REPORT DOCUMENTATION PAGE		Form Approved OMB NO. 0704-0188

1. REPORT DATE (DD-MM-YYYY) 30-09-2015	2. REPORT TYPE Final Report	3. DATES COVERED (From - To) 1-Jul-2014 - 30-Jun-2015

4. TITLE AND SUBTITLE	5a. CONTRACT NUMBER
Final Report: Research Area 4: Electronics: A Special Event at the International Conference on Molecular Beam Epitaxy	W911NF-14-1-0342
	5b. GRANT NUMBER
	5c. PROGRAM ELEMENT NUMBER 611102

6. AUTHORS	5d. PROJECT NUMBER
Yong-Hang Zhang	
	5e. TASK NUMBER
	5f. WORK UNIT NUMBER

7. PERFORMING ORGANIZATION NAMES AND ADDRESSES	8. PERFORMING ORGANIZATION REPORT NUMBER
Arizona State University ORSPA P.O. Box 876011 Tempe, AZ 85287 -6011	

9. SPONSORING/MONITORING AGENCY NAME(S) AND ADDRESS (ES)	10. SPONSOR/MONITOR'S ACRONYM(S) ARO
U.S. Army Research Office P.O. Box 12211 Research Triangle Park, NC 27709-2211	11. SPONSOR/MONITOR'S REPORT NUMBER(S) 65942-EL-CF.2

12. DISTRIBUTION AVAILIBILITY STATEMENT
Approved for Public Release; Distribution Unlimited

13. SUPPLEMENTARY NOTES
The views, opinions and/or findings contained in this report are those of the author(s) and should not contrued as an official Department of the Army position, policy or decision, unless so designated by other documentation.

14. ABSTRACT

The International Conference on Molecular Beam Epitaxy (Flagstaff, Arizona, September 7-12, 2014) provided an international forum for the latest research in the area of molecular beam epitaxy (MBE), including the fundamentals of MBE, the latest developments in III-V, II-VI, IV-VI, and IV semiconductors, oxides, nitrides, and wide gap materials, nanowires, quantum dots, spintronics, emerging materials, heterogeneous epitaxy, devices, and production MBE. The conference included 432 attendees from 24 countries and a contributed technical program

15. SUBJECT TERMS
molecular beam epitaxy, MBE, conference, crystal growth

16. SECURITY CLASSIFICATION OF:			17. LIMITATION OF ABSTRACT	15. NUMBER OF PAGES	19a. NAME OF RESPONSIBLE PERSON Yong-Hang Zhang
a. REPORT UU	b. ABSTRACT UU	c. THIS PAGE UU	UU		19b. TELEPHONE NUMBER 480-727-2795

Standard Form 298 (Rev 8/98)
Prescribed by ANSI Std. Z39.18

Report Title

Final Report: Research Area 4: Electronics: A Special Event at the International Conference on Molecular Beam Epitaxy

ABSTRACT

The International Conference on Molecular Beam Epitaxy (Flagstaff, Arizona, September 7-12, 2014) provided an international forum for the latest research in the area of molecular beam epitaxy (MBE), including the fundamentals of MBE, the latest developments in III-V, II-VI, IV-VI, and IV semiconductors, oxides, nitrides, and wide gap materials, nanowires, quantum dots, spintronics, emerging materials, heterogeneous epitaxy, devices, and production MBE. The conference included 432 attendees from 24 countries and a contributed technical program with 90 oral presentations and 143 poster presentations, with more than 60% of the contributed presentations given by students. The proceedings are published in the internationally renowned Journal of Crystal Growth, volume 425, pages 1-400 (2015). In addition, there were 3 plenary talks, 16 invited presentations, 26 vendor exhibits, and a one day special symposium "Meeting with MBE Pioneers" (Sunday, September 7, 2014) that vividly delivered the legendary history of some of the most prominent MBE pioneers, capturing their history and personal reflections during the development, evolution, and use of MBE. They shared their valuable experience with the community and most importantly with students and junior researchers.

Enter List of papers submitted or published that acknowledge ARO support from the start of the project to the date of this printing. List the papers, including journal references, in the following categories:

(a) Papers published in peer-reviewed journals (N/A for none)

<u>Received</u>   <u>Paper</u>

TOTAL:

Number of Papers published in peer-reviewed journals:

(b) Papers published in non-peer-reviewed journals (N/A for none)

<u>Received</u>   <u>Paper</u>

TOTAL:

Number of Papers published in non peer-reviewed journals:

(c) Presentations

Number of Presentations: 0.00

Non Peer-Reviewed Conference Proceeding publications (other than abstracts):

<u>Received</u>   <u>Paper</u>

TOTAL:

Number of Non Peer-Reviewed Conference Proceeding publications (other than abstracts):

Peer-Reviewed Conference Proceeding publications (other than abstracts):

<u>Received</u>   <u>Paper</u>

09/30/2015 1.00 Yong-Hang Zhang. The 18th International Conference on Molecular Beam Epitaxy (MBE 2014),
The International Conference on Molecular Beam Epitaxy (MBE 2014). 07-SEP-14, . : ,

TOTAL: **1**

Number of Peer-Reviewed Conference Proceeding publications (other than abstracts):

(d) Manuscripts

<u>Received</u>   <u>Paper</u>

TOTAL:

Number of Manuscripts:

Books

Received   Book

  TOTAL:

Received   Book Chapter

  TOTAL:

Patents Submitted

Patents Awarded

Awards

Graduate Students

NAME	PERCENT_SUPPORTED
FTE Equivalent:	
Total Number:	

Names of Post Doctorates

NAME	PERCENT_SUPPORTED
FTE Equivalent:	
Total Number:	

Names of Faculty Supported

NAME   PERCENT_SUPPORTED

FTE Equivalent:
Total Number:

Names of Under Graduate students supported

NAME   PERCENT_SUPPORTED

FTE Equivalent:
Total Number:

Student Metrics
This section only applies to graduating undergraduates supported by this agreement in this reporting period

The number of undergraduates funded by this agreement who graduated during this period: 0.00

The number of undergraduates funded by this agreement who graduated during this period with a degree in science, mathematics, engineering, or technology fields:...... 0.00

The number of undergraduates funded by your agreement who graduated during this period and will continue to pursue a graduate or Ph.D. degree in science, mathematics, engineering, or technology fields:...... 0.00

Number of graduating undergraduates who achieved a 3.5 GPA to 4.0 (4.0 max scale):...... 0.00

Number of graduating undergraduates funded by a DoD funded Center of Excellence grant for Education, Research and Engineering:...... 0.00

The number of undergraduates funded by your agreement who graduated during this period and intend to work for the Department of Defense 0.00

The number of undergraduates funded by your agreement who graduated during this period and will receive scholarships or fellowships for further studies in science, mathematics, engineering or technology fields:...... 0.00

Names of Personnel receiving masters degrees

NAME

Total Number:

Names of personnel receiving PHDs

NAME

Total Number:

Names of other research staff

NAME   PERCENT_SUPPORTED

FTE Equivalent:
Total Number:

Sub Contractors (DD882)

Inventions (DD882)

Scientific Progress

Technology Transfer

Editorial

Preface of the 18th International Conference on Molecular Beam Epitaxy (MBE 2014)

The first International Conference on Molecular Beam Epitaxy (IC-MBE) was held in Paris in 1978, chaired by Alfred Y. Cho. Every other year since, with the exception of a four-year break after the initial meeting, the IC-MBE has been held in European, Asian, and North American venues. The 18th and latest IC-MBE was held in Flagstaff, Arizona, USA, September 7–12, 2014, and was chaired by Yong-Hang Zhang (Arizona State University). MBE is an advanced crystal growth method that benefits areas from the study of fundamental physics, all the way through the production of devices used in countless fields. IC-MBE brings together researchers from all over the world, and is the premier forum for scientific and technological exchange among researchers investigating all types of materials growth using the MBE technique.

The 18th IC-MBE included 432 attendees from 24 countries. The technical program featured 90 oral presentations in three parallel sessions, as well as 143 poster presentations. Importantly, more than 60% of the presentations were given by students, which affords great confidence for the future of MBE. In addition to the contributed work, there were 16 invited presentations and three plenary talks. Ted Moustakas (Boston University, USA) spoke on the fundamental differences between cubic III–V compounds and wurtzite nitride semiconductors produced by MBE. Tomasz Wojtowicz (Polish Academy of Sciences) described the MBE growth of II–VI dilute magnetic semiconductor nanostructures for spintronic research. Qi-Kun Xue (Tsinghua University, China) explained the role of MBE in the study of topological insulators and high temperature superconductivity. These plenary sessions were extremely well-attended and well-received.

IC-MBE 2014 included a special Sunday event, *Meeting with MBE Pioneers,* which captured the history of the development of MBE and the personal reflections of researchers integral to the

evolution of the technology and its use. Ray Tsu gave the session's keynote speech on *The Birth of Semiconductor Superlattices*. Other highlights during the week included a conference excursion to Sunset Crater and the Wupatki National Monuments, and a conference banquet showcasing a variety of entertainment from the Southwest region of the United States.

In this special issue of the Journal of Crystal Growth, we have collected 91 papers associated with presentations at the 18th IC-MBE held in Flagstaff, Arizona. The papers in this issue reflect the breadth of the meeting, demonstrating continued progress in MBE fundamentals, elemental and compound semiconductors, oxides and novel materials, nanostructured materials, and devices. This issue provides a valuable snapshot of the state of the field of MBE during this time, and will help to enable future success in MBE-related research.

Finally, we wish to thank everyone who helped to make the 18th IC-MBE a success, including the Conference Chair and Organizing Committee, the Program Committee for assembling stimulating technical sessions, the authors and reviewers who contributed to this issue, all of the companies and organizations that contributed financial resources, as well as Naveen J. Raja, Yanli Gao, and Xiaolin Li at Elsevier who were instrumental in creating the final record. We look forward to seeing you at the next IC-MBE Conference in 2016 in Montpellier, France, which will be chaired by Eric Tournie.

Guest Editors
April S. Brown, Aaron J. Ptak
United States
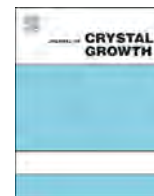
Determination of N-/Ga-rich growth conditions, using in-situ auger electron spectroscopy

S.P. Svensson [a,*], W.L. Sarney [a], K.M. Yu [b,c], M. Ting [b,d], W.L. Calley [e], S.V. Novikov [f], C.T. Foxon [f], W. Walukiewicz [b]

[a] US Army Research Laboratory, 2800 Powder Mill Rd., Adelphi, MD 20783, USA
[b] Materials Sciences Division, Lawrence Berkeley National Laboratory, Berkeley, CA 94720, USA
[c] Department of Physics and Materials Science, City University of Hong Kong, Kowloon, Hong Kong
[d] Department of Mechanical Engineering, University of California, Berkeley, CA 94720, USA
[e] Staib Instruments, Inc., 101 Stafford Court, Williamsburg, VA 23185, USA
[f] School of Physics and Astronomy, University of Nottingham, Nottingham, NG7 2RD, UK

ABSTRACT

In-situ Auger electron spectroscopy was used to determine the 1:1 flux ratios of Ga and N during growth of GaN by molecular beam epitaxy at low substrate temperatures. By linearly ramping the Ga-flux, while keeping the N-flux constant, and simultaneously measuring the chemical composition by monitoring N and Ga Auger peaks, the time of deviation from stoichiometry could be determined. The method was applied at very low substrate temperatures where reflection high-energy electron diffraction does not reveal clear growth mode changes. The importance of the N- vs Ga-rich conditions were confirmed with transmission electron microscopy which showed a distinct change in crystallinity between material at the top and bottom of the film, which are in agreement with previous findings.

Published by Elsevier B.V.

1. Introduction

Conventional III–V molecular beam epitaxy (MBE) growth is typically performed under group-V rich conditions. It has been known for some time that state-of-the-art GaN grown by plasma-assisted MBE requires slightly Ga-rich conditions [1] at very high substrate temperatures ($\sim$700–800 °C). Early work [1] asserted that N-rich conditions led to three-dimensional, columnar growth and low electron mobilities [2]. Some research has concluded that growth must be done with the fluxes set to obtain films as close to the stoichiometric condition as possible [3], while others maintain that it must be done in the 'intermediate range' (Ga-rich but just short of droplet formation) [4,5]. In any case the window for obtaining Ga rich films without inducing Ga droplet formation is small, and precise determination of the 1:1 condition is important.

For Ga-rich conditions, the GaN (0001) surface is terminated by approximately one bilayer of Ga atoms [6–8], which results in a smoother morphology than found in films grown under N rich conditions [9,10]. Feenstra et al., explains in detail the mechanisms of the N-rich and Ga-rich growth modes, and also discusses that

while the Ga-rich conditions lead to smoother films, there is a cost to be paid in terms of Ga-droplet formation and leakage current induced by Ga-filled threading dislocation cores [9].

We have been investigating highly mismatched alloys (HMAs) that consist of various amounts of Sb [11,12] and As [13] incorporated in GaN for solar water splitting applications. The bandgap of these materials is drastically reduced for even very small amounts of Sb and As, and the absorption seems to be unaffected by the film's crystallinity or lack thereof. 'Low temperature' growth of GaN onto sapphire or SiC substrates typically refers to temperatures that are as high as 700 °C. Our samples are grown at extremely low temperature, as low as 80 °C, and more recently, at $\sim$300 °C. The initial low temperatures were initially chosen in order to avoid phase segregation, and to demonstrate that films with the desired bandgap properties could be grown on 'cheap' substrates such as glass. We are experimenting with higher temperatures to see if Sb can still be incorporated, and because it is likely that higher crystalline quality is desirable for device applications.

Although we were aware of no comparative studies of Ga vs N rich films grown at these extreme low temperature regimes, or for polycrystalline and amorphous films, it made sense to start with Ga-rich conditions given the prior research. Also, others had noted that the sensitivity to the V/III ratio is even more pronounced for low temperature growth. Heying et al., found that for 'low-T' MBE

* Corresponding author. Tel.: +1 301 394 0605.
E-mail address: stefan.p.svensson.civ@mail.mil (S.P. Svensson).

($\sim$720 °C) grown GaN, impurity incorporation, point defect densities, and electrical properties were extremely sensitive to the Ga/N flux ratio, with slightly Ga-rich conditions being favorable [14].

Surprisingly, we found that it was not possible to change the bandgap with increasing Sb-concentration for Ga-rich conditions [12]. Instead, the bandgap appeared to be dominated by a defect state. However, by switching to N-rich conditions, the bandgap was observed to change and roughly followed the predictions of the band-anti-crossing model [15].

These examples illustrate that determining the critical conditions where the growth changes from N- to Ga-rich is very important, even for non-single crystalline films grown under non-ideal conditions. For MBE growth of III–V materials, the flux ratios from the group III and V elements can be measured by an in situ beam flux monitor and the fluxes for stoichiometric growth can be determined using reflection high-energy electron diffraction (RHEED) oscillations on a single sample. However, in the case of plasma assisted nitride growth, the active N-content in the beam from a nitrogen RF plasma source is usually not known and RHEED oscillations are not observed. For conventional GaN growth the typical procedure for determining the critical Ga-flux is therefore to fix the N-flow while increasing the Ga-flux. Under these conditions it may be possible to observe a change in the RHEED pattern on a single sample, but more typically a series of films are produced and the growth rate is determined. Ga-rich conditions are established when the growth rate as a function of Ga-flux ceases to increase. For highly mismatched alloy (HMA) growth [12,15] this would be the only method available since the RHEED pattern does not exhibit a clear transition.

2. Experiment

The GaN films were grown on (0001)-oriented 2-inch double-side polished and uncoated, sapphire substrates by plasma-assisted MBE in a GENII system. We are primarily interested in growth on sapphire substrates, therefore those samples comprise most of the data and analysis discussed in this paper. The system has a Uni-bulb plasma source operated at 400 W with a flow rate of 0.58 sccm to provide active nitrogen, and elemental Ga was used as the other source. The absolute Ga fluxes were determined from growth rate characterization by RHEED oscillations of GaSb on GaSb. The N-flow was fixed to generate a steady-state background chamber pressure of 1.5×10^{-5} Torr, while the Ga source was set up to generate a linear flux ramp from 9.8×10^{16} to 3.9×10^{18} at/(m^2 s) over two hours. (The relationship between flux and cell temperature had been determined previously). The substrate temperature was set by the thermocouple and held at 325 °C. No attempt was made to relate this to the real temperature of the sapphire.

During the Ga ramp the Auger electron signals for N (KLL, 385 eV), and Ga (LMM, 1065 eV) were repeatedly recorded in the growth position using a *STAIB Auger Probe* [16]. The repetition rate was chosen to capture enough detail of the dynamic events but not optimized. The RHEED gun, operated at 12 kV and an emission current of $\sim$1.5 mA, is used to excite Auger electrons, and the electron detector/analyzer is located in a source port. Alignment was done on a separate very small sample centered on a In-bonded block. To ensure stable signals the sample was not azimuthally rotated during the deposition. This is irrelevant to the results since the physical center of the wafer is probed where the growth conditions represent the average of any off-center points when the sample is grown with azimuthal rotation.

3. Results and discussion

Typical Auger signal dynamics are shown in Fig. 1. As expected, both the Ga and N Auger electron signals initially increase as a GaN
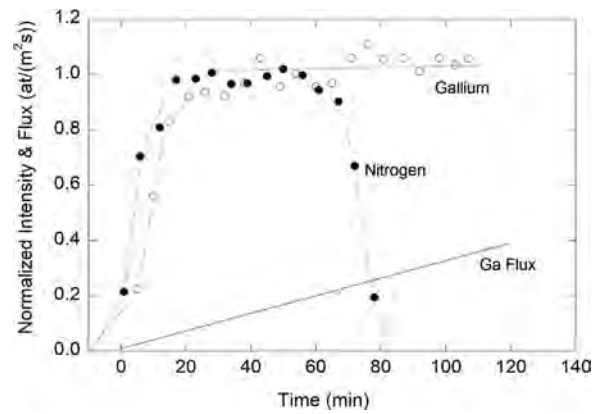
Fig. 1. Typical Auger electron signals from Ga and N recorded as a function of time, while linearly increasing the Ga flux. The broken lines are guides to the eye.
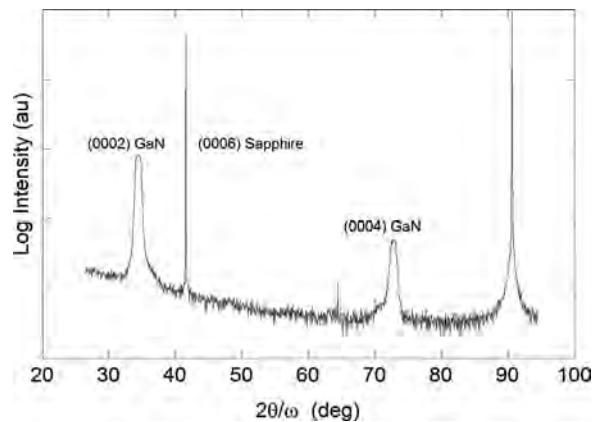
Fig. 2. 2θ-ω XRD scan of GaN film grown under an increasing Ga flux ramp.

film starts to form under N-rich conditions and reach a steady-state after $\sim$10 min. The increase is due to the electron escape depth exceeding the film thickness. At the start there is a time shift between N and Ga signals due to the sequential sampling of the two signals. In this experiment the N-signal started decreasing at about 65 min, which we define as the boundary between N- and Ga-rich conditions. The Ga-flux at this point was 2.5×10^{18} at/(m^2 s). The decrease is accompanied by a slight increase in the Ga-signal due to formation of Ga-droplets that cover the underlying GaN and prevent the Auger electrons from N to reach the surface.

GaN on sapphire grown under Ga and N rich conditions at 325 °C is polycrystalline, with a tendency to align along the (0002) growth plane. Fig. 2 shows the 2θ-ω x-ray scan for the sample grown under the ramped Ga flux. The two strong and sharp peaks correspond to the (0006) and (0012) sapphire planes. The two broader peaks correspond to the (0002) and (0004) GaN planes. The sample grown on Si had only a faint (0002) GaN peak and appeared to be primarily amorphous.

Rutherford backscattering depth profiles were collected, and the films were found to be stoichiometric throughout the thickness. Absorption measurements on the GaN film grown on sapphire indicate a bandgap of 3.25 eV.

Cross sectional transmission electron microscopy (TEM) of the GaN/sapphire sample grown in the N-rich growth region is shown in Fig. 3. Consistent with the XRD result, the film is polycrystalline with many regions strongly aligned with the sapphire substrate. Prior studies have shown that both Ga and N rich films grown at these low temperatures are columnar with the column boundaries lying along the growth direction [12]. Fig. 4 is a cross sectional TEM image of the Ga-rich growth region. The columnar structure seems
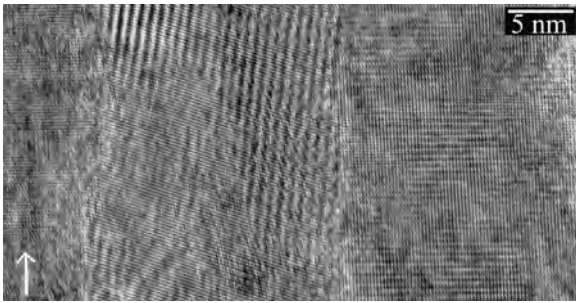
Fig. 3. N-rich region of GaN film grown under increasing Ga flux ramp. The arrow denotes the (0006) direction of the substrate (which is not shown in this image).
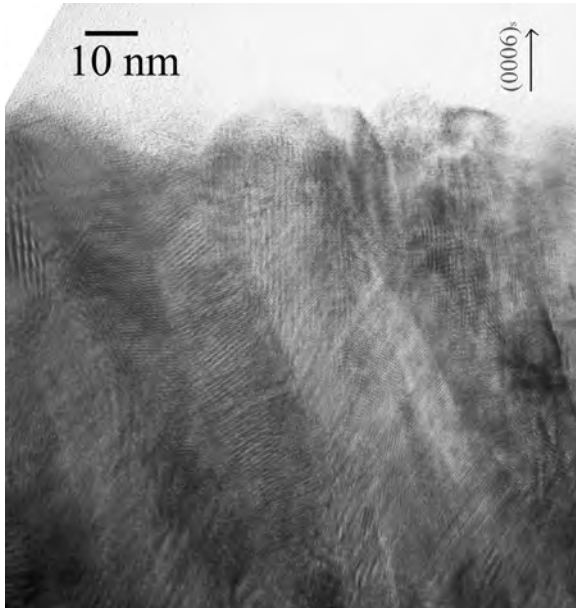
Fig. 4. Ga-rich region of GaN film grown under increasing Ga flux ramp. The arrow denotes the (0006) direction of the substrate (which is not shown in this image).

to rotate by approximately 30°. The polycrystalline nature of the diffraction pattern is the same throughout all regions of the film. We have not seen inclined columns in Ga rich films grown directly onto sapphire substrates in previous studies, so this feature may be related to the ramping of the Ga cell temperature.

Once the 1:1 Ga-N flux was determined, we grew bulk GaN and a series of GaNSb films on sapphire with the Ga flux fixed at 2.35×10^{18} at/(m^2 s). This Ga flux value should be just inside the N-rich region, but we do not want to be excessively N rich given that we find such conditions will increase the surface roughness [12]. The same substrate temperature of 325 °C was used, and Sb-flux ranged from 0 to 7.82×10^{18} at/(m^2 s). These conditions resulted in films that ranged in Sb composition from 0 to 16%. We found that the bandgap continuously shifted from 3.3 eV to 1.6 eV over this composition range. The shifting bandgap with Sb composition further indicates that we successfully identified the N-rich growth condition with the Auger probe.

4. Conclusion

It is important to define the growth parameters that result in N-rich/Ga-rich condition for GaN based alloys. We have used an in situ Staib Auger Probe to determine the boundary between Ga and N rich growth conditions of GaN grown on sapphire substrates by ramping the Ga source until the N signal dropped off. We then grew bulk GaN and GaNSb highly mismatched alloys under the growth conditions determined by the ramping experiment, and found that the resulting films had the desired properties of N-rich growths.

The 1:1 Ga/N flux ratio can now be determined within approximately 2 h for each substrate temperature. The exploration of ideal growth conditions for HMA materials as well as for conventional GaN growths can be significantly sped up this way with noticeable savings in time and substrate costs.

References

[1] R.J. Molnar, T.D. Moustakas, Growth of GaN by electronc-cyclotron resonance plasma-assisted molecular beam epitaxy:The role of the charged species, J. Appl. Phys. 76 (1994) 4587.

[2] A. Botchkarev, A. Salvador, B. Sverdlov, J. Myoung, H. Morkoc, Properties of GaN films grown under Ga and N rich conditions with plasma enhanced molecular beam epitaxy, J. Appl. Phys. 77 (1995) 4455.

[3] N. Grandjean, M. Leroux, J. Massies, M. Mesrine, M. Laugt, Molecular beam epitaxy of GaN under N-rich conditions using NH_3, Jpn. J. Appl. Phys. 38 (1999) 618.

[4] A.V. Sampath, G.A. Garrett, C.J. Collins, et al., Effect of Ga- rich growth conditions on the optical properties of GaN films grown by plasma-assisted molecular beam epitaxy, J. Vac. Sci. Technol. B 22 (2004) 1487.

[5] V. Ramachandran, R.M. Feenstra, W.L. Sarney, L. Salamanca-Riba, D.W. Greve, Optimized structural properties of wurtzite GaN on SiC(0001) grown by molecular beam epitaxy, J. Vac. Sci. Technol. A 18 (2000) 1915.

[6] A.R. Smith, R.M. Feenstra, D.W. Greve, M.-S. Shin, M. Skowronski, J. Neugebauer, J. Northrup, Reconstructions of GaN (0001) and (0001⁻) surfaces, J. Vac. Sci. Technol. B 16 (1998) 2242.

[7] C. Adelmann, J. Brault, G. Mula, B. Daudin, L. Lymperakis, J. Neugebauer, Ga adsorption on (0001) surfaces, Phys. Rev. B 67 (2003) 165419.

[8] G. Koblmüller, R. Averbeck, H. Riechert, P. Pongratz, Direct observation of different equilibrium Ga adlayer coverages and their desorption kinetics on GaN(0001) and (0001⁻) surfaces, Phys. Rev. B 69 (2004) 035325.

[9] R.M. Feenstra, Y. Dong, C.D. Lee, J.E. Northrup, Recent developments in surface sciences of GaN and AlN, J. Vac. Sci. Technol. B 23 (2005) 1174.

[10] B. Heying, R. Averbeck, L.F. Chen, E. Haus, H. Riechert, J.S. Speck, Control of GaN surface morphologies using plasma-assisted molecular beam epitaxy, J. Appl. Phys. 88 (2000) 1855.

[11] K.M. Yu, S.V. Novikov, M. Ting, W.L. Sarney, S.P. Svensson, M. Shaw, R.W. Martin, W. Walukiewicz, C.T. Foxon, Growth and characterization of highly mismatched $GaN_{1-x}Sb_x$ alloys, J. Appl. Phys. 116 (2014) 123704.

[12] W.L. Sarney, S.P. Svensson, S.V. Novikov, W. Walukiewicz, C.T. Foxon, $GaN_{1-x}Sb_x$ highly mismatched alloys grown by low temperature molecular beam epitaxy under Ga rich conditions, J. Cryst. Growth 383 (2013) 95.

[13] K.M. Yu, S.V. Novikov, R. Broesler, I.N. Demchenko, J.D. Denlinger, Z. Liliental-Weber, F. Luckert, R.W. Martin, W. Walukiewicz, C.T. Foxon, Highly mismatched crystalline and amorphous $GaN_{1-x}As_x$ alloys in the whole composition range, J. Appl. Phys. 106 (2009) 103709.

[14] B. Heying, I. Smorchkova, C. Poblenz, C. Elsass, P. Fini, S. DenBaars, U. Mishra, J.S. Speck, Optimization of the surface morphologies and electron mobilities in GaN grown by plasma-assisted molecular beam epitaxy, Appl. Phys. Lett. 77 (2000) 2885.

[15] K.M. Yu, W.L. Sarney, S.V. Novikov, D. Detert, R. Zhao, J.D. Denlinger, S.P. Svensson, O.D. Dubon, W. Walukiewicz, C.T. Foxon, Highly mismatched N-rich GaNSb films grown by low temperature molecular beam epitaxy, Appl. Phys. Lett. 102 (2013) 102104.

[16] Philippe G. Staib, In situ real time Auger analyses during oxides and alloy growth using a new spectrometer design, J. Vac. Sci. Technol. B 29 (2011) 03C125.

CrossMark
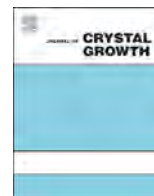
Desorption mass spectrometry: Revisiting the in-situ calibration technique for mixed group-V alloy MBE growth of ∼3.3 μm diode lasers

Ron Kaspi *, Chunte Lu, Chi Yang, Timothy C. Newell, Sanh Luong

Air Force Research Laboratory, Directed Energy Directorate, AFRL/RDLTD, 3550 Aberdeen Ave. Kirtland AFB, Albuquerque, NM 87117 USA

ARTICLE INFO

ABSTRACT

We apply the desorption mass spectrometry (DMS) technique and analyze the desorbed Sb species in-situ during MBE growth of mixed As/Sb heterostructures. We demonstrate how DMS is useful in pre-growth calibration of the V/III ratio, the group-III ratio, as well as the Sb-content in quaternary or quinary mixed As/Sb alloys. We also apply DMS to the digital alloy growth method. For demonstration purposes, we start with an un-calibrated MBE system, use the DMS technique to calibrate all of the previously undetermined MBE parameters and grow a ∼3.3 μm diode laser heterostructure in only one attempt. The results demonstrate that the DMS technique will allow the MBE to quickly converge toward a set of acceptable growth parameters without the need for ex-situ calibration of alloy composition.

Published by Elsevier B.V.

1. Introduction

Epitaxial growth of mixed group-V alloys such as $Al_xGa_{1-x}As_{1-y}Sb_y$ and $In_xGa_{1-x}As_{1-y}Sb_y$ are commonly employed in GaSb-based heterostructures. Achieving the desired composition in such alloys is complicated by the fact that, under typical MBE growth conditions, the sticking coefficients for the group-V fluxes are less than unity. As a result, the group-V beams compete with each other to determine the As/Sb content "y" in these alloys. This competition may be sensitive to the absolute value of each group-V flux, the ratio of the group-V fluxes, the substrate temperature and the alloy growth rate. There are many studies that have been conducted to illustrate the trend of compositional variation in the mixed group-V alloy as a function of one or more of these factors [1–3].

For the MBE practitioner, the group-III content "x" in the alloy can be predicted by routine in-situ RHEED oscillation measurements prior to growth. In contrast, there is no in-situ sensing technique that is sufficiently well developed to predict the group-V content "y" in these alloys. Consequently, ex-situ characterization such as x-ray diffraction measurements performed on representative samples is prescribed. However this is generally less accurate due to two main factors: (1) x-ray diffraction cannot uniquely determine composition in quaternary alloys, thus any uncertainty in the value of "x" will also cause uncertainty in the

determination of "y", and (2) Not all of the MBE parameters that influence "y" may be precisely duplicated and/or adjusted for growth after ex-situ characterization. An in-situ determination of "y", if it can eliminate the need for ex-situ characterization, can be very valuable in growing GaSb-based heterostructures with the 6.1 Angstrom family of ternary, quaternary and quinary mixed As/Sb alloys.

One method to determine y in $III\text{-}As_{1-y}Sb_y$ alloys during MBE was demonstrated nearly two decades ago, using a quadrupole mass spectrometer as the in-situ sensor [4]. It was shown that positioning a quadrupole mass spectrometer in line-of-sight of the substrate to monitor the desorbed antimony species, it is possible to quantify the rate of incorporation of antimony during mixed As/Sb alloy growth.

Historically, mass spectrometry techniques have played an important role in understanding some of the dynamics of the surface chemistry during III–V MBE growth. At various times and under various names, mass spectrometry techniques have been used to monitor surface dynamics [5–11], monitor sub-surface dynamics [12,13], and provide calibration and control [4,14,15]. These techniques are not widely used, partly due to lack of dedicated instrumentation and software, partly due to scarcity of ports in MBE reactors, and partly due to limited awareness of its range of usefulness.

In this paper, we revisit the desorption mass spectrometry (DMS) technique to demonstrate its usefulness in the growth of a multi quantum well diode laser emitting near 3.3 μm, containing strained $In_xGa_{1-x}As_{1-y}Sb_y$ quantum wells, lattice-matched

* Corresponding author. Tel.: +1 5058465879.
 E-mail address: ron.kaspi@us.af.mil (R. Kaspi).

$Al_zIn_xGa_{1-x-z}As_{1-y}Sb_y$ quinary barriers, and $Al_xGa_{1-x}As_{1-y}Sb_y$ quaternary alloy clad layers. We report the results of this growth, attempted without a-prior knowledge of fluxes and without any ex-situ testing. In the process, we also demonstrate how the DMS technique can be used to determine the mixed As/Sb alloy composition during "digital alloy growth" where a short period super-lattice is deposited to emulate that alloy.

2. Predicting conventionally grown alloy composition

A common inexpensive quadrupole mass spectrometer (Stanford Research 1–200 amu) is mounted facing the substrate at the central port of the bottom flange in a V-90 MBE system equipped to grow GaSb-based heterostructures. A copper gasket with a 3 mm diameter hole is positioned in front of the ionizing region in order to limit the line-of-sight to within the 2-in. diameter wafer.

The mass/charge of 121 amu/e signal from the mass spectrometer was previously shown to be insensitive to the partitioning (cracking and/or recombination) of the desorbed group-V species across a wide (320–740 °C) wafer temperature range [4]. We therefore assume that the 121 amu/e signal indicates a value that is proportional to the total rate of antimony desorption from the wafer surface in real-time. We conduct all DMS calibrations using a 2-in. diameter GaAs test wafer, although any wafer that ensures stoichiometric growth can be used. In Fig. 1, a typical time evolution of the 121 signal during composition calibration for a conventionally grown $Al_xGa_{1-x}As_{1-y}Sb_y$ is shown. At time < 200 s, first the gallium shutter then the aluminum shutter is opened resulting in a corresponding decrease (increase) in the rate of antimony desorption (incorporation) from the wafer surface. Due to the deposition of the stoichiometric compound, we have a direct way to quantify "x" in this alloy as $B/(A+B)$ where A is the antimony consumption rate during GaSb, and B is the additional antimony consumption rate during $Al_xGa_{1-x}Sb$. While composition can be determined in this manner, the growth rate cannot. In order to determine the growth rate, at least one of the group-III rates must be known, and act as the anchor to the rest of the calibrations. For example, if the anchoring flux were Ga with κ Monolayers (ML)/s on GaSb, then the Al flux would be $\kappa B/A$ ML/s and the alloy growth rate would be $\kappa + \kappa B/A$ ML/s on GaSb.

Note that the requirement for stoichiometric growth is satisfied even when the crystalline quality and surface smoothness of the deposited layer is not optimized. Consequently, the DMS calibration
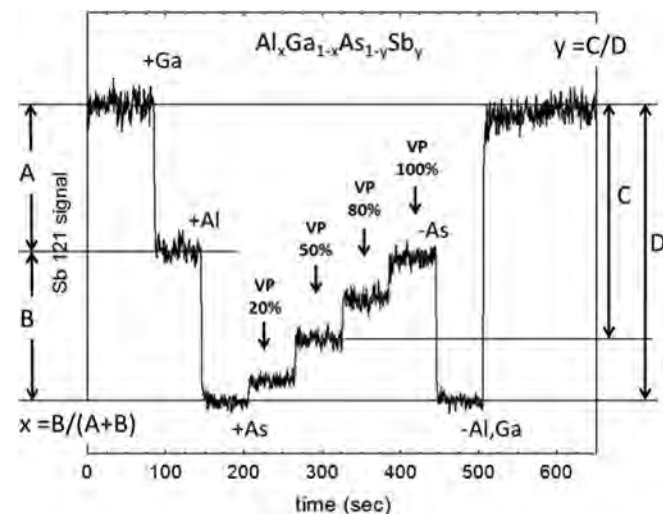
wafer, which in this case is largely mismatched GaAs, can be used and re-used many times without the worry of maintaining the near lattice-matched and layer-by-layer conditions that would be required for RHEED. Note also that the state of strain or relaxation in the DMS test layer can be ignored because the antimony consumption is measured relative to the anchoring Ga flux which remains fixed.

In the example shown in Fig. 1, arsenic is introduced to the growth at time > 200 s. Four different As cracker valve positions (As VP=20%, 50%, 80%, and 100%) are shown where each increasing level of As flux corresponds to an increased (decreased) rate of antimony desorption (incorporation). In this case, y(As VP) is computed as C/D, where C is the antimony consumption rate for a given As VP, and D is the maximum antimony consumption rate without arsenic. For added clarity, it is important to note that in this example, $D=A+B$. It is easy to see that this in-situ calibration procedure can be applied generally to all As/Sb alloys.

3. Predicting digital alloy composition

The digital alloy technique to grow quaternary and quinary mixed group-V alloys is gaining popularity because it provides several advantages [16–18]. These include the ability to grade the alloy composition, as well as the ability to make rapid compositional changes in the alloy without changing the effusion cell temperatures. The assumption is that when digitization is made with a small enough period (typically 4–8 monolayers) the alloy properties are largely unaffected.

In this work, we build toward the growth of a ~ 3.3 μm diode laser heterostructure which employs a quinary barrier with a nominal composition of $Al_{0.20}In_{0.25}Ga_{0.55}As_{0.25}Sb_{0.75}$. In doing so, we demonstrate how the DMS technique can be used to calibrate for this composition. The digital alloy growth for this alloy can be set up in many ways. In our case, the period consists of the GaSb/AlSb/InAsSb/InAs sequence. We choose to adjust the Arsenic cracker valve position, As-VP to reach the desired composition.

The DMS calibration of this quinary alloy is performed using a sequence shown in Fig. 2. Four sets of the digital alloy, each using a different As-VP is grown sequentially while the 121 amu/e signal is recorded as a function of time. Two anchoring values must also be determined before making a quantitative assessment of the digital alloy composition. The first is the maximum rate of antimony desorption, measured during periods of no growth; i.e. static surface. The other is the zero value of the 121 amu/e signal recorded when the antimony shutter is closed both at the start and at the end of the sequence. Fig. 2 shows a DMS calibration

Fig. 1. Typical sequence of DMS 121 data used to determine quaternary alloy composition. A is the antimony consumption rate due to Ga, B is the consumption rate due to Al. C is the Sb consumption rate for a given As-VP, and D is the maximum Sb consumption rate when $y=1$.
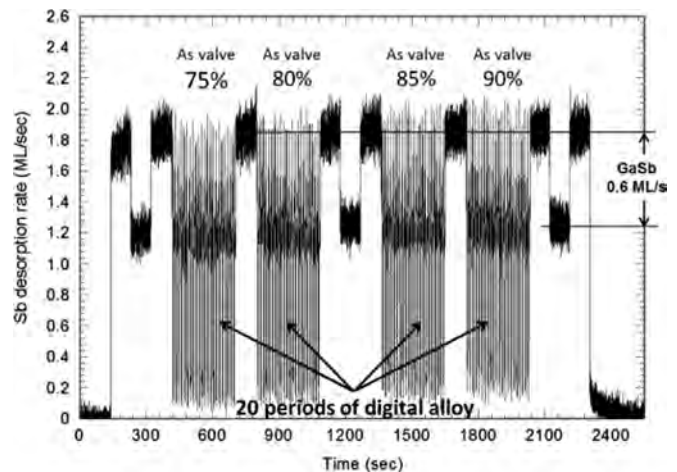
Fig. 2. Typical DMS sequence for calibrating digital alloy growth. Four consecutive growths of 20 periods, each with a different As-VP are shown. The desorption rate axis is calibrated using the known value of GaSb growth rate.
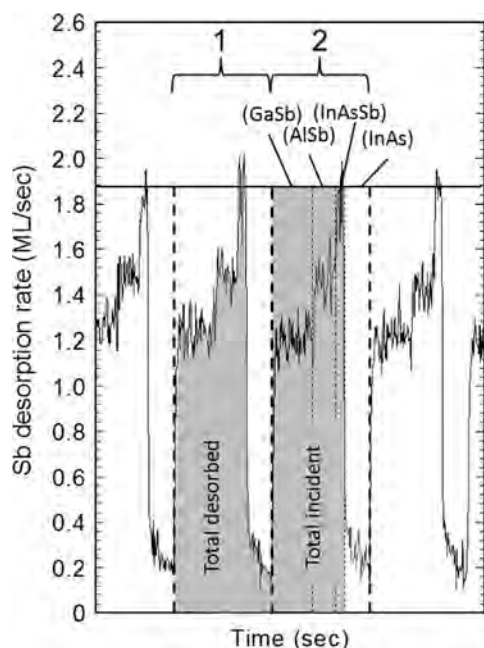
Fig. 3. A closer view of the desorption data during digital alloy. The total amount of Sb incident on the wafer, and the total amount of Sb desorbed during one period is given by the highlighted areas.
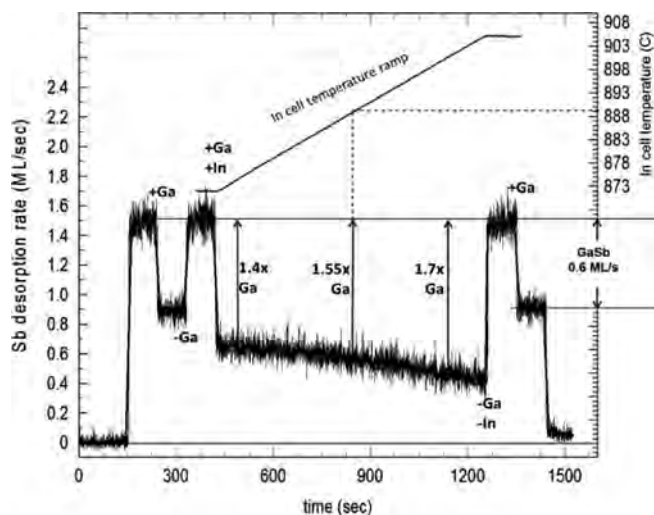
Fig. 4. DMS used to determine In cell temperature that produces 0.33 ML/s of In deposition rate using a known Ga-flux as the anchor.

sequence where 20 period of the digital alloy period is grown using an As-VP value of 75%, 80%, 85%, and 90%.

The prediction of the Sb-content y in the quinary alloy is made by quantifying the amount of Sb that is incorporated into each period. This is determined by subtracting the amount of Sb desorbed from the surface from the amount of Sb incident during one period. A close look at desorption data during digital alloy growth reveals how this can be done. In Fig. 3, two adjacent periods of the digital alloy are marked for the purpose of identification. In the first period, the total amount of desorbed Sb is shown as the gray area under the desorption curve. In contrast, the total amount of incident antimony is shown as the gray area in the second period. Note that the upper bound of this area is the maximum desorption rate during the static surface. To reduce measurement error, it is advised to compare these areas after the growth of a number of periods. The average Sb-content "y" is then calculated by computing the total amount of Sb incorporated over a number of digital alloy

periods divided by the total number of monolayers deposited. When an anchoring group-III flux is used, such as 0.6 ML/s of Ga in our case, then the y-axis is scaled to units of ML/s for this computation.

4. Growth of ~3.3 μm diode laser using DMS

Growth of > 3 μm diode lasers is difficult due to the diminishing valence band offset with the InGaAsSb quantum well and the AlGaAsSb barrier. Recently, it was shown that the quinary $Al_zIn_xGa_{1-x-z}As_{1-y}Sb_y$ alloy can provide sufficient valence band offset to allow room temperature lasing at 3.3 μm and beyond [19,20]. In a demonstration of the DMS technique, we chose to grow such a laser structure in one attempt, with only a prior knowledge of the Ga cell temperature for 0.6 ML/s to which all DMS calibrations can be anchored.

The laser heterostructure was designed to have a 2 μm thick top and bottom digitally grown $Al_{0.9}Ga_{0.10}As_{0.07}Sb_{0.93}$ clad layers, surrounding a 600 nm-thick digitally grown quinary $Al_{0.20}In_{0.25}Ga_{0.55}As_{0.25}Sb_{0.75}$ waveguide. At the center of the waveguide, three 10 nm-thick compressively strained $In_{0.52}Ga_{0.48}As_{0.24}Sb_{0.76}$ quantum wells were used. Dopant calibrations were also assumed to yield a Te-doped bottom clad with $n \sim 4 \times 10^{17}$/cm^3, and a Be-doped clad with $p \sim 1 \times 10^{18}$/cm^3.

Based on the growth plan, DMS was used to generate the required fluxes and As-VP prior to growth using the same GaAs test wafer. Following the procedures described above, using the 0.6 ML/s of Ga flux as the anchor, the Sb cracker valve position that gave a Sb/Ga ratio of ~3 was selected. The remaining group-III cell temperatures to produce indium flux of 0.33 ML/s, Al flux of 0.4 ML/s (waveguide) and a second Al flux of 0.8 ML/s (clads) were determined using DMS.

As an example, calibration of the indium cell temperature is shown in Fig. 4. Here we begin with the premise when both In and Ga are incident on the wafer, the Sb consumption rate should be a factor of $(0.6 + 0.33)/(0.6) = 1.55$ higher than the case when only Ga is present. We therefore start with an indium cell temperature that is too low, and monitor the Sb consumption rate while slowly raising the cell temperature. It is evident from the data that the correct rate of total Sb consumption rate is reached when the indium cell base temperature is ~889 °C. Time evolution of the Sb desorption rate in a similar manner was used to generate the Al cell base temperatures that give 0.4 ML/s and 0.8 ML/s.

DMS was then used to determine the As-VP necessary to attain the lattice-matched composition for the digitally grown alloys. Following the general procedure described in Section 3, and the specific example given for the desired $Al_{0.20}In_{0.25}Ga_{0.55}As_{0.25}Sb_{0.75}$ quinary alloy, it is possible to generate a plot of the Sb-content y as a function of As-VP, as shown in Fig. 5. For $y \sim 0.75$, an As-VP of 81% was selected to be necessary at the desired growth temperature. In a similar manner, the As-VP was determined to be 70% for the lattice-matched quaternary clad layers, and 95% for the strained quantum wells.

At this point, all cell temperatures and cracker valve positions are calibrated for the growth of the laser heterostructure, which is grown immediately following the DMS calibrations. The structural characterization is conducted using high resolution x-ray diffraction, and the (004) omega/2theta reflectivity is shown in Fig. 6. The central peak contains reflections from the GaSb substrate, both clad layers and the waveguide. The lattice mismatch is not evident on this scale, and is therefore well within acceptable limits. The envelope originating from the compressed quantum wells is clearly seen. Also, two pairs of satellite peaks ($+1$ and -1) are present; the inner pair originating from the waveguide alloy with a 6 ML periodicity, and the outer pair originating from the clad layers with a 5 ML periodicity. The small difference in the periodicity was deliberately designed to identify the 0th order of the corresponding layers.
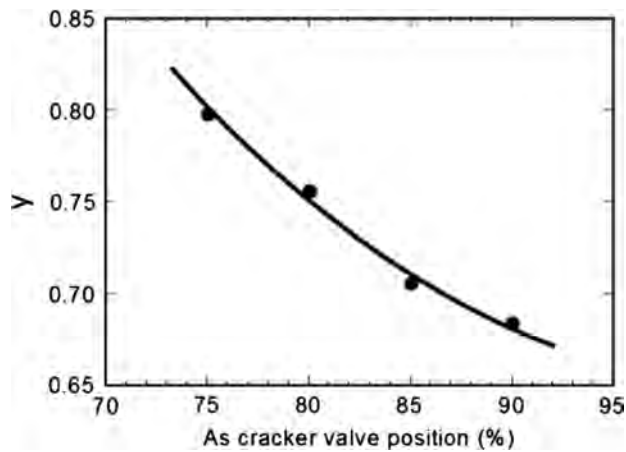
Fig. 5. Variation of y in the $Al_{0.20}In_{0.25}Ga_{0.55}As_{1-y}S_y$ alloy as a function of As-VP, calculated using the DMS data collected during digital alloy growth.
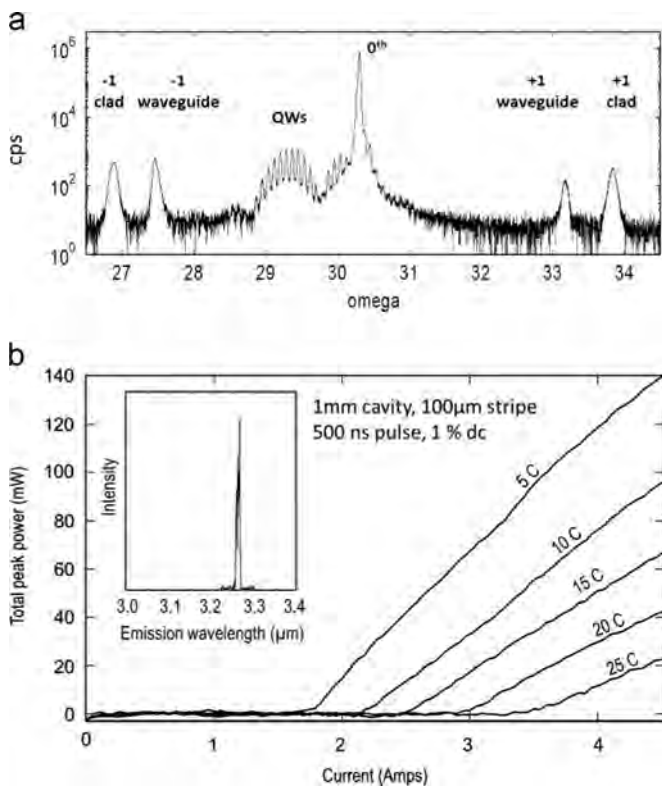
Fig. 6. Characterization of laser diode grown using DMS. (a) Omega/2theta (004) XRD diffraction spectrum. (b) LI curves at various temperatures. Emission spectrum is shown in the inset.

Lasing devices were fabricated from this demonstration wafer and tested using pulsed conditions in the epi-up configuration as a function of temperature. LI curves generated from a typical $100\,\mu m \times 1\,mm$ cavity device, as well as the wavelength spectrum, are shown in Fig. 6. At a 1% duty cycle, the total peak power was measured to be ~ 42 mW at 20 °C and ~ 140 mW at 5 °C. These device results show respectable, and constitute a fine baseline for further optimization. This demonstration shows that the DMS technique will allow the MBE to quickly converge toward a set of acceptable growth parameters without the need for ex-situ calibration.

5. Discussion and summary

The demonstration of the DMS technique presented in this paper lacks an adequate evaluation of precision and reproducibility due to lack of a sufficient sample size. To do this requires repeated growths, and even growths using different MBE tools and different DMS configurations. Rather than claiming precision, we merely want to demonstrate the plausibility, and describe the procedures used.

In terms of the accuracy of the DMS technique, note that the desorption signature is somewhat noisy. In this work, we simply smooth the data prior to analysis. In addition, a small drift may occur in the mass spectrometer signal during data collection. Both of these factors are strongly influenced by the quadrupole system, its ionizing chamber and its electronics. Making only relative measurements, and providing periodic measurements as reference, help alleviate the influence of drift.

If we examine the noise band in the DMS signal, we can put an upper bound to compositional accuracy by allowing the true DMS signal to be anywhere within the noise band. In this case, we can take a closer look at data shown in Fig. 4. At the selected indium cell temperature of 889 °C, the flux value including the maximum error is 1.55 ± 0.03. Therefore, the actual indium flux may range from 0.312 ML/s to 0.348 ML/s giving up to $\sim 6\%$ error in flux. However, given the fact that the data is monotonically varying when smoothed, this is likely to be an overestimation of the error.

In summary, we revisit the DMS technique and demonstrate its usefulness in avoiding ex-situ calibration prior to the growth of mixed As/Sb heterostructures, such as the 3.3 μm diodes, that may include digital alloy deposition.

Acknowledgments

References

[1] M. Yano, M. Ashida, A. Kawaguchi, Y. Iwai, M. Inoue, J. Vac. Sci. Technol. B7 (1989) 199.
[2] J. Klem, R. Fisher, T.J. Drummondm, H. Morkoc, A.Y. Cho, Electron. Lett. 19 (1983) 455.
[3] P. Gopaladasu, J.L. Cecchi, K.J. Malloy, R. Kaspi, J. Cryst. Growth 225 (2001) 556.
[4] R. Kaspi, W.T. Cooley, K.R. Evans, J. Cryst. Growth 173 (1997) 5.
[5] A.J. Springthorpe, P. Mandeville, J. Vac. Sci. Technol. B6 (1988) 754.
[6] J.Y. Tsao, T.M. Brennan, B.E. Hammons, Appl. Phys. Lett. 53 (1988) 288.
[7] J.Y. Tsao, T.M. Brennan, J.F. Klem, B.E. Hammons, J. Vac. Sci. Technol. A7 (1989) 2138.
[8] R. Kaspi, J.P. Loehr, Appl. Phys. Lett. 71 (1997) 3537.
[9] K.R. Evans, C.E. Stutz, D.K. Lorance, R.L. Jones, J. Vac. Sci. Technol. B7 (1989) 259.
[10] L. Lapena, P. Muller, G. Quentel, H. Guesmi, G. Treglia, Appl. Surf. Sci. 212–213 (2003) 715.
[11] S. Fernández-Garrido, G. Koblmüller, E. Calleja, J.S. Speck, J. Appl. Phys. 104 (2008) 33541.
[12] R. Kaspi, K.R. Evans, J. Cryst. Growth 175/176 (1997) 838.
[13] K.R. Evans, R. Kaspi, J.E. Ehret, M. Skowronski, C.R. Jones, J. Vac. Sci. Technol. B13 (1995) 1820.
[14] F.G. Celii, T.B. Harton, Y.-C. Kao, T.S. Moise, Appl. Phys. Lett. 66 (1995) 2555.
[15] J.Y. Tsao, T.M. Brennan, J.F. Klem, B.E. Hammons, Appl. Phys. Lett. 55 (1989) 777.
[16] Y.-H. Zhang, D.H. Chow, Appl. Phys. Lett. 65 (1994) 3239.
[17] R. Kaspi, G.P. Donatim, J. Cryst. Growth 251 (2003) 515.
[18] Y.-Y. Cao, Y.-G. Zhang, Y. Gu, X.-Y. Chen, L. Zhou, IEEE Photonics Technol. Lett. 26 (2014) 571.
[19] M. Grau, C. Lin, O. Dier, C. Lauer, M.-C. Amann, Appl. Phys. Lett. 87 (2005) 241104.
[20] G. Belenky, L. Shterengas, G. Kipshidze, T. Hosoda, IEEE J. Sel. Top. Quantum Electron. 17 (2011) 1426.
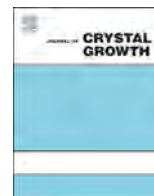
Pulsed growth techniques in plasma-assisted molecular beam epitaxy of $Al_xGa_{1-x}N$ layers with medium Al content ($x=0.4$–0.6)

D.V. Nechaev *, P.N. Brunkov, S.I. Troshkov, V.N. Jmerik, S.V. Ivanov

Ioffe Institute, Polytekhnicheskaya 26, St Petersburg 194021, Russia

ABSTRACT

Paper presents the comparative analysis of Metal Modulated Epitaxy (MME) and Droplet Elimination by Thermal Annealing (DETA) techniques in the low-temperature plasma-assisted MBE of thick $Al_xGa_{1-x}N$ layers with the medium Al content ($x=0.4$–0.6) grown under the highly metal-rich conditions. Atomically smooth surface with RMS of about 0.4 nm across the area of 2×2 μm² has been achieved for AlGaN layers grown at F^{III}/F^{N} flux ratio of 2.5 and substrate temperature of 700 °C by using DETA. The MME growth of AlGaN epilayers leads to their cracking due to the tensile stress introduced by relaxed GaN interlayers which are formed during the nitrogen exposure of the Ga-enriched AlGaN surface. A new technique based on IR-pyrometry measurements has been developed to monitor *in situ* metal accumulation and depletion on the growth surface.

© 2015 Published by Elsevier B.V.

1. Introduction

$Al_xGa_{1-x}N$ layers with high Al content ($x > 0.4$) is an attractive material for development of ultraviolet (UV) light emitting and laser diodes [1–3], photodiodes and photocathodes [4,5] highly demanded for numerous applications. Low temperature (< 800 °C), high vacuum ($\sim 10^{-5}$ Torr), and hydrogen-free environment of plasma-assisted molecular-beam epitaxy (PA MBE) gives rich possibilities in realization of quantum heterostructures, their strain engineering, and p-type doping. However, insufficiently high growth temperatures limit the achievement of two-dimensional growth of AlGaN layers with atomically smooth morphology (rms < 1 nm) by using thermal enhancement of the surface mobility of adatoms as it is usually done in high-temperature gas-phase epitaxial techniques. On the other hand, PA MBE enables one to raise the surface adatoms mobility through usage of metal-rich stoichiometric conditions, which provides sufficient mobility for 2D growth even at the low growth temperatures [6]. However, an essential shortcoming of this approach is the possible metal accumulation into microdroplets at small violations of growth conditions which must be maintained within a relatively narrow "growth window". Two kinds of pulsed growth techniques have been proposed to solve this problem, which are schematically illustrated in Fig. 1(a and b). The first one, the

so-called metal modulated epitaxy (MME) is based on consumption of excessive metal during short-term interruption of all metal fluxes at the constant values of activated nitrogen flux and substrate temperature. Initially this technique was developed by Ferro et al. [7] for growth of binary AlN layers and then it has been applied to growing the InGaN ternary alloys [8–10]. The second one, so-called Droplet Elimination by Thermal Annealing (DETA) initially developed by Terashima et al. [11] for the growth of GaN/AlGaN superlattices proceeds through thermal evaporation of the excessive metal (Ga) at the elevated substrate temperature during full growth interruption by shuttering all the fluxes. In both techniques, one can distinguish the Droplets Accumulation (DA) phase of ternary alloy growth under the metal rich conditions and the Droplet Elimination (DE) phase.

Both Laser Reflectometry (LR) and Reflection High-Energy Electron Diffraction (RHEED) are the techniques most frequently used to control growth rate, strain and surface morphology during MBE growth of different heterostructures [12]. In principle, RHEED allows one to evaluate Ga-coverage on the surface of the growing films [6,13], but these measurements are technically difficult for growth control of the films on rotating substrates.

In this paper we compare pulsed MME and DETA growth techniques for the PA MBE growth of $Al_xGa_{1-x}N$ ($x > 0.4$) bulk epilayers with the aim to achieve atomically smooth and droplets-free surface morphology, as well as uniform alloy composition along the growth direction. In addition, an original simple method using a common IR-pyrometer is developed for detection of the metal droplet occurrence on the growth surface.

* Corresponding author. Tel.: +7 812 2927124; fax: +7 812 297 36 20.
E-mail address: nechayev@mail.ioffe.ru (D.V. Nechaev).
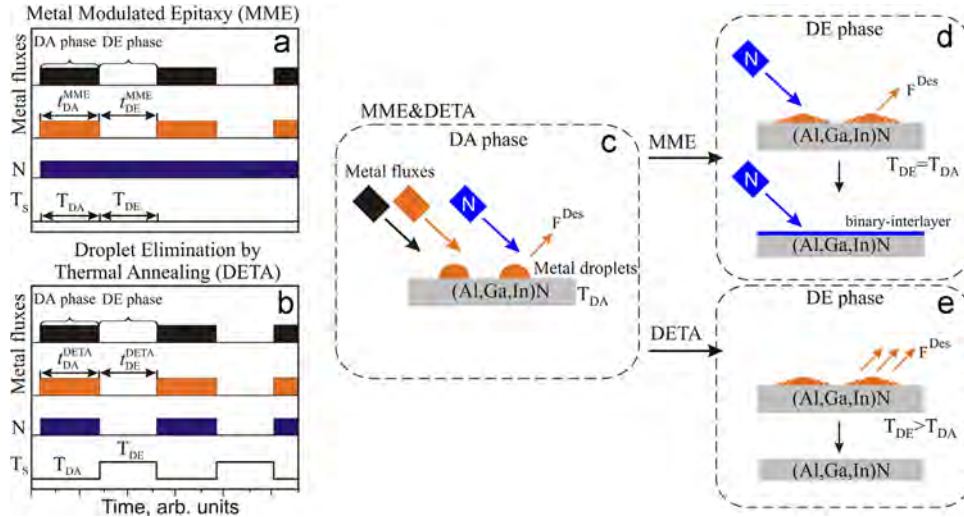
Fig. 1. Schematic illustrations of the flux modulation techniques applied to III-Nitrides growth in MBE: MME (a) and DETA (b). Schematic flux diagrams of DA phase (c) and DE phases for MME (d) and DETA (e) techniques are also presented.

Table 1
Characteristics of the AlGaN layers grown on AlN/c-Al$_2$O$_3$ templates.

Growth technique	Al$_x$Ga$_{1-x}$N growth parameters			Parameters of DA phase		Parameters of DE phase	
	x	Flux ratio F^{III}/F^N	Thickness, μm	Temperature T_{DA} (°C)	Duration t_{DA} (min)	Temperature T_{DE} (°C)	Duration t_{DE} (min)
Standard continuous	0.5	2.5	0.7	700	84	–	–
MME	0.4	2	0.9	700	10	700	1
DETA	0.6	2.5	0.5	700	2.5	730	1

2. Experimental

All AlGaN films were grown by using PA MBE setup Riber21T on c-Al$_2$O$_3$ substrates on top of a 500-nm-thick AlN/GaN buffer structures designed and grown as described earlier [14]. AlGaN layers were grown by both standard and pulsed techniques including MME and DETA ones. Table 1 summarizes the main growth parameters of the studied samples. The Al$_x$Ga$_{1-x}$N layers having thickness ranged from 500 to 900 nm were grown at the metal-rich (Ga-rich) conditions and the constant active nitrogen flux. The Al-content in the layers x, changing between 0.4 and 0.6, was controlled by variation of the Al flux between different growth runs. Main shutter closing was used to interrupt all the fluxes simultaneously and to rise the substrate temperature during DE phase of DETA technique owing to the heat reflectance effect, while the power supplied to a substrate heater was maintained constant.

Surface morphology was characterized by scanning electron (SEM), optical (OM), and atomic force microscopies (AFM). The former was also employed for observation of compositional contrast at the cross-section of the epilayers by using a back scattering electron mode. Substrate temperature was controlled in situ by IR pyrometer MIKRON M680 operating at $\lambda = 910$ nm. RHEED (Staib Instruments, 30 keV) and LR were used for evaluation of surface morphology and growth rate, respectively, the latter employed a green laser ($\lambda = 532$ nm) and a 1.3 MP CCD camera.

3. Results and discussion

It is well known that during growth of AlGaN ternary alloys Al adatoms are preferably incorporated to the film, which is related to the stronger bonding energy of Al-N as compared to

that of Ga-N [15]. Therefore, standard continuous growth of AlGaN layers under the highly Ga-rich conditions should cause Ga-droplets accumulation on the surface, as can be clearly seen in Fig. 2a. In opposite, Fig. 2(b and c) illustrates droplets-free surfaces of samples grown by using the droplets elimination techniques. An excess of Ga of about 50 ML for the DA phase was determined based on the incident fluxes (F^{III}, F^N) and metal desorption rate (F_{des}^{Ga}, Al desorption is negligible at these temperatures) as ($F^{III} - F^N - F_{des}^{Ga}$) for both MME and DETA samples. The minimum duration of DE phase providing the full droplets elimination is directly related to the growth conditions as

$$t_{DE}^{MME} = \frac{t_{DA}^{MME} \cdot \left[F^{III} - F^N - F_{des}^{Ga}(T_S^{DA})\right]}{F^N + F_{des}^{Ga}(T_S^{DE})} \quad (1)$$

for MME, and

$$t_{DE}^{DETA} = \frac{t_{DA}^{DETA} \cdot \left[F^{III} - F^N - F_{des}^{Ga}(T_S^{DA})\right]}{F_{des}^{Ga}(T_S^{DE})} \quad (2)$$

for DETA. Ga desorption rates of ~0.42 and ~1.05 ML/s at substrate temperatures of 700 and 730 °C, respectively, were experimentally estimated from Eqs. (1) and (2), using the minimum necessary t_{DE}^{DETA} values determined from the IR-pyrometry experiments as described below.

It has been found that IR-pyrometer signal is very sensitive to monitor in situ the excess metal (Ga) on the surface of growing films. Fig. 3 demonstrates the behaviors of LR and IR-pyrometer signals during growth of AlGaN layer by the MME technique at the metal-rich conditions with the flux ratio $F^{III}/F^N = 2.5$ and initial substrate temperature of 702 °C. Indeed, immediately after the initiation of growth pyrometer reading drops by 5 °C. Then, during the whole DA phase the pyrometer signal remains constant. Start

Fig. 2. SEM images of AlGaN samples grown by the standard (continuous) (a), MME (b) and DETA (c) techniques.

Fig. 3. The LR and IR-pyrometer signal variations during AlGaN layer growth by MME technique.

Fig. 5. AFM image of $Al_{0.6}Ga_{0.4}N$ layer grown by DETA technique with RMS of 0.4 nm over 2×2 μm^2.

phases. We believe that the dependence of the pyrometer data on the excess Ga accumulated at the surface of growing films is related to scattering and/or absorption of IR radiation by an ultra-thin Ga film and small droplets on the surface.

Comparative analysis of the morphologies of AlGaN layers grown by using MME and DETA techniques revealed for the former some inhomogeneities both on the plain and at the cross-section SEM images. First, the traces of cracking are observed by both OM (not shown) and SEM (see Fig. 2b) on the surface of the $Al_{0.4}Ga_{0.6}N$ layer grown by MME. In addition, Fig. 4 demonstrates formation of the relatively thick interlayers of a lighter contrast on the cross-sectional SEM images. The thickness of the layers of about 7 nm correlates well with the nominal thickness of about 50 ML of the excess Ga accumulated during the DA phase, estimated from Eq. (1) taking into account its partial evaporation during the DE stage. Therefore one can conclude that pure GaN interlayers are formed during the DE phase of an MME cycle. Furthermore, it is expected that elastic stress in such recrystallized layers relaxes, which generates the tensile strain in the subsequent thick AlGaN layers, causing the development of cracks. In contrast, such undesirable phenomena are not observed in the $Al_{0.6}Ga_{0.4}N$ layer grown by the DETA technique. This sample exhibits an atomically smooth, droplet-free surface morphology without any traces of cracking.

Thus, one can conclude that DETA method is more appropriate for the growth of AlGaN layers with perfect surface morphology having RMS of about 0.4 nm over the area of 2×2 μm^2 as shown in Fig. 5.

4. Conclusions

In summary, $Al_xGa_{1-x}N$ layers with medium Al-content ($x = 0.4$–0.6), having atomically smooth and droplet-free surface morphology, can be grown by low-temperature PA MBE using both MME and DETA techniques. However, the MME layers

Fig. 4. Cross-section SEM image of $Al_{0.4}Ga_{0.6}N$ layer grown by MME. Three Ga-enriched AlGaN interlayers (most probably GaN) can be clearly distinguished.

of the DE phase, when GaN film continues to grow from the excess Ga at the closed metal cell shutters, does not change significantly the pyrometer signal. The signal comes back to the initial level only when the excessive metal has been consumed by nitrogen and the surface becomes metal-free again. Analogous behavior was observed during AlGaN growth by the DETA technique, except for the DE growth stage, and was also used for determination of the minimum necessary time of the DE phase. In both cases the completeness of the DE phase is characterized by a negligible difference between the pyrometer data before DA and after DE

demonstrate traces of cracking probably related to the formation of rather thick relaxed GaN interlayers inside the AlGaN layer during metal droplet consumption under the nitrogen flux (DE phase). Contrary to that, the DETA technique provides the best surface morphology with RMS of 0.4 nm over 2×2 μm^2 without cracks. In addition, the IR-pyrometry has been demonstrated to be an efficient tool for detection of the excessive metal on the surface of growing AlGaN layers.

Acknowledgements

References

[1] Y. Liao, C. Thomidis, C.-k. Kao, T.D. Moustakas, Appl. Phys. Lett. 98 (2011) 081110. http://dx.doi.org/10.1063/1.3559842.

[2] S. Hwang, D. Morgan, A. Kesler, M. Lachab, B. Zhang, A. Heidari, H. Nazir, I. Ahmad, J. Dion, Q. Fareed, V. Adivarahan, M. Islam, A. Khan, Appl. Phys. Exp. 4 (2011) 032102. http://dx.doi.org/10.1143/APEX.4.032102.

[3] K. Takeda, K. Nagata, T. Ichikawa, K. Nonaka, Y. Ogiso, Y. Oshimura, M. Iwaya, T. Takeuchi, S. Kamiyama, I. Akasaki, H. Amano, H. Yoshida, M. Kuwabara, Y. Yamashita, H. Kan, Phys. Status Solidi C 8 (2011) 464–466. http://dx.doi.org/10.1002/pssc.201000588.

[4] P.E. Malinowski, J.-Y. Duboz, P. De Moor, K. Minoglou, J. John, P. Srivastava, F. Semond, E. Frayssinet, A. BenMoussa, B. Giordanengo, C. Van Hoof, R. Mertens, Proc. SPIE 8073 (2011) 807302. http://dx.doi.org/10.1117/12.886682.

[5] A.M. Dabiran, A.M. Wowchak, P.P. Chow, O.H.W. Siegmund, J.S. Hull, J. Malloy, A.S. Tremsin, Proc. SPIE 7212 (2009) 721213. http://dx.doi.org/10.1117/12.809503.

[6] C. Adelmann, J. Brault, G. Mula, B. Daudin, L. Lymperakis, J. Neugebauer, Phys. Rev. B 67 (2003) 165419. http://dx.doi.org/10.1103/PhysRevB.67.165419.

[7] G. Ferro, H. Okumura, T. Ide, S. Yoshida, J. Cryst. Growth 210 (2000) 429–434. http://dx.doi.org/10.1016/S0022-0248(99)00891-X.

[8] T. Yamaguchi, H. Umeda, T. Araki, Y. Nanishi, Jpn. J. Appl. Phys. 50 (2011) 04DH08. http://dx.doi.org/10.1143/JJAP.50.04DH08.

[9] M. Moseley, B. Gunning, J. Greenlee, J. Lowder, G. Namkoong, W.A. Doolittle, J. Appl. Phys. 112 (2012) 014909. http://dx.doi.org/10.1063/1.4733347.

[10] T. Yamaguchi, N. Uematsu, T. Araki, T. Honda, E. Yoon, Y. Nanishi, J. Cryst. Growth 377 (2013) 123–126. http://dx.doi.org/10.1016/j.jcrysgro.2013.05.009.

[11] W. Terashima, H. Hirayama, Phys. Status Solidi A 208 (2011) 1187–1190. http://dx.doi.org/10.1002/pssa.201000871.

[12] V.N. Jmerik, A.M. Mizerov, D.V. Nechaev, P.A. Aseev, A.A. Sitnikova, S.I. Troshkov, P.S. Kop'ev, S.V. Ivanov, J. Cryst. Growth 354 (2012) 188–192. http://dx.doi.org/10.1016/j.jcrysgro.2012.06.025.

[13] M. Moseley, D. Billingsley, W. Henderson, E. Trybus, W.A. Doolittle, J. Appl. Phys. 106 (2009) 014905. http://dx.doi.org/10.1063/1.3148275.

[14] S.V. Ivanov, D.V. Nechaev, A.A. Sitnikova, V.V. Ratnikov, M.A. Yagovkina, N.V. Rzheutskii, E.V. Lutsenko, V.N. Jmerik, Semicond. Sci. Technol. 29 (2014) 084008. http://dx.doi.org/10.1088/0268-1242/29/8/084008.

[15] E. Iliopoulos, T.D. Moustakas, Appl. Phys. Lett. 81 (2002) 295 http://dx.doi.org/10.1063/1.1492853.
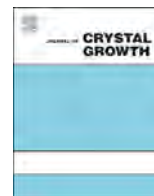
In situ three-dimensional X-ray reciprocal-space mapping of InGaAs multilayer structures grown on GaAs(001) by MBE

Takuo Sasaki [a,*], Masamitu Takahasi [a], Hidetoshi Suzuki [b], Yoshio Ohshita [c], Masafumi Yamaguchi [c]

[a] *Japan Atomic Energy Agency, 1-1-1 Koto, Sayo, Hyogo 679-5148, Japan*
[b] *University of Miyazaki, 1-1 Gakuenkibana-dai Nishi, Miyazaki 889-2192, Japan*
[c] *Toyota Technological Institute, 2-12-1 Hisakata, Tempaku-ku, Nagoya 468-8511, Japan*

ARTICLE INFO

ABSTRACT

In situ three-dimensional X-ray reciprocal space mapping (*in situ* 3D-RSM) was employed for studying molecular beam epitaxial (MBE) growth of InGaAs multilayer structures on GaAs(0 0 1). Measuring the symmetric 004 diffraction allowed us to separately obtain film properties of individual layers and to track the real-time evolution of both residual strain and lattice tilting. In two-layer growth of InGaAs, significant plastic relaxation was observed during the upper layer growth, and its critical thickness was experimentally determined. At the same thickness, it was found that the direction of lattice tilting drastically changed. We discuss these features based on the Dunstan model and confirm that strain relaxation in the multilayer structure is induced by two kinds of dislocation motion (dislocation multiplication and the generation of dislocation half-loops).

1. Introduction

The development of high quality (low dislocation density) and fully strain-relaxed III–V layers grown on lattice-mismatched substrates is required for future optoelectronic devices such as hetero-junction transistors and multi-junction solar cells [1–3]. To reduce lattice-mismatch strain, compositionally step-graded buffers (CSBs), which are step-like multilayer structures with different lattice constants, have often been inserted between active layers and substrates. While CSBs have been shown to function well as dislocation filters [4], efficient methods of strain relief still need to be explored, because reducing the total thickness of the CSBs lowers the production cost of devices. For this reason, it is important to understand the fundamental mechanisms of strain relaxation in multilayer structures.

To do this, the relaxation processes of individual layers need to be studied separately. For this purpose, *in situ* three-dimensional X-ray reciprocal-space mapping (*in situ* 3D-RSM) is suitable, since each layer differs in lattice constant and yields diffraction peaks at different points in reciprocal space [5]. This is in contrast to reflected high energy electron diffraction and surface reflectance monitoring, which are sensitive only to the top layer of the

multilayer [6,7], and monitoring of the substrate curvature, which provides average information over the entire multilayer [8]. In this study, we employed *in situ* 3D-RSM to study an InGaAs multilayer structure consisting of two InGaAs layers with different indium compositions. The *in situ* measurement of the X-ray intensity distribution around the symmetric 004 diffraction revealed the characteristic behavior of the residual strain and the lattice tilting of each layer.

2. Experimental procedure

The *in situ* 3D-RSM was carried out at a synchrotron radiation facility, SPring-8 (Beamline 11XU) using a surface X-ray diffractometer that is directly coupled to a MBE apparatus. A detailed system configuration can be found elsewhere [9,10]. The GaAs (001) ± 0.1° substrate was mounted on a molybdenum block, and loaded into the MBE chamber. After removal of the native oxide layer and the growth of a 100 nm-thick GaAs buffer layer, $In_{0.11}Ga_{0.89}As$ was deposited to a thickness of 300 nm. Subsequently, a 300 nm-thick $In_{0.20}Ga_{0.80}As$ layer was grown on the first layer, as shown in Fig. 1(a). The growth rate, temperature and vacuum pressure were 0.2 ML/s, 470 °C and 3×10^{-4} Pa, respectively. Synchrotron X-rays from an in-vacuum undulator were monochromatized to $\lambda = 0.827$ Å and focused to 0.3 mm horizontally and 0.1 mm vertically. X-rays diffracted by the symmetric 004

* Corresponding author.
E-mail address: sasaki.takuo@jaea.go.jp (T. Sasaki).
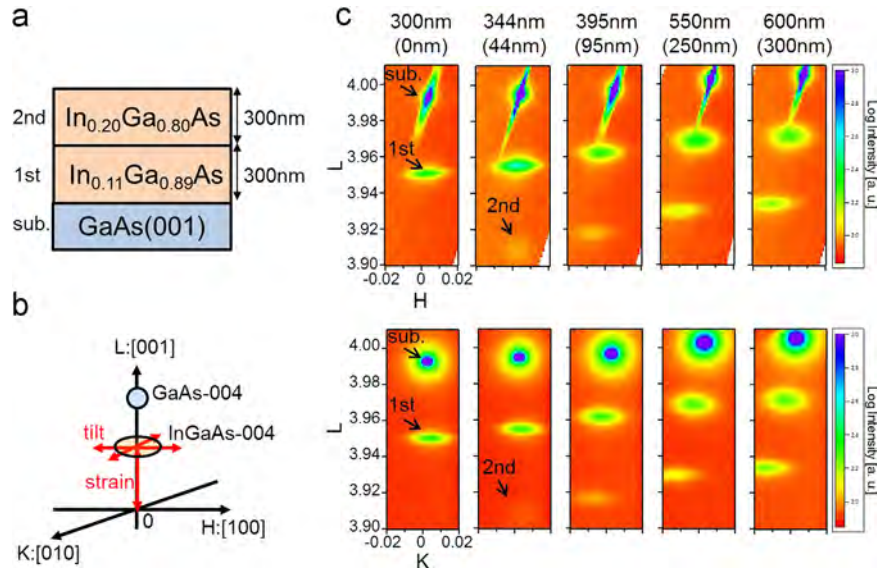
Fig. 1. (a) Structure of the InGaAs multilayer structure grown on GaAs(001) substrate. (b) Measured 004 reciprocal points in reciprocal space. (c) Typical *H–L* and *K–L* reciprocal space maps at different InGaAs total thicknesses. The thickness of the second layer is given in brackets.

plane were detected by a two-dimensional charge coupled device (CCD) camera. It took 72 s to obtain a single 3D-RSM, which was composed of 60 CCD images. This measuring time corresponds to a thickness of 3 nm for the employed growth rate of InGaAs. As shown in Fig. 1(b), the residual strain of the InGaAs multilayer structure can be estimated from peak positions along the L direction on the assumption of constant indium composition during the growth. The indium composition in each layer was confirmed by post-growth X-ray diffraction. The direction and magnitude of lattice tilting in each layer were evaluated from peak positions in the *H–K* plane.

3. Results

Typical *H–L* and *K–L* projections of the 3D-RSM at different layer thicknesses are shown in Fig.1(c). The upper and lower (in brackets) thicknesses indicate the thicknesses of the total film and the second layers, respectively. The peak positions for both the first and second layers move along the L direction with increasing second-layer thickness. This is due to a decrease in the residual strain in each layer. The peaks also move along the *H* and *K* directions. This corresponds to lattice tilting during the second layer growth.

Fig. 2 shows the peak shifts along the L direction for the first and second layers as a function of the total InGaAs thickness. During the growth of the first layer, the InGaAs layer is fully strained on the substrate up to a thickness of about 40 nm, and a large strain relaxation is observed at around 120 nm. Consequently, relaxation of the first layer reaches 56% at the end of the first layer growth. These observations agree with our previous work [11]. At a thickness of 344 nm, a large strain relaxation is observed again for both the first and second layers. As thickness increases further, strain relaxation of the first layer stays around 94%, even after additional growth of the second layer.

Fig. 3(a) shows the trajectory of the diffraction peak position of the first layer during the growth of the InGaAs layers, demonstrating the correlation between the strain relaxation and the lattice tilting. Since the lattice tilting is due to the in-plane anisotropic distribution of misfit dislocation Burgers vectors [12], the correlation is helpful to deduce the dislocation motion in the multilayer structure. Fig. 3(b) shows the projection of the peak positions on
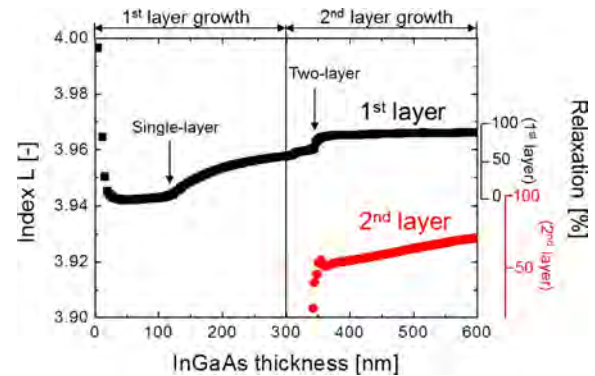
Fig. 2. Evolution of diffraction peak positions along index L associated with the residual strain for the 1st and 2nd layers as a function of total InGaAs thickness. The arrows indicate the thicknesses at which large strain relaxations were observed in the single (120 nm) and two-layer structures (344 nm).

the *H–L* plane. The direction of the lattice tilting changes from $<010>$ to $<110>$ concomitantly with the large strain relaxation at a thickness of 344 nm, where the increase in the magnitude of lattice tilting is accelerated as well. This indicates a strong correlation between strain relaxation and lattice tilting.

4. Discussion

The present *in situ* 3D-RSM results have revealed an interaction between the first and second InGaAs layers. One of the effects of the interaction is found in the significantly earlier strain relaxation of the second layer, which occurred at a thickness of 44 nm, compared to that of the first layer, which was observed at a thickness of 120 nm. This accelerated relaxation of the second layer can be explained by dislocation multiplication [13]. When the second layer is grown on the partially relaxed first layer, threading dislocations reaching from the first layer provide sources for misfit dislocations in the second layer. Thus, strains in the second layer are effectively relaxed through dislocation multiplication from the high density of sources.

Another indication of the interaction between the first and second layers is the fact that the residual strains in the first layer were relieved when the second layer was relaxed at a thickness of
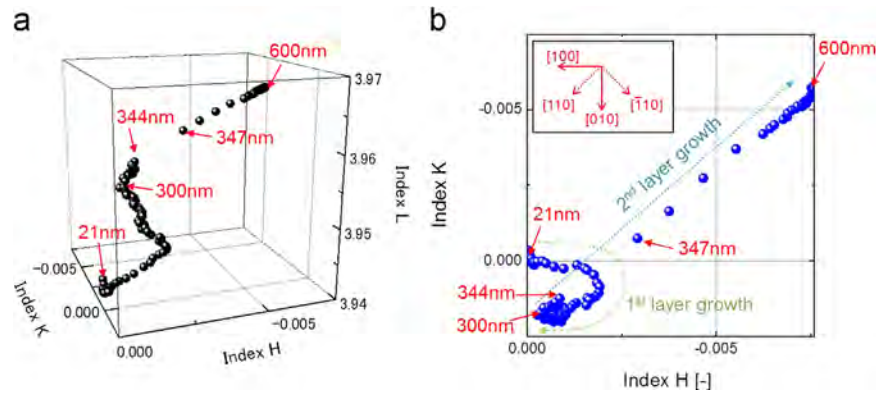
Fig. 3. Evolution of the diffraction peak positions of the 1st layer in *H–K–L* 3D reciprocal space (a) and in the projected *H–K* plane (b) during growth of the 1st and 2nd InGaAs layers. The peak positions shown in (b) are associated with the direction and the magnitude of lattice tilting. The magnitude of the tilt for the 1st layer with respect to the substrate was 0.13° along $< 110 >$ direction at a thickness of 600 nm. At this thickness, the tilt for the 2nd layer was 0.34°, and its direction was the same as that of the 1st layer (not shown in the figure).

Table 1
Comparison of model and experimental values of relaxation critical thickness t_c and residual strain $\varepsilon_r(d)$ for the single and two-layer structures. Thickness d is chosen to be 150 (single-layer) and 350 nm (two-layer) during the large relaxation where Dunstan's model is applicable [14].

	Single-layer structure		Two-layer structure	
	t_c^1	ε_r^1(150 nm)	t_c^2	ε_r^2(350 nm)
Model	100	0.0053	82	0.0029
Experiment	122	0.0059	44	0.0023

344 nm. At the same time, the lattice planes of the first layer started to tilt in a different way than before the growth of the second layer. Obviously, the altered relaxation found in the first layer is caused by the dislocation half-loops [14] extended from the interface between the first and second layers to the substrate. When reaching the interface between the first layer and the substrate, the dislocation half-loops newly generate misfit dislocations [15], the anisotropy of which causes the tilting of the lattice planes. It is not surprising that the in-plane anisotropic distribution of these post-generated dislocations is different from that of the preexisting dislocations because they have independent origins.

Dunstan et al. [16,17] proposed a model to deal with the relaxation of multilayer structures. In this model, the critical thickness of the *i*-th layer, t_c^i, is given by $t_c^i = k/\Delta\varepsilon_m^i$, where $\Delta\varepsilon_m^i$ is the misfit between the *i*-th and (*i*-1)-th layer. The average residual strain is defined as $\varepsilon_r^n(d) = k/\sum_{i=1}^{n} d^i$ for a multilayer structure consisting of *n* layers, with thicknesses $d^i (i = 1, 2,…n)$. The coefficient k has been experimentally determined to be about 0.8 nm [17]. The validity of this model for single layer structures has been demonstrated by X-ray diffraction and transmission electron microscopy [18,19]. A comparison of the present *in situ* X-ray diffraction results with the model is given in Table 1. The model well explains the critical thickness t_c^1 and residual strains ε_r^1 of the first layer. However, a significant discrepancy was found for the critical thickness of the second layer, t_c^2, which is experimentally determined to be 44 nm, and predicted to the model to be 82 nm. The reduction of the critical thickness suggests that the dislocation motion in the second layer is considerably altered by dislocation multiplication.

5. Summary

We have investigated the strain relaxation mechanisms in an InGaAs multilayer structure grown on a GaAs(001) substrate by MBE. The *in situ* measurement of 3D-RSM for the symmetric 004 reflection enabled a direct observation of the relationship between strain relaxation and lattice tilting. Based on the obtained experimental results, we clarified that there are two processes in terms of dislocation motion (dislocation multiplication and generation of dislocation half-loops) which occur during the growth of the multilayer structure. The validity of our interpretation is consistent with a comparison to Dunstan's model.

References

[1] K.E. Lee, E.A. Fitzgerald, J. Cryst. Growth 312 (2010) 250.
[2] R.M. France, J.F. Geisz, M.A. Steiner, B. To, M.J. Romero, W.J. Olavarria, R.R. King, J. Appl. Phys. 111 (2012) 103528.
[3] G.B. Galiev, I.S. Vasil'evskii, S.S. Pushkarev, E.A. Klimov, R.M. Imamov P.A. Buffat, B. Dwir, E.I. Suvorova, J. Cryst. Growth 366 (2013) 55.
[4] D. Araújo, D. González, R. García, A. Sacedón, E. Calleja, Appl. Phys. Lett. 67 (1995) 3632.
[5] H. Suzuki, T. Sasaki, A. Sai, Y. Ohshita, I. Kamiya, M. Yamaguchi, M. Takahasi, S. Fujikawa, Appl. Phys. Lett. 97 (2010) 041906.
[6] J. Pamulapati, P.K. Bhattacharya, J. Singh, P.R. Berger, C.W. Snyder, B.G. Orr R.L. Tober, J. Electron. Mater. 25 (1996) 479.
[7] Y. Wang, R. Onitsuka, M. Deura, W. Yu, M. Sugiyama, Y. Nakano, J. Cryst. Growth 312 (2010) 1364.
[8] J.F. Geisz, A.X. Levander, A.G. Norman, K.M. Jones, M.J. Romero, J. Cryst. Growth 310 (2008) 2339.
[9] M. Takahasi, Y. Yoneda, H. Inoue, N. Yamamoto, J. Mizuki, Jpn. J. Appl. Phys. 41 (2002) 6427.
[10] W. Hu, H. Suzuki, T. Sasaki, M. Kozu, M. Takahasi, J. Appl., Crystallography 45 (2012) 1046.
[11] T. Sasaki, H. Suzuki, M. Takahasi, Y. Ohshita, I. Kamiya, M. Yamaguchi, J. Appl. Phys. 110 (2011) 113502.
[12] M. Natali, F. Romanato, E. Napolitani, D. De Salvador, A.V. Drigo, Phys. Rev. B 62 (2000) 11054.
[13] R. Beanland, J. Appl. Phys. 72 (1992) 4031.
[14] A.G. Cullis, A.J. Pidduck, M.T. Emeny, Phys. Rev. Lett. 75 (1995) 2368.
[15] T. Sasaki, H. Suzuki, A. Sai, J-H Lee, M. Takahasi, S. Fujikawa, K. Arafune, I. Kamiya, Y. Ohshita, M. Yamaguchi, Appl. Phys. Express 2 (2009) 085501.
[16] D.J. Dunstan, S. Young, R.H. Dixon, J. Appl. Phys. 70 (1991) 3038.
[17] D.J. Dunstan, P. Kidd, P.F. Fewster, N.L. Andrew, R. Grey, J.P.R. David, L. González, Y. González, A. Sacedón, F. González-Sanz, Appl. Phys. Lett. 65 (1994) 839.
[18] D.J. Dunstan, P. Kidd, L.K. Howard, R.H. Dixon, Appl. Phys. Lett. 59 (1991) 3390.
[19] A. Sacedón, F. González-Sanz, E. Calleja, E. Muñoz, S.I. Molina, F.J. Pacheco, D. Araújo, R. García, M. Lourenço, Z. Yang, P. Kidd, D. Dunstan, Appl. Phys. Lett. 66 (1995) 3334.

CRYSTAL
GROWTH
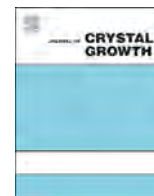
In-situ monitoring during MBE growth of InAs based heterostructures

CrossMark

Kunal Bhatnagar, Juan Rojas-Ramirez, Manuel Caro, Rocio Contreras, Bernd Henninger [1], Ravi Droopad *

Ingram School of Engineering, Texas State University, San Marcos, TX 78666, United States.

ARTICLE INFO

ABSTRACT

The use of reflectance anisotropy spectroscopy (RAS) for the real time monitoring of the growth of InAs based heterostructures by molecular beam epitaxy within the photon energy range 1.5–5.0 eV is reported. The complete desorption of the native oxide for InAs substrates was monitored using a single wavelength and epitaxial growth of InAs was also monitored under both the As- and In-rich surface reconstructions. Further the changes in the RAS and reflectance data for ternary and quaternary layers demonstrated the usefulness of this system as an *in-situ* tool for monitoring the composition of layers for this important class of narrow gap semiconductors. In addition, emissivity corrected pryometry temperature was measured using the RAS system. Growth rates for the individual layers in a heterostructure were also determined from an analysis of the reflectance data.

1. Introduction

III–V semiconductors in the lattice constant range between 6.05 and 6.3 Å are being actively considered for a number of applications. These materials when combined in a superlattice structure are potential alternatives to HgCdTe infrared detectors [1]. Because of their superior transport properties [2,3] they also represent a class of materials for future replacement of the channel in silicon based CMOS technology. Among the substrates in this family are InAs and GaSb materials with lattice constants of 6.06 Å and 6.096 Å respectively and bulk bandgaps, E_G of 0.35 eV and 0.726 eV respectively. While other III–V substrates can be made semi-insulating, the same is not true for InAs and GaSb. As a result, the fabrication of planar electronic devices on these substrates must be carried out on structures with suitable buffer layers so that the conducting substrate is completely isolated to eliminate parallel conduction. To overcome this limitation, a large bandgap buffer layer that is lattice matched to the substrates is required. One such buffer layer is the ternary mixed group V material, AlAsSb with an As composition of approximately 16% and for which careful control of the group V fluxes are necessary during growth. Such layers were successfully grown lattice matched on InAs substrates both by MBE [4] and MOCVD [5]. *In-situ* monitoring of the growth on these narrow bandgap substrates would be useful to provide an accurate measure of the substrate temperature and real time control of the layer composition and possibly doping. In this paper we will report on the use of reflectance anisotropy spectrometry

(RAS) to provide real time information during the MBE growth of InAs based heterostructures.

While the reflection high energy electron diffraction (RHEED) technique has been the normal *in-situ* monitoring technique used during MBE growth, various optical techniques such as spectroscopic ellipsometry [6] and reflectance difference spectroscopy [7] have been developed as alternative non-destructive techniques used for growth monitoring. The optical techniques are conducive to non-UHV growth techniques where RHEED cannot be used allowing for the monitoring of the surface during growth [8]. Reflectance anisotropy spectroscopy (RAS) is based on measuring the optical anisotropies associated with cubic semiconductors due to surface dimers [9]. The RAS technique measures the anisotropic optical response of the surface due to reconstructions, bonds and even doping by taking the difference in the reflectance of light polarized along two orthogonal axes of the crystal surface,

$$\frac{\Delta R}{R} = 2\frac{R_x - R_y}{R_x + R_y}$$

where R_x and R_y are the reflectances for linearly polarized light along the orthogonal [110] directions. The anisotropy signal is the result of surface reconstructions having characteristic configuration due to dimerization [10]. The RAS optical setup utilizes a near normal incidence angle and due to the cubic symmetry in bulk semiconductors with zincblende crystal structures, the isotropic bulk has nearly no contribution to the RAS signal. The RAS signal therefore originates solely from the anisotropy of the reconstructed surface and is ideal for the investigation of surface phenomenon in III–V semiconductors. The changes in the RAS signal can also be a function of the doping. Studies have shown

that for both GaAs and InP, the surface electric fields generated depend on the doping type [11,12]. In this study we will investigate the usefulness of this technique for narrow gap semiconductors.

2. Experimental

This study was carried out using a LayTec EpiRAS system mounted on the pyrometer port of a DCA III–V MBE system allowing for normal incidence beam paths. The MBE is used for the growth of high mobility narrow gap heterostructures with As and Sb valved crackers for the group V sources. Elemental group III sources include Ga, In and Al with Te and Be used for n- and p-type doping. To facilitated measurements using the EpiRAS system, a strain free window was mounted on the pyrometer port. During layer growth the group V valve crackers temperatures were set to obtain dimeric species. Because of the high group V overpressure needed for MBE growth the viewport windows were coated in a very short time after growth initiation resulting in a dramatic reduction of the RAS signal. To overcome this problem the strain-free window was heated during all MBE growth and during data acquisition.

All experiments were carried out on epiready InAs substrates that were mounted in indium free holders. To remove the native oxide, the substrate was ramped to a temperature of 640 °C as measured by manipulator thermocouple with the As flux during this process fixed at 8×10^{-6} mbar until the diffraction pattern transitions for a $3 \times$ to $2 \times$ reconstruction along the [110] azimuth. To ensure complete removal of the surface oxide the sample was annealed at 10–15 °C higher for 30 min. An InAs epitaxial buffer layer was grown at 500 °C using an initial growth rate of 0.15 ML/s for a thickness of 20 nm followed by a growth rate of 0.5 ML/s for subsequent growths. AlAsSb growth lattice matched to InAs was carried out using a digital growth scheme as outlined in ref. 4 at a temperature of 500 °C. The As content for this layer to be lattice matched to InAs is 16.8% as determined by high resolution XRD measurements.

The EpiRAS system used consists of a XBO arc bow lamp as light source. The light, in the wavelength region from 1.5 eV to 5 eV, from this source is polarized by a Glan-air type polarizing prism and is focused on the sample using spherical mirrors. Using the strain free window on the pyrometer port, the light path is close to normal incidence on the substrate and allows for the use of a spherical mirror in the anti-wobble mirror configuration needed

to optically compensate for the wobbling generated by sample rotation. The reflected light is generally elliptically polarized and carries information about the sample encoded in the intensity (reflectivity) and polar angle (reflection anisotropy signal). The state of polarization is analyzed using photo-elastic modulator and a Si detector. An additional light path is used to provide a measure of the sample surface temperature, using the emissivity corrected pyrometry.

3. Results and discussions

The growth on InAs substrates requires a careful removal of the native oxide and RHEED signatures are typically used to determine the onset of oxide desorption. However this change is gradual and in our laboratory we use a RHEED transition from $3 \times$ to $2 \times$ reconstruction along the [110] azimuth as the onset for oxide desorption followed by an anneal for 30 mins at a temperature that is 10–15 °C higher. We take this temperature as a calibration point to represent a real temperature of 520 °C. Fig. 1 shows a typical 2D plot of the time resolved spectroscopic RAS signal during this InAs oxide desorption process followed by the homo-epitaxial growth of an InAs buffer and an AlAsSb ternary layer also lattice matched to InAs. The complete structure represented in the 2D plot is shown on the right of Fig. 1. In addition to extracting RAS and reflectance information, the system also measures the emissivity corrected substrate temperature in real time. Fig. 2 shows a plot of the RAS signal at a single wavelength of 3.4 eV (364.6 nm) during the growth of the structure. The emissivity corrected temperature extracted is also shown in the plot. As a reference a system thermocouple reading of 650 °C corresponds to an emissivity corrected temperature 546 °C as measured by the RAS system. This suggests that the RAS system overestimates the temperature by approximately 16 °C. Fig. 3 plots the spectra for various emissivity corrected temperatures as the InAs substrate is heated from room temperature during the oxide desorption process. An inspection of the spectra shows that gradual changes occur as the temperature is ramped from room temperature until a measured temperature of around 520 °C with significant changes in the spectra occurring between 520 °C and 530 °C above which these spectra remained fairly constant in shape. This result show that while RHEED may be able to suggest an onset of oxide desorption, the surface structure is dynamic and would require additional time/higher temperature to achieve a clean oxide free surface. The plot also suggests that by monitoring a single
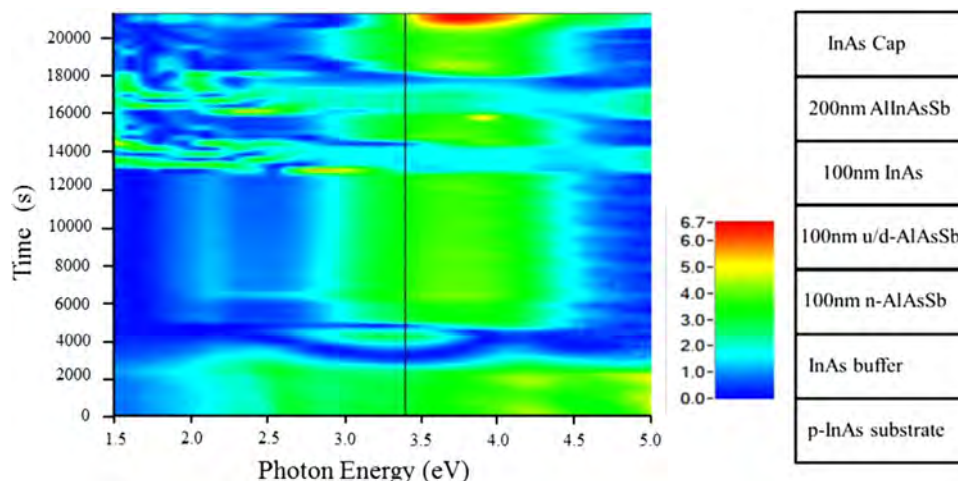
Fig. 1. 2D plot of the absolute value of the time resolved RAS spectra during MBE growth of an InAs based heterostructure shown on the right. The vertical line is at a photon energy of 3.4 eV.
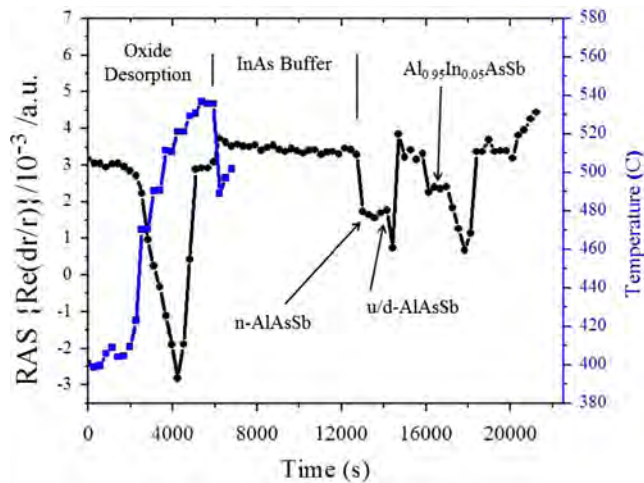
Fig. 2. Plot of the RAS signal the growth of the heterostructure shown in Fig. 1 for a single wavelength at a photon energy of 3.4 eV. Also shown is the emissivity corrected temperature measured by the RAS system during the InAs oxide desorption process.
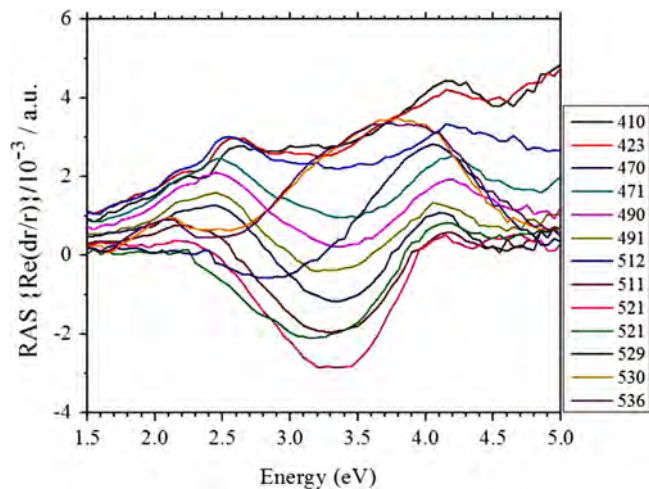
Fig. 3. Plot of the RAS spectra during InAs oxide desorption. The temperature shown in the legend is in °C is taken from the plot of Fig. 2.

Fig. 4. RAS signal measured during the growth of InAs initially during the As-rich (2×4) conditions, followed by an In-rich (4×2) surface reconstruction and finally back to an As-stabilized (2×4) reconstruction achieved by increasing the incident As flux.

wavelength the oxide desorption process can be followed. An inspection of Figs. 1 and 2 showed that significant changes in the spectra occur at the 3.4 eV (364.6 nm) wavelength.

Since the RAS signal gives a measure of the surface anisotropy, this measurement technique will be sensitive to the surface reconstruction. Reports suggest that InAs can be grown using a low As/In flux ratio albeit with high defects. However it is the experience in our laboratory that any InAs surface haze that is due to non-ideal growth parameters can be completely eliminated when growth is carried out under slightly In-rich conditions. Growth under these 2 conditions results in dramatic change in the RAS signal since the surface anisotropy is switched. Fig. 4 shows the spectral plot of the RAS data during the growth of InAs under the two surface reconstructions. The data was initially taken during the growth of InAs under an As stabilized (2×4) recon- struction. To achieve an In stabilized (4×2) reconstruction, the As flux was reduced gradually and the RHEED monitored until the required reconstruction was achieved. After increasing the As back to the level required for the (2×4) surface, the RAS spectrum is almost identical to that prior to the growth under the In-rich regime. The growth under the In-rich (4×2) regime had no effect on the subsequent As-rich growth of InAs with respect to its surface crystallinity and stoichiometry as confirmed by the RHEED

observations, suggesting that both RHEED and RAS techniques are not sensitive to surface defects present when growth is carried out under In-rich conditions as reported in the literature [4,13]

Lattice matching of III–V heterostructures on InAs requires careful control of the alloy composition of ternary and quaternary layers. While the composition of the group III fluxes can be determined from RHEED oscillations, the group V flux ratios are inherently more difficult due to the non-unity sticking coefficients of both As and Sb and the fact that the incorporation rates are dependent on growth temperature. An initial investigation of the growth of ternary lattice matched layer was also monitored in the 2D plot of Fig. 1. In this structure, 2 ternary layers were grown each 100 nm thick but with the bottom ternary layer doped n-type with Te to a level of 2×10^{17} cm^{-3}, while the rest of the structure was undoped. From the plot of Fig. 2, there appears to be some difference in the RAS signal for the 2 layers suggesting that the RAS signal may be used as an in-situ tool to monitor doping during growth. Further, the RAS signal at 3.4 eV for the growth of the quaternary layer is much higher than those for the ternary layers, indicating the potential for using this technique for composition monitoring and control. To investigate the use of the reflectance anisotropy spectroscopy to monitor and control composition, the structure shown on the left of Fig. 5 was grown which includes two 300 nm quaternary layers separated by an InAs layer. The bottom quaternary layer having a low indium composition was grown using a digital alloy techniques while the top quaternary layer was growth using conventional MBE by adjusting the group V fluxes to give the required composition. The plot shows on the right of Fig. 5 represent the RAS and reflectance data extracted from the 2D plot for a wavelength of 4.1 eV. The plot shows that both the RAS signal and the reflectance is a function of the composition of the layers. The combination of the RAS and reflectance data can be used to fully characterize the grown layer. The reflectance data is sensitive to the growth rate which solely depends on the group III fluxes and intensity oscillations can be used to monitor the In and Al ratios. The RAS signal on the other hand is more surface sensitive and can be used to assess the As to Sb ratio of the quaternary layers [14]. As seen in plot of Fig. 5, the reflectance signal increases significantly with higher Al concentra- tion in the quaternary layer while the RAS signal decreases with increasing As to Sb ratio. A more comprehensive study for
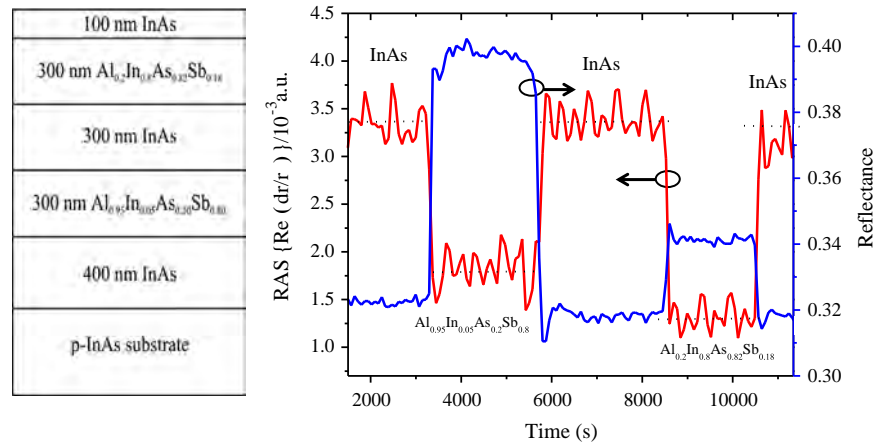
Fig. 5. Shown on the left, the MBE structure including 2 quaternary layer lattice matched to InAs to investigate the suitability of RAS for composition monitoring, the plot on the right represents the RAS and reflectance data extracted from the 2D plot for at a photon energy of 4.1 eV for the growth of the heterostructure.

different alloy compositions lattice-matched to InAs can provide a clear trend line for monitoring the ratios for both the group III and group V elements using the reflectance and RAS data in conjunction.

Oscillations in the reflectance data can be used to calculate the growth rate and thickness of the layers grown and can also be used for determination of the alloy composition for multicomponent layers. The oscillation in the reflectance data occurs due to change in thickness of the epilayer resulting in the interference of optical beam as they reflected from the interface and surface. The thickness of the layer represented by the period of the oscillations is a function of the dielectric constants of the growing layer and the wavelength used. For optically thick materials, these oscillations disappear altogether. Fig. 6 shows the reflectance data extracted at 1.5 eV for the structure grown as represented in Fig. 5. Clear oscillations can be seen for the growth of the various layers with the exception of the first InAs buffer layer. The oscillation is absent for homoepitaxial growth as there is no difference in dielectric constants between the substrate and epitaxial film. Each layer was fitted for n, k and growth rate, the results of which are shown in the Table 1 giving values at 1.5 eV at growth temperature of around 500 °C. The growth rates agree with those determined by RHEED oscillations and high resolution x-ray diffraction measurements.

4. Conclusions

The capability of the RAS technique as an *in-situ* tool to monitor the MBE growth heterostructures has been demonstrated. In particular, this represents an important technique for the MBE development of the narrow gap InAs based heterostructures, critical for applications in a number of important device technologies, including infrared detectors and next generation CMOS transistors. The oxide desorption from the substrates was monitored spectrally from 1.5 eV to 5.0 eV and the data suggest that a single wavelength is sufficient for determining the complete removal of the native oxide. In addition, the surface reconstruction during growth was monitored to determine whether InAs was being grown under In-rich or As-rich conditions. Both the RAS and reflectance signals were sensitive to alloy composition and to some extent doping. Fitting the reflectance data, the growth rates and optical constants of the individual layers were extracted. The growth temperature was also measured using the RAS setup with the temperatures representing the emissivity corrected values that can be used with certainty during MBE growth of multilayer
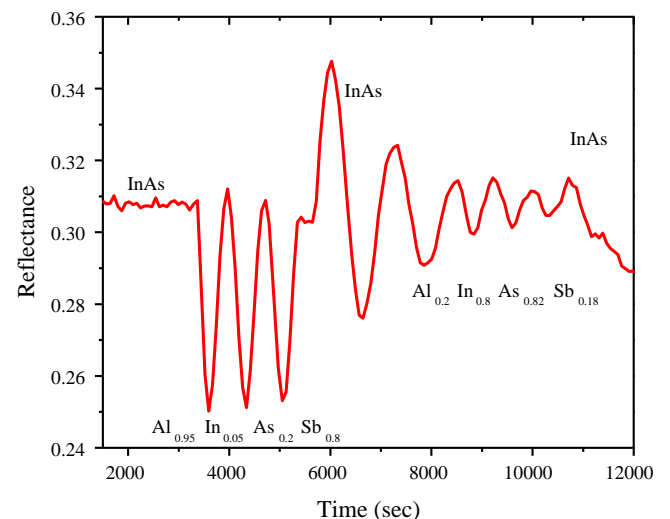
Fig. 6. Reflectance data taken at 1.5 eV for the structure shown in Fig. 5 in which the oscillations can be used for the fit for the optical parameters at growth temperature of the various layers and to determine a growth rate for each layer.

Table 1

Optical constants obtained for the various layers in Fig. 4(a) obtained by fitting oscillations in the reflectance data. Also shown is the calculated growth rate.

Layer	Refractive index (n)	Extinction coefficient (k)	Growth rate (μm/h)
$Al_{0.95}In_{0.05}As_{0.2}Sb_{0.8}$	3.499	0.016	0.54
InAs	3.679	0.433	0.32
$Al_{0.2}In_{0.8}As_{0.82}Sb_{0.18}$	3.742	0.29	0.52

structures. The data presented in this paper demonstrate the usefulness of the RAS technique for growth monitoring and possibly control. In addition to its application for monitoring layer growth during MBE, this all optical technique is also ideal for use in non-UHV deposition tools where it is not possible to use RHEED.

References

[1] A. Rogalski, Recent progress in infrared detector technologies, Infrared Phys. Technol. 54 (2011) 136.
[2] R. Chau, B. Doyle, S. Datta, J. Kavalieros, K. Zhang, Nat. Mater. 6 (2007) 810–812.
[3] J. Nah, H. Fang, C. Wang, K. Takei, M.H. Lee, E. Plis, S. Krishna, A. Javey, Nano Lett. 12 (2012) 3592.

[4] R. Contreras-Guerrero, S.W. Wang, M. Edirisooriya, W. Priyantha, J.S. Rojas-Ramirez, K. Bhuwalka, G. Doornbos, M. Holland, R. Oxland, G. Vellianitis, M. Van Dal, B. Duriez, M. Passlack, C.H. Diaz, R. Droopad, J. Cryst. Growth 378 (2013) 117.

[5] P. Ramvall, C.H. Wang, G. Astromskas, G. Vellianitis, M. Holland, R. Droopad, L. Samuelson, L.E. Wernersson, M. Passlack, C.H. Diaz, J. Cryst. Growth 374 (2013) 43.

[6] G.N. Maracas, J.L. Edwards, K. Shiralagi, K.Y. Choi, R. Droopad, B. Johs, J. Woollam, J. Vac. Sci. Technol. A 10 (1992) 1832.

[7] D.E. Aspnes, J.P. Harbison, A.A. Studna, L.T. Florez, J. Vac. Sci. Technol. A 6 (1988) 1327.

[8] W. Richter, J.T. Zettler, Appl. Surf. Sci. 100–101 (1996) 465.

[9] I. Kamiya, D.E. Aspnes, L.T. Florez, J.B. Harbison, Phys. Rev. B 46 (1992) 15894.

[10] W.G. Schmidt, N. Esser, A.M. Frisch, P. Vogt, J. Bernholc, F.B.M. Zorn, T. Hannappel, S. Visbeck, F. Willig, W. Richter, Phys. Rev. B 61 (2000) R16335.

[11] H. Tanaka, E. Colas, I. Kamiya, D.E. Aspnes, R. Bhat, Appl. Phys. Lett. 59 (1991) 3443.

[12] K. Knorr, A. Rumberg, M. Zorn, C. Meyne, T. Trepk, J.-T. Zettler, and W. Richter, P. Kurpas, M. Weyers, in: Proceedings of the 8th International Conference on InP and Related Materials, 1996, 590–593.

[13] J. Bubesh Babu, Kanji Yoh, Appl. Phys. Lett. 97 (2010) 072102.

[14] P. Wolfram, E. Steimetz, W. Ebert, B. Henninger, J.-T. Zettler, J. Cryst. Growth 248 (2003) 240–243.
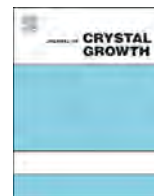
Reflectance-difference spectroscopy as a probe for semiconductor epitaxial growth monitoring

A. Lastras-Martínez [a,*], J. Ortega-Gallegos [a], L.E. Guevara-Macías [a], O. Nuñez-Olvera [a],
R.E. Balderas-Navarro [a], L.F. Lastras-Martínez [a], L.A. Lastras-Montaño [b],
M.A. Lastras-Montaño [c]

[a] Instituto de Investigación en Comunicación Optica, Universidad Autónoma de San Luis Potosí, Alvaro Obregón 64, San Luis Potosí, SLP 78000, México
[b] IBM T. J. Watson Research Center, Yorktown Heights, NY 10598, USA
[c] Department of Electrical and Computer Engineering, University of California, Santa Barbara, Santa Barbara, CA 93106, USA

ARTICLE INFO

ABSTRACT

We report on real-time reflectance-difference (RD) spectroscopic measurements carried out during the homoepitaxial grow of GaAs under As overpressures in the range from $P_{As} = 6 \times 10^{-7} - 5 \times 10^{-6}$ Torr. We found that the time-dependent RD spectrum is described in terms of two basic line shapes. One of these components is associated to the orthorhombic surface strain due to surface reconstruction while the second one has been assigned to surface composition. Results reported in this paper render RD spectroscopy as a powerful tool for the real-time monitoring of surface strains and its interplay with surface composition during growth.

1. Introduction

Reflectance-difference spectroscopy (RDS) is a noninvasive, contrasting technique that suppresses the bulk isotropic component of the optical reflectance spectrum of cubic semiconductors enhancing its surface-associated component. Both its noninvasive character and surface specificity make RDS a very attractive tool for monitoring the epitaxial growth of zincblende semiconductors, as it was first reported by Aspnes and collaborators [1]. The interpretation of reflectance-difference (RD) spectra, nevertheless, poses some challenges as the surface may become anisotropic for a number of physical mechanisms [2], including surface electric fields [3], α and β dislocations [4], surface reconstruction strains [5,6] and surface dimers [7,8]. At the same time, time-resolved RD spectra measured during epitaxial growth would lead to a great deal of information on the kinetics of epitaxial growth, provided we can resolve them into their different components and determine the time-evolution of such components during growth.

Previously we reported on real-time RDS of homoepitaxial GaAs (001) grown by molecular beam epitaxy (MBE) [9]. For the growth we employed a As overpressure (P_{As}) of 1×10^{-6} which led to a rich surface reconstruction evolution as growth progressed as well as to

considerable changes in RD spectrum line shape. We showed that the time-evolution of RD spectra during growth is well described in terms of two independent components, each with a specific physical origin. In this paper we report on the results of a study carried out within a range of As overpressures and demonstrate that our previous results can be extended to more general growth conditions.

2. Experimental details and results

Epitaxial growth was carried out on (001) GaAs substrates in a solid-source MBE chamber (Riber 32P). Epitaxial growth was carried out under four As overpressures (P_{As}) ranging from 6×10^{-7} to 5×10^{-6} Torr at a growth rates from 0.14 to 0.23 ML/s as determined from RHEED oscillations. Growth substrate temperature was 520 °C in all cases. Epitaxial growth was initiated/interrupted by opening/ closing the Ga shutter and lasted for about 45 s. Time-resolved spectroscopic RD measurements were performed with a rapid RD, 32-channel spectrometer attached to the epitaxial growth chamber. More details on the RD spectrometer are given elsewhere [10]. In order to correlate RD changes with surface reconstruction changes, RHEED patterns were acquired concurrently with RD spectra.

To prevent components associated to dislocations in the measured RD spectra, a 0.3 μm thick GaAs buffer layer was grown prior to carrying out the experiments. Further, to avoid electro-optical contributions that may hinder the analysis of the RD line shapes, we did not intentionally dope the GaAs films.

* Corresponding author.
  E-mail addresses: alm@cactus.iico.uaslp.mx,
alastras@gmail.com (A. Lastras-Martínez).
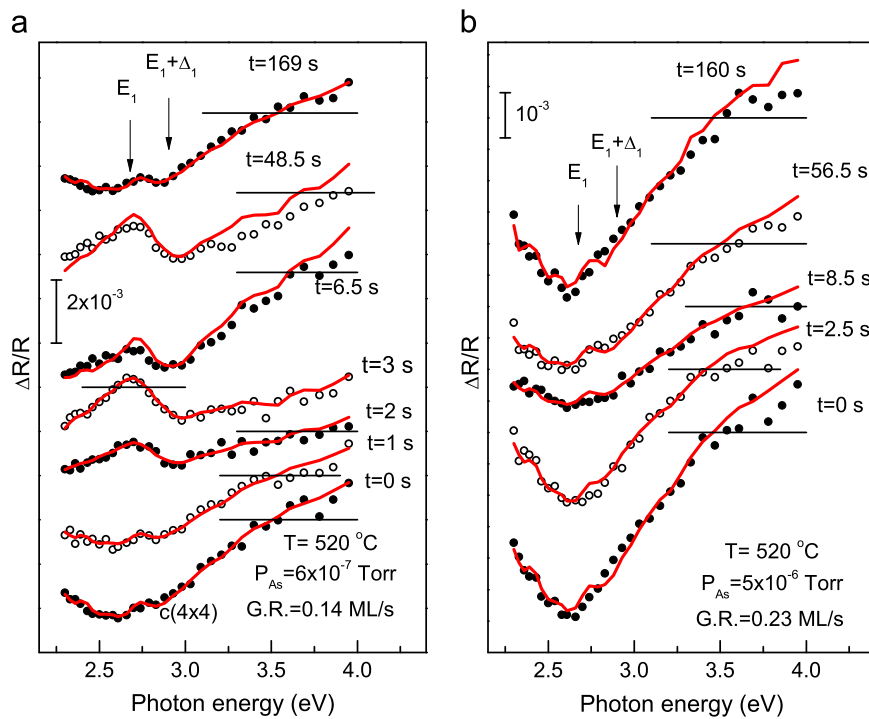
Fig. 1. Filled and open circles: representative time-resolved RD spectra during MBE GaAs homoepitaxy for two As overpressures. Panels (a) and (b) correspond to 6×10^{-7} Torr and 5×10^{-6} Torr, respectively. Growth temperature and growth rate are as indicated. Spectra have been displaced vertically for the sake of clarity with zeros as indicated with horizontal lines. Growth started at $t=0$ and was interrupted at $t=44.5$ s. Time shown next to each spectrum corresponds to time elapsed after starting growth. Lowermost spectra in both panels were measured just before starting growth, while uppermost spectra were measured long after closing the Ga shutter. Continuous lines correspond to line shapes synthesized in terms of two the basic line shape components $S_1(E)$ and $S_2(E)$ as discussed in the text.

In Fig. 1 we show time-resolved RD spectra of GaAs homoepitaxy for (a) $P_{As} = 6 \times 10^{-7}$ Torr and (b) $P_{As} = 5 \times 10^{-6}$ Torr. Lowermost spectra in both cases correspond to GaAs surfaces under As flux, just before starting growth. For $P_{As} = 6 \times 10^{-7}$ the evolution of the RD spectrum is rather involved. This is in correspondence with the evolution of the GaAs surface reconstruction which changes from $c(4 \times 4)$ before starting growth, to (2×4) after the deposition of about 0.5 ML GaAs, and to a Ga-rich (4×2) phase after steady state growth is reached. In comparison, the RD spectrum evolution for $P_{As} = 5 \times 10^{-6}$ Torr is simpler according to the less varied surface reconstruction changes. We note, nevertheless, that irrespective of P_{As} values, there is a change in RD spectrum line shape as growth progresses.

3. RD line shape analysis

The rather complex evolution of RD spectra during epitaxial growth is indicative that they comprise at least two components, each one with its own time-evolution. We may further expect these two components to result from different physical processes. As reported previously [9], a Singular Value Decomposition (SVD) [11] analysis of the experimental, time-dependent RD spectra measured during MBE GaAs homoepitaxial growth shows that for $P_{As} = 1 \times 10^{-6}$ the RD spectrum is written in terms of two independent components, allowing thus write

$$\frac{\Delta R}{R} = c_1(t)S_1(E) + c_2(t)S_2(E), \tag{1}$$

where $\Delta R/R$ is the experimental RD spectrum, $S_1(E)$ and $S_2(E)$ are independent line shape components, each one associated to a specific physical mechanism, and $c_1(t)$ and $c_2(t)$ are coefficients that account for the time-evolution during growth of components $S_1(E)$ and $S_2(E)$, respectively.
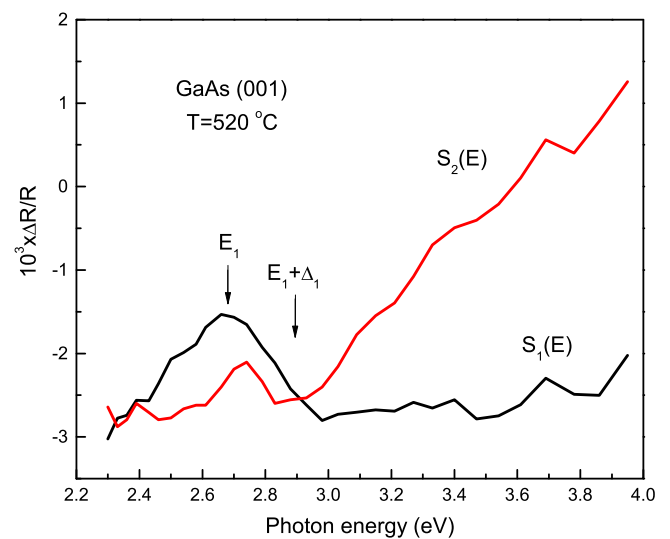
Fig. 2. $S_1(E)$ and $S_2(E)$ line shapes employed to model the time-dependent RD experimental spectra. These line shapes were obtained from a SVD analysis of time-dependent RD spectra measured during the MBE homoepitaxial growth of GaAs under a 1×10^{-6} Torr As overpressure.

Provided we have access to $S_1(E)$ and $S_2(E)$ line shapes, as well as to their physical interpretation, a great deal of information on epitaxial growth dynamics may be obtained from the fitting of Eq. (1) to real-time RD spectra. In this regard, we note that while the SVD analysis yields by construction orthogonal independent line shapes, in our case these line shapes may correspond to linear combinations of $S_1(E)$ and $S_2(E)$ and may have therefore a mixed physical origin.

Previously we took advantage of the substantial changes in RD line shape that occur during the homoepitaxial growth of GaAs
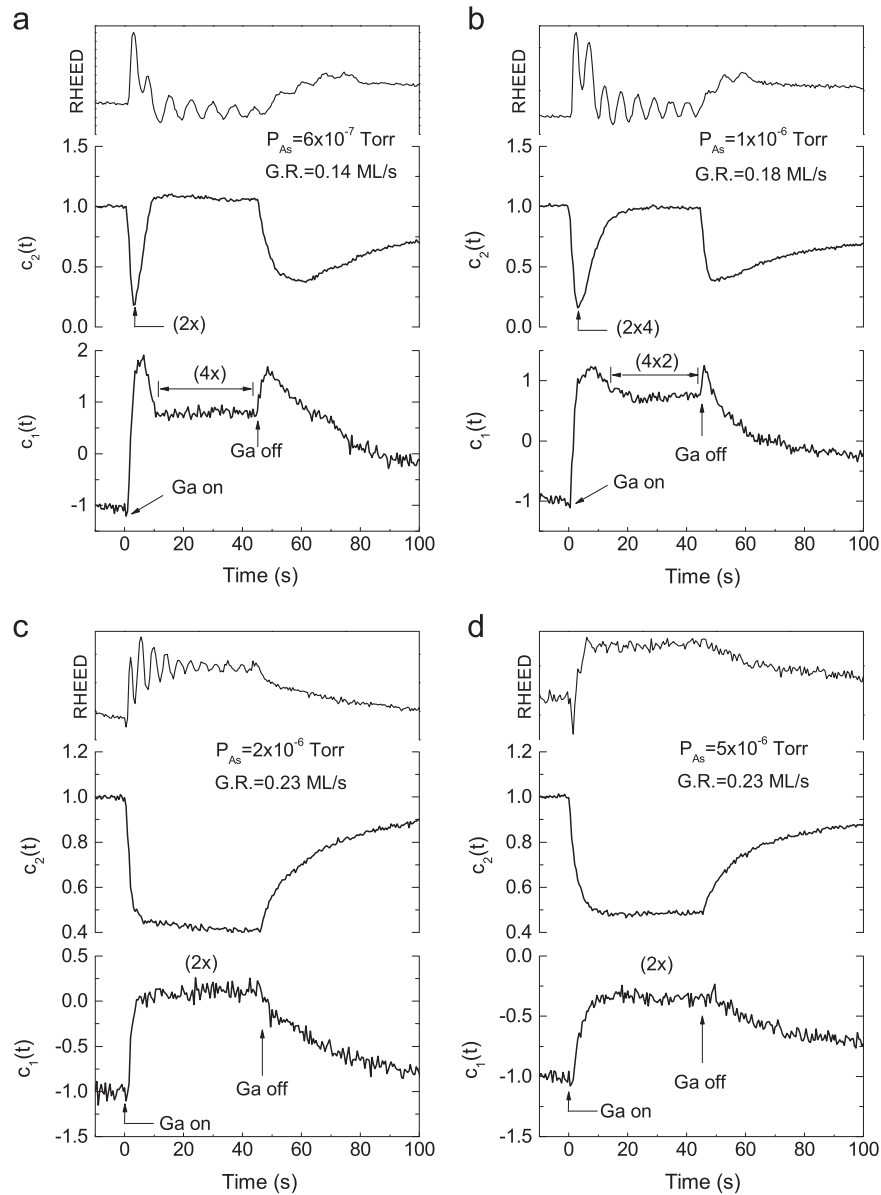
Fig. 3. Time evolution of coefficients $c1(t)$ and $c2(t)$ upon opening and closing the Ga shutter. Arsenic overpressures are as indicated. Surface reconstruction before opening the Ga shutter to start growth was $c(4 \times 4)$. At the top of each panel the corresponding amplitude of the RHEED specular reflection is shown. Upon opening the Ga shutter a transient in surface reconstruction is observed.

under low As overpressure conditions to identify two independent $S_1(E)$ and $S_2(E)$ components with specific physical origins [9]. $S_1(E)$ was found to be associated to the surface strain induced by surface reconstruction and has a resonant-like line shape with prominent optical features around E_1 and $E_1 + \Delta_1$ transitions. $S_2(E)$ has an energy-extended line shape and was suggested to be associated to surface stoichiometry. $S_1(E)$ and $S_2(E)$ line shapes are shown in Fig. 2. They were obtained from a SVD analysis of time-dependent RD spectra measured during the MBE homoepitaxial growth of GaAs as discussed elsewhere [9].

Continuous lines in Fig. 3 correspond to spectra synthesized on the basis of Eq. (1) employing the $S_1(E)$ and $S_2(E)$ line shapes shown in Fig. 2. As it can be seen, for both higher and lower pressure growth Eq. (1) accounts for all the essential features of the time-resolved RD spectra. Namely, (1) the resonant structure around E_1 and $E_1 + \Delta_1$ and (2) the extended broad-energy line shape. The largest discrepancy between the experimental spectra and the modeled spectra, which is, nevertheless, rather small, occurs for a few spectra measured just after closing the Ga shutter, the worst case being illustrated by the spectrum

corresponding to $t = 48.5$ s in Fig. 1. This result shows that the basic $S_1(E)$ and $S_2(E)$ line shapes obtained for $P_{As} = 1 \times 10^{-6}$ Torr work as well for both lower and higher As fluxes.

4. Discussion and conclusions

Fitting Eq. (1) to time-resolved RD spectra yields both $c_1(t)$ and $c_2(t)$ coefficients. In Fig. 3 we plot these coefficients as a function of time for the four studied As overpressures as indicated. Transients are observed for both $c_1(t)$ and $c_2(t)$ upon opening/closing the Ga shutter to initiate/interrupt epitaxial growth. At the top of each panel of Fig. 3 we further show the amplitude of the specular RHEED spot. Fig. 3 shows that for $P_{As} \leq 1 \times 10^{-6}$ Torr the time evolution of coefficients $c_1(t)$ and $c_2(t)$ is more involved than for $P_{As} \geq 2 \times 10^{-6}$. This is in agreement with the three-step $c(4 \times 4) \rightarrow (2 \times 4) \rightarrow (4 \times 2)$ transformation in surface reconstruction observed during growth for $P_{As} \leq 1 \times 10^{-6}$ Torr. For $P_{As} \geq 2 \times 10^{-6}$ Torr, in contrast, the Ga-rich (4×2) reconstruction is never reached and the GaAs surface

remains As-rich all along growth. We further note that for $P_{As} \leq 1 \times 10^{-6}$ Torr (two upper panels in Fig. 3) the time-evolution of coefficient $c_1(t)$ is qualitatively different from that of $c_2(t)$. This result indicates that $S_1(E)$ and $S_2(E)$ are no correlated, in spite of the fact that both components respond to changes in the surface composition occurring upon opening or closing the Ga shutter. In what follows we discuss the results shown in Fig. 3.

We will first consider coefficient $c_1(t)$. As reported previously, coefficient $c_1(t)$ corresponds to the RD component associated to the surface strain due to surface reconstruction [9]. In this regard, it is known that due to the preferential orientation of surface dimers, surface reconstruction induces an orthorhombic strain in the near-surface region of GaAs thus leading to a surface anisotropy [5]. Accordingly, as shown in Fig. 3a and b, for $P_{As} \leq 1 \times 10^{-6}$ Torr coefficient $c_1(t)$ swings from negative to positive values as surface reconstruction changes from $c(4 \times 4)$ to (2×4), which is consistent with the 90° rotation of the GaAs As dimers upon the $c(4 \times 4) \rightarrow (2 \times 4)$ surface transformation [12]. Further, Fig. 3a and b shows that the value of coefficient $c_1(t)$ decreases upon the $(2 \times 4) \rightarrow (4 \times 2)$ transformation. No zero crossing was observed, nevertheless, as it could had been expected for a surface changing from As-rich to Ga-rich. Upon closing the Ga shutter $c_1(t)$ rises sharply as the surface becomes As-rich and then decreases slowly towards stabilization.

For $P_{As} \geq 2 \times 10^{-6}$, as pointed out above, the high Arsenic flux prevents the surface from becoming Ga-rich (as a matter of fact, it even prevents its full transformation to the (2×4) phase). As a result, as Fig. 3c and d shows, coefficient $c_1(t)$ does not change sign during growth. How close to zero $c_1(t)$ becomes depends on how low P_{As} is. After the end of growth $c_1(t)$ rises slowly and reaches a steady state value at a time $t > 100$ s.

Regarding coefficient $c_2(t)$, we point out that while the physical origin of spectrum $S_2(E)$ is not fully understood at present, it may be associated to surface stoichiometry as suggested previously [9]. In agreement with this hypothesis, Fig. 3a and b shows that for $P_{As} \leq 1 \times 10^{-6}$ coefficient $c_2(t)$ decreases rapidly after starting growth, reaching a minimum when the sharpest (2×4) RHEED pattern is observed. Afterwards, $c_2(t)$ increases gradually and attains a constant value as steady state growth is reached. Upon closing the Ga shutter, $c_2(t)$ first decreases sharply and then gradually recovers. Thus, coefficient $c_2(t)$ follows closely the various changes in surface composition taking place during growth.

For $P_{As} \geq 2 \times 10^{-6}$, as Fig. 3c and d shows, the time evolution of coefficient $c_2(t)$ is simpler as changes in surface stoichiometry are not that varied. Upon starting growth, $c_2(t)$ sharply decreases and then remain approximately constant. After closing the Ga shutter $c_2(t)$ slowly rises to recover its starting value.

We note that not taking into account RHEED oscillations, the time-dependence of the intensity of the specular RHEED spot mimics that of coefficient $c_2(t)$, albeit multiplied by minus one. This is true for low as well as for high As overpressures. This adds further support the association of the $S_2(E)$ component with the surface composition.

In conclusion, we carried out real-time RD spectroscopic measurements during the homoepitaxial grow of GaAs under As overpressures in the range from $P_{As} = 6 \times 10^{-7} - 5 \times 10^{-6}$ Torr. We found that the time-dependent RD spectrum is described in terms of two basic line shapes, which are the same independently of P_{As}. One of these components is associated to the orthorhombic surface strain due to surface reconstruction while the second one has been assigned to surface composition. Results reported in this paper render RD spectroscopy as a powerful tool for monitoring the epitaxial growth of zincblende semiconductors as well as for the study of the kinetics of epitaxial growth processes. In particular, it allows for the real-time monitoring of surface strains and its interplay with surface composition during growth.

Acknowledgments

References

[1] D.E. Aspnes, J.P. Harbison, A.A. Studna, L.T. Florez, Phys. Rev. Lett. 59 (1987) 1687.
[2] See for instance P. Weightman, D.S. Martin, R.J. Cole, T. Farrell, Rep. Prog. Phys. 68 (2005) 1251, and references therein.
[3] S.E. Acosta-Ortiz, A. Lastras-Martínez, Phys. Rev. B 40 (1989) 1426.
[4] L.F. Lastras-Martínez, A. Lastras-Martínez, Solid State Commun. 98 (1996) 479; L.F. Lastras Martínez, A. Lastras-Martínez, Phys. Rev. B 54 (1996) 10,726.
[5] L.F. Lastras-Martínez, D. Ronnow, P.V. Santos, M. Cardona, K. Eberl, Phys. Rev. B 64 (2001) 245303.
[6] K. Hingerl, R.E. Balderas-Navarro, W. Hiber, A. Bonanni, D. Stifter, Phys. Rev. B 62 (2000) 13048.
[7] Yia-Chung Chang, Shang-Fen Ren, D.E. Aspnes, J. Vac. Sci. Technol. A 10 (1992) 1056.
[8] A.I. Shkrebtii, N. Esser, W. Richter, W.G. Schmidt, F. Bechstedt, B.O. Fimland, A. Kley, R. Del Sole, Phys. Rev. Lett. 81 (1998) 721.
[9] A. Lastras-Martínez, J. Ortega-Gallegos, L.E. Guevara-Macías, O. Núñez-Olvera, R. Balderas-Navarro, L.F. Lastras-Martínez, L.A. Lastras-Montaño, M.A. Lastras-Montaño, Appl. Phys. Lett. Mater. 2 (2014) 032107.
[10] O. Núñez-Olvera, R.E. Balderas-Navarro, J. Ortega-Gallegos, L.E. Guevara-Macías, A. Armenta-Franco, M.A. Lastras-Montaño, L.F. Lastras-Martínez, A. Lastras-Martínez, Rev. Sci. Instrum. 83 (2012) 103109.
[11] G.H. Golub, C.F. Van Loan, Matrix Computations, 3rd edition, Johns Hopkins University Press, Baltimore, MD, USA, 1996.
[12] See for instance A. Ohtake, Surf. Sci. Rep 63 (2008) 295.

CrossMark
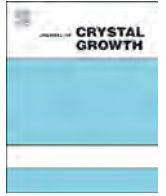
Control of anion incorporation in the molecular beam epitaxy of ternary antimonide superlattices for very long wavelength infrared detection

H.J. Haugan [a,*], G.J. Brown [a], S. Elhamri [b], L. Grazulis [a]

[a] Air Force Research Laboratory, Materials and Manufacturing Directorate, Wright-Patterson Air Force Base, Ohio 45433, United States
[b] Department of Physics, University of Dayton, Ohio 45469, United States

A B S T R A C T

Authors discuss how anion incorporation was controlled during the epitaxial growth process to develop InAs/GaInSb superlattice (SL) materials for very long wavelength infrared applications. A SL structure of 47.0 Å InAs/21.5 Å $Ga_{0.75}In_{0.25}Sb$ was selected to create a very narrow band gap. Although a molecular beam epitaxy growth developed can produce a strain balanced ternary SL structure with a precisely controlled band gap around 50 meV, the material quality of grown SL layers is particularly sensitive to growth defects formed during an anion incorporation process. Since Group III antisites are the dominant structural defects responsible for the low radiative efficiencies, the authors focus on stabilizing III/V incorporation during SL layer growth by manipulating the growth surface condition for a specific anion cracking condition. The optimized ternary SL materials produced an overall strong photoresponse signal with a relatively sharp band edges and a high mobility of $\sim 10{,}000$ cm^2/V s that is important for developing infrared materials.

© 2015 Elsevier B.V. All rights reserved.

1. Introduction

The InAs/GaInSb superlattice (noted as "ternary SL") system provides several distinctive theoretical advantages suitable for very long wavelength infrared (VLWIR) detection [1]. With increasing indium composition, a very narrow band gap can be achieved with a smaller period for the ternary SL system, leading to a larger absorption coefficient due to enhanced electron and hole wavefunction overlap [2]. More importantly, the strain can create a large splitting between the heavy-hole and light-hole bands in the ternary SLs, which reduces the hole–hole Auger recombination process and increases the minority carrier lifetime, thus improving the device detectivity. Based on minimizing the Auger recombination, Grein et. al. [3] proposed a strain balanced VLWIR ternary SL of 47.0 Å InAs/21.5 Å $Ga_{0.75}In_{0.25}Sb$, which is the design used in our studies. Haugan et al. [4,5] have shown improvements in the quality of the ternary materials produced using molecular beam epitaxy (MBE) growth process for this design. Their optimized SL materials produced a strong photoresponse signal, a high mobility, and a long 300 K carrier lifetime. Although longer carrier lifetimes have been reported in mid-wave

InAs/InAsSb (noted as "Ga-free") SLs [6], unfortunately to strain balance these Ga-free SLs in a VLWIR design requires a much wider period, ~ 147 Å [7] versus the 68.5 Å used in this study, significantly impacting the absorption coefficient. Therefore, the ternary SL materials are still important for VLWIR detection.

In this work, using a combination of high-resolution X-ray diffraction (HRXRD), atomic force microscopy (AFM), temperature-dependent Hall (TdH) effect, and photoconductivity measurements, we continuously refined the MBE process and tuned growth conditions to produce high-quality ternary SL materials to be used for VLWIR detection. Since most MBE-grown III–V heterostructures are affected by a large number of growth defects generated during the III–V surface reconstruction process, we optimized the III/V stoichiometry by manipulating the growth surface condition such as anion fluxes, Sb cracking condition, and growth temperature. We used a SL structure of 47.0 Å InAs/21.5 Å $Ga_{0.75}In_{0.25}Sb$ to create the band gap around 50 meV.

2. Ternary superlattice growths

The InAs/GaInSb SL materials in this study were grown in a Varian MBE reactor equipped with dual-filament effusion cells for the Group III elements, and valved cracker cells for the Group V elements. The repeated SL stacks (0.5 μm-thick) and the undoped

* Corresponding author.
  E-mail address: heather.haugan.ctr@us.af.mil (H.J. Haugan).

GaSb buffer layer (0.5 μm-thick) were deposited on GaSb (100) wafers, and several series of 47.0 Å InAs/21.5 Å Ga$_{0.75}$In$_{0.25}$Sb SL samples were grown over a wide range of anion flux conditions to preset the growth rates of Group III elements and the V/III flux ratio. To grow the intended ternary structure under minimum cross contamination environment of the anion fluxes, the V/III beam equivalent pressure (BEP) ratio was set at ∼3 for both GaInSb and InAs layer depositions and the growth rates of 1.6 and 0.3 Å/s were used for GaInSb and InAs layers, respectively. The Sb cracking zone temperature was varied between 850 and 1000 °C in order to investigate the III-Sb incorporation during a growth, while the As cracking zone temperature was set at 900 °C. Fig. 1 shows a typical strain-balanced ternary structure with an excellent crystalline quality that can be achieved by using the shutter sequence described in the inset of Fig. 1. With measured period of 68.0 Å, the grown structure produced a band gap of 53 meV, or a

corresponding onset wavelength of 23 μm, as demonstrated in the photoresponse (PR) spectrum in Fig. 2.

3. Results and discussions

In order to stabilize the III-Sb incorporation, a comparative deposition temperature (T_g) study was performed using various Sb cracking conditions to generate beams of tetramers, dimers, and monomers. Although some studies showed that a nearly 100% yield of Sb monomers can be achieved at a cracker temperature above ∼1100 °C [8,9], no systematic study has been done to determine Sb mole fraction as a function of cracker temperature for our EPI Model 200 cc Mark V Corrosive Series Valved Cracker. Since the most obvious effect one would expect from a III/V ratio not equal to one is morphological disorder induced by the nucleation of surface defects, we used 50 μm × 50 μm area scans by AFM to monitor surface roughness as a function of the T_g. For a series of samples grown under a low Sb cracking condition (Sb cracker temperature of 850 °C), the SL roughens very quickly as the T_g is increased above 420 °C. Fig. 3 top shows the apparent surface damage observed by AFM for the sample grown at the highest T_g of 440 °C. The root-mean-square (RMS) value quickly changes from 2 to 61 Å as the T_g increases from 420 to 430 °C and further increases up to 80 Å at higher temperatures highlighting the noticeable surface damage that occurred at 430 °C and above. While the exact surface pitting mechanism is undetermined, it is common to see pitted surfaces in the SL layers grown under a metal-rich condition due to the higher desorption rate of anion fluxes at the growth surfaces [10].

To relate the observed surface pitting phenomena to the spectral response, low temperature photoconductivity measurements were performed and Fig. 4d plots their results. The PR spectra were collected with fourier transform infrared spectrometer over a wavelength range from 2 to 50 μm at a temperature of 10 K. Due to the relatively low resistivity of the samples, the photoconductivity was measured in the current-biased mode, with a current of 0.5 mA between two parallel strip contacts on the surface. The PR intensities in Fig. 4d were measured at 100 meV above the onset. Although these intensities are given in arbitrary units (a.u.), the relative signal strengths can still be compared as the test conditions for all the samples were kept constant. The typical band gap energies of SLs grown at the same low T_g were around 48 ± 5 meV. However for $T_g > 420$ °C, the band gap did increase, as listed in Table 1. The PR intensity gradually decreases from 1.07 to 0.8 a. u. as T_g increases from 410 to 420 °C, when SL layers were grown under low Sb cracking condition generating low fraction of Sb monomers. The result of much lower PR intensity for the samples deposited at high temperatures does follow the severe surface damage trend observed in AFM scans.

Although there is a variety of ways of controlling surface roughness, such as by increasing V/III flux ratio, we increased Sb cracker temperature to generate more Sb monomers to enhance III-Sb incorporation. For a series of samples grown under high Sb cracking condition (Sb cracker temperature of 950 °C), the SL layers were deposited without any noticeable surface defects at temperature as high as 470 °C. Fig. 4a plots the RMS values as a function of T_g from SL samples grown with the Sb cracker at 950 °C. In contrast to the AFM results observed in Fig. 3 top, there were no significant changes in the RMS roughness for the SL samples deposited at T_g between 410 and 450 °C, and the RMS values remained in a range of ∼3 Å. Although there were no noticeable surface damages occurring at elevated temperatures (see Fig. 3 bottom), the PR signal strength was still affected by T_g. Fig. 4d indicates that the PR intensity gradually increases as T_g
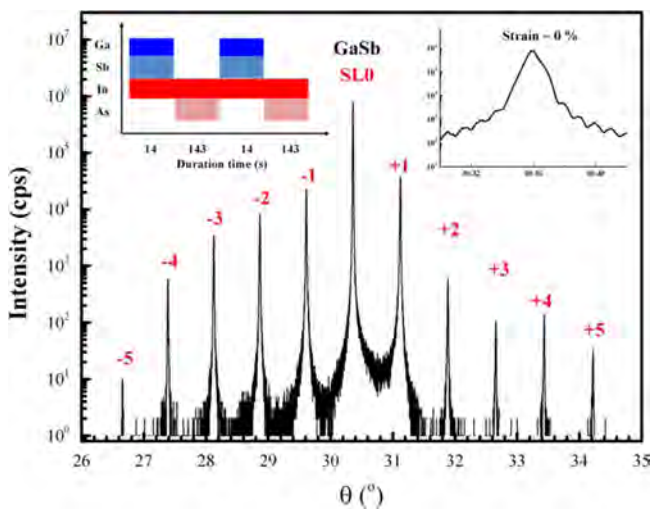
Fig. 1. X-ray diffraction patterns of a 68.0 Å period superlattice (SL) sample containing a 0.5 μm thick 47.0 Å InAs/21.5 Å Ga$_{0.75}$In$_{0.25}$Sb SLs. Inset is the shutter sequence employed to create a strain-balanced ternary structure.
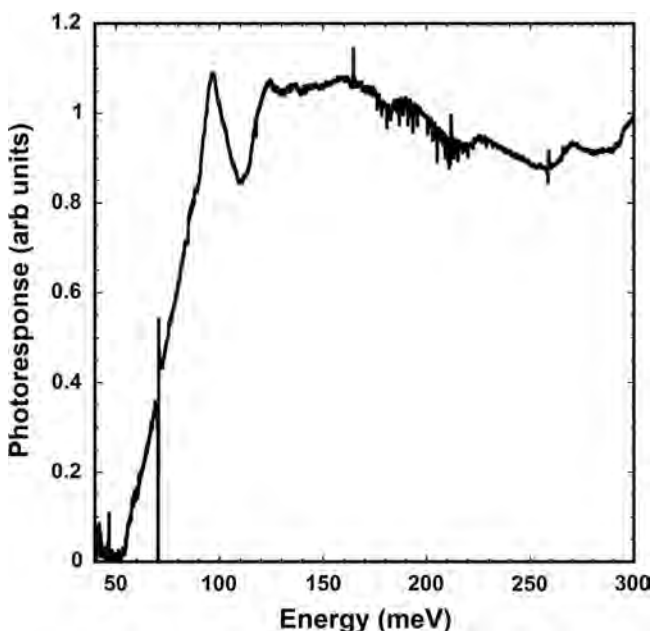
Fig. 2. Photoresponse spectrum at 10 K for the 47.0 Å InAs/21.5 Å Ga$_{0.75}$In$_{0.25}$Sb superlattices.
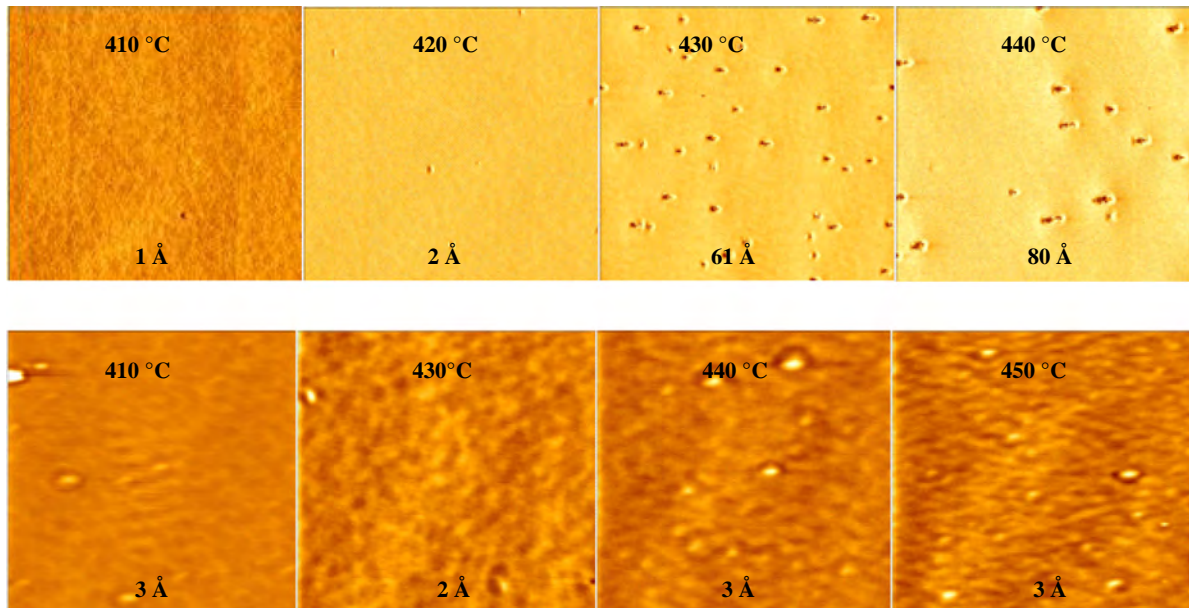
Fig. 3. AFM images of 50 μm × 50 μm area scans of 0.5 μm thick 47.0 Å InAs/21.5 Å Ga$_{0.75}$In$_{0.25}$Sb superlattices grown at substrate temperature (T_s) of 410–450 °C (from left to right) performed under (top) antimony cracking temperature of 850 °C and (bottom) 950 °C, respectively. The value listed on the top (the bottom) of each image represents a T_s (an average root-mean-square roughness).
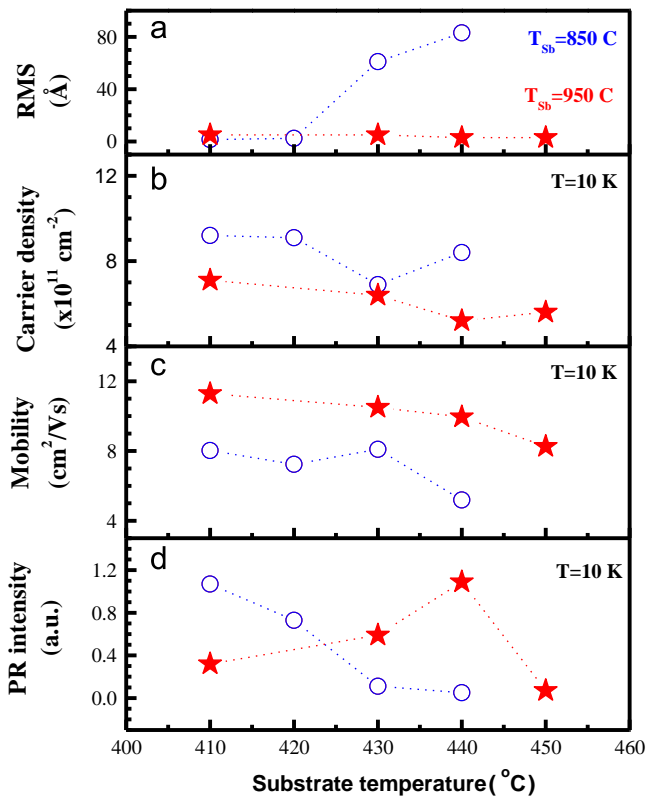
Fig. 4. (a) The root-mean-square (RMS) of 50 μm × 50 μm scans in AFM, (b) the 10 K carrier density, (c) mobility, and (d) photoresponse (PR) intensity as a function of substrate temperature for the sample series grown under antimony cracker temperature of 850 (open red circle) and 950 °C (closed blue star). For interpretation of the references to color in this figure legend, the reader is referred to the web version of this article.

Table 1
Summary of the measurements results for the sample set. The photoresponse (PR) results are from measurements at 10 K. The cut-off wavelength λ_c is selected at the point, where the PR intensity drops by 50 %. The PR intensity was measured at 100 meV above the band gap. Antimony cracker temperature and growth temperature were noted by T_{Sb} and T_s, respectively.

Sample	T_{Sb} (°C)	T (°C)	P (Å)	E_g (meV)	λ_c (μm)
SL1	850	410	68.0	53	16.4
SL2	850	420	68.0	53	16.7
SL3	850	430	68.2	62	14.7
SL4	850	440	67.0	80	13.8
SL5	950	410	67.5	44	20.1
SL6	950	430	68.0	46	19.0
SL7	950	440	67.5	53	17.0
SL8	950	450	68.6	50	16.2

correlated to the III-Sb stoichiometry during a growth and depend directly to the quality of grown layers.

In addition to the spectral PR measurements, TdH measurements were also performed to track changes in the electrical properties under the various growth conditions. For the first series, the average sheet concentration was 8.4×10^{11} cm^{-2} at 10 K and varied by only about 1×10^{11} cm^{-2}. All of the VLWIR samples were n-type. The average carrier mobility at 10 K was 7800 cm^2/V s for the first three samples but dropped to 5190 cm^2/V s at the 440 °C of T_g. While this agrees with the lowest PR result, we do not see a matching trend of degrading Hall results with increasing T_g similar to the AFM or PR intensity trends. The TdH measurements appear to be less sensitive to growth defects. The photoresponse on the other hand is very sensitive to growth defects and recombination centers. Still the Hall results do indicate when growth improvements have been made, which either decrease intrinsic carrier concentration or increase mobility, or both. For instance, for the second series of samples with the 950 °C cracker temperature, the average carrier concentration was 6.0×10^{11} cm^{-2} at 10 K, which is lower than in the first set. For the second set, the average mobility was 10,600 cm^2/V s at 10 K for

increases from 410 to 440 °C, reaching a maximum at 440 °C, and then drops rapidly to less than 0.1 a.u. at 450 °C. This is in contrast to the first series, where the PR was very low at 440 °C. Evidently deposition temperature and Sb cracking condition are intimately

the three samples with $T_g \leq 440\ °C$ and the 10 K mobility dropped to 8500 cm^2/V s. In this case the Hall measurements are similar to the AFM trend of very little change in the RMS roughness but again do not track the changes in the PR.

4. Conclusions

In summary, there is a complex interplay between growth temperature, and flux condition during the MBE growth of type-II ternary superlattices. This makes determining the optimum growth conditions non-trivial. This report focused on the optimization of anion incorporation conditions, by manipulating anion fluxes, anion species, and growth temperature (T_g). As shown, changes in the Sb cracker temperature (T_{Sb}) selectively impact the T_g, where the photoresponse was optimized. At $T_{sb} = 850\ °C$, the photoresponse was the strongest at 410 °C, while at $T_{sb} = 950\ °C$ the photoresponse was optimum at 440 °C. The inherent residual carrier concentration was slightly decreased in samples grown with the higher Sb cracker temperature and the electron mobility was higher. However, changes in the Hall and photoresponse measurements as a function of deposition conditions are very different. One of the key differences between these two experiments would be the impact of carrier recombination and lifetime on the results. The AFM results were a better indicator of the PR results. The average surface roughness of SL samples that produce a strong photoresponse was around 3 Å.

References

[1] D.L. Smith, C. Maihiot, Rev. Mod. Phys. 62 (1990) 173.
[2] H. Kroemer, Physica E 20 (2004) 196.
[3] C.H. Grein, W.H. Lau, T.L. Harbert, M.E. Flatté, Proc. SPIE 4795 (2002) 39.
[4] H.J. Haugan, G.J. Brown, S. Elhamri, W.C. Mitchel, K. Mahalingam, M. Kim, G.T. Noe, N.E. Ogden, J. Kono, Appl. Phys. Lett. 101 (2012) 171105.
[5] Heather J. Haugan, Gail J. Brown, Krishnamurthy Mahalingam, Larry Grazulis, Gary T. Noe, Nathan E. Ogden, Junichiro Kono, J. Vac. Sci. Technol. B 32 (2014) 2C109.
[6] B.V. Olson, E.A. Shaner, J.K. Kim, J.F. Klem, S.D. Hawkins, L.M. Murray, J.P. Prineas, M.E. Flatté, T.F. Boggess, Appl. Phys. Lett. 101 (2012) 052106.
[7] A.M. Hoang, G. Chen, R. Chevallier, A. Haddadi, M. Razeghi, Appl. Phys. Lett. 104 (2014) 251105.
[8] P.D. Brewer, D.H. Chow, R.H. Miles, J. Vac. Sci. Technol. B **14** (1996) 2335.
[9] R.H. Miles, D.H. Chow, Y.H. Zhang, P.D. Brewer, R.G. Wilson, Appl. Phys. Lett. 66 (1995) 1921.
[10] B.Z. Nosho, B.R. Bennett, L.J. Whitman, M. Goldenbergen, J. Vac. Sci. Technol. B 19 (2001) 1626.
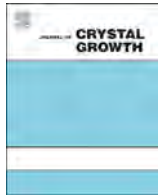
Growth of InAs–InAsSb SLS through the use of digital alloys

T. Schuler-Sandy *, B. Klein, L. Casias, S. Mathews, C. Kadlec, Z. Tian, E. Plis, S. Myers, S. Krishna **

Center for High Technology Materials, Department of Electrical and Computer Engineering, University of New Mexico, Albuquerque, NM 87106, USA

ARTICLE INFO

ABSTRACT

In order to improve the stability and repeatability of the growth of InAs–InAsSb (Ga-free) superlattices (SLs), we have investigated the use of an InAs–InSb digital alloy in place of the InAsSb ternary material. We report on a PIN structure made from Ga-free SL material grown using the digital alloy method, and compare the results to a reference PIN device composed of the InAs–InAsSb SL. The results for both devices show $\lambda_{\text{cutoff,0\%}} = 5\,\mu\text{m}$ at $T = 80\,\text{K}$, which is in agreement with the 14 ML InAs–12 ML InAs$_{0.81}$Sb$_{0.19}$ SL design used. At $T = 80\,\text{K}$ and a bias voltage of $V_b = -0.01\,\text{V}$ ($V_b = -0.25\,\text{V}$), the average dark currents (from 5 measured devices for each sample) for the ternary and digital alloy based devices are 0.1315 (4.249) A/cm^2 and 0.1068 (3.522) A/cm^2, respectively. The quantum efficiencies under the same conditions are 24.1% (24.0%) for the ternary and 39.7% (39.9%) for the digital alloy. This improvement in quantum efficiency is attributed to superior crystalline quality in the digital alloy sample. These initial results show that the digital alloy sample is comparable to or better than the reference sample in each tested metric, and thus is worthy of further investigation.

© 2015 Elsevier B.V. All rights reserved.

1. Introduction

Strained-layer superlattices (SLs) have become an increasingly active topic of research since their conception in the 1970s. The InAs–GaSb SL material system has demonstrated a long Auger lifetime, which makes it a promising candidate for improving on current HgCdTe (MCT) devices [1,2]. However, devices made from this material system have not shown the expected improvement due to a comparatively high level of Generation–Recombination (G–R) dark current. This G–R current arises from a low Shockley–Read–Hall (SRH) carrier lifetime [3–5], which is currently attributed to native defects in the GaSb layer [6]. The InAs–InAsSb (Ga-free) SL was developed to avoid the low lifetimes associated with the GaSb layer, and has shown significant improvement in SRH carrier lifetimes [7–10]. This is expected to result in improved performance in infrared detectors made from this material.

One downside to the Ga-free SL material arises from the ternary material (InAsSb) present in the system. Since III–V materials are generally grown under group V rich conditions, balancing the incorporation of two group V materials requires great care. This can become a problem if the system is not perfectly stable, since any

drift in either source beam equivalent pressure (BEP) values or in growth temperature can radically change the InAsSb material composition. This, in turn, causes unwanted changes to the Ga-free SL material properties.

Digital alloy materials were developed as a tool to alleviate the strong compositional dependence of mixed group V materials (such as InAsSb) on growth temperature and source BEP. The reduction in dependence on both of these parameters has been demonstrated in the literature [11]. For the Ga-free SL, this would mean a marked improvement in growth stability and repeatability, which is highly desirable for both research and production purposes. Improved crystalline quality in the Ga-Free SL obtained through the use of digital alloys has been demonstrated previously [12–15]. This paper provides some preliminary findings on the use of a digital alloy in place of the InAsSb ternary in a Ga-free SL infrared detector device, and compares the electrical characteristics of this device to a reference ternary-containing Ga-free SL device. This digital alloy, composed of 1.7 ML InAs–0.3 ML InSb, was grown by keeping the In shutter open and alternating the As and Sb shutters to provide the desired layer thicknesses.

2. Ga-free SL material growth considerations

In order to demonstrate the difficulties with As/Sb ternary materials, a series of Ga-free SL test samples with a 14 ML InAs–12 ML InAs$_{0.81}$Sb$_{0.19}$ design were grown using varying Sb BEPs and

growth temperatures. This design was used in previous studies [16,17], and thus provided a good candidate for this study. Once grown, high-resolution X-ray diffraction (XRD) was performed with a Phillips X-ray diffractometer using the Cu–K$_{\alpha 1}$ line. The peak separation between the substrate peak and the superlattice 0th order peak is measured in arcseconds in order to provide an indication of the degree of lattice mismatch present in the samples. This difference can also be expressed as $\Delta a/a$ by calculating each lattice constant using the measured XRD peaks. This is done using Bragg's law:

$$d = \frac{n\lambda}{2\,\sin(\theta)} \tag{1}$$

where θ values are in degrees and d is the material lattice constant (a) divided by 2 (calculated for the superlattice by using the 0th order peak). The lattice mismatch can then be calculated using

$$\Delta a/a = \frac{d_{0th} - d_{substrate}}{d_{substrate}} \tag{2}$$

This equation can then be re-written [18] as

$$\Delta a/a = \frac{\sin(\theta_{substrate})}{\sin(\theta_{substrate} + \Delta\theta)} - 1 \tag{3}$$

where $\theta_{substrate}$ is the angle in degrees of the substrate peak measured by XRD and $\Delta\theta$ is the angular difference between the substrate peak and the epitaxial peak (the 0th order SL peak in this case) in degrees. This does not take relaxation into account, and thus does not directly calculate the level of strain in the system. However, it is a good metric for determining whether the epilayer has achieved a good lattice match with the substrate. Epitaxial layers are generally considered lattice matched when the peak separation is below 100 arcseconds, or $|\Delta a/a| \lesssim 0.0825\%$ for GaSb substrates. The results for the Ga-free SL tests are shown in Fig. 1.

The degree of angular peak separation in the samples that appears even with slight variations in temperature or Sb BEP demonstrates the difficulty with growing the Ga-free SL with a high degree of repeatability. The dependence on these variations can also cause issues during long growth periods, since the source BEPs may drift slightly, thereby inducing undesired strain in the growth. In order to alleviate these issues, a digital alloy growth was employed as a replacement for the InAsSb ternary material. This replacement hinges on the digital alloy behaving similar to the ternary material, which means the electrical performance of the device grown using a digital alloy must be comparable to that of devices that use the ternary material traditionally present in Ga-free SL growth. This paper provides data on an initial attempt at growing a PIN device using the digital alloy method.
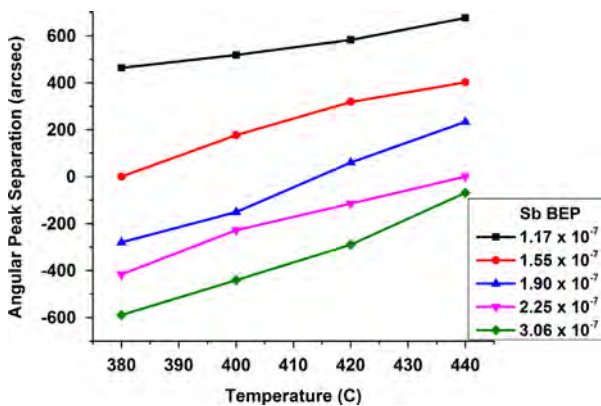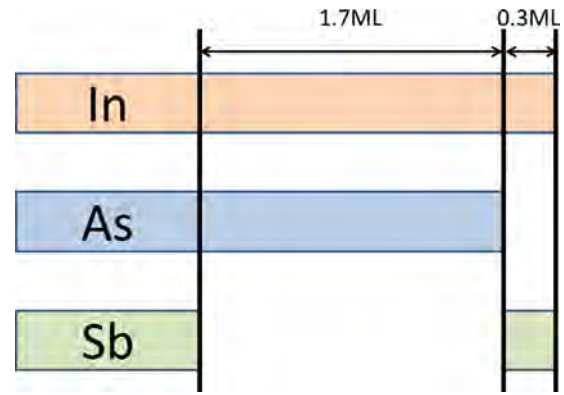
Fig. 2. Shuttering sequence used to grow the InAs/InSb digital alloy used to replace the InAsSb ternary material. The As shutter was closed just as the Sb shutter opened (and vice-versa), while the In shutter remained open throughout the growth.

3. Device growth and fabrication

Two Ga-free SL PIN homojunction devices were grown for this study, one reference ternary sample and one using a digital alloy in place of the InAsSb material. The PIN architecture was chosen to allow for device comparisons between these samples and previous results obtained for Ga-free SL devices. The sample growth was accomplished using a VG V80H reactor equipped with valved As and Sb crackers. In both cases, oxide desorption was performed by heating a GaSb:Te substrate to 540 °C for 30 min. After the desorption was completed, a 250 nm thick buffer layer of GaSb doped with Te at 2×10^{18} cm^{-3} was grown at 500 °C to smooth the surface prior to device growth. Each sample was composed of a 2 µm thick absorber doped at 3×10^{16} cm^{-3} p-type, and P and N contact layers each doped at 2×10^{18} cm^{-3}. Both samples were grown at 420 °C. For the reference sample, a material composition of 14 ML InAs–12 ML InAs$_{0.81}$Sb$_{0.19}$ was used. For the digital alloy sample, the composition was 14 ML InAs–12 ML DA, where the digital alloy (DA) was composed of 1.7 ML InAs–0.3 ML InSb. The shuttering sequence used to grow this digital alloy is shown in Fig. 2.

This alloy composition was chosen to mimic the composition of the InAsSb in the reference sample and to maintain the 12 ML layer thickness. Though this composition of digital alloy would normally be expected to result in $x_{Sb} = 15\%$, which should result in an overall tensile strain on the epilayer, the resulting angular peak separation as measured by XRD demonstrated a good lattice match, which indicates that the composition of the ternary is correct ($x_{Sb} = 19\%$). The difference in composition is attributed to an undesirable incorporation of Sb into the InAs layers, thereby forming an intermediary InAsSb compound at the InSb/InAs boundary. To compensate for this, the thickness of the InSb layer was reduced from the initial 0.38 ML to 0.3 ML. The angular peak separation demonstrated by both the digital alloy and ternary devices was measured using XRD, and showed good lattice match (< 100 arcsec separation between the substrate peak and the 0th order SL peak). The full-width at half-maximum (FWHM) for the 0th order epilayer peak was better for the digital alloy sample than for the ternary sample (28.8 arcsec vs. 34.2 arcsec). This indicates that the digital alloy has superior crystalline quality. The XRD curves can be seen in Fig. 3. These curves demonstrate that the superlattice structure formed with a digital alloy layer is comparable to one formed with a ternary layer.

The grown devices were processed into single-pixel mesas with varying aperture sizes using a standard photolithography process and an ICP dry etch. These samples were passivated using SiN$_x$, and Ti/Pt/Au metallization was used for both top and bottom contacts.

Fig. 1. Angular peak separation induced in Ga-free SL samples by varying growth temperatures and Sb BEPs, as measured by XRD. The As:In BEP ratio and In growth rates were kept consistent for these growths. The variation in this peak separation indicates an undesired variation in InAsSb composition.
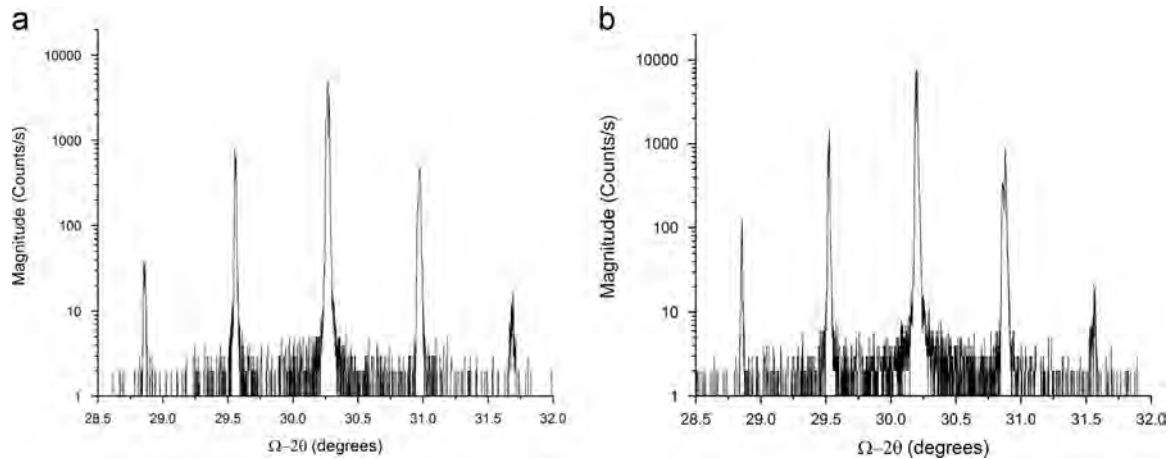
Fig. 3. XRD rocking curves taken from each grown sample. These curves show good lattice match in both cases. For the digital alloy, the full-width at half-maximum of the 0th order SL peak (28.8 arcsec) is thinner than that of the ternary (34.2 arcsec). This indicates superior crystalline quality in the digital alloy sample. (a) Ternary reference sample. (b) Digital alloy sample.

4. Electrical characteristics

In order to determine whether the InAs–InSb digital alloy can make a suitable replacement for the InAsSb ternary material, the processed devices were characterized for spectral response, dark current, and quantum efficiency (QE).

The dark current characteristics from these devices are reported in Fig. 4. These results demonstrate that both the average (of 5 measured devices for each sample) and best-device results from the digital alloy sample are slightly better than those of the reference sample. The average dark current levels for the ternary reference sample and the digital alloy sample at a voltage bias of $V_b = -0.01$ V ($V_b = -0.25$ V) and $T = 80$ K are 0.1315 (4.249) A/cm^2 and 0.1068 (3.522) A/cm^2, respectively. The best-device dark currents under the same conditions are 0.1227 (2.859) A/cm^2 and 0.0853 (2.115) A/cm^2, respectively. This is summarized in the table in Fig. 5. The high levels of dark current are attributed to both the lack of barriers in the PIN structure and the non-optimized As:In BEP ratios used for these preliminary devices. The BEP ratio is suspected to be non-optimal due to these devices being grown in a different MBE chamber from the previously reported devices. This has been reported for InAs–GaSb superlattices to cause detrimental effects to the resulting device performances due to increased interface roughness and, in the case of excess group V material, the incorporation of impurities into the device [19]. The same effect is expected to occur in the Ga-free SL.

Normalized spectral response characteristics were measured for each device at $V_b = 0$ V and $T = 80$ K, and are shown in Fig. 6. The measurements were not changed when a slight bias ($V_b = -0.01$ V) was applied. The two samples show very similar response characteristics. More notably, the cutoff wavelength $\lambda_{cutoff,0\%} = 5$ μm at 80 K for both devices. This cutoff wavelength is expected from the 14 ML InAs–12 ML InAs$_{0.81}$Sb$_{0.19}$ SL design, and has been demonstrated previously [17]. This gives further indication that the digital alloy sample has electrical characteristics that are comparable to the reference sample. The digital alloy sample showed operation up to a slightly higher temperature (220 K vs. 200 K for the ternary), indicating that the material quality in the digital alloy sample is slightly better.

The QE of the devices was measured by taking photocurrent measurements with a calibrated Mikron blackbody source at 627 °C. At $V_b = -0.01$ V ($V_b = -0.25$ V) and $T = 80$ K, the QE of the ternary and digital alloy samples are 24.1% (24.0%) and 39.7% (39.9%), respectively. The increase in quantum efficiency present in the digital alloy is attributed to the superior crystalline quality shown
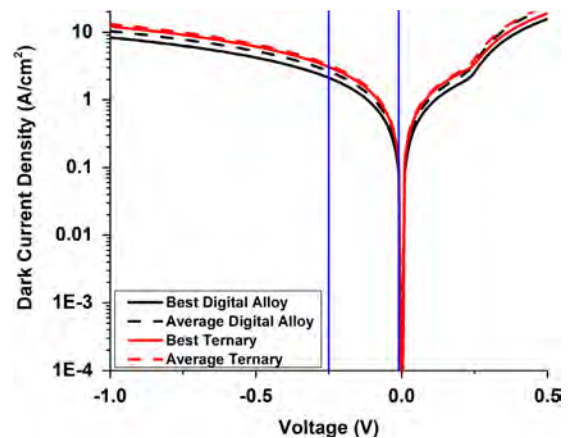
Fig. 4. Dark current density characteristics of Ga-free reference (ternary) and digital alloy-based samples. The average dark current densities at a bias of $V_b = -0.01$ V ($V_b = -0.25$ V) and $T = 80$ K are 0.1315 (4.249) A/cm^2 for the ternary reference sample and 0.1068 (3.522) A/cm^2 for the digital alloy sample. The blue lines indicate $V_b = -0.01$ V and $V_b = -0.25$ V. (For interpretation of the references to color in this figure caption, the reader is referred to the web version of this paper.)

Sample	Average Dark Current (A/cm³)	Best Device Dark Current (A/cm²)	Quantum Efficiency
Digital Alloy (-0.01V, 80K)	0.1068	0.0853	39.7
Ternary (-0.01V, 80K)	0.1315	0.1227	24.1
Digital Alloy (-0.25V, 80K)	3.522	2.115	39.9
Ternary (-0.25V, 80K)	4.249	2.859	24.0

Fig. 5. Table comparing the results of the reference (ternary) sample with the digital alloy sample. These results show that the digital alloy is comparable to or better than the ternary reference results for each measured parameter.

in the XRD results. The reduced FWHM of the 0th order digital alloy peak indicates improved superlattice layer interfaces. The improvement of these interfaces is believed to improve device performance [12,20]. The results from this measurement are plotted against bias voltage, and can be seen in Fig. 7. These results are comparable to previously reported device results [17].

In all cases, the digital alloy sample is comparable to or better than the ternary reference sample. This provides preliminary evidence that
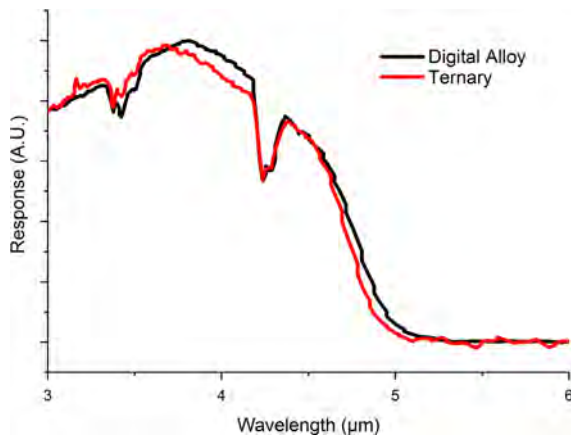
Fig. 6. Normalized spectral response measured for both the ternary and digital alloy samples. These measurements were taken at $V_b = 0$ V and $T = 80$ K, demonstrating a photovoltaic response in these devices. The addition of a slight bias ($V_b = -0.01$ V) did not result in any significant changes in these measurements. These results demonstrate comparable response from the two devices.
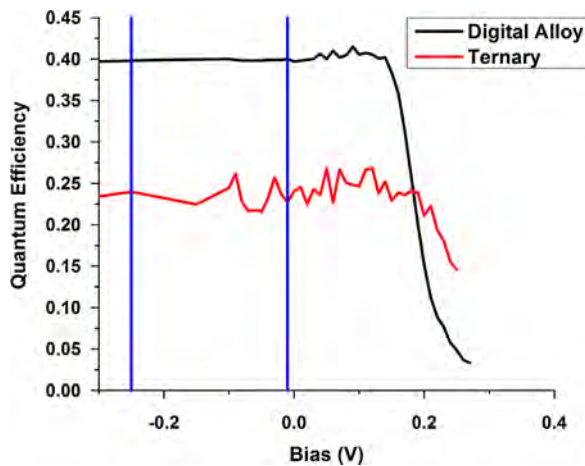
Fig. 7. Quantum efficiency vs. voltage for both the reference (ternary) and digital alloy samples. These measurements were taken at 80 K using a calibrated Mikron blackbody set to 627 °C. The blue lines indicate $V_b = -0.01$ V and $V_b = -0.25$. (For interpretation of the references to color in this figure caption, the reader is referred to the web version of this paper.)

the use of a digital alloy does not negatively affect the electrical performance of a Ga-free SL device and may prove to be a successful replacement for the InAsSb ternary material, thereby improving the growth stability of the Ga-free SL material.

5. Summary

In summary, two MWIR detectors were grown using a 14 ML InAs–12 ML $InAs_{0.81}Sb_{0.19}$ design. One device was used as a reference, while the other was grown using a 1.7 ML InAs–0.3 ML InSb digital alloy in place of the InAsSb ternary. Electrical and optical characterizations of these devices demonstrate that the digital alloy device performs comparable to or better than the reference sample in each metric. This provides preliminary evidence that a digital alloy is suitable for use in Ga-free SL-based devices, thereby eliminating the

InAsSb ternary and easing the degree of dependence on growth temperature and source BEP stability observed in the Ga-free SL material system.

Acknowledgements

References

[1] C.H. Grein, P.M. Young, H. Ehrenreich, Minority carrier lifetimes in ideal InGaSb/InAs superlattices, Appl. Phys. Lett. 61 (1992).
[2] E.R. Youngdale, J.R. Meyer, C.A. Hoffman, F.J. Bartoli, C.H. Grein, P.M. Young, H. Ehrenreich, R.H. Miles, D.H. Chow, Auger lifetime enhancement in InAs–$Ga_{1-x}In_xSb$ superlattices, Appl. Phys. Lett. 64 (1994).
[3] C.H. Grein, J. Garland, M. Flatté, Strained and unstrained layer superlattices for infrared detection, J. Electron. Mater. 38(8) (2009).
[4] D.R. Rhiger, Performance comparison of long-wavelength infrared type II superlattice devices with HgCdTe, J. Electron. Mater. 40(8) (2011).
[5] D. Donetsky, S.P. Svensson, L.E. Vorobjev, G. Belenky, Carrier lifetime measurements in short-period InAs/GaSb strained-layer superlattice structures, Appl. Phys. Lett. 95 (2009).
[6] S.P. Svensson, D. Donetsky, D. Wang, H. Hier, F.J. Crowne, G. Belenky, Growth of type II strained layer superlattice, bulk InAs and GaSb materials for minority lifetime characterization, J. Cryst. Growth 334 (2011) 103–107.
[7] E.H. Steenbergen, B.C. Connelly, G.D. Metcalfe, H. Shen, M. Wraback, D. Lubyshev, Y. Qiu, J.M. Fastenau, A.W.K. Liu, S. Elhamri, O.O. Cellek, Y.-H. Zhang, Significantly improved minority carrier lifetime observed in a long-wavelength infrared III–V type-II superlattice comprised of InAs/InAsSb, Appl. Phys. Lett. 99 (2011).
[8] B.V. Olson, E.A. Shaner, J.K. Kim, J.F. Klem, S.D. Hawkins, L.M. Murray, J.P. Prineas, M.E. Flatté, T.F. Boggess, Time-resolved optical measurements of minority carrier recombination in a mid-wave infrared InAsSb alloy and InAs/InAsSb superlattice, Appl. Phys. Lett. 101 (2012).
[9] A. Haddadi, G. Chen, R. Chevallier, A.M. Hoang, M. Razeghi, InAs/$InAs_{1-x}Sb_x$ type-II superlattices for high performance long wavelength infrared detection, Appl. Phys. Lett. 105 (2014).
[10] A.M. Hoang, G. Chen, R. Chevallier, A. Haddadi, M. Razeghi, High performance photodiodes based on InAs/$InAs_{1-x}Sb_x$ type-II superlattices for very long wavelength infrared detection, Appl. Phys. Lett. 104 (2014).
[11] R. Kaspi, G. Donati, Digital alloy growth in mixed As/Sb heterostructures, J. Cryst. Growth 251 (1–4) (2003) 515–520.
[12] A.Y. Lew, E.T. Yu, Y.-H. Zhang, Atomic-scale structure of InAs/$InAs_xSb_{1-x}$ superlattices grown by modulated molecular beam epitaxy, Appl. Phys. Lett. 14 (1996).
[13] Y.-H. Zhang, A. Lew, E. Yu, Y. Chen, Microstructural properties of InAs/$InAs_xSb_{1-x}$ superlattices and $InAs_xSb_{1-x}$ ordered alloys grown by modulated molecular beam epitaxy, J. Cryst. Growth 270 (2004) 359–363.
[14] L. Ouyang, E.H. Steenbergen, Y.-H. Zhang, K. Nunna, D.L. Huffaker, D.J. Smith, Structural properties of InAs/$InAs_{1-x}Sb_x$ type-II superlattices grown by molecular beam epitaxy, J. Vac. Sci. Technol. B 18 (2) (2000) 746–750.
[15] H. Li, S. Liu, O.O. Cellek, D. Ding, X.-M. Shen, E.H. Steenbergen, J. Fan, Z. Lin, Z.-Y. He, Q. Zhang, P.T. Webster, S.R. Johnson, L. Ouyang, D.J. Smith, Y.H. Zhang, A calibration method for group V fluxes and impact of V/III flux ratio on the growth of InAs/InAsSb type-II superlattices by molecular beam epitaxy, J. Cryst. Growth 378 (2013).
[16] T. Schuler-Sandy, M. Malone, Z. Tian, L. Treider, E. Plis, T. Rotter, C. Morath, V. Cowan, S. Krishna, Absorber Doping in Gallium-Free Superlattice Photodetectors, Appl. Phys. Lett. 101 (2012).
[17] T. Schuler-Sandy, S. Myers, B. Klein, N. Gautam, P. Ahirwar, Z.B. Tian, T. Rotter, G. Balakrishnan, E. Plis, S. Krishna, Gallium free type II InAs/$InAs_xSb_{1-x}$ superlattice photodetectors, Presented at the US Workshop on the Physics & Chemistry of II–VI materials, Chicago, Il, October 2013.
[18] M. Sardela, X-ray analysis methods, Presented at the 6th Advanced Materials Characterization Workshop, Urbana-Champaign, Il, June 2012.
[19] E. Plis, B. Klein, N. Gautam, S. Myers, M.N. Kutty, M. Naydenkov, S. Krishna, Performance optimization of long-wave infrared detectors based on InAs/GaSb strained layer superlattices, in: Infrared Technology and Applications XXXVII, vol. 8012, 2011.
[20] E. Plis, S. Annamalai, K.T. Posani, S. Krishna, R.A. Rupani, S. Ghosh, Midwave infrared type-II InAs/GaSb superlattice detectors with mixed interfaces, J. Appl. Phys. 100 (2006).

CRYSTAL
GROWTH

ELSEVIER
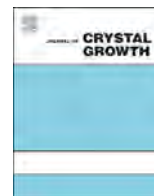
Al$_x$In$_{1-x}$As$_y$Sb$_{1-y}$ alloys lattice matched to InAs(1 0 0) grown by molecular beam epitaxy

CrossMark

J.S. Rojas-Ramirez [a], S. Wang [c], R. Contreras-Guerrero [a], M. Caro [a], K. Bhatnagar [b], M. Holland [c], R. Oxland [c], G. Doornbos [c], M. Passlack [c], C.H. Diaz [d], R. Droopad [a,b,*]

[a] Ingram School of Engineering, Texas State University, San Marcos, TX 78666, United States
[b] Material Science, Engineering & Commercialization, Texas State University, San Marcos, TX 78666, United States
[c] TSMC R&D, Europe B. V., 3001 Leuven, Belgium
[d] TSMC R&D, Hsinchu Science Park, Hsinchu 300, Taiwan, ROC

ARTICLE INFO

ABSTRACT

Al$_x$In$_{1-x}$As$_y$Sb$_{1-y}$ quaternary alloys lattice-matched to InAs were successfully grown by molecular beam epitaxy (MBE) for use as buffer layers for substrate isolation in InAs channel devices. The use of In-containing quaternary buffer layers with 5% In was found to dramatically improve the heterointerface between the buffer and a surface InAs channel layer. The composition of these alloys and the extent of lattice matching were accurately determined by double crystal X-ray measurements. A simple model was used to estimate the variation of critical thickness with lattice mismatch for AlInAsSb epitaxially grown on an InAs substrate. Layers with high Al content and low As mole fraction were grown by modulated MBE technique which was found to significantly improve the surface morphology and the composition control of the alloys. In contrast, quaternary alloys with low Al content were grown by conventional MBE and had an rms roughness of less than 0.2 nm.

© 2015 Elsevier B.V. All rights reserved.

1. Introduction

Due to their high mobilities and electron velocities, III–V semiconductors are ideal contenders for use as channel materials in future MOSFET transistors. In particular, InAs which has a bulk band gap of 0.35 eV, a room temperature electron mobility of 30,000 cm^2/V s and an electron velocity of 4×10^7 cm/s, is being considered [1]. In this material system, it is possible to unpin the Fermi level through the formation of a gate dielectric using atomic layer deposition [2]. InAs is also technologically important for use in infrared detectors and is one of the main components in the type II superlattice structures [3,4]. For electronic devices, determining the transport properties of thin InAs channels without a suitable insulating buffer layer on native substrates is problematic because of the narrow band gap of InAs. Possible insulating buffers are quaternary Al$_x$In$_{1-x}$As$_y$Sb$_{1-y}$ alloys since they can be lattice matched to InAs and have a high enough band gap (when a high Al content is used).

The introduction of quaternary layers to the device design also gives more flexibility to tune the band gap and band offsets of lattice matched heterostructures on InAs. Compared to conventional AlGaAsSb, AlInAsSb provides higher valence band offset in InAs-based type-I quantum wells [5]. However, this enhanced flexibility comes at the expense of a more complex growth scheme when using molecular beam epitaxy. In a mixed group V quaternary system like AlInAsSb, it is extremely difficult to control the composition because of the high group V vapor pressure and the strong dependence of the incorporation rate on growth temperature. To avoid strain relaxation of thick buffer layers, these layers must be lattice-matched to the specific substrates by accurate controlling of the alloy composition. To accurately fix the composition, a number of calibration runs are typically required. Also, there are wide regions of possible quaternary compositions that are unstable [6]. In thermal equilibrium, the quaternary components tend to segregate into inhomogeneous mixtures of binaries and ternaries. However, the non-equilibrium growth process afforded by the MBE process can extend the miscibility boundaries considerably. Even with MBE, inaccessible composition gaps remain for some of the III–V quaternary systems.

In this study, Al$_x$In$_{1-x}$As$_y$Sb$_{1-y}$ alloys lattice matched to InAs have been grown by conventional molecular beam epitaxy (MBE) and modulated molecular beam epitaxy (MMBE) techniques on InAs(1 0 0) substrates with the Al content ranging from $x=0.19$ to $x=1$. In the MMBE scheme, the As and Sb shutters are alternately opened and closed resulting in the variation of the As incident flux within the layer and As content in the film.

* Corresponding author at: Material Science, Engineering & Commercialization, Texas State University, San Marcos, TX 78666, United States.
E-mail address: rdroopad@txstate.edu (R. Droopad).

2. Experimental

Samples were grown in a DCA 3-in. capable molecular beam epitaxy (MBE) reactor using elemental sources for group III (Ga, Al, and In). Two crackers were used to supply the group V species (As and Sb). The dopant sources were Te, Si, and Be. The cracker temperature was set to 950 °C for As_2 and to 900 °C for Sb_2. In-situ reflection high energy electron diffraction (RHEED) was used to monitor the surface quality in real time and obtain the growth rate calibration for binary compounds. Fluxes were measured using beam flux monitor consisting of a moveable ion gauge. Substrate temperature was determined by emissivity corrected pyrometry using the LayTec EpiRAS system and crossreferences using the different well-known GaAs, InAs, and GaSb surface reconstruction transitions monitored by RHEED.

Epi-ready Zn-doped InAs(1 0 0) substrates with nominal donor density of 2×10^{17} cm^{-3} were used in this study. The InAs oxide removal process occurs at a substrate temperature of 520 °C. This process is accompanied by a surface reconstruction transition monitored by RHEED from a $3 \times$ to $2 \times$ reconstruction along the [1 1 0] azimuth under an overpressure of arsenic [7] at a flux of 8×10^{-6} mbar. A thermal anneal for 30 min was carried out at a temperature 15 °C higher to complete the native oxide desorption. Following the oxide desorption, an InAs epitaxial buffer layer was grown. The optimal growth conditions for InAs homoepitaxy have been reported elsewhere [8] which include an initial low growth rate of 0.15 ML/s. at a substrate temperature of 500 °C followed by a bulk growth rate of 0.5 ML/s with an arsenic flux pressure of 3.5×10^{-6} mbar. The growth of the quaternary layers were carried out at a temperature around 490 °C.

Double crystal X-ray measurements were carried out to obtain alloy compositions and to monitor material defectivity. Dark field optical microscopy was used to estimate surface defects. Atomic force microscopy (AFM) was used to determine the surface morphology and transmission electron micrograph (TEM) was used to characterize the defectivity and interface of the grown structures.

3. Results and discussion

3.1. Critical thickness of AlInAsSb on InAs

Lattice mismatch is defined as

$$\frac{\Delta a}{a} = \frac{a_f - a_0}{a_f} = -f \tag{1}$$

where a_f is the lattice constant of the unstrained epilayer and a_0 is that of the substrate. The lattice constant in the direction perpendicular to the interface is
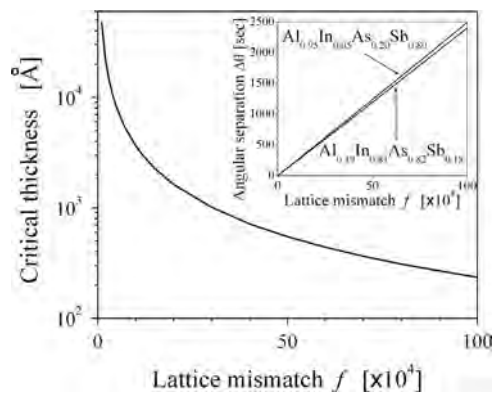
$$a_\perp = (1 - \sigma_{ST}f)a_f \tag{2}$$

where $\sigma_{ST} = c_{11}/2c_{12}$ and c_{11} and c_{12} are elastic constants of the epilayer. The in-plane coordinate directions are x and y, and growth occurs along the z-direction. These equations are only valid when the z-direction coincides with the (0 0 1) crystallographic axis.

The critical thickness depends on a number of factors: (i) the amount of the lattice mismatch (ii) the materials parameters and (iii) the properties of the dislocations that form in the particular material. In the case of misfit dislocations forming at the interface when the critical thickness is exceeded, it has been shown that [9]

$$h_c = \frac{a_0\left(1 - v_{PR}/4\right)\left[\ln\left(\sqrt{2}h_c/a_0\right) + 1\right]}{2\sqrt{2}\pi|f|(1 + v_{PR})} \tag{3}$$

where $v_{PR} = \left(c_{12}/(c_{11} + c_{12})\right)$ is the Poisson ratio. The variation of critical thickness as a function of lattice mismatch for AlInAsSb on InAs substrate is plotted in Fig. 1. The materials parameters listed in Table 1 were used for the calculation. The ternary and quaternaries values were obtained by linear interpolation of the binary constants. According to this model, the maximum strained layer thickness for a lattice mismatch of 3×10^{-3} is 100 nm and 300 nm for a lattice mismatch of 1.3×10^{-3}.

The inter-planar spacing d in the Bragg's condition,

$$2d \sin \theta = n\lambda \tag{4}$$

coincides with the perpendicular lattice constant. Using Eqs. (1) and (2) gives:

$$d = a_\perp = \frac{(1 - \sigma_{ST}f)}{1 + f}a_0 \tag{5}$$

Table 1
Elastic constants of single crystal semiconductor compounds at 300 K [10,11].

Compound	c_{11} [dyn/cm^2]	c_{12} [dyn/cm^2]	σ_{ST}	v_{PR}
AlAs	12.02×10^{11}	5.70×10^{11}	1.054	0.322
AlSb	8.939×10^{11}	4.427×10^{11}	1.009	0.331
InAs	8.34×10^{11}	4.54×10^{11}	0.918	0.352
InSb	6.67×10^{11}	3.65×10^{11}	0.914	0.354
AlAs$_{0.16}$Sb$_{0.84}$	9.432×10^{11}	4.631×10^{11}	1.016	0.329
Al$_{0.95}$In$_{0.05}$As$_{0.20}$Sb$_{0.80}$	9.428×10^{11}	4.639×10^{11}	1.013	0.328
Al$_{0.19}$In$_{0.81}$As$_{0.82}$Sb$_{0.18}$	8.690×10^{11}	4.587×10^{11}	0.942	0.345

Fig. 1. Calculated variation of critical thickness with lattice mismatch for epitaxy of AlInAsSb on an InAs substrate. The inset shows the corresponding separation between the substrate and strained epilayer (0 0 4) Bragg angles.
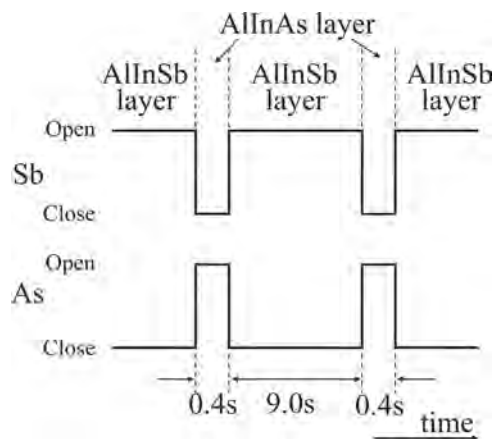
Fig. 2. The time sequence of the As and Sb shutters during the MMBE growth of Al$_x$In$_{1-x}$As$_y$Sb$_{1-y}$ lattice-matched to InAs. The Al and In shutters remained open throughout the deposition while the As and Sb shutters opened and closed sequentially for deposition of AlInAs and AlInSb for 0.4 s and 9.0 s, respectively.

The difference, $\Delta\theta$, between the substrate and epilayer (0 0 4) Bragg angles is proportional to the lattice mismatch as shown in the inset of Fig. 1.

3.2. Digital growth of $Al_xIn_{1-x}As_ySb_{1-y}$ alloys

The lattice-match condition of $Al_xIn_{1-x}As_ySb_{1-y}$ on InAs with high Al content ($x > 0.9$) requires a low As to Sb composition ratio (< 0.3). Because As_2 has a high incorporation rate relative to that of Sb_2 at the growth temperature used, it is more difficult to control the composition of mixed group V alloys with low As fractions. At 500 °C, the As flux has to be limited to one order of magnitude lower than the Sb flux. In order to overcome this issue, MMBE growth of AlInAsSb was used. MMBE allows comparable group V fluxes to be used for As and Sb while the incorporation of the group V is controlled by shuttering the As or Sb sources. The

growth rate for the quaternary alloy was 0.5 ML/s with the Sb-flux kept at 3.1×10^{-6} and the As-flux varied from 1.9×10^{-6} to 2.3×10^{-6} mbar.

The modulated growth scheme employed for the quaternaries layer is shown schematically in Fig. 2. The Al and In shutters remain open while the As and Sb shutters alternately open and closed so that a superlattice structure consisting of AlInAs and AlInSb is grown. The thickness of the layers is controlled so that each individual layer is less than the critical thickness. Each pair of ternary layers is strain compensated. This allows for very thick, defect free, quaternary layers to be grown lattice matched to InAs.

The MBE growth development for insulating buffers on InAs started with the lattice matching of AlAsSb, the alloy with the largest bandgap, to the InAs substrate. The shutter times and the Sb flux were kept constant while the effect of changing the As flux was investigated. Fig. 3(a) shows the X-ray rocking curves for a
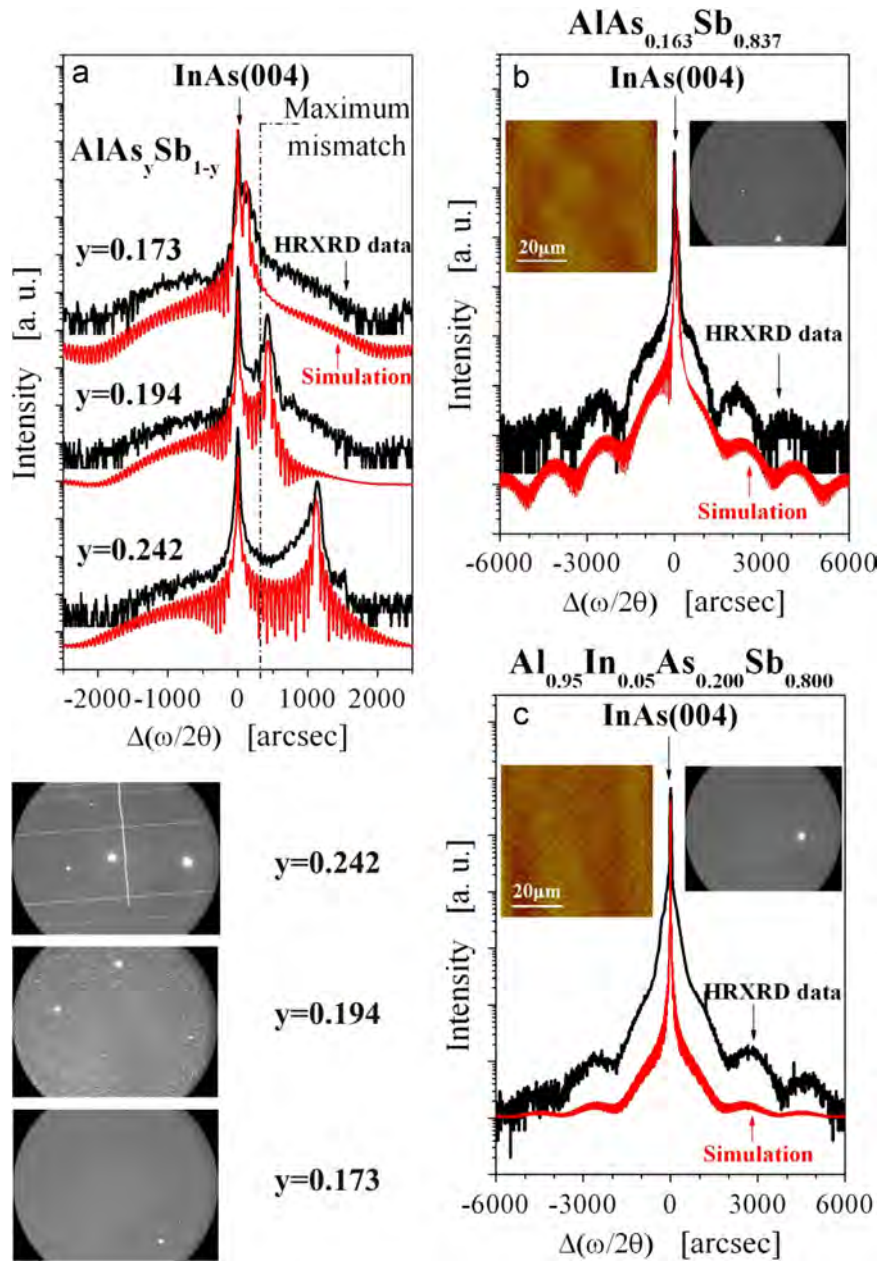
Fig. 3. XRD rocking curves and dark field OM images of ternary and quaternary layers grown on InAs substrate along with a simulation to obtain the alloys compositions. (a) Relaxed and pseudomorphic AlAsSb epilayers. The dark field optical micrographs shows the surface quality of the 3 surfaces. The dashed line represents maximum mismatch for a 300 nm layer. (b) 500 nm-thick AlAsSb lattice matched layer. Inset shows a 60×60 μm^2 AFM micrograph of the sample with an rms roughness of 0.21 nm. (c) 500 nm-thick $Al_{0.95}In_{0.05}As_{0.20}Sb_{0.80}$ layer lattice matched to InAs with an rms AFM roughness of 0.24 nm.

series of growths of AlAsSb buffer layer on InAs substrate with the composition determined using simulations. The satellite peak in the X-ray diffractograms corresponds to the ternary alloy. A clear shift towards the substrate peak is seen as the As flux is decreased. The layer with 24.2% of arsenic has relaxed as revealed in the corresponding dark field optical micrograph which shows a cross-hatched surface. The vertical dashed line in Fig. 3(a) indicates the maximum mismatch for a layer with a nominal thickness of 300 nm according to the calculation in previous section. The sample with an arsenic composition of 19.4% did not relax but was strained as evidenced from the narrow linewidth and the smooth optical micrograph. An AFM analysis of the surface also showed no indication of partial relaxation. This would suggest that the model in Eq. (3) slightly underestimates the critical thickness as it predicts the 19.4% arsenic layer should relax. The sample with 17.3% of arsenic has the lowest tensile strain, a much better surface morphology with a low rms roughness of 0.197 nm. Using the MMBE method, 500 nm thick $AlAs_{0.163}Sb_{0.837}$ and $Al_{0.95}In_{0.05}As_{0.20}Sb_{0.80}$ layers lattice matched to InAs were successfully grown (Fig. 3b and c). HRXRD fringes seen for these layers indicate high quality material and abrupt interfaces. The rms roughness for these layers was < 0.25 nm over a 60 μm × 60 μm scan region.

The motivation for investigating the growth of In-containing quaternary layer was the surface and interface roughness seen when InAs surface channel layer was grown on AlAsSb buffer layers. The large band gap AlAsSb layer serves to isolate the conducting InAs substrates in the fabrication of high mobility electronic devices. The TEM image in Fig. 4(a) shows the structure consisting of InAs substrate, a ternary AlAsSb buffer followed by a thin InAs surface channel. While the micrograph shows a sample with no detectable

defects and layer thicknesses as predicted from RHEED growth rates a close examination InAs/AlAsSb interface in the right micrograph showed an undulation of the top AlAsSb surface. This undulation results in a non-uniform thickness of the top InAs layer presenting a major problem for a surface channel device. However, the top surface of the InAs layer is smooth suggesting that the addition of In into the AlAsSb layer may help to improve the device structures by reducing the long range roughness at the interface. To maintain a large enough band gap to isolate the InAs channel, the indium content has to be kept low.

Fig. 4(b) shows the effect of the addition of a small amount of indium to the buffer layer. In this case, the In composition of 5% is shown to virtually eliminate the AlAsSb undulation. The interfaces are smoother and the surface InAs channel thickness is uniform. This quaternary layer is grown using the modulated MBE method with a modification of the group V composition in order to satisfy the lattice match condition.

3.3. Non-modulated growth of $Al_xIn_{1-x}As_ySb_{1-y}$ alloys

For high In composition quaternary alloys the use of digital growth (as shown in Fig. 1) is not possible. This is because, at high In content, the thickness of the AlInSb can exceed the critical thickness. For this reason, the growth of high In composition quaternary layers was carried out using conventional MBE. Fig. 5 shows the XRD rocking curves for a series of 100 nm thick quaternary layers with In composition of 81% on InAs substrate that were grown using conventional MBE deposition. RHEED oscillations were used to set the group III composition assuming a unity sticking coefficient at the growth temperature of 490 °C. The As and Sb fluxes
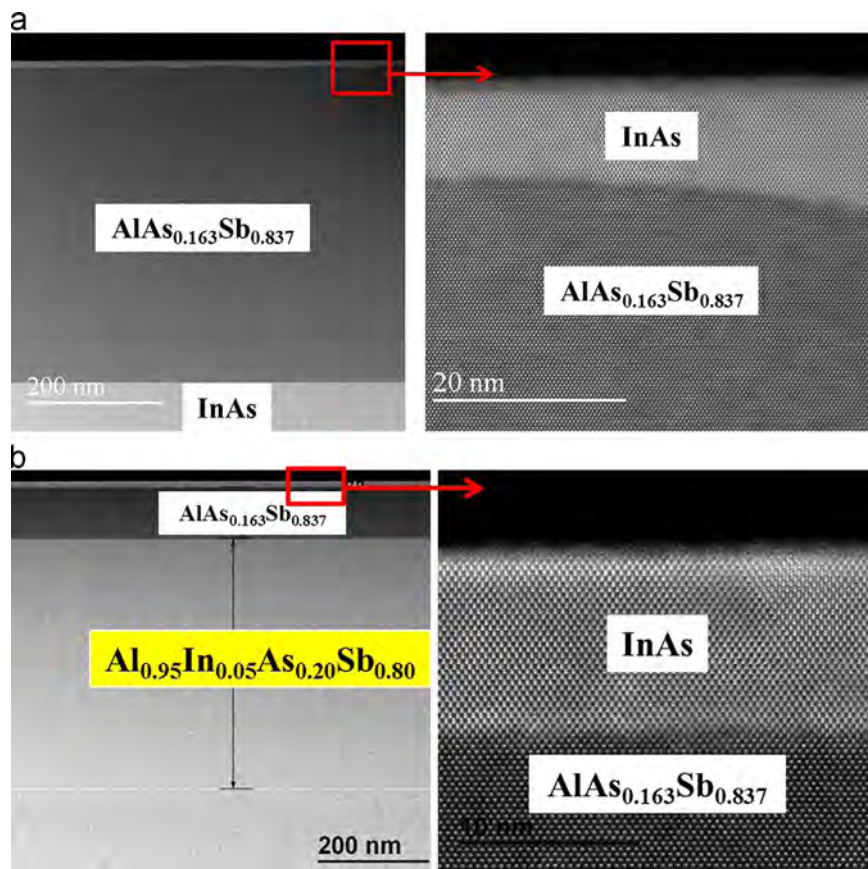
Fig. 4. (a) Cross-sectional TEM images of ternary AlAsSb layer lattice matched to InAs with a top InAs channel layer. On the right micrograph, a close inspection shows the undulating ternary interface with the top InAs layer resulting in the top InAs layer having non-uniform thickness. (b) Cross-sectional TEM images of quaternary AlInAsSb layer with 5% In content lattice matched to InAs with a top InAs channel layer. As shown in the right micrograph the addition on In in the buffer layer resulted in smoother interfaces and uniform InAs surface channel layer.
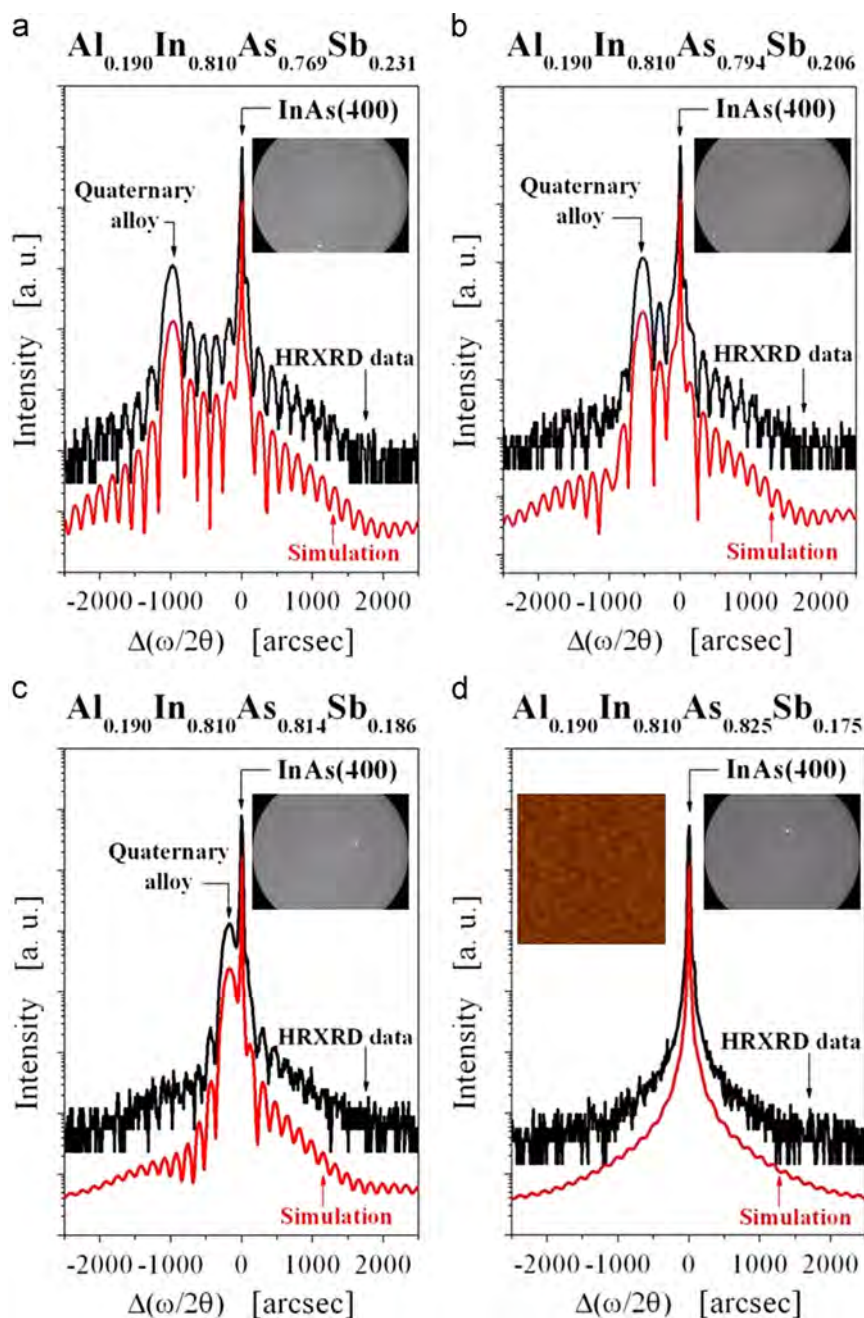
Fig. 5. XRD rocking curves of 100 nm-thick quaternary layers with 81% In grown on an InAs substrate. XRD simulations are also shown (in red) to obtain the alloys compositions. As the As flux was increased, the lattice matched condition was approached (a–c). Perfect lattice matching of the buffer layer is seen in (d). (For interpretation of the references to color in this figure legend, the reader is referred to the web version of this article.)

were adjusted to obtain lattice matching. The Sb flux was kept constant with a BEP (beam equivalent pressure) measured value of 5.6×10^{-6} mbar and the As flux was varied. The quaternary layers shown in Fig. 5(a–c) were determined to be in compression. Fringe oscillations in the rocking curve data and the excellent fit with simulation suggest the layers have low defectivity and smooth interfaces. By adjusting the As flux, exact lattice matching the substrate was achieved (Fig. 5d).

4. Conclusions

$Al_x In_{1-x} As_y Sb_{1-y}$ quaternary alloys were grown successfully lattice matched to an InAs substrate by MBE. Double crystal X-ray measurements were used to determine the alloy composition and the degree of mismatch of the strained layers. A simple model (which assumes misfit dislocations formation at the interface when the critical thickness is exceeded) was used to predict the variation of critical thickness with lattice mismatch for AlInAsSb on an InAs substrate. Comparison of the model with as-grown layers suggests the model slightly underestimates the critical thickness.

$AlAs_y Sb_{1-y}$ ternary alloy which represent a lattice matched buffer with the largest band offsets for an InAs surface channel results in long range roughness at the interface with the top layer. The use of quaternary buffer layers with 5% of In drastically improved this heterointerface by eliminating the long range roughness. For low In% quaternary buffers, a digital growth scheme was used in which the As and Sb shutters were alternately switched. For high In content, conventional MBE was used in which the As flux controlled the group V composition. The successful growth of the AlInAsSb buffers

lattice matched to InAs can provide greater freedom than ternary buffers in the design of high speed optoelectronic devices which use narrow band gap materials.

References

[1] J. Nah, H. Fang, C. Wang, K. Takei, M.H. Lee, E. Plis, S. Krishna, A. Javey, Nano Lett. 12 (2012) 3592.

[2] S.W. Chang, X. Li, R. Oxland, S.W. Wang, C.H. Wang, R. Contreras-Guerrero, K.K. Bhuwalka, G. Doornbos, T. Vasen, M.C. Holland, G. Vellianitis, M.J.H. van Dal, B. Duriez, M. Edirisooriya, J.S. Rojas-Ramirez, P. Ramvall, S. Thoms, U. Peralagu, C.H. Hsieh, Y.S. Chang, K.M. Yin, E. Lind, L.E. Wernersson, R. Droopad, I. Thayne, M. Passlack, C.H. Diaz, IEEE Int. Electron. Devices Meet. (2013) 16.1.

[3] A. Rogalski, Recent progress in infrared detector technologies, Infrared Phys. Technol. 54 (2011) 136.

[4] Z. Tian, R.T. Hinkey, R.Q. Yang, Y. Qiu, D. Lubyshev, J.M. Fatenau, Amy W.K. Liu, M.B. Johnson, J. Appl. Phys. 111 (2012) 024510.

[5] G.W. Turner, M.J. Manfra, H.K. Choi, M.K. Connors, J. Cryst. Growth 175/176 (1997) 825.

[6] A.N. Semenov, V.A. Solov'ev, B.Ya. Meltser, Ya.V. Terent'ev, L.G. Prokopova, S.V. Ivanov, J. Cryst. Growth 278 (2005) 203.

[7] M.P.J. Punkkinen, P. Laukkanen, J. Lång, M. Kuzmin, J. Dahl, H.L. Zhang, M. Pessa, M. Guina, L. Vitos, K. Kokko, Surf. Sci. 606 (2012) 1837.

[8] R. Contreras-Guerrero, S. Wang, M. Edirisooriya, W. Priyantha, J.S. Rojas-Ramirez, K. Bhuwalka, G. Doornbos, M. Holland, R. Oxland, G. Vellianitis, M. Van Dal, B. Duriez, M. Passlack, C.H. Diaz, R. Droopad, J. Cryst. Growth 378 (2013) 117.

[9] Shumin Wang, Lattice Engineering: Technology and Applications, Pan Stanford Publishing Pte. Ltd., 2013.

[10] ⟨http://www.ioffe.ru/SVA/NSM/Semicond/index.html⟩.

[11] D.I. Bolef, M. Menes, J. Appl. Phys. 31 (1960) 1426.
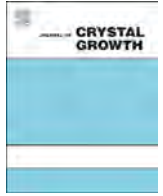
Overgrowth of wrinkled InGaAs membranes using molecular beam epitaxy

S. Filipe Covre da Silva [a,b], E.M. Lanzoni [a], A. Malachias [c], Ch. Deneke [a,*]

[a] Laboratório Nacional de Nanotecnologia (LNNano/CNPEM), Rua Giuseppe Máximo Scolfaro 10000, 13083-100, Campinas, Brazil
[b] Departamento de Física, Universidade Federal de Viçosa, 36570-000 Viçosa, MG, Brazil
[c] Departamento de Física, Universidade Federal de Minas Gerais, 30123-970 Belo Horizonte, MG, Brazil

ARTICLE INFO

ABSTRACT

Partly released InGaAs layers forming a wrinkled network are used as templates for InAs growth. A systematic growth study was carried out, where InAs amounts from 0 ML to 3 ML were deposited on the patterned samples. The material migration during growth is evaluated by distinct microscopy techniques. We find a systematic accumulation of the deposited material on the released, wrinkled areas of the sample, whereas no material accumulation or formation of three-dimensional nanostructures is observed on the unreleased areas of the sample.

© 2015 Elsevier B.V. All rights reserved.

1. Introduction

The thickness for the defect free growth of InGaAs/GaAs heterostructures is limited due to the mismatch strain between the two materials [1]. Such mismatch strain is at the origin of the formation of dislocations or the formation of three-dimensional nanostructures, depending on the growth rate, temperature and total coverage [2]. In the late 90s, a new class of compliant substrates was proposed and realized [3–7]. They can extend the threshold of maximum allowed thickness (critical thickness) before the formation of dislocations or other growth defects. Recently, such compliant substrates have been realized [8–11] using freestanding semiconductor structures formed by the release and rearrangement of thin solid films [12–16].

We use in this work partly release $In_{0.33}Ga_{0.67}As$ membranes forming a wrinkled network [17,18] as virtual substrate for the growth of InAs nanostructures. Molecular beam epitaxy (MBE) was used to deposited different amounts of material. The evolution of the material at the top of the membranes was studied with atomic force microscopy (AFM) and scanning electron microscopy (SEM). We find that in our systematical growth study that only InAs nanostructures form on the released parts of the sample. Furthermore, we observe a migration and accumulation to the deposited material at the released, wrinkled areas of the sample. The SEM images show that the InAs deposits form large structures preferably on the top of the freestanding parts of the released

membrane. This is ascribed to the smaller lattice misfit between the virtual substrate and the deposited material as well as to the compliance of the freestanding, wrinkled membranes.

2. Experimental details

Fig. 1a and b shows a schematic illustration of the main steps to produce the wrinkles membranes. A commercial heterostructure (EpiNova) composed of an AlAs (20 nm) sacrificial layer and $In_{0.33}Ga_{0.67}As$ (5 nm) grown on a GaAs (001) substrate was used to prepare the samples. In the first step, we patterned circular mesas (150 μm) using photolithography. After defining the pattern, the sample is cleaned as described in Ref. [19]. To obtain partly release membranes and consequently the wrinkle structures, we selectively remove the AlAs sacrificial layer with a HF:H_2O (1:30) solution (Fig. 1b). The light microscopy image in Fig. 1c shows the defined circular mesas with 150 μm after the process. For better illustration, we show a detailed representation of the etched sample in Fig. 1d, visualizing the 10 μm deep wrinkled area as well as a mark of the size of a typical AFM scan (red rectangle).

All samples were grown using the MBE facility of the LNNano (CNPEM, Brazil). The samples were heated to 350 °C for 2 h before growth and hydrogen cleaning. After this step, cleaning with atomic hydrogen was carried out to remove the native top oxide and carbon contaminants without damaging the thin membrane. After hydrogen cleaning, we observed a streak reflective high energy electron diffraction (RHEED) pattern, proofing the removal of the native surface oxide. The sample was then transferred to the main chamber, where the InAs was deposited with a growth rate

* Corresponding author.
E-mail address: christoph.deneke@lnnano.cnpem.br (Ch. Deneke).
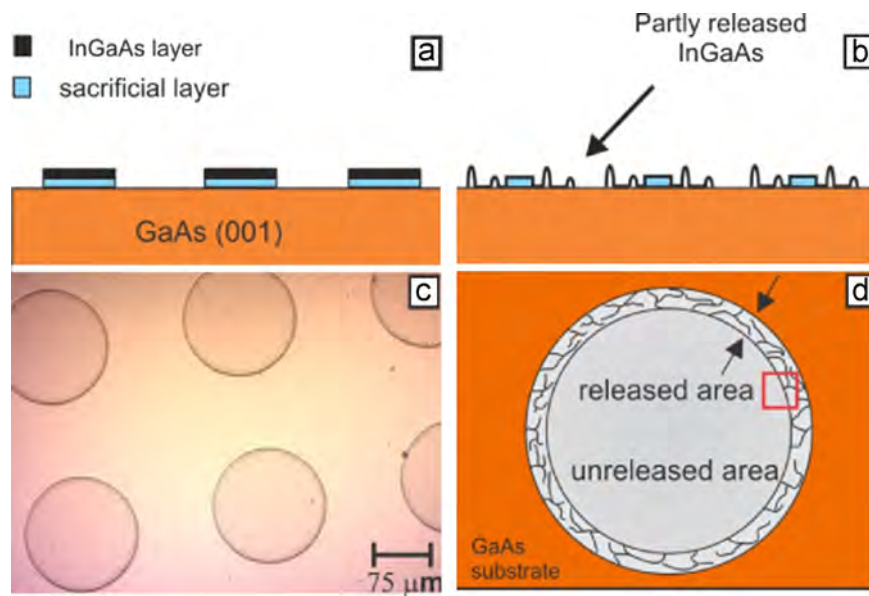
Fig. 1. Sketch of the sample fabrication procedure: (a) processed sample before membrane release and (b) after partial underetching with wrinkle formation at the mesa border regions. (c) Light microscopy image of the mesas after partial layer release. (d) Schematic illustration of the wrinkled region after the partial releasing of the InGaAs layer. (For interpretation of the references to color in this figure legend, the reader is referred to the web version of this article.)

(given in monolayers (ML) per second) of 0.022 ML/s at a substrate temperature of ca. 490 °C. After material deposition, a post-growth annealing of 5 min was carried out. In-situ RHEED monitoring was used during the whole growth process. Dot formation could be confirmed by the change of the RHEED pattern from streaky to spotty.

The topography of the samples was studied with atomic force microscopy (AFM) using two different systems (NX10 Park System and Digital Instruments Nanoscope IIIa). An Inspect F50 (FEI instruments) scanning electron microscopy (SEM) operating in 10 keV was used for a complementary study of the topography and material accumulation at the top of the membranes. Grazing-incidence X-ray diffraction (GI-XRD) maps were measured at the beamline XRD2 of the LNLS (Campinas, Brazil) using a beam energy of 9.5 keV. The sample is illuminated with a 0.2° incident angle and the diffraction signal detected using a Pilatus 100 K area detector covering an exit angle ranging from 0 to 2.5°. Reciprocal space maps as well as cuts through the reciprocal space were obtained near the in-plane (220) GaAs reflection.

3. Results and discussion

In Fig. 2a–d, we show a systematic growth study for a InAs deposition of 0 ML, 1 ML, 2 ML and 3 ML. Fig. 2a depicts an AFM image of the surface of the 0 ML sample. This sample was submitted to the normal growth process but without opening the In shutter. We can identify the wrinkles formed after the release process, the frontier between the released and unreleased parts of the sample as well as the flat unreleased areas. No material accumulation or migration is observed in the released or unreleased part. The unreleased part stays attached in the substrate and exhibits a flat surface. The released and back-bond areas exhibit the typical wrinkled network previously observed for such type of samples [17,18]. This proofs that the wrinkle network stays intact during the growth process and no Indium segregation and migration from the released or unreleased InGaAs film occurs.

In our study, we monitored the InAs nanostructure formation on different positions of the sample. Already on the surface of the sample with 1 ML deposited, some InAs accumulation can be observed

(Fig. 2b, marked by black circles for clarity). No Indium dots or other type of deposit is observed on the unreleased area; even so we could already expect some dot formation as the critical thickness for the unreleased parts of the sample should be below the 1.8 ML for a bare GaAs (001) surface. For 2 ML InAs deposition a large amount of InAs accumulation can be observed in form of chain-like structures on the wrinkled structures of the released parts (Fig. 2c). Furthermore, InAs accumulates on the frontier between the etched and unetched parts of the sample. No major formation of InAs structures is observed on the flat, back-bond parts of the released membrane. Finally, for the sample with 3 ML InAs deposited (Fig. 2(d)), InAs dot formation is observed on the flat parts of the released areas. Further, all wrinkles are completely covered with InAs. InAs also accumulates on the frontier between the released and unreleased parts. For none of the samples, InAs nanostructures form on the unreleased areas indicating that the material migrates from the released to the unreleased parts. Further studies (see Ref. [19]), show a migration length up to 60 μm in similar samples.

To better estimate the size and position of the InAs nanostructures formed on top of the wrinkled areas of the sample, SEM was carried out on the sample with 2 ML deposited.

Fig. 3a shows an SEM image of the edge between the released and unreleased parts of the sample. In the image, the wrinkles formed after the release of the membrane can be identified. Furthermore, the frontier between the released and unreleased parts is visible. On top of the membranes, InAs nanostructures can be recognized by their contrast compared to the dark background of the wrinkled-up, three-dimensional membrane. The SEM image shows that InAs only accumulates in big quantities on top of the freestanding parts of the membrane, which can act as complied substrates. No major InAs structure with comparable height and width is observed neither on the released, back-bond areas nor on the unreleased parts of the sample. Fig. 3b depicts a magnification SEM image of a single wrinkle structure seen in Fig. 3a. Again, the InAs accumulation on top of the wrinkle is clearly identifiable. Besides the large structure, which exhibits some crystal facets, only a very small InAs structure on the etching frontier (left side of the image) can be seen. This clearly supports our hypothesis that the top of the wrinkle is the preferred place of the material accumulation at these unique growth templates. We ascribe the
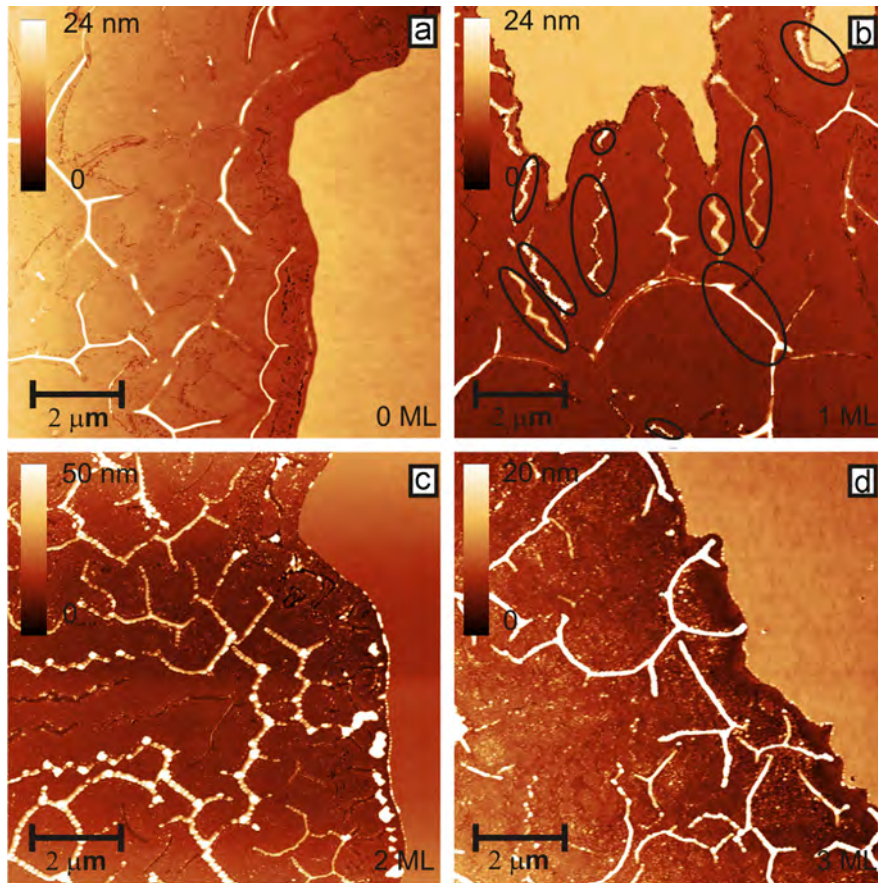
Fig. 2. Growth series with different amounts of deposited InAs material in partly released membranes. All images above show 10×10 μm^2 areas in the etching front that separates the released and unreleased parts, as represented in the square mark in Fig. 1(d). (a) 0 ML of InAs deposition (b) 1 ML of InAs deposition (black circles mark the area with material accumulation) (c) 2 ML of InAs (d) 3 ML of InAs deposition.
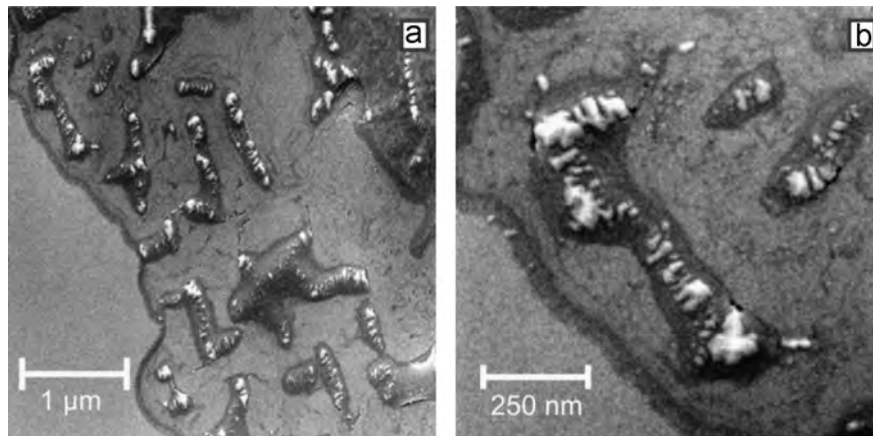
Fig. 3. (a) SEM image of wrinkled region and (b) a magnification of this area.

InAs accumulation to a non-homogeneous chemical potential due to changes on the misfit strain between unreleased, released backbond and released wrinkled parts of the sample [19].

To understand, if the InAs accumulation leads to a partial relaxation (either elastic or inelastic), GI-XRD was carried out on the 2 ML sample.

Fig. 4a depicts a radial-angular reciprocal space map obtained around the (220) GaAs reflection. Besides the intense peak ascribed to the GaAs position ($q_r = 3.14$ Å^{-1}), a shoulder towards the expected position of the InAs lattice parameter ($q_r = 2.94$ Å^{-1}) is observed. This is attributed to material deposited on the InGaAs

membrane, in which a lattice parameter gradient continually develops from unrelaxed, epitaxial material to nearly fully relaxed material with the InAs lattice parameter.

To better understand the material origin of the continuous lattice parameter distribution, the lateral domain size L of the scattering material is evaluated from the Δq_a width of the map – $L = 2\pi/\Delta q_a$ – at several reciprocal space conditions (denoting distinct lattice parameters within the lattice gradient) and plotted in Fig. 4b. From the graph, we can clearly attribute the L values retrieved at lattice parameters close to GaAs (5.653 Å) as originated from large areas, found in bond-back parts of the
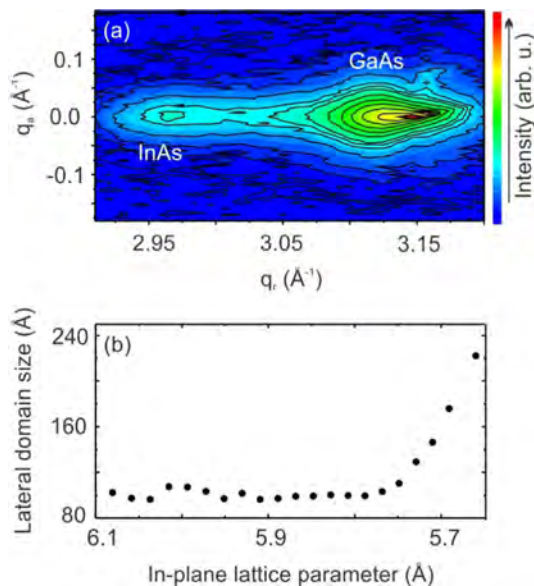
Fig. 4. (a) Reciprocal space map around the GaAs (220) reflection. (b) Crystalline domain size obtained from the q_a profile widths along the reciprocal space map.

membrane, as well as on the pseudomorphic unreleased film. Starting from a lattice parameter of 5.75 Å, we retrieve a smaller domain size of ca. 90 Å. Such type of domain is related to the InAs deposits observed in wrinkled regions by AFM and SEM images and is comparable with the size of individual InAs islands grown on flat substrates. This indicates that InAs deposits partly relax, hence exhibiting a lattice parameter closer to InAs – either elastically by straining its substrate as seen before [5,8] or plastically by the introduction of crystal defects.

4. Conclusion

We describe the formation of InAs nanostructures by material migration during the growth of InAs on partly released, wrinkled InGaAs membranes. AFM images obtained from surfaces of a systematic growth series indicates that the InAs migrates from the unreleased to the released areas of the sample and accumulates preferably on top of wrinkled structures. Our AFM and SEM results additionally show that InAs nanostructures are not formed on the unreleased parts of the samples. SEM results confirm that a major amount of the material migrates to the compliant free-standing parts of the samples.

Our work demonstrates that released wrinkled InGaAs networks can be used as compliant substrates for the growth of InAs/GaAs heterostructures. Furthermore, the growth on such partly released membranes turns out to be fundamentally different from the growth on rigid substrates as the deposited material migrates over large distances. The origin is ascribed to a non-homogeneity of the chemical surface potential due to the change of the lattice parameter between the released and the unreleased areas of the sample [19]. GI-XRD indicates that the deposited material undergoes a partial relaxation. Further experiments have to show, if this relaxation is mostly elastic or plastic.

References

[1] B.A. Joyce, D.D. Vvedensky, Self-organized growth on GaAs surfaces, Mater. Sci. Eng. R Rep. 46 (2004) 127–176. http://dx.doi.org/10.1016/j.mser.2004.10.001.
[2] A. Pimpinelli, J. Villain, Physics of Crystal Growth, University Press, Cambridge, New York, Melbourne, 1998.
[3] Y.H. Lo, New approach to grow pseudomorphic structures over the critical thickness, Appl. Phys. Lett. 59 (1991) 2311. http://dx.doi.org/10.1063/1.106053.
[4] C.L. Chua, W.Y. Hsu, C.H. Lin, G. Christenson, Y.H. Lo, Overcoming the pseudomorphic critical thickness limit using compliant substrates, Appl. Phys. Lett. 64 (1994) 3640. http://dx.doi.org/10.1063/1.111229.
[5] A.M. Jones, J.L. Jewell, J.C. Mabon, E.E. Reuter, S.G. Bishop, S.D. Roh, et al., Long-wavelength InGaAs quantum wells grown without strain-induced warping on InGaAs compliant membranes above a GaAs substrate, Appl. Phys. Lett. 74 (1999) 1000. http://dx.doi.org/10.1063/1.123435.
[6] P.M. Mooney, G.M. Cohen, J.O. Chu, C.E. Murray, Elastic strain relaxation in free-standing SiGe/Si structures, Appl. Phys. Lett. 84 (2004) 1093. http://dx.doi.org/10.1063/1.1646464.
[7] F.E. Ejeckam, Y.H. Lo, S. Subramanian, H.Q. Hou, B.E. Hammons, Lattice engineered compliant substrate for defect-free heteroepitaxial growth, Appl. Phys. Lett. 70 (1997) 1685. http://dx.doi.org/10.1063/1.118669.
[8] C. Deneke, A. Malachias, A. Rastelli, L. Merces, M. Huang, F. Cavallo, et al., Straining nanomembranes via highly mismatched heteroepitaxial growth: InAs islands on compliant Si substrates, ACS Nano 6 (2012) 10287–10295. http://dx.doi.org/10.1021/nn304151j.
[9] C.S. Ritz, H.J. Kim-Lee, D.M. Detert, M.M. Kelly, F.S. Flack, D.E. Savage, et al., Ordering of nanostressors on free-standing silicon nanomembranes and nanoribbons, New J. Phys. 12 (2010) 103011. http://dx.doi.org/10.1088/1367-2630/12/10/103011.
[10] P. Sookchoo, F.F. Sudradjat, A.M. Kiefer, H. Durmaz, R. Paiella, M.G. Lagally, Strain engineered SiGe multiple-quantum-well nanomembranes for far-infrared intersubband device applications, ACS Nano 7 (2013) 2326–2334. http://dx.doi.org/10.1021/nn305528t.
[11] H.J. Kim-Lee, D.E. Savage, C.S. Ritz, M.G. Lagally, K.T. Turner, Control of Three-Dimensional Island Growth with Mechanically Responsive Single-Crystal Nanomembrane Substrates, Phys. Rev. Lett. 102 (2009) 226103. http://dx.doi.org/10.1103/PhysRevLett.102.226103.
[12] V.Y. Prinz, Precise semiconductor nanotubes and nanocorrugated quantum systems, Phys. E-Low-Dimens. Syst. Nanostruct. 24 (2004) 54–62. http://dx.doi.org/10.1016/j.physe.2004.04.024ISSN.
[13] O.G. Schmidt, N. Schmarje, C. Deneke, C. Muller, N.Y. Jin-Phillipp, Three-dimensional nano-objects evolving from a two-dimensional layer technology, Adv. Mater. 13 (2001) 756–759.
[14] O.G. Schmidt, C. Deneke, N. Schmarje, C. Muller, N.Y. Jin-Phillipp, Free-standing semiconductor micro- and nano-objects, Mater. Sci. Eng. C-Biomim. Supramol. Syst. 19 (2002) 393–396.
[15] C. Deneke, R. Songmuang, N.Y. Jin-Phillipp, O.G. Schmidt, The structure of hybrid radial superlattices, J. Phys. -Appl. Phys. 42 (2009) 103001. http://dx.doi.org/10.1088/0022-3727/42/10/103001.
[16] C. Deneke, O.G. Schmidt, Structural characterization and potential x-ray waveguiding of a small rolled-up nanotube with a large number of windings, Appl. Phys. Lett. 89 (2006) 123121. http://dx.doi.org/10.1063/1.2356998iissn.
[17] A. Malachias, Y.F. Mei, R.K. Annabattula, C. Deneke, P.R. Onck, O.G. Schmidt, Wrinkled-up nanochannel networks: Long-range ordering, scalability, and X-ray investigation, ACS Nano 2 (2008) 1715–1721. http://dx.doi.org/10.1021/nn800308p.
[18] Y.F. Mei, S. Kiravittaya, M. Benyoucef, D.J. Thurmer, T. Zander, C. Deneke, et al., Optical properties of a wrinkled nanomembrane with embedded quantum well, Nano Lett. 7 (2007) 1676–1679. http://dx.doi.org/10.1021/nl070653eISSN.
[19] S. Filipe, Covre da Silva, E.M. Lanzoni, V. de Araujo Barboza, A. Malachias, S. Kiravittaya, Ch. Deneke InAs migration on released, wrinkled InGaAs membranes used as virtual substrate, Nanotechnol. 25 (2014) 455603. http://dx.doi.org/10.1088/0957-4484/25/45/455603.

CRYSTAL
GROWTH

CrossMark
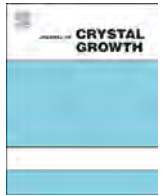
Defect creation in InGaAs/GaAs multiple quantum wells–I. Structural properties

Matthias M. Karow [a,*,1], Nikolai N. Faleev [a], David J. Smith [b], Christiana B. Honsberg [a]

[a] Solar Power Laboratory Arizona State University, Tempe, AZ 85287, USA
[b] Department of Physics Arizona State University, Tempe, AZ 85287, USA

ARTICLE INFO

ABSTRACT

We present a systematic study of extended defect creation in InGaAs/GaAs multiple quantum well (MQW) structures. Three sets of samples, grown by molecular beam epitaxy, were characterized by high-resolution x-ray diffraction and transmission electron microscopy. First, in a temperature series, optimal deposition temperature of 505 °C was found for the In composition of 20% as determined from dislocation loop (DL) density and inspection of diffuse scattering patterns. InGaAs decomposition and lateral layer thickness undulations were observed above this optimal temperature. Second, increase of MQW periodicity from $\times 5$ to $\times 10$ revealed a thickness-related cumulative deterioration, characterized by increased likelihood of defect intersection with continued MQW growth, as suggested by an increase of the secondary DL density from $\sim 1.6 \times 10^7\,\mathrm{cm}^{-2}$ to $\sim 6 \times 10^8\,\mathrm{cm}^{-2}$. Additional strained layers experienced an ever-degrading quality of the growth surface. Third, a set consisting of samples with three different MQW periods was investigated. Different stages, suggested by a model of defect creation, were obtained for these different MQW periods, allowing specification of particular type, density, and spatial distribution of extended defects for each stage of defect creation.

© 2015 Elsevier B.V. All rights reserved.

1. Introduction

Defect creation as an inherent process in epitaxial growth has impeded the realization and practical application of many electronic and optoelectronic devices. Physical properties and hence final device performance depend critically on the crystal quality of the epitaxial structure [1–5]. In multiple-quantum-well (MQW) solar cells, which appear to offer a superior approach compared to their homojunction counterparts [6–8], crystal quality deterioration still inhibits tapping of their full potential [9].

We report here on investigations of defect creation in InGaAs/GaAs MQWs and describe new findings about the main structural features, such as type, density, and spatial distribution of crystal defects, as dependent on growth conditions. Observations are interpreted in the framework of a model describing defect creation as a multi-stage process, starting from accommodation of initial elastic stress and point defect (PD) creation on the growth front, followed by inward diffusion and accumulation at pre-dislocation clusters, and finally transformation to extended defects in the

volume of epitaxial structure [10–12]. The crystalline properties of these structures as dependent on growth conditions are related to optical properties in the companion paper [13].

2. Experimental details

The $\mathrm{In}_x\mathrm{Ga}_{1-x}\mathrm{As/GaAs}$ MQW samples were grown by molecular beam epitaxy (MBE) on undoped (001)-oriented GaAs-wafers. MQW growth was preceded by a deoxidation step at 580 °C, followed by the growth of a 250-nm-thick GaAs buffer and AlGaAs cladding layers at a deposition temperature of 595 °C. Completion of deoxidation and the surface morphology transformation were monitored by in situ reflection-high-energy electron diffraction (RHEED). Growth rates of MQW structures were chosen as ~ 0.1 nm/s and 0.08 nm/s for InGaAs and GaAs layers, respectively, adjusted $\sim 20\%$ In composition.

Three sample sets were grown in order to allow defect creation in the InGaAs MQWs to be studied systematically as a function of deposition temperature, total MQW thickness, and average elastic strain.

(I) four samples, MQW period 8+8 nm (well and barrier thickness), grown at various deposition temperatures between 475 and 520 °C, with $\times 5$ periodicity;

* Corresponding author. Tel.: +1 480 965 6898.
E-mail addresses: Matthias.Karow@asu.edu (M.M. Karow),
Nikolai.Faleev@asu.edu (N.N. Faleev), David.Smith@asu.edu (D.J. Smith),
Christiana.Honsberg@asu.edu (C.B. Honsberg).
[1] Present address: Institute of Solid State Physics, Technical University Berlin,
Hardenbergstraße 36, 10623 Berlin, Germany.

(II) two samples, MQW period $8+8$ nm, grown at 490 °C, with periodicity $\times 5$ and $\times 10$;

(III) three structures, grown at 490 °C, periodicity $\times 10$, with MQW periods $4+8$ nm, $8+8$ nm, and $8+16$ nm.

These grouped structures were then analyzed to determine the influence of the growth parameters on defect creation. Crystalline properties were investigated with a PANalytical X'Pert Pro MRD high-resolution x-ray diffractometer (HRXRD) in double- and triple-crystal (DC and TC) modes for acquisition of DC and TC ω–2θ and TC ω rocking curves (RC). In TC geometry, an analyzer crystal in front of the x-ray detector is used to spatially separate coherent and diffuse scattered radiation. Shape, position, and full-width-at-half-maximum (FWHM) of diffraction peaks in respective RCs were examined to obtain structural information about the substrate and the epitaxial layers to suggest the type, density, and spatial location of the crystal defects resulting from epitaxial growth [10–12,14–16]. Symmetrical (004) and asymmetrical (224) ω–$2\theta/\omega$ TC reciprocal space maps (RSM) revealed the spatial distribution of diffuse scattered radiation, and hence showed structural features of the created defects. Asymmetric RSMs enable estimates to be made of the extent of relaxation of initial elastic stress, and correct specification of the preferred type of crystal defects [10–12].

Plan-view and cross-section transmission electron micrographs were compared to results from RHEED and HRXRD characterization.

3. Results and discussion

3.1. Deterioration regimes at different deposition temperature

Changes in crystal deterioration between deposition temperatures of 475 °C and 520 °C are observed in DC ω–2θ scans (Fig. 1). These curves are dominated by (004) GaAs diffraction and MQW superlattice (SL) peaks. In the curves for samples grown at temperatures ≤ 505 °C, coinciding angular positions of the SL peaks indicate the target In composition of $\sim 20\%$ and MQW period of ~ 16 nm. Interference patterns with clear SL peaks and interference fringes over a wide angular range correspond to a total MQW thickness of 80 nm and low deterioration of vertical coherence. RSMs reveal low density of diffuse scattered radiation and zero relaxation of the initial elastic stress. In cubic lattice heterostructures, this indicates low density of 60° dislocation loops (DLs) as the primary extended defects created in the volume of the epitaxial structures and on the interface(s), along with a lack

of closing-edge segments (Lomer dislocations) formed where the 60° DLs intersect in the volume of the MQWs [10–12].

In contrast, the DC ω–2θ scan of structure $T_{dep}=520$ °C reveals a lower In composition of $\sim 18.5\%$, as the SL interference pattern is shifted towards the substrate peak. Further, the SL peaks and the interference fringes are diffuse as a result of inferior vertical coherence. Quantitative results obtained from the FWHM of MQW peaks in TC ω–2θ scans demonstrate diminished vertical coherence ~ 75 nm (Table 1), while samples $T_{dep} \leq 505$ °C exhibit larger vertical coherence length ~ 97 nm.

TC ω RCs (Fig. 2) are used to specify type, density, and spatial distribution of preferred defects. The structures grown at $T_{dep} \leq 505$ °C (Fig. 2a) reveal ω RCs with a narrow central coherent peak on wider base and a clear interference wing on the tails indicating lateral ordering of the secondary 60° DLs on the MQW/substrate interface [10–12,14]. On the contrary, weak lateral ordering of small defects occurs at elevated temperature, as indicated by the broad range of scattering contributions in the respective TC ω RC (Fig. 2b). Azimuthal asymmetry observed for the lower growth temperatures is not present in this structure. The analysis of shape and linewidths in TC ω RCs allowed estimates to be made of the densities of 60° DLs as listed in Table 1. The density of both primary and secondary 60° DLs decreased with increasing deposition temperature until a minimum ($\sim 3 \times 10^5$ cm^{-2} and $\sim 1.5 \times 10^7$ cm^{-2} for primary and secondary DLs, respectively) is reached for a growth temperature of 505 °C. Diffuse scattering on the tails of the ω RCs caused by these loops is also minimal for this sample.

Symmetric and asymmetric RSMs (not shown) confirm the differences in crystal quality deterioration. While symmetrical RSMs for structures $T_{dep} \leq 505$ °C reveal narrow diffraction spots connected by a streaky truncation rod due to high vertical coherence of entire MQW structure, wide areas of diffuse scattering are observed in the RSM of the structure grown at 520 °C. The latter indicates deterioration of crystallinity with a broad range of length scales that is attributed to InGaAs decomposition leading to reduced In composition ($\sim 18.5\%$) and the creation of small scattering objects like In clusters. Asymmetrical RSMs with coinciding Q_x diffraction vector for (224) GaAs and InGaAs SL spots indicate a lack of initial stress relaxation for structures grown at ≤ 505 °C because primary DLs having their bottom edge segment in the volume of the substrate do not contribute to relaxation. Likewise, the density of secondary DLs is not sufficient to initiate relaxation. Asymmetrical RSMs in which the position of substrate and InGaAs SL spots causes specific Q_x gap ($T_{dep}=520$ °C), indicate an initial stage of stress relaxation (~ 2–3%).

Cross-section transmission electron microscopy (TEM) of the structure grown at 520 °C revealed a structural instability in the MQW structure with regard to the growth of morphological perturbations. In contrast to the other three samples, the MQW interfaces are not smooth, but show lateral thickness undulations with a period of ~ 100 nm (Fig. 3). This type of deterioration is attributed to the structural instability caused by the elevated growth temperature. This growth interval 505–520 °C resembles the critical temperature (surface diffusivity) predicted by [17] based on a theoretical stability analysis of strained-layer superlattice epitaxial growth. In this critical range, MQW growth is supposed to transition from a stable to an unstable regime, characterized by the lateral modulations in layer thickness.

Structural analysis identified the deposition temperature of 505 °C as the optimum for low deposition rate (~ 0.1–0.15 nm/s) epitaxial growth of the In$_{0.2}$Ga$_{0.8}$As MQWs. Further, two different regimes of crystal deterioration were found. At the optimal growth temperature and below, primary and secondary 60° DLs with pronounced lateral ordering served as the primary crystal defects that stabilize initially deteriorated epitaxial growth. DL densities
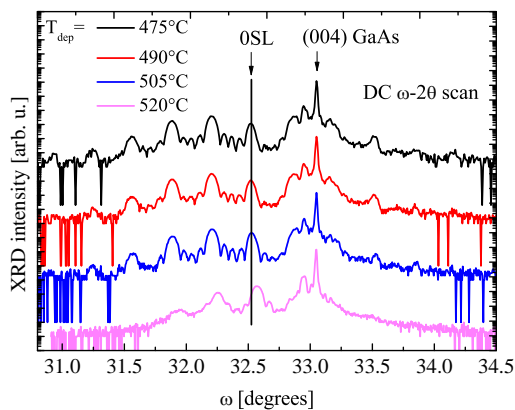
Fig. 1. DC ω–2θ scans in (004) reflection of four $\times 5$ MQW structures, period $8+8$ nm (well+barrier width) grown at different temperatures. SL peaks resultant from MQW periodicity and fast interference fringes related to total MQW thickness are clear for structures $T_{dep} \leq 505$ °C. Scan for the structure $T_{dep}=520$ °C demonstrates decrease of In composition and reduced vertical coherence of the MQW.

Table 1
Structural parameters as obtained from high-resolution x-ray diffraction around (004) InGaAs/GaAs MQW peaks.

T_{dep} [°C]	475	490	505	520
FWHM TC ω–2θ (0SL peak) [arc sec]	176	174	176	228
FWHM TC ω RC (-1SL peak) [arc sec]	12.2	11.2	9.4	10.1
$L_{vert.coh.}$ (MQW structure) [nm]	97	98	97	75
$N_{primary\ DLs}$ [cm^{-2}]	5.5×10^5	4.3×10^5	3.0×10^5	3.7×10^5
$N_{secondary\ DLs}$ [cm^{-2}]	2.7×10^7	1.6×10^7	1.0×10^7	1.2×10^7
Relaxation [%]	0	0	0	2–3
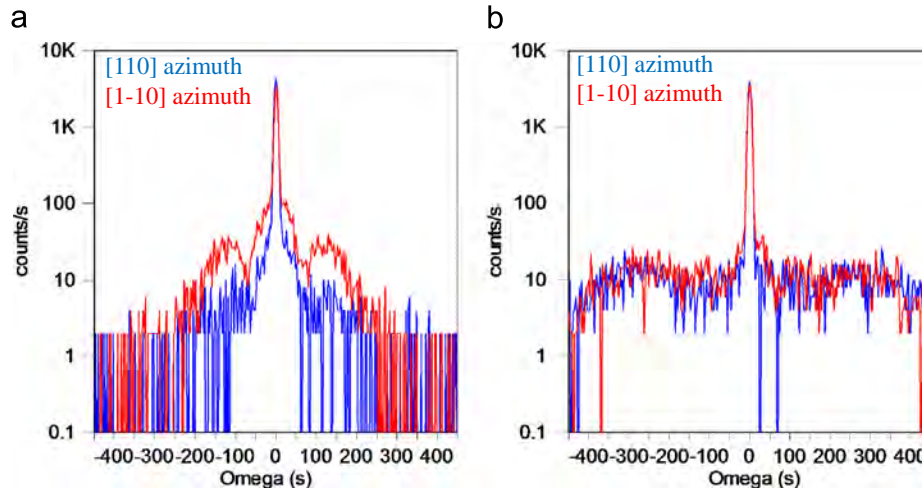
Fig. 2. TC ω RC in (004) reflection on -1SL of structure grown at: (a) optimal T_{dep}=505 °C and (b) elevated temperature T_{dep}=520 °C. Pronounced interference wings on the curve tails (a) contrast broad range of diffuse scattering (b) as a result of lateral ordering of extended defects.
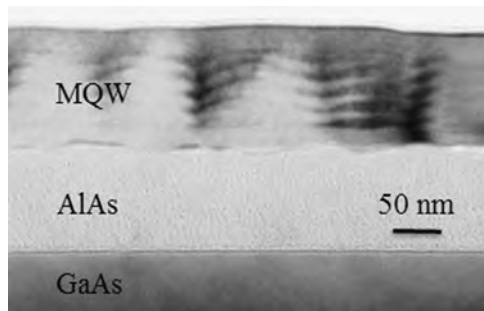
Fig. 3. Cross-section TEM of the $\times 5$ MQW structure grown at T_{dep}=520 °C. Lateral layer undulations (period ~100 nm) result from elevated deposition temperature and partial In decay.

decrease with increasing deposition temperature up to the optimum. Exceeding this temperature, a different type of deterioration, characterized by a range of lateral length scales and diminished vertical coherence is created. InGaAs decomposition as a material instability occurs at elevated growth temperature and a structural instability is manifested in lateral layer undulations.

An In composition ~20% was chosen for this particular study. However, there is possibly a different optimal temperature for each In composition and deposition rate with highest crystallinity and two distinct regimes of primary crystal deterioration below and above this temperature.

3.2. Effect of MQW periodicity

The increase of MQW periodicity from $\times 5$ to $\times 10$, for a fixed growth temperature of 490 °C and MQW period of 8+8 nm, is characterized by greater deterioration of crystal quality. Whereas the vertical coherence length of the $\times 5$ structure (~98 nm)

resembles its physical thickness (~80 nm), the $\times 10$ structure reveals vertical coherence (~110 nm) in comparison to MQW total physical thickness (~160 nm). This reduction results from an increased density of secondary DLs, their intersection, and creation of coherency-deteriorating edge segments (Lomer dislocations) in the volume of the SL.

TC ω RCs collected around the SL peaks reveal a strong decrease in coherent scattering and a prominent increase of diffuse scattering on the tail of the RC as the total MQW thickness is doubled. The increase in diffuse scattering is related to the increase in total density of secondary 60 °C DLs from ~1.6×10^7 cm^{-2} ($\times 5$) to ~6×10^8 cm^{-2} ($\times 10$) and augmented formation of edge segments resulting from DL intersection in the volume of MQW. The lateral coherence of the epitaxial layers is thus reduced.

Enhanced creation of secondary DLs and reduced vertical and lateral coherence are visible in the (004) RSMs (Fig. 4). While the narrow SL spots of the $\times 5$ MQW structure (Fig. 4a) are connected by a continuous narrow surface truncation rod due to high spatial coherence, Fig. 4b shows a broken truncation rod and diffuse SL spots visually elongated in the lateral direction.

The increase in secondary DL density shifts creation of next "tertiary" DLs close to the interface. This type of 60° DLs originates from single-atom pre-dislocation clusters, which gradually occupy vacant positions on the interface (minimal distance between these loops is $\approx |\boldsymbol{b}|\ /\varepsilon_{xx}$, where $|\boldsymbol{b}|$ is the modulus of the Burgers vector and ε_{xx} the initial elastic strain). These positions became available between already created primary and secondary DL extraplanes, which, diminishing atomic migration on the growth front, enable the creation of single-atom pre-dislocation clusters. Single-atom size of these pre-dislocation clusters induces secondary elastic stress to create DLs close to the interface and finally onset relaxation of the initial elastic stress [12], but insufficient to let created dislocation core glide into the substrate. In fact, the compressively strained SL is fully stressed in the $\times 5$ structure,

a b
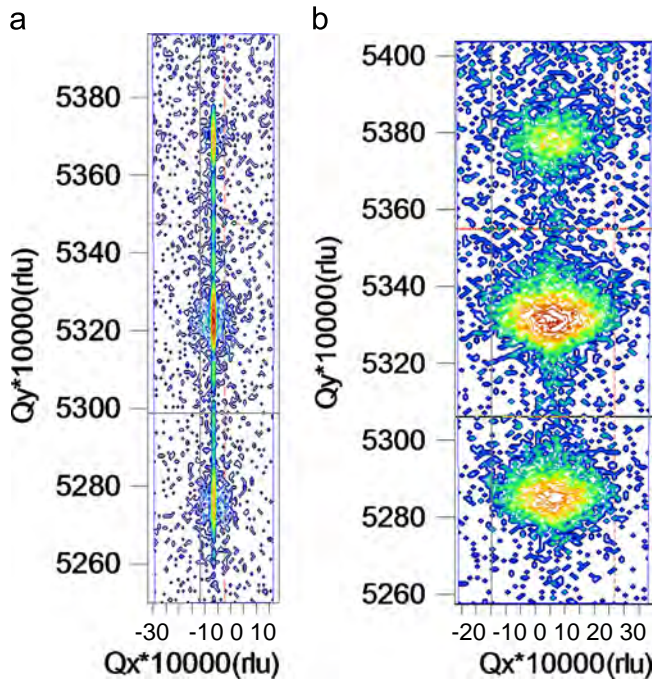
Fig. 4. Symmetrical (004) reciprocal space maps for two $8+8$ nm structures grown at the same deposition temperature and MQW period, but varied MQW periodicity (a) $\times 5$, (b) $\times 10$. Extended diffraction spots for $\times 10$ structure illustrate spatial coherence diminution and initial stage of relaxation caused by secondary DLs.

Fig. 5. TC ω RCs in (004) reflection of three MQW structures with varied MQW period. Three different, preceding stages of defect creation are realized. For the $8+16$ nm structure RCs for two azimuthal directions [110] and [1-10] are shown, whereas the two other samples do not show azimuthal anisotropy.

whereas a relaxation of ~ 12–15% is observed in the (224) RSM for the $\times 10$ structure.

Contrasting these two samples with different MQW periodicity (total thickness), while T_{dep} and MQW period were kept fixed, revealed a cumulative thickness-related deterioration as the elastic strain is accommodated during epitaxial growth by the gradual occupation of pre-dislocation positions on the interface(s).

3.3. Effect of MQW period

Growth of $\times 10$-periodicity MQW structures was carried out at a common deposition temperature. Starting from the MQW period $8+8$ nm (well and barrier widths), as used in all structures discussed so far, the thickness of the strained well layers was reduced to 4 nm. In a second approach, the strained layer thickness was kept at 8 nm, while the unstrained barrier width was doubled to 16 nm. This set of samples allows an evaluation of how changes in the total incorporated elastic strain affect and possibly mitigate defect creation related to lattice-mismatched epitaxial growth.

The sample with the lowest MQW period of $4+8$ nm revealed best crystal quality with a sharp coherent SL peak in the TC ω RC (Fig. 5). FWHM of the central and diffuse peaks of symmetric RCs allowed estimates to be made of the density of primary and secondary DLs of ~ 5–7.5×10^4 cm^{-2} and $\sim 1 \times 10^7$ cm^{-2}, respectively. From the linewidth of the SL peaks in the TC ω–2θ scans, the vertical coherence length of the MQW was calculated to be ~ 120 nm, which coincides with the physical thickness of the structure. Symmetrical RSM (Fig. 6a) revealed SL spots elongated along the vertical diffraction vector forming a faint surface truncation rod. The narrow lateral extent of diffraction spots correlates with a weak diffuse scattering contribution in TC ω RC. Total density of the primary and secondary DLs was insufficient to onset noticeable creation of tertiary DLs and relaxation of the initial elastic stress. The growth surface, deteriorated by InGaAs deposition was "healed" by barrier GaAs layers,
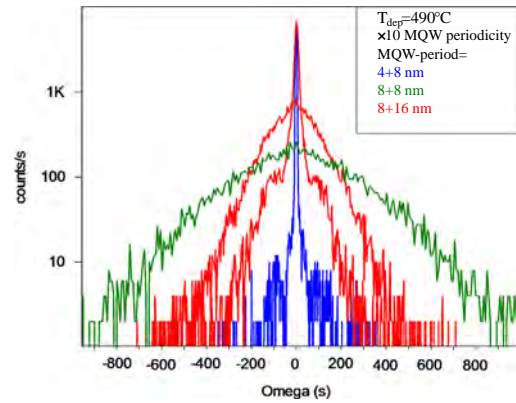
diminishing the depth of dislocation trenches, the main deteriorating factor on the growth surface [11]. Both effects terminated the defect creation at an early stage, individually for each SL pair (well and barrier), as less strain needed to be accommodated and fewer surface migration obstacles to overcome.

In contrast, the samples with increased MQW periods of $8+16$ nm and $8+8$ nm with thicker strained layers showed reduced crystal quality. Coherent scattering was considerably weakened and diffuse contributions were enhanced, as apparent from the TC ω RC (Fig. 5). The structure with $8+16$ nm demonstrates an intermediate stage of crystal perfection, between those observed in the $4+8$ nm and the $8+8$ nm structures. For [110] azimuth direction, coherent scattering from the MQW structure is rather intense and a primary DL density of ~ 7–8×10^5 cm^{-2} is estimated from the FWHM of this peak (Fig. 5). Visual azimuthal asymmetry of the ω RCs for [1-10] direction corresponds to the anisotropic spatial distribution of extended defects. This distribution results in secondary DL density estimates differing by about an order of magnitude, namely of $\sim 1.3 \times 10^7$ cm^{-2} and 1.7×10^8 cm^{-2} for [110] and [1-10] azimuths, respectively. The anisotropic spatial distribution of secondary DLs is also confirmed by the different degree of relaxation of the strained layers. Whereas the lower DL density along [110] and the respective number of tertiary DLs on the interface is insufficient to initiate the relaxation of initial elastic stress, higher DL density along [1-10] led to creation of a sufficient number of DLs close to the epitaxial interfaces for a relaxation of $\sim 5\%$ in the [1-10] direction. This corresponds to the linear density of tertiary DLs at the bottom interface of $\sim 1.8 \times 10^4$ cm^{-1}.

Despite the increased total number of primary and secondary DLs in the volume, the calculated vertical coherence length (based on the FWHM of 0SL peak in ω–2θ scans) is close to the physical thickness (240 nm), as for the $4+8$ nm structure. The unstrained barrier layers of doubled thickness retained the crystalline properties of the MQW structures. The barrier layers, serving as a defect protector, helped to realize defect "healing" after a single deteriorated well layer is grown. During growth of further strained-well layers, these were exposed to fewer extended defects originating from the previous strained layers.

In the $8+8$ nm structure, the density of secondary DLs in the volume increased to $\sim 6 \times 10^8$ cm^{-2}, which is more than an order of magnitude higher than in the $4+8$ nm structure and about half an order of magnitude higher than for the $8+16$ nm structure. The spatial distribution of extended defects had no azimuthal asymmetry. The vertical coherence length was estimated as ~ 110 nm, which is $\sim 30\%$ below the 160 nm physical thickness of the MQW
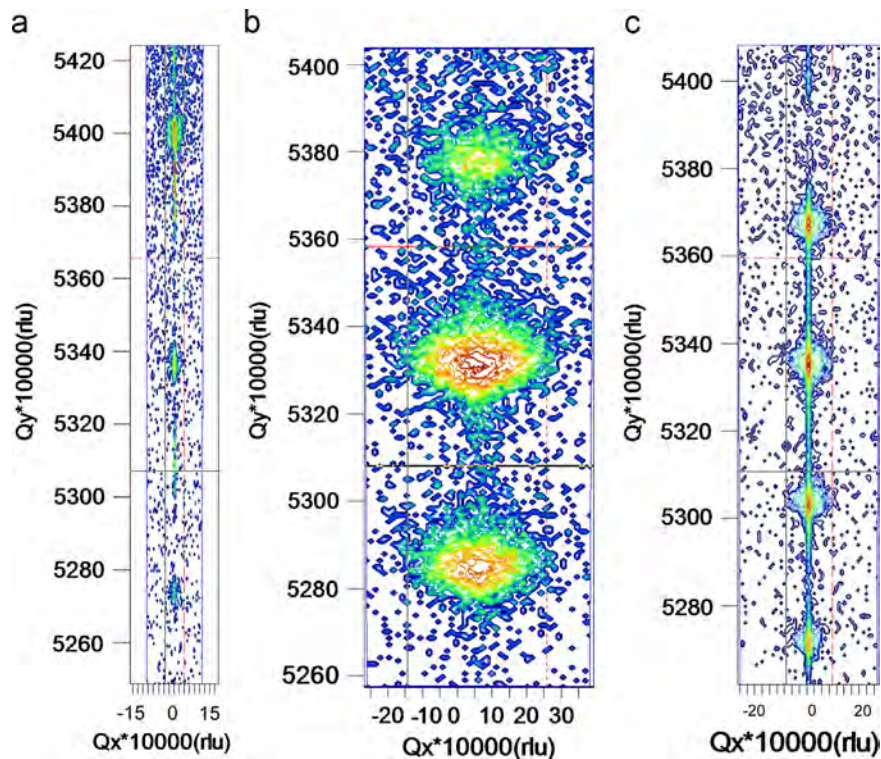
Fig. 6. Symmetric (004) RSMs for three MQW structures with different MQW period, (a) 4+8 nm, (b) 8+8 nm, (c) 8+16 nm. The streaky vertically running surface truncation rod suggests high vertical coherence due to low density of edge segments, but laterally elongated diffraction spots indicate high deterioration due to intersecting secondary DLs and edge segments created in the MQW volume.

structure. The increased thickness of the strained layers led to higher deterioration of every single quantum well as larger elastic strain had to be accommodated. In turn, more secondary and tertiary DLs were created and the density of closing-edge segments (Lomer dislocations) increased. The latter was manifested in reduced vertical coherence length as compared to the physical thickness and relaxation of the initial elastic stress.

In direct comparison, the decrease of the strained layer width (8+8 nm vs. 4+8 nm) reduced the crystalline deterioration more effectively than increasing the unstrained layer thickness (8+8 nm vs. 8+16 nm), as defect creation was terminated at an earlier stage. For a multi-stage defect creation process, this early stage is characterized by the creation of primary DLs as the main deterioration cause. Increasing the unstrained layer thickness used as "healing" element, resulted in reductions in the total amount of PDs created on the growth front and hence to the lower density of secondary DLs. The likelihood of tertiary DL and Lomer dislocation formation close to substrate/epi-structure interface and in the MQW volume was hence reduced. The latter explains why the extent of stress relaxation decreased from $\sim 15\%$ to 0–5%.

4. Discussion and conclusions

The experimental results emphasize that defect creation in epitaxial growth is a complicated multi-stage process. All types of 60° DLs originate from PDs, created at the growth front. Upon inward diffusion of PDs they accumulate in pre-dislocation clusters and finally transform to DLs under secondary elastic stress, induced by these clusters. In a continuous process, primary and secondary DLs reconstruct the growth surface for the generation of tertiary DLs. Creation of these DLs stabilizes the growth procedure.

Three sets of InGaAs/GaAs MQW structures were grown by MBE and characterized by HRXRD and TEM with regard to their crystal quality. Probing the influence of the deposition temperature revealed two distinct deterioration regimes, separated by the optimal growth temperature of ~ 505 °C. Deposition below this temperature resulted in the creation of primary and secondary 60° DLs as the main deterioration type, with a decreasing density trend as the temperature was increased and a minimum at the optimal temperature. Elevated temperature led to InGaAs decomposition and a structural instability of the MQW growth, forming laterally undulated MQW layers and interfaces.

Increasing the periodicity and total thickness of the MQWs revealed a cumulative deteriorating effect. The intersection of already created DLs for continued MQW growth increased the number of edge segments created at substrate/epi-structure interface and in the volume of the MQWs. The former led to the onset of relaxation of initial elastic stress, while the latter led to deterioration of the spatial coherence.

Three distinct stages of defect creation were obtained by varying the MQW period. While a diminished thickness of the QW layers (4+8 nm structure) revealed primary DLs as the main type of deterioration, the 8+16 nm structure led to enhanced creation of secondary DLs representing the succeeding deterioration stage. Closing-edge segments were formed at a density on the substrate/MQW interface not sufficient for noticeable stress relaxation. The 8+8 nm structure represented an even more advanced stage of defect creation in which the creation of tertiary DLs on the interface, and most importantly, their intersection in the volume of MQW and the location of closing-edge segments close to epitaxial interfaces were sufficient to initiate relaxation of elastic stress.

Acknowledgments

References

[1] G.W. Pickrell, K.L. Chang, J.H. Epple, K.Y. Cheng, K.C. Hsieh, J. Vac. Sci. Technol. B 18 (6) (2000) 2611–2614.
[2] J.F. Klem, W.S. Fu, P.L. Gourley, E.D. Jones, T.M. Brennan, J.A. Lott, Appl. Phys. Lett. 56 (14) (1990) 1350–1352.
[3] A. Madhukar, K.C. Rajkumar, Li Chen, S. Guha, K. Kaviani, R. Kapre, Appl. Phys. Lett. 57 (1990) 2007–2009.
[4] B. Grandidier, H. Chen, R.M. Feenstra, D.T. McInturff, P.W. Juodawlkis, S. E. Ralph, Appl. Phys. Lett. 74 (10) (1999) 1439–1441.
[5] J. Zou, D.J.H. Cockayne, Appl. Phys. Lett. 69 (8) (1996) 1083–1085.
[6] K. Barnham, I. Ballard, J. Connolly, N. Ekins-Daukes, B. Kluftinger, J. Nelson, C. Rohr, Physica E 14 (2002) 27–36.
[7] C.B. Honsberg, S.P. Bremner, R. Corkish, Physica E 14 (2002) 136–141.
[8] A. Freundlich, G.K. Vijaya, A. Mehrotra, Proceedings of the 39th IEEE Photovoltaic Specialist Conference, 1635–1638, 2013.
[9] F.W. Ragay, J. Wolter, A. Marti, G. Araujo, Proceedings of IEEE First World Conference on Photovoltaic Energy Conversion, 2, 1754–1758, 1994.
[10] N. Faleev, N. Sustersic, N. Bhargava, J. Kolodzey, A. Yu. Kazimirov, C. Honsberg, J. Cryst. Growth 365 (2013) 44–53.
[11] N. Faleev, N. Sustersic, N. Bhargava, J. Kolodzey, S. Magonov, D.J. Smith, C. Honsberg, J. Cryst. Growth 365 (2013) 35–43.
[12] S.P. Bremner, K.-Y. Ban, N.N. Faleev, C.B. Honsberg, D.J. Smith, J. Appl. Phys. 114 (2013) 103511-1–103511-9.
[13] M.M. Karow, N.N. Faleev, A. Maros, C.B. Honsberg, Journal of Crystal Growth, x (x), pp. xx-xx, 201x. (Companion paper: Defect Creation in InGaAs/GaAs Multiple Quantum Wells – II. Optical Properties).
[14] V.M. Kaganer, R. Kohler, M. Schmidbauer, R. Opitz, B. Jenichen, Phys. Rev. B 55 (1997) 1793–1810.
[15] U. Pietsch, V. Holy, T. Baumbach, High Resolution X-Ray Scattering, Springer, Berlin, 1999.
[16] J.E. Ayers, J. Cryst. Growth 135 (1994) 71–77.
[17] L.E. Shilkrot, D.J. Srolovitz, J. Tersoff, Phys. Rev. B 62 (12) (2000) 8397–8409.

CRYSTAL
GROWTH

CrossMark
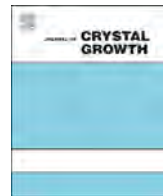
Defect Creation in InGaAs/GaAs Multiple Quantum Wells – II. Optical Properties

Matthias M. Karow [*,1], Nikolai N. Faleev, Aymeric Maros, Christiana B. Honsberg

Solar Power Laboratory Arizona State University, Tempe, AZ 85287, USA

ARTICLE INFO

ABSTRACT

The optical properties of three sets of InGaAs/GaAs multiple quantum well (MQW) structures grown by molecular beam epitaxy and previously characterized by x-ray diffraction for crystal perfection were investigated. The correlations between growth conditions, crystal defects, and optical properties are discussed. Evaluation of the relative importance of non-radiative Shockley-Read-Hall (SRH) recombination was carried out according to a method presented herein. The optimal deposition temperature was determined based on both proper carrier confinement in the nanostructures and the least non-radiative recombination. Growing below this temperature increased SRH-recombination whereas higher growth temperatures led to carrier localization in local band edge minima. Varying the MQW periodicity and MQW period allowed the study of their effects on the strength of SRH-recombination. MQW periodicity results are explained in the frame of a cumulative deterioration effect with continued epitaxial growth, while MQW period data shows correlations between relaxation of the initial elastic stress and SRH-strength. Limitations of the underlying model for SRH-analysis are pointed out.

1. Introduction

High device performance requires optimized growth processes tailored to the underlying epitaxial structures, in an effort to reduce crystalline deterioration as a possible origin for device capability shortcomings [1–3]. In this respect, crystal defects are known to mediate loss mechanisms [4], to be responsible for leakage channels [5], and to be roots of device degradation [6]. In the context of optoelectronic applications, their impact on optical properties has hence been studied extensively for various material systems.

In the InGaAs/GaAs material system, for instance, it was shown that dislocation edge segments particularly enhance non-radiative recombination. The involved carrier states, mediating this loss mechanism were revealed to be associated with dislocation cores, and did not originate from spatially separated defect sites [7].

Our x-ray diffraction investigations [8] previously revealed distinct dependencies of the crystalline properties of InGaAs/GaAs multiple-quantum-well (MQW) structures on molecular beam epitaxy (MBE) growth conditions. In this paper, these findings

are related to conclusions drawn from optical studies. In particular, non-radiative recombination is assessed by means of a model developed herein, in order to establish correlations between growth conditions, crystal quality, and optical properties for the particular structures investigated herein.

2. Experimental procedure

Three sets of $In_xGa_{1-x}As$/GaAs MQW samples were grown by MBE on undoped (0 0 1)-oriented GaAs wafers. The first set consists of four samples grown at varied deposition temperature 475–520 °C, the second set was grown with varied periodicity × 5 and × 10, and finally a third set features a MQW period series of 4+8 nm, 8+8 nm, and 8+16 nm. A full description of the growth conditions and the setup used can be found in the companion paper [8]. In addition to characterization by means of high-resolution x-ray diffraction (HRXRD) described therein, optical properties were examined in various photoluminescence spectroscopy (PL) experiments.

Information about the electronic states present in the grown structures was extracted from temperature-dependent PL measurements. Placed in a He-flow cryostat between 5 and 300 K, the samples were excited with a 632.8 nm HeNe-laser at 10 mW optical power. The resultant PL transition energies were compared to the

* Corresponding author, Tel.: +1 480 965 6898.
E-mail addresses: Matthias.Karow@asu.edu (M.M. Karow),
Nikolai.Faleev@asu.edu (N.N. Faleev), Aymeric.Maros@asu.edu (A. Maros),
Christiana.Honsberg@asu.edu (C.B. Honsberg).
[1] Present address: Institute of Solid State Physics, Technical University Berlin,
Hardenbergstraße 36, 10623 Berlin, Germany.
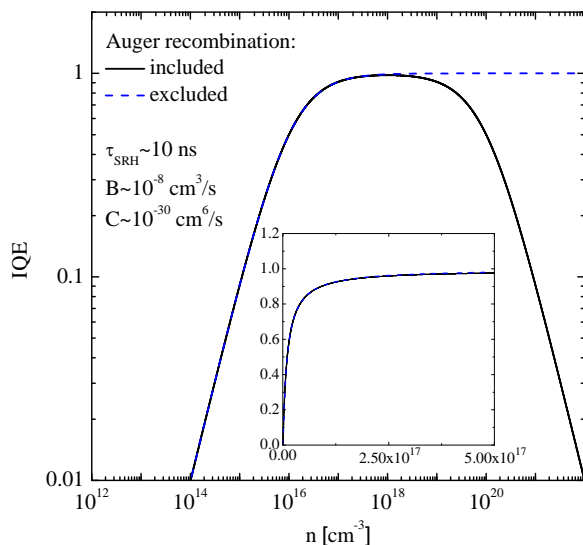
Fig. 1. Calculated internal quantum efficiency (IQE) based on a conservative low temperature life time estimate and appropriate B and C parameters [12,13]. Until the onset of the IQE drop at elevated carrier density n, Auger recombination can be neglected.

Fig. 2. Sample plot of the emitted PL intensity upon increase of the excitation power. Two distinct regimes, characterized by square and linear scaling, respectively are identified. The transition occurs at a higher pumping level the stronger SRH-recombination.

calculated confinement states of carriers in these nanostructures obtained using self-consistent Schrödinger Poisson methods [9].

Excitation power-dependent photoluminescence spectroscopy was utilized to characterize the strength of non-radiative recombination in the structures as a result of the defects created during epitaxial growth. The measurements were carried out at 12 K with excitation provided by a 376 nm laser diode and power varied over three orders of magnitude up to 70 mW.

3. Excitation-dependent PL for defect analysis

A model is presented as a means to characterize the strength of Shockley-Read-Hall (SRH)-recombination based on excitation power-dependent PL measurements. Fundamental to this model is a transition of the dominant carrier recombination process from one type to another depending upon the excess carrier density. This manifests as a change in scaling of the light output-excitation power relationship from a square to a linear dependence.

At low temperature and sufficient excitation power, the SRH-recombination rate per unit volume in undoped structures is given as $R_{SRH} = A \cdot \Delta n$, with the SRH-parameter A and the excess electron density Δn [10]. Optical excitation creates electron-hole-pairs $\Delta n = \Delta p$, (Δp is the excess hole density). In structures without carefully designed optical cavities, spontaneous radiative recombination occurs at a rate $R_{spo} = B \cdot (\Delta n)^2$, with the spontaneous emission coefficient B. A third recombination process, Auger recombination, occurs at the rate $R_{Auger} = C \cdot (\Delta n)^3$, with the Auger coefficient C^2. [11]

These recombination mechanisms compete with carrier generation by the excitation source (power P, wavelength λ). The generation rate G per volume V is proportional to the excitation power, $G(P) = P\lambda/hcV(1 - e^{-\alpha d})$ where h is Planck's constant, c is the speed of light, α is the absorption coefficient, and d is the length of the absorption region. At steady state, the rate equation for these processes reads $dn/dt = G - An - Bn^2 - Cn^3 = 0$. Simplifications are possible if Auger recombination is neglected. For that
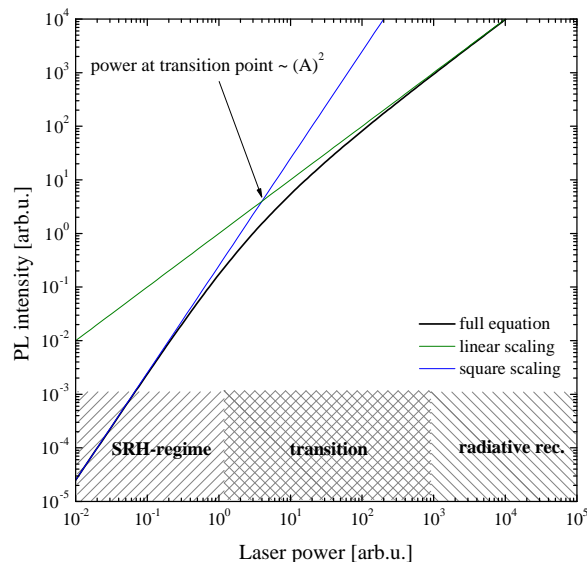
reason a means is introduced to determine from experimental data if this condition is met. The internal quantum efficiency IQE is given by IQE $= Bn^2 / An + Bn^2 + Cn^3$. Fig. 1 shows an example of the calculated dependence of IQE on carrier density n for selected values A, B, and C. Beyond a plateau within a carrier density range where radiative recombination dominates, a drop in IQE marks the onset of Auger recombination as the dominant mechanism. The external quantum efficiency EQE $\propto$ IQE is experimentally accessible since EQE $\propto I_{PL}/P$, where I_{PL} is the measured PL intensity. Thus a plot of the quantity I_{PL}/P versus the excitation power P allows one to determine the experimentally covered excitation range over which Auger recombination can be neglected. Indirect semiconductors with a low B parameter are not suitable for investigation in this manner.

From the approximated rate equation $0 = G(P) - A\,n(P) - B\,n(P)^2$, in which Auger recombination is neglected, the rate of emitted photons from the optical volume V is derived as

$$I_{PL}(P) = VB \cdot n(P)^2 = VB \left[-\frac{A}{2B} + \sqrt{\left(\frac{A}{2B}\right)^2 + \frac{G(P)}{B}} \right]^2. \qquad (1)$$

Approximation of this equation in low excitation limit ($BG/A \ll 1$) and at intermediate level ($n \approx \sqrt{B/G}$), shows square and linear scaling, respectively. A sample plot of Eq. (1) illustrates the two regimes (Fig. 2). At low pumping level, carriers mainly saturate trap states and only a small portion recombine radiatively. With increased pumping levels, non-radiative recombination sites become saturated and radiative recombination of electron-hole-pairs dominates. The transition between the two regimes occurs gradually $I_{PL} \propto P^k$ with a continuously decreasing scaling parameter $k \in (1, 2)$. A particular value of the power at which the transition occurs can be defined as the excitation level G_T at which the curves, approximated in the individual limits, intersect. Since the generation rate at this point is given by $G_T = A^2/B \propto A^2$, the excitation power at which this transition occurs can be used to measure the magnitude of the A parameter.

To summarize, excitation power-dependent PL measurements can be used to detect a transition from square to linear scaling in the relation between the intensity of the luminescence emitted from the sample and the excitation power. The higher the

---

^{2} In undoped structures held at low temperature the electron density n can be approximated as $n \approx \Delta n$.

excitation power at which this transition occurs, the stronger are the non-radiative processes. Applying this ABG-model allows one to draw conclusions about how defects created in epitaxial growth act as non-radiative recombination sites.

4. Results

The quantum confinement states of carriers in MQW nanostructures are studied using PL over a range of temperatures and excitation powers. The temperature evolution of the PL transition lines reveals the nature and origin of these states. Ideal behavior would reproduce the temperature-dependent transition energy behavior between electron and hole confinement states.

4.1. Effect of different deposition temperature

As described in the companion paper [8], one sample set consists of $\times 5$ MQW structures among which the deposition temperature was varied. Temperature-dependent PL revealed Varshni-like temperature dependence of the main PL transition line for all samples grown at $T_{dep} \leq 505\ ^\circ$C [14]. An example of the PL peak dependence on ambient temperature for the structure with $T_{dep} = 505\ ^\circ$C is shown in Fig. 3a. Good agreement with the calculated transition energy between heavy hole and electron MQW states (black, dashed) shows ideal carrier confinement in the nanostructures. The low temperature (12 K) linewidth of the PL peaks were as low as 8 meV, indicating a low density of defect centers at which carriers are scattered, which would otherwise lead to PL line broadening. This range of deposition temperatures ($\leq 505\ ^\circ$C) resulted in high quality $In_{0.2}Ga_{0.8}As/GaAs$ MQW structures with ideal carrier confinement.

The method described in Section 3 is applied to three samples with $T_{dep} \leq 505\ ^\circ$C. The ratio $I_{PL}/P \propto$ EQE vs. P is plotted in Fig. 4 to validate the assumption of negligible Auger recombination. It is apparent that the regime in which Auger recombination becomes significant is not entered, i.e. the EQE does not drop beyond the plateau as it would at higher excitation as shown in Fig. 1. Hence the simplified equations of the ABG-model (Eq. 1) can be used for further analysis.

The change in the scaling parameter k of an I_{PL} vs. P curve is a measure of the SRH-recombination strength. A suitable way to present this transition is shown in Fig. 5, in which the scaling exponent $k = d\log(I_{PL})/d\log(P)$ is plotted against the excitation power P. While square scaling corresponds to $k = 2$, linear scaling is indicated by $k = 1$. The plot of the scaling exponent shows different onsets of linear scaling over the covered excitation range. The structure $T_{dep} = 505\ ^\circ$C exhibits linear scaling over the entire excitation range as the scaling exponent scatters around 1. For the structure grown at 15 °C lower temperature the scaling exponent started off around 1.2 at the lowest pumping level, decreasing continuously with excitation power and finally reaching unity. In comparison to the structure grown at higher temperature, this sample required a higher excitation power to reach the linear regime. The lowest deposition temperature sample $T_{dep} = 475\ ^\circ$C manifested a high scaling exponent ~ 1.4 at lowest excitation. Although k decreased continuously with higher excitation, linear scaling was not observed in the covered range. The value $k = 1$ is hence likely to occur at even higher pumping. These measurements showed a gradual increase of the pumping level at which the linear PL regime is entered as deposition temperature is decreased, leading to the conclusion that the strength of non-radiative SRH-recombination increases likewise.

Whereas the structures with $T_{dep} \leq 505\ ^\circ$C showed Varshni-like behavior in the temperature-dependent PL experiments as a result of ideal carrier confinement, the sample with $T_{dep} = 520\ ^\circ$C deviates in this respect (Fig. 3a). In contrast to the simulated transition
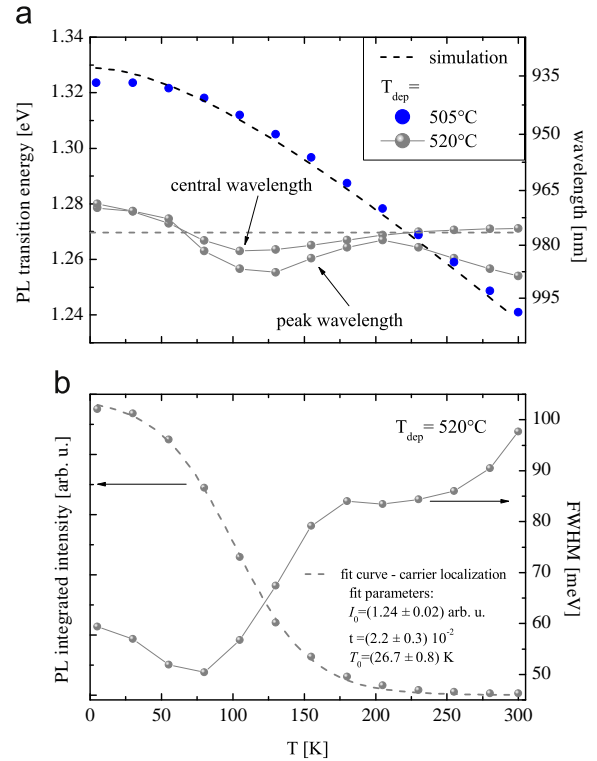
Fig. 3. a) Temperature-dependent PL signal for two MQW structures with the same periodicity and period. Whereas the structure grown at $T_{dep} = 505\ ^\circ$C reveals a behavior that follows closely the calculated trend (black, dashed), sample $T_{dep} = 520\ ^\circ$C is described by an S-shape curve. b) Characteristic non-monotonic linewidth temperature dependence and good fit of integrated PL intensity versus ambient temperature curve to $I_{PL} = I_0/(1 + t \cdot \exp(T/T_0))$ suggest the occurrence of carrier localization.
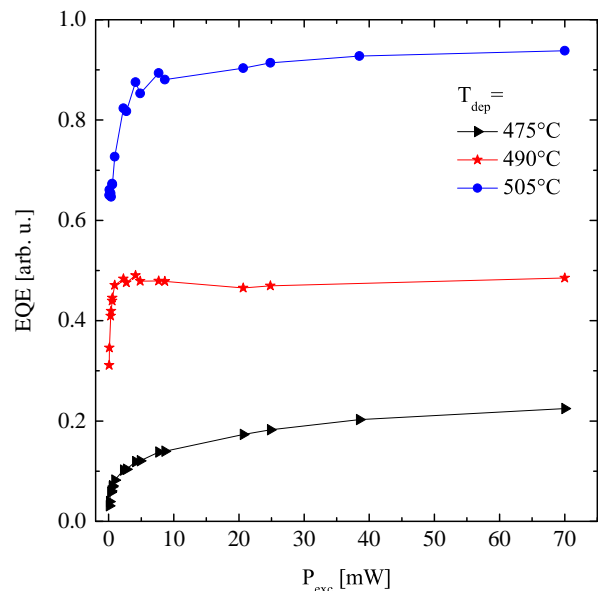
Fig. 4. The shape of the external quantum efficiency (EQE) curve as dependent on excitation power indicates that Auger recombination is negligible over the covered pumping range, if compared to Fig. 1.

energy dependence (black, dashed), this sample's PL response (grey) started off with a photon energy ~ 50 meV below the calculated value at low temperature and revealed a non-monotonic temperature dependence. This particular S-shape behavior and the non-monotonic variation in peak asymmetry (compare peak and central wavelength) hint at the localization of
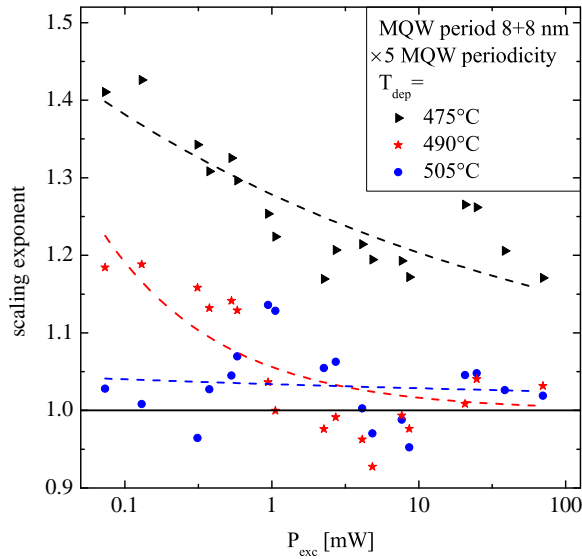
Fig. 5. Linear scaling occurs at a higher excitation power the lower the deposition temperature T_{dep}. High scattering of data points is to be expected as the plotted quantity (scaling exponent) is based on a differentiative evaluation method.

Fig. 6. Direct comparison of optical behavior at varied excitation power unveils the stronger SRH-recombination in the higher periodicity MQW.

Fig. 7. Increasing the unstrained barrier width reduces defect state mediated non-radiative recombination as apparent from particular scaling exponent behavior shown.

carriers in local energy minima. Redistribution of carriers among local minima is a temperature activated process and leads to the S-shape dependence observed here. Along with the non-monotonic linewidth behavior and a good fit of the temperature-dependent PL intensity data to a model proposed by [15,16] (both Fig. 3b) the results suggest the occurrence of carrier localization. This mechanism has been described previously in various other structures [15–17]. The identified presence of random band edge fluctuations is attributed to compound composition variations as a result of InGaAs decomposition at an elevated deposition temperature $T_{\text{dep}}=520$ °C.

4.2. Effect of MQW periodicity

This set of samples probes the influence of MQW periodicity on the optical properties of epitaxial structures. The PL response showed good carrier confinement in these epitaxially grown nanostructures with agreement between measured photon wavelength and calculated confinement states. To compare the influence of defect related recombination processes, excitation-dependent PL was carried out according to the ABG-model used above. As was shown above for the temperature series (Fig. 4), the behavior of the quantity I_{PL}/P was examined with regard to a possible EQE drop at highest pumping level, justifying neglecting Auger recombination in the ABG-model. The scaling exponent dependence on the pumping level is plotted in Fig. 6 for the samples with different MQW periodicities. It can be seen that the low-periodicity structure revealed a scaling exponent ~ 1.2 at the lowest excitation and rapidly transitioned into the linear region. In contrast, the high-periodicity sample started off with a higher scaling exponent ~ 1.9 and reached linear scaling at a comparatively higher pumping level. Based on the ABG-model it can be inferred that trap state mediated non-radiative recombination is stronger in the $\times 10$ structure. An increase in the periodicity of epitaxial MQW structures led to a reduced carrier lifetime as a result of more defect sites involved in SRH-recombination.

4.3. Effect of MQW period

The decrease of the MQW period from $8+16$ nm to $8+8$ nm of epitaxial structures is supposed to result in different densities of defects due to the different amount of total elastic strain.
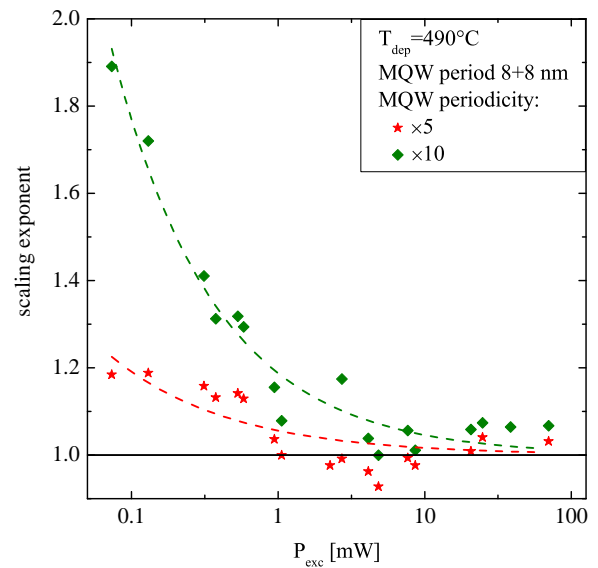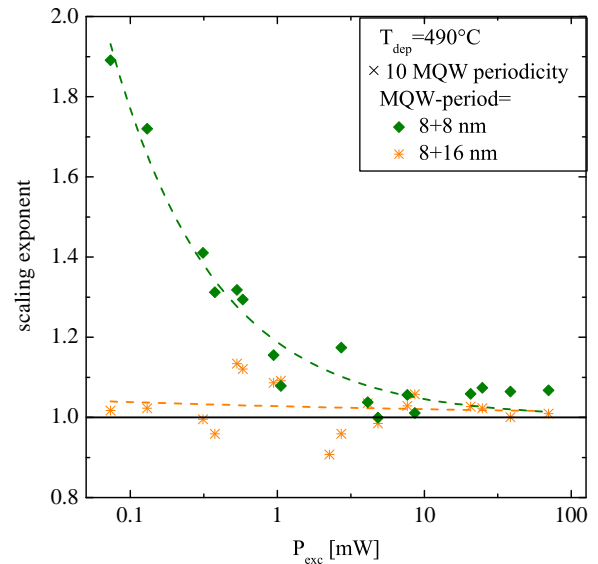
As before, the strength of SRH-recombination was investigated via excitation power-dependent PL. The evolution of the ratio I_{PL}/P confirmed that Auger recombination is negligible over the excitation power range of interest. A plot of the scaling exponent versus the pumping level is shown in Fig. 7. It is apparent that the sample with highest MQW period $8+16$ nm stays in a linear regime over the entire excitation range. The saturation of recombination sites in the epitaxial volume is expected to occur at even lower excitation power. Reducing the MQW period to $8+8$ nm reveals the higher pumping level necessary to enter the linear scaling regime.

Hence, the reduction of unstrained barrier layer thickness from 16 to 8 nm increased the strength of SRH-recombination considerably. This result, however, has to be put into perspective, as the limited absorption depth ($\sim$ 200 nm [18]) leads to partial excitation and hence examination of only part of the MQW volume of the structure with MQW period $8+16$ nm. The substrate/epi-structure interface, which due to relaxation of the initial elastic

stress [8] is a probable location of non-radiative recombination sites, most likely contributes only slightly to the emitted light and is thus of minor influence in this ABG-experiment because of the sample's thickness ($\times 10$, $8+16$ nm). If the scaling exponent curves of this structure and the $\times 5$, $8+8$ nm one (the latter revealing comparatively reduced edge segment density and no relaxation) are compared, it becomes apparent that non-radiative recombination is underestimated in the thick structure $8+16$ nm.

5. Correlation with crystalline properties

The optical properties of various InGaAs/GaAs MQW structures studied in this work were correlated with the particular growth conditions and crystalline properties from prior work as explained in detail in [8].

In the set of samples grown at varied deposition temperatures, HRXRD investigations found an optimal growth temperature $T_{dep}=505\ °C$ for $In_{0.2}Ga_{0.8}As$, characterized by smooth MQW interfaces, minimal dislocation loop (DLs) densities and the least amount of diffuse scattering in symmetric (0 0 4) reciprocal space maps. At this value and below ($T_{dep} \leq 505\ °C$) the main type of crystalline defects are $60°$ DLs with increasing density as T_{dep} is decreased. From the optical data, the primary and secondary DLs at the measured densities ($3.0\text{–}5.5 \times 10^5\ cm^{-2}$ and $1.0\text{–}2.7 \times 10^7\ cm^{-2}$) still allow proper confinement of charge carriers in the nanostructures as concluded from temperature-dependent PL experiments. The strength of non-radiative SRH-recombination increases along with the density of DLs for lowered T_{dep} and the optimal T_{dep} found in HRXRD experiments coincides with the one inferred from optical investigations.

Exceeding the optimal $T_{dep}=505\ °C$ revealed a material instability manifested in InGaAs decomposition and a structural instability visible as lateral layer thickness undulations in transmission electron micrographs. Both deteriorations cause local effective band gap fluctuations as both the compound composition and confining layer thicknesses determine carrier state energies. This correlates with random band edge fluctuations found in the optical investigations (Fig. 3) that led to carrier localization in local energy minima.

Varied MQW periodicity from $\times 5$ to $\times 10$ at the same T_{dep} and MQW period revealed reduced vertical and lateral coherence, an increased density of secondary $60°$ DLs, and visible relaxation of initial elastic stress up to $\sim 15\%$. As the densities of edge segments on the substrate/epi-structure interface and Lomer dislocations in the volume increase non-radiative SRH-recombination becomes prominently stronger. This finding was explained as a cumulative deterioration effect. Denser creation of edge segments close to substrate/epi-structure interface (tertiary DLs) giving rise to stress relaxation [19–21] accounts for the denser distribution of defect states involved in SRH-recombination.

Lastly, a set with different MQW periods, grown at the same T_{dep} with common MQW periodicity, showed in its optical properties the effect of thicker unstrained barriers as defect "healing" layers while the period was increased from $8+8$ nm (well+barrier width) to $8+16$ nm, in agreement with the conclusions drawn from HRXRD investigations.

6. Discussion and conclusion

In this work, a method capable of evaluating the strength of defect state mediated non-radiative recombination was introduced. This ABG-model is based on excitation power-dependent PL experiments. Its applicability was shown for several InGaAs/GaAs MQW structures. Limitations of this model were observed for structures with weak carrier confinement, such as shallow wells (e.g. GaAs/GaAs$_{0.92}$Sb$_{0.08}$) or comparatively thick single layers (e.g. 100–500 nm), based on data not presented herein. However, the proposed ABG-model can be applied to nanostructures with proper carrier confinement, as typical for, e.g. light emitting diodes and MQW solar cell structures.

Further, correlations between the crystalline and optical properties versus epitaxial growth conditions were presented. Investigation of three individual sample sets with variations in deposition temperature, total MQW thickness, and MQW period, allowed the creation of extended and optically active defects to be studied systematically.

The correlation between physical properties, such as the optical response and crystal perfection, as dependent on growth conditions are of special importance in the development of growth processes for device applications. In this context, optimization of the growth procedure and prevention of material quality deterioration improve device performance.

References

[1] I. Tångring, S. Wang, M. Sadeghi, A. Larson, Electronics Letters 42 (12) (2006) 691–693.
[2] K.J. Beernink, P.K. York, J.J. Coleman, R.G. Waters, J. Kim, C.M. Wayman, Applied Physics Letters 55 (21) (1989) 2167–2169.
[3] R.L.S. Devine, Semiconductor Science and Technology 3 (1988) 1171–1176.
[4] E.A. Fitzgerald, D.G. Ast, P.D. Kirchner, G.D. Pettit, J.M Woodall, Journal of Applied Physics 63 (1988) 693–703.
[5] A.G.U. Perera, S.G. Matsik, H.C. Liu, M. Gao, M. Buchanan, W.J. Schaff, W. Yeo, Applied Physics Letters 77 (5) (2000) 741–743.
[6] J. Jiménez, Comptes Rendus Physique 4 (2003) 663–673.
[7] G.P. Watson, D.G. Ast, T.J. Anderson, B. Pathangey, Y. Hayakawa, Journal of Applied Physics 71 (1992) 3399–3407.
[8] M.M. Karow, N.N. Faleev, A. Maros, C.B. Honsberg, Journal of Crystal Growth, (Companion paper: Defect Creation in InGaAs/GaAs Multiple Quantum Wells – I. Structural Properties).
[9] nextnano3: ⟨www.wsi.tum.de/nextnano3⟩ and ⟨www.nextnano.de⟩, accessed February 2013.
[10] W. Shockley, W.T. Read, Physical Review 87 (5) (1952) 835–842.
[11] E. Rosencher, B. Vinter, P.G. Piva, Optoelectronics, Cambridge University Press, 2002.
[12] Z. Garbuzov, Journal of Luminescence 27 (1982) 109–112.
[13] K.A. Bulashevich, S. Yu. Karpov, Physica Status Solidi C 5 (6) (2008) 2066–2069.
[14] Y.P. Varshni, Physica 34 (1) (1967) 149–154.
[15] T. Yamamoto, M. Kasu, S. Noda, A. Sasaki, Journal of Applied Physics 68 (10) (1990) 5318–5323.
[16] T.Y. Lin, J.C. Fan, Y.F. Chen, Semiconductor Science and Technology 14 (1999) 406–411.
[17] S.W. Feng, Y.C. Cheng, Y.Y. Chung, C. Yang, Y.S. Lin, C. Hsu, K.J. Ma, J.I. Chyi, Journal of Applied Physics 92 (8) (2002) 4441–4448.
[18] M.D. Sturge, Physical Review 127 (3) (1962) 768–773.
[19] N. Faleev, N. Sustersic, N. Bhargava, J. Kolodzey, A. Yu. Kazimirov, C. Honsberg, Journal of Crystal Growth 365 (2013) 44–53.
[20] N. Faleev, N. Sustersic, N. Bhargava, J. Kolodzey, S. Magonov, D.J. Smith, C. Honsberg, Journal of Crystal Growth 365 (2013) 35–43.
[21] S.P. Bremner, K.-Y. Ban, N.N. Faleev, C.B. Honsberg, D.J. Smith, Journal of Applied Physics 114 (2013) 103511-1–103511-9.
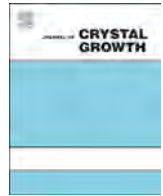
A study of MBE growth-related defects in InAs/GaSb type-II supperlattices for long wavelength infrared detectors

Olga Klin, Noam Snapi, Yossi Cohen, Eliezer Weiss *

SCD – Semi-Conductor Devices, P.O. Box 2250/99, Haifa 31021, Israel

ABSTRACT

The performance of focal plane arrays type-II InAs/GaSb superlattices (T2SL) based photo-detectors is limited by their operability (percentage of working pixels). Using preferential chemical etching we formed pits around "killer" defects found in InAs/GaSb T2SL epi-layers grown by MBE on GaSb (100). These pits were then studied with various microscopically methods, including optical, high resolution scanning electron (HRSEM), high resolution transmission electron (HRTEM), and cross-section scanning tunneling (XSTM) microscopies. We have found that these "killer" defects are related to both growth conditions and substrate imperfections. Adjusting these parameters allowed us to reduce "killer" defects density by several orders of magnitude. HRTEM inspection of the defects shows that at high growth temperatures they originate close to the T2SL–GaSb interface, and develop in size during only few SL loops to a straight and narrow "column" through the whole structure. At low growth temperatures most of them are nucleated on stacking fault defects formed on irregularities in the substrate surface.

© 2015 Elsevier B.V. All rights reserved.

1. Introduction

In the past few years, type-II InAs/GaSb superlattices (T2SL) photo-detectors have developed quickly. The material and device performances have improved significantly and large format focal plane arrays (FPAs) have been demonstrated, especially for applications in the long-wave infrared (LWIR) absorption band [1]. Despite the rapid progress, the performance of T2SL infrared detector arrays reported is limited by their operability (percentage of working pixels). Using preferential chemical etching and high resolution microscopies we studied "killer" defects found in our T2SL epi-layers. We found that defects, having a nail-like shape in high resolution transmission electron microscopy (HRTEM), were formed at the T2SL interfaces close to the T2SL–GaSb buffer layer (BfL) interface. Their density increased with the growth temperature and the InSb content in the T2SL interfaces but not with the density of threading dislocations in the BfL. Irregularities in the GaSb substrate also caused such defects. It seems that the formation of nail-like defects in superlattice growth is enhanced by the superlattice itself. This may be due to the local strains within the superlattice, existing even when the whole structure is lattice-constant balanced by InSb forced interfaces.

2. Experimental procedure

The T2SL studied, consisting of 13 ML of InAs and 7 ML of GaSb, were grown by MBE on 3 in. "epi-ready" GaSb (100) $1° → (111)$A wafers (supplied by WaferTech) with a $0.1~\mu m$ GaSb buffer layer. Most of the time we studied structures in which the T2SL layer was capped with a thinner aluminum-containing superlattice (ALSL) with 15 ML of InAs and 4 ML of AlSb. Both superlattices (SLs) had InSb forced interfaces for lattice parameter balancing. The material growths were carried out in a Veeco GenIII MBE system, equipped with valved arsenic and antimony cracker cells, and indium, gallium and aluminum SUMO cells. Substrate temperature was measured with a pyrometer (IRCON 3G-10C05). The BEP V/III ratios were 8 for InAs, 3.4 for GaSb and 4.8 for AlSb. The growth rate was ~0.5 ML/s.

We studied the defects in the epilayers, revealed by an SCD proprietary preferential etch, using optical (Nomarski mode) and scanning electron microscopies, as seen in Fig. 1 for growth at 430 °C. The SCD etch (Fig. 1a) forms large pits around "killer" defects that can be easily detected with an optical microscope. These large pits are formed only in ALSL. In T2SL it forms very small pits that can be detected only at higher magnifications (Fig. 1b). For comparison we used, sometimes, the etchant proposed by Aifer [2] (Aifer Etch – Fig. 1c). It develops etch pits (EPs) around few kinds of defects in the T2SL and not only at the "killer" defects as the SCD etchant.

We used these EPs as markers for the preparation of cross-section samples for TEM. We also used XSTM (Omicron) to study

* Corresponding author. Tel.: 972 4 990 2521.
E-mail address: eliweiss@scd.co.il (E. Weiss).

our T2SL structures. High-resolution X-ray diffraction (HRXRD, Jordan Valley QC3) and photoluminescence (PL) measurements were also performed.

3. Results and discussion

The SCD etch forms a typical pit in the ALSL cap layer around a "killer" defect as shown in Fig. 2a: the four corner "stars" appearing in the optical microscopy (Fig. 1a) are revealed as flat-bottom pits surrounded by steps (due to the SL structure) forming [110] oriented "double-arrowheads". In the center of each is a black rectangular (sometimes covered by debris). Fig. 2b shows schematically a cross-section in a pit formed in an ALSL–T2SL structure by the SCD etch: a small and narrow pit in the T2SL, in the center of the large EP in the ALSL layer. The flat bottom of the ALSL pit is at the ALSL–T2SL interface. At its center lies a hole etched in the T2SL as seen also in Fig. 1b.

Fig. 3 shows TEM images around the core of defects shown in Fig. 2a. At the top we see the etch pit itself (the bright cone). The dark cylinder below it is the defect, which looks like a nail, with a constant width from the top of the T2SL epi-layer down to about the 10th T2SL loop (Fig. 3b1). At that point, the dark cylinder turns into a dark narrow line which continues down to the T2SL–GaSb buffer layer interface. Inspection of more defects in the same epilayer (Fig. 3b2 and other images not shown here) shows that these transitions (from a column to a line – the tip of the "nail") lie at different levels above the T2SL–BfL interface for different defects. The dark lines end always close to this interface.

Looking closely at the "nail's" tip (Fig. 3c) we see that the dark line, originating at the T2SL–GaSb interface, is split, as it propagates, to a few thread-like defects in the structure. We did not reveal any irregularity close to the dark line origin or to where it splits into the "threads". Also, at this stage, we cannot say much about the nature of these dark thread-like lines, although they may be dislocations.

The main growth parameter affecting the density of the nail-like defects is the growth temperature. This is shown in Fig. 4: the high EPD shown in Fig. 1 ($\sim 5 \cdot 10^5$ cm^{-2}) drops rapidly as the
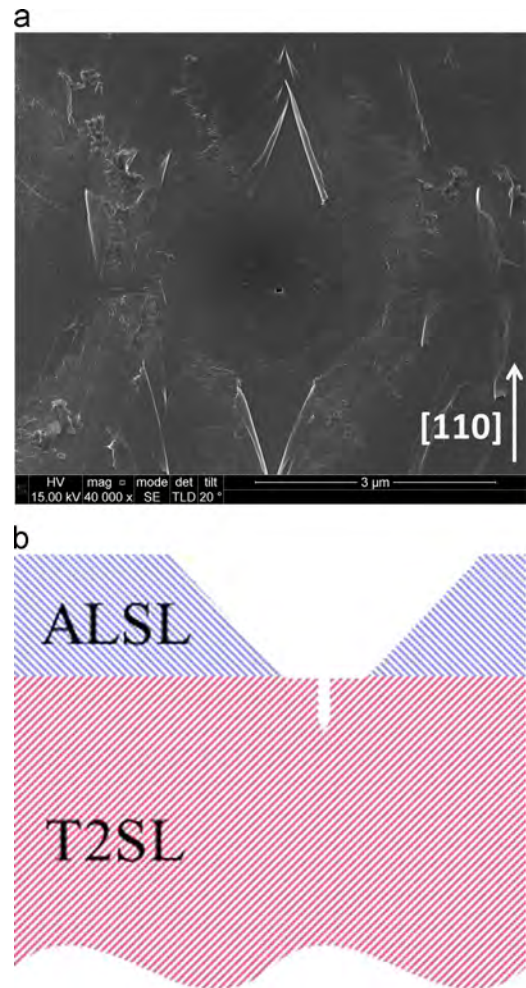
Fig. 2. Shape of etch pits formed by the SCD etchant in an ALSL–T2SL epilayer. (a) SEM image of the top surface after etching. (b) Schematic illustration of the pit formed in the structure: a small and narrow pit in the T2SL, in the center of the large etch pit in the ALSL layer. The flat bottom of the ALSL pit is at the ALSL–T2SL interface.
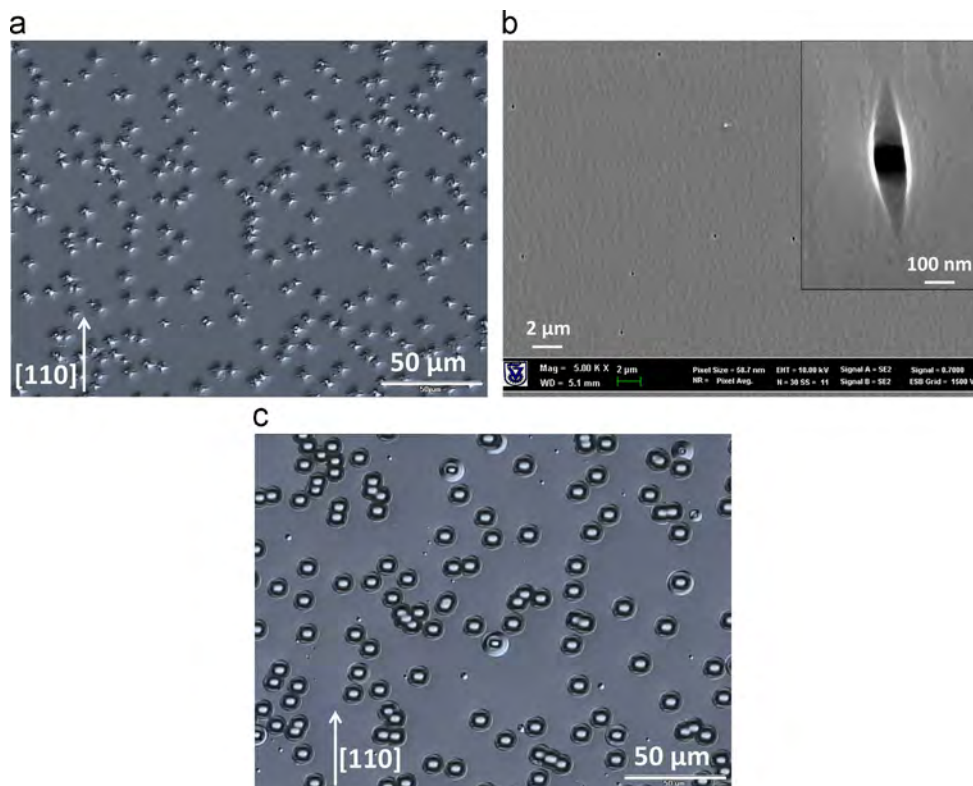
Fig. 1. Optical microscope in Nomarski mode (a,c) and SEM (b) micrographs of etch pits formed by the two preferential etchants used in this study in epilayers grown at 430 °C. (a) SCD etch in ALSL on T2SL, (b) SCD etch in T2SL epilayer (without the ALSL cap layer), and (c) Aifer Etch in T2SL.
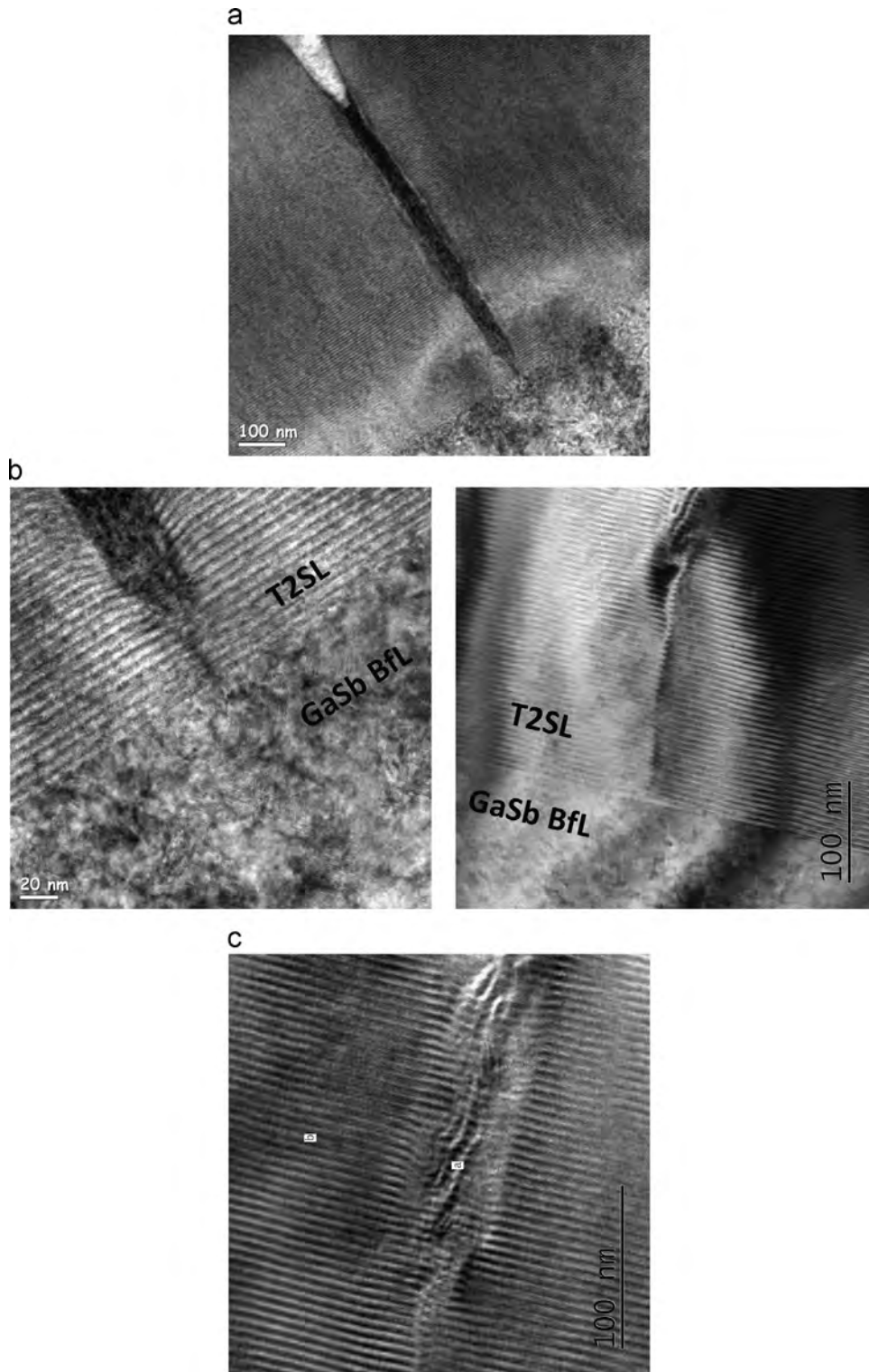
Fig. 3. HRTEM images of: (a) one of the EPs shown in Fig. 2a; (b) the defects in the vicinity of the T2SL–GaSb buffer layer interface at two magnifications; and (c) high magnification of the tip of the "nail-defect" of (b1).

growth temperature is reduced. The EPD value stabilizes at 400 °C on $\sim 5 \cdot 10^3$ cm^{-2}, slightly higher than the dislocation density in the GaSb substrates [3,4]. The same type of defects is formed in ALSL epilayers grown directly on GaSb, only the density of these defects in them is much lower than their density in T2SL epilayers grown at the same temperature. Apparently the formation of the defects is easier in a T2SL than in an ALSL grown on GaSb.

In order to test if the nail-like defects are due to threading dislocations (TDs), we grew the ALSL–T2SL structure on a virtual substrate (VS) at a low temperature (400 °C). The VS is a thick GaSb layer grown on a GaAs substrate. These VSs were found to have a TD density of $\sim 10^7$ cm^{-2} [5]. So, if the nail-like defects were due to TDs we should have gotten an EPD of about 10^7 cm^{-2}. However, as can be seen in Fig. 5a, the SCD etch gave low EPDs (in the 10^3 cm^{-2} range), as found in low temperature grown T2SL layers on lattice-matched GaSb. In contrast, the Aifer Etch (Fig. 5b), which decorates both dislocations and nail-defects, showed the expected density of TDs in a T2SL grown on GaAs.
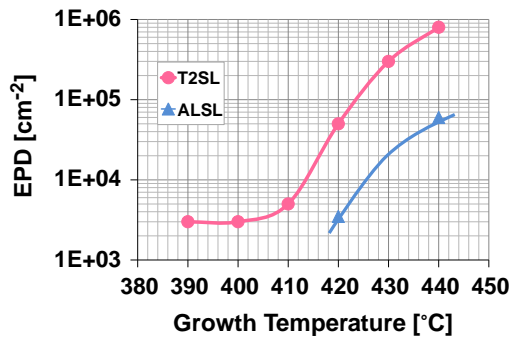
Fig. 4. The dependence of the EPD (SCD Etch) in T2SL (circles) and ALSL (triangles) as a function of the growth temperature.
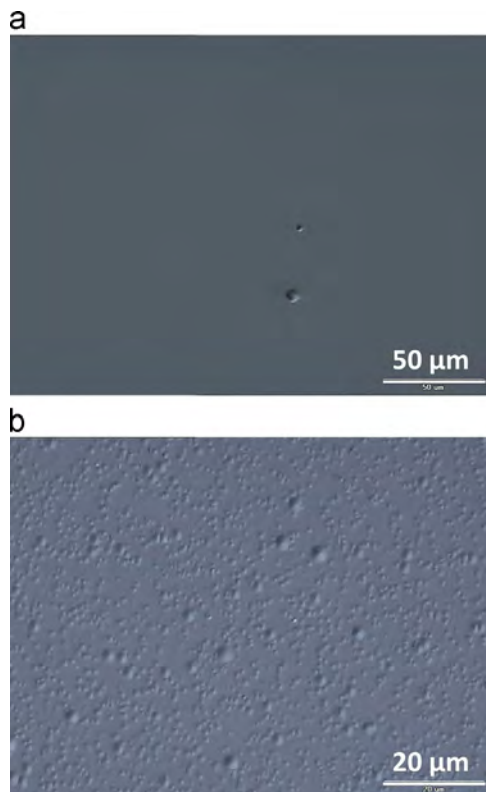
Fig. 5. Optical microscope (Nomarski mode) micrographs of the surface of a T2SL grown on GaSb on GaAs virtual substrate after SCD etch (a) and Aifer Etch (b). The EPDs are in the 10^3 cm^{-2} range in (a) and $\sim 10^7$ cm^{-2} in (b).

Fig. 6. XSTM image of a cleaved T2SL around the T2SL–GaSb BfL interface (lying to the left of the image). The bright triangles at the GaSb-to-InAs interfaces are believed to be small InSb islands. The structure was grown at 430 °C.

Table 1
The influence of the amount of InSb in the T2SL interfaces on various epilayer characteristics: the XRD peak separation between substrate and layer ($\Delta\theta$), the thickness of the SL loop, the 10 K photoluminescence peak wavelength (λ_{PL}) and the density of the pits formed by the SCD etch (EPD).

Interface type	$\Delta\theta$ [arcsec]	Loop thickness [Å]	λ_{PL} [μm]	EPD [cm^{-2}]
InSb forced	150	59.6	8.8	$\sim 3 \cdot 10^5$
InSb forced, thin	570	55.8	7.1	$\sim 5 \cdot 10^4$
Unforced	1225	54.4	6.3	$\sim 5 \cdot 10^3$

A clue regarding the origin of the nail defects was received by the XSTM measurements of T2SLs grown at different temperatures (Fig. 6). We found bright triangles near the GaSb buffer layer in one of the cross-sections in an epilayer with high "nail defect" density, grown at 430 °C. Since InSb has a bright signature in these XSTM images, we think that these bright triangles are InSb islands and that they cause the nails. Indeed, we found (Table 1) that as we lowered the amount of the InSb in the interfaces of the epilayers grown at a high temperature, we got a smaller EPD value. Without InSb at all at the interfaces, the EPD was much lower [a]. We hypothesize, therefore, that at high growth temperatures small InSb islands are formed at the forced superlattice interfaces, most probably due to the high mobility of the indium adatoms on the surface or strained-induced InSb melting [6]. Linear defects appear in the vicinity of these small InSb islands split or and multiply after 5–20 loops of SL transforming into nail-like defects. The lower defect density in ALSL grown directly on GaSb (Fig. 4) is due to the higher roughness of the AlSb-to-InAs interface (seen in XSTM images not reproduced here) then the GaSb-to-InAs interface. The indium adatom mobility on the AlSb surface is, therefore, lower than on the GaSb surface.

We found an EPD "background" level of $\sim 5 \cdot 10^3$ cm^{-2} in epilayers grown at low temperatures (Fig. 4) and the question is what caused it. Surface morphology analysis by optical microscopy (before etching) consistently detected single defects and aggregation of defects associated with the quality of the substrate surface. For instance, the preferential etching reveled many times defects arranged along a straight line which are due to a latent scratch on the substrate surface. Fig. 7a shows such scratch-related series of defects after etching with the SCD etch in an epilayer grown at 400 °C. At high magnification (Fig. 7b) we can see four of these pits arranged along the straight line. In the center of each of the four pits we found a stacking fault defect (SFD). The small black defects, mainly near the SFDs, are the small pits formed at nail defects in T2SL (see Fig. 2b). At a growth temperature of 440 °C we also detected SFDs, but the density of nail defects near them was much higher (image not shown). Nevertheless, at these high temperatures the majority of the nail defects was not related to SFDs as discussed above.

Fig. 7c is a TEM image obtained after a careful cross-section at the area shown in Fig. 7b. The SFD is the dark line in the T2SL epilayer (at 54° to the interfaces, i.e. in a {111} plane) and the nail defects are the perturbations coming out of it (at right angle to the interfaces). It can be seen that the SFD continues down from the T2SL into the GaSb buffer layer (the contrast is better in other images not shown here). It

---

[a] As expected, the amount of InSb at the interfaces affected the thickness of the SL loop, the photoluminescence peak wavelength (λ_{PL}) and the InSb lattice-parameter balancing: the XRD peak separation between substrate and layer ($\Delta\theta$) increased as the amount of InSb at the interface was reduced.
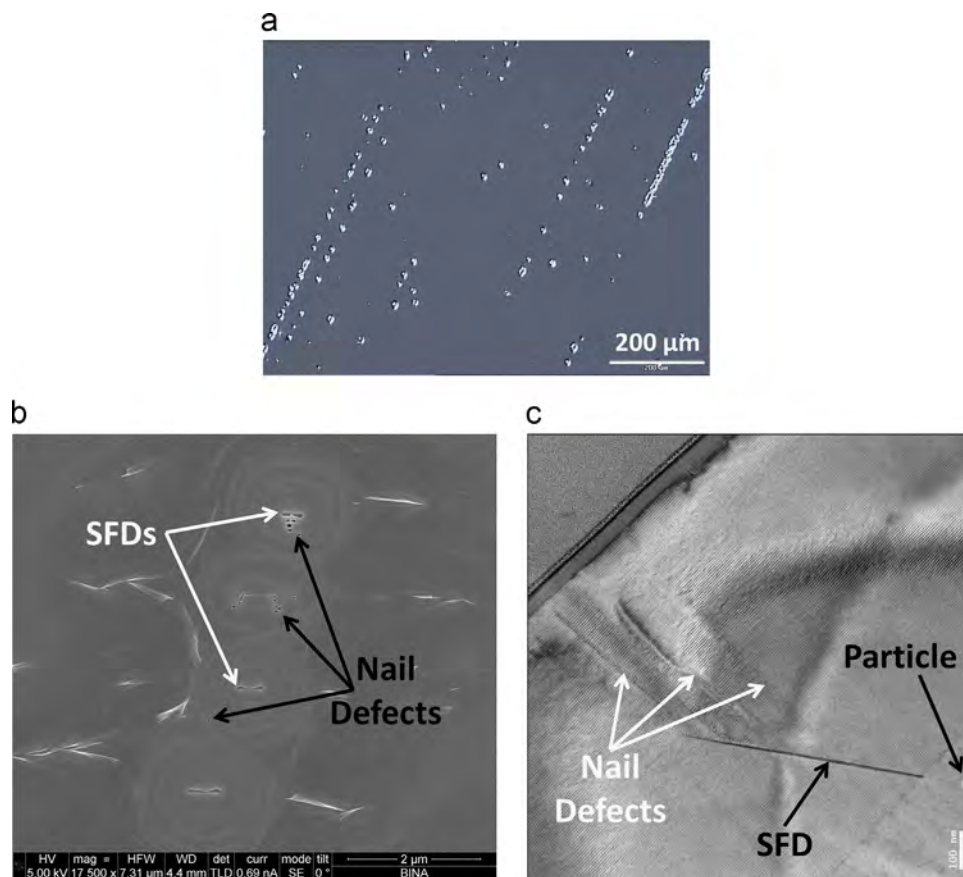
Fig. 7. (a) Optical (Nomarski mode) micrograph of a series of defects along a scratch defect in the substrate surface revealed by the SCD etch in an ALSL–T2SL–GaSb BfL structure. (b) HRSEM image of four pits along the "scratch" in (a) showing SFDs (horizontal linear defects) and nail-like defects (small dark rectangles). (c) HRTEM image from a sample prepared in the area shown in (b). The SFD (dark line) was formed by the white circular particle in the GaSb substrate surface. Three defects nucleated on the SFD and propagated linearly to the sample surface.

originates at the foreign particle (bright circle) which lies exactly 100 nm below the T2SL–GaSb buffer layer interface. That is, at the substrate-buffer layer interface. Even at low growth temperatures linear defects (similar or identical to the high temperature-related nail-like defects) are nucleated on these SFDs. The "background" substrate-related killer defects originate, therefore, from particles on the surface of the GaSb substrates. They may also be due to other irregularities in the substrate surface, like topographically uneven surfaces (scratches and voids), or fluctuations in the amount and composition of the oxide at the surface.

Further study is required to understand the mechanisms of generation and multiplication of the linear defects from irregularities, either in the substrate surface or at the SL interfaces, as well as to explain why these narrow column-like defects do not widen along the crystallographic planes in the structure. The defects reveled in our superlattices can be similar to dislocation dipoles [7], screw dislocations [8,9] and micropipes [10] described in previous studies. Nevertheless, it seems that their formation in superlattice growth is enhanced by the superlattice itself. This may be due to the local strains within the superlattice, existing even when the whole structure is lattice-constant balanced by InSb forced interfaces.

4. Conclusions

SCD proprietary etchant reveals "killer" defects in our T2SL test devices. They are related to both growth conditions and substrate imperfections. Adjusting these parameters allowed us to reduce "killer" defects density by several orders of magnitude. Because of their shape in cross-section HRTEM we named them "nails". At

high growth temperatures they originate close to the T2SL–GaSb interface, and develop in size during only few SL loops to a straight and narrow "column" through the whole structure. At low growth temperatures most of them are nucleated on stacking fault defects formed on irregularities in the substrate surface. The formation of these defects in superlattice growth may be enhanced by the superlattice itself. This may be due to the local strains within the superlattice, existing even when the whole structure is lattice-constant balanced by InSb forced interfaces.

Acknowledgments

References

[1] M. Sundaram, et al., Infrared Phys. Technol. **59** (2013) 12;
    M. Razeghi, et al., Infrared Phys. Technol. **59** (2013) 41;
    D.Z.-T. Ting, et al., Infrared Phys. Technol. **59** (2013) 146.
[2] E.H. Aifer, US Patent 2013/0122715 A1, 2013.

[3] M.J. Furlong, R. Martinez, S. Amirhaghi, D. Lubyshev, J.M. Fastenau, X. Gu, A.W.K. Liu, Proc. SPIE 7660 (2010) 48.
[4] M. Walther, A. Wörl, V. Daumer, R. Rehm, L. Kirste, F. Rutz, J. Schmitz, Proc. SPIE 8704 (2013) 87040U.
[5] E. Weiss, O. Klin, S. Grossman, N. Snapi, I. Lukomsky, D. Aronov, M. Yassen, E. Berkowicz, A. Glozman, P. Klipstein, A. Fraenkel, I. Strichman, J. Cryst. Growth 339 (2012) 31.
[6] M.A. Herman, W. Richter, H. Sitter, Epitaxy – Physical Principles and Technical Implementation, Springer, Berlin, 2010.
[7] H. Klapper, Generation and Propagation of Defects During Crystal Growth, (Springer HB Crystal Growth, 2010) Chap. 4.
[8] B. Brar, D. Leonard, Appl. Phys. Lett. 66 (1995) 463.
[9] C.C. Hsu, J.B. Xu, I.H. Wilson, T.G. Andersson, J.V. Thordson, Appl. Phys. Lett. 65 (1994) 1552.
[10] M. Dudley, X.R. Huang, W. Huang, A. Powell, S. Wang, P. Neudeck, M. Skowronski, Appl. Phys. Lett. 75 (1999) 784.

CRYSTAL
GROWTH
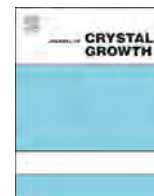
Unintentional boron contamination of MBE-grown GaInP/AlGaInP quantum wells

CrossMark

Antti Tukiainen [a,*], Jari Likonen [b], Lauri Toikkanen [a], Tomi Leinonen [a]

[a] Optoelectronics Research Centre, Tampere University of Technology, PO Box 692, FIN-33101 Tampere, Finland
[b] VTT, PO Box 1000, 02044 VTT, Finland

ARTICLE INFO

ABSTRACT

The effects of unintentional boron contamination on optical properties of GaInP/AlGaInP quantum well structures grown by molecular beam epitaxy (MBE) are reported. Photoluminescence and secondary-ion mass spectrometry (SIMS) measurements revealed that the optical activity of boron-contaminated quantum wells is heavily affected by the amount of boron in GaInP/AlGaInP heterostructures. The boron concentration was found to increase when cracking temperature of the phosphorus source was increased. Boron incorporation was enhanced also when aluminum was present in the material.

© 2015 Elsevier B.V. All rights reserved.

1. Introduction

Fabrication of high-power short-wavelength red-light emitting devices and high-efficiency multi-junction solar cells requires ability to fabricate high-purity III–V phosphide materials, such as $(Al_xGa_{1-x})_{1-y}In_yP$ (denoted as AlGaInP). Molecular beam epitaxy (MBE) of AlGaInP is a challenging task, not only because the material contains phosphorus which is a flammable material and easily generates toxic fumes when exposed to air and moisture but there are also several extrinsic atomic species that can generate defects in phosphide materials. This sets stringent requirements for the purity of the source materials.

One rather well documented source of detrimental extrinsic defects in AlGaInP is oxygen, which is reported to create deep levels in the material [1]. In previous studies, oxygen has also been shown to deteriorate the properties of AlGaInP-based heterostructures by reducing the carrier lifetime and optical activity [1–8]. The oxygen incorporation into AlGaInP has been shown to be related to the phosphorus cracker source and notably to the cracking zone temperature (T_{cr}). Therefore, one way to reduce oxygen contamination in MBE-grown AlGaInP has been to use low cracking tube temperature [2–4,12]. The recent findings, presented here, however, indicate that oxygen appears not to be the only detrimental contaminant whose incorporation into AlGaInP could be related to T_{cr}.

2. MBE growth and used measurement techniques

The samples were fabricated using solid-source MBE system (VG V80) equipped with standard conical effusion cells for group III elements and cracker sources for arsenic and phosphorus (Veeco Mark III). Phosphorus used in the study was manufactured by Rasa Industries, Ltd. The samples were prepared for growth by thermal oxide desorption at 620 °C for 10 min. Growth of the GaInP/AlGaInP QW structure was started by a 100 nm of GaAs buffer followed by 300 nm of $Al_{0.53}In_{0.47}P$ (hereinafter denoted as AlInP) and 60 nm of $(Al_{0.50}Ga_{0.50})_{0.52}In_{0.48}P$ waveguide after which a 5-nm-thick QW of $Ga_{0.49}In_{0.51}P$ was grown. After the QW the other half of the waveguide was finalized by 60 nm of $(Al_{0.5}Ga_{0.5})_{0.52}In_{0.48}P$ after which a 100 nm of AlInP was grown. The layer sequence of AlInP/AlGaInP/GaInP/AlGaInP/AlInP was used for insuring a good carrier confinement in the quantum well region. The layer structure was finalized by a 50-nm-thick $Ga_{0.51}In_{0.49}P$ to prevent the sample surface from oxidation. Growth rates used in the experiments were 0.5 μm/h, 1.2 μm/h, 2.0 μm/h, and 1.0 μm/h for GaAs, AlInP, AlGaInP and GaInP, respectively. The V/III BEP ratio was about 20 for all the phosphide layers. The sample temperature was kept at 490 °C for the QW and at ∼500 °C for the other phosphide layers. Growth temperature for GaAs was 580 °C. All four samples had nominally similar layer structure, but different T_{cr} values of 750 °C, 820 °C, 870 °C, and 920 °C were used during phosphide growth. The samples were grown during one day so that T_{cr} was decreased from the first to the last sample.

The samples were examined using standard room temperature photoluminescence (PL) to gain information about the effects of T_{cr} on the optical activity of the GaInP QWs. PL measurements were done using a commercial RPM2000 photoluminescence mapping tool.

* Corresponding author. Tel.: +358 40 198 1076; fax: +358 3 364 1436.
E-mail address: antti.tukiainen@tut.fi (A. Tukiainen).

Secondary-ion mass spectrometry (SIMS) measurements were done on GaInP/AlGaInP quantum well samples, as well as on selected AlInP bulk samples to reveal differences in trace element concentrations between the samples. SIMS measurements were done using VG Ionex IX-70S instrument. 12 keV Cs^+ and 5 keV O_2^+ ions were used as primary ions for generation of negative and positive secondary ions. The primary ion currents were 100 nA and 150 nA for Cs^+ and O_2^+ ions, respectively. The sputtered areas were 430 μm $\times$ 570 μm for Cs^+ ions and 320 μm $\times$ 420 μm for O_2^+. Analyzed areas were 10% of the sputtered areas. Depth profiles of a set of negative and positive secondary ions including the elements of the host matrix, $^{12}C^-$, $^{1}H^-$, $^{18}O^-$, and $^{11}B^+$ were recorded.

3. Experimental results and discussion

Room temperature PL measurements (Fig. 1a) revealed a QW-related emission peak at $\sim$644 nm irrespective of the phosphorus cracking tube temperature. Another weak PL signal was detected close to 850 nm due to GaAs buffer and n-GaAs substrate layers. The QW PL peak intensity values were found to reduce almost exponentially upon increasing T_{cr} (Fig. 1b). This behavior indicates that there has to be a large number of defects generated in the QW samples as a result of higher T_{cr}.

Earlier studies have pointed out that in some cases oxygen that is present in the MBE growth may be the cause of inferior quality of AlGaInP when grown at high T_{cr} [2–4,12]. The present results are difficult to explain using the previous observations, e.g., the ones seen in Ref. [3]. Previously, it was found that changing the T_{cr} from 800 to 900 °C would increase the oxygen concentration of GaInP bulk samples about 1.5 times [3], which resulted in room temperature PL intensity reduction to about 1/4 of the original value. However, for the present samples, the PL intensities dropped almost two orders of magnitude when T_{cr} was increased from 800 to 900 °C. Therefore, SIMS measurements were done to find out whether the cause for the reduction of PL was of the same origin as in the previous studies. The presence of other unwanted elements was monitored as well. The SIMS depth profiles for hydrogen, carbon, oxygen and boron were measured. The normalized SIMS signal of hydrogen, carbon, oxygen and boron measured in different parts of the structures are shown in Fig. 2a and b.

The SIMS measurements show that the amount of oxygen increases upon increasing T_{cr} up to 820–870 °C, above which, oxygen concentration decreases in all the layers. The SIMS signal can be considered to be proportional to the oxygen concentration and this means that there is $\sim$4–5 times increase in the amount of oxygen in the QW samples when T_{cr} is increased from 750 °C to 820 °C. The observation is well in line with oxygen concentrations measured in [3]

but in clear contrast with the present PL results. The amount of oxygen even starts to decrease when T_{cr} is increased above 870 °C. Therefore, the conclusion is that oxygen contamination alone cannot explain the drastic reduction of PL in the GaInP/AlGaInP QWs grown at higher T_{cr}. The SIMS profiles of hydrogen and carbon are very similar in all the measured samples with not any clear trends, and thus they cannot be regarded as the cause for the reduced PL intensity.

SIMS profiles were also measured for boron (Fig. 3a). The profiles reveal that there are substantial differences in the amount of boron between the samples and between different layers. The samples exhibit a clear accumulation of boron at the bottom AlGaInP/AlInP interface and top GaInP/AlInP interface. Also, a slightly smaller accumulation of boron is observed at the top AlInP/AlGaInP interface, and furthermore, the concentration of boron away from the interfaces shows a decaying profile. The amount of boron is also found to drastically increase with T_{cr}.

The SIMS signal of boron, i.e., the amount of boron, in almost all locations of GaInP/AlGaInP QW samples, appears to be strongly dependent on the cracking cell temperature and increases almost exponentially when T_{cr} is increased. The only one exception is the top GaInP which seems to have drastically reduced incorporation of boron even with the highest T_{cr}. This indicates that boron incorporation is enhanced in AlGaInP by the presence of aluminum.

The main question that arises from the above experimental results is where the boron contamination is originating from. Currently the exact cause for the boron contamination in these samples is not known for sure but some probable reasons are discussed shortly below.

The first one is that the origin of boron incorporation could be related to contaminated phosphorus ingot. At higher T_{cr} the boron-containing molecules entering the growth chamber together with phosphorus molecules would be cracked or activated in the phosphorus cracking zone more efficiently and therefore the boron incorporation to the growing crystal would increase exponentially with T_{cr}.

The second option is that there exist boron-containing or contaminated parts in the phosphorus source, either in the red zone, white zone, or in the cracking zone. When heated boron containing molecules could be evaporated or decomposed leading to boron contamination. Although boron itself has a very low vapor pressure at the temperatures used in the cracking zone, boron could get there in the volatile oxidized form, e.g., B_2O_3, which would have substantial vapor pressure at elevated temperatures. Formation of B_2O_3 in the phosphorus source could take place via a vacuum leak during operation of the source. Especially, during white phosphorus conversion process the red zone is heated to temperatures close to 400 °C, which could promote formation of B_2O_3 especially if water vapor and oxygen were
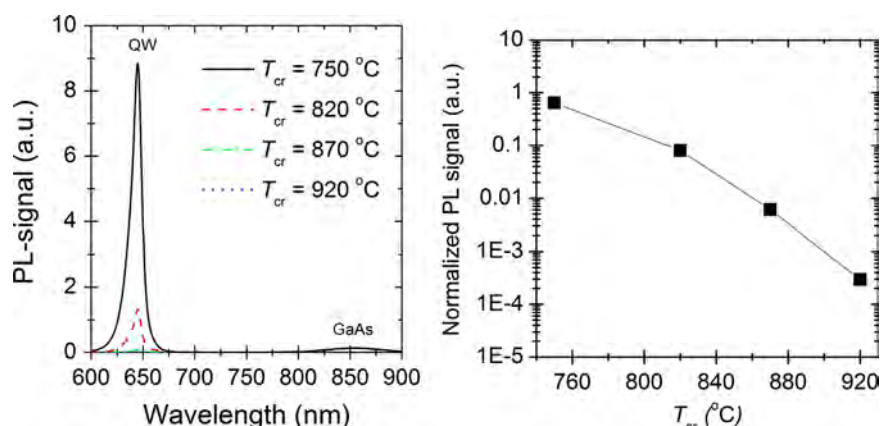
Fig. 1. (a) PL spectra for GaInP/AlGaInP quantum wells grown with different T_{cr}. (b) PL intensity of GaInP/AlGaInP QW samples grown with different phosphorus cracking zone temperatures.
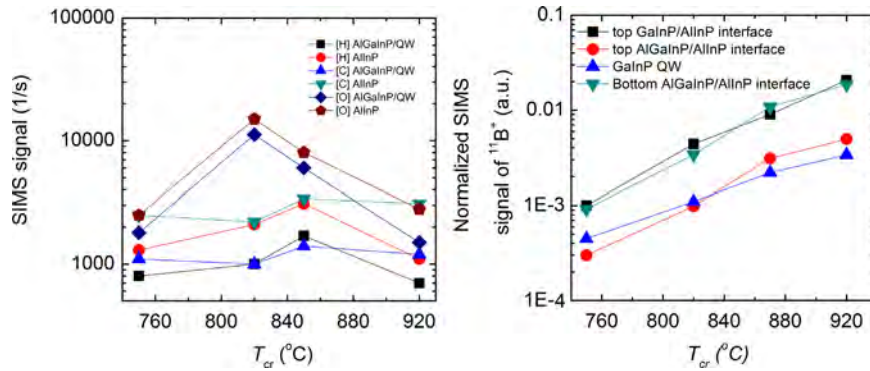
Fig. 2. (a) The SIMS signals for hydrogen, carbon and oxygen in GaInP/AlGaInP QWs and in AlInP layers with different values of T_{cr}. (b) The normalized SIMS signal of $^{11}B^+$ (SIMS signals of boron are normalized to the phosphorus signal in each sample) at different interface locations as a function of T_{cr}.
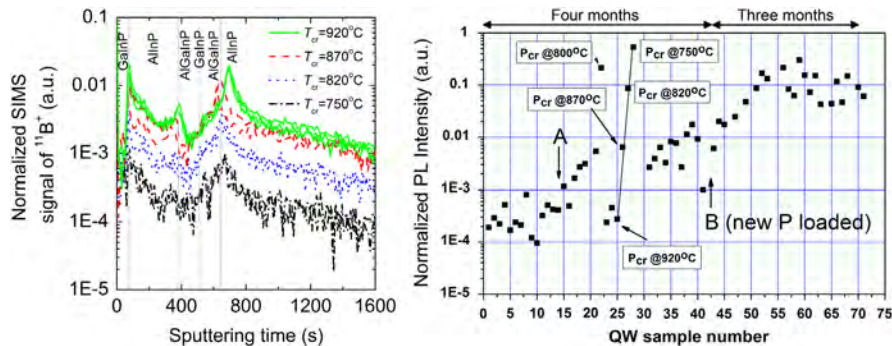
Fig. 3. (a) The SIMS profiles for Boron with different values of T_{cr}. Two measurements per sample were taken. The sample structure is drawn to the figure to show the interfaces between the layers. (b) The evolution of PL intensities of GaInP/AlGaInP QWs over seven months of growths. System openings/maintenance points are marked with A and B. All the QW samples had similar layer structure and T_{cr} was 920 °C except for the ones that are specifically mentioned. Altogether 185 III–V arsenide and phosphide samples including bulk layers, QW samples and laser structures were grown during the seven months.

present in the system. There is also a possibility that P_4O_6 contamination of phosphorus source described earlier by Hoke and Lemonias [13] could lead to formation of phosphoric acid which etches PBN when heated [14].

The third possible route for boron incorporation is related to vacuum parts and materials used in the MBE system. For example, some of the viewport glasses are made of borosilicate materials and it has been found earlier that in silicon MBE it is possible to have boron contamination of Si films if such vacuum viewports are used in the system [10]. Even some older papers describing boron contamination of Si in vacuum by a reaction between borosilicate glassware and water vapor have been presented [11]. The boron contamination in Ref. [11] was found to depend on the water vapor in the system and B_2O_3-rich surface of the glassware. The contamination was even found to be rather insensitive to the surface temperature of the glassware.

Unfortunately, it is impossible to confirm or rule out the first option because the SIMS measurements were done long time after the phosphorus ingot had been fully used and thus no phosphorus ingot material was left for SIMS analysis. There is however, some evidence that contamination of the red zone could be part of the problem. The PL evolution data, shown in Fig. 3b, indicate that after loading new phosphorus (point marked with B) the PL intensity rapidly increases and settles to a level which, at the time was acceptable but not top class, within one month. The increase of the PL intensity could be related to natural recovery of the growth chamber and the phosphorus source after opening. Also, additional SIMS measurements (described in detail on the next page) done on separate AlInP bulk layers point to the direction that phosphorus flux was responsible for the elevated boron levels.

The third option is quite unlikely but there is also some evidence in favor of that as well. The PL intensity of similar GaInP/AlGaInP samples

grown during a seven month time span was monitored and it was found out that after one maintenance operation (marked with A in Fig. 3b) the PL intensities started to increase almost exponentially from one growth to another. This could indicate that the one major source of contamination was removed from the MBE system and that the system started to recover itself. The part that was removed from the system was an old viewport window. If the viewport was the reason for boron contamination, then most likely, other parts of the system were still contaminated with boron-containing molecules even after removing the window and the effects seen when T_{cr} was increased could be due to heating the boron-contaminated areas of the system, and thus, enabling further contamination of the films.

To clarify whether the boron contamination originated from the vacuum system, additional SIMS measurements (Fig. 4) were done on AlInP films grown in the same MBE system equipped with two different phosphorus cracker sources; a new one and the old one which had been chemically cleaned. The crackers were kept at $T_{cr}=920$ °C during both growths. Additionally, the old cracker source did not have any shutter installed in the port, and therefore, any boron originating directly from the old cracker tube or areas nearby would have been seen also in the films grown using the new cracker. The SIMS analysis indicated that the films grown using the new cracker did not contain boron or boron concentrations were below the detection limit. Instead, the samples grown using the chemically cleaned cracker source exhibited a small but clearly elevated signal of boron. This result also suggests that the source of boron contamination was not related to the vacuum parts and materials but to the phosphorus flux coming from the cleaned old cracker source.

There exist very few published literature on the effects of boron in AlGaInP. In one published work, it was shown that boron implantation induces a deep mid-gap level at 0.9–1.0 eV in GaInP [9]. This
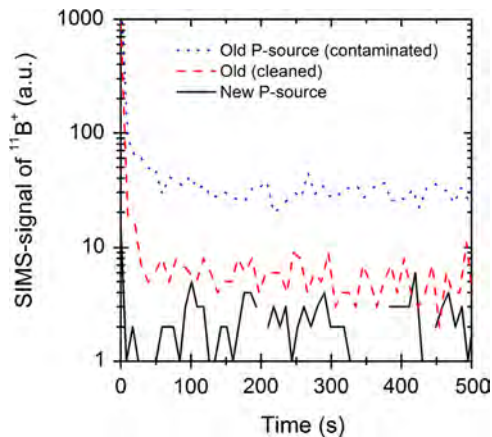
Fig. 4. An additional SIMS measurement done on AlInP bulk samples grown using different P-sources.

deep level acts as a very efficient carrier compensation center. The PL results obtained here could reflect a presence of a similar type of defect that acts as an efficient recombination center. Interestingly, the energy of the boron-generated mid-gap level is close to some of the deep levels observed in GaInP materials that were grown with high T_{cr} [3,12]. Unfortunately, in [3,12] boron was not measured and thus direct comparison cannot be made. Also, because boron is an isoelectronic impurity in AlGaInP, it should not as such generate deep levels but boron could form complexes with other types of defects which then could act as recombination centers. More detailed studies on the characteristics and origin of the boron impurities found in GaInP/AlGaInP heterostructures are currently underway.

4. Conclusions

We have studied the cause for phosphorus cracking tube temperature dependent reduction of PL intensity in GaInP/AlGaInP quantum well structures. The origin of the reduced PL intensity is related to enhanced boron incorporation when higher cracking tube temperatures are used during growth of AlGaInP layers. The exact origin of the source of boron contamination remains currently unresolved and new research is needed to clarify the issue.

References

[1] K. Domen, K. Sugiura, C. Anayama, M. Kondo, M. Sugawara, T. Tanahashi, K. Nakajima, J. Cryst. Growth 115 (1991) 529–532.
[2] W.E. Hoke, et al., J. Vac. Sci. Technol., B 16 (1998) 3041–3047.
[3] N. Xiang, et al., J. Cryst. Growth 227-228 (2001) 244–248.
[4] C. Soubervielle-Montalvo, et al., J. Cryst. Growth 311 (7) (2009) 1650–1654.
[5] M. Kondo, et al., J. Electron. Mater. 23 (3) (1994) 355–358.
[6] J.G. Cederberg, et al., J. Electron. Mater. 29 (4) (2000) 426–429.
[7] S.P. Najda, et al., J. Cryst. Growth 220 (2000) 226–230.
[8] K.A. Bertness, et al., J. Cryst. Growth 196 (1) (1999) 13–22.
[9] A. Henkel, S.L. Delage, M.A. di Forte-Poisson, H. Blanck, H.L. Hartnagel, Jpn. J. Appl. Phys., Part 1 36 (1A) (1997), http://dx.doi.org/10.1143/JJAP.36.175.
[10] R.A.A. Kubiak, W.Y. Leong, M.G. Dowsett, D.S. McPhail, R. Houghton, E.H. C. Parker, J. Vac. Sci. Technol., A 4 (1986) 1905. http://dx.doi.org/10.1116/1.573745.
[11] F.G. Allen, T.M. Buck, J.T. Law, J. Appl. Phys. 30 (1960) 979.
[12] N. Xiang, A. Tukiainen, M. Pessa, J. Dekker, J. Likonen, J. Mater. Sci.: Mater. Electron. 13 (2002) 549–552.
[13] W.E. Hoke, P.J. Lemonias, J. Vac. Sci. Technol., B 17 (5) (1999) 2009–2014.
[14] CRC Handbook of Metal Etchants, P. Walker, W.H. Tarn (Eds.), ISBN: 0-8493-3623-6 1991.
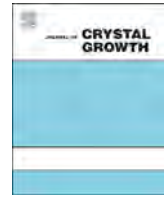
Improved electron transport properties of InSb quantum well structure using stepped buffer layer for strain reduction

S. Fujikawa *, T. Taketsuru, D. Tsuji, T. Maeda, H.I. Fujishiro

Department of Applied Electronics, Faculty of Industrial Science and Technology, Tokyo University of Science, 6-3-1 Niijuku Katsushika-ku, Tokyo 125-8585, Japan

ARTICLE INFO

ABSTRACT

We investigated a high-quality novel AlInSb buffer layer to increase the electron mobility of an InSb quantum well (QW) structure, which was grown on a (1 0 0) GaAs substrate by molecular beam epitaxy. We achieved high electron mobility in the InSb QW structure using an $Al_{0.25}In_{0.75}Sb/Al_{0.15}In_{0.85}Sb$ stepped buffer layer and realized reduced compressive strain and improved surface roughness. In addition, we investigated the dependence of the $Al_{0.25}In_{0.75}Sb$ layer thickness in the $Al_{0.25}In_{0.75}Sb/Al_{0.15}In_{0.85}Sb$ stepped buffer layer on the electron mobility characteristics. We only obtained increased electron mobility using the $Al_{0.25}In_{0.75}Sb$ layer within a critical thickness range.

© 2015 Elsevier B.V. All rights reserved.

1. Introduction

High electron mobility transistors (HEMTs) belonging to the III–V group are the most promising devices that can operate in the millimeter- and sub-millimeter-wave frequency ranges. So far, these devices have been improved by size scaling and channel engineering to increase electron velocity using indium-rich channel. However, progress in the cutoff frequency (f_T) in the last 10 years has not been so rapid: 562 GHz in 2002 using an $In_{0.7}Ga_{0.3}As$ channel layer with gate length (L_g) of 25 nm [1], 688 GHz in 2011 using an $In_{0.7}Ga_{0.3}As$ channel layer with L_g of 40 nm [2], and 710 GHz in 2013 using an $In_{0.7}Ga_{0.3}As/InAs/In_{0.7}Ga_{0.3}As$ channel layer with L_g of 60 nm [3]. Meanwhile, InSb has the highest electron mobility in the III–V group compound semiconductors. Therefore, HEMTs that use InSb for the channel is expected to be the next-generation ultrafast low-power-consumption devices [4,5]. However, the performance of InSb HEMTs remains in the early stages yet, e.g., the record for f_T in 2005 was 340 GHz with L_g of 85 nm [6], because of the absence of a reliable technique for device process and the large lattice mismatch (~14.6%) between the InSb and the GaAs substrate. Because of the latter, the epitaxial growth of InSb-related materials has tend to involve high-density threading dislocation and self-interface rough-ness, which affect the transport characteristics of two-dimensional electron gas in the InSb channel. High electron mobility has been reported with the reduction of microtwin defects and threading dislocation by introducing AlInSb/InSb strained-layer superlattice

using 2° off-axis GaAs(0 0 1) substrates and so on [7–10]. Another reason is that the effective mass (m) of the InSb channel is increased by the compressive strain from the AlInSb buffer layer [4,5]. In the present study, we investigate a high-quality novel AlInSb buffer layer to increase the electron mobility of the InSb channel. We show that the electron mobility of an InSb quantum well (QW) structure is increased using an $Al_{0.25}In_{0.75}Sb/Al_{0.15}In_{0.85}Sb$ stepped buffer layer, which reduces the compressive strain in the channel. In addition, we investigate the dependence of the $Al_{0.25}In_{0.75}Sb$ layer thickness in the $Al_{0.25}In_{0.75}Sb/Al_{0.15}In_{0.85}Sb$ stepped buffer layer on the electron mobility. The increase in electron mobility is only observed when using the $Al_{0.25}In_{0.75}Sb$ layer within a critical thickness range.

2. Experiment

The samples were grown on a (1 0 0) semi-insulating GaAs substrate by molecular beam epitaxy (MBE). Fig. 1 shows the schematic structures of the InSb QW. Structure (a) has a 3-μm-thick $Al_{0.25}In_{0.75}Sb$ buffer layer on 250-nm-thick AlSb/3.5-nm-thick low-temperature (LT) AlSb/15-nm-thick GaAs layers. Structure (b) has a 50-nm-thick $Al_{0.25}In_{0.75}Sb/3$-μm-thick $Al_{0.15}In_{0.85}Sb$ stepped buffer layer on 250-nm-thick AlSb/3.5-nm-thick LT-AlSb/15-nm-thick GaAs layers. Structures (a) and (b) have a 3-nm-thick InSb cap layer, a 25-nm-thick $Al_{0.25}In_{0.75}Sb$ barrier layer, a Te-sheet-doped $Al_{0.25}In_{0.75}Sb$ supply layer, a 5-nm-thick $Al_{0.25}In_{0.75}Sb$ spacer layer, and a 20-nm-thick InSb channel layer on the buffer layers. The substrate temperatures (T_s) for LT-AlSb, AlSb, $Al_xIn_{1-x}Sb$, and InSb growths were 455, 530, 455, and 455 °C, respectively. The growth

* Corresponding author. Tel.: +81 3 5876 1439; fax: +81 3 5876 1639.
E-mail address: fujikawa@te.noda.tus.ac.jp (S. Fujikawa).

rates of the AlSb, $Al_{0.15}In_{0.85}Sb$, $Al_{0.25}In_{0.75}Sb$, and InSb layers were 277, 549, 587, and 413 μm/h, respectively. The substrates were rotated at approximately 8 rpm during the MBE growth.

Table 1 shows the critical thickness (h_c) of the InSb channel in Structure (a), and the InSb channel layer and the $Al_{0.25}In_{0.75}Sb$ buffer layer in Structure (b), which are calculated on the basis of the Matthew's equation [11]. The parameters used in the calculation are also shown in Table 1. Here, we assume simply that the $Al_{0.25}In_{0.75}Sb$ buffer layer in Structure (a) and the $Al_{0.15}In_{0.85}Sb$ lower buffer layer in Structure (b) are lattice-relaxed completely. These show that the 20-nm-thick InSb channel and the 50-nm-thick $Al_{0.25}In_{0.75}Sb$ buffer layers in Structure (b) are lattice-strained and both those lattice constants parallel to the (1 0 0) plane coincide with that of the $Al_{0.15}In_{0.85}Sb$ buffer layer.

3. Results and discussion

Fig. 2 shows the relationship between m and strain ratio ($\varepsilon_{//}$) along the [0 0 1], [1 0 0], and [0 1 0] axes for the InSb layer, which is calculated using the empirical pseudo-potential band calculation with rigid-ion approximation [4,12]. Here we assume that the InSb layer is on (1 0 0) substrate and its lattice constant parallel to the (1 0 0) plane is the same as that of the substrate (a_s). Then the biaxial strain is applied on the InSb layer by the substrate. $\varepsilon_{//}$ is defined as $\varepsilon_{//} = (a_0 - a_s)/a_s$, where a_0 is an original lattice constant without the strain. The lattice constant perpendicular to the (1 0 0) plane is calculated by the elastic theory [13]. We can see that the compressive strain ($\varepsilon_{//} < 0$) yields a larger m and the tensile strain ($\varepsilon_{//} > 0$) a smaller m. In Structures (a) and (b), the compressive strains are applied to the InSb-QW channel layers by the buffer layers, and m then becomes larger. The thickness of the $Al_{0.25}In_{0.75}Sb$ layer in Structure (b) is within the critical thickness range. Then, $\varepsilon_{//}$ of the

InSb-QW channel layers are estimated roughly to be −1.3% and −0.8% for Structures (a) and (b), respectively. Consequently, m in Structure (b) is expected to be smaller than that in Structure (a).

Fig. 3 shows the (5 1 1) and (4 0 0) plane X-ray reciprocal space maps (RSMs) of Structures (a) and (b). As shown in the (5 1 1) plane X-ray RSM, the Q_x value of the InSb channel layer almost coincides with that of the $Al_{0.25}In_{0.75}Sb$ buffer layer in Structure (a), and the Q_x value of the InSb channel layer almost coincides with those of the $Al_{0.15}In_{0.85}Sb$ and also $Al_{0.25}In_{0.75}Sb$ buffer layers in Structure (b). Meanwhile, the Q_y value of the InSb channel layer in the (4 0 0) plane X-ray RSM increases in Structure (b). From these results, we estimate the $\varepsilon_{//}$ values of the InSb channel layers, which are −1.2 % in Structure (a) and −0.9 % in Structure (b), respectively. Then, we confirm that the strain in the InSb channel layer in Structure (b) is reduced compared with that in Structure (a).

Fig. 4 shows the surface images of the InSb-QW structures where Structure (a) is $Al_{0.25}In_{0.75}Sb$ and Structure (b) is $Al_{0.25}In_{0.75}Sb$/$Al_{0.15}In_{0.85}Sb$ stepped buffer layers on the GaAs substrates, as observed by an atomic force microscope (AFM) in 20 μm × 20 μm and 500 nm × 500 nm scales. The root-mean-square (RMS) values of the surface roughness of Structures (a) and (b) are 0.36 and 0.14 nm, respectively. From these results, we also found that the surface roughness of the InSb-QW structure is significantly improved using the $Al_{0.25}In_{0.75}Sb$/$Al_{0.15}In_{0.85}Sb$ stepped buffer layer. The effect of the $Al_{0.25}In_{0.75}Sb$/$Al_{0.15}In_{0.85}Sb$ stepped buffer layer on the dislocation and defect densities will also be described elsewhere.

Fig. 5 shows the electron mobility (μ) and the sheet carrier density (N_s) of the InSb-QW structures by Hall measurement. The μ values at room temperature of Structures (a) and (b) are 11,200 and 16,500 cm^2/(V s), respectively (an increase of 47%). Meanwhile, the N_s values of Structures (a) and (b) are 1.1×10^{12} and 1.2×10^{12} cm^{-2}, respectively. These results suggest that the $Al_{0.25}In_{0.75}Sb$/$Al_{0.15}In_{0.85}Sb$
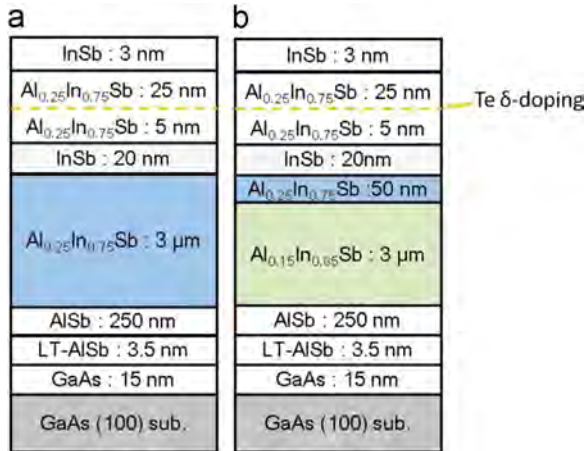
Fig. 1. Schematic structures of the InSb-QW with (a) $Al_{0.25}In_{0.75}Sb$ buffer layer and (b) $Al_{0.25}In_{0.75}Sb$/$Al_{0.15}In_{0.85}Sb$ stepped buffer layer.
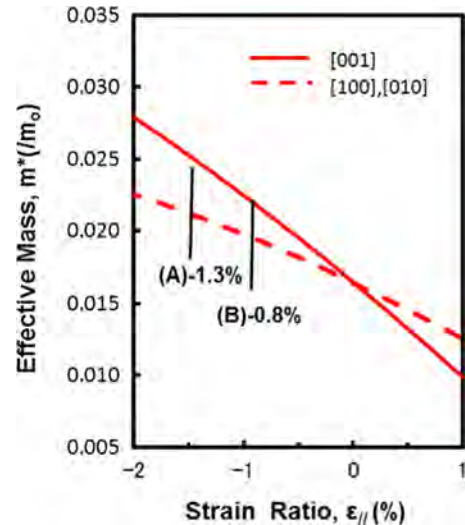
Fig. 2. Relationship between effective mass m and strain ratio $\varepsilon_{//}$.

Table 1
Critical thickness (h_c) of InSb channel layer in Structure (a) and InSb channel layer and $Al_{0.25}In_{0.75}Sb$ buffer layer in Structure (b). Parameters used in the calculation are also shown.

		h_c	f	b	ν	A	λ
Structure (a)	InSb channel on $A_{0.25}In_{0.75}Sb$ buffer layer	25	0.00804	4.5813	0.286	90	0
Structure (b)	InSb channel on $A_{0.25}In_{0.75}Sb$/$Al_{0.15}In_{0.85}Sb$ buffer layer	49	0.00481	4.5813	0.284	90	0
	$A_{0.25}In_{0.75}Sb$ layer on $Al_{0.15}In_{0.85}Sb$ buffer layer	81	0.00320	4.5206	0.290	90	0
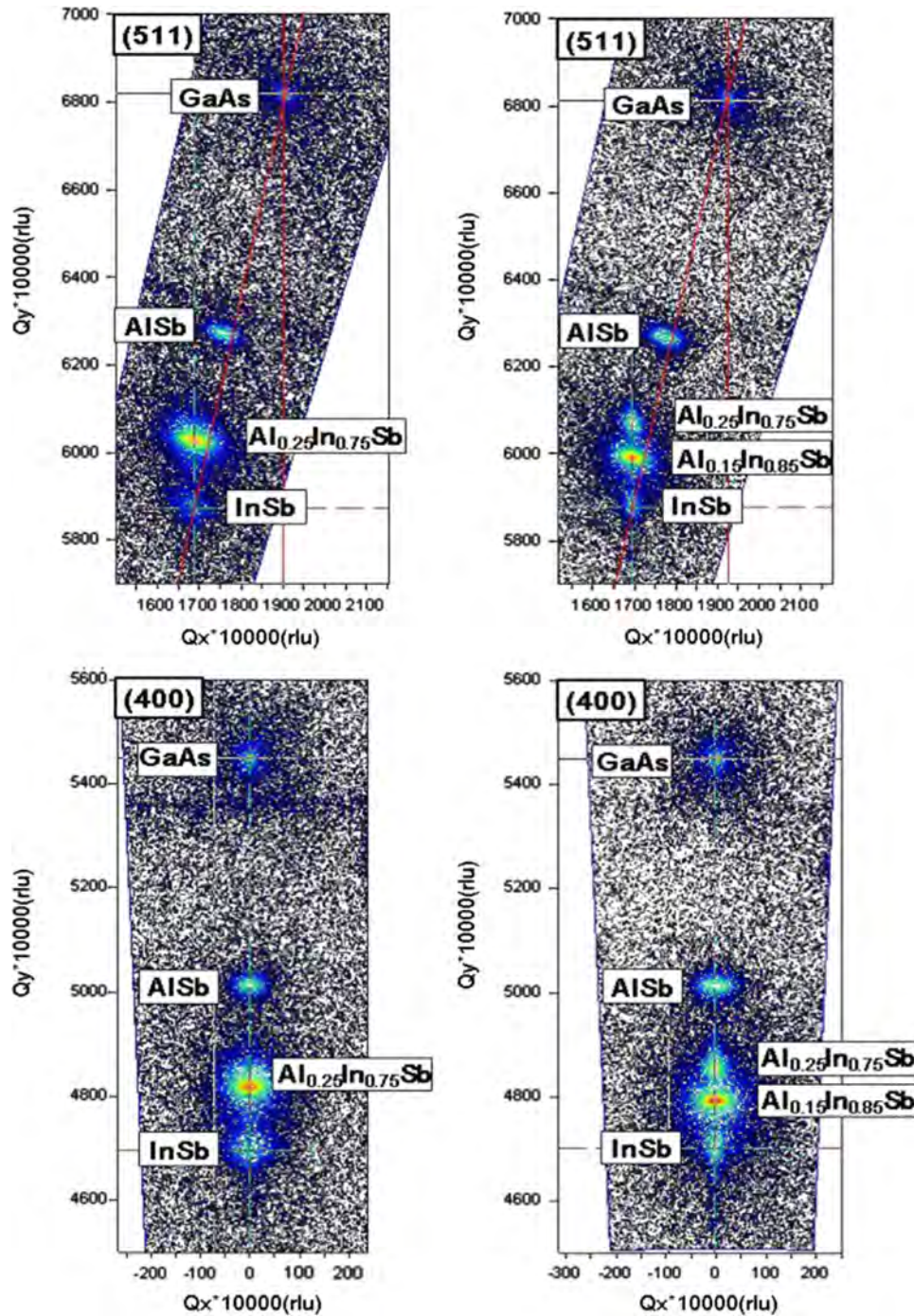
Fig. 3. (5 1 1) and (4 0 0) plane X-ray RSM of Structures (a) and (b).

stepped buffer layer is beneficial in increasing μ of the InSb-QW structure. The Monte Carlo simulation shows that the μ of InSb layer increases by about 10% as changing $\varepsilon_{//}$ from -1.3% to -0.8%, because of the decrease in m [12]. Therefore, the increase in μ using the $Al_{0.25}In_{0.75}Sb/Al_{0.15}In_{0.85}Sb$ stepped buffer layer is thought to come from the strain reduction and also the improvement of the crystalline quality including the surface roughness.

Then, we investigate the dependence of the $Al_{0.25}In_{0.75}Sb$ layer thickness below the InSb-channel layer on the μ characteristic. Fig. 6 shows the schematic sample structures. The $Al_{0.25}In_{0.75}Sb$ layer thickness below the InSb-channel layer are varied as 0, 20, 50, 100, and 200-nm thick, respectively, for Structures (c)–(g).

These samples have a 500-nm-thick $Al_{0.15}In_{0.85}Sb$ layer, a 750-nm-thick graded $Al_xIn_{1-x}Sb$ ($x=0.40 \to 0.15$) layer and a 500-nm-thick $Al_{0.40}In_{0.60}Sb$ layer below the $Al_{0.25}In_{0.75}Sb$ layer.

Fig. 7 shows the (5 1 1) plane X-ray RSMs for Structures (c)–(e) and (g). The Q_x value of the InSb channel layer approaches from the position of $Al_{0.15}In_{0.85}Sb$ to $Al_{0.25}In_{0.75}Sb$ as it transforms from Structure (e) into Structure (g). Then, the $Al_{0.25}In_{0.75}Sb$ layer is obviously lattice-relaxed when its thickness is 200 nm.

Fig. 8 shows the surface images of the InSb-QW structures of Structures (c)–(g) by AFM for 20 μm × 20 μm and 500 nm × 500 nm scales. The RMS values of Structures (c)–(g) are 0.24, 0.15, 0.14, 0.35, and 0.22 nm, respectively. Then, we confirm that the surface
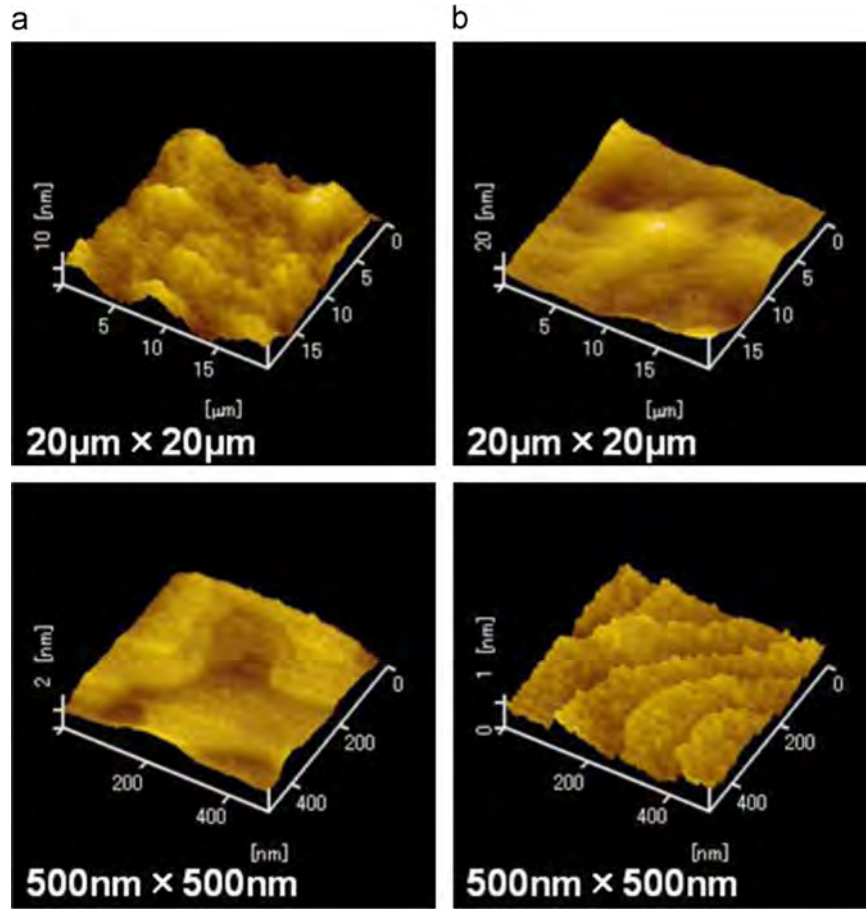
Fig. 4. AFM images of InSb-QW Structures (a) and (b). RMS values of the surface roughness for (a) 0.39 nm and (b) 0.14 nm.
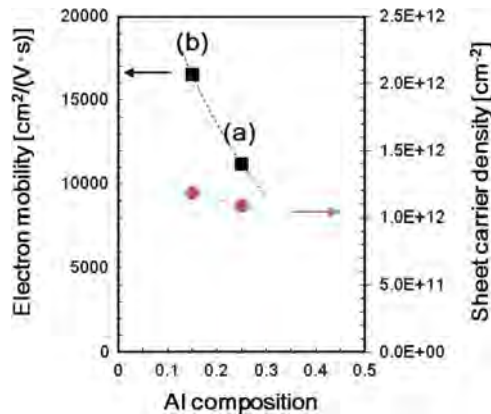
Fig. 5. Electron mobility and sheet electron density of Structures (a) and (b).

roughness is improved using the $Al_{0.25}In_{0.75}Sb$ layer within the critical thickness range, such as in Structures (d) and (e).

Fig. 9 shows the μ and the N_s values of Structures (c)–(g) by Hall measurement. The μ values of these structures are 14,482, 15,399, 15,333, 15,107, and 13,202 cm²/(V s), respectively. The N_s values are 1.35×10^{12}, 1.29×10^{12}, 1.28×10^{12}, 1.25×10^{12}, and 1.19×10^{12} cm^{-2}, respectively. We find that the μ and the N_s values gradually decrease when the $Al_{0.25}In_{0.75}Sb$ layer thickness exceeds the critical thickness.

4. Summary and conclusions

We have demonstrated the increase in electron mobility of the InSb QW structure on a (1 0 0) GaAs substrate using the $Al_{0.25}In_{0.75}Sb/Al_{0.15}In_{0.85}Sb$ stepped buffer layer. The $Al_{0.25}In_{0.75}Sb/Al_{0.15}In_{0.85}Sb$ stepped buffer layer has reduced the electron effective mass in the InSb channel by reducing the compressive strain and has improved the surface roughness. Consequently, the electron mobility of the InSb QW structure improved from 11,200 to 16,500 cm²/(V s) using the $Al_{0.25}In_{0.75}Sb/Al_{0.15}In_{0.85}Sb$ stepped buffer layer. Additionally,
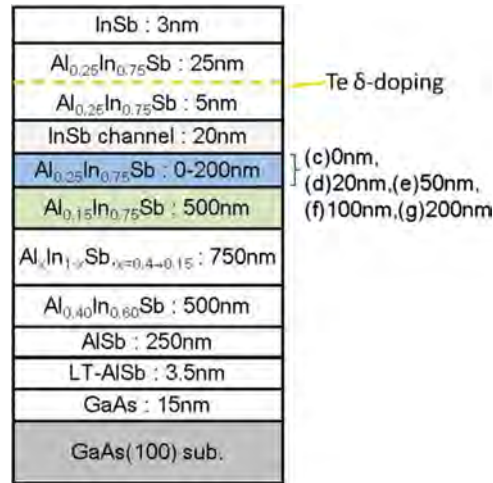
Fig. 6. Schematic structures of InSb-QW with (c) 0-nm, (d) 20-nm, (e) 50-nm, (f) 100-nm, and (g) 200-nm-thick $Al_{0.25}In_{0.75}Sb$/500-nm-thick $Al_{0.15}In_{0.85}Sb$ stepped buffer layers.
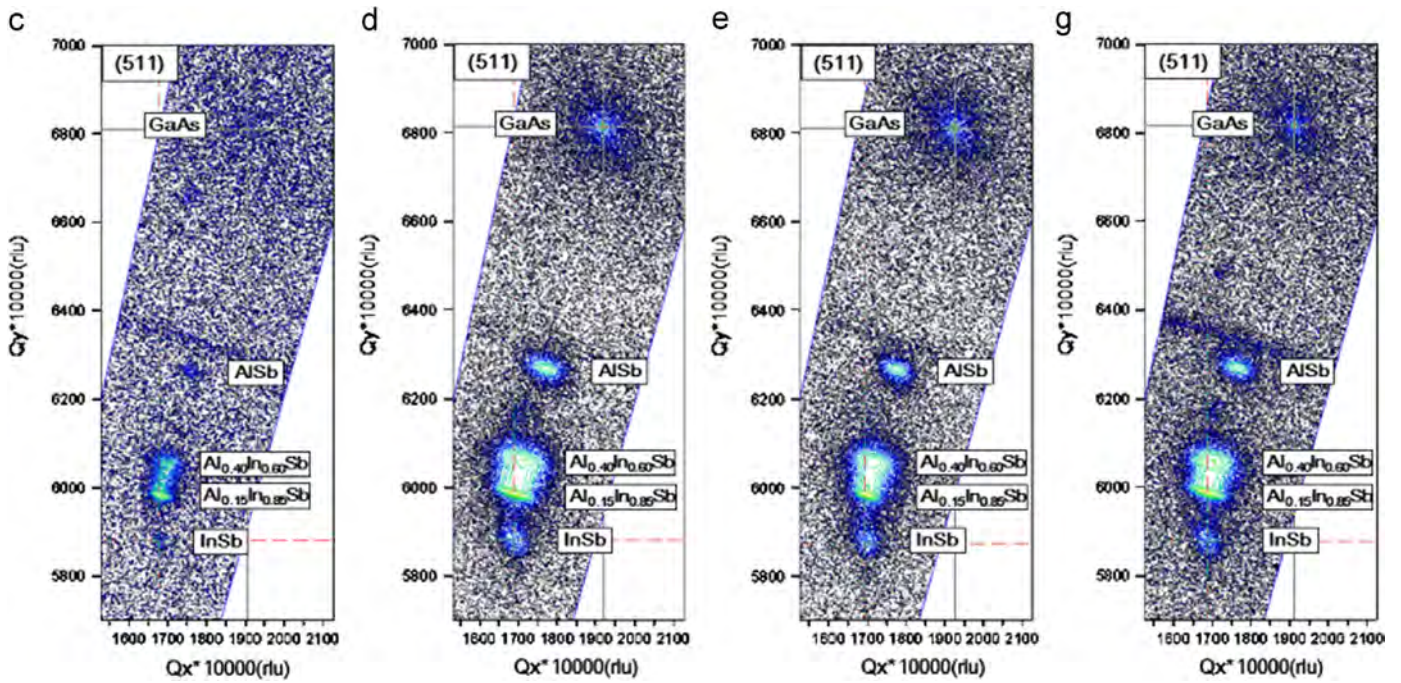
Fig. 7. (5 1 1) plane X-ray RSM of Structures (c)–(e) and (g).
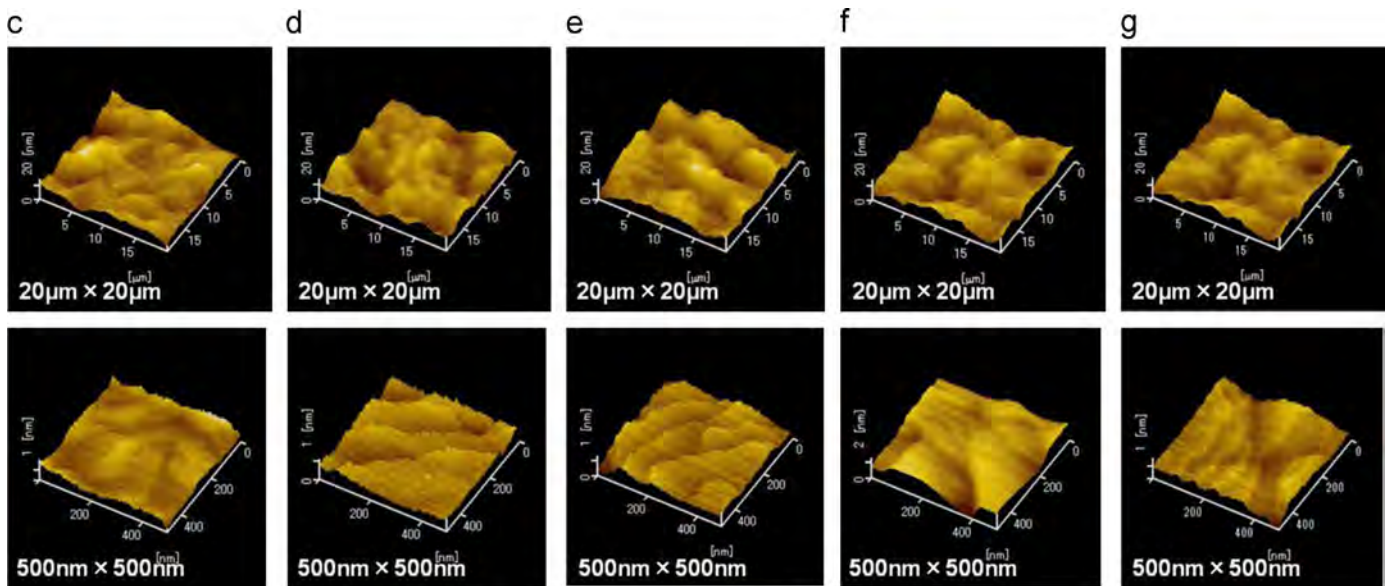
Fig. 8. AFM images of InSb-QW Structures (c)–(g). RMS value of the surface roughness for (c) 0.24 nm, (d) 0.15 nm, (e) 0.14 nm, (f) 0.35 nm, and (g) 0.22 nm.
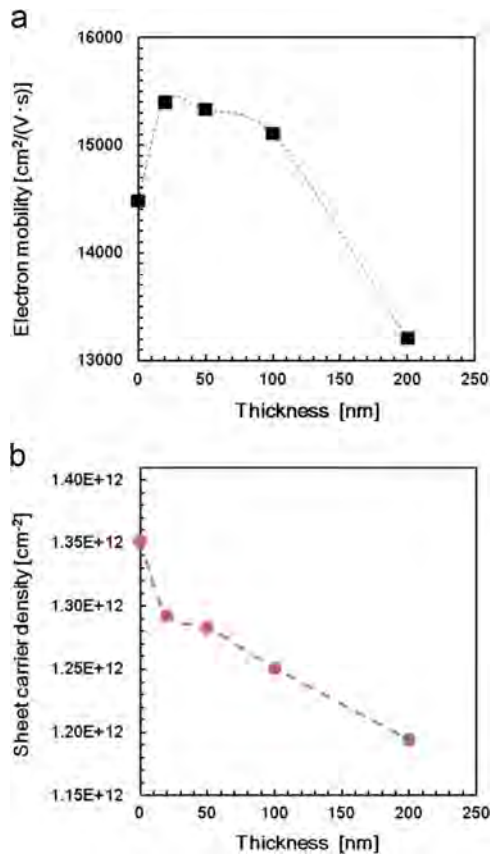
Fig. 9. Electron mobility and sheet carrier density dependence of Structures (c)–(g).

we found that the thickness of the $Al_{0.25}In_{0.75}Sb$ layer in the $Al_{0.25}In_{0.75}Sb/Al_{0.15}In_{0.85}Sb$ stepped buffer layer is crucial for high electron mobility, i.e., the electron mobility and sheet carrier density gradually decrease when the thickness of the $Al_{0.25}In_{0.75}Sb$ layer exceeds the critical thickness. In conclusion, a well-designed $Al_{0.25}In_{0.75}Sb/Al_{0.15}In_{0.85}Sb$ stepped buffer layer will be useful in increasing the electron mobility of InSb-QW structures.

References

[1] Y. Yamashita, A. Endoh, K. Shinohara, K. Hikosaka, T. Matsui, S. Hiyamizu, T. Mimura, IEEE Electron Device Lett. 23 (2002) 573.
[2] D.H. Kim, B. Brar, J.A. del Alamo, IEDM Tech. Dig. (2011) 13.6.1.
[3] E.-Y. Chang, C.-I. Kuo, H.-T. Hsu, C.-Y. Chiang, Y. Miyamoto, Appl. Phys. Express 6 (2013) 034001.
[4] J. Sato, Y. Nagai, S. Hara, H.I. Fujishiro, A. Endo, I. Watanabe, Proceedings of 24th International Conference on IPRM, 2012, We-2E.4.
[5] Y. Nagai, S. Nagai, J. Sato S. Hara, H.I. Fujishiro, A. Endoh, I. Watanabe, A. Kasamatsu,, Proceedings of 25th International Conference on IPRM, 2013, ThD2-4.
[6] T. Ashley, L. Buckle, M.T. Emeny, M. Fearn, D.G. Hayes, K.P. Hilton, R. Jefferies, T. Martin, T.J. Phillips, J. Powell, A.W.H. Tang, D. Wallis, P.J. Widing, Conf. Proc. CSICS 2006, 2006, 121.
[7] T.D. Mishima, J.C. Keay, N. Goel, M.A. Ball, S.J. Chung, M.B. Johnson, M.B. Santos, Physica E 20 (2004) 260.
[8] T.D. Mishima, J.C. Keay, N. Goel, M.A. Ball, S.J. Chung, M.B. Johnson, M.B. Santos, J. Cryst. Growth 251 (2003) 551.
[9] T.D. Mishima, M. Edirisooriya, N. Goel, M.B. Santos, Appl. Phys. Lett. 88 (2006) 191908.
[10] X. Weng, N.G. Rudawski, P.T. Wang, R.S. Goldman, D.L. Partin, J. Heremans, J. Appl. Phys. 97 (2005) 043713.
[11] J.W. Matthews, A.E. Blakeslee, J. Cryst. Growth 27 (1974) 118.
[12] H. Nishino, I. Kawahira, F. Machida, S. Hara, H.I. Fujishiro., Proceedings of 24th International Conference on IPRM, 2010, 1.
[13] S.C. Jain, et al., Adv. Phys. 39 (1990) 127.

CRYSTAL GROWTH

CrossMark
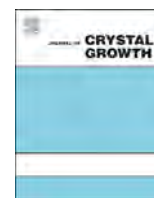
Growth variations and scattering mechanisms in metamorphic $In_{0.75}Ga_{0.25}As/In_{0.75}Al_{0.25}As$ quantum wells grown by molecular beam epitaxy

Chong Chen [a,*], Ian Farrer [a], Stuart N. Holmes [b], Francois Sfigakis [a], Marc P. Fletcher [a], Harvey E. Beere [a], David A. Ritchie [a]

[a] Cavendish Laboratory, University of Cambridge, JJ Thomson Avenue, Cambridge CB3 0HE, United Kingdom
[b] Toshiba Research Europe Limited, Cambridge Research Laboratory, 208 Cambridge Science Park, Milton Road, Cambridge CB4 0GZ, United Kingdom

ARTICLE INFO

ABSTRACT

Modulation doped metamorphic $In_{0.75}Ga_{0.25}As/In_{0.75}Al_{0.25}As$ quantum wells (QW) were grown on GaAs substrates by molecular beam epitaxy (MBE) with step-graded buffer layers. The electron mobility of the QWs has been improved by varying the MBE growth conditions, including substrate temperature, arsenic over pressure and modulation doping level. By applying a bias voltage to SiO_2 insulated gates, the electron density in the QW can be tuned from 1×10^{11} to 5.3×10^{11} cm^{-2}. A peak mobility of 4.3×10^5 cm^{2}V^{-1}s^{-1} is obtained at 3.7×10^{11} cm^{-2} at 1.5 K before the onset of second subband population. To understand the evolution of mobility, transport data is fitted to a model that takes into account scattering from background impurities, modulation doping, alloy disorder and interface roughness. According to the fits, scattering from background impurities is dominant while that from alloy disorder becomes more significant at high carrier density.

© 2015 Elsevier B.V. All rights reserved.

1. Introduction

$In_xGa_{1-x}As/In_xAl_{1-x}As$ quantum wells (QWs) are attractive because of the low electron effective mass, large g-factor, large Rashba spin–orbit coupling and highly transmissive metal–semiconductor interface at high indium composition compared to GaAs/AlGaAs [1]. It also provides a way of varying these parameters by changing the composition of the indium.

However, when compared with its counterpart GaAs/AlGaAs, there is a fundamental issue regarding growth. There is no lattice matched substrate for growing InGaAs except for $In_{0.53}Ga_{0.47}As/In_{0.52}Al_{0.48}As$ on InP. Researchers have incorporated graded InGaAs or InAlAs layer to grow high percentage InGaAs on InP or GaAs [2–4] and managed to achieve control of dislocation propagation due to strain [2,4–6]. Virtually strain-free, defect-free layers can be achieved through the use of step-graded buffer layers with compositional "overshoot" [5]. An electron mobility of 2.9×10^5 cm^2 V^{-1} s^{-1} was obtained at 4.0×10^{11} cm^{-2} [5].

Scattering mechanisms in relaxed and strained InGaAs/InAlAs quantum wells have been studied by several researchers [1,2,7]. Their research has shown that scattering from background impurities limits the mobility at lower carrier densities, scattering from alloy disorder becomes more important at higher carrier densities. Capotondi et al. [1] reduced the impact of alloy disorder by inserting binary InAs into the quantum well. Understanding how each scattering mechanism influences the total mobility is crucial when attempting to further improve mobility in InGaAs which could make the realisation of spin and/or Josephson FETs possible [8,9].

In this paper, we present a transport study on a series of wafers grown under different conditions with nominally the same layer structure to investigate the difference in mobility. AFM (Atomic Force Microscope) images of the free surface are used to provide supplementary information of the surface or interface morphology. The transport measurements were performed at 1.5 K. The mobility fits were using the theory provided by Gold [10]. This work aims to understand the influence of different scattering mechanisms and therefore, make possible suggestions for further improvements to the layer structure or growth conditions.

2. Experiment

The quantum wells studied in this paper were grown by solid-source molecular beam epitaxy (MBE) using a Veeco Gen III system on

* Corresponding author.
  E-mail address: cc638@cam.ac.uk (C. Chen).

Fig. 1. Schematic layer structure of $In_{0.75}Ga_{0.25}As/In_{0.75}Al_{0.25}As$ quantum wells.

Table 1
Growth detail.

Wafer no.	W0401	W0402	W0413	W0414	W0435	W0436
T_B (°C)	416	391	360	341	331	337
T_P (°C)	470	462	437	431	428	429
P_{As_2} ($\times 10^{-5}$ torr)	1.2	1.2	1.4	1.4	1.2	1.0
N_{Si} ($\times 10^{17}$ cm^{-3})	0	2.3	2.3	2.3	1.8	1.8

T_B/T_P: Substrate temperature measured by BandiT/Pyrometer at the start of SGB/QW growth; P_{As_2}: As$_2$ Beam Flux; N_{Si}: Si Modulation Doping Level.

gate. The chips were taken from the same position on each wafer. Shubnikov–de Haas oscillations and Hall effect are measured at 1.5 K to obtain electron density and mobility.

3. Result and discussion

3.1. AFM

The morphology of the free surface is studied as an indirect reference to the buried $In_{0.75}Al_{0.25}As/In_{0.75}Ga_{0.25}As$ interface, since we assume that the lattice is fully relaxed according to [11] and the surface undulation results from the misfit dislocation network buried in the buffer layer [5]. The digitisation lateral step size of the following images is 20 nm.

As seen in Fig. 2, the surface grown at the highest temperature Fig. 2a has the roughest morphology with long 3D islands due to the tensile strain during crystal growth [15]. When the temperature is decreased from 416 °C to 390 °C the size of the islands reduces, with a further decrease of the growth temperature, the islands become less visible but more aligned. The surface begins to show the well-known cross-hatched pattern. A change from 3D growth mode (Fig. 2a and b) to 2D growth mode (Fig. 2c–f) and a corresponding reduction, by a factor of 3, of the RMS value can be seen when the growth temperature is decreased. This is because the surface diffusion length is reduced and therefore the layer-by-layer growth regime is extended [15].

The surface morphology is clearly anisotropic. The islands seen in 2a and 2b are elongated along [1$\bar{1}$0]. There are striations aligned to [1$\bar{1}$0] in other samples. The period of surface oscillation appears to be crystallographic direction dependent. This difference in surface undulation was also observed previously [5,16,17].

3.2. Transport

Fig. 3 shows the electron mobility (μ) as a function of electron density (n_{2d}) for $In_{0.75}Ga_{0.25}As$ quantum wells. Electron density was varied by applying a gate voltage from the beginning of 2DEG depletion to the saturation of electron density. In Ref. [12], the growth at 410 °C showed the highest mobility. In the present set of wafers, sample grown at a similar temperature (W0401 at 416 °C) did not conduct without illumination. The mobility of W0401 (416 °C) is only comparable with the crystal grown at 470 °C (Fig. 3 in [12]) but with slightly higher carrier densities. Extra carriers in W0401 could come from unintentional dopants from the thicker buffer layer compared with InGaAs QWs grown on the InP substrate [12]. The growth temperature at the quantum well region in W0401 is 470 °C which is a comparable growth temperature in [12]. Therefore, the two samples have similar mobility although based on different substrates.

The fact that the surface morphology of wafer W0401 is rough and does not conduct in the dark indicates that it has been grown at a too high temperature. In order to improve the surface morphology, the growth temperature was lowered to 391 °C when growing the next wafer W0402. Modulation doping was

3 inch semi-insulating (001) GaAs substrates that are indium-free mounted. A schematic layer structure adapted from [5,11,12] is shown in Fig. 1. Arsenic dimers (As$_2$) rather than arsenic tetramers (As$_4$) are used to try and reduce antisite defects at the low growth temperatures used (330–420 °C) [13]. Three growth parameters, substrate temperature (T_B), arsenic over pressure (P_{As_2}) and Si modulation doping level (N_{Si}) were adjusted to improve the electron mobility in this structure. T_B was measured using a kSA BandiT system [14] and where possible also with an optical pyrometer. T_B was set at the start of the graded buffer layer growth and not intentionally further altered during the growth. Growth temperatures quoted throughout this work refer to those measured by BandiT unless specified.

After oxide removal and degassing, the GaAs/AlAs/GaAs buffer was grown at 580 °C. Then the substrate temperature is ramped down over a period of 20 min before growing the step-graded buffer (SGB) layer. The step-graded buffer layer was grown at six different starting substrate temperatures: 416 °C, 390 °C, 360 °C, 341 °C, 331 °C and 337 °C. The first growth temperature was chosen according to Simmonds' study [12] where the growth temperature for devices grown on InP substrates was optimised. The quantum wells are grown at slightly higher substrate temperatures as the substrate becomes more absorbing during growth. To alter the indium composition in the structure, the aluminium cell temperature is ramped down while the indium cell temperature is ramped up rapidly at the start of each layer in the SGB sequence. To change the arsenic over pressure, the needle valve in the arsenic cell was adjusted and the pressure is measured by the beam flux gauge prior to growth. The nominal growth rate is kept the same (around 1.0 μm/h) throughout the structure. Growth was interrupted to stabilise the In cell to grow the 75% InAlAs buffer. This interruption introduces the possibility of impurity accumulation [12], therefore a further 250 nm InAlAs layer is grown afterwards to separate the impurities from the conduction channel. The first sample was grown undoped to replicate the growth condition in [12], however it did not conduct without illumination at 1.5 K. The remaining 5 wafers were then modulation doped to ensure conductance in the dark. The modulation doping concentration is controlled by altering the Si cell temperature. The major differences in growth conditions are highlighted in Table 1.

The AFM images are taken with a Veeco Dimension 3000 SPM (Scanning Probe Microscope) and Nanoworld pointprobe. The size of the scanned area is 10×10 μm^2 which is large enough to be representative of the surface morphology. High Electron Mobility Transistors (HEMTs) were fabricated using standard wet chemical etching. AuGeNi alloy was used for Ohmic contacts, PECVD Silicon dioxide (100 nm) for insulator and thin NiCr (20 nm) for transparent

Fig. 2. $10 \times 10\ \mu m^2$ AFM images show significant improvement in surface morphology when decreasing the growth temperature. The z-axis scale is adjusted to be 100 nm in each image for comparison. The root mean square (RMS) roughness value, given in the caption, is averaged from 5 images taken from different positions on the wafer: (a) 416 °C (14.25 nm); (b) 391 °C (14.19 nm); (c) 360 °C (4.68 nm); (d) 341 °C (5.33 nm); (e) 331 °C (4.98 nm); and (f) 337 °C (4.92 nm).
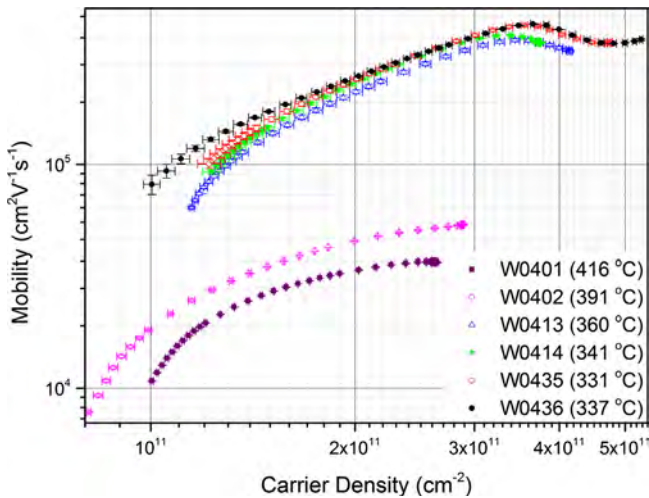
Fig. 3. Electron mobility as a function of electron density at 1.5 K.

implemented to make the wafer conduct in the dark. As shown in Figs. 2 and 3, the surface morphology and the mobility of W0402 improved comparing with W0401, but it is not comparable with that presented in [1]. The growth temperature was further reduced to 360 °C and the arsenic over pressure was increased in W0413 which lead to significant improvements in both morphology and mobility. Although a further reduction in growth temperature in W0414 (341 °C) did not improve surface morphology, it did improve the mobility. High arsenic over pressure would improve the surface morphology, however, it may introduce more background impurities. Steps to improve the mobility were then made by controlling the scattering from ionised impurities, reducing the arsenic over pressure and the modulation doping level as for W0435 while keeping the growth temperature at roughly the same level (10 °C lower at the start of SGB and 3 °C lower at the beginning of QW). The arsenic over pressure was further reduced in W0436 while maintaining the growth temperature. The

mobility of W0435 and W0436 is similar over whole density range except that W0436 shows a slightly higher peak mobility around $4.3 \times 10^5\ cm^2\ V^{-1}\ s^{-1}$ at $3.7 \times 10^{11}\ cm^{-2}$. Transport data from W0436 will be discussed in more detail in the following sections.

In all wafers, the μ increases monotonically with n_{2d} to its peak value; a decrease is seen in mobility above a critical density (n_c) in the four wafers the density of which reaches $3.4 \times 10^{11}\ cm^{-2}$. This decrease was also observed by Capotondi in their undoped relaxed structures [1] and Ramvall in their strained structures [7]; however, only two of the best mobility structures showed an increase in mobility after the minimum mobility. This feature, due to the second-subband population, is confirmed by multiple frequencies in the Shubnikov–de Haas oscillation as shown in Fig. 4. Fast Fourier transform performed at different carrier densities demonstrates the evolution of the second subband. The electron density in the first subband (F1 in Fig. 4) is constant while that inside the second subband increases as the total density increases. No clear beating effect is observed in the Shubnikov–de Haas effect nor spin-splitting in the FFT. Therefore, the multiple frequencies in the Shubnikov–de Haas effect are not due to the Rashba effect but due to the second subband population [18].

Using a magnetic field modulation technique [19], the Rashba coefficient (α) was measured to be $0.7 \pm 0.1 \times 10^{-11}$ eV m in W0436 where peak splittings in the FFTs can be quantified. This corresponds to an energy splitting of 1.6 meV at the Fermi energy. The detailed measurement is not included in this work. The asymmetry of the confining potential in the doped wafer does not enhance the Rashba coefficient compared to the nominally undoped wafers grown on InP in the authors' previous work [19]. Although modulation doping changes quite dramatically the symmetry of the confining potential, the spin-splitting in a quantum well system is mainly determined by the band offsets with the barrier material, not the electric field in the z-direction [20].

There are three main scattering mechanisms operating in these structures: ionised impurity scattering, alloy disorder scattering (AD), and interface roughness scattering (IR) [21]. The ionised impurity scattering can come from the background impurities (BG) or the modulation doping (MD). An example fit is shown in Fig. 5

(left). There are some reports about charged dislocations acting as scattering centres [6,16], however the mobility in these samples is only 50,000 cm² V⁻¹s⁻¹ at 3.6 × 10¹¹ cm⁻². Consequently,

scattering from charged dislocations is not considered in this paper since a study on a similar structure has demonstrated a defect-free conducting layer and the mobility in this work is comparable with that of [1].

Single scattering mechanism fitting is done first to extract the reasonable range of the parameters, the background impurity level N_B, the activated dopants level N_D, the alloy disorder potential V_{ad}, the interface correlation length Λ and the average height of the surface Δ. V_{ad} will be the same for each wafer since the alloy composition is identical among them. We assume that the dopant activation rate is the same across this set of wafers. According to [22], we assume that at the doping level in this paper, Si is fully activated with an activation rate of 1. Scattering from MD is not the limiting scattering mechanism since the mobility limited by MD is one magnitude larger (see Fig. 5). Therefore to simplify the fitting procedure the data using only BG and AD was carried out according to [1]. The extracted parameters are summarised in Table 2. By assuming the scattering from interface roughness is not significant, background impurity levels extracted from the fitting are very sensitive to changes in growth temperature and arsenic over pressure. One example fit is shown in Fig. 5 (right). As a comparison, the fitting that considers all four scattering mechanisms is presented in the same diagram. R-squared value has been calculated from 1.7×10^{11} cm⁻² to 3.8×10^{11} cm⁻² for these two fittings, the value from the four-mechanism fitting is 0.9573 and that from the two-mechanism fitting is 0.8386, therefore the four-mechanism fitting is more representative of the experimental data. Consequently, even though scattering from IR is not dominant, it has a significant contribution to the total mobility.

The four-mechanism fitting is applied to the four high density wafers. The results are shown in Fig. 6 and the parameters used
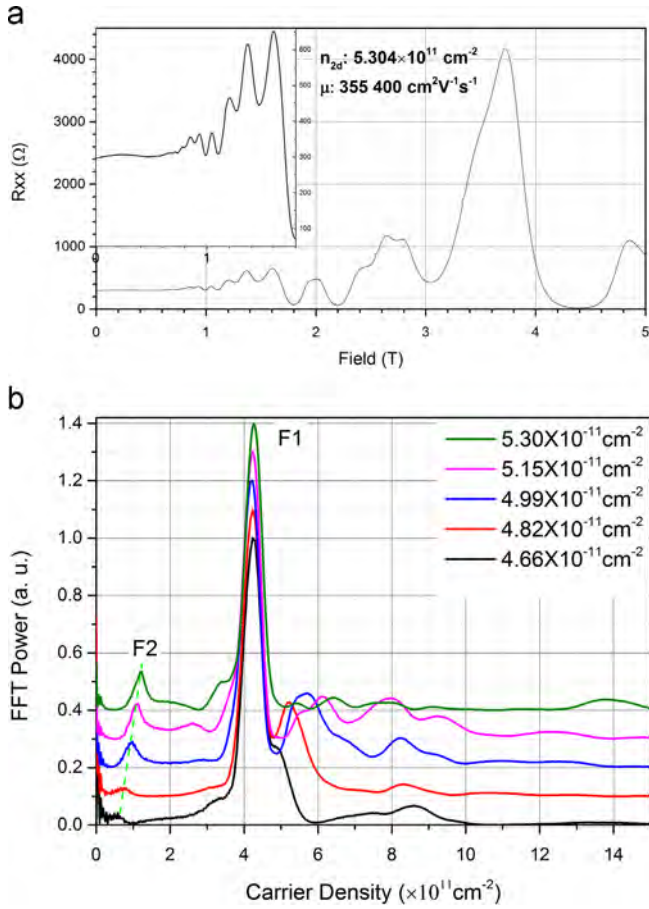
Fig. 4. (a) A representative longitudinal resistance measurement on W0436 shows multiple frequencies in the Shubnikov–de Haas oscillations; the inset shows the low field region in more detail; (b) Fast Fourier Transform results from Shubnikov–de Haas oscillations at different densities by changing the gate voltage in enhancement mode (F1 and F2 are the first and second subband). The legends are carrier densities obtained from the Hall measurement slopes which agree well with densities calculated from FFT.

Table 2
Fitting parameters only considering background impurities and alloy disorder.

Wafer no.	Background impurity level N_B (cm⁻³)	Alloy disorder potential V_{ad} (eV)
W0401 (416 °C)	3.7×10^{16}	0.2
W0402 (391 °C)	2.9×10^{16}	0.2
W0413 (360 °C)	6.5×10^{15}	0.2
W0414 (341 °C)	5.8×10^{15}	0.2
W0435 (331 °C)	$> 5.6 \times 10^{15}$	0.2
W0436 (337 °C)	$< 5.6 \times 10^{15}$	0.2
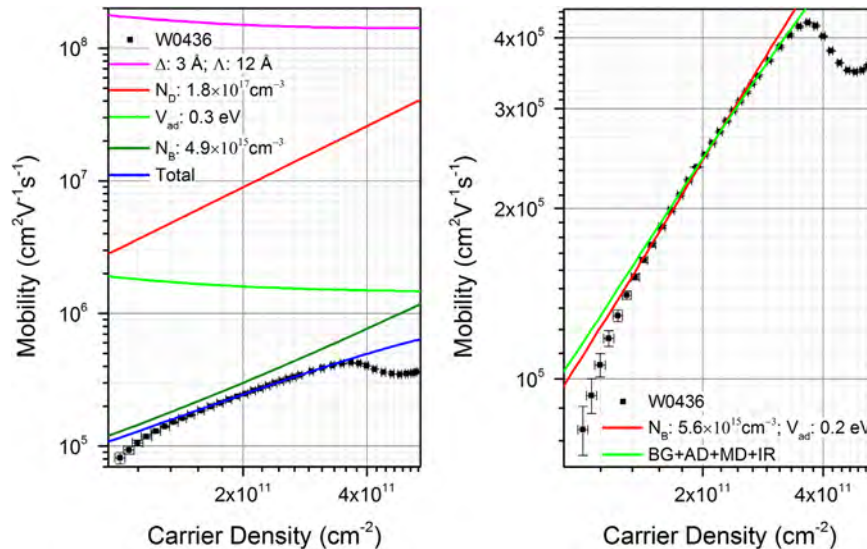
Fig. 5. Left: fitting example of taking Interface Roughness (IR: Δ, Λ), Modulation Doping (MD: N_D), Alloy Disorder (AD: V_{ad}), and Background Impurity (BG: N_B) scattering into consideration; right: comparison of two fittings: one with four scattering mechanisms ($R^2 = 0.9573$) and the other with only two of them (BG and AD, $R^2 = 0.8386$).
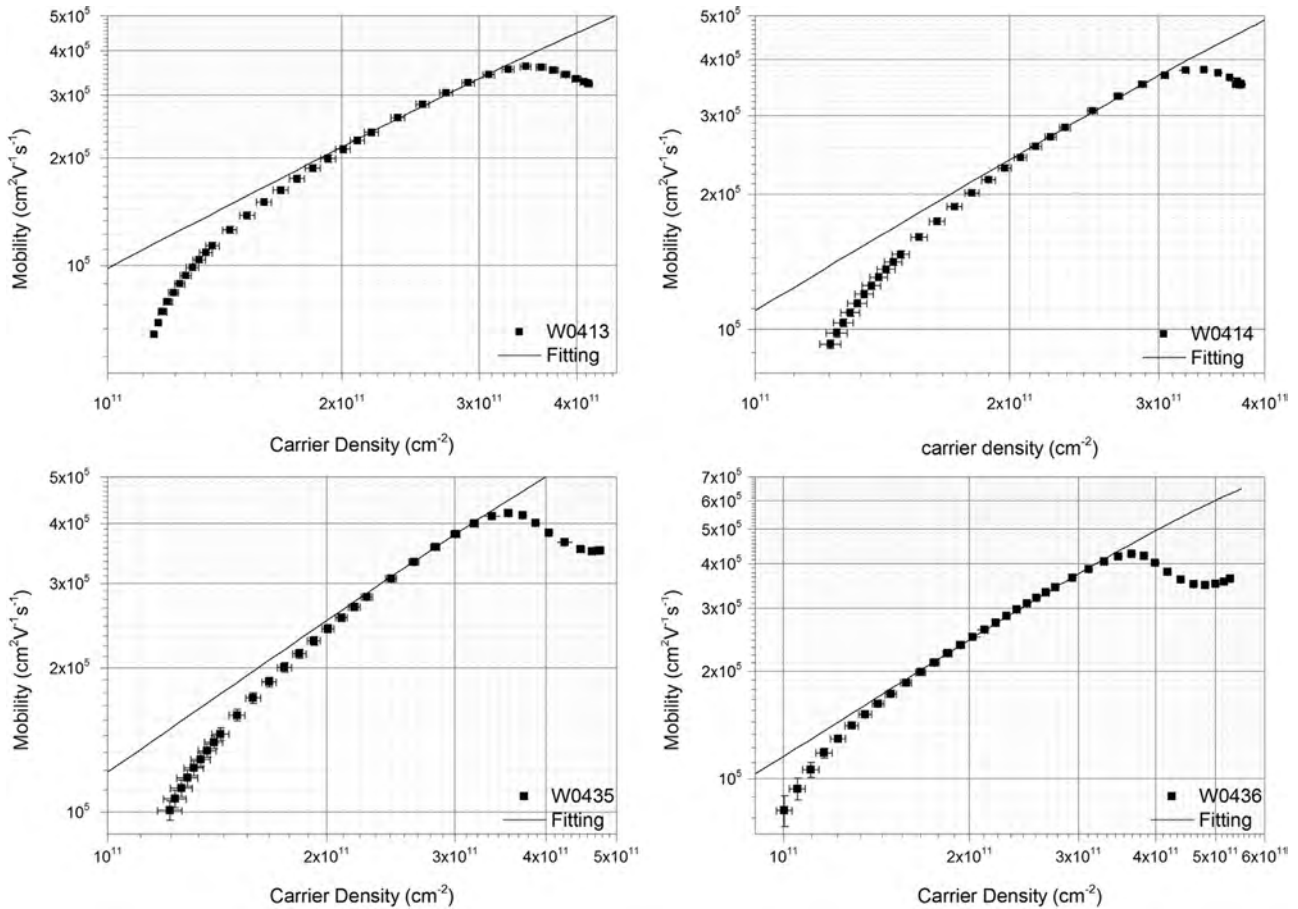
Fig. 6. Four mechanisms fitting of all four wafers, the fitting parameters are listed in Table 3. The straight line is a fit to the data.

Table 3
Fitting parameters used in Fig. 6.

Wafer no.	MD	BG	AD	IR	
	N_d (cm^{-3})	N_B (cm^{-3})	V_{ad} (eV)	Λ (Å)	Δ (Å)
W0413 (360 °C)	2.3×10^{17}	5.5×10^{15}	0.3	300	6
W0414 (341 °C)	2.3×10^{17}	4.8×10^{15}	0.3	300	6
W0435 (331 °C)	1.8×10^{17}	4.5×10^{15}	0.3	100	3
W0436 (337 °C)	1.8×10^{17}	4.9×10^{15}	0.3	12	3

MD: Modulation Doping; BG: Background Impurities; AD: Alloy Disorder; IR: Interface Roughness.

are listed in Table 3. The average height is chosen to be a multiple of the thickness of one monolayer. To be noted, the parameters for interface roughness are not taken from the AFM information. Since the lateral resolution of AFM is limited by both digitisation step size and the tip size which are 20 nm and 10 nm in this study, respectively. This is 2 orders larger than the lattice constant of InGaAs. A good fit can be made to each set of data by adjusting the background impurity level and the interface roughness. The extracted alloy disorder potential is 0.3 eV which agrees with the result, around 0.3 eV, reported by [7] for In$_{0.75}$Ga$_{0.25}$As however smaller than the value (0.5 eV) reported by [5]. The extracted background impurity level is of the order of 10^{15} cm^{-3}. The fitted data agrees well with the experimental data from around 1×10^{11} cm^{-2} to the point where the second subband populates. At the low density end where neither fitting method applies, the mobility is dominated by percolation which can only be fitted using metal-insulator transition theory [23]. At the high density
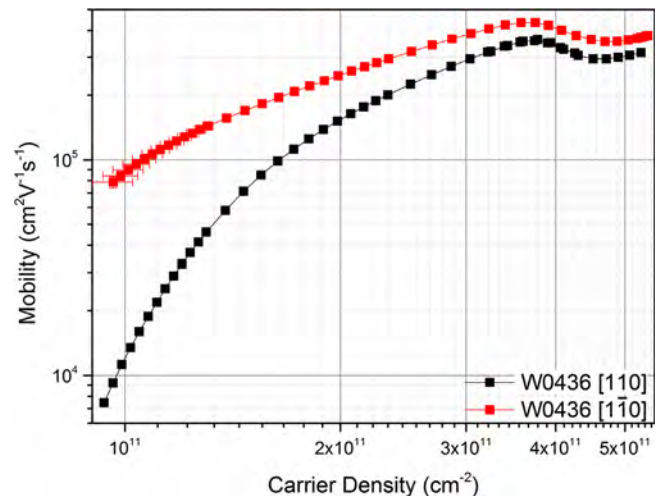
Fig. 7. Anisotropy of mobility in two different crystallographic directions at 1.5 K which is present at all gate voltages.

end where the second-subband populates (see Fig. 4), the mobility is limited by inter-subband scattering. The scattering from background impurities is dominating the whole density range, while alloy disorder scattering becomes increasingly important as the carrier density increases. To extract more accurate growth parameters, a further study has to be carried out to verify the assumptions made in this work, eg. relaxation of the crystal during growth.

It is interesting to see that all these wafers show anisotropy in mobility. The measured mobility difference in both direction on

W0436 is shown in Fig. 7. This had been observed by many researchers [24,17,7]. This could result from a number of reasons such as interface roughness, indium concentration modulation or anisotropic ordering appeared in the structures. In this work, the mobility anisotropy appears to follow the surface morphology anisotropy: the higher mobility is along [1$\bar{1}$0] which has larger undulation period. To verify the factors that account for this phenomenon, a more detailed study is required.

4. Conclusion

The growth conditions for modulation doped In$_{0.75}$Ga$_{0.25}$As/In$_{0.75}$Al$_{0.25}$As quantum wells on GaAs were studied. A sample grown under 1.0×10^{-5} torr arsenic over pressure with 1.8×10^{17} cm^{-3} modulation doping at 337 °C has the highest mobility. A peak mobility of 4.3×10^5 cm^2 V^{-1} s^{-1} is obtained at 3.7×10^{11} cm^{-2} at 1.5 K with a gated structure. The SiO$_2$ insulated gates provides high reproducibility and low hysteresis from depletion to $\simeq 5 \times 10^{11}$ cm^{-2}. We have demonstrated a promising fit to experimental data using Gold's model considering four different scattering mechanisms, background impurities, modulation doping, alloy disorder and interface roughness scattering. We estimate the alloy disorder potential to be around 0.3 eV and the background impurity level of the order of $\sim 10^{15}$ cm^{-3}. This could be used as a method to extract growth parameters [23] if the growth conditions or the layered structure is designed in a systematic way. Anisotropy in surface morphology and mobility is observed in all wafers. The Rashba coefficient calculated in these structures is similar to that in undoped structures. Although modulation doping enhances the asymmetry across the quantum well, the measured Rashba coefficient is insensitive to this confirming the theory presented in [20].

Acknowledgement

References

[1] F. Capotondi, G. Biasiol, D. Ercolani, L. Sorba, Scattering mechanisms in undoped In$_{0.75}$Ga$_{0.25}$As/In$_{0.75}$Al$_{0.25}$As two-dimensional electron gases, J. Cryst. Growth 278 (1–4) (2005) 538–543.

[2] S. Gozu, T. Kita, T. Kikutani, S. Yamada, Critical layer thickness study in In$_{0.75}$Ga$_{0.25}$As/In$_{0.5}$Al$_{0.5}$As pseudomorphic resonant tunneling diode structure grown on GaAs substrates, J. Cryst. Growth 227–228 (2001) 161–166.

[3] M. Bergh, E. Olsson, T.G. Andersson, H. Zirath, Molecular beam epitaxy growth and characterization of In$_x$Ga$_{1-x}$As ($0.57 < x < 1$) on GaAs using InAlAs graded buffer, J. Cryst. Growth 175/176 (1997) 1016–1021.

[4] K. Inoue, J.C. Harmand, T. Matsuno, High-quality In$_x$Ga$_{1-x}$As/InAlAs modulation-doped heterostructures grown lattice-mismatched on GaAs substrates, J. Cryst. Growth 111 (1–4) (1991) 313–317.

[5] F. Capotondi, G. Biasiol, D. Ercolani, V. Grillo, E. Carlino, Strain induced effects on the transport properties of metamorphic InAlAs/InGaAs quantum wells, Thin Solid Films 484 (2005) 400–407.

[6] C. Heyn, S. Mendach, S. Löhr, S. Beyer, S. Schnüll, Growth of shallow InAs HEMTs with metamorphic buffer, J. Cryst. Growth 251 (2003) 832–836.

[7] P. Ramvall, N. Carlsson, P. Omling, L. Samuelson, W. Seifert, Q. Wang, K. Ishibashi, Y. Aoyagi, Quantum transport in high mobility modulation doped Ga$_{0.25}$In$_{0.75}$As/InP quantum wells, J. Appl. Phys. 84 (4) (1998) 2112–2122.

[8] S. Gozu, T. Kita, Y. Sato, S. Yamada, M. Tomizawa, Characterization of high indium content metamorphic InGaAs/InAlAs modulation-doped heterostructures, J. Cryst. Growth 227–228 (2001) 155–160.

[9] P. Chuang, S. Ho, L.W. Smith, F. Sfigakis, M. Pepper, C. Chen, J. Fan, J.P. Griffiths, I. Farrer, H.E. Beere, G.A.C. Jones, D.A. Ritchie, T. Chen, All-electric all-semiconductor spin field-effect transistors, Nat. Nanotechnol. 10 (2015) 35–39.

[10] A. Gold, Scattering time and single-particle relaxation time in a disordered two-dimensional electron gas, Phys. Rev. B 38 (1988) 10798.

[11] F. Capotondi, G. Biasiol, I. Vobornik, L. Sorba, F. Giazotto, A. Cavallini, B. Fraboni, Two-dimensional electron gas formation in undoped In$_{0.75}$Ga$_{0.25}$As/In$_{0.75}$Al$_{0.25}$As quantum wells, J. Vac. Sci. Technol. B: Microelectron. Nanometer Struct. 22 (2) (2004) 702–706.

[12] P.J. Simmonds, H.E. Beere, D.A. Ritchie, S.N. Holmes, Growth-temperature optimization for low-carrier-density In$_{0.75}$Ga$_{0.25}$As-based high electron mobility transistors on InP, J. Appl. Phys. 102 (8) (2007) 083518.

[13] R.P. Campion, K.W. Edmonds, L.X. Zhao, K.Y. Wang, C.T. Foxon, B.L. Gallagher, C.R. Staddon, The growth of GaMnAs films by molecular beam epitaxy using arsenic dimers, J. Cryst. Growth 251 (2003) 311–316.

[14] I. Farrer, J.J. Harris, R. Thomson, D. Barlett, C.A. Taylor, D.A. Ritchie, Substrate temperature measurement using a commercial band-edge detection system, J. Cryst. Growth 301–302 (2007) 88–92.

[15] N. Grandjean, J. Massies, Epitaxial growth of highly strained In$_x$Ga$_{1-x}$As on GaAs (001): the role of surface diffusion length, J. Cryst. Growth 134 (1993) 51–61.

[16] C. Lavoie, T. Pinnington, E. Nodwell, T. Tiedje, R.S. Goldman, K.L. Kavanagh, J.L. Hutter, Relationship between surface morphology and strain relaxation during growth of InGaAs strained layers, Appl. Phys. Lett. 67 (25) (1995) 3744.

[17] D. Ercolani, G. Biasiol, E. Cancellieri, M. Rosini, C. Jacoboni, F. Carillo, S. Heun, L. Sorba, F. Nolting, Transport anisotropy in In$_{0.75}$Ga$_{0.25}$As two-dimensional electron gases induced by indium concentration modulation, Phys. Rev. B 77 (2008) 235307.

[18] P.J. Simmonds, S.N. Holmes, H.E. Beere, D.A. Ritchie, Spin–orbit coupling in an In$_{0.52}$Ga$_{0.48}$As quantum well with two populated subbands, J. Appl. Phys. 103 (8) (2008) 124506.

[19] S.N. Holmes, P.J. Simmonds, H.E. Beere, F. Sfigakis, I. Farrer, D.A. Ritchie, M. Pepper, Bychkov–Rashba dominated band structure in an In$_{0.75}$Ga$_{0.25}$/In$_{0.75}$Al$_{0.25}$ device with spin-split carrier densities of $< 10^{11}$ cm^{-2}, J. Phys.: Condens. Matter 20 (2008) 472207.

[20] R. Winkler, Spin–Orbit Coupling Effects in Two-Dimensional Electron and Hole Systems, Springer, Berlin, Heidelberg, 2003.

[21] A. Gold, Electronic transport properties of a two-dimensional electron gas in a silicon quantum-well structure at low temperature, Phys. Rev. B 35 (1987) 723.

[22] Y. Fedoryshyn, M. Beck, P. Kaspar, Characterization of Si volume- and delta-doped InGaAs grown by molecular beam epitaxy, J. Appl. Phys. 107 (2010) 093710.

[23] W.Y. Mak, K. DasGupta, H.E. Beere, I. Farrer, F. Sfigakis, D.A. Ritchie, Distinguishing impurity concentrations in GaAs and AlGaAs using very shallow undoped heterostructures, Appl. Phys. Lett. 97 (2010) 242107.

[24] A. Richter, M. Koch, T. Matsuyama, C. Heyn, U. Merkt, Transport properties of modulation-doped InAs-inserted-channel In$_{0.75}$Al$_{0.25}$As/In$_{0.75}$Ga$_{0.25}$As structures grown on GaAs substrates, Appl. Phys. Lett. 77 (20) (2000) 3227.

CRYSTAL GROWTH

CrossMark
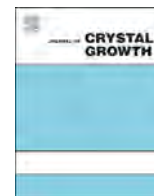
Low temperature transport property of the InSb and InAsSb quantum wells with $Al_{0.1}In_{0.9}Sb$ barrier layers grown by MBE

I. Shibasaki [a,b,*], S. Ishida [c], H. Geka [d], T. Manago [e]

[a] The Noguchi Institute, 1-8-1 Kaga, Itabashi, Tokyo 173-0003, Japan
[b] Toyohashi University of Technology, 1-1, Hibarigaoka, Tempaku, Toyohashi 441-8580, Japan
[c] Tokyo University of Science, Yamaguchi, Sanyo-Onoda, Yamaguchi 756-0884, Japan
[d] Asahi Kasei Corporation, Samejima 2-1, Fuji, Shizuoka 416-8501, Japan
[e] Fukuoka University, 8-19-1 Nanakuma, Jonan, Fukuoka 814-0180, Japan

ARTICLE INFO

ABSTRACT

We investigated difference in the transport properties between $Al_{0.1}In_{0.9}Sb/InSb$ and $Al_{0.1}In_{0.9}Sb/InAs_{0.1}Sb_{0.9}$ quantum wells (QWs). The resistivity of InSb QWs increases exponentially with decreasing temperature, while that of $InAs_{0.1}Sb_{0.9}$ QWs is much lower than that of InSb QWs, showing low resistivity even at low temperature. Energy band diagram calculations of $InAs_xSb_{1-x}/Al_{0.1}In_{0.9}Sb$ quantum wells (QWs) revealed that the bottom of the conduction band of the $InAs_xSb_{1-x}$ well moves downward with increasing As content x. The bottom of the InSb QWs lies above the Fermi level (E_F), resulting in depletion of the QW, while that in $InAs_{0.1}Sb_{0.9}$ QWs lies under E_F at low temperature. These calculation results support the experimental difference of the resistivity and sheet carrier density between two types of the QWs well.

© 2015 Elsevier B.V. All rights reserved.

1. Introduction

Two-dimensional electron systems (2DES) using narrow-gap semiconductors are important for high-speed devices, infrared detectors, highly sensitive magnetic sensors and spintronic applications because of high electron mobility and large effective g-factor. Among the binary narrow-gap III–V semiconductors, InSb has the smallest band gap and the highest intrinsic mobility. When Sb atoms are partially substituted by As atoms in InSb, $InAs_xSb_{1-x}$ with $x < 0.7$ has a smaller band gap than InSb [1]. Hence, the $InAs_xSb_{1-x}$ has a possibility of overcoming a limit of III–V device performance in terms of high speed and quantum effects because of small effective mass. However, the lattice mismatch between InSb and GaAs which is the widely used substrate for epitaxial growth of InSb and InAs is very large ($\sim 14\%$). The defects at the interface due to the lattice mismatch are known to cause the decrease of mobility [2,3]. In order to reduce or eliminate the lattice mismatch, we used the QW structure with a thick buffer layer and a cap layer of $Al_{0.1}In_{0.9}Sb$, which has a lattice constant close to InSb and also with insulating property. The lattice mismatch between $Al_{0.1}In_{0.9}Sb$ and InSb is only about 0.5% [4], and that between $Al_{0.1}In_{0.9}Sb$ and $InAs_{0.1}Sb_{0.9}$ is achieved to 0% [5]. Therefore, we grew InSb quantum wells (QWs) of $Al_{0.1}In_{0.9}Sb/InSb/Al_{0.1}In_{0.9}Sb/GaAs$ substrate and $InAs_{0.1}Sb_{0.9}$ Qws of $Al_{0.1}In_{0.9}Sb/$

$InAs_{0.1}Sb_{0.9}/Al_{0.1}In_{0.9}Sb/GaAs$ substrate by using MBE, and their transport properties under magnetic field and Hall sensor applications were studied [4–12]. These QWs show the marked improvement of transport properties compared with InSb thin films directly grown on GaAs. On the other hand, we found a large difference in the transport properties between the InSb and $InAs_{0.1}Sb_{0.9}$ QWs at very low temperature. The sheet resistivity of InSb QWs is much larger than that of $InAs_{0.1}Sb_{0.9}$ QWs, although the compositional difference of these QWs is only 10% As substitution of Sb.

In this paper, we studied systematically the well-width dependence of carrier density of InSb and $InAs_{0.1}Sb_{0.9}$ QWs sandwiched by $Al_{0.1}In_{0.9}Sb$ insulating layers grown on GaAs substrates by MBE. Especially, the difference of transport properties of both QWs is discussed in conjunction with their band diagrams. The band-diagrams of these quantum wells were calculated. It was revealed that the difference of low temperature transport properties must be caused by the corresponding difference of band-diagram of these QWs due to their composition.

2. Experimental procedures

The samples were grown by using MBE (V100 production scale MBE system by VG Semicon). The sample structure is GaAs cap (6.5 nm)/$Al_{0.1}In_{0.9}Sb$ cap (50 nm)/InSb or $InAs_{0.1}Sb_{0.9}$ active layer (L_W)/$Al_{0.1}In_{0.9}Sb$ buffer (700 nm)/GaAs (100) substrate, which is shown in Fig. 1. The layer structure is the same except the active

* Corresponding author at: The Noguchi Institute, 1-8-1 Kaga, Itabashi, Tokyo 173-0003, Japan.
E-mail address: shibasakii@goo.jp (I. Shibasaki).

layer for both QW samples and barrier layer and cap layer are fixed. The substrate is a semi-insulating GaAs and all layers are undoped. The well width (L_W) of the active layer is 15–100 nm. The lattice mismatch at the hetero-interface between the barrier and active layers is 0.5% for InSb QW and 0% for $InAs_{0.1}Sb_{0.9}$ QW. The quantum well was achieved by optimizing the As_4/Sb_4 flux ratio under the MBE growth. Hall effect was measured at room temperature (RT), 77, and 4.2 K to estimate the carrier density. In order to eliminate the persistent-photoconductive effect on a sample, it was shielded from irradiation and kept in the dark at room temperature (RT) at least overnight, after setting it on the sample holder.

The band diagrams were calculated using a one-dimensional Poisson–Schrödinger solver, called "nextnano" [13]. We assumed in calculation that the surface state was pinned in middle of the gap of the GaAs cap layer and GaAs substrate because of the Fermi level pinning effect, and it did not take into account the strain of the lattice. The GaAs substrate was undoped and the thickness was set to 0.3 mm.

3. Results and discussions

The effect of lattice mismatch reduction is shown in Fig. 2, where the electron mobility of the InSb QWs and InAsSb QWs at 77 K is plotted with respect to well width. The mobility of the InAsSb QWs is much improved, compared with the InSb QWs. Thus, the effect of lattice mismatch reduction is very large.

Fig. 3 shows the typical temperature dependence of sheet resistivity of InSb and $InAs_{0.1}Sb_{0.9}$ QWs with a 70-nm-thick active layer. The resistivity of InSb QWs increases remarkably with lowering temperature, while that of $InAs_{0.1}Sb_{0.9}$ QWs shows a small increase below RT, but does not rise very much even at low temperature. Additionally the resistivity of $InAs_{0.1}Sb_{0.9}$ QWs is much smaller than that of InSb QWs for whole temperature range. Thus, sheet resistivity of the two types of QWs is quite different in spite of the little difference in As contents only by 0.1. Moreover, it cannot be

explained by the difference of the electron mobility at very low temperature.

The L_W dependence of the sheet carrier density is shown in Fig. 4. The sheet carrier density at RT reduces with decreasing thickness for both InSb and InAsSb QWs. However, it is clearly seen that the sheet carrier density of the InSb QWs is smaller than that of the $InAs_{0.1}Sb_{0.9}$ QWs. On the other hand, at 77 K sheet carrier density of both QWs does not show thickness dependence. The value of carrier density of both QWs is almost comparable at 77 K. For InSb QWs, it is expected that there are almost no intrinsic electrons in conduction band, and electrons in conduction band must be of other origin which may come from the defects from hetero-interface at InSb/AlInSb. At 4.2 K, we cannot measure the sheet carrier density of the InSb QWs because of the hopping transport. On the other hand, surprisingly, the sheet carrier density of the InAsSb QWs at 4.2 K is almost same as that of 77 K. This difference in sheet carrier density at 4.2 K is important and the problem is to be understood.

Fig. 3. Temperature dependence of sheet resistivity of InSb and $InAs_{0.1}Sb_{0.9}$ QWs with a well width of 70 nm.

Fig. 1. Sample structure of InSb and $InAs_xSb_{1-x}$ quantum wells.
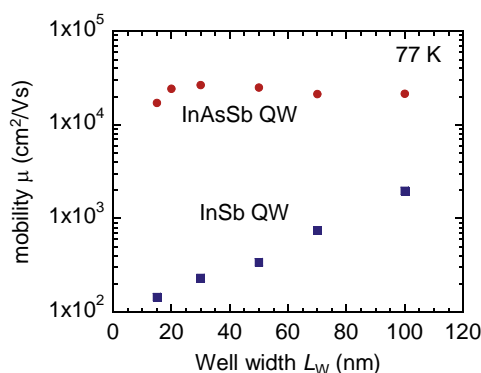
Fig. 2. Electron mobility of InSb QW and InAsSb QW at 77 K.
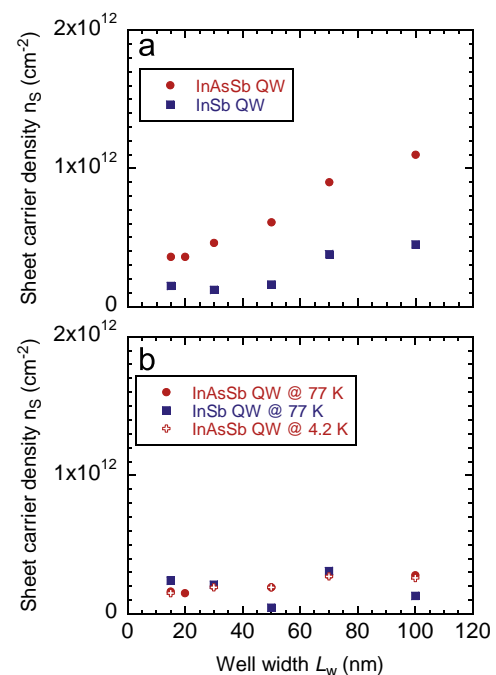
Fig. 4. Well width dependence of the sheet carrier density of InSb and $InAs_{0.1}Sb_{0.9}$ QWs (a) at RT and (b) at low temperature.

In order to investigate this carrier density difference, we intended to calculate the band diagrams of these QWs concerned with As composition. Fig. 5 shows the energy band diagrams for InSb and InAsSb QWs with respect to As content x; $x=0$ (InSb QW), 0.1 (our InAs$_{0.1}$Sb$_{0.9}$ QW), and 0.3. The barrier layer was Al$_{0.1}$In$_{0.9}$Sb, the L_W of the active layer was 50 nm, and the calculated temperature was 4 K. The results clearly showed that InSb QW ($x=0$) shows a type I QW structure, and the bottom of the conduction band of InSb QWs is above the Fermi level (E_F). When intrinsic electrons are not excited at low temperature, the well will be depleted. For InAs$_{0.1}$Sb$_{0.9}$ QW ($x=0.1$), the band diagram changes from type I to type II because of increasing band offset between the active layer and barrier layer, and the bottom of conduction band of the QW becomes under E_F. Therefore, the InAs$_{0.1}$Sb$_{0.9}$ QWs are not depleted even at very low temperature. These results support the experimental results that the carriers of the InAsSb QWs still remain at low temperature, and the sheet carrier density at 4.2 K is almost the same as that at 77 K. Thus, it clearly explains the difference of the resistivity and carrier density between InSb and InAsSb QWs. Therefore, we concluded that the carrier density difference comes from the difference in the band diagram between the two kinds of QWs. These facts suggest us a control method of the carrier density of the GaAs/InAs$_x$Sb$_{1-x}$/Al$_{0.1}$In$_{0.9}$Sb/GaAs (substrate) QW by varying the As content x, which is different from doping method. Additionally, the calculation of band diagram showed that the QW changes into the type III structure when $x=0.3$. Thus, the calculation of the band diagrams of the GaAs/Al$_{0.1}$In$_{0.9}$Sb/InAs$_x$Sb$_{1-x}$/Al$_{0.1}$In$_{0.9}$Sb/GaAs (substrate) QWs showed the transfer from type I to type III via type II with increasing As content x. The bottom of the conduction band of the QW becomes lower with increasing x (addition of As to the QW layer), and finally, it lies under Fermi level E_F.

The temperature dependences of the calculated energy band diagrams for the InSb and InAs$_{0.1}$Sb$_{0.9}$ QWs with thickness of 70 nm are shown in Fig. 6. For InSb, the band gap increases with decreasing temperature, and then the bottom of the InSb well gradually rises, but not so much. As a result, for InSb QW, bottom of the conduction band is far from the Fermi level E_F at very low
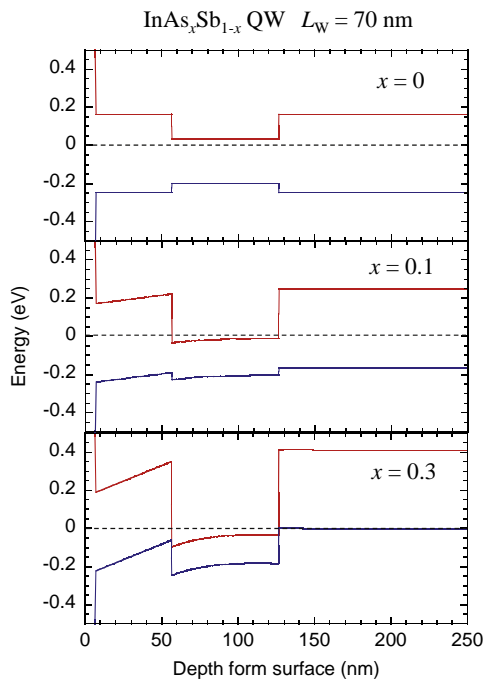
Fig. 6. Temperature dependence of the calculated energy band diagrams for the (a) InSb QW and (b) InAs$_{0.1}$Sb$_{0.9}$ QW. The well width is 70 nm.

temperature, since intrinsic electrons are not excited and then the well becomes depleted. This means that the resistivity of InSb QW at very low temperature will be extremely a high value or diverges, which corresponds to experimental result shown in Fig. 3. In contrast, the bottom of the conduction band of the InAs$_{0.1}$Sb$_{0.9}$ QWs is under E_F at all temperatures, which means that the InAs$_{0.1}$Sb$_{0.9}$ QW is not depleted and sufficient conduction electrons exist even at very low temperature. Therefore the sheet resistivity of the InAs$_{0.1}$Sb$_{0.9}$ QWs remains small at very low temperature, which is different from that of the InSb QWs. These results are consistent with the experimental results.

4. Conclusion

In summary, transport properties of InSb and InAs$_{0.1}$Sb$_{0.9}$ QWs were investigated covering a wide range of well width and the band diagram of the GaAs (cap layer)/Al$_{0.1}$In$_{0.9}$Sb/InAs$_x$Sb$_{1-x}$/Al$_{0.1}$In$_{0.9}$Sb/GaAs (substrate) QW with $x=0$–0.3 was calculated. The band diagram calculation revealed the origin of the small sheet carrier density and high resistivity of the InSb QWs. We found that the bottom of the conduction band of the InSb QWs is above the Fermi level, so that the well is depleted at low temperature. On the other hand, the bottom of the conduction band of the InAs$_{0.1}$Sb$_{0.9}$ QWs is under the Fermi level, and these QWs show low resistivity even at low temperature. The results of this study will be useful for designing InAsSb-based QW devices and applications.

Fig. 5. Energy band diagrams for InSb and InAsSb QWs with respect to As content x; $x=0$ (InSb QW), 0.1 (our InAs$_{0.1}$Sb$_{0.9}$ QW), and 0.3. The well width is 70 nm. The calculated temperature was 4 K.

References

[1] S. Adachi, Properties of Semiconductor Alloys; Group–IV, III–V and II–VI Semiconductors, John Wiley & Sons Ltd., UK (2009) 182.
[2] A. Okamoto, I. Shibasaki, J. Cryst. Growth 251 (2003) 560.

[3] A. Okamoto, H. Geka, I. Shibasaki, K. Yoshida, J. Cryst. Growth 278 (2005) 604.

[4] H. Geka, A. Okamoto, S. Yamada, H. Goto, K. Yoshida, I. Shibasaki, J. Cryst. Growth 301–302 (2007) 152.

[5] I. Shibasaki, H. Geka, A. Okamoto, in: B.N. Murdin, S.K. Clowes (Eds.), Narrow Gap Semiconductors, Springer Proceedings in Physics, vol. 199, 2007, p. 89.

[6] S. Ishida, T. Manago, K. Oto, A. Fijimoto, H. Geka, A. Okamoto, I. Shibasaki, in: B. N. Murdin, S.K. Clowes (Eds.), Narrow Gap Semiconductors, Springer Proceedings in Physics, vol. 199, 2007, p. 203.

[7] T. Manago, N. Nisizako, S. Ishida, H. Geka, I. Shibasaki, J. Cryst. Growth 311 (2009) 1711.

[8] N. Nishizako, T. Manago, S. Ishida, H. Geka, I. Shibasaki, J. Cryst. Growth 311 (2009) 2128.

[9] N. Nishizako, T. Manago, S. Ishida, H. Geka, I. Shibasaki, Physica E 42 (2010) 975.

[10] S. Ishida, T. Manago, N. Nishizako, H. Geka, I. Shibasaki, Physica E 42 (2010) 984.

[11] T. Manago, N. Nishizako, S. Ishida, H. Geka, I. Shibasaki, K. Makise, K. Mitsuishi, Phys. Procedia 3 (2010) 1219.

[12] S. Ishida, T. Manago, N. Nishizako, H. Geka, I. Shibasaki, Phys. Procedia 3 (2010) 1213.

[13] Software for the simulation of electronic and optoelectronic semiconductor nanodevices and materials, ⟨http://www.nextnano.de/⟩.
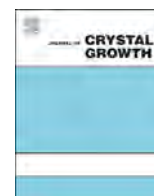
InAs nanowires with $Al_xGa_{1-x}Sb$ shells for band alignment engineering

Torsten Rieger *, Detlev Grützmacher, Mihail Ion Lepsa

Peter Grünberg Institute and JARA-FIT, Forschungszentrum Jülich GmbH, 52425 Jülich, Germany

ABSTRACT

InAs nanowires surrounded by $Al_xGa_{1-x}Sb$ shells exhibit a change in the band alignment from a broken gap for pure GaSb shells to a staggered type II alignment for AlSb. These different band alignments make InAs/$Al_xGa_{1-x}Sb$ core–shell nanowires ideal candidates for several applications such as TFETs and passivated InAs nanowires. With increasing the Al content in the shell, the axial growth is simultaneously enhanced changing the morphological characteristics of the top region. Nonetheless, for Al contents ranging from 0 to 100 % conformal overgrowth of the InAs nanowires was observed. AlGaSb shells were found to have a uniform composition along the nanowire axis. High Al content shells require an additional passivation with GaSb to prevent complete oxidation of the AlSb. Irrespective of the lattice mismatch being 1.2% between InAs and AlSb, the shell growth was found to be coherent.

© 2015 Elsevier B.V. All rights reserved.

1. Introduction

The combination of different semiconductor materials into low-dimensional heterostructures offers new possibilities ranging from fundamental physics [1] to devices being suitable for "More than Moore". For the latter, especially tunnel field effect transistors (TFETs) are considered as ideal candidates since they allow a subthreshold slope of less than 60 mV/dec with a high on and low off current [2]. Here, TFETs make use of either a staggered or even a broken band alignment. III–V semiconductors belonging to the 6.1 Å family (InAs, GaSb and AlSb) cover the different types of band alignment [3] and are therefore suitable materials for TFETs. Additionally, the low lattice mismatch ($\leq 1.2\%$) results in low dislocation density or even coherent growth. Taking such devices into the nanowire (NW) geometry should even enhance the region of coherent growth due to improved strain accommodation [4]. Applying classical Matthews–Blakeslee theory [5] to InAs/GaSb and InAs/AlSb results in critical thicknesses of 20 nm and 10 nm, respectively.

While several NW-TFET devices based on the broken gap InAs/GaSb system have been demonstrated [6,7], staggered InAs/AlGaSb TFETs have been limited to planar structures [8,9]. However, Knoch and Appenzeller [10] showed that the staggered band alignment with an Al content of about 60% should result in the best performance. Considering InAs NWs embedded in high Al content shells, the large electron barrier of up to 1.35 eV can significantly enhance the electron mobility due to reduced surface scattering [3,11,12]. Therefore, this in-situ passivation of InAs NWs with an almost lattice matched shell is of particular interest for high-mobility devices.

In this context, we present the growth, morphological and structural analyses of InAs/$Al_xGa_{1-x}Sb$ core–shell NWs with Al contents varying from 0 to 100% using molecular beam epitaxy.

2. Experimental details

Si (111) substrates were cleaned in hydrofluoric acid to remove the native oxide and absorbents. A thin silicon oxide was subsequently prepared wet chemically by placing the samples for 60 s in hydrogen peroxide. Hereafter, they were loaded into the molecular beam epitaxy (MBE) system and degased at 200 °C and 400 °C in the load lock and buffer chamber, respectively. After introduction in the MBE chamber, additional outgasing at 600 °C takes place and subsequently, the temperature was lowered to the growth temperature of the InAs NWs being 490 °C. Vapor solid InAs NWs were grown with an In rate of 0.035 μm/h and an As_4 beam equivalent pressure of 10^{-5} mbar for 1 h [13]. Hereafter, the substrate temperature was decreased to 360 °C keeping the As shutter open. After reaching this temperature, the As shutter was closed and the Sb shutter was opened 2 min prior to the Ga and Al shutters. The Sb flux was set to 7×10^{-7} mbar and the total flux of the group III elements was kept constant at a planer growth rate of 0.1 μm/h. If not mentioned differently, the growth duration of the shell was 60 min resulting in shell thicknesses of $\sim$20–25 nm. These growth conditions have been previously determined to be optimal for GaSb shells covering InAs NWs [14]. Considering planar growth, the critical thickness according to Matthews–Blakeslee is 20 nm for GaSb and decreases to 10 nm for AlSb.

The grown samples have been analyzed by scanning and transmission electron microscopy (SEM and TEM). In the latter

* Corresponding author. Tel.: +49 2461 61 2732; fax: +49 2461 61 2333.
E-mail address: t.rieger@fz-juelich.de (T. Rieger).

one, also energy dispersive x-ray spectroscopy (EDX), selective area electron diffraction (SAED) and high angle annular dark field (HAADF) have been used. High resolution TEM (HRTEM) images were filtered by applying a mask to the fast Fourier transform (FFT) maintaining solely the {111} lattice planes.

3. Results and discussion

Fig. 1 shows overview SEM micrographs of InAs/Al$_x$Ga$_{1-x}$Sb core–shell NWs with x ranging from 0 to 1 in steps of 0.2. For all Al contents, the NWs have uniform dimensions, no clustering is observed. The only remarkable difference is found at the top of the NWs. For pure GaSb shells, a platform develops at the top, having a flat facet as well as a diameter expansion compared to the rest of the NW. The InAs NW itself does not have this flat facet but a rounded or tapered shape [14,15]. By increasing the Al content in the shell, the platform slowly vanishes and the flat top facet transforms into a rounded and faceted top similar to the pure InAs NW. The transition from a flat to a tapered shell occurs roughly in the region of 40–60% Al, however, it might also depend on the growth time of the shell. The flat top facet for GaSb shells can be attributed to a low growth rate of the {111}B facet compared to the {110} and {211} facets, the diameter expansion to radial growth occurring on zinc blende (ZB) GaSb inducing additional twins [14]. Contrary, when pure AlSb shells are grown, the growth rate of the {111}B facet is higher than that of the {110} and {211} facets. In this sense, using TEM micrographs the length of the axially grown GaSb was measured to be ∼ 0 nm while it increased to ∼50 nm, ∼80 nm and ∼95 nm for x=0.2, 0.6 and 1, respectively. Considering axial growth solely be caused by direct impingement, an axially AlGaSb segment of 100 nm would be expected. Thus, the presence of Al reduces the adatom mobility and therefore favors the axial growth of Al$_x$Ga$_{1-x}$Sb.

The successful and homogenous incorporation of Al into the shells was confirmed by EDX line scans, two exemplary scans are shown in Fig. 2 together with bright field TEM images. Fig. 2a and b is taken from a core–shell NW with a nominal content of 20% Al. As can be seen, the Al signal in the EDX line scan is very weak, but could be clearly identified in the spectra. The TEM image being acquired from the < 211 > zone axis shows very smooth surfaces and interfaces. No evidence of phase separation or an inhomogeneous alloy is found. The thickness of the native oxide of the Al$_{0.2}$Ga$_{0.8}$Sb shell is in the same range as that of pure GaSb shells, i.e., 3–4 nm. However, an increase of the Al content in the shell to 60% significantly increases the thickness of the native oxide being in the range of 8–10 nm (not shown). This is in fact a direct evidence for the incorporation of a higher amount of Al which has a stronger tendency for the formation of a native oxide layer. Consequently, an additional thin GaSb cap layer was grown around InAs/Al$_x$Ga$_{1-x}$Sb core–shell nanowires with Al contents above 20%. Fig. 2c and d depicts the TEM micrograph and corresponding EDX profile for an InAs/Al$_{0.6}$Ga$_{0.4}$Sb core–shell nanowire. As seen in the TEM image, the native oxide thickness is again in the order of ∼4 nm and a corresponding delayed onset of the Al signal in the EDX profile is found. The Al/Ga is significantly higher than in Fig. 2b, thus the amount of incorporated Al in the shell increased. This not only proves that the thin GaSb shell prevents oxidation of the underlying AlGaSb, it is also a first demonstration of a multiple core–shell system based on arsenides and antimonides.

However, although the incorporation of Al into the shell is proven, the actual composition of the AlGaSb shell might vary along the growth axis. This can be caused by a temperature gradient along the nanowire axis [16,17] or different adatom diffusion lengths for Ga and Al. Consequently, EDX spectra were acquired at different positions along the nanowire axis of a core–shell nanowire with an Al$_{0.6}$Ga$_{0.4}$Sb shell. In order to compensate for thickness variations and sample drift, the intensities of Ga and Al were normalized to that one of Sb. The TEM micrograph, HAADF image as well as the corresponding EDX profile displayed in Fig. 3 show a uniform shell thickness along the NW axis as well as a relatively uniform composition. Slight variations should rather be caused by the limited time used to acquire the spectra than by a temperature gradient or differences in the adatom mobilities.

When pure AlSb shells are grown, the necessity of a GaSb cap preventing oxidation becomes even more evident. A pure, nominally 20 nm thick AlSb shell oxidizes completely if not protected by a GaSb cap. This can be clearly seen in the HAADF image in Fig. 4a with its
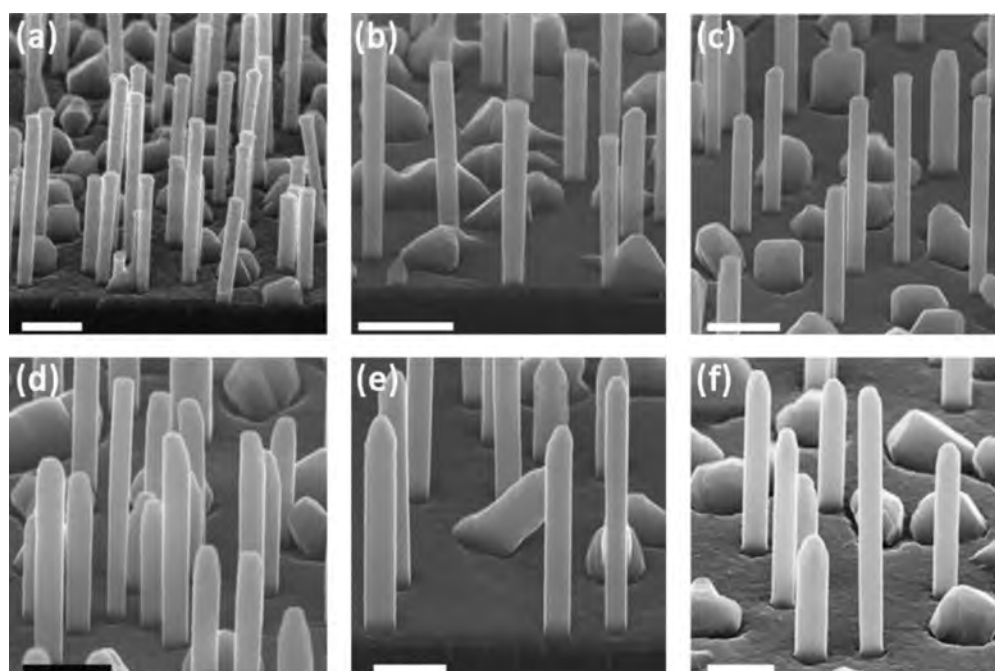
Fig. 1. SEM micrographs of InAs/Al$_x$Ga$_{1-x}$Sb core–shell NWs with Al contents of 0, 0.2, 0.4, 0.6, 0.8 and 1 in (a), (b), (c), (d), (e) and (f), respectively. All scale bars are 500 nm.
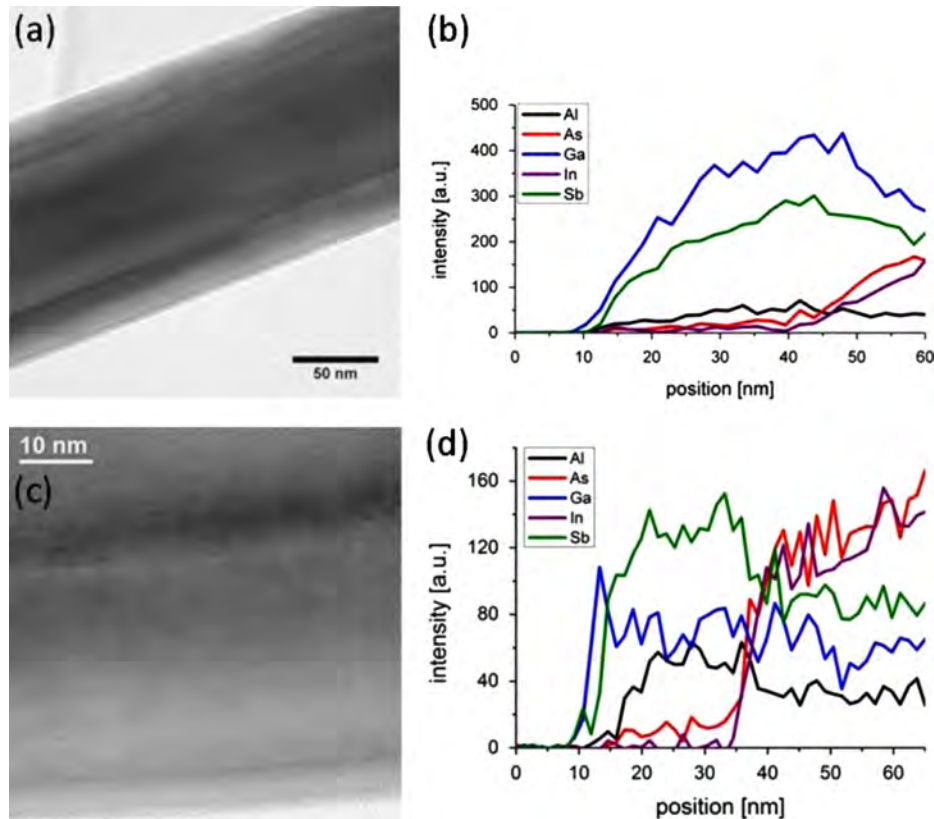
Fig. 2. TEM micrographs acquired from the $<211>$ zone axis of (a) InAs/Al$_{0.2}$Ga$_{0.8}$Sb and (c) InAs/Al$_{0.6}$Ga$_{0.4}$Sb core–shell NWs. EDX profiles shown in (b) and (d) demonstrate the incorporation of Al into the shell as well as a GaSb cap layer on the InAs/Al$_{0.6}$Ga$_{0.4}$Sb core–shell NW.

superimposed EDX profile. As obvious, a strong signal corresponding to oxygen is detected. The shell is entirely amorphous while the InAs core is still crystalline (see Fig. 4b). Due to the addition of oxygen, the thickness of the shell increases significantly to around ~ 40 nm. However, no peel-off of the shell is observed which makes it possible to use the oxidized shell as a passivation or gate dielectric. By adding an additional GaSb shell around the AlSb shell, the oxidation can be circumvented. This can already be seen by the EDX profile shown in Fig. 4c, being superimposed over a HAADF image. At the NW edges, intensity peaks belonging to Ga and Oxygen can be seen, both having similar extents. Hereafter, the Oxygen signal in the EDX spectra sinks drastically, indicating only a thin oxide. The thickness of the GaSb cap can be approximated both from the EDX profile as well as the HAADF image (bright edges) to about 4–5 nm, being in agreement with a growth time of 15 min and a planar growth rate of 100 nm/h, considering also the NW and MBE geometry. The absence of an oxidized AlSb shell is further evidenced by the TEM image depicted in Fig. 4d. Clearly, the crystalline structure of the NW with stacking faults and twins continues from the core to the NW edge, with a thin native oxide layer only. The contrast allows estimating the AlSb shell thickness to be in the range of 25–30 nm, i.e., more than twice as high as the critical thickness in planar systems. Due to the high density of stacking faults and twins being present in vapor solid grown InAs NWs, the analyses of misfit dislocations becomes difficult when NWs are evaluated from the $<110>$ zone axis. By tilting the NWs into the $<211>$ zone axis, contrast arising from stacking faults and twins disappears. Nonetheless, misfit dislocation, i.e. extra or missing planes in the $<111>$ direction, will still be visible [14]. Consequently, Fig. 4e and f depicts HRTEM images from the $<211>$ zone axis. The AlSb shell thicknesses are about 10 and ~ 25 nm, respectively, thus just the critical thickness and above. For the 10 nm thick shell (Fig. 4e) the contrast arising from the core and shell can clearly be seen, the interface is smooth. A native oxide of about 4–5 nm is detected, which
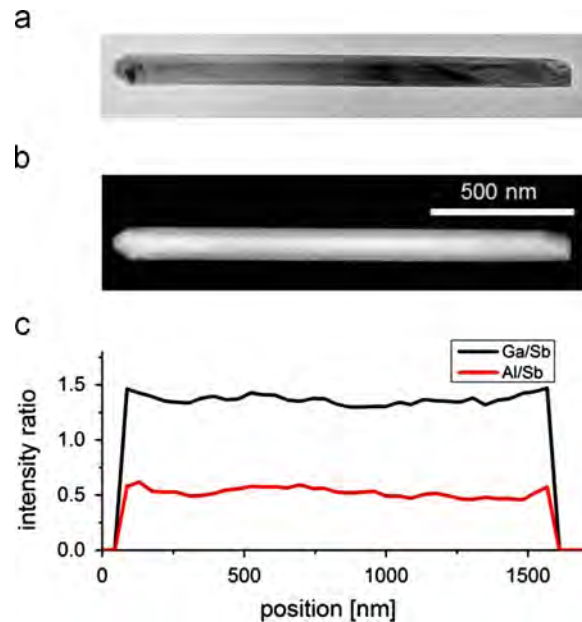
Fig. 3. (a) TEM image and (b) HAADF image of an InAs/Al$_{0.6}$Ga$_{0.4}$Sb core–shell NW, (c) EDX profile taken along the NW axis with Ga and Al normalized to the Sb intensity. The EDX profile demonstrates a uniform shell composition along the NW, the homogenous shell thickness can be seen in the HAADF image.

is limited to the additional GaSb shell. As expected due to the low lattice mismatch as well as small shell thickness, no misfit dislocations are detected. However, even by increasing the shell thickness to ~ 25 nm, a thorough analysis of TEM images did not reveal any misfit dislocations. Exemplarily, a HRTEM image is shown in Fig. 4f, the interface from InAs to AlSb is marked by the white line. Also after long
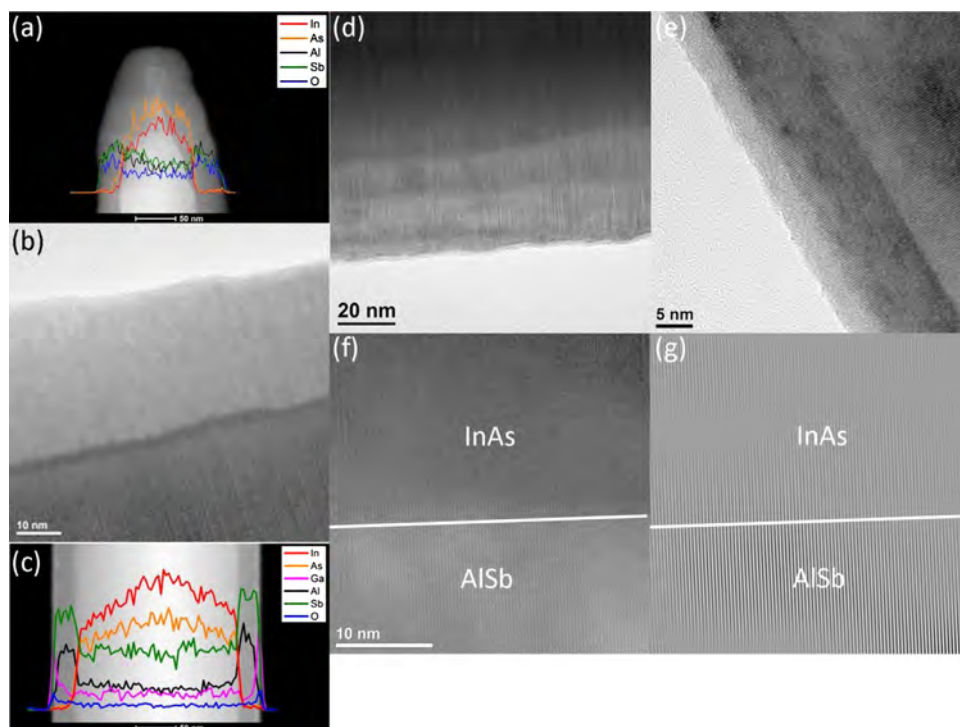
Fig. 4. InAs/AlSb core–shell nanowires. (a) HAADF image with superimposed EDX profile demonstrating complete oxidation of the shell when not covered by a GaSb cap layer. (b) Bright field image of the same NW showing the amorphous, 30–40 nm thick shell. (c) HAADF image with superimposed EDX line scan of an InAs/AlSb/GaSb core–shell NW. The thin GaSb cap prevents the underlying AlSb from oxidation. As seen, by the EDX profile, the oxidation is limited to the GaSb shell. (d) Bright field TEM image from the $<110>$ zone axis of an InAs/AlSb core–shell NW with 20–25 nm thick shell. (e) HRTEM micrograph from the $<211>$ zone axis of a ~10 nm thick shell. (f) HRTEM image from the $<211>$ zone axis revealing the interface for a 20–25 nm thick shell and its FFT-filtered image in (g). White lines in (f) and (g) indicate the InAs-AlSb interface.

shell growth times, the interface appears to be smooth, indicating only a low temperature induced intermixing. In order to examine the presence of misfit dislocations, HRTEM images were filtered using only the {111} reflections in the FFTs. The FFT-filtered image of Fig. 4f showing only the {111} planes is displayed in Fig. 4g. By following each of the {111} planes from the InAs core into the AlSb shell and searching for terminating planes, possible misfit dislocations can be identified. Similar as in the image in Fig. 4e, no terminating planes and therefore no misfit dislocations were found. Thus, coherent growth in a core–shell NW system is achieved significantly exceeding the critical thickness of planar structures. Similar as for InAs/GaSb core–shell NWs [14], the critical thickness in NWs is at least twice as high as for planar systems. Here it should be mentioned that this is even the case for relatively thick NWs such as that one shown in Fig. 4c. There, the InAs core has a diameter of about 175–200 nm. This further demonstrates the excellent suitability of core–shell NWs of various dimensions for the dislocation-free integration of lattice mismatched material systems.

Although the second GaSb shell was used as a protection layer for the AlSb only, a thicker GaSb shell might also provide a radial hole gas, confined by the type I band alignment between GaSb and AlSb.

4. Conclusions

InAs/Al$_x$Ga$_{1-x}$Sb core–shell NWs with an Al content dependent staggered or broken gap band alignment were successfully grown by self-assisted MBE. The presented NW structures are potential candidates for future TFETs and the in-situ passivation of InAs NWs. For high Al content shells, an additional thin GaSb cap was found to be crucial in order to prevent a strong oxidation of the Al$_x$Ga$_{1-x}$Sb shell. A 4 nm thick GaSb shell limits the oxidation to the GaSb, keeping the AlSb shell non-oxidized. Despite of the

maximal lattice mismatch of 1.2% between InAs and AlSb and shell thicknesses of more than 20 nm, misfit dislocations have not been detected making the 6.1 Å family ideal for NW devices.

References

[1] Ö. Gül, N. Demarina, C. Blömers, T. Rieger, H. Lüth, M.I. Lepsa, et al., Flux periodic magnetoconductance oscillations in GaAs/InAs core/shell nanowires, Phys. Rev. B 89 (2014) 045417.
[2] A.M. Ionescu, H. Riel, Tunnel field-effect transistors as energy-efficient electronic switches, Nature 479 (2011) 329–337.
[3] H. Kroemer, The family (InAs, GaSb, AlSb) and its heterostructures: a selective review, Phys. E Low-Dimens. Syst. Nanostruct. 20 (2004) 196–203.
[4] S. Raychaudhuri, E.T. Yu, Calculation of critical dimensions for wurtzite and cubic zinc blende coaxial nanowire heterostructures, J. Vac. Sci. Technol. B Microelectron. Nanom. Struct. 24 (2006) 2053.
[5] J.W. Matthews, A.E. Blakeslee, Defects in epitaxial multilayers, J. Cryst. Growth 27 (1974) 118–125.
[6] B.M. Borg, K.A. Dick, B. Ganjipour, M.-E. Pistol, L.-E. Wernersson, C. Thelander, InAs/GaSb heterostructure nanowires for tunnel field-effect transistors, Nano Lett. 10 (2010) 4080–4085.
[7] A.W. Dey, J. Svensson, M. Ek, E. Lind, C. Thelander, L.-E. Wernersson, Combining axial and radial nanowire heterostructures: radial Esaki diodes and tunnel field-effect transistors, Nano Lett. 13 (2013) 5919–5924.
[8] R. Li, Y. Lu, G. Zhou, Q. Liu, S.D. Chae, T. Vasen, et al., AlGaSb/InAs tunnel field-effect transistor with on-current of 78 µA/µm at 0.5 V, IEEE Electron Device Lett. 33 (2012) 363–365.
[9] R. Li, Y. Lu, S.D. Chae, G. Zhou, Q. Liu, C. Chen, et al., InAs/AlGaSb heterojunction tunnel field-effect transistor with tunnelling in-line with the gate field, Phys. Status Solidi 9 (2012) 389–392.
[10] J. Knoch, J. Appenzeller, Modeling of high-performance p-type III–V heterojunction tunnel FETs, IEEE Electron Device Lett. 31 (2010) 305–307.

[11] L. Desplanque, D. Vignaud, X. Wallart, High mobility metamorphic AlSb/InAs heterostructures grown on InP substrates, J. Cryst. Growth 301–302 (2007) 194–198.

[12] G. Tuttle, H. Kroemer, J.H. English, Electron concentrations and mobilities in AlSb/InAs/AlSb quantum wells, J. Appl. Phys. 65 (1989) 5239.

[13] T. Rieger, D. Grützmacher, M.I. Lepsa, Si substrate preparation for the VS and VLS growth of InAs nanowires, Phys. Status Solidi Rapid Res. Lett. 7 (2013) 840–844.

[14] T. Rieger, D. Grützmacher, M. I. Lepsa, M. I., Misfit dislocation free InAs/GaSb core–shell nanowires grown by molecular beam epitaxy Nanoscale 7, 2015, 356–364.

[15] S. Hertenberger, D. Rudolph, S. Bolte, M. Döblinger, M. Bichler, D. Spirkoska, et al., Absence of vapor–liquid–solid growth during molecular beam epitaxy of self-induced InAs nanowires on Si, Appl. Phys. Lett. 98 (2011) 123114.

[16] F. Glas, J.-C. Harmand, Calculation of the temperature profile in nanowhiskers growing on a hot substrate, Phys. Rev. B 73 (2006) 155320.

[17] P. Krogstrup, R. Popovitz-Biro, E. Johnson, M.H. Madsen, J. Nygård, H. Shtrikman, Structural phase control in self-catalyzed growth of GaAs nanowires on silicon (111), Nano Lett. 10 (2010) 4475–4482.
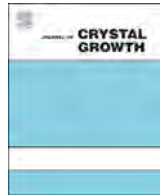
Si-doped AlGaAs/GaAs(6 3 1)A heterostructures grown by MBE as a function of the As-pressure

Víctor-Hugo Méndez-García [a,*], S. Shimomura [b], A.Yu. Gorbatchev [c], E. Cruz-Hernández [a], D. Vázquez-Cortés [b]

[a] Center for the Innovation and Application of Science and Technology, Universidad Autónoma de San Luis Potosí, Av. Sierra Leona # 550, Col. Lomas 2a Sección, C.P. 78210 San Luis Potosí, Mexico
[b] Graduate School of Science and Engineering, Ehime University, 3 Bukyo-cho, Matsuyama 790-8577, Ehime, Japan
[c] Instituto de Investigación en Comunicación Óptica, Universidad Autónoma de San Luis Potosí, Av. Karakorum # 1470, Col. Lomas 2a Secc., C.P. 78210 San Luis Potosí, Mexico

ARTICLE INFO

ABSTRACT

The effects of doping with silicon (Si) AlGaAs layers grown by molecular beam epitaxy on GaAs (6 3 1)-oriented substrates as a function of the arsenic pressure (P_{As}) is presented and compared with layers grown on (1 0 0) oriented substrates. The surface texture of the AlGaAs (6 3 1) films is composed by nanogrooves, whose dimensions depend on P_{As}. On the contrary, the MBE growth on the (1 0 0) plane resulted on rough surfaces, without evidence of formation of terraces. Mobility and carrier density of AlGaAs:Si layers grown on substrates (6 3 1) were studied as a function of P_{As}. The doping type conversion from p-type to n-type as a function of the As pressure is corroborated for high index samples. All the films grown on (1 0 0) exhibited silicon n-type doping. These observations were related with the amphotericity of Si, where it acts as a donor impurity occupying Al or Ga-sites or as an acceptor when it takes an As-site, depending on the competition that the Si atoms encounters with As for any of these sites. The acceptor and donor lines close to the AlGaAs transition observed by photoluminescence spectroscopy (PL) were affected by the incorporation of Si. When increasing P_{As} the energy of the main PL peak is redshifted for n-type AlGaAs layers, but it is shifted back towards high energy once the conduction type conversion takes place. X-ray diffraction patterns revealed high crystalline quality for samples grown at the highest P_{As}.

1. Introduction

Recently nanotechnology is generating new technological developments and it is envisaged as the most powerful and promising engine for the development of the society. In this emerging area, nanostructured materials are investigated for applications in electronics, optoelectronic and electro-mechanical devices. For example, semiconductor nanowires (NWRs) have emerged as one of the most versatile building blocks for integration of nanoscale devices with current technology. In addition, NWRs has been used for the investigation of basic aspects of one-dimensional systems (1D) [1–4]. In this direction, the growth of semiconductor materials on high-index substrates is a very important subject since it has been proved that, under suitable growth conditions, nanoscale step arrays and

nanogrooves can be self-assembled and later employed as templates for the synthesis of high quality semiconductor NWRs. Recently, highly ordered nanoscale step arrays were obtained in the homoepitaxial growth of GaAs on (6 3 1) oriented substrates [5], opening opportunities to the self-assembling of 1D arrays. Nevertheless, for the further application of these 1D systems, several challenges must be overcome. For example, the obtaining of n- and p-type doped AlGaAs layers is an essential step for the application of NWRs in optoelectronic devices. Si is known to be amphoteric dopant in III–V compounds [6,7]. For example in GaAs, Si behaves as donor or acceptor depending on the lattice site occupation: a Si atom occupying an As (Ga) site acts like an acceptor (donor). In the growth on high index substrates, the doping type strongly depends on both, growth conditions and on the particular substrate orientation [6–11].

In this work the Si doping of AlGaAs layers grown on (6 3 1)-oriented substrates as a function of the As$_4$-beam equivalent pressure (P_{As}) is studied. The electrical properties obtained by

* Corresponding author.
   E-mail address: victor.mendez@uaslp.mx (V.-H. Méndez-García).

Hall effect measurements indicated the doping type conversion, which occurs after experiencing high Si-doping compensation in the layers. The optical properties, studied by photoluminescence spectroscopy, are modified accordingly with the electrical characteristics. P_{As} also affected the crystalline quality of both (6 3 1) and (1 0 0) oriented samples as observed by X-ray diffraction experiments.

2. Experimental

The samples were grown in a VG molecular beam epitaxy (MBE) system on GaAs (6 3 1)A $\pm 0.1°$ semi-insulating commercially available substrates. Before being loaded into the MBE system, substrates were etched in a "Semico Clean" (Furuuchi Chemical Corp., Japan) solution over the course of one hour and then were loaded into the MBE preparation chamber and pre-degassed at 380 °C for 20 min. Once transferred to the growth chamber, the oxide desorption process was carried out at 640 °C for 15 min under As_4 flux. A 100 nm-thick GaAs layer was grown as a buffer layer (BL) at 660 °C and a growth rate of 0.3 μm/h. Once concluded the deposition of the GaAs layer, the substrate temperature was set at 700 °C in order to continue with the deposition of 1 μm-thick Si-doped AlGaAs layer, at the growth rate of 0.3 μm/h. The Si-effusion cell temperature was chosen such that the target Si concentration was 1×10^{18} cm^{-3} in (1 0 0) grown GaAs under normal growth conditions. Finally a 2.4 nm thick undoped GaAs layer was grown at 700 °C in order to avoid the oxidation of the samples. The Ga and Al-beam equivalent pressures were 2.7×10^{-7} and 1×10^{-7} mbar, respectively. Different samples were prepared with the As_4 overpressure (P_{As}), in the range of 0.5 to 4×10^{-5} mbar. The morphology of the nanostructure was studied by Atomic Force Microscopy (AFM) operated in contact mode. The Van der Pauw technique in Hall measurements at room temperature was employed in order to determine the doping type and mobility and the free carrier concentration of these samples. 12 K photoluminescence (PL) spectroscopy was employed with the 442 nm line of a He–Cd laser.

3. Results and discussion

Fig. 1a–d shows the AFM images of the AlGaAs films grown at 0.5 and 1.9 $\times 10^{-5}$ mbar. Wavy surfaces composed of nanochannels oriented along the [−1 1 3] direction can be observed when growing on the (6 3 1) orientation, Fig. 1a and b. On the contrary, the growth on the (1 0 0) substrate orientation resulted on rough but non-corrugated surfaces as observed in Fig. 1c and d. Some holes are perceived for the growth on (1 0 0) at the lowest P_{As} that might be related with the As desorption of the surface that frequently occurs at high temperature. At higher As pressures from 1×10^{-5} to 1.9×10^{-5} mbar the roughness is increased, and by increasing As pressure up to 4×10^{-5} the morphology of the AlGaAs(1 0 0) films improves significantly. The root mean square (rms) roughness from samples is plotted as a function of P_{As} in Fig. 2a. It is observed that samples grown on the (1 0 0) presented higher values of roughness, as compared to AlGaAs(6 3 1). Due to the differences of atomic configuration of singular and high index substrates, the surface free energy related to the atomic configuration and bonding structure, is expected to be different, and so are the optimal growth conditions that can conduce to flat surfaces. While for (1 0 0) the typical growth temperatures are around the 600 °C [12], for (6 3 1) 700 °C are more explored. The main reason for exploring such a high temperatures in the growth on the (6 3 1) plane is related to the searching for nanoscale corrugation or self-assembled surface faceting. The faceting is driven by the minimization of the surface energy. The increase in the length of the surface migration of adatoms by decreasing the As /Ga flow rate is frequently observed. In the case of high index substrates the spontaneous augmentation of the surface migration length of the adatoms along a preferential direction related to the anisotropic nature of the substrate promotes the formation of highly ordered arrays [13]. At $P_{As}=0.5 \times 10^{-5}$ mbar the formation of nanoscale corrugation seems to be initiated as observed in Fig. 1a, which presents tiny grooves, where the average step-height corrugation is equal to 2 nm, and the terrace width is close to 125 nm. At higher As pressure, $P_{As}=1.9 \times 10^{-5}$ mbar, the corrugation becomes clear, the height of nanochanels
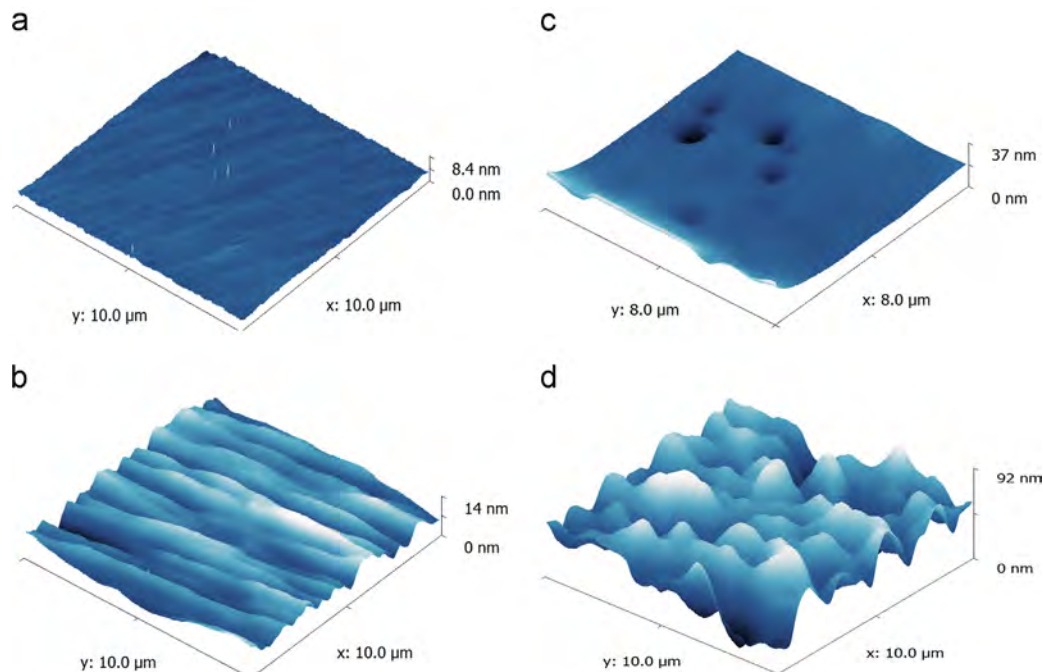
Fig. 1. AFM images of the AlGaAs layers grown on GaAs (6 3 1)A-orientes substrates at (a) $P_{As} \approx 0.5 \times 10^{-5}$ mbar and (b) $P_{As} \approx 1.9 \times 10^{-5}$ and grown on the GaAs(1 0 0) substrates at (c) $P_{As} \approx 0.5 \times 10^{-5}$ mbar and (d) $P_{As} \approx 1.9 \times 10^{-5}$ mbar.
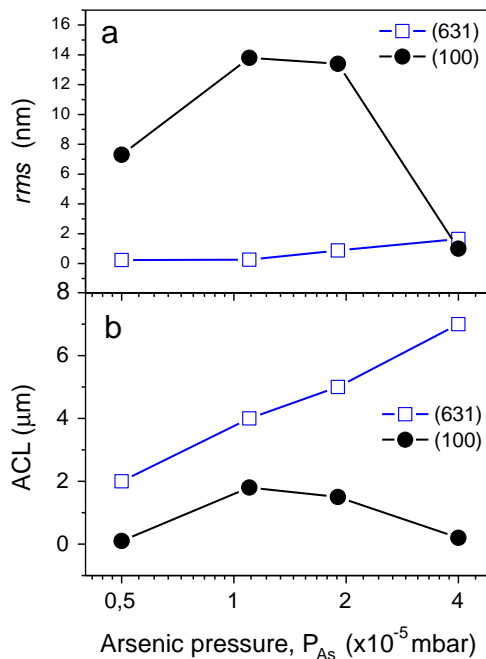
Fig. 2. (a) AlGaAs surface roughness as a function of P_{As} for samples grown on GaAs (6 3 1) and GaAs(1 0 0) substrates. (b) Autocorrelation length taken for the AlGaAs (6 3 1) samples along the corrugation, [-1 1 3], and for the AlGaAs(1 0 0) films along the [0 1 -1] direction.

increases up to 6.2 nm and the terrace width up to 500 nm, Fig. 1b. A quantitative measure of the corrugation uniformity is provided by the autocorrelation function analysis (ACF). In Fig. 2b the autocorrelation length, ξx, which provides a quantitative length parameter to distinguish between short- and long-range ordering in the surface morphology [14], is plotted as a function of P_{As}. The ξx of AlGaAs(1 0 0) films showed no clear dependence on the As pressure corroborating the isotropic nature of this plane. On the contrary, for the AlGaAs(6 3 1) layers, ξx measured along the [−1 1 3] direction increases with P_{As}, in other words, the nanoscale corrugation gets straighter along [−1 1 3] and the dispersion in the terrace width decreases. Similar dependence of surface corrugation on P_{As} in the range from 2.2×10^{-6} to 4.5×10^{-6} Torr has been observed for the homoepitaxial growth of GaAs(6 3 1) [15]. It is worth to comment that the terrace width for the nanoscale corrugation of GaAs was found to be 75 nm, for $P_{As} = 1.1 \times 10^{-5}$ mbar and in contrast, for AlGaAs layers grown at similar growth conditions the terrace width reaches the 500 nm; six times larger. This flattening effect is attributed to the presence of Al, whose alloys are frequently reported to smooth the growth front [16].

Fig. 3 summarizes the electrical characterization of the samples by room temperature Hall measurements. The free carriers concentration of the AlGaAs(1 0 0) films was nearly independent of P_{As}, close to 7×10^{16} cm^{-3}, and all the samples are n-type. Different behavior of both the free carriers density and type of doping was observed for AlGaAs(6 3 1) films. Between $P_{As} = 1.1 \times 10^{-5}$ and 1.9×10^{-5} mbar the doping type conversion from p- to n-type took place. The conversion of doping type implies highly compensated samples related to the amphoteric nature of Si on high index substrates, occupying both III- and V-sites in detriment of the electrical properties [7–9,17–19]. Note that the samples grown close to the P_{As} doping conversion exhibited low free carries concentration as well as very low carriers mobility. For GaAs the amphoteric behavior of Si has been related to the number of Si atoms Si_{III} (Si_V) substituting on the III (V) sublattice and the amount of V (III)
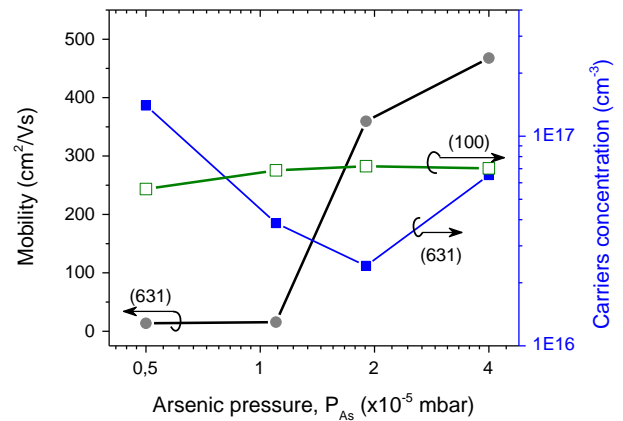
Fig. 3. Carrier concentration of the AlGaAs films grown as a function of P_{As} and on the substrates orientations (6 3 1) and (1 0 0). The carrier concentration of the films is almost constant for samples grown on (1 0 0). The carriermobility or the AlGaAs films, which is very low for the p-type samples, is also presented.

vacancies, X_V (X_{III}), on the growth surface, through the equation [20]

$$\ln \frac{[Si_{III}]}{[Si_V]} = \ln \frac{X_V}{X_{III}} + \frac{1.4 \times 10^3}{T_s} \qquad (1)$$

where T_s is the substrate temperature. It is clear that both, high substrate temperature and low V/III ratio enhance Si incorporation on As sites. Li et al. employed this equation in order to explain the amphoteric behavior of Si in of GaAs and AlGaAs films grown on GaAs (3 1 1) and in a wide variety of growth conditions. In our experiments the substrate temperature was kept at $T_s = 700$ °C while P_{As} was varied, and in complete agreement with Eq. (1) the for low V/III ratio, Si predominantly incorporates in As sites. On the other hand, depending on the substrate miss-orientation and face (A or B face, referred to Ga or As terminated surface, respectively), the dangling bond density and configuration changes, and with this, the probability of getting or not As/Ga vacancies. For example in the A face, it has been demonstrated that the boundary between n and p-type decreases as the substrate angle increases away from (1 1 1)A [6]. The (6 3 1)A surface is 65° off from the (1 1 1), so the boundary at low P_{As} of the n to p-type is expected, and indeed observed in Fig. 3.

Low-temperature PL measurements were carried out in order to investigate the effects on the optical properties of doping conversion. In Fig. 4 we show typical 12 K-PL spectra from AlGaAs layers grown on (6 3 1) oriented substrates at $P_{As} = 0.5 \times 10^{-5}$ and 4×10^{-5} mbar and on the (1 0 0) singular plane. The PL spectra of the AlGaAs/GaAs(1 0 0) layers exhibited four lines. The highest energy peak in Fig. 4a at 1.992 eV is attributed to the band to band recombination (BB). The peak at 1.902 eV is due to the donor-acceptor pair recombination (D,C), where the acceptor is carbon in As-site (C_{As}) and the donor is likely to be Si in the Al/Ga site. At 1.931 eV the donor to acceptor pair recombination (D,Si) involving the Si acceptor is found. A broad transition located around 1.875 eV could be tentatively attributed to the recombination of the V_{As}–Si_{Ga} complex [19]. The PL spectra of the samples AlGaAs(1 0 0) grown at higher P_{As} are very similar. An apparent redshift is observed but, as observed in Fig. 4(b) for $P_{As} = 4 \times 10^{-5}$, it is a consequence that the (D,Si) transition becomes more intense than (D,C) as we increase P_{As}. Since the carrier density of the AlGaAs(1 0 0) films did not vary significantly (Fig. 3), the PL changes are explained as a consequence of an improvement of the crystal quality. On the other hand, the main peak of the PL spectra of the AlGaAs(6 3 1) films showed redshift as the As pressure was increased. When increasing P_{As}, the energy of the PL-peak red-shifts in the p-type region, but it shifts back towards high energy once the doping type conversion takes place, which is in the n-type region. Similar shifts of the PL spectra have been reported to occur during the carriers compensation for the growth on (n 1 1)A substrates for $n = 1,2, 3$ [4,9,19,21]. In Fig. 4(c) it is observed that the 12 K-PL spectra from AlGaAs layers grown on (6 3 1) oriented
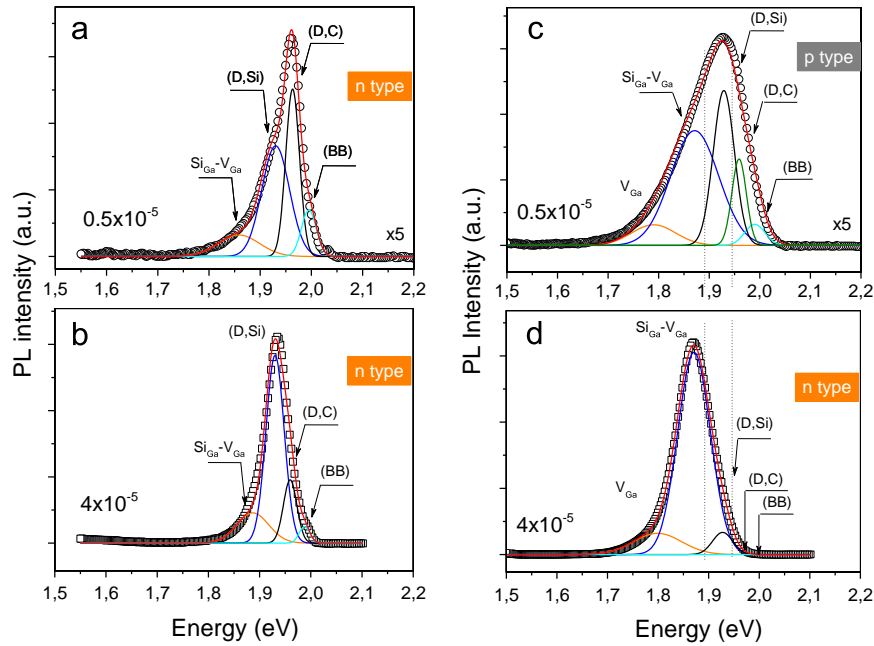
Fig. 4. 12 K PL spectra from the AlGaAs films grown on (a) and (b) GaAs(1 0 0) substrates and (c) and (d) GaAs(6 3 1). P_{As} is indicated in the graphs. The solid lines represents Gaussian fittings of the spectra.

substrates at $P_{As}=0.5 \times 10^{-5}$, p-type sample, can be fitted to the same four lines that presented the PL spectra of the AlGaAs(1 0 0) films, plus an additional broad line which is is associated to a Ga vacancy, V_{Ga}. The doping conversion usually broadens the lineshape and more PL transitions are involved, which explains the broad lineshape for $P_{As}=0.5 \times 10^{-5}$. The PL spectra of the AlGaAs film grown at $P_{As}=4 \times 10^{-5}$ mbar, n-type, is principally composed of transitions related to defect emissions. While for the p-type samples the peak close to 1.871 eV can be attributed to V_{As} related emissions [19], for n-type samples it is more likely to be attributed to Si_{Ga}–V_{Ga} aitisite related defects [22]. The presence of V_{Ga} transition, and the moderate slope of the n-type region of the carriers concentration in dependence of P_{As}, indicates that under these growth conditions, we are still close to the doping convertion range, and in order to get higher carrier concentration n- (p-) type samples we should further increase (decrease) the As beam equivalent pressure during the growth of the AlGaAs films on GaAs (6 3 1). All these observations resemble the doping of GaAs in high-index directions, where the amphoteric nature of Si is corroborated [4,7–9,17–19,21].

4. Conclusions

The doping type conversion of AlGaAs doped with Si was studied as a function of the As4-beam equivalent pressure. For (6 3 1) oriented samples at low P_{As} the Si is incorporated into As sites, acting as acceptor and producing p-type AlGaAs layers. For a further increase in P_{As} the Si is incorporated into Ga or Al sites, acting as donor and producing n-type AlGaAs layers. It is important to remark that the n-type (6 3 1) samples showed carriers concentration as high as that obtained for those samples grown on the (1 0 0) substrates, besides of sustaining nanoscale surface corrugation. Therefore, for the formation of optoelectronic devices the subsequent growth of a thin AlGaAs layer with lower Al content (i.e. lower bandgap) might conduce to the assembling of semiconductor quantum wires (QWRs), and the latter capping of the structure with a p-type AlGaAs layers can be easily achieved by decreasing P_{As}. Concerning to the optical properties, the redshift of the main peak of PL frequently observed for the growth on non-singular high-index substrates and high intensity Si_{Ga}–V_{Ga} antisite related defect emission was observed. It is important to comment that high resolution X-ray diffraction of the films (not shown here) exhibited higher crystal quality for those samples grown at high P_{As}.

References

[1] H. Sakaki, Jpn. J. Appl. Phys. 19 (1980) L735.
[2] T. Ogawa, T. Takagahara, Phys. Rev., B 43 (1991) 14325.
[3] E. Wigner, Phys. Rev. 46 (1934) 1002.
[4] S. Tomonaga, Prog. Theor. Phys. 5 (1950) 544.
[5] E. Cruz-Hernández, S. Shimomura, M. López-López, D. Vázquez-Cortes, V.H. Méndez-García, J. Cryst. Growth 316 (2011) 149.
[6] A. Miyagawa, T. Yamamoto, Y. Ohnishi, J.T. Nelson, T. Ohachi, J. Cryst. Growth 237–239 (2002) 1434.
[7] L. Pavesi, M. Henini, D. Johnston, Appl. Phys. Lett. 66 (1995) 21.
[8] N. Sakamoto, K. Hirakawa, T. Ikoma., Appl. Phys. Lett. 67 (1995) 1444.
[9] Y. Okano, M. Shigeta, H. Seto, H. Katahama, S. Nishine, I. Fujimoto, Jpn. J. Appl. Phys. 29 (1990) L1357.
[10] W.I. Wang, E.E. Mendez, T.S. Kuan, L. Esaki, Appl. Phys. Lett. 47 (1985) 826.
[11] J.M. Ballingal, C.E.C. Wood, Appl. Phys. Lett. 41 (1982) 947.
[12] G. Biasiol, F. Reinhardt, A. Gustafsson, E. Martinet, E. Kapon, Appl. Phys. Lett. 69 (1996) 2710.
[13] N.N. Ledentsov, D. Litvinov, A. Rosenauer, D. Gerthsen, I.P. Soshnikov, V.A. Shchukin, V.M. Ustinov, A. Yu., A.E. Egorov, Zukov, V.A. Volodin, Phys. Rev., B 51 (1995) 17767.
[14] H Assender, V Bliznyuk, K Porfyrakis, Science 297 (2002) 976.
[15] E. Cruz-Hernandez, S. Shimomura, V.H. Mendez-Garcia, Appl. Phys. Lett. 101 (2012) 073112.
[16] J. Saito, K. Kondo, J. Vac. Sci. Technol. B 8 (6) (1990) 1264.
[17] D Vazquez Cortés, E. Cruz-Hernandez, V.H. Méndez-García, S. Shimomura, M. Lopez-Lopez, J. Vac. Sci. Technol., B 30 (2012) 02B125.
[18] N Galbiati, E Grilli, M Guzzi, P Albertini, L Brusaferri, L Pavesi, M Henini, A. Gasparotto, Semicond. Sci. Technol. 12 (1997) 555.
[19] D. Johnston, L. Pavesi, M. Henini, Microelec. J. 26 (1995) 759.
[20] W.Q. Li, P.K. Bhattacharya, S.H. Kwok, R. Merlin, J. Appl. Phys. 72 (7) (1992) 3129.
[21] L. Pavesi, M. Henini, Appl. Phys. Lett. 68 (1996) 652.
[22] Chul Lee Young-Ki Ha, Hae Yong Jae-Eun Kim, S.B. Kim Park, H. Lim, Bong-Cheol Kim, Hee-Chul Lee, J. Kor. Phys. Soc. 36 (2000) 48.
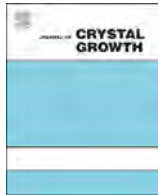
Effect of bismuth on structural and electrical properties of InAs films grown on GaAs substrates by MBE

H. Zhao [a,*], A. Malko [a], Z.H. Lai [b]

[a] Terahertz and Millimeter Wave Laboratory, Department of Microtechnology and Nanoscience, Chalmers University of Technology, Göteborg 41296, Sweden
[b] Nanofabrication Laboratory, Department of Microtechnology and Nanoscience, Chalmers University of Technology, Göteborg 41296, Sweden

ARTICLE INFO

ABSTRACT

InAs films were grown on GaAs substrates by molecular beam epitaxy (MBE) without or with different Bi fluxes. The effect of Bi on the structural and electrical properties of the InAs films was studied. Atomic Force Microscopy (AFM) measurement showed clear surface steps in all samples, indicating an over-flow growth mode. A more uniform distribution and narrower spacing of the surface steps were observed with increased Bi fluxes. Small area AFM scans showed reduced surface roughness with increased Bi fluxes. Whereas from large area scans, reduced surface roughness was only observed in samples grown under low Bi fluxes, and a deteriorated surface was obtained in the sample grown under the highest Bi flux. Bi was not compositionally incorporated to the InAs films confirmed by X-ray diffraction (XRD) and Second Ion Mass Spectroscopy (SIMS) measurements. The electron mobility of the InAs films, measured at room temperature, decreased monotonically with increased Bi fluxes. This is correlated to the Transmission Electron Microscopy (TEM) results in which increased threading dislocation (TD) densities were shown with increased Bi fluxes. Therefore, Bi-mediated growth deteriorates the electron mobility of the MBE-grown InAs films, whereas smoother surface can be obtained by applying low Bi fluxes. Possible mechanisms were proposed to explain these phenomena.

1. Introduction

The compound semiconductor InAs has a narrow band gap and a small effective electron mass, which makes it an important material in applications such as infrared detectors and high-speed electronics [1–3]. In some cases, the device performance requires insulating substrates. However, semi-insulating (SI) or high resistivity InAs or GaSb substrates are difficult to produce due to their narrow band gap nature. Hence, considerable effort has been devoted to grow InAs films on GaAs and other commonly used substrates [4–13]. But the large lattice mismatch between InAs and heterogeneous substrates leads to numerous dislocations, thus growth of high quality InAs films is challenging. Several methods were suggested to overcome these problems such as a two-step growth method and the use of a graded buffer layer [6–8]. Many studies using misoriented GaAs substrates were also carried out to evaluate the microstructure and development of defects in epitaxial InAs films [9,10]. On the other hand, surfactants such as Te [11,12] and Bi [13,14] were used to ameliorate the surface quality in such mismatched systems. It was demonstrated that two-dimensional (2D) growth mode can be obtained by adding Te before the InAs growth. Bi surfactant-mediated growth of InAs films was carried out using metalorganic

vapor phase epitaxy (MOVPE), in which Bi flux leaded to a reduction of full widths at half-maxima (FWHM) of the diffraction rocking curves, a reduction of growth rate, a degraded surface morphology and an enhancement of electron mobility [13,14]. However, there is few report on Bi surfactant-mediated growth of InAs films by molecular beam epitaxy (MBE).

In this paper, we study the effect of Bi on the structural and electrical properties of InAs films grown on GaAs substrates by MBE. InAs films were grown without or with different Bi fluxes. The structural and electrical properties of the InAs films were characterized using cross-section Transmission Electron Microscopy (TEM), high resolution X-ray diffraction (XRD), Second Ion Mass Spectroscopy (SIMS), Atomic Force Microscopy (AFM) and Hall Effect measurements. It was found Bi-mediated growth could reduce surface roughness of the InAs films in small scales. Whereas in large scales, reduced surface roughness were only observed in samples grown under low Bi fluxes, and a deteriorated surface was obtained in the sample grown under the highest Bi flux. The electron mobility of the InAs films decreased with increased Bi fluxes, which was explained by increased threading dislocation (TD) densities observed from the cross-section TEM measurements. All the samples have shown identical InAs film thickness, indicating Bi flux does not influence the growth rate. Possible mechanisms were proposed to explain these phenomena.

The paper is organized as follows. In the next section, the experiment details of epitaxial growth and characterization methods are described. Then the AFM, XRD, SIMS, Hall measurement, and TEM results are presented, and the effects of Bi on the structural and electrical properties of the InAs films are discussed. Finally, a short summary is given.

1.1. Experiment

All the samples in this study were grown by a Riber C21 MBE system. Four InAs films were grown on semi-insulating (100) GaAs without or with different Bi fluxes. The growth rate of InAs was 1 μm/h and all the samples were designed to be 1.5 μm thick. The growth temperature and V/III ratio were set to be 510 °C and 15, respectively.

Sample A was grown without Bi flux as a reference sample. Samples B–D were grown under different Bi fluxes. The Bi/As ratios in samples B, C, and D were approximately 0.0005, 0.001 and 0.01 respectively.

AFM was employed in a tapping mode to study the surface morphologies of the samples right after the growth. High resolution XRD was performed in a Phillips X'Pert double crystal analyzer and the ω-2θ rocking-curves on the (115) diffraction plane were scanned. SIMS measurements were carried out to verify whether Bi was incorporated. Electrical properties of the InAs films were investigated at room temperature with Hall Effect measurement using the Van der Pauw configuration. Cross-section of the materials were characterized using a TEM, Phillips CM200. The samples for the analysis were prepared using the focused ion beam (FIB) equipment, FEI Strata 235 Dual Beam.
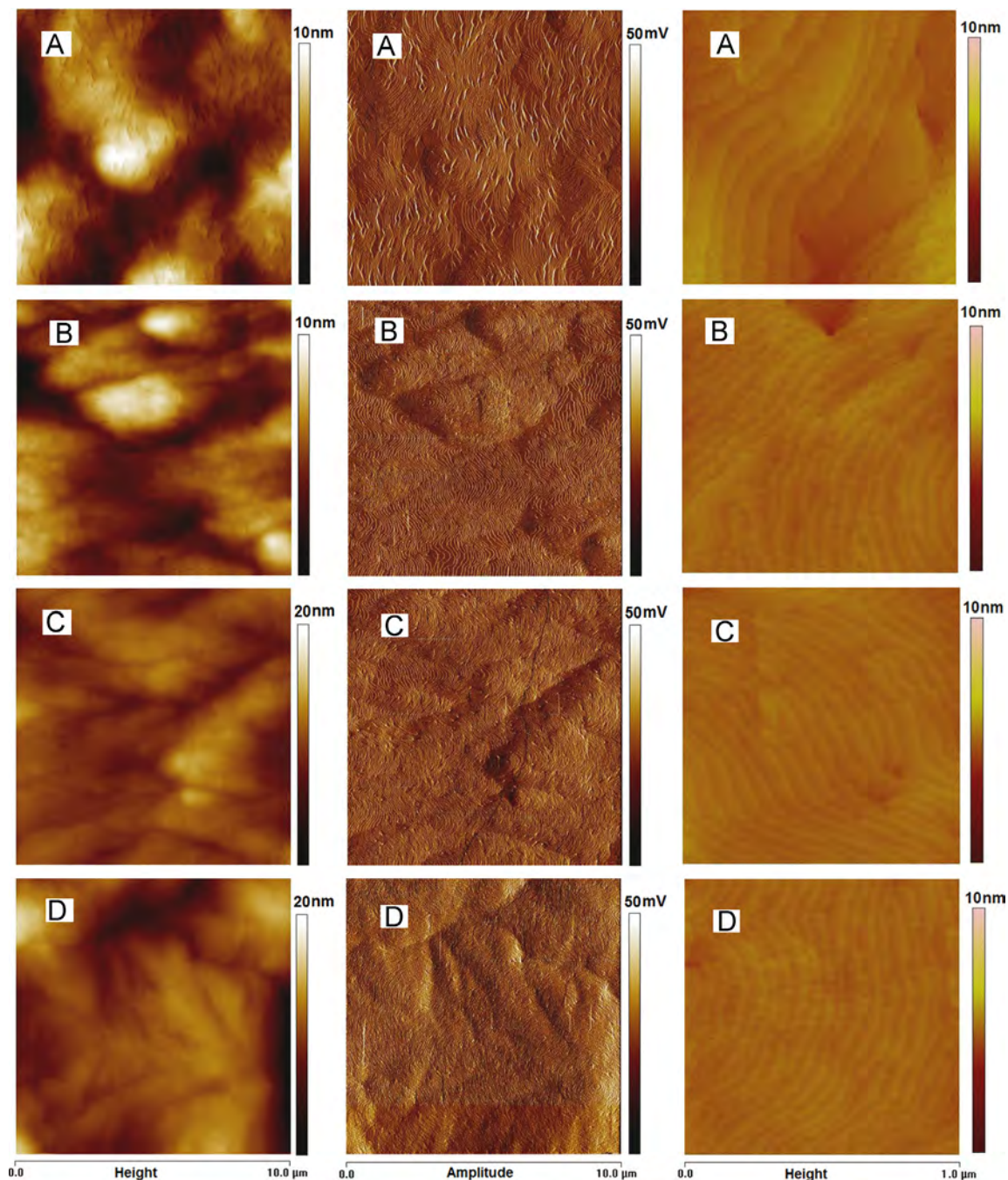
Fig. 1. From left to right: $10 \times 10 \ \mu m^2$ height, $10 \times 10 \ \mu m^2$ amplitude, and $1 \times 1 \ \mu m^2$ height AFM images of samples A–D.

2. Results and discussions

Fig. 1 shows both 10×10 μm^2 and 1×1 μm^2 AFM scans of the four samples. Both height and amplitude images are presented since the amplitude image provides kinds of error signals and highlights the changes in surface height, e.g. slopes and edges. The 1×1 μm^2 scan shows a closer look at the surfaces, but one should notice it could be not representative since the surface morphology are non-uniform in a large scale. The root mean square (RMS) roughness of samples A–D is 0.327 nm, 0.207 nm, 0.150 nm and 0.153 nm for a 1×1 μm^2 scan area, and 1.7 nm, 1.45 nm, 1.42 nm and 2.39 nm for a 10×10 μm^2 scan area, respectively. Therefore, the surfaces of the InAs films locally becomes smoother as the increased Bi fluxes, whereas seen from the large scale scans an increased surface roughness is obtained in sample D. As shown in the 10×10 μm^2 amplitude and the 1×1 μm^2 height images, surface steps are clearly observed in all the samples indicating an over-flow growth mode, and these steps become smaller and more uniform with increased Bi fluxes.

The smoother surfaces in samples B and C are likely attributed to the surfactant effect of Bi. Indeed Bi was not incorporated in all the samples which was confirmed by High resolution XRD and SIMS measurements. Fig. 2 shows (115) diffraction rocking curves for the four samples, the position and shape of the InAs peaks are almost identical for the four samples. Fig. 3 shows the SIMS results of sample D. The signal of Bi in the InAs film is very low that incorporation of Bi can be neglected. The long tail of the In/Ga

Fig. 2. The (115) XRD ω-2θ rocking curves of samples A–D.

Fig. 3. SIMS profile of sample D showing depth distribution of different elements.

signal at the GaAs/InAs interface can be related to the SIMS resolution, and/or the In–Ga inter-diffusion.

The major effect of surfactant on III–V semiconductors, as Grandjean et al. suggested, was to reduce the surface free energy by surfactant segregating on the surface, and thus altered the growth mode to 2D growth [12]. There was another point of view attributing the effects of surfactants on the surface diffusion, while both enhanced and suppressed surface diffusion by the surfactant effect were proposed to explain different experimental observations [15]. However, neither a suppressed nor an enhanced surface diffusion can explain the non-monotonic change of the RMS roughness with increased Bi fluxes observed in this work. For sample A the deeper (darker) areas in the height image correspond to wider-step areas in the amplitude images, see 10×10 μm^2 AFM scans in Fig. 1. This correlation can also be found in sample B, whereas the total darker (wider-step) regions in sample B are less than that in sample A. A more uniform step distribution and a narrower surface step spacing are shown in sample B, corresponding to a smoother surface. In sample C, the deeper and wider-step areas are partly correlated. And the surface step spacing of sample C is similar to that of sample B, see 1×1 μm^2 scans. In sample D the surface step spacing becomes even more uniform and smaller, the correlation between the deeper and wider-step areas disappears. Compared these four samples, some 'wedding-cake' structures (spiral terraces) are observed on the surface of samples B, C, and D but not on that of sample A, indicating some near-surface screw dislocations introduced by Bi fluxes. Quite a few pits are seen on the surface of sample C, and only a few pits are visible in samples B and D.

The locally reduced RMS roughness in samples B–D, seen from small area scans, can be attributed to a more uniform surface step distribution and narrower surface step spacing. It has been reported that surfactant alters the attachment kinetics of group III adatoms at descending and ascending steps, modifies the step motions and changes the surface morphology [16,17]. According to Schwoebel's kinetics model of step motions, coalescence of steps or stabilization of step spacing can occur as a consequence of assuming that captures probability depends on the direction from which adatoms approach the step [18,19]. By using this kinetics model, the observations in this work can be explained: the additional Bi atoms at the growth front reduce the Ehrlich–Schwoebel barrier and thus increase sticking coefficient of adatoms at 'up' steps, hence an arbitrary initial distribution of step spacing tends toward a sequence of uniformly spaced steps. The formation of pits on the surface of samples B, C, and D can be attributed to a suppressed surface diffusion. Pit nucleation is sensitive to the adatom concentration and elastic calculations have shown that pits can relieve elastic energy more efficiently than islands [20]. More stain relieved through pit nucleation results in less surface undulation, explaining the smoothest surface observed in sample C. The surface undulation observed in samples C and D, which is not represented by the deeper–wider area correlation and thus is not related to step coalescence, will be discussed together with Hall and TEM measurement results.

Room temperature Hall Effect measurements were carried on the four samples using the Van der Pauw configuration. Fig. 4 shows that the electron mobility of the InAs films decreases as the Bi flux increases. Sample A shows a mobility of 14,600 cm^2/V s with a sheet density of 9.92×10^{12}/cm^2, while in sample D a mobility of 3500 cm^2/V s with a sheet density of 1.7×10^{15}/cm^2 was measured. The cross-section TEM images of the four samples are shown in Fig. 5. The layer thicknesses of the samples are identical, indicating Bi flux does not influence the growth rate. However, increased TD densities are observed with increased Bi fluxes, which explains the deteriorated electron mobility due to the scattering effect [21]. Now the rough surface in sample D can be explained by the high density TDs near the surface, since high strain energy density near the dislocation core exerts a force inward toward
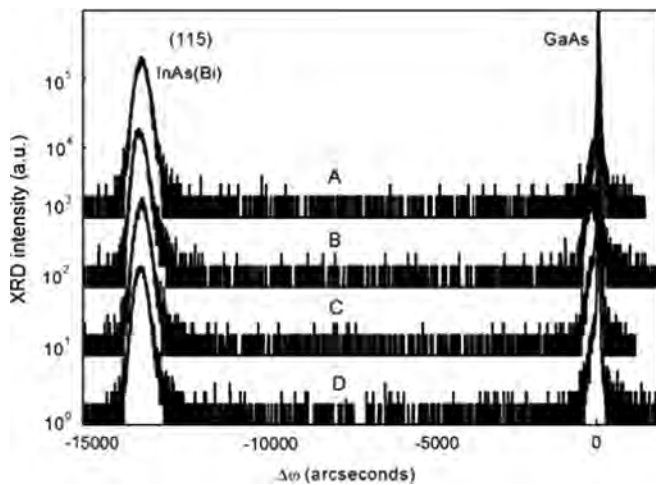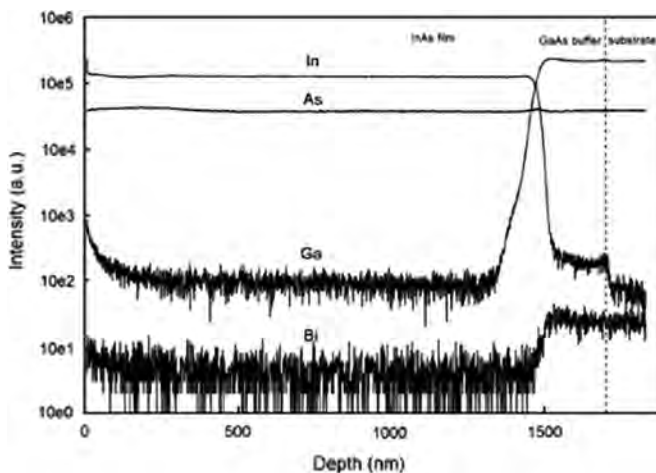
the material which must be balanced by the surface energy. Therefore, the effect of Bi on the surface morphology of the InAs films is a combined effect of surface step motions and the near-surface dislocation density.

The reason for the TDs introduced by Bi fluxes can be explained by interaction between Bi atoms and structural defects. It is well known that TD density in a strained layer decreases with the layer thickness and this can be explained by a reaction model [22]. The two reduction reactions are annihilation, in which TDs with opposite Burgers vectors meet, or fusion, in which two TDs react to form a single TD. Relative motion between TDs is necessary to bring them within a reaction
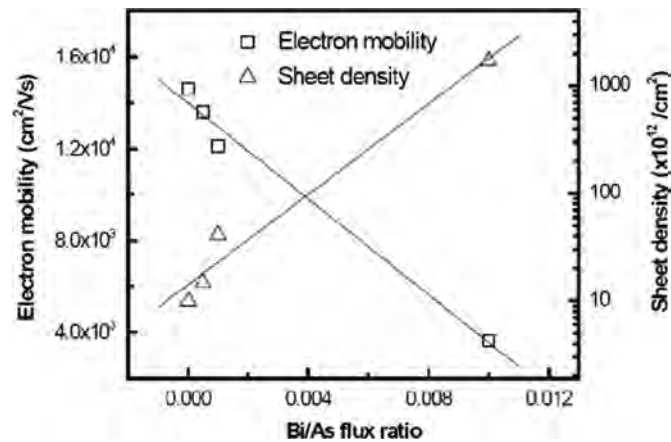
Fig. 4. Electron mobility and sheet density of the samples as a function of Bi/As flux ratio. The solid are for guiding eyes.

distance. The inclined geometry of 60° mixed type TDs enables TDs to move with film thickness and two TDs originating from two initially far separated misfit dislocations may have chances to interact. However, it has been found that a dislocation in a crystal originally mobile can become immobile when impurities precipitates on it [23–25]. The interaction between the structural defects and individual impurity atoms, due to the overlapping of their strain field, could result in an impurity-rich region developed around an extended structural defects. And the strength of immobilization of a dislocation due to the impurity precipitation is determined not only by the amount of impurity atoms accumulated on the dislocation, but also by the morphology of precipitates developed on the dislocation. Though the calculated Bi solubility in InAs was found to be as low as 0.025% [26] and Bi incorporation was excluded by the XRD and SIMS measurement, undetectable Bi atoms are probably trapped by structural defects during growth, e.g. vacancy trails associated with screw and 60° dislocations [24]. The interaction between Bi atoms and dislocations reduces the dislocation velocity, suppressing the dislocation interaction and thus resulting in a high TD density.

3. Summary

We have grown a set of InAs film samples by MBE without or with different Bi fluxes. The effect of Bi on the structural and electrical properties of the InAs films was studied. XRD and the SIMS measurements show that Bi was not compositionally incorporated. AFM measurements show clear surface steps in all the samples, indicating an over-flow growth mode. Small area AFM scans show reduced surface roughness with increased Bi fluxes.
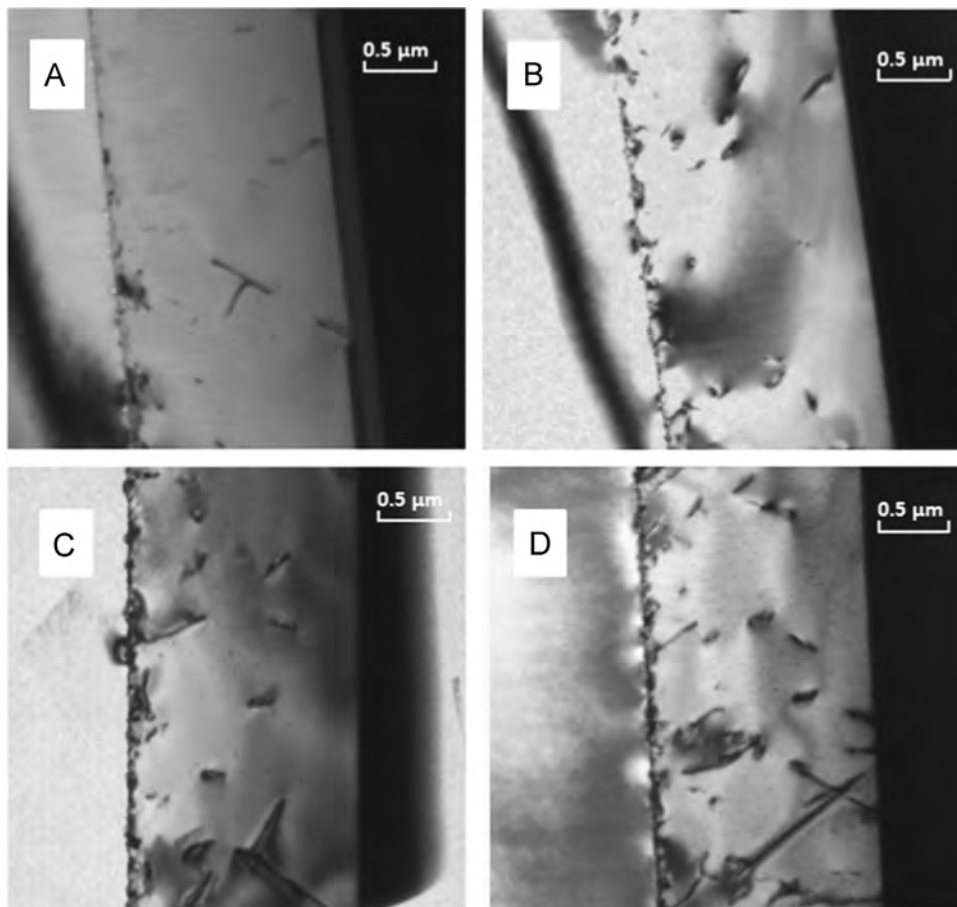
Fig. 5. Cross-section TEM images of samples A–D.

Whereas from large area scans, reduced surface roughness was only observed in the samples grown under low Bi fluxes, and a deteriorated surface was obtained in the sample grown under the largest Bi flux. The locally reduced surface roughness in the Bi-mediated grown samples is attributed to a more uniformly spaced surface steps, which was also observed from the AFM images. This can be explained by Schwoebel's kinetics model of step motions, where a stabilization of step spacing occurs as a consequence of Bi modified step attachment kinetics. The electron mobility of the InAs films, measured at room temperature, was monotonically decreased with increased Bi fluxes. This is correlated to the TEM results in which increased TD densities were observed with increased Bi fluxes, which can be explained by interaction between Bi atoms and structural defects. The interaction between Bi atoms and e.g. $60°$ dislocations reduces the dislocation mobility and chance to annihilate or fuse with another dislocation, thus results in a high TD density in the InAs films. Therefore, the surface of MBE-grown InAs films can be smoothed by applying low Bi fluxes, at a cost of an increased TD density and a deteriorated electron mobility. Further improvement in both surface morphology and electron mobility could be achieved by periodically opening the Bi flux.

Acknowledgments

References

[1] M.J. Yang, F.C. Wang, C.H. Yang, B.R. Bennett, T.Q. Do, Appl. Phys. Lett. 69 (1996) 85.
[2] P.Y. Aghdam, H. Zhao, Phys. Status Solidi C 10 (2013) 777.
[3] N.P. Esina, N.V. Zotova, I.I. Markov, B.A. Matveev, A.A. Rogachev, N.M. Stus, G.N. Talalakin, J. Appl. Spectrosc. 42 (1985) 465.
[4] P. Laukkanen, M. Ahola, M. Kuzmin, R.E. Perälä, I.J. Väyrynen, J. Sadowski, Surf. Sci. 598 (2005) L361.
[5] G.H. Kim, J.B. Choi, J.Y. Leem, J.I. Lee, S.K. Noh, J.S. Kim, J.S. Kim, S.K. Kang, S.I. Ban, J. Cryst. Growth 234 (2002) 110.
[6] H. Yuan, S.J. Chua, Z.L. Miao, J.R. Dong, Y.J. Wang, J. Cryst. Growth 273 (2004) 63.
[7] Y. Takano, M. Umezawa, S. Shirakata, S. Fuke, Jpn. J. Appl. Phys. 43 (2004) 944.
[8] Y. Jeong, H. Choi, T. Suzuki, J. Cryst. Growth 301–302 (2007) 235.
[9] Y. Nabetani, A. Wakahara, A. Sasaki, J. Appl. Phys. 78 (2009) 6461.
[10] H. Naceur, T. Mzoughi, I. Moussa, A. Rebey, B.E. Jani, Nucl. Instrum. Methods Phys. Res. B 268 (2010) 236.
[11] W.N. Rodriguesa, V.H. Etgensb, M. Sauvage-Simkinc, G. Rossid, F. Sirotti, R. Pinchauxe, F. Rochet, Solid State Commun. 95 (1995) 873.
[12] N. Grandjean, J. Massies, V.H. Etgens, Phys. Rev. Lett. 69 (1992) 796.
[13] T. Mzoughi, H. Fitouri, I. Moussa, A. Rebey, B.E. Jani, J. Alloy. Compd. 524 (2012) 26.
[14] H. Naceur, T. Mzoughi, I. Moussa, L. Nguyen, A. Rebey, B.E. Jani, Physica E 43 (2010) 106.
[15] D. Kandel, E. Kaxiras, Solid State Phys. 54 (2000) 219.
[16] S.W. Jun, G.B. Stringfellow, J.K. Shurtleff, R.T. Lee, J. Cryst. Growth 235 (2002) 15.
[17] S.H. Lee, G.B. Stringfellow, Appl. Phys. Lett. 73 (1998) 1703.
[18] R.L. Schwoebel, E.J. Shipsey, J. Appl. Phys. 37 (1966) 3682.
[19] R.L. Schwoebel, J. Appl. Phys. 40 (1969) 614.
[20] M. Bouville, J.M. Millunchick, M.L. Falk, Phys. Rev. B. 70 (2004) 235312.
[21] R.J. Egan, V.W.L. Chin, T.L. Tansley, J. Appl. Phys. 75 (1994) 2473.
[22] A.E. Romanov, W. Pompe, S. Mathis, G.E. Beltz, J.S. Speck, J. Appl. Phys. 85 (1999) 182.
[23] P.A. Kirkby, IEEE J. Quantum Electron. 11 (1975) 562.
[24] V. Czlrr, M. Kabler, T. Nrnolxrya, R. Thomson, Phys. Rev. 131 (1963) 58.
[25] K. Sumino, Phys. Status Solidi A 171 (1999) 111.
[26] K.Y. Ma, Z.M. Fang, R.M. Cohen, G.B. Stringfellow, J. Appl. Phys. 70 (1991) 3940.
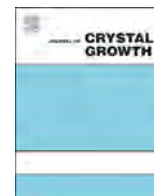
Structural properties of AlGaP films on GaP grown by gas-source molecular-beam epitaxy

S. Dadgostar [a,*], E.H. Hussein [a], J. Schmidtbauer [b], T. Boeck [b], F. Hatami [a], W.T. Masselink [a]

[a] Department of Physics, Humboldt Universität zu Berlin, Newton-Str. 15, D-12489 Berlin, Germany
[b] Leibniz-Institute für Kristallzüchtung, Max-Born-Str. 2, 12489 Berlin, Germany

ARTICLE INFO

ABSTRACT

The growth of $Al_{0.85}Ga_{0.15}P$ on GaP using gas-source molecular-beam epitaxy is investigated using in situ high-energy electron diffraction, high-resolution x-ray diffraction, atomic-force microscopy, and scanning electron microscopy. Growth temperature and phosphorus flux were varied. The 1.0-μm AlGaP films were grow on a GaP buffer layer and capped with GaP. The investigation indicates that a growth temperature of 490 °C and a cracked PH3 flux of 2.7 sccm resulted in the best AlGaP quality, while maintaining very good GaP quality.

© 2015 Elsevier B.V. All rights reserved.

1. Introduction

Photonic crystal cavities are optoelectronic devices that reduce optical energy loss by confining light in a very small volume. Photonic crystal cavities can be used in spectroscopic devices and can also be incorporated into single-photon light emitters based on quantum dots, nitrogen vacancies, or organic molecules [1–3]. For applications in the range of visible wavelengths, photonic crystal cavities based on GaAs and Si cannot be used because of their small band gaps. Photonic crystal cavities with shorter wavelength transparency are usually fabricated based on the GaN, SiN, and GaP systems. Difficult fabrication process and the low refractive index are the problems of GaN systems [4,5]. Low refractive index is also a disadvantage of SiN which limits the quality (Q) factor of device [6]. GaP, on the other hand, is a good candidate for short wavelengths photonic crystals due to its large indirect band gap energy of 2.26 eV and high refractive index in the range of 3.44–3.25 for the wavelengths between 555 and 700 nm [7]. Moreover, the quantum efficiency of the light emitters in visible wavelengths can be increased by fabrication of the GaP photonic crystal in coupling with InP or InGaAs quantum dots [8]. Recently fabrication of high quality photonic crystal cavities based on GaP using a sacrificial layer of AlGaP has been reported [9–11]. The high Q factor of the photonic crystal cavities is limited by the crystal quality of GaP membrane that is, in turn, dependent on the AlGaP sacrificial layer crystal quality. AlGaP, however, is a reactive material which can be easily oxidized therefore to prevent the oxidation a thin GaP layer grown on the AlGaP layer. Since the growth of the AlGaP layer with minimum density of dislocation- and oval-defects and

minimum surface roughness is a difficult challenge, limiting the quality of the GaP top layer that should be fabricated into a membrane. The impact of the III/V ratio and growth temperature on surface structure of GaP grown by MBE has been reported [12,13] as well x-ray diffraction investigations of GaP/AlGaP heterostructures [14,15]. The impact of growth temperature and PH_3 flux on the crystal structure of AlGaP, however, has not been investigated. This work investigates the relationship between the growth temperature and PH_3 flux and the crystal quality of AlGaP layer.

2. Experimental

The growth of AlGaP was made using a Riber 32P gas-source molecular-beam epitaxy (GSMBE) system, using PH_3 as the phosphorus source and solid Al and Ga sources. The PH_3 was cracked at 850 °C by a low-pressure high-temperature cracker and its flux was controlled by a flow meter. The growth temperature was measured by a thermocouple located directly behind the GaP substrate held by its rim. Structural properties were characterized using in situ reflection high-energy electron diffraction (RHEED), x-ray diffractometer, scanning electron microscopy (SEM), and atomic force microscopic (AFM).

Samples were grown on one-side polished S-doped GaP (100) substrates with thickness of 300 μm. Fig. 1 illustrates the grown structures. Each sample consists of a 0.2-μm GaP buffer, 1.0-μm $Al_{0.85}Ga_{0.15}P$, and a 80-nm GaP cap layer. The GaP layers were grown at 1.1-μm/h and the AlGaP at 1.6-μm/h. The PH_3 flux during the GaP growth was in every case 1.9 sccm; the PH_3 flux for the AlGaP growth was 2.3 or 2.7 sccm according to Table 1 A constant growth temperature was used for each sample of 480, 490, or 500 °C, again as given in Table 1. Note that we grew and characterized 17 AlGaP/GaP samples. Therefore, our conclusion that the growth window is small for AlGaP

* Corresponding author. Tel.: +49 30 20938076.
E-mail address: dadgostar@physik.hu-berlin.de (S. Dadgostar).

layer is based on the results of RHEED, XRD, AFM, and SEM of all grown samples. We chose, however, 5 samples with the defined growth conditions in the paper as representative of our work.
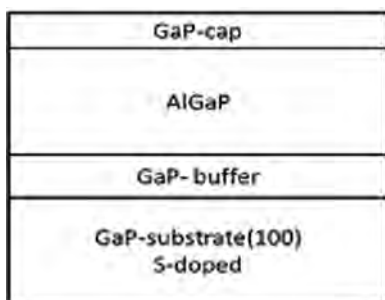
Fig. 1. Scheme of structures. Al content for all samples was set to be 85%. GaP buffer and cap layer were grown under 1.9 sccm PH$_3$ while to grow AlGaP layer different fluxes of 2.3 and 2.7 were used. Same growth temperature was applied during the growth of GaP and AlGaP.

Table 1
Growth temperature and PH$_3$ flux of the AlGaP layer for different samples.

Sample	Growth T (°C)	PH$_3$ (sccm)
S1	480	2.3
S2	480	2.7
S3	490	2.7
S4	500	2.7
S5	500	2.3
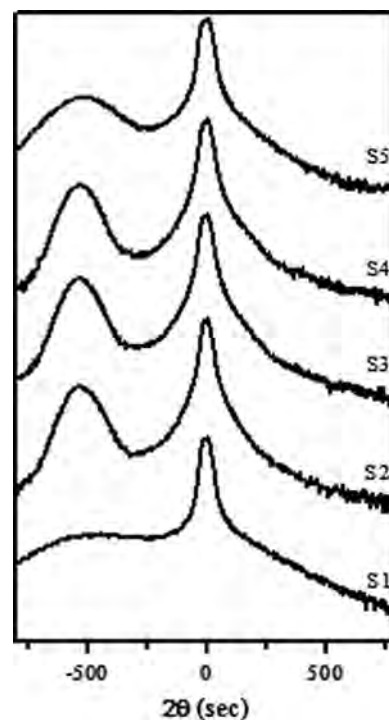
Fig. 3. X-ray measurement results for samples grown at different temperature and under different PH$_3$ flux. The sharper peak belongs to the GaP and the other peak is related to Al$_{0.85}$Ga$_{0.15}$P layer.
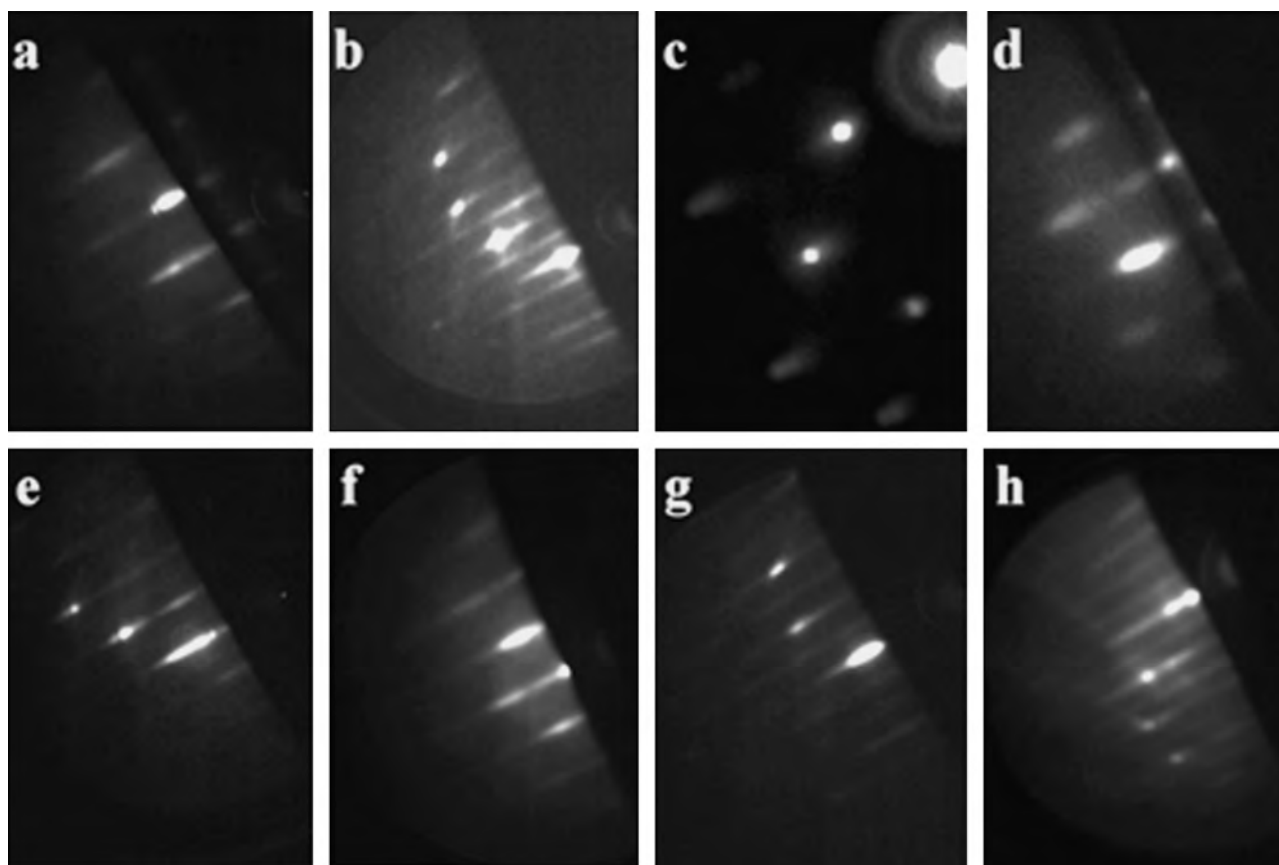
Fig. 2. RHEED pattern images: (a) sharp lines of the 2 × 4 reconstruction of GaP surface after oxide desorption at 580 °C, (b) GaP buffer layer of S1, (c) and (f) first MLs growth of AlGaP layer of S1 and S3, (d) and (g) after the growth of AlGaP layer, (e) and (h) GaP cap layer of S1 and S3. It is notable that RHEED pattern of GaP buffer of S3 was as sharp and streaky as the first MLs of AlGaP layer.

3. Results and discussions

We grew and characterized several GaP/GaP samples. AFM results indicate that under PH_3 flux of 1.9 sccm, the growth temperatures higher than 520 °C is followed by the high surface roughness for the epitaxial GaP layer on GaP substrate. Results show also that the growth under a high PH_3 flux of 2.7 sccm increases the roughness. Our results indicate that the optimum conditions for GaP growth are a PH_3 flux of 1.9 sccm and a growth temperatures of 490 ± 10 °C, so that in every case the GaP was grown within this range.

The native oxide of the GaP substrate was removed by heating the substrate to 580 °C under a PH_3 over pressure and the RHEED pattern of GaP substrate shows the sharp lines of 2×4 reconstruction after oxide desorption (Fig. 2a).

For all samples, the RHEED patterns of GaP buffer layers demonstrate a very sharp and streaky pattern (Fig. 2b). Upon initiation of the AlGaP growth, the samples grown using the lower PH_3 flux (2.3 sccm) showed a spotty RHEED pattern for the first monolayers (Fig. 2c) that became better by the time the full 1.0 μm AlGaP layer was grown (Fig. 2d). After overgrowth with the GaP cap layer, the RHEED was again sharp (Fig. 2e). The RHEED from the AlGaP grown under the higher PH_3 flux (2.7 sccm), however, showed sharper and streakier patterns for both AlGaP and GaP cap layers (Fig. 2f–h). It may be associated to the better crystal quality of AlGaP layer grown under higher PH_3 flux which can also improve the crystal quality of the GaP cap layer.

X-ray diffraction was measured using a Bede-QC1 diffractometer. The spectra presented in Fig. 3 indicate that the full width at half maximum (FWHM) of AlGaP peak strongly decreases with increase of PH_3 flux from 2.3 sccm (S1 and S5) to 2.7 sccm (S2, S3 and, S4) and this suggests the reduction of the density of defects. For 2.3 sccm PH_3 flux, however, FWHM of AlGaP peak decreases with the increase of growth temperature from 480 °C (S1) to 500 °C (S5) while it changes slightly with growth temperature under the higher PH_3 flux (Table 2). Density of dislocation defects can be calculated based on the Hirsch model as

$$N = \beta^2/(9b^2) \tag{1}$$

where β is the FWHM of AlGaP peak in radian and b is the Burgers vector in cm [16]. Calculated results show that for S1 and S2, N decreases from 7.4×10^8 to 0.1×10^8 cm^{-2}. These results may be associated with the sharper RHEED patterns of AlGaP layer grown under higher PH_3 flux.

Since the GaP buffer and cap layers were grown at the optimum growth temperatures and PH_3 flux, therefore the structural quality of the cap layer may be affected by the quality of AlGaP layer. Therefore AFM and SEM measurements' results can be related to the structural quality of AlGaP layer. The AFM measurements were done using a Bruker Icon Dimension AFM operating in peak force mode and to

Table 2
Extracted result from the x-ray measurements of rocking curve.

Sample	FWHM $\times 10^{-3}$ (rad)	$N \times 10^8$ (cm^{-2})
S1	2.24	7.4
S2	0.38	0.1
S3	0.32	0.1
S4	0.34	0.1
S5	0.74	0.8

Table 3
Extracted result from AFM and SEM measurements of different samples. The PH_3 flux was 1.9 sccm for the cap layer of all samples, while it was 2.3 sccm for S1 and S5 and 2.7 sccm for S2, S3 and, S4 for the AlGaP layer.

Sample	rms (nm)	AFM—oval defect d (μm)	AFM—oval defect density $\times 10^8$ (cm^{-2})	SEM—oval defect d (μm)	SEM—oval defect density $\times 10^8$ (cm^{-2})
S1	14.8	0.287	12.8	0.33	7.6
S2	0.58	0.230	0.1	0.33	0.07
S3	0.48	No	No	No	No
S4	1.03	No	No	0.33	0.28
S5	3.78	0.285	2.0	0.33	4.0
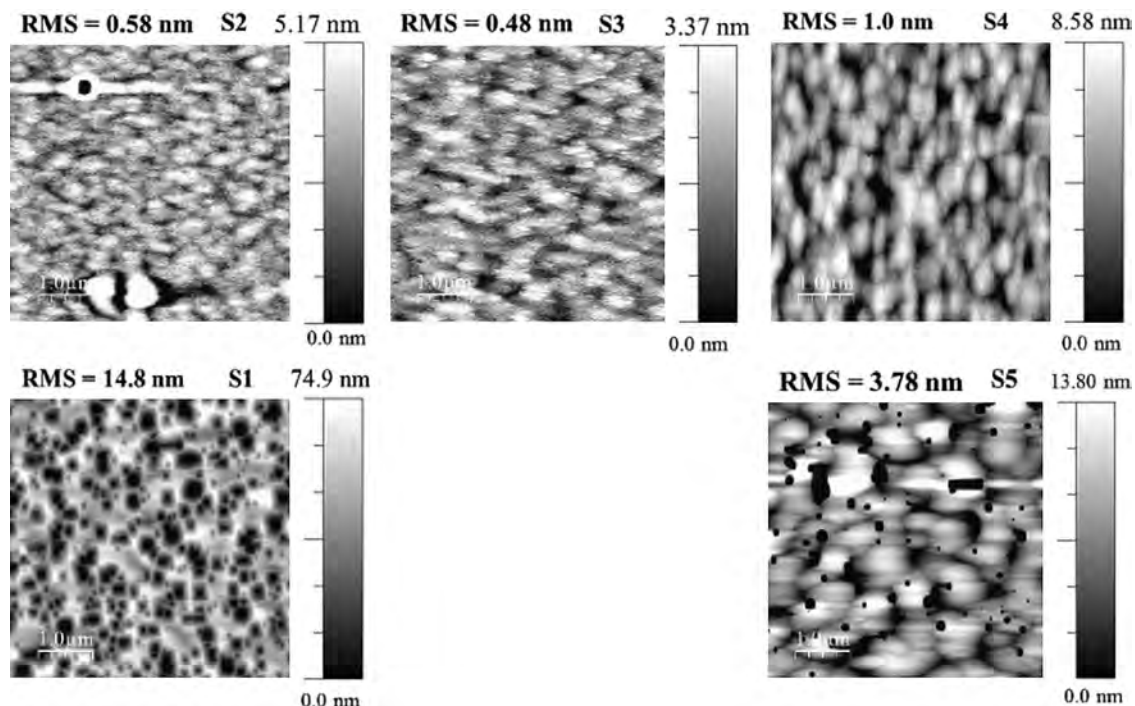
Fig. 4. AFM images of the grown samples at different temperatures. The PH_3 flux was 1.9 sccm for the cap layer of all samples, while it was 2.3 sccm for S1 and S5 and 2.7 sccm for S2, S3 and, S4 for the AlGaP layer. All the AFM measurements were done on the 5×5 μm scale.
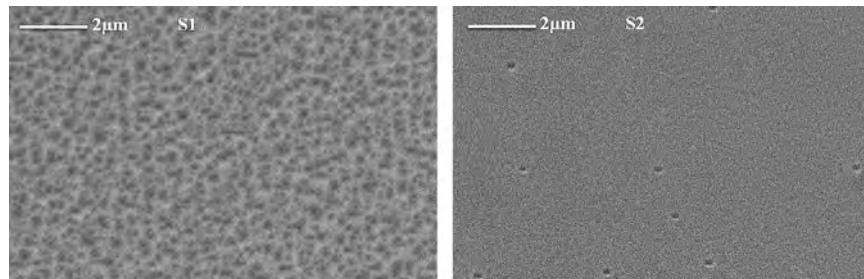
Fig. 5. SEM image of S2 and S3. Reduction of the growth temperature from 490 °C to 480 °C is followed by the formation of oval-defects.

analyze the AFM results, we used the WSxM v5.0 [17]. Fig. 4 presents the AFM images of the different samples on which their GaP cap layer was grown under the optimized growth conditions but however the results are different for them and this can be due to the AlGaP layers. Using the AFM results we can find the optimum growth conditions for the AlGaP layer which can cause the minimum surface roughness and density of oval defects for the GaP cap layer.

AFM results indicate that the rise of the PH_3 flux for the AlGaP layer growth is followed by strong decrease of surface roughness and density of oval defects for the GaP cap layer of S2 and S3 in comparison with S5 (Table 3). This may be associated to the narrowing of x-ray peak of AlGaP. For samples with AlGaP layer grown under higher PH_3 flux, however, AFM measurements indicate that decrease of the growth temperature causes the formation of the oval defects. These results indicate the oval defects with density of $1.1 \times 10^7 \, cm^{-2}$ and size of $0.23 \pm 0.05 \, \mu m$ for S2 and therefore the root mean square (rms) of surface roughness of S2 (0.58 nm) is slightly larger than S3 (0.48 nm). This result may be related to the slight increase of the FWHM of AlGaP x-ray peak of S2 in comparison with S3 (Table 2).

SEM measurements are consistent with the AFM results (Fig. 5). We used a Jeol-6350 microscopy for SEM measurements and the results do not show any oval defects for S3 while they indicate the hole-shape oval defects with the average size of $0.33 \pm 0.02 \, \mu m$ on the surface of the GaP cap layers of other samples. According to these measurements the density of defects strongly decreases with the increase of the PH_3 flux (Table 3).

It is possible that the 25% increase of the PH_3 flux improves the crystal quality by decreasing the surface mobility, resulting in smoother surfaces. Under low PH_3 flux, the probability of formation of the 3D islands or agglomeration of group-III adatoms increases [12,13,18]. The insufficient availability of P_2 might be the reason for the wide FWHM of x-ray peak and therefore high density of the dislocation defects of the AlGaP layers grown under lower PH_3 flux. The low crystal quality of AlGaP layer can affect the crystal quality of the GaP cap layer and therefore the high roughness and density of oval defects of S4 and S5 may be associated to the high density of dislocation defects. The AFM and SEM results, however, indicate that S3 has the lowest surface roughness and density of oval defects. Therefore under high PH_3 flux, 490 °C is the optimum growth temperature. This may be related to the better crystal quality of the AlGaP layer of S3 which is confirmed by its less FWHM in comparison to S2 and S4. Increase of growth temperature can be followed by less availability of P_2 and consequently increase of the diffusivity of group-III adatoms. Thus a higher probability for the agglomeration of group-III adatoms [12,13,18] can be predicted which results in the rise of the density of dislocation defects and therefore wider FWHM for AlGaP layer. However, for the growth temperature lower than 490 °C, the insufficient surface energy may be the reason of the formation of dislocation defects [15]. The mobility reduction of group-III adatoms may be related to the increase of the FWHM of AlGaP which can be followed by the oval defects formation on the GaP cap layer for S2.

4. Conclusions

In summary, the x-ray results imply that the grown sample at 490 °C under 2.7 sccm PH_3 flux (S3) has the minimum FWHM of AlGaP layer and AFM and SEM measurements also show that the GaP cap layer has the minimum density for both oval defects and surface roughness. Density of defects and surface roughness rise with PH_3 flux reduction which may be due to the insufficient availability of P_2 and it can be the origin of higher probability for formation of 3D islands of group III adatoms. Under high PH_3 flux (2.7 sccm), both increase and decrease of the growth temperatures than 490 °C show the rise of FWHM of AlGaP and roughness of cap layer. The growth temperatures below 490 °C might bring the insufficient mobility of group-III adatoms due to the low surface energy which may be the reason of the formation of defects while above 490 °C less availability of P_2 may cause the defects.

Acknowledgments

References

[1] J.D. Joannopoulos, P.R. Villeneuve, S. Fan, Photonic crystals: putting a new twist on light, Nature 386 (1997) 143.

[2] T. Tanabe, M. Notomi, S. Mitsugi, A. Shinya, E. Kuramochi, All-optical switches on a silicon chip realized using photonic crystal nanocavities, Appl. Phys. Lett. 87 (2005) 151112.

[3] I. Fushman, E. Waks, D. Englund, N. Stoltz, P. Petroff, J. Vuckovic, Ultrafast nonlinear optical tuning of photonic crystal cavities, Appl. Phys. Lett. 90 (2007) 091118.

[4] Y.-S. Choi, K. Hennessy, R. Sharma, E. Haberer, Y. Gao, S.P. DenBaars, et al., GaN blue photonic crystal membrane nanocavities, Appl. Phys. Lett. 87 (2005) 243101.

[5] C.-F. Lai, P. Yu, T.-C. Wang, H.-C. Kuo, T.-C. Lu, S.-C. Wang, et al., Lasing characteristics of a GaN photonic crystal nanocavity light source, Appl. Phys. Lett. 91 (2007) 041101.

[6] A.M. Adawi, A.R. Chalcraft, D.M. Whittaker, D.G. Lidzey, Refractive index dependence of L3 photonic crystal nano-cavities, Opt. Express. 15 (2007) 14299.

[7] D.F. Nelson, Electro-optic and piezoelectric coefficients and refractive index of gallium phosphide, J. Appl. Phys. 39 (1968) 3337.

[8] S. Buckley, K. Rivoire, F. Hatami, J. Vuckovic, Quasiresonant excitation of InP/InGaP quantum dots using second harmonic generated in a photonic crystal cavity, Appl. Phys. Lett. 101 (2012) 161116.

[9] K. Rivoire, S. Buckley, F. Hatami, J. Vuckovic, Second harmonic generation in GaP photonic crystal waveguides, Appl. Phys. Lett. 98 (2011) 263113.

[10] K. Rivoire, A. Faraon, J. Vuckovic, Gallium phosphide photonic crystal nano-cavities in the visible, Appl. Phys. Lett. 93 (2008) 063103.

[11] K. Rivoire, A. Kinkhabwala, F. Hatami, W.T. Masselink, Y. Avlasevich, K. Müllen, et al., Lithographic positioning of fluorescent molecules on high-Q photonic crystal cavities, Appl. Phys. Lett. 95 (2009) 123113.

[12] C. Ratcliff, T.J. Grassman, J.A. Carlin, S.A. Ringel, High temperature step-flow growth of gallium phosphide by molecular beam epitaxy and metalorganic chemical vapor deposition, Appl. Phys. Lett. 99 (2011) 141905.

[13] J.N. Baillargeon, K.Y. Cheng, K.C. Hsieh, Surface structure of (100)GaP grown by gas source molecular beam epitaxy, Appl. Phys. Lett. 56 (1990) 2201.

[14] W.G. Bi, High resolution x-ray diffraction studies of AlGaP grown by gas-source molecular-beam epitaxy, J. Vac. Sci. Technol. B Microelectron. Nanom. Struct. 13 (1995) 754.

[15] J.N. Baillargeon, K.Y. Cheng, K.C. Hsieh, G.E. Stillman, The gas source molecular beam epitaxial growth of $Al_xGa_{1-x}P$ on (100) GaP, J. Appl. Phys. 68 (1990) 2133.

[16] P. Gay, P.B. Hirsch, A. Kelly, Acta Metall. 1 (1953) 315.

[17] I. Horcas, R. Fernndez, J.M. Gmez-Rodrguez, J. Colchero, J. Gmez-Herrero A.M. Baro, WSXM: a software for scanning probe microscopy and a tool for nanotechnology, Rev. Sci. Instrum. 78 (2007) 013705.

[18] S. Matteson, H.D. Shih, Morphological studies of oval defects in GaAs epitaxial layers grown by molecular beam epitaxy, Appl. Phys. Lett. 48 (1986) 47.

CrossMark
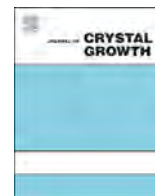
Crystal structure of low-temperature-grown $In_{0.45}Ga_{0.55}As$ on an InP substrate

Yoriko Tominaga *, Yuki Tomiyasu, Yutaka Kadoya

Graduate School of Advanced Sciences of Matter, Hiroshima University, 1-3-1, Kagamiyama, Higashihiroshima, Hiroshima 739-8530, Japan

ARTICLE INFO

ABSTRACT

We grew low-temperature-grown (LTG) $In_{0.45}Ga_{0.55}As$ on an InP substrate by molecular beam epitaxy at a substrate temperature of 200–240 °C; it was characterized by high-resolution X-ray diffraction (XRD) and Rutherford backscattering spectrometry (RBS). The XRD results indicated deterioration of crystalline quality at a growth temperature between 200–220 °C, and a transformation of excess As in the crystal of LTG $In_{0.45}Ga_{0.55}As$ into As precipitates by thermal annealing. The RBS for LTG $In_{0.45}Ga_{0.55}As$ grown at 220 °C indicated that the In atoms were located in interstitial sites along the [110] direction. The ratio of the interstitial In atoms was estimated to be almost 40% of all In atoms in the LTG $In_{0.45}Ga_{0.55}As$, and this ratio did not change abruptly after annealing to 550 °C.

© 2015 Elsevier B.V. All rights reserved.

1. Introduction

Low-temperature-grown (LTG) GaAs-based III-V semiconductor materials have been actively studied for photoconductive antennas (PCAs) activated by femtosecond-regime optical pulses in terahertz time-domain spectroscopy (THz-TDS). LTG GaAs has a relatively good carrier mobility ($\sim 200\ cm^2/V\ s$), an ultrashort carrier lifetime ($< 1\ ps$), and large resistivity ($\sim 10^7\ \Omega\ cm$); therefore, the PCAs made of LTG GaAs are well suited to generate and detect THz waves using mode-locked Ti:sapphire lasers with wavelengths of approximately 0.8 μm. Recently, an attempt has been made to develop PCAs that can be excited by femtosecond fiber lasers with wavelengths of approximately 1.5 μm [1–13]. Because fiber lasers are portable and stable, using them to excite PCAs as a light source will allow less expensive and more compact THz-TDS systems to be used. These systems have attracted considerable attention because of their potential to become a powerful tool in pharmaceutical and semiconductor testing and in imaging, molecular spectroscopy, and other fields. Therefore, it is imperative that we develop more practical THz-TDS systems.

To fabricate PCAs activated by fiber lasers, LTG-GaAs-based semiconductor alloys with bandgaps that correspond to the 1.5 μm-region such as LTG-InGaAs [4,5,8,9], -GaNAsSb [11], and -GaAsBi [12,13] have been used. However, endeavors for these LTG-narrow-bandgap semiconductors have not been completely successful. Although one of the authors (Y. K.) and other research groups succeeded in observing THz-wave emission and detection using

LTG-InGaAs PCAs [4,5,8,9], the detailed fundamental properties and optimized growth condition of LTG InGaAs are still unknown. The high resistivity of LTG GaAs originates from the high density of defects caused by excess As incorporated during low-temperature growth as well as from the high density of As precipitates formed after annealing [14]. Therefore, observation of excess As incorporation and As precipitates in LTG InGaAs has been performed by using X-ray diffraction (XRD) measurement and cross-sectional transmission electron microscope (TEM) observation [15,16]. There is no report for In atoms, however, in the LTG-InGaAs crystal, which can be presumed to affect the fundamental properties of LTG InGaAs.

In this paper, we report on the crystal structure of LTG $In_{0.45}Ga_{0.55}As$ on an InP substrate, focusing on the lattice site of In atoms in an LTG-$In_{0.45}Ga_{0.55}As$ crystal as the first step in obtaining the characteristics mentioned previously in achieving efficient PCAs with LTG-GaAs-based semiconductors for THz-wave emission and detection. To reveal this crystal structure, XRD measurement and Rutherford backscattering spectrometry (RBS) were performed.

2. Experiment

Using solid sources of In, Ga, and As, the LTG $In_{0.45}Ga_{0.55}As$ samples were grown on semi-insulating (001)-oriented InP substrates by molecular beam epitaxy (MBE). We kept each flux almost constant at 9.9×10^{-8}, 6.9×10^{-8}, and 1.7×10^{-5} Torr for In, Ga, and As, respectively. Thermal flashing of the InP substrate was performed at a substrate temperature (T_{sub}) of 500 °C to desorb native oxides of the substrate, and then, the LTG-$In_{0.45}Ga_{0.55}As$ layer was grown on an InP substrate directly with a thickness of 2.0 μm at a T_{sub} of 200–240 °C.

* Corresponding author. Tel: +81 82 424 7649.
  E-mail address: ytominag@hiroshima-u.ac.jp (Y. Tominaga).

The LTG-$In_{0.45}Ga_{0.55}As$ layer was doped with a Be concentration of 3.0×10^{18} cm^{-3} for a future fabrication of PCAs because Be doping has been reported to reduce the residual carrier density and lifetime through the compensation of donor states formed by the antisite As [15,17–20]. After growth, the In content for an as-grown sample was measured with electron probe microanalysis. The samples were then annealed at 400 and 550 °C for 1 h in an H_2 atmosphere with a cover wafer of GaAs. The structural properties of the samples were characterized by using a high-resolution XRD machine (Rigaku ATX-E) with a double-crystal diffractometer. A Ge(220) monochromator and horizontal divergence slits selected Cu Kα_1 radiation. The RBS measurements were performed with a 1.4-mm-collimated beam of 2.0 MeV He$^+$ ions. We mounted the sample on a three-axis goniometer in a vacuum chamber for precisely controlling the orientation of the sample relative to the He$^+$ beam. The backscattered particles were detected by ion implanted silicon charged particle detectors placed at an angle of 165° with respect to the direction of the incident beam.

3. High-resolution X-ray diffraction

Fig. 1 shows XRD spectra of LTG-$In_{0.45}Ga_{0.55}As$ samples grown at a T_{sub} of 200, 220, and 240 °C. Although we could see diffraction peaks for samples grown at 220 and 240 °C, these observed peaks were broad. We calculated ratio of the full width at half maximum of the XRD peak of LTG-$In_{0.45}Ga_{0.55}As$ layer to that of InP substrate, and it turned out to be about 3.2 times larger in comparison with the case of $In_xGa_{1-x}As$ with high crystalline quality reported in ref. [21]. These results suggest that the crystalline quality of LTG $In_{0.45}Ga_{0.55}As$ should be low because of its low growth temperature and/or the lattice mismatch of the relatively thick epitaxial layer. The sample grown at 200 °C exhibited no XRD peaks, indicating that it was relatively amorphous, and that its crystalline quality drastically deteriorates at a T_{sub} between 200 and 220 °C. Fig. 2 shows the XRD spectra of LTG-$In_{0.45}Ga_{0.55}As$ samples before and after annealing. Diffraction peaks of the annealed samples shifted to a higher angle with increasing annealing temperature. This result, which is similar to the case of the LTG $In_xGa_{1-x}As$ lattice matched to the InP substrate [15], implies that annealing caused a transformation of excess As in the crystallization of LTG $In_{0.45}Ga_{0.55}As$ into As precipitates. A future study requires detailed observation of this transformation using a TEM.

4. Rutherford backscattering spectrometry

In order to reveal the crystal structure of the LTG $In_{0.45}Ga_{0.55}As$, we focused on the sample grown at a T_{sub} of 220 °C because this
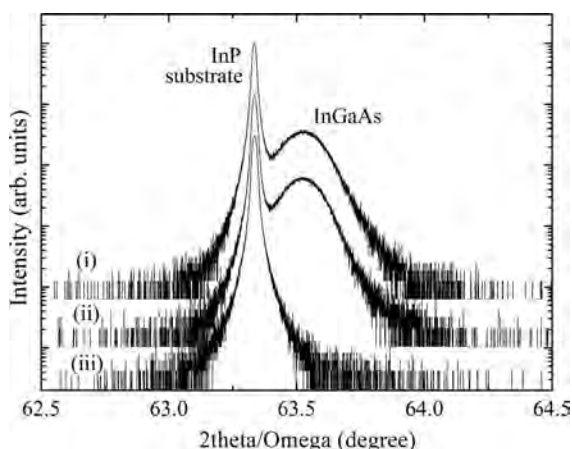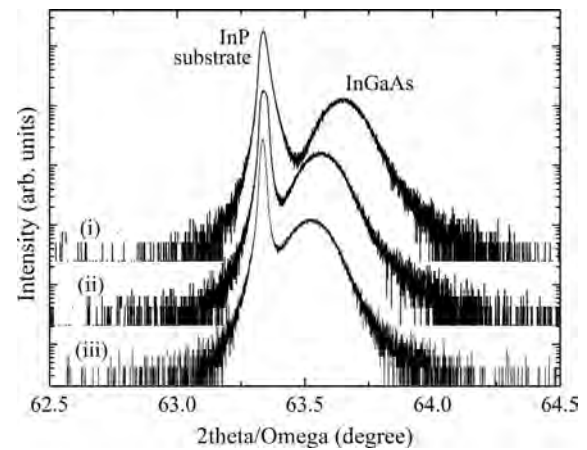
Fig. 2. XRD spectra of as-grown and annealed LTG $In_{0.45}Ga_{0.55}As$. The annealing temperatures were (i) 550 °C, (ii) 400 °C, and (iii) as-grown.
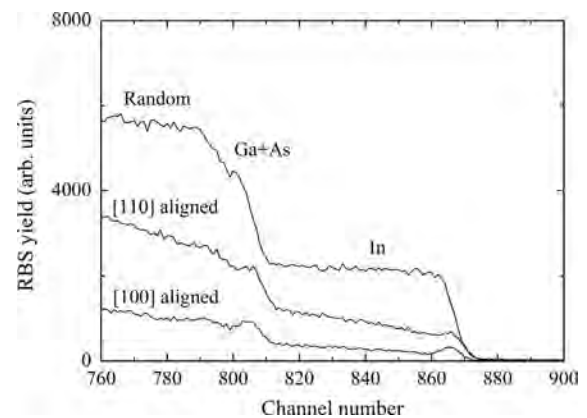
Fig. 3. RBS spectra of as-grown LTG $In_{0.45}Ga_{0.55}As$.

T_{sub} is the minimum temperature at which the sample showed an XRD peak. Fig. 3, which indicates the components of In, Ga, and As, shows random and aligned RBS spectra of as-grown LTG-$In_{0.45}Ga_{0.55}As$ at 220 °C. Since the signals from Ga and As cannot be separated due to their similar atomic weight, they are marked as Ga+As. In Fig. 3, the [110]-aligned signal is much higher than the [100]-aligned signal, with a clear contrast between the random and [100]-aligned signals. This result indicates that interstitial constituent atoms are present in more numbers along the [110] direction than along the [100] direction for the as-grown LTG $In_{0.45}Ga_{0.55}As$. Fig. 4 shows the RBS angular scans of In signals for the same as-grown and annealed LTG $In_{0.45}Ga_{0.55}As$ as in Fig. 3. In Fig. 4(a), dips are confirmed at a tile angle of 0° for both as-grown and annealed samples when He$^+$ ions were irradiated along the [100] direction. During irradiation of He$^+$ ions along the [110] direction, as Fig. 4(b) shows, the tilt angles of dip differ from 0°, and each angle of dips for as-grown, annealed at 400 °C and 550 °C are 0.79°, 2.54°, and 2.11°, respectively. This result probably reflects the lattice distortion of LTG-$In_{0.45}Ga_{0.55}As$ layers to the InP substrate. For the sample annealed at 400 °C, the dip is slightly deeper than those of the others (Fig. 4(a)), and the dip shifts to the highest angle (Fig. 4(b)). Although the cause for this phenomenon is not clear so far, it can be presumed that the lattice distortion of the LTG-$In_{0.45}Ga_{0.55}As$ layer was affected first by thermal treatment up to 400 °C. In addition, the depths of dip in the irradiation of the He$^+$ ions along the [110] direction are shallower than in the case of the [100] direction. Therefore, In atoms are incorporated at interstitial sites into LTG $In_{0.45}Ga_{0.55}As$ due to the low-temperature growth, and more interstitial In atoms are

Fig. 1. XRD spectra of LTG $In_{0.45}Ga_{0.55}As$. The growth temperatures were (i) 240 °C, (ii) 220 °C, and (iii) 200 °C.
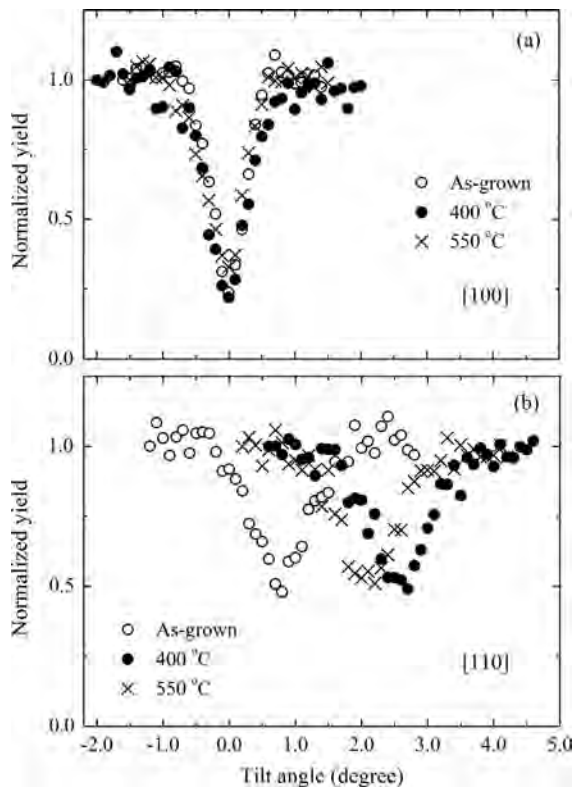
Fig. 4. RBS angular scans of In signals for as-grown and annealed LTG In$_{0.45}$Ga$_{0.55}$As, aligned toward [100] ((a)) and [110] ((b)).

Table 1
Ratio of substitutional In atoms in the crystal of LTG In$_{0.45}$Ga$_{0.55}$As.

Sample	[100] (%)	[110] (%)
As-grown	89.2	60.0
Anneal 400 °C	91.3	58.8
Anneal 550 °C	78.6	56.5

lo-
cated in the crystal along the [110] direction than along the [100] direction for both as-grown and annealed LTG In$_{0.45}$Ga$_{0.55}$As.

To estimate the ratio of substitutional In atoms R in the crystal of LTG In$_{0.45}$Ga$_{0.55}$As, the results of the RBS angular scans were applied to the following equation:

$$R = \frac{1 - \chi_{min}(\text{In})}{1 - \chi_{min}(\text{GaAs})},\qquad(1)$$

where $\chi_{min}(\text{In})$ and $\chi_{min}(\text{GaAs})$ are the minimum yields of In and As+Ga scattering intensity, respectively [22,23]. The LTG-In$_{0.45}$Ga$_{0.55}$As samples in this study did not include any GaAs and/or In$_x$Ga$_{1-x}$As layers with high-crystalline quality and therefore, it was difficult to separate the RBS signals of In and As+Ga clearly in these samples. Therefore, we measured the RBS of a commercial semi-insulating (001)-oriented GaAs substrate as a reference for high quality crystal with zincblende structure, and applied the results to $\chi_{min}(\text{GaAs})$ in eq. (1). Table 1 shows the estimated R of as-grown and annealed LTG In$_{0.45}$Ga$_{0.55}$As, revealing that almost 60% of all In atoms incorporated into LTG In$_{0.45}$Ga$_{0.55}$As at 220 °C are substitutional. In other words, 40% of the In atoms are located in interstitial sites, and the amount of these interstitial In atoms does not change abruptly after annealing to 550 °C.

5. Conclusions

LTG In$_{0.45}$Ga$_{0.55}$As was grown on an InP(001) substrate by MBE at a T_{sub} of 200–240 °C. Although XRD peaks in LTG In$_{0.45}$Ga$_{0.55}$As grown at 220 °C were observed, there was no peak in the sample grown at 200 °C, suggesting that crystalline quality drastically deteriorated at a T_{sub} between 200 and 220 °C. The XRD peak shifted to a higher angle with increasing annealing temperature, which implies a transformation of excess As in the crystal of LTG In$_{0.45}$Ga$_{0.55}$As into As precipitates by thermal treatment. The result of the RBS for LTG In$_{0.45}$Ga$_{0.55}$As at 220 °C indicated that more In atoms were located in interstitial sites along the [110] direction than the [100] direction. The ratio of the interstitial In atoms was estimated to be almost 40% of all In atoms in LTG In$_{0.45}$Ga$_{0.55}$As, and this ratio did not change abruptly after annealing to 550 °C.

Acknowledgments

References

[1] M. Tani, K.-S. Lee, X.-C. Zhang, Appl. Phys. Lett. 77 (2000) 1396.
[2] T. Kataoka, K. Kajikawa, J. Kitagawa, Y. Kadoya, Y. Takemura, Appl. Phys. Lett. 97 (2010) 201110.
[3] M. Suzuki, M. Tonouchi, Appl. Phys. Lett. 86 (2005) 051104.
[4] A. Takazato, M. Kamakura, T. Matsui, J. Kitagawa, Y. Kadoya, Appl. Phys. Lett. 90 (2007) 101119.
[5] A. Takazato, M. Kamakura, T. Matsui, J. Kitagawa, Y. Kadoya, Appl. Phys. Lett. 91 (2007) 011102.
[6] A. Schwagmann, Z.-Y. Zhao, F. Ospald, H. Lu, D.C. Driscoll, M.P. Hanson, A.C. Gossard, J.H. Smet, Appl. Phys. Lett. 96 (2010) 141108.
[7] C.D. Wood, O. Hatem, J.E. Cunningham, E.H. Linfield, A.G. Davies, P.J. Cannard, M.J. Robertson, D.G. Moodie, Appl. Phys. Lett. 96 (2010) 194104.
[8] H. Roehle, R.J.B. Dietz, H.J. Hensel, J. Böttcher, H. Künzel, D. Stanze, M. Schell, B. Sartorius, Opt. Express 18 (2010) 2296.
[9] R.J.B. Dietz, B. Globisch, H. Roehle, D. Stanze, T. Göbel, M. Schell, Opt. Express 22 (2014) 19411.
[10] J. Sigmund, C. Sydlo, H.L. Hartnagel, N. Benker, H. Fuess, F. Rutz, T. Kleine-Ostmann, M. Koch, Appl. Phys. Lett. 87 (2005) 252103.
[11] K.H. Tan, S.F. Yoon, S. Wicaksono, W.K. Loke, D.S. Li, N. Saadsaoud, C. Tripon-Canseliet, J.F. Lampin, D. Decoster, J. Chazelas, Appl. Phys. Lett. 103 (2013) 111113.
[12] A. Arlauskas, P. Svidovsky, K. Bertulis, R. Adomavičius, A. Krotkus, Appl. Phys. Express 5 (2012) 022601.
[13] B. Heshmat, M. Masnadi-Shirazi, R.B. Lewis, J. Zhang, T. Tiedje, R. Gordon, T.E. Darcie, Adv. Opt. Mater. 1 (2013) 714.
[14] I.S. Gregory, C.M. Tey, A.G. Cullis, M.J. Evans, H.E. Beere, I. Farrer, Phys. Rev. B 73 (2006) 195201.
[15] R.A. Metzger, A.S. Brown, L.G. McCray, J.A. Henige, J. Vac. Sci. Technol. B 11 (1993) 798.
[16] J.P. Ibbetson, J.S. Speck, A.C. Gossard, U.K. Mishra, Appl. Phys. Lett. 62 (1993) 2209.
[17] R. Takahashi, Y. Kawamura, T. Kagawa, H. Iwamura, Appl. Phys. Lett. 65 (1994) 1790.
[18] P.W. Joudawlkis, D.T. McInturff, S.E. Ralph, Appl. Phys. Lett. 69 (1996) 4062.
[19] Y. Chen, S.S. Prabhu, S.E. Ralph, D.T. McInturff, Appl. Phys. Lett. 72 (1998) 439.
[20] B. Grandidier, H. Chen, R.M. Feenstra, D.T. McInturff, P.W. Juodawlkis, S.E. Ralph, Appl. Phys. Lett. 74 (1999) 1439.
[21] B.R. Bennett, J.A. del Alamo, J. Appl. Phys. 73 (1993) 3195.
[22] L.C. Feldman, J.M. Mayer, S.T. Picraux, Materials Analysis by Ion Channeling, Academic, New York, 1982, Chap. 2.
[23] T. Nebiki, T. Narusawa, A. Kumagai, T. Saito, S. Takagishi, Nucl. Instrum. Methods Phys. Res B 249 (2006) 501.
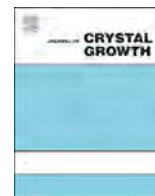
CRYSTAL
GROWTH

Crystal quality of InGaAs/AlAs/InAlAs coupled double quantum wells for intersubband transition devices

CrossMark

Shin-ichiro Gozu *, Teruo Mozume

National Institute of Advanced Industrial Science and Technology (AIST), 1-1-1 Umezono, Tsukuba 205-8568, Japan

ARTICLE INFO

ABSTRACT

The crystal quality of coupled double quantum wells (CDQWs) having different barrier structures was investigated by evaluating optical properties and structural interface quality. Photoluminescence (PL) spectra revealed that the CDQW samples with an AlAs/InAlAs combined barrier (CDQW$_{CB}$) exhibited a narrower PL emission peak than those with an AlAsSb barrier. CDQW$_{CB}$ also showed the best excitation dependence of PL intensity. X-ray reflectivity (XRR) measurements revealed that better interface quality was confirmed in CDQW$_{CB}$. We conclude that CDQW$_{CB}$ has the best crystal quality among those evaluated.

1. Introduction

Intersubband transitions (ISBTs) in InGaAs-based material systems are attractive for ultra-high-speed all-optical signal processing for the optical communication wavelength of 1.55 μm [1]. We have demonstrated InGaAs/AlAsSb-based coupled double quantum wells (CDQWs) exhibiting optical absorption around 1.55 μm due to ISBTs [2]. Using a waveguide device that consisted of CDQWs, 172-Gbit/s optical time domain multiplex transmission [3] and all-optical wavelength conversion [4] have been realized. The functional capability of this waveguide device can be greatly enhanced by integrating it with other optical devices such as laser diodes, photodiodes, and electro-optic modulators. However, their incorporation in an integrated optical device is problematic given the presence of Sb because Sb is not a common material for the optical devices operating at 1.55 μm [5]. To overcome this problem, we used an AlAs/InAlAs combined barrier (CB$_{AlAs/InAlAs}$) to replace the AlAsSb barrier, and demonstrated a clear optical absorption at 1.55 μm due to ISBTs [5]. However, our previous study has focused to realize 1.55 μm of ISBT, and thus, investigation is further required, that is crystal quality of CDQWs with CB$_{AlAs/InAlAs}$ as well as their band structure. In the present study, the crystal quality of the CDQWs with CB$_{AlAs/InAlAs}$ was investigated.

2. Experiment

Three different CDQW samples were prepared for this study: CDQW samples with CB$_{AlAs/InAlAs}$ [5], an AlAsSb/Al(Ga)As/InGaAs-based

CDQW sample (prev. a) [6], and an AlAsSb/InGaAs-based CDQW sample (prev. b) [2]. The sample structure was differed among the samples. But, the growth condition for the molecular beam epitaxy was same among the samples. Fig. 1 shows the samples used in this study. Quantum well widths for the CDQW samples with CB$_{AlAs/InAlAs}$ were 2.6, 2.8, and 3.0 nm. The samples were labeled W:2.6, W:2.8, and W:3.0. Detailed information of all samples are described in Refs. [5,6,2]. Prev. a and prev. b were chosen for comparison since they used AlAsSb barriers with different interface structures between the InGaAs well and AlAsSb barrier, and they operate at 1.55 μm [2,6]. The prev. a structure contained an AlAs layer at the interface, while prev. b structure did not. It was revealed that Sb atoms interdiffused between layers [7]. However, the AlAs layer prevented the interdiffusion, resulting in abrupt interfaces [8]. The CDQW samples used in this study were undoped. Photoluminescence (PL) measurements were performed to evaluate the crystal quality of the CDQW samples. PL spectra were measured using a 514.5 nm Ar-ion excitation laser at both 77 K and room temperature (RT), with an excitation power that varied between 4 mW and 120 mW. X-ray reflectivity (XRR) spectra of the CDQW samples were also taken using a high-resolution X-ray diffractometer system. Because XRR measurements were performed under glancing incidence, the same sample size (10 mm × 5 mm) was utilized.

3. Results and discussion

Fig. 2 shows PL spectra for all samples at a measurement temperature of 77 K; the peaks evident in the spectrum of prev. b will be discussed further below. Note that the PL peak shifts to lower energy as the well width is increased for the CDQW samples with CB$_{AlAs/InAlAs}$, an effect due to the quantized energy in the

* Corresponding author. Tel.: +81 29 861 5814; fax: +81 29 861 3260.
  E-mail address: s-gozu@aist.go.jp (S.-i. Gozu).
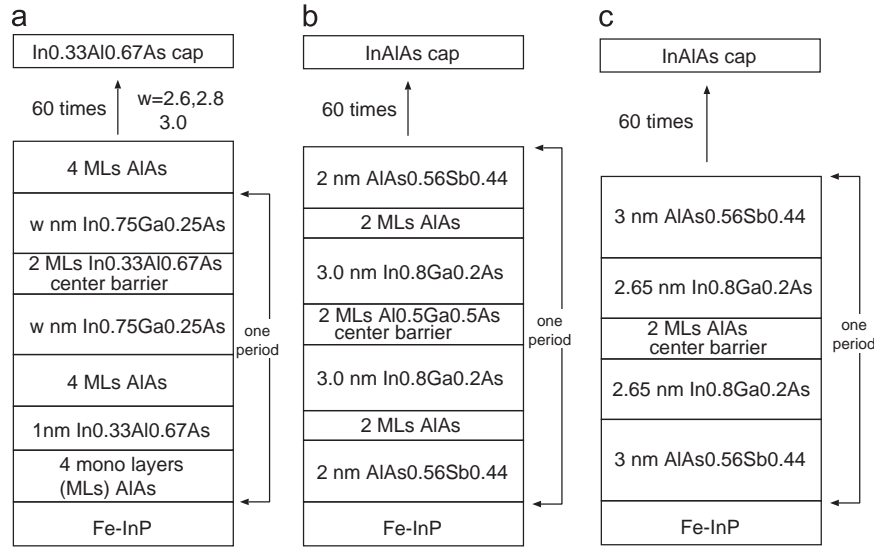
Fig. 1. Schematic structure of the coupled double quantum wells (CDQWs) used in this study. (a) CDQW samples with AlAs/InAlAs combined barrier (CDQW$_{AlAs/InAlAs}$). (b) AlAsSb/Al(Ga)As/InGaAs-based CDQW sample (prev. a). (c) AlAsSb/InGaAs-based CDQW sample (prev. b).

quantum wells. The band structure of lattice matched AlAsSb/InGaAs on InP substrate was type-I with a large conduction band offset of 1.6 eV [9]. InGaAs/InAlAs material system also showed type-I band structure. Thus, the band structure for all investigated samples was type-I. Prev. a and prev. b exhibited lower PL energies than the CDQW samples with CB$_{AlAs/InAlAs}$. According to our previous study [10], interband transition energy (IBT) for the CDQW samples was most likely attributed to the differences in indium content of the InGaAs wells, where these samples used In$_{0.8}$Ga$_{0.2}$As (In 80%). This is because the well width is almost same for obtaining same ISBT energy. The full width at half maximum (FWHM) of the PL spectra was found to vary considerably; FWHM values were 19, 22, 30, 24, and 98 meV for W:3.0, W:2.8, W:2.6, prev. a, and prev. b, respectively. This variation arose from different conditions of interface disorder among the samples. When PL linewidth enhancement due to the interface disorder was discussed, wavefunction penetration over whole structure should be clarified. Using band parameter for AlAsSb/InGaAs [10] and InAlAs/InGaAs, conduction band offset between the barriers and the wells for all CDQW samples was extremely high. As a result, wavefunction for ground subband was well confined in InGaAs wells. The quantized energy fluctuations arising from the interface disorder increase as the well width decreases, resulting in wider FWHM of the PL spectra for the CDQW samples having narrow well width. The well widths of prev. a and prev. b were 3.0 nm and 2.65 nm, respectively, which were almost the same as those of W:3.0 and W:2.6. The interface disorder for the samples of W:x (x=3.0, 2.8, and 2.6) was assumed to be same, since they were grown under identical conditions, the only difference being their well width. Using this assumption, we could directly compare all investigated samples to each other and concluded that the CDQW samples with CB$_{AlAs/InAlAs}$ and prev. b had the best and the worst interface quality among all investigated samples, respectively. An interesting similarity was found in X-ray diffraction (XRD) measurements of the samples. The satellite peaks of the XRD pattern were narrower for the CDQW samples with CB$_{AlAs/InAlAs}$ than for the CDQW samples with AlAsSb barrier [5]. To verify the crystal quality of the samples, the radiative phenomena of PL were investigated by evaluating the excitation power dependence of the PL peak intensity. This relation: PL peak intensity $\propto$ (excitation power density)$^{\beta}$ reveals that the PL emission is dominated by a radiative process ($\beta = 1$) or a non-radiative process ($\beta = 2$) [11]. Fig. 3(a), (b), and (c) shows the excitation power dependence of the PL spectra for W:3.0, prev. a, and prev. b, respectively. The excitation
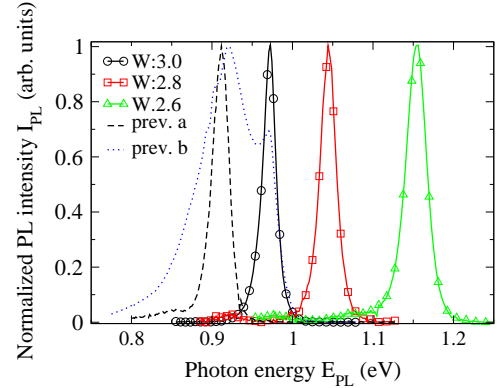
Fig. 2. Photoluminescence spectra of the samples. These spectra were taken at 77 K using 40 mW of a 514.5 nm laser. Sample captions of W:x (x=3.0, 2.8, 2.6), prev. a, and prev. b correspond to sample structures shown in Fig. 1(a), (b), and (c), respectively.

power was varied between 3 mW and 120 mW. To evaluate the PL peak intensity, it is necessary to identify the PL peak related to IBT between the lowest quantized energies of conduction and valence bands. PL peaks of W:3.0 and prev. a were easily revealed because the PL spectra exhibited single peaks. It was difficult, however, to identify the primary peak from the PL spectrum of prev. b. By fitting the prev. b PL spectrum to a Gaussian function, at least three peaks (P1, P2, and P3) could be distinguished, as shown in Fig. 3(c). The peak positions for P1 and P2 exhibited excitation power dependence, while that for P3 was constant for the same experimental conditions. In our previous study [10], IBT energy of prev. b for RT was investigated using photoreflectance measurements with theoretical calculations. When measurement temperature was changed, IBT energy of CDQWs varied according to temperature dependence of band gap energy for the well material. This is because band gap energy exhibits the largest temperature dependence among band parameters. By considering change of InGaAs band gap energy due to temperature change using the Varshini relation [12], P3 peak of prev. b was attributed to IBT and the other peaks (P1, P2) arose from the interface-related states [13] originating from the interdiffusion of Sb atoms between layers [7]. When Sb atoms were incorporated into InGaAs well, quaternary InGaAsSb was formed at the interface. This incorporation will lead to an upward shift in the conduction band and valence band edges. As a result, the quaternary interface

a

b

c
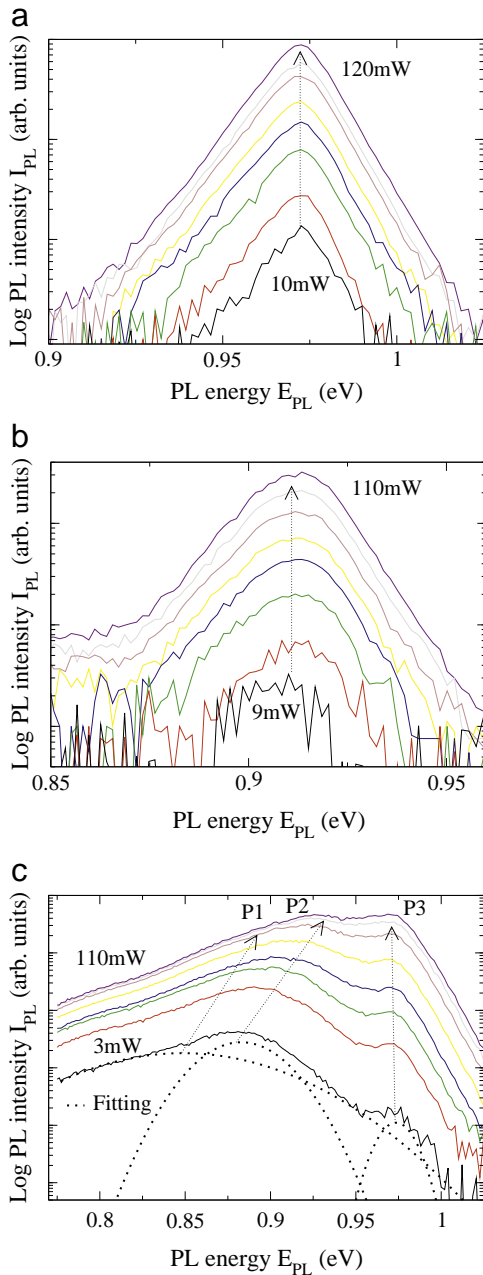
Fig. 3. Excitation power dependence of photoluminescence spectra of the samples. (a) W:3.0, (b) prev. a, (c) prev. b. P1, P2, and P3 in (c) indicate separate peaks that are obtained by curve fitting. Arrows in (c) represent peak energies and intensities of the separated peaks.

Table 1
Excitation power dependence of photoluminescence (PL) intensity (β) and full width at half maximum (FWHM) of PL spectra for W:3.0, prev. a, and prev. b, where PL spectra were measured at 77 K. FWHM values are in units of meV.

	W:3.0	prev. a	prev. b
β	1.69	1.89	1.92
FWHM	19	24	98
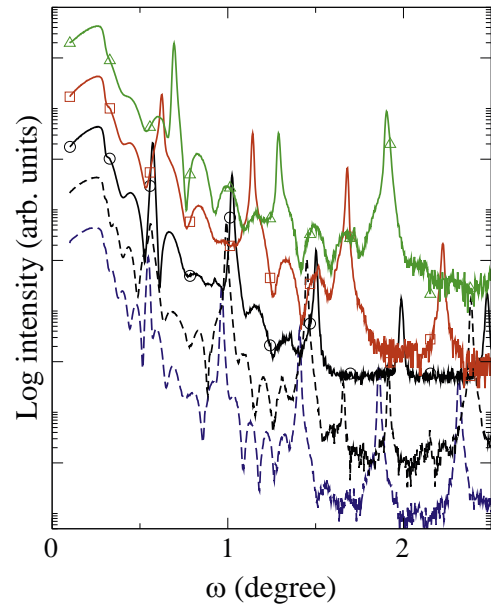
Fig. 4. X-ray reflectivity (XRR) spectra of the samples. From top to bottom, XRR spectra correspond to W:2.6, W:2.8, W:3.0, prev. a, prev. b. The data lines are offset for clarity.
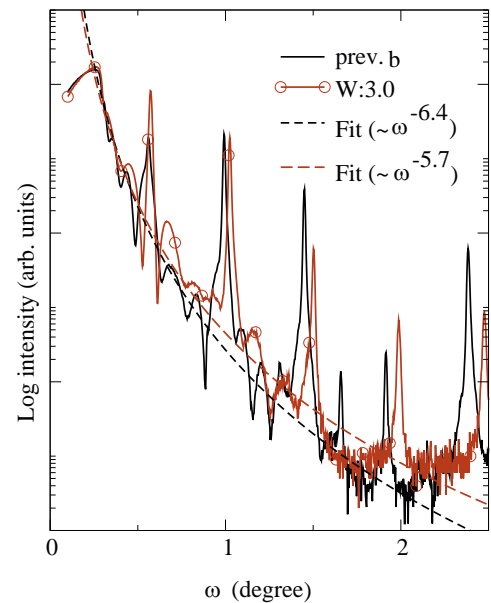
Fig. 5. X-ray reflectivity (XRR) spectra of prev. b and W:3.0 together with fitting results to ω^n.

acted as additional quantum states for holes [13]. Table 1 shows β values for W:3.0, prev. a, and prev. b, together with FWHM values of PL spectra at 77 K. This sample dependence of β values clearly indicates that W:3.0 exhibits the best radiative PL spectrum performance among the evaluated samples, although the absolute value of β was high. The FWHM values exhibit a sample dependence similar to that of the β values. Because tendency of FWHM linewidth and excitation power dependence was same for RT (not shown), PL spectra for all CDQW samples at RT were not discussed in this study.

To reveal interface quality of the CDQW samples, XRR measurements were performed. XRR can evaluate quantitatively electron density, thickness and roughness of thin layers on a flat substrate without any crystal information. Fig. 4 shows XRR spectra of all CDQW samples. There was no information of the thin layers for

incident angle narrower than critical angle around $0.3°$. When the incident angle was wider than the critical angle, reflected X-ray intensity (I_{X-ray}) decreased rapidly with oscillations. Periods and amplitudes of the oscillations corresponded to thickness of the

Table 2
Decay rates for X-ray reflectivity measurements.

Sample	W:2.6	W:2.8	W:3.0	prev. a	prev. b
Decay rate	−5.7	−5.8	−5.7	−6.2	−6.4

thin layer and electron density difference between the thin layers and interface roughnesses, respectively. Overall decay rate was related to overall interface roughness [14]. Oscillation periods between the largest peaks arose from one periods of the CDQW samples. Estimated one periods of all CDQW samples were agreed with those from XRD analysis. The amplitudes of the oscillations contained a lot of information. As a result, spectrum simulations were required to reveal the information. Because a model structure strongly affected the result of the spectrum simulations, overall interface roughness was evaluated by obtaining the decay rate of ($I_{X\text{-}ray}$). Fig. 5 shows an example of the evaluation for prev. b and W:3.0. The other samples were also evaluated under the same manner as shown in Fig. 5. The ideal decay rate was -4 ($I_{X-ray} \sim \omega^{-4}$). Additional decay clearly revealed that all samples had a rough interface structure. Thus, the absolute higher value of β might be attributed to this rough interface. Table 2 shows the decay rate ($I_{X-ray} \sim \omega^{-n}$) of I_{X-ray}. These values are divided into two groups. They are around -5.7 for CDQW samples with $CB_{AlAs/InAlAs}$ and -6.3 for CDQW samples having AlAsSb barrier, respectively. As previously mentioned Sb atoms interdiffused between layers and the interdiffusion caused rough interface [7]. The decay rates clearly reveal the rough interface due to the interdiffusion. On the other hand, FWHM value which could be strongly influenced by the rough interface dose not correspond to the decay rate for prev. a. This is because of the position of the rough interface. The superior decay rate, FWHM and β values of W:3.0 allow us to conclude that the CDQW samples with $CB_{AlAs/InAlAs}$ had the best crystal quality of all samples studied.

4. Conclusion

In this study, the crystal quality of CDQW samples with $CB_{AlAs/InAlAs}$ was investigated by evaluating their PL properties and the decay rates of XRR spectra. CDQW samples with $CB_{AlAs/InAlAs}$ showed a narrower PL emission compared with CDQW samples with an AlAsSb barrier. The excitation power dependence of the PL intensity of CDQW sample with the $CB_{AlAs/InAlAs}$ also indicated its superior radiative quality. Samples containing the AlAsSb barrier were found to have Sb-related states at the interface that degraded PL performance. The decay rates of XRR spectra clearly indicated inferior interface quality due to Sb interdiffusion. From these experimental findings, we can conclude that CDQW samples with $CB_{AlAs/InAlAs}$ have superior crystal quality relative to samples containing an AlAsSb barrier.

References

[1] H. Tsuchida, T. Simoyama, H. Ishikawa, T. Mozume, M. Nagase, J. Kasai, Opt. Lett. 32 (2007) 751.
[2] S. Gozu, T. Mozume, H. Ishikawa, J. Cryst. Growth 311 (2009) 1700.
[3] T. Kurosu, et al., OFC/NFOEC 2012, PDP5C.10.
[4] R Akimoto, H. Kuwatsuka, S. Gozu, T. Mozume, H. Ishikawa, ECOC 2012, We.2.E.6.
[5] S. Gozu, T. Mozume, H. Kuwatsuka, H. Ishikawa, J. Cryst. Growth 378 (2013) 134.
[6] S. Gozu, et al., Appl. Phys. Express 2 (2009) 042201.
[7] N. Georgiev, T. Mozume, J. Crst. Growth 209 (2000) 247.
[8] J. Kasai, T. Mozume, J. Cryst. Growth 278 (2005) 183.
[9] N. Georgive, T. Mozume, J. Appl. Phys. 89 (2001) 1064.
[10] T. Mozume, S. Gozu, Phys. Status Solidi C 9 (2012) 234.
[11] H. Sugawara, K. Itaya, M. Ishikawa, G. Hataoshi, Jpn. J. Appl. Phys. 31 (1992) 2446.
[12] I. Vurgaftman, J.R. Meyer, L.R. Ram-Mohan, J. Appl. Phys. 89 (2001) 5815.
[13] T. Mozume, N. Georgiev, Physica E 13 (2002) 361.
[14] T. Roch, et al., CEJP 5 (2007) 244.

CrossMark
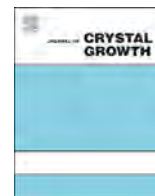
Suppression of photoluminescence from wetting layer of InAs quantum dots grown on (311)B GaAs with AlAs cap

X.M. Lu [a,*], S. Matsubara [a], Y. Nakagawa [a,b], T. Kitada [a], T. Isu [a]

[a] *Center for Frontier Research of Engineering, Institute of Technology and Science, Tokushima University, Tokushima 770-8506, Japan*
[b] *Nichia Corporation, Anan, Tokushima 774-8601, Japan*

ABSTRACT

Self-assembled InAs quantum dots (QDs), without and with an AlAs cap, were grown on (311)B GaAs substrates by molecular beam epitaxy. Surface morphologies of QDs were characterized by atomic force microscopy. Photoluminescence (PL) was performed in the 4–300 K temperature range. For QDs without AlAs cap, sharp and intense PL emitted from wetting layer was observed. PL from QDs was relatively weak at 4 K. The PL intensity of QDs decreased as measurement temperature increased and was not observed at 300 K. For QDs with AlAs cap, PL from WL vanished while PL from QDs were substantially enhanced at 300 K. Suppression of PL from WL indicates that the thickness of WL was reduced due to phase separation result from AlAs cap, which is an effective way to improve the PL of InAs QDs grown on (311)B GaAs substrate.

© 2015 Elsevier B.V. All rights reserved.

1. Introduction

In the past several decades, self-assembled quantum dots (QDs) have been extensively investigated because its three-dimensional quantum carrier confinement properties can provide new opportunities for novel device applications such as QD lasers [1] and quantum information processing [2]. QDs are the products of strain-induced hetero-epitaxial growth, in which the formation of QDs takes place after a thin elastically strained epitaxial wetting layer (WL). The WL plays a key role in carrier capture for QDs grown with SK mode. It is well established that most of carriers are firstly injected into WL from the barrier layers and then they are captured by QDs or recombine in the WL [3–6].

Many studies about InAs QDs grown by MBE have been concentrated on (100) GaAs substrates. However, potential advantages would also be offered by InAs QDs grown on high-index substrates, which are essential for terahertz emission devices based on the difference frequency generation (DFG) [7,8] because the effective second-order nonlinear coefficient is zero on the (100) orientation due to the crystal symmetry [9,10]. Several attempts have been taken on QDs grown on (311)B GaAs substrates. Photoluminescence (PL) from WL were observed in (311)B QDs either grown by MBE [11,12] or metal-organic chemical-vapor deposition (MOCVD) [13], while emission from WL were not observed in reference QDs samples grown on (100) GaAs in their research. In our previous study, PL from WL were

also observed for all (311)B QDs with different coverage of InAs [14]. The results indicated that carriers were easier recombined in WL other than captured by QDs. Therefore, it would be highly advantageous if we can explore a new growth method to suppress WL PL. A novel mechanism of QD formation have been proposed by V. Shchukin et al. [15]. The InAs WL can be reduced or even removed if an AlAs layer was deposited on the InAs QDs because of phase separation. Tutu et al. have found the absence of WL after depositing an AlAs cap layer over InAs QDs grown on (100) GaAs [16]. The phase separation are driven by the effects of wetting and non-wetting phenomenon which was defined by wetting constant. $\Phi_{BA} = \gamma_B^{surf} + \gamma_{BA}^{int} - \gamma_A^{surf}$. Here γ_B^{surf}, γ_{BA}^{int}, and γ_A^{surf} are surface energy of B, interface energies for B–A, and surface energy of A. $\Phi_{BA} < 0$ and $\Phi_{BA} > 0$ denoted wetting and non-wetting respectively. For AlAs/InAs/GaAs (100) system, InAs/GaAs is wetting ($\Phi_{InAs-GaAs} < 0$) but AlAs/GaAs is non-wetting ($\Phi_{AlAs-GaAs} > 0$). If a thin AlAs layer was deposited on InAs, InAs and AlAs will separate into local InAs-rich and AlAs-rich domains on the surface.

In this work, we investigated the influence of AlAs layer on the optical properties of InAs QDs grown on (311)B GaAs substrate. Surface morphologies of QDs were characterized by atomic force microscopy (AFM). The optical properties of QDs were investigated by PL. We have suppressed the PL from InAs WL by depositing AlAs cap on InAs QDs.

2. Experiments

Fig. 1 shows the epitaxial layer structure of InAs QDs with AlAs cap grown on (311)B GaAs substrate by Varian GEN-II MBE. InAs QDs

without AlAs cap were also grown on both (100) and (311)B GaAs as references. QDs with and without AlAs cap hereafter termed as QD-W and QD-W/O respectively. Native oxides on the GaAs substrates were removed by heating up to a substrate temperature (T_S) of 630 °C under As$_4$ atmosphere of 1.3×10^{-5} Torr. AlGaAs layer were introduced in order to prevent photoexcited carrier escape from the GaAs barrier layer to the substrate or surface. InAs QDs were grown at T_S of 500 °C with a coverage of 2.3 ML at a growth rate of 0.163 ML/s. Buried and surface QDs were grown under identical conditions for PL and AFM measurements, respectively.

Surface morphologies of the QDs were characterized by a tapping-mode AFM. The optical properties of buried QDs were investigated by PL using an excitation laser at a wavelength of 532 nm. Samples were mounted into a helium cryostat that allowed the temperature to be controlled in the range of 4–300 K. The PL spectra was dispersed by a spectrometer and detected by a liquid-nitrogen-cooled InGaAs photodiode array.

3. Results and discussion

Fig. 2(a) and (b) shows the PL (4 K) of QD-W/O grown on (100) and (311)B GaAs substrate, respectively. Only one strong PL peak assigned to QDs was observed for (100) QD-W/O as shown in Fig. 2(a). On the contrary, the PL spectrum of (311)B QD-W/O can be fitted by two Gaussian profiles as shown in Fig. 2(b). The broad long-wavelength one is related to the QD ensemble, whereas the sharp short-wavelength emission at 875 nm is attributed to the electron–hole recombination in the WL. Insets are the corresponding 1×1 μm^2 AFM images of surface QDs. The density of (100) QD-W/O is 4.1×10^{10} cm^{-2}, which is not larger than 3 times of (311)B QD-W/O of 1.8×10^{10} cm^{-2}. However, the integrated PL intensity of (100) QD-W/O is more than 6 times than that of (311)B QD-W/O indicating the inefficient capture of carriers in (311)B QD-W/O.

Fig. 3(a) shows the PL spectra measured from (311)B QD-W/O with various excitation power density at 4 K. The intensity of WL PL increased as excitation power density increased from 3 to 150 mW/cm^2. Moreover, as can be seen in Fig. 3(b), when the temperature increased from 4 to 140 K, the peak intensity of the QD decreased considerably while the WL emission intensity increased quickly.

Ohmori et al. [17] have observed that the intensity of PL from (100) QDs is smaller than that from WL as long as the QD density is less than 10^8 cm^{-2}, that is, the inter-dot distance is larger than 1 μm. It is because that carriers were firstly supplied to a zone of the WL which is within the diffusion length (L_D) from QDs in order to achieve an efficient injection into a specific QD. Otherwise, carriers will recombine in WL if they are further than L_D away from the QD. Note that the direct pathway of carriers from the barrier layer to QDs can be almost negligible for low-density QDs which cover an area smaller than WL. In our study, InAs QDs grown on (100) GaAs have the dot density of 4.1×10^{10} cm^{-2}. Therefore the carriers can be captured by QDs easily and the carriers trapped in WL is almost negligible. However, it is clearly not true for the InAs QDs grown on (311)B GaAs where intense PL peak from WL was observed, even (311)B QDs have a dot density of 1.8×10^{10} cm^{-2}. Considering that short L_D means strong WL PL and weak QD PL, we inferred that L_D is quite short for QDs grown on (311)B GaAs substrate.

Fig. 4(a) and (b) shows power and temperature dependence of (311)B QD-W. Compared with (311)B QD-W/O, a striking feature was observed that the WL PL disappeared while QDs PL emerged at varied excitation power density and temperature.

PL of (311)B QD-W/O and QD-W measured at 300 K are shown in Fig. 5. PL of WL and GaAs buffer were apparent around 865 and 920 nm, respectively. However, PL emission from QD was not
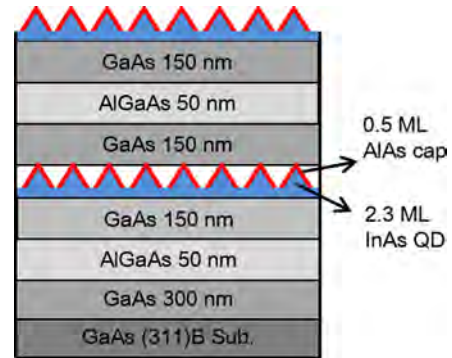
Fig. 1. Epitaxial layer structure of QDs grown on (311)B GaAs substrate. InAs QDs were grown at T_S of 500 °C with a coverage of 2.3 ML and then capped by 0.5 ML AlAs layer. Buried and surface QDs were grown under identical conditions for PL and AFM measurements, respectively.
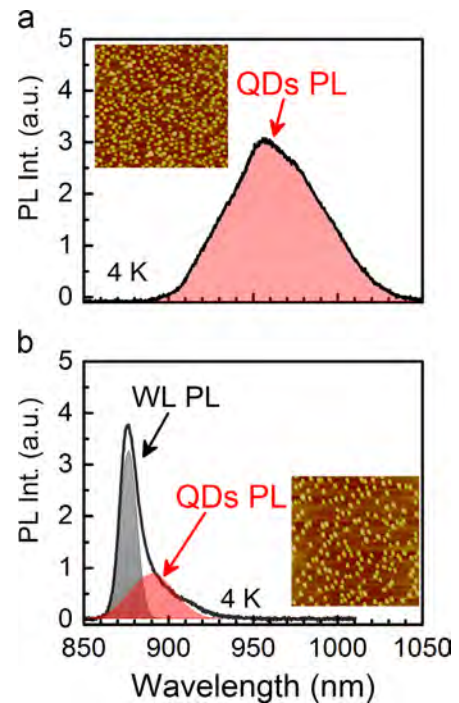
Fig. 2. PL of QDs without AlAs cap grown on (100) GaAs substrate (a) and (311)B GaAs substrate (b). The PL originated form WL of QDs grown on (311)B GaAs substrate can be seen in (b) at 875 nm. Insets show the corresponding 1×1 μm^2 AFM image of surface QDs.

observed. For (311)B QD-W, The WL PL disappeared and the PL from QDs is clearly observed. The vanishing of WL PL indicated that the thickness of WL was reduced due to phase separation. The probability of carrier recombination in WL was decreased because of reduction of WL. On the other hand, the chance of directly injecting carriers from barrier layer into QDs was increased. The results suggested that it is an effective way to suppress the PL from WL and to improve the PL of InAs QDs grown on (311)B GaAs substrate by an AlAs cap.

Several researches have reported that AlAs cap has a large influence on the structural and optical properties of QDs grown on (100) GaAs [18,19]. A small blue-shift has been observed when the AlAs thickness is increased from 3 to 5 ML [19], reflecting the effect of the higher potential barrier. However, such effect of ultra-thin (0.5 ML) AlAs cap can be neglected in our case. Therefore, the substantially enhanced PL of InAs QDs can be regarded as the result of reduction of WL. It is reasonable to inferred that the phase separation in AlAs/InAs/GaAs(100) [15] also occurred in
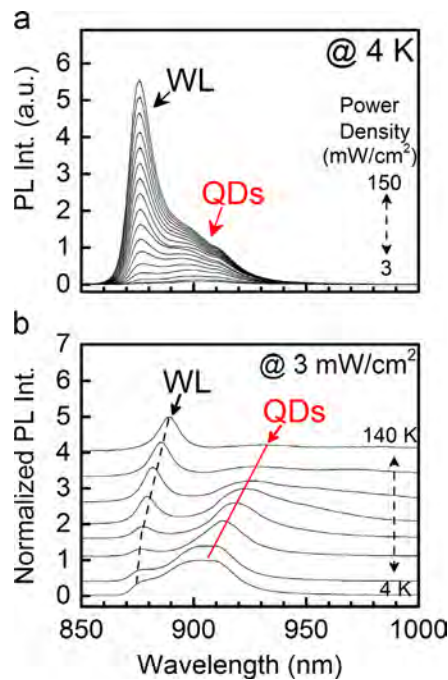
Fig. 3. Power (a) and temperature (b) dependence of PL of QDs without AlAs cap grown on (311)B GaAs substrate. Although the intensity of WL PL decrease with power density decreasing as shown in (a), it increased as the temperature was increased as shown in (b).
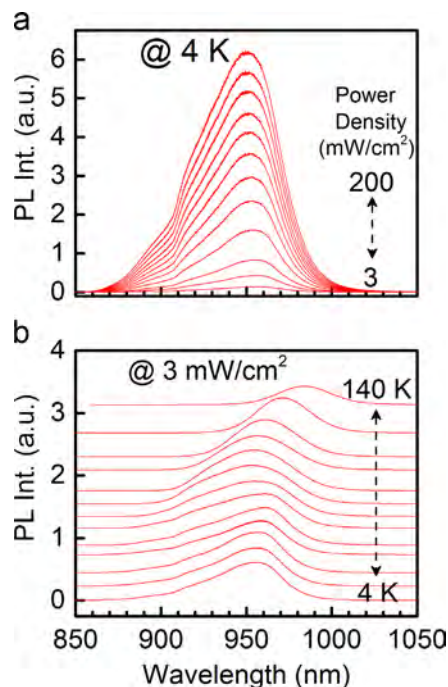
Fig. 4. Power (a) and temperature (b) dependence of PL of QDs with 0.5 ML AlAs cap grown on (311)B GaAs substrate. The PL originated from WL vanished.

AlAs/InAs/GaAs(311)B system. InAs/GaAs(311)B is wetting but AlAs/GaAs(311)B is non-wetting, that is, $\Phi_{InAs-GaAs} < 0$ and $\Phi_{AlAs-GaAs} > 0$. However, it should be noted that larger surface migration of Ga adatoms and longer surface segregation length of In atoms on high-index GaAs [20] could affect the numerical value of $\Phi_{InAs-GaAs}$ and $\Phi_{AlAs-GaAs}$ on (311)B GaAs substrate.
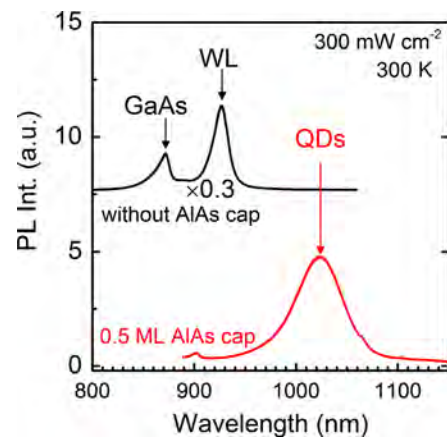
Fig. 5. PL of (311)B QDs without and with AlAs cap measured at 300 K. The excitation power density is 300 mW/cm^{-2}.

4. Summary

We have investigated self-assembled InAs QDs, without and with an AlAs cap, grown on (311)B GaAs substrate by molecular beam epitaxy. AlAs cap were introduced to suppress the WL PL. Surface morphologies of QDs were characterized by AFM. PL measurements were performed in 4–300 K temperature range. For QDs without AlAs cap, sharp and intense PL emitted from wetting layer was observed at 4 K. PL from QDs was relatively weak around 900 nm and was not observed at 300 K. For QDs with AlAs cap, PL from WL was vanished with varied excitation power and temperature. Moreover, the PL from QDs were observed from 4 to 300 K. Suppression of PL from WL indicates that the thickness of WL was reduced due to phase separation result from AlAs cap, which is an effective way to improve the PL of InAs QDs grown on (311)B GaAs substrate.

Acknowledgments

References

[1] Y. Arakawa, H. Sakaki, Multidimensional quantum well laser and temperature dependence of its threshold current, Appl. Phys. Lett. 40 (1982) 939. http://dx.doi.org/10.1063/1.92959.

[2] A. Imamoglu, D.D. Awschalom, G. Burkard, D.P. DiVincenzo, D. Loss, M. Sherwin, A. Small, Quantum information processing using quantum dot spins and cavity QED, Phys. Rev. Lett. 83 (1999) 4204–4207. http://dx.doi.org/10.1103/PhysRevLett.83.4204.

[3] A.V. Uskov, J. McInerney, F. Adler, H. Schweizer, M.H. Pilkuhn, Auger carrier capture kinetics in self-assembled quantum dot structures, Appl. Phys. Lett. 72 (1998) 58. http://dx.doi.org/10.1063/1.120643.

[4] D.R. Matthews, H.D. Summers, P.M. Smowton, P. Blood, P. Rees, M. Hopkinson, Dynamics of the wetting-layer-quantum-dot interaction in InGaAs self-assembled systems, IEEE J. Quantum Electron 41 (2005) 344–350. http://dx.doi.org/10.1109/JQE.2004.841275.

[5] T.S. Shamirzaev, D.S. Abramkin, A.V. Nenashev, K.S. Zhuravlev, F. Trojánek, B. Dzurnák, P. Malý, Carrier dynamics in InAs/AlAs quantum dots: lack in carrier transfer from wetting layer to quantum dots, Nanotechnology 21 (2010) 155703. http://dx.doi.org/10.1088/0957-4484/21/15/155703.

[6] M. Syperek, M. Baranowski, G. Sęk, J. Misiewicz, A. Löffler, S. Höfling, S. Reitzenstein, M. Kamp, A. Forchel, Impact of wetting-layer density of states on the carrier relaxation process in low indium content self-assembled (In,Ga)As/GaAs quantum dots, Phys. Rev. B 87 (2013) 125305. http://dx.doi.org/10.1103/PhysRevB.87.125305.

[7] T. Kitada, F. Tanaka, T. Takahashi, K. Morita, T. Isu, GaAs/AlAs coupled multi-layer cavity structures for terahertz emission devices, Appl. Phys. Lett. 95 (2009) 111106. http://dx.doi.org/10.1063/1.3226667.

[8] T. Kitada, S. Katoh, T. Takimoto, Y. Nakagawa, K. Morita, T. Isu, Terahertz waveforms generated by second-order nonlinear polarization in GaAs/AlAs

coupled multilayer cavities using ultrashort laser pulses, IEEE Photonics J. 5 (2013) 6500308. http://dx.doi.org/10.1109/JPHOT.2013.2267536.

[9] N. Yamada, Y. Ichimura, S. Nakagawa, Y. Kaneko, T. Takeuchi, N. Mikoshiba, Second-harmonic generation in vertical-cavity surface-emitting laser, Jpn. J. Appl. Phys. 35 (1996) 2659. http://dx.doi.org/10.1143/JJAP.35.2659.

[10] Y. Kaneko, S. Nakagawa, Y. Ichimura, N. Yamada, D.E. Mars, T. Takeuchi, Blue vertical-cavity surface-emitting lasers based on second-harmonic generation grown on (311)B and (411)A GaAs substrates, J. Appl. Phys. 87 (2000) 1597. http://dx.doi.org/10.1063/1.372065.

[11] K. Nishi, R. Mirin, D. Leonard, G. Medeiros-Ribeiro, P.M. Petroff, A.C. Gossard, Structural and optical characterization of InAs/InGaAs self-assembled quantum dots grown on (311)B GaAs, J. Appl. Phys. 80 (1996) 3466. http://dx.doi.org/10.1063/1.363216.

[12] Q. Gong, R. Nötzel, J.H. Wolter, Strain-driven (In,Ga)As growth instability on GaAs (311)A and (311)B: self-organization of template for InAs quantum dot nucleation control, J. Cryst. Growth 251 (2003) 150–154. http://dx.doi.org/10.1016/S0022-0248(02)02387-4.

[13] C. Lobo, N. Perret, D. Morris, J. Zou, D.J.H. Cockayne, M.B. Johnston, M. Gal, R. Leon, Carrier capture and relaxation in Stranski-Krastanow $In_xGa_{1-x}As/As$ GaAs (311)B quantum dots, Phys. Rev. B 62 (2000) 2737–2742. http://dx.doi.org/10.1103/PhysRevB.62.2737.

[14] T. Takahashi, T. Mukai, K. Morita, T. Kitada, T. Isu, Photoluminescence properties of self-assembled InAs quantum dots grown on (001) and (113)B GaAs substrates by molecular beam epitaxy under a slow growth rate condition, Jpn. J. Appl. Phys. 48 (2009) 04C128. http://dx.doi.org/10.1143/JJAP.48.04C128.

[15] V. Shchukin, N. Ledentsov, S. Rouvimov, Formation of three-dimensional Islands in subcritical layer deposition in Stranski–Krastanow growth, Phys. Rev. Lett. 110 (2013) 176101. http://dx.doi.org/10.1103/PhysRevLett.110.176101.

[16] F.K. Tutu, P. Lam, J. Wu, N. Miyashita, Y. Okada, K.-H. Lee, N.J. Ekins-Daukes, J. Wilson, H. Liu, InAs/GaAs quantum dot solar cell with an AlAs cap layer, Appl. Phys. Lett. 102 (2013) 163907. http://dx.doi.org/10.1063/1.4803459.

[17] M. Ohmori, P. Vitushinskiy, H. Sakaki, Diffusion process of excitons in the wetting layer and their trapping by quantum dots in sparsely spaced InAs quantum dot systems, Appl. Phys. Lett. 98 (2011) 133109. http://dx.doi.org/10.1063/1.3574080.

[18] F. Ferdos, S. Wang, Y. Wei, M. Sadeghi, Q. Zhao, A. Larsson, Influence of initial GaAs and AlAs cap layers on InAs quantum dots grown by molecular beam epitaxy, J. Cryst. Growth 251 (2003) 145–149. http://dx.doi.org/10.1016/S0022-0248(02)02471-5.

[19] M. Arzberger, U. Käsberger, G. Böhm, G. Abstreiter, Influence of a thin AlAs cap layer on optical properties of self-assembled InAs/GaAs quantum dots, Appl. Phys. Lett. 75 (1999) 3968. http://dx.doi.org/10.1063/1.125509.

[20] T. Kitada, S. Shimomura, S. Hiyamizu, Surface segregation of indium atoms during molecular beam epitaxy of InGaAs/GaAs superlattices on (n11)A GaAs substrates, J. Cryst. Growth 301–302 (2007) 172–176. 10.1016/j.jcrysgro.2006.11.170.
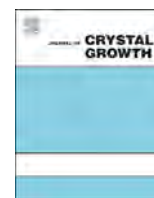
Monolayer-by-monolayer compositional analysis of InAs/InAsSb superlattices with cross-sectional STM

M.R. Wood [a,*], K. Kanedy [a], F. Lopez [a], M. Weimer [a], J.F. Klem [b], S.D. Hawkins [b], E.A. Shaner [b], J.K. Kim [b]

[a] Department of Physics and Astronomy, Texas A&M University, College Station, TX 77843, United States
[b] Sandia National Laboratories, Albuquerque, NM 87185, United States

ARTICLE INFO

ABSTRACT

We use cross-sectional scanning tunneling microscopy (STM) to reconstruct the monolayer-by-monolayer composition profile across a representative subset of MBE-grown InAs/InAsSb superlattice layers and find that antimony segregation frustrates the intended compositional discontinuities across both antimonide-on-arsenide and arsenide-on-antimonide heterojunctions. Graded, rather than abrupt, interfaces are formed in either case. We likewise find that the incorporated antimony per superlattice period varies measurably from beginning to end of the multilayer stack. Although the intended antimony discontinuities predict significant discrepancies with respect to the experimentally observed high-resolution x-ray diffraction spectrum, dynamical simulations based on the STM-derived profiles provide an excellent quantitative match to all important aspects of the x-ray data.

© 2015 Elsevier B.V. All rights reserved.

1. Introduction

It has been recognized for some time that type-II superlattices based on the GaSb/InAs system might hold distinct advantages over HgCdTe in long-wave-infrared detector applications [1]. For many years, research attention focused largely on the non-common-atom binary materials, and their closely-related, ternary variant InAs/Ga(In)Sb, despite early recognition of the potential offered by a simpler, common-atom analog, namely InAs/InAsSb [2]. With the recent demonstration that InAs/InAsSb superlattices exhibit minority carrier lifetimes up to two orders of magnitude greater [3,4] than those observed in InAs/Ga(In)Sb [5,6], there has been renewed interest in the prospects for competitive devices built from this material.

The deliberate tailoring of optical transitions in these, and similar, quantum-confined structures typically relies on theoretical or empirical paradigms whose predictive utility is judged against assumed (intended) rather than empirically determined (as-grown) constituent-layer sequences. Accurate knowledge concerning the as-grown atomic arrangements responsible for the confining potentials that make these structures unique is rarely available.

Here, we show how atomic-resolution scanning tunneling microscopy (STM) may be used to reconstruct the monolayer-by-monolayer

composition profile throughout one such structure, an $InAs_{0.67}Sb_{0.33}$ strained-layer superlattice (Fig. 1), following cleavage in ultra-high vacuum (UHV). We also show how STM may be used to quantify the changes in superlattice composition as growth progresses from beginning to end by selectively examining a subset of periods at various points along the multilayer stack. Finally we demonstrate these results are globally representative by comparing x-ray simulations based on the STM findings to high-resolution x-ray diffraction (HRXRD) data from the same wafer.
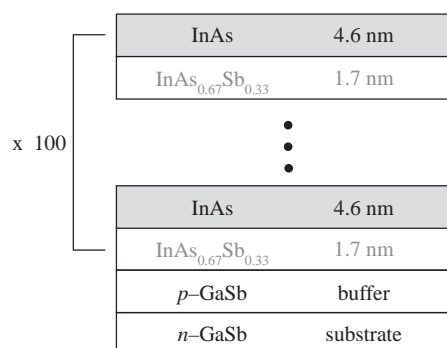
Fig. 1. Intended superlattice layer sequence. Growth direction is from bottom to top.

* Corresponding author. Tel.: +1 979 845 7815.
  E-mail address: mrwood@physics.tamu.edu (M.R. Wood).
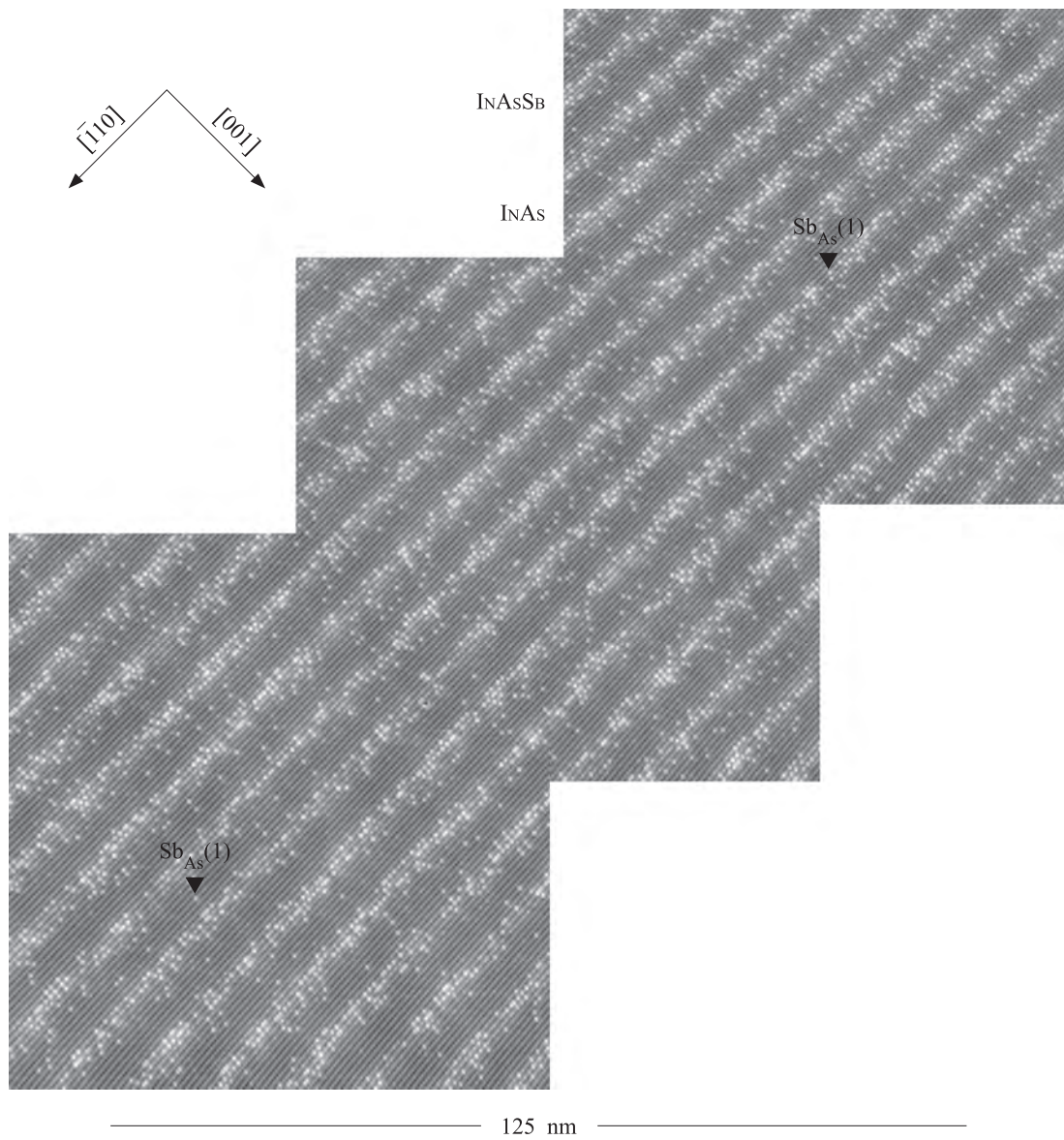
Fig. 2. Anion images from a large-area STM survey of superlattice periods 73–84. Antimony-for-arsenic replacement within the top-layer, cleavage-exposed plane is identified by carets. Growth direction is from top left to bottom right.

2. Experimental details

Epitaxial growth of the superlattice shown in Fig. 1 was carried out by solid-source molecular beam epitaxy at Sandia National Laboratories. The layers were deposited on a (001)–oriented GaSb substrate under an anion overpressure[1] of ∼1.5:1 and growth rate of 0.9 monolayers/s (ML/s). The substrate was held at approximately 420 °C and rotated continuously throughout deposition. Subsequent HRXRD examination of the (004) reflections in a triple-axis configuration revealed a period of 6.28 nm (corresponding to 20.6 ML) and substrate mismatch of −0.05% following analysis of nine superlattice satellite orders.

Select dies from this wafer were transferred to a dedicated UHV–STM system, with base pressures below 1E-13 Torr for all reactive species save hydrogen (at the 1E-11 Torr level), where the completed structure was exposed in cross section by cleavage along (1$\bar{1}$0) or (110) planes. Precise position control allowed placement of an STM tip above any desired subset of layers from the 100-period stack as well as navigation across the entire structure in the [001] growth direction and up to a micron in the orthogonal ⟨110⟩ direction.

Large-area surveys were assembled from overlapping atomic-resolution images along periods near the initiation and completion of growth for multiple locations on the substrate wafer. Fig. 2 shows a representative portion of one such survey, obtained with negative sample bias to image the filled-state densities associated with As and Sb. Isovalent replacement of arsenic with antimony at the cleavage-exposed surface is unmistakably pinpointed here by the change in covalent radius and back-bond length attending any such non-native, InSb-like pairing. As we will see shortly, the evident intermixing along each and every interface is due to segregation of vapor-deposited antimony atoms.

To facilitate compilation of the requisite bulk antimony profile, a counting window extending 62 surface monolayers in the growth direction, thus encompassing 6 repeats of the bulk superlattice period, was overlaid on each image of the survey. The ⟨110⟩ width of these

---
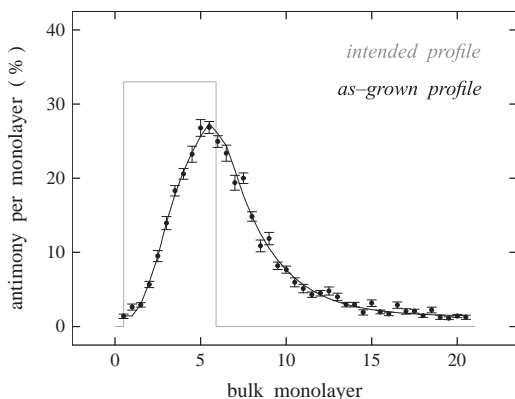
Fig. 3. Intended antimony profile (gray), with compositionally abrupt interfaces, contrasted against the compositionally-graded as-grown profile (black) reconstructed from STM. The data (assembled, here, from superlattice periods 76–81) exhibits exponential growth, and subsequent decay, consistent with antimony segregation; detailed fit likewise includes constant background incorporation.

windows was chosen to maximize counting statistics yet avoid double counting due to the overlap of adjoining STM images from the survey mosaic. It is a straightforward matter to then count the number of top-layer Sb sites within each surface atomic row (whose identification across the entire mosaic is preserved by careful spatial alignment of each image relative to its neighbors)—and normalize this count to the total number of anion sites sampled in all windows—to obtain an antimony fraction versus surface monolayer and corresponding binomial error.

3. Results and discussion

Reconstruction of the bulk composition profile from the surface samplings obtained with STM follows a well-defined algorithm for the case of zincblende {110} facets. The distinction between surface and bulk identified here arises because only every second bulk (001) anion plane actually projects dangling bonds into the vacuum following cleavage. Any single surface sampling of the bulk period therefore represents, at best, every other plane of the bulk anion layer sequence. It is, in fact, this very phenomenon that underlies the factor of two disparity between surface-and bulk-monolayer counts per period in Fig. 2. Whenever the bulk period is even-integer valued, this under sampling recurs with each surface repeat. For bulk periods that adopt odd-integer values, on the other hand, two sequential surface samplings suffice to sample every bulk monolayer once, revealing even and odd anion subsequences of the complete bulk profile in turn. The general principle may be recognized as a strobing of the bulk by the surface, whose surface period is dictated by commensurability of the bulk period with an integer number of surface monolayers. For bulk periods with a rational fraction remainder, this commensurability is still guaranteed, but its rigorous fulfillment may be experimentally inaccessible due to the large number of surface monolayers required. Given a 20.6 bulk monolayer period, for example, strict commensurability occurs every 103 surface monolayer samplings (or ten surface repeats), well beyond our accessible counting window. Simply approximating the period by 20.5 monolayers, on the other hand, reduces that requirement to 41 surface monolayers, or four surface repeats.[2]

The as-grown antimony profile reconstructed by a systematic fold back[3] of the six (four minimum plus two additional) surface repeats sampled with STM for nearly three-quarters of a micron along the
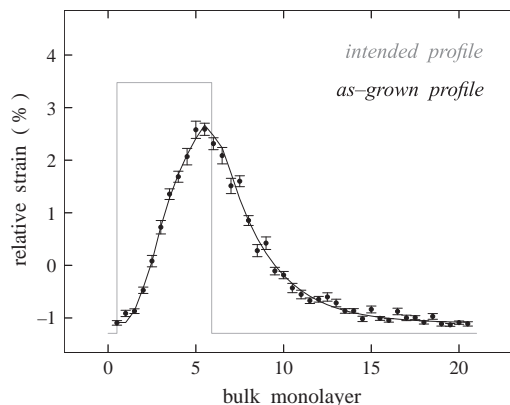
Fig. 4. Inferred bulk strain along the [001] growth direction directly mirrors the composition profile shown in Fig. 3.

⟨110⟩ direction is plotted in Fig. 3, where it is compared against the intended profile for a single bulk period. The reconstructed data display an exponential-like growth in the incorporated antimony fraction at the antimonide-on-arsenide interface, followed by a corresponding exponential-like decay at the arsenide-on-antimonide interface. Both are qualitatively consistent with antimony segregation.

To conclusively establish segregation as the physical mechanism behind the compositional grading observed along both interfaces, we fit the data in Fig. 3 to a continuum generalization (solid black line) of a standard segregation model originally formulated by Muraki et al. [7], and previously employed to quantitatively describe antimony segregation in GaInSb/InAs superlattices [8]. The essential features of this model are embodied in Eq. (1), where x_{ss} represents the steady-state antimony fraction, z a continuously-varying coordinate along the growth direction, d the (arbitrary) duration (in monolayers) of a (presumed) spatially-invariant antimony exposure, Λ the superlattice period, and R the corresponding segregation coefficient, equivalently parameterized in terms of a segregation length λ[4]. The discrete Muraki model is recovered when z and d are restricted to integer values and the spatially invariant offset introduced by background incorporation (represented here by x_o) is neglected

$$x(z) = x_{ss}\left(1 - R^z\right) + x_o \quad 0 < z \le d$$
$$x(z) = x_{ss}\left(1 - R^d\right)R^{z-d} + x_o \quad d < z \le \Lambda$$
$$R = \exp(-1/\lambda) \tag{1}$$

A presumed boundary condition of the Muraki model, necessarily abandoned in Ref.[8] but imposed here in Eq. (1), is that a floating layer established atop the arsenide-on-antimonide interface by antimony segregation during vapor deposition ($0 < z \le d$) supplies the seed for subsequent segregation throughout the remainder of the period.[5]

Fig. 4 shows the monolayer-by-monolayer strain accompanying the compositional grading in Fig. 3. This strain profile serves as an important touch point for alternative characterization techniques, such as TEM [9] (which measures strain in order to infer composition), and likewise enters into various calculations of superlattice optical properties [10]. It directly mirrors the antimony fraction in Fig. 3 on account of a near degeneracy [11] in InAs and InSb Poisson ratios that, in turn, causes the [001] lattice constant of coherently-strained InAsSb on GaSb to depend (nearly) linearly on composition.

---

[2] It is worth pointing out that the commensurability number attending a bulk period of 20 3/5 (103) versus 20 1/2 (41) MLs is odd in either case.

[3] This fold back entails assigning a bulk index = 2 ● surface index modulo ($n-1$) ● superlattice period to each surface layer from the nth (observed) surface repeat.

[4] Eq. (1) may be further generalized to accommodate substrate vicinality by adding another, spatially-abrupt source term representing a second terrace. When the z-offset between terraces is left free to vary it naturally settles at one monolayer, providing the accurate fit shown in Fig. 3.

[5] The segregation coefficient and cross-incorporated background so obtained nevertheless appear reasonable in light of Ref. [8].
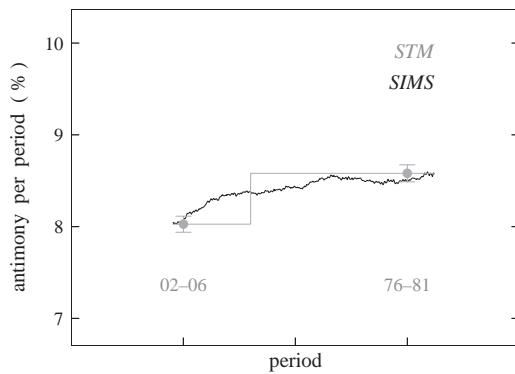
Fig. 5. Total antimony per period from early- and late-period STM surveys (gray points) agrees, here, with the antimony depth profile obtained from SIMS (black line). A piecewise-constant approximation to this continuously-varying depth profile that matches both the mean antimony per period as well as the asymptotic STM data (gray line) is employed for x-ray simulation.

As already noted, controlled navigation across the entire multi-layer stack illustrated in Fig. 1 is easily achieved with STM. Comparison of early-, middle-, and late-period surveys from distinct cleaves at multiple locations on the same wafer reveals an increase in the incorporated antimony per period from beginning to end in each case. This is illustrated for one particular instance in Fig. 5, where an approximately 7% increase distinguished the total change between initiation and termination of growth.[6] A small piece from a remote location on the wafer was subsequently selected for depth profiling with secondary ion mass spectrometry (SIMS). These SIMS data[7] are likewise plotted in Fig. 5—here as a moving average over 9 periods—and they support the STM results on this point.

A convincing argument that the monolayer-by-monolayer composition profile and evolving substrate mismatch reconstructed with STM are indeed characteristic of the superlattice as a whole may be made by appealing to dynamical x-ray simulations. Fig. 6 contrasts the anticipated HRXRD spectrum, assuming abrupt interfaces and compositional uniformity throughout the structure, with the experimental facts. Predicted and observed satellite peak locations agree, demonstrating the as-grown period and mismatch are close to their intended values, but predicted and observed peak intensities differ by up to two orders of magnitude bringing the assumed structure into question. In addition to this conspicuous quantitative discrepancy, the assumed structure likewise fails to capture the evident broadening at the base of each satellite peak.

Adopting the fit in Fig. 3 to include segregation and cross incorporation, together with the piecewise constant approximation in Fig. 5 to include the evolution in antimony incorporation during growth, decisively remedies both these deficiencies of the intended structure. As seen in Fig. 7, the resulting HRXRD spectrum accurately accounts for every significant feature of the x-ray data, including satellite peak intensities, peak widths, and overall background.

4. Conclusions

Large-area, atomic-resolution STM surveys over subsets of the full layer sequence comprising an MBE-grown InAs/InAsSb superlattice have established the existence of compositional grading at both the antimonide-on-arsenide and aresenide-on-antimonide heterojunctions. Detailed fits to a standard segregation model pinpoint the
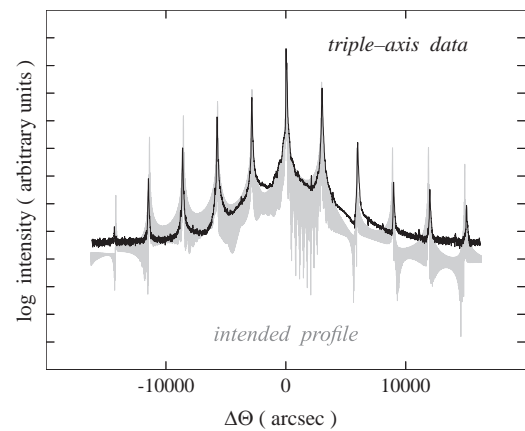
Fig. 6. Dynamical x-ray simulation (gray)—normalized to the observed substrate peak intensity—assuming the intended composition profile shown in Fig. 3, as well as uniform antimony-per-period throughout the superlattice. Comparison with the experimental HRXRD spectrum (black) reveals the assumed structure provides a comparatively poor global description of the x-ray data.
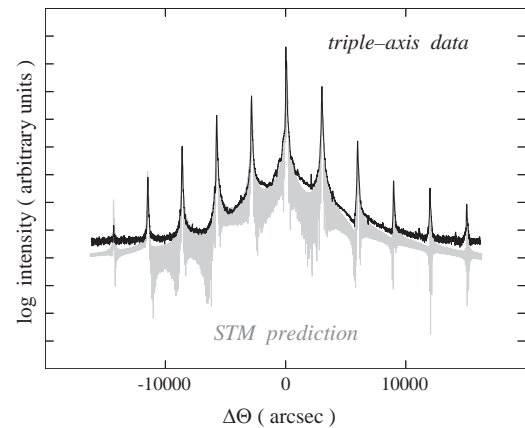
Fig. 7. Dynamical x-ray simulation (gray)—again normalized to the observed substrate peak intensity—assuming the as-grown profile deduced from STM in Fig. 3, as well as the piecewise-constant total antimony-per-period illustrated in Fig. 5. Comparison with the experimental HRXRD spectrum (black) demonstrates this structure provides an excellent global description of the observed x-ray mismatch, satellite peak intensities, peak widths, and overall background.

physical origin of this compositional grading as a combination of antimony segregation and background incorporation that, in turn, produces exponentially-increasing or exponentially-decreasing antimony fractions across the respective interfaces. Cross-sectional STM also reveals a systematic increase in the incorporated antimony per period from beginning to end of the multilayer stack that is independently confirmed with SIMS. Dynamical x-ray simulations that take into account the compositional grading observed with STM, as well as the evolution in substrate mismatch occasioned by variable antimony per period, provide a convincingly accurate match to the full, as-grown HRXRD spectrum. Since this compositional grading exerts a similarly pronounced influence on local strain and band structure, one may reasonably expect such as-grown profiles to play an equally important part in the reliable prediction of superlattice optical properties.

---

[6] Comparable measurements at different locations on the wafer yield somewhat larger variations.
[7] Evans Analytical Group.

References

[1] D.L. Smith, C. Mailhiot, Proposal for strained type II superlattice infrared detectors, J. Appl. Phys. 62 (1987) 2545–2548 http://dx.doi.org/10.1063/1.339468.

[2] Y.–H. Zhang, Continuous wave operation of InAs/InAs$_{(x)}$Sb$_{(1-x)}$ midinfrared lasers, Appl. Phys. Lett. 66 (1995) 118 http://dx.doi.org/10.1063/1.113535.

[3] B.V. Olson, E.A. Shaner, J.K. Kim, J.F. Klem, S.D. Hawkins, L.M. Murray, J.P. Prineas, M.E. Flatte, T.F. Boggess, Time-resolved optical measurements of minority carrier recombination in a mid-wave infrared InAsSb alloy and InAs/InAsSb superlattice, Appl. Phys. Lett. 101 (2012) 092109 http://dx.doi.org/10.1063/1.4749842.

[4] E.H. Steenbergen, B.C. Connelly, G.D. Metcalfe, H. Shen, M. Wraback, D. Lubyshev, Y. Qiu, J.M. Fastenau, A.W.K. Liu, S. Elhamri, O.O. Cellek, Y.-H. Zhang, Significantly improved minority carrier lifetime observed in a long-wavelength infrared III–V type-II superlattice comprised of InAs/InAsSb, Appl. Phys. Lett. 99 (2011) 251110 http://dx.doi.org/10.1063/1.3671398.

[5] B.C. Connelly, G.D. Metcalfe, H. Shen, M. Wraback, Direct minority carrier lifetime measurements and recombination mechanisms in long-wave infrared type II superlattices using time-resolved photoluminescence, Appl. Phys. Lett. 97 (2010) 251117 http://dx.doi.org/10.1063/1.3529458.

[6] D. Donetsky, S.P. Svensson, L.E. Vorobjev, G. Belenky, Carrier lifetime measurements in short-period InAs/GaSb strained-layer superlattice structures, Appl. Phys. Lett. 95 (2009) 212104 http://dx.doi.org/10.1063/1.3267103.

[7] K. Muraki, S. Fukatsu, Y. Shiraki, R. Ito, Surface segregation of In atoms during molecular beam epitaxy and its influence on the energy levels in InGaAs/GaAs quantum wells, Appl. Phys. Lett. 61 (1992) 557–559 http://dx.doi.org/10.1063/1.107835.

[8] J. Steinshnider, J. Harper, M. Weimer, C.-H. Lin, S.S. Pei, D.H. Chow, Origin of antimony segregation in GaInSb/InAs strained-layer superlattices, Phys. Rev. Lett. 85 (2000) 4562–4565 http://dx.doi.org/10.1103/PhysRevLett.85.4562.

[9] K. Mahalingam, E.H. Steenbergen, G.J. Brown, Y.-H. Zhang, Quantitative analysis of strain distribution in InAs/InAs$_{(1-x)}$Sb$_x$ superlattices, Appl. Phys. Lett. 103 (2013) 061908 http://dx.doi.org/10.1063/1.4817969.

[10] Y. Sun, S.E. Thompson, T. Nishida, Strain Effect in Semiconductors: Theory and Device Applications, Springer Science & Business Media, New York (2009) 291 http://dx.doi.org/10.1007/978-1-4419-0552-9.

[11] S. Adachi, Properties of Group-IV, III–V and II–VI Semiconductors, Wiley, West Sussex England (2005) 56 http://dx.doi.org/10.1002/0470090340.

[12] S. Stepanov, Dynamical x-ray diffraction from multilayers on the web, ⟨http://x-server.gmca.aps.anl.gov/GID_sl.html⟩, 2014, accessed October .
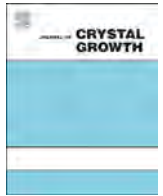
Low-temperature growth of InGaN films over the entire composition range by MBE

CrossMark

Chloe A.M. Fabien [a], Brendan P. Gunning [a], W. Alan Doolittle [a,*], Alec M. Fischer [b], Yong O. Wei [b], Hongen Xie [b], Fernando A. Ponce [b]

[a] School of Electrical and Computer Engineering, Georgia Institute of Technology, Atlanta, GA 30332, USA
[b] Department of Physics, Arizona State University, Tempe, AZ 85281, USA

ABSTRACT

The surface morphology, microstructural, and optical properties of indium gallium nitride (InGaN) films grown by plasma-assisted molecular beam epitaxy under low growth temperatures and slightly nitrogen-rich growth conditions are studied. The single-phase InGaN films exhibit improved defect density, an absence of stacking faults, efficient In incorporation, enhanced optical properties, but a grain-like morphology. With increasing In content, we observe an increase in the degree of relaxation and a complete misfit strain relaxation through the formation of a uniform array of misfit dislocations at the InGaN/GaN interface for InGaN films with indium contents higher than 55–60%.

© 2015 Published by Elsevier B.V.

1. Introduction

The ternary indium gallium nitride (InGaN) alloy system is of great interest for optoelectronics applications due to its direct band gap varying from 0.65 to 3.42 eV and thus, spanning the entire visible to near-infrared spectrum [1]. However, the epitaxial growth of InGaN over the entire composition range faces many issues such as (i) the lack of appropriate substrates, which leads to dislocation formation [2], (ii) the control of In incorporation, which depends on the growth chemistry and temperature [3], and (iii) the miscibility gap between InN and GaN, which results in phase separation [4].

A precise control and optimization of the III/N ratio and the growth temperature is required to obtain single-phase, high-quality InGaN films. The growth of single-phase InGaN by molecular beam epitaxy (MBE) has been previously reported using various approaches [5–8]. Metal-rich growth favors a 2D growth mode, which promotes smoother surfaces but results in compositional alloy fluctuations and high threading dislocation densities [5,6]. On the other hand, N-rich growth leads to more uniform InGaN alloys but reduces surface adatom mobility, resulting in 3D growth mode and grain-like morphology [6–8]. The structural and optical properties of InGaN films also strongly depend on growth temperature [9]. An optimized growth temperature must account for a tradeoff between enhanced compositional homogeneity and In incorporation at low temperatures and improved surface morphology and threading dislocation density at high temperatures.

In order to take advantage of both metal-rich and N-rich conditions, several modulated growth methods have been studied [10,11]. Metal-modulated epitaxy (MME), a growth technique that uses constant N flux, shuttered Ga and In fluxes under metal-rich conditions, and extremely low substrate temperatures (400–450 °C), has enabled the growth of InGaN films throughout the miscibility gap [12,13]. While the moderate In-content films (22–46% InGaN) display high density of dislocations and stacking faults, InGaN films with In content higher than 60% exhibit a significant improvement in the crystalline quality and optical properties due to a complete misfit strain relaxation through the formation of a uniform array of misfit dislocations at the InGaN/GaN interface [14]. However, it is unclear whether this complete misfit strain relaxation originates from (i) the fundamental lattice mismatch between In-rich InGaN films and GaN, (ii) the MME growth technique, or (iii) the use of low temperatures. In this work, we report on the growth of InGaN films over the entire composition range under very low growth temperatures and slightly N-rich growth conditions.

2. Experiments

The InGaN films were grown in a Riber 32 MBE system using a standard effusion cell for In, a Veeco SUMO cell for Ga, and a Veeco Unibulb plasma source for N. Lumilog MOCVD-grown GaN (0 0 0 1) templates on sapphire were used as substrates and were backside metallized with tantalum to enable radiative heating. Substrates were

degreased in H_2SO_4:H_2O_2 (4:1) and outgassed in the introductory chamber at 150 °C for 30 min. A ~130 nm GaN buffer was grown at 600 °C via MME to bury the native surface oxide.

InGaN growth was performed at various low growth temperatures (360–450 °C) depending on the targeted compositions. All InGaN films were grown under N-rich conditions using a constant III/N ratio of ~0.9 with group-III fluxes normalized by Z-number to account for differences in ion-gauge sensitivity between In and Ga. The In/(Ga+In) ratio was varied to obtain InGaN alloys over the entire composition range. Nitrogen flow rate and RF-plasma power were set at 1.3 sccm and 350 W, respectively. The growth rate was ~1 μm/h and the nominal InGaN film thickness was 55 nm. The InGaN layers were then capped with a ~10 nm GaN film to prevent thermal decomposition of the surface upon cool down.

The growth of the InGaN films was monitored in situ by reflection high-energy electron diffraction (RHEED). The structural properties of the samples were characterized by X-ray diffraction (XRD) including 2θ–ω diffraction scans, ω rocking curves, and reciprocal space maps (RSM). The surface morphology, microstructural, and optical properties of all these samples were analyzed by atomic force microscopy (AFM), transmission electron microscopy (TEM), and photoluminescence/cathodoluminescence (PL/CL), respectively.
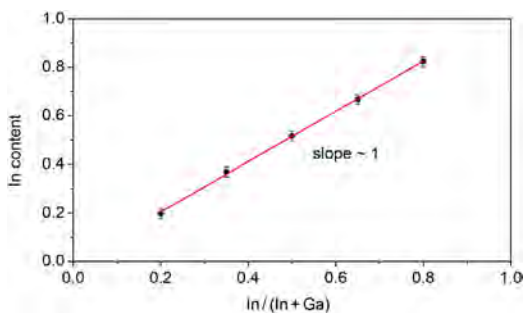
Fig. 1. In content of InGaN films as a function of the ratio of In to total metal flux. The slope represents the In incorporation efficiency.
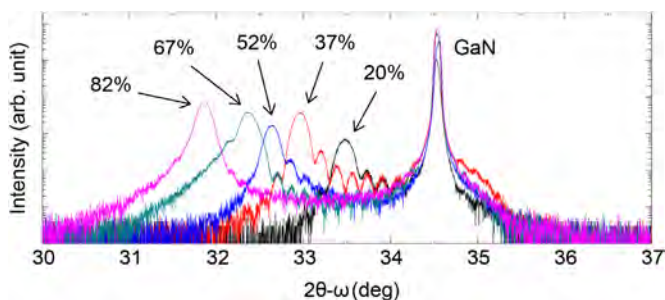
Fig. 2. 2θ–ω diffraction scans of single-phase InGaN films over the entire composition range.
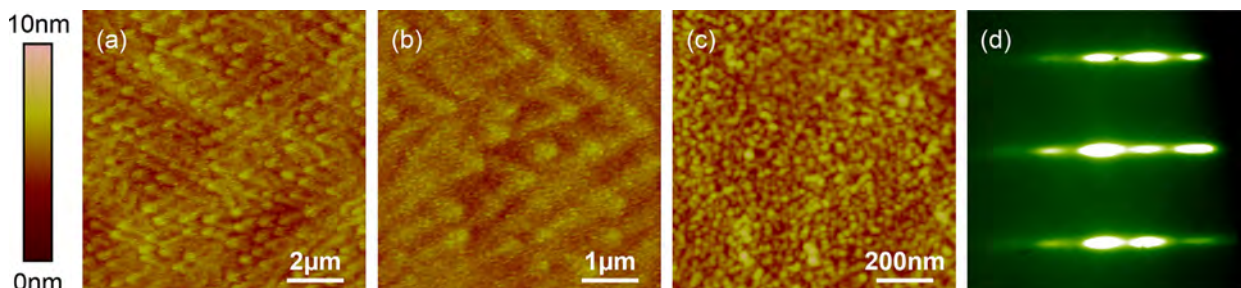
3. Results and discussion

Fig. 1 shows the In content determined by XRD as a function the ratio of the indium (In) to the total group-III (In+Ga) flux. The experimental data points follow a linear behavior with a slope equal to one. This slope can be interpreted as the incorporation efficiency of In into the InGaN layer, which depends on the desorption and the segregation of In atoms [8,15]. At the low substrate temperatures used for these growths, desorption of In atoms from the surface is negligible. Under N-rich growth, the influence of In segregation is limited due to the reduced surface adatom mobility. Therefore, at low substrate temperatures and under slightly N-rich conditions, the In incorporation efficiency is approximately unity.

The 2θ–ω scans depicted in Fig. 2 show the absence of phase separation for all the InGaN films grown throughout the miscibility gap. The suppression of phase separation can be attributed to kinetically-limited adatom diffusion enhanced by the N-rich growth regime [6] and the low substrate temperatures [9]. The (0 0 0 2) rocking curve FWHMs of all InGaN films are comparable to those of the underlying GaN templates, indicating negligible tilt. Film thicknesses were measured to be 52–60 nm from the Pendellösung fringes, which are also indicative of smooth interfaces. The surface morphology of the InGaN films was investigated by AFM. The AFM images shown in Fig. 3 display smooth surfaces with sub-nm RMS roughness. The low adatom mobility from the slightly N-rich growth conditions results in a combination of long-range 2D atomic steps (Fig. 3a) with short-range 3D granular domains (Fig. 3c) that are 25–50 nm diameter wide. This grainy morphology is confirmed by the slightly spotty RHEED pattern observed during growth as shown in Fig. 3d.

The composition and strain of the InGaN films were derived from XRD reciprocal space maps. Fig. 4 depicts the InGaN/GaN RSMs for the (1 0 $\bar{1}$ 5) reflections of the five InGaN samples with In compositions ranging from 20% to 82%. The fully-strained and fully-relaxed lines are also represented as vertical and diagonal dashed lines, respectively. With increasing In content, the InGaN reciprocal lattice point shifts from a fully-strained to a fully-relaxed position. The 20% InGaN film is fully coherent to the GaN underlayer. The degree of relaxation increases for the 37% and the 52% InGaN films and for In composition of 67% and 82%, the films are fully relaxed. This relaxation trend is confirmed by TEM as shown in Fig. 5. The 20% InGaN film exhibits residual strain. The 37% InGaN layer follows an island-nucleation growth mechanism, resulting in isolated islands, with different tilt and twist, which coalesce. The onset of moiré fringes, which are associated with misfit dislocations, is observed at the GaN/InGaN interface for the 52% InGaN as demonstrated by the periodic peaks from the line scan (Fig. 5c inset). The N-rich 67% InGaN sample clearly exhibits moiré fringes at the interface, indicating a complete misfit strain relaxation through misfit dislocations. Similar to the MME-grown InGaN samples [14], we observe a transition in the structural properties of the N-rich InGaN films for In content higher than 55–60%. This transition coincides with the calculated critical thickness reaching a value close to a monolayer. At this composition, due to the large lattice

Fig. 3. (a) 10 × 10 μm, (b) 5 × 5 μm, and (c) 1 × 1 μm representative AFM images of InGaN films grown under slightly N-rich conditions at low temperatures. (d) Typical RHEED pattern during growth.
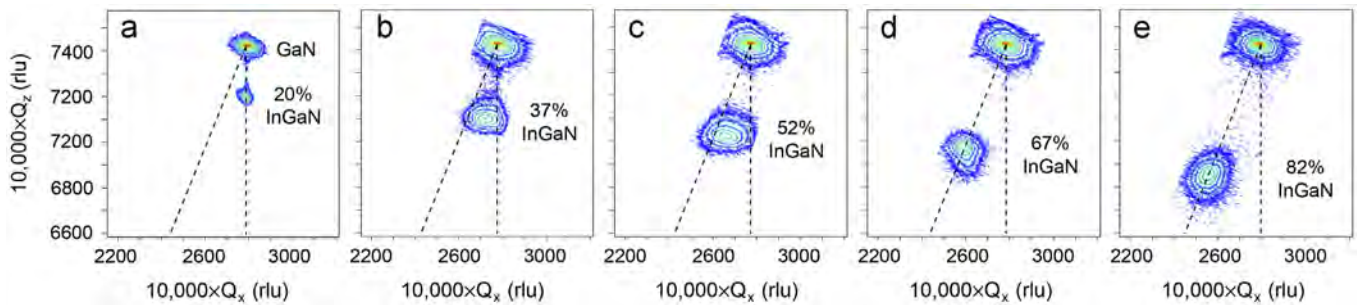
Fig. 4. Reciprocal space maps along the $(1\,0\,\bar{1}\,5)$ reflection of the (a) 20%, (b) 37%, (c) 52%, (d) 67%, and (e) 82% InGaN films. The vertical and diagonal dashed lines corresponds to the fully-strained and fully-relaxed positions, respectively.
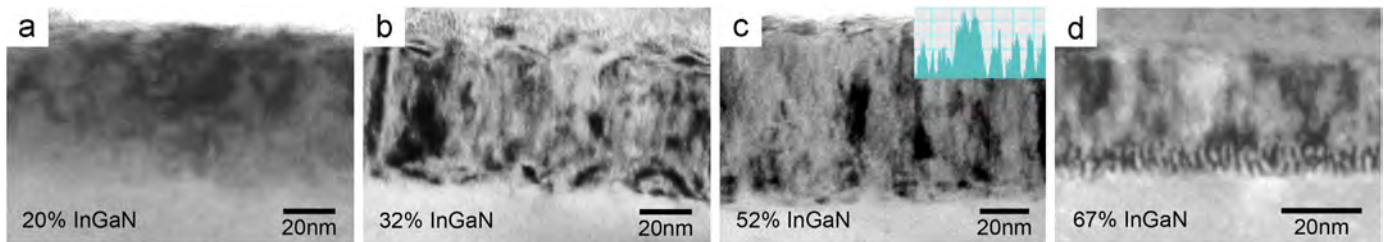
Fig. 5. Cross-section TEM images of the InGaN films, taken along the 1 1 2 0 projection with diffraction contrast set at $g = [1\,\bar{1}\,0\,0]$. Residual strain and island formation are observed for the (a) 20% and (b) 37% InGaN films, respectively. Moiré fringes indicating misfit strain relaxation are observed at the InGaN/GaN interfaces for the (c) 52% and (d) 67% InGaN films. The inset shows periodic peaks from the line scan at the bottom InGaN/GaN interface.
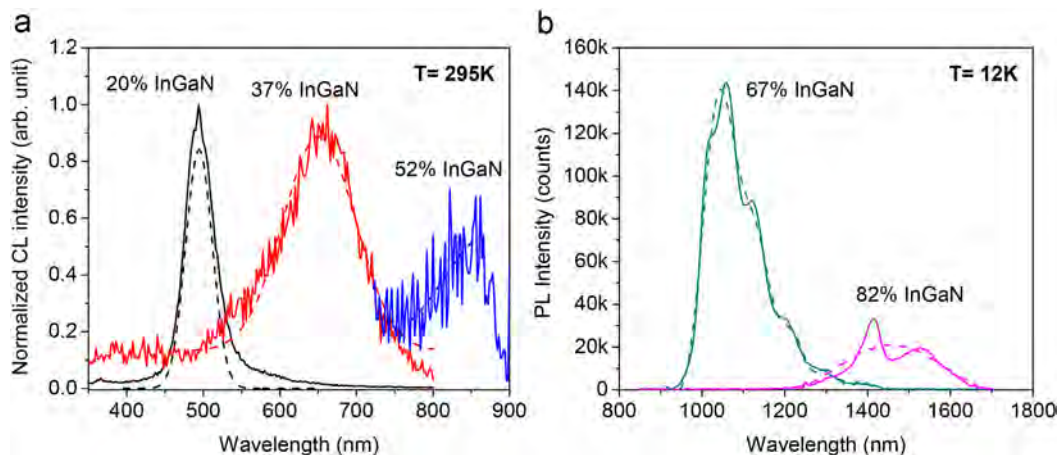
Fig. 6. (a) Cathodoluminescence spectra of the 20%, 37%, and 52% InGaN films and (b) photoluminescence spectra of the 67% and 82% InGaN films. The dashed lines represent the Gaussian fittings after removal of Fabry–Pérot interference effects.

mismatch between GaN and In-rich InGaN, the material spontaneously nucleates in a fully relaxed state, with the formation of a uniform array of misfit dislocations at the interface. While the complete strain relaxation through misfit dislocations is independent of the growth method, further experiments are needed to determine the influence of low growth temperatures.

All these InGaN films exhibit luminescence either by CL (Fig. 6a) or PL (Fig. 6b) possibly due to reduced defect density compared to the MME-grown InGaN films [14] and the absence of stacking faults as demonstrated by the TEM. The additional peaks and shoulders in the 67% and 82% InGaN spectra are attributed to Fabry–Pérot interference from the GaN underlayer.

4. Conclusions

In summary, single-phase InGaN films over the entire composition range have been grown by plasma-assisted MBE under slightly N-rich growth regime at extremely low temperatures. These growth conditions resulted in low defect density, notably no observation of stacking faults, efficient In incorporation, the suppression of phase separation, an improvement in the optical properties, and a grainy surface morphology. We observed an increase in the relaxation degree with higher In content and a transition in the structural properties of the InGaN films for In content higher than 60%. The enhancement of In incorporation and the improvement in structural and optical properties of InGaN films over the entire composition range will benefit the development of InGaN-based optoelectronic devices.

References

[1] J. Wu, When group-III nitrides go infrared: new properties and perspectives, J. Appl. Phys. 106 (2009) 011101.

[2] L. Liu, J.H. Edgar, Substrates for gallium nitride epitaxy, Mater. Sci. Eng., R 37 (2002) 61–127.

[3] F.K. Yam, Z. Hassan, InGaN: an overview of the growth kinetics, physical properties and emission mechanisms, Superlattices Microstruct 43 (2008) 1–23.

[4] R. Singh, D. Doppalapudi, T.D. Moustakas, L.T. Romano, Phase separation in InGaN thick films and formation of InGaN/GaN double heterostructures in the entire alloy composition, Appl. Phys. Lett. 70 (1997) 1089–1091.

[5] J. Ju, B. Loitsch, T. Stettner, F. Schuster, M. Stutzmann, G. Koblmüller, Trade-off between morphology, extended defects, and compositional fluctuation induced carrier localization in high In-content InGaN films, J. Appl. Phys. 116 (2014) 053501.

[6] H. Komaki, R. Katayama, K. Onabe, M. Ozeki, T. Ikari, Nitrogen supply rate dependence of InGaN growth properties, by RF-MBE, J. Cryst. Growth 305 (2007) 12–18.

[7] Ž. Gačević, V.J. Gómez, N.G. Lepetit, P.E.D. Soto Rodríguez, A. Bengoechea, S. Fernández-Garrido, R. Nötzel, E. Calleja, A comprehensive diagram to grow (0 0 0 1)InGaN alloys by molecular beam epitaxy, J. Cryst. Growth 364 (2013) 123–127.

[8] A. Kraus, S. Hammadi, J. Hisek, R. Buß, H. Jönen, H. Bremers, U. Rossow, E. Sakalauskas, R. Goldhahn, A. Hangleiter, Growth and characterization of InGaN by RF-MBE, J. Cryst. Growth 323 (2011) 72–75.

[9] H. Komaki, T. Nakamura, R. Katayama, K. Onabe, M. Ozeki, T. Ikari, Growth of In-rich InGaN films on sapphire via GaN layer by RF-MBE, J. Cryst. Growth 301–302 (2007) 473–477.

[10] C. Song-Bek, S. Takuro, M. Tomoyasu, W. Xinqiang, I. Yoshihiro, Y. Akihiko, Effect of precise control of V/III ratio on in-rich InGaN epitaxial growth, Jpn. J. Appl. Phys. 45 (2006) L1259.

[11] T. Yamaguchi, N. Uematsu, T. Araki, T. Honda, E. Yoon, Y. Nanishi, Growth of thick InGaN films with entire alloy composition using droplet elimination by radical-beam irradiation, J. Cryst. Growth 377 (2013) 123–126.

[12] M. Moseley, J. Lowder, D. Billingsley, W.A. Doolittle, Control of surface adatom kinetics for the growth of high-indium content InGaN throughout the miscibility gap, Appl. Phys. Lett. 97 (2010) 191902.

[13] M. Moseley, B. Gunning, J. Greenlee, J. Lowder, G. Namkoong, W.A. Doolittle, Observation and control of the surface kinetics of InGaN for the elimination of phase separation, J. Appl. Phys. 112 (2012) 014909.

[14] A.M. Fischer, Y.O. Wei, F.A. Ponce, M. Moseley, B. Gunning, W.A. Doolittle, Highly luminescent, high-indium-content InGaN film with uniform composition and full misfit-strain relaxation, Appl. Phys. Lett. 103 (2013) 131101.

[15] E. Iliopoulos, A. Georgakilas, E. Dimakis, A. Adikimenakis, K. Tsagaraki, M. Androulidaki, N.T. Pelekanos, InGaN(0 0 0 1) alloys grown in the entire composition range by plasma assisted molecular beam epitaxy, Phys. Status Solidi A 203 (2006) 102–105.
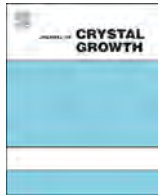
Indium incorporation dynamics in N-polar InAlN thin films grown by plasma-assisted molecular beam epitaxy on freestanding GaN substrates

M.T. Hardy [a,*], D.F. Storm [b], N. Nepal [c], D.S. Katzer [b], B.P. Downey [b], D.J. Meyer [b]

[a] National Research Council Postdoctoral Fellow residing at the Naval Research Laboratory, 4555 Overlook Avenue SW, Washington, DC 20375, USA
[b] Electronics Science & Technology Division, Naval Research Laboratory, 4555 Overlook Avenue SW, Washington, DC 20375, USA
[c] Sotera Defense Solutions, 2200 Defense Hwy Suite 405, Crofton, MD 21114, USA

ARTICLE INFO

ABSTRACT

N-polar InAlN thin films were grown by plasma-assisted molecular beam epitaxy on freestanding GaN substrates under N-rich conditions. Indium and aluminum fluxes were varied independently at substrate temperatures below and above the onset of thermal desorption of indium. At low temperatures, the InAlN composition and growth rate are determined by the group-III fluxes. With increasing substrate temperature, the surface morphology transitions from quasi-3D to a smooth, 2D morphology at temperatures significantly above the onset of indium loss. At higher temperatures, we observe increased indium evaporation with higher indium fluxes and a suppression of indium evaporation with increased aluminum flux. The final optimized InAlN thin film results in step-flow morphology with rms roughness of 0.19 nm and high interfacial quality.

© 2015 Elsevier B.V. All rights reserved.

1. Introduction and background

InAlN has emerged as a promising alternative to more conventional InGaN and AlGaN III-nitride alloys for use in both optoelectronic and electronic devices. $In_xAl_{1-x}N$ can be grown lattice matched to GaN while maintaining a significant refractive index and spontaneous polarization difference with GaN [1–4]. The refractive index contrast with GaN makes InAlN attractive as a thick, strain-free cladding layer in GaN based laser diodes and in distributed Bragg reflectors [5,6]. High electron mobility transistors (HEMTs) take advantage of the large spontaneous polarization difference between $In_{0.18}Al_{0.82}N$ and GaN to induce a high carrier density two dimensional electron gas (2DEG) [1–4].

While the majority of InAlN growth studies have focused on metal-polar growth, N-polar devices have several potential advantages for next generation, high frequency GaN-based HEMTs. In N-polar oriented devices, the barrier is located below the channel, allowing easier access for low resistance ohmic contact formation and improved electron confinement via a built-in back-barrier [7,8]. N-polar HEMTs also offer improved scalability through independent control of the gate-2DEG thickness and the barrier thickness, allowing the barrier design to compensate for the loss of sheet charge density as the channel thickness is scaled down [9]. In addition, the

quantum displacement of the 2DEG towards the surface relative to the barrier/channel interface places the 2DEG closer to the gate, reducing short-channel effects and improving frequency performance [10]. In contrast to metal-polar grown InAlN, N-polar oriented indium-containing films have shown significantly higher indium incorporation for a given set of growth conditions [11–15], suggesting that the optimal growth conditions for N-polar InAlN may be significantly different than for metal-polar InAlN.

InAlN layers have been demonstrated by metalorganic chemical vapor deposition (MOVCD) [16,17], NH_3-based molecular beam epitaxy (MBE) [18] and plasma-assisted MBE (PAMBE) [2]. PAMBE has potential advantages for HEMT growth due to its capability to produce higher chemical purity and more abrupt AlN interlayers (ILs), relative to MOCVD and NH_3-MBE [19]. However, InAlN has proven to be a difficult material to grow with high quality, in part due to the large In–N and Al–N bond strength difference that leads to very different optimal growth temperatures for InN and AlN [11,20]. Historically, PAMBE grown InAlN layers have suffered from both vertical and lateral compositional inhomogeneity [21,22]. In addition, there have been reports of poorly understood compositional changes with respect to supplied indium and aluminum flux (Φ_{In} and Φ_{Al}) [23,24]. InAlN layers are frequently grown with the total $\Phi_{In} + \Phi_{Al}$ approximately equal to the supplied active nitrogen flux (Φ_{N^*}) to take advantage of enhanced surface mobility in the metal-rich regime, similar to metal-rich GaN growth [4,12]. However, metal rich growth generally requires varying Φ_{In} and Φ_{Al} together to avoid crossing from N-rich to metal-rich regimes,

* Corresponding author.
  E-mail address: matthew.hardy.ctr@nrl.navy.mil (M.T. Hardy).

and is complicated by possible indium accumulation and indium/aluminum liquid phase segregation [25]. Growth temperatures are generally chosen to be low enough to avoid thermal decomposition of InN: around 500 °C for metal-polar InAlN and 550 °C for N-polar InAlN [4,12,23]. Recently, InAlN layers grown in the N-rich regime at somewhat higher temperatures have been demonstrated with improved compositional homogeneity [26,27].

In this work we investigate the dependence of $In_xAl_{1-x}N$ composition and surface morphology on systematically varying Φ_{In} and Φ_{Al}, both at temperatures below and above the onset of InN thermal decomposition. We then report on the indium incorporation behavior and the impact on the growth mode in both temperature regimes.

2. Experiments

All samples in this study were grown in an Omicron PRO-75 PAMBE system, equipped with a Veeco Unibulb® RF nitrogen plasma source and dual-filament indium, gallium and aluminum effusion cells. The plasma was operated at 300 W with an N_2 flow rate of 1 sccm, giving a chamber pressure of approximately 2×10^{-5} Torr during growth. InAlN layers were grown on N-polar oriented free-standing substrates provided by Kyma, having a nominal threading dislocation density (TDD) of 5×10^6 cm^{-3}. The low grown-in TDD substrates reveal the native surface morphology rather than the screw dislocation-mediated spiral hillock morphology generally found in III-N MBE. The varying step edge character present around the hillock circumference in spiral-mediated growth may modify indium incorporation and degrade layer homogeneity [28].

Wafers were cleaned *ex situ* using a trichloroethane, acetone, isopropanol, deionized water degrease, followed by an HF dip and deionized water rinse, and were then placed into an indium-free wafer mount. After loading into the preparation chamber, wafers were outgassed at 700 °C for 30 min. Growth was initiated with a three period Ga deposition and desorption procedure to remove excess oxygen from the sample surface [29,30], followed by a two minute nitridation. After InAlN growth, the wafer was immediately cooled and no capping layer was grown.

Growth conditions were chosen well within the N-rich regime to allow independent Φ_{In} and Φ_{Al} series without crossing the N-rich-to-metal-rich transition, avoiding potential issues with indium accumulation and indium/aluminum liquid phase segregation [25]. Φ_{N*} was calculated from the growth rate of GaN grown in the Ga-rich regime measured by X-ray diffraction (XRD), and converted to equivalent $In_{0.18}Al_{0.82}N$ growth rate units using the respective *c*-lattice constants for relaxed GaN and coherently strained InAlN. Φ_{Al} was measured from the composition of a metal-rich AlGaN sample, as determined by XRD, given the known Φ_{N*}. Φ_{In} was calculated from Φ_{Al} using the measured aluminum and indium beam equivalent pressure (BEP) and relative ion gauge sensitivities for indium and aluminum from Ref. [31]. Φ_{In} and Φ_{Al} were also calculated from the growth rate and composition of N-rich InAlN samples, assuming group-III controlled composition and growth rate, and found to be in good agreement with the previously calculated values. All substrates temperature measurements are from a thermocouple mounted in the substrate heater; wafer surface temperatures are estimated to be 100–150 °C below the measured thermocouple temperature (T_{TC}). The T_{TC} for the initial growth series was set at 600 °C, and was chosen to be at least 100 °C below the onset of InN thermal decomposition.

A series of samples was grown varying Φ_{In} from 0.08 to 0.89 nm/min while holding Φ_{Al} and Φ_{N*} constant at 0.64 and 3.2 nm/min, respectively. The corresponding III/V ratio ranged from 0.23 to 0.47, well within the N-rich regime. Next, Φ_{In} was fixed at 0.14 nm/min and Φ_{Al} was varied from 0.54 to 0.73 nm/min. Both series described above had an InAlN layer growth time of 40 min, and were grown at

Table 1
Summary of InAlN experimental growth series.

Series	T_{TC} (°C)	Φ_{In} (nm/min)	Φ_{Al} (nm/min)	III/V Ratio
Low T Φ_{In}	600	0.11–0.89	0.64	0.23–0.47
Low T Φ_{Al}	600	0.14	0.54–0.73	0.21–0.27
T_{TC}	600–815	0.14	0.64	0.24
High T Φ_{In}	815	0.14–0.86	0.64	0.24–0.46
High T Φ_{Al}	815	0.86	0.64–1.28	0.46–0.66
Final	825	0.86	0.95	0.56

$T_{TC}=600$ °C corresponding to a real surface temperature of 450–500 °C.

To identify the onset of indium loss under our growth conditions, Φ_{In} and Φ_{Al} were fixed at 0.14 and 0.64 nm/min, respectively, and T_{TC} was stepped between 600 and 815 °C for a series of growths. Φ_{In} and Φ_{Al} series were then repeated with $T_{TC}=815$ °C to investigate the change in indium incorporation behavior in the desorption regime. For the high temperature Φ_{In} series, Φ_{In} was increased from 0.14 to 0.86 nm/min, with a T_{TC} of 815 °C. Next, a series of samples was grown varying Φ_{Al} from 0.64 to 1.28 nm/min, also at 815 °C. The temperature series and high temperature Φ_{In} and Φ_{Al} series had InAlN layer growth times of 60 min, giving InAlN film thicknesses of 45–50 nm. A final sample was then grown with optimized conditions, adjusting T_{TC} to yield a nominally $In_{0.17}Al_{0.83}N$ layer. A summary of growth experiments is given in Table 1.

All samples were characterized using a Rigaku Smartlab high-resolution XRD system with a rotating anode X-ray source, four bounce Ge (2 2 0) monochromator and an open detector with 0.25 mm incident and receiving slits. Composition was calculated from the InAlN–GaN peak separation in (0 0 0 2) $2\theta/\omega$ measurements, assuming Vegard's law for the lattice constants and elastic constants taken from Ref. [32]. Layer thicknesses were measured by fitting a dynamical XRD simulation to the Pendellösung fringes in the same XRD measurement [33]. Surface morphology was characterized using a Bruker Dimension FastScan atomic force microscope (AFM).

3. Results and discussion

3.1. Low temperature flux series

The $In_xAl_{1-x}N$ composition as a function of the group-III flux ratio $\Phi_{In}/(\Phi_{In} + \Phi_{Al})$ for samples from the low temperature Φ_{In} series is shown in Fig. 1(a). The line plotted in Fig. 1(a) shows the ideal relationship of the composition with the group-III ratio. Also plotted in Fig. 1(a) is the indium incorporation efficiency k_{In}, which is defined as

$$k_{In} \equiv \frac{\Phi_{In*}}{\Phi_{In}}, \tag{1}$$

where Φ_{In*} is the effective indium flux incorporated into the InAlN layer. The indium incorporation efficiency can then be rearranged to give

$$k_{In} = \frac{x}{1-x} \frac{\Phi_{Al}}{\Phi_{In}}, \tag{2}$$

allowing calculation of k_{In} from the supplied fluxes and measured InN fraction x, assuming N-rich growth.

In Fig. 1(a), the InN fraction x followed the group-III flux ratio over a wide range of compositions, as indicated by a near unity k_{In} for $\Phi_{In} \leq 0.31$ nm/min. Indium droplets were observed on the highest Φ_{In} sample from the low temperature Φ_{In} series, in spite of a III/V ratio of only 0.6. The reduction of k_{In} concurrent with indium droplet formation suggests a competition for the incoming Φ_{In} between droplet and layer incorporation and/or an indium self-blocking mechanism [34]. The surface In–In interactions for a
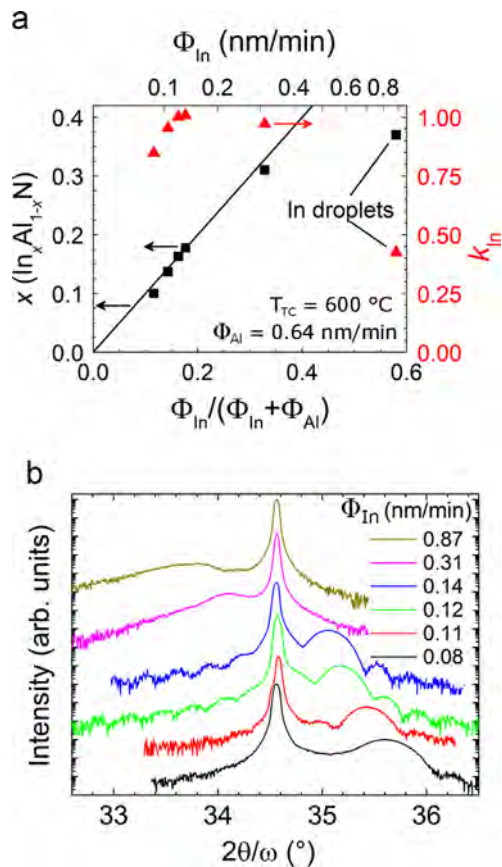
Fig. 1. (a) Composition and indium incorporation efficiency k_{In} as a function of supplied indium flux to group-III-ratio and (b) XRD (0002) $2\theta/\omega$ scans for samples in the low temperature Φ_{In} series. The line in (a) represents the ideal composition determined by the group-III flux ratio.

Fig. 2. (a) $In_xAl_{1-x}N$ composition x as a function of the indium flux to group-III ratio and (b) growth rate measured from XRD Pendellösung fringes as a function of the total group-III flux for the low temperature Φ_{Al} series. For both plots the line indicates expected ideal group-III controlled behavior.

sufficiently high indium surface coverage may lead to droplet formation even under N-rich conditions. If so, there may be a critical Φ_{In} above which droplet formation is unavoidable for a given Φ_{Al} and substrate temperature. Indium droplet formation has also been observed for N-rich InGaN grown by NH_3-MBE [35]. Further investigation into the mechanism for droplet formation under N-rich conditions is ongoing.

XRD scans in Fig. 1(b) show good single peaked InAlN layers accompanied by Pendellösung fringes for samples with $\Phi_{In}=0.08$–0.14 nm/min ($x=0.10$–0.18). The InAlN layer peaks become much broader and even multi-peaked for the samples with $\Phi_{In}=0.31$–0.87 nm/min ($x=0.31$–37), indicating a degradation of crystal quality and/or loss of coherency for these highly compressively strained samples.

Fig. 2(a) gives composition and k_{In} as a function of group-III ratio, and Fig. 2(b) shows the measured growth rate and k_{In} as a function of total group-III flux for the low temperature Φ_{Al} series. The line in each plot is the expected behavior assuming ideal N-rich group-III flux determined composition and growth rate. While there is some experimental variation, overall there is good agreement with expected composition and growth rate. k_{In} is near unity, suggesting negligible indium loss, as expected for low temperature InAlN growth.

Both the low temperature Φ_{In} and Φ_{Al} series showed clear control of composition and growth rate by varying the group-III flux. The variation of composition shown in Figs. 1(a) and 2(b) agrees closely with the predicted composition from the group-III flux ratio, excluding the sample with indium droplets. Likewise, varying Φ_{Al} gave the expected changes in both

composition and growth rate as predicted by the total group-III flux and the group-III flux ratio, respectively.

3.2. Substrate temperature series

The dependence of composition on T_{TC} is given in Fig. 3(a). The composition remains constant below approximately 760 °C, and then decreases as temperature increases. The two highest temperature samples had a low density of surface cracks due to tensile misfit stress in the reduced InN fraction InAlN films.

The variation of $In_xAl_{1-x}N$ composition with temperature shown in Fig. 3(a) is quantitatively similar to Ref. [4], with the exception that no indium droplets were observed at an intermediate temperature regime. The absence of indium droplets is likely related to growth under N-rich growth conditions, as compared to $\Phi_{In} + \Phi_{Al} \approx \Phi_{N^*}$. Excess Φ_{N^*} can re-incorporate the additional indium resulting from InN decomposition on the surface, as long as the surface coverage remains below some critical value for droplet formation. At higher temperatures, the indium evaporation rate becomes larger than the InN decomposition rate, preventing indium accumulation on the surface [4]. A single indium loss mechanism (evaporation) results in a delayed, but sharper decrease in composition with increasing temperature.

The surface morphologies of the samples in the temperature series are shown in Fig. 3(b–g). All samples are reasonably smooth, with no systematic variation in the rms roughness with temperature. At low temperature the surface has a bumpy, quasi-3D morphology. With increasing temperature, this morphology remains fairly constant until after the onset of indium evaporation. For temperatures greater than 40 °C above the onset of indium evaporation, the morphology evolves to a smooth and fully 2D surface.

Given that the growth temperature for the highest temperature sample is at least 100 °C less than optimal for AlN growth [20], it is
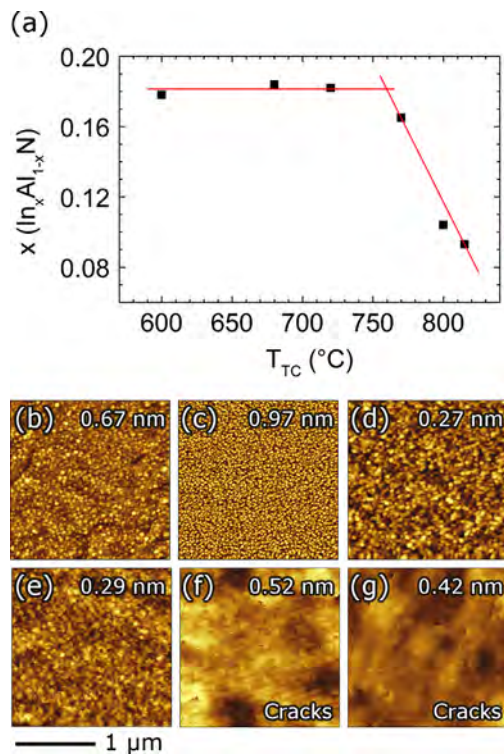
Fig. 3. (a) $In_xAl_{1-x}N$ composition with increasing substrate thermocouple temperature. $2 \times 2 \ \mu m^2$ AFM scans for samples grown at a substrate temperature of (b) 600 °C, (c) 680 °C, (d) 720 °C, (e) 770 °C, (f) 800 °C and (g) 815 °C. The rms roughness (averaged over the wafer for $5 \times 5 \ \mu m^2$ scans) and the presence of surface cracks is indicated.

unlikely that the increase in temperature alone led to a significant increase in Al ad-atom mobility. The clear shift in InAlN surface morphology occurs significantly after the onset of indium evaporation, and under these conditions it is likely that some steady-state indium surface layer is present. This indium surface layer may act as a surfactant to improve Al and N ad-atom mobility, similar to Ga ad-layers for GaN or AlN growth [26,36].

3.3. High temperature flux series

Fig. 4(a) shows the dependence of composition and k_{In} on the group-III ratio for the high temperature Φ_{In} series. With increasing Φ_{In} the composition increases sub-linearly and consequently k_{In} decreases with increasing Φ_{In}. Fig. 4(b) and (c) show $5 \times 5 \ \mu m^2$ AFM images of the lowest Φ_{In} sample (0.14 nm/min) and the highest Φ_{In} sample (0.86 nm/min), respectively. A low density of cracks was present for $\Phi_{In}=0.14$ nm/min; no indium droplets were present on any sample in this series.

Fig. 5(a) gives the dependence of k_{In} on Φ_{Al} for the high temperature Φ_{Al} series. While the InN fraction decreased with increasing Φ_{Al}, it decreased significantly less than predicted by the changing group-III ratio; therefore, indium evaporation decreased with increasing Φ_{Al}. This is reflected in Fig. 5(a) by an increase in k_{In} with increasing Φ_{Al}. $5 \times 5 \ \mu m^2$ AFM images of the samples in this series are shown in Fig. 5(b)–(d). Steps are visible in the AFM image of the sample with $\Phi_{Al}=0.95$ nm/min, shown in Fig. 5(c).

The high temperature Φ_{In} and Φ_{Al} series showed significantly different behavior than the corresponding low temperature series. The sub-linear increase in x and linear decrease in k_{In} with increasing Φ_{In} in Fig. 4(a) indicates saturation of indium incorporation, accompanied by increased indium evaporation. Several effects may contribute to indium composition saturation, including indium site saturation [37] and indium self-blocking [38]. In
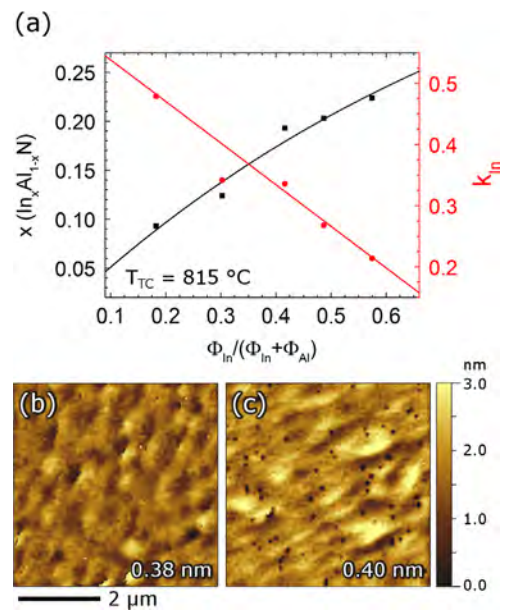
Fig. 4. (a) Dependence of the measured $In_xAl_{1-x}N$ composition x and indium incorporation efficiency k_{In} on the group-III ratio for the high temperature Φ_{In} series. The lines are an exponential fit to x and a linear fit to k_{In}, and are meant as a guide to the eye. $5 \times 5 \ \mu m^2$ AFM scans of samples with Φ_{In} of (b) 0.14 nm/min and (c) 0.86 nm/min, with rms roughness indicated.
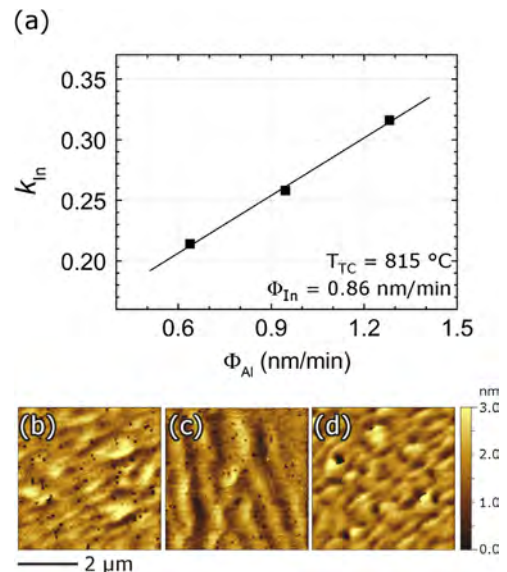
Fig. 5. (a) Indium incorporation efficiency k_{In} for the high temperature Φ_{Al} series. The line shown is a linear fit to the data. $5 \times 5 \ \mu m^2$ AFM images of the sample with Φ_{Al} of (b) 0.64 nm/min, (c) 0.95 nm/min and (d) 1.28 nm/min grown at $T_{TC}=815$ °C.

addition, strain-related composition pulling effects may increase or reduce indium incorporation in tensily or compressively strained InAlN, respectively. Additional investigation is required to separate and clarify the indium incorporation mechanisms.

The Φ_{Al} series showed an increase in k_{In} with increasing Φ_{Al}. The reduction in indium loss is likely due to an indium trapping or burying effect, as the higher total growth rate allows surface steps to move more quickly and incorporate a larger fraction of the indium ad-atoms before they can evaporate. Reduction of evaporating indium with changing Φ_{Al} will cause a different slope for the composition versus temperature behavior and higher Φ_{Al} should allow higher growth temperatures with the same group-III ratio and composition. Similar growth rate dependent composition effects have been observed for InGaN grown by MBE and MOCVD [39,40].
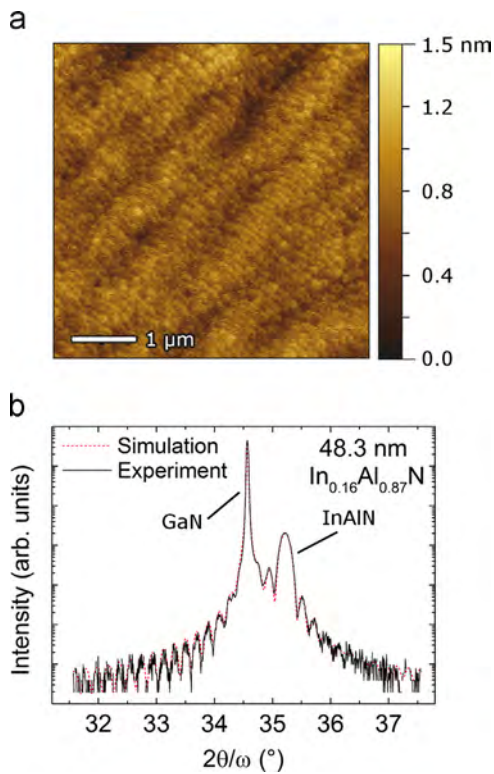
Fig. 6. (a) $5 \times 5\ \mu m^2$ AFM scan having an rms roughness of 0.19 nm and (b) 0 0 0 2 $2\theta/\omega$ XRD scan of an optimized 48 nm thick $In_{0.16}Al_{0.84}N$ sample. The XRD data shows excellent agreement with simulation and at least 15 Pendellösung fringes are visible to the low angle side of the InAlN layer peak.

Surface pits are visible in Figs. 4(c) and 5(a) and (b). Line scans indicate the pits are fairly shallow, with typical depths less than 1 nm. The pit density is approximately $2-3 \times 10^8\ cm^{-2}$ for all of the high temperature grown samples. Upon careful examination of Fig. 3(f), (g) and (b) small surface depressions can be observed, having a density similar to the pit density. All samples having pits have $In_xAl_{1-x}N$ composition $x > 0.18$ and are under compressive strain, while the samples tensily strained with $x < 0.18$ have much smaller surface depressions. Thus the pits may be similar to V-defects in InGaN, which nucleate on screw component dislocations and can relieve compressive stress via elastic relaxation [41,42]. Alternatively, higher composition and more compressive strain may promote surface segregation around the surface perturbation caused by screw component dislocations, leading to InN-rich regions localized on the dislocations that are more prone to thermal decomposition and subsequent evaporation at elevated growth temperatures. The pit density is over an order of magnitude higher than the nominal TDD. Unless there is significant dislocation generation at the re-growth interface [29], it is likely that a screw dislocation is not required for pit formation.

3.4. Optimized InAlN

Fig. 6 shows AFM and XRD data for a sample grown with the final optimized growth conditions. Φ_{Al} was 0.95 nm/min (the mid-point from the high temperature Φ_{Al} series) and Φ_{In} was 0.86 nm/min, and the substrate temperature was increased by 10 °C to adjust the composition. The average rms roughness was 0.19 nm measured on $5 \times 5\ \mu m^2$ scans, and parallel step edges were observed suggesting step-flow growth mode.

The XRD scan in Fig. 6(b) shows a large number of Pendellösung fringes, indicating a high quality InAlN/GaN interface, although XRD may not be sensitive to short range compositional inhomogeneity

[43]. The InAlN layer peak width is primarily controlled by limited coherence length broadening due to the low thickness of the film. However dynamical diffraction simulations [33], with only a single broadening parameter for both the GaN and InAlN peak, show good agreement with the XRD measurement.

N-polarity of the InAlN films was confirmed by the observation of a two-dimensional electron gas (2DEG) on a separate sample with a 20 nm GaN channel, in combination with the absence of a 2DEG on any other sample in this series (which had no GaN cap). In addition, InAlN layers grown on Ga-polar substrates at the high growth temperatures used in this study exhibited little to no indium incorporation.

4. Conclusions

N-polar $In_xAl_{1-x}N$ growth series independently varying Φ_{In} and Φ_{Al} have been grown at temperatures both below and above the onset of indium desorption. In the low temperature regime the composition and growth rate are determined by the group-III fluxes, and are limited by indium droplet formation even for N-rich conditions. InAlN surface morphology changed from quasi-3D for low growth temperature grown InAlN to 2D for samples grown at least 40 °C above the indium desorption transition temperature. An Φ_{In} series grown at high temperature showed increased indium evaporation with increasing Φ_{In}, indicating saturation of indium incorporation in the absence of droplet formation. A high temperature grown Φ_{Al} series resulted in suppressed indium evaporation with increasing Φ_{Al}. Optimized growth conditions resulted in step-flow growth of N-polar InAlN layers with rms roughness less than 0.2 nm and excellent interfacial quality as measured by XRD.

References

[1] J. Kuzmik, Power electronics on InAlN/(In) GaN: prospect for a record performance, IEEE Electron Device Lett. 22 (2001) 510–512.
[2] M. Higashiwaki, T. Matsui, InAlN/GaN heterostructure field-effect transistors grown by plasma-assisted molecular-beam epitaxy, Jpn. J. Appl. Phys. 43 (2004) L768.
[3] D.F. Brown, Nidhi, F. Wu, S. Keller, S.P. DenBaars, U.K. Mishra, N-polar InAlN/ AlN/GaN MIS-HEMTs, IEEE Electron Device Lett. 31 (2010) 800–802.
[4] S. Dasgupta, S. Choi, F. Wu, J.S. Speck, U.K. Mishra, Growth, structural, and electrical characterizations of N-polar InAlN by plasma-assisted molecular beam epitaxy, Appl. Phys. Express 4 (2011).
[5] A. Castiglia, E. Feltin, G. Cosendey, A. Altoukhov, J.-F. Carlin, R. Butte, N. Grandjean, $Al_{0.83}In_{0.17}N$ lattice-matched to GaN used as an optical blocking layer in GaN-based edge emitting lasers, Appl. Phys. Lett. 94 (2009) 193506.
[6] J.-F. Carlin, J. Dorsaz, E. Feltin, R. Butte, N. Grandjean, M. Ilegems, M. Laugt, Crack-free fully epitaxial nitride microcavity using highly reflective AlInN/GaN Bragg mirrors, Appl. Phys. Lett. 86 (2005) 031107.
[7] S. Dasgupta, Nidhi, D.F. Brown, S. Wu, J.S. Keller, U.K. Speck, Mishra, Ultralow nonalloyed Ohmic contact resistance to self aligned N-polar GaN high electron mobility transistors by In(Ga)N regrowth, Appl. Phys. Lett. 96 (2010) 143504.
[8] D.J. Meyer, D.S. Katzer, R. Bass, N.Y. Garces, M.G. Ancona, D.A. Deen, D.F. Storm, S.C. Binari, N-polar n+ GaN cap development for low ohmic contact resistance to inverted HEMTs, Phys. Status Solidi C 9 (2012) 894–897.
[9] J. Lu, X. Zheng, M. Guidry, D. Denninghoff, E. Ahmadi, S. Lal, S. Keller, S.P. DenBaars, U.K. Mishra, Engineering the (In, Al, Ga)N back-barrier to achieve high channel-conductivity for extremely scaled channel-thicknesses in N-polar GaN high-electron-mobility-transistors, Appl. Phys. Lett. 104 (2014) 092107.
[10] M.H. Wong, S. Keller, S. Nidhi, D.J. Dasgupta, S. Denninghoff, D.F. Kolluri, J. Brown, N.A. Lu, E. Fichtenbaum, U. Ahmadi, A. Singisetti, S. Chini, S.P. Rajan, J.S. DenBaars, U.K. Speck, N-polar Mishra, GaN epitaxy and high electron mobility transistors, Semicond. Sci. Technol. 28 (2013) 074009.

[11] C.S. Gallinat, G. Koblmüller, J.S. Brown, J.S. Speck, A growth diagram for plasma-assisted molecular beam epitaxy of In-face InN, J. Appl. Phys. 102 (2007) 064907.
[12] S. Fernández-Garrido, Ž. Gačević, E. Calleja, A comprehensive diagram to grow InAlN alloys by plasma-assisted molecular beam epitaxy, Appl. Phys. Lett. 93 (2008) 191907.
[13] G. Koblmüller, C.S. Gallinat, J.S. Speck, Surface kinetics and thermal instability of N-face InN grown by plasma-assisted molecular beam epitaxy, J. Appl. Phys. 101 (2007) 083516.
[14] D.N. Nath, E. Gur, S.A. Ringel, S. Rajan, Molecular beam epitaxy of N-polar InGaN, Appl. Phys. Lett. 97 (2010) 071903.
[15] K. Xu, A. Yoshikawa, Effects of film polarities on InN growth by molecular-beam epitaxy, Appl. Phys. Lett. 83 (2003) 251–253.
[16] C. Hums, J. Bläsing, A. Dadgar, A. Diez, T. Hempel, J. Christen, A. Krost, K. Lorenz, E. Alves, Metal–organic vapor phase epitaxy and properties of AlInN in the whole compositional range, Appl. Phys. Lett. 90 (2007) 022105.
[17] D.F. Brown, S. Keller, T.E. Mates, J.S. Speck, S.P. DenBaars, U.K. Mishra, Growth and characterization of In-polar and N-polar InAlN by metal organic chemical vapor deposition, J. Appl. Phys. 107 (2010) 033509.
[18] M.-H. Wong, F. Wu, C.A. Hurni, S. Choi, J.S. Speck, U.K. Mishra, Molecular beam epitaxy of InAlN lattice-matched to GaN with homogeneous composition using ammonia as nitrogen source, Appl. Phys. Lett. 100 (2012) 072107.
[19] B. Mazumder, S.W. Kaun, J. Lu, S. Keller, U.K. Mishra, J.S. Speck, Atom probe analysis of AlN interlayers in AlGaN/AlN/GaN heterostructures, Appl. Phys. Lett. 102 (2013) 111603.
[20] G. Koblmüeller, R. Averbeck, L. Geelhaar, H. Riechert, W. Hösler, P. Pongratz, Growth diagram and morphologies of AlN thin films grown by molecular beam epitaxy, J. Appl. Phys. 93 (2003) 9591–9596.
[21] J.M. Mánuel, F.M. Morales, J.G. Lozano, D. González, R. García, T. Lim, L. Kirste, R. Aidam, O. Ambacher, Structural and compositional homogeneity of InAlN epitaxial layers nearly lattice-matched to GaN, Acta Mater. 58 (2010) 4120–4125.
[22] L. Zhou, D.J. Smith, M.R. McCartney, D.S. Katzer, D.F. Storm, Observation of vertical honeycomb structure in InAlN/GaN heterostructures due to lateral phase separation, Appl. Phys. Lett. 90 (2007) 081917.
[23] D.S. Katzer, D.F. Storm, S.C. Binari, B.V. Shanabrook, A. Torabi, L. Zhou, D. J. Smith, Molecular beam epitaxy of InAlN/GaN heterostructures for high electron mobility transistors, J. Vac. Sci. Technol., B 23 (2005) 1204–1208.
[24] T. Ive, O. Brandt, X. Kong, A. Trampert, K.H. Ploog, Al,In)N layers and (Al,In)N/GaN heterostructures grown by plasma-assisted molecular beam epitaxy on 6H-SiC(0 0 0 1), Phys. Rev. B 78 (2008) 035311.
[25] M. Moseley, B. Gunning, J. Greenlee, J. Lowder, G. Namkoong, W. Alan Doolittle, Observation and control of the surface kinetics of InGaN for the elimination of phase separation, J. Appl. Phys. 112 (2012) 014909.
[26] S.W. Kaun, E. Ahmadi, B. Mazumder, F. Wu, E.C.H. Kyle, P.G. Burke, U.K. Mishra, J.S. Speck, GaN-based high-electron-mobility transistor structures with homogeneous lattice-matched InAlN barriers grown by plasma-assisted molecular beam epitaxy, Semicond. Sci. Technol. 29 (2014) 045011.
[27] E. Ahmadi, R. Shivaraman, F. Wu, S. Wienecke, S.W. Kaun, S. Keller, J.S. Speck, U.K. Mishra, Elimination of columnar microstructure in N-face InN, lattice-matched to GaN, grown by plasma-assisted molecular beam epitaxy in the N-rich regime, Appl. Phys. Lett. 104 (2014) 072107.
[28] C. Skierbiszewski, M. Siekacz, P. Perlin, A. Feduniewicz-Żmuda, G. Cywiński, I. Grzegory, M. Leszczyński, Z.R. Wasilewski, S. Porowski, Role of dislocation-free GaN substrates in the growth of indium containing optoelectronic structures by plasma-assisted MBE, J. Cryst. Growth 305 (2007) 346–354.
[29] D.F. Storm, T. McConkie, D.S. Katzer, B.P. Downey, M.T. Hardy, D.J. Meyer, D.J. Smith, Effect of interfacial oxygen on the microstructure of MBE-grown homoepitaxial N-polar GaN, J. Cryst. Growth 409 (2014) 14.
[30] D.F. Storm, D.S. Katzer, D.J. Meyer, S.C. Binari, Oxygen incorporation in homoepitaxial N-polar GaN grown by radio frequency-plasma assisted molecular beam epitaxy: mitigation and modeling, J. Appl. Phys. 112 (2012) 013507.
[31] T.A. Flaim, P.D. Ownby, Observations on Bayard–Alpert ion gauge sensitivities to various gases, J. Vac. Sci. Technol. 8 (1971) 661.
[32] A.E. Romanov, T.J. Baker, S. Nakamura, J.S. Speck, E.J.U. Group, Strain-induced polarization in wurtzite III-nitride semipolar layers, J. Appl. Phys. 100 (2006) 023522.
[33] O. Brandt, P. Waltereit, K.H. Ploog, Determination of strain state and composition of highly mismatched group-III nitride heterostructures by x-ray diffraction, J. Phys. D: Appl. Phys., 35 (2002) 577. "MadMax" executable program courtesy of Patrick Waltereit of Fraunhofer IAF.
[34] D.F. Storm, Incorporation kinetics of indium and gallium in indium gallium nitride: a phenomenological model, J. Appl. Phys. 89 (2001) 2452–2457.
[35] V.P. Chaly, B.A. Borisov, D.M. Demidov, D.M. Krasovitsky, Y.V. Pogorelsky, A.P. Shkurko, I.A. Sokolov, S.Y.-. Karpov, Indium droplet formation during molecular beam epitaxy of InGaN, J. Cryst. Growth 206 (1999) 147–149.
[36] B. Heying, R. Averbeck, L.F. Chen, E. Haus, H. Riechert, J.S. Speck, Control of GaN surface morphologies using plasma-assisted molecular beam epitaxy, J. Appl. Phys. 88 (2000) 1855–1860.
[37] F. Jiang, R.-V. Wang, A. Munkholm, S.K. Streiffer, G.B. Stephenson, P.H. Fuoss, K. Latifi, C. Thompson, Indium adsorption on GaN under metal–organic chemical vapor deposition conditions, Appl. Phys. Lett. 89 (2006) 161915.
[38] D.F. Storm, C. Adelmann, B. Daudin, Incorporation kinetics of indium in indium gallium nitride at low temperature, Appl. Phys. Lett. 79 (2001) 1614–1615.
[39] C. Skierbiszewski, Z.R. Wasilewski, I. Grzegory, S. Porowski, Nitride-based laser diodes by plasma-assisted MBE—from violet to green emission, J. Cryst. Growth 311 (2009) 1632–1639.
[40] S. Keller, B.P. Keller, D. Kapolnek, A.C. Abare, H. Masui, L.A. Coldren, U.K. Mishra, S.P. DenBaars, Growth and characterization of bulk InGaN films and quantum wells, Appl. Phys. Lett. 68 (1996) 3147–3149.
[41] X.H. Wu, C.R. Elsass, A. Abare, M. Mack, S. Keller, P.M. Petroff, S.P. DenBaars, J.S. Speck, S.J. Rosner, Structural origin of V-defects and correlation with localized excitonic centers in InGaN/GaN multiple quantum wells, Appl. Phys. Lett. 72 (1998) 692–694.
[42] S. Srinivasan, L. Geng, R. Liu, F.A. Ponce, Y. Narukawa, S. Tanaka, Slip systems and misfit dislocations in InGaN epilayers, Appl. Phys. Lett. 83 (2003) 5187–5189.
[43] S. Choi, F. Wu, R. Shivaraman, E.C. Young, J.S. Speck, Observation of columnar microstructure in lattice-matched InAlN/GaN grown by plasma assisted molecular beam epitaxy, Appl. Phys. Lett. 100 (2012) 232102.

Molecular beam epitaxy of free-standing wurtzite $Al_xGa_{1-x}N$ layers

CrossMark

S.V. Novikov [a,*], C.R. Staddon [a], R.W. Martin [b], A.J. Kent [a], C.T. Foxon [a]

[a] *School of Physics and Astronomy, University of Nottingham, Nottingham NG7 2RD, UK*
[b] *Department of Physics, SUPA, University of Strathclyde, Glasgow, G4 0NG, UK*

ARTICLE INFO

ABSTRACT

Recent developments with group III nitrides present $Al_xGa_{1-x}N$ based LEDs as realistic devices for new alternative deep ultra-violet light sources. Because there is a significant difference in the lattice parameters of GaN and AlN, $Al_xGa_{1-x}N$ substrates would be preferable to either GaN or AlN for ultraviolet device applications. We have studied the growth of free-standing wurtzite $Al_xGa_{1-x}N$ bulk crystals by plasma-assisted molecular beam epitaxy (PA-MBE). Thick wurtzite $Al_xGa_{1-x}N$ films were grown by PA-MBE on 2-in. GaAs (111)B substrates and were removed from the GaAs substrate after growth to provide free standing $Al_xGa_{1-x}N$ samples. X-ray microanalysis measurements confirm that the AlN fraction is uniform across the wafer and mass spectroscopy measurements show that the composition is also uniform in depth. We have demonstrated that free-standing wurtzite $Al_xGa_{1-x}N$ wafers can be achieved by PA-MBE for a wide range of AlN fractions. In order to develop a commercially viable process for the growth of wurtzite $Al_xGa_{1-x}N$ substrates, we have used a novel Riber plasma source and have demonstrated growth rates of GaN up to 1.8 μm/h on 2-in. diameter GaAs and sapphire wafers.

1. Introduction

At present there is great interest in the development of ultraviolet (UV) light sources for solid-state lighting, optical sensors, surface decontamination and water purification. UV disinfection is one of the most promising methods for water treatment. Unlike chemical water treatment it will be fast and easy to use and will not require hazardous materials. 250 nm deep ultra-violet (DUV) light attacks the DNA of micro-organisms. Until recently the main UV sources for such applications were mercury lamps, however, these lamps are fragile, have a limited lifetime and present a disposal problem due to the toxic mercury.

Recent developments with group III nitrides allows researchers world-wide to consider $Al_xGa_{1-x}N$ based LEDs as possible new alternative DUV light sources. If efficient devices can be developed they will be easy to use, will potentially have a long life time, will not be fragile and will be suitable for battery operation allowing their use in remote locations. The first UV LEDs are now being successfully manufactured using the $Al_xGa_{1-x}N$ material system. DUV LEDs require $Al_xGa_{1-x}N$ layers with compositions in the mid-range between AlN and GaN. For example for efficient water purification the $Al_xGa_{1-x}N$ LEDs need to emit in the wavelength range 250–280 nm. However, there are significant differences in the lattice parameters of GaN

$(a \sim 3.19$ Å and $c \sim 5.19$ Å$)$ and AlN $(a \sim 3.11$ Å and $c \sim 4.98$ Å$)$ [1]. Therefore $Al_xGa_{1-x}N$ substrates would be preferable to those of either GaN or AlN for deep ultraviolet device applications, that has stimulated an active search for methods to produce bulk $Al_xGa_{1-x}N$ substrates with variable AlN content.

MBE is normally regarded as an epitaxial technique for the growth of very thin layers with monolayer control of their thickness. However, we have recently used MBE for bulk crystal growth and have produced layers of zinc-blende GaN up to 100 μm in thickness [2–4]. We have also demonstrated the scalability of the process by growing free-standing zinc-blende GaN layers up to 3-in. in diameter.

We have shown that our newly developed PA-MBE process for the growth of bulk zinc-blende GaN layers can also be used to achieve free-standing wurtzite $Al_xGa_{1-x}N$ wafers [5,6]. Thick wurtzite $Al_xGa_{1-x}N$ films with an AlN content, x, from 0 to 0.5 were successfully grown by PA-MBE on 2-in. GaAs (111)B substrates.

In this paper we will describe our recent results in development of our PA-MBE approach for the growth of free-standing wurtzite $Al_xGa_{1-x}N$ bulk crystals.

2. Experimental details

Wurtzite (hexagonal) GaN and $Al_xGa_{1-x}N$ films were grown on different substrates by plasma-assisted molecular beam epitaxy (PA-MBE) in a MOD-GENII system [2–6]. 2-in. diameter sapphire and GaAs (111)B substrates were used. The active nitrogen for the

---

* Corresponding author. Tel.: +44 115 9515138; fax: +44 115 9515180.
E-mail address: Sergei.Novikov@Nottingham.ac.uk (S.V. Novikov).

growth of the group III-nitrides was provided by RF activated plasma sources. We compared different nitrogen plasma sources for the growth of thick wurtzite GaN and $Al_xGa_{1-x}N$ films including a standard HD25 plasma source from Oxford Applied Research and a modified novel high efficiency plasma source from Riber.

A GaAs buffer layer was grown on the GaAs (111)B substrates in order to improve the properties of the $Al_xGa_{1-x}N$ films. A thin GaN buffer was deposited before the growth of the $Al_xGa_{1-x}N$ layers of the desired composition. All the $Al_xGa_{1-x}N$ layers were grown under strongly group III-rich conditions in order to achieve the best structural quality layers. In the current study the $Al_xGa_{1-x}N$ layers were grown at temperatures of $\sim 700\ °C$.

Thick ($\sim 10\ \mu m$) $Al_xGa_{1-x}N$ layers were grown by MBE on GaAs substrates and the GaAs was subsequently removed using a chemical etch (20 ml H_3PO_4:100 ml H_2O_2) in order to achieve free-standing $Al_xGa_{1-x}N$ wafers. From our previous experience with MBE growth of zinc-blende GaN [2–4], such a thickness is already sufficient to obtain free-standing GaN and $Al_xGa_{1-x}N$ layers without cracking and at the same time it does not require very long growth runs. To increase the thickness even further to 50–100 μm is merely a technical task, which we have shown earlier is possible. Therefore, for this demonstration of the feasibility of the method, we have chosen to grow the majority of the bulk wurtzite $Al_xGa_{1-x}N$ layers $\sim 10\ \mu m$ thick.

The structural properties of the samples were studied in-situ using reflection high-energy electron diffraction (RHEED) and after growth ex-situ measurements were performed using X-ray diffraction (XRD). To investigate the optical properties of free-standing $Al_xGa_{1-x}N$ layers we have studied photoluminescence (PL) and cathodoluminescence (CL). The PL was excited by a quadrupled tuneable ps Ti:Sapphire laser operating at 190–330 nm. The CL was measured using a telescopic collection system on field emission gun scanning electron microscope [7].

We have studied Al incorporation in the $Al_xGa_{1-x}N$ layers by secondary ion mass spectrometry (SIMS) using Cameca IMS-3F and IMS-4F systems and by electron probe microanalysis (EPMA) using a Cameca SX100 apparatus.

3. Results and discussion

At the first stage we carried out PA-MBE growth of thin ($\sim 1\ \mu m$) wurtzite $Al_xGa_{1-x}N$ layers on two-in. diameter (111)B GaAs substrates for AlN fractions ranging from 0 up to 0.5. This substrate orientation was chosen in order to initiate the growth of the hexagonal phase of material. Wurtzite GaN buffers, of thickness $\sim 50\ nm$, were deposited before the growth of all the $Al_xGa_{1-x}N$ layers. As expected, in $2\theta–\omega$ XRD plots, with increasing Al content we observed a gradual shift of the position of the $Al_xGa_{1-x}N$ XRD peak to higher angle. PL and CL studies confirmed an increase of the band gap of $Al_xGa_{1-x}N$ layers with increasing Al content.

Based on these results then grew $\sim 10\ \mu m$ thick wurtzite $Al_xGa_{1-x}N$ layers under similar growth conditions with x ranging from 0 up to 0.5. Fig. 1 shows a $2\theta–\omega$ XRD plot for a 10 μm thick freestanding wurtzite $Al_xGa_{1-x}N$. The GaAs substrate had been chemically removed from the substrate after growth. In XRD studies we have observed a single peak at ~ 35 degrees, which is the correct position for a wurtzite $Al_xGa_{1-x}N$ layer. Using Vegard's law, we can estimate the composition of the $Al_xGa_{1-x}N$ layer shown in Fig. 1 to be $x \sim 0.1$. The value of AlN fraction in this $Al_xGa_{1-x}N$ layer was also confirmed by EPMA measurements. From high resolution XRD scans we can estimate the zinc-blende fraction, which in this case was below our detection limit ($< 0.1\%$). It is important to note that for $Al_xGa_{1-x}N$ layers with a similar composition ($x \sim 0.1$), but with a thickness of only $\sim 0.5\ \mu m$ the FWHM was similar. This data confirms that we are able to sustain the same good structural quality of wurtzite $Al_xGa_{1-x}N$ layers, whilst increasing the thickness from the very thin layers up to
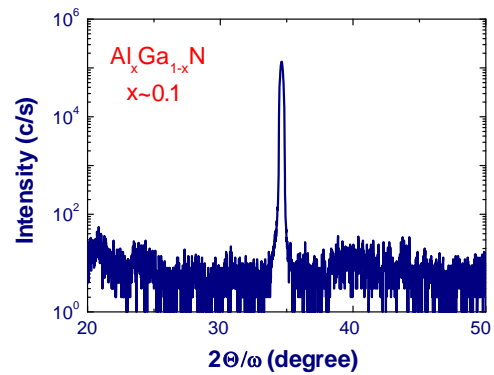
Fig. 1. A $2\theta–\omega$ XRD scan showing the 0002 peak at the centre of a $\sim 10\ \mu m$ thick 2-in. diameter free-standing wurtzite $Al_xGa_{1-x}N$ layer with composition $x \sim 0.1$.
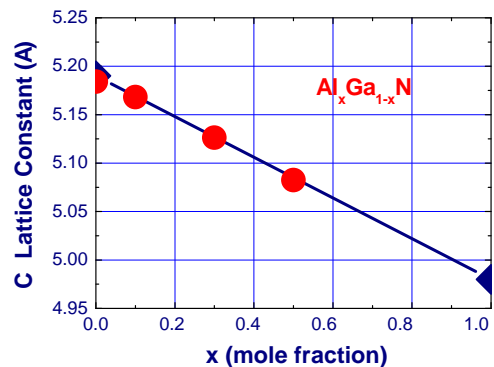
Fig. 2. C-lattice constants for 10 μm thick wurtzite $Al_xGa_{1-x}N$ layers with the different AlN contents.

$\sim 10\ \mu m$. This is a very significant result, because it shows that MBE can be a viable method for the growth of bulk free-standing wurtzite $Al_xGa_{1-x}N$ crystals.

From XRD data the dependence of the lattice constants for $Al_xGa_{1-x}N$ were measured as a function of the AlN content and the results for c-lattice are shown in Fig. 2. The estimated $Al_xGa_{1-x}N$ composition data were later confirmed by EPMA studies. On the figure we have also plotted c-lattice constants for GaN and AlN [1] and a linear estimate for $Al_xGa_{1-x}N$ alloys c-lattice constants using Vegard's law. Fig. 2 shows that c-lattice parameter for freestanding $Al_xGa_{1-x}N$ layers decreases linearly with decreasing AlN content in good agreement with Vegard's law.

We have investigated reciprocal space maps and rocking curves for this series of samples and observed a gradual increase in FWHM ω and decrease in XRD peak intensity with increasing AlN fraction in $Al_xGa_{1-x}N$ layers from 0 to $x \sim 0.5$. The intensity of the XRD peak is still strong and the FWHM ω is relatively narrow for all $Al_xGa_{1-x}N$ layers, which confirms that MBE can be used as a method for the growth of bulk wurtzite $Al_xGa_{1-x}N$ crystals for a wide range of the Al compositions.

The depth uniformity of Al incorporation into the $Al_xGa_{1-x}N$ layers was studied using SIMS. Fig. 3 shows SIMS profiles for Al, Ga, As and N at the centre of free-standing $Al_xGa_{1-x}N$ layer with $x \sim 0.3$ on the side previously in contact with the GaAs substrate. After sputtering through the initial GaN layer we have observed a uniform distribution of Al, Ga and N within the bulk of $Al_xGa_{1-x}N$ layers with different AlN fractions. There is no significant As incorporation into the bulk of $Al_xGa_{1-x}N$ layers, which was confirmed by the fact that the As signal is at the background level of the SIMS system.

In order to study the lateral distribution of the elements across the 2-in. diameter $Al_xGa_{1-x}N$ wafer, we have performed EPMA studies on the surface of the $Al_xGa_{1-x}N$ crystal previously attached
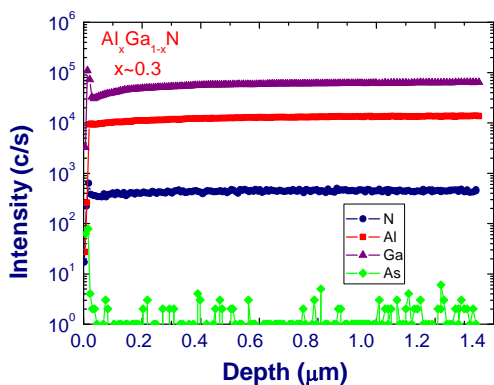
Fig.3. SIMS profiles for Al, Ga, As and N at the centre of free-standing wurtzite $Al_xGa_{1-x}N$ layer with a composition $x\sim0.3$ on the side previously in contact with the GaAs substrate.

Fig. 4. Growth rate for GaN layers grown on 2-in. sapphire substrates using the different Ga fluxes.

Fig. 5. Thickness of wurtzite GaN layers grown on 2-in. GaAs (111)B substrates as a function of the growth time.

to the GaAs substrate. We were able to achieve a uniform distribution of Al content across the diameter for the central part of the 2-in. $Al_xGa_{1-x}N$ wafer. However, close to the edge of the wafer the Al distribution becomes less uniform, with the maximum Al content close to the edge of the wafer. This is similar to EPMA results from zinc-blende $Al_xGa_{1-x}N$ wafers and can be attributed to the strong dependence of the Al incorporation on the group III:N ratio during MBE [5,6]. In our case we have slightly more group III-rich conditions at the edges of the 2-in. wafer due to temperature non-uniformity.

The maximum GaN and $Al_xGa_{1-x}N$ growth rate in our MBE system is limited by the efficiency of our HD25 nitrogen plasma source. In the current MBE configuration the maximum growth rates for HD25 were less than 1 μm/h. Recently, Riber has developed a novel plasma source for the fast growth of GaN layers. Riber have modified the construction of the source and optimised the pyrolytic boron nitride (PBN) crucible and PBN aperture arrangement. The first tests of the novel Riber source were performed for the growth of very thin GaN layers grown for 5 min on small wafers [8]. The authors of that work demonstrated that with this novel source it was possible to achieve GaN growth rates up to 2.65 μm/h [8].

We have installed this novel Riber source in our custom designed MBE system. Growth of GaN layers was performed on large area 2-in. sapphire (0001) wafers. In this study, all the GaN layers were grown for 2 h, which was significantly longer than in the earlier study [8]. The transition from N-rich to Ga- rich growth was also investigated. The N flow rate was fixed at 3 sccm, which was established to be an optimal N flow rate for efficient performance of the novel Riber source [8]. A fixed RF power of 500 W was used in all our experiments.

Fig. 4 shows the dependence of the growth rate for GaN layers grown on 2-in. sapphire for different Ga fluxes. We measured the thickness of the GaN layers after growth by an optical interference method. Under N-rich conditions we observed a clean surface and the growth rate increased linearly with increasing Ga flux. Under strongly Ga-rich growth conditions we observed Ga droplets on the surface and a fixed growth rate, so in this regime the growth is limited by the amount of active nitrogen. The dependence in Fig. 4 is in excellent agreement with the classical papers on the kinetics of PA-MBE of GaN [9]. The highest growth rate achieved under these growth conditions was 1.8 μm/h, which is in agreement with the earlier Riber results on the very thin GaN layers [8].

For the growth of free-standing GaN and $Al_xGa_{1-x}N$ layers we normally use GaAs substrates [2–4]. Therefore, we checked the performance of Riber source for the growth of GaN layers on GaAs (111)B substrates and have obtained results similar to the growth on sapphire shown in Fig. 4.

Fig. 5 shows the thicknesses of three wurtzite GaN layers grown for 2, 4 and 6 h respectively on 2 in. GaAs (111)B substrates. The N flow was kept at 3 sccm and the Ga flux was fixed at a BEP $\sim2.8\times$
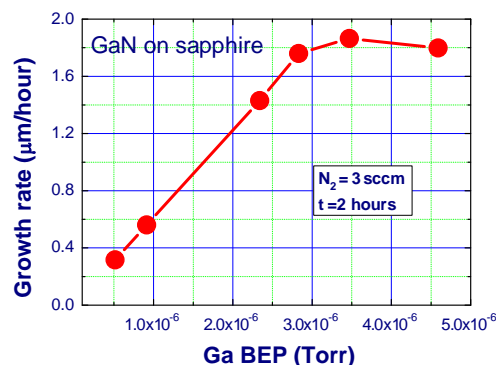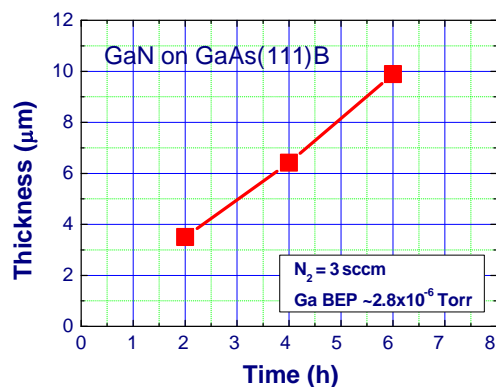
10^{-7} Torr. This Ga flux value allowed us to stay under slightly Ga-rich conditions during the growth, as can be seen from Fig. 4. We have checked the stability of the GaN growth rate during the PA-MBE process. We observed a linear increase in the GaN thickness with time as expected and so GaN layers with a thickness of $\sim10\,\mu$m can be obtained in 6 h. We have demonstrated previously [2–6] that for the use as a substrate the GaN layer thickness needs to be greater than 50 μm. With the new Riber source we can achieve such a thickness in less than 2 days growth, and that makes the production of wurtzite $Al_xGa_{1-x}N$ a commercially viable process.

4. Summary and conclusions

We have studied the growth of free-standing wurtzite $Al_xGa_{1-x}N$ bulk crystals by PA-MBE. Thick wurtzite $Al_xGa_{1-x}N$ films were grown by PA-MBE on 2-in. GaAs (111)B substrates and were removed from the GaAs substrate after growth to provide free standing $Al_xGa_{1-x}N$ samples. EPMA measurements confirm that the Al content is uniform across the wafer and SIMS measurement show that the composition is also uniform in depth. We demonstrated that free-standing wurtzite $Al_xGa_{1-x}N$ wafers can be achieved by PA-MBE for a wide range of AlN fractions. In order to develop a commercially viable process for the growth of wurtzite $Al_xGa_{1-x}N$ substrates, we used a novel Riber plasma source and have demonstrated growth rates of GaN up to 1.8 μm/h on 2-in. diameter GaAs and sapphire wafers.

References

[1] J.H. Edgar, S. Strite, I. Akasaki, H. Amano, C. Wetzel (Eds.), Part A1.2. Lattice parameters of the group III nitrides, in: Properties, Processing and Applications of Gallium Nitride and Related Semiconductors, INSPEC, Stevenage, 1999, ISBN 0 85296 953 8.

[2] S.V. Novikov, N.M. Stanton, R.P. Campion, R.D. Morris, H.L. Geen, C.T. Foxon A.J. Kent, Semicond. Sci. Technol. 23 (2008) 015018.

[3] S.V. Novikov, N.M. Stanton, R.P. Campion, C.T. Foxon, A.J. Kent, J. Cryst. Growth 310 (2008) 3964.

[4] S.V. Novikov, N. Zainal, A.V. Akimov, C.R. Staddon, A.J. Kent, C.T. Foxon, J. Vac. Sci. Technol. B 28 (2010) C3B1.

[5] S.V. Novikov, C.R. Staddon, R.E.L. Powell, A.V. Akimov, F. Luckert, P.R. Edwards, R.W. Martin, A.J. Kent, C.T. Foxon, J. Cryst. Growth 322 (2011) 23.

[6] S.V. Novikov, C.R. Staddon, F. Luckert, P.R. Edwards, R.W. Martin, A.J. Kent C.T. Foxon, J. Cryst. Growth 350 (2012) 80.

[7] P.A. Edwards, J L Krishnan, J. Bruckbauer, C. Liu, P. Shields, D. Allsopp, T. Wang, R.W. Martin, Microsc. Microanal. 18 (2012) 1212.

[8] B.M. McSkimming, F. Wua, T. Huault, C. Chaix, J.S. Speck, J. Cryst. Growth 386 (2014) 168.

[9] B. Heying, R. Averbeck, L.F. Chen, E. Haus, H. Riechert, J.S. Speck, J. Appl. Phys. 88 (2000) 1855.
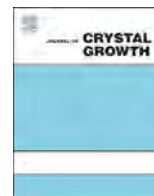
High growth speed of gallium nitride using ENABLE-MBE

CrossMark

J.J. Williams [a,*], A.M. Fischer [b], T.L. Williamson [c], S. Gangam [d], N.N. Faleev [d],
M.A. Hoffbauer [c], C.B. Honsberg [d]

[a] Materials Science Engineering, Arizona State University, P.O. Box 875706, Tempe, AZ 85287-5706, USA
[b] Department of Physics, Arizona State University, P.O. Box 871504, Tempe, AZ 85287-1504, USA
[c] Chemistry Division, Los Alamos National Laboratory, P.O. Box 1663, MS J964, Los Alamos, NM 87545, USA
[d] School of Electrical, Computer and Energy Engineering, Ira A. Fulton Schools of Engineering, Solar Power Lab, Arizona State University, P.O. Box 875706,
Tempe, AZ 85287-5706, USA

ARTICLE INFO

ABSTRACT

Films of gallium nitride were grown at varying growth speeds, while all other major variables were held constant. Films grown determine the material impact of the high flux capabilities of the unique nitrogen plasma source ENABLE. Growth rates ranged from 13 to near 60 nm/min. X-ray ω scans of GaN (0002) have FWHM in all samples less than 300 arc sec. Cathodoluminescence shows radiative recombination for all samples at the band edge. In general material quality overall is high with slight degradation as growth speeds increase to higher rates.

© 2015 Published by Elsevier B.V.

1. Introduction

Over the past two decades gallium nitride has reached maturity as a technologically pivotal semiconductor. The uses for GaN range from power electronics, to high electron mobility transistors, and to light emitting diodes [1,2]. Currently, material for all of these applications has been predominantly produced by metal organic vapor phase epitaxy (MOVPE).

Molecular beam epitaxy (MBE) has unique advantages over MOVPE due to its inherent lower background contamination, ability to make abrupt stops in incoming growth species (important for sharp quantum wells), and kinetically driven capability to access metastable phases that are not available to growth processes of thermodynamic equilibrium. However, any commercial interest in MBE based growth of GaN has been passed over due to slow growth rates that make it hard to meet demand thus challenging the economics of an MBE based industry. These slow growth rates are mostly due to the low fluxes of active nitrogen associated with conventional plasma nitrogen sources [3].

The Energetic Neutral Atom Beam Lithography and Epitaxy (ENABLE) plasma source developed at Los Alamos National Laboratory (LANL) is a unique source. ENABLE is capable of delivering a high flux of neutral nitrogen atoms (or other gases as well) as the active species to the surface of a wafer [4]. This technique has the potential to keep pace with the Ga fluxes supplied by the industry standard Ga effusion cells. This should lead to higher growth speeds for gallium nitride films by MBE. These high speed growth rates and their effects on structural and luminescent properties will be explored herein.

2. Experimental

Film growth was performed in a custom built MBE chamber. This chamber exhibited a background pressure of 3.1×10^{-9} Torr during the time prior to sample growth. Samples are thermally heated by radiative transfer from a pyrolytic boron nitride (PBN) heater plate 5 mm offset from the back of the wafer. Samples are rotated during growth at 5 rpm to promote film uniformity. Reflection high energy electron diffraction (RHEED) is used to monitor the condition of the crystal surface. A residual gas analyzer (RGA) is used to measure partial pressures of relevant gases: N, NH_3, H_2O, Ar, and CO_2. Transients of each signal are used to determine deviations from stoichiometry. A gallium beam is supplied to the surface of the sample from a Veeco SUMO thermal evaporator. This provides high quality Ga flux uniformity across the wafer surface. [5] A nitrogen beam is supplied to the sample from the LANL built ENABLE source.

The ENABLE source uses a focused infrared laser ($\lambda = 10.6$ µm) to sustain a plasma in an antechamber. Mass flow controllers are used to create a source gas mixture of Ar and N_2. The flow rate of the N_2 controls the flux of N atoms in the beam. The beam is created when the focused plasma is inserted into a supersonic nozzle. The expansion from this nozzle passes through several apertures and is introduced into the main growth chamber. This

creates a beam of neutral nitrogen atoms with kinetic energies tunable from 0.5 to 3.0 eV [6].

Samples were grown on two-inch c-plane oriented α-Al$_2$O$_3$ wafers. Wafers were outgassed for 30 min at 900 °C followed by nitridation at 350 °C for 30 min. An aluminum nitride buffer layer was grown at 850 °C for 10 min at a nominal growth rate of 15 nm/min. Subsequently, the GaN layer was grown for 10 min at 850 °C with varying growth rates. Growth rates were based on a nominal growth of 15 nm/min for a Ga cell base temperature of 950 °C. Samples were also grown with the Ga cell base temperature at 1000 and 1050 °C. Under the assumption that the ratio of vapor pressures (based on Eq. (1), where T is in Kelvin and P is in atmospheres [7]) at these temperatures will produce an equivalent ratio in Ga flux to the sample surface it was estimated that the growth rates should be 30 nm/min and 60 nm/min, respectively. Growths were not investigated at higher speeds due to concerns of the Ga cell spitting above 1050 °C. However, it should be noted that the ENABLE source was only running at 20% nitrogen capacity for the fastest growth. In keeping consistency with other growth protocol on this tool (focused on In-rich InGaN [8]) films were grown in a slightly nitrogen rich regime. This was verified by monitoring the transient of the nitrogen signal in the RGA after metal shuttering

$$\ln(P_{Ga,vap}) = \frac{-14,900}{T} - 0.515 \ \ln(T) + 7.34 \qquad (1)$$

The thickness and surface roughness of the samples were measured using a J.A. Woollam variable angle spectroscopic ellipsometer. Incident light with wavelengths ranging from 400 to 800 nm was used. The resulting data was fitted to n (index of refraction) and k (extinction coefficient) values for GaN and AlN. Surface roughness at the AlN-GaN interface was assumed to be negligible. This assumption was based on the RHEED pattern of the AlN layer showing strong surface reconstruction, indicative of a near atomically flat surface.

Structural properties of the samples were characterized using a PANalytical MRD high resolution X-ray diffractometer (HRXRD). A hybrid X-ray mirror with asymmetrical Ge (220) 4-bounce crystal produces an incident Cu Kα$_1$ X-ray beam with $\lambda = 0.1540598$ nm and 19 arc sec divergence. A triple crystal scheme (TC) utilizing a three-bounce Ge(220) analyzer crystal in front of the detector was used to collect high resolution ω–2θ and ω scans to separate coherent and diffused scattered radiation. A double crystal scheme (DC) with only a receiving slit on the detector was used to perform rough alignments and collect ω–2θ and ω-scans. A JEOL JSM 6300 scanning electron microscope (SEM) equipped with MonoCL2 cathodoluminescence spectrometer was used to measure the optical properties of the samples.

3. Results and interpretations

Ellipsometry values for roughness and thickness are presented in Table 1. Most of these values track well with the X-ray diffraction based calculations. Both of the measured values trail the vapor pressure curve approximations. The offset in growth rates is due to the slight inaccuracy of the known growth rate. The reference growth rate was thought to be 15 nm/min, but these conditions yielded a growth rate of 13 nm/min.

A symmetric ω–2θ scan of all three samples is shown in Fig. 1. The GaN (0002) and AlN (0002) can be clearly seen, with no irregular phases present. Additional scans (not shown here) included the Al$_2$O$_3$ (0006) substrate peak. These scans confirmed that measurements were made with the sapphire peak well aligned in the diffractometer at $2\theta = 41.67°$. The high resolution TC ω-2θ scan resolves interference fringes (i.e. Pendellosüng fringes) about the main diffraction peaks. The angle spacing of the fringes can be used to estimate the layer thickness [9]. The fringes around the AlN peak correspond to a thickness of ∼160 nm for all three films, and hence a growth rate of 16 nm/min. The GaN peaks for the "15 nm/min" and "30 nm/min" both have fringes, while the "60 nm/min" does not due to increased volumetric structural deteriorations. The interference fringes on the former two correspond to thicknesses of 132 and 275 nm, respectively. These values come from growth rates of 13.2 and 27.5 nm/min for the nominal "15 nm/min" and "30 nm/min" respectively. This is in
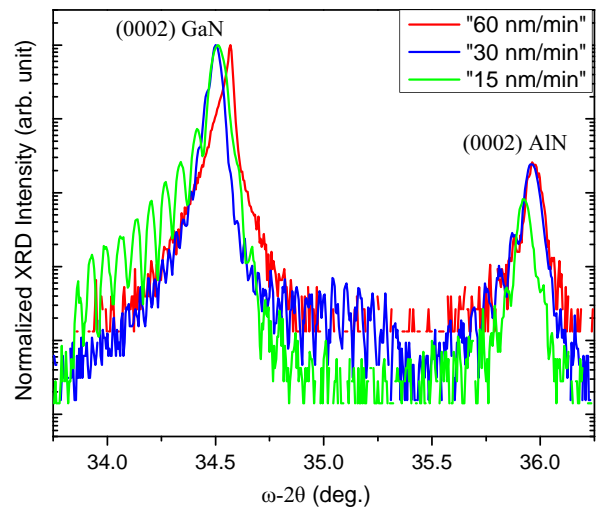
Fig. 1. Semi-log plots of ω–2θ scans taken with the TC schematic, resolving the interference fringes on the main diffraction peak. Since these scans are symmetric the ω–2θ schematic is equivalent to θ–2θ scans.

Table 1
Lists XRD and Ellipsometry measurements for the films. The "Coh. FWHM" column represents the full-width-half-maximum (FWHM) of a Gaussian peak representative of the narrow coherent peak for the TC ω-scans. The "Diff. FWHM" represents the FWHM of the complimentary broad diffuse peak from the same de-convolution process of TC ω-scan. The "DC FWHM" values are taken from ω-scans with double crystal scheme and no receiving slits.

		X-ray diffraction					Ellipsometry	
		2θ Pos.	Coh. FWHM	Diff. FWHM	DC FWHM	Thickness[a]	Thickness[b]	Roughness
"15 nm/min"	AlN	35.92°	0.0022°	0.0353°	0.0290°	160 nm	177 nm	–
	GaN	34.41°	0.0025°	0.0470°	0.0396°	132 nm	134 nm	3.0 nm
"30 nm/min"	AlN	35.98°	0.0029°	0.0333°	0.0360°	154 nm	163 nm	–
	GaN	34.50°	0.0029°	0.0602°	0.0510°	275 nm	283 nm	4.5 nm
"60 nm/min"	AlN	35.96°	0.0036°	0.0334°	0.0350°	160 nm	181 nm	–
	GaN	34.57°	0.0034°	0.0343°	0.0280°	–	782 nm[c]	15.3 nm

[a] Thicknesses from XRD.

[b] Thicknesses from ellipsometry.

[c] The thickness for the "60 nm/min" speed GaN does not follow the trend of the other two that is falling just short of the vapor pressure approximation. This value produced a high mean-squared error and is likely off due to surface roughness and non-ideal n and k values.

Fig. 2. The top graph depicts the GaN(0002) DC "no slit" ω-scans of all samples. Peaks show a slight asymmetry. In the "15 nm/min" sample this is due to interference fringes. The bottom graph shows TC ω-scans of the same peaks. Strong coherent peaks are flanked by wide diffuse peaks. The shape of the diffuse tails of the red RC suggest co-existence of two different types of crystal defects in the volume of GaN layer.

Fig. 3. Cathodoluminescence spectra taken at room temperature. All spectra show band edge or near band edge emission. The "15 nm/min" sample has a significantly weaker intensity, likely due to a film thickness smaller than the excitation depth of the electron beam. The "60 nm/min" sample shows weak broad blue band and yellow band emission. Likely associated with point defects.

close agreement with the initial vapor curve based approximations, and nearly identical agreement with the ellipsometry data. If it was to be assumed that the "60 nm/min" sample follows the same trend it would have a thickness of 550 nm and a growth rate of 55 nm/min. It is a noteworthy trend that the Pendellosüng fringes become more diffuse with faster growth rates. This is likely due to increased bulk defect densities with increased growth rates, defects which may not show up in ω-scans.

Fig. 2 shows semi-log plots of ω-scans about the GaN (0002) peak, taken with the double crystal and triple crystal schematic, respectively. The ω-scan with the double crystal schematic was collected with no receiving slits. The triple crystal schematic uses the analyzer crystal to separate coherent diffraction of the lattice planes from diffuse radiation due to crystal imperfections. These scans have been de-convoluted into two Gaussian peaks representing the coherent and diffuse components. The FWHM for each of these component peaks is listed in Table 1. For the double crystal and diffuse scattered radiations the FWHM is never wider than 0.083° or 300 arc sec. This value been classically assigned as a benchmark for device grade GaN. There have been accounts that narrower peaks can lead to material with worse device quality [10]. Additional characterization of background carrier concentrations, TEM, and polarity measurements would indicate if this is valid for these samples.

Cathodoluminescence (CL) spectra of the three samples, taken at 295 K, are shown in Fig. 3. The "60 nm/min" sample exhibits a near-band-edge emission (NBE) at 364 nm with a FWHM of 11 nm. Two additional broad emissions are observed at ∼450 (blue) and 575 nm (yellow). The origin of the latter band is associated to nitrogen vacancies [11]. As the growth speed decreases, the intensity of the NBE and of the yellow band quench. A decrease in the yellow band luminescence may be associated to a decrease in the nitrogen vacancy density (*i.e.* material grows more stoichiometrically). CL images taken at the NBE emission of the three samples are shown in Fig. 3. We observe an improvement in the film surface quality from large grains (∼500 nm) to smooth surfaces as the growth speed decreases. For example, Fig. 3 ("30 nm/min") exhibits bright and dark regions. The dark regions correspond to regions with lower NBE intensity, possibly due to lower crystalline quality. The decrease in the NBE for the lowest growth speed sample may be explained by a lower background carrier concentration.

4. Conclusion

The use of the source technology ENABLE has been implemented in an MBE chamber to deliver high fluxes of active nitrogen for growth of gallium nitride. These high fluxes have been used to investigate nominal growth rates of 15, 30, and 60 nm/min. These films have been characterized by ellipsometry, X-ray diffraction and cathodoluminescence. Structures all show narrow FWHM for ω-scans of (0002) GaN and interference fringes on the AlN buffer layer. The nominal 15 and 30 nm/min films show interference fringes around the ω-2θ GaN (0002) peak, indicating high vertical coherence of these films. The 60 nm/min film shows no

interference fringes and broader almost diffuse ω-scans, indicating that at high growth speeds the crystal quality is more deteriorated. This trend is also seen in the ellipsometry fittings. Both the ellipsometry fittings and the interference fringe spacing give good agreement for thicknesses in the "15 nm/min" and "30 nm/min" sample thicknesses. Real rates were slightly slower than anticipated, 13 and 28 nm/min. However, the relative ratio for the rates was as expected.

All samples show band edge or near band edge emission in the cathodoluminescence measurements. This indicates that the growth rates can be pushed to high speeds while still sustaining crystal quality good enough for photo-active material. Some broad low intensity emissions in the blue and yellow range start to show up for the 60 nm/min GaN, likely due to deviations in stoichiometry.

The characteristics of stable growth rate, narrow rocking curves, and photoactive material are all promising results. They indicate that using ENABLE as a source of active nitrogen species, nitride MBE can achieve growth of respectable material at growth rates up to at least 55 nm/min. This rate of 3.3 μm/hr was achieved with the ENABLE source at 20% of maximum nitrogen capacity opening the possibility for MBE to achieve even faster nitride based growth.

Acknowledgments

References

[1] H. Morkoc, Nitride Semiconductors and Devices, Springer, Heidelberg, New York, 1999.
[2] S. Nakamura, The Blue Laser Diode, Springer, 2000.
[3] N. Newman, The energetics of the GaN MBE reactions: A case study of meta-stable growth, J. Cryst. Growth 178 (1997) 102–112.
[4] E.A. Akhadov, D.E. Read, A.H. Mueller, J. Murray, M.A. Hoffbauer, Innovative approach to nanoscale device fabrication and low-temperature nitride film growth, J. Vac. Sci. Technol. B 23 (2005) 3116.
[5] F. Ren, Proceedings of the Symposium on High Speed III-V Electronics for Wireless Applications and the Twenty-Fifth State-of-the-Art Program on Compound Semiconductors, The Electrochemical Society, Inc., Pennington, New Jersey, 1996.
[6] J.J. Williams, T.L. Williamson, M.A. Hoffbauer, Y. Wei, N.N. Faleev, C.B. Honsberg, Growth of high crystal quality InN by ENABLE-MBE, Phys. Status Solidi C 11 (2014) 577–580.
[7] C.N. Cochran, L.M. Foster, Vapor pressure of gallium, stability of gallium suboxide vapor, and equilibria of some reactions producing gallium suboxide vapor, J. Electrochem. Soc. 109 (1962) 144–148.
[8] T.L. Williamson, A.L. Salazar, J.J. Williams, M.A. Hoffbauer, Improvements in the compositional uniformity of In-rich $In_xGa_{1-x}N$ films grown at low temperatures by ENABLE, Phys. Status Solidi C 8 (2011) 2098–2100.
[9] V. Holý, U. Pietsch, T. Baumbach, High resolution x-ray scattering from thin films and multilayers, in: Springer Tracts in Modern Physics, ,Ch. 7, 149, 1999.
[10] H. Morkoc, Nitride Semiconductors and Devices, Springer, Heidelberg, New York (1999) 124.
[11] E.R. Glaser T.A. Kennedy, J.A. Freitas, Jr, M. Asif Khan, D.T. Olsen, and J.N. Kuznia, Silicon Carbide and Related Materials, in: Proceedings of the IOP Conference, 137 IOP, Bristol, 1994, p. 443.

CRYSTAL
GROWTH
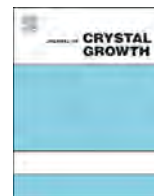
Low temperature AlN growth by MBE and its application in HEMTs

CrossMark

Faiza Afroz Faria *, Kazuki Nomoto, Zongyang Hu, Sergei Rouvimov, Huili (Grace) Xing, Debdeep Jena

Department of Electrical Engineering, University of Notre Dame, Notre Dame, IN 46556, USA

ABSTRACT

Low temperature growth of AlN from 470 °C down to room temperature has been studied by RF-plasma assisted molecular beam epitaxy (PAMBE). Partially amorphous AlN was achieved at growth temperatures below 250 °C. We demonstrate the application of the low temperature (LT-) AlN as an in-situ surface passivation technique for III-nitride based high electron mobility transistors (HEMTs). High 2DEG densities $> 2 \times 10^{13}$ cm^{-2} and sheet resistance < 250 $\Omega/\square$ at room temperature were first obtained for MBE grown AlN/GaN HEMT structures with thin high temperature AlN barrier, then capped with LT-AlN (< 4 nm). Using this novel technique, low DC–RF dispersion with gate lag and drain lag below 2% is demonstrated for an AlN/GaN HEMT.

© 2015 Elsevier B.V. All rights reserved.

1. Introduction

MBE growth of AlN at low temperature (< 600 °C) has not been explored and a systemic study of it is still missing. Epitaxial growth of high quality single crystal AlN is possible at high temperatures, preferably above 700 °C using metal–organic chemical vapor deposition (MOCVD) or MBE. This is due to the fact that Al has low adatom mobility at low growth temperatures. In contrast, low temperature growth of AlN is common in other thin film deposition techniques, such as, atomic layer deposition (ALD), plasma enhanced chemical vapor deposition (PECVD) or sputter deposition. The quality of the AlN films obtained by these techniques differs from the MBE or MOCVD grown AlN in terms of crystallinity. MBE and MOCVD are employed to achieve single crystal AlN. On the other hand, ALD, PECVD or sputtering techniques are used for applications in which single crystal AlN is not essential.

In this work, we perform a systematic study of low temperature MBE growth of AlN. We investigate the possible application of MBE grown LT-AlN as an in-situ surface passivation layer for performance enhancement of III-nitride HEMTs. Although reports of various passivation techniques exist in literature [1–6], further improvement is desired. DC–RF dispersion in HEMTs is an issue still to be addressed effectively by the III-nitride community [7]. AlN has a wide bandgap (~ 6.2 eV) and a high thermal conductivity (285 W/m/K for wurtzite single crystal) [8]. Its unique properties make it a strong candidate compared to other materials typically chosen for III-nitride surface passivation [1–4]. Furthermore, in-situ passivation within the ultra high vacuum environment of MBE prevents the surface from being exposed to atmosphere/moisture before it is passivated. Therefore, MBE offers an advantage over other tools used for ex-situ passivation, for example, ALD or PECVD. To the best of our knowledge, the MBE grown LT-AlN, and its application for in-situ passivation of III-nitride surfaces have not been reported yet. The aim of this work is to provide some insight into this rather unexplored field of III-nitride research.

2. MBE growth of low temperature AlN

All III-nitride growths in this work were performed using a Veeco Gen 930 RF-plasma assisted MBE system. The growths were done along the [0 0 0 1] direction on *c*-plane substrates. Reflection high-energy electron diffraction (RHEED) was used for in-situ film characterization. For ex-situ structural characterization of the MBE grown films, Atomic Force microscopy (AFM), X-ray diffraction (XRD) and Transmission electron microscopy (TEM) were used.

2.1. AlN films grown at different temperatures

The goal of the first experiment was to study the change in structural properties of AlN as a function of the growth temperature. A series of AlN/GaN (15/50 nm) films were grown on semi-insulating (SI) GaN on Sapphire templates prepared by MOCVD. The growth of 50 nm GaN was performed under slightly metal-rich conditions at $T_{Tc} \sim 660$ °C as measured by the thermocouple.

* Corresponding author.
E-mail addresses: ffaria@nd.edu, faizafaria2011@yahoo.com (F.A. Faria).

The excess Ga was desorbed in-situ at $T_{Tc} \sim 700$ °C before growing the AlN layer. Five 15 nm thick AlN layers were grown at $T_{Tc} \sim 800$, 660, 470, 250 °C and at room temperature (RT) with Al/N flux ~ 1. A growth interruption (GI) was applied to reach the desired temperature before growing the AlN layer. A growth rate of ~ 180 nm/h was used with a RF-plasma power of 190 W and a nitrogen flow rate of 1.1 sccm.

To characterize the films, ω–2θ scan along the 002 reflection were performed using XRD. The presence of the AlN peaks in addition to the GaN substrate peaks are observed in all 5 samples (Fig. 1). However, the FWHM of the AlN peak increases with decreasing growth temperature. This is expected as the quality of the single crystal AlN degrades at lower growth temperature and the film becomes less oriented along the c-axis. Due to the $\sim 2.4\%$ lattice mismatch, AlN grown on GaN is tensile strained and beyond a critical thickness of ~ 6.5 nm it starts to crack [9]. In this experiment, the thickness of the AlN films grown on GaN was larger than the critical thickness. AFM images show cracks on the surface of the 15 nm AlN layers grown at $T_{Tc} \sim 800$, 660 and 470 °C (Fig. 2a–c, respectively). The density of the cracks reduces by more than 50% as T_{Tc} is lowered from 800 to 470 °C. No cracks are observed on the surface of the 15 nm AlN grown on GaN at $T_{Tc} \sim 250$ °C and at RT (Fig. 2d and e). A possible explanation of this observation would be the difference in thermally-induced stress in AlN when grown on GaN at different temperatures. Figge et al., experimentally calculated the thermal expansion coefficient of wurtzite AlN as a function of temperature [10]. Based on their hypothesis, the mismatch between the in-plane lattice constants of AlN and GaN induced only by thermal expansion is maximum
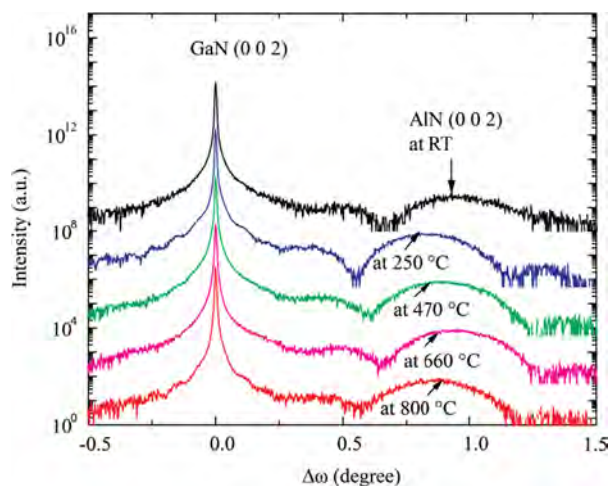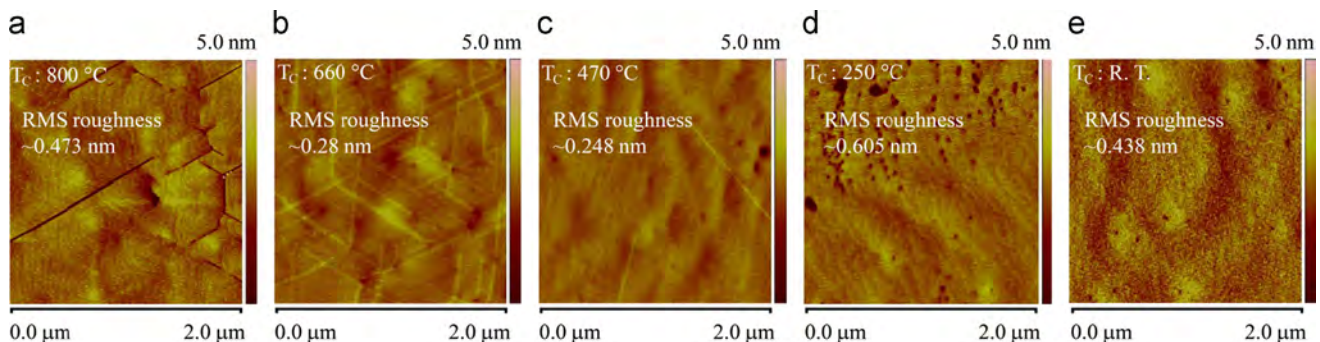
($\sim 0.055\%$) at a temperature of ~ 700 K (427 °C). As temperature is decreased beyond this value, the thermally-induced mismatch decreases monotonically. So, a low growth temperature as opposed to conventional high temperature (> 600 °C) may reduce the possibility of crack formation as the substrate is cooled down. The AFM image in Fig. 2d shows presence of pits on the AlN surface for $T_{Tc} \sim 250$ °C. However, no pits are observed and atomic steps do not appear on the surface of the AlN grown at RT (Fig. 2e) unlike high quality single crystal AlN. The RMS roughness of the AlN film is plotted as a function of growth temperature in Fig. 3.

2.2. AlN growth below 250 °C

To further study the crystal quality of AlN grown at low temperature ($T_{Tc} < 250$ °C), the following experiment was performed. A 15 nm thick AlN film was grown at RT under slightly N-rich regime on a GaN on sapphire template. The Al/N flux ratio was ~ 0.97. Under similar growth condition, a thicker (~ 200 nm) AlN film was grown on a similar template. A control sample was prepared by growing 15 nm AlN at a high temperature of $T_{Tc} \sim 660$ °C on a similar substrate. In-situ measurement by RHEED showed 1×1 reconstruction for the GaN substrate and the high temperature (HT-) AlN oriented along the c-axis. On the other hand, diffused ring like features were observed in RHEED for the AlN films grown at RT. This indicates polycrystalline quality of the films near the surface. The ω–2θ scan along the 002 reflection (Fig. 4) shows the AlN peak only for the control sample. The absence of AlN peak for the other two samples suggests that the RT AlN is not oriented along the [0 0 0 1] direction and is partially or fully amorphous [11].

AFM scans over large (400 μm^2) and small (4 μm^2) areas reveal that the surface roughness is relatively higher for the 200 nm thick film compared to the 15 nm film (Fig. 5). A relatively higher density of accumulated metal is observed on the surface of the thicker film (Fig. 5a and b). However, both 15 and 200 nm films show RMS roughness < 1 nm over small areas (Fig. 5c and d). The lack of adatom mobility of Al at room temperature leads to the formation of occasional voids and accumulation of Al on the surface. For thicker films this effect is more pronounced. Further studies by varying the Al/N flux ratio in N-rich regime and by applying shutter modulation method may lead to a better understanding of the surface roughness limits of PAMBE grown RT AlN.

To further analyze the structural property of LT-AlN grown on different substrates, the following experiment was performed. MOCVD grown AlN on sapphire and SI GaN on sapphire were chosen as the substrates. The substrates were co-loaded into the reactor chamber and ~ 130 nm LT-AlN films were grown. The targeted growth temperature was $T_{Tc} \sim 160$ °C. Al/N flux ratio was ~ 1. The RF plasma power was set to 275 W with a nitrogen flow rate of 1.25 sccm to achieve a growth rate of ~ 260 nm/h. A ω–2θ scan along the 002 reflection was performed for the 130 nm LT-AlN film grown

Fig. 1. ω–2θ scan along the 002 reflection for the series of 5 samples show peak for 15 nm AlN grown at different temperatures on GaN.

Fig. 2. AFM scan over an area of 4 μm^2 shows the surface morphology of the 15 nm AlN grown at different temperatures on GaN.
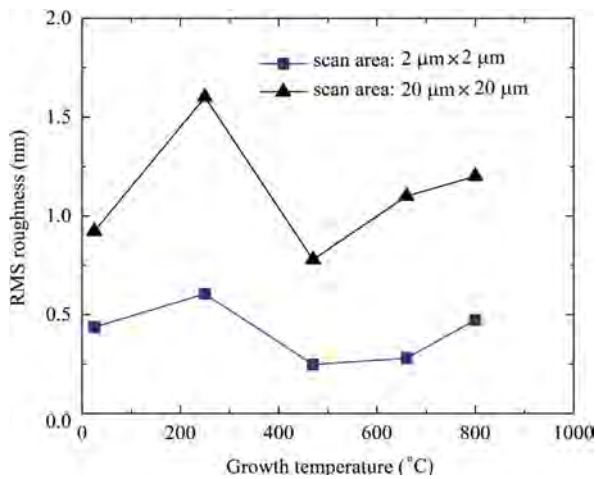
Fig. 3. RMS roughness obtained from AFM scan of the 15 nm AlN films grown at different temperatures on GaN.
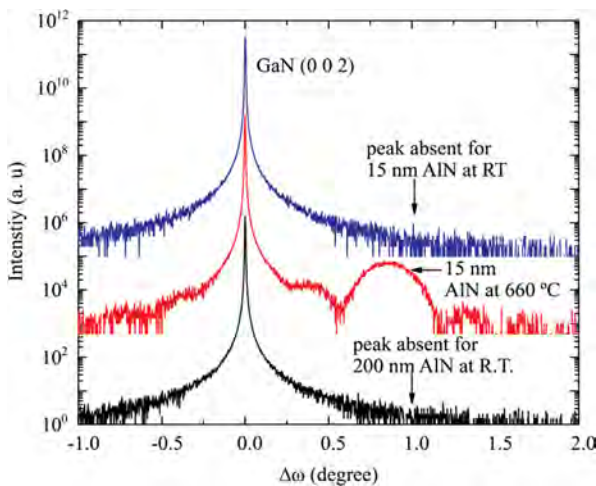
Fig. 4. ω–2θ scan along the 002 reflection show the absence of AlN peak for 15 and 200 nm AlN grown at RT on GaN templates. The peak for the 15 nm AlN grown at 660 °C on a similar GaN template is present.

Fig. 5. AFM scan over an area of 4 μm^2 and 400 μm^2 for 15 nm AlN (a, c, respectively) and 200 nm AlN (b, d, respectively) grown at room temperature on GaN templates.

on SI GaN substrate. The AlN peak was absent. Cross-section TEM image confirms that continuous films of ~130 nm LT-AlN were grown on both substrates with no preferential orientation. The coexistence of polycrystalline and amorphous regions within the LT-AlN film is manifested in both samples (Fig. 6b and c). The inset of Fig. 6c shows the Fast Fourier Transform (FFT) for the region highlighted in the LT-AlN film. The FFT represents the diffraction pattern of that region and confirms the presence of amorphous region in the LT-AlN film. It was also confirmed by TEM (not shown) that the growth rate of AlN at the low temperature remains same as that at high temperature with Al/N flux ratio ~1.

3. Application of MBE grown LT-AlN in HEMT

With a goal to demonstrate the application of MBE grown LT-AlN in HEMTs a series of AlN barrier GaN HEMT structures were grown by MBE with an additional LT-AlN (<4 nm) cap layer. The HEMT structures grown underneath the LT-AlN cap consisted of GaN/HT-AlN/GaN/HT-AlN (~2/3.5/250/1 nm) layers with ±0.5 nm variation in the HT-AlN barrier within the series of samples. 1 cm × 1 cm pieces of MOCVD grown SI GaN on sapphire were chosen as the substrate. A growth temperature of ~665 °C was used for all the

layers of the HEMT structures and GI was applied before growing the LT-AlN cap. The HT-AlN barrier and the buffer GaN layer were grown under slightly metal rich condition and N-rich condition was used for the HT-AlN nucleation layer. Indium dot contacts were formed on the as-grown HEMT structures for the Hall-effect measurement. Decently high 2DEG densities exceeding 2×10^{13} cm^{-2} with mobility ~1000 cm^2/V/s and sheet resistance below 250 Ω/□ were measured at room temperature for all the samples. The Hall-effect data measured at room temperature and 77 K are illustrated in Figs. 7a and 6b. These data indicate that the LT-AlN cap layer does not have adverse effect on the carrier transport properties of the 2DEG channel formed at the HT-AlN/GaN interface. Therefore, the 2DEG channels can be employed to fabricate high performance AlN/GaN HEMTs. HEMTs with annealed Ti/Al/Ni/Au contacts were fabricated using the heterostructures containing the LT-AlN cap. We report a maximum current density of ~1.6 A/mm at 0 V gate bias and peak extrinsic transconductance of ~420 mS/mm at 6 V drain bias for a 55 nm long, 25 μm wide device. Low DC–RF dispersion was observed for the as-fabricated device in terms of low gate lag (~1.8%) and drain lag (~1.4%) from pulsed I–V measurement (Fig. 8a) near 1 MHz. The increase in dynamic on resistance is only ~5%. Note that the relatively lower value of the current density at DC condition compared to the pulsed condition indicates possible self-heating of the substrate. This may be due to the low thermal conductivity of the SI GaN on sapphire substrate. However, the high drain current density approaching 2 A/mm and the low gate and drain lag (<2%) are encouraging results for further study of MBE grown LT-AlN for performance boost of III-nitride HEMTs. The transfer curves with dual sweep are plotted for drain current, gate current and extrinsic transconductance (g_m) in Fig. 8b for drain bias of 6 V. The peak g_m was measured to be ~424 mS/mm at V_{DS} of 6 V. The reason
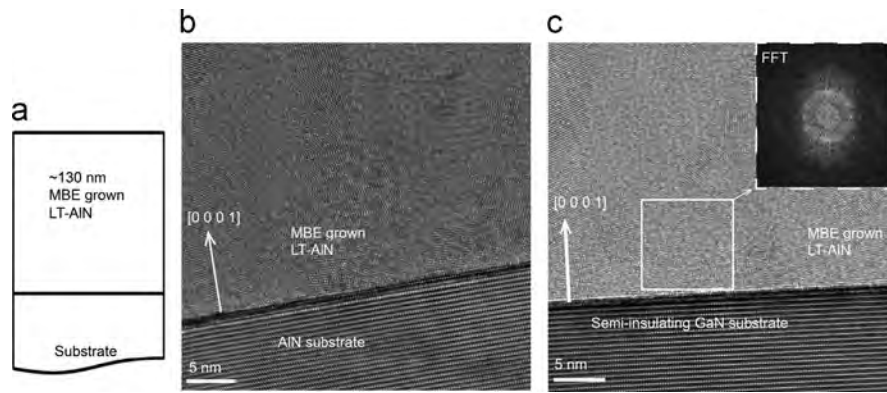
Fig. 6. Schematic of the grown structure is shown in (a). Cross section transmission electron micrographs show presence of partially amorphous regions in 130 nm LT-AlN grown on (b) AlN substrate and (c) semi-insulating GaN substrate. The inset in (c) shows FFT of the area selected by the square.
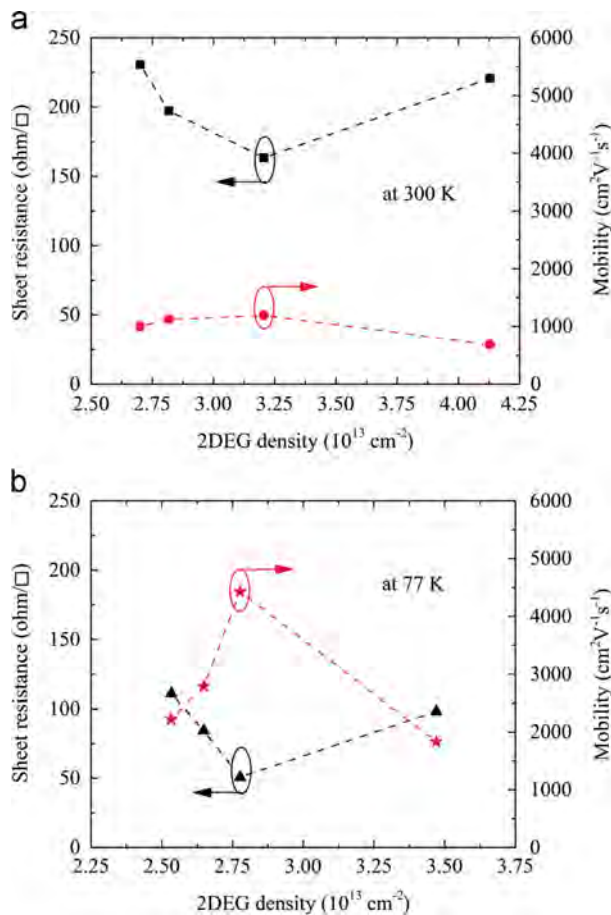
Fig. 7. Sheet resistance and mobility as a function of 2DEG density measured for the as-grown LT-AlN passivated HEMT structures at (a) room temperature (300 K) and (b) 77 K.

and mechanism of the high gate leakage will be identified in further studies where the DC performance of AlN/GaN HEMTs with LT-AlN passivation cap will be compared with control samples having no LT-AlN cap.

4. Conclusion

Low temperature growth of AlN was studied using PAMBE. Up to ~200 nm of thick crack-free LT-AlN films were grown on GaN substrate. The presence of partially amorphous regions in 130 nm
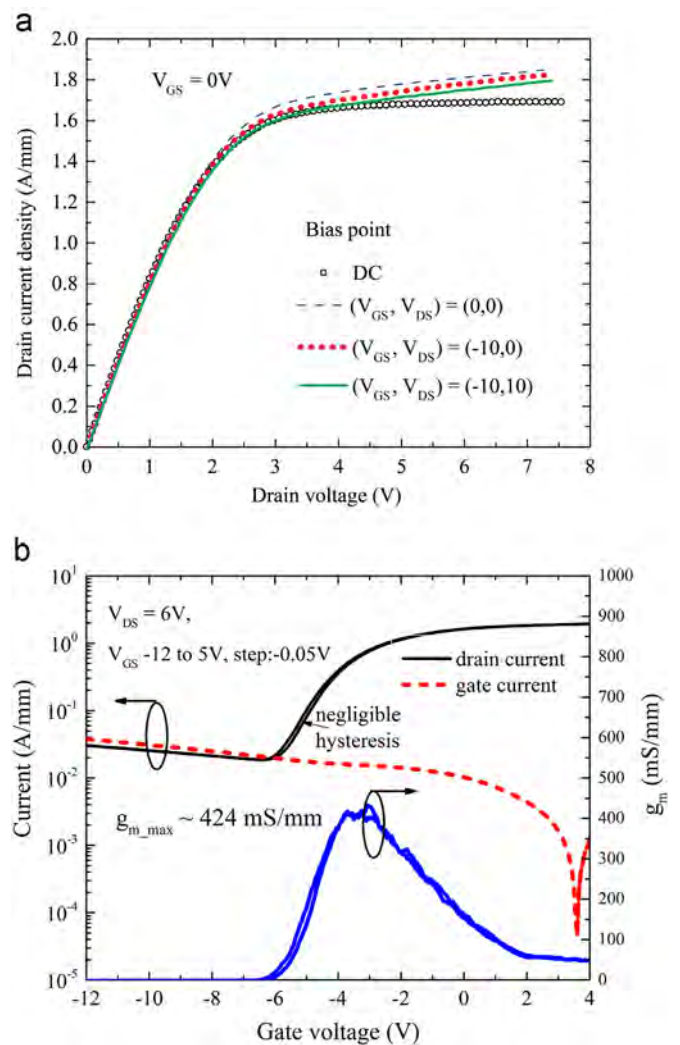
Fig. 8. (a) Pulsed I–V measured for an AlN/GaN HEMT for which MBE grown LT-AlN was applied as in-situ surface passivation. 0.3 μs wide pulses were used with a duty cycle of 99.94%. The gate is 55 nm long and 25 μm wide, (b) Transfer curves with dual sweep shown for drain current, gate current and extrinsic transconductance at a drain bias of 6 V.

thick LT-AlN film was confirmed by TEM. MBE grown LT-AlN was applied for in-situ surface passivation of AlN barrier GaN HEMT structures. Upon fabricating 55 nm long, 25 μm wide devices, low DC–RF dispersion was observed in terms of gate lag and drain lag

below 2% from pulsed I–V measurements. The HEMT showed a maximum drain current density of $\sim$1.6 A/mm at 0 V gate bias and peak extrinsic transconductance of $\sim$420 mS/mm at 6 V drain bias. To the best of our knowledge this is the first report of application of MBE grown LT-AlN in III-nitride HEMTs for in-situ surface passivation.

Acknowledgements

References

[1] S. Huang, et al., IEEE Electron Device Lett. 33 (2012) 516–518. http://dx.doi.org/10.1109/LED.2012.2185921.

[2] A.D. Koehler, et al., IEEE Electron Device Lett. 34 (9) (2013) 1115–1117. http://dx.doi.org/10.1109/LED.2013.2274429.

[3] J. Hwang, et al., Solid State Electron. 48 (2) (2004) 363–366. http://dx.doi.org/10.1016/S0038-1101(03)00324-1.

[4] S.L. Selvaraj, et al., Appl. Phys. Lett. 90 (2007) 173506. http://dx.doi.org/10.1063/1.2730751.

[5] J. Derluyn, et al., J. Appl. Phys. 98 (2005) 054501. http://dx.doi.org/10.1063/1.2008388.

[6] D.H. Kim, et al., Electron. Lett. 43 (129) (2007), http://dx.doi.org/10.1049/el:20073494.

[7] R. Wang, et al., IEEE IEDM Dig. (2013).

[8] AlN—Aluminium Nitride. Ioffe Database.

[9] Y. Cao, et al., Appl. Phys. Lett. 90 (2007) 182112. http://dx.doi.org/10.1063/1.2736207.

[10] S. Figge, et al., Appl. Phys. Lett. 94 (2009) 101915. http://dx.doi.org/10.1063/1.3089568.

[11] J.M. Khoshman et al., J. Non-Cryst. Solids, 351, 40–42, 3334–3340 (http://dx.doi.org/10.1016/j.jnoncrysol.2005.08.009).
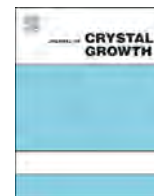
A new AlON buffer layer for RF-MBE growth of AlN on a sapphire substrate

T. Makimoto [a,*], K. Kumakura [b], M. Maeda [a], H. Yamamoto [b], Y. Horikoshi [a,c]

[a] Faculty of Science and Engineering, Waseda University, 3-4-1 Okubo, Shinjuku-ku, Tokyo 169-8555, Japan
[b] NTT Basic Research Laboratories, NTT Corporation, 3-1 Morinosato Wakamiya, Atsugi, Kanagawa 243-0198, Japan
[c] Kagami Memorial Laboratory for Materials Science and Technology, Waseda University, 2-8-26 Nishi-Waseda, Shinjuku-ku, Tokyo 169-0051, Japan

ARTICLE INFO

ABSTRACT

A 20 nm-thick AlON buffer layer consisting of Al_2O_3, graded AlON, AlN, and thin Al_2O_3 amorphous films was used to grow AlN on a sapphire substrate by molecular beam epitaxy with radio frequency plasma for nitrogen source (RF-MBE). Mirror-smooth AlN layers were successfully obtained using this new AlON buffer layer. The total threading dislocation densities of AlN layers are comparable to those reported for the high-quality AlN layers grown by RF-MBE using the conventional low-temperature (LT) buffer layer.

© 2015 Elsevier B.V. All rights reserved.

1. Introduction

AlN is a promising material for short wavelength light emitting devices [1] and high-power electronic devices [2]. This AlN layer is often grown on a sapphire substrate using a LT buffer layer [3,4]. In our previous paper, we reported that we developed a new AlON buffer layer to grow a GaN layer on a sapphire substrate [5], instead of the LT buffer layer. In this method, the composition of oxygen and nitrogen atoms in the AlON layer is gradually changed from an aluminum oxide to an aluminum nitride, that is, from a sapphire (Al_2O_3) substrate to a nitride compound. Using this method, we obtained high-quality nitride layers grown by metalorganic vapor phase epitaxy (MOVPE). The undoped GaN shows resistance higher than 100 k ohm/sheet and AlGaN/GaN heterostructure shows high electron mobility of 1760 cm^2/V, meaning that these characteristics are favorable especially for an AlGaN/GaN heterostructure field effect transistor [6]. In addition to the growth of such a high quality nitride layer, the growth process using this AlON buffer layer reduces the growth time and the number of the growth parameters compared with the two step growth using a LT buffer layer.

Although this new AlON buffer layer is used to grow a high-quality GaN layer by MOVPE, it has not been used for the growth by molecular beam epitaxy (MBE) yet. In this paper, therefore, we will report the result that we have applied this method to grow AlN on a sapphire substrate by RF-MBE.

2. Materials and methods

An AlON buffer layer consists of Al_2O_3, graded AlON, AlN, and thin Al_2O_3 amorphous films, which were sputtered on a c-face (0001) sapphire substrate using electron cyclotron resonance (ECR) Ar-plasma sputtering at room temperature. The thickness of this buffer layer was around 20 nm. An AlN layer was grown directly on the AlON buffer layer in a similar way to the GaN MOVPE growth using an AlON buffer layer [5]. In the RF-MBE growth, nitrogen gas flow rate of 2 sccm and RF-plasma power of 500 W were used. The growth temperature of AlN was 800 °C. The thickness of the AlN layer was changed from 0.5 μm to 2 μm to investigate the influence of the thickness on the threading dislocation density. Scanning electron microscopy (SEM) was used to observe surface and cross-sectional images of the AlN layer grown on a sapphire substrate using the AlON buffer layer. X-ray diffractometry (XRD) was used to characterize the AlN layer. The XRD ω-rocking curves of symmetric (0002) and skew-symmetric (1–102) reflections were used to estimate screw and edge threading dislocation densities [7].

3. Results

Using an AlON buffer layer, mirror-smooth AlN layers were successfully grown by RF-MBE. Fig. 1(a and b) shows surface and cross-sectional SEM images of 1 μm-thick AlN. These figures show good surfaces and uniform growth of AlN using the AlON buffer layer.

Fig. 2 shows XRD symmetric 2θ–ω scan. An AlN (0002) diffraction peak was observed at 2θ of 36.00°, so the c-lattice constant of the AlN layer is calculated to be 0.4985 nm. Since the

c-lattice constant of strain-free AlN is 0.4979 nm, the AlN layer has a compressive strain as is reported on an AlN layer grown on a c-face sapphire substrate [8].

Figs. 3 and 4 show XRD rocking curves of symmetric (0002) and asymmetric (1–102) reflections for 1 μm-thick AlN. The full width at half-maximum (FWHM) values for these two curves are 2412 and 3024 arcsec. Using these values, the screw and edge threading dislocation densities were calculated to be 1.3×10^{10} cm^{-2} and 7.3×10^{10} cm^{-2}, respectively. These values are comparable to those reported for the high-quality AlN layer grown using the LT buffer layer with two 3 nm-thick GaN interlayers [4]. These GaN interlayers are reported to decrease the threading dislocation

densities effectively [9]. Therefore, the threading dislocation densities obtained in this experiment mean that a high-quality AlN layer was grown using the AlON buffer layer.

Fig. 5 shows the AlN thickness dependence of the screw and edge threading dislocation densities. As the thickness increases, the threading dislocation densities decrease. The total threading dislocation density of a 0.5 μm-thick AlN was less than 1×10^{11} cm^{-3}. It was reported that the total dislocation densities of the 0.25 μm-thick AlN grown by RF-MBE on a sapphire substrate using the LT buffer layer exceeds 10^{11} cm^{-2} [3], even though this AlN layer was used for optically pumped lasing at 303 nm, meaning that the quality of this AlN layer is relatively high for its thickness. Therefore, the quality of
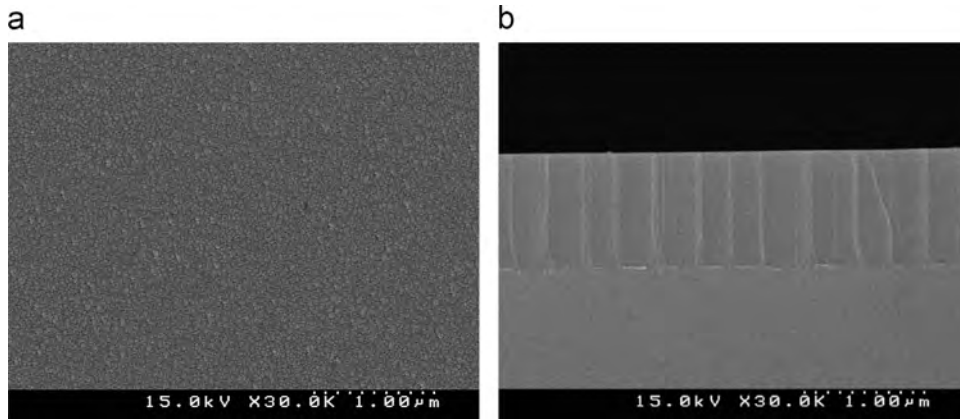
Fig. 1. (a) Surface and (b) cross-sectional SEM images of 1 μm-thick AlN.
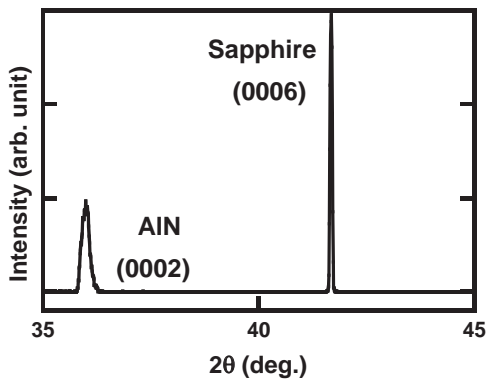
Fig. 2. XRD symmetric 2θ–ω scan of AlN.
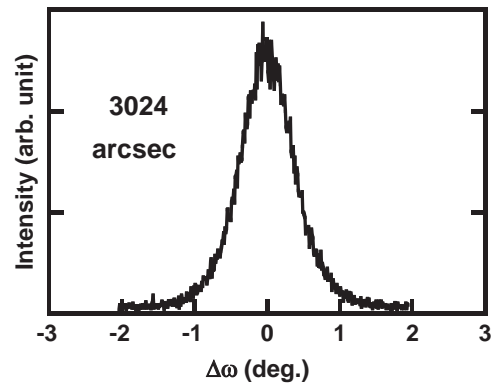
Fig. 4. XRD rocking curve of asymmetric (1–102) reflection for 1 μm-thick AlN.
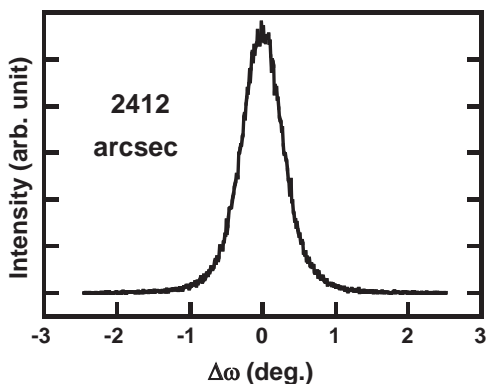
Fig. 3. XRD rocking curve of symmetric (0002) reflection for 1 μm-thick AlN.
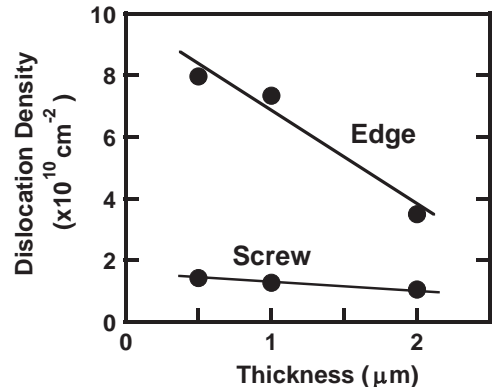
Fig. 5. AlN thickness dependence of screw and edge threading dislocation densities.

the 0.5 μm-thick AlN layer grown using the AlON buffer layer in this experiment is as high as that of the AlN layer used for optically pumped lasing.

4. Conclusions

We have applied a new AlON buffer layer to grow AlN on a sapphire substrate by RF-MBE. This AlON buffer layer is 20-nm thick and consists of Al_2O_3, graded AlON, AlN, and thin Al_2O_3 amorphous films. The surface and cross-sectional SEM images show that good surfaces and uniform growth of AlN using the AlON buffer layer. The XRD analysis shows that the total threading dislocation density is comparable to those reported for high-quality AlN layers grown on a sapphire substrate by RF-MBE using the conventional LT buffer layer. After optimizing parameters of AlN itself in the RF-MBE growth process, the dislocation density is expected to be decreased further. Therefore, from the results obtained in this experiment, it can be concluded that the new AlON buffer layer is promising for RF-MBE growth of high-quality group-III nitride layers on a sapphire substrate.

References

[1] Y. Taniyasu, M. Kasu, T. Makimoto, Nature 441 (2006) 325.
[2] S. Imanaga, H. Kawai, J. Appl. Phys. 82 (1997) 5843.
[3] V.N. Jmerik, A.M. Mizerov, A.A. Sitnikova, P.S. Kop'ev, S.V. Ivanov, E.V. Lutsenko, N.P. Tarasuk, N.V. Rzheutskii, G.P. Yablonskii, Appl. Phys. Lett. 96 (2010) 141112.
[4] D.V. Nechaev, P.A. Aseev, V.N. Jmerik, P.N. Brunkov, Y.V. Kuznetsova, A.A. Sitnikova, V.V. Ratnikov, S.V. Ivanov, J. Cryst. Growth 378 (2013) 319.
[5] K. Kumakura, T. Makimoto, J. Cryst. Growth 292 (2006) 155.
[6] J.-Y. Shiu, J.-C. Huang, V. Desmaris, C.-T. Chang, C.-Y. Lu, K. Kumakura, T. Makimoto, H. Zirath, N. Rorsman, E.Y. Chang, IEEE Electron Device Lett. 28 (2007) 476.
[7] S.R. Lee, A.M. West, A.A. Allerman, K.E. Waldrip, D.M. Follstaedt, P.P. Provencio, D.D. Koleske, C.R. Abernathy, Appl. Phys. Lett. 86 (2005) 241904.
[8] Z.Y. Fan, G. Rong, J. Browning, N. Newman, Mater. Sci. Eng. B67 (1999) 80.
[9] H. Jiang, T. Egawa, M. Hao, Y. Liu, Appl. Phys. Lett. 87 (2005) 241911.
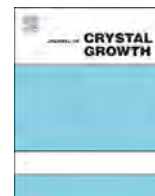
Dislocation reduction in GaN grown on nano-patterned templates

W.C. Yang, K.Y. Chen, Kai-Yuan Cheng *, Y.L. Wang, K.C. Hsieh, K.Y. Cheng

Department of Electrical Engineering, National Tsing Hua University, Hsinchu, Taiwan 30013, Republic of China

ARTICLE INFO

ABSTRACT

A nano-holes patterned GaN-on-patterned sapphire substrate template has been developed to reduce the threading dislocation (TD) density in homoepitaxy GaN layer grown by plasma-assisted molecular beam epitaxy. The grown layers characterized by high resolution x-ray diffraction, photoluminescence, and cross-section transmission electron microscopy confirm that the TD density of GaN epilayer has been successfully reduced an order of magnitude to $\sim 10^7 \, cm^{-2}$ by optimizing the depth and coverage area percentage of patterned nano-holes.

© 2015 Elsevier B.V. All rights reserved.

1. Introduction

The large energy band gap, high breakdown field, and high electron saturation velocity of GaN make it useful for optoelectronic, high-speed, and high power device applications. The majority of current device structures are grown on sapphire, 6H-SiC, or silicon substrates. The large difference of lattice constants and thermal expansion coefficients between the substrates and GaN epitaxial films lead to the generation of a high threading dislocation (TD) density and even cracks [1–3]. These defects degrade the performance and shorten the lifetime of devices. Although 6H-SiC and freestanding GaN are promising substrate materials with a misfit of less than 3.5%, these wafers are still too expensive at the moment. Currently, epitaxial GaN is mainly grown by metalorganic chemical vapor deposition (MOCVD) and plasma-assisted molecular beam epitaxy (PAMBE). Using appropriate nucleation layer allows the reduction of the dislocation density to the $\sim 10^8 \, cm^{-2}$ range. In general, epitaxial lateral overgrowth (ELOG) and selective area growth (SAG) are commonly used techniques in MOCVD to reduce TD density ($\sim 10^6$–$10^8 \, cm^{-2}$) [4–6]. However, it can only reduce TDs regionally such as the wing region of the ELOG structure [7]. Also, dielectric layers used as the growth mask may generate stress and incorporated as impurities in GaN epitaxial films [8]. On the other hand, several groups have used patterned sapphire substrates (PSS) to reduce TD density near 10^8 [9]. In this study, we report PAMBE growth of GaN epilayer on nano-holes patterned GaN templates without complex processes. By optimizing the depth and the periodicity of nano-holes fabricated on GaN-on-PSS templates by NIL, the TD density of the regrown GaN has been effectively reduced. Improvement of

crystalline quality and decrease of dislocation density are identified by HRXRD and EPD measurements.

2. Experiment

The 4 μm GaN template with a dislocation density about $3 \times 10^8 \, cm^{-2}$ is prepared on the c-plane of a 2-in. diameter patterned sapphire substrate (PSS) by MOCVD. Prior to the growth of GaN epilayers, nano-hole patterns are fabricated on GaN templates by nanoimprint lithography (NIL) technique. The homoepitaxial growth of GaN is performed in a Veeco GEN20 MBE system where atomic nitrogen flux is generated from a RF plasma source that operates at 300–450 W under a nitrogen flow of 0.5–2 sccm. The group-III Ga flux is supplied by an effusion cell. A 1 μm thick Ti metal layer is first evaporated on the back surface of PSS in order to ensure a uniform and efficient heat transfer from the heater to the substrate. Before loading into the MBE growth chamber, substrates are first degreased in acetone, rinsed in methanol, and followed by etched in a solution of HF:DI-water (1:10) for 2 min. The substrates are then thermally cleaned in the MBE system at 830 °C for 20 min prior to the growth of 800 nm GaN layers. All films are grown at a temperature of 750 °C.

In this study, the nano-holes patterned in the GaN template are used to reduce the TD density of the GaN epilayer. The NIL technique is used to fabricate nano-hole patterns in GaN templates [10]. The imprint molds used have square patterns with periodicities of 350, 450, and 750 nm, and diameters of 200, 200, 400 nm, respectively. The NIL process begins with depositing a SiO_2 thin film on GaN template by plasma-enhanced chemical vapor deposition as a pattern transfer layer. Next, nano-hole patterns of different periodicities are transferred to the SiO_2 film by NIL method. Nano-holes of different depths ranging from 100, 200,

* Corresponding author.
E-mail address: kycheng@ee.nthu.edu.tw (K.Y. Cheng).

to 300 nm are etched into the GaN template by inductively coupled plasma etching. The pattern transfer process is finished by removing the SiO₂ layer in hydrofluoric (HF) acid. During the GaN growth, the two-dimensional growth mode under a slightly Ga-rich condition (III/V flux ratio=1.2) is used to promote lateral growth over nano-holes, where the high adatom mobility helps recovering the surface smoothness as indicated by streaky reflection high-energy electron diffraction patterns.

The crystal quality of samples is evaluated by room temperature photoluminescence (PL) and high-resolution x-ray diffraction (HRXRD). The 325 nm line of a 45 mW He–Cd laser is used to excite the sample. The signal is detected by a photomultiplier in a 0.55 m spectrometer with a lock-in amplifier configuration. x-ray ω scan and rocking curves are measured using a Philips X'PERT MRD triple-axis diffractometer. Both symmetric (002) and asymmetric (102) diffractions are investigated to determine the defect properties of the GaN film. The dislocation density of samples is determined by counting the etch pits density (EPD) from the atomic force microscope (AFM) image. Etching is carried out in a molten KOH at 210 °C for 5 min. The information of dislocation annihilation by nano-hole voids and the morphology of the growth evolution are studied using cross-sectional transmission electron microscopy (TEM). The electron-transparent sample is examined with JOEL JEM-3000F at 300 kV in conventional and scanning TEM modes.

3. Results and discussions

In GaN films, TDs can be divided into three categories including pure screw, mixed, and pure edge dislocations. The predominant TDs are pure edge TDs perpendicular to the c-axis with Burgers vectors **b** in either $\pm 1/3[11\bar{2}0]$, $\pm 1/3[1\bar{2}10]$, or $\pm 1/3[2110]$. The other types of TDs are either pure screw or mixed TDs in $\pm 1/3[11\bar{2}3]$, which parallel to the c-axis and correlate to the electrical and optical properties of the material [11–13]. Although it is difficult to separate these different types of TDs, the HRXRD rocking curve measurements could be used to investigate the properties of the GaN material in specific crystallographic planes. The results of symmetric (002) reflection reveal the density of pure screw and mixed TDs, and the asymmetry (102) reflections correlate the pure edge TD density [14]. Additionally, the density of TDs can be simultaneously calculated by counting EPD of KOH etched sample surface that reveals pure screw and mixed TDs [15,16]. In this study, the design parameters including the depths and periods of nano-hole patterns in GaN templates, the measured full-width at half-maximum (FWHM) of HRXRD rocking curves in symmetric (002) and asymmetric (102) reflections of the grown GaN, and the dislocations density of homoepitaxy GaN films determined from EPD count are all summarized in Table 1.

In the first series of experiments, the diameter and periodicity of nano-holes patterns are fixed at 200 and 350 nm, respectively, while the nano-hole depth is varied ranging from 100 nm (Sample A), 200 nm (Sample B) to 300 nm (Sample C). Both the FWHM of (002) and (102) reflections decrease with increasing the depth of nano-patterned holes from 100 to 300 nm as compared to GaN templates. Comparing to the GaN template, the narrower FWHM achieved in sample B for (002) and (102) reflections are 218 and 180 arcsec, respectively, indicating the quality of the GaN material is improved with a lower TD density [17]. This is confirmed by the EPD count of 1.2×10^7 cm^{-2} in sample B, which is one order of magnitude fewer than the GaN template (3×10^8 cm^{-2}). It is clear that the nano-hole depth of 200 nm is an optimal value for dislocation reduction. The FWHM of (002) and (102) rocking curves for all samples having various EPDs are shown in Fig. 1. It is observed that the (002) FWHM decreases much faster than the

Table 1
The relationships between the geometry of nano-holes patterns in GaN templates, and the measured FWHMs of HRXRD (002) and (102) rocking curves and EPDs of samples A, B, C, D, and E. The homoepitaxy GaN samples are 800 nm thick. The results measured in a 4 μm GaN-on-PSS template are also listed for reference purpose.

Sample	Nano-holes		FWHM of HRXRD		Etch pits density (cm^{-2})
	Period (nm)	Depth (nm)	(002) (arcsec)	(102) (arcsec)	
A	350	100	255	201	8.0×10^7
B	350	200	218	180	1.2×10^7
C	350	300	236	191	2.0×10^7
D	450	200	250	206	6.0×10^7
E	750	200	228	190	2.8×10^7
Template	–	–	348	244	3.0×10^8
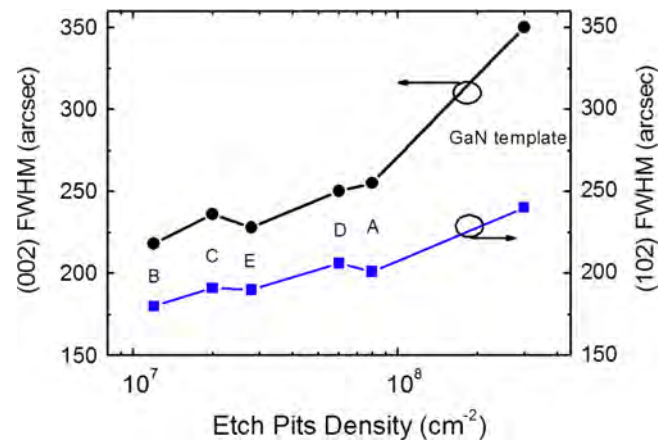
Fig. 1. The measured FWHM of (002) and (102) HRXRD rocking curves for all samples as functions of measured EPDs.
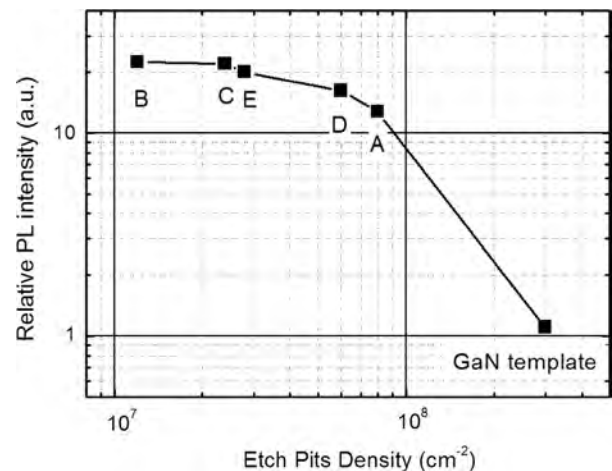
Fig. 2. Measured room temperature PL intensity as functions of EPDs in all samples using the data of GaN-on-PSS template as the reference.

(102) FWHM as the EPD drops, which represents the reduction of pure screw/mixed TDs is much more efficient than for edge TDs. To reveal the effectiveness of screw/mixed TD annihilation, the PL luminescence efficiency is shown in Fig. 2. A stronger PL intensity is obtained for samples with a lower EPD due to the reduction of the screw and mixed dislocations which directly link to the density of nonradiative recombination centers [13,16,18]. The PL spectra of sample B and the GaN template with the highest and lowest EPDs,
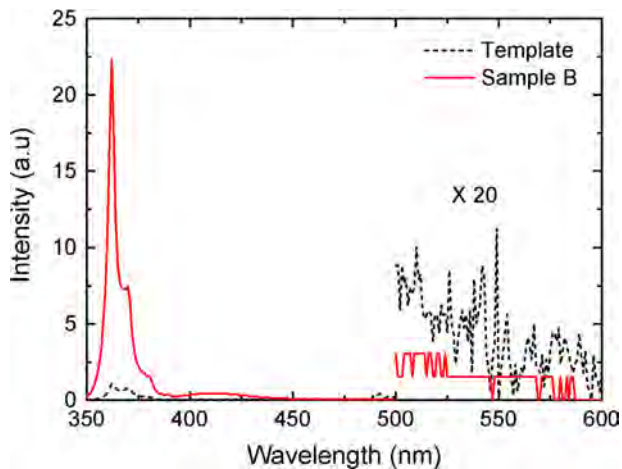
Fig. 3. Comparison of room temperature PL spectra of Sample B and the GaN template. The yellow emission band is not visible even under magnified scale of $20\times$.

Table 2
A list of the periods and diameters of nano-holes used to calculate the area of the hole, the number of holes within an area of 25 μm², and the percentage of area coverage of holes per unit area for samples B, E, and F.

Sample	Period (nm)	Diameter (nm)	Area (μm^{-2})	Number (per 5×5 μm²)	Area coverage percentage (%)
B	350	200	0.0314	196	24.6
E	450	200	0.0314	121	15.2
F	750	400	0.125	49	24.5

respectively, are compared in Fig. 3. The yellow emission band is not observed even under magnified scale ($20\times$) from all samples.

Next, we investigate the influence of the percentage of the surface area covered by nano-holes on the GaN quality. This is done by varying the periodicity of nano-holes from 350 nm (Sample B), 450 nm (Sample D) to 750 nm (Sample E) while fixing the hole depth at 200 nm, which is the best value deduced above. The diameters of nano-holes used in samples B, D, and E are 200, 200, and 400 nm, respectively. The percentage of hole coverage areas are calculated to be 24.6%, 15.2%, and 24.5% for samples B, D and E, respectively, and are tabulated in Table 2. Assuming the effectiveness of reducing TD density dependents on the percentage of hole covered area, a high percentage of hole coverage is more effective in reducing the TD density. Again, the HRXRD rocking curves in specific crystallographic planes are used to evaluate the reduction of TD density [11]. The FWHM of symmetric (002) and asymmetry (102) rocking curves for samples B, D, and E with different hole coverage percentages are compared in Table 1. Both samples B and E show the narrowest FWHM of 218 and 228 arcsec for (002) rocking curve, and 180 and 190 arcsec for (102) rocking curve, respectively. It confirms that the sample with a high percentage of hole area coverage leads to a narrow HRXRD FWHM, which corresponds to a low defect density. Samples B and E also show lower EPDs of 1.2×10^7 cm^{-2} and 2.8×10^7 cm^{-2} comparing 6×10^7 cm^{-2} for sample D. Therefore, the improvement of the quality on the GaN material is associated with the percentage of hole area coverage. The surface hole coverage area could be increased beyond 25% to further reduce EPD pending on the successful development of suitable patterning and regrowth techniques.

Finally, in order to further understand the TD reduction mechanism, the bright field cross-section TEM images are studied. Fig. 4 shows a cross-section TEM image of sample B. It clearly confirms that TDs can be stopped and annihilated at the void,
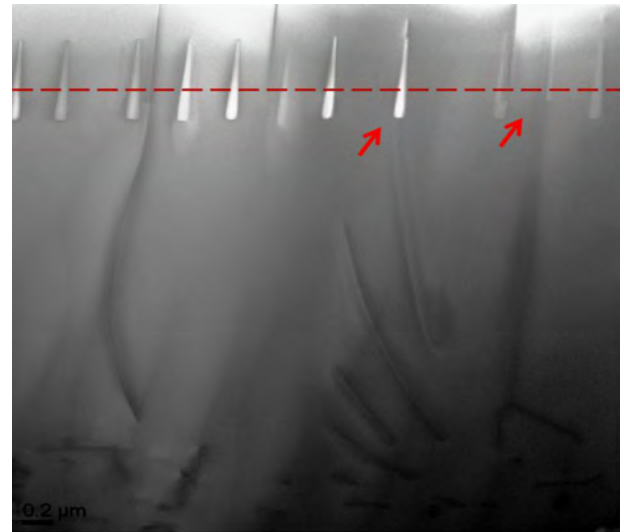
Fig. 4. The cross-section TEM bright field image of sample B showing that two TDs are terminated at voids as indicated by arrows. The dashed line indicates the regrown interface between the template surface and the homoepitaxy GaN layer.

while others threading up to the surface. Since the regrowth would occur inside nano-holes, the shallower holes (100 nm) could lead to an incomplete void formation where TDs extend upward continuously. On the other hand, further increase the nano-hole depth above 300 nm will suffer from increased dry etching related defects during NIL processes. Together with the FWHM data of HRXRD, PL intensity, and EPD count, it tangibly demonstrates that TDs could be reduced by an array of nano-holes patterned on the GaN template using optimized nano-hole depth (200 nm) as well as percentage of hole area coverage. Moreover, the reduction of the screw/mixed dislocation is most effective which is helpful to improve the electrical and optical properties of GaN-based devices in the future.

4. Summary and conclusion

The PAMBE growth of GaN epilayer on a nano-holes patterned template surface of the GaN-on-PSS structure is investigated. Cross-sectional TEM directly reveals the act of annihilation of vertically propagating TD at the void, which is a major reason of crystalline quality amelioration. High quality GaN is successfully obtained by optimizing the depth of nano-holes (200 nm) and percentage of hole area coverage ($\sim$25%) leading to a low TD density of 1.2×10^7 cm^{-2}. Through HRXRD using different reflections, it also reveals that the reduction of dislocations is more effective for screw/mixed type TDs comparing to edged type TDs.

References

[1] D. Kapolenek, X.H. Wu, B. Heying, S. Keller, B. Keller, U.K. Mishra, S.P. Denbaars, J.S. Speck, Appl. Phys. Lett. 67 (1995) 1541.
[2] S.D. Lester, F.A. Ponce, M.G. Crawford, D.A. Steigerwald, Appl. Phys. Lett. 66 (1995) 1249.

[3] W. Qian, M. Skowronski, M. Degraef, K. Doverspike, L.B. Rowland, D.K. Gaskill, Appl. Phys. Lett. 66 (1995) 1252.
[4] A. Sakai, H. Sunakawa, A. Usui, Appl. Phys. Lett. 71 (1997) 2259.
[5] O.H. Nam, T.S. Zheleva, M.D. Bremser, R.F. Davis, J. Electron. Mater. 27 (1998) 233.
[6] X.L. Fang, Y.Q. Wang, H. Meidia, S. Mahajan, Appl. Phys. Lett. 84 (2004) 484.
[7] S. Nagahama, N. Iwasa, M. Senoh, T. Matsushita, Y. Sugimoto, H. Kiyoku, T. Kozaki, M. Sano, H. Matsumura, H. Umemoto, K. Chocho, T. Mukai, Jpn. J. Appl. Phys. 39 (2000) L647.
[8] X. Li, P.W. Bohn, J.J. Coleman, Appl. Phys. Lett. 75 (1999) 4049.
[9] D.S. Wu, W.K. Wang, K.S. Wen, S.C. Huang, S.H. Lin, R.H. Hrong, Y.S. Yu, M.H. Pan, J. Electrochem. Soc. 153 (2006) G765.
[10] K. Meneou, K.Y. Cheng, J. Vac. Sci. Technol. B 26 (2008) 156.
[11] X.H. Wu, L.M. Brown, D. Kapolnek, S. Keller, B. Keller, S.P. Denbaars, J.S. Speck, J. Appl. Phys. 80 (1996) 3228.
[12] J.W.P. Hsu, M.J. Manfra, S.N.G. Chu, C.H. Chen, L.N. Pfeiffer, R.J. Molnar, Appl. Phys. Lett. 78 (2001) 3980.
[13] D. Cherns, S.J. Henley, F.A. Ponce, Appl. Phys. Lett. 78 (2001) 2691.
[14] B. Heying, X.H. Wu, S. Keller, Y. Li, D. Kapolnek, B.P. Keller, S.P. Denbaars, J.S. Speck, Appl. Phys. Lett. 68 (1996) 643.
[15] P. Visconti, K.M. Jones, M.A. Reshchikov, R. Cingolani, H. Morkoç, R.J. Molnar, Appl. Phys. Lett. 77 (2000) 3532.
[16] T. Hino, S. Tomiya, T. Miyajima, K. Yanashima, S. Hashimoto, M. Ikeda, Appl. Phys. Lett. 76 (2000) 3421.
[17] H. Heinke, V. Kirchner, S. Einfeldt, D. Hommel, Appl. Phys. Lett. 77 (2000) 2145.
[18] T. Langer, H. Jonen, A. Kruse, H. Bremers, U. Rossow, A. Hangleiter, Appl. Phys. Lett. 103 (2013) 022108.
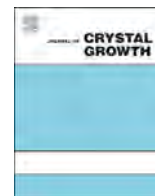
Influence of the substrate grade on structural and optical properties of GaN/AlGaN superlattices

F. Schubert [a,*], S. Zybell [b], J. Heitmann [b], T. Mikolajick [a,c], S. Schmult [c]

[a] NaMLab gGmbH, Nöthnitzer Straße 64, D-01187 Dresden, Germany
[b] TU Bergakademie Freiberg, Institut für Angewandte Physik, Leipziger Straße 23, D-09599 Freiberg, Germany
[c] TU Dresden, Institute of Semiconductor and Microsystems, Nöthnitzer Straße 64, D-01187 Dresden, Germany

ARTICLE INFO

ABSTRACT

The aspect of superior interfaces is studied using short-period GaN/AlGaN superlattices grown by Molecular Beam Epitaxy (MBE) on various substrates as versatile test structures for investigations of interface and layer properties. High-resolution x-ray diffraction pattern compared with simulations of ideal structures prove coherent 2-dimensional growth of structures with homogenous layer composition and atomically smooth and abrupt interfaces. The influence of structural perfection on optical properties is investigated in time-resolved photoluminescence measurements of selected superlattices. The recombination behavior of the excitons, their life time and the photoluminescence emission energy depend on the substrate quality and the superlattice structure. Furthermore it could be demonstrated that for optimal growth conditions the limiting factor for structural and optical properties of our MBE grown layers and heterostructures is the substrate.

© 2015 Elsevier B.V. All rights reserved.

1. Introduction

Due to GaNs wide direct bandgap of 3.4 eV and the high thermal conductivity GaN based devices have gained increasing significance in optoelectronics and high-power applications [1–3]. Modern electronic devices based on high-mobility two-dimensional electron gases e.g. formed at the interface between epitaxially grown AlGaN and GaN layers are promising devices for energy-efficient high-frequency and high-power applications. Superior interface quality and well defined layer properties are prerequisites for the high-end performance of these GaN based devices [4,5]. This study focuses on the aspect of interface perfection using short-period GaN/AlGaN superlattices as versatile test structures for investigations of interface and layer properties. Furthermore time-resolved photoluminescence measurements (PL) were performed to investigate the exciton recombination behaviors dependent on the substrate choice.

2. Experimental procedure

The investigated superlattice structures (consisting of the $5.5-6$ nm thick AlGaN tunnel barrier layers also called multiple quantum wells (MQW)) were grown in a VG Semicon V80H MBE system under slightly Ga-rich conditions in uninterrupted growth runs at constant substrate temperature of 750 °C measured by optical pyrometry. Previous experiments with different growth conditions showed that nitrogen-rich conditions result in rough surfaces and interfaces of the grown layers. At Ga-rich conditions, the formation of Ga-droplets at the surface is favored resulting in microscopic defects. Just a narrow Ga/N-ratio window for slightly Ga-rich conditions exists where smooth and droplet-free crystal surfaces with atomically flat steps could be achieved [6]. The growth experiments were performed on sapphire and GaN substrates prepared by metal-organic chemical vapor deposition (MOCVD), hydride vapor phase epitaxy (HVPE) and ammonothermal growth with dramatically different properties of the bulk and surfaces. All substrates were backside-coated with titanium to optical opaqueness and degased at 400 °C under ultra-high vacuum conditions for at least 2 hours before growing the epitaxial layers. In the growth chamber the substrates were heated to growth temperature under nitrogen plasma exposure. For all growth runs active nitrogen was supplied by an RF-plasma source with 220 W forward power and 0.6 sccm (standard cubic centimeter) nitrogen flow rate, as discussed in a previous work [7]. The growth on sapphire was initiated by a few nanometer thick AlN nucleation layer to assure Ga-polarity. All substrates were overgrown with a 1.5 μm thick GaN buffer prior to the superlattice growth along the c-axis of the Ga-polar substrates. Aluminum mole fractions of the respective $Al_xGa_{1-x}N$ layers up to $x=0.33$ were investigated with layer thicknesses always below the critical thickness for defect formation described by the Matthews–Blakeslee criterion [8].

The crystal surface morphology was in-situ monitored by reflection high energy electron diffraction (RHEED) and ex-situ by atomic force microscopy (AFM) before and after MBE growth using a DI/Veeco

---

* Corresponding author. Tel.: +49 351212499038; fax: +49 35147583900.
E-mail address: Felix.Schubert@namlab.com (F. Schubert).

Table 1
Summary of relevant properties for the GaN-substrates used in this study.

	GaN thickness (μm)	FWHM ($\omega-2\theta$) of the (002) reflex (arc sec)	FWHM (Rocking curve) of the (002) reflex (arcsec)
MBE-GaN buffer on c-sapphire (*home-made*)	1.5	80	1713
MOVPE-GaN (*commercially available*)	1.9	65	457
HVPE-GaN (*project partner supplied*)	91	43	180
Ammonothermal-GaN (*commercially available*)	bulk	< 36[a]	57

[a] Limited by tool resolution.

DIMENSION 3100 AFM operated in contact mode. High-resolution x-ray diffraction (HRXRD) scans of the crystals were measured with a Bruker D8 Discover x-ray diffractometer equipped with a 2 Bounce Ge monochromator. In this configuration, the tool resolution is 36 arc sec for the angle of incidence Omega and the diffraction angle Theta. Table 1 summarizes relevant properties of the investigated substrates. The differences in the FWHM of the Rocking curves corresponds to differences in the mosaicity and depends primarily on the nucleation conditions of the grown substrate. As a general trend it is known that with increasing thickness of the heteroepitaxially grown GaN on sapphire substrate the crystallinity and crystal perfection increases [9]. The FWHM of the Rocking curves was taken into account to gauge the TDD (threading dislocation density) by using the equations of Metzger et al. [10]. From this we estimated TDDs for the MBE-GaN buffer on c-sapphire in the mid-10^9 cm^{-2}, for the MOVPE-GaN in the mid-10^8 cm^{-2}, for HVPE-GaN in the mid-10^7 cm^{-2} and for the Ammonothermal-GaN in the mid-10^6 cm^{-2}. HRXRD-patterns were simulated using the commercial software Diffrac Plus Laptos 7.04 from Bruker AXS GmbH based on dynamical x-ray diffraction theory. Time-resolved photoluminescence measurements were performed using the second harmonic generation of a mode-locked Ti:Sapphire laser, providing 2.5 ps long pulses with a repetition rate of 78 MHz. Laser pulses at 3.548 eV photon energy excited the material above the absorption edge of the GaN quantum well and bulk layer. The samples were mounted in an optical cryostat and were thermally coupled to a 6 K cold-finger. The full time dependent PL spectra are detected by a HAMAMASTSU streak camera connected to a grating spectrometer. The experimental time resolution of the system is less than 10 ps. The measurements were performed with an incident energy density of about 0.7 μJ/cm^2 per laser pulse. The time constants of the PL signal are evaluated from the PL transients by an exponential fit [11].

3. Results and discussion

Fig. 1 compares exemplarily experimentally recorded diffraction pattern of a symmetrically 10-period GaN/Al$_{0.33}$Ga$_{0.67}$N superlattice with 11 nm period length grown on ammothermal GaN with the according simulation. For superlattices grown on such outstanding substrates, key features of the simulations can be accurately recovered experimentally. Namely intense narrow superlattice satellite peaks up to the -11th order, pronounced interface fringes and oscillatory peak intensity trends among higher orders are clearly identified. These results prove coherent 2-dimensional growth with abrupt and smooth interfaces over a wide range of aluminum mole fraction in the AlGaN layers up to x=0.33. Fig. 2 shows exemplarily an AFM scan over a 5×5 μm^2 surface area of this superlattice sample. The roughness can be determined to a root mean square value of 0.5 nm, clearly
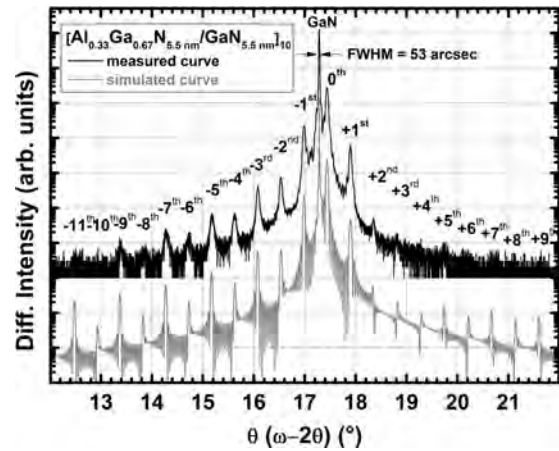
Fig. 1. Experimentally obtained (black) and simulated (gray) x-ray diffraction pattern in $\omega-2\theta$ geometry around the GaN (002) Bragg-reflex of a 10-period superlattice with aluminum mole fraction x=0.33 and individual GaN and AlGaN layer thicknesses of 5.5 nm grown on bulk GaN prepared by ammonothermal synthesis.
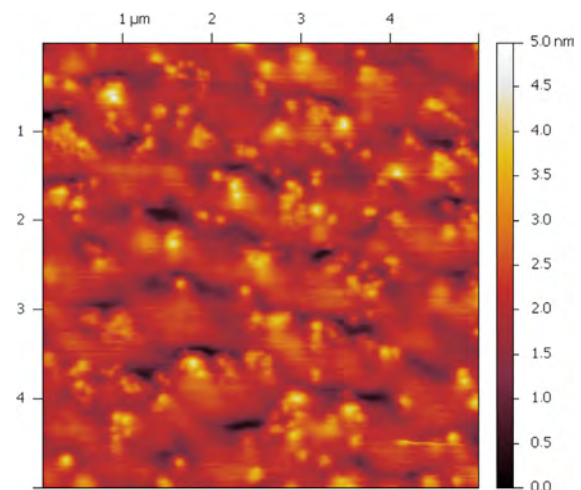
Fig. 2. Atomic force microscopy image of a 10-period superlattice surface with aluminum mole fraction x=0.33 and individual GaN and AlGaN layer thicknesses of 5.5 nm grown on GaN prepared by ammonothermal synthesis. The surface roughness root mean square (RMS) value equals 0.5 nm.
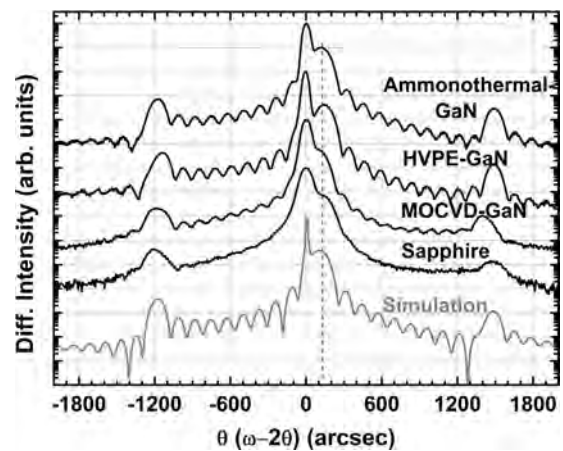
Fig. 3. X-ray diffractogram in $\omega-2\theta$ gerometry around the GaN (002) Bragg-reflex of identically grown 10-period superlattices with aluminum mole fraction x=0.08 and individual GaN and AlGaN layer thicknesses of 6 nm grown on 1.5 μm MBE-GaN buffer grown on different substrates.
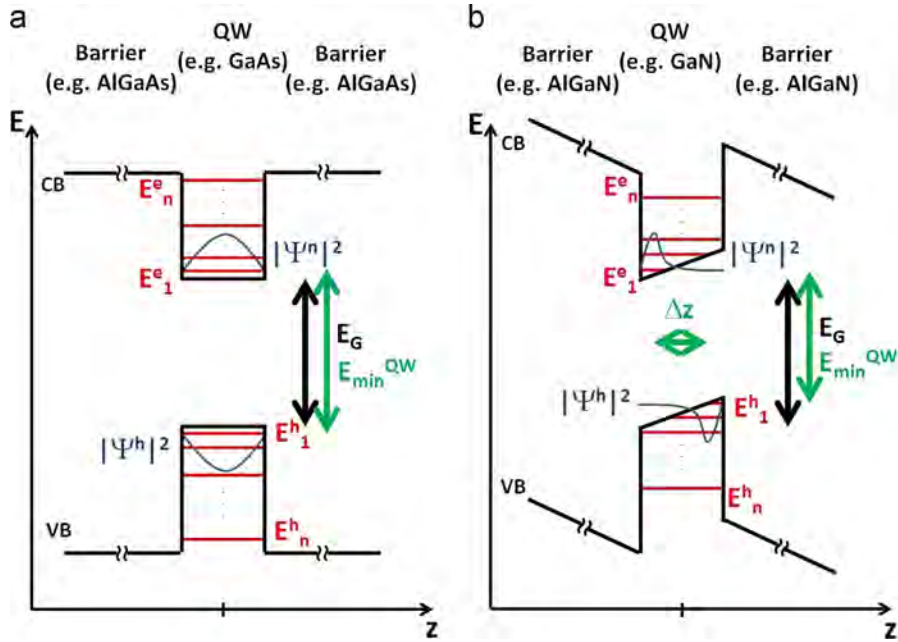
Fig. 4. Theory of the quantum confined Stark effect: Band diagram (energy vs. spatial position z) of a quantum well (QW) (a) without electric field and (b) with intrinsic polarization fields including energy levels E of quantum-mechanically confined states for electrons (e) and holes (h) and there probabilities ($|\Psi|^2$) as well as the bulk band gap E_G of the well material.

indicating the 2-dimensional growth mode. For such superior MBE growth conditions the comparative plot of the HRXRD pattern of 10-period GaN/Al$_{0.08}$Ga$_{0.92}$N superlattices with 12 nm period grown on various substrates (Fig. 3) points out that the substrate properties limit the structural quality of our MBE grown layers and heterostructures. This is clearly visible from the less pronounced superlattice features in the diffraction pattern with deteriorating substrate grade. As known from the HRXRD precharacterization of the templates and from the literature [9] the crystallinity of the GaN template increases with increasing thickness. Already on sapphire weak interface fringes of the on-top grown superlattice structure are visible indicating sufficient interface perfection. As a result of the known increasing crystallinity with the GaN substrate thickness, more pronounced key features of the superlattices occur with increasing substrate thickness. This trend joins to an excellent agreement between simulation and measured intensity profile for the superlattice grown on bulk ammonothermal GaN templates. This result shows clearly that the substrate is the limiting factor for the structure perfection grown in our MBE system.

Based on these structural results time-resolved PL measurements were performed on selected superlattices (MQWs) grown on bulk ammonothermal and 1.9 μm MOVPE produced GaN substrates. In MQWs the GaN layers are sandwiched between two Al$_x$Ga$_{1-x}$N barriers. This confinement results in new discrete energy states in this quantum well which differ from the GaN bulk energy states. The spontaneous recombination of excitons according to these new energy states results in new photon energies in the detected PL. Fig. 4(a) illustrates this effect schematically. The lattice parameters and the spontaneous polarization field of Al$_x$Ga$_{1-x}$N differ from GaN dependent on the aluminum mole fraction. This variation in lattice parameters [12] results in the epitaxial growth of strained layers. By the interplay of spontaneous polarization of Al$_x$Ga$_{1-x}$N and GaN and the resulting piezoelectric polarization inherent electric polarization fields occur. The resulting electric field changes the rectangular quantum well shape into a triangular shape leading to an additional modification of the energy states and a local separation of electrons and holes. [13] Fig. 4(b) illustrates this so called quantum-confined-Stark-effect (QCSE). The triangular potential shape induces asymmetric wave functions and probability of presence ($|\Psi|^2$) for electrons and holes. In consequence the electron–hole-separation should cause an increase of the exciton life

time with increasing quantum well width. Fig. 5 shows a time-resolved PL spectrum for a 10-period MQW (quantum well width 9 monolayers (MLs, 1 ML = 0.259 nm, barrier width 6 nm) grown on 1.9 μm MOCVD-GaN. The MQW emission energy (3.505 eV) is clearly separated from the bulk GaN (3.48 eV) what allows the determination of the respective life times. The energy shift of the main peak of the MQW PL in the first few picoseconds to slightly lower energy can be explained by the shielding of the inherent polarization field by generated minorities. Their number reduces relatively fast due to exciton recombination. Thereby the inherent polarization field reached the unshielded value and according to the QCSE the energy reaches a constant level (dotted red line). From the time-resolved PL of the investigated MQW we extracted the quantum well energy position and the time dependent intensity trend. Fig. 6 shows the MQW PL energy for MQWs grown on 1.9 μm MOVPE GaN substrates for different quantum well widths at barrier aluminum mole fraction $x = 0.08$. The experimentally determined values are in good agreement with values published by Grandjean et al. [14] (gray). The slightly lower determined energy of the quantum well peak compared with the literature results may be explained with the point that we do not plot the energy of the absolute PL intensity maximum in the time-resolved PL because this value seems to be shifted due to the further described polarization field shielding. Furthermore we extracted the time dependent intensity profile of the MQW PL signal after turning off the excitation laser. Fig. 7 shows exemplarily the extracted intensity profile for the MQW with 9 ML quantum well width from Fig. 6. The curve can be fitted by a stretched exponential function

$$It = I_0 e^{-\left(\frac{t-t_0}{\tau}\right)^{\beta}} \tag{1}$$

where $I(t)$ is the time t dependent PL intensity and I_0 is the amplitude scaling factor, t_0 is the starting time of the intensity decrease, τ expresses the exciton life time and β is the stretch parameter. The inset of Fig. 7 plots the extracted exciton life time for different quantum well thicknesses and aluminum mole fraction.

The MQWs with 7 and 9 ML and aluminum mole fraction $x = 0.08$ were grown on 1.9 μm MOVPE GaN templates and show 127 for the MQW PL and 130 ps exciton life time for the MQW PL and 71 ps and 126 ps for the sheer GaN PL respectively. The MQW
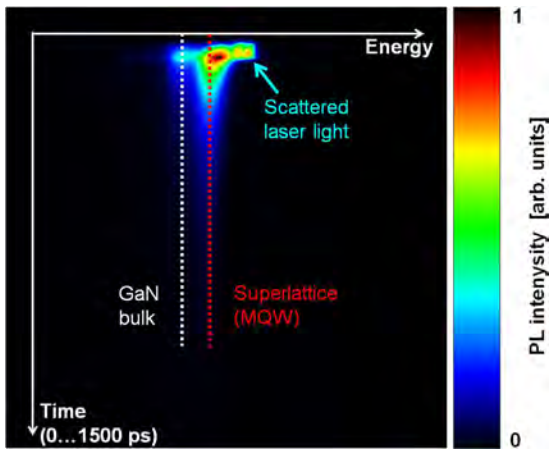
Fig. 5. Example for time-resolved photoluminescence measurements detected by a streak camera connected to a grating spectrometer for [Al$_{0.08}$Ga$_{0.92}$N$_{6\ nm}$/GaN$_{9\ ML}$]$_{10}$ superlattice on 1.9 μm MOCVD-GaN. The Energy of GaN bulk PL (3.48 eV) and MQW PL (3.505 eV) is marked by dotted lines. (For interpretation of the references to color in this figure, the reader is referred to the web version of this article.)
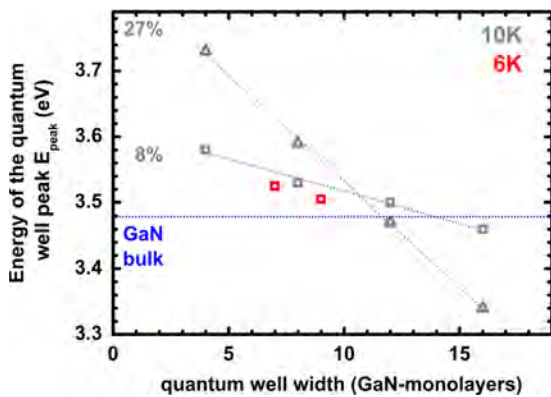
Fig. 6. Photoluminescence energy of the grown GaN/AlGaN MQW vs. well width (red) and literature results (gray) after Granjean et al. [14]. (For interpretation of the references to color in this figure legend, the reader is referred to the web version of this article.)
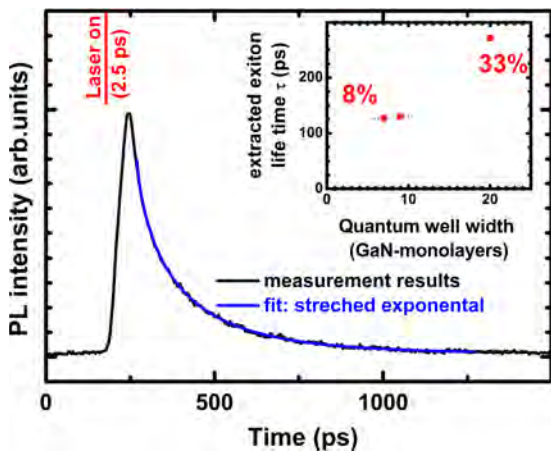
Fig. 7. Time-dependent MQW PL signal after stimulation for a 10-period 9 ML GaN/6 nm Al$_{0.08}$Ga$_{0.92}$N MQW grown on 1.9 μm MOVPE-GaN substrate: The inset shows the extracted time constant for the photoluminescence. The Spatial separation of electrons and holes results in an increase in exciton lifetime.

with 20 ML and $x=0.33$ was grown on ammonothermal bulk GaN and shows a significantly higher exiton life time of 271 ps and

161 ps for the GaN buffer. These results show that MQWs grown on substrates with better crystallinity exhibit higher exciton life times in bulk GaN as well as in the quantum well. In addition we consider the curve shape parameter β and recognized for both the 7 and 9 ML MQW on MOVPE-GaN values of 0.8 for the MQW PL and 0.54 and 0.66 for the GaN PL respectively. For the MQW grown on ammonothermal GaN we could determine β for the MQW PL to be 1 and for the GaN PL 0.94 reflecting a nearly single exponential behavior as expected for perfect spontaneous exciton recombination [11,15]. We believe that the decrease in β for thin defect-rich GaN can be explained by the realization of multiple recombination paths for the excitons correlating with structural defects as centers.

4. Summary

In our study we re-visited the aspect of interface perfection using short-period GaN/AlGaN superlattices as versatile test structures for investigations of interface and layer properties with consequences for a proper GaN substrate choice. The superlattice structures have been grown by MBE under equal growth conditions along the c-axis of Ga-polar substrates prepared by different growth methods. HRXRD pre-characterization indicates the defect reduction in the GaN substrates with increasing thickness as empirically expected. Therefore no deviation from this trend could be determined for the different preparation methods. HRXRD pattern obtained from the grown superlattices have been compared with simulations based on dynamical x-ray diffraction theory of ideal structures with homogeneous composition and atomically smooth and abrupt interfaces and show that for freestanding bulk GaN prepared by a ammonothermal growth method the best structural quality could be achieved. Based on these results, time-resolved PL measurement on selected superlattices confirm this trend with regard to exciton life times as well as recombination mechanisms.

References

[1] I. Akasaki, J. Cryst. Growth 300 (1) (2007) 2–10.
[2] M.S. Shur, in: Proceedings of the Spanish Conference on Electron Devices 0-7803-88 10-0/05/$20.00 02005 IEEE (2005).
[3] U.K. Mishra, et al., Proc. IEEE 96 (2) (2008) 287–305.
[4] T. Aggerstam, et al., Thin Solid Films 515 (2006) 705–707.
[5] R. Oberhuber, et al., Appl. Phys. Lett. 73 (1998) 6.
[6] G. Koblmüller, et al., Appl. Phys. Lett. 91 (2007) 161904.
[7] F. Schubert, et al., J. Appl. Phys. 115 (2014) 083511.
[8] J.W. Matthews, A.E. Blakeslee, J. Cryst. Growth 27 (1974) 118–125.
[9] A. Bchetnia, et al., J. Cryst. Growth 308 (2007) 283–289.
[10] T. Metzger, et al., Philos. Mag. A 77 (1998) 1013–1025.
[11] M. Pophristic, et al., Appl. Phys. Lett. 73 (1998) 24.
[12] O. Ambacher, et al., J. Phys.: Condens. Matter 14 (2002) 3399–3434.
[13] R. Kajitani, et al., Mater. Sci. Eng. B 139 (2007) 186–191.
[14] N. Grandjean, et al., Appl. Phys. Lett. 74 (1999) 2361.
[15] H.E. Romany, L. Pavesiz, J. Phys.: Condens. Matter 8 (1996) 5161–5187.
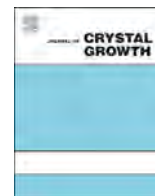
Comparison of stress states in GaN films grown on different substrates: Langasite, sapphire and silicon

Byung-Guon Park [a,1], R. Saravana Kumar [a,1], Mee-Lim Moon [a], Moon-Deock Kim [a,*], Tae-Won Kang [b], Woo-Chul Yang [b], Song-Gang Kim [c]

[a] Department of Physics, Chungnam National University, 220 Gung-dong, Yuseong-gu, Daejeon 305-764, South Korea
[b] Department of Physics, Dongguk University, Pil-dong, Jung-gu, Seoul 100-715, South Korea
[c] Department of Information and Communications, Joongbu University, Chungnam 132-940, South Korea

ABSTRACT

We demonstrate the evolution of GaN films on novel langasite (LGS) substrate by plasma-assisted molecular beam epitaxy, and assessed the quality of grown GaN film by comparing the experimental results obtained using LGS, sapphire and silicon (Si) substrates. To study the substrate effect, X-ray diffraction (XRD), scanning electron microscopy (SEM), Raman spectroscopy and photoluminescence (PL) spectra were used to characterize the microstructure and stress states in GaN films. Wet etching of GaN films in KOH solution revealed that the films deposited on GaN/LGS, AlN/sapphire and AlN/Si substrates possess Ga-polarity, while the film deposited on GaN/sapphire possess N-polarity. XRD, Raman and PL analysis demonstrated that a compressive stress exist in the films grown on GaN/LGS, AlN/sapphire, and GaN/sapphire substrates, while a tensile stress appears on AlN/Si substrate. Comparative analysis showed the growth of nearly stress-free GaN films on LGS substrate due to the very small lattice mismatch ($\sim$3.2%) and thermal expansion coefficient difference ($\sim$7.5%). The results presented here will hopefully provide a new framework for the further development of high performance III-nitride-related devices using GaN/LGS heteroepitaxy.

© 2015 Elsevier B.V. All rights reserved.

1. Introduction

Gallium nitride (GaN) has long been viewed as a promising semiconductor due to its fascinating intrinsic properties like wide direct band gap (3.4 eV), strong binding energies, excellent thermal stability and conductivity, mechanical and chemical robustness, which triggered a fast technological progress in the fabrication of electronics and optoelectronic devices such as high brightness light emitting diodes (LEDs), high-electron-mobility transistors as well as high temperature, high frequency, and high power semiconductor devices [1–4]. Despite the remarkable progresses made in the commercialization of GaN systems achievement of their full potential has however been limited due to the lack of native/lattice-matched substrates. The inevitable heteroepitaxy of GaN on foreign substrates like sapphire, Si or SiC results in stress, and generates high density of threading dislocations (TD, $\sim 10^8$–10^{10} cm^{-2}), cracks and other defects (stacking faults, voids, inversion domains, point defects) due

to the large lattice mismatch and thermal expansion coefficient incompatibility, which deteriorates the optical and electrical properties of GaN-based devices [5,6]. Ever since Amano et al. successfully demonstrated the growth of high quality crack-free GaN epilayers on sapphire substrate using an AlN buffer layer a variety of strain compensating layers like low-temperature GaN, SiN, AlN–GaN superlattices, AlGaN and rare earth oxides have been used to mitigate the stress and to reduce the TD density in GaN epilayers [1,7–10]. Use of these buffer layers, to some extent, has shown considerable improvement in the crystalline quality of GaN epilayers and their device performances, yet there still exist many defects and thus, the growth of high-quality GaN raises many interrogations and requires further research. Hence there is great research interest in finding new methods and substrate materials to overcome these issues, and in particular, the development of novel and futuristic substrate material with better lattice and thermal matching would be an effective and pioneering solution for addressing the problems in GaN-based devices. Erstwhile, Fukuda et al. observed langasite (La$_3$Ga$_5$SiO$_{14}$, LGS) family materials as viable substrate materials for GaN heteroepitaxy due to their small lattice and thermal mismatch as well as domain matching epitaxy [11]. LGS has been extensively used in piezoelectric applications, and belongs to a trigonal crystal system

with space group P321, having high melting point (1475 °C), in-plane structure with hexagonal symmetry and lattice constants $a = 8.161$ Å, $c = 5.087$ Å [11–13]. Besides, the thermal expansion coefficient difference between GaN (5.59×10^{-6} K^{-1}) and LGS (5.20×10^{-6} K^{-1}) is very small ($\sim 7.5\%$) when compared to the conventional substrates like sapphire (7.5×10^{-6} K^{-1}, 25.5%) and Si (3.77×10^{-6} K^{-1}, 48.3%) [14–16]. Despite these potential virtues, the growth of GaN epilayers on LGS substrate has not been reported so far, and hence in this work we report the successful growth of GaN film on novel LGS substrate by plasma-assisted molecular beam epitaxy (PA-MBE). Also, the effectiveness of LGS substrate was demonstrated by comparing the stress states in GaN films grown on various substrates namely LGS, Si (111) and c-plane sapphire. The study of stress or strain effects in GaN films is indispensable for better understanding of the film's property and for realizing high performance GaN-based devices. Experimental results obtained from X-ray diffraction (XRD), scanning electron microscopy (SEM), Raman spectroscopy, and photoluminescence spectra (PL) showed the growth of stress-free GaN on LGS substrate.

2. Experimental details

All the unintentionally doped (UID) GaN films were grown on different substrates namely LGS (Fomos-Materials Co.), sapphire, and Si(111) by PA-MBE. High purity material sources such as gallium (7 N) and aluminum (6 N) were supplied by a standard Knudsen cell, while active N$_2$ (6 N) was provided by a radio-frequency (rf) plasma source. Schematics of four different sample structures used in the present work are shown in Fig. 1. In growing GaN on LGS substrate, a 5 nm thick LT-GaN layer was firstly deposited at 480 °C followed by the growth of 620 nm top GaN layer at 640 °C. For the samples on sapphire, two different buffer layers were deposited, one consisting of 35 nm thick AlN layer deposited at 800 °C and the other consisting of 10 nm LT-GaN deposited at 550 °C prior to the deposition of 680 nm GaN at 680 °C. For GaN on Si(111) a 10 nm thick LT-AlN layer was grown at 600 °C followed by the growth 65 nm thick high-temperature AlN layer at 800 °C, and then final 1000 nm thick GaN layer deposited at 570 °C. During the growth of GaN films on different substrates, the N$_2$ flow rate, RF power, and Ga partial pressure was maintained at 3.0 sccm, 450 W, and 1.2×10^{-6} Torr, respectively. For simplicity, GaN films grown on LGS, AlN/sapphire, GaN/sapphire, and AlN/Si(111) were denoted as samples A, B, C, and D, respectively.

Wet etching experiments were performed to analyze the polarity of GaN films on different substrates by immersing the substrates in 2 M KOH aqueous solution at 90 °C for 1 min. Surface morphology of as-grown and KOH etched GaN films were analyzed by SEM. Stress states in GaN films was investigated by HR-XRD (Cu Kα, 1.541 Å), Raman (Ar$^+$ laser, 532 nm), PL (He–Cd laser, 325 nm, 20 K) measurements.

3. Results and discussion

Fig. 2 shows the SEM images of GaN films grown on different substrates before and after KOH etching. SEM images of as-grown GaN films (Fig. 2(a)–(d)) grown on various substrates before KOH

Fig. 2. SEM images of GaN films grown on different substrates (a)–(d) before etching and (e)–(h) after KOH etching.

etching exhibited flat and comparatively uniform morphology with some hillock pits at the surfaces. After KOH etching (Fig. 2(e)–(h)), the surface morphology of samples A, B, and D remains unaltered, while sample C (Fig. 2(g)) exhibited hexagonal pyramidal structure. This suggest that GaN films grown on LGS, AlN/sapphire and AlN/Si substrates possess Ga-polarity, while the film grown on GaN/sapphire substrate have N-polarity.

The $2\theta - \omega$ XRD patterns of GaN films grown on various substrates are shown in Fig. 3. The (0002) diffraction peaks of all the samples exhibited some shift relative to the bulk GaN ($2\theta = 34.5701°$) [17]. The (0002) diffractions peaks of samples A, B, and C are shifted to lower 2θ angles at 34.5648°, 34.532°, and 34.5618°, respectively, while that of sample D is shifted to higher 2θ angle at 34.5918° relative to the bulk value, indicating the different stress states in the four samples. The shift in the (0002) diffraction peak position to higher and lower 2θ values generally indicates the tensile and compressive stress, respectively [18]. Hence, the samples A, B, and C are under compressive stress, while the sample D is under tensile stress. The calculated values of 'c' axis lattice parameter and the corresponding residual strain in GaN films deposited on various substrates are given in Table 1. The residual strain in z-direction is estimated using the relation,

$$\varepsilon_\perp = \frac{(c_s - c_o)}{c_o} \tag{1}$$

Fig. 1. Schematics of GaN films grown on different substrates.
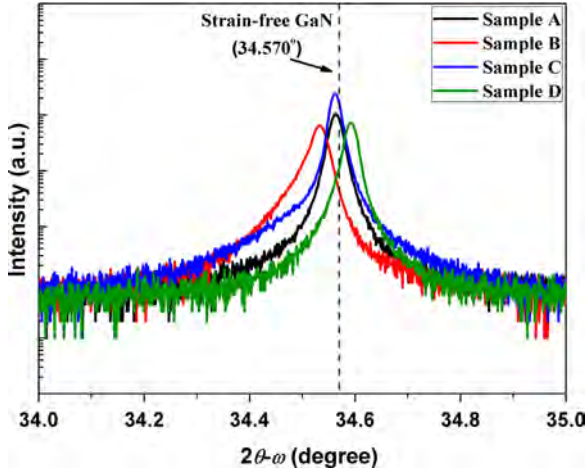
Fig. 3. $2\theta-\omega$ XRD-scan of (0002) diffraction peaks of GaN films.
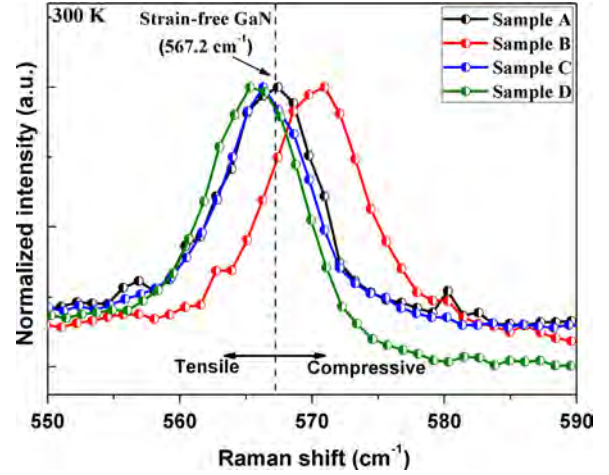
Fig. 4. Raman spectra of E_2(high) phonon shift of GaN films.

Table 1
Structural and optical parameters of GaN films grown on different substrates.

Sample Code	XRD		Raman	PL
	Lattice constant, c (Å)	Strain, $\varepsilon_\perp$ (%)	Stress (GPa)	Band gap energy (eV)
Sample A	5.1858	+0.0140	0.047	3.524
Sample B	5.1906	+0.1067	0.881	3.546
Sample C	5.1860	+0.0196	−0.209	3.533
Sample D	5.1818	−0.0617	−0.395	3.495
Unstrained GaN	5.1850	0	0	3.510

where, 'c_s' and 'c_o' are the lattice parameter values of strained and unstrained GaN epilayers [15]. The estimated values indicate a tensile stress for GaN film grown on AlN/Si substrate while compressive stress on other substrates, which is consistence with the analysis of XRD patterns.

Fig. 4 shows the Raman spectrum of GaN films grown on various substrates. The E_2(high) mode is very sensitive to strain and has been extensively used to quantify the stress in GaN epilayers. Usually, a blue-shift in E_2(high) phonon peak indicates a compressive stress, while a red-shift indicates the tensile stress. It can be observed from figure that the E_2(high) position is substrate dependent, clearly implying different stress states in different samples. The E_2(high) peak of samples A, B, C, and D were observed at 567.4, 570.9, 566.3, and 565.5 cm^{-1}, respectively. Comparing with the intrinsic value of 567.2 cm^{-1} for stress-free GaN [19], the samples A and B are under compressive stress, while the samples C and D are under tensile stress. The stress in the GaN films were quantitatively evaluated using $\Delta\omega = k \cdot \sigma$, where '$\Delta\omega$' is the shift in the frequency of phonon, 'k' is the Raman stress coefficient (4.3 cm^{-1}/GPa), and 'σ' is the stress. The calculated values of stress for different samples are given in Table 1. Among the four samples, GaN film deposited on LGS substrate has the minimum stress, and is very close to the stress-free state.

It is well known that the energy band gap of a semiconductor is affected by the residual stress. A tensile stress narrows the band gap while a compressive stress widens it [20]. Fig. 5(a) shows the neutral donor bound excitons (D^{O}X) emission peak of GaN films deposited on various substrates. The D^{O}X peak originating from the neutral Si- and O-related exciton recombinations [21] was observed between 3.459 and 3.493 eV depending on the substrate. The band gap energy of GaN films deposited on different

substrates is estimated using the relation [15],

$$E_g = E_{D^O X} + E_a s \tag{2}$$

where, 'E_g' is the band gap, '$E_{D^O X}$' is the energy position of D^{O}X, and 'E_a' is the activation energy of D^{O}X. The activation energy was estimated from the temperature dependent PL spectra using the Arrhenius curve [15],

$$I = \frac{I_O}{[1 + a\exp(-E_a/k_B T)]} \tag{3}$$

where 'a' is a factor related to the ratio of the radiative lifetime and the ground state lifetime. Fig. 5(b) shows the typical Arrhenius plot of sample A displaying the variation in the PL intensity with $1000/T$. The activation energy estimated from the Arrhenius plot was found to be 36.15, 53.38, 52.38, and 36.05 meV for samples A, B, C, and D, respectively.

According to Eq. (2) the band gap of GaN was calculated, and a plot showing the energy dependence on substrate is given in Fig. 6(a). From the figure it can be observed that the energy band gap of GaN film deposited on LGS substrate is very close to the free-standing GaN, indicating the growth of nearly stress-free GaN on LGS. Fig. 6(b) shows the relationship between the luminescent band gap and the vertical strain of Ga-polar GaN films namely samples A, B, and D. The plot showed the linear dependence of band gap with strain from quasicubic approximation, and by least-square fitting of the data the band gap of GaN at 20 K as a function of biaxial stress can be expressed by [15]

$$E_g(\varepsilon) = E_g(0) + b_g \varepsilon_\perp = 3.51 + 30.2\varepsilon_\perp \text{ (eV)} \tag{4}$$

where, '$E_g(\varepsilon)$' is the band gap of strained GaN film, '$E_g(0)$' is the strain-free band gap transition energy, 'b_g' is the linear coefficient, and '$\varepsilon_\perp$' is the strain component in the z-direction obtained from XRD measurement in Fig. 3.

From the above results, it can be observed that the GaN films grown on LGS substrate is nearly stress-free, which can be attributed to the small lattice mismatch (~3.2%) and thermal expansion coefficient difference (~7.5%) between GaN and LGS when compared to sapphire and Si. However, these are early investigations of GaN films on LGS substrate, and further work in optimizing the growth conditions and the buffer design are underway to have a better understanding on the growth kinetics of GaN films on LGS substrate.
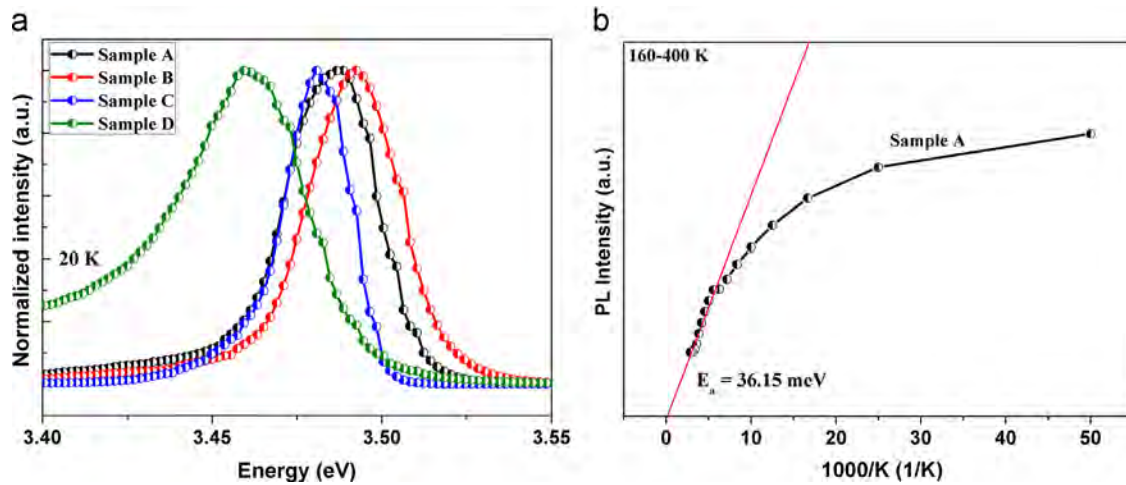
Fig. 5. (a) D^{O}X PL spectra of GaN films and (b) typical Arrhenius plot of sample A showing the variation in PL intensity as a function of 1000/*T*.
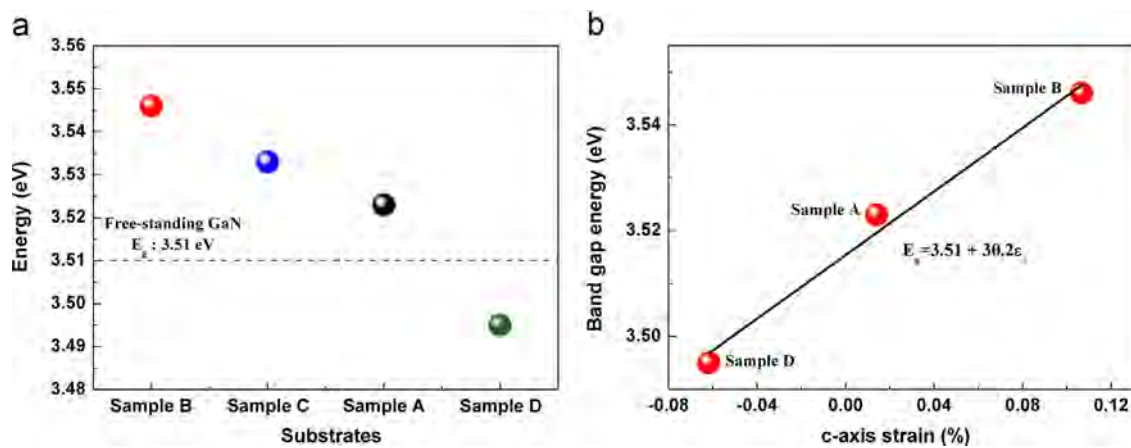
Fig. 6. (a) Band energy dependence on substrate and (b) variation in band gap energy of GaN films with strain.

4. Conclusion

We have investigated the feasibility using novel and nearly lattice-matched LGS substrate for the growth of GaN films by PA-MBE. Stress analysis by XRD, Raman and PL revealed that the film grown on LGS substrate exhibited minute peak shift relative to unstrained GaN when compared to other substrates, indicating the stress-free state. A linear relationship between energy band gap and strain was observed, and a linear coefficient of 30.2 eV is obtained at 20 K. The present work sheds light on the potentiality of using LGS as a futuristic and ideal substrate material for the growth of III-nitride materials with improved device performance.

References

[1] H. Xu, X. Hu, X. Xu, Y. Shen, S. Qu, C. Wang, S. Li, Gallium vacancies related yellow luminescence in N-face GaN epitaxial film, Appl. Surf. Sci. 258 (2012) 6451–6454.
[2] Y.L. Wang, F. Ren, U. Zhang, Q. Sun, C.D. Yerino, T.S. Ko, Y.S. Cho, I.H. Lee, J. Han, S.J. Pearton, Improved hydrogen detection sensitivity in N-polar GaN Schottky diodes, Appl. Phys. Lett. 94 (2009) 212108.
[3] S.W. Pak, D.U. Lee, E.K. Kim, S.H. Park, K. Joo, E. Yoon, Defect states of *a*-plane GaN grown on *r*-plane sapphire by controlled integration of silica nano-spheres, J. Cryst. Growth 370 (2013) 78–81.
[4] Y. Lu, H. Kondo, K. Ishikawa, O. Oda, K. Takeda, M. Sekine, H. Amano, M. Hori, Epitaxial growth of GaN by radical-enhanced metalorganic chemical vapor deposition (REMOCVD) in the downflow of a very high frequency (VHF) N$_2$/H$_2$ excited plasma – effect of TMG flow rate and VHF power, J. Cryst. Growth 391 (2014) 97–103.
[5] M.K. Ozturk, E. Arslan, I. Kars, S. Ozcelik, E. Ozbay, Strain analysis of the GaN epitaxial layers grown on nitridated Si(111) substrate by metal organic chemical vapor deposition, Mater. Sci. Semicond. Process. 16 (2013) 83–88.
[6] Z.M. Chen, Z.Y. Zheng, Y.D. Chen, H.L. Wu, C.S. Tong, G. Wang, Z.S. Wu, H. Jiang, Threading edge dislocation arrays in epitaxial GaN: formation, model and thermodynamics, J. Cryst. Growth 387 (2014) 48–51.
[7] H. Amano, N. Sawaki, I. Akasaki, Y. Toyoda, Metalorganic vapor phase epitaxial growth of a high quality GaN film using an AlN buffer layer, Appl. Phys. Lett. 48 (1986) 353–355.
[8] E. Arslan, O. Duygulu, A. Arslan Kaya, A. Teke, S. Ozcelik, E. Ozbay, The electrical, optical, and structural properties of GaN epitaxial layers grown on Si (111) substrate with SiN$_x$ interlayers, Superlattice Microstruct. 46 (2009) 846–857.
[9] L. Ravikiran, M. Agrawal, N. Dharmarasu, K. Radhakrishnan, Effect of stress mitigating layers on the structural properties of GaN Grown by ammonia molecular beam epitaxy on 100 mm Si(111), Jpn. J. Appl. Phys. 52 (2013) 08JE05.
[10] J. Leathersich, E. Arkun, A. Clark, P. Suvarna, J. Marini, R. Dargis, F. (Shadi) Shahedipour-Sandvik, Deposition of GaN films on crystalline rare earth oxides by MOCVD, J. Cryst. Growth 399 (2014) 49–53.
[11] T. Fukuda, K. Shimamura, V.V. Kochurikhin, V.I. Chani, B.M. Epelbaum, S. L. Baldochi, H. Takeda, A. Yoshikawa, Crystal growth of oxide and fluoride materials for optical, piezoelectric and other applications, J. Mater. Sci.: Mater. Electron. 10 (1999) 571–580.
[12] O.A. Gurbanova, E.L. Belokoneva, Topology-symmetry analysis of the mixed frameworks in the structures of phosphates, germanates, gallates, and silicates based on fundamental building blocks, Crystallogr. Rep. 51 (2006) 577–583.

[13] C. Klemenz, High-quality langasite films grown by liquid phase epitaxy, J. Cryst. Growth 237–239 (2002) 714–719.

[14] J. Kraublich, S. Hofer, U. Zastrau, N. Jeutter, C. Baehtz, Temperature dependence of lattice parameters of langasite single crystals, Cryst. Res. Technol. 45 (2010) 490–492.

[15] L. Zhang, K. Cheng, S. Degroote, M. Leys, M. Germain, G. Borghs, Strain effects in GaN epilayers grown on different substrates by metal organic vapor phase epitaxy, J. Appl. Phys. 108 (2010) 073522.

[16] X. Pan, M. Wei, C. Yang, H. Xiao, C. Wang, X. Wang, Growth of GaN film on Si (111) substrate using AlN sandwich structure as buffer, J. Cryst. Growth 318 (2011) 464–467.

[17] J. Wang, H.B. Ryu, M.S. Park, W.J. Lee, Y.J. Choi, H.Y. Lee, Epitaxy of GaN on Si (111) substrate by the hydride vapor phase epitaxy method, J. Cryst. Growth 370 (2013) 249–253.

[18] K.M.A. Saron, M.R. Hashim, M.A. Farrukh, NH$_3$-free growth of GaN nanostructure on n-Si (111) substrate using a conventional thermal evaporation technique, J. Cryst. Growth 349 (2012) 19–23.

[19] G. Nootz, A. Schulte, L. Chernyak, A. Osinsky, J. Jasinski, M. Benamara, Z.L. Weber, Correlations between spatially resolved Raman shifts and dislocation density in GaN films, Appl. Phys. Lett. 80 (2002) 1355–1357.

[20] C.C. Chen, R.Z. Wang, P. Liu, M.K. Zhu, B.B. Wang, H. Yan, Structural effects of field emission from GaN nanofilms on SiC substrates, J. Appl. Phys. 115 (2014) 153705.

[21] A. Lundskog, C.W. Hsu, D. Nilsson, K.F. Karlsson, U. Forsberg, P.O. Holtz, E. Janzen, Controlled growth of hexagonal GaN pyramids by hot-wall MOCVD, J. Cryst. Growth 363 (2013) 287–293.
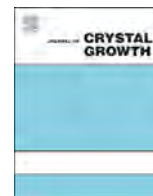
Influence of (7 × 7)–"1 × 1" phase transition on step-free area formation in molecular beam epitaxial growth of Si on Si (111)

Andreas Fissel*, Ayan Roy Chaudhuri, Jan Krügener, H. Jörg Osten

Institute of Electronic Materials and Devices, Leibniz University Hannover, Schneiderberg 32, 30167 Hannover, Germany

ABSTRACT

The step-flow growth condition of Si on Si (111) near the (7 × 7)–"1 × 1" surface phase transition temperature T_C is analysed within the framework of Burton–Cabrera–Frank theory. In particular, coexistence of both surface phases well below T_C and their specific influence on the step-flow growth behaviour is considered. We presume that under dynamical condition of growth, the surface initially covered by only the (7 × 7) phase separates into domains surrounded by "1 × 1" areas. On such a surface, the overall supersaturation should be reduced drastically compared to a surface with only (7 × 7), resulting in much larger critical terrace width for nucleation.

© 2015 Elsevier B.V. All rights reserved.

1. Introduction

The Si (111) surface exhibits a surface phase transition from (7 × 7) to disordered "1 × 1" surface structure at a temperature $T_C \approx 1100$ K. Recently, we investigated the development of surface morphology in Si molecular beam epitaxy (MBE) on mesastructured Si (111) surfaces near T_C [1]. For a small increase in T, significant changes in surface morphology were found, accompanied by a strong increase in step-free area dimension (Fig.1), what has not been reported so far.

Therefore, a deeper understanding of the unusual observation is needed. In our earlier studies, the coexistence of "1 × 1" and (7 × 7) surfaces under certain growth conditions and their specific influence on the growth behaviour was already discussed in such a context [1]. Here, we present a more quantitative interpretation to support this prediction using a simple step-flow growth model and data known from the literature. The results show that indeed under dynamical condition of growth the coexistence of both surface phases well below 1100 K could explain our experimental findings.

2. Results and discussion

At $T < T_C$, the 7 × 7 surface phase exhibits a smaller surface energy than the "1 × 1" surface. However, long range order elastic and electrostatic interactions of surface structure domains allow the coexistence of (7 × 7) and "1 × 1" domains over an extended T-range around T_C [2]. Thereby, the size of the domains is dependent on T and the rate of T changes. Moreover, area fraction of the two surface phase domains was found to be also strongly dependent on the terrace width. Triangular domains with up to 1 μm side length were observed on terraces > 4 μm [3]. The size of domains for a given T is determined by the difference in surface free energy $\Delta\gamma$ between the 7 × 7 and "1 × 1" surface phase, where the T-dependence of $\Delta\gamma$ is determined by the entropy difference ΔS between both phases and can be expressed near T_c by: $\Delta\gamma = (T - T_C)\Delta S$, with $\Delta S = 0.013 k_b$ (k_b - Boltzmann constant) [3].

Further studies show, that surface supersaturation has also a strong impact on the formation and extension of surface phases. Hannon et al. found that near T_C the size of individual (7 × 7) domains within a "1 × 1" surface matrix decreases under the presence of an external Si flux [4]. The external Si flux results in a supersaturation of adatom concentration n with respect to the equilibrium mobile adatom density (n_{eq}) at the surface, giving rise to an adatom chemical potential $\Delta\mu = k_b T \times \ln(n/n_{eq})$. They pointed out that the energy cost of (7 × 7) domain formation relative to the uniform "1 × 1" phase with higher n_{eq} has to be modified by the energy associated with the transfer of excess adatom density to the surrounding "1 × 1" area on the terrace. This energy is expressed by: $\Delta\mu \times (n_{"1 \times 1"} - n_{7 \times 7}) = \Delta\mu \times \Delta n$, [4] where $n_{"1 \times 1"}$ and $n_{7 \times 7}$ are the n_{eq} values of the "1 × 1" and (7 × 7) phase, respectively. From STM investigations $n_{"1 \times 1"} \approx 0.2$ monolayer's (ML) and $n_{7 \times 7} \approx 0.08$ ML were obtained, [5] which results in an excess mobile adatom density of $\Delta n \approx 0.12$ ML (1 ML = 7.83×10^{14} atoms/cm²). This effect changes the surface free energy $\Delta\gamma$ by $\Delta\mu \times \Delta n$, which makes the "1 × 1" phase more favourable than the (7 × 7) phase (Fig. 2). Consequently, phase transition is shifted by $\Delta T = T_C - T_C$ to lower T. Assuming no change of γ around T_C, ΔT can be roughly estimated by $\Delta T = -(\Delta n \times \Delta\mu)/\Delta S$ [4].

Hannon et al. estimated $\Delta T = -3$ K for a Si flux of 4.4×10^{12} atoms/cm² s, which corresponds to $\Delta\mu = 2 \times 10^{-4}$ on a

---

* Corresponding author.
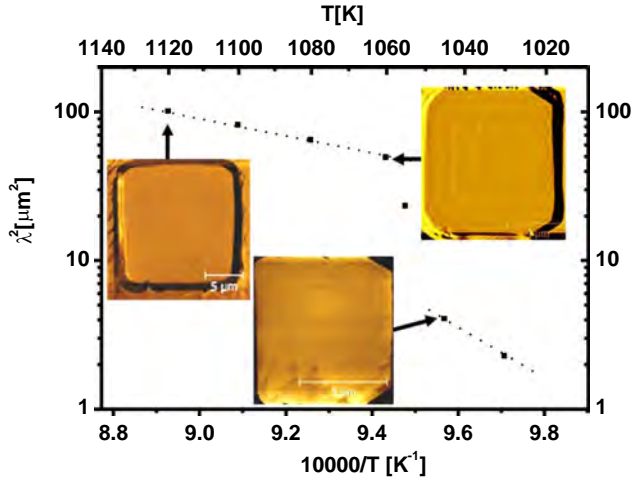
Fig. 1. Summarised data of step-free areas (λ^2) (λ – step-free terrace width) as a function of temperature (T) (Arrhenius graph), with corresponding AFM images of the mesa surfaces.
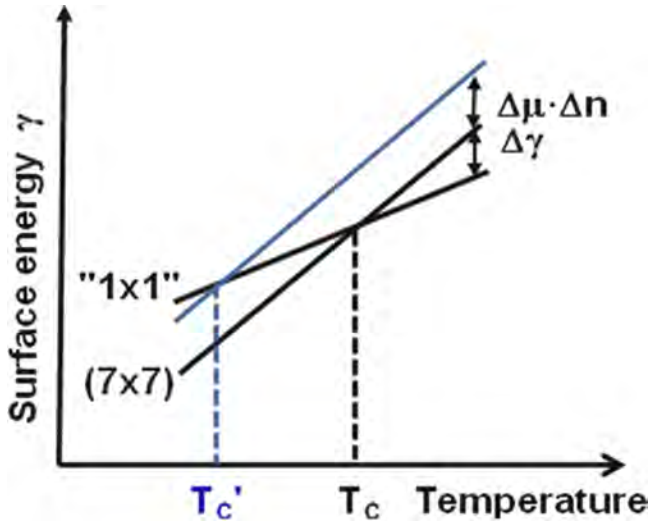
Fig. 2. Schematic illustration of the change in surface energy of the "1×1" and 7×7 phase at T around T_C and the shift in T_C due to the energy associated with the transfer of excess adatom density ($\Delta\mu \times \Delta n$).

2 μm wide terrace [4]. They also suggested already that typical growth rates used in semiconductor epitaxy lead to a more significant change in T_C. In our experiments, we use a Si flux of about 4×10^{13} atoms/cm² s, which results in a change in T_C by at least 30 K considering the same terrace width. Moreover, $\Delta\mu$ becomes larger on wider terraces, which consequently could result in a further increase in "1×1" domains or shrinking of (7×7) domains, respectively. Since we observed the (7×7)–"1×1"phase transition at 1100 K under static conditions, a significant amount of "1×1" domains could be present already at $T \leq 1070$ K under the dynamical conditions of growth in our experiments. This is the T-range, where we observed a drastic change in surface morphology and a strong increase in step-free areas.

The supersaturation is determined by the ratio of the actual density of mobile adatoms at the surface to n_{eq}. Following the work of Burton, Cabrera and Frank (BCF) [6], the adatom density n on a terrace is governed by the diffusion equation. The diffusion equation in the steady state regime valid for complete condensation, fast attachment–detachment kinetics as well as slow moving straight steps in x-direction scan can be written in a form

$$D\frac{d^2 n(x)}{dx^2} + R = 0 \tag{1}$$

with D is the diffusion coefficient, and R is the rate of atom flux towards the surface. The assumption of complete condensation is justified in view of the very low desorption rate (between 10^8 and 10^{10} atoms/cm² s¹ [7]) at T used in our experiments compared to the deposition rate (10^{13} atoms/cm² s¹). Furthermore, it has been shown that surface mass transport on Si (111) is governed by diffusion of adatoms on terraces rather than attachment/detachment of atoms at steps within the T-range of our investigation [8]. Therefore, it can be suggested that $n(x)$ at the step edges is equal to n_{eq}: $n(0) = n(\lambda) = n_{eq}$. Introducing the dimensionless terrace width $X = x/\lambda$, solution of Eq. (1) is

$$\frac{n(x)}{n_{eq}} = 1 + \frac{R \times \lambda^2}{2D \times n_{eq}}X - \frac{R \times \lambda^2}{2D \times n_{eq}}X^2 \tag{2}$$

where $D \times n_{eq}$ represents the so-called mass diffusion constant. The corresponding supersaturation $\Delta\mu$, i.e. the adatom chemical potential, is given by

$$\Delta\mu = k_b T \times \ln\left[\frac{n(x)}{n_{eq}}\right] = k_b T \times \ln\left[1 + \frac{R \times \lambda^2}{2D \times n_{eq}}X - \frac{R \times \lambda^2}{2D \times n_{eq}}X^2\right] \tag{3}$$

Midway the steps ($\lambda/2$), $\Delta\mu$ reaches its maximum value with

$$\Delta\mu = k_b T \times \ln\left[\frac{n(\lambda/2)}{n_{eq}}\right] = k_b T$$
$$\times \ln\left[1 + \frac{R \times \lambda^2}{4D \times n_{eq}} - \frac{R \times \lambda^2}{8D \times n_{eq}}\right] = k_b T \times \ln\left[1 + \frac{R \times \lambda^2}{8D \times n_{eq}}\right] \tag{4}$$

or with simplification for small $\Delta\mu$

$$\Delta\mu = k_b T \times \frac{R \times \lambda^2}{8D \times n_{eq}} \tag{5}$$

Values in the range from $D \times n_{eq} = 10^7$–10^8 s⁻¹were reported for the "1×1" surface [9,10]. In our analysis, we use a value of $D \times n_{eq} = 8 \times 10^7$ s⁻¹derived for $T = 1140$ K [8]. Furthermore, $D \times n_{eq}$ can be suggested to be thermally activated [10]

$$D \times n_{eq} = const. e^{-[(E_D + E_a)/k_b T]} \tag{6}$$

where E_D is the surface diffusion barrier and E_a is the adatom creation energy [10]. At $T \geq 1100$ K, $E_D + E_a = 1.3$ eV on "1×1"; with $E_D = 1.1$ eV and $E_D = 0.2$ eV were reported [8,10]. If this is applied to the value of $D \times n_{eq} = 8 \times 10^7$ s⁻¹at 1140 K, we get $D \times n_{eq} = 6.3 \times 10^7$ s⁻¹ at 1120 K.
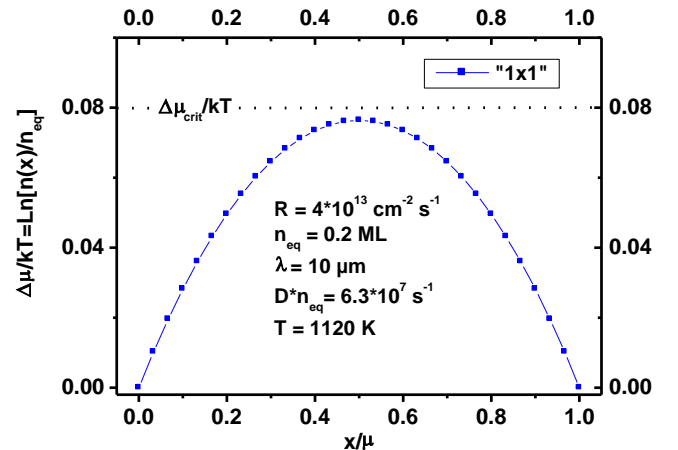
Fig. 3. Excess chemical potential profile across a 10 μm wide terrace calculated for a Si flux of 4×10^{13} cm⁻² s⁻¹ at 1120 K, where only the "1×1" surface phase was observed. Critical supersaturation for nucleation is also indicated by the dotted line.

Fig. 3 shows the $\Delta\mu$ profile across a 10 μm wide terrace calculated for a flux of 4×10^{13} cm^{-2} s^{-1}. Since 10 μm corresponds to the observed maximum step-free terrace width, $\Delta\mu_{crit}/k_bT = 0.08$ obtained widway the steps corresponds nearly to the critical value before nucleation occurs. This value is quite low indicating that the surface conditions are near to the thermodynamic equilibrium. Considering $n_{"1 \times 1"} = 0.2$ ML, $\Delta\mu_{crit}/k_bT = 0.08$ corresponds to a critical excess mobile adatom density of 0.016 ML (1.25×10^{13} cm^{-2}) on Si (111) at 1120 K.

Next, we analysed the conditions for 1030 K, where only (7×7) surface structure appears. Here, we assume that $\Delta\mu_{crit}/k_bT$ for island formation is comparable to "1×1". That simply means with respect to the terrace centre

$$\frac{n(\lambda/2)}{n_{eq}} = \text{const.} = 1 + \frac{R \times \lambda^2}{8D \times n_{eq}} \qquad (7)$$

At 1030 K, we obtain a critical terrace width of only 1.5 μm. Since $[(10 \mu m)^2/(1.5 \mu m)^2] = 44$, $(D \times n_{eq})_{"1 \times 1"}$ at 1120 K should be larger than $(D \times n_{eq})_{7 \times 7}$ at 1030 K to an equal extent, which gives $(D \times n_{eq})_{7 \times 7} = 1.4 \times 10^6$ s^{-1}. That is similar to results obtained from studies of the island and void decay performed at similar temperatures [8].

To analyse the conditions of phase coexistence, we have to calculate the relevant data for $D \times n_{eq}$ at $T = 1060$ K. For "1×1", $(D \times n_{eq})_{"1 \times 1"} = 8 \times 10^7$ s^{-1} at 1140 K and $E_D + E_a = 1.3$ eV give $(D \times n_{eq})_{"1 \times 1"} = 3 \times 10^7$ s^{-1} at 1060 K. For (7×7), it is known that n_{eq} is much smaller compared to the "1×1" surface and $(D \times n_{eq})_{7 \times 7}$ cannot be simple estimated from the high temperature value known for the "1×1" surface.

An activation energy of 3.6 ± 0.2 eV was obtained for mass transport on the Si (111) at 880 K $\leq T \leq$ 980 K [11]. Similar energies (3.2–3.8 eV) were reported recently for the mass transport during the (7×7)–"1×1" surface phase transition [12]. It was suggested that the phase transition is governed by the rate at which the material is exchanged between the first layer of the crystal and the surface. Additional adatoms are assumed to be formed in the first layer of the crystal and the activation energy is related to the adatom-vacancy generation. That means that terraces appear to produce most mobile adatoms rather than step edges. It is interesting to note that for vacancy diffusion on Si (111) at 850 K $\leq T \leq$ 1000 K similar activation energy (3.0 ± 0.2 eV) was reported, which was assumed to consists of the energy to create monovacancy and diffusion barrier [13]. In our estimation, we use $E_D + E_a = 3.6$ eV and $(D \times n_{eq})_{7 \times 7} = 1.4 \times 10^6$ s^{-1} at 1030 K, which gives a value of $(D \times n_{eq})_{7 \times 7} = 4.3 \times 10^6$ s^{-1} for 1060 K.

Furthermore, a surface diffusion barrier of $E_D = 1.1$ eV was also reported for the (7×7) surface [14]. That results in $E_a = 2.5$ eV for

the (7×7) surface, a value which is comparable to the Si–Si binding energy [15]. As mentioned above, $n_{7 \times 7} = 0.08$ ML was estimated for the (7×7) surface phase from STM investigations. However, this value was obtained from the evaluation of island densities formed from excess adatoms during fast quenching surfaces from $T > T_C$ and represents n_{eq} at or near T_C. Therefore, n_{eq} for (7×7) should be smaller at 1060 K. Considering $n_{eq(7 \times 7)} = 0.08$ ML at 1100 K and $E_a = 2.5$ eV results in $n_{eq(7 \times 7)} = 0.03$ ML at 1060 K.

The adatom density and the corresponding $\Delta\mu$ across a terrace with coexisting surface phases were calculated using a simple model presented by Hibino et al. [16]. In this model, the terrace is separated into two parts, with (7×7) and "1×1" surface phase, respectively. Thereby, the phase boundary is parallel to the step edges and moves with the same velocity during growth (Fig. 4a). Both the step edges and the phase boundaries are straight. Indeed, such configuration was observed experimentally under certain conditions, however, only on small terraces [2].

Furthermore, the surface mass transport on Si (111) was assumed to be only governed by the diffusion of adatoms on the terraces. Moreover, the continuity of the chemical potential with respect to the mobile adatom density and conservation of adatoms at the phase boundary were considered for solving the diffusion equations. The solution of the diffusion equation provides for the different parts of the terrace [16]

$$\frac{n(x)}{n_{eq("1x1")}} = 1 + \frac{R \times \lambda^2 (p \times a^2 - a^2 - p)}{2(D \times n_{eq})_{"1 \times 1"} (p \times a - a - p)} X$$
$$- \frac{R \times \lambda^2}{2(D \times n_{eq})_{"1 \times 1"}} X^2 \quad (0 \leq X \leq \ell/\lambda) \qquad (8)$$

$$\frac{n(x)}{n_{eq(7 \times 7)}} = 1 + \frac{R \times \lambda^2 (p \times a^2 - a^2 - p)}{2(D \times n_{eq})_{(7 \times 7)} (p \times a - a - p)} (X - 1)$$
$$- \frac{R \times \lambda^2}{2(D \times n_{eq})_{(7x7)}} (X^2 - 1) \quad (\ell/\lambda \leq X \leq 1) \qquad (9)$$

where ℓ is the position of the domain boundary, p is the ratio $(D \times n_{eq})_{"1 \times 1"}/(D \times n_{eq})_{7 \times 7}$ and $a = \ell/\lambda$. Using the values estimated for the $(D \times n_{eq})_{7 \times 7}$ and $(D \times n_{eq})_{"1 \times 1"}$ we obtain $p = 7$ at 1060 K.

Fig. 4b shows the calculated supersaturation across a 4 μm terraces with coexisting "1×1" and (7×7) surface phases, with phase boundary in the centre of terrace ($\ell = \lambda/2$), and for comparison with only the (7×7) surface phase. It is clearly visible that in case of phase coexistence, $\Delta\mu$ remains below the critical value, whereas for terrace with only (7×7) $\Delta\mu$ becomes much larger than the critical value expected for nucleation. That means that
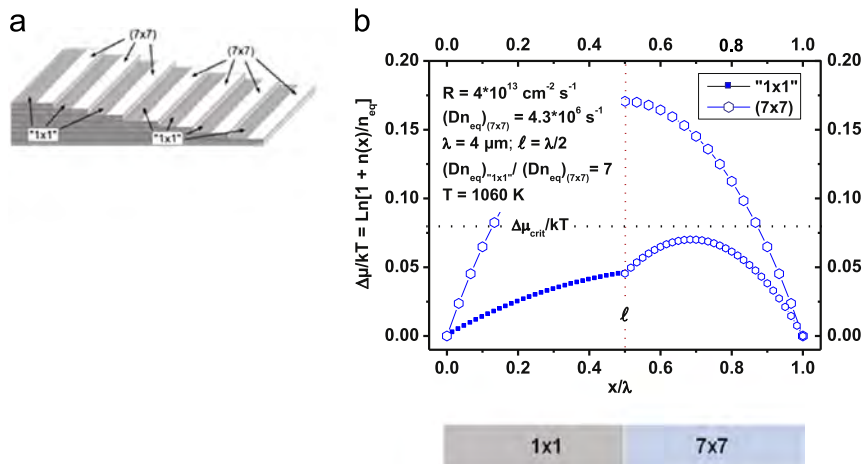
Fig. 4. (a) Illustration of step and phase boundary configuration used for the calculation; (b) profile of $\Delta\mu$ across a 4 μm wide terrace with coexisting (7×7) and "1×1" domains (phase boundary ℓ at $\lambda/2$) and with only (7×7) superstructure. $\Delta\mu_{crit}$ for nucleation is also indicated by the dotted line.

the overall supersaturation on surfaces with coexisting surface phases is drastically reduced in comparison to surfaces with only the (7×7) phase. That is in close agreement to earlier predictions based on the finite-difference method with iteration scheme [17].

3. Summary and conclusion

We observed a steeply increase in step-free areas during MBE at T near the (7×7)–"1×1" phase transition. This behaviour could be explained within the framework of classical BCF theory considering the coexistence of (7×7) and "1×1" surface phases, which exhibit different mass diffusion coefficients due to different equilibrium mobile adatom densities. On surfaces with coexisting surface phases overall supersaturation should be drastically reduced compared to those with only the (7×7) phase. Phase coexistence under dynamically conditions of growth is suggested to appear well below T_C obtained under static conditions. Despite the fact that the used model is very abstract and extremely simplified, we get reasonable good results to explain the experimental findings.

In reality, steps act as effective sinks for adatoms and, therefore, a shift in T_C due to a Si supply can only be expected on wide terraces, where surface phase domains are not associated with steps. It means that a strong increase in step-free areas well below T_C can only be expected for very low growth rates, where wide terraces could be formed. This could explain why such behaviour was not reported so far. On very wide step-free surfaces, however, structure domains form a random granular network in which phase boundaries are indeed not inevitably associated with steps. During Si supply (or heating from below T_C) the "1×1"-regions appear and broaden between the (7×7) domains and the surface initially covered by only (7×7) separates into smaller (7×7) domains. This results in local variation in supersaturation. This, however, should result in the same effect as demonstrated with the simple model, the overall supersaturation drops.

References

[1] A. Fissel, J. Krügener, H.J. Osten, Phys. Status Solidi C 10 (2012) 139;
    J. Krügener, H.J. Osten, A. Fissel, Surf. Sci. 618 (2013) 27.
[2] J.B. Hannon, et al., Phys. Rev. Lett. 86 (2001) 4871.
[3] J.B. Hannon, J. Tersoff, M.C. Reuter, Science 295 (2002) 299.
[4] J.B. Hannon, J. Tersoff, M.C. Reuter, R.M. Tromp, Phys. Rev. Lett. 89 (2002) 266103.
[5] Y.-N. Yang, E.D. Williams, Phys. Rev. Lett. 72 (1994) 1862.
[6] W.K. Burton, N. Cabrera, F.C. Frank, Philos. Trans. R. Soc. London A 243 (1951) 299.
[7] E. Kasper, Appl. Phys. A 28 (1982) 129.
[8] H. Hibino, C.-W Hu, T. Ogino, I.S.T. Tsong, Phys. Rev. B 63 (2001) 245402.
[9] A.B. Peng, et al., Phys. Rev. B 77 (2008) 115424.
[10] A. Pimpinelli, J. Villain, Physica A 204 (1994) 521.
[11] B.Z. Ol'shanetskii, S.M. Repinskii, A.A. Shklyaev, JETP Lett. 27 (1978) 378.
[12] J.B. Hannon, et al., Nature 405 (2000) 552.
[13] H. Watanabe, M. Ichikawa, Phys. Rev. B 54 (1996) 5574.
[14] K. Cho, E. Kaxiras, Europhys. Lett. 39 (1997) 287;
    S.M. Bedair, Surf. Sci. 42 (1974) 595;
    T. Sato, et al., J. Vac. Sci. Technol. A 18 (2000) 960.
[15] I. NoorBatcha, L.M. Raff, D.L. Thompson, J. Chem. Phys. 82 (1965) 1543.
[16] H. Hibino, Y. Homma, M. Uwaha, T. Ogino, Surf. Sci. 527 (2003) L222.
[17] V.A. Zinovyev, et al., Phys. Status Solidi B 173 (1992) K5.
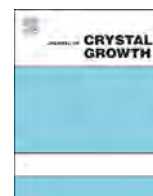
Evaluation of the electronic states in highly Ce doped Si films grown by low temperature molecular beam epitaxy system

CrossMark

Yusuke Miyata, Yukinori Nose, Takeshi Yoshimura, Atsushi Ashida, Norifumi Fujimura *

Graduate School of Engineering, Osaka Prefecture University, 1-1 Gakuen-cho, Naka-ku, Sakai, Osaka 599-8531, Japan

ARTICLE INFO

ABSTRACT

Highly Ce doped single crystalline Si films with high crystallinity, smooth surface and uniformly distributed Ce were deposited by low-temperature grown molecular beam epitaxy (LT-MBE) system. The lattice parameter increases with increasing Ce concentration below 0.2 at%, suggesting that the formation of substitutionally dissolved Ce increases. The donor level of Si homoepitaxial film without Ce doping is calculated as 57 meV originated in the formation of dangling bonds probably due to low temperature growth. Although all films show n-type conduction, electron density decreases with increasing the Ce concentration below 0.5 at%, suggesting Ce^{3+} ion at substitutional site in Si acts as an acceptor. However, the conduction type does not change from n-type to p-type, indicating that the density of the Ce^{3+} ion is not enough to change the conduction type. J–V characteristics at the measurement temperature from 180 to 300 K were evaluated by using metal–insulator–semiconductor (MIS) structure. The generation energy of electron–hole pair is calculated by Arrhenius plot of resistance at depletion layer. The charged state at the mid gap in Si is formed by Ce doping.

1. Introduction

Rare earth (RE) doped semiconductors have been paid much attention because they show unique optical and magnetic characteristics. As matrixes, GaAs [1–3], GaN [4–9], AlGaAs [10], Si [1,11–16,22–32], and SiO_2 [17–21] have been reported. Er [1–3,10–21], Eu [4,5,9], Gd [6–8], Yb [10] and Ce [22–32] have been studied as rare earth dopants. For example, Er doped materials have been attracted enormous interest due to the emission at the photon energy of 1.54 μm originated in an intra 4f shell transition between the $^4I_{12/2}$ and the $^4I_{15/2}$ levels [13], that is attractive for silica optical fibers and optical amplifier [16]. On the other hand, Gd doped GaN shows ferromagnetic with high Curie temperature above 400 K [8]. The detection of an induced magnetic moment of Eu^{3+} ions in GaN which is associated with the $^7F_2$ final state of $^5D_0$ to $^7F_2$ optical transitions emitting at 622 nm has also been reported [9].

We have been interested in RE doped single crystalline Si films. Ce, which has one 4f electron, is one of the most interesting RE elements because Ce-based compounds show attractive phenomena originated in valence fluctuation [33–35]. Therefore, we have studied the magnetic and magneto-transport properties of Ce doped Si (Si:Ce) epitaxial films using solid source molecular beam epitaxy system (MBE) that show very interesting phenomena such

as ferromagnetic ordering [26,27], spin-glass-like behavior and giant magneto-resistance effect [25,31]. Although most of them were observed in the p-type Si:Ce, we have not elucidated if the phenomena are originated from spin–hole interaction, because the films slightly include silicides. Low temperature growth enables to obtain Si:Ce films with high concentration and uniform distribution of Ce without including precipitation of a second phase such as Ce silicides [24–28,30–32]. However, these films show n-type conduction with high carrier concentration and paramagnetic behavior [30,32]. To discuss the origin of above mentioned ferromagnetic related interesting phenomena, we have to investigate the solid solubility of the Ce and the electronic state in Si epitaxial films because the magnetic and electronic properties of magnetic impurity doped semiconductors depends on the distribution and local environment of the dopant [36]. In this paper, change in the carrier density, formation energies of electron and hole, and the lattice constant against the Ce concentration were evaluated and the solid solubility state and the electronic states of Ce for low temperature grown Si:Ce epitaxial films with the Ce concentration below 1.0 at% are discussed.

2. Experiment

Si:Ce epitaxial thin films were deposited on (001) Si or Si on insulator (SOI) substrates by a solid source MBE method at a base

* Corresponding author. Fax: +81 72 254 9327.
E-mail address: fujim@pe.osakafu-u.ac.jp (N. Fujimura).

pressure in the order of 10^{-10} Torr. The substrate was chemically cleaned with Semico Clean 23 (Furuuchi Chemical). After immersion in 1.0% HF solution for 2 min, the substrate was inserted into an ultra-vacuum MBE chamber. The substrate was carefully outgassed at 600 °C and β-SiC was intentionally formed at 830 °C to fix carbon at the surface. After the growth of the 30-nm-thick Si buffer layer, the sample was annealed at 750 °C in order to form a step and terrace surface structure with the double domained reconstructed surface structure of 2×1 and 1×2 observed by Reflection High Energy Electron Diffraction (RHEED). An 100-nm-thick Si:Ce layer was grown by simultaneously evaporated on the Si buffer layer at 600 °C by using Knudsen cells (k-cell) of Si and Ce. A 5-nm-thick Si capping layer was finally deposited at the same temperature after the Si:Ce deposition. The deposition rate evaluated by RHEED oscillation is fixed as 40 nm/h. The Ce concentration was varied from 0.1 to 1.0 at% evaluated by electron prove micro analyzer calibrated with Rutherford backscattering and secondary ion mass spectroscopy. The substrate and k-cell temperature was measured with a thermocouple and a pyrometer. The surface morphology and structure were analyzed by in-situ RHEED operated at the incident electron energy of 30 keV. The crystal structural analysis was also performed by ex-situ x-ray diffraction (XRD). For the electrical measurement, the Al electrode was deposited on the samples through a shadow mask after removal of native oxide at the surface. The electrical resistivity and the Hall Effect were performed in the van der Pauw configuration at the temperature from 70 to 300 K. In order to evaluate the electron states of Si:Ce films, the metal insulator semiconductor (MIS) capacitor structure was fabricated. Around 10-nm-thick Si oxy-nitride was prepared by Atmospheric Pressure Plasma Enhanced Chemical Vapor Deposition (APE-CVD) system [37,38]. The capacitance–voltage (C–V) and current–voltage (J–V) characteristics were also evaluated by using a LCR meter (HP4284A) and a pico-ampere meter (4140B) at the measurement temperature from 180 to 300 K.

3. Results and discussion

Fig. 1 shows the in-situ RHEED images of Si:Ce films grown at 600 °C. All films show a 2×1 reconstructed surface throughout the growth without the Ce concentration above 1.0 at%. And the root mean square of these samples measured by Atomic Force Microscopy is below 0.5 nm. Although the streak pattern diffraction gradually changes to spotty pattern suggesting the three dimensional growth under the Ce concentration of 1.0 at%, the RHEED image of Si:1.0 at% Ce shows sharp streaky pattern with 3-folded structure. Although this reconstructed surface structure appears in highly Ce doping Si films, the surface becomes smooth [32] probably due to the relaxation of stress induced by incorporation of Ce with very large ionic radius.

The 004 diffraction peak of XRD for Si:Ce films has interference fringes indicating that the films have very smooth surface. However, the strong peak of substrate prevents from calculation of the lattice constant of the films normal to the surface. In order to

deconvolute the diffraction of the film from that of the substrate, the lattice spacing of (113) (d_{113}) is evaluated. Fig. 2(a) shows the change in the d_{311} as a function of Ce concentration. The d_{311} of the Si homoepitaxial film without Ce is smaller than that of Si single crystal probably originated from the formation of defect formation such as Si vacancy. The d_{311} increases with increasing the Ce concentration below the 0.2 at% suggesting that the formation of Ce^{3+} ion in substitutional site of Si because the covalent radius of Ce^{3+} ion is larger than that of Si. However, it decreases with increasing Ce concentration between 0.3 and 0.6 at%, suggesting that the defects such as Si vacancy or Ce related defects, which make the lattice constant small, increase. The formation of these defect and the solid solubility state of Ce change the carrier concentration in films. Fig. 2(b) shows the change in the carrier concentration as a function of Ce concentration. The Si homo-epitaxial film without doping Ce shows n-type conduction with the carrier density 5×10^{16} cm^{-3}. Because the donor level of this film is calculated as 57 meV by Arrhenius plot of carrier density, this n-type conduction is originated in the formation of dangling bonds due to low temperature growth of Si. With increasing Ce concentration, carrier density decreases below the Ce concentration of 0.3 at%, indicating that the electrons are compensated by the holes generated by substitutionally dissolved Ce^{3+} ions. This tendency is similar to the increase of d_{113}. However, the conduction type does not change from n-type to p-type, indicating that the density of the Ce^{3+} ion in substitutional site of Si is not enough to change the conduction type. It is also considered that the lattice strain due to the Ce^{3+} ion, which has large covalent radius, forms the Si vacancy. So there are many electrons and holes in Si:Ce films. Although the Hall Effect measurement was done at low temperature from 70 to 300 K, high resistivity of the film below 250 K prevents from evaluating the Hall voltage at low temperature.

In order to discuss the electronic state of Si:Ce thin films, MIS structure has been fabricated. As the insulator layer, ultra-thin SiON layer with the thickness of less than 10 nm was formed using atmospheric pressure (AP) plasma. AP plasma oxynitridation enables to low temperature fabrication of highly resistive dielectric ultra-thin films. Hayakawa et al. have reported that the nitridation thickness of Si saturates at 2 nm (self-limitation), which is independent on the substrate temperature [39]. Pure nitrogen gas (99.999%) of 10/min
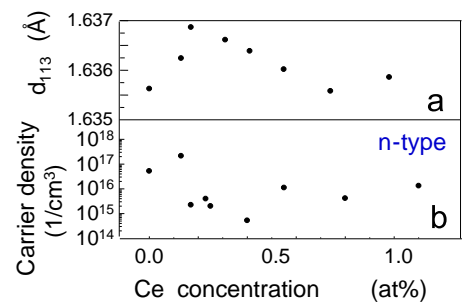
Fig. 2. Change in the lattice parameter of (113) (d_{113}) (a) and carrier density (b) as a function of the Ce concentration. All samples show n-type conduction.
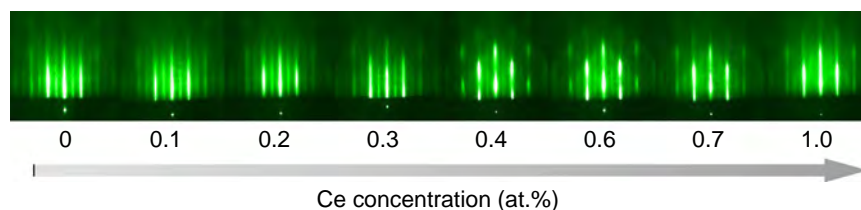
Fig. 1. Change in the RHEED images of Si:Ce films grown at 600 °C with increasing Ce concentration. Incident direction of the electron beam was parallel to [110] direction. The film thickness is 100 nm.

was introduced into an ultrahigh-vacuum chamber with the base pressure below 8×10^{-8} Torr. AP plasma was generated by applying an alternating voltage with the peak to peak value of 3 kV and the frequency of 160 kHz. SiON layer was formed by irradiating AP plasma to the surface of the samples remotely. The optical emissions corresponding to the electron transition of N_2 second positive system was dominant observed by optical emission spectroscopy. To evaluate the AP SiON thin films works as a dielectric layer, p-type Si substrate
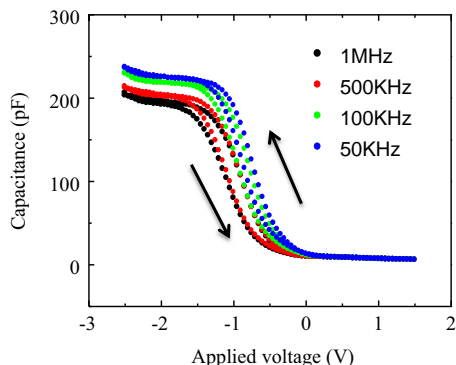
Fig. 3. C–V characteristics of Al/SiON/Si metal–insulator–semiconductor (MIS) capacitor measured at room temperature.
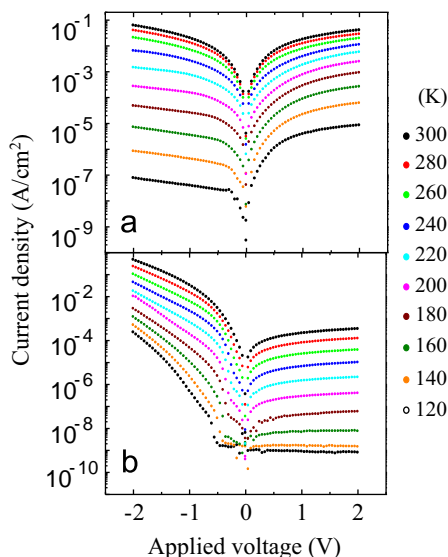
Fig. 4. Change in the J–V characteristics of Al/SiON/Si:1.0 at%Ce films MIS structure measured at the temperature from 300 K to 120 K. Although these samples show n-type conduction measured by Hall effect, there are two samples which are formed carrier accumulation layer at positive voltage (a) and negative voltage (b).
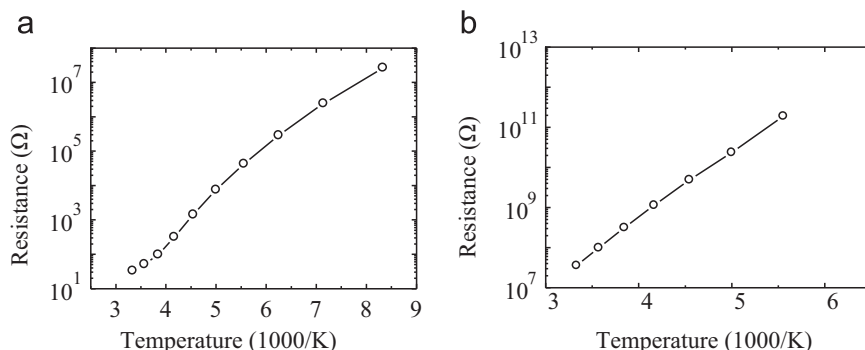
without Si:Ce layer was used for MIS structure. Fig. 3 shows typical C–V properties of Al/SiON/p-type Si substrate capacitor. The bias voltage was applied to the top electrode and changed from −3 V to 2 V. The frequency was varied from 50 kHz to 1 MHz. Although the clockwise hysteresis caused by charge injection is recognized, carrier accumulation and depletion clearly observed at negative and positive bias voltage, respectively. Considering the capacitance at accumulation region, the chemical composition of SiON layer should be almost equal to SiO_2 with the thickness of 7 nm because unintentional oxidants in a gas cylinder such as H_2O and O_2 strongly enhance the oxidation of Si layer.

Fig. 4 shows temperature dependence of J–V properties of Al/ SiON/Si:1.0 at%Ce capacitors. Although the surface morphology and the crystallinity deteriorate with increasing the Ce concentration, those drastically improved for the Si:1.0 at%Ce films due to the formation of re-constructed surface as shown Fig. 1. Therefore, the Si:1.0 at%Ce film was used for the electrical and dielectrical measurements. Although these samples show n-type conduction by Hall effect at room temperature, the J–V characteristics does not show carrier depletion near room temperature because these samples include large amount of holes originated from the substitution of Ce into Si site together with electrons due to the formation of the dangling bonds. However, with decreasing the measurement temperature, the formation of depletion layer is observed at positive bias voltage region as shown Fig. 4(a) and (b). Fig. 5 shows Arrhenius plots of the resistance obtained at depletion region. The activation energy is deduced by fitting with using the Arrhenius equation described below.

$$R(T) \propto e^{\frac{Q}{k_B T}}$$

where $R(T)$, k_B, T and Q indicate the resistance of the depletion layer, Boltzmann constant, temperature and the activation energy. The activation energies of the resistance observed at negative (a) and positive bias voltage (b) are calculated as 0.19 eV and 0.32 eV, respectively. These activation energies are equal to the generation energy of electron–hole pair at depletion layer. In the case of the depletion layer formed at negative bias voltage, electron–hole pair generates at 0.19 eV below conduction band. The generated electrons excite to conduction band and acts as free carrier, and holes are compensated by charged state at 0.38 eV below conduction band. On the other hand, in the case of the depletion layer formed at positive bias voltage, electron–hole pair generates at 0.32 eV above valence band. The generated holes excite to valence band and acts as free carrier and electrons compensated by charged state at 0.64 eV above valence band suggesting. Therefore, these results conduct the formation of the charged state at the mid gap by Ce doping. Fig. 6 shows the schematic image of the electronic states of Si:Ce films. Shallow donor level at 57 meV below conduction band is originated in

Fig. 5. Arrhenius plots of the resistance at depletion layer obtained by Fig. 4. The activation energy calculated at negative voltage (a) is 0.19 eV and at negative voltage (b) is 0.32 eV.
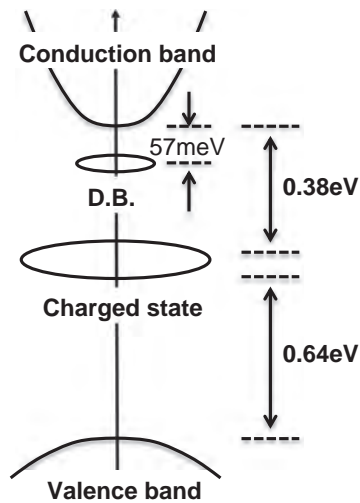
Fig. 6. Schematic image of the electronic states in Si:Ce films.

dangling bond of Si. The charged state at the mid gap is formed by Ce doping.

4. Conclusion

Si:Ce films with high crystallinity, smooth surface, uniform distributed Ce were deposited by LT-MBE system. The substitutionally dissolved Ce^{3+} ion acting as an acceptor is observed by change in the d_{311} and carrier density. SiON ultra-thin films were prepared on Si:Ce films by oxynitridation using atmospheric pressure (AP) plasma for the evaluation of the electronic state of Ce in Si. The formation of the depletion layer is clearly observed in this MIS structure. The generation energy of electron–hole pair is calculated by Arrhenius plots of resistance in depletion region. We conclude the charged state at mid gap is formed by Ce doping.

References

[1] E. Ennen, J. Schneider, G. Pomrenke, A. Axmann, Appl. Phys. Lett. 43 (1983) 943.
[2] M. Yoshida, K. Hiraka, H. Ohta, Y. Fujiwara, A. Koizumi, Y. Takeda, J. Appl. Phys. 96 (2004) 4189.
[3] K. Takahei, A. Taguchi, J. Appl. Phys. 74 (1993) 1979.
[4] A. Nishikawa, T. Kawasaki, N. Furukawa, Y. Terai, Y. Fujiwara, Appl. Phys. Express 2 (2009) 071004.
[5] J.H. Park, A.J. Steckl, Appl. Phys. Lett. 85 (2004) 4588.
[6] G.H. Zhong, J.L. Wang, Z. Zeng, J. Phys.: Condens. Matter 20 (2008) 295221.
[7] S. Dhar, O. Brandt, M. Ramsteiner, V.F. Sapega, K.H. Ploog, Phys. Rev. Lett. 94 (2005) 037205.
[8] N. Teraguchi, A. Suzuki, Y. Nanishi, Y.K. Zhou, M. Hashimoto, H. Asahi, Solid State Commun. 122 (2002) 651.
[9] V. Kachkanov, M.J. Wallace, G. van der Laan, S.S. Dhesi, S.A. Cavill, Y. Fujiwara, K.P. O'Donnell, Sci. Rep. 2 (2012) 969.
[10] T. Araki, S. Uekusa, Phys. Status Solidi (a) 205 (2008) 60.
[11] J. Stimmer, A. Reittinger, J.F. Nutzel, G. Abstreiter, H. Holzbrecher, C. Buchal, Appl. Phys. Lett. 68 (1996) 3290.
[12] J. Palm, F. Gan, B. Zheng, J. Michel, L.C. Kimerling, Phys. Rev. B 54 (1996) 17603.
[13] F. Priolo, G. Franzo, S. Coffa, A. Polman, S. Libertino, R. Barkline, D. Carey, J. Appl. Phys. 78 (1995) 3874.
[14] D.J. Eaglesham, J. Michel, E.A. Fitzgerald, D.C. Jacobson, J.M. Poate, J.L. Benton, A. polman, Y.H. Xie, L.C. Kimerling, Appl. Phys. Lett. 58 (1991) 2797.
[15] M.S. Bresler, O.B. Gusev, P.E. Pak, N.A. Sobolev, I.N. Yassievich, J. Lumin. 80 (1999) 375.
[16] A. Reittinger, J. Stimmer, G. Abstreiter, Appl. Phys. Lett. 70 (1997) 2431.
[17] A.G. Raffa, P. Ballone, Phys. Rev. B 65 (2002) 12309.
[18] S.Y. Seo, J.H. Shin, Appl. Phys. Lett. 78 (2001) 2709.
[19] Z.F. Krasilnik, B.A. Andreev, D.I. Kryzhkov, L.V. Krasilnikova, V.P. Kuznetsov, D.Y. Remizov, V.B. Shmagin, M.V. Stepikhova, A.N. Yablonskiy, T. Gregorkievicz, N.Q. Vinh, W. Jantsch, H. Przybylinska, V.Y. Timoshenko, D.M. Zhigunov, J. Mater. Res. 21 (2006) 574.
[20] K. Masaki, H. Isshiki, T. Kimura, Opt. Mater. 27 (2005) 876.
[21] J.H. Shin, J.H. Jhe, S.Y. Seo, Y.H. Ha, D.W. Moon, Appl. Phys. Lett. 76 (2000) 3567.
[22] T. Yokota, N. Fujimura, Y. morinaga, T. Ito, Physica E 10 (2001) 237.
[23] T. Yokota, N. Fujimura, T. Ito, Appl. Phys. Lett. 81 (2002) 4023.
[24] T. Yokota, N. Fujimura, T. Wada, S. Hamasaki, I. Ito, J. Appl. phys. 91 (2002) 7905.
[25] T. Yokota, N. Fujimura, I. Ito, J. Appl. Phys. 93 (2003) 4045.
[26] T. Yokota, N. Fujimura, T. Wada, S. Hamasaki, T. Ito, J. Appl. Phys. 93 (2003) 7679.
[27] T. Terao, Y. Nishimura, D. Shindo, T. Yoshimura, A. Ashida, N. Fujimura, J. Magn. Magn. Mater. 310 (2007) e726.
[28] T. Terao, Y. Nishimura, D. Shindo, N. Fujimura, J. Cryst. Growth 307 (2007) 30.
[29] D. Shindo, T. Yoshimura, N. Fujimura, Appl. Surf. Sci. 254 (2008) 6218.
[30] T. Terao, K. Fujii, D. Shindo, T. Yoshimura, N. Fujimura, Jpn. J. Appl. Phys. 48 (2009) 033003.
[31] D. Shindo, K. Fujii, T. Terao, S. sakurai, S. Mori, K. Kurushima, N. Fujimura, J. Appl. Phys. 107 (2010) 09C308.
[32] D. Shindo, S. Sakurai, N. Fujimura, Jpn. J. Appl. Phys. 50 (2011) 065701.
[33] H. Okamura, T. Watanabe, M. Matsunami, T. Nishihara, N. Tsuji, T. Ebihara, H. Sugawara, H. Sato, Y. Onuki, Y. Isikawa, T. Takabatake, T. Nanba, J. Phys. Soc. Jpn. 76 (2007) 023703.
[34] A. koizumi, G. Motoyama, Y. Kubo, T. Tanaka, Y. Sakurai, Phys. Rev. Lett. 106 (2011) 136401.
[35] N.D. Mathur, F.M. Grosche, S.R. Julian, I.R. Walker, D.M. Freye, R.K. W. Haselwimmer, G.G. Lonzarich, Nature 394 (1998) 39.
[36] Y.L. Soo, S.W. Huang, Z.H. Ming, Y.H. Kao, H. Munekata, L.L. Chang, Phys. Rev. B 53 (1996) 4905.
[37] R. Hayakawa, M. Nakae, T. Yoshimura, A. Ashida, N. Fujimura, T. Uehara, M. Tagawa, Y. Teraoka, J. Appl. Phys. 100 (2006) 073710.
[38] R. Hayakawa, M. Nakae, T. Yoshimura, A. Ashida, N. Fujimura, T. Uehara, Jpn. J. Appl. Phys. 45 (2006) 9025.
[39] R. Hayakawa, T. Yoshimura, A. Ashida, T. Uehara, N. Fujimura, Thin Solid Films 506–507 (2006) 423.
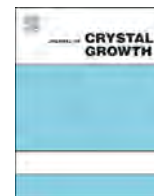
Electrical characteristics of amorphous Si:H/crystalline $Si_{0.3}Ge_{0.7}$ heterojunction solar cells grown on compositionally graded buffer layers

Ryuji Oshima *, Mitsuyuki Yamanaka, Hitoshi Kawanami, Isao Sakata, Koji Matsubara, Takeyoshi Sugaya

Research Center for Photovoltaic Technologies, National Institute of Advanced Industrial Science and Technology, 1-1-1 Umezono, Tsukuba, Ibaraki 305-8568, Japan

ABSTRACT

We examined the influence of the processing temperature on hydrogenated amorphous Si/crystalline $Si_{0.3}Ge_{0.7}$ heterojunction solar cells with a bandgap of 1.0 eV, which were grown on Si(001) by solid-source molecular beam epitaxy. Stepwise, compositionally graded buffer $Si_{1-x}Ge_x$ layers were applied to prepare $Si_{0.3}Ge_{0.7}$ films with low dislocation density. We studied the influence of the annealing temperature applied at the buffer layer on the diode characteristics. The diode factor was minimized to 1.45 at 800 °C, and the saturation current density monotonically decreased from 7.5×10^{-4} A/cm² for an annealing temperature of 650 °C to 5.0×10^{-5} A/cm² for that of 900 °C, as a result of the promotion of dislocation annihilation. Consequently, the $Si_{0.3}Ge_{0.7}$ heterojunction solar cell showed a maximum conversion efficiency of 1.50% when the annealing temperature was 850 °C. We also studied the influence of the growth temperature of the p-$Si_{0.3}Ge_{0.7}$ active layer (absorber) on the cell performance. The short circuit current density increased from 16.03 mA/cm² for 520 °C to 20.95 mA/cm² for 600 °C. This result corresponded to an improvement of quantum efficiency response in the longer wavelength region due to the reduction of crystal defects caused by oxygen contamination. However, the $Si_{0.3}Ge_{0.7}$ active layer processed at a higher temperature showed an accumulation of threading dislocations and roughening of the surface, resulting in the degradation of both the open circuit voltage and the fill factor.

© 2015 Elsevier B.V. All rights reserved.

1. Introduction

$Si_{1-x}Ge_x$ alloys are of significant interest to researchers for the development of future complementary metal oxide semiconductor (CMOS) devices, such as hetero-MOS field-effect transistors (HMOSFET) [1,2], and Si-based bandgap-engineered devices, such as photodetectors [3,4] and solar cells [5]. It is possible to continuously tune the bandgap of these alloys between 0.66 eV (pure Ge) and 1.11 eV (pure Si) by simply changing the compositional ratio [6]. In solar cell applications using tandem cell designs, which stack multiple p–n junctions, one can boost the conversion efficiency (η) by increasing the number of layers. In particular, an ideal η of over 40% was predicted in a stacked 1.8 eV/1.4 eV/0.9–1.0 eV configuration under concentrated sunlight [7,8]. Si-based alloy materials with a bandgap in the range of 1.0 eV are good candidates for future cost effective, high efficiency multi-junction cells [9,10].

For single-junction cells using single-crystalline $Si_{1-x}Ge_x$ films, one option is to construct a heterojunction-emitter-based solar cell in which the emitter is a large-bandgap hydrogenated amorphous Si (a-Si:H) [11,12]. Although an n-type substrate is commonly used as the absorber (to form a so-called p-i-n structure, where i is the intrinsic layer) for heterojunction with intrinsic thin layer (HIT) cells [13,14], we have concentrated instead on developing $Si_{1-x}Ge_x$ heterojunction cells on p-type Si substrates (forming n–i–p structures) for two main reasons. First, a low processing temperature of less than 200 °C for the deposition of a-Si:H can be adopted to prevent the unexpected lifetime degradation of $Si_{1-x}Ge_x$ films during the construction of the solar cell. Second, it has been reported that the valence band offset is much larger than the conduction band offset in both a-Si:H/crystalline-Si [15] and a-Si:H/crystalline-Ge [16] systems. These characteristics would be advantageous if electrons were used as minority carrier in n–i–p cells.

Due to the 4.2% lattice mismatch between Si and Ge, a strain-relaxed SiGe buffer layer can be achieved by creating misfit dislocations. The strain in the SiGe epitaxial layer is generally relaxed by introducing 60° dislocations [17]. A certain fraction of these misfit dislocations ends in threading dislocations, which move to the surface of the epitaxial layer. The threading dislocations in the active region cause a short minority carrier lifetime, resulting in a significant degradation in diode characteristics. The aim of the development of the various buffer structures is to reduce the threading dislocation density, the surface roughness, and the residual internal stress. Examples of these buffer structures include layers grown with Sb surfactants [18], Si-strained layers [19,20], ion-implanted layers [21], and patterned Si substrates [2]. A compositionally graded buffer layer [22] and high-temperature annealing [23] are other promising approaches to reduce threading dislocation densities. We reported the fabrication of 3-μm-thick $Si_{1-x}Ge_x$ films with a Ge content of up to $x=0.84$, and the application of these films to heterojunction solar cells [24]. However, the η values of these $Si_{1-x}Ge_x$ heterojunction solar cells were still less than 4% because, despite the successful establishment of the graded buffer structure, the overall material quality was poor [11,24–26]. In addition, the studies described above mostly focused on structural characterization using very thin films ($\sim$100 nm thick) grown on buffer layers. To date, there are few reports that examined the influence of the processing temperature on the cell performance using thick ($\sim$3 μm) $Si_{1-x}Ge_x$ absorbers, which is important for producing practical $Si_{1-x}Ge_x$ heterojunction devices. In this study, we systematically examined these influences on $Si_{0.3}Ge_{0.7}$ heterojunction solar cells with a bandgap of 1.0 eV, and focused specifically on the electrical properties of the cells.

2. Experiments

All samples were grown by solid-source molecular-beam epitaxy (SS-MBE) using a system equipped with two electron guns for the Si and Ge solid sources. First, 2-inch, low-resistivity (1×10^{-3} Ω cm), p-type Si(001) substrates were cleaned using the Radio Corporation of America (RCA) method and annealed at 750 °C for 10 min in a growth chamber to remove an ultra-thin oxide layer. The base pressure of the growth chamber was typically 4.0×10^{-10} Torr. A 100-nm-thick, p-type Si buffer layer was deposited in order to obtain an atomically flat and contamination-free surface. Next, 10 stepwise, compositionally graded $Si_{1-x}Ge_x$ buffer layers and a $Si_{0.23}Ge_{0.77}$ strain-inverted layer were deposited; these acted as a metamorphic virtual substrate. The Ge content was increased by 7% per step, and the thickness of each step layer was 300 nm. This gave a total thickness of 3.3 μm and an average Ge gradient rate of $\sim$20% μm. The growth temperature of the buffer layer (T_{Buffer}) was 420 °C or 500 °C. Thermal annealing was performed for 2 min after the deposition of each step. The annealing temperature (T_{Anneal}) was varied from 650 °C to 900 °C. Then, a 150-nm-thick $Si_{0.3}Ge_{0.7}$ back surface field (BSF) layer and a 3-μm-thick $Si_{0.3}Ge_{0.7}$ active layer were consecutively grown. The growth temperature of the active layer (T_{Active}) was varied from 520 °C to 600 °C. The deposition rate was 2.8 Å/s for all layers. The $Si_{1-x}Ge_x$ buffer layers and the BSF layer were doped with p-type dopants (Ga) to a concentration of approximately $\sim$3 $\times 10^{17}$ cm^{-3}, while the $Si_{0.3}Ge_{0.7}$ active layer was doped with Ga at a concentration of 1.0×10^{16} cm^{-3}. Finally, the $Si_{0.3}Ge_{0.7}$ active layer was capped with an intrinsic 2-nm-thick Si strained layer in an attempt to passivate the deleterious defects
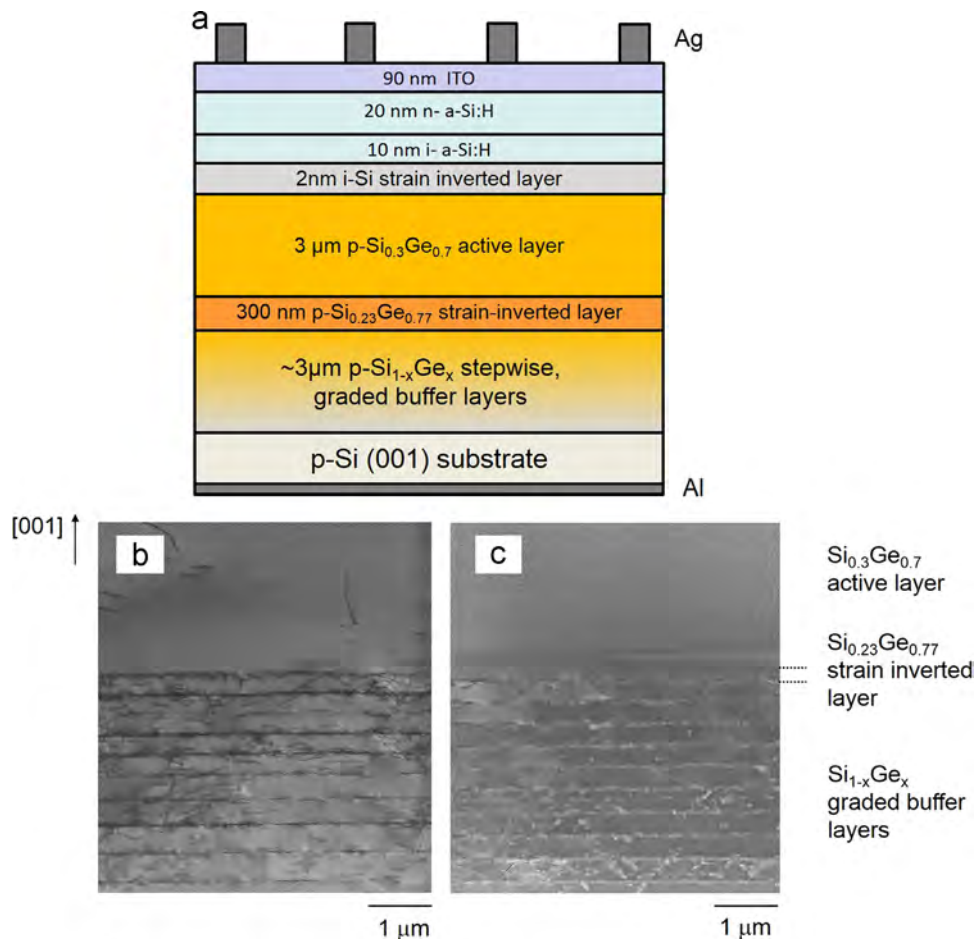
Fig. 1. (a) Schematic structure of $Si_{0.3}Ge_{0.7}$ heterojunction solar cells. Cross-sectional TEM images of $Si_{0.3}Ge_{0.7}$ films grown at (b) $T_{Anneal}=700$ °C and (c) $T_{Anneal}=850$ °C.

possibly present at SiGe surfaces, and to produce interfacial properties similar to those of Si cells [11,24]. For solar cell characterization, the layers were capped with a combination of 100-Å-thick intrinsic a-Si:H and 200-Å-thick n-type a-Si:H films fabricated by plasma-enhanced chemical vapor deposition at 200 °C. A 90-nm-thick In$_2$O$_3$:Sn (ITO) layer then followed; silver and aluminum were deposited for the front and back contact electrodes, respectively, as shown in Fig. 1(a). The cell size was 5 mm × 5 mm. Structural properties were studied using reflection high-energy electron diffraction (RHEED), cross-sectional transmission electron microscopy (TEM) and secondary ion mass spectroscopy (SIMS). For solar cell characterization, quantum efficiency (QE) measurements were carried out under a constant photon flux of 1×10^{14} cm^{-2}. The light current–density voltage (J–V) characteristics were measured under air mass 1.5 global (AM 1.5 G) illumination at 1 sun.

3. Results and discussion

We examined the influence of T_{Anneal} on the dark I–V curves of Si$_{0.3}$Ge$_{0.7}$ heterojunction solar cells, as shown in Fig. 2. T_{Anneal} was varied from 650 °C to 900 °C. T_{Buffer} and T_{Active} were fixed at 500 °C and 520 °C, respectively. A significant decrease in dark current density was clearly observed with increasing T_{Anneal} up to 850 °C. These curves were fitted by a familiar form [27] to estimate J_0 and n

$$J = J_0 \cdot \exp(\frac{q(V - R_s \cdot J)}{nkT} - 1) + \frac{V - R_s \cdot J}{R_{sh}} \qquad (1)$$

where J_0 is the saturation current density, R_s and R_{sh} are series and shunt resistances, and q, n, k, and T are electron charge, diode factor, Boltzmann's constant, and measurement temperature, respectively. Because the n-a-Si:H layer used here was very thin (~20 nm), these junction properties seemed to be determined by the Si$_{0.3}$Ge$_{0.7}$ active layer, where the depletion region mainly extends. Fig. 3 plots J_0 and n as a function of T_{Anneal}. The sample grown at 650 °C exhibited larger values of $J_0 = 7.5 \times 10^{-4}$ A/cm^2 and $n = 1.83$, which implies the predominance of the recombination current component in the diode characteristics. The value of n was minimized to 1.45 at 800 °C, which was larger than that of Si HIT cells (~1.2) [27]. The larger value of n in our cells was presumably due to both the thicker i-a-Si:H layer as well as an insufficient surface passivation. The thickness of the i-a-Si:H layer (10 nm) is much greater than that of Si heterojunction cells (2–5 nm) [28,29]. In our devices, significant degradations in both short circuit current density (J_{SC}) and open circuit voltage (V_{OC}) were observed for a thinner i-layer, where the thickness was less than 10 nm. This was due to the surface roughness of Si$_{1-x}$Ge$_x$
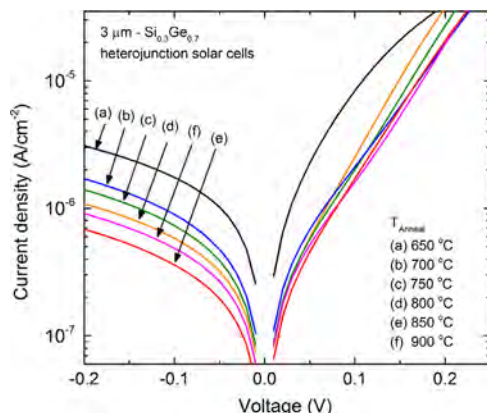
Fig. 2. T_{Anneal} dependence on the dark I–V curves of Si$_{0.3}$Ge$_{0.7}$ heterojunction solar cells. T_{Anneal} was varied from 650 °C to 900 °C.
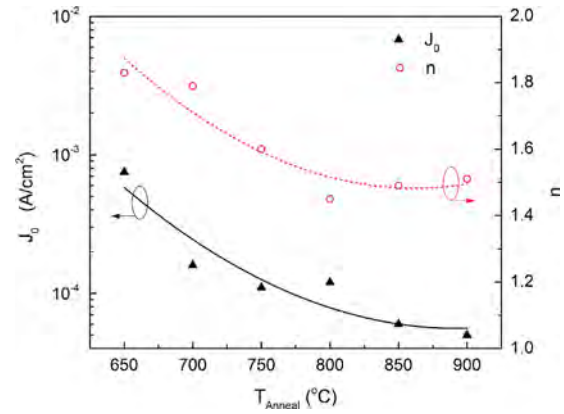
Fig. 3. Saturation current density (J_0) and diode factor (n) as a function of T_{Anneal}.
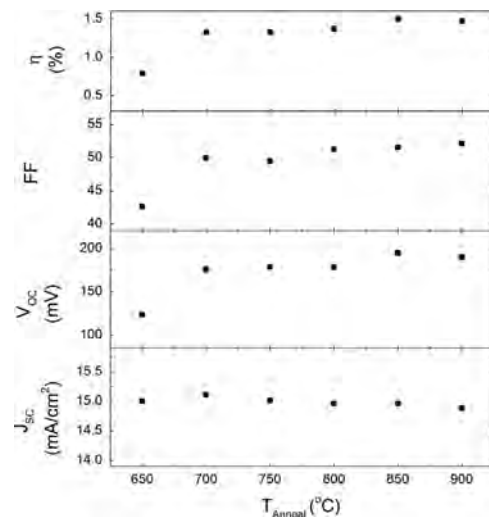
Fig. 4. Characteristics of Si$_{0.3}$Ge$_{0.7}$ heterojunction solar cells with various T_{Anneal}.

layers. The root mean square (RMS) of the surface roughness of Si$_{1-x}$Ge$_x$ layers was typically larger than ~2 nm due to the formation of cross-hatch patterns, which differed from the atomically flat surface of Si wafers; hence, a thicker i-layer is needed to passivate the surface in order to suppress surface recombination. In order to improve the diode characteristics, further investigation of this observation is needed. Moreover, J_0 monotonically decreases from 7.5×10^{-4} A/cm^2 for 650 °C to 5.0×10^{-5} A/cm^2 for 900 °C. J_0 obtained in this study is more closer to that obtained for Ge cells (~3×10^{-5} A/cm^2) [30,31] than to that obtained for Si cells (~3×10^{-11} A/cm^2) [32]. The J_0 of Si$_{0.3}$Ge$_{0.7}$ heterojunction cells fabricated in this work is roughly consistent with their inherent bulk characteristics, though further improvements of both the device structure and material quality are needed. On the other hand, we observed obvious spotty patterns in RHEED measurements during the annealing processes at temperatures higher than 950 °C, which resulted from strong phase separation.

Fig. 4 plots the solar cell parameters: J_{SC}, V_{OC}, fill factor (FF), and η as a function of T_{Anneal}. It can be seen that T_{Anneal} strongly affects V_{OC} and FF, while J_{SC} is almost identical for all samples. V_{OC} increases significantly until 700 °C and then increases slightly with increasing T_{Anneal} up to 850 °C. V_{OC} of 194.6 mV for 850 °C was slightly larger than that of 189.9 mV for 900 °C. The FF shows similar behavior to V_{OC}, except that the largest FF, 52.11, was obtained for 900 °C. As a result, the Si$_{0.3}$Ge$_{0.7}$ solar cell with the maximum η of 1.50% ($V_{OC} = 189.9$ mV, $J_{SC} = 14.96$ mA/cm^2, FF = 51.52) was obtained at

the optimum T_{Anneal} of 850 °C. Cross-sectional TEM images obtained for the samples grown at (b) $T_{Anneal}=700$ °C and (c) $T_{Anneal}=850$ °C are shown in Fig. 1. A certain fraction of threading dislocations still propagated to the $Si_{0.3}Ge_{0.7}$ active layer in (b). By contrast, most dislocations terminated at the interfaces at each $Si_{1-x}Ge_x$ buffer layer in (c) and thus, threading dislocations were not observed in the $Si_{0.3}Ge_{0.7}$ active layer. The threading dislocation density at the surface was found to be on the order of 10^5 cm^{-2} for (c). These results suggest higher T_{Anneal} is responsible for the decrease in threading dislocation density in the active layer, which results in a decrease in recombination current components in the diode characteristics.

Fig. 5 shows the light J–V curves obtained for the cells grown at various T_{Active}: (a) 520 °C, (b) 560 °C, and (c) 600 °C. T_{Anneal} and T_{Buffer} were fixed at 850 °C and 420 °C, respectively. A low growth temperature during deposition is known to be effective in reducing the accumulation of threading dislocations [33]. As the layers typically contain high-density intrinsic vacancy-type point defects, these point defects can reduce the mechanical stress particularly in the region where the stress is concentrated and thus decrease the rate of dislocation nucleation. Because impurities in the atmosphere can easily contaminate a Si wafer at a low growth temperature and cause crystal defects, we adopted the low growth temperature only for the buffer layers. We examined the influence of growth temperature on the oxygen concentration in the $Si_{0.3}Ge_{0.7}$ layer by SIMS, as shown in Fig. 6. A high O concentration of 4.3×10^{17} cm^{-3} was detected at 420 °C, and the concentration monotonically decreased with increasing the temperature. The light J–V curves are summarized in Table 1. It can be seen that V_{OC} and FF monotonically increased as the T_{Buffer} decreased, while J_{SC} increased
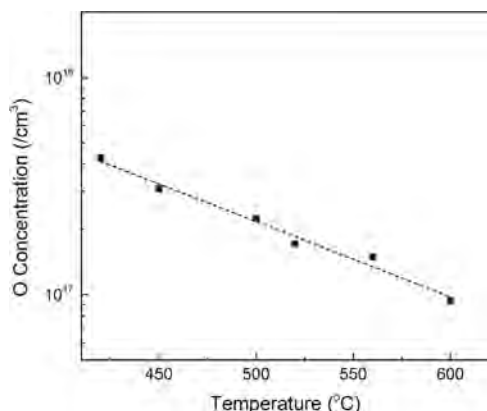
Table 1
Parameters obtained from J–V curves measured in Fig. 5.

T_{Active} (°C)	n	J_0 (A/cm^2)	η (%)	J_{SC} (mA/cm^2)	V_{OC} (mV)	FF
520	1.40	7.0×10^{-5}	1.51	16.03	178	53.12
560	1.42	1.8×10^{-4}	1.41	18.56	155	48.95
600	1.60	3.0×10^{-4}	1.15	20.95	132	41.68
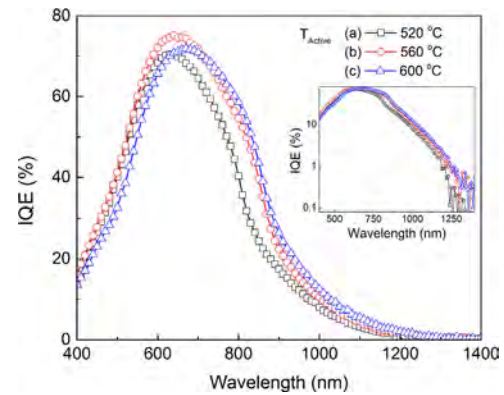
Fig. 7. Internal quantum efficiency (IQE) spectra for 3-µm-thick $Si_{1-x}Ge_x$ heterojunction solar cells grown at various T_{Active} of (a) 520 °C, (b) 560 °C, and (c) 600 °C. The inset shows the log-scale IQE spectra for each cell.

from 16.0 mA/cm^2 for 520 °C to 21.0 mA/cm^2 for 600 °C, as a result of the decrease in O contamination in the $Si_{0.3}Ge_{0.7}$ layer.

Fig. 7 shows the internal quantum efficiency (IQE) spectra measured from the cells shown in Fig. 5. The IQE spectra were obtained by taking into account the reflection at the surface. An absorption edge of roughly 1.0 eV (~ 1240 nm) was clearly observed (inset of Fig. 5); these are consistent with the inherent bandgap characteristics of the cells [6]. The poor IQE response for longer wavelengths is primarily due to the lack of absorption thickness of the active layer. Based on the absorption coefficient of $Si_{1-x}Ge_x$ [11], an absorber with a thickness of ~ 10 µm would achieve sufficient absorption for solar cell applications, while a relatively shorter minority lifetime of 1–20 µs in $Si_{1-x}Ge_x$ [34] may impede carrier collection in such thicker cells. It should be noted that the longer wavelength IQE increased for higher T_{Active}, presumably due to a decrease in crystal defects caused by O contamination, as shown in Fig. 6. In our devices, the thicker a-Si:H layer (30 nm) leads to a decrease in the IQE response for wavelengths shorter than 450 nm. Because the absorption depth for 450-nm light is typically smaller than ~ 30 nm in an a-Si:H layer [29], the carriers generated in an a-Si:H layer resulted in absorption losses. However, high temperature growth of 600 °C caused both the accumulation of the threading dislocation and roughening of the surface, as shown in Fig. 8, which resulted in the degradation of the diode characteristics. Reduction of IQE in the wavelength range shorter than 600 nm observed for the cell with T_{Active} of 600 °C (Fig. 7) can be also ascribed to the roughening of the surface in this sample. Furthermore, the misfit dislocation density in $Si_{1-x}Ge_x$ buffer layers clearly increased for 600 °C, probably due to the effect of thermal annealing during the growth of the active layer. For this reason, applying a low growth temperature would likely achieve good device operation. Studies of this hypothesis are currently underway.

Fig. 5. Light J–V curves obtained for the solar cells grown at various T_{Active} of (a) 520 °C, (b) 560 °C, and (c) 600 °C.

Fig. 6. Oxygen (O) concentration in $Si_{0.3}Ge_{0.7}$ layer measured by SIMS as a function of growth temperature.

4. Conclusions

We studied the influence of the processing temperature on $Si_{0.3}Ge_{0.7}$ heterojunction solar cells grown on Si(001) by MBE. Stepwise compositionally graded $Si_{1-x}Ge_x$ buffer layers were
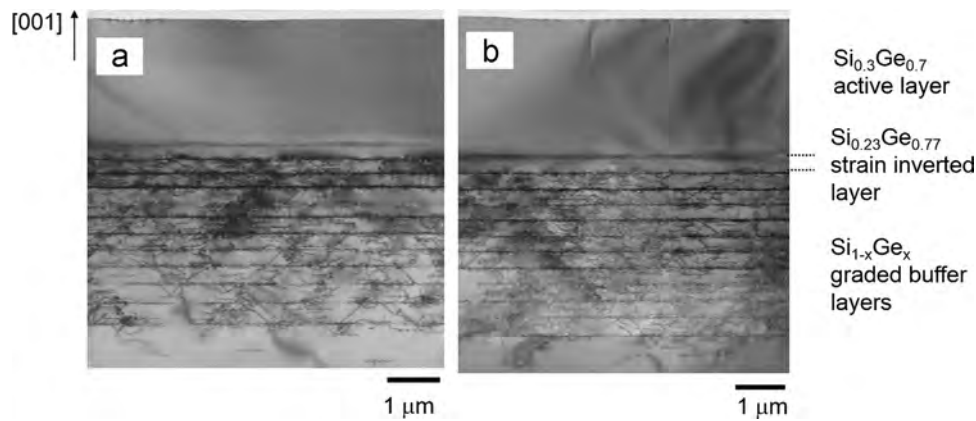
Fig. 8. Cross-sectional TEM images of $Si_{0.3}Ge_{0.7}$ films grown at (a) $T_{Active} = 560\ ^\circ C$ and (b) $T_{Active} = 600\ ^\circ C$.

successfully applied to prepare the $Si_{0.3}Ge_{0.7}$ films with low dislocation density. Annealing at a sufficiently high temperature (greater than 800 °C) promoted dislocation annihilation at the interfaces of each buffer layer, resulting in a decrease in recombination current components in diode characteristics. The diode factor was minimized to 1.45 at 800 °C, while J_0 monotonically decreased from 7.5×10^{-4} A/cm^2 for 650 °C to 5.0×10^{-5} A/cm^2 for 900 °C. An extended absorption edge up to 1.0 eV (1240 nm) was clearly observed for the $Si_{0.3}Ge_{0.7}$ cells. The $Si_{0.3}Ge_{0.7}$ cell grown at 600 °C exhibited both a higher short circuit current density of 20.95 mA/cm^2 and an improved IQE response in the longer wavelength region, presumably due to the reduction of crystal defects caused by oxygen contamination. At the same time, the accumulation of threading dislocation and roughening of the surface was observed, resulting in the degradation of the open circuit voltage and the fill factor.

Acknowledgments

References

[1] V.I. Kuznetsov, R.V. Veen, E. van der Drift, K. Werner, A.H. Verbruggen, S. Radelaar, J. Vac. Sci. Technol. B 13 (1995) 2892.
[2] G. Wöhl, V. Dudek, M. Graf, H. Kibbel, H.-J. Herzog, M. Klose, Thin Solid Films 369 (2000) 175.
[3] K.L. Wang, R.P.G. Karunasiri, J. Vac. Sci. Technol. B 11 (1993) 1159.
[4] M. Bauer, C. Schöllhorn, K. Lyutovich, E. Kasper, M. Jutzi, M. Berroth, Mater. Sci. Technol. B 89 (2002) 77.
[5] K. Said, J. Poortmans, M. Caymax, R. Loo, A. Daami, G. Bremond, O. Kruger, M. Kittler, Thin Solid Films 337 (1999) 85.
[6] Y. Shiraki, A. Sakaki, Surf. Sci. Rep. 59 (2005) 153.
[7] S.P. Philipps, G. Peharz, R. Hoheisel, T. Hornung, N.M. Al-Abbadi, F. Dimroth, A.W. Bett, Sol. Energy Mater. Sol. Cells 94 (2010) 869.
[8] D.C. Law, R.R. King, H. Yoon, A. Boca, C.M. Fetzer, S. Mesropian, T. Isshiki, M. Haddad, K.M. Edmondson, D. Bhusari, J. Yen, R.A. Sherif, H.A. Atwater, N. H. Karam, Sol. Energy Mater. Sol. Cells 94 (2010) 1314.
[9] D.J. Friedman, J.F. Geisz, S.R. Kurtz, J.M. Olson, J. Cryst. Growth 195 (1998) 409.
[10] H. Mizuno, K. Makita, K. Matsubara, Appl. Phys. Lett. 101 (2012) 191111.
[11] S.A. Hadi, P. Hashemi, N. DiLello, E. Polyzoeva, A. Nayfeh, J.L. Hoyt, Sol. Energy 103 (2014) 154.
[12] S. Nakano, Y. Takeuchi, T. Kaneko, M. Kondo, J. Non-Cryst. Solids 358 (2014) 2249.
[13] M. Tanaka, M. Taguchi, T. Matsuyama, T. Sawada, S. Tsuda, S. Nakano, H. Hanafusa, Y. Kuwano, Jpn. J. Appl. Phys. 31 (1992) 3518.
[14] J. Furlan, F. Smole, P. Popovič, M. Topič, M. Kamin, Sol. Energy Mater. Sol. Cells 53 (1998) 15.
[15] H. Mimura, Y. Hatanaka, Appl. Phys. Lett. 50 (1987) 326.
[16] T. Kaneko, M. Kondo, Jpn. J. Appl. Phys. 50 (2011) 120204.
[17] T. Egawa, A. Sakai, T. Yamamoto, N. Taoka, O. Nakatsuka, S. Zaima, Y. Yasuda, Appl. Surf. Sci. 224 (2004) 104.
[18] J.L. Liu, Z. Yang, K.L. Wang, J. Appl. Phys. 99 (2006) 024504.
[19] N. Usami, R. Nihei, Y. Azuma, I. Yonegawa, K. Nakajima, K. Sawano, Y. Shiraki, Thin Solid Films 517 (2008) 14.
[20] T.S. Yoon, J. Liu, A.M. Noori, M.S. Goorsky, Y.H. Xie, Appl. Phys. Lett. 87 (2005) 012104.
[21] Y. Hoshi, K. Sawano, Y. Hiraoka, Y. Sato, Y. Ogawa, A. Yamada, N. Usami, K. Nakagawa, Y. Shiraki, J. Cryst. Growth 311 (2009) 825.
[22] P.I. Gaiduk, A.N. Larsen, J.L. Hansen, Thin Solid Films 367 (2000) 120.
[23] N. Taoka, A. Sakai, S. Mochizuki, O. Nakatsuka, M. Ogawa, S. Zaima, Thin Solid Films 508 (2006) 147.
[24] R. Oshima, M. Yamanaka, H. Kawanami, I. Sakata, K. Matsubara, T. Sugaya, Jpn. J. Appl. Phys. 54 (2015) 12301.
[25] R. Oshima, Y. Watanabe, M. Yamanaka, H. Kawanami, I. Sakamoto, K. Matsubara, I. Sakata, J. Cryst. Growth 378 (2013) 226.
[26] Y. Wang, A. Gerger, A. Lochtefeld, L. Wang, C. Kerestes, R. Opila, A. Barnett, Sol. Energy Mater. Sol. Cells 108 (2013) 146.
[27] M. Taguchi, E. Maruyama, M. Tanaka, Jpn. J. Appl. Phys. 47 (2008) 814.
[28] L. Zhao, C.L. Zhou, H.L. Li, H.W. Diao, W.J. Wang, Sol. Energy Mater. Sol. Cells 92 (2008) 673.
[29] C.-H. Lin, T.-H. Tsai, C.-M. Wang, W.-T. Yeh, Appl. Surf. Sci. 275 (2013) 269.
[30] M. Bosi, A. Attolini, C. Ferrari, C. Frigeri, J.C. Rimada Herrera, E. Gombia, C. Pelosi, R.W. Peng, J. Cryst. Growth 310 (2008) 3282.
[31] R. Hoheisel, F. Dimroth, A.W. Bett, S.R. Messenger, P.P. Jenkins, R.J. Walters, Sol. Energy Mater. Sol. Cells 108 (2013) 235.
[32] S.S. Ang, J. Appl. Phys. 78 (1995) 1322.
[33] Y.B. Bolkhovityanov, A.S. Deryabin, A.K. Gutakovskii, M.A. Revenko, L.V. Sokolov, J. Appl. Phys. 96 (2004) 7665.
[34] S. Chakraborty, M.K. Bera, S. Bhattachara, P.K. Bose, C.K. maiti, Thin Solid Films 504 (2006) 73.
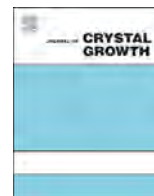
Strain-compensated Ge/Si$_{1-x}$C$_x$ quantum dots with Si mediating layers grown by molecular beam epitaxy

Kazuhiro Gotoh [a], Ryuji Oshima [b,*], Takeyoshi Sugaya [b], Isao Sakata [b], Koji Matsubara [b], Michio Kondo [a,b]

[a] Department of Innovative and Engineered Materials, Tokyo Institute of Technology, 4259 Nagatsuta-cho, Midori-ku, Yokohama, Kanagawa 226-8502, Japan
[b] National Institute of Industrial Science and Technology, 1-1-1 Umezono, Tsukuba, Ibaraki 305-8568, Japan

ABSTRACT

We fabricated 20-layer-stacked Ge/Si$_{1-x}$C$_x$ quantum dots (QDs) by solid source molecular beam epitaxy, for the realization of Si-based, strain-compensated Ge QDs. We inserted 2-nm-thick Si mediating layers between the Ge QDs and the Si$_{1-x}$C$_x$ strain-compensating spacer layers (SCLs) and evaluated their influence on the structural and optical properties of the obtained system. High density QDs with a size fluctuation of approximately 14% were successfully maintained independent of the number of stacked layers in the case of QDs with Si mediating layers, while the QD size monotonically increased with a number of stacked layers in the case of QDs without Si mediating layers. The sheet density of QDs with Si mediating layers reached 1.2×10^{11} cm^{-2}. A strong photoluminescence (PL) emission with a line-width of 96.7 meV was obtained for the QDs with Si mediating layers. The improvement of the aforementioned properties was caused by both the absence of C bonds at the surface and the improved surface roughness obtained by introducing Si mediating layers. The QD size increased for the 20-layer-stacked Ge/Si QDs samples grown with 10-nm-thick spacer layers, due to the accumulation of internal strains. By contrast, the size distribution of QDs was almost constant for the range of spacer layer thicknesses used in the present work (between 10 nm and 40 nm), implying that the tensile-strained Si$_{1-x}$C$_x$ SCLs compensated a certain fraction of the strain field created by the compressive-strained Ge QDs.

© 2015 Elsevier B.V. All rights reserved.

1. Introduction

Self-assembled Ge quantum dots (QDs) have been widely employed in devices such as field-effect transistors (FETs) [1], infrared photodetectors (IPs) [2,3], light emitting diodes (LEDs) [4,5] and solar cells [6,7]. Recently, it has been discovered that QD intermediate band solar cells (QD-IBSCs) may achieve a higher conversion efficiency than conventional single-junction solar cells by utilizing two-step optical transitions via intermediate band (IB) states (transitions from the valence band (VB) to the IB and from the IB to the conduction band (CB)), in addition to the conventional optical transition from the VB to the CB [8,9]. In particular, applying group-IV Ge/Si self-assembled QDs to QD-IBSCs is thought to be advantageous in several respects. First, the photo-generated electron–hole pairs can be efficiently separated in real and k spaces, because they have type-II heterointerfaces and indirect band structures [10,11]. Second, Ge/Si QD-IBSCs can be processed using cost-effective, mature Si technologies. Furthermore, in Ge/Si systems the absorption edge can expand toward longer wavelengths, typically in the 1.5-μm region, compared to the more

conventional, well-studied GaAs-based systems, such as the In(Ga)As QDs, which present an absorption edge in the range of 1.0–1.3 μm [12,13].

In order to realize practical QD-IBSCs, QDs should be dense, homogeneous in size, and periodically distributed to form the mini-bands utilized as IB states. The most popular QD fabrication technique is based on the exploitation of a spontaneous self-assembly mechanism forming coherent three-dimensional islands during growth, which is known as Stranski–Krastanov (S–K) growth and occurs during lattice-mismatched epitaxy. Increasing the number of stacked self-assembled QDs is a promising way to increase the total QD density, though some difficulties may arise from the accumulation of compressive strains induced by QD layers. If the host material used for burying the QDs was the same as the substrate, the QDs in a stacked configuration would be generally accompanied by an increase in size and in case their thickness exceeded a critical value, they would generate misfit dislocations. More recently, a strain compensation growth technique was employed for GaAs-based [14,15] and InP-based QD [16] systems. The compressive strain induced by the QDs was compensated by the tensile strain due to the presence of spacer layers, which have a smaller lattice constant than that of the substrate [17,18]. In the case of Ge/Si QDs, a Si$_{1-x}$C$_x$ material

* Corresponding author. Tel.: +81 29 861 3621; fax: +81 29 861 3142.
E-mail address: r.oshima@aist.go.jp (R. Oshima).

having a small amount of carbon ($\sim$1%) in a Si matrix can be used as a strain-compensating spacer layer (SCL). Though the growth of Ge QDs on the carbon-mediated Si surface has been intensively studied [19–30], there are few reports on the use of $Si_{1-x}C_x$ materials as SCLs. The present paper presents the structural and optical properties of multi-stacked, strain-compensated $Ge/Si_{1-x}C_x$ QDs grown by solid source molecular beam epitaxy (MBE).

2. Experimental methods

All samples were grown on Si (001) substrates by solid source MBE equipped with electron beam guns for the Si and Ge solid sources. A pyrolithic graphite filament cell heated at 1400 °C was used to incorporate C into the layer. Before the Si substrates were loaded into the growth chamber, they were chemically cleaned using the Radio Corporation of America (RCA) procedure [31]. The base pressure of the growth chamber was typically 4.0×10^{-10} Torr. After a thermal cleaning at 750 °C to remove the superficial ultra-thin oxide layer, a 150-nm-thick Si buffer layer was grown at 600 °C at a rate of 2.5 Å/s. Then, a spacer layer with a selected thickness and 4.6 monolayers (ML) of Ge QDs were consecutively grown in pairs at 500 °C, until either 10 or 20 cycles were completed. The growth was interrupted for 5 s after the deposition of Ge to enhance the three-dimensional islanding growth. This growth procedure has been previously reported as a pulse growth technique [32]. The thickness of the spacer layer (y) was varied from 10 nm to 40 nm. We compared two kinds of spacer layer structures in $Ge/Si_{1-x}C_x$ QDs as shown in Fig. 1(c) and (d): the first one included a y-nm-thick $Si_{1-x}C_x$ SCL, and the other one included a ($y-4$)-nm-thick $Si_{1-x}C_x$ SCL sandwiched between 2-nm-thick Si mediating layers. The growth rate of Ge QDs and $Si_{1-x}C_x$ SCLs were 2.6 Å/s and 2.0 Å/s, respectively. A stack of 20 layers consisting of 5.0 ML of Ge QDs

and Si spacer layers were fabricated as a reference. The C content in the $Si_{1-x}C_x$ layers used in this work was $x=0.001$, which was estimated by a separate set of experiments performed using high resolution X-ray diffraction (HR-XRD) on 200-nm-thick $Si_{1-x}C_x$ layers grown onto Si substrates using the same conditions used for the growth of the $Ge/Si_{1-x}C_x$ QD samples.

The structural properties of the achieved systems were evaluated by atomic force microscopy (AFM) and scanning transmission electron microscopy (STEM). For optical characterization, photoluminescence (PL) measurements were carried out at 12 K using a Ge photodetector cooled by liquid nitrogen in a standard lock-in configuration. A 532 nm green laser with a spot diameter of 500 μm at an excitation intensity of 101.8 mW was employed as excitation light source.

3. Results and discussion

Fig. 1 shows the AFM images of the topmost QD layer of the 10-layer-stacked $Ge/Si_{1-x}C_x$ QDs samples grown (a) with and (b) without the 2-nm-thick Si mediating layers. The spacer layer thickness (y) was 40 nm for both samples. The average height, average lateral size, fluctuation in lateral size, and sheet density were determined to be 1.7 nm, 28.3 nm, 14.0%, and 1.3×10^{11} cm^{-2} for (a), and 2.0 nm, 31.0 nm, 16.7%, and 5.1×10^{10} cm^{-2} for (b), respectively. Although the QD size was roughly the same for both samples, high-density Ge QDs with a better uniformity in size were obtained by using Si mediating layers, as shown in Fig. 1(a). Leifeld et al. argued that the formation of islands of Ge on the surface of a Si–C alloy starts at a lower coverage than on bare Si [23]. In that system, a Volmer–Weber growth mode was responsible for Ge QD formations instead of the S–K growth mode, which is typical for Ge QD formations on a Si surface. This occurred because Ge tends to wet the Si region first, since the C-rich areas
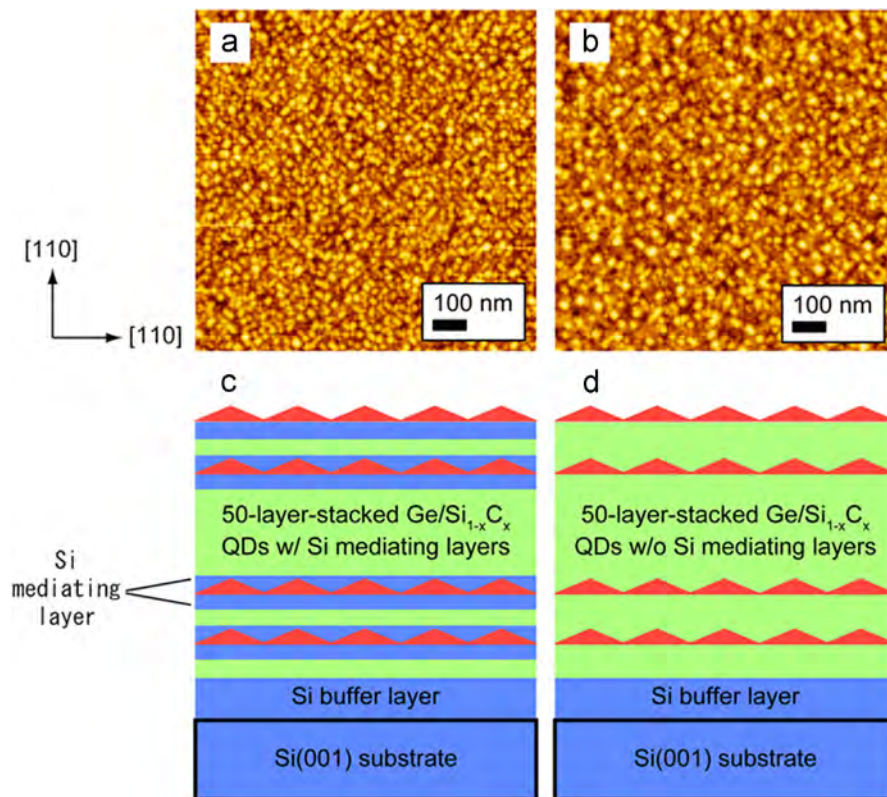
Fig. 1. AFM images of the topmost QD layer for the 10-layer-stacked $Ge/Si_{1-x}C_x$ QDs samples grown (a) with and (b) without Si mediating layers. The scan size is 1×1 μm^2. (c) and (d) Show schematic illustrations of the sample structures corresponding to (a) and (b).

repel the Ge ad-atoms. Indeed, we observed spotty patterns in reflection high-energy electron diffraction, which indicate a three-dimensional growth at an earlier stage of Ge deposition of ~4 ML for (a) compared to that of ~3 ML for (b). Furthermore, we observed that the root-mean-square (RMS) of the surface roughness before the Ge deposition was reduced from 8.02 Å for (b) to 6.45 Å for (a) by introducing 2-nm-thick Si mediating layers. Thus, the improvement in the homogeneity of the QD size for (a) is presumably caused by both the absence of C bonds at the surface
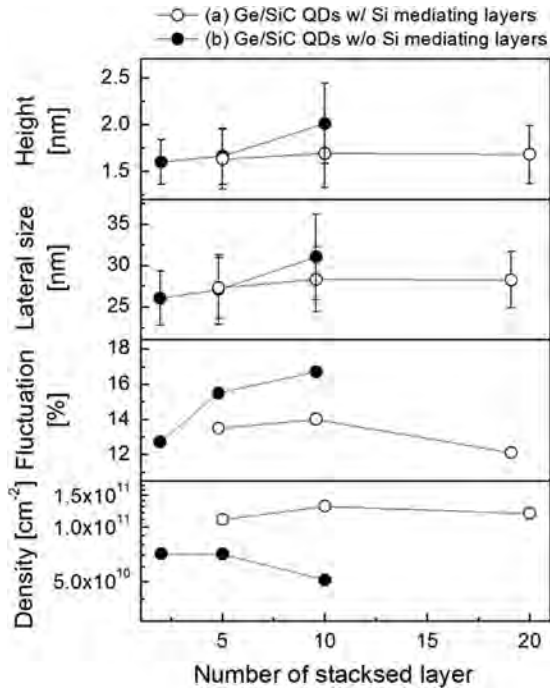
Fig. 2. Parameters of size distribution of multi-stacked Ge/Si$_{1-x}$C$_x$ QDs grown (a) with and (b) without Si mediating layers as a function of the number of stacked layers.

and the improved surface roughness. Fig. 2 shows a plot of the parameters related to the size distribution of multi-stacked Ge/Si$_{1-x}$C$_x$ QDs grown (a) with and (b) without Si mediating layers as a function of the number of stacked layers. Fig. 2(b) shows that all the parameters except the sheet density increased with increasing the number of stacked layers. The decrease in the sheet density was due to the increase in QD size, since the total volume of Ge QDs should be maintained regardless of the number of stacked layers. Conversely, Fig. 2(a) shows that these parameters were successfully maintained independent on the number of stacked layers for the QDs grown with Si mediating layers. Fig. 3(a) and (b) shows the bright field (BF) and high-angle annular dark field (HAADF) STEM images of the cross section obtained from the top portion of the 10-layer-stacked Ge/Si$_{1-x}$C$_x$ QDs sample grown with Si mediating layers, while (c) and (d) show the images taken for the stacked Ge QDs sample without Si mediating layers. Both misfit dislocations and C atoms clusters were not observed for any of the two QD samples in (a) and (c). Furthermore, an unexpected undulation at the heterointerface between the Ge QDs and the underlying spacer layer was observed for (d), in excellent agreement with the RMS of the surface roughness before the Ge deposition.

Fig. 4 shows the PL spectra at 12 K for the 10-layer-stacked Ge/Si$_{1-x}$C$_x$ QDs samples grown (a) with and (b) without Si mediating layers. Fig. 4(c) shows the spectra obtained for the 10-layer-stacked Ge QDs reference sample grown with Si spacer layers. The spacer layer thickness (y) was 40 nm for all the samples. The PL peak energy and the full width at half maximum (FWHM) for Ge QDs were 0.828 eV and 96.7 meV, respectively, in case (a); 0.845 eV and 198.2 meV, respectively, in case (b); and 0.818 eV and 85.2 meV, respectively, in case (c). The PL peaks of 1.08 eV and 1.02 eV for (c) are originated from the transverse-optical (TO$_{Si}$) phonon replica and two components of TO$_{Si}$ and zero center (O$^\Gamma$) phonons (TO$_{Si}$+O$^\Gamma$) of Si, respectively [33], although their emission energies were slightly deviated from those obtained from intrinsic Si bulks (1.099 eV for TO$_{Si}$ and 1.053 eV for TO$_{Si}$+O$^\Gamma$ lines, respectively, denoted as dash lines in Fig. 4) due to the tensile strain induced by Ge QDs. The broad PL peak near 1.0 eV was
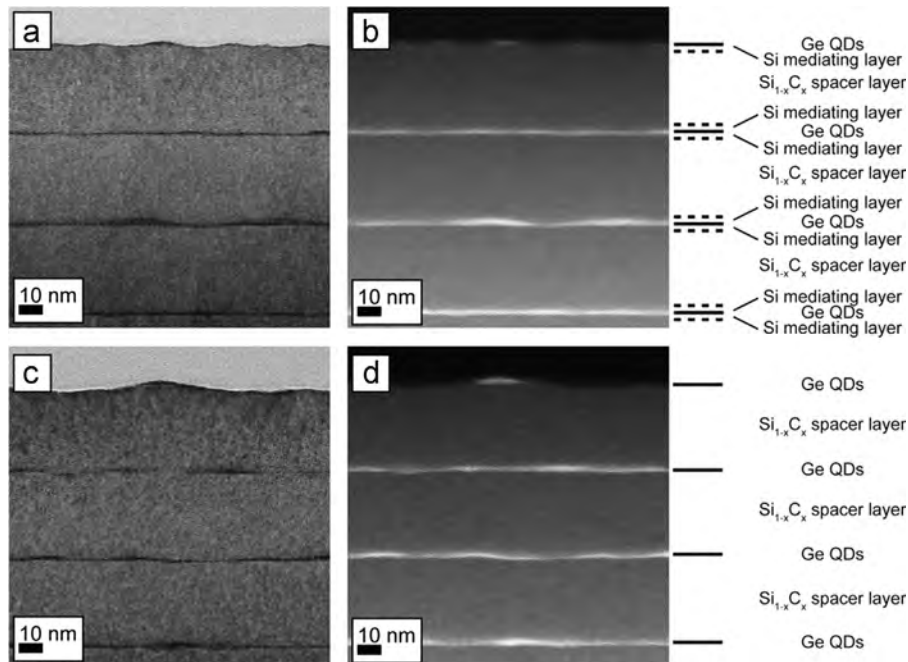
Fig. 3. (a) BF and (b) HAADF STEM images of the top portion of the 10-layer-stacked Ge/Si$_{1-x}$C$_x$ QDs sample grown with Si mediating layers. (c) and (d) Show the images taken for the stacked Ge QDs sample without Si mediating layers.

mainly composed of 3 small peaks, such as 1.06 eV for the TO phonon replica of the $Si_{1-x}C_x$ layers (TO_{SiC}), and 1.00 eV and 0.95 eV for the no-phonon transition (NP_{Ge}) and the TO phonon replica (TO_{Ge}) of Ge wetting layers [34,35]. The PL peak energy of the TO_{SiC} was shifted toward 1.06 eV from the peak observed at 1.08 eV for the TO_{Si}, due to the reduction of the Δ valley in the conduction band induced by the incorporation of C in a Si matrix [36,37]. The PL emission intensity for (a) was 2.5 times stronger than that for (b). Further, the FWHM was 198.2 meV for (b) and 96.7 meV for (a). The introduction of Si mediating layers may benefit both the QD homogeneity and the heterointerfaces formed at the surface of the Ge QDs. However, the PL intensity and the

FWHM for (a) were not as good as those observed for Ge/Si QDs, as shown in (c), implying that an optimization of the structure, as well as of the growth condition for $Si_{1-x}C_x$ SCL, are still needed. On the other hand, the PL peak energy for (a) was shifted toward the blue region of approximately 10 meV compared with (c). This was caused by an increase in the local strain fields around the QDs, due to the tensile strains caused by the $Si_{1-x}C_x$ SCLs and/or by the strong confinement effects occurring as a result of the formation of smaller Ge QDs on the combined set of $Si_{1-x}C_x$ SCLs and Si mediating layers compared with the Ge QDs formed on the plain Si spacer layers, as shown in Fig. 5.

Fig. 5 shows the AFM images of the topmost QDs on the 20-layer-stacked Ge QDs samples grown with (a) 10-nm, (b) 20-nm, and (c) 40-nm-thick $Si_{1-x}C_x$ SCLs and Si mediating layers, and with (d) 10-nm, (e) 20-nm, and (f) 40-nm-thick Si spacer layers. Smaller QDs with a higher sheet density were observed for (a), (b), and (c) compared with (e), (f), and (g), respectively. This indicates that the C atoms in the $Si_{1-x}C_x$ SCLs keep affecting the QD formation even if a 2-nm-thick Si mediating layer embeds the $Si_{1-x}C_x$ layer. The parameters relative to the size distribution of the 20-layer-stacked Ge QDs samples grown with (a) a combined set of $Si_{1-x}C_x$ SCLs and Si mediating layers and (b) Si spacer layers as a function of the spacer layer thickness (y) are shown in Fig. 6. The QD size and size fluctuation for (a) were successfully maintained independent on the spacer layer thickness, while those for (b) monotonically increased with decreasing the spacer layer thickness. A significant decrease in the sheet density, accompanied by an increase in QD size, was observed for $y = 10$ nm for both the structures, though the decreasing rate of the sheet density for (a) was much smaller than that for (b). In general, the second sheet of QDs grows in the strain field created by the buried first sheet of QDs in a multi-stacked configuration. This type of vertical correlation has been observed in various material systems, including Ge/Si [38–40]. In the Ge/$Si_{1-x}C_x$ QD system, the tensile-strained $Si_{1-x}C_x$ SCL seems to compensate a certain fraction of strain field induced by the Ge QDs, though 1.7% of C content in $Si_{1-x}C_x$ SCL

Fig. 4. PL spectra at 12 K for the 10-layer-stacked Ge/$Si_{1-x}C_x$ QD samples grown (a) with Si mediating layers and (b) without Si mediating layers. (c) PL spectra at 12 K for the 10-layer-stacked Ge QD sample grown with 40-nm-thick Si spacer layers used as a reference. Dash lines denote each emission line obtained from Ref. 33–37.(For interpretation of the references to color in this figure, the reader is referred to the web version of this article.)

Fig. 5. AFM images of the topmost QD layer for the 20-layer-stacked Ge QD samples grown with (a) 10-nm, (b) 20-nm, and (c) 40-nm-thick $Si_{1-x}C_x$ spacer layers and Si mediating layers. AFM images for the samples grown with (d) 10-nm, (e) 20-nm, and (f) 40-nm-thick Si spacer layers.
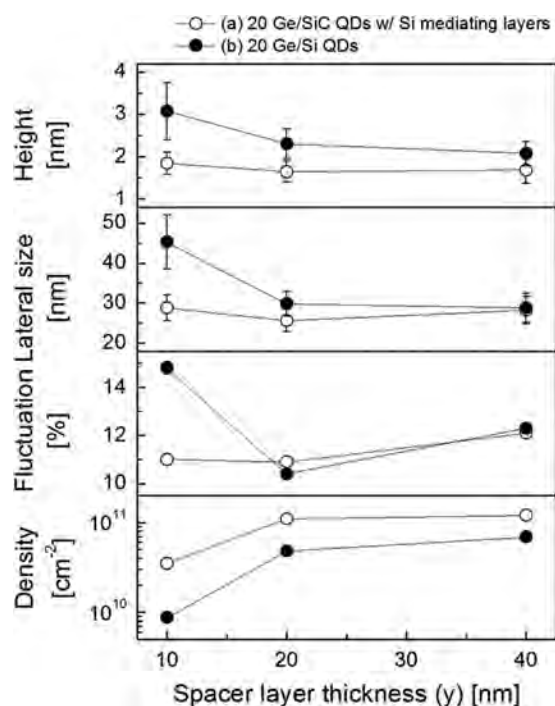
Fig. 6. Parameters of size distribution of 20-layer-stacked Ge QD samples grown with (a) a set of $Si_{1-x}C_x$ spacer layers and Si mediating layers and (b) Si spacer layers as a function of the spacer layer thickness (y).

would be still necessary to completely compensate the compressive strain for $y = 10$ nm.

4. Conclusions

We fabricated multi-stacked, strain-compensated Ge/$Si_{1-x}C_x$ QDs with Si mediating layers using solid source MBE. The influence on the structural and optical properties of the introduction of 2-nm-thick Si mediating layers between the Ge QDs and the $Si_{1-x}C_x$ SCLs was investigated. The distribution of several parameters (including QD size, lateral size fluctuation, and sheet density) relative to the Ge/$Si_{1-x}C_x$ QDs grown with Si mediating layers was successfully maintained independent of the number of stacked QD layers, while the distribution of the same parameters relative to the QDs grown without Si mediating layers increased with the number of stacked QD layers. As a result, the PL emission for the QDs with Si mediating layers was 2.5 times stronger than that for the QDs without Si mediating layers. The improvement of the properties was presumably caused by both the absence of C bonds at the surface and the improved surface roughness due to the introduction of Si mediating layers. Furthermore, we revealed that the increase in the QD size observed in the case of 10-nm-thick spacer layers was effectively suppressed by using a combination of a $Si_{1-x}C_x$ SCLs and Si mediating layers. This suggests that tensile-strained $Si_{1-x}C_x$ SCLs compensated a certain fraction of the strain field created by compressive-strained Ge QDs.

Acknowledgments

References

[1] A.I. Yakimov, A.V. Dvurechenskii, V.V. Kirienko, A.I. Nikiforov, Appl. Phys. Lett. 80 (2002) 4783.
[2] M. Elkurdi, P. Boucaud, S. Sauvange, O. Kermarrec, Y. Campidelli, D. Bensahel, G. Saint-Girons, I. Sagnes, Appl. Phys. Lett. 80 (2002) 509.
[3] A.I. Yakimov, A.V. Dvurechenskii, A.I. Nikiforov, Y.Y. Proskuryakov, J. Appl. Phys. 89 (2001) 5676.
[4] X. Xu, T. Chiba, T. Nakama, T. Maruizumi, Y. Shiraki, Appl. Phys. Express 5 (2012) 102101.
[5] X. Xu, T. Tsuboi, T. Chiba, N. Usami, T. Maruizumi, Y. Shiraki, Opt. Express 20 (2012) 14714.
[6] M.L. Lee, G. Dezsi, R. Venkatasubramanian, Thin Solid Films 518 (2010) S76.
[7] N. Usami, A. Alguno, K. Sawano, T. Ujihara, K. Fujiwara, G. Sazaki, Y. Shiraki and K. Nakajima, vol. 451–452, 2004, pp. 604.
[8] A. Luque, A. Martí, Adv. Mater. 22 (2010) 160.
[9] A. Luque, A. Martí, Phys. Rev. Lett. 78 (1997) 5014.
[10] Z. Liu, T. Zhou, L. Li, Y. Zuo, C. He, C. Li, C. Xue, B. Cheng, Q. Wang, Appl. Phys. Lett. 103 (2013) 082101.
[11] T. Tayagaki, N. Usami, W. Pan, Y. Hoshi, K. Ooi, Y. Kanemitsu, Appl. Phys. Lett. 101 (2012) 133905.
[12] Y. Shoji, K. Akimoto, Y. Okada, J. Phys. D: Appl. Phys. 46 (2013) 024002.
[13] T. Sugaya, O. Numakami, R. Oshima, S. Furue, H. Komaki, T. Amano, K. Matsubara, Y. Okano, S. Niki, Energy Environ. Sci. 5 (2012) 6233.
[14] K. Akanahane, N. Yamamoto, T. Kawanishi, Phys. Status Solidi A 208 (2011) 425.
[15] R. Oshima, T. Hashimoto, H. Shigekawa, Y. Okada, J. Appl. Phys. 100 (2006) 083110.
[16] P. Lever, H.H. Tan, C. Jagadish, J. Appl. Phys. 95 (2004) 5710.
[17] D. Alonso-Álvarez, J.M. Ripalda, B. Alén, J.M. Llorens, A. Rivera, F. Briones, Adv. Mater. 23 (2011) 5256.
[18] N.J. Ekins-Daukes, K. Kawaguchi, J. Zhang, Cryst. Growth Des. 2 (2002) 287.
[19] A. Beyer, E. Müller, H. Sigg, S. Stutz, D. Grützmacher, O. Leifeld, K. Ensslin, Appl. Phys. Lett. 77 (2000) 3218.
[20] A. Beyer, O. Leifeld, E. Müller, S. Stutz, H. Sigg, D. Grützmacher, Thin Solid Films 380 (2000) 246.
[21] O. Leifeld, A. Beyer, E. Müller, D. Grützmacher, K. Kern, Thin Solid Films 380 (2000) 176.
[22] J.Y. Kim, S.H. Ihm, J.H. Seok, C.H. Lee, Y.H. Lee, E.-K. Suh, H.J. Lee, Thin Solid Films 369 (2000) 96.
[23] O. Leifeld, A. Beyer, E. Müller, K. Kern, D. Grützmacher, Mater. Sci. Eng. B74 (2000) 222.
[24] J. Stangl, V. Holý, P. Mikulík, G. Bauer, I. Kegel, T.H. Metzger, O.G. Schmidt, C. Lange, K. Eberl, Appl. Phys. Lett. 74 (1999) 3785.
[25] K. Eberl, O.G. Schmidt, S. Schieker, N.Y. Jin-Phillipp, F. Phillipp, Solid-State Electron. 42 (1998) 1593.
[26] O.G. Schmidt, K. Eberl, Appl. Phys. Lett. 73 (1998) 2790.
[27] O.G. Schmidt, S. Shieker, K. Eberl, O. Kienzle, F. Ernst, Appl. Phys. Lett. 73 (1998) 659.
[28] S. Schieker, O.G. Schmidt, K. Eberl, N.Y. Jin-Phillipp, F. Phillipp, Appl. Phys. Lett. 72 (1998) 3344.
[29] O.G. Schmidt, C. Lange, K. Eberl, O. Kienzle, F. Ernst, Thin Solid Films 321 (1998) 70.
[30] O.G. Schmidt, C. Lange, K. Eberl, O. Kienzle, F. Ernst, Appl. Phys. Lett. 71 (1997) 2340.
[31] W. Kern, J. Electrochem. Soc. 137 (1990) 1887.
[32] K. Gotoh, R. Oshima, T. Sugaya, I. Sakata, K. Matsubara, M. Kondo, Thin Solid Films 557 (2014) 80.
[33] P.J. Dean, J.R. Haynes, W.F. Flood, Phys. Rev. 161 (1967) 711.
[34] G. Abstreiter, P. Schittenhelm, C. Engel, E. Silveria, A. Zrenner, D. Meertens, W. Jäger, Semicond. Sci. Technol. 11 (1996) 1521.
[35] H. Sunamura, N. Usami, Y. Shiraki, S. Fukatsu, Appl. Phys. Lett. 66 (1995) 3024.
[36] H.J. Osten, Thin Solid Films 367 (2000) 101.
[37] K. Brunner, K. Eberl, W. Winter, Phys. Rev. Lett. 76 (1996) 303.
[38] O.G. Schmidt, K. Eberl, Phys. Rev. B 61 (2000) 13721.
[39] V.L. Thanh, V. Yam, P. Boucaud, F. Fortuna, C. Ulysse, D. Bouchier, L. Vervoort, J.M. Lourtioz, Phys. Rev. B 60 (1999) 5851.
[40] J. Tersoff, C. Teichert, M.G. Lagally, Phys. Rev. Lett. 76 (1996) 1675.
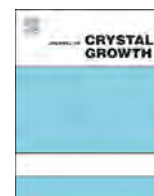
Sn-rich cubic phase nanocrystals in a SiGe/Si(001) quantum well

A.A. Tonkikh [a,b,*], N.D. Zakharov [b], V.G. Talalaev [a,d], C. Eisenschmidt [c], J. Schilling [a], P. Werner [b]

[a] ZIK SiLi-nano Martin Luther University of Halle-Wittenberg, Karl-Freiherr-von-Fritsch-Str. 3, 06120 Halle (Saale), Germany
[b] Max Planck Institute of Microstructure Physics, Weinberg 2, 06120 Halle (Saale), Germany
[c] Insitute of Physics, Martin Luther University Halle-Wittenberg, Von-Danckelmann-Platz 3 D-01620, Halle (Saale), Germany
[d] Fock Institute of Physics, St. Petersburg State University, St. Petersburg, 198504, Russia

ARTICLE INFO

ABSTRACT

We report on Sn-contained nanocrystals formed in Si and SiGe matrixes *via* Sn precipitation upon annealing of thin metastable $Si_{1-x-y}Ge_xSn_y$ layers grown by molecular beam epitaxy. The nanocrystals exhibit a cubic lattice, which is coherent with the matrix. The density of the nanocrystals decreases with the annealing temperature revealing a kinetic formation pathway. New optical spectral features below the Si band gap are observed in photoluminescence spectra of the samples with nanocrystals. The origin of these new spectral features is discussed.

© 2015 Elsevier B.V. All rights reserved.

1. Introduction

During the recent 15 years Si became a viable platform for photonics applications owing to the commercialization of SOI wafers [1]. At present the creation of a variety of active and passive CMOS-integrated photonic devices is demonstrated [2]. Particular efforts are devoted to an active light-emitting media, which requires the direct band gap material. Recently, several groups have reported on direct band gap SiGeSn alloys grown epitaxially on Si [3–5]. This achievement became possible due to a low energy gap between indirect L and direct Γ valleys in Ge of approximately 140 meV, which shrinks by embedding a few percent of Sn [3,6]. Unlike Ge, Si is a strongly indirect band gap semiconductor ($E_\Gamma - E_X > 2$ eV). Thus, a low Sn fraction should not transform Si to the direct band gap semiconductor. Theoretically, the direct bang gap could be achieved in a SiSn alloy at Sn fractions of less than 50 at%, if Ge is added to the SiSn system [3,7,8]. Experimentally, thin defect-free SiSn/Si layers having Sn fractions of up to only 9 at% (10 nm thick) [9] or 16 at% (1 nm thick) [10] were reported up to the date. These values are much lower than those required to achieve the direct band gap. Thereby, pseudomorphic epitaxial SiGeSn layers grown on Si could not be the candidates for the direct band gap material.

However, an increase in the Sn fraction could be achieved by applying annealing to the metastable SiSn alloys [11]. Then, Sn precipitation takes place due to the phase separation between Sn and Si, which is a commonly observed phenomenon in the immiscible systems [12]. These precipitates (nanocrystals) may contain pure Sn [11]. Moreover, a SiSn compound could also be expected in the nanocrystals by analogy to the GeSn system [13]. As the Sn fraction in the SiSn alloy increases, the band gap of the SiSn alloy should decrease [8]. Thus, a coherent SiSn nanocrystal in a Si matrix could be considered as a quantum dot, which may result in the radiative recombination of charge carriers. Although, the photoluminescence (PL) of α-Sn QDs in a Si matrix has not yet been confirmed [14], the idea of Sn-rich quantum dots in Si remains promising.

In our current study we experimentally re-examine this idea. Furthermore, we modify the composition of the Sn precipitates placing them in a GeSi quantum well. In this case the transition to the direct band gap semiconductor may occur at lower Sn fractions in the $Si_{1-x-y}Ge_xSn_y$ nanocrystals [7,8].

2. Experiment

The investigated samples were obtained in two stages. Firstly, the Sn-contained thin layers were coherently embedded in a Si matrix by applying non-equilibrium molecular beam epitaxy (MBE, SIVA45 setup by Riber). The MBE growth was carried out on a Si(001) substrate. Secondly, the as-grown samples were *ex situ* annealed in the Ar atmosphere at temperatures between 450 and 900 °C for one hour.

An experimental evidence of the formation of Sn precipitates in Si has been already reported elsewhere [11,15]. These

* Corresponding author at: ZIK SiLi-nano Martin Luther University of Halle-Wittenberg, Karl-Freiherr-von-Fritsch-Str. 3, 06120 Halle (Saale), Germany. Tel.: +49 345 5582643; fax: +49 345 5511223.
E-mail address: tonkikh@mpi-halle.de (A.A. Tonkikh).

experiments have revealed that when the thickness of a SiSn layer remains ~100 nm, annealing results in α- and β-Sn precipitates [16]. However, for relatively thin SiSn layers (~2 nm) only α-Sn precipitates have been found after annealing [11]. Therefore, the thickness of the Sn-contained layer in our experiments was limited to approximately 4 nm in order to form preferably cubic phase nanocrystals.

The structure of the as-grown samples was as follows: a 50 nm thick Si buffer layer, a 4 nm thick $Si_{1-x-y}Ge_xSn_y$ layer sandwiched between two 2 nm thick $Si_{1-x}Ge_x$ cladding layers (x=0.33), and a 30 nm thick Si capping layer. The buffer and capping layers were grown at 450 °C, while Sn-contained layers were deposited at 200 °C to suppress Sn segregation [9]. The compounds were grown using a co-deposition of Ge, Si, and Sn. The nominal Sn composition (y) in the $Si_{1-x-y}Ge_xSn_y$ layer was kept at approximately y=7 at%. The Ge content in the $GeSi/Si_{1-x-y}Ge_xSn_y/GeSi$ layers was varied. Four samples having x=0, 0.25, 0.5, 0.93 denoted as samples 1, 2, 3, 4 respectively, were grown. In the case of the two samples (1 and 4) the cladding GeSi layers were not grown.

The two sets of samples (as-grown and annealed) were characterized by using transmission electron microscopy (TEM), X-ray diffraction (XRD), and photoluminescence (PL). The crystal structure and composition of the samples were investigated in the cross-section and plan-view geometries using high-resolution TEM (HR TEM, JEM 4010), scanning TEM (STEM, FEI TITAN 80/300), and energy-dispersive x-ray spectroscopy (EDX, FEI TITAN 80/300). The XRD reciprocal space mapping (XRD RSM) was carried out for the Si 115+ reflections using a Bruker high-resolution diffractometer D8 with a Göbel mirror and a channel cut monochromator for Cu $K_{\alpha1}$ radiation, and a Vantec detector. The PL investigation was carried out in a He-cryostat at 10 K. The samples were excited by a 488 nm line of an Ar^+ laser at a power density of 20 Wcm^{-2}. The PL spectra were recorded using a LN_2-cooled InGaAs detector having the long-wavelength detection limit of 2400 nm.

3. Results

Fig. 1 shows the results of the plan-view TEM investigation of the set of annealed samples. Fig. 1a illustrates the nanocrystals in Ge-free sample 1. The dependence of the density of precipitates on the annealing temperature and Ge composition is depicted in Fig. 1b. All Ge-contained samples reveal precipitation at lower temperatures in comparison to Ge-free sample 1. No precipitates are detected in the Ge-free sample at temperatures of 600 °C and below. The plan-view TEM images reveal that the mean diameter of nanocrystals in Ge-contained samples remains in the range 3–5 nm, while the diameter in the Ge-free samples is 5–10 nm. The smaller nanocrystals are formed at lower annealing temperatures.

Fig. 2 shows two STEM images of as-grown and annealed sample 2, depicted in Fig. 2a and b, respectively. The bright stripe in both samples indicates the Ge-contained region (a quantum well). Due to a low Sn fraction in the as-grown sample no contrast modulation between SiGe and SiGeSn layers is observed. However, as sample 2 is annealed (Fig. 2b), the bright spots become visible revealing an increase in the Sn fraction in the nanocrystals. In this particular sample the nanocrystals possess a shape of oblate ellipsoids elongated in the SiGeSn plane. The length of the semi-principal axe along the growth direction is approximately 3 nm, while the both large axes are approximately 5 nm.

Quantitatively, the EDX measurement gives the Sn fraction in the specimen section containing nanocrystals between 14 and 25 at%. Since the TEM specimen thickness remains an unknown parameter in the EDX-experiment, the resulting Sn fraction within the nanocrystals is underestimated. In order to approach more realistic data we applied electron energy loss spectroscopy (EELS)
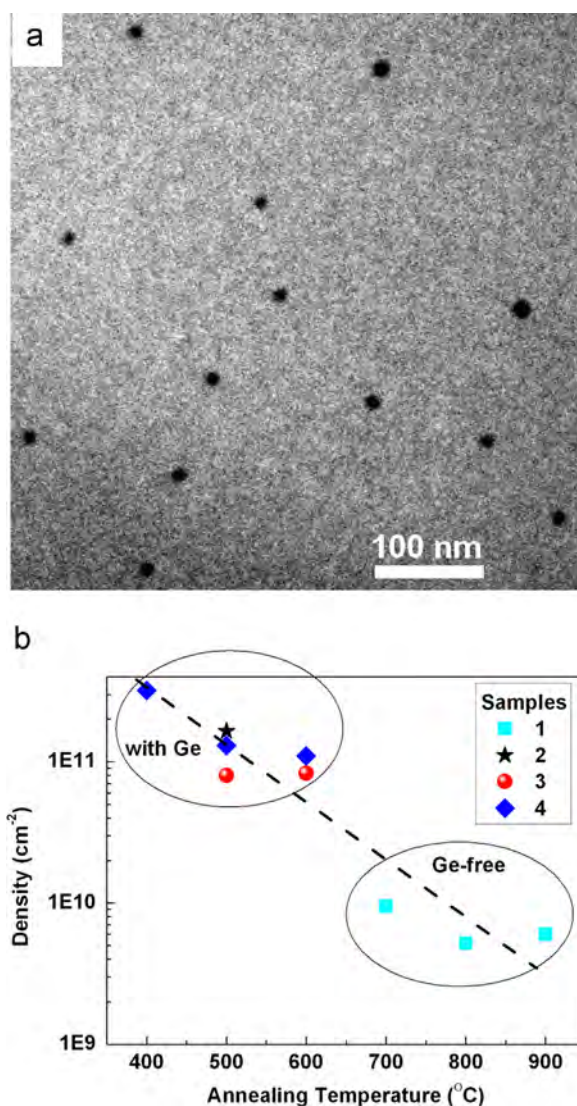
Fig. 1. (a) Plan-view TEM image of sample 1 annealed at 800 °C, black dots are Sn-rich nanocrystals of approximately 10 nm in diameter; (b) dependence of the nanocrystals density on the annealing temperature and Ge fraction in the GeSi quantum well, the line is guide to the eyes. Data points are collected by applying plan-view TEM.

to measure locally the specimen thickness. Then, the composition of nanocrystals was recalculated taking into account the specimen thickness, the mean size of nanocrystals, and the EDX-measured Sn fractions within the nanocrystals. This combined method gave us a much higher distribution of Sn fractions inside the nanocrystals: 40–100 at%. We note that such high distribution may originate from a limited accuracy of EDX and EELS methods.

Along with the composition inside the Sn-rich precipitates, their crystallographic structure is of particular importance. Therefore, we have carried out XRD RSM of sample 2. The results of XRD RSM are shown in Fig. 2c (as-grown sample 2) and d (annealed sample 2). Interestingly, both RSM images look very similar: SiGeSn-related RSM peaks lie at the same in-plane coordinate (Qx) as the fundamental Si peak, while being separated from the Si peak in the out-of-plane direction (Qz). This observation unambiguously reveals the pseudomorphic nature of both the as-grown and annealed SiGeSn films. Despite Fig. 2c and d looks identical, the positions of the XRD maxima of SiGeSn layers in the as-grown and annealed samples are different. The XRD peak of the SiGeSn layer in the annealed sample is shifted towards fundamental Si peak in comparison to the
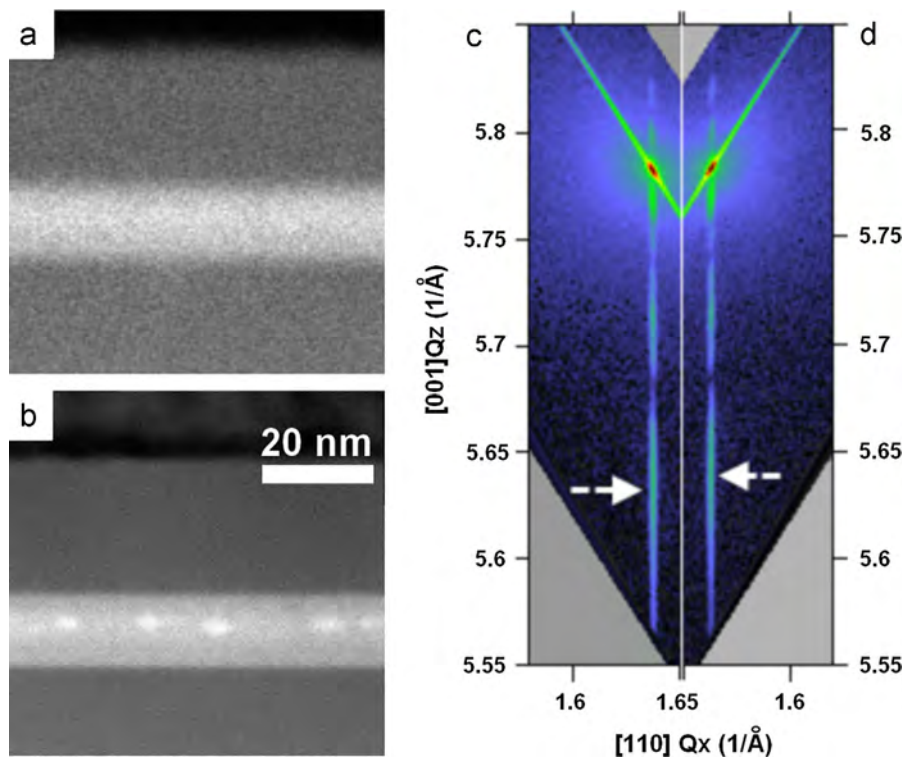
Fig. 2. (a), (b) Cross-section STEM images and (c), (d) HR XRD RSM-s of sample 2; (a) and (c) as-grown sample 2; (b) and (d) sample 2 annealed at 450 °C. Bright stripes in (a) and (b) depict regions with heavy-mass elements, *i.e.* Ge and Sn, bright spots in (b) show Sn-rich nanocrystals. White arrows in (c) and (d) indicate the positions of RSM intensity maxima of GeSnSi layers in both samples.

position of the SiGeSn peak in the as-grown sample. This fact may indicate that Sn atoms are transferred from the 2D SiGeSn layer to nanocrystals. No other indications of nanocrystals formation have been revealed by applying our lab XRD.

A confirmation of the cubic nature of nanocrystals has been received applying HR TEM. Fig. 3a shows HR TEM image of one of such precipitates. The HR TEM image reveals cubic lattice within the nanocrystal. The diffractogram of the HR TEM image is depicted in Fig. 3b. These two images indicate that the crystal lattice within and nearby the nanocrystal is cubic.

Fig. 4 shows four PL spectra: two spectra of sample 1 annealed at 500 and 800 °C, the spectrum of as-grown sample 2, and the spectrum of sample 2 annealed at 450 °C. All samples reveal an intensive spike at 1.136 µm (1.092 eV), which is related to the phonon-assisted radiative recombination in Si. This spike is accompanied by two weaker satellites 1.095 µm (1.132 eV) and 1.206 µm (1.028 eV) revealing a fingerprint of the B-doped substrate. No other spectral features are observed in the as-grown sample. Additional spectral features appear in the PL spectra of annealed samples. The PL spectra of two different samples: sample 1 (curve c) and sample 2 (curve b), annealed at 450 °C and 500 °C, respectively, show an additional broad band in the range 1.6–1.8 µm. Moreover, the Ge-free sample 1 (curve c) reveals additional spectral features next to the fundamental Si-TO band at 1.295 µm (0.957 eV) and 1.344 µm (0.922 eV). In the case of 800 °C-annealed sample 1 (curve d), no spectral features appear between 1.6–1.8 µm. However, a new triplet band appears in the PL spectrum of this sample close to the fundamental Si TO-line. These triplet lines are peaked at 1.192 µm (1.040 eV), 1.256 µm (0.987 eV), and 1.323 µm (0.937 eV). Their positions are marked with downward arrows in Fig. 4.

4. Discussion

The limited solubility in the SiSn system makes MBE-grown SnSi alloys metastable. An annealing activates precipitation. Our

experiments reveal that the addition of Ge to the SiSn system leads to the Sn precipitation at lower temperatures, than in the Ge-free samples. Moreover, we observed that as the annealing temperature increases the density of the nanocrystals decreases and the mean size of nanocrystals increases. The latter two phenomena indicate that the diffusion of Sn atoms towards existing precipitates at high temperatures makes nucleation of new precipitates less probable. Both these phenomena are signs of the kinetic precipitation mechanism. Moreover, our results (Fig. 1b) indicate that an addition of Ge results in nucleation of Sn-rich nanocrystals at lower temperatures, than without Ge. This phenomenon may be understood as a reduction of the nucleation barrier of nanocrystals formation or as an increase in the Sn diffusivity in Si due to presence of Ge.

The HR TEM images show that SiGeSn nanocrystals having the size of 3–5 nm exhibit a cubic structure. Moreover, the diffractogram of the HR TEM image (Fig. 3b) reveals no doubling of diffraction reflexes, which might give a sign of a relaxed lattice within the precipitates [15]. Thus, we believe that such nanocrystals remain coherent with the Si matrix. The XRD RSM investigation reveals the pseudomorphic nature of both types of the samples: as-grown and annealed. Thus, we claim the coherence of our structures with the matrix.

The coherent SiGeSn precipitates reported in the current study are approximately 3–5 nm in diameter. Interestingly, this size is larger than the size, which may have a coherent pure α-Sn nano-crystal in Si equaling to approximately 1 nm [16]. The critical diameter of a coherent nanocrystal scales as $d_{\mathrm{crit}} \sim 1/y^2$, where y is the Sn fraction in the nanocrystal. Therefore, the nanocrystals containing 60-to-30 at% Sn may become coherent with the Si host, while having a diameter of 3-to-5 nm, respectively. A comparison of this estimation with our quantitative EDX-measurements gives a realistic range of Sn fractions in the nanocrystals: 40–60 at%.

As the Sn fraction in Si or SiGe solid solution increases, the band gap of this solid solution should decrease. Thus, independently of the type of the heterojunction SiGeSn/Si, at least one type of the
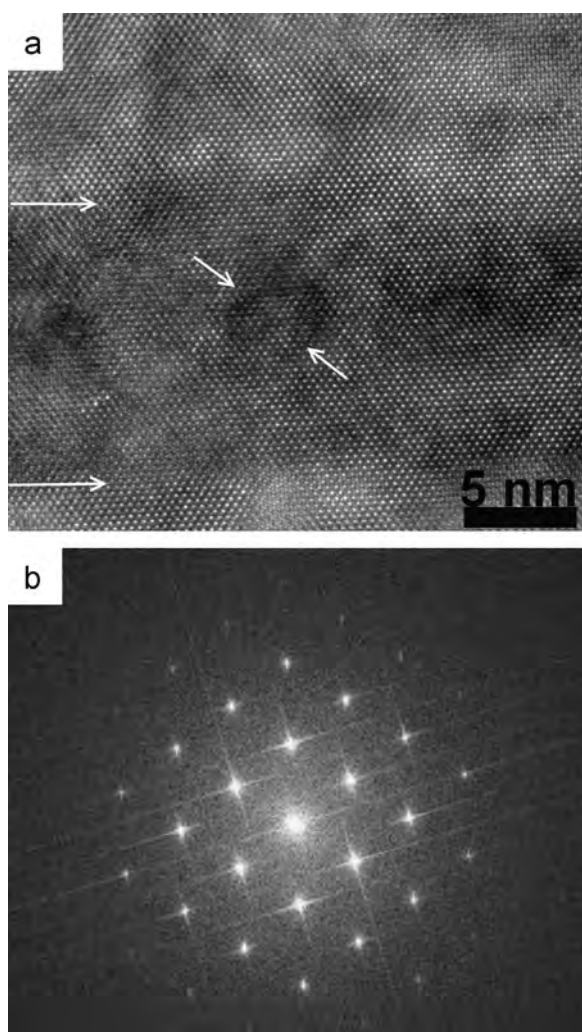
Fig. 3. (a) Cross-section HR TEM image of annealed sample 2 taken in the [110] crystallographic direction. Two horizontal arrows indicate positions of the SiGe/Si interfaces, while two inclined arrows depict the nanocrystal; (b) Fourier-transformed diffractogram taken on (a) shows cubic lattice reflexes only.
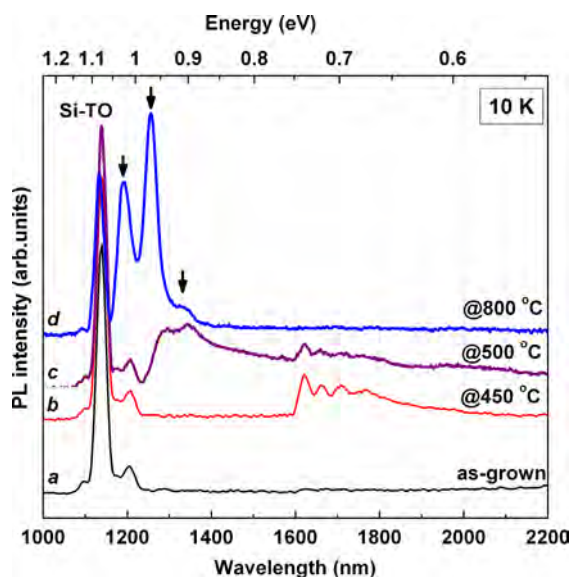
Fig. 4. The PL spectra taken at 10 K of four different samples: (a) as-grown sample 2; (b) sample 2 annealed at 450 °C; (c) sample 1 annealed at 500 °C; (d) sample 1 annealed at 800 °C.

charge carriers should be localized in the Sn-contained nanocrystals. This allows referring them to as quantum dots. A PL investigation of such quantum dots may reveal new quantum dot-related features in the energy range below the Si fundamental band gap.

Indeed, our PL experiments show several additional spectral features in the samples containing nanocrystals (curves b and d, Fig. 4) in comparison with the spectrum of the as-grown sample (curve a, Fig. 4). The moderate annealing of samples at 450 °C and 500 °C results in the appearance of a PL spectral band between 1.6 and 1.8 μm (curves b and c). The Ge-contained sample 2 annealed at 450 °C already reveals precipitation, while Ge-free sample 1 annealed at 500 °C does not (Fig. 1b). This fact prompted us to the assumption that the 1.6–1.8 μm spectral band has no relation to the nanocrystals. The spectral position and the specific shape of this band exhibiting a long wavelength fringe have led us to the conclusion that this is a so-called "P-line" caused by oxygen complexes in the Czochralski-grown substrates [17]. A long wavelength fringe ($\lambda > 1.8$ μm) of this band may contain not-resolved peaks related to carbon complexes in Si. This "P-line" should not appear in the spectrum of Czochralski-grown substrates annealed above 500 °C [17]. This is exactly the case of Ge-free sample 1 annealed at 800 °C.

The PL spectrum of this sample (curve d, Fig. 4) reveals an additional well-resolved triplet band. The peaks in this band are separated from each other and from the fundamental Si peak by approximately 55 meV. Therefore, an assumption of the phonon-assisted nature of this triplet band seems to be feasible. For example, Arguirov et al. [18] have reported on the PL observation of the 987 meV and 1040 meV peaks at 80 K in solar-grade Si arguing that the phonon-mediated transitions are responsible for the appearance of these two lines.

The line peaked at 937 meV (curve d, Fig. 4) could be a multiple-phonon assisted radiative recombination in Si. It is unlikely that this line originates from the defects in Si, despite its position fits well to the position of the so-called D3-line [18]. In the latter case other defect-related lines (D1, D2, and D4) should accompany the D3-line, which is not the case.

It is worth noting that the observed triplet band (curve d, Fig. 4) is unusual in the PL spectra of Si at 10 K. It is found in the PL spectrum of the sample containing Sn-rich nanocrystals. Therefore, we assume that this triplet band could be originated from the phonon-assisted optical transitions in the Sn-rich nanocrystals.

5. Conclusions

The formation of Sn-enriched nanocrystals in Si and SiGe matrixes has been investigated. It is found that the nanocrystals having diameters of 3–5 nm and Sn fractions in the range 40–60 at% form in the SiGe quantum well in Si. The PL spectra of the samples with nanocrystals reveal new spectral lines below the fundamental band gap of Si, which might be related to the optical transitions in the nanocrystals.

Acknowledgments

References

[1] M. Hochberg, T. Baehr-Jones, Nat. Photonics 4 (2010) 492.
[2] R. Soref, Proc. of SPIE 8629 (2013) 862902.
[3] J.D. Gallagher, C. Xu, L. Jiang, J. Kouvetakis, J. Menendez, Appl. Phys. Lett. 103 (2013) 202104.

[4] R. Chen, S. Gupta, Y.-C. Huang, Y. Huo, C.W. Rudy, E. Sanchez, Y. Kim, T.I. Kamins, K.C. Saraswat, J.S. Harris, Nano Lett. 14 (2014) 37.

[5] H.H. Tseng, K.Y. Wu, H. Li, V. Mashanov, H.H. Cheng, G. Sun, R.A. Soref, Appl. Phys. Lett. 102 (2013) 182106.

[6] A.A. Tonkikh, C. Eisenschmidt, V.G. Talalaev, N.D. Zakharov, J. Schilling, G. Schmidt, P. Werner, Appl. Phys. Lett. 103 (2013) 032106.

[7] P. Moontragoon, P. Pengpit, T. Burinprakhon, S. Maensiri, N. Vukmirovic, Z. Ikonic, P. Harrison, J. Non-Cryst. Solids 358 (2012) 2096.

[8] A. Attiaoui, O. Moutanabbir, J. Apply. Phys. 116 (2014) 063712.

[9] A.A. Tonkikh, N.D. Zakharov, C. Eisenschmidt, H.S. Leipner, P. Werner, J. Cryst. Growth 392 (2014) 49.

[10] K.S. Min, H.A. Atwater, Appl. Phys. Lett. 72 (1998) 1884.

[11] R. Ragan, H.A. Atwater, Appl. Phys. Lett. 77 (2001) 3418.

[12] W. Heiss, H. Groiss, E. Kaufmann, G. Hesser, M. Böberl, G. Springholz, F. Schäffler, K. Koike, H. Harada, M. Yano, Appl. Phys. Lett. 88 (2006) 192109.

[13] A.A. Tonkikh, N. Zakharov, A. Suvorova, C. Eisenschmidt, J. Schilling, P. Werner, Cryst. Growth Des. 14 (2014) 1617.

[14] A. Karim, G.V. Hansson, W.-X. Ni, P.O. Holtz, M. Larsson, H.A. Atwater, Opt. Mater. 27 (2005) 836.

[15] M.F. Fyhn, J. Chevallier, A.N. Larsen, R. Feidenhans'l, M. Seibt, Phys. Rev. B 60 (1999) 5770.

[16] L.M. Brown, G.R. Woolhouse, U. Valdrè, Philos. Mag. 17 (148) (1968) 781.

[17] W. Kürner, R. Sauer, A. Dornen, K. Thonke, Phys. Rev. B 39 (1989) 13327.

[18] T.Z. Arguirov, W. Seifert, M. Kittler, J. Reif, J. Phys.: Condens. Matter 14 (2002) 13169.
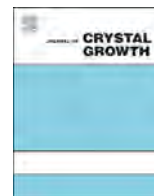
Transferring-free and large-area graphitic carbon film growth by using molecular beam epitaxy at low growth temperature

CrossMark

Meng-Yu Lin [a,b], Cheng-Hung Wang [c], Chun-Wei Pao [b], Shih-Yen Lin [a,b,*]

[a] Graduate Institute of Electronics Engineering, National Taiwan Univeristy, Taipei, Taiwan, ROC
[b] Research Center for Applied Science, Academia Sinica, Nankang, Taipei, Taiwan, ROC
[c] Institute of Display, National Chiao-Tung University, Hsinchu, Taiwan, ROC

ARTICLE INFO

ABSTRACT

Graphitic carbon films prepared by using molecular beam epitaxy (MBE) on metal templates with different thicknesses deposited on SiO_2/Si substrates are investigated in this paper. With thick Cu templates, only graphitic carbon flakes are obtained near the Cu grain boundaries at low growth temperatures on metal/SiO_2 interfaces. By replacing the Cu templates with thin Ni templates, complete graphitic carbon films with superior crystalline quality is obtained at 600 °C on SiO_2/Si substrates after removing the Ni templates. The enhanced attachment of the graphitic carbon film to the SiO_2/Si substrates with reduced Ni thickness makes the approach a promising approach for transferring-free graphene preparation at low temperature by using MBE.

© 2015 Elsevier B.V. All rights reserved.

1. Introduction

Since the first discovery of graphene film obtained by the exfoliation method from graphite in 2004 [1], many researchers have studied methods to enlarge the film size and its crystalline quality. Unlike flakes of graphene obtained via the exfoliation method, SiC sublimation and chemical vapor deposition (CVD) on metal templates are two approaches, which have demonstrated large-area graphene growth [2–7]. In the SiC sublimation method, it requires high substrate temperature ∼1400 °C during the process to desorb Si atoms from the substrate surface such that the remaining C atoms may undergo graphitization [2–4]. In this case, although the SiC sublimation method can achieve high quality graphene, the high growth temperature and high substrate price become a major concern on its practical application. For the CVD method, Ni and Cu are two metal templates commonly adopted for graphene growth. With the mechanism of C atoms dissolved and precipitated in the Ni templates, high quality graphene films can be observed on the metal surface after high-temperature annealing and fast cooling procedure [5]. However, because the C atoms would only precipitate from the defect locations on the Ni surface, un-uniform layer number of graphene films is usually obtained by using Ni templates. Unlike the growth mechanism of Ni templates, low solubility of the C atoms in Cu foil

results in different graphene growth mechanisms of surface migration and self-align arranged construction on Cu foil by using CVD [6,7]. Due to the self-limited process of C atoms, uniform single layer graphene is usually obtained on Cu foil surface by using CVD. However, due to the requests of methane decomposition and C atom dissolution into Ni templates, the growth temperatures of the CVD methods based on Cu and Ni templates are usually up to 1000 °C. The high processing temperature would become a major drawback for the practical application of CVD-prepared graphene films. On the other hand, graphene film transferring from the metal templates to other substrates required for CVD-prepared graphene would usually bring defects such as wrinkles and small holes on the film surface. This would become the other disadvantage of CVD-prepared graphene for practical applications.

Since good crystalline quality and large-area films have been demonstrated on CVD-prepared graphene on metal templates, graphene grown on metal templates can still be very useful if both transferring-free and low growth temperature can be achieved. In one of our previous publications, graphene formation on the interface between Ni templates and the dielectric substrate is observed [8]. The underneath graphene formation mechanism is based on the C atom dissolution and precipitation to the two Ni template surfaces. Therefore, the growth temperature ∼1050 °C is required and multilayer graphene is obtained by using this approach. Similar experiment result is also observed by replacing the metal with Cu [9]. Because of its low C solubility, Cu templates show different mechanisms on underneath graphene formation. The C atoms would migrate along the grain boundaries and reach

* Correspondence to: 128 Sec. 2, Academia Rd., Nankang, Taipei 11529, Taiwan.
Tel.: +886 2 27873187; fax: +886 2 27873122.
E-mail address: shihyen@gate.sinica.edu.tw (S.-Y. Lin).

the interface between metal templates and dielectric substrates. From their result, the processing temperature is reduced to 900 °C, which is mainly due to the request of methane decomposition. Although the growth temperature has decreased 150 °C after replacing the metal from Ni to Cu, the growth temperature is still too high for applications. To decrease the growth temperature, supplying C atoms directly for graphene growth could be the solution. By using the molecular beam epitaxy technique (MBE), the C atoms can be directly supplied by using heated pyrolithic graphite (PG) filament or cracked ethylene and then reach the substrate in atomic form [10–12]. In this case, the growth temperature of the graphene films can be greatly depressed, which could be a major improvement for graphene preparation and applications.

In this paper, graphitic carbon films are prepared by using MBE on metal templates with different thicknesses. With thick Cu templates, C atoms would diffuse to the Cu/SiO$_2$ interfaces through the grain boundaries and form graphitic carbon films. However, only graphitic carbon flakes are obtained near the boundaries at low growth temperatures. By replacing the Cu templates with thin Ni templates, complete graphitic carbon films with superior crystalline quality is obtained. The results suggest that similar C migration and graphitic carbon film growth mechanisms observed on Cu foil could also be observed on Ni templates given lower carbon solubility at low growth temperatures.

2. Experiment

The samples prepared in this paper are fabricated by using a customer-designed MBE system linked with a thermal coater. The first part of the experiments is focused on the investigations of Cu templates for graphene growth. The preparation procedure is as following: (1) a 600 nm SiO$_2$/Si substrate is loaded to the thermal coater connected to the MBE chamber, (2) a 300 nm Cu template is deposited on the sample surface, (3) the sample is annealed at 750 °C for 30 min after transferring the sample into growth chamber without exposure to the environment, (4) depositing C atoms on the sample surface for 1 h with different substrate temperatures and (5) removing the Cu templates by using FeNO$_3$ solution after transferring the sample out of the MBE system. During the C atoms deposition, two growth temperatures 400 and 700 °C are adopted. The C source is supplied by using a Riber C filament effusion cell [10]. The other set of graphene growth is done on Ni templates with different thicknesses. The growth procedure is as following: (1) a 600 nm SiO$_2$/Si substrate is loaded to the thermal coater connected to the MBE chamber, (2) Ni templates with different thicknesses is deposited on the sample surface with exposure to the environment, (3) depositing C atoms on the sample surface for 20 min at 600 °C and (4) removing the Ni templates with HCl solution after transferring the sample out of the MBE system. The Raman spectrums of the films are measured by using a HORIBA Jobin Yvon HR800UV spectrum system equipped with 532 nm laser.

3. Result and discussion

The picture of the Cu template taken under an optical microscope after 750 °C annealing is shown in Fig. 1(a). As shown in the figure, Cu crystal grains are formed on the substrate surface, which would facilitate C atom migration and underneath graphitic carbon growth [9]. After removing the Cu templates, the pictures of the graphitic carbon films formed underneath the metal templates at growth temperatures 400 and 700 °C are shown in Fig. 1(b) and (c), respectively. As shown in Fig. 1(b), only strip-like
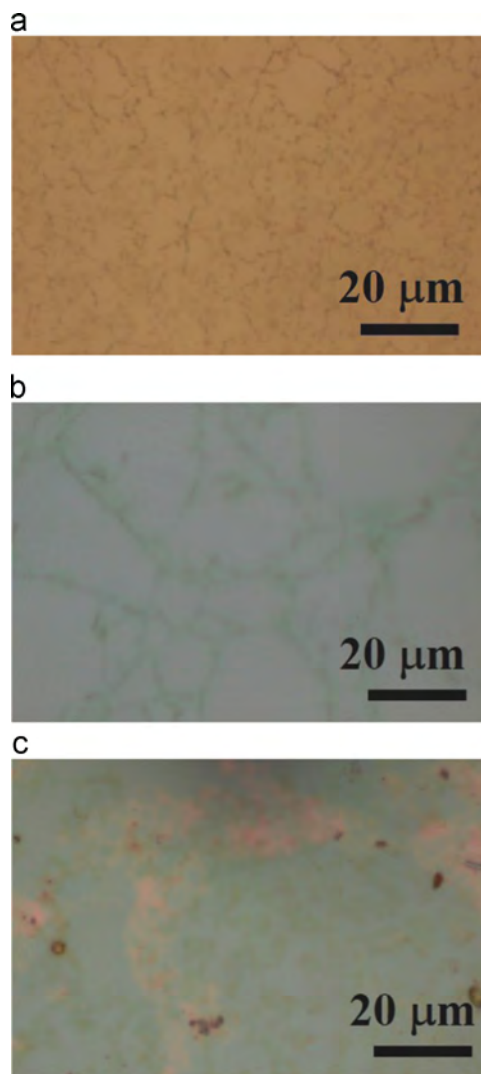
Fig. 1. The optical microscope pictures of (a) the 300 nm Cu template surface after 750 °C annealing and the graphene films formed underneath the metal templates at growth temperatures (b) 400 and (c) 700 °C.

graphitic carbon flakes are observed on the surface for the sample grown at 400 °C. With growth temperature raised up to 700 °C, denser graphitic carbon flakes are obtained on the sample surface. The results suggest that although C source decomposition is no longer required by using the atomic C source in the MBE chamber, higher growth temperature is still required for C atom migration on the Cu/SiO$_2$ interface for complete film formation [9]. Therefore, when the substrate is grown at 400 °C, the C atoms could only migrate through the grain boundary and accumulate along the grain boundary without further migration away the boundaries. When the growth temperature is raised up to 700 °C, enhanced C atom migration length would be obtained. In this case, instead of accumulating near the grain boundaries, the C atoms would migrate further on the Cu/SiO$_2$ interface and form denser graphitic carbon flakes.

To further investigate the crystalline quality of the graphitic carbon films, the Raman spectrums of the two samples are shown in Fig. 2. As shown in the figure, for the sample grown at 400 °C, except for the D and G peaks observed at around 1350 and 1590 cm^{-1}, dispersed G peak is also observed at around 1500 cm^{-1} [13]. The results indicate that both sp^2 and sp^3 bonding C structures are observed on the graphitic carbon film. The result indicates that most C atoms are accumulated near the grain
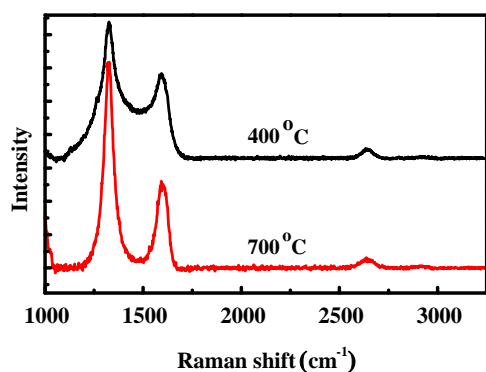
Fig. 2. The Raman spectrums of the graphene films grown at 400 and 700 °C.
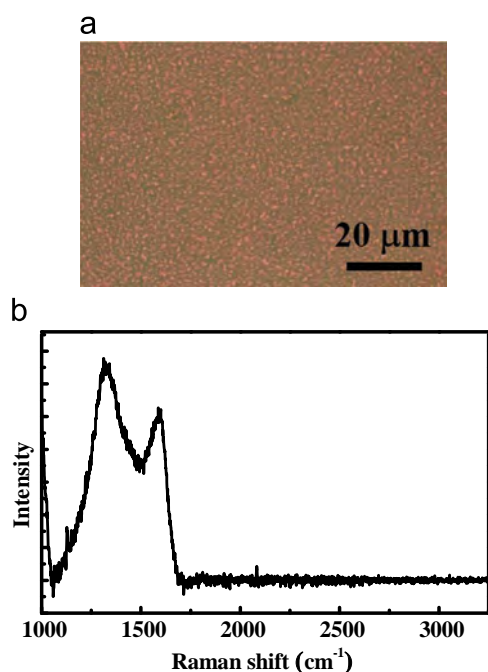
Fig. 3. (a) The optical microscope picture of the 20 nm Cu template after 600 °C annealing and (b) the Raman spectrum of the film after removing the metal template.

boundaries instead of further migration for graphitic carbon growth. For the sample grown at 700 °C, D, G and 2D peaks can be clearly identified at 1325, 1590 and 2630 cm^{-1}, respectively. The peak intensity ratio of the D and G peaks is 2.4, which corresponds to a nano-crystal graphitic carbon size ~8 nm [14]. The results have demonstrated that with increasing growth temperatures, as has been observed in Fig. 1(c), enhanced C migration between metal templates/SiO$_2$ interfaces is obtained. Improved crystalline quality can also be obtained for the graphitic carbon films. However, the still required high growth temperature for C atom migration would limit the application of this approach.

The other possible solution to enhance the C atom migration length at low growth temperatures is to reduce the metal template thickness. With the reduced metal template thickness, the C atoms may easily migrate to the SiO$_2$ surface and undergo graphitic carbon growth. Another sample with similar preparation procedure is grown except for the reduced Cu film thickness 20 nm and annealing temperature 600 °C. The optical microscope picture of the Cu template after 600 °C annealing is shown in Fig. 3(a). Instead of grain structures observed in Fig. 1(a), only Cu clusters are observed on the sample surface and the film is not continuous.

The Raman spectrum of the graphitic carbon film obtained after removing the Cu template is shown in Fig. 3(b). As shown in the figure, very poor crystalline quality is obtained for the film. Since the formation mechanism of graphitic carbon films underneath the Cu templates is through the C atom migration on the interfaces, the incomplete Cu templates would directly bring up poor graphitic carbon films. In this case, although graphitic carbon formation can be observed underneath Cu templates at low growth temperature by using MBE, complete films cannot be obtained via this approach. To effectively lower the growth temperature for large-area graphene growth, it is important to select a template material with the possibility of graphene growth directly on the smooth thin metal surfaces.

The other commonly adopted metal templates in CVD grown graphene are Ni films. Different from the growth mechanisms of graphene on Cu foils, C atom dissolution and then precipitation to the surfaces with fast cooling procedure are the main mechanisms for graphene growth above and below Ni templates [5,8]. With reduced growth temperatures, the same growth procedure may not happen due to the decreasing C solubility in Ni films. In this case, it seems that Ni templates may not be a good choice for graphene growth at low temperature. However, considering the low C flux of the C source in the MBE chamber, thin Ni templates may still act as efficient C atom traps and force graphene growth on the Ni surfaces. To investigate this possibility, graphitic carbon films grown on Ni templates with different thicknesses at 600 °C are performed by using the MBE chamber. The Raman spectrums of the films are shown in Fig. 4. The measurements are done after removing the Ni templates. As shown in the figure, with increasing Ni thickness, more significant 2D peaks located at ~2630 cm^{-1} are observed. The results have demonstrated that (a) similar growth mechanisms with graphene grown on Cu films can also take place on thin Ni films at a low growth temperature 600 °C and (b) the increasing 2D peak intensities with increasing Ni thickness suggest improved crystalline quality of the graphitic carbon films. Different from the case of 20 nm Cu templates, at the low growth temperature 600 °C, complete Ni templates are observed for all the samples with different thicknesses. However, since smoother surfaces are obtained with thicker Ni templates, the inferior crystalline quality of the graphitic carbon films prepared by using Ni template thickness thinner than 10 nm suggests that C atom migration still plays an important role by using this approach. On the other hand, the growth of the graphitic carbon films on Ni surfaces has confirmed that the Ni templates may undergo similar growth mechanisms with Cu foils at low growth temperatures.

The other advantage of using thin metal templates for graphene growth is the possible improved top-layer graphene attachment to the SiO$_2$/Si substrates after moving the metal templates. The optical microscope pictures of the graphitic carbon films
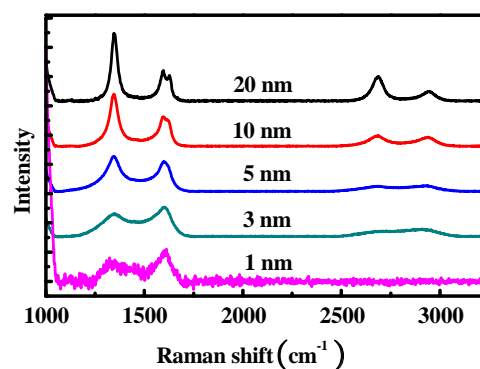
Fig. 4. The Raman spectrums of the graphene films grown on Ni templates with different thicknesses.
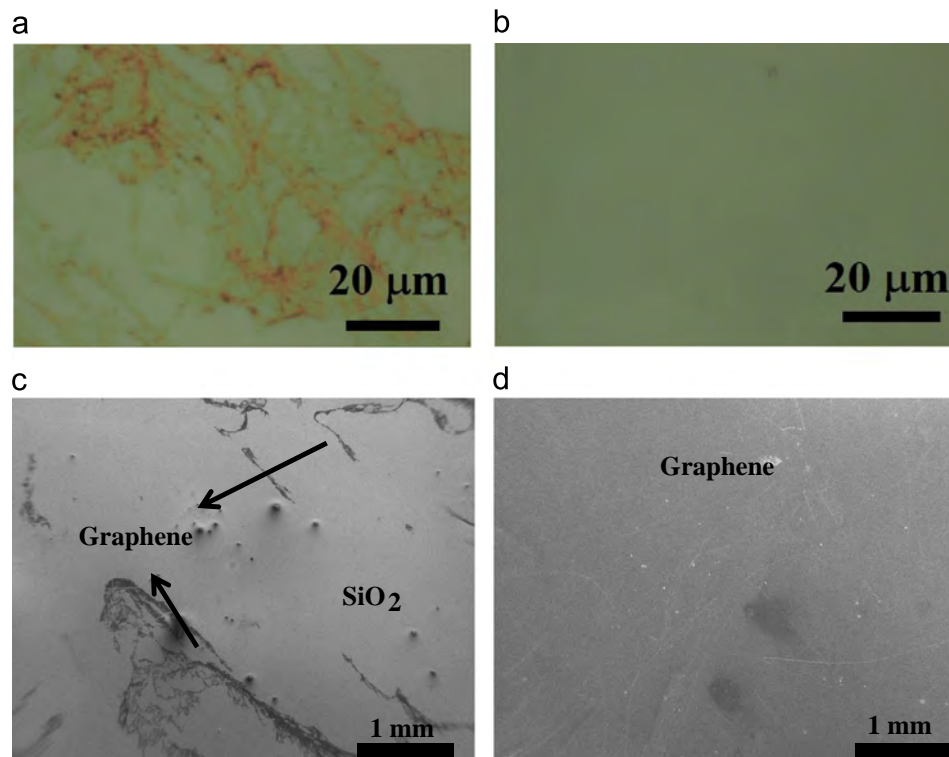
Fig. 5. The optical microscope and SEM images of the graphene films grown on (a), (c) 20 and (b), (d) 10 nm Ni templates.

grown on 20 and 10 nm Ni templates are shown in Fig. 5(a) and (b), respectively. Although better crystalline quality is obtained for the sample grown on 20 nm Ni template, the worse attachment to the SiO_2/Si substrates and the surface tension of the top-layer graphitic carbon would force the film to shrink such that wrinkled films would be obtained during the etching procedure. The phenomenon is observed in Fig. 5(a). For the film grown on 10 nm Ni template, such phenomenon is not observed. In this case, wrinkle-free and complete film is observed in Fig. 5(b). Further investigates the completeness of the films, the scanning electron microscope (SEM) images of the graphitic carbon films grown on 20 and 10 Ni templates are shown in Fig. 5(c) and (d), respectively. Similar with the results observed in Fig. 5(a) and (b), wrinkled and broken graphitic carbon films are obtained on 20 nm Ni templates while complete films are obtained on 10 nm Ni templates. The results suggest that by using thin Ni templates and the atomic carbon source in the MBE chamber, similar CVD-grown graphene mechanisms on Cu foils can also be observed on Ni surface. The low growth temperature and transferring-free graphitic carbon films prepared by this method has provided an alternate approach for graphene growth.

4. Conclusion

In conclusion, graphitic carbon films are prepared by using MBE on metal templates with different thicknesses. By using thin Ni templates and the atomic carbon source in the MBE chamber, similar growth mechanisms of graphene on Cu foils by using CVD are also observed on Ni templates. The enhanced attachment of the graphitic carbon film to the SiO_2/Si substrates makes thin Ni templates a promising candidate for transferring-free graphene preparation at low temperature by using MBE. The low growth temperature and transferring-free graphitic carbon films prepared by this method has provided an alternate approach for graphene growth.

References

[1] K.S. Novoselov, A.K. Geim, S.V. Morozov, D. Jiang, Y. Zhang, S.V. Dubonos, I. V. Grigorieva, A.A. Firsov, Science 306 (2004) 666.
[2] C. Riedl, A.A. Zakharov, U. Starke, Appl. Phys. Lett. 93 (2008) 033106.
[3] N. Camara, G. Rius, J.-R. Huntzinger, A. Tiberj, L. Magaud, N. Mestres, P. Godignon, J. Camassel, Appl. Phys. Lett. 93 (2008) 263102.
[4] N. Camara, G. Rius, J.-R. Huntzinger, A. Tiberj, N. Mestres, P. Godignon, J. Camassel, Appl. Phys. Lett. 93 (2008) 123503.
[5] K.S. Kim, Y. Zhao, H. Jang, S.Y. Lee, J.M. Kim, K.S. Kim, J.H. Ahn, P. Kim, J.Y. Choi, B.H. Homg, Nature 457 (2009) 706.
[6] X. Li, W. Cai, L. Colombo, R.S. Ruoff, Nano Lett. 9 (2009) 4268.
[7] G.A. Lopez, E.J. Mittemeijer, Scr. Mater. 51 (2004) 1.
[8] M.Y. Lin, Y.S. Sheng, S.H. Chen, C.Y. Su, L.J. Li, S.Y. Lin, J. Vac. Sci. Technol. B 29 (2011) 061202.
[9] C.Y. Su, A.Y. Lu, C.Y. Wu, Y.T. Li, K.K. Liu, W. Zhang, S.Y. Lin, Z.Y. Juang, Y. L. Zhong, F.R. Chen, L.J. Li, Nano Lett. 11 (2011) 3612.
[10] M.Y. Lin, W.C. Guo, M.H. Wu, P.Y. Wang, T.H. Liu, C.W. Pao, C.C. Chang, S.C. Lee, S.Y. Lin, Appl. Phys. Lett. 101 (2012) 221911.
[11] G. Lippert, J. Dabrowski, Y. Yamamoto, F. Herziger, J. Maultzsch, M.C. Lemme, W. Mehr, G. Lupina, Carbon 52 (2013) 40.
[12] F. Maeda, H. Hibino, Diam. Relat. Mater. 34 (2013) 84.
[13] A. Ferrari, J. Robertson, Phys. Rev. B 64 (2001) 075414.
[14] L. Cancado, K. Takai, T. Enoki, M. Endo, Y. Kim, H. Mizusaki, A. Jorio, L. Coelho, R. Magalhaes-Paniago, M. Pimenta, Appl. Phys. Lett. 88 (2006) 163106.
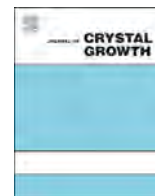
Molecular beam epitaxial re-growth of CdTe, CdTe/CdMgTe and CdTe/CdZnTe double heterostructures on CdTe/InSb(1 0 0) substrates with As cap

Shahram Seyedmohammadi [a,*], Michael J. DiNezza [b], Shi Liu [b], Paul King [a], Elizabeth G. LeBlanc [c], Xin-Hao Zhao [d], Calli Campbell [d], Thomas H. Myers [c], Yong-Hong Zhang [b], Roger J. Malik [a]

[a] First Solar, Inc., Santa Clara, CA 95050, USA
[b] School of Electrical, Computer and Energy Engineering, Arizona State University, Tempe, AZ 85287, USA
[c] Materials Science, Engineering, and Commercialization Program, Texas State University, San Marcos, TX 78666, USA
[d] School for Engineering of Matter, Transport and Energy, Arizona State University, Tempe, AZ 85287, USA

ABSTRACT

Molecular beam epitaxial growth on CdTe substrates is challenging since the CdTe film crystalline and optical quality is limited by residual defects including threading dislocations and stacking faults. This remains an obstacle in spite of exhausting variables including pre-growth substrate preparation as well as epitaxial growth conditions including thermal oxide desorption, growth temperature, and II/VI flux ratios. We propose a new technique to re-grow structures with low defect densities and high optical and structural quality on InSb substrates. The "CdTe virtual wafer" is made by growing a thin CdTe film on an InSb(1 0 0) substrate which is then covered with a thin As cap layer to prevent oxidation of the CdTe surface. The As cap can be removed by thermal desorption at about 300 C leaving a clean CdTe surface for subsequent epitaxial growth. This method eliminates the need for chemical etching of CdTe substrates which has been found to lead to an atomically rough surface with residual Carbon and Oxygen contamination. XRD and SEM characterization show a smooth transition from the buffer CdTe to re-grown CdTe layer with identical crystalline quality as for virtual wafer. Steady-state PL and time-resolved PL from CdTe/CdMgTe double heterostructures show substantial improvement in luminescence intensity and carrier lifetime comparable to values for identical samples grown without exposure to atmosphere. We will also report on CdTe/CdZnTe double heterostructures grown on virtual wafers compared to identical structures on conventional CdTe(2 1 1)B substrates.

© 2015 Elsevier B.V. All rights reserved.

1. Introduction

In CdTe-based solar cells, it is critical to have a low defect density absorber material to enhance minority carrier lifetime. Modeling studies have shown that single crystal CdTe solar cells have a potential to achieve efficiencies over 25% [1]. In order to enhance CdTe solar cell efficiency, it is necessary to increase the minority carrier lifetime as well as absorber carrier density [2]. The electrically-active absorber carrier density is directly correlated to material defect density [3,4]. These defects are as form of dislocations, twins, and anything else non-radiative, but they predominantly appear to be dislocations. In this work, we show how to significantly reduce defect densities and demonstrate the growth of test structures with high minority carrier lifetime in CdTe epitaxial films.

There have been extensive attempts to grow molecular beam epitaxial (MBE) CdTe films on CdTe substrates using different crystal orientations over a range of substrate temperature and Cd/Te flux ratio to improve the crystalline quality and reduce defect density. However these efforts have resulted in limited success and cannot reduce defect density below approximately $1 \times 10^6 \, \text{cm}^{-2}$ using currently available commercial CdTe substrates. Fig. 1 shows confocal photoluminescence (c-PL) images for a series of samples including a 1 µm thick CdTe grown on single crystal CdTe(2 1 1)B substrate. The Cd/Te flux ratio is one and is derived from direct thermal decomposition of CdTe using a single effusion cell. The substrate temperature was varied from 250 C to 300 C. Identical samples with different Cd/Te flux ratio in a range of 1.0 to 1.4 using an additional Cd effusion cell have also shown a similar trend with defect density values not less than $1 \times 10^6 \, \text{cm}^{-2}$. Table 1 shows a
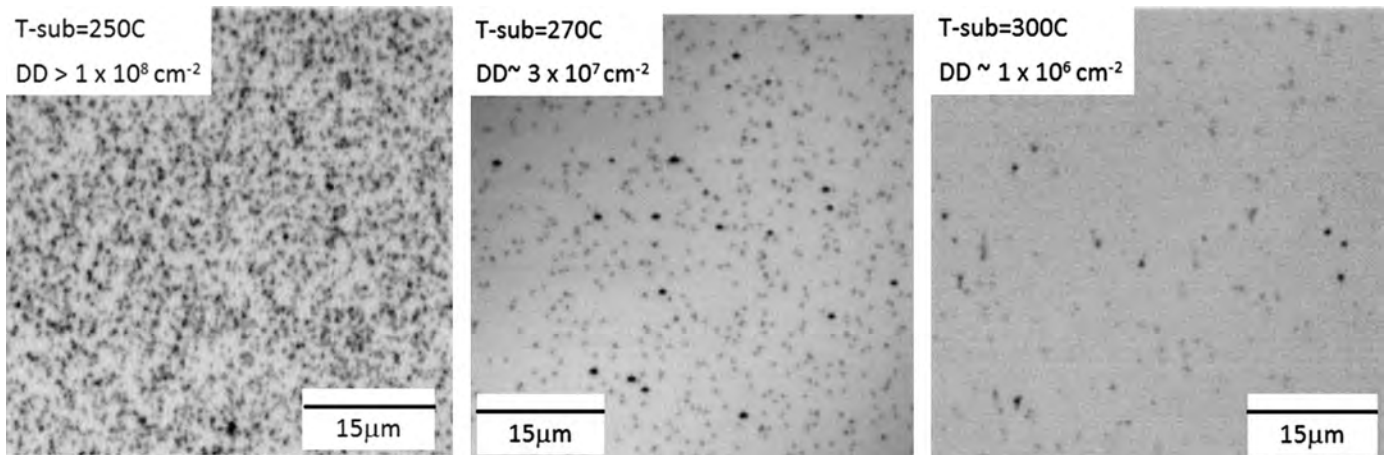
Fig. 1. Confocal PL images from buffer CdTe layer grown on CdTe(2 1 1)B substrates, showing correlation between defect density and substrate temperature at constant Cd/Te ratio of one.

Table 1
Defect density as a function of optimized CdTe growth condition on CdTe(2 1 1)B substrate. In best growth condition, defect density does not decrease below 10^6 cm^{-2}.

		Substrate temperature (C)		
		250	270	300
Cd/Te ratio	1.0	1×10^8	3×10^7	1×10^6
	1.2	2×10^7	3×10^7	5×10^6
	1.4	1×10^8	1×10^8	3×10^7

summary of defect density values for the whole matrix. These residual defect densities limit the minority carrier lifetime and optical characteristics of any structures grown on these CdTe wafers.

2. Experimental procedure

The growth of CdTe-on-InSb is carried out in two separate III–V and II–VI MBE chambers which are connected by a UHV transfer chamber. In the first step, an InSb buffer layer of about 600 nm is grown in the III–V chamber which is then transferred in-vacuo to the II–VI chamber to grow an epitaxial CdTe buffer layer. In the second step, the wafer is transferred back to the III–V chamber to deposit a thin As cap layer to protect the CdTe surface from oxidation. The next step of epitaxial growth can be performed either in this chamber or in an ex-vacuo II–VI MBE chamber. Crystalline and expitaxial quality were examined by rocking curve XRD and plan-view and cross-section SEM. Optical quality of the samples was measured by room temperature photoluminescence (PL) with a 660 nm excitation laser. Defect densities were measured using a laser scanning confocal photoluminescence (c-PL) system with a 0.25 μm resolution. Time-resolved photoluminescence (TRPL) was used to determine carrier lifetime.

2.1. Epitaxial re-growth of CdTe on CdTe/InSb(1 0 0) virtual wafers

MBE growth of CdTe on InSb(1 0 0) has been shown to be promising due to very small lattice mismatch between these two binary semiconductors [5] and easier surface preparation of InSb substrates. c-PL and XRD measurements show a high crystalline quality with low defect density in the re-grown CdTe layers on these substrates.

We consider two different methods to prepare the CdTe/InSb substrates before re-growth of the next CdTe layer. In the first approach, the sample is dipped in a diluted HCl mix with DI water,

followed by a sequence of DI water and Methanol rinse. The sample was then transferred into the MBE chamber where CdTe growth was performed after thermal desorption of the native oxide. This growth is determined to be epitaxial as the XRD from the CdTe layer lies over the CdTe peak from the starting CdTe/InSb(1 0 0) substrate, as indicted in Fig. 2(b). The peak broadening however indicates a degraded crystalline quality for the top CdTe layer. In fact, the interface between two CdTe layers is readily observable by cross-section SEM image shown in Fig. 2(a). We could improve the second CdTe epitaxial layer growth to obtain comparable crystalline quality to the starting CdTe/InSb wafer by optimizing chemical etch step and in-situ heat treatment for oxide desorption. However this process was not well repeatable in a series of identical growth runs.

In the second approach, we utilized the CdTe/InSb which included a 10 nm As cap layer to protect the CdTe surface from oxidation in atmosphere. The "CdTe virtual wafers" are prepared by growth of an InSb buffer layer on InSb(1 0 0) substrate in a III–V MBE chamber. The wafer is then transferred in-vacuo to the second II–VI MBE chamber for growth of CdTe buffer layer. The wafer is finally transferred back to the III–V MBE chamber for deposition of the As cap layer. This virtual wafer can be exposed to atmosphere at this point and stored in a N2 purged desiccator for subsequent epitaxial growths. A virtual wafer is then loaded into another MBE chamber for re-growth of a II–VI structure. Before MBE growth, the substrate is annealed at 300 C for 15 min to thermally desorb the oxidized As cap layer. No wet chemical treatment step is applied in this process.

Fig. 3(a and b) shows top view as well as cross-section image of the CdTe layer grown on a virtual wafer, after As desorption. No interface is observed between CdTe layer from the virtual wafer and the second epitaxial layer of CdTe indicating a clean transition between the two separately grown CdTe layers. The smooth top surface is comparable with the surface quality of the CdTe virtual wafer with no As cap layer. Fig. 3(c) shows the XRD from this sample. The peak from CdTe lays directly over the one from the virtual wafer with comparable FWHM indicating high crystalline quality of the second epitaxial CdTe layer. The average defect density measured by c-PL of the CdTe epitaxial layer grown on such a virtual substrate is in the low 2×10^5 cm^{-2}. One of the c-PL images is shown in Fig. 4 indicating a local defect density of less than 4×10^4 cm^{-2} as no defect was observed in this region of sample.

2.2. Epitaxial re-growth of CdTe/CdMgTe and CdTe/CdZnTe double heterostructures on CdTe/InSb(1 0 0) virtual wafers

Ternary II–VI group semiconductors have been studied in the past as electronic barrier material to confine carriers in CdTe due
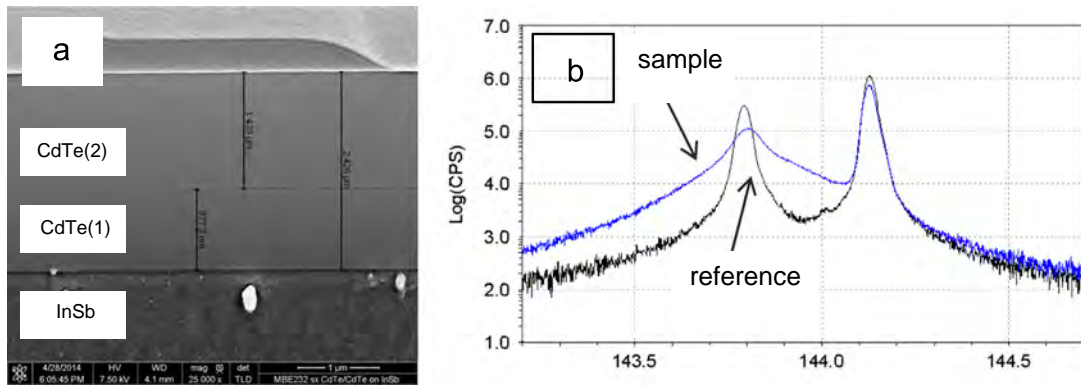
Fig. 2. (a) Cross section SEM of CdTe layer grown on a virtual wafer; an interface is observable between the two CdTe layers. The second layer of CdTe is grown after chemical treatment of a virtual wafer followed by conventional in-situ heat treatment pre-growth. (b) XRD shows some peak broadening due to degraded crystalline quality in second CdTe layer.
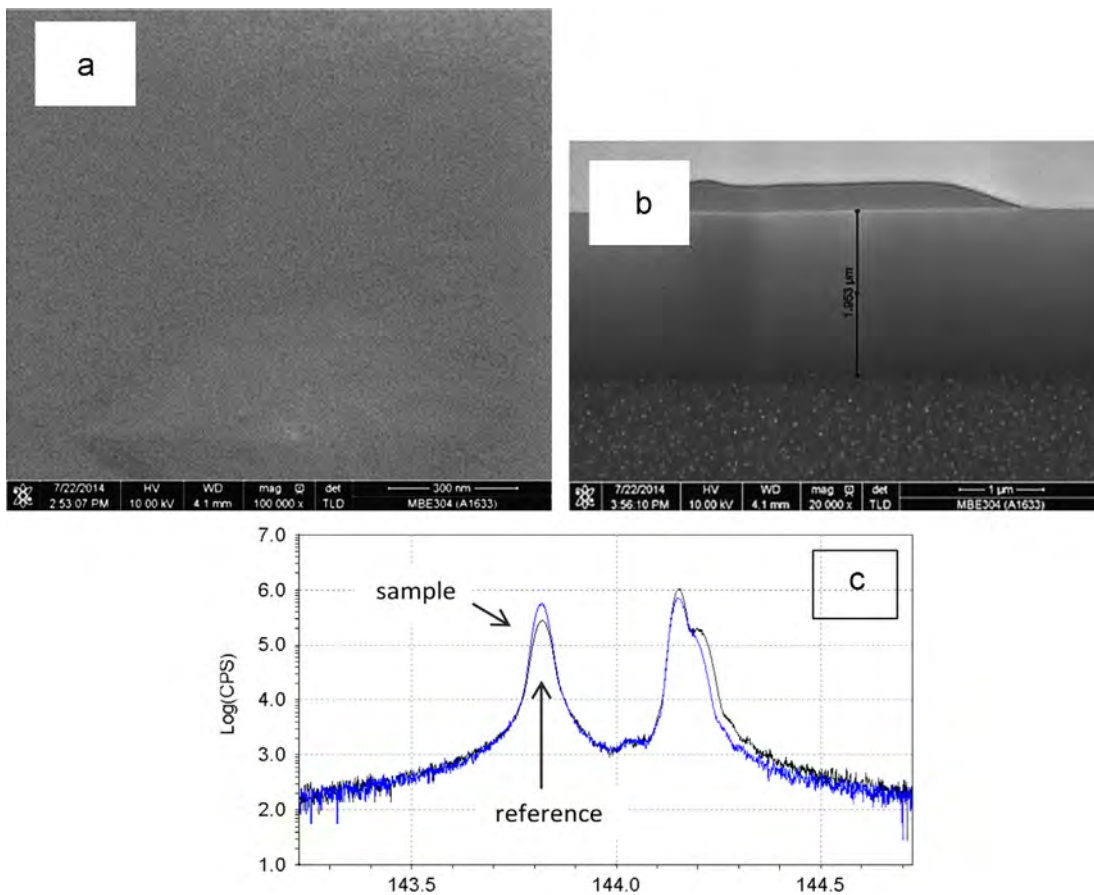
Fig. 3. (a) Plain-view SEM indicates a very smooth surface on top CdTe layer grown on a virtual wafer after As removal; (b) Cross section SEM from two epitaxial CdTe layers; second CdTe layer is grown after thermal in-situ removal of As cap; no interface is observable. (c) XRD scan from such a structure, compared to reference virtual wafer with identical FWHM shows an improved crystalline quality.

to their larger gap, band offset [6–9]. A previous study on CdTe/CdMgTe double heterostructures growth on InSb(1 0 0) substrates showed strong photoluminescence (PL) intensity and a long carrier lifetime of 86 ns [10]; the whole structure was grown in-vacuo without exposure to atmosphere. We grew a similar structure on a virtual wafer after in-situ As cap removal. After this step, a second CdTe buffer layer was grown which was followed by a CdTe/CdMgTe double heterostructure growth. A generic schematic of such a stack is shown in Fig. 5.

Fig. 6 shows comparison between strong PL intensity from this sample and a GaAs/AlGaAs double heterostructure reference sample. Also as shown in Fig. 7, TRPL measurement on this sample shows that

carrier lifetime is comparable with an identical structure grown on substrates without exposure to atmosphere. This further demonstrates the effectiveness of the As cap to protect CdTe surface from oxidation.

Fig. 8 shows comparison of PL intensity for double heterostructures using ternary CdZnTe and CdMgTe, both grown on virtual wafers, after in-situ removal of the As cap and re-growth of a second CdTe buffer layer. CdTe/CdMgTe double heterostructure shows about three orders of magnitude larger PL intensity compared to CdTe/CdZnTe double heterostructure, with the same CdTe absorber thickness of 1 μm. This can be explained based on the fact that for an equal mole fraction of Mg and Zn in a ternary CdXTe, CdMgTe has a relatively larger valence band offset and conduction band offset to
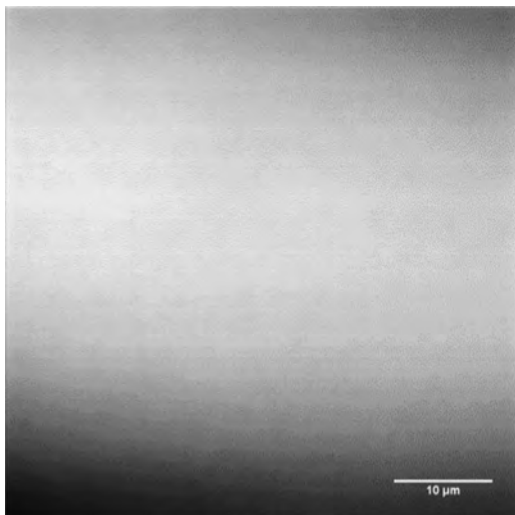
Fig. 4. Confocal-PL micrograph of CdTe grown on CdTe/InSb(1 0 0) substrate. No defects were observed in this region indicating a local defect density less than 4×10^4 cm^{-2}. Average defects density over the sample was 2×10^5 cm^{-2}.
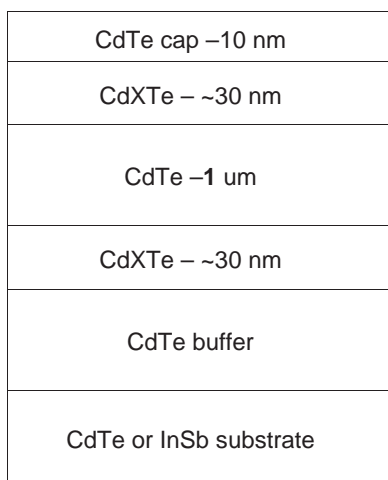
Fig. 5. Schematic stack of a CdTe/ternary CdXTe double heterostructure. X stands for Mg or Zn in this study.
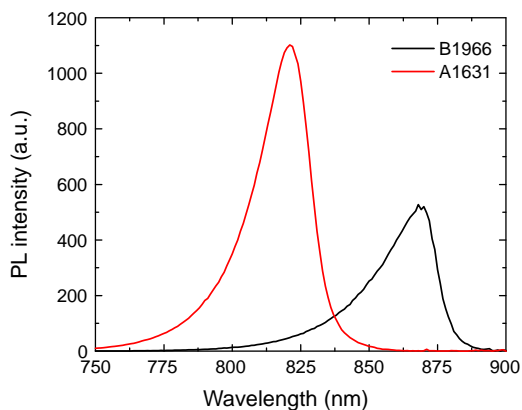
Fig. 6. Photoluminescence intensity comparison between a CdTe/MgCdTe double heterostructure grown on As capped CdTe/InSb virtual wafer, after As removal (A1631) and a GaAs/AlGaAs double heterostructure reference sample (B1966).

CdTe. This can be compared to CdZnTe which specifically has a much smaller valence band offset [6]. Therefore both electron and hole carriers are better confined within the CdTe layer between the ternary CdMgTe compared to the CdZnTe barriers. Furthermore, MgTe has a
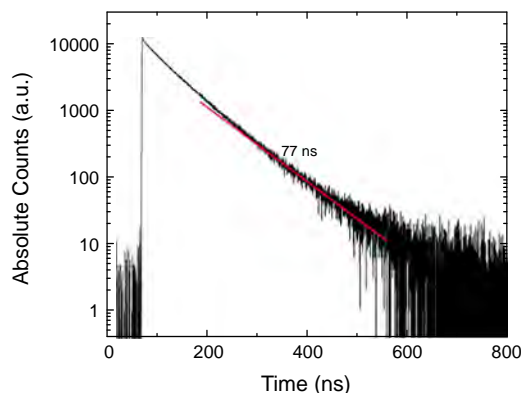
Fig. 7. Time-resolved photoluminescence measurement of a CdTe/MgCdTe double heterostructure grown on As capped CdTe/InSb virtual wafer, after As removal. The lifetime is 77 ns which is comparable to identical samples grown on CdTe/InSb substrates without exposure to atmosphere.
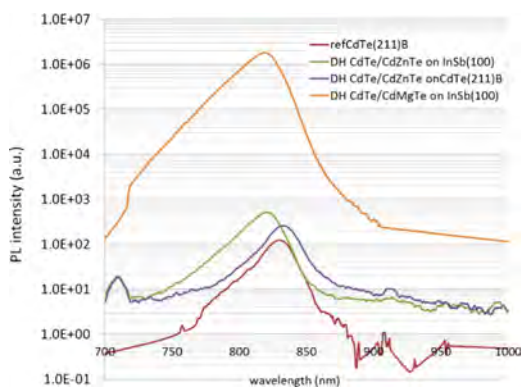
Fig. 8. Comparison of PL intensity for double heterostructures using ternary CdZnTe and CdMgTe.

significantly smaller lattice mismatch to CdTe (1.0%) compared to ZnTe (5.8%). A pseudomorphic layer of ternary CdXTe on CdTe with equal mole fraction of Zn and Mg has a larger strain in case of CdZnTe which is more likely to form strain-induced electronic defect states at heterojunction interfaces resulting in a larger surface recombination velocity. Experimentally, the CdTe/CdZnTe double heterostructure is not as effective as a CdTe/CdMgTe double heterostructure in confining carriers within the active CdTe region and it exhibits higher surface recombination velocity at the interfaces.

Fig. 8 also shows another PL signal from a CdTe/CdZnTe double heterostructure which was grown side by side to CdTe/InSb(1 0 0) virtual wafer but on a CdTe(2 1 1)B substrate. The structure grown on virtual wafer shows a relatively higher PL compared to the one grown on CdTe(2 1 1)B due to a lower level of defect density when using virtual wafer as was shown in previous section.

2.3. Issue with indium diffusion

We observed In diffusion from the substrate into epitaxial CdTe layer, as shown in Fig. 9. This is strongly correlated to the substrate temperature during the first layer of CdTe growth to form the virtual wafer. In diffusion from InSb substrate into CdTe has been reported before [11,12]. Diffusion of In is slower than what is predicted by Fick's law of diffusion [11]. This can be due to the fact that Fick's law assumes diffusion to take place in a static condition, while our experimental data is based on a dynamic epitaxial growth of CdTe [11]. In spite of this, diffusion extends into the CdTe top layer during the re-growth process. The spike in In concentration denotes the interface between the two CdTe layers. The In diffusion issue can be suppressed in both CdTe layers to some extent by
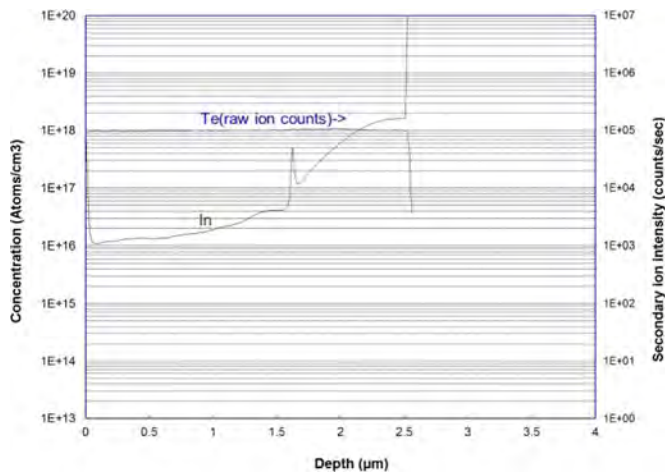
Fig. 9. SIMS profile shows indium diffusion from InSb substrate into epitaxial CdTe layer. Spike in profile indicates the interface between two CdTe layers, namely between virtual wafer and top (re-grown) CdTe layer, after As removal.

reducing the substrate temperature during growth. Further investigation is needed to fully control the In diffusion, as this can be a serious issue leading to residual In doping in epitaxial grown layers.

3. Conclusion

A new technique has been demonstrated to form CdTe virtual wafers for subsequent growth of CdTe in other MBE systems. The structure consists of a first InSb buffer layer grown on an InSb (1 0 0) substrate followed by the growth of a CdTe buffer layer and a final As cap layer to prevent the CdTe surface from oxidation. After thermal desorption of the As cap layer, the CdTe virtual wafer can be used to grow high quality CdTe heteroepitaxial films without the need for any chemical treatment of the wafer. Significant increase in PL intensity and carrier lifetime have been demonstrated in CdTe/CdMgTe double heterostructures grown on these CdTe virtual wafers. The characteristics of such samples are comparable to identical structures where the whole structure is grown in-vacuo, without exposure to atmosphere.

In diffusion from InSb substrate into the epitaxial layers is shown to be a dynamic process during the growth. This can result in unintentional In n-type doping that is an issue for growth of epitaxial films that require precise doping control. This In diffusion can be suppressed to some degree by reducing the substrate temperature during growth.

References

[1] A.P. Kirk, M.J. DiNezza, S. Liu, X.-H. Zhao, Y.-H. Zhang, in: Proceedings of the 39th IEEE Photovoltaic Specialists Conference, Tampa, FL, 16–21 June, 2013.
[2] T. Song, A. Kanevce, J.R. Sites, in: Proceeding of 40th IEEE Photovoltaic Specialists Conference, Denver, CO., 8–13 June, 2014.
[3] O. Astakhov, R. Carius, F. Finger, Y. Petrusenko, V. Borysenko, D. Barankov, Phys. Rev. B 79 (2009) 104205.
[4] J.J. Sheng, D. Leonhardt, S.M. Han, S.W. Johnston, J. Vac. Sci. Technol. 31 (2013) 051201–051208.
[5] T.D. Golding, M. Martinka, J.H. Dinan, J. Appl. Phys. 64 (1988) 1873.
[6] S.A. Nasrallah, S. Mnasri, N. Sfina, N. Bouarissa, M. Said, J. Alloys Compd. 509 (2011) 7677.
[7] Y.H. Kim, S.Y. An, J.Y. Lee, I. Kim, K.N. Oh, S.U. Kim, M.J. Park, J. Appl. Phys. 85 (1999) 7370.
[8] S.H. Cho, J.H. Suh, J.H. Won, K.H. Kim, J.K. Hong, S.U. Kim, Nucl. Instrum. Methods Phys. Res., Sect. A 591 (2008) 203.
[9] A. Waag, F. Fischer, Th. Litz, B.K. Heinrich, U. Zehnder, W. Ossau, W. Spahn, H. Heinke, G. Landwehr, J. Cryst. Growth 138 (1994) 155.
[10] M.J. DiNezza, X. Zhao, S. Liu, A.P. Kirk, Y.H. Zhang, Appl. Phys. Lett. 103 (2013) 193901.
[11] A.T.S. Wee, Z.C. Feng, H.H. Hng, K.L. Tan, R.F.C. Farrow, W.J. Choyke, J. Phys. Condens. Matter 7 (1995) 4359.
[12] M. Kimata, T. Suzuki, K. Shimomura, M. Yano, J. Cryst. Growth 146 (1995) 433.
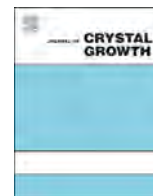
Growth and optical properties of ZnTe quantum dots on ZnMgSe by molecular beam epitaxy

W.C. Fan [a], S.H. Huang [a], W.C. Chou [a,*], M.H. Tsou [a], C.S. Yang [b], C.H. Chia [c], Nguyen Dang Phu [d], Luc Huy Hoang [d]

[a] Department of Electrophysics, National Chiao Tung University, HsinChu 30010, Taiwan, ROC
[b] Graduate Institute of Electro-Optical Engineering, Tatung University, Taipei 104, Taiwan, ROC.
[c] Department of Applied Physics, National University of Kaohsiung, Kaohsiung 81148, Taiwan, ROC
[d] Department of Physics, Hanoi National University of Education, 136 Xuanthuy Caugiay, Hanoi, Vietnam

ABSTRACT

Self-assembled type-II ZnTe quantum dots (QDs) were grown on GaAs (0 0 1) substrates with $Zn_{1-x}Mg_xSe$ ($x=0.24$ and 0.52) buffer layers by molecular beam epitaxy. The optical properties of ZnTe QDs were investigated by low-temperature photoluminescence (PL) and time-resolved PL. An abrupt variation of the PL peak energy with coverage implies the existence of wetting layer of 3.2 MLs and 4.0 MLs for the Mg concentration $x=0.24$ and 0.52, respectively. The thickness of wetting layer is larger than that of ZnTe QDs grown on ZnSe buffer layers because the strain between ZnTe and $Zn_{1-x}Mg_xSe$ is smaller. The non-mono-exponential decay profiles reflect the processes of carrier transfer and recapture. The Kohlrausch's stretching exponential well fits the decay profiles of ZnTe/$Zn_{1-x}Mg_xSe$ QDs.

© 2015 Elsevier B.V. All rights reserved.

1. Introduction

Compared with quantum dots (QDs) of type-I band alignment, type-II QDs exhibit unique physical properties. The interesting physical property of optical Aharonov–Bohm effect was observed in type-II ZnTe/ZnSe QDs [1,2]. Type II InAs/GaAs/GaAs$_{0.82}$As$_{0.18}$ QDs of long lifetime could be used for the application of high efficiency absorber in solar cell [3]. The formation of robust magnetic polaron was investigated in the ZnMnTe/ZnSe QDs [4]. However, the self-assembled QDs inevitably encounter the problem of size non-uniformity for the potential device application. The thickness of the wetting layer of the ZnMnTe/ZnSe QDs grown by the Stranski–Krastanov growth mode is fixed at 2.4 monolayers (MLs). In order to control the wetting layer thickness, dot size, dot density and the dot size uniformity, ZnTe QD structures were grown on $Zn_{1-x}Mg_xSe$ by molecular beam epitaxy (MBE). When parts of Zn atoms of ZnSe were replaced by Mg atoms to crystallize as $Zn_{1-x}Mg_xSe$, the lattice constant increases because of Mg having larger ionic radius than that of Zn atom. Therefore, the manipulation of Mg concentration (x) offers an extra degree of freedom to control the lattice mismatch between ZnTe and

$Zn_{1-x}Mg_xSe$ and to adjust the wetting layer thickness, dot size and dot density.

2. Experimental methods

The samples studied in this paper were grown on GaAs (1 0 0) substrates by MBE system. Prior to the growth procedure, GaAs (1 0 0) substrates were etched in the NH$_4$OH:H$_2$O$_2$:H$_2$O (5:1:50) solution for two minutes at room temperature, rinsed in flowing deionized water about two minutes and dried with high purity N$_2$. Desorption and growth procedures were monitored by the reflection high energy electron diffraction (RHEED). The growth processes of ZnTe QDs started with the deposition of $Zn_{1-x}Mg_xSe$ buffer layer, and the alternating supply method of ZnTe growth. The coverage of the single ZnTe QDs layer, grown on the flat $Zn_{1-x}Mg_xSe$ buffer layer, was varied from 2.4 to 4.4 MLs for $Zn_{1-x}Mg_xSe$ buffer layer of $x=24\%$ and 3.0 to 6.0 MLs for $x=52\%$. Finally, $Zn_{1-x}Mg_xSe$ capping layer was grown on the QDs for optical measurements. Samples were also grown without $Zn_{1-x}Mg_xSe$ capping layer for the morphology study using atomic force microscopy (AFM). The growth conditions of the ZnTe QDs on $Zn_{1-x}Mg_xSe$ were listed in Table 1. The ZnTe/$Zn_{1-x}Mg_xSe$ QDs with Mg concentration 24% and 52% are noted as series A and series B, respectively. The cell temperatures of Zn, Te and Se were set to 270 °C, 330 °C and 180 °C, respectively. The cell temperatures of Mg were 325 °C ($x=24\%$) and 360 °C ($x=52\%$).

* Corresponding author. Tel.: +886 3 571 2121; fax: +886 3 572 5230.
E-mail address: wuchingchou@mail.nctu.edu.tw (W.C. Chou).

The substrate surface temperature was maintained at 320 °C throughout the growth of the QDs. The Mg concentration was determined by energy dispersive X-ray diffraction using a $Zn_{1-x}Mg_xSe$ epilayer grown under the same conditions as the QDs structures.

The excitation source for conventional PL spectroscopy was a 325 nm-line of an He–Cd laser and the emissions were analyzed using a Horiba-Jobin Yvon iHR550 (1800 grooves/mm grating) spectrometer with a liquid nitrogen cooled CCD detector. For the excitation of time-resolved PL, the GaN 377 nm pulsed laser diode was used. The peak power of the pulse was estimated to be below 0.1 mW. The time-resolved PL spectra were analyzed using a high-speed photomultiplier tube. The overall time resolution of the detection system was about 300 ps.

3. Results and discussion

Fig. 1 shows the RHEED pattens (left) and AFM images (right) taken for the ZnTe QDs grown on ZnSe when the ZnTe coverages are 0, 1.8, 2.5, and 2.8 MLs. A clear transformation of the RHEED pattern from streaky to spotty, indicative of the onset of Stranski–Krastanow (SK) growth mode, could be observed when the coverage is above the critical thickness. The results from the RHEED patterns are further supported by the AFM images, clear QD formation starts when the effective thickness (coverage) of ZnTe is above 2.5 MLs. For the case of ZnTe QDs grown on $Zn_{1-x}Mg_xSe$, the RHEED patterns and AFM images are similar except that the critical thickness increases with increasing Mg concentration x.

Table 1
Coverage of the ZnTe QDs in different $Zn_{1-x}Mg_xSe$ matrices.

$Zn_{1-x}Mg_xSe/ZnTe/Zn_{1-x}Mg_xSe$			
$x=0.24$	Coverage	$x=0.52$	Coverage
A1	2.4 MLs	B1	3.0 MLs
A2	2.8 MLs	B2	3.5 MLs
A3	3.2 MLs	B3	4.0 MLs
A4	3.6 MLs	B4	4.5 MLs
A5	4.0 MLs	B5	5.0 MLs
A6	4.4 MLs	B6	6.0 MLs

Similar result was also observed for the CdTe QDs grown on $Zn_{1-x}Mg_xTe$ by F. Tinjod et al. [5].

Fig. 2 shows the low-temperature PL spectra of series A, ZnTe QDs on $Zn_{0.76}Mg_{0.24}Se$ with different values of ZnTe coverage thickness from 2.4 to 4.4 monolayers. The PL band between the spectral ranges of 2.9–3.1 eV is the near band edge emission (NBE) of $Zn_{1-x}Mg_xSe$ layers. The low-energy emission band (2.0–2.5 eV)
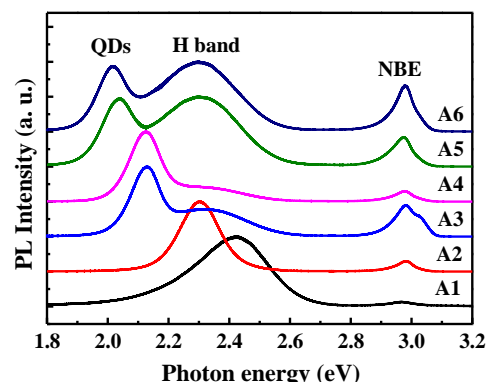
Fig. 2. PL spectra of ZnTe QDs on $Zn_{0.76}Mg_{0.24}Se$ with different ZnTe coverages.
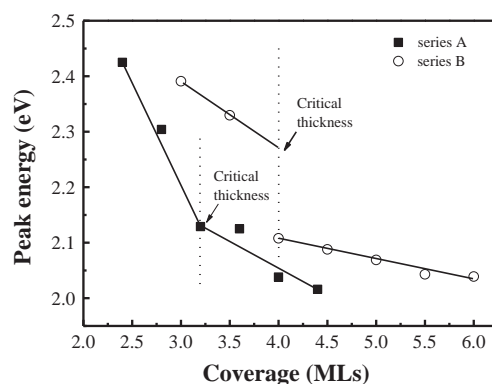
Fig. 3. PL emission peak energy of QD as a function of ZnTe coverage. Solid squares for ZnTe QDs self-assembled on $Zn_{0.76}Mg_{0.24}Se$; open circles for ZnTe QDs self-assembled on $Zn_{0.46}Mg_{0.52}Se$.
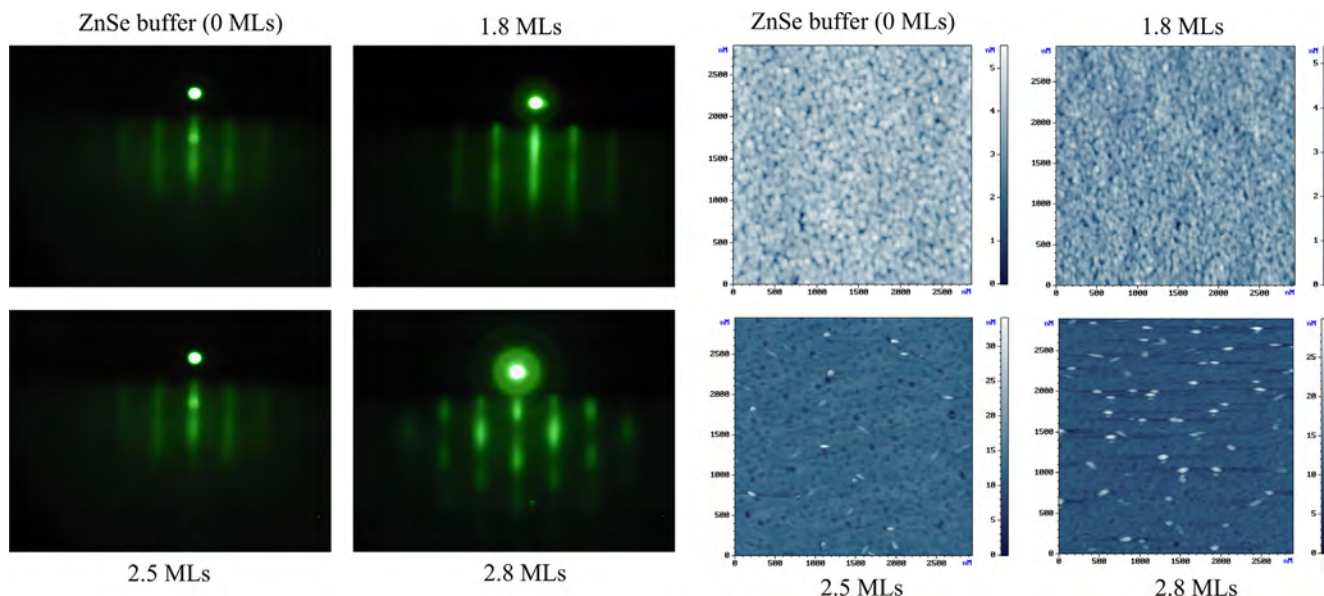
Fig. 1. RHEED pattens (left) and AFM images (right) taken when the ZnTe coverages are 0, 1.8, 2.5, and 2.8 MLs.

is due to the radiative recombination from QDs, because the corresponding PL peak energy is more sensitive to the change of coverage, as compared with the high-energy emission band noted as H in Fig. 2. The H emission remains constant after the dot-formation, but slightly redshifts when QDs start to form. This phenomenon is similar to the case of the two-dimensional platelet observed in the ZnMnTe QDs self-assembled on ZnSe by our previous study [6] and in CdTe QDs on ZnTe by Mackowski

et al. [7]. The red-shift in QDs emission is attributed to the decrease in the quantum confinement of holes in ZnTe.

There exists a critical coverage at 3.2 MLs, judging from the two different red-shift slopes for the QD emission energy versus the ZnTe coverage for ZnTe QDs self-assembled on $Zn_{0.76}Mg_{0.24}Se$, as shown by the solid squares in Fig. 3. The emission energy initially red-shifts with the coverage abruptly and followed by a gentle red-shift. This is a signature of the change from the two dimensional (2-D) layer growth to 0-D QD formation for type II ZnTe QDs self-assembled on ZnMgSe in current study and also ZnMnTe QDs self-assembled on ZnSe in our previous report [6]. On the other hand, for type I CdSe QDs self-assembled on ZnSe, because both electron and hole are confined in CdSe QD, the emission energy initially red-shifts slowly and then becomes more pronounced when the coverage is above 2.5 MLs [8]. The variation of emission energy with ZnTe coverage for ZnTe QDs self-assembled on high Mg concentration $Zn_{0.48}Mg_{0.52}Se$ is shown by the open circles in Fig. 3. The critical coverage for the change of red-shift slope is about 4.0 MLs, which is slightly larger than that of ZnTe QDs self-assembled on $Zn_{0.76}Mg_{0.24}Se$. It is due to the smaller lattice mismatch between ZnTe and $Zn_{0.48}Mg_{0.52}Se$ than that between ZnTe and $Zn_{0.76}Mg_{0.24}Se$. This result illustrates that the thickness of the 2D wetting layer between ZnTe and $Zn_{1-x}Mg_xSe$ can be manipulated by the control of Mg concentration x.

Fig. 4. FWHM change in the QDs by different coverages of ZnTe.
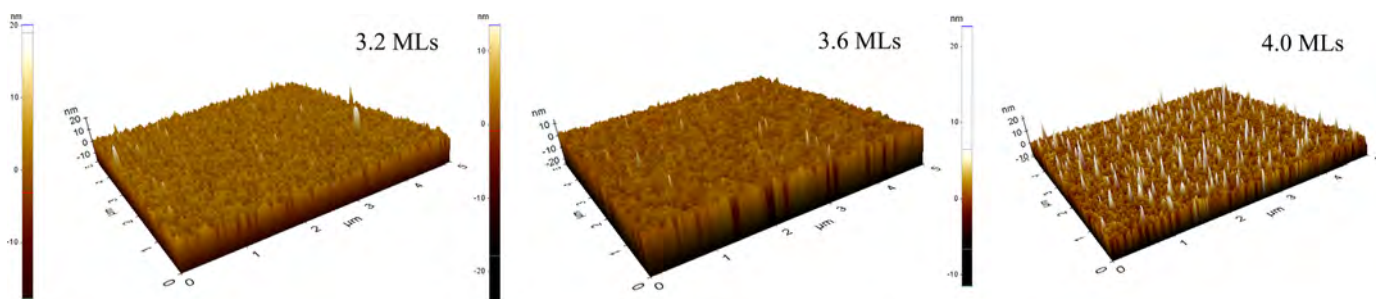
Fig. 5. AFM images of ZnTe QDs on $Zn_{0.76}Mg_{0.24}Se$.
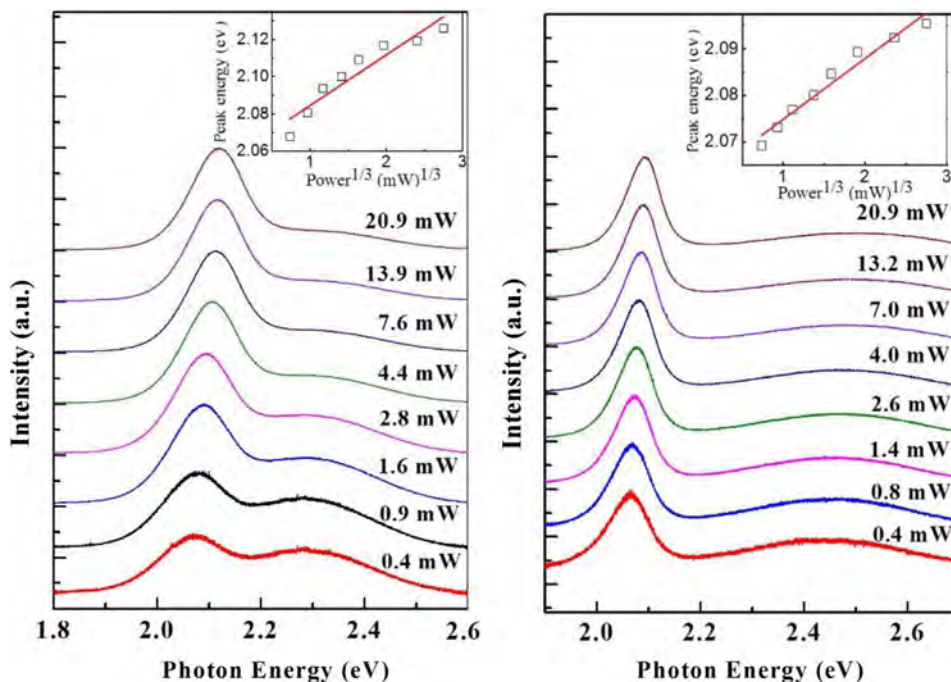
Fig. 6. PL spectra at various excitation powers: (a) for the sample A4 and (b) for the sample B4.

In Fig. 4, the full width at half maximum (FWHM) from the PL spectra of the ZnTe QDs on $Zn_{0.76}Mg_{0.24}Se$ and ZnTe QDs on $Zn_{0.48}Mg_{0.52}Se$ versus the ZnTe coverage are shown by the solid squares and open circles, respectively. This figure shows that all the values of FWHM in series B are smaller than that of series A. It implies that the dots size distribution in series B is more uniform than in series A. The result is similar to GeSi/Si QDs [9], which shows that the uniformity of dots improves with the decreasing mismatch between the buffer layer and QDs.

In order to study the morphology, size distribution, and dot density, the AFM images of 3.2 MLs, 3.6 MLs, and 4.0 MLs QDs on $Zn_{0.76}Mg_{0.24}Se$ are shown in Fig.5. The average height (H) and diameter (D) are 6 nm, 7 nm, 8 nm and 50 nm, 57 nm, 80 nm for the 3.2 MLs, 3.6 MLs, and 4.0 MLs samples, respectively. It confirms that dots self-assemble when the coverage of ZnTe over 3.2 MLs and also corroborates with the result obtained from two different red-shift slopes in Fig. 3. Both the size and density of QDs increases with increasing coverage of ZnTe. The densities of QDs in the samples are about the order of $10^8/cm^2$. In addition the non-uniformity, variation in height, increases with the ZnTe coverage. This also reflects the increasing FWHM of PL with ZnTe coverage from Fig. 4. Because, the PL emission energy is dominantly determined by the quantum confinement in height, which is much smaller than the diameter, the non-uniformity in height results the broadening in PL spectra.

In order to confirm the type-II emission nature of the ZnTe QDs on $Zn_{1-x}Mg_xSe$, the PL spectra under various excitation powers are shown in Fig. 6(a) and (b) for the samples A4 and B5, respectively. The PL bands blue-shift as excitation power increases. The emission peak energy linearly depends on the cubic root of the excitation power, as shown in the insets of Fig. 6. This phenomenon is caused by the band-bending effect at the hetero-interfaces [10] and is a fingerprint of the type II quantum structures. As the excitation density was increased, an increase in population of spatially confined electron–hole pairs enhanced the band-bending effect at the hetero-interfaces. In Fig. 6, there is no obvious PL band broadening with the increasing excitation power. It implies that the blue-shift of PL emission peak due to band filling effect can be excluded.

The transitions in type-II quantum structures show longer radiative lifetime than those of type-I quantum structures because of smaller overlap of electron–hole wave-functions [11]. The time-resolved PL (TRPL) measurements were carried out to study the carrier recombination dynamics in the type-II ZnTe/$Zn_{1-x}Mg_x$Se QDs. The temporal dependence of decay characteristics, detected at their PL peak energies, for ZnTe/$Zn_{0.76}Mg_{0.24}Se$ QDs of different ZnTe coverages is shown in Fig. 7. The decay profiles revealed non-single-exponential decays and could be better fitted by two components. The fast component was a mono-exponential decay, while the
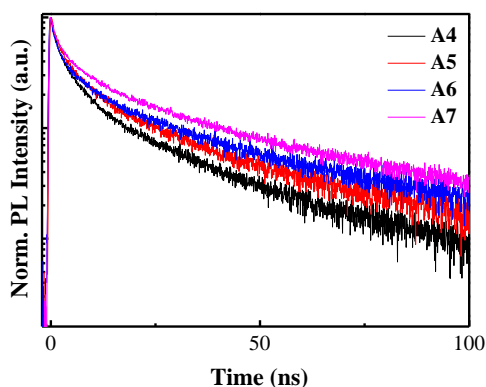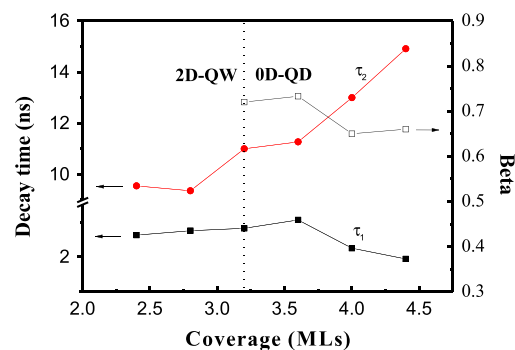
Fig. 8. Coverage dependences of decay times and β values obtained from the decay profiles of Fig. 6 using the profile fitting of Eq. (1).

slow component was a stretched-exponential decay. The decay curves were fitted using the following equation:

$$I_{PL}(t) = I_1 \exp(-t/\tau_1) + I_2 \exp(-(t/\tau_2)^\beta),$$ (1)

where $I_{PL}(t)$ is the PL intensity at time t, I_1 and I_2 are the relative intensity for fast component and slow component. τ_1 and τ_2 are lifetimes of the two different recombination mechanisms. β is the stretching parameter ($0 < \beta \leq 1$). The best fit yields that the decay time τ_1 is about 2–3 ns for all samples and the decay time τ_2 increases with the ZnTe coverage from 10 to 15 ns. τ_1 describes the transient dynamics for carriers relaxing to QDs after the excitation. The longer time τ_2 is due to the recombination of spatially separated electron and hole after the electrons and holes are in equilibrium.

Fig. 8 shows the coverage dependences of decay times (τ_1, τ_2) and β values. The value of β always decreases and τ_2 increases with increasing thickness of ZnTe. The increase in ZnTe coverage results in the enlarged size of QDs. The larger dot size further separates the electron and hole and reduces the wave-function overlapping, which increases recombination decay time. In addition, the increase in ZnTe coverage also increases QD density. The more QDs of different sizes offer more recombination channels. For the shallow (smaller) QDs, holes could be thermally activated and transfer to the neighboring lager QDs of lower energy. As a result, the decay profiles could not be simulated by the simple single exponential $\beta=1$. The increasing ZnTe coverage and dot density caused the decreasing of stretching exponent β [12]. We also monitored the decay profiles at the emission energy of the 2-D wetting layers. The TRPL-results show that the decay time of the wetting layer is shorter than the decay time of the QDs.

4. Conclusion

Self-assembled type-II ZnTe QDs were grown on GaAs (0 0 1) substrates with $Zn_{1-x}Mg_xSe$ ($x=0.24$ and 0.52) buffer layers by molecular beam epitaxy. Current study achieves the control of the critical thickness of Stranski–Kastonov ZnTe/$Zn_{1-x}Mg_xSe$ QDs from 3.2 to 4.0 MLs by manipulate the Mg concentration from $x=0.24$ to 0.52. The PL decay profiles were well correlated by the Kohl-rausch's stretched exponential to demonstrate the hole activation from smaller QDs followed by the transfer and re-capture to larger QDs.

Fig. 7. The decay profiles of the PL signal, detected at their PL peak energies, from ZnTe QDs on $Zn_{0.76}Mg_{0.24}Se$ with different ZnTe coverages.

References

[1] I.R. Sellers, V.R. Whiteside, I.L. Kuskovsky, A.O. Govorov, B.D. McCombe, Phys. Rev. Lett. 100 (2008) 136405.
[2] I.R. Sellers, V.R. Whiteside, A.O. Govorov, W.C. Fan, W.C. Chou, I. Khan, A. Petrou, B.D. McCombe, Phys. Rev. B 77 (2008) 241302.
[3] K. Nishikawa, Y. Takeda, T. Motohiro, D. Sato, J. Ota, N. Miyashita, Y. Okada, Appl. Phys. Lett. 100 (2012) 113105.
[4] I.R. Sellers, R. Oszwałdowski, V.R. Whiteside, M. Eginligil, A. Petrou, I. Zutic, W.C. Chou, W.C. Fan, A.G. Petukhov, S.J. Kim, A.N. Cartwright, B.D. McCombe, Phys. Rev. B 82 (2010) 195320.
[5] F. Tinjod, S. Moehl, K. Kheng, B. Gilles, H. Mariette, J. Appl. Phys. 95 (2004) 102.
[6] M.C. Kuo, J.S. Hsu, J.L. Shen, K.C. Chiu, W.C. Fan, Y.C. Lin, C.H. Chia, W.C. Chou, M. Yasar, R. Mallory, A. Petrou, H. Luo, Appl. Phys. Lett. 89 (2006) 263111.
[7] S. Mackowski, G. Prechtl, W. Heiss, F.V. Kyrychneko, G. Karczewski, J. Kossut, Phys. Rev. B 69 (2004) 205325.
[8] Y.J. Lai, Y.C. Lin, C.B. Fu, C.S. Yang, C.H. Chia, D.S. Chuu, W.K. Chen, M.C. Lee, W.C. Chou, M.C. Kuo, J.S. Wang, J. Cryst. Growth 282 (2006) 338.
[9] G. Abstreiter, P. Schittenhelm, C. Engel, E. Silveira, A. Zrenner, D. Meertens, W. Jager, Semiconduct. Sci. Technol. 11 (1996) 1521.
[10] N.N. Ledentsov, J. Böhrer, M. Beer, F. Heinrichsdorff, M. Grudmann, D. Bimberg, S.V. Ivanov, B. Ya., S.V. Meltser, I.N. Shaposhnikov, N.N. Yassievich, P.S. Faleev, Kop'ev, Zh.I. Alferov, Phys. Rev. B 52 (1995) 14058.
[11] Jai Verma, S.M. Islam, Vladimir Protasenko, Prem Kumar Kandaswamy, Huili Xing, Debdeep Jena, Appl. Phys. Lett. 104 (2014) 021105.
[12] B. Sturman, E. Podivilov, M. Gorkunov, Phys. Rev. Lett. 91 (2003) 176602.
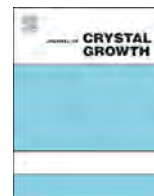
Control of domain orientation during the MBE growth of ZnTe on *a*-plane sapphire

T. Nakasu [a,*], T. Aiba [a], S. Yamashita [a], S. Hattori [a], W. Sun [a], K. Taguri [a], F. Kazami [a], M. Kobayashi [a,b], T. Asahi [c]

[a] *Waseda University, Department of Electrical Engineering and Bioscience, 3-4-1 Okubo Shinjuku, Tokyo 169-8555, Japan*
[b] *Waseda University, Kagami Memorial Research Institute for Materials Science and Technology, 2-8-26 Nishiwaseda, Shinjuku, Tokyo 169-0051, Japan*
[c] *JX Nippon Mining & Metals Corporation, Technology Development Center, 187-4, Usuba, Hanakawa-cho, Kitaibaraki 319-1535, Japan*

ARTICLE INFO

ABSTRACT

ZnTe epilayers were grown on transparent *a*-plane (11–20) sapphire substrates by molecular beam epitaxy (MBE). The insertion of a low-temperature nucleated buffer layer was carried out, and the influence of the buffer layer annealing prior to the film growth on crystallographic properties of the epilayer was investigated. Pole figure imaging and wide-range reciprocal space mapping (RSM) measurements were used to study the domain distribution within the layer, and epitaxial relationships between the ZnTe thin films and the sapphire substrates. The orientation of ZnTe domains formed on *a*-plane sapphire substrates was controlled by the annealing condition of the buffer layer. Two different {111} domains were formed from the sample the buffer layer was annealed at 350 °C, while (100) layers were obtained from the sample the buffer layer was annealed at 300 °C. These crystallographic features were probably originated from the atom arrangements of ZnTe and sapphire at the interface.

1. Introduction

Zinc-based II–VI compound semiconductors (e.g., ZnS, ZnSe and ZnTe) can be applied to optoelectronic devices such as light emitting diodes [1–3], UV sensors [4–6], waveguides [7–10], photovoltaic solar cells [11,12], and terahertz device applications [13,14]. ZnTe is one of the II–VI semiconductors that present good electrooptic (EO) properties with a direct optical band gap of 2.2–2.3 eV at room temperature, and high transparency in the visible spectral domain. To obtain a high EO effect from ZnTe, thin films with either (110) or (111) orientation are preferred [15,16]. Sapphire is an advantageous substrate for EO device structures using ZnTe thin films because it is a transparent material and simplifies the alignment of the optical path in the resulting device applications. Therefore, sapphire is a feasible substrate material choice for this device application.

In our previous study, ZnTe layers have been grown on various sapphire substrate surfaces by molecular beam epitaxy (MBE), and it was found that the arrangement of atoms on the sapphire's surface has affected the crystallographic orientation [17–22]. It was revealed that the (111)-oriented ZnTe layer was grown on the *c*-plane of sapphire substrates [18], and the (211)-oriented ZnTe layer was grown on the *m*-plane sapphire [19–22]. Improvement

of the ZnTe epilayer quality grown on the sapphire substrate by the insertion of thin buffer layers between the substrate and the epilayer was also reported in previous works [18–19,22]. ZnTe epilayers with reduced numbers of domains could be grown on *c*-plane sapphire substrates by tuning the buffer layer growth conditions (e.g., the layer thickness, the annealing time, and the annealing temperature) [18]. These studies were carried out by using an X-ray diffraction (XRD) pole figure imaging analysis, which was revealed to be a powerful method for ZnTe epilayers on sapphire substrates [17–22].

In this study, we focus on the growth of the ZnTe epilayer on the *a*-plane (11–20) sapphire substrate. Based on the previously obtained data, the *a*-plane of sapphire will cause the formation of the (110) oriented ZnTe layer since the *c*-plane in the sapphire substrate would be parallel to (111) plane of ZnTe and the *m*-plane in the sapphire substrate would be parallel to (211) plane of ZnTe. A single-domain ZnTe layer was sought on the *a*-plane sapphire substrate by tuning the buffer layer growth conditions (annealing condition of the buffer layer). Epitaxial relationships between the ZnTe epilayers and the *a*-plane sapphire substrates were studied via XRD pole figure measurements. In addition to the pole figure analysis, an XRD reciprocal space mapping (RSM) was employed to characterize the orientation relationship of the heterostructure. The RSM was used to evaluate the degree of the lattice mismatch strain relaxation in the MBE grown samples. The crystal quality, especially at the heterointerface region, was observed by the cross sectional TEM (JEOL JEM-2100F).

2. Experiments

ZnTe thin films were grown on *a*-plane sapphire substrates (Kyocera) in an MBE system (V80H; VG). Elemental Zn (6N super; Osaka Asahi Metal) and Te (6N super; Osaka Asahi Metal) were used as source materials. Sapphire substrate surface was cleaned using organic solvents at room temperature and was then introduced to the growth chamber. A 3.5 nm thick ZnTe layer buffer was deposited at 100 °C, and the annealing was performed for 5 min with varying the temperature between 300–350 °C. The substrate temperature during ZnTe growth was maintained at 340 °C. The growth rate and the film thickness were kept constant at 0.5 μm/h and 1 μm respectively.

The XRD pole figures were collected using a Rigaku Smart-Lab system [23]. In this instrument, the X-ray beam is focused on a sample located at the center of an Eulerian cradle, which provides four degrees of positioning freedom (2θ, ω, χ, and ϕ). In this study, pole figure measurement was performed wherein the diffraction angle 2θ is maintained at the diffraction of 111 ZnTe and 11–20 sapphire to analyze the relationship between the epilayer and the substrate, and the diffraction intensity was collected while two geometrical parameters are varied, such as the tilt angle (χ) from the sample surface normal and the rotation angle (ϕ) about the sample surface normal direction. The in-plane configuration was also used for this study. The origin of the pole figure image was aligned to the *a*-plane sapphire substrate orientation, and the
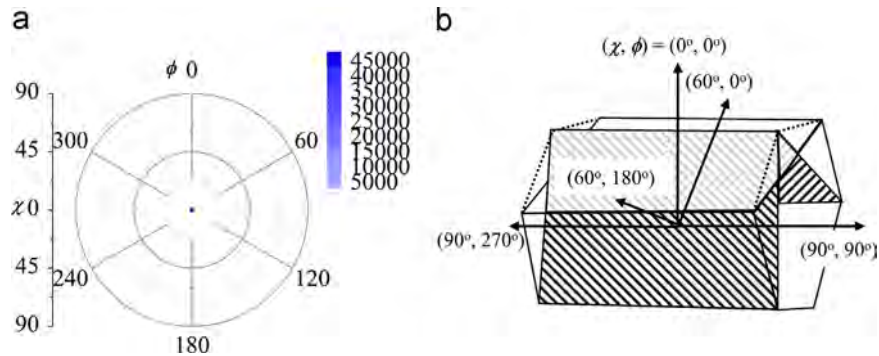
Fig. 1. (a) Pole figure of 11–20 sapphire reflection for a ZnTe/*a*-plane sapphire substrate sample, and (b) defined directions corresponding to the pole figure.
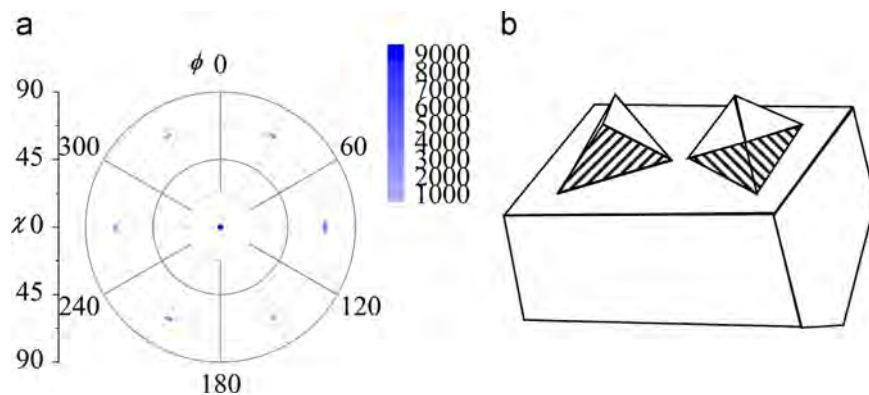
Fig. 2. (a) Pole figure of 111 ZnTe diffraction for the ZnTe/*a*-plane sapphire substrate sample, and (b) a schematic image of the two different {111} ZnTe domains formed on the *a*-plane sapphire lattice.
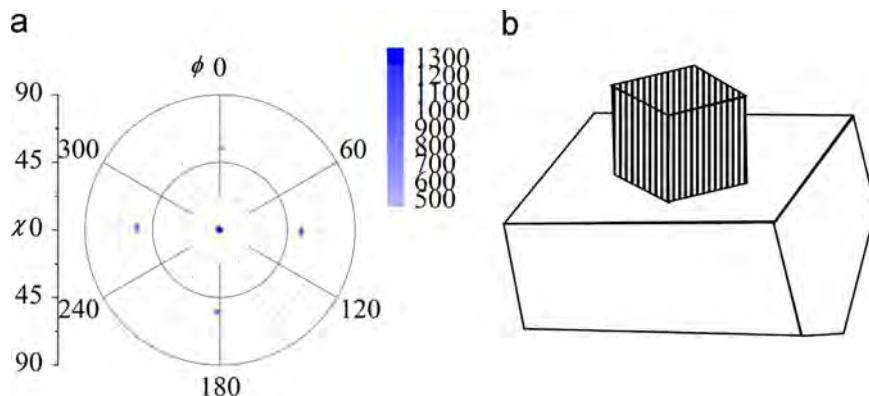
Fig. 3. (a) Pole figure of 111 ZnTe diffraction for another ZnTe thin film grown on the *a*-plane sapphire substrate, and (b) a schematic image of the (100) domain formed on the *a*-plane sapphire lattice.

common ϕ was obtained by measuring both ZnTe and sapphire diffraction signals without unmounting the sample. By comparing diffraction signal positions from the substrate with those from the epilayer, the crystallographic relationships were analyzed using the same (χ, ϕ).

The X-ray RSM was also conducted for the characterization of orientational relationships between the ZnTe epilayer and the *a*-plane sapphire substrate. The conventional RSM measurement uses ω-shift and $2\theta/\omega$ scan, and limited in a certain angular range. In this paper, the X-ray RSMs of wide angular ranges was performed employing a 2D detector (PILATUS; RIGAKU) instead of a 0-dimensional scintillation detector. The wide-range RSM data was obtained by χ steps and $2\theta/\omega$ scans. The 2D data could be shown either in the goniometer coordinates (the two coordinate axes χ angle and 2θ angles) or in the reciprocal space coordinates. Two axes of wide-range RSMs are employed in a scale of the reciprocal unit, those are the direction along the substrate surface plane and the direction normal to the substrate surface plane [23].

3. Results and discussion

A pole figure based on the diffraction peaks of 11–20 sapphire is shown in Fig. 1(a), and two peaks are observed at $(\chi, \phi)=(60°, 0°)$ and $(60°, 180°)$. Based on these peak positions, the (χ, ϕ) of the ZnTe/*a*-plane sapphire substrates were defined (as shown in Fig. 1(b)). It revealed that the sapphire's *c*-plane directions were located at $\phi=90°$ and $270°$. When the ZnTe layer was grown on a buffer layer that was annealed at 350 °C (Fig. 2(a)), a six-fold rotational symmetry pattern with diffraction peaks at $(\chi, \phi)=(0°, 0°)$, $(70°, 30°)$, $(70°, 90°)$, $(70°, 150°)$, $(70°, 210°)$, $(70°, 270°)$, and $(70°, 330°)$, was observed from a pole figure generated using 111 diffraction peaks of ZnTe. The sharpness of the signal originated from ZnTe suggested the high degree of crystallographic quality. The pattern was analyzed and two kinds of ZnTe {111} domains were formed on the *a*-plane sapphire; two different domains were rotated by 60° relative to each other [17]. The signal intensities from these two domains were approximately equal. It was therefore concluded that two kinds of {111}-oriented ZnTe domain with a similar ratio were formed on the *a*-plane sapphire. Because the diffraction peaks of {111} ZnTe were located on the line of the sapphire *c*-axis ($\phi=0°$ and $180°$), the {111} ZnTe domains on *a*-plane sapphire were aligned in the direction associated with the sapphire *c*-axis (Fig.2 (b)).

In contrast to this result, a four-fold rotationally symmetrical pattern peaking at $\chi=55°$ was obtained (Fig. 3(a)) for a pole figure of 111 ZnTe from the epilayer grown on a buffer layer that was annealed at 300 °C. The RHEED pattern observed after this annealing process was a dim harrow pattern indicating that the buffer layer was not crystalized. This result suggested that layer obtained was governed by a (100)-oriented domain. There was also an additional peak at the origin, suggesting that a small mixture ratio of the {111}-oriented domain was included in the epilayer.

Wide-range RSM images are compared in Fig. 4 for ZnTe layers grown on buffer layers with various annealing temperatures. Diffraction spots were analyzed and associated with (111) and $(-1-1-1)$ were clearly observed for a sample that the buffer layer was annealed at 350 °C while (111), $(-1-1-1)$, and (100) associated peaks were observed for a sample that the buffer layer was observed at 300 °C. These observations were the same as the data observed from the pole figure imaging. Different from the pole figure analysis, (511) associated peaks were observed from the sample that the buffer layer was annealed at 350 °C. Hence this sample included a small percentage of mis-oriented domains. Wide-range RSM images are probably advantageous to distinguish

domains which may have similar indexes (for example (511) and (333) could not be easily resolved by other methods).

A high-resolution lattice image of the *a*-plane sapphire/ZnTe interface region with the buffer layer annealed at 350 °C is shown in Fig. 5. While defects associated with lattice mismatch accommodation can be seen in the large area image, the ZnTe film shows lattice fringes trending in the same direction. This indicates the high quality of the ZnTe/sapphire interface.

The atom arrangements of *a*-plane sapphire, (111) ZnTe, and (100) ZnTe are summarized in Fig. 6(a)–(c). In an epitaxial growth system with large lattice misfits, the lattice mismatch is estimated based on the domains, and not on the unit cells [24]. The lattice mismatch between three unit cells of *a*-plane sapphire (rectangular shape as shown in Fig. 6(a)) and five unit cells of (111) ZnTe (rectangular shape as shown in Fig. 6(b)) is approximately 4.4%
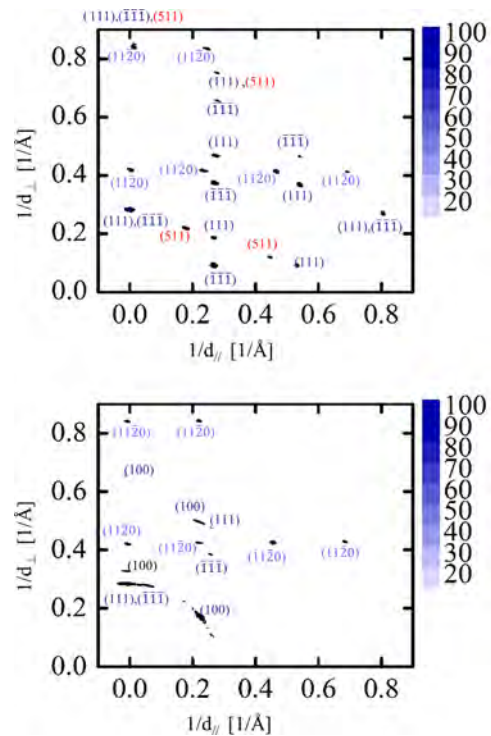
Fig. 4. The wide-range reciprocal space mappings of samples. (a) The buffer layer was annealed at 350 °C, and (b) the buffer layer was annealed at 300 °C. The horizontal axis corresponds to the direction of ⟨0001⟩ axis of the sapphire substrate, and the vertical axis corresponds to the direction of [11–20] axis of the sapphire substrate. Indexes of diffraction spots are the origin of the domain.
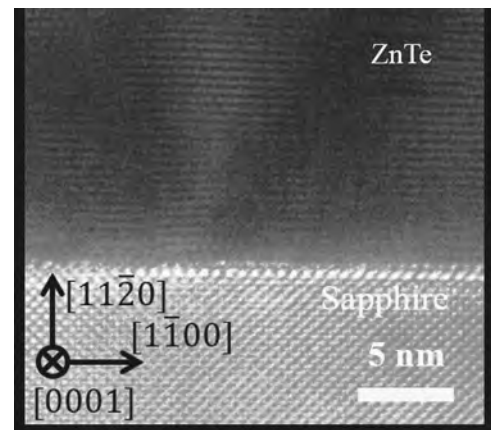
Fig. 5. High-resolution TEM image of the ZnTe/sapphire interface region.
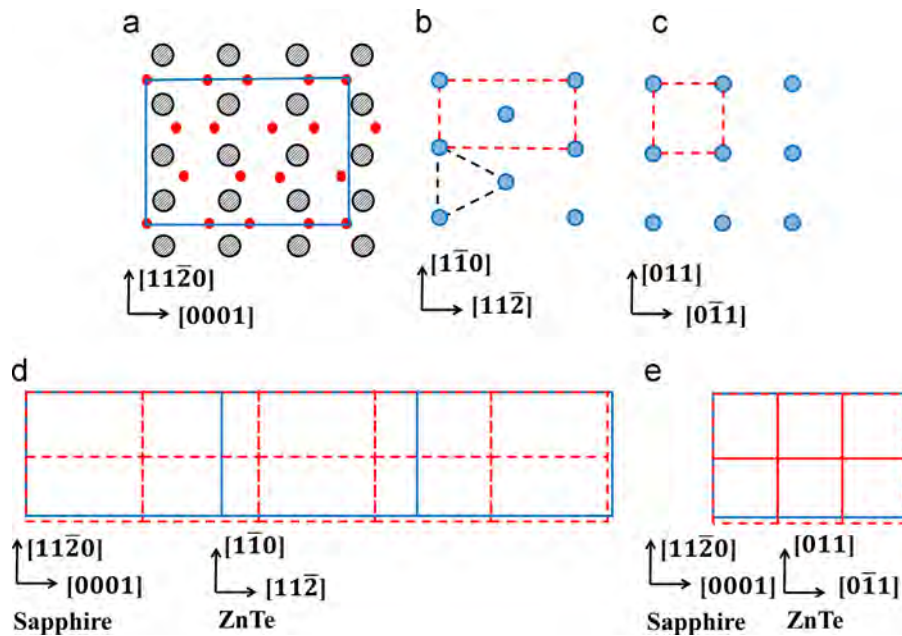
Fig. 6. Atom arrangements of (a) *a*-plane sapphire, (b) (111) ZnTe, and (c) (100) ZnTe. The alignment of (d) the (111) ZnTe and (11–20) sapphire, and (e) (100) ZnTe and (11–20) sapphire.

as shown in Fig. 6(d)), and between one unit cells of *a*-plane sapphire and three unit cells (100) ZnTe is approximately 0.64% (as shown in Fig. 6(e)). When ZnTe layers were grown on *c*-plane and *m*-plane sapphire substrates, (111) ZnTe and (0001) sapphire exhibited a certain relationship at the interface. That particular relationship was not observed so far for the ZnTe layer on the *a*-plane sapphire substrate. Since the diffraction peaks of (111) and (100) ZnTe domains on *a*-plane sapphire substrates are related to the *c*-axis direction of sapphire, there must be a crystallographic relationship between ZnTe and *a*-plane sapphire. The difference in the annealing temperature has resulted in the difference in the crystallization of the buffer layer, and the orientation of the epilayer. The detailed analysis is currently ongoing, and the surface atomic structure including kinks and terraces is probably another crucial factor for governing the orientation of the domain.

4. Conclusion

ZnTe epilayers were grown on *a*-plane (11–20) sapphire substrates by MBE. The insertion of a low-temperature buffer layer was carried out, and the influence of the buffer layer annealing prior to the growth of the epilayer on the crystallographic properties of the structure was investigated. The crystal orientation of ZnTe thin films prepared by MBE were studied via XRD pole figure and wide-range RSM measurements. Two different {111} domains were formed from the sample that the buffer layer was annealed at 350 °C, while (100) domains were preferentially formed for the sample that the buffer layer was annealed at 300 °C. These crystallographic features were also related to the atom arrangements of ZnTe and sapphire

References

[1] H. Jeon, J. Ding, W. Patterson, A.V. Nurmikko, W. Xie, D.C. Grillo, M. Kobayashi, R.L. Gunsor, Appl. Phys. Lett. 59 (1991) 3619.
[2] I. Nomura, Y. Ochiai, N. Toyomura, A. Manoshiro, A. Kikuchi, K. Kishino, Phys. Status Solidi B 241 (3) (2004) 483.
[3] H. Nishinaka, Y. Kamada, N. Kameyama, S. Fujita, Jpn. J. Appl. Phys. 48 (2009) 121103.
[4] M. Enami, K. Tsutsumi, F. Hirose, S. Katsuta, M. Kobayashi, Jpn. J. Appl. Phys. 42 (2003) L1047–L1049.
[5] M. Enami, K. Tsutsumi, F. Hirose, S. Katsuta, M. Kobayashi, Phys. Status Solidi C 1 (2004) 1038–1041.
[6] J. Ueno, K. Ogura, A. Ichiba, S. Katsuta, M. Kobayashi, K. Onomitsu, Y. Horikoshi, Phys. Status Solidi C 3 (2006) 1225–1228.
[7] S. Imada, T. Baba, S. Sakurasawa, M. Kobayashi, Phys. Status Solidi C **7** (2010) 1473.
[8] Y. Kumagai, M. Kobayashi, Jpn. J. Appl. Phys. 51 (2012) 02BH06.
[9] Y. Kumagai, S. Imada, T. Baba, M. Kobayashi, J. Cryst. Growth 323 (2011) 132.
[10] W. Sun, T. Nakasu, K. Taguri, T. Aiba, S. Yamashita, M. Kobayashi, H. Togo, T. Asahi, Phys. Status Solidi C 11 (7–8) (2014) 1252.
[11] T. Tanaka, M. Miyabara, Y. Nagao, K. Saito, D. Guo, M. Nishio, K.M. Yu, W. Walukiewicz, Appl. Phys. Lett. 102 (2013) 052111.
[12] W. Wang, A.S. Lin, J.D. Philips, Appl. Phys. Lett. 95 (2009) 011103.
[13] Q. Wu, M. Litz, X.C. Zhang, Appl. Phys. Lett. 68 (1996) 2924.
[14] Q. Guo, M. Nada, Y. Dling, T. Tanaka, M. Nishio, J. Appl. Phys. 107 (2010) 123525.
[15] Q. Chen, M. Tani, Z. Jiang, X.C. Zhang, J. Opt. Soc. Am. B 18 (6) (2001) 823.
[16] S. Namba, J. Opt. Soc. Am. 51 (1961) 77.
[17] M. Kobayashi, Y. Kumagai, T. Baba, S. Imada, Phys. Status Solidi C 9 (2012) 1748.
[18] T. Nakasu, Y. Kumagai, K. Nishimura, M. Kobayashi, H. Togo, T. Asahi, Appl. Phys. Express 5 (2012) 095502.
[19] T. Nakasu, M. Kobayashi, H. Togo, T. Asahi, Phys. Status Solidi C 10 (2013) 1381.
[20] T. Nakasu, M. Kobayashi, H. Togo, T. Asahi, J. Electron. Mater. 43 (2014) 921.
[21] T. Nakasu, W. Sun, S. Yamashita, T. Aiba, K. Taguri, M. Kobayashi, T. Asahi, H. Togo, Phys. Status Solidi C 11 (7–8) (2014) 1182.
[22] T. Nakasu, M. Kobayashi, T. Asahi, H. Togo, Jpn. J. Appl. Phys. 53 (2014) 015502.
[23] K. Inaba, S. Kobayashi, K. Uehara, A. Okada, S.L. Reddy, T. Endo, Adv. Mater. Phys. Chem 3 (2013) 72.
[24] J. Narayan, B.C. Larson, J. Appl. Phys. 93 (2003) 278.
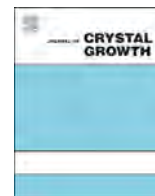
MBE growth and interfaces characterizations of strained HgTe/CdTe topological insulators

C. Thomas [a,*], X. Baudry [a], J.P. Barnes [a], M. Veillerot [a], P.H. Jouneau [b], S. Pouget [b], O. Crauste [c], T. Meunier [c], L.P. Lévy [c], P. Ballet [a]

[a] CEA—LETI, MINATEC Campus, 17 rue des Martys, 38054 Grenoble, France
[b] CEA—INAC & Univ. Grenoble Alpes, UMR-E, MINATEC, 17 rue des Martys, 38054 Grenoble, France
[c] Univ. Grenoble Alpes & CNRS, Inst. NEEL, BP 166, 38042 Grenoble, France

ARTICLE INFO

ABSTRACT

Topological insulator materials like HgTe exhibit unique electronic properties at their interfaces and so peculiar attention has to be paid concerning the growth optimization. Molecular beam epitaxy of tensile-strained HgTe/CdTe is investigated as a function of the growth temperature. Crystal quality is checked by using high resolution X-rays diffraction. By combining several material characterization techniques such as scanning transmission electronic microscopy, time-of-flight secondary ion mass spectroscopy and X-rays reflectivity, we report sharp interface morphology with nanometer-scale Hg/Cd diffusion lengths.

© 2015 Elsevier B.V. All rights reserved.

1. Introduction

First predicted by Kane and Mele [1] as a new class of matter, topological insulators are of main interest in condensed matter researches thanks to their unique electronic and spin properties that arise on theirs interfaces. It gather the graphene-like transport properties with Dirac fermions and the topological protection that prevent backscattering phenomena. These interfaces exhibit spin-momentum locking which polarizes the spin perpendicular to the momentum. Control of the spin and coherent spin transport are then easily achievable in topological insulators [2,3] making them very attractive for spintronic applications [4–6].

In this paper we will focus on topological insulator structures made of HgTe/CdTe. Bernevig, Hughes and Zhang [7] have made the prediction that CdTe/HgTe/CdTe quantum wells would be good candidate for 2D topological insulators. One year later, Fu and Kane [8] have extended this prediction to three dimension in the case where the semi-metal HgTe would have a bulk gap opening turning it into an insulator. This bulk gap can be obtained by growing tensile strained HgTe on a larger lattice constant substrate like CdTe. With a lattice mismatch of 0.3%, the growth of HgTe on CdTe(0 0 1) opens a bulk gap of about 25 meV.

The topological insulator HgTe exhibits its electronic and topological properties on its surfaces and interfaces. MBE growth optimization and interfaces characterization are so of main importance and are the subject of this paper. Time-of-flight secondary ion mass spectroscopy (TOF-SIMS), scanning transmission electronic microscopy (STEM) and X-rays reflectivity (XRR) measurements are used and their results compared to determine diffusion length at the interface between HgTe and CdTe.

2. MBE growth of HgTe/CdTe structures

Molecular beam epitaxy of HgTe/CdTe layers is achieved in a Riber 32 chamber [9]. HgTe layers are grown on either (1 0 0) CdTe or (2 1 1)B CdTe substrates. Growth rate of 1 monolayer/s and a Hg/Te ratio in excess of 1000/1 were used.

After thermal desorption of the substrate surface oxide, growth process starts with the deposition of a 200 nm-thick CdTe buffer layer with excess cadmium. The aim is to compensate the substrate remaining surface defects and so to perform the growth on a more flat surface. The substrate is then cooled down to the growth temperature for strained HgTe layer [9].

At the end of the growth process, a cooling down under Hg flux is performed allowing to improve roughness values lower than one nanometer [9]. This in-situ surface treatment prevents desorption of Hg from the HgTe surface and ensures flatness of the top HgTe interface. In these conditions, higher growth temperatures can be reached. HgTe layers have been successfully grown at temperatures up to 185 °C with equivalent crystal quality as shown in high resolution X-rays diffraction (HRXRD) spectra of Fig. 1 where CdTe and HgTe peaks are well-defined and surrounded by Pendellösung fringes.
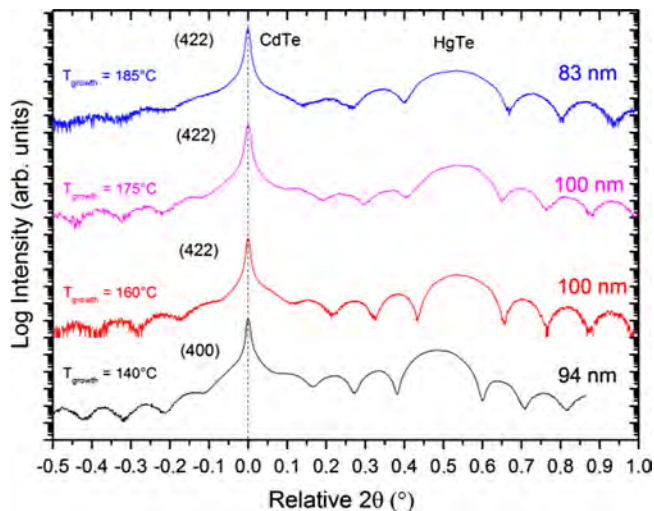
Fig. 1. HRXRD of HgTe grown on either (2 1 1)B CdTe or (1 0 0)CdTe susbtrates for different growth temperatures ranging from 140 °C to 185 °C.

However as reported by Oehling et al. [10], the HgTe growth experiences a transition from 2D growth mode to a step flow growth mode for surface temperatures larger than 175 °C. In the 140–175 °C range of available growth temperatures, the growth optimization must take into account bulk defects issues that appear for low growth temperature (140 °C) and interdiffusion issues that might appear for higher growth temperatures. Study of interdiffusion as a function of growth temperature is therefore needed to fully describe the interfaces.

2.1. HgTe/CdTe interface characterizations

Numerous studies concerning HgTe–CdTe superlattices interdiffusion have been carried out for infrared applications. As far as we know, interdiffusion characteristics were only determined after few hours of annealing at temperatures ranging from 110 °C [11] to more than 450 °C [12] under Hg saturated vapour pressure. One of these studies led by Tardot et al. [13] demonstrated diffusion coefficients of 2×10^{-16} cm²/s for Cd in HgTe in the case of superlattices annealed at 200 °C. Indeed the diffusion process between these two materials is characterized by the important diffusion of Cd into HgTe layer creating a HgCdTe intermixing layer at the interface. By extrapolation they also managed to estimate a diffusion length of 4 nm for a growth performed at 180 °C.

In this paper, we study the interdiffusion between HgTe and CdTe layers grown by MBE without any annealing step. We focus on the HgTe/CdTe interface characterizations for a sample of HgTe (83 nm)/CdTe (2 1 1)B grown at 185 °C to check values of interdiffusion for higher growth temperatures that usual ones. Three characterizations techniques are used: STEM, SIMS and XRR.

(a) Cross-sectional STEM measurements are performed on a FEI Osiris microscope at 80 kV with sample preparation done using a gallium-ion thinning in a focused-ion-beam microscope.
Fig. 2 shows bright-field mode (BF) image of HgTe/CdTe layer with well-defined and sharp interface. The sharpness of the interface is highlighted in Fig. 2(b) with TEM image. The HgTe layer exhibits low defect density but some local dislocation loops as it can be seen in the BF image (Fig. 2(a)). The enhanced top surface roughness is due to the change of growth mode from 2D to step flow as mentioned by Oehling et al. [10] for this growth temperature.

(b) To quantify the diffusion length at the interface, TOF-SIMS measurements are performed using Cs^+ ions at the energy of 500 eV. As shown in Fig. 3, chemical profiles with Hg and Cd
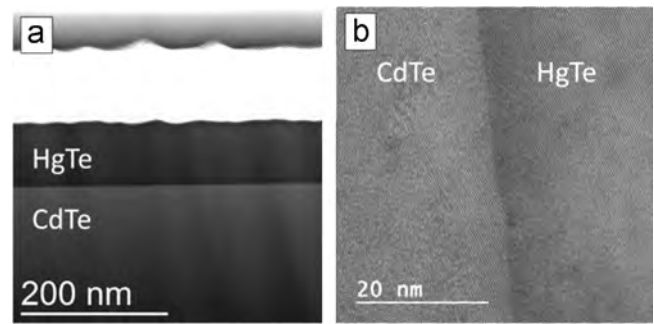
Fig. 2. (a) BF-STEM image in and (b) TEM image of the HgTe (83 nm)/CdTe (2 1 1) structure.

concentrations are obtained after normalization to the Te signal which is considered to be unity in the whole structure.
Chemical profiles are compared with second Fick's law of diffusion [14] applied for thin films where the diffusion coefficient D and the surface concentration of Hg C_0 are assumed to be constant. The concentration C of Hg through the structure evolves as:

$$C(x,t) = C_0 \exp\left(\frac{-x^2}{4Dt}\right) \qquad (1)$$

With respect to Eq. (1), diffusion length $x_{diff} = 2\sqrt{Dt}$ can be estimated as the length after which C_0 is divided by exp(1). On Fig. 3(b), a diffusion length of 6.1 nm is estimated. However, this result should be analyzed taking into account the TOF-SIMS depth resolution which is not known precisely for these materials but can be estimated to be within the range of at least 2 nm/decade for these experimental conditions. Therefore, the diffusion length can be considered between 2 and 4 nm for this structure.

(c) Due to the resolution issue of TOF-SIMS, X-rays Reflectivity is used to obtain a more accurate estimation of the interdiffusion between HgTe and CdTe layers. Measurements are done on a PANalytical Empyrean X-Rays diffractometer (using the cobalt $K\alpha1$ wavelength (1.789 A). Fig. 4 illustrates the reflectivity curve of HgTe (83 nm)/CdTe which was grown at 185 °C, as a function of grazing angle. Experimental data are fitted using the X'pert Reflectivity software [15–17] associated with a simple model composed of three layers: the HgTe thin film layer, a HgCdTe intermixing layer and the CdTe buffer layer. Best fitting parameters are obtained for a HgTe layer of 79.7 nm and roughness of 1.6 nm. This latter value is in perfect agreement with atomic force microscopy (AFM) measurement where top surface root mean square (RMS) roughness was determined to a value of 1.7 nm. Concerning the intermixing layer, the best fit is obtained for 3 nm of $Hg_{0.5}Cd_{0.5}Te$ with a roughness of 0.8 nm. Thanks to these fitting parameters, the diffusion length can be estimated to 3.4 ± 0.4 nm for this structure.

2.2. Discussion

With the combination of these three characterization techniques, diffusion length of about 3.4 nm was determined for HgTe layer grown at 185 °C. This value is consistent with the extrapolation of Tardot et al. [13] for growth at 180 °C and has to be considered as a maximum value for interdiffusion in our structures assuming our maximal growth temperature is 10 °C lower.

The corresponding diffusion coefficient D can be extracted using x_{diff} value and t which is chosen as the time of HgTe growth (i.e. 300 s) for first approximation. D is estimated to be about $9.6(\pm 2.3) \times 10^{-17}$ cm²/s.
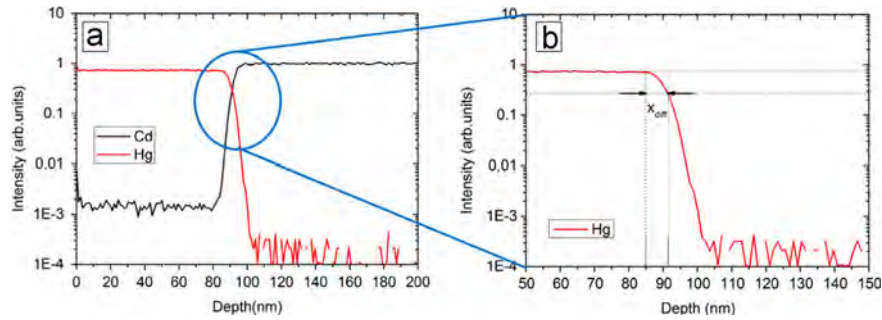
Fig. 3. SIMS measurements of HgTe (83 nm)/CdTe illustrating Hg and Cd concentration ratio evolution through the whole structure (a). (b) Determination of Hg diffusion length. Dashed horizontal lines represent C_0 and $C_0/exp(1)$.
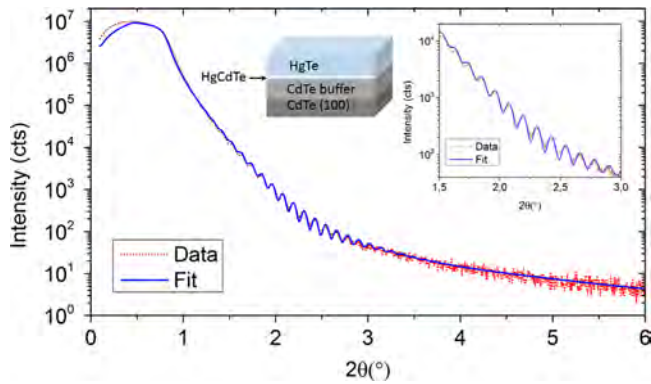
Fig. 4. XRR spectra of HgTe (83 nm)/CdTe. The model structure used for the fit is represented is the inset as well as the spectral range of main importance for the fit of the XRR spectra. The red dashed curve represents the experimental data and the blue curve is the fit using the X'pert Reflectivity software [15–17]. (For interpretation of the references to color in this figure legend, the reader is referred to the web version of this article.)

However, this value was calculated assuming that the time of diffusion is equal to the time of growth. This is not completely true since, after the growth process, the substrate is cooled down to 80 °C with a rate of about 4.5 °C/min and so diffusion may occur with a significant degree during this step. This effect appears not to be negligible until the substrate temperature reaches 140 °C but we are nowadays not able to differentiate properly the diffusion occurring during the growth from the diffusion occurring during this cooling down.

3. MBE growth and interfaces characterizations of capped HgTe structures

The sharpness of HgTe/CdTe interfaces has just been demonstrated. However, for magnetotransport measurements, HgTe layers are passivated with HgCdTe cap layers grown by MBE [9] just before and after HgTe. Interdiffusion and morphology of these HgCdTe/HgTe/HgCdTe interfaces are also interesting to study. In this paper, a 10 nm HgTe layer grown at 160 °C and capped with 40 nm $Hg_{0.3}Cd_{0.7}Te$ layers is used for characterization.

Fig. 5 shows STEM measurements done on this sample. Bright Field mode and High Angle Annular Dark Field (HAADF) mode images provide evidences of a HgTe layer with low defect density and having sharp and clear interfaces.

Chemical mapping (Fig. 5(c)) is also performed using energy dispersive X-ray spectroscopy (EDX) and a Cliff–Lorimer ratio analysis. Concerning EDX resolution, a compromise has to be taken between beam energy and time of acquisition to ensure accuracy of the measurement and not damage too fast the sample.

The extracted chemical profile (Fig. 5(d)) gives information about Hg, Cd and Te concentration ratio through the whole structure and confirms the abruptness of the interfaces.

Composition of cap layers is estimated to be 60% of Cd and 40% of Hg which is quite coherent with the nominal composition of 70/30%. Composition of Cd differs also from the nominal one in the HgTe layer where 10% are reported. This can be due to a residual deposit. However, topological aspect of HgTe layer is preserved since Cd fraction is under 15%. The HgTe layer thickness is estimated to be 8.3 nm.

To quantify the diffusion process in such structures, XRR is performed using a model composed of $Hg_{0.3}Cd_{0.7}Te$ cap layers and $Hg_{0.65}Cd_{0.35}Te$ intermixing layers surrounding the HgTe layer (see inset of Fig. 6). The diffusion between the $Hg_{0.3}Cd_{0.7}Te$ first barrier and the CdTe buffer layer was not taken into account in our model. This effect is expected to be negligible here because of the high concentration of Cd in the barrier layer.

HgTe layer of 8.3 nm with roughness of 0.6 nm is used for fitting. A CdTe-based oxide layer of 2.3 nm with 0.3 nm of roughness (this value is consistent with AFM RMS of 0.3 nm) is added to model the desorption of Hg at the top cap layer surface since cooling down is not performed under Hg flux for such capped structures.

With respect to these parameters, diffusion lengths are estimated for both interfaces.

The influence of bottom intermixing layer characteristics (especially its thickness) is visible in the fit for higher angle than for the top one due to the difference in depth.

The diffusion length for the bottom interface (HgTe/HgCdTe) is determined to be about 0.9 ± 0.3 nm for the best fitting conditions. Concerning the top interface (HgCdTe/HgTe), the fit stays suitable with the data with an intermixing layer thinner than 0.5 nm. The difference between these two diffusion lengths is explained by a different exposure time to growth temperature. Indeed the bottom interface is exposed at 160 °C in excess of 30 s (time for the growth of HgTe) with respect to the top interface.

With these growth conditions and by considering that $x_{diff}=2\sqrt{Dt}$ (we assume that at 160 °C the diffusion occurring during the end-of-growth cooling down is not predominant), the bottom diffusion length should be in theory 1.12 times longer than the top one.

4. Conclusion

We report the molecular beam epitaxy growth of HgTe/CdTe topological insulator structures with high crystal quality. As interfaces are carrying all the electronic transport in these structures, we focused on their characterization. STEM provides information about interface morphology and evidenced sharp interfaces. Chemical profiles using SIMS allow giving a first estimation of the diffusion length but XRR measurement are needed to provide a necessary accuracy. For growth temperature of 185 °C, diffusion length of about 3.4 nm is reported. In the case of HgTe capped layer grown at 160 °C,
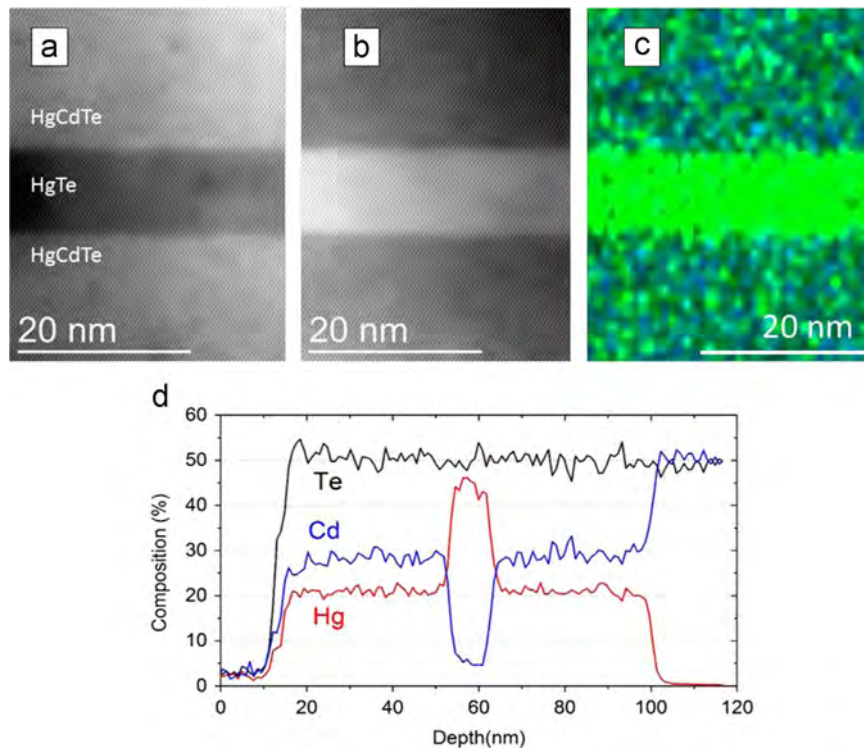
Fig. 5. STEM images of 10 nm HgTe capped structure: (a) BF mode, (b) HAADF mode, (c) EDX mapping with Hg in green, Cd in blue (d) extracted chemical profile of the whole structure with Hg in red, Cd in blue and Te in black. (For interpretation of the references to color in this figure legend, the reader is referred to the web version of this article.)
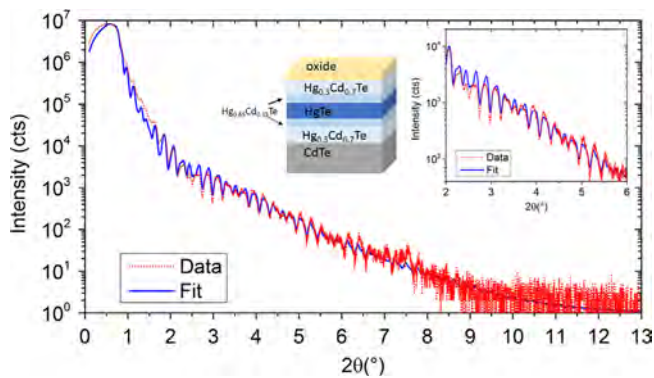
Fig. 6. XRR spectra of HgTe/HgCdTe capped structure. The model structure used for the fit is represented is the inset as well as the spectral range of main importance for the fit of the XRR spectra. The red dashed curve represents the experimental data and the blue curve is the fit. (For interpretation of the references to color in this figure legend, the reader is referred to the web version of this article.)

sharp interfaces of about 1 nm for the bottom interface and lower than 0.5 nm for the top interface are evidenced.

In a nutshell, with diffusion length on the nanometer order, HgTe interfaces are a perfect playground for topological properties.

References

[1] C.L. Kane, E.J. Mele, Phys. Rev. Lett. 95 (2005) 226801.
[2] C Brüne, A Roth, H Buhmann, E.M Hankiewicz, L.W Molenkamp, J Maciejko, X-L Qi, S-C Zhang, Nat. Phys. 8 (2012).
[3] C.H. Li, O.M.J. van't Erve, J.T. Robinson, Y. Liu, L. Li, B.T. Jonker, Nat. Nanotechnol. 9 (2014).
[4] V. Krueckl, K. Richter, Phys. Rev. Lett. 107 (2011) 086803.
[5] M. Zeng, G. Liang, J. Appl. Phys. 112 (2012) 073707.
[6] R. Citro, F. Romeo, N. Andrei, Phys. Rev. B 84 (2011) 161301(R).
[7] B.A. Bernevig, T.A. Hughes, S.C. Zhang, Science 314 (2006) 1757.
[8] L. Fu, C.L. Kane, Phys. Rev. B 76 (2007) 045302.
[9] P Ballet, C Thomas, X Baudry, C Bouvier, O Crauste, T Meunier, G Badano, M Veillerot, J.P Barnes, P.H Jouneau, L.P Lévy, J. Electron. Mater. 43 (2014) 2955–2962.
[10] S. Oehling, M. Ehinger, W. Spahn, A. Waag, C.R. Becker, G. Landwehr, J. Appl. Phys. 79 (1996) 748.
[11] D.K Arch, J.L Staudenmann, J.P Faurie, J. Appl. Phys. 48 (1986) 23.
[12] M.F.S Tang, D.A. Stevenson, J. Vac. Sci. Technol., A **5** (1987) 3124.
[13] A Tardot, A Hamoudi, N Magnea, P Gentile, J.L Pautrat, J. Appl. Phys. 62 (1993) 2548.
[14] J Crank, The Mathematics of Diffusion, Clarendon Press, Oxford, 1979.
[15] X'Pert Reflectivity software, PANalytical B.V., Almelo, The Netherlands.
[16] V Holý, U Pietsch, T Baumbach, High Resolution X-ray Scattering, Springer, ISBN 3-540-62029-X, 1999.
[17] V. Holý, J. Kubĕna, I. Ohlídal, K. Lischka, W. Plotz, Phys. Rev. B 47 (23) (1993) 15896–15903.

CRYSTAL
GROWTH
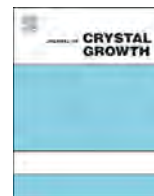
Investigation of p-side contact layers for II–VI compound semiconductor optical devices fabricated on InP substrates by MBE

CrossMark

Shingo Takamatsu, Ichirou Nomura *, Tomohiro Shiraishi, Katsumi Kishino

Department of Engineering and Applied Sciences, Sophia University, 7-1 Kioi-cho, Chiyoda-ku, Tokyo 102–8554, Japan

ARTICLE INFO

ABSTRACT

N-doped p-type ZnTe and ZnSeTe contact layers were investigated to evaluate which is more suitable for use in II–VI compound semiconductor optical devices on InP substrates. Contact resistances (R_c) between the contact layers and several electrode materials (Pd/Pt/Au, Pd/Au, and Au) were measured by the circular transmission line model (c-TLM) method using p-n diode samples grown on InP substrates by molecular beam epitaxy (MBE). The lowest R_c ($6.5 \times 10^{-5}\ \Omega\,cm^2$) was obtained in the case of the ZnTe contact and Pd/Pt/Au electrode combination, which proves that the combination is suitable for obtaining low R_c. Yellow light-emitting diode devices with a ZnTe and ZnSeTe p-contact layer were fabricated by MBE to investigate the effect of different contact layers. The devices were characterized under direct current injections at room temperature. Yellow emission at around 600 nm was observed for each device. Higher emission intensity and lower slope resistance were obtained for the device with the ZnTe contact layer and Pd/Pt/Au electrode compared with other devices. These device performances are ascribed to the low R_c of the ZnTe contact and Pd/Pt/Au electrode combination.

© 2015 Elsevier B.V. All rights reserved.

1. Introduction

II–VI compound semiconductors such as ZnCdSe, BeZnTe, and BeZnSeTe on InP substrates are very attractive for use in visible-to-infrared optical devices [1–9]. Using these materials, we are developing green and yellow laser diodes (LDs) and light-emitting diodes (LEDs) [3–9]. In the developments, lowering the contact resistance between (especially p-side) contact layers and electrodes is a crucial issue in obtaining high device performances. ZnTe and ZnSeTe are potential materials for the p-side contact layers of II–VI devices because of their high p-type doping properties and low electron affinity. However, they have merits and demerits as a contact layer. For example, ZnTe contact layers were used in previous *blue-green II–VI laser diodes on GaAs substrates* developed in the 1990s because of their high p-dopability. However, the ZnTe contact has a problem of crystal quality due to a large lattice mismatch with GaAs (8.0%) and InP (4.0%) substrates. On the other hand, ZnSeTe has the merit that lattice matching with InP substrates can be obtained when the Se and Te compositions are 0.54 and 0.46, respectively. However, the p-type doping property of ZnSeTe is lower than that of ZnTe. In addition, the doping property sensitively depends on the Se and Te compositions. For example, increasing the Se composition leads to a rapid decrease in the p-dopability. Therefore, we must precisely

control the composition to obtain high-quality, high doped ZnSeTe contact layers.

On the other hand, the suitable selection of electrode materials is also crucial for obtaining low contact resistances. Metal properties such as a high work function and adhesion to contact layers are required to obtain low-resistance ohmic p-side electrodes. For the p-side electrode of II–VI devices, Au, Pt, and Pd have been commonly used [10–13] because they have relatively high work functions (5.1, 5.6, and 5.1 eV for Au, Pt, and Pd, respectively). In addition, Pd has high adhesion due to its reaction with the contact layer, which is effective for lowering the contact resistance [11–13].

In this study, N-doped p-type ZnTe and ZnSeTe contact layers were investigated to evaluate which is more suitable for use in II–VI devices on InP substrates. Contact resistances (R_c) between the contact layers and some electrode materials (Pd/Pt/Au, Pd/Au, and Au) were measured using p-n diode samples grown on (100) InP substrates. Yellow light-emitting diode devices with a ZnTe or ZnSeTe p-contact layer were fabricated to investigate the effects of the *difference in* the contact layers. Device characteristics such as emission spectra and electrical properties were compared.

2. Sample preparation

The p-n diode samples with p-ZnTe or p-ZnSeTe contact layers were fabricated to investigate the contact resistances. The samples consisted of 250-nm-thick n-ZnCdSe, 700-nm-thick p-BeZnTe, and

* Corresponding author. Tel.: +81 332 383 095; fax: +81 332 383 311
E-mail address: i-nomura@sophia.ac.jp (I. Nomura).

p-ZnTe or p-ZnSeTe contact	30 nm
p-BeZnTe	700 nm
n-ZnCdSe	250 nm
LTn-ZnCdSe buffer	
n-InGaAs buffer	
n-InP substrate	
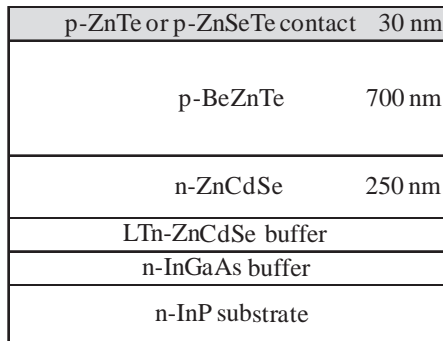
Fig. 1. A schematic diagram of the p-n diode samples with the ZnTe and ZnSeTe contact layers.

Fig. 2. Resistances (R) between the circle and outside electrodes for the ZnTe and ZnSeTe contact samples with Pd/Pt/Au electrodes as a function of the gap length (d).

Table 1

Experimental R_c values of the ZnTe and ZnSeTe contact layer samples with Au, Pd/Au, and Pd/Pt/Au electrodes made by the EB (for Au, Pd/Au, and Pd/Pt/Au) and RH (for Au) evaporation.

Electrode material	R_c (Ω cm^2)	
	ZnTe contact	ZnSeTe contact
Au (RH)	6.3×10^{-3}	3.1×10^{-3}
Au (EB)	7.2×10^{-4}	3.5×10^{-4}
Pd/Au (EB)	7.7×10^{-5}	2.7×10^{-3}
Pd/Pt/Au (EB)	6.5×10^{-5}	9.0×10^{-3}

thin (30 nm) p-ZnTe or p-ZnSeTe contact layers, as shown in Fig. 1. The samples were grown on S-doped (100) n-InP substrates employing a double-chamber molecular beam epitaxy (MBE) system consisting of II–VI and III–V growth chambers connected by an ultrahigh-vacuum transfer (UVT) chamber. The elemental sources used in this growth were In (7N), Ga (7N), P (7N), As (7.5N), Be (4N), Zn (7N), Se (6N-S), Cd (7N), and Te (7N). Standard Knudsen effusion cells were used to supply Be, Zn, Cd, Te, In, and Ga molecular beam fluxes. Se, P, and As fluxes were supplied from valved cracker cells.

First, thermal cleaning of the InP substrate surface was performed under P flux irradiation at 500 °C in the III–V chamber. Then, 30-nm-thick Si-doped n-InP and 90-nm-thick Si-doped n-InGaAs buffer layers were grown at 450 and 470 °C, respectively, After that, the samples were transferred into the II–VI chamber to grow II–VI layers. Before the II–VI growth, Zn flux was irradiated onto the n-InGaAs buffer surface at 240 °C. Then, 6-nm-thick n-ZnCdSe low-temperature (LT) buffer and 250-nm-thick n-ZnCdSe buffer layers were grown at 240 and 280 °C, respectively. Following the buffer growth, 700-nm-thick p-BeZnTe and 30-nm-thick p-ZnTe or p-ZnSeTe contact layers were grown at 300 °C. The ZnCdSe, BeZnTe, and ZnSeTe layers were grown under lattice-matching conditions with the InP substrate. That is, the Zn and Cd compositions for ZnCdSe were 0.47 and 0.53, those of Be and Zn for BeZnTe were 0.48 and 0.52, and those of Se and Te for ZnSeTe were 0.54 and 0.46, respectively. The n- and p-type doping sources were ZnCl$_2$ and radio-frequency (RF) radical nitrogen, respectively. In the p-doping, the RF power and partial pressure of nitrogen in the growth chamber were 450 W and 1.0×10^{-7} Torr, respectively.

After the growth, patterned electrodes were formed on the contact layers by conventional photolithography and standard evaporation techniques. Pd/Pt/Au, Pd/Au, and Au electrodes were formed by an electron beam (EB) method. In particular, the Pd/Pt/Au electrode was evaporated in the order of Pd, Pt, and Au from the contact surface. The thicknesses of Pd, Pt, and Au were 10, 50, and 100 nm, respectively. In addition, samples with Au electrodes formed by resistant heating (RH) evaporation were prepared for comparison. In this experiment, no annealing was performed after the evaporation.

3. Contact resistance measurements

The contact resistances of the samples were measured by the circular transmission line model (c-TLM) method [14]. In this method, circle-patterned electrodes with several gap lengths between the circle and the outside electrodes [14] are used, and the contact resistances were estimated from the relationship between the gap length and the resistance between the circle and the outside electrodes. In this experiment, the resistances between the electrodes were obtained from the I–V characteristics at room

temperature (RT). The I–V curves showed ideal ohmic characteristics for each sample. Fig. 2 shows the resistances (R) between the electrodes as a function of gap length (d) for the ZnTe and ZnSeTe contact samples with Pd/Pt/Au electrodes. Almost linear relationships between R and d were obtained for both samples. Similar linearity was also confirmed for all other samples. From the relationships, values of twice the transfer length (L_t) of each sample were estimated by determining the gap length when $R=0$ by extrapolation. Then, the contact resistances (R_c) were estimated from the L_t and R values and the radii of the circle electrodes. The electrode geometry and size and the calculation method of R_c were the same as those in Ref. [15].

The R_c values obtained for the ZnTe and ZnSeTe contact layer samples with various electrode combinations (i.e., Pd/Pt/Au, Pd/Au, Au formed by EB evaporation, and Au formed by RH evaporation) are summarized in Table 1. In these data, the lowest R_c value is 6.5×10^{-5} Ω cm^2 for the ZnTe sample with the Pd/Pt/Au electrode, showing that this combination is the most suitable for use as a low-resistance contact. On the other hand, the highest R_c value was 9.0×10^{-3} Ω cm^2 for the ZnSeTe sample with Pd/Pt/Au electrodes. Also in the case of the Pd/Au electrode R_c for ZnSeTe was higher than that for ZnTe. These results can be ascribed to the disruption of ZnSe by the deposited Pd [16]. In general, Pd is known to be a reactive transition metal when it is used as an electrode material on semiconductors such as GaAs [11–13]. The reactive transition metal promotes some reactions between the metal and the semiconductor surface, which is effective for lowering the contact resistance. In the case of the Pd/ZnSe combination, however, Pd is known to be not reactive but disruptive to ZnSe [16]. From this, it is considered that the disruption of ZnSe components in the ZnSeTe contact layer is due to the *deposited* Pd forming some barrier layer such as an insulating layer, which resulted in the high R_c of the ZnSeTe sample. The disruptive effect was particularly enhanced in the case of the Pd/Pt/Au electrode as a result of the ion irradiation of the sample surface during the EB evaporation of Pt. The amount and effects of

Pt ions from the evaporation source must have been greater than those of Pd and Au because the emission current for the EB evaporation of Pt was very high (130 mA) owing to the very low vapor pressure of Pt compared with those of Pd and Au (20 mA). This is considered to be the reason behind the highest R_c value in the case of the ZnSeTe sample with the Pd/Pt/Au electrode.

On the other hand, the lower R_c values of the ZnTe samples with the Pd/Pt/Au and Pd/Au electrodes are ascribed to various factors, i.e., the *reactive transition metal effect* of Pd described above, the high p-doping of the ZnTe contact layer, the higher valence-band maximum of ZnTe, and the large work functions of the metals (especially Pt). In our previous work, the net acceptor densities of 500-nm-thick N-doped ZnTe and ZnSeTe layer samples grown under the same conditions as the samples in this study were evaluated by C–V measurements employing a UCVpro-UV device (Nanometrics). As a result, the acceptor densities of the ZnTe and ZnSeTe layers were found to be 2.0×10^{19} and 6.0×10^{18} cm^{-3}, respectively. This high p-doping of the ZnTe layer must have contributed to reducing R_c for the ZnTe samples with the Pd/Pt/Au and Pd/Au electrodes. In addition, the valence-band maximum of ZnTe was higher than that of ZnSeTe, which is effective for obtaining ideal ohmic contacts and low R_c. Comparing the Pd/Au and Pd/Pt/Au electrodes, the Pd/Pt/Au electrode is more effective for lowering R_c because it includes Pt, which has a larger work function than Pd and Au.

Contrary to the case of the Pd/Pt/Au and Pd/Au electrodes, the R_c values of the ZnSeTe samples were lower than those of the ZnTe samples in the case of the Au electrodes, although the doping level and the valence band top of ZnSeTe were lower than those of ZnTe. This is ascribed to the difference in the crystal quality of the ZnTe and ZnSeTe layers. ZnTe had a highly compressive strain (4.0%) to InP substrates, which led to the crystal degradation and surface roughness of the contact layer [15]. This low crystal quality causes the interface state and deep levels to function as carrier traps because of the crystal defects, and they suppress the hole injection from the metal to the contact layer. In contrast, high crystal quality was obtained for the ZnSeTe contact because it was lattice-matched with the InP substrate [15], which resulted in lower R_c than that of ZnTe. Therefore, it is considered that the high crystal quality of ZnSeTe is more effective for determining the R_c than the high p-doping and high valence band top of ZnTe in the case of the Au electrode.

In addition, it is interesting that the R_c values of both the ZnTe and ZnSeTe samples with the Au electrodes formed by EB evaporation were lower than the those of samples with the Au electrode formed by RH evaporation. This was probably due to the difference in the migration energy of Au adatoms (and/or molecules) evaporated onto the contact layers by EB and RH evaporation. That is, the

migration energy of Au adatoms and molecules in the case of EB evaporation was higher than that in the case of RH evaporation, which was effective for enhancing the uniformity and adhesion of the Au electrodes, and thus lowering the R_c.

In this study, the lowest R_c was 6.5×10^{-5} Ω cm^2 in the case of p-ZnTe contact layers and Pd/Pt/Au electrodes. In general, it is preferable for practical use that R_c is the order of 10^{-6} Ω cm^2 or less. Therefore, it is necessary to decrease the R_c a little more. On the other hand, the above result is comparable to reported values for other semiconductor/metal contacts. For example, the R_c value in the case of p-InGaAs contact layers and Au/Pt/Ti electrodes with no annealing after the metal deposition was 8.3×10^{-5} Ω cm^2 [17]. Here, the doping level of the p-InGaAs layer was 2×10^{19} cm^{-3}, which was the same as one in our case. In addition, the R_c in the p-InGaAs case decreased to 7.5×10^{-6} Ω cm^2 by increasing the doping level of the contact layer to 1×10^{20} cm^{-3}, and it decreased to 4.8×10^{-8} Ω cm^2 by annealing [17]. Therefore, we expect that the R_c in our case also can be decreased furthermore by increasing the doping level and annealing.

4. Characteristics of light-emitting devices

Yellow light-emitting diode devices with ZnTe and ZnSeTe contact layers were fabricated to investigate the effects of different contact layers. The devices consisted of a 30-nm-thick BeZnTe/ZnSeTe superlattice (SL) active layer sandwiched by MgSe/BeZnTe barrier layers and MgSe/ZnCdSe SL n-cladding, MgSe/BeZnTe SL p-cladding, and 30-nm-thick ZnTe or ZnSeTe p-contact layers. The devices were grown on S-doped (100) n-InP substrates by double-chamber MBE. *Details of* the device structure and growth conditions are described in Ref. [15]. After the growth, 50-μm-wide stripe-geometry Pd/Pt/Au and Au electrodes were formed on the p-contact layers by conventional photolithography and the evaporation techniques described in Sec. II. The Pd/Pt/Au and Au electrodes were formed by EB and RH evaporation, respectively. For the n-side contact, Au electrodes were formed by RH evaporation on the back of the substrate. Then the device wafers were cleaved to produce chips with a length of approximately 500 μm. The devices were characterized by direct current (DC) injection at RT.

Fig. 3 shows emission spectra of the ZnTe and ZnSeTe contact devices with (a) Pd/Pt/Au and (b) Au electrodes under a current density of 50 A/cm^2. In Fig. 3(a), the peak wavelengths of the ZnTe and ZnSeTe contact devices are 608 and 604 nm, and the full width at half maximum (FWHM) values of the peaks are 87.7 and 97.2 meV, respectively. In Fig. 3(b), the peak wavelengths are 610 and 598 nm,
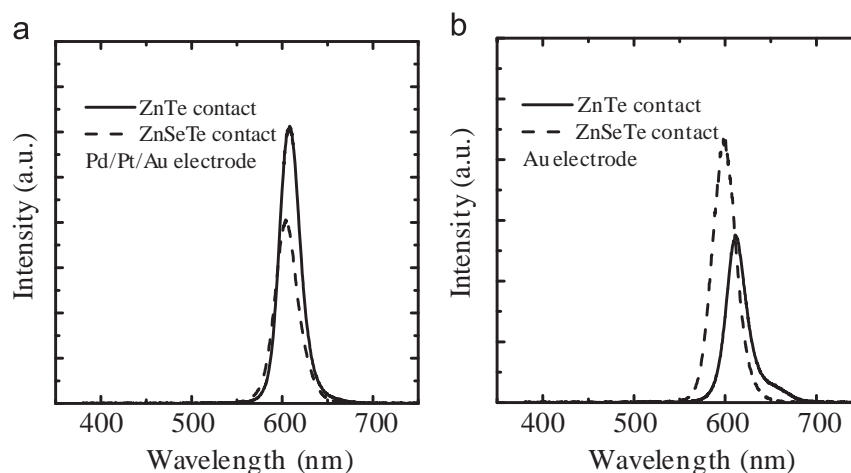
Fig. 3. Emission spectra of the light emitting devices with a ZnTe and ZnSeTe p-contact layers in the case of (a) Pd/Pt/Au and (b) Au electrodes under the current density of 50 A/cm^2 at RT.
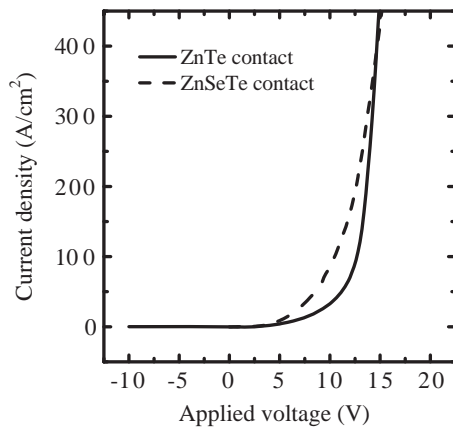
Fig. 4. J–V characteristics of the light emitting devices with a ZnTe and ZnSeTe p-contact layers with the Pd/Pt/Au electrodes.

and the FWHM values are 85.6 and 103.7 meV for the ZnTe and ZnSeTe devices, respectively. In Fig. 3(a) and (b), there are differences between the emission intensities of the ZnTe and ZnSeTe contact devices. The peak intensity of the ZnTe device is higher than that of the ZnSeTe in the case of the Pd/Pt/Au electrodes (Fig. 3(a)). In contrast, the peak intensity of the ZnTe device is lower than that of the ZnSeTe in the case of the Au electrodes. Here, we note that this trend is consistent with the results for R_c shown in Table 1. That is, R_c for the ZnTe contact is lower than that for the ZnSeTe contact, and the emission intensity of the ZnTe device is higher than that of the ZnSeTe device in the case of the Pd/Pt/Au electrodes. Meanwhile, the case of the Au electrodes was the contrary. The cause of these results (i.e., *the difference in* the intensity and the relationship with the R_c) have not yet been made clear. However, as one of possible causes, it is considered that the difference in the emission intensities is due to heat generation under DC injection by the device resistance. For example, the higher R_c in the case of the ZnSeTe contact and Pd/Pt/Au electrode combination increased the device temperature by the heat generation at the contact layer, which caused the decrease of the emission intensity. As another cause, the disruption of the ZnSeTe contact due to Pd deposition in the case of the Pd/Pt/Au electrode described in Sec. III might have affected not only the p-contact but also other parts of the device such as the active layer, which led to the deterioration of the device performances such as the emission intensity.

Fig. 4 shows the injection current density versus applied voltage (J–V) characteristics of the ZnTe and ZnSeTe contact devices with the Pd/Pt/Au electrodes. As shown in Fig. 4, the slope resistance of the ZnTe device is lower than that of the ZnSeTe device. In fact, the slope resistances of the ZnTe and ZnSeTe devices are 4.4×10^{-3} and $1.1 \times 10^{-2}\,\Omega\,cm^2$, respectively. Assuming that the contact resistances of the devices are the same as the R_c values shown in Table 1, the series resistances without the p-contact resistances are estimated by subtracting the R_c values from the slope resistances. As a result, the series resistances (not including the p-contact resistances) of the ZnTe and ZnSeTe devices are 4.3×10^{-3} and $3.0 \times 10^{-3}\,\Omega\,cm^2$, respectively. The two values are similar, which is consistent with the fact that the structures of the ZnTe and ZnSeTe devices are the same except for the p-contact layers and p-electrodes. Therefore, the low slope resistance of the ZnTe device is ascribed to the low R_c. From these results, it is concluded that the combination of the ZnTe p-contact layers and Pd/Pt/Au electrodes is very effective for lowering the R_c and improving the device performances.

On the other hand, current densities of the ZnSeTe device were higher than those of the ZnTe device in the applied voltage range from 5 to 15 V as shown in Fig. 4, which means lower total resistances of the ZnSeTe device in that range. This can be ascribed

to lower crystal quality especially around the p-n junction including the active layer of the ZnSeTe device. That is, the rectification characteristic slightly became dull due to leakage currents through defect levels such as interface states for the ZnSeTe device, which was probably caused by accidental deviation of the crystal growth condition and compositional fluctuations of the layers around the junction. Or the disruption of the ZnSeTe contact layer due to Pd deposition might have affected the crystal quality around the junction, as discussed about the emission properties in Fig. 3. At all events, the cause has not yet been identified at the moment.

5. Conclusions

N-doped p-type ZnTe and ZnSeTe contact layers were more investigated to evaluate which is suitable for use in II–VI devices on InP substrates. The R_c values between the contact layers and some electrodes (Pd/Pt/Au, Pd/Au, and Au) were measured by the c-TLM method using p-n diode samples grown on InP substrates by MBE. The lowest R_c ($6.5 \times 10^{-5}\,\Omega\,cm^2$) was obtained in the case of the ZnTe contact and Pd/Pt/Au electrode combination, which shows that the combination is suitable for obtaining low R_c. Yellow light-emitting diode devices with a ZnTe or ZnSeTe p-contact layer were fabricated to investigate the effects of different contacts layer. Device characteristics such as the emission spectra, J–V characteristics, and series resistances were evaluated. Yellow emission around at 600 nm was observed for the devices. Higher emission intensity and lower slope resistance were obtained for the device with the ZnTe contact and Pd/Pt/Au electrode. The low slope resistance was ascribed to the low R_c. These results prove that the combination of the ZnTe p-contact layers and Pd/Pt/Au electrodes is very effective for lowering the R_c and improving the device performances.

References

[1] T. Morita, A. Kikuchi, I. Nomura, K. Kishino, J. Electron. Mater. 25 (1996) 425.
[2] M.C. Tamargo, A. Cavus, L. Zeng, N. Dai, N. Bambha, A. Gray, F. Semendy, W. Krystek, F.H. Pollak, J. Electron. Mater. 25 (1996) 259.
[3] Y. Takashima, I. Nomura, Y. Nakai, A. Kikuchi, K. Kishino, Phys. Status Solidi B 241 (2004) 747.
[4] Y. Nakai, I. Nomura, Y. Takashima, A. Kikuchi, K. Kishino, Phys. Status Solidi A 201 (2004) 2708.
[5] I. Nomura, Y. Nakai, K. Hayami, T. Saitoh, K. Kishino, Phys. Status Solidi B 243 (2006) 924.
[6] I. Nomura, K. Kishino, T. Ebisawa, Y. Sawafuji, R. Ujihara, K. Tasai, H. Nakamura, T. Asatsuma, H. Nakajima, Appl. Phys. Lett. 94 (2009) 021104.
[7] T. Ebisawa, I. Nomura, K. Kishino, K. Tasai, H. Nakamura, T. Asatsuma, H. Nakajima, J. Cryst. Growth 311 (2009) 2291.
[8] I. Nomura, Y. Sawafuji, K. Kishino, Jpn. J. Appl. Phys. 50 (2011) 031201.
[9] T. Kobayashi, I. Nomura, K. Murakami, K. Kishino, J. Cryst. Growth 378 (2013) 263.
[10] P.A. Tupenevich, V.K. Kononenko, A.K. Lyakhovich, Instrum. Exp. Tech. USSR 17 (1974) 1509.
[11] L.C. Wang, X.Z. Wang, S.S. Lau, T. Sands, W.K. Chan, T.F. Kuech, Appl. Phys. Lett. 56 (1990) 2129.
[12] D Marchal, B. Zhang, L.C. Wang, P. E Jiao, W.X. Chen, T. Sawada, S.S. Lau, K.L. Kavanagh, T.F. Kuech, J. Appl. Phys. 62 (1987) 942.
[13] M. Ozawa, F. Hiei, M. Takasu, A. Ishibashi, K. Akimoto, Appl. Phys. Lett. 64 (1994) 1120.
[14] M. Ahmad, B.M. Arora, Solid-State Electron 35 (1992) 1441.
[15] S. Takamatsu, I. Nomura, T. Kobayashi, K. Murakami, T. Shiraishi, K. Kishino, Phys. Status Solidi C 11 (2014) 1273.
[16] M. Vos, F. Xu, S.G. Anderson, J.H. Weaver, H. Cheng, Phys. Rev. B 39 (1989) 10744.
[17] G. Stareev, H. Künzel, G. Dortmann, J. Appl. Phys. 74 (1993) 7344.
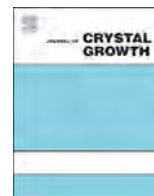
Study of single crystal CuInSe₂ thin films and CuGaSe₂/CuInSe₂ single quantum well grown by molecular beam epitaxy

Sathiabama Thiru [a,c,*], Masaki Asakawa [a], Kazuki Honda [a], Atsushi Kawaharazuka [b],
Atsushi Tackeuchi [a], Toshiki Makimoto [a,b], Yoshiji Horikoshi [a,b]

[a] School of Advanced Science and Engineering, Waseda University, 3-4-1, Okubo, Shinjuku, Tokyo 169-8555, Japan
[b] CREST, JST, 4-1-8, Honcho Kawaguchi, Saitama 332-0012, Japan
[c] Razak School of Engineering and Advanced Technology, University Technology Malaysia, Kuala Lumpur, Malaysia

ABSTRACT

High quality CuGaSe₂ and CuInSe₂ single crystalline layers are grown on GaAs (001) by employing the deposition sequence of migration enhanced epitaxy using a solid source molecular beam epitaxy system. When CuGaSe₂ is grown on CuInSe₂ at moderate temperatures, severe interdiffusion takes place at the heterojunction of CuGaSe₂/CuInSe₂. This problem has been solved by optimizing the growth temperature and deposition rates of the constituent elements. Thus, we have successfully grown CuGaSe₂/CuInSe₂ single quantum well with sharp interfaces on GaAs (001) for the first time. Intense photoluminescence from the single quantum well with 10 nm well width is demonstrated.

© 2015 Elsevier B.V. All rights reserved.

1. Introduction

Growth of chalcopyrite materials such as CuInSe₂ (CIS) and CuGaSe₂ (CGS) has been done on glass substrates by variety of deposition methods for solar cell application. Therefore, grown layers have been polycrystalline. In addition, only p-type conduction is obtained in these materials. Therefore, solar cells have been usually constructed by making p–n heterojunctions using n-type CdS/ZnO [1,2]. These structures suffer from the poor interface flatness and thin film crystal quality, mainly due to the large lattice mismatching at the heterointerface. As a result, high density of defects could be introduced. Nevertheless, resulting solar cells show high performances as used for practical application. We expect that the solar cell performances could be much more improved by using high quality single crystal thin films of CIS and CGS instead of polycrystalline layers. If the high quality single crystal layers are available, flat interfaces are easily achieved. In addition, we expect that such low defect density single crystal layers could be useful to achieve materials with n-type conduction. If the heterojunction interface issues are eliminated, dramatic increase in efficiency of solar cells can be expected. In addition, if the flat interfaces are obtained in CIS/CGS and CGS/CIS heterostructures, CGS/CIS quantum wells and superlattices (SLs) can be grown. Thus, this material system can be applied to variety of electro-optic devices in addition to solar cells. Growth and

characterization of single crystal CIS and CGS layers have so far been grown by using molecular beam epitaxy (MBE) [3–6]. By optimizing Cu/Ga, and Cu/In ratios they improved the hole mobility of CGS and CIS. However, the values were still not very high compared with those of the samples grown by a chemical vapor transport method [7,8].

In the present work, we have found that during epitaxial growth of CGS on GaAs (001) by MBE, the intensity of RHEED pattern decreases and disappears after several tens of MLs growth. When the migration enhanced epitaxy (MEE) deposition sequence is applied instead of simultaneous deposition of conventional MBE, the intense RHEED patterns are conserved throughout the growth. Resulting CGS layers exhibit hole mobility as high as 220 cm²/Vs at 300 K and 2000 cm²/Vs at 100 K [9,10]. Therefore, we have adopted the MEE deposition sequence where cations (Cu and Ga) and anions (Se) are alternately deposited. Similar improvement is observed for CIS growth on GaAs (001).

Thus, we have grown high quality CIS and CGS thin films by using MEE. By optimizing the growth temperature and fluxes of constituent elements, CGS/CIS double heterostructures and single quantum wells (SQW) are successfully grown on GaAs (001) substrates for the first time. The grown structures are evaluated by means of X-ray diffraction (XRD) and photoluminescence (PL).

2. Experimental procedure

A VG80H MBE system equipped with a RHEED gun having an acceleration voltage of 20 kV and an incident angle of 1.5° has

been used in this work. Single crystal CIS and CGS thin films and CGS/CIS SQWs have been grown by using MEE deposition sequence. The MEE growth of CGS for example is composed of repetition of Cu+Ga deposition followed by Se deposition. The variation of RHEED specular beam intensity is monitored during growth. We have employed GaAs (001) as substrates because its lattice constant is close to those of CIS and CGS. The lattice mismatch between CGS and GaAs is only 0.7% and, for CIS and GaAs it is 2.3%.

Optimized beam equivalent pressures of Cu, In, Ga and Se used in this experiment are 1×10^{-7} mbar, 3×10^{-7} mbar, 3×10^{-7} mbar and 1×10^{-5} mbar, respectively. The duration of the deposition cycle is 2 s for each of Cu+In(Ga) and Se deposition which provides about 2.0 MLs/cycle. With the flux intensities stated above, 2 MEE cycles complete one unit cell of chalcopyrite crystal. Background pressure of the growth chamber is as low as 5.0×10^{-10} mbar. After removing the native oxide from the GaAs (001) substrate at 590 °C, we have confirmed (2×4) reconstruction. After that, we have grown CGS, CIS and CGS/CIS single quantum wells. Growth has been performed at temperatures between 580 °C and 350 °C.

For structural studies, XRD measurements were performed for grown structures. We have measured and analyzed PL of CGS, CIS thin films and CGS/CIS SQWs. In the present PL study, we have employed cooled InGaAs–CCD detector and the excitation laser energy of 2.33 eV. Hall measurements were also performed at room temperatures.

3. Results and discussion

As described above MEE deposition sequence keeps the RHEED pattern bright throughout the epitaxial growth. This is probably caused by the fact that, in MEE, cations and anions of constituent elements are separately deposited on the surface. During cation deposition, Cu+Ga/In atoms have enough time to find their preferable nucleation sites and able to produce well-ordered and smooth surface layer [11–13]. Indeed, MEE has been proved useful for producing high mobility CGS and CIS compared with those grown by conventional MBE [9]. Undoped CGS with hole concentration of 1×10^{17}/cm^3 shows a hole mobility higher than 200 cm^2/Vs at room temperature.

Another difficulty of the growth of this system is severe intermixing at the CGS/CIS interface. It is found that less intermixing occurs when CIS is grown on CGS, while drastic intermixing is observed when CGS is grown on CIS at temperatures higher than 500 °C. This intermixing problem is circumvented by lowering the growth temperature and optimizing the deposition fluxes. The intermixing is directly detected through in-situ RHEED specular beam intensity observation. The details are reported elsewhere [14].

Such intermixing occurs even between GaAs substrate and over grown CIS layer. Fig. 1 shows the results of double-crystal X-ray 2θ–ω scans of CIS grown on GaAs (001) at temperatures 580 and 530 °C in the vicinity of (004) GaAs Bragg angle. Each sample has a CIS thickness of about 1 μm. The sample grown at 530 °C exhibits well-distinguished diffraction peaks close to its strain-free angle of CIS (008) as shown by a dashed vertical line [15]. In the sample grown at 580 °C, however, the diffraction peak appears at 64.74°, which corresponds to a smaller vertical lattice constant c compared to CIS (11.616 Å). Plausible reason for this obvious shift is due to the Ga incorporation into CIS layer from the GaAs substrate during growth. Even the CIS layer grown at 530 °C has diffraction peak shifts slightly to the higher angle direction, suggesting also an intermixing between CIS and GaAs. Assuming that Vegard's law is operative in this system, the CIS layer grown at 580 °C contains 16% of Ga in average, while 2% of Ga contamination is expected in the sample grown at 530 °C. This implies that even when temperature is as low
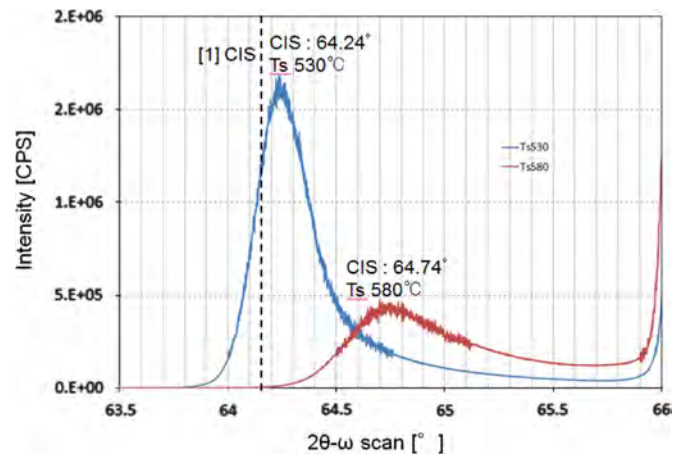
Fig. 1. XRD measurement results of CIS grown on GaAs (001) at 580 and 530 °C.
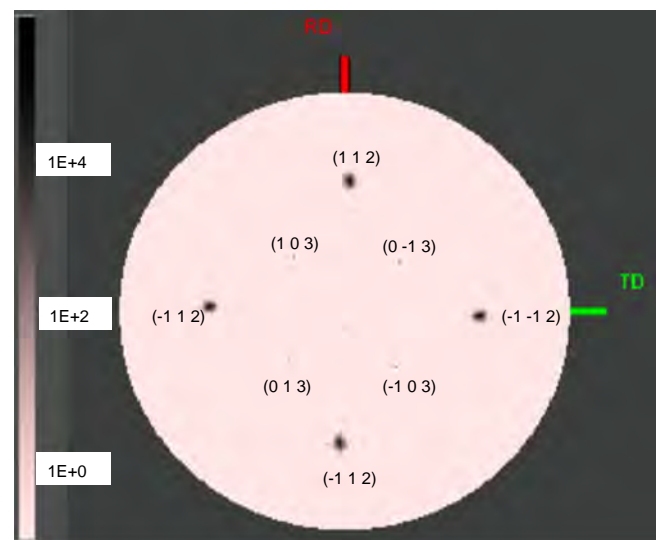
Fig. 2. {112} and {103} pole figure of CIS/GaAs.

as 530 °C, Ga diffusion from GaAs substrate into growing CIS occurs prominently. Rather broad diffraction bands of CIS related peaks are probably caused by the gradual variation of Ga/In ratio in the epitaxial layers. Thus, low temperature growth is vital to achieve an abrupt interface of CIS on GaAs. However, there are no other domain phases, microstructures or twining in the {112} and {103} pole as confirmed by the pole figure of epitaxial CIS single crystal on GaAs (001) shown in Fig. 2. Previously, we have reported the pole figure results of CGS on GaAs (001) [9], similarly it confirms that there are no other microstructures in the epitaxial CGS layers.

For the growth of CIS/CGS quantum wells, we have first deposited 500 nm-thickness of CGS layer at 580 °C because no discernible intermixing occurs at CGS/GaAs interface at 580 °C. Then the substrate temperature is lowered to 350 °C, where a 10 nm-thickness of CIS well is grown. Next, at the same temperature (350 °C) a 30 nm-thickness of CGS growth is continued. Then the growth is suspended and the substrate temperature is increased to 580 °C. Then the CGS growth is continued until the total CGS thickness reaches 500 nm. This process anneals the previously grown CIS and CGS at 350 °C. As a result, the crystal quality of the SQW is improved.

PL measurements are carried out on the CIS thin films grown on GaAs at 530 °C. PL measurements are performed between 10 and 300 K using 532 nm excitation source with 2~30 mW and a InGaAs CCD detector. The PL spectra measured at different temperatures are shown in Fig. 3. At 10 K, the dominant peak appears at 1.043 eV,
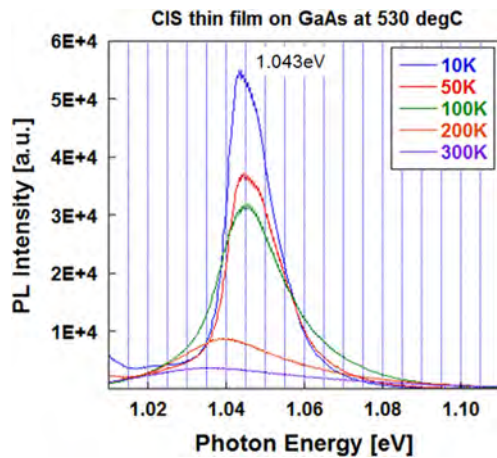
Fig. 3. PL emissions of CIS thin film grown on GaAs at 530 °C.

Fig. 5. PL emissions of CGS/CIS SQW grown at 350 °C.
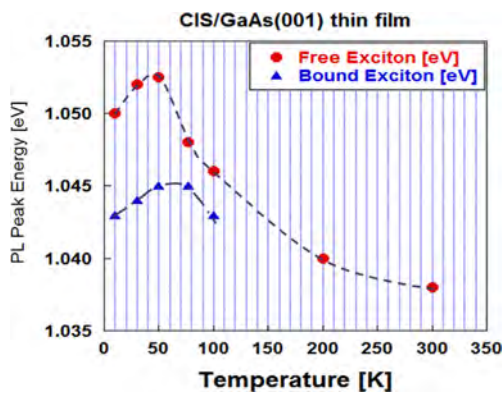
Fig. 4. Temperature dependence of excitonic emissions of CIS thin film grown on GaAs at 530 °C.

Fig. 6. PL emissions of CGS barrier grown at 580 °C.

which is probably caused by the CIS excitonic transition. Even though CIS grown at 530 °C has 2% of Ga incorporation, intense and sharp spectra of near band edge emissions are obtained which confirms high crystal quality. Using results from Fig. 3, a multi-peak Gaussian fitting is performed to analyze the superpositioned emission peaks. The PL peak fitting results are used to discuss the temperature effect in CIS material. In Fig. 4 the temperature dependence of the radiative recombination peaks for both bound and free excitons are shown. The PL peak energy difference between temperatures at 300 and 10 K is only 10 meV, indicating that the bandgap variation on temperature is very small. This value is one order of magnitude smaller than that of GaAs. This is one of the characteristics of CIS which may be useful for optical devices. In Fig. 4, PL peak energies for both emission lines show a slight increase when the temperature is raised from 10 K to 50 K. This phenomenon could be related to the characteristics of thermal expansion coefficient of this material. Above 100 K, the bound exciton peak disappears probably due to the excitation to free excitons.

The PL spectra from a CGS/CIS SQW composed of 500 nm of CGS barrier and 1 nm of CIS well are shown in Fig. 5. The excitonic emission from the SQW appears at 1.11 eV, while the excitonic transition feature from CGS barrier layer is seen at 1.71 eV. PL emission peak of pure CIS should be around 1.05 eV at 10 K. The calculated energy of the transition between the lowest quantized levels of 10 nm quantum well is about 30 meV higher than the bulk CIS band-to-band transition. Therefore, the SQW emission occurs at 30 meV higher than the calculated value. This discrepancy is probably caused by the possible small amount of Ga diffusion into the CIS well during the growth of upper CGS barrier layer. Furthermore, the full-width-at-half-maximum (FWHM) of the PL
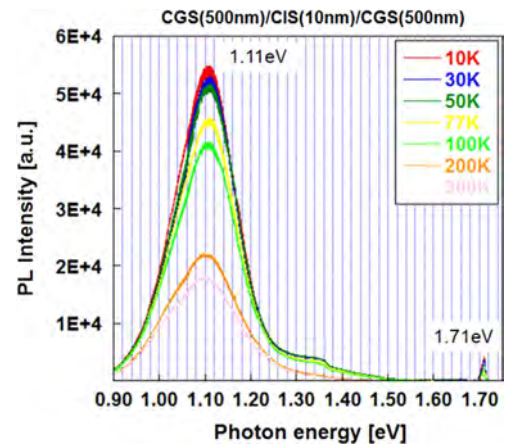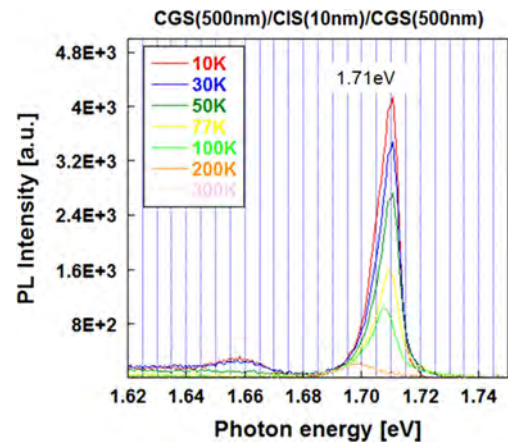
spectra of SQW (~140 meV) is much broader than that of the excitonic emission of CGS (~10 meV). In addition, the FWHM is almost independent on the temperature. Therefore, this broadness of SQW emission is probably caused by the Ga and In interdiffusion at the interface of CGS and CIS. On the other hand, there is no obvious temperature variation in the PL emission energies in CIS SQW. This is quite an interesting feature of this material system, which makes it attractive for future device application. Fig. 6 shows PL emission spectra from the CGS barrier. Here, we are able to confirm much larger temperature dependence than those of CIS. The peak energy variation between 10 K and 300 K is as large as 25 meV which is attributed to the CGS bandgap characteristics.

Electrical properties are also investigated for undoped CIS and CGS single layer films. CIS thin films grown at 530 and 580 °C exhibit similar hole concentrations between $3 \sim 4 \times 10^{17}$/cm^3. The hole mobility of these CIS samples is 86 and 220 cm^2/Vs. CGS thin films also show similar mobility characteristics as CIS. The CGS samples grown at 580 °C exhibit a hole mobility of approximately 200 cm^2/Vs, while those grown at 550 °C give only about 70 cm^2/Vs. However, n the latter, the resulting hole concentration is very different; the samples grown at 580 °C show a hole concentration of $\sim 1 \times 10^{17}$/cm^3, while the sample grown at 550 °C gives 4×10^{16}/cm^3. These results suggest that higher temperature growth is preferable for obtaining high mobility material for both CIS and CGS. However, in our SQW samples, low-temperature grown CIS well and a part of CGS are annealed during the growth of upper CGS barrier. Thus, the quality of the well region is predicted to be good. This may be the major reason of the intense PL emission from the well.

4. Conclusion

In conclusion, we have successfully grown CIS thin films and CGS/CIS SQWs on GaAs (001) substrates using MEE growth sequence. In order to prevent intermixing between CIS and CGS, a special temperature control process is developed in the growth of CGS barrier on CIS well, in particular. Grown structures are characterized by X-ray diffraction and PL. The PL from 10 nm CIS well appears at 1.11 eV which is higher than the predicted value by about 30 meV. Since the intensity of quantum well PL emission is much higher than those observed in CGS barrier layer, photo-excited carriers are efficiently injected into the quantum well. Moreover, PL from SQW shows no obvious temperature variation which could be a useful characteristic for optical devices.

Acknowledgments

References

[1] I. Repins, M.A. Contreras, B. Egaas, C. DeHart, J. Scharf, C.L. Perkins, B. To, R. Noufi, Prog. Photovolt.: Res. Appl. 16 (3) (2008) 235–239.
[2] M.A. Green, K. Emery, Y. Hishikawa, W. Warta, E.D. Dunlop, Prog. Photovolt.: Res. Appl. 19 (2011) 565–572.
[3] A. Yamada, Y. Makita, S. Niki, A. Obara, P. Fons, H. Shibata, Microelectron. J. 27 (1) (1996) 53.
[4] S. Niki, P.J. Fons, H. Shibata, T. Kurafuji, A. Yamada, Y. Okada, H. Oyanagi, W.G. Bi, C.W. Tu, J. Crys Growth 175/176 (1997) 1051.
[5] K. Yoshino, H. Yokoyama, K. Maeda, T. Ikari, A. Fukuyama, P.J. Fons, A. Yamada, S. Niki, J. Appl. Phys. 86 (8) (1999) 4354.
[6] S. Chichibu, T. Mizutani, K. Murakami, T. Shioda, T. Kurafuji, H. Nakanishi, S. Niki, P.J. Fons, A. Yamada, J. Appl. Phys. 83 (7) (1998) 3678.
[7] J.H. Schon, J. Phys. D: Appl. Phys. 33 (2000) 286.
[8] J.H. Schon, F.P. Baumgartner, E. Arushanov, H. Riazi-Nejad, C.h. Kloc, E. Bucher, J. Appl. Phys. 79 (9) (1996) 6961.
[9] M. Fujita, A. Kawaharazuka, J. Nishinaga, K.H. Ploog, Y. Horikoshi, Jpn. J. Appl. Phys. 50 (2011) 125502.
[10] M. Fujita, T. Sato, T. Kitada, A. Kawaharazuka, Y. Horikoshi, J. Vac. Sci. Tech. B 30 (2) (2012) 5.
[11] Y. Horikoshi, M. Kawashima, H. Yamaguchi, Jpn. J. Appl. Phys. 25 (1986) L868.
[12] Y. Horikoshi, M. Kawashima, H. Yamaguchi, Jpn. J. Appl. Phys. 27 (1988) 169.
[13] N. Kobayashi, Y. Horikoshi, Jpn. J. Appl. Phys. 28 (1989) L1880.
[14] S. Thiru, M. Asakawa, K. Honda, A. Kawaharazuka, A. Tackeuchi, T. Makimoto, Y. Horikoshi, AIP Advances 5 (2015) 027120-1.
[15] H.W. Spiess, U. Haeberlen, G. Brandt, A. Rauber, J. Schneider, Phys. Status Solidi B 62 (1974) 183.
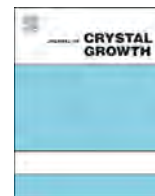
Strain compensated CdSe/ZnSe/ZnCdMgSe quantum wells as building blocks for near to mid-IR intersubband devices

Joel De Jesus [a], Guopeng Chen [b], Luis C. Hernandez-Mainet [c], Aidong Shen [b], Maria C. Tamargo [c,*]

[a] Physics Department, The Graduate Center and The City College of New York (CUNY), 160 Convent Avenue, New York, NY 10031, USA
[b] Electrical Engineering Department, The City College of New York (CUNY), 160 Convent Avenue, New York, NY 10031, USA
[c] Chemistry Department, The Graduate Center and The City College of New York (CUNY), 160 Convent Avenue, New York, NY 10031, USA

ABSTRACT

In order to increase the conduction band offset of the ZnCdMgSe-based material system we studied the incorporation of strained CdSe layers to obtain deeper quantum wells for shorter wavelength intersubband transitions than those obtained in lattice-matched structures. Five CdSe/ZnSe/ZnCdMgSe multi-quantum wells (QW) samples grown by molecular beam epitaxy are studied in detail by transmission electron microscopy (TEM), X-ray diffraction (XRD), cw-photoluminescence (PL), and Fourier Transform Infrared (FTIR) absorption experiments. TEM and XRD results confirmed good structural quality of the samples. All the multi-QW PL energies were below the ZnCdSe lattice-matched to InP alloy bandgap (2.1 eV), which serves as first evidence of having achieved deeper quantum wells. FTIR absorptions from 3.83 to 2.56 μm were measured, shorter than those achieved by the lattice matched system. Simulations based on these results predict that absorptions as low as 2.18 μm can be obtained with these materials.

© 2015 Elsevier B.V. All rights reserved.

1. Introduction

Quantum wells (QW) are the building blocks of intersubband (ISB) devices such as quantum well infrared photodetectors (QWIPs) [1], quantum cascade (QC) lasers [2] and QC detectors [3]. Commercially available ISB devices cover the mid-infrared wavelengths from 4 to 13 μm, and have many applications in science (spectroscopy), medicine (non-invasive glucose monitoring), environment (monitoring of trace pollutants), industry (process monitoring) and military (countermeasure). Achieving room temperature ISB activity shorter than 4 μm wavelengths, to expand their range, has been an area of research since the past decade. The commercially available ISB devices are made from the InGaAs/InAlAs alloys grown on InP. When lattice matched, this material system has a conduction band offset (CBO) of 0.52 eV [4], not enough to reach the 3–5 μm range. Larger offsets can be obtained when strained layers are used, but devices made from those structures have reached a short wavelength fundamental limit of ∼4 μm, due to intervalley scattering [5,6]. In order to achieve shorter IR wavelengths one must increase the CBO, while avoiding intervalley scattering. Some material systems have been investigated for shorter IR wavelength response, including, among

the III–Vs, GaN/Al(Ga)N [7–9], InGaAs/AlAs/InAlAs [10,11], InGaAs/AlAsSb/InP [12], InAs/AlSb [13,14], and, among the II–VIs, (CdS/ZnSe)/BeTe [15,16], and the ZnCdMgSe-based structures [17]. The last example is the focus of our current research.

Calculated band structures of ZnCdSe/ZnCdMgSe-based materials lattice-matched to InP [18,19], and experimental measurements of their CBOs [20] confirm that this system has favorable properties to go beyond the commercially available wavelength range. It has a lattice matched CBO$_{MAX}$ of ∼1.1 eV, and the Γ and X valleys are farther apart than the III–Vs, promising no intervalley scattering. With this system we have reported several novel results in ISB devices, including the first II–VI QWIP operating up to room temperature [21] and the first II–VI QC detector [22], with detectivities around 2.6 and 3.6 μm. Even though the maximum lattice-matched CBO is large enough to expand their operating wavelengths by simply using higher barriers and thinner wells, growth of high bandgap barrier materials, which require high Mg content, is difficult, and the materials are unstable to oxidation. Here we explore the use of the low bandgap CdSe material to make deeper quantum wells as an alternative approach.

Within the ZnCdMgSe alloy system, CdSe is the lowest bandgap binary at our disposal ($E_g = 1.7$ eV). However, it has a large +3.5% mismatch with our substrate of choice, InP. An approach that can be used to incorporate such a highly strained layer in a device structure is strain compensation. We will use ZnSe ($E_g = 2.7$ eV) layers, which has −3.4% mismatch to the InP as strain

compensating layers. As long as the CdSe layers remain below their critical thickness on InP, estimated to be 10 ML, a similar amount of ZnSe can be deposited to achieve strain compensation on InP. ZnSe/CdSe quantum dots have been previously studied and grown on GaAs substrates, where the strain compensation approach for the growth of QWs cannot be easily applied. The optical properties of ZnSe/CdSe short period superlattices on InP have been reported [23,24], but there are no reports of the use of the combination of these binaries to form isolated QWs.

In this paper we will discuss the growth of multi-QW structures grown by Molecular Beam Epitaxy (MBE) using a ZnCdMgSe alloy with a bandgap of 3.0 eV, lattice matched to InP, as the barrier material, compressively strained CdSe as the well material, and tensile strained ZnSe for strain compensation, all grown on InP substrates. We will choose to sandwich the CdSe layer with two ZnSe layers to form a symmetric step QW system. The multi-QW structures grown exhibit narrow short IR wavelength ISB absorption peaks as low as 2.56 μm at room temperature. Simulations based on these results confirm that these structures can be used to cover the 2–3 μm range.

2. Experimental details and methods

2.1. Molecular beam epitaxy growth and samples description

The samples were grown in a dual-chamber MBE system on semi-insulating InP (001) substrates. We chose InP substrates because: 1) it is widely used in currently commercially available InGaAs based intersubband devices, 2) there is a wide range of accessible energy gaps of ZnCdMgSe-based alloys that can be grown lattice matched to it, and 3) strain compensation can be readily be achieved on this substrate. Epi-ready substrates were bonded to molybdenum blocks using indium and loaded to the MBE system in a clean environment. The substrate's native oxide was removed under an arsenic flux in the chamber dedicated to the growth of III–V materials by heating the surface to $\sim 500\,^{\circ}\mathrm{C}$ while monitoring the reflection high energy electron diffraction (RHEED) patterns. After the oxide was removed, a 130 nm buffer layer of InGaAs lattice-matched to InP was grown, and transferred via ultra-high vacuum transfer modules to a second chamber used to grow II–VI materials.

In the II–VI chamber, the surface was exposed to atomic Zn flux for 30 s, and then a 7 nm ZnCdSe layer was grown at a low temperature of 200 °C. The substrate temperature was then raised and kept at the optimal growth temperature of 300 °C for the deposition of the remaining layers. A 120 nm ZnCdSe layer was first grown, followed by 110 nm of ZnCdMgSe. Then the ZnSe/CdSe/ZnSe symmetric step QW structure was grown, followed by a 9.2 nm ZnCdMgSe barrier layer. The deposition times (and therefore the thicknesses) of the ZnSe and CdSe layers were varied to explore the properties for different QW thickness and different strain. This set of 4 layers was repeated 35 times, to create a multi-QW structure. After growth of the multi-QWs, a 110 nm layer of ZnCdMgSe was grown. We capped the structure by growing a 10 nm ZnCdSe layer, to protect the Mg containing layers from oxidation. Brief growth interruptions of 10 s, during which the sample was only irradiated with a molecular flux of Se, were used at the interfaces between layers throughout the entire structure.

A Se-to group-II flux ratio of 6 was used to ensure Se-stabilized growth conditions. Growth of the materials was monitored by RHEED, and streaky 2×1 patterns were observed throughout the growth. Prior to the growth of the multi-QW samples, the compositions of ZnCdSe and ZnCdMgSe were calibrated by growing and characterizing ~ 1 μm thick layers to ensure that they are closely lattice-matched to the InP substrate. No change of the cells

temperatures was made after this calibration for the deposition of the ZnSe and CdSe compounds. RHEED oscillations were used to obtain growth rates, which were 0.38 μm/h for ZnCdSe, and 0.80 μm/h for the ZnCdMgSe layers. RHEED oscillations could not be observed for CdSe, therefore we will vary the deposition times of the CdSe and ZnSe layers to vary the QW thickness and strain. Information for the samples investigated here is given in Table 1, which includes deposition times used for the CdSe (t_{CdSe}), the ratio between t_{CdSe} and total ZnSe deposition time (t_{ZnSe}), and the samples characteristics.

2.2. Post-growth characterization

Structural information of the grown samples was obtained by performing high resolution transmission electron microscopy (TEM), and X-ray diffraction (XRD). A Bruker D8 Discover X-ray diffractometer was used to obtain $2\theta - \omega$ scans around several Bragg reflections of the InP substrate. The electron microscope used was a Hitachi HD2700 scanning transmission electron microscope (STEM) with spherical aberration correction. It was operated at 200 kV acceleration voltage. Dark field transmitted electron images were acquired in atomic number contrast mode (ZC) detected with a High Angle Annular Dark Field (HAADF) detector.

Steady-state PL and Fourier Transform infrared (FTIR) absorption measurements were performed to investigate the optical properties of the structures. The steady-state PL studies were carried out at room temperature by optically pumping the samples with a 30 mW 325 nm He–Cd laser line. The laser radiation was incident at an angle of 45 to the sample surface normal, then the photoluminescence from the sample was collected and the spectra analyzed by an spectrometer (Ocean Optics HR2000). Prior to the FTIR absorption experiments the sample was polished into a multipass geometry, in order to enhance the absorption signal. The ISB absorption was measured using a Nicolet Nexus-870 FTIR spectrometer with a white light source, CaF$_2$ lenses and beam splitter, a wire-grid polarizer, and a liquid-nitrogen-cooled HgCdTe detector. The absorbance for the samples is obtained by taking the negative natural logarithm of the p-polarized transmittance over the s-polarized transmittance.

To obtain the anticipated energy values for the FTIR absorption the symmetric step QW was simulated and the Schrodinger equation for the electron solved using a one-band conduction band model with an energy dependent effective mass that accounts for non-parabolicity, and pseudo-potential parameter to account for strain.

3. Results and discussion

3.1. Structural properties: TEM

TEM images of sample 2 are shown in Fig. 1. In the low magnification image on the left we see the full structure described earlier. The InP substrate is at the bottom, followed by the InGaAs and ZnCdSe buffer layers. Although the contrast between the InGaAs and ZnCdSe is low, the interface could be identified (marked by arrows in the figure). Then there is a darker region corresponding to the first ZnCdMgSe layer, followed by the multi-QW structure. The second ZnCdMgSe and cap layer of ZnCdSe are seen on top. The first two wells of the multi-QW region exhibit diffuse interfaces, but the remaining 33 wells have sharp well-defined interfaces. No dislocations are seen in these low magnification images, indicative of coherent structures.

A higher magnification image of the multi-QW region is also shown in Fig. 1 (right side). Uniform ZnCdMgSe barriers layer
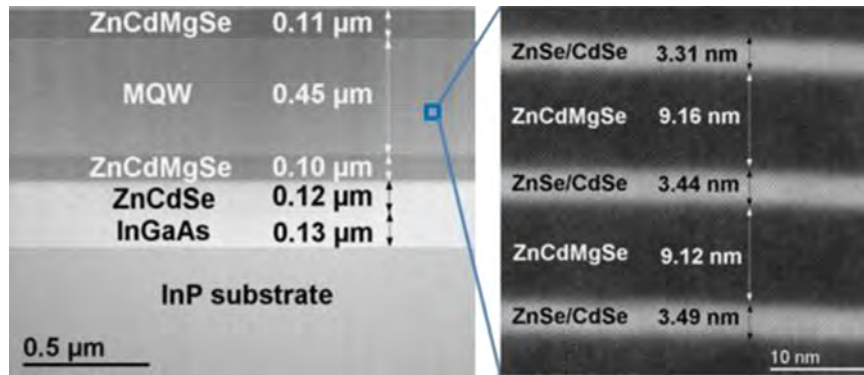
Fig. 1. TEM images of a multi-QW sample 2. In the left a lower magnification image shows the whole sample structure. On the right a higher magnification image around the quantum wells.
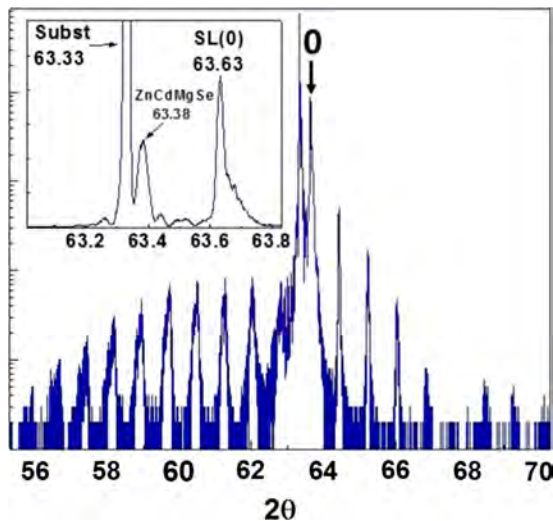
Fig. 2. Plot of the $2\theta-\omega$ scan around the InP (004) reflection for the multi-QW sample 2. The inset is a linear-scale plot near the substrate peak.

Table 1
Information of the multi-QW samples investigated here. The second and third column gives the deposition times of the CdSe and ZnSe layers. Following are the $\Delta a/a$ of the 0th order superlattice peak obtained from XRD. Then the PL and FTIR absorption measurements, ending with the calculated CdSe thickness obtained by simulations.

Sample #	tCdSe (s)	tCdSe/ tZnSe	$\Delta a/a$ (%)	RT PL (eV)	FTIR absorption (μm)	Simulated CdSe thickness (ML)
1	51	1.34	−1.0	1.77	3.8	9
2	40	2.5	−0.42	1.86	3.04	7
3	32	2.6	−0.23	1.95	2.65	6
4	28	2.8	+0.90	2.01	2.59	~5.5
5	24	3	+1.0	2.06	2.56	~5.5
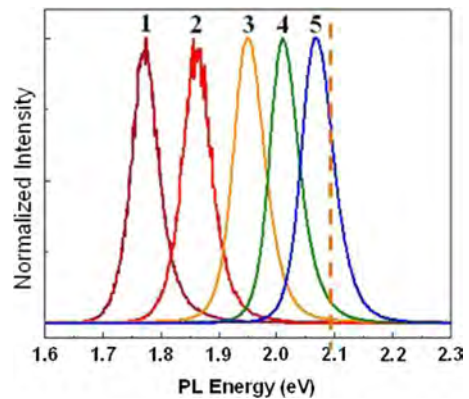
Fig. 3. Room temperature cw-PL of the samples investigated here. On top of each spectrum is the sample number. The dotted line shows the 2.1 eV bandgap for the ZnCdSe alloy lattice-matched to InP.

thicknesses of 9.2 nm, and 3.4 nm for the ZnSe/CdSe layers were obtained. The contrast between the ZnSe/CdSe layers was not evident, and the layers could not be resolved individually. CdSe is known to produce quantum dots (QDs) when grown on ZnSe on GaAs substrates due to the large lattice mismatch when that substrate is used. The TEM images confirm that when grown on InP substrates and with strain compensation, good two-dimensional QW formation was achieved through the structure.

3.2. Structural Properties: XRD

Fig. 2 shows the $2\theta-\omega$ scans for sample 2, which is representative of all the samples studied. For the measurement shown we aligned to the InP substrate (004) Bragg reflection. The main graph is plotted on a log-scale, and the scan was made over a wide range of 2θ values (55.3–70.3). Many superlattice peaks are present in the scan, evidence of an excellent layered structure. The inset shows a linear scale plot over a narrow 2θ range, close to the substrate peak. Based on the results of the calibration samples we could identify the ZnCdMgSe (shown), and ZnCdSe (not shown) 004 diffraction peaks.

Because of the highly strained nature of this system and to clearly identify the 0th order superlattice peak, we scanned the (004), (115), (113), (224) and (333) Bragg reflections and performed a graphical identification of the 0th order superlattice peak [25–27] for all the samples, and followed its evolution as the

tCdSe/tZnSe was changed. From this we deduced the perpendicular lattice mismatch from the structures, which varied from −1.0% to +1.0%. The data are summarized in Table 1. The lowest mismatch was −0.23% for sample 3. Further adjustments of the relative thicknesses of the CdSe and ZnSe layers should result in a fully strain compensated structure with the desired mismatch value of less than 0.2% [28].

3.3. Optical properties: room temperature cw-photoluminescence

We investigated the intra-band optical transitions by performing PL measurements. Fig. 3 shows the room temperature cw-PL spectra of the samples. Bright PL emission was observed in the visible range, from red (700 nm, 1.77 eV) to orange (602 nm,
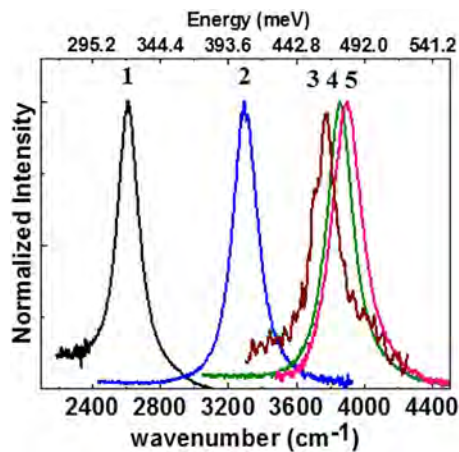
Fig. 4. FTIR absorption of the multi-QW samples investigated here. On top of each spectrum is the number of the sample. The peak absorption in wavelengths was 3.83 μm, 2.65 μm, 2.59 μm, and 2.56 μm for samples 1 to 5, respectively.

Fig. 5. Simulations results for the moduli square of the wavefunctions of the CdSe/ZnSe/ZnCdMgSe step QW. Below each well is the corresponding CdSe thickness in monolayers (ML), followed by the energy and wavelength of the predicted intersubband transition.

2.06 eV). The PL emission energy of all the multi-QW samples studied is below the bandgap of the ZnCdSe lattice-matched to InP ($E_g=2.1$ eV). This is the first indication that the system provides deeper QWs, and hence a larger CBO, by using strained CdSe layers as the well material. Single narrow peaks (FWHM 48–67 meV) were obtained at room temperature for all the samples, and no deep level emission was present, indicative of high quality samples.

3.4. Optical properties: room temperature IR absorption and intersubband simulations

Room temperature FTIR absorption measurements gives us insight about the optical response due to ISB transitions in the infrared. The FTIR absorption spectra for the samples are shown in Fig. 4. Single peaks in the absorption are obtained as expected for symmetric QW structure due to the selection rules. Peak absorption was tailored from 3.83 μm (324 meV) in sample 1 to 2.56 μm (484 meV) in sample 5, well below the values achieved with the InGaAs/InAlAs system on InP.

Simmulations of the conduction band energy levels in single symmetric step QWs were done to obtain the wavefunctions and discreet energy values expected for these structures. The 3.0 eV ZnCdMgSe barrier thickness of 9 nm is thick enough to prevent coupling in the QWs. In the simulations we vary the CdSe layer thickness from 9 ML to 3 ML, with integer ML values. The ZnSe total thickness was set such that the structure would be strain balanced, that is, the same number of MLs of ZnSe as MLs of CdSe. The QW structure was assumed to be symmetric, so that the ZnSe total thickness is distributed equally on each side of the CdSe layers (for example: 4.5 ML ZnSe/9 ML CdSe/4.5 ML ZnSe). The simulation parameters include the effective mass of the electron in the conduction band of $0.11m_e$, $0.15m_e$, and $.23m_e$ for CdSe (RT E_g = 1.7 eV), ZnSe (RT E_g = 2.7 eV), and MgSe (RT E_g = 3.6 eV), respectively, and a conduction band offset of 80% of the total band offset. From the simulations, shown in Fig. 5, only one electron bound state was obtained for 3 ML of CdSe, 2 bound states for 4–6 ML, and 3 bound states from 7–9 ML. We calculated $e1-e2$ transitions energies of 3.85 μm (322 meV) for 9 ML CdSe well, 3.43 μm (361 meV) for 8 ML, 3.04 μm (407 meV) for 7 ML, 2.68 μm (461 meV) for 6 ML, 2.39 μm (518 meV) for 5 ML, and 2.18 μm (569 meV) for 4 ML of CdSe. By comparing the simulation values with the measured absorption we could estimate the actual thickness of the CdSe layers to be ∼9 ML for sample 1, 7 ML for sample 2, 6 ML for sample 3, and around 6–5 ML for samples 4 and 5.
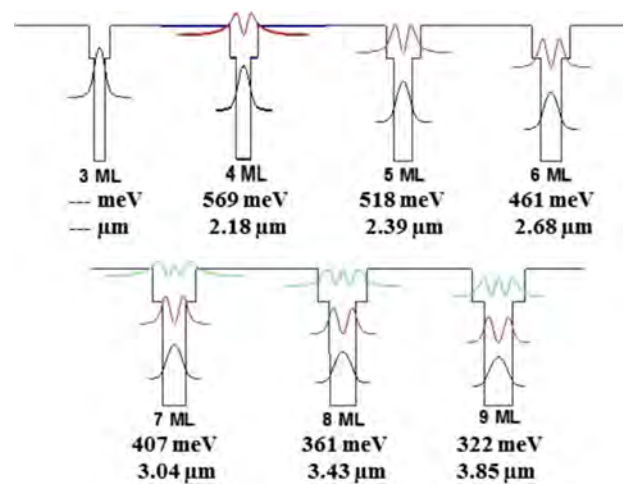
Based on the simulation results we predict that we can reach wavelengths as low as 2.18 μm with the materials used here by reducing the CdSe (and corresponding ZnSe) thickness to 4 ML. Even shorter wavelengths for QW thinner than 4 ML can be obtained by increasing the barrier height using a higher MgSe fraction in the quaternary material. The binaries CdSe (as the well material) and MgSe (as the barrier) provide the maximum band-gap difference of the ZnCdMgSe alloy system, but if the strain between them and the InP substrate is not balanced it can lead to lattice relaxation and defects. An improvement of the structure quality is clearly evidenced by XRD scans when ZnSe is used for strain compensation [29] as compared to when no strain compensation is used [30]. The incorporation of binary compounds in the active region of these structures may have other positive impacts on the material quality due to the absence of alloy disorder, which could result in more abrupt interfaces [31].

4. Conclusions

We presented the MBE growth and characterization of strain balanced CdSe/ZnSe/ZnCdMgSe-based multi-QW structures grown on InP substrates. TEM, XRD and PL confirm the good structural and optical quality of the samples. The ISB absorption of these multi-QW structures was observed at wavelengths as low as 2.56 μm, shorter than those possible with the commonly used InGaAs-based structures. Simulations based on these results predict that using a 3.0 eV ZnCdMgSe barrier wavelengths as short as 2.18 μm are possible with these strained compensated materials.

References

[1] H. Schneider, H.C. Liu, Quantum Well Infrared Photodetectors, in: William T. Rhodes (Ed.), Springer Publications, New York, http://dx.doi.org/10.1007/978-3-540-36324-8.

[2] J. Faist, F. Capasso, D.L. Sivco, C. Sirtori, A.L. Hutchinson, A.Y. Cho, Quantum cascade laser, Science 264 (1994) 553. http://dx.doi.org/10.1126/science.264.5158.553.

[3] F.R. Giorgetta, E. Baumann, M. Graf, Q. Yang, C. Manz, K. Köhler, H.E. Beere, D.A. Ritchie, E. Linfield, A.G. Davies, Y. Fedoryshyn, H. Jäcket, M. Fischer, J. Faist, D. Hofstetter, Quantum cascade detectors, IEEE J. Quantum Electron. 45 (2009) 1039. http://dx.doi.org/10.1109/JQE.2009.2017929.

[4] N. Georgiev, T. Dekorsy, F. Eichhorn, M. Helm, M.P. Semtsiv, W.T. Masselink, Short-wavelength intersubband absorption in strain compensated InGaAs/AlAs quantum well structures grown on InP, Appl. Phys. Lett. 83 (2003) 210. http://dx.doi.org/10.1063/1.1592315.

[5] N. Bandyopadhyay, Y. Bai, S. Tsao, S. Nida, S. Slivken, M. Razeghi, Room temperature continuous wave operation of lambda similar to 3–3.2 μm quantum cascade lasers, Appl. Phys. Lett. 101 (2012) 241110. http://dx.doi.org/10.1063/1.4769038.

[6] I.P. Marko, A.R. Adams, S.J. Sweeney, R. Teissier, A.N. Baranov, S. Tomic, Evidence of carrier leakage into the L-valley in InAs-based quantum cascade lasers under high hydrostatic pressure, Phys. Status Solidi B 246 (2009) 512. http://dx.doi.org/10.1002/pssb.200880501.

[7] K. Driscoll, Y.T. Liao, A. Bhattacharyya, L. Zhou, D.J. Smith, T.D. Moustakas, R. Paiella, Optically pumped intersubband emission of short-wave infrared radiation with GaN/AlN quantum wells, Appl. Phys. Lett. 94 (2009) 081120. http://dx.doi.org/10.1063/1.3089840.

[8] C. Gmachl, H.M. Ng, S.N.G. Chu, A.Y. Cho, Intersubband absorption at lambda similar to 1.55 μm in well- and modulation-doped GaN/AlGaN multiple quantum wells with superlattice barriers, Appl. Phys. Lett. 77 (2000) 3722. http://dx.doi.org/10.1063/1.1332108.

[9] M. Beeler, E. Trichas, E. Monroy, III-nitride semiconductors for intersubband optoelectronics: a review, Semicond. Sci. Technol. 28 (2013) 074022. http://dx.doi.org/10.1088/0268-1242/28/7/074022.

[10] S. Gozu, T. Mozume, H. Kuwatsuka, H. Ishikawa, InGaAs/AlAs/InAlAs coupled double quantum wells for intersubband transition devices operating at 1550 nm, J. Cryst. Growth. 378 (2013) 134. http://dx.doi.org/10.1016/j.jcrysgro.2012.11.023.

[11] M.P. Semtsiv, M. Ziegler, W.T. Masselink, N. Georgiev, T. Dekorsy, M. Helm, Near-infrared intersubband transitions in InGaAs–AlAs–InAlAs double quantum wells, J. Appl. Phys. 97 (2005) 113538. http://dx.doi.org/10.1063/1.1931037.

[12] S.Y. Zhang, D.G. Revin, J.W. Cockburn, K. Kennedy, A.B. Krysa, M. Hopkinson, Lambda similar to 3.1 μm room temperature InGaAs/AlAsSb/InP quantum cascade lasers, Appl. Phys. Lett. 94 (2009) 031106. http://dx.doi.org/10.1063/1.3073865.

[13] D. Barate, R. Teissier, Y. Wang, A.N. Baranov, Short wavelength intersubband emission from InAs/AlSb quantum cascade structures, Appl. Phys. Lett. 87 (2005) 051103. http://dx.doi.org/10.1063/1.2007854.

[14] J. Devenson, D. Barate, O. Cathabard, R. Teissier, A.N. Baranov, Very short wavelength (lambda=3.1–3.3 μm) quantum cascade lasers, Appl. Phys. Lett. 89 (2006) 191115. http://dx.doi.org/10.1063/1.2387473.

[15] B.S. Li, R. Akimoto, A. Akita, T. Hasama, Lambda 1.49–3.4 μm intersubband absorptions in (CdS/ZnSe)/BeTe quantum wells grown by molecular beam epitaxy, Appl. Phys. Lett. 88 (2006) 221915. http://dx.doi.org/10.1063/1.2208963.

[16] R. Akimoto, K. Akita, F. Sasaki, T. Hasama, Sub-picosecond electron relaxation of near-infrared intersubband transitions in n-doped (CdS/ZnSe)/BeTe quantum wells, Appl. Phys. Lett. 81 (2002) 2998. http://dx.doi.org/10.1063/1.1515371.

[17] A. Shen, W.O. Charles, B.S. Li, K.J. Franz, C.F. Gmachl, Q. Zhang, M.C. Tamargo, Wide band gap II-VI selenides for short wavelength intersubband devices, J. Cryst. Growth. 311 (2009) 2109. http://dx.doi.org/10.1016/j.jcrysgro.2008.10.102.

[18] H. Hakan Gürel, H. Ünlü, Density functional and tight binding theories of electronic properties of II–VI heterostructures, Mater. Sci. Semicond. Process. 16 (2013) 1619. http://dx.doi.org/10.1016/j.mssp.2013.05.021.

[19] O. Zakharov, A. Rubio, X. Blase, M.L. Cohen, S.G. Louie, Quasiparticle band structures of six II–VI compounds: ZnS, ZnSe, ZnTe, CdS, CdSe, and CdTe, Phys. Rev. B 50 (1994) 10780. http://dx.doi.org/10.1103/PhysRevB.50.10780.

[20] M. Munoz, H. Lu, X. Zhou, M.C. Tamargo, F.H. Pollak, Band offset determination of $Zn_{0.53}Cd_{0.47}Se/Zn_{0.29}Cd_{0.24}Mg_{0.47}Se$, Appl. Phys. Lett. 83 (2003) 1995. http://dx.doi.org/10.1063/1.1606875.

[21] A.P. Ravikumar, G. Chen, K. Zhao, Y. Tian, P. Prucnal, M.C. Tamargo, C.F. Gmachl, A. Shen, Room temperature and high responsivity short wavelength II–VI quantum well infrared photodetector, Appl. Phys. Lett. 102 (2013) 161107. http://dx.doi.org/10.1063/1.4802955.

[22] A.P. Ravikumar, T.A. Garcia, J. De Jesus, M.C. Tamargo, C.F. Gmachl, High detectivity short-wavelength II–VI quantum cascade detector, Appl. Phys. Lett. 105 (2014) 061113. http://dx.doi.org/10.1063/1.4893359.

[23] Y. Nabetani, H. Takahashi, T. Kato, T. Matsumoto, CdSe/ZnSe strained layer superlattices grown on InP, J. Cryst. Growth. 184 (1998) 26. http://dx.doi.org/10.1016/S0022-0248(98)80287-X.

[24] Y. Nabetani, Y. Kobayashi, T. Kato, T. Matsumoto, High resolution transmission electron microscope analysis of CdSe/ZnSe strained layer superlattices grown on InP, Phys. Status Solidi B 229 (2002) 209.

[25] K. Nakashima, H. Sugiura, A novel graphical analysis method for double crystal X-ray diffraction measurements of strained layer superlattices grown on (100) substrate, Jpn. J. Appl. Phys. Part 1 36 (1997) 5351. http://dx.doi.org/10.1143/JJAP.36.5351.

[26] K. Nakashima, Y. Kawaguchi, X-ray-diffraction analysis of complex structures in ZnCdSe/ZnSe strained-layer superlattices, J. Appl. Phys. 76 (1994) 5111. http://dx.doi.org/10.1063/1.357223.

[27] K. Nakashima, Evaluation of $In_{1-x}Ga_xAs/In_{1-y}Ga_y$ As strained layer superlattice structures by X-ray-diffraction measurements with a novel discrimination method of the fundamental peak, J. Appl. Phys. 71 (1992) 1189. http://dx.doi.org/10.1063/1.351286.

[28] T.A. Garcia, S. Hong, M. Tamargo, J. De Jesus, V. Deligiannakis, A. Ravikumar, C. Gmachl, A. Shen, Improved electrical properties and crystalline quality of II–VI heterostructures for quantum cascade lasers, J. Vacuum Sci. Technol. B 31 (2013) 03C133. http://dx.doi.org/10.1116/1.4803837.

[29] G. Chen, J. DeJesus, M.C. Tamargo, A. Shen, MgSe/ZnSe/CdSe coupled quantum wells grown on InP substrate with intersubband absorption covering 1.55 μm, Appl. Phys. Lett. 105 (2014) 232107. http://dx.doi.org/10.1063/1.4903823.

[30] G. Chen, K. Zhao, M.C. Tamargo, A. Shen, Near infrared intersubband absorption of CdSe/MgSe quantum wells grown on InP substrate with an InAlAs buffer layer, J. Vacuum Sci. Technol. B 32 (2014) 02C105. http://dx.doi.org/10.1116/1.4863496.

[31] Y. Kawakami, M. Funato, S. Fujita, S. Fujita, Y. Yamada, Y. Masumoto, Localized excitons in cubic $Zn_{1-x}Cd_xS$ lattice matched to GaAs, Physical Review B 50 (1994) 14655. http://dx.doi.org/10.1103/PhysRevB.50.14655.
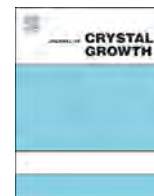
MBE growth, structural and transport properties of alternately-strained ZnSSe/CdSe superlattices with effective band-gap 2.5–2.6 eV

S.V. Sorokin *, S.V. Gronin, E.A. Evropeytsev, I.V. Sedova, A.A. Toropov, S.V. Ivanov

Ioffe Physical-Technical Institute, Politekhnicheskaya Street 26, St. Petersburg 194021, Russia

ABSTRACT

Short-period ZnS_ySe_{1-y}/CdSe superlattices (SLs) with an effective energy gap $E_g = 2.5$–2.6 eV ($T = 300$ K) are grown by molecular beam epitaxy pseudomorphically on GaAs (001), and their structural properties are studied by using X-ray diffraction (XRD) and transmission electron microscopy. Both sulfur content and thickness of the ZnS_ySe_{1-y} SL barriers have been determined via analysis of the XRD curves, taking account of the thickness of the CdSe SL layers estimated independently from the low-temperature ($T = 77$ K) PL spectra of the single CdSe quantum dot (QD) layer (nominal thickness of 2.8 monolayer) embedded into each SL. The evaluated SL parameters are shown to be in good agreement with the intended ones. The efficient non-equilibrium carrier transport in the SLs along the growth direction at 300 K is demonstrated by photoluminescence (PL) spectroscopy through the relative temperature variation of the intensities of the PL peaks originated from the buried CdSe/ZnSe QD layers and the ZnSSe/CdSe SLs.

1. Introduction

An increase in the efficiency of multi-junction solar cells (SCs) is of great importance due to the rapid growth in the worldwide demand for renewable energy. Today, the highest values of conversion efficiency ($\sim$44%) have been reported for the concentrator triple-junction compound SCs based on metamorphic InGaP/GaAs/InGaAs [1] and pseudomorphic GaInP/GaAs/GaInNAs [2] structures. Nevertheless, it is expected that adjunction of a II–VI pseudomorphic cascade to the existing three-cascade III–V SCs can further increase the SCs efficiency due to optimization of photoelectric conversion of the short-wavelength part of the solar radiation spectrum [3]. Short-period alternately-strained ZnS_ySe_{1-y}/CdSe superlattices (SLs) lattice matched to GaAs (or Ge) look as a suitable material for such wide-gap cascade. The SLs could be realized in a relatively wide energy gap range (2.5–2.6 eV), while maintaining the high crystallinity and efficient vertical transport of photo-excited carriers. Moreover, the using of SLs instead of bulk alloys results in narrower effective band gap of the structures in comparison with the bulk alloy with the same composition [4]. And finally, the proposed ZnS_ySe_{1-y}/CdSe SLs could be matched not only to GaAs(Ge) substrates, but also to the lattice

parameter of metamorphic $In_xGa_{1-x}As$ ($x \sim 0.2$–0.3) structures, demonstrating even lower (down to $\sim$2.1 eV) energy gap value.

This paper reports on MBE growth of pseudomorphic short-period ZnS_ySe_{1-y}/CdSe SLs with the effective band-gap energy $E_g^{eff} = \sim$2.5–2.6 eV (300 K) and studies of their structural properties by using X-ray diffraction (XRD) and transmission electron microscopy (TEM) techniques as well as the photo-excited carrier transport in the SLs along the growth direction by using photoluminescence (PL) spectroscopy.

2. Experiment and ZnSSe/CdSe superlattices design

The ZnS_ySe_{1-y}/CdSe SL structures were grown by molecular beam epitaxy (MBE) at growth temperature $T_S \sim 250\ ^\circ$C on GaAs (001) substrates via GaAs buffer layers by using a double-chamber setup (SemiTEq, Russia). Conventional Zn, Cd, ZnS cells, and Se valve cracking cell were employed as molecular beam sources. The low T_S value is governed by the strong temperature dependence of the sulfur sticking coefficient and requirements of the high ($y = 0.3$–0.4) sulfur content in the ZnS_ySe_{1-y} layers of the SLs, obtained under stoichiometric growth conditions (VI/II $\sim$1) [5]. The structures under the study comprise sequentially from the substrate: fifty SL periods followed by a single CdSe/ZnSe quantum dot (QD) layer with a nominal thickness of 2.8–3.0 monolayers (MLs), and then ninety additional SL periods on top (see Fig. 1). The nominal thicknesses of

* Corresponding author. Tel.: +7 812 2927124; fax: +7 812 2973620.
E-mail address: sorokin@beam.ioffe.ru (S.V. Sorokin).

CdSe ($w_{CdSe}^{(SL)}$) and ZnS$_y$Se$_{1-y}$ ($t_{ZnSSe}^{(SL)}$) SL layers were varied within the 1.3–1.6 and 4–6 ML ranges, respectively. Both the thicknesses and S content in the SL layers were chosen to implement the strain balance between the tensile-strained ZnSSe and compressively strained CdSe layers. Taking into account the difference in elastic properties of the constituent SL layers [6], the lattice-matching conditions of the average SL lattice parameter to GaAs substrate can be expressed as

$$a_{SL} = \frac{a_{ZnSSe} t_{ZnSSe}^{(SL)} G_{ZnSSe} + a_{CdSe} w_{CdSe}^{(SL)} G_{CdSe}}{t_{ZnSSe}^{(SL)} G_{ZnSSe} + w_{CdSe}^{(SL)} G_{CdSe}} = a_S = a_{GaAs}, \qquad (1)$$

where a_{ZnSSe}, a_{CdSe} are the lattice constants of the respective bulk (unstrained) layers, and G_{ZnSSe} G_{CdSe} are the shear modulus. The choice of the SL design is strongly affected by the necessity to provide the efficient vertical transport of photo-excited carriers into the SL. To do this, the heavy-hole miniband in the SL should be as wide as at least $\sim$30 meV. The calculated dependencies of the ZnS$_y$Se$_{1-y}$/CdSe SL effective band-gap energy on the width of heavy-hole miniband at $T=300$ K are presented in Fig. 2.

The calculations carried out in the envelope function approximation (the details have been reported elsewhere [7]) predict, in particular, that the 4 ML-ZnS$_{0.4}$Se$_{0.6}$/1.3 ML-CdSe SL with E_g^{eff} $\sim$2.55 eV, lattice-matched to GaAs, satisfies the above mentioned requirements (structure 1-371).

Both intended and measured parameters of the structures are summarized in Table 1. The S content in the SL barrier layers of the structure **B** has been intentionally lowered down to $y \sim 0.3$ in an attempt to reduce the SL effective bandgap. Despite the relatively high mismatch of the average SL lattice parameter with that of a GaAs substrate, one can expect the absence of stress relaxation in this structure due to its relatively small thickness ($\sim$300 nm) and a higher value of critical thickness of alternately-strained SL in comparison with that of bulk layer having the same lattice-mismatch [8].

The single CdSe/ZnSe QD layers has been introduced into the structures to study the vertical carrier transport in SLs as well as for the express estimation of the extended defects density in as-grown structures using a PL microscopy technique [9]. To minimize the density of stacking faults (SFs) at the III–V/II–VI heterointerface the low-temperature ($\sim$210 °C) migration enhanced epitaxy (MEE)
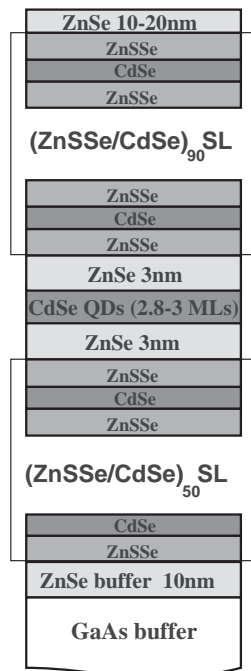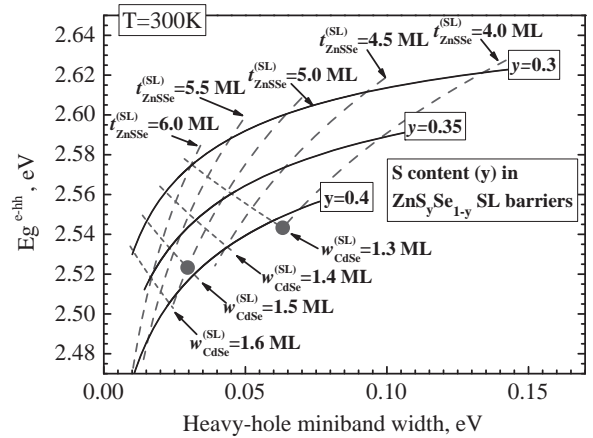
Fig. 2. Dependences of the effective band-gap energy on the width of the heavy-hole mini-band in the ZnS$_y$Se$_{1-y}$/CdSe SLs. The solid, dashed and short-dashed curves are calculated respectively for the fixed S content (y) in ZnS$_y$Se$_{1-y}$ SL layers, ZnSSe ($t_{ZnSSe}^{(SL)}$) and CdSe ($w_{CdSe}^{(SL)}$) SL layer thicknesses, with the other parameters varied to satisfy the expression (1). The lattice-matched to GaAs SLs chosen for experimental realization are shown as filled circles.

growth mode has been applied at the initial growth stage of a ZnSe buffer layer. This procedure allows reducing the SFs density below 10^5 cm^{-2} [9,10]. The growth rates of Zn(S,Se) were controlled in-situ by recording RHEED specular spot intensity oscillations after the II–VI growth initiation immediately before the SLs growth. In this case the S content (y) in SL barriers (y_{osc} column in Table 1) could be estimated via the difference between the growth rates of ZnSSe, grown under the stoichiometric conditions (VI/II $\sim$1) using ZnS and Se fluxes only (Se+S fluxes), and ZnSe, grown under the Zn-rich conditions using the same Se flux (Se flux).

The temperature dependent PL spectra were measured using the emission of a tungsten lamp, dispersed by a monochromator, and recorded by a PIXES 265E cooled CCD-camera. The PL microscopy images were taken using a LUMAM PM-11 microscope. XRD curves (in Θ–2Θ scan mode) were measured using a D8 Discover (Bruker-AXS, Germany) diffractometer in a parallel X-ray beam geometry. A Philips EM-420 microscope was employed for the TEM cross-section measurements.

3. Structural properties of ZnSSe/CdSe superlattices

The CdSe/ZnSe QD layer placed in the center of the SL structures allows accurate *ex-situ* estimation of thickness of the CdSe wells in SLs, both being grown under the same conditions. For that aim, the CdSe QD layer nominal thickness is determined from its low-temperature PL peak position in accordance with the empirical dependence (see, e.g. [11]) obtained earlier by analyzing PL spectra of a series of CdSe/ZnSe nanostructures with different $w_{CdSe}^{(QD)}$, as well as their TEM and XRD [12] data, in comparison with numerous results published by other groups. Then the nominal thickness of CdSe wells in the SL is derived by using the growth time extrapolation. In particular, for structure **A** (1-371) exhibiting the CdSe/ZnSe QD PL peak position at $\sim$2.39 eV (77 K), the nominal thickness $w_{CdSe}^{(QD)}$ is $\sim$2.8 ML ($t_{gr}=20.5$ s), which results in $w_{CdSe}^{(SL)} \sim 1.3$ ML ($t_{gr}=9.5$ s). As soon as the CdSe layer thickness in SLs is known, both the S content (y) and the thickness of the ZnS$_y$Se$_{1-y}$ SL barriers can be determined from the analysis of the Θ–2Θ XRD curves of the SL structures (Fig. 3) by using in calculations the SL period and position of a "0"-order SL peak. The values estimated in assumption of the completely pseudomorphic SL structure are in reasonable agreement with the intended ones (see Table 1).

Fig. 1. Schematic diagram of the structures with short-period ZnS$_y$Se$_{1-y}$/CdSe SLs (y=0.3–0.4).

Table 1
Parameters of the SL structures under the study.

Sample no.	SL design	T_{SL} (Å)	T_{SL} (Å)	$w_{CdSe}^{(SL)}$ (ML)	$t_{ZnSSe}^{(SL)}$ (ML)	y_{osc}	y_{XRD}	$(\Delta a/a)$ (%)
	Intended parameters		Parameters measured by XRD and PL					
1–371 (**A**)	4 ML-ZnS$_{0.4}$Se$_{0.6}$/1.3 ML-CdSe	15.3	16.0	1.3	4.3	0.35	0.34	0.16
1–397 (**B**)	5 ML-ZnS$_{0.3}$Se$_{0.7}$/1.5 ML-CdSe	18.7	20.0	1.63	5.3	–	0.27	0.46
1–419 (**C**)	5 ML-ZnS$_{0.38}$Se$_{0.62}$/1.5 ML-CdSe	18.7	20.0	1.45	5.5	–	0.43	−0.3
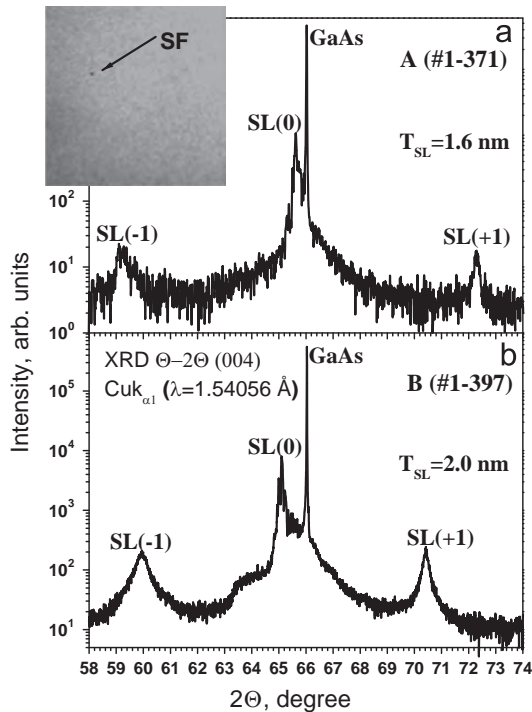
Fig. 3. Θ–2Θ XRD curves for the structures **A** (a) and **B** (b). The inset shows the PL microscopy image of the structure **A**. Side of the square is ~ 200 μm.

Fig. 4. Cross-section TEM image of structure **A**.

Fig. 5. PL spectra of the SL structures measured at 77 K (a) and 300 K (b).

Despite the relatively high value of lattice-mismatch with GaAs followed from the position of the "0"-order SL peak (e.g. $\sim 1600''$ for structure **B**), TEM measurements reveal negligibly small density of misfit dislocations (below 10^6 cm^{-2}) in all the SL structures, thus confirming their pseudomorphic growth. Fig. 4 shows the cross-section TEM image of structure **A**. Both the individual layers of the SL and the CdSe/ZnSe QD layer are clearly distinguished, T_{SL} calculated from the image being of ~ 16.5 Å. This value, as well as the total thickness of the structure (~ 260 nm), are in good agreement with the intended parameters. The PL microscopy image of structure **A** (see inset in Fig. 3) demonstrates an absence of any features associated with dislocations (dark lines), and the stacking fault density (black dots) can be estimated as below 10^4 cm^{-2}.

4. Vertical carrier transport in superlattices

PL spectra of the structures, measured at 77 and 300 K, are presented in Fig. 5. All three structures demonstrate bright PL, the PL spectra containing two well separated peaks associated with the emission from either SL or QDs. The PL intensities of these two peaks are comparable at cryogenic temperatures, whereas the QD peak strongly dominates at 300 K. Such behavior can be attributed to the temperature induced activation of the carrier vertical transport through the SL [13,14]. More detailed data on the efficiency of vertical carrier transport in SLs are obtained through the measurements of

temperature dependences (Fig. 6) of the integral intensity of the PL bands originated from the SL (circles) and the buried CdSe/ZnSe QDs (triangles).
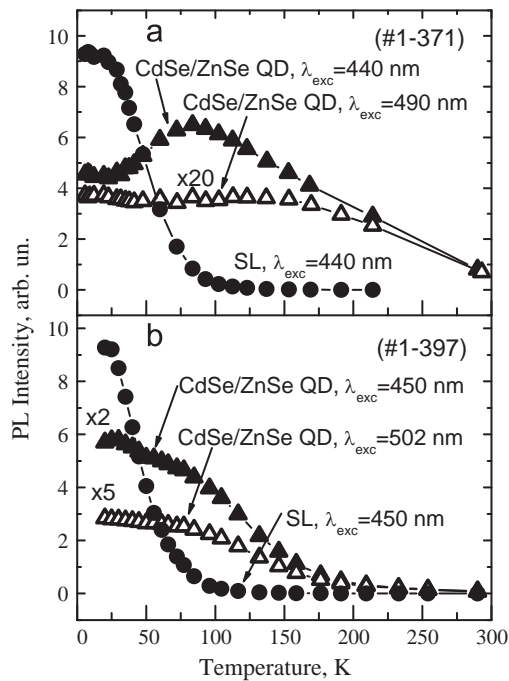
Fig. 6. Temperature dependences of integral intensity of PL in the SL and buried CdSe/ZnSe QD under excitation both above and below the SL effective bandgap.

The QD PL spectra were measured for the excitation energies either above the SL absorption edge ($E^{exc} > E_g^{eff(SL)}$) or between the SL absorption edge and the QD peak position ($E^{QD} < E^{exc} < E_g^{eff(SL)}$). The excitation wavelengths are indicated in Fig. 6. Only minor variations in the integral intensity of the PL line associated with SL (for the structures **A** and **B**) are observed at temperatures below 20 K that corresponds to the emission of localized excitons in the SL. At $T > 20$ K the intensity of the SL PL drastically decreases with an increase in temperature and reduces by more than two orders of magnitude at $T \sim 100$ K. In contrast to that, the temperature dependence of the PL from QDs is a non-monotonic function at $E^{exc} > E_g^{eff(SL)}$ with a maximum at about 80 K (for structure **A**), demonstrating the increase of the vertical carrier transport efficiency in the SL with temperature. However, this tendency is much less pronounced for the structure **B** that could be explained by worse conditions of carrier vertical transport due to the lower width of a heavy-hole miniband (see Fig. 2). The decrease of the QD PL integral intensity at temperatures above 150 K can be ascribed to the temperature induced escape of the carriers localized within the QDs.

5. Conclusions

Summarizing, the ZnS_ySe_{1-y}/CdSe SLs pseudomorphic to GaAs (001) with the effective bandgap energy within the range $E_g \sim 2.5$–2.6 eV have been grown by MBE. Main geometric parameters of the SL structures were evaluated via joint analysis of the low-temperature PL and XRD data. The SLs have demonstrated the parameters close to the intended ones, as well as the low density of extended defects at a thickness (~ 300 nm) significantly exceeding the critical one reported previously for bulk II–VI layers possessing the same lattice mismatch. PL studies of the vertical carrier transport in the SL structures with an incorporated CdSe/ZnSe QD layer confirm the Bloch-type transport of carriers at the temperatures above 100 K. The defect-free ZnS_ySe_{1-y}/CdSe SLs pseudomorphic to GaAs (001) may be considered as a suitable material for a wide band-gap cascade of a multi-junction SC comprising both III–V and II–VI materials.

References

[1] M.A. Green, K. Emery, Y. Hishikawa, W. Warta, E.D. Dunlop, Prog. Photovolt.: Res. Appl. 22 (7) (2014) 701–710. http://dx.doi.org/10.1002/pip.2525 (Solar cell efficiency tables (version 44)).

[2] H. Yuen, M. Wiemer, V. Sabnis, High efficiency solar cells at solar junction, in: Renewable Energy and the Environment, OSA Technical Digest (CD) (Optical Society of America), paper SRWB3, 2011, http://dx.doi.org/10.1364/OSE.2011.SRWB3.

[3] S.-N. Wu, D. Ding, S.R. Johnson, S.-Q. Yu, Y.-H. Zhang, Prog. Photovolt.: Res. Appl. 18 (5) (2010) 328–333. http://dx.doi.org/10.1002/pip.962.

[4] A.W. Jia, M. Kobayashi, A. Yoshikawa, J. Electron. Mater. 24 (3) (1995) 117–121. http://dx.doi.org/10.1007/BF02659883.

[5] S.V. Ivanov, S.V. Sorokin, P.S. Kop'ev, J.R. Kim, H.D. Jung, H.S. Park, J. Cryst. Growth 159 (1) (1996) 16–20. http://dx.doi.org/10.1016/0022-0248(95)00588-9.

[6] Chris G. Van de Walle, Phys. Rev. B 39 (3) (1989) 1871–1883. http://dx.doi.org/10.1103/PhysRevB.39.1871.

[7] E.A. Evropeytsev, S.V. Sorokin, S.V. Gronin, I.V. Sedova, G.V. Klimko, S.V. Ivanov, A.A. Toropov, Semiconductors 49 (3) (2015) 352–357.

[8] Jan H. van der Merwe, W.A. Jesser, J. Appl. Phys. 63 (5) (1988) 1509–1517. http://dx.doi.org/10.1063/1.339934.

[9] S.V. Gronin, I.V. Sedova, S.V. Sorokin, G.V. Klimko, K.G. Belyaev, A.V. Lebedev, A.A. Sitnikova, A.A. Toropov, S.V. Ivanov, Phys. Status Solidi C 9 (8–9) (2012) 1833–1836. http://dx.doi.org/10.1002/pssc.201100606.

[10] A. Colli, E. Pelucchi, A. Franciosi, Appl. Phys. Lett. 83 (1) (2003) 81–83. http://dx.doi.org/10.1063/1.1589195.

[11] S.V. Ivanov, A.A. Toropov, S.V. Sorokin, T.V. Shubina, I.V. Sedova, A.A. Sitnikova, P.S. Kop'ev, Zh.I. Alferov, A. Waag, H.-J. Lugauer, G. Reuscher, M. Keim, G. Landwehr, Appl. Phys. Lett. 74 (4) (1999) 498–500. http://dx.doi.org/10.1063/1.123167.

[12] R.N. Kyutt, A.A. Toropov, S.V. Sorokin, T.V. Shubina, S.V. Ivanov, M. Karlsteen, M. Willander, Appl. Phys. Lett. 75 (3) (1999) 373–375. http://dx.doi.org/10.1063/1.124379.

[13] T.V. Shubina, A.A. Toropov, S.V. Ivanov, S.V. Sorokin, P.S. Kop'ev, G. Pozina, J.P. Bergman, B. Monemar, Thin Solid Films 336 (1–2) (1998) 377–380. http://dx.doi.org/10.1016/S0040-6090(98)01256-5.

[14] A. Lebedev, S. Sorokin, A. Toropov, T. Shubina, N. Il'inskaya, O. Nekrutkina, S. Ivanov, G. Pozina, J.P. Bergman, B. Monemar, Acta Phys. Polon. A 94 (3) (1998) 421–426.
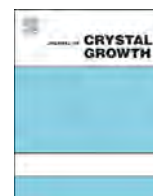
Low resistivity and low compensation ratio Ga-doped ZnO films grown by plasma-assisted molecular beam epitaxy

Cheng-Yu Chen [a], Li-Han Hsiao [a], Jen-Inn Chyi [a,b,c,∗]

[a] Department of Electrical Engineering, National Central University, Jhongli, Taiwan ROC
[b] Research Center for Applied Sciences, Academia Sinica, Taipei, Taiwan ROC
[c] National Applied Research Laboratories, Taipei, Taiwan ROC

ARTICLE INFO

ABSTRACT

In this study, Ga-doped ZnO (GZO) thin films were deposited on GaN templates by using plasma-assisted molecular beam epitaxy. To obtain low resistivity GZO films, *in-situ* post-annealing under Zn over-pressure was carried out to avoid the generation of acceptor-liked Zn vacancies. The resultant films showed optical transparency over 95% in the visible spectral range. By reducing the acceptor-like defects, GZO films with compensation ratio near 0.4 and resistivity simultaneously lower than $1 \times 10^{-4}\,\Omega\,cm$ have been successfully demonstrated.

© 2015 Elsevier B.V. All rights reserved.

1. Introduction

Al-doped ZnO (dubbed AZO) and Ga-doped ZnO (dubbed GZO) have been recently studied extensively as materials with potential to replace indium tin oxide and fluorine-doped tin oxide for transparent electrodes applied in light-emitting diodes, flat-panel displays, and transparent thin film transistors because of their low resistivity, high transparency, non-toxic, easy to deposit as well as their low cost [1]. Among these dopants, Ga might be the most promising one based on its similar atomic radius to Zn atom, lower reactivity to oxygen as well as uniform doping in ZnO films [2]. GZO films have been prepared by sputtering [3,4], pulsed laser deposition (PLD) [5] and molecular beam epitaxy (MBE) [6]. But the resistivity achieved so far falls only at about $2 \times 10^{-4}\,\Omega\,cm$. In order to achieve lower resistivity GZO films, post-thermal annealing in different environment has also been proposed to improve crystal quality, including eliminating native defects [3,7]. However, several reports have shown that the annealed GZO exhibit degraded electrical properties especially the electron concentration [8,9]. It is attributed to the desorption of Zn and migration of Ga in the films [9]. The generation of resultant acceptor-like defects during growth and post-treatments can also be reflected on the compensation ratios (N_A/N_D). The compensation ratios extracted from reported data are limited to the range of 0.4–0.5, which is still unsatisfactory for practical applications.

In this study, GZO films are grown by plasma-assisted molecular beam epitaxy (PA-MBE). An *in-situ* post-annealing process under Zn overpressure is used to improve the electrical properties and suppress the generation of acceptor-like defects. GZO films with different growth temperatures are also investigated with respect to the electrical, structural and optical properties.

2. Experiments

GZO films were grown on high resistivity MOCVD-grown GaN templates by plasma-assisted molecular beam epitaxy. Solid sources, including 7 N Zn and 8 N Ga, were evaporated by Knudsen cells. Oxygen radical was generated by introducing 6 N oxygen through a 13.6 MHz radio frequency (RF) plasma cell. Before the growth, GaN templates were cleaned by heating at 700 °C for 20 min in the growth chamber. A nearly 5 nm-thick undoped ZnO buffer layer was firstly grown on the GaN templates, and Ga doping was incepted after the buffer layer. The thickness of the GZO films is about 250 nm. The growth temperature in this study was controlled in the range from 200 °C to 400 °C. A Zn-rich environment was employed during the growth in order to suppress the formation of Zn vacancy-complexes, which are acceptor-like defects [6]. The Zn-rich condition was determined by checking the growth rate with Zn flux under a fixed oxygen flux. Under Zn-rich condition, the growth rate will not increase with Zn flux. In this study, the Zn/O ratio was determined at 350 °C and was not changed with changing substrate temperature. For the growth carried out below 350 °C, Zn-rich condition was automatically ensured because less Zn would be desorbed from the sample surface. The Zn/O ratio used in the work was set large enough to maintain Zn-rich condition for the growth at 400 °C. It could be verified by the fact that the resistivity of the GZO films did not increase significantly as the films grown under O-rich environment. *In-situ* thermal annealing

∗ Corresponding author.

under Zn flux in the growth chamber for 5 min was performed after the film growth. Hall measurement was carried out using Van der Pauw method to obtain electron concentration, mobility and resistivity of the films. Temperature-dependent Hall measurements were carried out at the temperature ranging from 15 to 310 K in a closed-cycle cryostat. Surface morphology was checked by HITACHI S-4300 scanning electron microscopy (SEM). The crystal quality of the GZO films was evaluated by x-ray diffraction (XRD). Optical transmission spectra from ultraviolet to near infrared were obtained by using a HITACHI-U4100 spectrophotometer.

3. Characterization of GZO films

3.1. Influence of thermal annealing under Zn overpressure

All the GZO samples were annealed at various temperatures to achieve their lowest resistivity. It was found that the annealing temperature for achieving the lowest resistivity of each GZO film was about 50 °C higher than its growth temperature. Fig. 1 shows the carrier concentration, Hall mobility, and resistivity of the GZO films that were grown at 350 °C and subject to *in-situ* thermal annealing under Zn overpressure and *ex-situ* thermal

Fig. 1. Electrical properties of the GZO films that were grown at 350 °C and subject to (a) *in-situ* thermal annealing under Zn overpressure and (b) *ex-situ* thermal annealing in nitrogen ambient at various temperatures.

annealing in nitrogen ambient at various temperatures. The lowest resistivity of $1.8 \times 10^{-4}\,\Omega$ cm is obtained at an annealing temperature of 400 °C due to the increase in electron mobility. As the annealing temperature is increased to 700 °C, the resistivity increases from 1.8×10^{-4} to $4.5 \times 10^{-4}\,\Omega$ cm. This increase is well correlated with the reduction of electron concentration in the GZO films. In addition, the change in resistivity with temperature is smaller than that of the GZO films annealed in nitrogen ambient, as displayed in Fig. 1(b). The significant decrease in electron concentration upon annealing in nitrogen ambient supports the finding that Zn desorption and Ga migration occur during the annealing process. The desorption of Zn atoms might have increased the number of acceptor-like vacancies in the films and reduced the number of free carriers for conduction. This degradation of electrical properties by thermal desorption could also be correlated with the surface morphology of the films, as shown by the SEM images in Fig. 2. No morphological change is observed in the GZO films subject to annealing at temperatures below 500 °C. Increased surface roughness upon annealing at 600 °C suggests the onset of thermal desorption from the surface, consistent with the degradation of electrical properties revealed by the Hall results.

3.2. Effects of growth temperature

Fig. 3 shows the x-ray diffraction peaks of the annealed GZO films, which have the lowest resistivity for each growth temperature. The peak at 34.56° represents the diffraction peak of the GaN template. Diffraction peaks that correspond to the (004) reflection dominate the spectra, indicating that the c-axis of the GZO film is perpendicular to the substrate plane. The 2θ diffraction peak at 34.44°, close to that of the undoped ZnO, appears to be slightly influenced by the size mismatch between Zn and Ga atoms [10]. Apparently, the growth temperature significantly affects the crystal quality of GZO films, as depicted in Fig. 3. On the GZO films grown at 200 °C, the diffraction peak of GZO is not observed and the ring shape RHEED pattern (not shown) during the growth indicates that the film is polycrystalline. Even though post-thermal annealing is performed on these films, they remain to be polycrystalline, in good agreement with the low mobility of these films. At higher substrate temperatures, the intensity of the (002) peaks increases and the full width at half maximum values decreases as the growth temperature is increased, indicating that high growth temperature improve their crystallinity. It can be concluded that to achieve high mobility, the growth temperature of MBE-grown GZO films should exceed 300 °C.

The electrical properties of GZO films grown at various growth temperatures with optimal annealing temperature to reach the lowest resistivity are summarized in Table 1. The electron concentration varies from the order of 10^{22} cm^{-3} to the order of 10^{20} cm^{-3} and the mobility increases from 2 to 52 cm^2/V s as the growth temperature is increased from 200 to 400 °C. The resistivity of GZO films easily reaches $2 \times 10^{-4}\,\Omega$ cm upon annealing under Zn overpressure. The resistivity as low as $9.2 \times 10^{-5}\,\Omega$ cm is obtained on the GZO films grown at 300 °C with electron concentration of 2.2×10^{21} cm^{-3} and mobility of 26 cm^2/V s. Temperature-dependent resistivity of the GZO films with room temperature electron concentrations of 5.6×10^{20} and 2.2×10^{21} cm^{-3} are measured in the temperature range of 15–310 K, as displayed in Fig. 4. Both samples exhibit the same temperature-dependent behavior in spite of their difference in electron concentration. For the film with electron concentration of the order of 10^{20} cm^{-3}, the presence of a large number of carriers shifts the Fermi level toward or even into the conduction band, and become degenerate semiconductors. Therefore, the activation energy required for
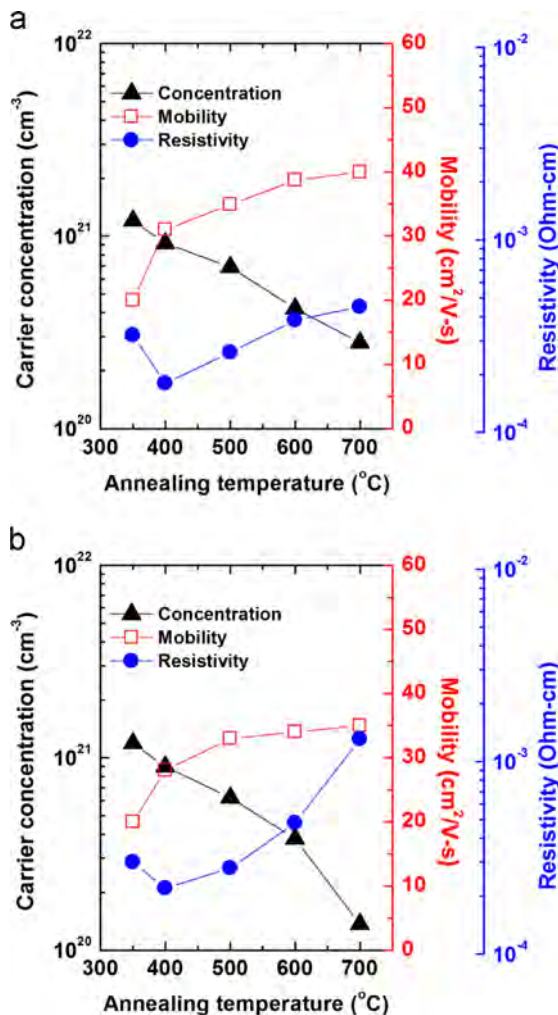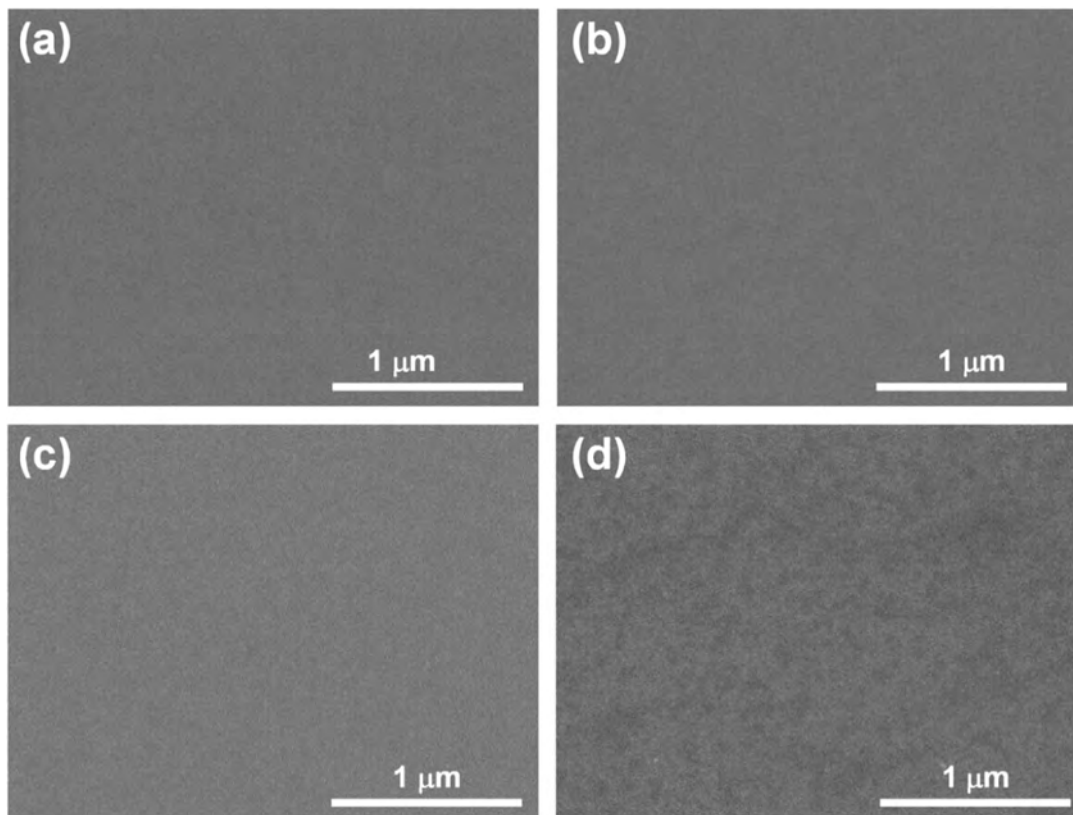
Fig. 2. SEM images of the GZO film grown at 350 °C and annealed under Zn flux at various temperatures: (a) as-deposited, (b) 400 °C, (c) 500 °C, and (d) 600 °C.
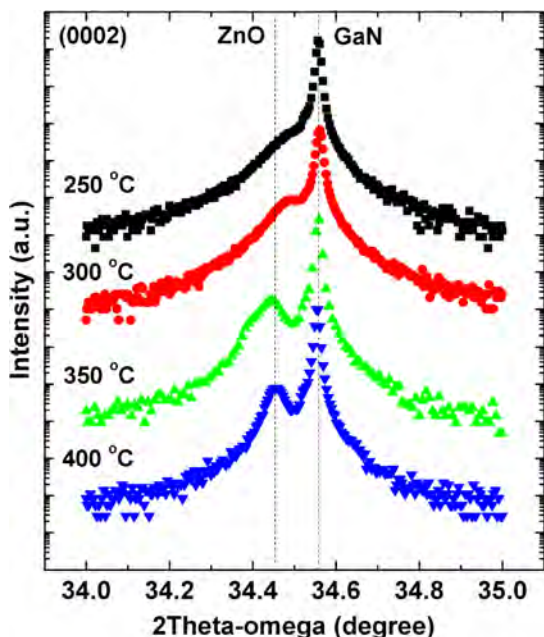
Fig. 3. X-ray diffraction spectra of the annealed GZO films, which have the lowest resistivity for each growth temperature.

Table 1
Electrical properties of the annealed GZO films, which have the lowest resistivity for each growth temperature.

Growth temperature (°C)	Electron concentration (cm^{-3})	Electron mobility (cm^2 V^{-1} s^{-1})	Resistivity (Ω cm)	Compensation ratio
200	1.7×10^{22}	2	1.8×10^{-4}	0.93
250	3.1×10^{21}	15	1.6×10^{-4}	0.64
300	2.2×10^{21}	26	9.2×10^{-5}	0.47
350	9.0×10^{20}	36	1.6×10^{-4}	0.39
400	5.6×10^{20}	52	2.4×10^{-4}	0.30

resistivity and causes metallic transport behavior. The negative temperature coefficient of resistivity (TCR) at low temperatures, which reflects the transport behavior, arises from the thermally activated motion of carriers. This transport behavior could be attributed to the weak localization effect of electrons in disordered electron systems. As a consequence, the transition temperature of the GZO film with an electron concentration of 2.2×10^{21} cm^{-3} shifts to 120 K. The shift of metal-semiconductor transition temperature is found to be related to the doping concentration of GZO and is attributed to the increase in disordering of the crystal [11,12].

Fig. 5 presents the optical transmission spectra of the GZO films with various carrier concentrations. Oscillations at wavelengths longer than 450 nm are caused by interference of light that is reflected from the GZO surface and the ZnO/GaN interface. The transmittance being higher than 100% is a measurement artifact caused by the Fabry–Pérot interference. The optical transmittance measurements between 300 and 1000 nm show that the films with a concentration of the order of 10^{20}–1×10^{21} cm^{-3} are highly

electrons jumping from the valence band to the conduction band continuously decreases and even vanishes. However, the resistivity of the GZO films is constant as the temperature is below 90 K. Increasing the measurement temperature to 90 K and above increases the
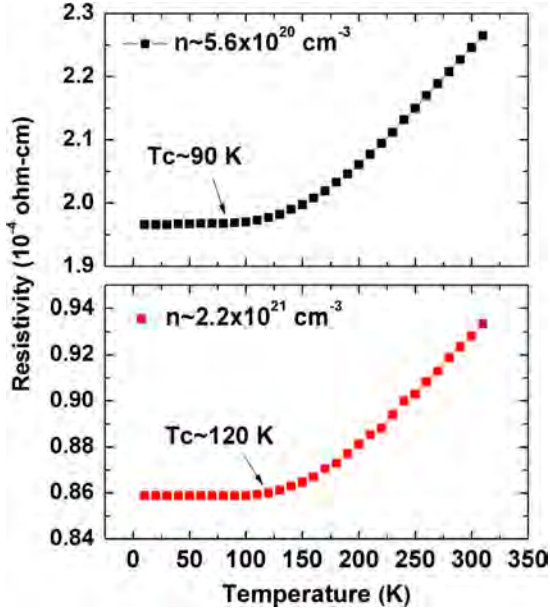
Fig. 4. Temperature-dependent Hall measurements on GZO films with two different electron concentrations.

Fig. 6. Figure of merit of GZO films grown by different methods. Resistivity of $2 \times 10^{-4}\ \Omega$ cm for various electron concentration and mobility is depicted in solid line.

Fig. 5. Optical transmittance of the GZO films with various carrier concentrations. Oscillations at wavelengths > 450 nm are due to interference of light reflected from GZO surface and ZnO/GaN interface. (Note that transmittance higher than 100% is a measurement artifact due to the Fabry–Pérot interference.)

transparent in the visible range. The GZO films with transmittance near 90% in the visible range compare favorably to the conventional ITO with transmittance of about 85%. However, the spectra reveal serious degradation in transmittance as the carrier concentration increases above 2.2×10^{21} cm^{-3}. The GZO films become opaque eventually at concentrations over 10^{22} cm^{-3}. Calculation based on Drude's theory also suggests high reflectivity at concentrations of over 10^{22} cm^{-3} [13].

3.3. Compensation ratio

Acceptor-like defects greatly influence electron concentration and mobility. The influence can be quantified by the compensation ratio, i.e. the ratio of acceptor concentration and donor concentration (N_A/N_D), which is a key parameter in determining the performance of conductive films.

Based on the Coulomb interaction between electrons and the impurities, theoretical electron mobility of the degenerate form can be estimated by the Brooks–Herring formula shown below [14]

$$
\begin{aligned}
\mu_{ii} &= \frac{24\pi^3 \varepsilon_0^2 \hbar^3}{Z^2 e^3 m^{*2}} \frac{n}{N_{ii}} \frac{1}{\ln[1+y(n)] - (y(n)/1+y(n))} \\
&= \frac{146.9}{\ln(1+6.46 n_{20}^{1/3}) - (6.46 n_{20}^{1/3}/1 + 6.46 n_{20}^{1/3})} \frac{1-K}{1+K} \\
&= \mu_{\max} \frac{1-K}{1+K}\ \text{cm}^2/\text{V s}
\end{aligned}
\tag{1}
$$

where, the dielectric constant ε_0 and effective mass m^* are set to 8.12 and 0.3, respectively, and Z is the ionization charge in units of e, which is assumed to be unity for both donors and acceptors [14]. The concentration of the ionized centers N_{ii} is given by $N_{ii} = N_D + N_A = 2N_A + n$, and the compensation ratio K is N_A/N_D. If the concentration is 5.6×10^{20} cm^{-3}, then an ideal $\mu_{\max} = 97$ cm^2/V s can be derived from Eq. (1), yielding a compensation ratio equal to zero. Using a mobility of 52 cm^2/V s measured in this work, a compensation ratio of 0.30 is obtained. This compensation ratio is lower than those reported elsewhere, and is believed to be due to the suppression of acceptor-like defects by in-situ annealing under Zn overpressure.

Fig. 6 summarizes the variation of electron concentration with mobility of polycrystalline and epitaxial GZO films [3,4,6,15–22]. The experimental data of this work are marked in solid circles. Dash lines refer to the compensation ratios of zero and 0.4, calculated using Eq. (1), and the solid line corresponds to a resistivity of $2 \times 10^{-4}\ \Omega$ cm for various combinations of electron concentration and mobility. This figure reveals that most of the reported works have a high compensation ratio over 0.4 and even worse for the cases with electron concentration over 10^{21} cm^{-3}.

4. Conclusions

Ga-doped ZnO films have been grown on GaN templates by plasma-assisted molecular beam epitaxy and characterized in terms of structural, electrical, and optical properties. In-situ post-growth annealing under Zn overpressure can effectively reduce the resistivity

of the GZO films by minimizing the concentration of acceptor-like Zn vacancy caused by thermal desorption of Zn atoms. A minimal resistivity of 9.2×10^{-5} Ω cm is achieved on the GZO films grown at 300 °C. The metal–semiconductor transition temperature is dependent on the dopant concentration in the GZO films and related to the increased disorder induced by Ga atoms. Optical transmittance over 95% in the visible range is obtained on the films with electron concentration on the order near 10^{21} cm^{-3}. By minimizing the acceptor-like defects, we have successfully demonstrated GZO films with compensation ratio near 0.4 and resistivity below 1×10^{-4} Ω cm, simultaneously.

Acknowledgments

References

[1] T. Minami, Transparent conducting oxide semiconductors for transparent electrodes, Semicond. Sci. Technol. 20 (2005) S35–S44.
[2] A.V. Kvit, A.B. Yankovich, V. Avrutin, H. Liu, N. Izyumskaya, U. Özgür, H. Morkoç, P.M. Voyles, Impurity distribution and microstructure of Ga-doped ZnO films grown by molecular beam epitaxy, J. Appl. Phys. 112 (2012) 123527.
[3] P.K. Song, M. Watanabe, M. Kon, A. Mitsui, Y. Shigesato, Electrical and optical properties of gallium-doped zinc oxide films deposited by dc magnetron sputtering, Thin Solid Films 411 (2002) 82–86.
[4] V. Assunção, E. Fortunato, A. Marques, H. Águas, I. Ferreira, M.E.V. Costa, R. Martins, Influence of the deposition pressure on the properties of transparent and conductive ZnO:Ga thin-film produced by r.f. sputtering at room temperature, Thin Solid Films 427 (2003) 401–405.
[5] Z.F. Liu, F.K. Shan, Y.X. Li, B.C. Shin, Y.S. Yu, Epitaxial growth and properties of Ga-doped ZnO films grown by pulsed laser deposition, J. Cryst. Growth 259 (2003) 130–136.
[6] H.Y. Liu, V. Avrutin, N. Izyumskaya, M.A. Reshchikov, Ü. Özgür, H. Morkoç, Highly conductive and optically transparent GZO films grown under metal-rich conditions by plasma assisted MBE, Phys. Status Solidi-Rapid Res. Lett. 4 (2010) 70–72.
[7] B. Du Ahn, S.H. Oh, C.H. Lee, G.H. Kim, H.J. Kim, S.Y. Lee, Influence of thermal annealing ambient on Ga-doped ZnO thin films, J. Cryst. Growth 309 (2007) 128–133.
[8] H. Makino, N. Yamamoto, A. Miyake, T. Yamada, Y. Hirashima, H. Iwaoka, T. Itoh, H. Hokari, H. Aoki, T. Yamamoto, Influence of thermal annealing on electrical and optical properties of Ga-doped ZnO thin films, Thin Solid Films 518 (2009) 1386–1389.
[9] T. Yamada, A. Miyake, H. Makino, N. Yamamoto, T. Yamamoto, Effect of thermal annealing on electrical properties of transparent conductive Ga-doped ZnO films prepared by ion-plating using direct-current arc discharge, Thin Solid Films 517 (2009) 3134–3137.
[10] C. Kittel, Introduction to Solid State Physics, sixth ed., Wiley, New York, 1986.
[11] Y. Li, Q. Huang, X. Bi, The change of electrical transport characterizations in Ga doped ZnO films with various thicknesses, J. Appl. Phys. 113 (2013) 053702.
[12] V. Bhosle, A. Tiwari, J. Narayan, Electrical properties of transparent and conducting Ga doped ZnO, J. App. Phys. 100 (2006) 033713.
[13] J.R. Bellingham, W.A. Phillips, C.J. Adkins, Intrinsic performance limits in transparent conducting oxides, J. Mater. Sci. Lett. 11 (1992) 263–265.
[14] D.C. Look, K.D. Leedy, D.H. Tomich, B. Bayraktaroglu, Mobility analysis of highly conducting thin films: application to ZnO, Appl. Phys. Lett. 96 (2010) 062102.
[15] H.J. Ko, Y.F. Chen, S.K. Hong, H. Wenisch, T. Yao, D.C. Look, Ga-doped ZnO films grown on GaN templates by plasma-assisted molecular-beam epitaxy, Appl. Phys. Lett. 77 (2000) 3761.
[16] E. Fortunato, V. Assunção, A. Gonçalves, A. Marques, H. Águas, L. Pereira, I. Ferreira, P. Vilarinho, R. Martins, High quality conductive gallium-doped zinc oxide films deposited at room temperature, Thin Solid Films 451 (2004) 443–447.
[17] G.A. Hirata, J. McKittrick, T. Cheeks, J.M. Siqueiros, J.A. Diaz, O. Contreras, O.A. Lopez, Synthesis and optelectronic characterization of gallium doped zinc oxide transparent electrodes, Thin Solid Films 288 (1996) 29–31.
[18] X. Yu, J. Ma, F. Ji, Y. Wang, X. Zhang, C. Cheng, H. Ma, Preparation and properties of ZnO:Ga films prepared by r.f. magnetron sputtering at low temperature, Appl. Surf. Sci. 239 (2005) 222–226.
[19] Q.-B. Ma, Z.-Z. Ye, H.-P. He, S.-H. Hu, J.-R. Wang, L.-P. Zhu, Y.-Z. Zhang, B.-H. Zhao, Structural, electrical, and optical properties of transparent conductive ZnO:Ga films prepared by DC reactive magnetron sputtering, J. Cryst. Growth 304 (2007) 64–68.
[20] M. Miyazaki, K. Sato, A. Mitsui, H. Nishimura, Properties of Ga-doped ZnO films, J. Non-Cryst. Solids 218 (1997) 323–328.
[21] G.K. Paul, S.K. Sen, Sol–gel preparation, characterization and studies on electrical and thermoelectrical properties of gallium doped zinc oxide films, Mater. Lett. 57 (2002) 742–746.
[22] T. Yamamoto, T. Sakemi, K. Awai, S. Shirakata, Dependence of carrier concentrations on oxygen pressure for Ga-doped ZnO prepared by ion plating method, Thin Solid Films 451 (2004) 439–442.
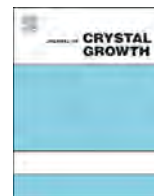
Intersubband absorption in ZnO/ZnMgO quantum wells grown by plasma-assisted molecular beam epitaxy on c-plane sapphire substrates

Kuaile Zhao [a], Guopeng Chen [a], Juliana Hernandez [b], Maria C. Tamargo [c], Aidong Shen [a,*]

[a] *Department of Electrical Engineering, The City College of New York, NY 10031, USA*
[b] *Department of Electrical Engineering, University of California Santa Cruz, Santa Cruz, CA 95064, USA*
[c] *Department of Chemistry, The City College of New York, NY 10031, USA*

ARTICLE INFO

ABSTRACT

The authors report the growth of ZnO/ZnMgO multiple quantum well (MQW) structures by plasma-assisted molecular beam epitaxy. A set of three MQW samples with different well thicknesses were grown on c-plane sapphire substrates. Structural and optical properties of the samples were characterized by reflection high-energy electron diffraction, high-resolution x-ray diffraction (XRD) and photoluminescence measurements. Clear superlattice satellite peaks and thickness fringes observed in XRD measurements indicate the formation of periodic structure with good interfacial quality and high crystalline quality. Mid infrared absorptions around 3 µm are observed from Fourier transform infrared spectroscopy measurement. The polarization-dependent absorption proves that the absorptions are originated from intersubband transitions.

© 2015 Elsevier B.V. All rights reserved.

1. Introduction

Although the challenges associated with p-type doping in ZnO have hindered the realization of efficient interband optical emitters, ZnO and related structures may find applications in intersubband (ISB) devices [1,2]. ISB devices are unipolar devices, in which electron (or hole) transitions happen between energy subbands within the conduction (or valence) band and only one kind of conduction carriers are needed. Since the observation of ISB transitions in semiconductor quantum wells (QWs) [3], various ISB devices such as quantum cascade lasers [4–6], quantum-well infrared photodetectors [7–11], and all-optical switches [12,13] have been fabricated. The mature technology for achieving high n-type doping in ZnO makes it possible to employ ZnO-based heterostructures in ISB devices. The large band offset in ZnO-based heterostructures suggests a large conduction band offset (CBO), which makes the material system a very promising candidate for ISB devices working in the short wavelength infrared (IR) region. ZnO-based materials may find more applications in high speed devices due to their higher ionicity and thereby shorter carrier lifetime compared to their III–V counterparts.

Here we report the growth of ZnO/ZnMgO multiple QWs (MQWs) on c-plane sapphire substrates by plasma-assisted molecular beam epitaxy (MBE). The structural and optical properties were characterized by x-ray diffraction (XRD) and photoluminescence (PL) measurements. ISB absorptions were measured by Fourier-transform IR (FTIR) spectroscopy. At room temperature (RT), ISB absorptions at around 3 µm were observed in ZnO/ZnMgO MQWs.

2. Experiments

Three ZnO/ZnMgO MQW samples (samples A, B, and C) and a Ga-doped ZnO reference sample (sample D) are reported here. All these samples were grown on 2-in. c-plane sapphire substrates by plasma-assisted MBE in a modified DCA 350 system. Prior to the growth, the substrates were outgassed at 670 °C for half an hour. After the outgassing, the substrate temperature was ramped down to 650 °C. At that temperature, the substrates were exposed to the active oxygen for another 30 min. The growth started with the growth of a thin (about 2 nm) MgO buffer (at 650 °C). On the thin MgO buffer, a thick ZnO buffer layer (500 nm) was grown (at 650 °C). After that the substrate temperature was lower down to 450 °C to grow the ZnO/ZnMgO MQWs. The low growth temperature (450 °C) is to avoid the phase separation in ZnMgO.

* Corresponding author. Tel.: +1 212 650 8376.
 E-mail address: ashen@ccny.cuny.edu (A. Shen).

All growths were performed under group-II-rich (oxygen limited) conditions. Typical beam equivalent pressures for Zn, Mg, and Ga (used as n-type dopant) fluxes are 2.0×10^{-7} Torr, 2.5×10^{-8} Torr, and 0.3×10^{-9} Torr, respectively. The oxygen flow rate was kept at 0.6 SCCM (standard cubic centimeter per minute). The RF source (OAR CARS25AI) was operated under a forward power of 350 W.

High-resolution XRD measurements were performed with a Bruker D8 Advance x-ray Diffractometer. PL measurements were carried out at room temperature (RT) using a 266 nm line of a solid-state laser as the excitation source. The ISB absorption was measured at RT with a parallel $45°$ multiple-pass waveguide geometry using a Nicolet Nexus-670 Fourier-transform IR (FTIR) spectrometer with a white light source, a CaF_2 beam splitter, a wire-grid polarizer, and a liquid-nitrogen-cooled HgCdTe detector. Hall Effect measurements were performed with the Van der Pauw method in a Lake Shore 7604 Hall System.

3. Results and discussions

Samples A and B have 14 periods and sample C has 15 periods. The ZnO well thicknesses are 26.2 Å, 29.1 Å, and 31.2 Å for sample A, B, and C, respectively. The ZnMgO barrier thickness for sample A is 39.4 Å, for sample B is 43.7 Å, and that for sample C is 46.9 Å. Growth rates are obtained from dividing the film thicknesses by the growth time in separate calibration samples. The film thicknesses are calculated from thickness fringes in high-resolution XRD curve. Fig. 1 shows the XRD curve for sample D obtained with coupled $\theta/2\theta$ scan. Numerous thickness fringes were observed, indicating high crystalline quality and good surface/interface quality of the sample. From the angular spacing between the fringes, the thickness of the ZnO film was calculated. The growth rate thus determined is 0.28 Å/s. The ZnO well layers in Samples A, B, and C were doped with Ga with a carrier concentration of 1×10^{19} cm^{-3}. The electron concentration is obtained from Hall Effect measurements on the reference sample (sample D). Band-gap energies of the ZnMgO barrier layers are 4.045 eV, 4.364 eV, and 4.364 eV for samples A, B, and C respectively, which are also obtained from separated calibration samples. According to the reported empirical formula [14], the corresponding Mg compositions are 28.4%, 39.7%, and 39.7% in samples A, B, and C, respectively.

Fig. 2a shows the reflection high-energy electron diffraction (RHEED) pattern after the thick ZnO buffer growth for sample C. A streaky (3×3) pattern with bright Kikuchi lines indicates the

high crystalline quality and good surface morphology of the ZnO buffer layer. The streaky pattern maintained until the growth of the complete structure is finished, as shown in Fig. 2b. Similar RHEED patterns were observed for other samples.

Clear satellite peaks were observed in the MQW samples (samples A, B, and C), indicating the formation of periodic structure and good interfacial quality in the samples. Fig. 3 shows the XRD curve obtained with coupled $\theta/2\theta$ scan for sample B. The periodicity thus determined for sample B is 72.8 Å, very close to the designed value of 72 Å. A large number of thickness fringes from the thick ZnO buffer layers were observed around the ZnO (0002) peaks (see the inset of Fig. 3). The observation of thickness fringes is an indication of excellent crystalline quality of the sample. Thickness fringes corresponding to the total MQWs thickness are also observed around the satellite peaks (indicated by the downwards arrows in Fig. 3). The periodicities of samples A and C determined from XRD measurements are 65.6 Å and 78.1 Å, respectively. These results demonstrate that ZnO/ZnMgO MQWs can be grown on c-plane sapphire substrates with high structural quality.

The emission energies of the MQW samples obtained from PL measurements are higher than that of the reference sample (sample D—a Ga-doped ZnO thin film). The higher emission energy (blue-shift) is the result of quantum confinement effect
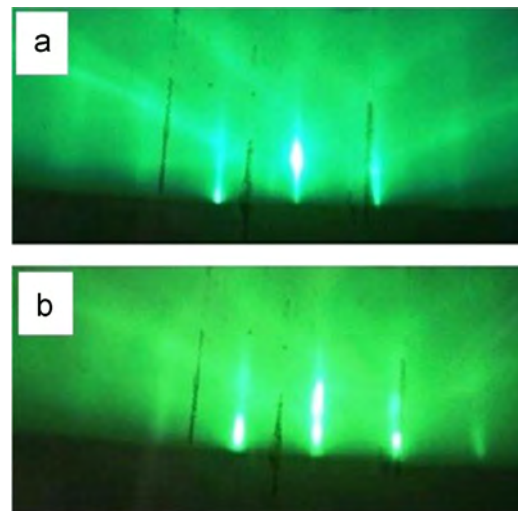
Fig. 2. RHEED pattern of sample C took (a) after the growth of ZnO buffer layer; and (b) after the MQW structure is finished.
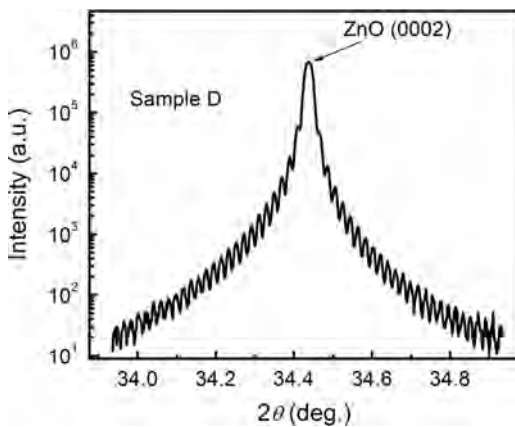
Fig. 1. A high-resolution XRD curve obtained with couple $\theta/2\theta$ scan for sample D. The observation of clear thickness fringes is an indication of high structural quality of the ZnO film. The thickness of the ZnO layer can be determined from the angular spacing between the fringes.
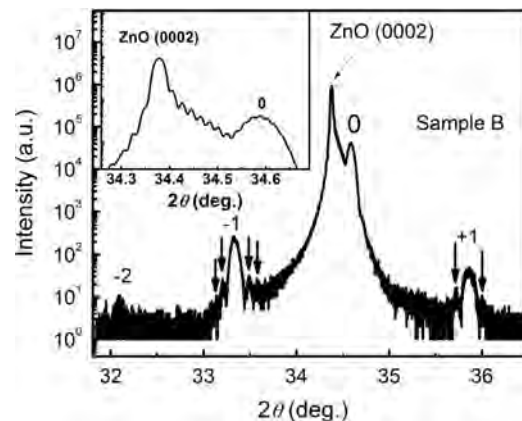
Fig. 3. A high-resolution XRD curve obtained with couple $\theta/2\theta$ scan for sample B. Satellite peaks originated from the periodic QW structure were observed. Inset shows the magnified view around the ZnO (0002) peak and the 0th superlative peak.
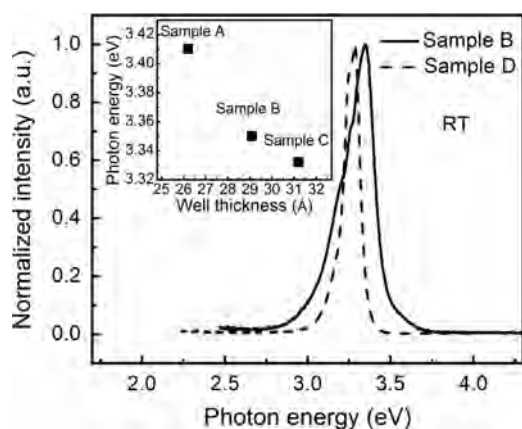
Fig. 4. PL spectra of samples B and D measured at RT. Inset shows the emission energy as a function of ZnO well thickness.
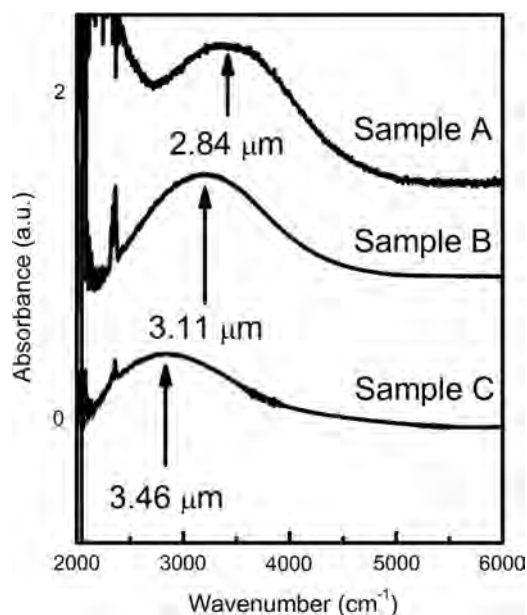
Fig. 5. Absorbance spectra obtained with FTIR measurements at RT for samples A, B, and C.

Fig. 6. Absorbance spectra of sample C measured at different polarization angles, with 0° (the topmost curve) corresponding to p-polarized light and 90° s-polarized light.

in the MQWs. At RT, the emission energies are 3.410 eV, 3.350 eV, and 3.332 eV for samples A, B, and C respectively. Fig. 4 shows the PL spectra for the samples B in reference to sample D. The inset of Fig. 4 shows the emission energy as a function of ZnO well thickness. The blue-shift in the MQW samples is also an indication of moderate electric field in the ZnO well, since a significantly high field can cause the red-shift due to the strong quantum-confined Stark effect.

Fig. 5 shows the absorbance of the MQW samples obtained by FTIR measurements at RT. The absorbance was obtained by taking the negative natural logarithm of the ratio between the p-polarized light and the s-polarized light. Due to the ISB transition selection rule, only the p-polarized light is absorbed by the QWs. Clear ISB absorptions in the mid IR spectral region are observed at 2.84 μm for sample A, 3.11 μm for sample B, and 3.46 μm for sample C. The difference in absorption wavelength (energy) is mainly due to different well width of the samples. All spectra have the Lorentzian line shapes. The full width at half maximum (FWHM) of absorption spectra for sample A is 180 meV ($\Delta E/E=41\%$), for B is 158 meV ($\Delta E/E=40\%$), and for C is 146 meV ($\Delta E/E=40.7\%$). The large FWHM may result from the very thin wells used. With such thin wells ($\sim$3 nm), a fluctuation of one

monolayer in well thickness (about 3 Å) can cause the change of ISB transition energy of more than 40 meV. We note that non-uniformity exists across the wafer. Both the layer thickness and the alloy composition decrease from the center to the edge of the wafer.

The absorptions observed in all the MQW samples are strongly polarization dependent. Fig. 6 shows the absorbance spectra of sample C measured at different polarization angles, with 0° corresponding to p-polarized light and 90° s-polarized light. The strongly polarization-dependent absorptions are clear signatures of ISB absorption. The result is a direct proof that the observed absorptions are originated from ISB transitions in ZnO/ZnMgO QWs.

4. Summary

In summary, ZnO/ZnMgO MQW structures have been grown on c-plane sapphire by plasma-assisted MBE with high structural quality and good interfacial quality. Formation of high quality MQW structures was demonstrated by the observation of satellite peaks in high-resolution XRD measurements. PL measurements demonstrated the expected quantum confinement effect of these samples. Clear mid IR absorptions at 2.84 μm, 3.11 μm, and 3.46 μm have been observed. Polarization-dependent FTIR measurement results indicate that these absorptions were originated from ISB transitions. The observation of ISB absorptions demonstrates the potential to use the ZnO/ZnMgO heterostructures for ISB devices.

References

[1] K. Zhao, G. Chen, B.-S. Li, A. Shen, Appl. Phys. Lett. 104 (2014) 212104.
[2] M. Belmoubarik, K. Ohtani, H. Ohno, Appl. Phys. Lett. 92 (2008) 191906.
[3] L.C. West, S.J. Eglash, Appl. Phys. Lett. 46 (1985) 1156.

[4] J. Faist, F. Capasso, D.L. Sivco, C. Sirtori, A.L. Hutchinson, A.Y. Cho, Science 264 (1994) 553.
[5] C. Gmachl, F. Capasso, D.L. Sivco, A.Y. Cho, Rep. Prog. Phys. 64 (2001) 1533.
[6] N. Bandyopadhyay, Y. Bai, S. Tsao, S. Nida, S. Slivken, M. Razeghi, Appl. Phys. Lett. 101 (2012) 241110.
[7] M. Razeghi, A. Haddadi, A.M. Hoang, E.K. Huang, G. Chen, S. Bogdanov, S.R. Darvish, F. Callewaert, R. McClintock, Infrared Phys. Technol. 59 (2013) 41.
[8] A. Shen, A.P. Ravikumar, G. Chen, K. Zhao, A. Alfaro-Martinez, T. Garcia, J. de Jesus, M.C. Tamargo, C. Gmachl, J. Vac. Sci. Technol. B 31 (2013) 03C113.
[9] S.D. Gunapala, S.V. Bandara, S.B. Rafol, D.Z. Ting, Advances in Infrared Photodetectors, Semiconductors and Semimetals, Academic, San Diego (2011) 59–151.

[10] S. Krishna, D. Forman, S. Annamalai, P. Dowd, P. Varangis, T. Tumolillo Jr., A. Gray, J. Zilko, K. Sun, M. Liu, J. Campbell, D. Carothers, Appl. Phys. Lett. 86 (2005) 193501.
[11] A. Shen, H.C. Liu, M. Gao, E. Dupont, M. Buchanan, J. Ehret, G.J. Brown, F. Szmulowicz, Appl. Phys. Lett. 77 (2000) 2400.
[12] T. Simoyama, H. Yoshida, J. Kasai, A.V. Gopal, H. Ishikawa, IEEE Photonics Technol. Lett. 15 (2003) 1363.
[13] R. Akimoto, B.S. Li, K. Akita, T. Hasama, Appl. Phys. Lett. 87 (2005) 181104.
[14] H. Morkoç, Ü. Özgür, Zinc Oxide: Fundamentals Materials and Device Technology, Wiley, Weinheim (2009) 352–356.
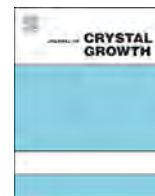
Molecular beam epitaxy growth of niobium oxides by solid/liquid state oxygen source and lithium assisted metal-halide chemistry

M. Brooks Tellekamp, Jordan D. Greenlee, Joshua C. Shank, W. Alan Doolittle *

Georgia Institute of Technology, Atlanta, GA, United States

ARTICLE INFO

ABSTRACT

In order to consistently grow high quality niobium oxides and lithium niobium oxides, a novel solid/liquid state oxygen source, $LiClO_4$, has been implemented in a molecular beam epitaxy (MBE) system. $LiClO_4$ is shown to decompose into both molecular and atomic oxygen upon heating. This allows oxidation rates similar to that of molecular oxygen but at a reduced overall beam flux, quantified by in situ Auger analysis. $LiClO_4$ operation is decomposition limited to less than 400 °C, and other material limitations are identified. The design of a custom near-ambient $NbCl_5$ effusion cell is presented, which improves both short and long term stability. Films of Nb oxidation state $+2$, $+3$, and $+5$ are grown using these new tools, including the multi-functional sub-oxide $LiNbO_2$.

© 2015 Elsevier B.V. All rights reserved.

1. Introduction

Transition metal oxides have enabled and improved many technologies such as hydrogen production, methane production, photocatalysis, resistive ram, and memristors [1–3]. Often novel material properties are made possible by the d-orbital electrons found in transition metals such as niobium, which allow for various bonding mechanisms and oxidation states. In particular, several stable niobium oxides exist with different niobium to oxygen ratios due to the various niobium oxidation states. Examples include a Nb^{2+} semimetal (NbO) [4], a Nb^{4+} semiconductor (NbO_2) [5], and a Nb^{5+} insulator (Nb_2O_5) [6]. Lithium bearing niobium oxide ternaries exhibit optical waveguiding and ferro/piezoelectric properties in lithium niobate ($LiNbO_3$, Nb^{5+}) [7–9] while the sub-oxide lithium niobite ($LiNbO_2$, Nb^{3+}) has memristive [10] and low T_c superconducting properties [11], as well as applications as a battery cathode material [12].

Many properties such as ferromagnetism, piezoelectricity, and pyroelectricity rely on single crystalline material of the highest quality in order to maximize their effect, and many multi-functional devices have been realized by perovskite materials, heterojunctions, and superlattices such as $BiFeO_3$ and $BiTiO_3/SrTiO_3$ [13,14]. It is therefore desirable to develop a method for growing high quality metal oxide films of varying metal oxidation state to exploit these multi-functional properties.

Molecular beam epitaxy (MBE) provides monolayer control and high quality material. However, the growth of stoichiometric refractory metal oxides by molecular beam epitaxy (MBE) is traditionally difficult because of inadequate oxygen and low vapor pressure metal sources leading to extremely low growth rates [15]. Transition metals are difficult to evaporate controllably due to high temperature requirements and the poor compatibility of a hot electron beam filament with an oxygen environment. $LiNbO_3$ is very difficult to grow stoichiometric in oxygen, and it is often annealed post-growth to incorporate the correct amount of oxygen in the film [16]. It is difficult for any niobium film to reach full oxidation in an MBE environment at the high growth temperatures required for quality single crystalline material, and therefore a more reactive oxidizer is desirable to reach these fully oxidized states. Previous work has explored oxidizers such as oxygen plasmas and dangerous ozone sources [17]. This work investigates a solid/liquid state oxygen source as an alternative to these gas based methods, as well as a new style of MBE effusion cell for the evaporation of metal-halide sources which offer much lower evaporation temperatures and therefore greater flux stability [18].

2. Experimental methods

2.1. Custom cell design

Historically, refractory metals have been evaporated by electron beam to achieve growth level fluxes in MBE; however, the hot filament used to create the electron beam oxidizes and breaks easily in an oxide growth environment. For this reason, niobium

* Corresponding author.
  E-mail address: alan.doolittle@ece.gatech.edu (W.A. Doolittle).

Fig. 1. (a) Custom NbCl5 cell with (b) tip filament, bulk water, tip and bulk thermocouple feedthroughs, and (c) a 5 × 5 hole pattern aperture plate.
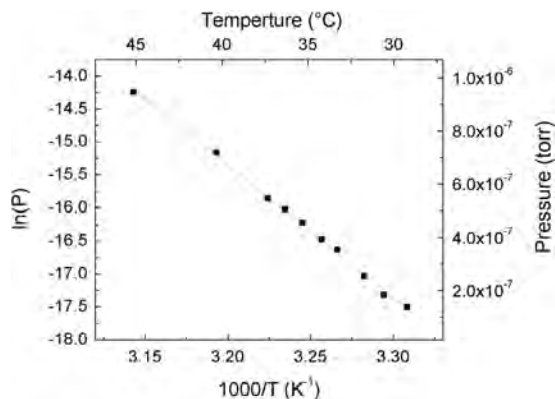
Fig. 2. The measured NbCl$_5$ flux (BEP) versus temperature on an Arrhenius plot follows an expected linear trend. Growth level fluxes occur above ∼30 °C. The included fit gives an equation $\ln(P) = 49.0 - 20.1\ (1000/T(K))$.
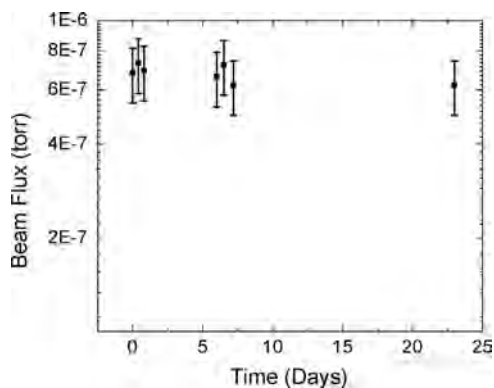
Fig. 3. Measured NbCl$_5$ flux at a single setpoint over a period of 24 days. The cell remains stable within the error range (20%) of a standard ion flux gauge, depicted by error bars ($\sigma = 4.39 \times 10^{-8}$ Torr).

oxides have been previously deposited using a lithium assisted metal-halide growth chemistry [10,16,18]. In this method the niobium source is NbCl$_5$, present as the dimer Nb$_2$Cl$_{10}$, which has an equilibrium vapor pressure of ∼1×10^{-4} Torr at 20 °C. The chlorine from NbCl$_5$ is gettered by lithium forming LiCl that desorbs from the substrate surface at growth level temperatures (vapor pressure=3.61 Torr at 900 °C). This growth method is described in depth by Doolittle et al. [16], Greenlee et al. [10] and Henderson et al. [18]. In this previous work, the material was evaporated from a Createc NATC-40-40-290 oil/water heated cell, which provided temperature stability of ∼0.1%. Despite this stability, radiation from the hot substrate (∼900 °C) caused the NbCl$_5$ cell temperature to rise, increasing the growth rate gradually over the course of the growth.

To overcome this problem, a custom evaporation cell was designed featuring two zone heating and an aperture plate. The

cell, shown in Fig. 1, was manufactured by VESCO-NM. The bulk material zone of the cell is, like the former case, temperature controlled by an oil or water bath to maintain stable temperatures in the near-ambient range. A second heating zone was added at the tip of the cell, heated by a traditional filament that along with a PBN aperture plate provides thermal isolation from the substrate radiation. The hot zone also prevents condensation on the aperture plate and allows a back pressure of NbCl$_5$ for more stable flux control. The crucible is an 82 cm^3 elongated quartz tube, which is filled half full of material to avoid evaporation from the hot zone.

The vapor flux from the new cell design, measured in beam equivalent pressure (BEP), follows a linear trend with temperature on an Arrhenius plot, shown in Fig. 2, as is expected for Knudson flow. Growth level NbCl$_5$ fluxes can be achieved at 30–60 °C compared to previous work at 25–35 °C, indicating flow retardation by the aperture plate. After 6 months of use, the aperture plate shows no corrosion or clogging, indicating the hot zone operating temperature of 100–150 °C is sufficient to prevent any condensation. The cell was measured for long term flux stability over a period of 24 days, shown in Fig. 3, and shows stability within the quoted error range of a standard ion flux gauge (20% within a pressure decade), indicating that flux drift is reasonably controlled with this design.

2.2. Lithium perchlorate

Previous work has indicated that oxygen incorporation into a niobium oxide films at high temperatures (>650 °C) is difficult, with the fully oxidized state of niobium (chemical valence +5) difficult to achieve. LiNbO$_3$ films have been grown by MBE in the past, as well as the ceramics Li$_3$NbO$_4$ and LiNb$_3$O$_8$, but the repeatability of these growths is poor due in part to low and variable oxygen incorporation [16]. This oxygen incorporation issue has led to the use of a stronger oxidizer than molecular oxygen, lithium perchlorate (LiClO$_4$), as an alternative to a higher reactivity sources such as ozone and oxygen plasmas which require a very specific flow control and in the case of the former extensive safety regulation due to reactivity. Lithium perchlorate has the highest volumetric density of oxygen of any material, including liquid oxygen, and is the only material in the perchlorate family that is stable above its melting point [19]. The material is traditionally used as a chemical oxygen generator for emergency oxygen candles as well as a method of chemical oxygen storage [19,20]. Lithium perchlorate is also highly soluble in a number of solvents and is used in this form as a soluble electrolyte for lithium ion batteries.

Lithium perchlorate exists in the solid state as salt granules at room temperature. The substance melts at 236 °C in its anhydrous form, although it is highly hygroscopic and must be handled in a dry environment. Once hydrated, its melting point shifts to ∼247 °C. Lithium perchlorate begins to decompose near 400 °C, with the reaction becoming exothermic around 420 °C [19,21,22]. The material decomposes according to the following equations:

$$LiClO_4(l) \rightarrow LiCl(sol.) + 2O_2(g) \tag{1}$$

$$LiClO_4(sol.) + LiCl(sol.) \rightarrow LiClO_3(sol.) + LiCl(sol.) + O(g) \tag{2}$$

$$LiClO_3(sol.) \rightarrow LiCl(sol. \text{ or } s) + 3/2O_2(g) \tag{3}$$

The decomposition of $LiClO_4$ is autocatalytic, catalyzed by the product LiCl [21], where the formation of LiCl appears to assist in rupturing the Cl–O bond. This theory is consistent with an observed activation energy of 222 kJ [22]. The decomposition is shown to simplify to a standard first order reaction at a LiCl composition of ~40%, at which point the solution is saturated. Eqs. (2) and (3) are the physical realization of this reaction with both molecular and atomic oxygen species evolved during the decomposition process. The presence of atomic oxygen provides the potential for higher reactivity and stronger oxidation. The LiCl autocatalysis necessitates preconditioning the material by prolonged heating or pre-mixing of LiCl to reach the 40% LiCl saturation point. In addition, the 400 °C decomposition temperature places an upper limit on the operational temperature of the cell as well as the temperature ramp rate to prevent local heating exceeding the full decomposition temperature.

Lithium compounds have been proven incompatible with quartz and PBN, and in a previous attempt $LiClO_4$ catastrophically reacted with a niobium crucible. Thus, the $LiClO_4$ bulk material was heated in a beryllia crucible in a standard Knudsen effusion cell. Following six months of use there has been no observable degradation of the crucible, indicating that BeO is resistant to lithium perchlorate corrosion on this timescale.

Oxygen evolution begins shortly after the material melts, with growth level fluxes of oxygen obtained at cell temperatures between 250 and 350 °C. The measured flux is shown on an Arrhenius plot in Fig. 4 for the range 250 to 325 °C, showing the expected linear trend with a measured flux of approximately 1.5×10^{-5} Torr at 325 °C.

3. Results and discussion

3.1. Niobium thin films

Niobium films have been grown using the aforementioned cell on sapphire substrates by a lithium assisted growth chemistry. The $NbCl_5$ cell is operated at a tip temperature of 130 °C, while the bulk is maintained at 50 °C by a heated recirculating water bath, with a measured flux by ion gauge of $\sim 7 \times 10^{-7}$ Torr. The $NbCl_5$ is reduced to Nb with a coincident Li flux, which is maintained in the range of 5×10^{-7} Torr and varied to adjust the growth rate. Films are deposited slowly, at approximately 20–50 nm/h at a substrate temperature of 850–950 °C. The Nb thin films are analyzed for crystalline
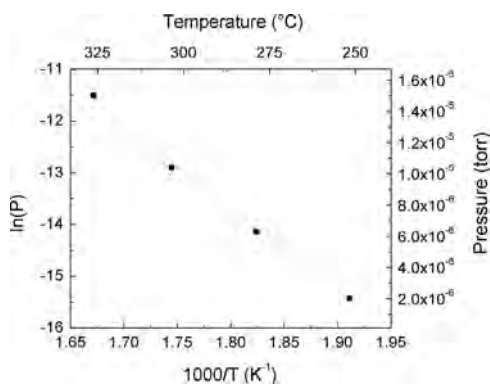
Fig. 4. The measured $LiClO_4$ flux (BEP) versus temperature on an Arrhenius plot follows an expected linear trend. Growth level fluxes occur above ~250 °C, the approximate temperature at which oxygen evolution begins. The included fit gives an equation $\ln(P) = 15.5 - 16.2(1000/T(K))$.
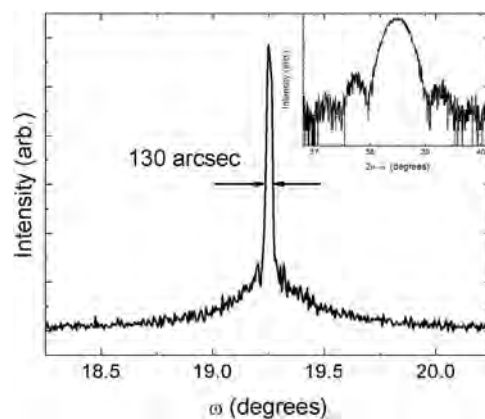
Fig. 5. XRD rocking curve of the BCC Nb film with a FWHM of 130″ indicating excellent crystalline uniformity. **Inset** X-ray diffraction scan showing (1 1 0) oriented BCC Nb with Pendellösung fringes indicating a smooth film.
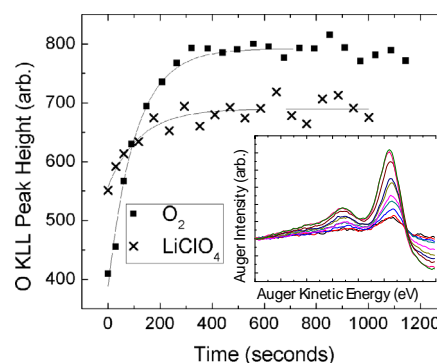
Fig. 6. Auger oxygen KLL peak height as a function of time. The included fit is a first order exponential, characteristic of the oxidation time constant for the given system for (a) $LiClO_4$ at 300 °C, beam flux 8×10^{-7} torr, $\tau = 120$ s, and (b) 1 SCCM O_2, beam flux 3×10^{-6} torr, $\tau = 110$ s. Inset Successive Auger oxygen KLL peak height scans showing increasing surface oxidation.

quality using a Panalytical MRD X-ray Diffraction (XRD) system (Cu-K_α). The Nb nucleates (1 1 0) oriented BCC on c-plane sapphire, indicated by the diffraction scan shown in the inset of Fig. 5. The presence of Pendellösung fringes indicates a smooth film. The film also exhibits an omega rocking curve FWHM of ~ 130 ″, shown in Fig. 5, indicating excellent crystal quality. Secondary ion mass spectroscopy (SIMS) profiling of the films show no chlorine or lithium contamination with the signals for both elements below the detection limit of the spectrometer.

3.2. In situ oxidation rate studies

To quantify the oxidation rate of niobium using the $LiClO_4$ oxygen source, the oxygen KLL Auger peak is monitored for changes in overall intensity. An in situ Auger probe (Staib Instruments) is used to examine reactions on the surface of the growing film. In this configuration, an electron probe is used to analyze Auger electrons excited by the RHEED gun and the probe is mounted in the pyrometer port of a Varian Gen II MBE system normal to the substrate. This system has sub-monolayer surface sensitivity to changing elemental compositions [23,24]. Unlike traditional Auger systems, the Staib Auger probe supplies the direct, non-differentiated signal representing the $E \times N(E)$ spectra. In this experiment, crystalline BCC Nb is deposited on sapphire, growth is halted, and the surface is exposed to oxygen while monitoring the Auger signal in real time. Upon opening the $LiClO_4$ shutter, the oxygen KLL peak immediately begins to intensify. When plotted against time the Auger peak height follows

a first order exponential relation, saturating as the surface reaction comes to completion as shown in Fig. 6. The Auger peak height is proportional to the overall number of oxygen KLL auger electrons which is directly related to the number of oxygen atoms present in the energized volume, which increases exponentially toward a saturated value representing the final (but not necessarily full) oxidation state.

Multiple data points are taken from 40 eV wide scans of the oxygen KLL peak with a resolution of 0.5 meV. The measurement time is 30 s. Scatter plots are fit to a first order exponential following the form of Eq. (4), where measured peak intensity is taken from the $E \times N(E)$ spectra, shown in the inset of Fig. 6.

$$I = I_0 - Ae^{-(t/\tau)} \tag{4}$$

I_0 is the final peak height, t is time, τ is the time constant characteristic of the oxidation, and A is a fitting constant not equal to I_0, indicating a non-zero initial concentration of surface oxide due to background level oxygen in the MBE system.

Characteristic oxidation peak height transients are shown in Fig. 6 for 1 SCCM O_2 and $LiClO_4$ at 300 °C. While these two transients have similar time constants, the measured beam flux for $LiClO_4$ is about 4 times lower than that of O_2. It is theorized that the mixture of molecular and atomic species present in the $LiClO_4$ oxygen evolution allows faster oxidation, providing the possibility of faster growth rates for oxide films than previously possible.

3.3. Niobium oxide thin films

Using the custom $NbCl_5$ cell and the solid/liquid state $LiClO_4$ source, niobium oxide films of various niobium oxidation states have been grown. Films are grown at a substrate temperature of 850 °C, a $NbCl_5$ flux of $\sim 7 \times 10^{-7}$ Torr, and constant oxygen flux. The niobium incorporation and oxidation state is controlled by adjusting the lithium flux and therefore growth rate. Fig. 7 shows the x-ray diffraction scan of an NbO film (Nb^{2+}) oriented (1 1 1) cubic on c-plane sapphire. The peak at 18.6° $2\theta-\omega$ is an interface layer caused by lithium reacting with the sapphire surface forming (0 0 3) oriented α-$LiAlO_2$.

A c-oriented $LiNbO_2$ film (Nb^{3+}) was grown using this technique and capped with c-oriented $LiNbO_3$ (Nb^{5+}). Using the growth rate to control oxidation state, Li flux was decreased at the end of growth to allow higher oxygen incorporation into the film. The x-ray diffraction scan of this film is shown in Fig. 8. The growth of these various films demonstrates the capability of $LiClO_4$ as a solid/liquid state oxygen source to oxidize Nb at 850 °C from the +2 to +5 oxidation state.
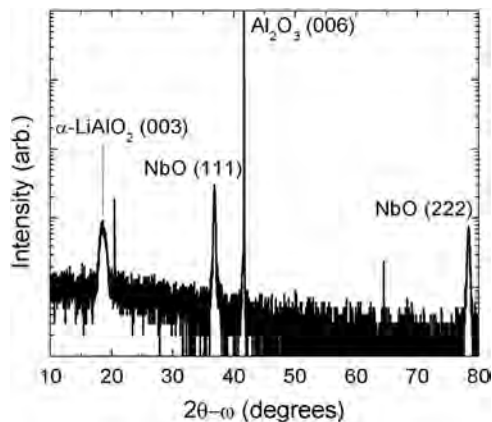
Fig. 7. XRD $2\theta-\omega$ scan of (1 1 1) oriented NbO with an interface layer of α-$LiAlO_2$.
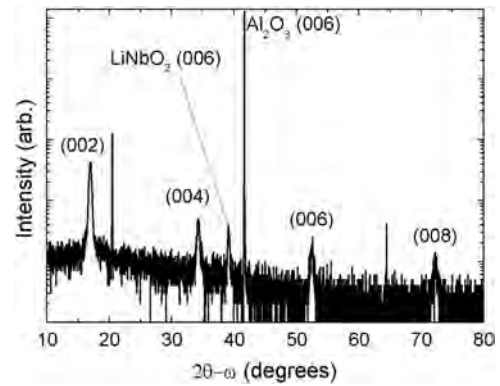
Fig. 8. XRD $2\theta-\omega$ scan of c-oriented $LiNbO_2$ capped with $LiNbO_3$.

3.4. Lithium perchlorate pressure instabilities

During the operation of the $LiClO_4$ cell, pressure variations become an issue significantly affecting the overall chamber pressure. Once oxygen evolution begins at approximately 250 °C, the pressure in the growth chamber, as measured by cold cathode gauge, rises sharply with the decomposition of the $LiClO_4$ bulk material. Monitoring gases by residual gas analysis (RGA), the only signals with corresponding rapid pressure variations are molecular oxygen at m/q 32 and doubly ionized molecular oxygen or atomic oxygen at m/q 16, indicating that oxygen is the source of the pressure variations. For comparison, the oxygen RGA signal during $LiClO_4$ decomposition varies around its mean by $\pm 5 \times 10^{-8}$ Torr, an order of magnitude larger than the signal variation for molecular oxygen flow, which is only $\pm 2 \times 10^{-9}$ Torr.

While the source of the pressure instabilities is unknown, it is hypothesized that they could be caused by bubbling as the oxygen evolution occurs and/or droplets of liquid $LiClO_4$ spitting from the cell. If true, then a valved or aperture sealed cell such as the $NbCl_5$ cell described in this work could resolve these instabilities. Previous reports of chemical additives used to stabilize the decomposition of $LiClO_4$ such as $AgNO_3$ and $AgClO_4$ could also be used [25].

3.5. Comparisons with molecular oxygen

RGA signals exhibit specific cracking patterns for various materials relating to the probability of double ionization as well as the probability of cracking a dimer such as O_2. For molecular oxygen, the measured ratio of the RGA signals at mass to charge ratio 16 to 32 is 5.67%, while that ratio is 8.42% for $LiClO_4$. This corresponds to a 48.5% increase in signal at mass to charge ratio 16. This increase supports the mixed oxygen species theory, suggesting that the $LiClO_4$ is evolving both molecular and atomic oxygen. It is conjectured that this is the mechanism behind the faster oxidation rate per flux beam equivalent pressure revealed by the in situ Auger transient experiment in Section 5.2.

4. Conclusions

It has been demonstrated that a liquid heated bulk, filament heated tip, two zone effusion cell with an aperture plate is effective for the stable and controllable evaporation of metal-halide sources in an MBE environment. Using this source, high quality Nb thin films on sapphire have been grown. It has also been shown that the salt $LiClO_4$ can be used as a solid/liquid state oxygen source evaporated from a standard effusion cell. Through an in situ Auger experiment, $LiClO_4$ is shown to be a stronger

oxidizer than molecular oxygen providing a pathway to potentially higher growth rates, likely due to the presence of both molecular and atomic oxygen evolving from the molten salt. Using the $LiClO_4$ cell niobium oxides have been grown in Nb oxidation states $+2$, $+3$, and $+5$, including the multi-functional sub-oxide $LiNbO_2$. It is also shown that pressure instabilities from the $LiClO_4$ must be addressed to improve the quality of films grown by this method.

Acknowledgements

References

[1] S. Matsuda, A. Kato, Titanium oxide based catalysts—a review, Appl. Catal. 8 (1983) 149–165. http://dx.doi.org/10.1016/0166-9834(83)80076-1.

[2] A. Sawa, Resistive switching in transition metal oxides, Mater. Today 11 (2008) 28–36. http://dx.doi.org/10.1016/S1369-7021(08)70119-6.

[3] S.D. Ha, S. Ramanathan, Adaptive oxide electronics: a review, J. Appl. Phys. 110 (2011) 071101. http://dx.doi.org/10.1063/1.3640806.

[4] W.W. Schulz, R.M. Wentzcovitch, Electronic band structure and bonding in Nb_3O_3, Phys. Rev. B: Condens. Matter 48 (1993) 16986. http://dx.doi.org/10.1103/PhysRevB.48.16986.

[5] M.D. Pickett, G. Medeiros-Ribeiro, R.S. Williams, A scalable neuristor built with Mott memristors, Nat. Mater. 12 (2013) 114–117. http://dx.doi.org/10.1038/nmat3510.

[6] T. Cardinal, E. Fargin, G. Le Flem, M. Couzi, L. Canioni, P. Segonds, L. Sarger, A. Ducasse, F. Adamietz, Non linear optical properties of some niobium (V) oxide glasses, Eur. J. Solid State Inorg. Chem. 33 (1996) 597–606.

[7] E. Lim, M. Fejer, R. Byer, W. Kozlovsky, Blue light generation by frequency doubling in periodically poled lithium niobate channel waveguide, Electron. Lett. 25 (1989) 731–732. http://dx.doi.org/10.1049/el:19890495.

[8] L.E. Myers, R.C. Eckardt, M.M. Fejer, R.L. Byer, W.R. Bosenberg, J.W. Pierce, Quasi-phase-matched optical parametric oscillators in bulk periodically poled $LiNbO_3$, J. Opt. Soc. Am. B 12 (1995) 2102–2116. http://dx.doi.org/10.1364/JOSAB.12.002102.

[9] R. Weis, T. Gaylord, Lithium niobate: summary of physical properties and crystal structure, Appl. Phys. A 37 (1985) 191–203. http://dx.doi.org/10.1007/Bf00614817.

[10] J.D. Greenlee, W. Calley, W. Henderson, W.A. Doolittle, Halide based MBE of crystalline metals and oxides, Phys. Status Solidi C 9 (2012) 155–160. http://dx.doi.org/10.1002/pssc.201100468.

[11] E. Moshopoulou, P. Bordet, J. Capponi, Superstructure and superconductivity in $Li_{1-x}NbO_2$ ($x \approx 0.7$) single crystals, Phys. Rev. B: Condens. Matter 59 (1999) 9590. http://dx.doi.org/10.1103/PhysRevB.59.9590.

[12] M.J. Geselbracht, A.M. Stacy, A.R. Garcia, B.G. Silbernagel, G.H. Kwei, Local environment and lithium ion mobility in lithium niobate ($LiNbO_2$): inferences from structure, physical properties, and NMR, J. Phys. Chem. 97 (1993) 7102–7107. http://dx.doi.org/10.1021/j100129a030.

[13] A. Soukiassian, W. Tian, V. Vaithyanathan, J. Haeni, L. Chen, X. Xi, D. Schlom, D. Tenne, H. Sun, X. Pan, Growth of nanoscale $BaTiO_3/SrTiO_3$ superlattices by molecular-beam epitaxy, J. Mater. Res. 23 (2008) 1417–1432. http://dx.doi.org/10.1557/JMR.2008.0181.

[14] R. Ramesh, N.A. Spaldin, Multiferroics: progress and prospects in thin films, Nat. Mater. 6 (2007) 21–29. http://dx.doi.org/10.1038/nmat1805.

[15] F. Gitmans, Z. Sitar, P. Günter, Growth of tantalum oxide and lithium tantalate thin films by molecular beam epitaxy, Vacuum 46 (1995) 939–942. http://dx.doi.org/10.1016/0042-207x(95)00077-1.

[16] W.A. Doolittle, A. Carver, W. Henderson, W.L. Calley, Molecular beam epitaxy of lithium niobate multifunctional materials using a chloride refractory metal chemistry, ECS Trans. 2 (2006) 103–114.

[17] D. Schlom, A. Marshall, J. Sizemore, Z. Chen, J. Eckstein, I. Bozovic, K. Von Dessonneck, J. Harris Jr, J. Bravman, Molecular beam epitaxial growth of layered Bi–Sr–Ca–Cu–O compounds, J. Cryst. Growth 102 (1990) 361–375.

[18] W.E. Henderson, W. Laws Calley, A.G. Carver, H. Chen, W. Alan Doolittle, A versatile metal-halide vapor chemistry for the epitaxial growth of metallic, insulating and semiconducting films, J. Cryst. Growth 324 (2011) 134–141. http://dx.doi.org/10.1016/j.jcrysgro.2011.03.049.

[19] J.A. Peters, M. Klanchar, T.G. Hughes, J.C. Mankin, Means for Heating and Holding Liquid Lithium Perchlorate for Decomposition into Lithium Chloride and Oxygen, The Penn State Research Foundation, 1994.

[20] M.M. Markowitz, D.A. Boryta, H. Stewart Jr, Lithium perchlorate oxygen candle. Pyrochemical source of pure oxygen, Ind. Eng. Chem. Prod. Res. Dev. 3 (1964) 321–330. http://dx.doi.org/10.1021/i360012a016.

[21] M.M. Markowitz, D.A. Boryta, The decomposition kinetics of lithium perchlorate, J. Phys. Chem. 65 (1961) 1419–1424. http://dx.doi.org/10.1021/j100826a034.

[22] K.H. Stern, High Temperature Properties and Thermal Decomposition of Inorganic Salts with Oxyanions, CRC Press, 2000.

[23] P.G. Staib, In situ real time Auger analyses during oxides and alloy growth using a new spectrometer design, J. Vac. Sci. Technol. B 29 (2011) 03C125. http://dx.doi.org/10.1116/1.3562195.

[24] W.L. Calley, J.D. Greenlee, W.E. Henderson, J. Lowder, M.W. Moseley, W.A. Doolittle, P.G. Staib, In situ Auger probe enabling epitaxy composition control of alloys by elemental surface analysis, J. Vac. Sci. Technol. B 31 (2013) 03C126. http://dx.doi.org/10.1116/1.4798653.

[25] M.M. Markowitz, D.A. Boryta, Retardation of the thermal decomposition of lithium perchlorate, J. Phys. Chem. (1962), http://dx.doi.org/10.1021/j100808a505 358-358.

CRYSTAL
GROWTH
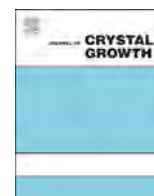
Epitaxial growth of high quality La$_2$CuO$_4$ film on LaSrAlO$_4$ substrate with introduction of ultrathin amorphous layer of La$_2$CuO$_4$

CrossMark

B.-S. Li [a,b,c,*], Y. Matsui [b], T. Miyamoto [b], H. Yada [b], A. Sawa [c,**], H. Okamoto [b,**]

[a] Academy of Fundamental and Interdisciplinary Sciences, Harbin Institute of Technology (HIT), Harbin City 150080, China
[b] Department of Advanced Materials Science, University of Tokyo, Kashiwa, Chiba 277-8561, Japan
[c] National Institute of Advanced Industrial Science and Technology (AIST), Tsukuba, Ibaraki 305-8562, Japan

ARTICLE INFO

ABSTRACT

The authors present the apparent improvement of quality of La$_2$CuO$_4$ (LCO) thin films with the introduction of an amorphous layer (AL) of LCO. The samples were grown on LaSrAlO$_4$ substrates by pulsed laser deposition. X-ray diffraction (XRD) measurements demonstrate that the introduction of the AL of LCO significantly improves the structural quality of LCO thin films. The linewidth of XRD peaks is significantly narrowed down to 129 arcsec. Atomic force microscopy (AFM) shows that the surface precipitates are sufficiently suppressed for the LCO films with ALs. The spectra of optical absorption indicate that the ALs can improve the stoichiometry of the LCO films. The mechanism for the improved quality of LCO films with the ALs is discussed based on the results of XRD and AFM measurements.

© 2015 Elsevier B.V. All rights reserved.

1. Introduction

Epitaxial growth of high T_c cuprate superconductor (HTCS) thin films, such as YBa$_2$Cu$_3$O$_7$ and La$_{2-x}$Sr$_x$CuO$_4$ (LSCO), has been paid great attention in the viewpoint of both fundamental physics and optoelectronic-device applications [1,2]. The parent compound of HTCS such as La$_2$CuO$_4$ (LCO) is a Mott insulator. With carrier doping into the CuO$_2$ plane of the parent compound of HTCS, the superconductivity appears [3]. Therefore, the physics of the carrier (hole and/or electron) creation in a Mott insulator is the crucial concept to understand the superconductivity of cuprates [4]. Among HTCSs, LSCO is a model system to investigate the carrier doping into CuO$_2$ plane, because of its simple structure. Moreover, thin films of HTCS are suitable for optical measurements to reveal the doping-dependent evolution of the electronic structures.

For the LSCO film deposition, LaSrAlO$_4$ (LSAO) is a favored substrate in term of lattice-matching [2]. Furthermore, the LSAO substrate can give a compressive strain in the LSCO thin film, resulting in the increase of the critical temperature of super-conductivity [5]. It is well known that the conditions of substrate surface and the initial nucleation are crucial in the epitaxial growth of thin films. For the LSAO substrate, the transmission electron microscopy (TEM) study reveals that the surface suffers a serious degradation due to the segregation of Sr oxides, when the substrate is annealed at high temperature under oxygen envior-onment [6]. This surface degradation induces the surface defect accompanied by the reduced structural quality in the LSCO films. Recently, we succeeded in the improvement of the surface morphology of LSAO substrate by introducing the homoepitaxial layer and successfully suppressed precipitates, i.e., impurity phases, in the LSCO films [7].

In this study, we demonstrate another method to improve the quality of LCO thin films on the LSAO substrates. The kernel of this idea is to protect the surface of LSAO substrate by depositing an amorphous layer of LCO (AL-LCO) at low temperature. This amorphous layer crystallizes during the ramp-up of the substrate temperature, and then serves as nucleation sites for the subsequent growth of the LCO epitaxial film. Based on the results of the X-ray diffraction (XRD), atomic force microscope (AFM), and optical absorption experiments, we discuss the effect of the AL-LCO on the growth of LCO epitaxial films.

2. Experimental procedure

The samples were deposited on LSAO (001) substrates by pulsed laser deposition (PLD) utilizing a KrF eximer laser as an exciting light source. Laser fluence and the repetition rate were $\sim$2 J/cm^2 and 4 Hz, respectively. Stoichiometric ceramic LCO

* Corresponding author at: Academy of Fundamental and Interdisciplinary Sciences, Harbin Institute of Technology (HIT), Harbin City 150080 China.
Tel./fax: +86 451 8641 8440.
** Corresponding authors.
E-mail addresses: libingsheng@hit.edu.cn (B.-S. Li), a.sawa@aist.go.jp (A. Sawa), okamotoh@k.u-tokyo.ac.jp (H. Okamoto).
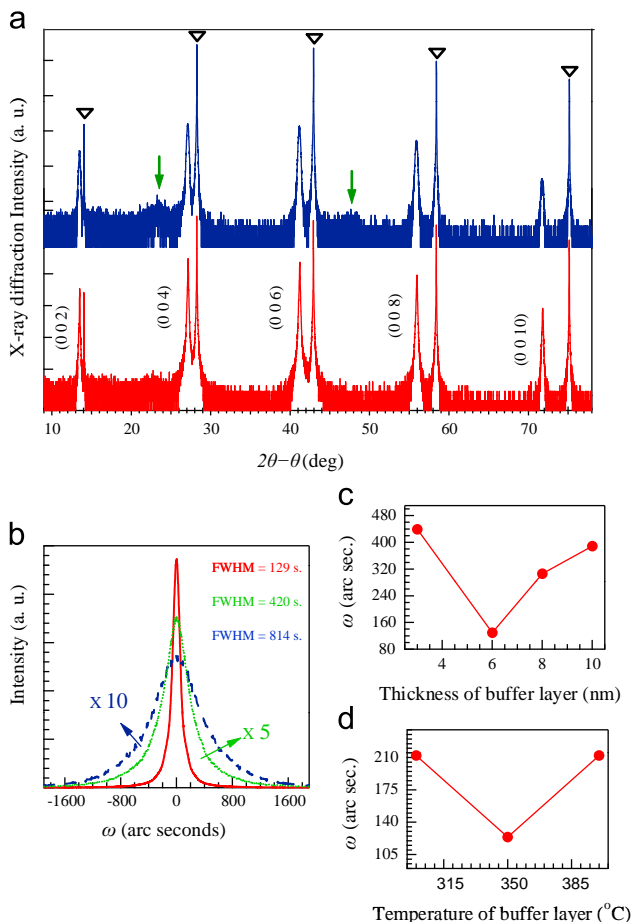
Fig. 1. (a) X-ray diffraction curves of La$_2$CuO$_4$ (LCO) films prepared without (top) and with (bottom) low-temperature-deposited amorphous layer of LCO (AL-LCO). Triangles and arrows indicate the peaks of the LaSrAlO$_4$ (LSAO) substrate and the impurity phases, respectively. (b) The rocking curves around (006) of LCO thin films with (solid line) and without (dash line) AL-LCO. Data (dotted line) obtained from the control sample of LCO film with AL-LCO is also plotted (see text for details). (c,d) Full width at half-maximum dependence of rocking curves of LCO thin films on the thickness and substrate temperature of the AL-LCO, respectively.

Fig. 2. Absorption spectra obtained from transmittance and reflectance measured at room temperature for LCO thin films with (solid line) and without (dotted line) AL-LCO.
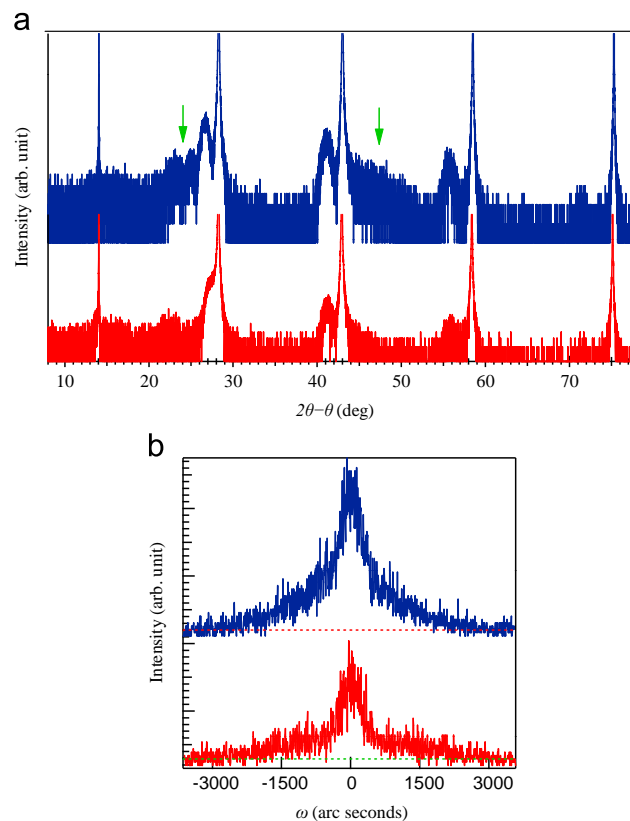
Fig. 3. (a) XRD curves of 5-nm-thick LCO films directly deposited on LSAO substrate at high temperature (top) and deposited at low temperature and subsequently annealed at high temperature (bottom). The arrows indicate the peaks from impurity phases in LCO film. (b) Rocking curves of (006) diffraction peak for the corresponding samples in (a).

targets were used in the present study. A 5-nm-thick AL-LCO was first deposited at a substrate temperature (T_s) of 350 °C in an oxygen pressure (P_O) of 250 mTorr. Then, T_s was increased to ∼780 °C, and a LCO film with a thickness of about 100 nm was deposited again. After the depositions, the sample was in situ annealed at 400 °C under 400 Torr of O$_2$ for 30 min. For comparison, LCO films without ALs of LCO were also prepared. The structural quality of the thin films was evaluated by XRD measurements. AFM was used to investigate the surface morphology. The optical properties were studied by optical absorption spectrum in a range of mid-infrared to UV wavelength at room temperature.

3. Results and discussions

The effect of AL-LCO on the structural quality of thin films is summarized in Fig. 1. The 2θ–θ scans of the LCO films without and with the AL-LCO [Fig. 1(a)] indicate that both LCO films were c-axis oriented. However, there are some additional peaks in the 2θ–θ scans of the LCO films without the AL-LCO, marked with arrows in the top of Fig. 1(a), indicating the presence of impurity phases. Note that it is hard to eliminate these additional peaks by any optimizations of deposition parameters such as T_s, P_O, and ablation

power of KrF excimer laser. However, the introduction of an AL-LCO can apparently suppress the formation of impurity phases. Fig. 1(b) shows the rocking curves around the (006) peaks of the LCO films without and with the AL-LCO. The linewidth of the diffraction curve with the AL-LCO is much narrower than that

without the AL-LCO, indicating a higher structural quality. These results suggest that the AL-LCO can avoid the surface degradation of the LSAO substrate, resulting in the improvement of epitaxial growths. This can be identified by the following experiment. Before depositing AL-LCO, the LSAO substrate was annealed at ~800 °C, which may lead the degradation of the substrate surface. After the annealing, the T_s was decreased to 350 °C, and then the AL-LCO was deposited. As shown by the green dash line in Fig. 1 (b), the linewidth is broadened, but still narrower than the blue dotted line (without the AL-LCO). This result indicates that the AL-LCO can improve the surface condition of the LSAO substrate. We also investigated the effects of the growth temperature and the thickness of AL-LCO on the structural quality. As shown in Fig. 1 (c) and (d), under optimized conditions, the film quality can be sufficiently improved.

Fig. 2 is the optical absorption of the LCO films with and without the AL-LCO. Both films show an optical absorption edge at 2.0 eV, which corresponds to the charge-transfer (CT) gap in LCO [8,9]. However, there are several differences in the two spectra. With the AL-LCO, the absorption edge becomes much steeper, suggesting that the film becomes more homogeneous. Above the CT gap, three peaks have been observed in the sample with the

AL-LCO. Without the AL-LCO the low energy peak vanishes and the spectrum weight is slightly reduced after structure degrades for the sample. There have been some reports to discuss the origin for these peaks [10]. They may come from the excitonic effect in the cuprate. In the sample without the AL-LCO, there is still some absorption in the lower energy region and an obvious middle infrared peak is observed. The transfer of spectrum weight from the high energy region to the low energy region is attributed to the introduction of hole carriers in the CuO_2 plane, which has been reported in the optical studies of LSCO with various Sr doping concentrations [8,9]. This suggests that additional holes are generated in the sample without the AL-LCO. One possibility is that Sr oxides segregated on the LSAO surface [6] diffuses into the LCO film without the AL-LCO. On the other hand, the AL-LCO is expected to suppress the segregation of Sr oxides. As a result, the LCO film with the AL-LCO has good stoichiometry.

In order to confirm the suppression of the impurity-phase formation by the AL-LCO, we performed the following annealing experiments. A 5-nm-thick AL-LCO was deposited on LSAO at low temperature of 350 °C and was subsequently annealed at 780 °C. We also directly grew a 5-nm-thick LCO on LSAO at 780 °C for comparison. Fig. 3 shows the XRD curves for these films. Note that
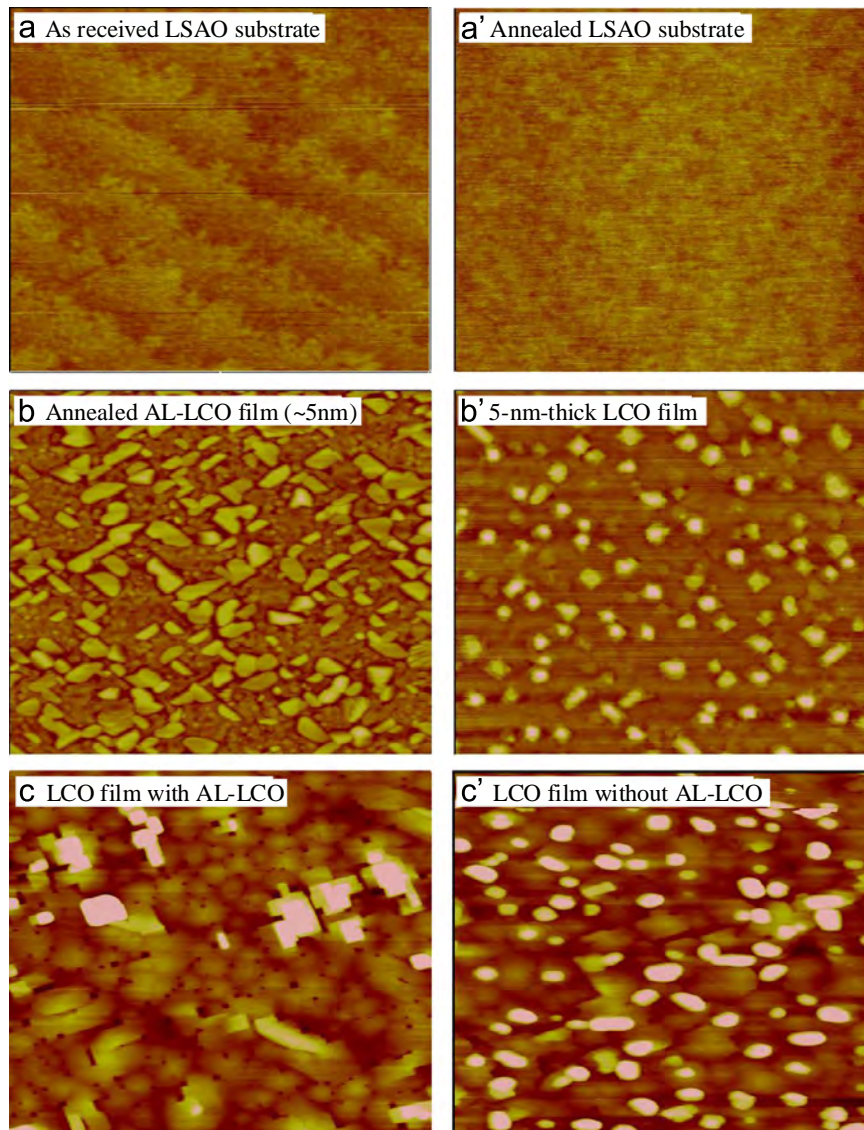
Fig. 4. AFM images of surfaces for (a) as-received LSAO substrate, (a′) LSAO substrate annealed at 800 °C under 100 mTorr of O_2 for 10 min, (b) AL-LCO film annealed at 780 °C, (b′) 5-nm-thick LCO film deposited at 780 °C, (c) LCO film grown on AL-LCO at 780 °C, and (c′) 100-nm-thick LCO film grown at 780 °C without AL-LCO.

before annealing, the AL-LCO showed no diffraction peak (data not shown), indicating the formation of amorphous film. After annealing, (00l) peaks of LCO appear in the XRD of the AL-LCO film. This suggests that crystallization occurs in the annealing process. For the LCO film directly deposited at high temperature, it also shows the (00l) diffraction peaks. As indicated by arrows in the top panel of Fig. 3(a), however, several broadened peaks from impurity phases also appear in the XRD of the LCO film. These results suggest that the AL-LCO can suppress the formation of impurity phases, which may relate to the segregation of Sr oxides on the LSAO surface at high temperature.

Fig. 3(b) is the rocking curve scan around (006) for the annealed AL-LCO film (bottom) and the LCO film deposited at 780 °C (top). The linewidth (~490 arcsec) from the annealed AL-LCO film is much narrower than that of the LCO film (~712 arcsec). From this result, we can expect that the *in-situ* annealed AL-LCO film has better structural quality than that of the initial growth stage of the LCO film directly deposited on the LSAO substrate at high temperature.

In order examine the impact of the AL-LCO on the surface condition, we investigated the surface morphology for the substrates and LCO films by AFM. Fig. 4 shows AFM images of surfaces for (a) an as-received LSAO substrate, (a') an LSAO substrate annealed at 800 °C under 100 mTorr of O_2 for 10 min, (b) a 5-nm-thick AL-LCO film annealed at 780 °C, (b') a 5-nm-thick LCO film deposited directly on the substrate at 780 °C, (c) a 100-nm-thick LCO film grown on the AL-LCO at 780 °C, and (c') a 100-nm-thick LCO film grown directly on the substrate at 780 °C. The surface of an as-received substrate has a step-and-terrace structure [Fig. 4(a)], which is suitable for the epitaxial film growth. After annealing, however, the step-and-terrace structure disappears, as seen in Fig. 4(a'). There are lots of islands and holes (or pits) on the annealed surface. This is consistent with the previous report [7]. This result confirms that the surface of an LSAO substrate is not stable at high temperature under oxygen environment. The degradation of the LSAO surface observed in the present study may be related to the segregation of Sr oxides at high temperature as confirmed by the TEM experiments [6]. Reflecting the LSAO-surface degradation at high temperature, a lot of precipitates with various shapes appeared on the surface of a 5-nm-thick LCO film directly on the substrate, as shown in Fig. 4(b'). The size of the precipitates increased with the increase of the film thickness, as can be seen in Fig. 4(c'). Note that, generally, the precipitates are nonstoichiometric species containing a high percentage of Cu. On the other hand, the surface morphology of the annealed AL-LCO looks completely different from the LCO film directly deposited at high temperature. Before annealing, the film is composed of uniform spheroids with very small size (data not shown). After annealing, a lot of rectangle-shaped grains appeared, as can be seen in Fig. 4(b). We confirmed that most of the grains aligned with [100] and [010] of the LSAO substrate. From this

result and the XRD [Fig. 3(a)], we can consider that crystallization of the AL-LCO occurs along [100] and [010] of the LSAO substrate during the annealing process. As can be seen in Fig. 4(c), this crystallized AL-LCO suppressed the formation of precipitates in the subsequent growth of the LCO film, resulting in the improvement of its stoichiometry. Furthermore, from the XRD of the LCO film with the AL-CLO [Fig. 1(a)] we can consider that the crystallized AL-LCO acts as nucleation sites and thus improve the structural quality of the LCO film.

4. Conclusions

We have studied the effect of AL-LCO on the quality of LCO films grown on LSAO (001) substrates by the pulsed laser deposition method. The experimental results indicate that the AL-LCO suppresses the degradation of the LSAO-substrate surface at high temperature. As a result, the introduction of AL-LCO significantly improved the structural quality and stoichiometry of the LCO films. We also found that when LCO films were deposited directly on LSAO substrates at high temperature, the formation of precipitates occurred in the initial growth stage. This result is attributable to the degradation of the LSAO-substrate surface such as the segregation of Sr oxides. These findings demonstrate that the surface engineering of LSAO substrates is crucial for preparing LCO thin films with high quality.

References

[1] T. Terashima, K. Iijima, K. Yamamoto, Y. Bando, and H. Mazaki, Jpn. J. Appl. Phys. 27(1988) L91; J.C. Nie, H. Yamasaki, Y. Nakagawa, K. Develos-Bagarinao, M. Murugesan, H. Obara, and Y. Mawatari, Appl. Phys. Lett. 86 (2005) 192507.
[2] G. Logvenov, A. Gozar, I. Bozovic, Science 326 (2009) 699; I.E. Trofimov, L.A. Johnson, K.V. Ramanujachary, S. Guha, M.G. Harrison, M. Greenblatt, M.Z. Cieplak, P. Lindendeld, Appl. Phys. Lett. 65 (1994) 2481; H. Sato, A. Tsukada, M. Naito, A. Matsuda, Phys. Rev. B 61 (2000) 12447.
[3] J.G. Bednorz, K.A. Müller, Z. Phys. B 64 (1986) 189.
[4] Patrick A. Lee, Naoto Nagaosa, Xiao-Gang Wen, Rev. Mod. Phys. 78 (2006) 17.
[5] J.-P. Locquet, J. Perret, J. Fompeyrine, E. Mächler, J.W. Seo, G. Van Tendeloo, Nature 394 (1998) 453.
[6] A.E. Becerra-Toledo, L.D. Marks, Surf. Sci. 604 (2010) 1476.
[7] B.S. Li, A. Sawa, H. Okamoto, Jpn. J. Appl. Phys. 50 (2011) 093101.
[8] S. Uchida, T. Ido, H. Takagi, T. Arima, Y. Tokura, S. Tajima, Phys. Rev. B 43 (1991) 7942.
[9] M. Suzuki, Phys. Rev. B 39 (1989) 2312.
[10] K. Waku, T. Katsufuji, Y. Kohsaka, T. Sasagawa, H. Takagi, H. Kishida, H. Okamoto, M. Azuma, M. Takano, Phys. Rev. B 70 (2004) 134501.
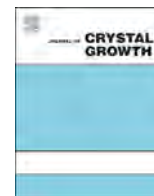
Growth temperature and surfactant effects on the properties of mixed group V alloys

S.P. Svensson [a,*], W.L. Sarney [a], B.C. Connelly [a], E.M. Anderson [b], J.M. Millunchick [b]

[a] U.S. Army Research Laboratory, Adelphi, MD 20783, USA
[b] Department of Materials Science and Engineering, University of Michigan, Ann Arbor, MI 48109, USA

ARTICLE INFO

ABSTRACT

The optical properties of InAsSb, nominally lattice matched to GaSb, grown at varying substrate temperatures with and without Bi-surfactant exposure, were studied with photoluminescence (PL). Both Bi exposure and increasing substrate temperatures reduce the Sb-incorporation and produce strained layers. The bandgap of lattice mismatched layers grown in this way is lowered compared to unstrained material. The PL intensity decreases dramatically when the lattice mismatch increases. The PL intensity also shows significant broadening that can be interpreted as evidence for inhomogeneous alloy distributions induced by the Bi.

Published by Elsevier B.V.

1. Introduction

InAsSb has become a material of increasing interest due to its use in infrared (IR) detector applications. By combining it with InAs in a superlattice, a wide range of bandgaps can be reached, although the absorption becomes increasingly weak at longer wavelengths [1]. This problem is avoided in bulk InAsSb, which has an absorption very similar to that of bulk HgCdTe [2]. It has recently been demonstrated that the bandgap bowing parameter of InAsSb is large enough that the entire long wavelength infrared (LWIR) band can be reached (8–12 μm) [3–5]. This was enabled by development of an efficient lattice constant shifting buffer technology that allows the growth of unstrained, unrelaxed material.

Optimization of the growth parameters of InAsSb for a desired bandgap requires that the interplay between the parameters is known so that a mole fraction can be maintained when one parameter is varied [6]. It is also of interest to explore the feasibility of further materials quality improvements from surfactants, such as Bi [7].

In this work we have studied the effects on the structural and optical properties and the As/Sb composition in InAsSb nominally lattice matched to GaSb as a function of substrate temperature and Bi-exposure (without incorporation).

2. Experimental

Molecular beam epitaxy (MBE) was used to grow InAsSb on (001) GaSb substrates, with conditions as described previously [7].

The samples consist of two layers, a 0.59-μm InAsSb layer without Bi exposure and a top 0.27-μm layer of InAsSb with Bi exposure. Both layers of all samples were grown with the Sb/As flux ratio that was previously determined for obtaining lattice matched InAsSb$_{0.089}$ on GaSb at a substrate temperature of 415 °C [9]. The substrate temperature was varied (400–490 °C) so that the combined effect of Bi exposure and substrate temperature on the Sb incorporation could be determined. The Bi beam equivalent pressure (BEP) of 4.8×10^{-7} Torr does not induce incorporation at alloy levels using these growth conditions [8]. The composition of the InAsSb layers was determined from triple axis x-ray diffraction using (004) and (115) reflections. Selected samples were studied with symmetric and asymmetric reciprocal space maps and with transmission electron microscopy (TEM). Sample bandgaps were determined from low-temperature 8-K photoluminescence (PL). Samples were excited using a continuous-wave 975-nm laser tuned between 9.9 and 231 mW. PL spectra were acquired using a Fourier transform infrared (FTIR) spectrometer with a liquid-nitrogen cooled HgCdTe detector through a 2.4-μm longpass filter to isolate the PL signal from pump laser scattering. The sample temperature was varied between 8 and 300 K using a closed-cycle He cryostat.

3. Results

An increase in the substrate temperature results in a decrease of the Sb content with or without Bi exposure. Adding Bi to the surface during growth induces a further reduction of the Sb content, although it becomes less pronounced for higher growth temperatures.

With a kinetic model we could fit the data, taking several surface processes into account including, deposition, desorption, removal of one anion by another (such as Sb removal by As) and segregation. The results suggested that the composition of the film was altered by the replacement of Bi with As [6].

In order to explore the optical properties of these structures, low-temperature PL was performed. A typical 8 K spectrum is shown in Fig. 1, where two distinct peaks can be seen in the PL signal, which can be attributed to the two layers in the structure. We observe a relatively sharp peak, with a broad high-energy shoulder. By decomposing the structure into two Bi-Gaussian peaks, which is used to account for the observed asymmetry in the broad high-energy shoulder, we obtain peaks with similar height but very different widths. By assuming that the broad peak originated from the Bi-exposed layer we could plot the peak positions as a function of substrate temperature as seen in Fig. 2. Using the same assignment of the peaks we can plot the same energies as a function of composition in Fig. 3. A monotonic change in bandgap as a function of Sb composition was observed. The overlapping composition ranges of the data from the Bi-exposed and un-exposed layers give confidence in the peak assignments. The dependence of the bandgap is significantly different than expected from unstrained material as shown in Fig. 3a. The energy is noticeably lower than expected. Another striking effect is the strong sensitivity of the PL intensity as the Sb-composition deviates from the lattice matched condition.

The one sample grown at 415 °C in this series has an InAsSb layer with 8.95% Sb, followed by a 6.30% Sb layer (grown in presence of Bi). The initial layer has a very small ($\sim 0.003\%$) compressive strain relative to the substrate and the second layer has a small tensile strain (0.184%) relative to the first layer. (004) and (444) reciprocal space maps show that the in-plane lattice constant is constant throughout the film thickness, and that the strain is accommodated by tetragonal distortion. TEM images show a narrow, high contrast strain band at the interfaces (Fig. 4a), but no threading dislocations within the field of view. The layers are flat and there is no evidence of compositional inhomogenieties, but there is also no contrast between the two layers, as would be expected for such small composition differences (Fig. 4b). Reciprocal space maps of the sample grown at 430 °C also shows that the lattice mismatch is accommodated by tetragonal distortion, although in this case both layers are tensile strained (0.051% and 0.200%).
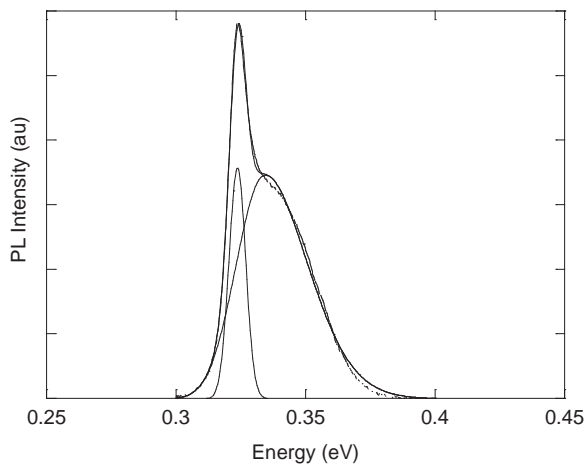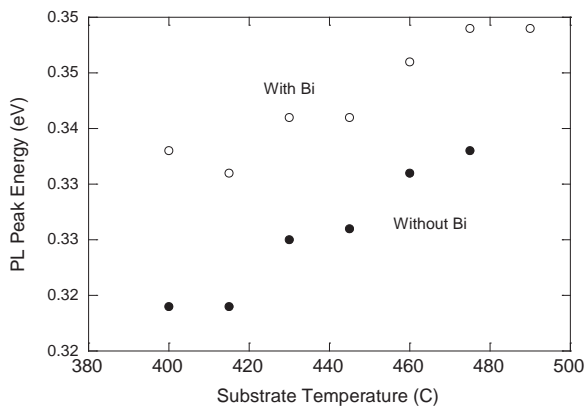
The first layer of the sample grown at 460 °C was mostly relaxed within the resolution afforded reciprocal space maps and triple axis x-ray diffraction, however the relaxation was anisotropic along the two orthogonal [110] directions. This anisotropy was seen in all three samples grown at or above 460 °C, and results in a small residual strain. As the temperature increases, the Sb composition decreases and becomes closer to InAs, which is known to show anisotropic strain relaxation via misfit dislocations [9]. TEM shows relaxation at the GaSb/InAsSb$_{0.061}$ interface (mismatch strain of 0.15%), although no dislocations thread through the structure within the field of view (Fig. 4c), which is not unexpected given the very low density of dislocations expected to be generated by such a small mismatch. There is no strain contrast band at the interface between the InAsSb$_{0.061}$ and InAsSb$_{0.046}$ (mismatch strain of 0.15%) layers. As the temperature increased, the presence of the Bi had less effect on the composition; therefore it is not surprising that the interface is less pronounced.

4. Discussion

A reduction in the bandgap compared to the expected unstrained case as seen here was also observed by Marciniak, et al. in thick InAsSb films [10]. They assumed that this was due to residual strain in the films, even though the thicknesses were of the order of a micron or more. They also discussed the possibility

Fig. 1. 8K PL spectrum decomposed in to two Bi-Gaussian peaks.

Fig. 2. The PL peak positions from InAsSb layers as a function of substrate temperature. The solid circles represent layers without Bi exposure and the open circles with Bi.
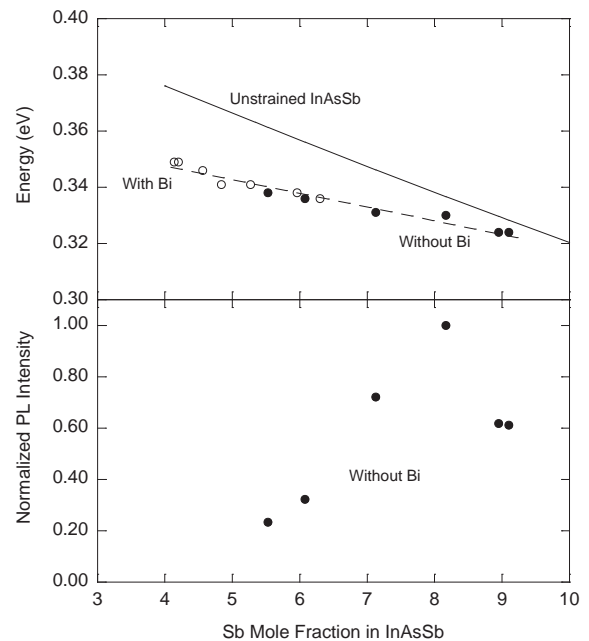
Fig. 3. The upper figure shows the bandgap of unstrained InAsSb (solid line) and the PL peak positions from the layers without Bi exposure (solid circles) and with Bi exposure (open circles). The lower figure is the normalized PL peak areas as a function of Sb-mole fraction in InAsSb without Bi exposure. The broken line is a guide to the eye.
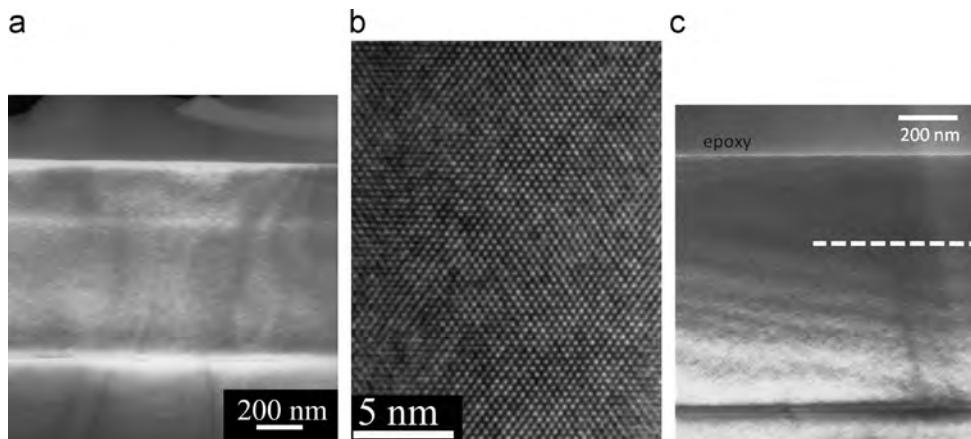
Fig. 4. (a) Two layer structure grown at 415 °C. (b) High resolution image of top layer in (a) that was grown with Bi surfactant. (c) Sample grown at 460 °C showing no contrast between the layers grown with or without the Bi surfactant (indicated by the dashed line).

of CuPt ordering but did not favor that explanation. The InAsSb alloys in this study have Sb compositions ranging from 4.20–9.10%, and it seems indeed unlikely that ordering can play a significant role in alloys with compositions that are so far from $InAs_{0.50}Sb_{0.50}$. Our observations of residual strain support this as the dominant mechanism for the bandgap shift.

The PL intensity from both the Bi-exposed and non-exposed layers goes down rapidly as the lattice mismatch increases. We cannot determine the direct cause for this. None of the layers showed threading dislocations. It is possible that the increasingly strained interfaces with GaSb may have localized recombination centers.

The PL intensity from the Bi-exposed layers, relative to the non-Bi-exposed bottom layers, is more perplexing. When the non-Bi-exposed bottom layer is close to lattice matched, the integrated intensity from each peak is comparable. However, as the lattice mismatch of the non-Bi-exposed bottom layer is increased, the integrated PL intensity of the Bi-exposed layer is ~ 3–6 times greater than the non-Bi-exposed bottom layer. Since the laser light is incident upon the Bi-exposed top layer first, more light is absorbed in that layer. Further, a portion of the PL emitted by the non-Bi-exposed bottom layer will be absorbed by the top layer. Using an absorption coefficient of $\sim 2 \times 10^{-4} \, cm^{-1}$, we would expect the integrated PL intensity from the Bi-exposed top layer to be a factor of ~ 1.5 greater than from the non-Bi-exposed bottom layer (assuming comparable material quality), falling short of the observed factor of 3–6.

Also, the peaks from the Bi-exposed layers are significantly broader than the peaks from the layers that were not exposed to Bi. The observed peak width is seen to increase from 6 to 9 meV at low injection from 12 to18 meV at high injection, which suggests filling of the higher energy states that are present due to compositional inhomogeneities. These widths can be compared with the 4–6 meV peak widths observed in the non-Bi-exposed layer at all injection levels. It seems likely that the wide peak widths of the Bi-exposed layers are due to non-uniformities in the alloy concentration that are below what can be detected by TEM. Inhomogeneties in the As/Sb distribution would lead to variations in the bandgap that would be further enhanced by the strain effect. This would also lead to localization that could help explain the unexpectedly large luminescence intensity. The localized states may collect the excited carriers preventing non-radiative recombination through defect states, thus increasing the contribution from radiative recombination.

5. Conclusion

Although this set of experiments does not rule out a possible benefit to InAsSb growth from a Bi surfactant, it demonstrates the

sensitivity of the material to lattice mismatch, which may be enhanced in a negative way by Bi. In order for InAsSb to exhibit its real bandgap, it needs to be strain-free. During mismatched growth Bi appears to induce alloy broadening.

Since both raising the growth temperature and using Bi surfactants suppresses Sb incorporation, it induces strain and/or strain-relieving defects. Therefore, one would need to grow perfectly lattice matched material with and without the Bi surfactant in order to make a conclusive comparison of the material's properties.

References

[1] E.H. Steenbergen, K. Nunna, L. Quyang, B. Ullrich, D.L. Huffaker, D.J. Smith, Y.-H. Zhang, Stain balanced InAs/InAs1-xSbx type II superlattices grown by molecular beam epitaxy on GaSb substrates, J. Vac. Sci. Technol. B 30 (2012) 107.
[2] Y. Lin, D. Wang, D. Donetsky, G. Kipshidze, L. Shterengas, L.E. Vorobjev, G. Belenky, Transport properties of holes in bulk InAsSb and performance of barrier long-wavelength infrared detectors, Semicond. Sci. Technol. 29 (2014) 112002.
[3] D. Wang, Y. Lin, D. Donetsky, L. Shterengas, G. Kipshidze, G. Belenky, W.L. Sarney, H. Hier, S.P. Svensson, Unrelaxed bulk InAsSb with novel absorption, carrier transport and recombination properties for MWIR and LWIR photodetectors, Proc. SPIE 8353 (2012) 8353.
[4] G. Belenky, D. Donetsky, G. Kipshidze, D. Wang, L. Shterengas, W.L. Sarney, S.P. Svensson, Properties of unrelaxed InAs1-xSbx alloys grown on compositionally graded buffers, Appl. Phys. Lett. 99 (2011) 141116.
[5] S.P. Svensson, W.L. Sarney, H. Hier, Y. Lin, D. Wang, D. Donetsky, L. Shterengas, G. Kipshidze, G. Belenky, Band gap of InAs1−xSbx with native lattice constant, Phys. Rev. B 86 (2012) 245205.
[6] J.M. Millunchick, E.M. Anderson, C. Pearson, W.L. Sarney, S.P. Svensson, Incorporation kinetics in mixed anion compound semiconductor alloys, J. Appl. Phys. 114 (2013) 234907.
[7] W.L. Sarney, S.P. Svensson, E.M. Anderson, A.M. Lundquist, C. Pearson, J.M. Millunchick, The influence of growth temperature on Sb incorporation in InAsSb, and the temperature-dependent impact of Bi surfactants, J. Cryst. Growth 8 (2014) 406.
[8] E.M. Anderson, A.M. Lundquist, W.L. Sarney, S.P. Svensson, P.J. Carrington, C. Pearson, J.M. Millunchick, Influence of a Bi surfactant on Sb incorporation in InAsSb alloys, J. Appl. Phys. 116 (2014) 014901.
[9] A. Trampert, K.H. Ploog, E. Tournié, Anisotropic misfit dislocation nucleation in two-dimensional grown InAs/GaAs(001) heterostructures, Appl. Phys. Lett. 73 (1998) 1074.
[10] M.A. Marciniak, R.L. Hengehold, Y.K. Yeo, G.W. Turner, Optical characterization of molecular beam epitaxy grown InAsSb nearly lattice mismatched in GaSb, J. Appl. Phys. 84 (1998) 480.
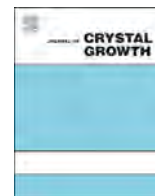
MBE grown GaAsBi/GaAs multiple quantum well structures: Structural and optical characterization

Robert D Richards [a,*], Faebian Bastiman [a], John S Roberts [a], Richard Beanland [b], David Walker [b], John P R David [a]

[a] Department of Electronic and Electrical Engineering, University of Sheffield, Sheffield S1 3JD, UK
[b] Department of Physics, University of Warwick, Coventry CV4 7AL, UK

ARTICLE INFO

ABSTRACT

A series of GaAsBi/GaAs multiple quantum well p–i–n diodes were grown by molecular beam epitaxy. Nomarski images showed evidence of sub-surface damage in each diode, with an increase in the cross-hatching associated with strain relaxation for the diodes containing more than 40 quantum wells. X-ray diffraction ω–2θ scans of the (004) reflections showed that multiple quantum well regions with clearly defined well periodicities were grown. The superlattice peaks of the diodes containing more than 40 wells were much broader than those of the other diodes. The photoluminescence spectra showed a redshift of 56 meV and an attenuation of nearly two orders of magnitude for the 54 and 63 well diodes. Calculations of the quantum confinement and strain induced band gap modifications suggest that the wells in all diodes are thinner than their intended widths and that both loss of quantum confinement and strain probably contributed to the observed redshift and attenuation in the 54 and 63 well diodes. Comparison of this data with that gathered for InGaAs/GaAs multiple quantum wells, suggests that the onset of relaxation occurs at a similar average strain–thickness product for both systems. Given the rapid band gap reduction of GaAsBi with Bi incorporation, this data suggests that GaAsBi is a promising photovoltaic material candidate.

1. Introduction

The large, non-linear bowing coefficient of Bi in GaAs [1] makes it a promising candidate for infrared detectors and the band gap temperature dependence and split-off band modification suggest applications in telecommunications [2,3]. Little attention has been paid to the potential of GaAsBi and related materials for photovoltaic (PV) applications. The large band gap reduction per unit strain on GaAs (750 meV/%strain [4,5]) makes GaAsBi/GaAs multiple quantum wells (MQWs) a candidate material system for the middle junction in triple junction PV. For this application, well numbers in excess of 60 are required [6]. GaAsBi/GaAs structures with up to 24 wells have previously been investigated [7] and this project aims to characterize structures containing up to 60 wells with a view to the development of GaAsBi as a 1 eV absorbing photovoltaic material candidate.

2. Experimental

In this work, GaAsBi/GaAs MQW p–i–n diodes were grown on 2 in. epi-ready n+ GaAs:Si substrates cleaved into 11.4 mm × 11.8 mm sections to fit the sample holder of an Omicron molecular beam epitaxy–scanning tunnelling microscopy (MBE–STM) system. Details of the sample preparation and growth calibration protocols are discussed elsewhere [8]. A 200 nm n-type GaAs:Si buffer was grown at 580 °C on each sample before the heterostructure was deposited (see Fig. 1 for sample structures). The Ga flux was 3.44 atoms nm^{-2} s^{-1}, which is equivalent to a GaAs growth rate of 0.55 μm/h, with an As$_2$ flux of 6 atoms nm^{-2} s^{-1}. The n-type AlGaAs cladding was also grown at 580 °C using the same Ga flux, an Al flux of 1.47 atoms nm^{-2} s^{-1} and an As$_2$ flux of 7 atoms nm^{-2} s^{-1} to produce Al$_{0.3}$Ga$_{0.7}$As. The sample was cooled to 380 °C and the arsenic cracker was cooled from 1000 °C to 650 °C to provide As$_4$ for growth of the MQW region. As$_4$ was used for the growth of GaAsBi because it has been shown that there is a much larger As:Ga flux ratio growth window for GaAsBi using As$_4$ than As$_2$ with no reduction in material quality [8,9]. The MQW i-region was grown using an As$_4$ flux of 6 atoms nm^{-2} s^{-1}. Prior to growth of the first GaAsBi well a Bi pre-layer was deposited on the growth surface. The pre-layer was deposited in the absence of a Ga flux by exposing
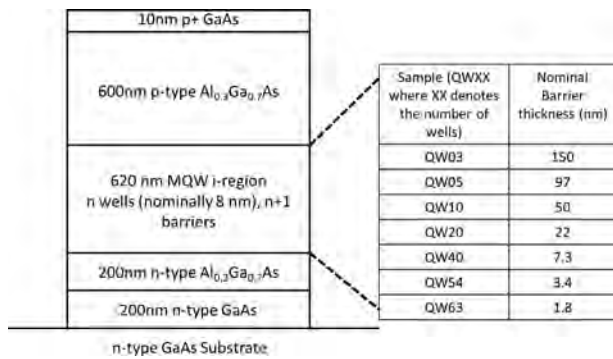
Fig. 1. Diagram of the p–i–n diode structure grown in this work. The number in each sample's name is the number of wells in that sample.

the growth surface to the same Bi flux as that used during well growth (0.24 atoms $nm^{-2}\,s^{-1}$) for 30 s. The pre-layer was intended to prevent compositional fluctuations caused by the finite time taken to build up a surface Bi layer as reported by Fan et al. [10]. After deposition of the Bi pre-layer, growth was halted for 30 s before growth of the first quantum well (QW). The nominal well thickness in every sample was 8 nm. Growth was interrupted at each well/barrier interface for 1 min to allow excess Bi (i.e. the Bi layer that forms on top of the reconstructed surface) to desorb; the Bi surface reconstruction lifetime at this temperature is significantly longer [8,10], so Bi desorption from the reconstructed Bi layer was considered to be negligible. After the growth of the QWs, the sample was heated back up to 580 °C and the As cracker was heated back up to 1000 °C to produce As_2 before deposition of the upper AlGaAs cladding and GaAs cap layers, which were grown using the same temperatures and fluxes as the first AlGaAs and GaAs layers.

The photoluminescence (PL) measurements made during this work were performed with a 532 nm continuous wave, diode pumped solid state laser. The PL signal was spectrally separated using a monochromator and the signal was passed through a phase sensitive lock-in amplifier to eliminate background noise from the measurements.

The ω–2θ X-ray diffraction (XRD) measurements throughout this work were taken on a Bruker D8 Discover XRD machine using Cu $k\alpha_1$ radiation and the measured diffraction patterns were modelled using RADS Mercury software assuming a GaBi lattice constant of 6.28 Å [11].

3. Results

3.1. Nomarski

Nomarski differential interference microscopy images of the surfaces of the diodes (Fig. 2) showed signs of sub-surface structural damage. For the diodes with up to 40 wells, the sub-surface damage lines were not all orthogonal and straight, so it seems unlikely that they were caused by strain relaxation [12]. QW54 and QW63 showed a much greater density of damage lines and a significant proportion of the lines were straight and orthogonal, indicating that strain relaxation may have played a part in their formation.

3.2. XRD

Initial (004) XRD scans of the diodes are shown in Fig. 3. The presence of clear superlattice (SL) peaks indicates that MQW regions of well-defined periodicity were formed. There is a significant broadening of the SL peaks for QW54 and QW63, which is often an indication of strain relaxation [14]. As only the symmetrical 004 scan was performed on these diodes, only the MQW period and

average Bi content have been extracted from this data, assuming no strain relaxation. By assuming 8 nm wells of uniform Bi content, the measured MQW period and average Bi content were used to calculate the average strain in the MQW region. The predicted average strain was calculated using the nominal well and barrier thicknesses. The predicted average strain most accurately matched the measured average strain when the Bi content was set to be 2.83%.

3.3. PL

The PL spectra from the diodes grown in this work are shown in Fig. 4. The diodes with up to 40 wells show a slight variation in peak position and peak intensity. This variation is probably due to variations in the substrate temperature and atomic fluxes during growth. The growth temperature uncertainty is ± 10 °C, the flux uncertainties are all $\pm 10\%$, and Bi incorporation is very sensitive to the growth temperature and atomic fluxes during growth [8].

The diodes containing more than 40 wells show a significant redshift and attenuation of their PL spectra. The redshift between the mean PL peak energies of the diodes with up to 40 wells and those with more than 40 wells is 56 meV. The significant redshift and attenuation of the spectra from QW54 and QW63 could be caused by two effects: strain relaxation and loss of quantum confinement. The redshift associated with each effect was calculated to determine which was responsible for the observed redshift and attenuation in the PL spectra.

3.4. Analysis

From the Nomarski, XRD and PL data, there appears to have been a strain relaxation event in QW54 and QW63. The analysis was, therefore, only conducted for the diodes with up to 40 wells as the average strain estimated from the XRD data and the Bi content estimated from the PL spectra would be affected by relaxation.

First, the quantum confinement energy in each sample was calculated assuming a uniform Bi content throughout the QWs. This assumption was necessary to complete the calculations; however, it has been shown that GaAsBi QWs do not always have uniform Bi contents [15]. The numbers derived from these calculations are, therefore, only effective well widths and Bi contents, which are used to estimate the quantum confinement and band gap modification due to strain in each diode. By varying the estimated QW widths and Bi contents in each diode in order to match the first calculated QW transition to the observed peak PL energy (as in Fig. 4), while maintaining the observed average strain in the MQW region (as in Fig. 3b), new estimates of the average QW width, Bi content and quantum confinement energy in each MQW were obtained. These parameters were then used to estimate the redshift of the first QW transition associated with a total loss of strain in the MQW region. The calculations were performed using the finite QW confinement energy estimates of Singh [16], electron and hole reduced masses of $0.06m_0$ [17] and $0.55m_0$ [18] respectively and the calculations of the effect of strain on the band structure of GaAsBi by Batool et al. [19]. The results are shown in Table 1. All of the calculated well widths are thinner than expected. TEM images like that shown in Fig. 5 suggest that the well thicknesses are around 4.8 ± 0.6 nm. It is probable that the wells are not uniform in profile, which would explain why the calculated well thicknesses are larger than the thickness estimated from TEM.

It seems likely that a relaxation event has occurred in QW54 and QW63 from the XRD and Nomarski measurements and the calculated redshift associated with the complete relaxation of strain in the other MQWs is sufficient to account for the observed redshift in the PL spectra of these samples (56 meV) as seen in Table 1. However, the estimated quantum confinement energy in each MQW is also sufficient to account for the observed redshift. These
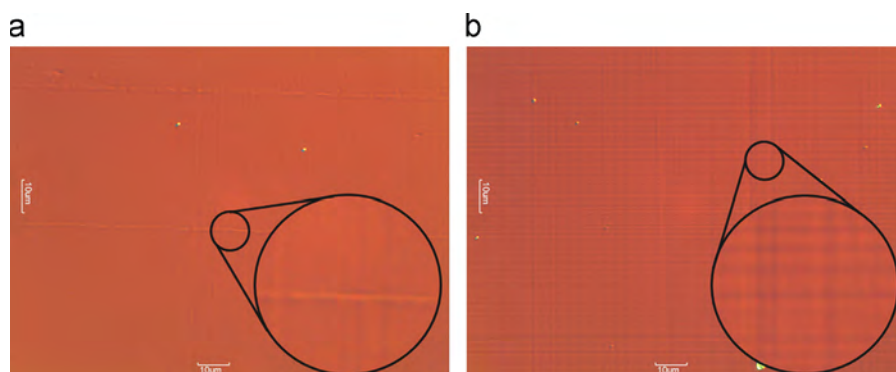
Fig. 2. Nomarski images of a) QW40 and b) QW54.
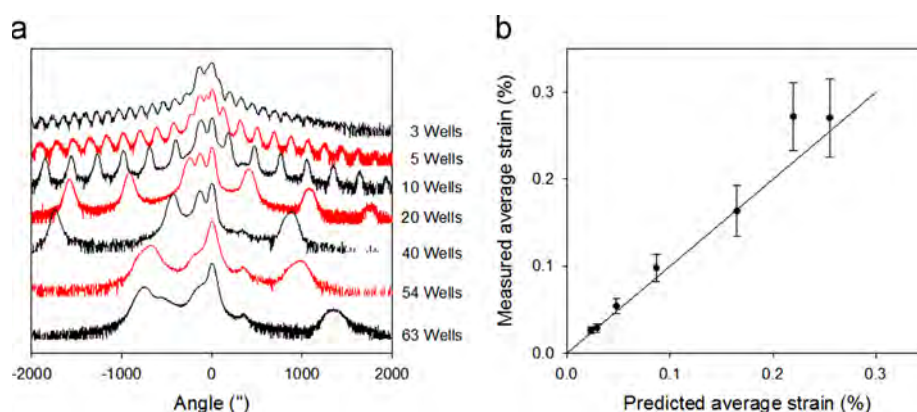
Fig. 3. Data from the initial XRD characterization of the diodes. a) (004) ω–2θ scans of each diode, the y-axis is on a log scale and the scans have been vertically offset for clarity and b) the average strain in each MQW region measured by XRD, plotted against the estimated average strain in each MQW region assuming 8 nm wells of 2.83% Bi. The calculations were performed using the method of Ref. [13]. The error bars were estimated from the range of Bi contents that produced a reasonable fit between the measured and modelled XRD scans.
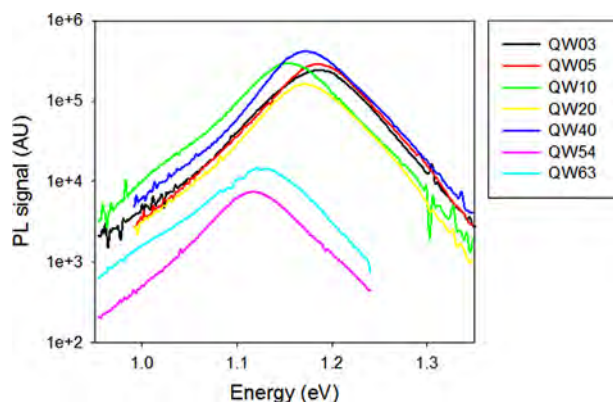
Fig. 4. PL spectra from all diodes in this work.

Table 1

Well widths, Bi contents, quantum confinement energies, and strain induced band gap modifications for each diode in this work. QW54 and QW63 were omitted as the MQW regions in these diodes are expected to have relaxed. The uncertainties associated with the parameters in this table are derived from the uncertainties in the average strain in each MQW as shown in Fig. 3 and the uncertainty in the estimate of the band gap from the PL spectra.

Sample	Estimated well width (nm)	Estimated Bi content (%)	Estimated quantum confinement energy (meV)	Estimated band gap modification due to strain (meV)	Estimated first transition blueshift due to strain (meV)
QW03	6.4 ± 1.0	4.0 ± 0.5	59 ± 11	62 ± 8	51 ± 16
QW05	5.3 ± 0.9	4.8 ± 0.5	75 ± 13	66 ± 9	50 ± 17
QW10	5.3 ± 1.0	4.2 ± 0.5	67 ± 13	76 ± 11	61 ± 20
QW20	5.8 ± 0.9	4.4 ± 0.5	66 ± 12	69 ± 9	53 ± 17
QW40	5.0 ± 0.9	4.5 ± 0.5	73 ± 14	71 ± 9	57 ± 19

estimates represent upper limits of the redshift associated with each effect. In practice, it is unlikely that either quantum confinement or strain will be completely lost. Therefore, it seems reasonable to assume that both effects contribute to the redshift of the PL spectra from QW54 and QW63. Further investigation is required to differentiate between the two effects in these layers.

The greatest number of wells grown before the onset of strain relaxation in this work was 40, at a band gap of around 1.18 eV. The mean well width in this work is 5.6 nm and, in order to reach 1 eV, the Bi content of 5.6 nm wells would need to be ~8%. The maximum number of such wells that could be contained in a 620 nm MQW without dislocation multiplication is around 30. Strain balancing will be required to realise thicker GaAsBi/GaAs MQWs.

3.5. Comparison with InGaAs/GaAs

The results from this work are compared to those of Griffin et al. [13] from the InGaAs/GaAs material system in Fig. 6. It seems that GaAsBi/GaAs MQWs undergo strain relaxation at a similar average strain–thickness product to InGaAs/GaAs MQWs. The samples analysed by Griffin et al. were grown at 500 °C [21] and the low growth temperature used for the GaAsBi layers in this work could freeze defects into the MQW regions and make them seem less susceptible to strain relaxation. Even so, this data suggests that GaAsBi could be a suitable alternative to InGaAs for PV applications
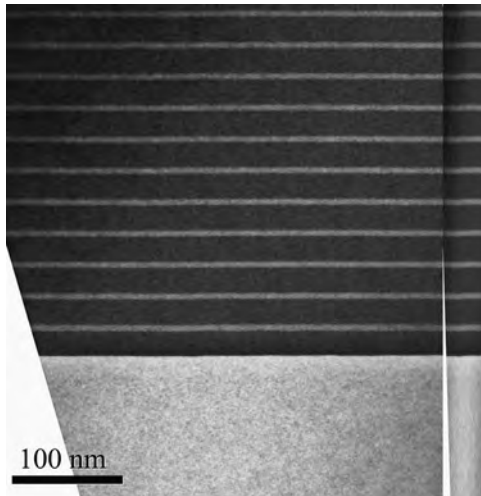
Fig. 5. Dark field TEM image of QW20.
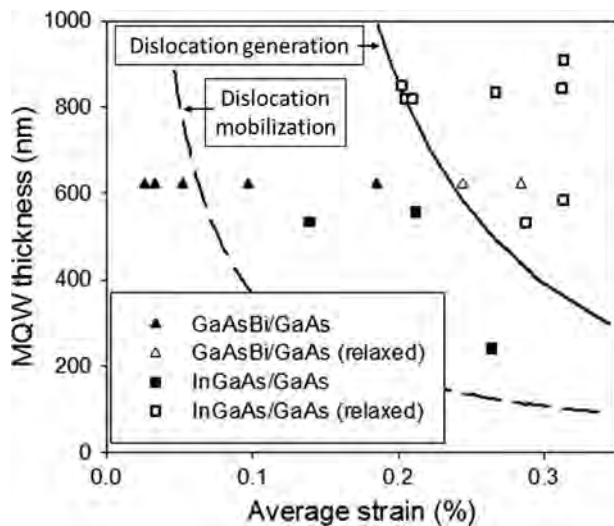
Fig. 6. Plot of the thicknesses and average strains of the samples reported by Griffin et al. [13]. The dashed line is the calculated Matthews–Blakeslee critical thickness for dislocation propagation; the solid line is the dislocation generation critical thickness taken from the data of Drigo et al. [20]; the squares represent InGaAs/GaAs MQWs; the triangles represent GaAsBi/GaAs MQWs; and the empty symbols represent samples which exhibit significant relaxation.

as the rapid reduction in band gap with Bi incorporation allows for better tailoring of the absorption edge of the material.

4. Conclusions

GaAsBi/GaAs MQW diodes were grown. Nomarski images of the sample surfaces and XRD ω–2θ measurements suggest that lattice relaxation occurred in the diodes with more than 40 wells. The PL spectra from the diodes with more than 40 wells show a redshift and attenuation compared to the other diodes. Calculations of the quantum confinement energies and strain induced band gap modifications

of each diode suggest that strain relaxation and a loss of quantum confinement have occurred in the diodes with more than 40 QWs. The GaAsBi/GaAs MQWs appear to relax at a similar average strain–thickness product to InGaAs/GaAs MQWs. This suggests that replacing InGaAs with GaAsBi in multi-junction photovoltaics could produce a middle junction with a better optimized band gap. However, strain balancing with a material such as GaAsP needs to be investigated. Further work is also required to assess the electrical characteristics of these diodes for their suitability for photovoltaic applications.

References

[1] T. Tiedje, E.C. Young, A. Mascarenhas, Growth and properties of the dilute bismide semiconductor GaAs1−xBix a complementary alloy to the dilute nitrides, Int. J. Nanotechnol. 5 (9–12) (2008) 963–983.
[2] S.J. Sweeney, S.R. Jin, Bismide-nitride alloys: promising for efficient light emitting devices in the near- and mid-infrared, J. Appl. Phys. 113 (4) (2013) 043110.
[3] C.A. Broderick, et al., Band engineering in dilute nitride and bismide semiconductor lasers, Semicond. Sci. Technol. 27 (2012) 9.
[4] S. Francoeur, et al., Band gap of GaAs$_{1−x}$Bi$_x$, $0 < x < 3.6\%$, Appl. Phys. Lett. 82 (22) (2003) 3874–3876.
[5] S. Tixier, et al., Molecular beam epitaxy growth of GaAs$_{1−x}$Bi$_x$, Appl. Phys. Lett. 82 (14) (2003) 2245–2247.
[6] D.B. Bushnell, et al., Effect of well number on the performance of quantum-well solar cells, J. Appl. Phys. 97 (12) (2005) 124908–124911.
[7] Y. Tominaga, et al., Structural investigation of GaAs$_{1−x}$Bi$_x$/GaAs multiquantum wells, Appl. Phys. Lett. 93 (13) (2008) 131915.
[8] R.D. Richards, et al., Molecular beam epitaxy growth of GaAsBi using As$_2$ and As$_4$, J. Cryst. Growth 390 (0) (2014) 120–124.
[9] F. Bastiman, et al., Non-stoichiometric GaAsBi/GaAs (100) molecular beam epitaxy growth, J. Cryst. Growth 338 (1) (2012) 57–61.
[10] D. Fan, et al., MBE grown GaAsBi/GaAs double quantum well separate confinement heterostructures, J. Vac. Sci. Technol. B: Microelectron. Nanometer Struct. 31 (3) (2013) 181103–181106.
[11] H. Achour, et al., Structural and electronic properties of GaAsBi, Superlattices Microstruct. 44 (2) (2008) 223–229.
[12] D.J. Dunstan, Strain and strain relaxation in semiconductors, J. Mater. Sci.: Mater. Electron. 8 (6) (1997) 337–375.
[13] P.R. Griffin, et al., Effect of strain relaxation on forward bias dark currents in GaAs/InGaAs multiquantum well p-i-n diodes, J. Appl. Phys. 80 (10) (1996) 5815–5820.
[14] P.F. Fewster, X-ray diffraction from low-dimensional structures, Semicond. Sci. Technol. 8 (11) (1993) 1915.
[15] Y.I. Mazur, et al., Effects of spatial confinement and layer disorder in photoluminescence of GaAs$_{1−x}$Bi$_x$/GaAs heterostructures, J. Phys. D: Appl. Phys. 46 (6) (2013) 065306–065313.
[16] J. Singh, Analytical closed form expressions for the effective band edges in shallow quantum wells, Appl. Phys. Lett. 64 (20) (1994) 2694–2696.
[17] B. Fluegel, et al., Shubnikov-de Haas measurement of electron effective mass in GaAs$_{1−x}$Bi$_x$, Appl. Phys. Lett. 99 (16) (2011) 162108–162108-3.
[18] J. Hwang, J.D. Phillips, Band structure of strain-balanced GaAsBi/GaAsN superlattices on GaAs, Phys. Rev. B 83 (19) (2011) 195327.
[19] Z. Batool, et al., The electronic band structure of GaBiAs/GaAs layers: influence of strain and band anti-crossing, J. Appl. Phys. 111 (11) (2012) 113108.
[20] A.V. Drigo, et al., On the mechanisms of strain release in molecular-beam-epitaxy-grown In$_x$Ga$_{1−x}$As/GaAs single heterostructures, J. Appl. Phys. 66 (5) (1989) 1975–1983.
[21] J.P.R. David, et al., Barrier width dependence of leakage currents in InGaAs/GaAs multiple quantum-well P-I-N-diodes, J. Electron. Mater. 20 (4) (1991) 295–297.
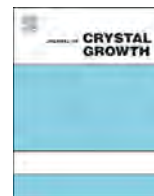
Bi flux-dependent MBE growth of GaSbBi alloys

M.K. Rajpalke [a], W.M. Linhart [a], K.M. Yu [b,c], T.S. Jones [d], M.J. Ashwin [d], T.D. Veal [a,*]

[a] *Stephenson Institute for Renewable Energy and Department of Physics, School of Physical Sciences, University of Liverpool, Liverpool L69 7ZF, United Kingdom*
[b] *Materials Sciences Division, Lawrence Berkeley National Laboratory, 1 Cyclotron Road, Berkeley, CA 94720, USA*
[c] *Department of Physics and Materials Science, City University of Hong Kong, Kowloon, Hong Kong*
[d] *Department of Chemistry, University of Warwick, Coventry CV4 7AL, United Kingdom*

ABSTRACT

The incorporation of Bi in $GaSb_{1-x}Bi_x$ alloys grown by molecular beam epitaxy is investigated as a function of Bi flux at fixed growth temperature (275 °C) and growth rate (1 μm h^{-1}). The Bi content is found to vary proportionally with Bi flux with Bi contents, as measured by Rutherford backscattering, in the range $0 < x \leq 4.5\%$. The GaSbBi samples grown at the lowest Bi fluxes have smooth surfaces free of metallic droplets. The higher Bi flux samples have surface Bi droplets. The room temperature band gap of the GaSbBi epitaxial layers determined from optical absorption decreases linearly with increasing Bi content with a reduction of ~ 32 meV/%Bi.

1. Introduction

The incorporation of a dilute amount of Bi in III–V arsenide semiconductors has shown great promise for optoelectronics device applications operating in the near- and mid-infrared ranges [1–5]. The interest in the incorporation of a dilute amount of N or Bi in GaSb is similarly motivated by mid-infrared applications as alloying with these elements produces a large reduction of the band gap per %N or %Bi, taking the band gap from 1.7 μm for GaSb to beyond 3 μm.

There are recent reports on controlled N incorporation and the band gap reduction in GaN_xSb_{1-x} alloys [6,7]. The incorporation of Bi as an isoelectronic dopant in GaSb was reported nearly two decades ago [8,9]. However, very few studies of the growth of $GaSb_{1-x}Bi_x$ alloys have been reported. A detailed understanding of Bi incorporation in GaSb is required in order to determine the properties of GaSbBi alloys and also to be able to develop GaNSbBi alloys lattice matched to GaSb substrates. The earliest reports on epitaxial GaSbBi alloys show very low Bi incorporation up to 0.8% [10,11]. The $GaSb_{1-x}Bi_x$ alloys grown by liquid phase epitaxy (LPE) showed the expected lattice dilation [11], whereas the initial films grown by molecular-beam epitaxy (MBE) exhibited lattice contraction with respect to GaSb [10].

The incorporation of Bi in III–V semiconductors while maintaining a droplet-free smooth surface is challenging, but is achievable by using low growth temperatures and a near-stoichiometric V:III ratio [12–14]. Some recent attempts to grow GaSbBi alloys with high Bi content show Sb/Bi droplets on the surface as well as unintentional arsenic incorporation [15]. Our first studies of growth temperature- and growth rate-dependent MBE of GaSbBi used a fixed Bi flux and achieved Bi incorporation of up to 9.6% with high substitutionality and generally metallic droplet-free surfaces [16,17]. Optical absorption, photoreflectance and photoluminescence studies showed band gap reduction of ~ 30–36 meV/%Bi [16,17,19,20]. However, while the Bi flux has been varied at the same time as varying the growth temperature in one previous study [10], the effect of Bi flux alone on Bi incorporation into GaSb has yet to be explored. The present work deals with the control of Bi content in GaSbBi alloys by varying the Bi flux, at fixed growth temperature and growth rate, and determination of the resulting band gap variation.

Fig. 1 shows the calculated $\mathbf{k} \cdot \mathbf{P}$ band structure close to the Γ point of GaSb and a $GaSb_{0.95}Bi_{0.05}$ alloy to illustrate the Bi-induced band gap reduction based on previous reports [16,17]. The calculation was carried out under the assumption that the valence band edge moves according to the valence band anticrossing (VBAC) model and the conduction band minimum (CBM) shifts according to the virtual crystal approximation (VCA) [16–18]. Fig. 1(a) also depicts the localised Bi 6p-like states at 1.17 eV below the GaSb VBM (valence band maximum) [16]. Fig. 1(b) illustrates the changes in band edge positions with respect to those of GaSb for a Bi content of 5% of the anion sublattice. According to the VBAC model, the VBM moves upward by ~ 10 meV/%Bi, whereas the CBM moves downward by 26.0 meV/%Bi.

* Correspondence to: Stephenson Institute for Renewable Energy and Department of Physics, School of Physical Sciences, Chadwick Building, Peach Street, University of Liverpool, Liverpool, L69 7ZF, United Kingdom. Tel.: +44 151 794 3872.
E-mail address: T.Veal@liverpool.ac.uk (T.D. Veal).
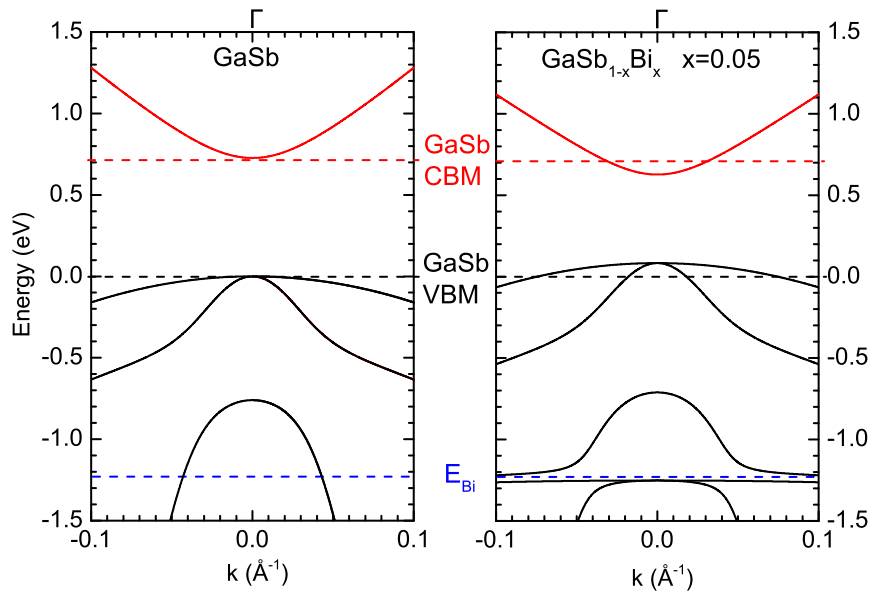
Fig. 1. (Color online) Band dispersion for (a) GaSb and (b) GaSb$_{0.95}$Bi$_{0.05}$ calculated using $\mathbf{k} \cdot \mathbf{p}$ model. The band gap changes from 720 to 545 meV with the incorporation of 5% Bi.

2. Experimental details

The GaSbBi epilayers were grown on undoped GaSb(001) substrates by solid-source MBE. The sources and substrate preparation procedure are described elsewhere [16]. For each GaSbBi film, a GaSb buffer layer of 100 nm thickness was grown at 500 °C and the substrate was then cooled to 275 °C. The Bi beam equivalent pressure (BEP) flux was varied from approximately 2.0×10^{-8} to 5.8×10^{-8} mbar. The Sb BEP was fixed at 1.25×10^{-6} mbar. The substrate temperature was measured by thermocouple calibrated by pyrometer measurements. The samples were grown under nominally slightly group V-rich conditions (Sb:Ga ratio of approximately 1.05:1) using a growth rate of 1.0 μm h^{-1}, at fixed growth temperatures of 275 °C. The film thicknesses were found to be 400 nm by modelling the interference fringes in 004 HRXRD ω–2θ scans and this was confirmed by RBS.

The Bi incorporation in the GaSbBi epilayers was characterised using RBS with 3.72 MeV He^{2+} ions and by HRXRD using a Philips X'Pert diffractometer equipped with a Cu Kα_1 X-ray source (λ=0.15406 nm). The surface morphology was investigated by JEOL JSM-7001F field emission scanning electron microscopy (SEM), with energy dispersive X-ray spectroscopy (EDS) used to identify any surface metallic droplets. To remove any droplets, samples were dipped in dilute HCl (10:1H$_2$O:HCl) for 60 s at room temperature and then rinsed in deionised water and dried in flowing nitrogen gas. Transmittance measurements were carried out at room temperature to determine the band gap of the alloys using a Bruker Vertex 70 V Fourier-transform infrared (FTIR) spectrometer, using a liquid nitrogen-cooled HgCdTe detector.

3. Results and discussion

Accurate values of Bi content in GaSbBi films cannot be obtained from XRD measurements of the lattice constant by applying Vegard's law because the lattice constant of zinc blende GaBi is experimentally unknown. Therefore, RBS was used to calculate the Bi content in the GaSbBi epilayers. Fig. 2 shows the RBS Bi content in GaSbBi epilayers as a function of Bi flux. The Bi content increases linearly with the Bi flux, at fixed growth temperature and growth rate, reaching 4.5% at the highest flux used. Channeling RBS
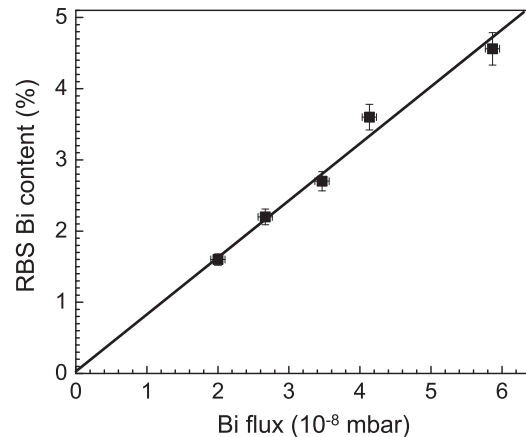
Fig. 2. (Color online) RBS Bi content of Bi flux dependent GaSbBi samples. The solid line is a linear fit to the Bi content.

measurements show that for up to 3.6% Bi content, the films are of high crystallinity with greater than 97% of Bi atoms on substitutional group V lattice sites. This falls to 93% for the sample grown using the highest Bi flux. The error bars in Fig. 2 reflect the uncertainties in the measurements of the Bi content and Bi flux. Earlier report on Bi incorporation in GaSbBi was found to saturate with higher Bi flux [10] and the maximum Bi incorporation was found to be 0.7% of the anion sublattice. The low Bi incorporation reported previously even with a high Bi flux ($\sim 2.7 \times 10^{-7}$ mbar) is probably due to the high growth temperature (390 °C). Our earlier report showed that Bi incorporation reduces drastically at higher growth temperature ($\sim$350 °C) [16].

Fig. 3 shows the HRXRD ω–2θ scans of GaSbBi samples with Bi contents 1.6, 2.7, and 3.6%. In each case, the peak corresponding to the GaSbBi film is at a lower Bragg angle than that of the substrate. This corresponds to the expansion of the lattice of the GaSbBi epilayers with respect to the GaSb substrate. Lattice dilation has previously been observed in GaSbBi films in our previous temperature-dependent and growth rate-dependent MBE growth [16,17] and with low Bi content ($< 1\%$) material grown by liquid phase epitaxy [11]. The previously observed lattice contraction for MBE-grown GaSbBi was explained in terms of group V vacancies [10]. The Pendellösung interference fringes observed indicates that the interfaces are smooth and the composition

is uniform. The diffraction peak from GaSbBi epilayers shifts towards lower angle with an increase in the Bi flux, indicating more Bi incorporation in agreement with the RBS results.

The surface morphology of the Bi flux dependent GaSbBi films was studied using SEM. Fig. 4 shows the SEM images of the GaSbBi samples with Bi contents 1.6, 2.7, 3.6, and 4.5% grown at Bi fluxes 2.0, 3.5, 4.1, and 5.8×10^{-8} mbar, respectively. Fig. 4(a) and (b) shows droplet-free smooth surfaces and are typical of GaSbBi samples with lower Bi flux ($< 4.1 \times 10^{-8}$ mbar). At higher Bi fluxes, the films show surface Bi droplets. Fig. 4(c) and (d) shows the formation of Bi droplets, identified by EDS, on the surface of the GaSbBi films grown at higher Bi fluxes ($\geq 4.1 \times 10^{-8}$ mbar). The excess Bi on the growth surface was etched using dilute HCl. The inset of Fig. 4(d) shows the SEM image of the same sample

after HCl etching. The Bi droplets are completely removed by HCl etching.

The optical properties of the GaSbBi epilayers as a function of Bi content were studied using transmittance measurements. The absorption coefficient, α, was calculated from the transmittance data. The transmission data from each sample was divided by the transmission from a GaSb substrate so that the remaining signal corresponds to transmission through a ~ 400-nm thick GaSbBi layer. Fig. 5 shows the absorption spectra derived from the transmission data for the GaSbBi epilayers. The absorption edge energy red shifts with increasing Bi content. The absorption edge decreases in energy to 575 ± 20 meV as the Bi content is increased to $x=4.5\%$.

The determined band gaps are plotted in Fig. 6 along with the data points from our earlier reports on growth temperature- and

Fig. 3. (Color online) HRXRD scans of the 004 Bragg reflection of Bi flux dependent GaSbBi films on GaSb substrates with Bi content 1.6, 2.7, and 3.6% grown at 275 °C with nominal growth rate 1 μm h^{-1}.
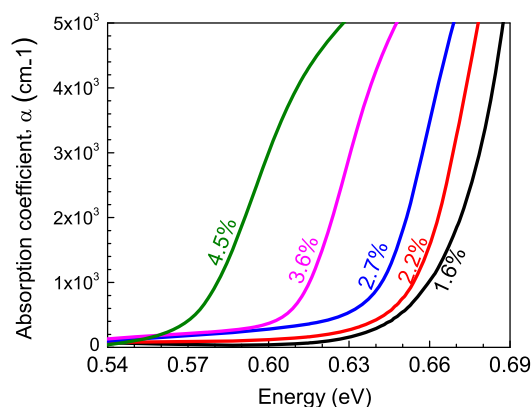
Fig. 5. (Color online) The absorption spectra for Bi flux-dependent GaSb$_{1-x}$Bi$_x$ films at a growth temperature of 275 °C. The composition of each film is given in the figure.
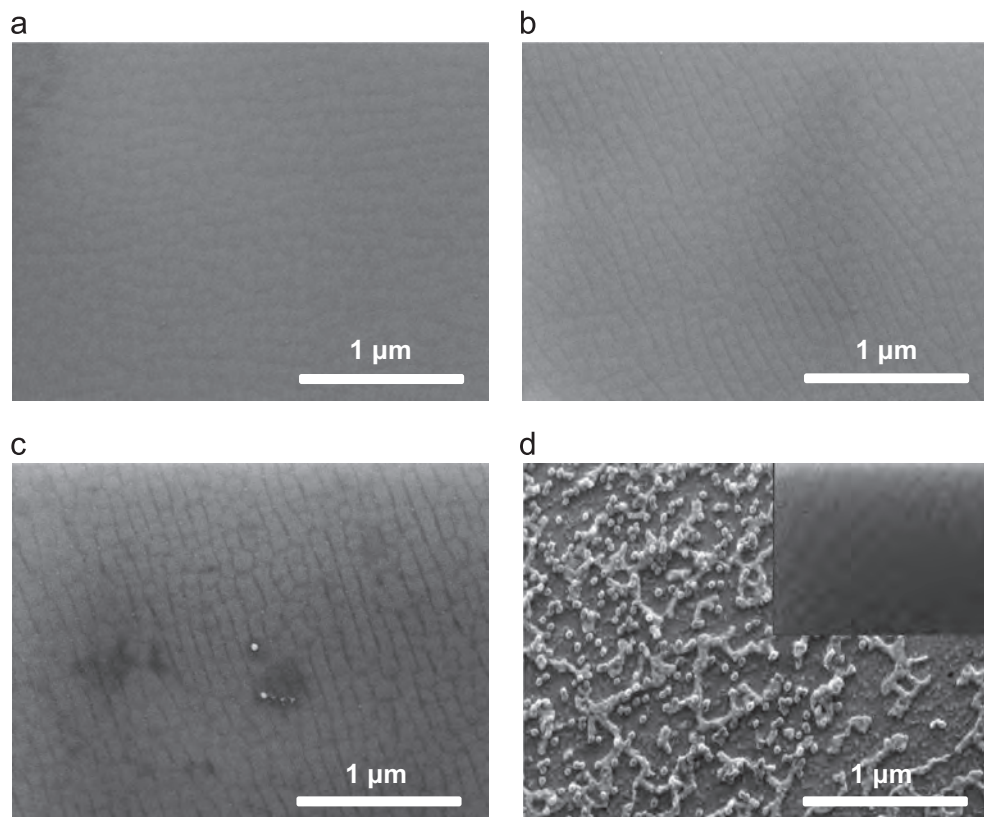
Fig. 4. (Color online) SEM images of GaSbBi samples with Bi contents (a) 1.6, (b) 2.7, (c) 3.6, and (d) 4.5% grown at Bi fluxes 2.0, 3.5, 4.1, and 5.8×10^{-8} mbar, respectively. The inset of (d) shows an SEM image of the same sample after HCl etching, indicating the removal of Bi droplets.
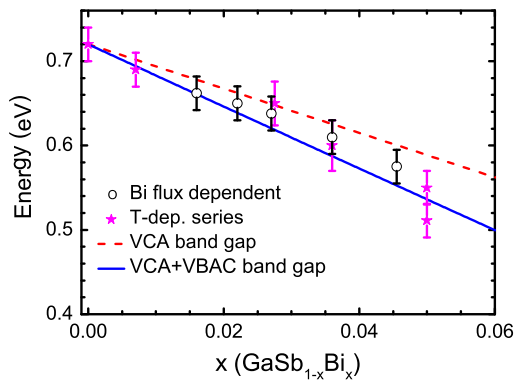
Fig. 6. (Color online) The band gap versus Bi content determined from the absorption spectra for the Bi flux-dependent GaSbBi samples (open circles). Calculated composition dependence of the band gap of $GaSb_{1-x}Bi_x$ based on the VCA variation of both the CBM and the VBM (dashed line) and from combining the VCA variation of the CBM with VBAC (solid line). The band gaps of $GaSb_{1-x}Bi_x$ films grown at different temperature (stars) from Ref. [16] are also plotted.

growth rate-dependent samples [16,17]. The band gap reduction for the Bi flux-dependent samples, obtained by a linear fit of the data points constrained to pass through 720 meV for GaSb, is found to be ∼32 meV/%Bi, greater than the value from the VCA model (dashed line) of about 25 meV/%Bi [16,18]. Additional band gap reduction has previously been accounted for by the VBAC model (solid line), implemented using a 12×12 $\mathbf{k} \cdot \mathbf{p}$ Hamiltonian [18]. The band gap reduction observed for the flux dependent samples is within the range ∼30–36 meV/%Bi previously reported for temperature- and growth-rate dependent samples [16,19,17,21].

4. Conclusion

Epitaxial thin films of $GaSb_{1-x}Bi_x$ with $0 < x \leq 4.5\%$ have been achieved by varying the Bi flux. The samples grown at lower Bi flux show droplet-free smooth surfaces. All the samples show high crystalline quality with greater than 97% of the incorporated Bi found to be substitutional on the group V sublattice. The Bi incorporation is found to be proportional to the Bi flux. Room temperature absorption studies show band gap reduction of 32 meV/% as the Bi content of the GaSbBi alloys is increased.

References

[1] Y. Tominaga, Y. Kinoshita, K. Oe, M. Yoshimoto, Appl. Phys. Lett. 93 (2008) 131915.
[2] P.M. Asbeck, R.J. Welty, C.W. Tu, H.P. Xin, R.E. Welser, Semicond. Sci. Technol. 17 (2002) 898.
[3] B. Fluegel, S. Francoeur, A. Mascarenhas, S. Tixier, E.C. Young, T. Tiedje, Phys. Rev. Lett. 97 (2006) 067205.
[4] S. Francoeur, M.-J. Seong, A. Mascarenhas, S. Tixier, M. Adamcyk, T. Tiedje, Appl. Phys. Lett. 82 (2003) 3874.
[5] X. Lu, D.A. Beaton, R.B. Lewis, T. Tiedje, Y. Zhang, Appl. Phys. Lett. 95 (2009) 041903.
[6] M.J. Ashwin, D. Walker, P.A. Thomas, T.S. Jones, T.D. Veal, J. Appl. Phys. 113 (2013) 033502.
[7] J.J. Mudd, N.J. Kybert, W.M. Linhart, L. Buckle, T. Ashley, P.D.C. King, T.S. Jones, M.J. Ashwin, T.D. Veal, Appl. Phys. Lett. 103 (2013) 042110.
[8] P. Gladkov, E. Monova, J. Weber, J. Cryst. Growth 146 (1995) 319.
[9] A. Danilewsky, S. Lauer, J. Meinhardt, K. Benz, B. Kaufmann, R. Hofmann, A. Dornen, J. Electron. Mater. 25 (1996) 1082.
[10] Y. Song, W. Shumin, I.S. Roy, P. Shi, A. Hallen, J. Vac. Sci. Technol. B 30 (2012) 02B114.
[11] S.K. Das, T.D. Das, S. Dhar, M. de la Mare, A. Krier, Infrared Phys. Technol. 55 (2012) 156.
[12] X. Lu, D.A. Beaton, R.B. Lewis, T. Tiedje, M.B. Whitwick, Appl. Phys. Lett. 92 (2008) 192110.
[13] A.J. Ptak, R. France, D.A. Beaton, K. Alberi, J. Simon, A. Mascarenhas, C.-S. Jiang, J. Cryst. Growth 338 (2012) 107.
[14] G. Vardar, S.W. Paleg, M.V. Warren, M. Kang, S. Jeon, R.S. Goldman, Appl. Phys. Lett. 102 (2013) 042106.
[15] A. Duzik, J.M. Millunchick, J. Cryst. Growth 390 (2014) 5.
[16] M.K. Rajpalke, W.M. Linhart, M. Birkett, K.M. Yu, D.O. Scanlon, J. Buckeridge, T.S. Jones, M.J. Ashwin, T.D. Veal, Appl. Phys. Lett. 103 (2013) 142106.
[17] M.K. Rajpalke, W.M. Linhart, M. Birkett, K.M. Yu, J. Alaria, J. Kopaczek, R. Kudrawiec, T.S. Jones, M.J. Ashwin, T.D. Veal, J. Appl. Phys. 105 (2014) 112102.
[18] K. Alberi, J. Wu, W. Walukiewicz, K.M. Yu, O.D. Dubon, P.S. Watkins, C.X. Wang, X. Liu, Y.-J. Cho, J. Furdyna, Phys. Rev. B 75 (2007) 045203.
[19] J. Kopaczek, R. Kudrawiec, W.M. Linhart, M.K. Rajpalke, K.M. Yu, T.S. Jones, M.J. Ashwin, J. Misiewicz, T.D. Veal, Appl. Phys. Lett. 103 (2013) 261907.
[20] J. Kopaczek, R. Kudrawiec, W. Linhart, M. Rajpalke, T. Jones, M. Ashwin, T. Veal, Appl. Phys. Express 7 (2014) 111202.
[21] M.P. Polak, P. Scharoch, R. Kudrawiec, J. Kopaczek, M.J. Winiarski, W.M. Linhart, M.K. Rajpalke, K.M. Yu, T.S. Jones, M.J. Ashwin, T.D. Veal, J. Phys. D: Appl. Phys. 47 (2014) 355107.
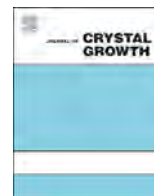
Bandedge optical properties of MBE grown GaAsBi films measured by photoluminescence and photothermal deflection spectroscopy

M. Beaudoin [a,*], R.B. Lewis [b,c], J.J. Andrews [a,d], V. Bahrami-Yekta [b], M. Masnadi-Shirazi [b,e], S.K. O'Leary [d], T. Tiedje [b]

[a] Advanced Materials and Process Engineering Laboratory (AMPEL), University of British Columbia, 2355 East Mall, Vancouver, B.C., Canada V6T 1Z4
[b] Department of Electrical and Computer Engineering, University of Victoria, P.O. Box 1700 STN CSC, Victoria, B.C., Canada V8W 2Y2
[c] Department of Physics and Astronomy, University of British Columbia, 6224 Agricultural Road, Vancouver, B.C., Canada V6T 1Z1
[d] School of Engineering, The University of British Columbia, 3333 University Way, Kelowna, B.C., Canada V1V 1V7
[e] Department of Electrical and Computer Engineering, University of British Columbia, 5500 – 2332 Main Mall, Vancouver, B.C., Canada V6T 1Z4

ARTICLE INFO

ABSTRACT

The bandedge optical properties of GaAsBi films, as thick as 470 nm, with Bi content varying from 0.7% Bi to 2.8% Bi grown by molecular beam epitaxy on GaAs substrates are measured by photoluminescence (PL) and photothermal deflection spectroscopy (PDS). The PDS spectra were fit with a modified Fernelius model which takes into account multiple reflections within the GaAsBi layer and GaAs substrate. Three undoped samples and two samples that are degenerately doped with silicon are studied. The undoped samples show a clear Urbach absorption edge with a composition dependent bandgap that decreases by 56 meV/% Bi and a composition independent Urbach slope parameter of 25 meV due to absorption by Bi cluster states near the valence band. The doped samples show a long absorption tail possibly due to absorption by gap states and free carriers in addition to a Burstein–Moss bandgap shift. PL of the undoped samples shows a lower energy emission peak due to defects not observed in the usually available thin samples (50 nm or less) grown under similar conditions.

© 2015 Elsevier B.V. All rights reserved.

1. Introduction

The dilute bismide semiconductor GaAsBi, grown epitaxially on GaAs substrates, is a promising III–V semiconductor alloy for applications in the 1.3–1.55 μm wavelength range [1,2]. GaAsBi has a large spin–orbit splitting which makes it an interesting candidate for spintronic devices [3]. The large spin orbit splitting may also help suppress Auger recombination processes involving the spin split-off hole band for alloys with high Bi concentrations [4]. The bandgap reduction in GaAsBi alloys varies from 44 to 88 meV/% Bi [1,5–7], with the composition dependence declining with increasing Bi content. Emission of light in crystalline semiconductors depends on the continuum states near the bandgap and in the case of disordered semiconductors on the localized states below the bandgap due to the presence of structural disorder [8,9]. Recently, Gogineni et al. used photoluminescence (PL) spectroscopy to study the tail states emission of GaAsBi quantum wells over the 10–300 K temperature range [10]. They found that the Urbach tail had two characteristic energies: the low energy part of the Urbach tail is temperature independent with a

characteristic energy of 29 meV while the part of the Urbach tail nearer to the bandgap is temperature dependent with characteristic energy of 17–29 meV [10]. Broadening of the main bandgap and spin–orbit transition has also been observed by Kudrawiec et al. using modulation spectroscopy [11] and was explained in the context of Bi-induced changes in the valence band and localized states inside the energy gap of GaAsBi.

In this paper, we use the mirage effect photodeflection spectroscopy (PDS) technique to measure the absorption of GaAsBi thick films (up to 470 nm) grown by solid source molecular beam epitaxy (MBE) with Bi concentrations up to 2.8% and compare the results with the photoluminescence (PL) spectra. We extracted GaAsBi absorption bandedge parameters by modifying the Fernelius [12] extension to the Rosencwaig–Gersho [13] PDS model to account for multiple reflections [14] in the sample as was used previously to measure the bandedge of GaAsN films [15]. Photothermal deflection spectroscopy [16] is a powerful technique for the investigation of low absorptions in thin films. PDS holds several advantages over transmission measurements, the method most commonly used to measure absorption. A major limitation of transmission is that it cannot distinguish between light absorption and scattering effects. PDS is relatively insensitive to scattering since only the absorbed light produces thermal effects. PDS is also sensitive to weak absorptions and was shown to reliably detect

an absorbance of $\sim 10^{-5}$ as opposed to $\sim 10^{-2}$ commonly demonstrated for transmission techniques [16,17]. Since the PDS signal depends on the thermal as well as the optical properties of the samples, extraction of the optical absorption coefficient requires modeling [12–15].

2. Experiment

Three (3) nominally undoped GaAsBi films and two Si-doped GaAsBi films, ranging from 230 nm to 470 nm in thickness, were grown on 350 μm thick rough backside semi-insulating GaAs(001) substrates in a VG-V80H MBE reactor as described by Lewis et al [18]. During operation, the MBE shroud was cooled to approximately −80 °C with a polysiloxane heat transfer fluid (instead of conventional liquid nitrogen cooling) [19]. Ga type effusion cells were used for Ga and Bi and a valved As cracker was used for As$_2$. The GaAs buffer layers were grown at substrate temperatures between 550 °C and 575 °C as measured by diffuse reflectance spectroscopy (DRS) [20], with As$_2$:Ga beam equivalent pressure ratio (BEPR) between 7 and 12 and a growth rate of 1 μm/h. To grow the GaAsBi layers, the As$_2$:Ga BEPR is reduced between 2.5 and 3.2 (atomic flux ratio between 1.1 and 1.4) while the growth temperature is decreased to 330 °C. A Bi flux (BEP between 1×10^{-8} Torr and 5×10^{-8} Torr) is added while maintaining a growth rate of 1 μm/h. A Si flux from a standard solid source Si effusion cell was present during the growth of the two doped GaAsBi layers, resulting in Si concentrations of 3×10^{18} cm^{-3} and 1×10^{19} cm^{-3}. Hall measurements gave free carrier concentrations of 1×10^{18} cm^{-3} and 3×10^{18} cm^{-3}, indicating high concentrations of compensating acceptors in the samples.
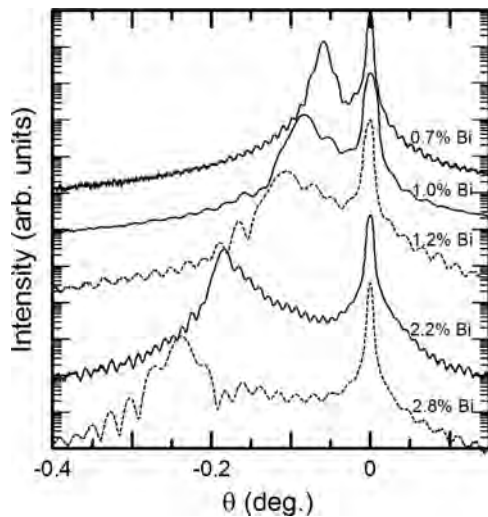
High resolution x-ray diffraction (HRXRD) (004) θ–2θ scans of the GaAsBi/GaAs samples, collected with a Bruker D8 Discover system, are shown in Fig. 1. The Bi contents and layer thicknesses, reported in Table 1, were obtained by dynamically simulating the (004) HRXRD scans assuming uniform pseudomorphic GaAsBi layers and Vegard's law with a GaBi lattice constant of 6.33 Å extrapolated from Rutherford backscattering spectrometry measurements [6]. The scans show clear Pendellösung fringes, suggesting abrupt interfaces, and the simulations gave good agreement with the data. For the doped samples, the effect of Si incorporation on the GaAsBi lattice constant is negligible compared to the effect of Bi. In addition to symmetric (004) HRXRD scans, asymmetric reflection reciprocal lattice maps (RLM) were collected in a different lab using a Philips X'Pert Pro MRD system equipped with a triple axis crystal. Fig. 2 shows the RLM for one of the undoped samples, with 2.2% Bi, and one of the doped sample with 2.8% Bi. The asymmetric scans were optimized along one of the (011) directions and a second RLM was collected for the same sample along the other (011) direction by rotating the sample by 90°. The layer peaks line up along the $\mathbf{k}_\parallel$ direction, indicative of negligible relaxation in the films. (004) Symmetric scans performed on the Philips diffractometer gave results identical to those obtained on the Bruker machine.

Photoluminescence from the undoped samples was excited at room temperature with a 532 nm frequency-doubled Nd:YLF laser with 20 ns long pulses at a 2 kHz repetition rate, having an average power of 2.6 mW. The spectra were collected in the wavelength range 700–1300 nm with an optical spectrometer equipped with a liquid nitrogen cooled InGaAs array detector. Spectra were corrected for the throughput of the optical system.

The optical absorption of the series of samples was measured using PDS in the spectral range 1100–700 nm in 2 nm steps. In mirage effect PDS, a modulated monochromatic light source at normal incidence to the sample is used as a pump. When the pump beam is absorbed, it creates a periodic heating of the sample which causes a temperature

Fig. 1. (004) θ–2θ HRXRD scans of the undoped (solid lines) and doped (broken lines) GaAsBi/GaAs samples. The compositions and thicknesses of the GaAsBi layers are obtained by dynamically simulating the (004) scans. Scans are offset for clarity.
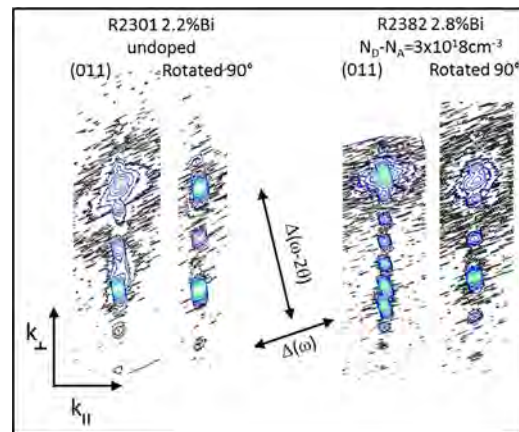
Fig. 2. Asymetric (115) reciprocal lattice maps (RLM) for sample R2301 (undoped, 2.2% Bi) and R2382 (doped, 2.8% Bi). The RLMs are collected along both (011) directions. The RLMs show that the films grow coherently on the GaAs substrates.

Table 1
Summary of sample properties and PL and PDS results for the GaAsBi films.

Sample #	x (% Bi)	N_D–N_A(cm^{-3})	Thickness (nm)	PL (eV)		From PDS fits	
				Bandedge	Defects	$E_g \pm 0.004$ (eV)	$E_0 |^{-2}_{+5}$ (meV)
r2358	0.7	–	470	1.38	1.20	1.384	27
r2300	1.0	–	240	1.36	1.21	1.364	26
r2301	2.2	–	450	1.28	1.17	1.305	25
r2372	1.2	1×10^{18}	230			1.38	25
r2382	2.8	3×10^{18}	230	–	–	1.33	70

gradient $d\Theta/dx$, in the medium immediately in front of the sample. By choosing a medium whose refractive index depends on temperature, $dn/d\Theta$, a modulated refractive index gradient is induced near the sample surface. A laser probe beam passing through this refractive index gradient, grazing the surface of the sample, will be deflected by its lensing effect with an angle, ϕ, that depends on the absorption of the sample. Our PDS setup uses a quartz tungsten–halogen lamp (150 W), a 0.5 m f/4 monochromator, a CCl_4 thermal deflection medium and a position sensitive detector (UDT®) with a home built preamplifier whose output is fed into a lock-in amplifier. All data presented here has been collected at a chopper frequency of 18 Hz. In PDS, since the signal depends on the thermal response in addition to optical response [12,13], higher frequencies yield information closer to the sample surface while lower frequencies yield information deeper inside the sample. In practical terms, higher frequencies tend to improve the PDS signal to noise ratio while reducing the absolute magnitude of the signal (for 18 Hz used in our experiments, the signal comes from the entire sample thickness including the substrate). The probe beam is sourced from a 4 mW, 632 nm laser diode focused to a waist size of less than 15 μm in front of the sample. Samples for PDS were cleaved into pieces about 1 mm wide (the PDS interaction length) by 8 mm long. The data was collected using LABVIEW® software. Normalization is achieved by dividing the raw PDS spectra with a PDS spectrum collected from a 1 mm wide sample of graphite paint on glass. Each spectrum is then normalized to its saturation value.

3. Results and analysis

Fig. 3 shows PL emission from the undoped GaAsBi layers. The higher energy peak in each spectrum corresponds to the band edge emission and the lower energy peak is believed to correspond to emission from localized states. The energies of the PL emission edge are reported in Table 1; it should be noted that the position of this edge is only an approximate measure of the bandgap. The 1.0% Bi film band edge emission appears as a doublet, possibly due to slight composition non-uniformity within the film: we reported the higher intensity (lower energy) peak in Table 1. It should be noted that the localized states emission is not generally observed in thin GaAsBi samples (typically less than 50 nm thick) grown under the same conditions. It is reasonable to observe such emission in thick samples even if it is absent from thin samples. In thin samples, the electron–hole pairs have a reduced diffusion length, making it more difficult for carriers to find the isolated deep levels.

Fig. 4 shows the normalized PDS spectra for the undoped samples in this study; the spectra are plotted on a log scale and
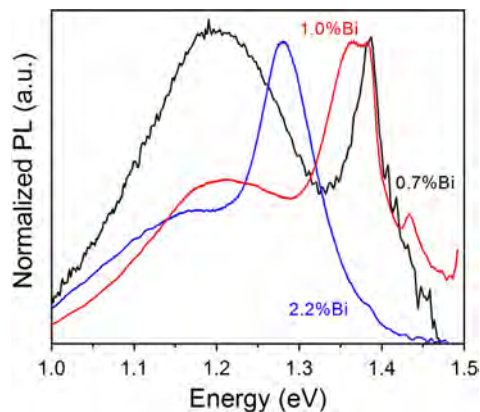
Fig. 3. Room temperature PL spectra of the undoped GaAsBi/GaAs samples. Note a high energy peak associated with GaAsBi bandedge absorption and a low energy peak due to localized states.
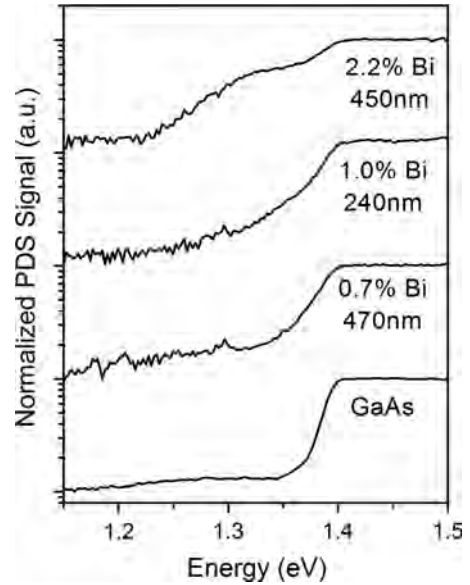
Fig. 4. PDS spectra of the undoped GaAsBi films showing clear low energy absorption due to GaAsBi overlayed on the GaAs background absorption. GaAs PDS is shown for comparison. The spectra are shown on a log scale and shifted for clarity.

shifted for clarity. The PDS spectrum from a semi-insulating GaAs substrate is also shown on the same figure for comparison. The GaAsBi PDS spectra show a low energy shoulder, from the GaAsBi absorption, superimposed on a higher energy spectrum due to the GaAs substrate absorption. The onset of the low energy shoulder is indicative of the GaAsBi bandgap while its steepness depends on the sharpness of the absorption edge.

To extract the substrate and film absorption, we fit the normalized PDS spectra using the Fernelius [12] extension to the Rosencwaig–Gersho [13] one dimensional (1D) model theory, which includes the effect of a thin absorbing film on an absorbing substrate as adapted by Chan and Beaudoin [14,15] to account for multiple reflections within the film and substrate. The full details of this model can be found in reference [14] The GaAs substrate and the GaAsBi film absorption coefficients, α_S and α_C respectively, are modeled with the Urbach expression

$$\alpha_{s,c}(h\nu) = \begin{cases} \alpha_d(h\nu) + \alpha_0 \exp\left(\frac{h\nu - E_g}{E_0}\right); & h\nu \le E_g \\ \alpha_d(h\nu) + \alpha_0 + A_0(h\nu - E_g); & h\nu > E_g \end{cases} \quad (1)$$

where $h\nu$ is the photon energy, the exponential term represents the Urbach edge absorption, E_g the optical bandgap and E_0 the Urbach parameter, are the quantities we extract from the fit. The values for E_g and E_0 for GaAs are taken from Beaudoin et al. [8] while the bandgap absorption coefficient $\alpha_0 = 8000$ cm^{-1} and the above bandgap slope $A_0 = 56,300$ cm^{-1} eV^{-1} are taken from Sturge [21]. We found that below the Urbach edge, the best fit to our PDS data for the GaAs substrate was obtained with $\alpha_d(h\nu) = (11.1 - 9.1/h\nu)$ cm^{-1}; although this is not a physical fit, it does agree very well with other published PDS data for GaAs [22] and is valid for the energy range over which we are probing ($h\nu > 1.13$ eV; $\lambda < 1100$ nm). These GaAs model parameters were kept constant in all fits to the GaAsBi thin films; we set $\alpha_d(h\nu) = 0$ for the GaAsBi subgap absorption because it does not contribute significantly to the PDS signal since the substrate absorption dominates at those energies. More details on the fitting procedure can be found in reference [15].

Fig. 5 shows a typical fit (red line) of the model to data (open blue circles) for the undoped samples. The extracted E_g and E_0 values and their estimated uncertainties are reported in Table 1.
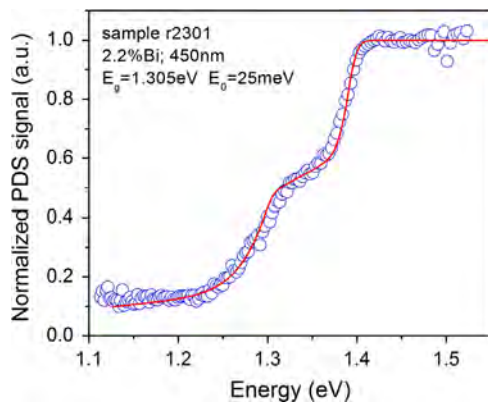
Fig. 5. Typical PDS fit, red line, to the data sample r2301 (2.2% Bi and 450 nm thick). (For interpretation of the references to color in this figure legend, the reader is referred to the web version of this article.)

Fig. 6. Bandgap of the undoped GaAsBi samples deduced from PL (●) and the undoped (■) and doped (♦) samples deduced form PDS. The lines are linear least squares fits to the data with the 0% Bi intercept fixed at the GaAs value. The 56 meV/% Bi bandgap reduction extracted from PDS closely matches the DFT predictions of the Janotti [25] model.

The MATLAB cftool function returned uncertainties of ± 4 meV for E_g and ± 5 meV for E_0. By doing simulations instead of fits and visually comparing the results with the PDS spectra, we believe these uncertainties are quite representative of the E_g error while the error bars for E_0 are different: uncertainty is -2 meV lower or $+5$ meV higher than the values reported in Table 1. For the 3 undoped samples, simulations with E_0 ranging from -2 meV to $+5$ meV difference from the values reported in Table 1 still gave acceptable fits. The Urbach parameter is, within fitting uncertainty, constant at ~25 meV. This value is consistent with the results of Gogineni et al. [10] on GaAsBi quantum wells and is higher than the E_0 values of dilute nitride (GaAsN) which were found to be ~18 meV in the previous studies [15]. This E_0 value can possibly be explained by the presence of Bi clusters states near the valence band. Clusters of Bi atoms will form randomly and Bi nano-clustering has been demonstrated by Z-contrast imaging [23]. Bi clustering effects have also been evidenced by the Monte-Carlo simulation work of Imhof et al. on the temperature depencence of photoluminescence in 30 nm thick GaAsBi films [24]. Since there is no reason to expect these states to have a well defined energy, broadening into an exponential distribution depending on the local density is reasonable.

Fig. 6 shows the PL and PDS deduced bandgaps as a function of Bi concentration in the films along with linear least squares fits where the 0% Bi intercept is fixed at the GaAs value. For the undoped samples, fitting the PL data yields a bandgap reduction of 66 meV/% Bi while the fit to the PDS data gives a bandgap reduction of 56 meV/% Bi. While both are within the reported bandgap variations for this material system [1,5–7], we note that the absorption (PDS) deduced bandgap is at a higher energy than the PL emission. This is consistent with previous studies, for example our own on GaAsN films [15] and is expected since PL emission takes place below the gap in the tail states.

Janotti et al. [25]. performed theoretical calculations of GaAs(N)(Bi) alloys using the density functional theory (DFT) [25,26], and predict a quadratic dependence (bowing) of the bandgap on Bi composition. For Bi compositions below 3% Bi, their model is well approximated with a linear reduction of 50 meV/% Bi; this is very close to the bandgap we determine here from PDS. While a similar offset between PL and PDS gaps, where PL emission is at a lower energy, have also been observed in the past for low N content GaAsN epitaxial films [15], the effect for the GaAsBi samples shown here is more pronounced, especially for the 2.2% Bi film.

Fig. 7 shows the PDS spectrum of the Si doped sample with 2.8% Bi (r2382). The spectrum is broad with a long low energy tail; this spectrum can be well fit by assuming a film with an
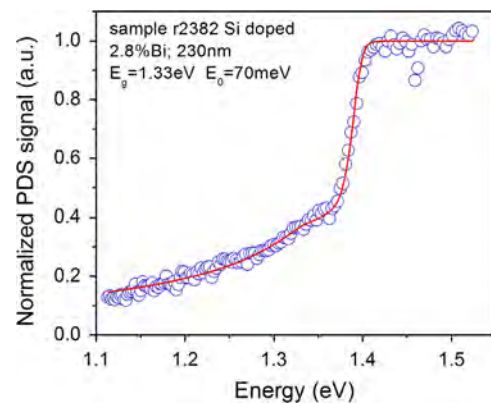
Fig. 7. PDS fit, red line, to the doped $GaAs_{0.972}Bi_{0.028}$ sample (r2382). The modeled fit with $E_g = 1.33$ eV and $E_0 = 70$ meV is indicative of absorption by filled acceptor-like states below the bandgap, which do not absorb in undoped materials. The higher than expected E_g is due to the Burstein–Moss shift. (For interpretation of the references to color in this figure legend, the reader is referred to the web version of this article.)

absorption profile in the form of Eq. (1) with a large Urbach tail of $E_0 = 70$ meV. The long low absorption tail is likely due to absorption by gap states. Since high Bi content samples are usually p-type [27], acceptor-like states are introduced by the Bi clustering. These states will absorb when the material is n-doped and will broaden E_0 in addition to the usually observed E_0 increase that is introduced by high doping in GaAs [28]. Sample r2372, with a carrier concentration of 1×10^{18} cm^{-3}, has a PDS spectrum not much different from that of pure GaAs; our best fit to the PDS gave $E_g = 1.38$ eV and $E_0 = 25$ meV. In this low range of Bi contents, Bi cluster densities are expected to increase as the Bi content raised to the power of the cluster size [29]. Therefore, the higher Bi-content in sample r2382 can result in much higher concentrations of localized states than for the other samples. For these doped samples, the PDS deduced bandgaps are larger than would be expected from the Bi concentrations in the films. At carrier densities above mid 10^{17} cm^{-3}, n-type GaAs becomes degenerate [30], hence, the larger absorption bandgap is likely due to the Burstein–Moss shift [31]. Hall effect measurements of these samples gave carrier concentrations of 1×10^{18} cm^{-3} and 3×10^{18} cm^{-3} carriers which yields a Burstein–Moss shift of up to 0.11 eV if one assumes the same effective masses as GaAs. Hence, the bandgap deduced from PDS for the doped samples is consistent with both a bandgap reduction from Bi incorporation and a

Burstein–Moss shift due to Si doping. These bandgaps are also shown in Fig. 6.

4. Conclusion

In conclusion, using PL and PDS, we have measured the room temperature bandedge optical properties of MBE grown GaAsBi films ranging from 230 nm to 470 nm in thickness. In addition to the edge emission, the PL spectra also have a lower energy emission peak that is not observed in thin samples (50 nm or less) grown under similar conditions. While both the PL edge emission and PDS deduced bandgap closely follow the reported gap reduction cited in the literature for GaAsBi, the bandgap extracted by PDS more closely follows the predictions from first principles DFT calculations of Janotti et al. [25]. While it is common for PL emission to be at lower energy than absorption deduced bandgaps, we find that for the films studied, this difference is larger than for other materials systems, such as GaAsN [15]. This result is consistent with GaAsBi having a larger Urbach parameter. For undoped GaAsBi samples a composition independent Urbach parameter E_0 value of 25 $(-2/+5)$ meV is found for our samples. We attribute this E_0 to absorption by localized Bi cluster states near the valence band. For degenerately Si-doped GaAsBi films, we find a smaller PDS deduced bandgap reduction consistent with a Burstein–Moss shift and a broad 70 meV exponential absorption tail possibly from filled acceptor-like states which do not absorb in undoped materials.

Acknowledgments

References

[1] T. Tiedje, E.C. Young, A. Mascarenhas, Int. J. Nanotechnol. 5 (2008) 963.
[2] Chris J. Hunter, Faebian Bastiman, Adbul R. Mohmad, Robert Richards, Jo Shien Ng, Stephen J. Sweeney, John P.R. David, IEEE Photonics Technol. Lett. 24 (2012) 2191.
[3] B. Fluegel, S. Francoeur, A. Mascarenhas, S. Tixier, T. Tiedje, E.C. Young, Phys. Rev. Lett. 97 (2006) 067205.
[4] M. Usman, C.A. Broderick, A. Lindsay, E.P. O'Reilly, Phys. Rev. B 84 (2011) 245202.
[5] O.E. Kunishige, Jpn. J. Appl. Phys. 41 (2002) 2801.
[6] S. Tixier, M. Adamcyk, T. Tiedje, S. Francoeur, A. Mascarenhas, Peng Wei, F. Schiettekatte, Appl. Phys. Lett. 82 (2003) 2245.
[7] Nebiha Ben Sedrine, Imed Moussa, Hedi Fitouri, Ahmed Rebey Belgacem El Jani, Radhouane Chtourou, Appl. Phys. Lett. 95 (2009) 0119110.
[8] M. Beaudoin, A.J.G. DeVries, S.R. Johnson, H. Laman, T. Tiedje, Appl. Phys. Lett. 70 (1997) 3540.
[9] G.D. Cody, in: J.I. Pankove (Ed.), Semiconductors and semimetals, vol. 21, Academic, Montréal, 1984 (Chapter 2).
[10] Chaturvedi Gogineni, Nathaniel A. Riordan, Shane R. Johnson, Xianfeng Lu, Tom Tiedje, Appl. Phys. Lett. 103 (2013) 041110.
[11] R. Kudrawiec, J. Kopaczek, P. Sitarek, J. Misiewicz, M. Henini, S.V. Novikov, J. Appl. Phys. 111 (2012) 066103.
[12] Nils C. Fernelius, J. Appl. Phys. 51 (1980) 650.
[13] A. Rosencwaig, A. Gersho, J. Appl. Phys. 47 (1976) 64.
[14] I.C.W. Chan, M. Beaudoin, J. Appl. Phys. 106 (2009) 103510.
[15] M. Beaudoin, I.C.W. Chan, D. Beaton, M. Elouneg-Jamroz, T. Tiedje, M. Whitwick, E.C. Young, J.F. Young, N. Zangenberg, J. Cryst. Growth 311 (2009) 1662.
[16] A.C. Boccara, D. Fournier, J. Badoz, Appl. Phys. Lett. 36 (1980) 130.
[17] J.I. Pankove, Semiconductors and Semimetals, vol. 21, Academic Press, Montréal, 1984.
[18] R.B. Lewis, M. Masnadi-Shirazi, T. Tiedje, Appl. Phys. Lett. 101 (2012) 082112.
[19] R.B. Lewis, V. Bahrami-Yekta, M.J. Patel, T. Tiedje, M. Masnadi-Shirazi, J. Vac. Sci. Technol. B 32 (2014) 02C102.
[20] M.K. Weilmeier, K.M. Colbow, T. Tiedje, T. Van Buuren, L. Xu, Can. J. Phys. 69 (1991) 422.
[21] M.D. Sturge, Phys. Rev. 127 (1962) 768.
[22] U. Zammit, F. Gasparrini, M. Marinelli, R. Pizzoferrato, F. Scudieri, S. Martellucci, Appl. Phys. A 52 (1991) 112.
[23] D.L. Sales, E. Guerrero, J.F. Rodrigo, P.L. Galindo, A. Yáñez, M. Shafi, A. Khatab, R.H. Mari, M. Henini, S. Novikov, M.F. Ghisholm, S.I. Molina, Appl. Phys. Lett. 98 (2011) 101902.
[24] Sebastian Imhof, Angela Thränhardt, Alexej Chernikov, Martin Koch, Niko S. Köster, Kolja Kolata, Sangam Chatterjee, Stephan W. Koch, Xianfeng Lu, Shane R. Johnson, Dan A. Beaton, Thomas Tiedje, Oleg Rubel, Appl. Phys. Lett. 96 (2010) 131115.
[25] A. Janotti, Su-Huai Wei, S.B. Zhang, Phys. Rev. B 65 (2002) 115203.
[26] P. Hohenberg, W. Kohn, Phys. Rev. 136 (1964) B864;
W. Kohn, L.J. Sham, Phys. Rev. 140 (1965) A1133.
[27] K. Bertulis, A. Krotkus, G. Aleksejenko, V. Pačebutas, R. Adomavičius, G. Molis, S. Marcinkevičius, Appl. Phys. Lett. 88 (2006) 201112.
[28] H.C. Casey Jr., Frank Stern, J. Appl. Phys. 47 (1976) 631.
[29] M.M. Kreitman, D.L. Barnett, J. Chem. Phys. 43 (1965) 364.
[30] Henry Mathieu, Physique des semiconducteurs et des composants électroniques, Masson, Paris (1987) 62.
[31] T.S. Moss, Proc. Phys. Soc. Lond.B 76 (1954) 775;
E. Burstein, Phys. Rev. 93 (1954) 632.

CrossMark
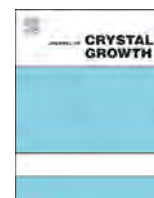
Investigation of MBE-grown InAs$_{1-x}$Bi$_x$ alloys and Bi-mediated type-II superlattices by transmission electron microscopy

Jing Lu [a,b,*], P.T. Webster [a,c], S. Liu [a,c], Y.-H. Zhang [a,c], S.R. Johnson [a,c], David J. Smith [a,d]

[a] Center for Photonics Innovation, Arizona State University, Tempe, AZ, USA
[b] School for Engineering of Matter, Transport and Energy, Arizona State University, Tempe, AZ, USA
[c] School of Electrical, Computer and Energy Engineering, Arizona State University, Tempe, AZ, USA
[d] Department of Physics, Arizona State University, Tempe, AZ 85287, USA

ARTICLE INFO

ABSTRACT

The microstructure of InAs$_{1-x}$Bi$_x$ ($x\sim4.5\%$ and $\sim5.8\%$) films and Bi-mediated InAs/InAs$_{1-x}$Sb$_x$ type-II superlattices grown by molecular beam epitaxy on GaSb (0 0 1) substrates has been investigated by electron microscopy techniques. Lateral compositional modulation exists in both smooth and hazy regions of all InAsBi films observed but no atomic ordering is apparent using current imaging projections. Surface droplets present in hazy regions assume a zincblende crystalline structure that is usually tilted relative to the underlying dilute bismide film. Study of Bi-mediated InAs/InAs$_{0.81}$Sb$_{0.19}$ type-II superlattices indicates that the InAs-on-InAsSb interface still appears broadened relative to the InAsSb-on-InAs interface.

© 2015 Elsevier B.V. All rights reserved.

1. Introduction

III-V-Bi alloys have potential applications in uncooled long-wavelength infrared photo-detectors and lasers due to their large bandgap reduction and relatively temperature-insensitive band gap, and the synthesis of dilute bismides has been actively pursued with different growth techniques to take advantage of such properties [1–4]. Despite the great promise that the dilute bismides hold, the successful growth of such thin films is very challenging and suffers from a large miscibility gap because the alloys are formed through isoelectronic substitution of group-V elements with very different atomic size. Microstructural studies done on epitaxial GaAs$_{1-x}$Bi$_x$ films grown by molecular beam epitaxy (MBE) have shown that the film morphology departs from homogeneity in several ways, including phase separation [5], atomic ordering [5,6] and surface-droplet formation [7], despite all the efforts directed towards optimizing the growth. In comparison, the growth of InAs$_{1-x}$Bi$_x$ alloys by MBE has only recently been established [8–10], and there is a need for detailed microstructural study of such alloys.

An alternative design for long-wavelength infrared photo-detection is the strain-balanced type-II superlattice (T2SL) system [11], where bandgap engineering can be achieved by varying the superlattice period (layer thickness/composition) and coherent interfacial strain.

Recent progress has been made in the design, growth and characterization of Ga-free InAs/InAs$_{1-x}$Sb$_x$ T2SL with very high structural quality, and the SL interface abruptness seems to play a significant role in affecting the emission properties [12–14]. Growth front coverage with surfactants of at most a few monolayer thickness has been used in MBE to help improve the surface/interface morphology and material properties. For example, Sb was used as a non-reactive surfactant for the growth of AlGaAs, and the surface morphology was improved at all growth temperatures investigated [15]. It continues to be of interest to investigate the effectiveness of surfactants on interface roughness.

In this study, the microstructures of 1-µm InAs$_{1-x}$Bi$_x$ films and bismuth-mediated InAs/InAs$_{1-x}$Sb$_x$ type-II superlattices grown on GaSb (0 0 1) substrates were investigated by transmission electron microscopy (TEM). Incorporation of bismuth into the InAs$_{1-x}$Bi$_x$ films was studied with different imaging techniques, while the emphasis for the T2SL studies was on characterization of the interface abruptness and thus the possible beneficial effect of the Bi surfactant.

2. Experimental details

All samples were grown on (0 0 1) GaSb substrates using a VG-V80H solid source MBE system. The two InAs$_{1-x}$Bi$_x$ samples ($x\sim4.5\%$ and $\sim5.8\%$) investigated here were grown at a substrate temperature of 280 °C with different V/III flux ratios. As shown by the schematic in Fig. 1(a), after growth of the 600-nm-thick GaSb

buffer, a 15-nm InAs spacer layer was grown, followed by a 1-μm InAs$_{1-x}$Bi$_x$ film and a 10-nm InAs capping layer. The T2SL sample studied consisted of 56.5 periods of 8-nm InAs$_{1-x}$Sb$_x$ ($x=19\%$) and 9-nm InAs layers, as indicated in Fig. 1(b), and was grown at a substrate temperature of 430 °C. The Bi flux (Bi/In flux ratio$=3\%$) was switched on during growth of the last 40 nm of the GaSb buffer layer, and was kept on throughout the growth of the entire super-lattice structure as well as the 100-nm GaSb capping layer. Additional growth details are provided elsewhere [10].

TEM samples were prepared for cross-section observation along $\langle 1\,1\,0 \rangle$-type projections using standard mechanical polishing and dimple grinding, followed by argon-ion-milling (maximum beam energy 2.3 keV) under liquid-nitrogen cooling in order to reduce the ion-beam damage [16]. Electron microscopy was performed using a JEOL JEM-4000EX high-resolution electron microscope with an accelerating voltage of 400 kV and structural resolution of 1.7 Å. Geometric phase analysis (GPA) to extract information about interfacial strain [17] was applied to the high-resolution electron micrographs using a Digital Micrograph script [18].

3. Results and discussion

3.1. InAs$_{1-x}$Bi$_x$ alloys

All surfaces of the InAs$_{1-x}$Bi$_x$ films had smooth droplet-free regions and hazy droplet-forming regions [10], and measurements using X-ray diffraction (XRD) indicated less Bi incorporation in InAs$_{1-x}$Bi$_x$ films under the hazy regions. Moreover, broadened X-ray peaks were observed for the droplet-free regions, suggesting non-uniform composition [10]. Reciprocal space maps in the vicinity of the (1 1 5) reflection indicate that the InAsBi layers are pseudomorphically strained to the GaSb substrate.

The first sample studied by TEM had a maximum Bi incorporation of 5.8% as measured by (0 0 4) $\omega - 2\theta$ high-resolution XRD scan, assuming a theoretical lattice-constant calculation for InBi. A TEM sample was prepared from the droplet-free region. As indicated by the bright-field image in Fig. 2(a), very few structural defects were visible over wide lateral distances. Selected-area electron diffraction patterns, as shown by the inset, gave no indication of atomic ordering along this viewing projection. Diffraction-contrast images such as Fig. 2(b) gave enhanced contrast due to differences in mass/thickness: The vertical stripe features visible in this micrograph thus indicate the occurrence of lateral compositional modulation on the scale of several tens of nanometers.

High-resolution electron micrographs to investigate the interfacial coherence were taken close to the substrate, and near the top, of the InAs$_{1-x}$Bi$_x$ films, as shown in Figs. 3(a) and 4(a), respectively. These lattice-fringe images showed the excellent crystallinity of the film. The
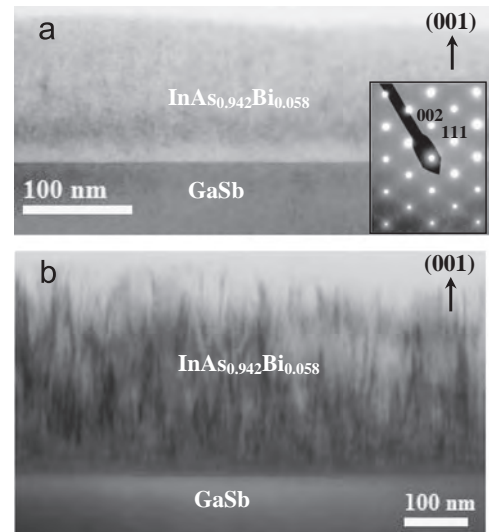
Fig. 2. (a) Bright-field TEM image of InAs$_{0.942}$Bi$_{0.058}$ alloy sample and the corresponding selected-area electron diffraction pattern (inset); (b) diffraction contrast image showing vertical stripe features, indicating lateral compositional modulation.

technique of geometric phase analysis can then be used to extract both in-plane and out-of-plane strain across the epitaxial layers, where the out-of-plane strain (in the $\langle 0\,0\,1 \rangle$ growth direction) due to the tetragonal distortion of the alloy lattice is defined by the expression:

$$\xi_{zz} = \frac{c_{\text{alloy}} - c_{\text{reference}}}{c_{\text{reference}}} \tag{1}$$

In Eq. (1), c is the lattice parameter along the growth direction.

The in-plane strain (not shown) extracted from both images was negligible, as expected. For the out-of-plane strain analysis of the lattice-fringe image recorded close to the substrate, the unstrained GaSb buffer layer was used as the reference in Eq. (1). The InAs spacer under tensile strain was readily identifiable in the strain map obtained and in the averaged line profile (averaged perpendicular to the growth direction). Bi started incorporating into the InAs$_{1-x}$Bi$_x$ layer shortly after, if not immediately after, growth of the InAs spacer layer, as evident from the reduced tensile strain in the InAs$_{1-x}$Bi$_x$ layer compared with that in the InAs spacer. Bi incorporation increased the lattice spacing in the InAs$_{1-x}$Bi$_x$ film, which is similar to the lattice expansion observed in GaAsBi [19], but contrary to the cases of lattice contraction in GaSbBi or InSbBi [20]. Thus, its lattice mismatch is reduced with respect to the unstrained GaSb buffer. However, insufficient Bi was incorporated to achieve exact lattice match so that the InAs$_{1-x}$Bi$_x$ layer remained under slight tensile strain.

Fig. 4(a) shows the excellent crystallinity near the top surface, and the coherent interface between the InAs$_{1-x}$Bi$_x$ film and the InAs capping layer. Again GPA analysis brings out the strain information embedded in high-resolution micrographs and the out-of-plane strain map obtained is shown in Fig. 4(b). In this case, the InAs capping layer was used as the reference. Thus, the InAs$_{1-x}$Bi$_x$ was under compressive strain as shown by the positive strain value in the averaged line profile (Fig. 4(c)). A qualitative comparison of the averaged out-of-plane strain in the InAs$_{1-x}$Bi$_x$ film close to the cap in Fig. 4(c) and close to the substrate (Fig. 4(d), obtained from further GPA analysis of Fig. 3(a) but using InAs as the reference) shows that the strain difference of the InAs cap and the top region of the InAs$_{1-x}$Bi$_x$ film is less than that of the InAs spacer and the bottom region of the InAs$_{1-x}$Bi$_x$ film, indicating that less Bi was incorporated close to the top of the InAs$_{1-x}$Bi$_x$ film.

The second sample investigated by TEM had a maximum Bi incorporation of 4.5%, as determined from the (0 0 4) $\omega - 2\theta$ high-
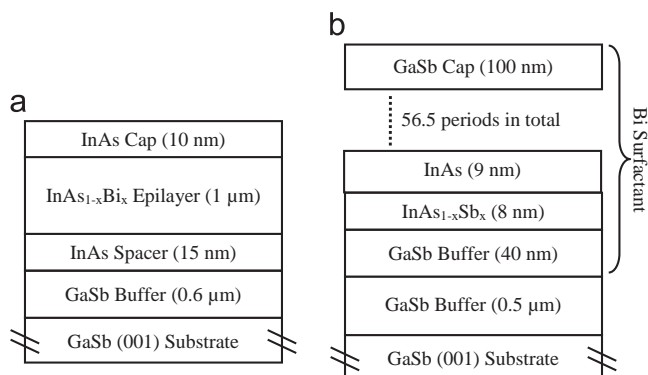
Fig. 1. Schematic illustration of samples studied: (a) InAs$_{1-x}$Bi$_x$ alloys and (b) Bi-mediated InAs/InAs$_{1-x}$Sb$_x$ T2SLs.
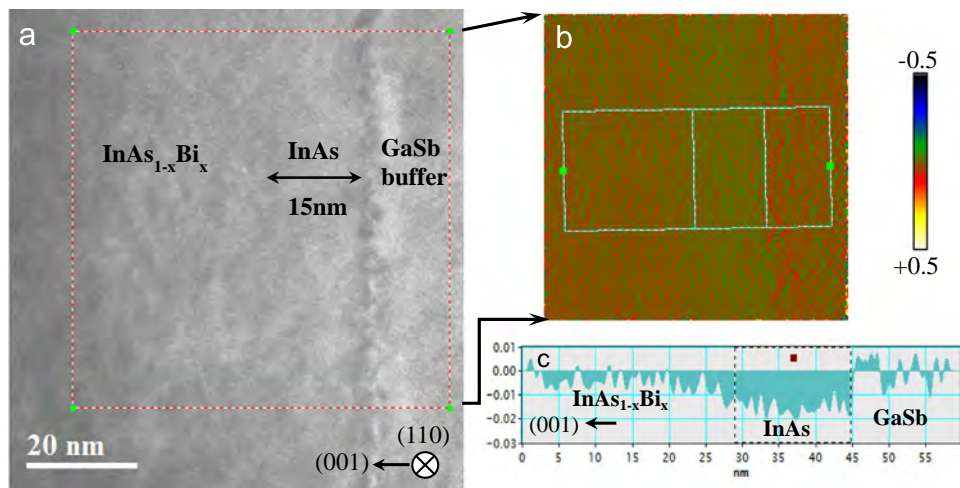
Fig. 3. (a) High-resolution image of $InAs_{0.942}Bi_{0.058}$ sample showing region close to the GaSb buffer, (b) corresponding out-of-plane strain map, and (c) average strain line profile.
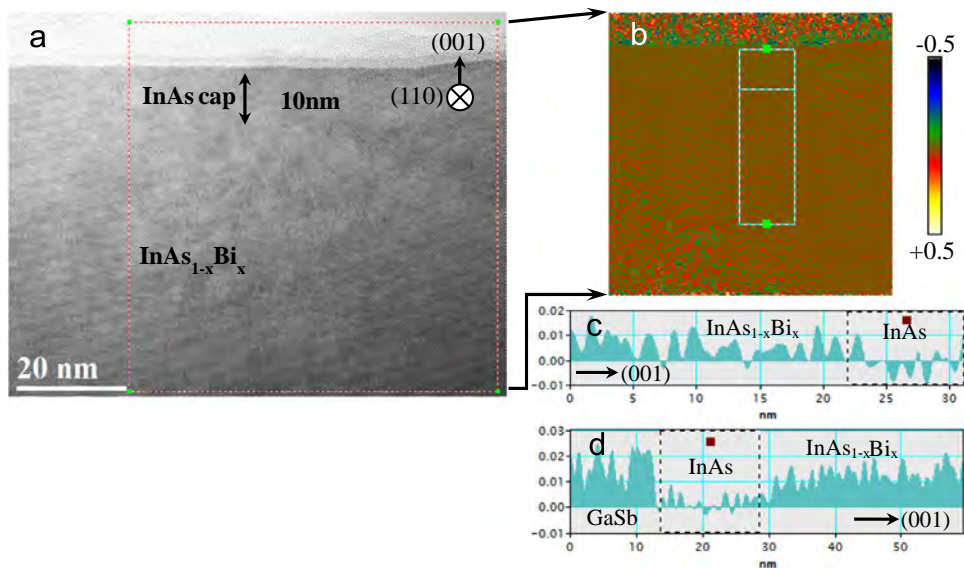
Fig. 4. (a) High-resolution image of $InAs_{0.942}Bi_{0.058}$ sample showing region close to the top InAs capping layer, (b) corresponding out-of-plane strain map, (c) average strain line profile, and (d) the average out-of-plane strain line profile obtained from further GPA analysis of Fig. 3 (a) using InAs as the reference.
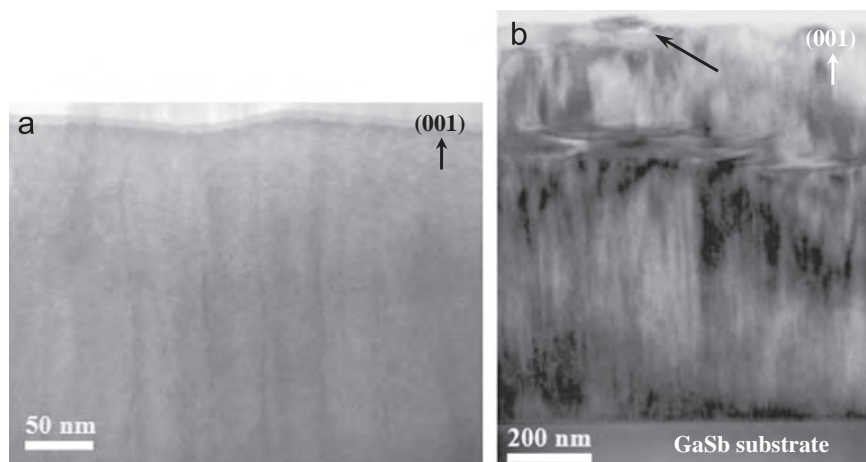
Fig. 5. (a) Bright-field TEM image of $InAs_{0.955}Bi_{0.045}$ sample, and (b) diffraction contrast image showed vertical stripe features, indicating lateral compositional modulation. Horizontal growth defects also visible.

resolution XRD scan. In this case, the TEM sample was prepared from the droplet-forming region. The bright-field image in Fig. 5(a) shows vertical stripe features similar to Fig. 2(b), as well as surface droplets at the surface (example arrowed in Fig. 5(b)). No apparent atomic ordering was visible, although horizontal growth defects were sometime observed—see the example in Fig. 5(b).

The lattice-fringe image of a representative surface droplet, which is about 100 nm in length and 40 nm in maximum height is shown in Fig. 6(a). Twinning and V-shaped surface grooves ((1 1 1) surface faceting) were observed in the droplet. Fast-Fourier-transform analysis was performed from regions of the capping layer (Fig. 6(b)) and the droplet (Fig. 6(c)), respectively, and the measured spacings of different lattice planes and angles were labelled. Judging from the length ratio and the angle between diffraction vectors in the diffractogram, the surface droplet has adopted a distorted zincblende structure, with a lattice constant in the range of 0.64–0.67 nm and an $\sim 80°$ tilt away from the matrix. EDX analysis performed on various droplet positions indicates that the droplet consists predominantly of Bi. In comparison, Bi-rich zincblende Ga(As, Bi) clusters and rhombohedral Bi clusters were reported for GaAsBi after annealing [21], and InBi clusters with distorted PbO structure were reported in InAsBi [22]. Such phase separation is attributed to the difficulties associated with Bi incorporation.

3.2. Bi-mediated InAs/InAs$_{1-x}$Sb$_x$ type-II superlattices

The low-magnification bright-field images of the whole InAs/InAs$_{0.81}$Sb$_{0.19}$ superlattice stack, such as the examples shown in Fig. 7 where the bottom half and top half of the T2SL were captured, indicated no extended structural defects over wide lateral distances. The averaged intensity line profile of the higher magnification bright-field image shown in Fig. 8(a) was extracted in order to study the interface abruptness and the effect of the Bi surfactant. The valleys shown in Fig. 8(b) correspond to InAs layers while the peaks correspond to the InAsSb layers. The gradual intensity drop at the interface of InAs-on-InAsSb compared to the interface of InAsSb-on-
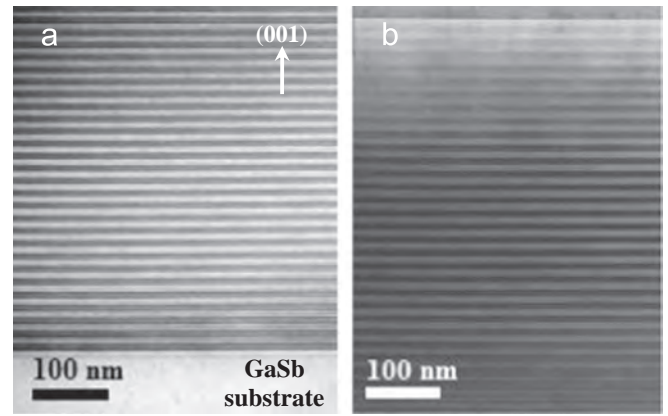
Fig. 7. (a) Bright-field images of Bi-mediated InAs/InAs$_{0.81}$Sb$_{0.19}$ T2SL showing: (a) bottom half, and (b) top half, also indicating no extended defects over large lateral distances.
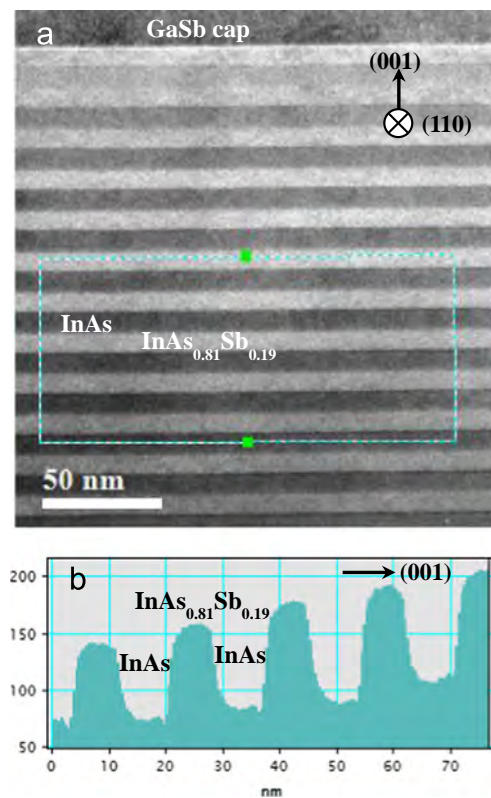
Fig. 8. (a) Bright-field TEM image showing upper part of InAs/InAs$_{0.81}$Sb$_{0.19}$ T2SL, and (b) the averaged line intensity profile from region indicated in (a).

InAs indicated interfacial broadening, as observed previously for samples grown without any surfactant [13]. Thus, it appears that use of the Bi surfactant during growth did not significantly improve the asymmetrical interfacial abruptness.

4. Conclusions

Bright-field and diffraction contrast imaging has revealed that lateral compositional modulation on the scale of several tens of nanometers exists in both the smooth and hazy regions of the InAs$_{1-x}$Bi$_x$ alloy films. However, no atomic ordering was observed in selected area electron diffraction patterns. The surface droplets seem to assume a tilted zincblende structure in the hazy regions, with a lattice constant between those of InAs and InBi, which is possibly a

Fig. 6. (a) High-resolution image showing surface droplet on the InAs$_{0.955}$Bi$_{0.045}$ film. Fast Fourier transform from square region of interest chosen in (b) capping layer, (c) droplet region, with measured spacings of different lattice planes and angles as shown labelled.

phase of $InAs_{1-x}Bi_x$. As evident from the averaged line intensity profile of bright-field image of the Bi-mediated $InAs/InAs_{0.81}Sb_{0.19}$ type-II superlattices, the InAs-on-InAsSb interface appears to be broadened compared with the InAsSb-on-InAs interface.

Acknowledgments

References

[1] K. Oe, H. Asai, IEICE Trans. Electron. E79C (1996) 1751.
[2] H. Okamoto, K. Oe, Jpn. J. Appl. Phys. 37 (1998) 1608.
[3] S. Tixier, M. Adamcyk, T. Tiedje, Appl. Phys. Lett. 82 (2003) 2245.
[4] S. Francoeur, M.-J. Seong, A. Mascarenhas, S. Tixier, M. Adamcyk, T. Tiedje, Appl. Phys. Lett. 82 (2003) 3874.
[5] A.G. Norman, R. France, A.J. Ptak, J. Vac. Sci. Technol. B 29 (2011) 03C121.
[6] M. Wu, E. Luna, J. Puustinen, M. Guina, A. Trampert, Appl. Phys. Lett. 105 (2014) 041602.
[7] G. Vardar, S.W. Paleg, M.V. Warren, M. Kang, R.S. Goldman, Appl. Phys. Lett. 102 (2013) 042106.
[8] S.P. Svensson, H. Hier, W.L. Sarney, D. Donetsky, D. Wang, G. Belenky, J. Vac. Sci. Technol. B 30 (2012) 02B109.
[9] L. Dominguez, D.F. Reyes, F. Bastiman, D.L. Sales, R.D. Richards, D. Mendes, J.P.R. David, D. Gonzalez, Appl. Phys. Express 6 (2013) 112601.
[10] P.T. Webster, N.A. Riordan, C. Gogineni, S. Liu, J. Lu, X.-H. Zhao, D.J. Smith, Y.-H. Zhang, S.R. Johnson, J. Vac. Sci. Technol. B 32 (2014) 02C120.
[11] D.L. Smith, C. Mailhiot, J. Appl. Phys. 62 (1987) 2545.
[12] E.H. Steenbergen, B.C. Connelly, G.D. Metcalfe, H. Shen, M. Wraback, D. Lubyshev, Y. Qiu, J.M. Fastenau, A.W.K. Liu, S. Elhamri, O.O. Cellek, Y.-H. Zhang, Appl. Phys. Lett. 99 (2011) 251110.
[13] L. Ouyang, E.H. Sttenbergen, Y.-H. Zhang, K. Nunna, D.L. Huffaker, D.J. Smith, J. Vac. Sci. Technol. B 30 (2012) 02B106.
[14] K. Mahalingam, E.H. Steenbergen, G.J. Brown, Y.-H. Zhang, Appl. Phys. Lett. 103 (2013) 061908.
[15] S.R. Johnson, Yu.G. Sadofyev, D. Ding, Y. Cao, S.A. Chaparro, K. Franzreb, Y.-H. Zhang, J. Vac. Sci. Technol. B 22 (2004) 1436.
[16] C. Wang, S. Tobin, T. Parodos, J. Zhao, Y. Chang, S. Sivananthan, D.J. Smith, J. Vac. Sci. Technol. A 24 (2006) 995.
[17] M.J. Hytch, E. Snoeck, R. Kilaas, Ultramicroscopy 74 (1998) 131.
[18] Digital Micrograph script developed by C. Koch (Ulm).
[19] Y. Takehara, M. Yoshimoto, W. Huang, J. Saraie, K. Oe, A. Chayahara, Y. Horino, Jpn. J. Appl. Phys. 45 (2006) 67.
[20] S. Wang, Y. Song, I.S. Roy, 13th International Conference on Transparent Optical Networks (ICTON), IEEE, New York, USA (2011).
[21] M. Wu, E. Luna, J. Puustinen, M. Guina, A. Trampert, Nanotechnology 25 (2014) 205605.
[22] L. Dominguez, D.F. Reyes, F. Bastiman, D.L. Sales, R.D. Richards, D. Mendes, J.P.R. David, D. Gonzalez, Appl. Phys. Express 6 (2013) 112601.

Journal of Crystal Growth
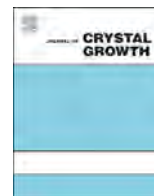
Exploration of the growth parameter space for MBE-grown GaN$_{1-x}$Sb$_x$ highly mismatched alloys

W.L. Sarney [a,*], S.P. Svensson [a], S.V. Novikov [b], K.M. Yu [c,d], W. Walukiewicz [c], M. Ting [c,e], C.T. Foxon [b]

[a] US Army Research Laboratory, 2800 Powder Mill Road, Adelphi, MD 20783, USA
[b] School of Physics and Astronomy, University of Nottingham, Nottingham NG7 2RD, UK
[c] Materials Sciences Division, Lawrence Berkeley National Laboratory, 1 Cyclotron Road, Berkeley, CA 94720 USA
[d] Department of Physics and Materials Science, City University of Hong Kong, Kowloon, Hong Kong
[e] Department of Mechanical Engineering, University of California, Berkeley, CA 94720, USA

ARTICLE INFO

ABSTRACT

Highly mismatched GaN$_{1-x}$Sb$_x$ alloys were grown under N-rich conditions at low substrate temperatures (325–550 °C) at a growth rates of ~0.09 μm/hr on sapphire. The alloys ranged in Sb composition from 0% to 16%, with the bandgap shifting from 3.3 to 1.6 eV in accordance with the band anticrossing (BAC) model. We compare these results to growths from another chamber, having a different N source, and using a faster growth rate (~0.24 μm/hr), much lower substrate temperatures (as low as 80 °C), different III/V ratios and absolute fluxes. Despite the range of morphologies obtained, all alloys follow the predictions of the BAC model with the bandgap only depending on the Sb composition.

Published by Elsevier B.V.

1. Introduction

Highly mismatched alloys (HMAs) based on GaN have small fraction of a group V element, such as As or Sb incorporated in the N sublattice. The 'mismatch' refers to the large difference in electronegativity and/or size between the anion of the host alloy (N) and the minority incorporant (As or Sb). Although adding such mismatched components invokes challenges such as phase segregation and the introduction of strain, there are benefits in terms of the drastic increase in the range of the bandgaps normally inaccessible to GaN-based compounds. In accordance with the band anticrossing (BAC) [1] model, first-principle density functional theory (DFT) [2], and with experimental evidence, very small amounts of Sb (5%), for instance, reduce the bandgap of the alloys from ~3.4 eV to 2.0 eV. This is a bandgap size that is of interest for solar water splitting applications, which require an inert, robust material like GaN.

The challenge of growing GaN based HMAs involves an enormous, largely unexplored parameter space. The N source type and efficiency is a major parameter, as are the power it is operated at and the N flow rate. The Sb or As absolute flux and III/V ratios, and the Ga growth rate are also major factors. Even the substrate choice is not obvious. Since the bandgap properties seem to be unaffected by the crystal morphology [3], and since we are growing at substrate temperatures that are well below what it is typical for high quality GaN, we are exploring the other numerous growth parameters using relatively inexpensive sapphire substrates. Certain device properties, however, may ultimately require that this technology be refined on better quality SiC substrates with buffer layers or GaN templates.

2. Experiment

The samples from our previously published studies [4,5] were grown in a MOD-GENII system with a HD-25 Oxford Applied Research rf activated plasma source to provide active nitrogen, and elemental Ga and Sb were used as the other sources. We are now growing these samples in an additional GENII system with a Veeco Uni-bulb plasma source to provide active N, elemental Ga and a Veeco valved cracker-sources for Sb. In both systems the uncoated sapphire substrate temperature was set by the thermocouple. The source and pumping arrangement in the second system produces significantly less atomic N; therefore we have to grow at a lower rate. Samples produced in this second chamber are the subject of this paper.

Because phase separation is a likely problem for growths at typical (~800 °C) GaN temperatures, we have focused on much lower growth temperatures, with many of our published studies discussing samples grown at 80 °C [4,5]. For this paper, we are exploring samples grown at somewhat higher temperatures, typically from 325 °C to 550 °C. Previously we have shown that under
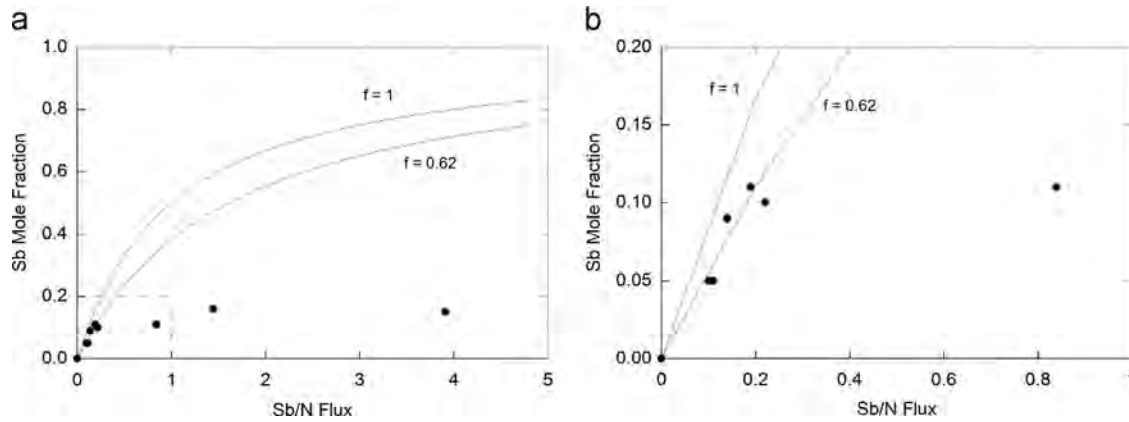
Fig. 1. (a) The Sb mole fraction (x) in GaN$_{1-x}$Sb$_x$ as a function of Sb/N flux with the inset expanded in (b). The symbol f refers to the interaction parameter between N and Sb.

Ga-rich conditions growth condition at low growth temperature ($\sim$80 °C), the optical properties of GaN was dominated by a defect state and it was not possible to control the bandgap by increasing the Sb-concentration in the alloy. In this study, we have grown all subsequent samples under N rich conditions. We note that growing under group V rich conditions is advantageous for most III–V semiconductors, such as GaAs, but it is not typically used for high quality GaN films [6]. The composition of the films was determined by Rutherford Backscatter Spectroscopy and the bandgaps determined from optical transmission measurements by linear extrapolation of the absorption coefficient to zero intensity.

3. Results and discussion

Our past studies from samples grown at higher growth rates ($\sim$0.24 μm/hr) showed that GaN grown at 80 °C was polycrystalline and columnar, and that the crystallinity markedly decreased as any Sb was incorporated and the films eventually became amorphous for Sb compositions exceeding 7% [4,5]. We find that for slower growth rates ($\sim$0.09 μm/hr), the crystallinity is maintained for higher Sb incorporations as the substrate temperature is raised. For instance, at 325 °C, we incorporated up to 16% Sb, and the polycrystalline morphology was maintained, although the preferential alignment with the substrate diminished.

The absolute Ga and Sb fluxes were determined from reflection high-energy electron diffraction (RHEED) oscillations: Assuming unity sticking, the GaSb growth rate was recorded as a function of decreasing Sb over pressure and the 1:1 flux defined at the point when the rate began to decrease (the onset of group V limited growth). The growth rate was converted to flux using the known lattice constant of the substrate. In another experiment the (fixed) N-flux was determined from the chemical composition of GaN as a function of a linearly increasing Ga-flux, using in-situ Auger electron spectroscopy. The 1:1 flux was defined at the point when the N-signal began to disappear due to formation of metallic Ga [7]. The Ga-flux as a function of temperature was known from the mentioned GaSb RHEED experiment.

For the first series of HMAs samples, we fixed the substrate temperature at 325 °C, the N flux at 2.00×10^{18} at/(m^2 s), the Ga flux at 2.35×10^{18} at/(m^2 s), and the Sb flux ranging from 0 to 7.82×10^{18} at/(m^2 s). The Sb mole fraction (x) in GaN$_{1-x}$Sb$_x$ as a function of Sb/N is plotted in Fig. 1a, and the region in the inset is expanded in Fig. 1b. As with any alloy system, to first order, the Sb concentration can be described by $[Sb] = (f\Phi_{Sb}/(f\Phi_{Sb} + \Phi_N))$ where Φ_{Sb} and Φ_N refer to the Sb and N flux, respectively, and f is an interaction parameter that describes the deviation from ideal incorporation. The solid lines in Fig. 1 shows calculations using
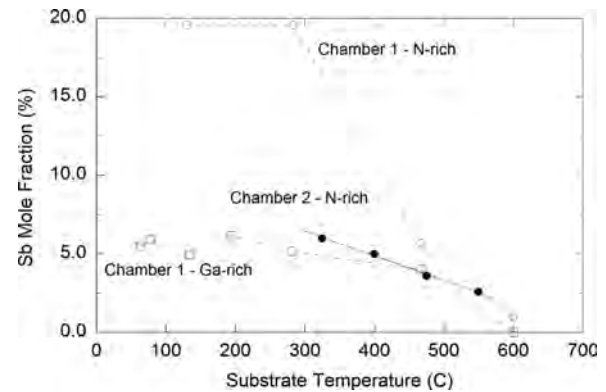
Fig. 2. The Sb mole fraction as a function of substrate temperature for N and Ga rich samples grown in chamber 1 (subject of prior studies) and N rich samples grown in chamber 2 (this publication).

$f = 1$ and $f = 0.62$. Up to the Sb/N flux ratio of 0.2, the incorporation is well-behaved with an interaction parameter slightly below 1. However, it appears that the Sb composition dramatically levels off at about 18% at this growth temperature. In contrast, we had earlier been able to grow across the composition spectrum at 80 °C [5]. It is unclear if the Sb composition is limited by the increased substrate temperature, or if it is because of the difference in absolute fluxes, etc, used in the two different MBE systems.

In a second series of growths, we fixed the Sb flux at 2.24×10^{17} at/(m^2 s), the Ga at 2.36×10^{18} at/(m^2 s) and the N at 2×10^{18} at/(m^2 s), and we varied the substrate temperature between 325 °C and 550 °C. The Sb incorporation decreases linearly with substrate temperature, as shown in Fig. 2 and in qualitative agreement with N-rich growth in the first MBE system [8].

Despite differences between samples grown in the two MBE systems, the behavior of the bandgap with Sb composition follow closely and agree with the trend predicted by the BAC model. All of the samples shown in Fig. 3 were grown at 325 °C, and are polycrystalline with Sb compositions ranging from 0% to 16%. The samples from Fig. 2 with the lowest composition are not included in Fig. 3 due to the difficulty of determining a bandgap from transmission measurements since the density of states of the Sb-derived valence band is quite small in the very dilute regime.

4. Conclusion

We have grown N-rich GaN$_{1-x}$Sb$_x$ highly mismatched alloys with various Sb fluxes and substrate temperatures. Samples grown in two chambers with different N sources and various substrate
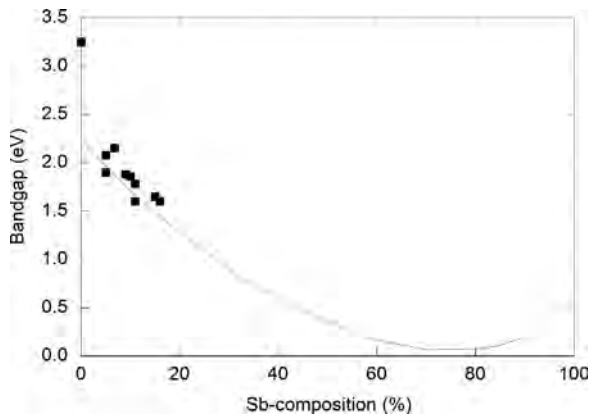
Fig. 3. Bandgap as a function of Sb composition for N-rich samples grown at 325 °C, with the line indicating the fit according to the BAC model.

temperatures, III/V ratios, absolute fluxes, and growth rates have different morphologies, but all follow the predictions of the band anticrossing model. Although the growth parameter space is enormous, the sole factor for obtaining specific bandgaps is dictated by the Sb composition. The control of many other materials properties required for device applications need to be studied and optimized separately.

Acknowledgments

References

[1] W. Walukiewicz, K. Alberi, J. Wu, W. Shan, K.M. Yu, J.W. Ager III, in: Ayse Erol (Ed.), Physics of Dilute III–V Nitride Semiconductors and Material Systems: Physics and Technology, Springer-Verlag Berlin-Heidelberg, New York, 2008.

[2] R.M. Sheetz, E. Richter, A.N. Andriotis, C. Pendyala, M.K. Sunkara, M. Menon, Visible light absorption and large band gap bowing in dilute alloys of gallium nitride with antimony, Phys. Rev. B 84 (2011) 075304.

[3] K.M. Yu, S.V. Novikov, R. Broesler, I.N. Demchenko, J.D. Denlinger, Z. Liliental-Weber, F. Luckert, R.W. Martin, W. Walukiewicz, C.T. Foxon, Highly mismatched crystalline and amorphous $GaN_{1-x}As_x$ alloys in the whole composition range, J. Appl. Phys. 106 (2009) 103709.

[4] K.M. Yu, W.L. Sarney, S.V. Novikov, D. Detert, R. Zhao, J. Denlinger, S.P. Svensson, O.D. Dubon, W. Walukiewicz, C.T. Foxon, Highly mismatched N-rich $GaN_{1-x}Sb_x$ films grown by low temperature molecular beam epitaxy, Appl. Phys. Lett. 102 (2013) 102104.

[5] W.L. Sarney, S.P. Svensson, SV Novikov, K.M. Yu, W. Walukiewicz, C.T. Foxon, $GaN_{1-x}Sb_x$ highly mismatched alloys grown by low temperature molecular beam epitaxy under Ga-rich conditions, J. Cryst. Growth 383 (2013) 95.

[6] V. Ramachandran, R.M. Feenstra, W.L. Sarney, L. Salamanca-Riba, D.W. Greve, Optimized structural properties of wurtzite GaN on SiC(0001) grown by molecular beam epitaxy, J. Vac. Sci. Technol. A 18 (2000) 1915.

[7] S.P. Svensson, W.L. Sarney, K.M. Yu, W.L. Calley, S.V. Novikov, M. Ting, W. Walukiewicz, Determination of N-/Ga-rich growth conditions, using in-situ auger electron spectroscopy, J. Cryst. Growth, in press, http://dx.doi.org/10.1016/j.jcrysgro.2015.02.035.

[8] K.M. Yu, S.V. Novikov, M. Ting, W.L. Sarney, S.P. Svensson, M. Shaw, R.W. Martin, W Walukiewicz, C.T. Foxon, Growth and characterization of highly mismatched $GaN_{1-x}Sb_x$ alloys, J. Appl. Phys. 116 (12) (2014) 123704.
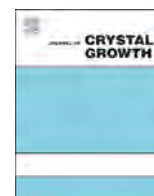
Physical properties of InGaO$_3$(ZnO)$_m$ with various content ratio grown by PAMBE

Chu Shou Yang [a,b,*], Shin Jung Huang [a], Yu Chung Kao [a], Guan He Chen [a], Wu-Ching Chou [c]

[a] Graduate Institute of Electro-optical Engineering, Tatung University, Taipei, Taiwan, ROC
[b] Department of electrical Engineering, Tatung University, Taipei, Taiwan, ROC
[c] Department of Electrophysics, National Chiao Tung University, Hsinchu, Taiwan, ROC

ABSTRACT

The quaternary compound semiconductor (InGaO$_3$(ZnO)$_m$); $m=1,2,3\ldots$)(IGZO) thin films were fabricated by plasma-assisted molecular beam epitaxy. First, the IGZO thin films were grown under the variation of gallium cell temperature to evaluate the fundamental properties of IGZO. A phase transformation between crystalline and amorphous is observed when the gallium content ratio is higher than 28 at%. It revealed redundancy in the metal, which would self-assist the channel or defect state to destroy the crystal structure. The highest mobility of 74.3 cm^2/V s was obtained at 28 at% of gallium. By tuning the element content of quaternary compounds, the ternary plots distribution of IGZO thin films exhibits an amorphous structure in most regions. Therefore, the stoichiometric condition of IGZO, which is 1:1:1:4, is demonstrated at the amorphous structure. Additionally, it transitions to crystalline structure after a 1100 °C annealing process.

© 2015 Elsevier B.V. All rights reserved.

1. Introduction

There are great advantages of oxide-based semiconductors such as wide bandgaps, and exceptional optical and electrical properties. ZnO has a direct bandgap of 3.37 eV and has a significant advantage over GaN, such as the higher exciton binding energy of 60 meV. It also is a good transparent oxide semiconductors (TOSs) material because of its high transmission above 90%. These features provide attractive potential to develop optoelectronic devices, for example, light emitted diode (LED), organic light emitted diode (OLED), and thin film transistor (TFT). The easy method of fabricating quaternary oxide semiconductor which is based on (RMO$_3$(ZnO)$_m$, $m=$integer) was developed on Reactive Solid-Phase Epitaxy (R-PSE) [1–5]. IGZO was also prepared by pulsed laser deposition (PLD) [6,7]. IGZO thin films had already been investigated for TFT devices and applications widely [8–13]. There were significant contributions on amorphous IGZO (a-IGZO) TFT in recent years and single-crystalline IGZO (sc-IGZO) thin films were applied to CAAC-IGZO (C-Axis Aligned Crystal IGZO) [14–17]. There are conspicuous advantages in a-IGZO TFT, e.g., the mobility is 20–30 times higher than amorphous silicon-based and cut-off voltage is 100 times higher than low-temperature poly silicon. For a-IGZO, the mechanism of electrical transition is not very clear. Takeda et al. found the mobility increased when they raised the free carrier concentration in the material [18]. They inferred the mechanism of electrical

transition between a-IGZO and sc-IGZO is similar because of identical electron effect mass [19]. This conception is contrary to the relationship between carrier concentration and mobility in semiconductor devices and physics technology. In general, they display an inverse proportion because high carrier concentrations mean high impurities interfere with transmission in thin films. Sc-IGZO was first fabricated in 2004 [20] on Yttria-stabilized zirconia (YSZ) substrate. The relationship between room-temperature Hall mobility and carrier concentration for a-IGZO films and sc-IGZO is reported to be 10 cm^2/V s at carrier concentrations greater than 10^{18}/cm^3 [21]. According this theory, a-IGZO TFT was studied and developed extensively, and proved to be an emerging product in recent years. Therefore, fundamental properties like structure phase change, transparency, and ions composition relation of amorphous and crystalline IGZO are not examined and evaluated in subsequent reports. In this work, we adjust the contents of ions Ga, Zn, and In by using plasma-assisted molecular beam epitaxy (PA-MBE) to figure out the related characteristics.

2. Experiments

InGaZnO thin films were grown on sapphire substrate by a PA-MBE system. Regarding MBE system, the growth chamber is consistently maintained by a Cryo-pump for an ultra-high vacuum

* Correspondence author at: Graduate Institute of Electro-optical Engineering, Tatung University, Taipei, Taiwan, ROC. Tel.: +886 2 21822928x6612.
  E-mail address: csyang@ttu.edu.tw (C.S. Yang).

situation at less than 1×10^{-8} Torr without sample growth and at 1×10^{-5} Torr vacuum for oxide growth process. First, the Ga cell temperature was varied between 500 and 800 °C and the cell temperature of In and Zn was fixed to figure out the ions contents relationship. The oxygen plasma was set up at 350 W (W) and 0.8 standard cubic centimeter per minute (sccm). In order to fabricate $(InGaO_3(ZnO)_m; m=1)$, cell temperatures of In, Ga, and Zn were adjusted. The detailed growth parameters and the atomic percentage of each metallic element, which are taken from energy dispersive spectrometer (EDS), are displayed in Table 1. In order to guarantee the credibility of EDS results, detailed analysis was carried out more than three times and area analysis was conducted on the samples. The data were presented as error bar which was similar to 0.5–1.5%. The optimum condition of $(InGaO_3(ZnO)_m; m=1)$, which denoted as sample-I, was 31, 36, and 32 at% of In, Ga, and Zn, respectively. Thickness of the sample was around 250 nm. The annealing temperature is controlled at 1100 °C with 30 min in the furnace. The structural and crystalline characterizations were performed by x-ray diffraction (XRD) measurements. The electric properties were determined by four-point Hall Measurements. Surface morphology and thickness were identified using scanning electron microscope (SEM).

3. Result and discussion

Contents of IGZO thin films are displayed in Fig. 1 with increasing T_{Ga} from 500 °C to 800 °C, i.e. sample A to E. According to EDS results, the trend of Ga composition appeared as a smooth linear phenomenon with T_{Ga} increasing. Additionally, the zinc atomic percentage decreased with increase in gallium. This caused some influence on indium and zinc elemental ratio interaction. A theoretical calculation of O_{II}/O_{Total} shows that the formation of oxygen vacancies is easier than the replacement of Zn by Ga and In [22]. By the selection relation, the relation of the bonding strength of these metals is Ga > In > Zn. Therefore, we suggested a reasonable explanation that Ga–O and In–O bonding energies are stronger than Zn–O [23,24]. These EDS results support this suggestion. On the other hand, T_{In} was reduced from 650 °C to 500 °C to realize the adjustment of ions ratio. It is carried out in sample-F to -I, which is shown in Table 1. Atomic percentage of In was displayed from 41.2% to 10.6% (650–500/°C), respectively. It proved the supposition just mentioned previously. The highest Ga content was present at 87.3% when In was at 10.6%. The EDS results were presented in an error bar, which was smaller than two percentages. According to experimental data, the difference between each sample was very huge. In this case, EDS results can be believed. SEM image of thin-films IGZO surface morphology is shown in Fig. 2. In the IGZO growth process, Ga^{3+} and Zn^{2+} ions randomly share a site in the oxidation process [19]. It can be clearly seen that crystal grain has a low Ga content as shown in Fig. 2(a)–(c). The sample surfaces became flat and the grain distribution was reduced when T_{Ga} was above 700 °C. Excess of Ga would destroy
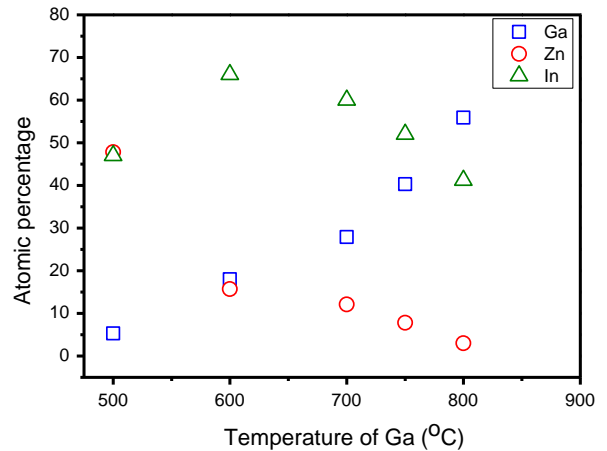
Fig. 1. IGZO thin films elemental contents verse gallium cell temperature. The open square, cycle, and triangle represent gallium, zinc, and indium, respectively.

structure quality to occur defect state and Ga interstitial. The reduction of grain distribution implied that a phase transition occurred.

Structure performance of IGZO thin films which was determined by XRD analysis is shown in Fig. 3. There is a phase transition from crystalline to amorphous with Ga atomic percentage increasing from 6% to 40%, i.e. the T_{Ga} from 500 to 750 °C. This was in agreement with the discussion of SEM. Note that the surface morphology of amorphous structure is flat in many ternary or quaternary compound systems. For example, in InO–ZnO system, a smooth surface (average roughness < 0.4 nm) is observed at the indium composition range of 55–84 cation %, which is amorphous [25]. Too many Ga ions led IGZO thin films to deprecate. The diffraction peak of IGZO became broad and wide. Furthermore, the diffraction peak is shifted from 30.7° to 31.1° with increasing gallium content. The reason is that the Ga ion radius (62 pm) is smaller than Zn (74 pm) and In (80 pm) elements. Increase in the gallium content would reduce the lattice constant.

The highest mobility 74 cm²/V s was obtained at T_{Ga} 700 °C (27.9%) by Hall measurement, as shown in Fig. 4. In low Ga contents, high crystal quality, which implies low carrier concentration, results in high resistance. However, the mobility is around 36.3 cm²/V s. It is compatible with crystalline ZnO. When Ga contents increased, the structure became worse and amorphous, but mobility reached 74 cm²/V s. The results do not agree with the rule that mobility depends on the structure quality in crystalline materials. IGZO quaternary compounds semiconductors are usually fabricated in amorphous nature for TFT devices. The reason was because there were great advantages in mobility of amorphous IGZO thin films. The carrier transmission mechanism of IGZO is still not clear. The authors expect to reach such a result by the analysis of different compositions. According to the Hall measurement results, the authors consider that this should be divided into two parts: the crystalline region (IZO-based) and amorphous region (IGZO-based). In the IZO-based region, mobility depends on the structure quality. When Ga atomic ratio increases, the mechanism switches to IGZO system. In this case, the carrier transition mechanism is suggested to be metallic transition channel which is different from the crystal. IGZO thin films were fabricated by MBE but the composition ratio between metal elements (In, Ga, Zn) was not achieved in ideal stable equilibrium concentration. Usually chemical equilibrium concentration whose content ratio (In:Ga:Zn:O, 1:1:1:4) is considered the most steady state [19,26,27]. Furthermore, we modulated the growth parameters to fabricate $InGaO_3(ZnO)$ thin film whose content ratio of In, Ga, Zn, and oxygen is 1:1:1:4, respectively. The modulated parameters are displayed in Table 1.

Ternary plots distribution of IGZO thin films with different element content ratio is displayed in Fig. 5. Sample (A–H) expressed

Table 1
The growth parameters and the atomic percentage of IGZO.

Sample	T_{Ga}/°C	Ga at%	T_{In}/°C	In at%	T_{Zn}/°C	Zn at%
A	500	6	650	44	325	50
B	600	18	650	66	325	16
C	700	28	650	60	325	12
D	750	40	650	52	325	8
E	800	56	650	41	325	3
F	800	67	600	28	325	5
G	800	80	550	16	325	5
H	800	87	500	11	325	0.2–1.2
I	700	37	600	31	330	32
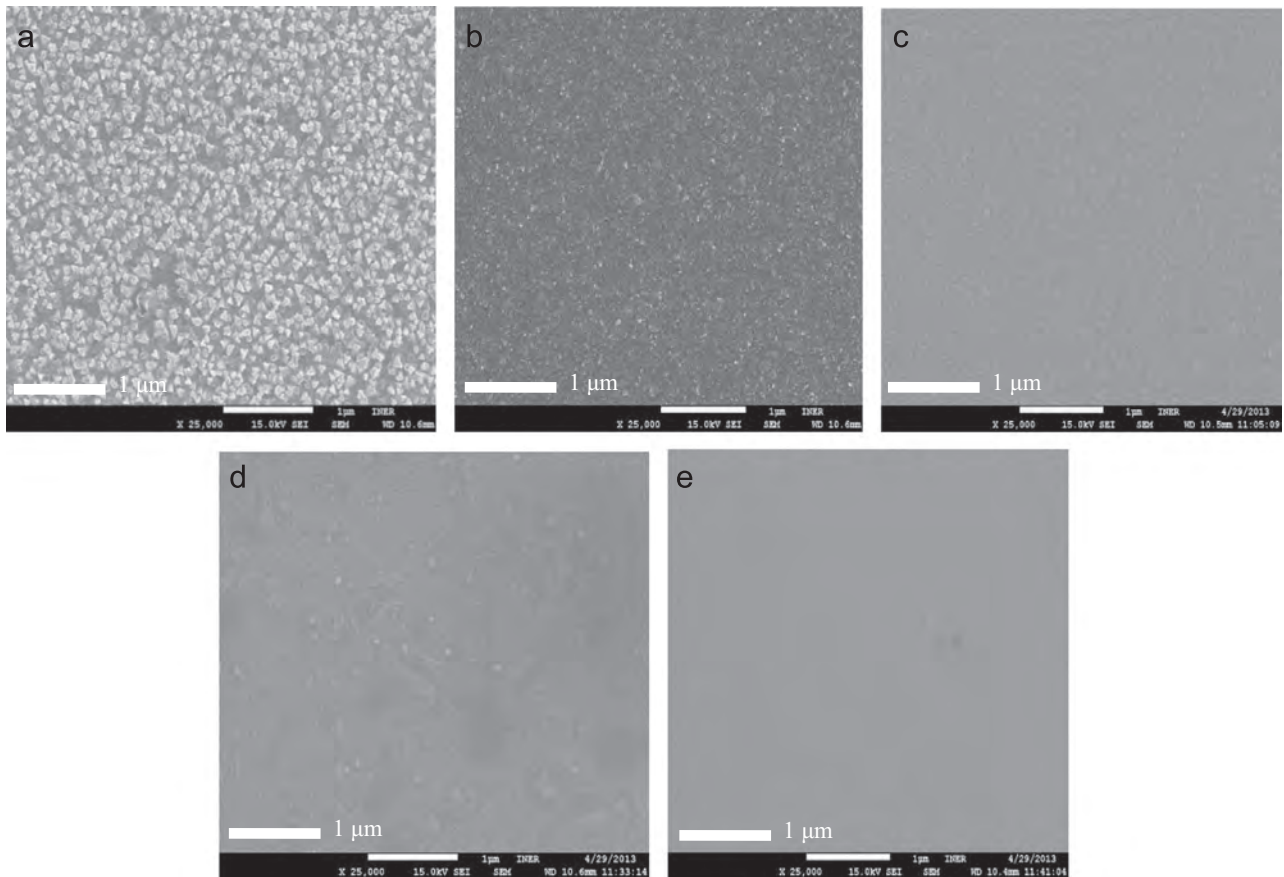
Fig. 2. Top-view SEM image with different Ga fluxes: (a) T_{Ga}: 500 °C (b) T_{Ga}: 600 °C (c) T_{Ga}: 700 °C (d) T_{Ga}: 750 °C (e) T_{Ga}: 800 °C.
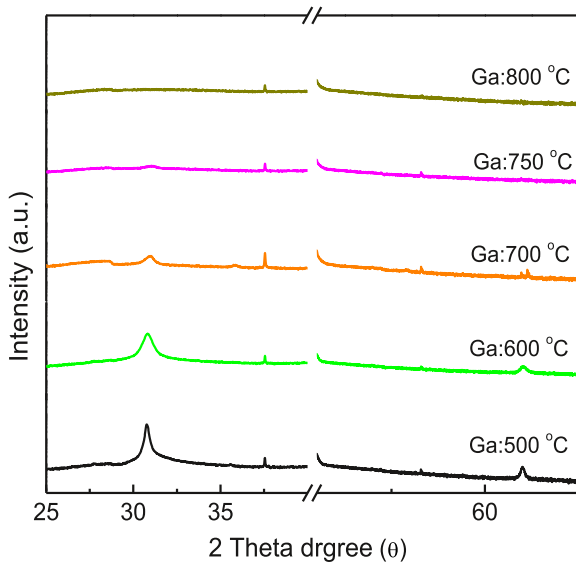
Fig. 3. X-ray diffraction pattern of samples A to E, whose T_{Ga}=500, 600, 700, 750, and 800 °C, respectively.

Fig. 4. Resistance and mobility versus the gallium content.

a curved line related to Ga contents from 6% to 87%. Samples A, B, and C presented crystalline properties, the others did not. Such a result demonstrates the structure variation from IZO-based to complicate IGZO-based. Triangular distribution usually displayed crystalline properties at acme, which demonstrated ZnO, Ga_2O_3, and In_2O_3. In this case this phenomenon has not been observed. It means the crystalline array of IGZO thin films were difficult to self-generate. There was elemental influence of In and Zn interaction due to the

results. By tuning the metal flux, Sample-I whose contents ratio was very closely related to 1:1:1:4 was obtained and the structure was found to be amorphous. The XRD patterns of as-grown and annealed sample-I are displayed in Fig. 6(a) and (b), respectively. Before the annealing process, the weak IGZO XRD pattern implies the structure tends to amorphous. After 1100 °C annealing for 30 min, the crystal IGZO's preferred orientation appeared. High temperature provided the migration kinetic energy to result in the IGZO self-assisted crystal structure during the heating process.

4. Conclusion

InGaZnO thin films were demonstrated by PA-MBE. With Ga flux increasing, crystal growth along with defect worsened the
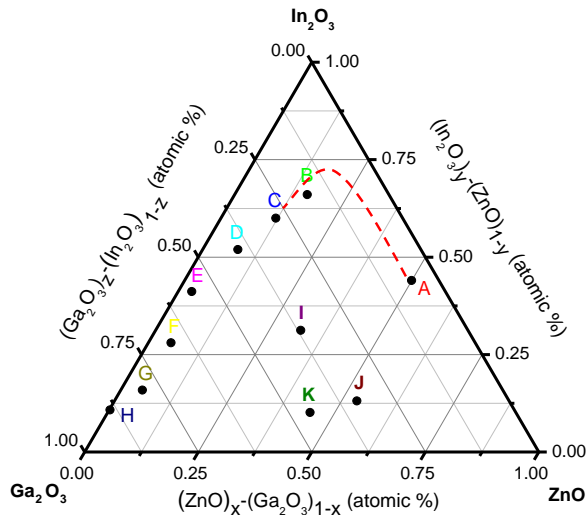
Fig. 5. Ternary plots distribution of IGZO thin films with different element contents ratio, where x, y, and z denote the atomic percentage of zinc, indium and gallium, respectively. Samples A to C revealed a crystal structure. Otherwise, samples D to K exhibit an amorphous structure.
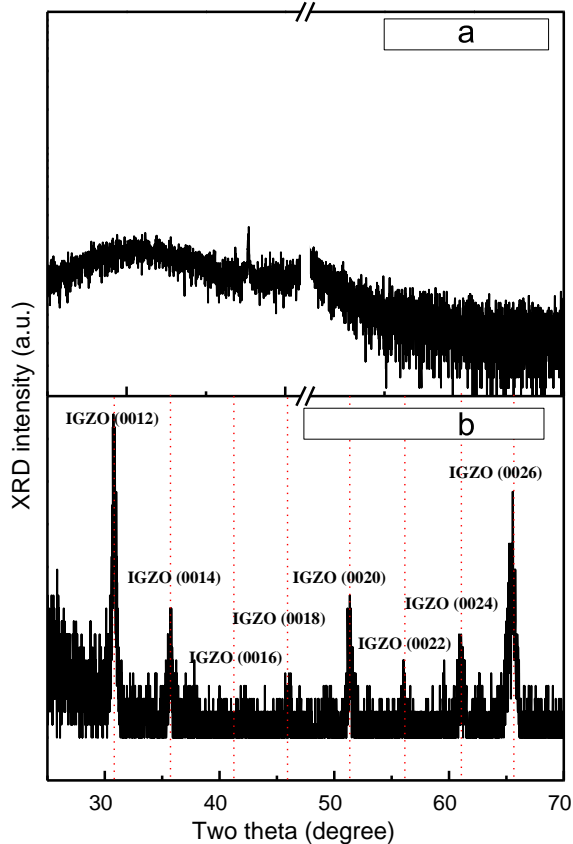
Fig. 6. XRD results of sample-I as (a) as-grown and (b) after annealing at 1100 °C within 30 min.

atomic percentages. The highest mobility of 74 cm^2/V s was also obtained. The content ratio of In:Ga:Zn:O related to 1:1:1:4 was obtained. Crystalline InGaO$_3$(ZnO) quaternary compounds were successfully demonstrated by annealing process at 1100 °C.

References

[1] H. Otha, H. Tanji, M. Orita, H. Hosono, H. Kawazoe, Mater. Res. Soc. Symp. Proc 570 (1999) 309.
[2] H. Ohta, K. Nomura, M. Orita, M. Hirano, K. Ueda, T. Suzuki, Y. Ikuhara, H. Hosono, Adv. Funct. Mater. 13 (2003) 139.
[3] K. Nomura, H. Ohta, K. Ueda, M. Orita, M. Hirano, H. Hosono, Thin Solid Films 411 (2000) 147.
[4] H. Hiramatsu, K. Ueda, H. Ohta, M. Orita, M. Hirano, H. Hosono, Appl. Phys. Lett. 81 (2002) 598.
[5] H. Ohta, H. Mizoguchi, M. Hirano, S. Narushima, T. Kamiya, H. Hosono, Appl. Phys. Lett. 82 (2003) 823.
[6] A. Suresh, P. Gollakota, P. Wellenius, A. Dhawan, J.F. Muth, Thin Solid Films 516 (2008) 1326–1329.
[7] J. Chen, L. Wang, X. Su, Vacuum 86 (2012) 1313–1317.
[8] H. Yabuta, M. Sano, K. Abe, T. Aiba, T. Den, H. Kumomi, Appl. Phys. Lett. 89 (2006) 112123.
[9] M. Kim, J.H. Jeong, H.J. Lee, T.K. Ahn, H.S. Shin, J.-S. Park, J.K. Jeong, Y.-G. Mo, H.D. Kim, Appl. Phys. Lett. 90 (2007) 212114.
[10] J.-S. Park, J.K. Jeong, Y.-G. Mo, H.D. Kim, S. Kim, Appl. Phys. Lett. 90 (2007) 262106.
[11] J.K. Jeong, J.H. Jeong, H.W. Yang, J.-S. Park, Y.-G. Mo, H.D. Kim, Appl. Phys. Lett. 91 (2007) 113505.
[12] A. Sato, K.a. Abe, R. Hayashi, H. Kumomi, K. Nomura, T. Kamiya, M. Hirano, H. Hosono, Appl. Phys. Lett. 94 (2009) 133502.
[13] J.-S. Park, T.-W. Kim, D. Stryakhilev, J.-S. Lee, S.-G. An, Y.-S. Pyo, D.-B. Lee, Y.G. Mo, D.-U. Jin, H.K. Chung, Appl. Phys. Lett. 95 (2009) 013503.
[14] S. Yamazaki, To promote the spirit of inventing, presented at the International Workshop Private Sector–Academia Interactions, 2011.
[15] S. Yamazaki, J. Koyama, Y. Yamamoto, and K. Okamoto, SID symposium digest, 43, 2012, p. 183.
[16] S. Yamazaki, M. Sakakura, R. Watanabe, J. Sakata, K. Akimoto, A. Miyanaga, T. Hirohashi, and H. Kishida, US Patent 8492758 2010.
[17] S. Yamazaki, M. Tsubuku, K. Akimoto, H. Ohara, T. Honda, T. Omata, Y. Nonaka, M. Takahashi, and A. Miyanaga, US Patent 8669556 2011.
[18] Y. Takedaa, K. Nomura, H. Ohta, H. Yanagi, T. Kamiya, M. Hirano, H. Hosono, Thin Solid Films 486 (2005) 28–32.
[19] A. Takagi, K. Nomura, H. Ohta, H. Yanagi, T. Kamiya, M. Hirano, H. Hosono, Thin Solid Films 486 (2005) 38–41.
[20] K. Nomura, H. Ohta, A. Takagi, T. Kamiya, M. Hirano, H. Hosono, Nature 432 (2004) 488.
[21] K. Nomura, H. Ohta, K. Ueda, T. Kamiya, M. Orita, M. Hirano, J. Appl. Phys. 95 (2004) 5532.
[22] G.C. Park, S.M. Hwang, J.H. Choi, Y.H. Kwon, H.K. Cho, S.-W. Kim, J.H. Lim, J. Joo, Phys. Status Solidi A 210 (8) (2013) 1552–1556.
[23] H. Wang, S. Baek, J. Song, J. Lee, S. Lim, Nanotechnology 19 (2008) 075607.
[24] Y.Y. Kim, B.H. Kong, H.K. Cho, J. Cryst. Growth 330 (2011) 17.
[25] M.P. Taylor, D.W. Readey, M.F.A.M. van Hest, C.W. Teplin, J.L. Alleman, M.S. Dabney, L.M. Gedvilas, B.M. Keyes, B. To, J.D. Perkins, D.S. Ginley, Adv. Funct. Mater. 18 (2008) 3169.
[26] H. Jeon, S. Na, M.R. Moon, D. Jung, H. Kim, H.-J. Lee, J. Electrochem. Soc. 158 (2011) 10.
[27] K. Lee, K. Nomura, H. Yanagi, T. Kamiya, H. Hosono, Thin Solid Films 520 (2012) 3808–3812.

structure quality. EDX results show that the bonding strength of Ga–O is stronger than In–O and Zn–O. Amorphous structure dominates when the content of gallium and indium reach several
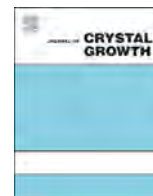
CRYSTAL
GROWTH

Heterointegration of III–V on silicon using a crystalline oxide buffer layer

CrossMark

K. Bhatnagar [a], J.S. Rojas-Ramirez [b], R. Contreras-Guerrero [b], M. Caro [b], R. Droopad [a,b,*]

[a] Materials Science, Engineering & Commercialization, Texas State University, San Marcos, TX 78666, United States
[b] Ingram School of Engineering, Texas State University, 601 University Drive, San Marcos, TX 78666, United States

ARTICLE INFO

ABSTRACT

The integration of III–V compound semiconductors with Si can combine the cost advantage and maturity of Si technology with the superior performance of III–V materials. We have achieved the heteroepitaxial growth of III–V compound semiconductors on a crystalline $SrTiO_3$ buffer layer grown on Si(0 0 1) substrates. A two-step growth process utilizing a high temperature nucleation layer of GaAs, followed by a low-temperature GaAs layer at a higher growth rate was employed to achieve highly crystalline thick GaAs layers on the $SrTiO_3$/Si substrates with low surface roughness as seen by AFM. The effect of the GaAs nucleation layer on different surface terminations for the $SrTiO_3$ layer was studied for both on axis and miscut wafers, which led to the conclusion that the Sr terminated surface on miscut substrates provides the best GaAs films. Using GaAs/STO/Si as virtual substrates, we have optimized the growth of high quality GaSb using the interfacial misfit (IMF) dislocation array technique. This work can lead to the possibility of realizing infrared detectors and next-generation high mobility III–V CMOS within the existing Si substrate infrastructure.

1. Introduction

The cost effectiveness of silicon combined with the extremely mature processing technology have made silicon one of the most important materials of the 21st century. Even with its cadre of undeniable advantages, the silicon technology still suffers from low optical efficiency and has degraded electrical properties in scaled CMOS devices [1]. On the other hand, III–V semiconductors are ideal candidates for optoelectronic and photonic applications and because of their high carrier mobilities, they are being considered for the channel material in future Si based MOSFETs [2]. However, such implementation would require the monolithic integration of various III–V materials on silicon with low enough defects to fabricate surface channel MOS devices. The integration of III–V compound semiconductors with Si can also combine the cost advantage and maturity of the Si technology with the superior performance of III–V materials resulting in highly integrated semiconductor circuits.

The heterointegration of III–V on Si presents several challenges including the growth of polar on non-polar substrate, high-lattice mismatch and large differences in the coefficients of thermal expansion leading to the formation of anti-phase domain boundaries, dislocations and surface defects [3]. Various schemes have been used to reduce the density of threading dislocations which include low temperature buffers, superlattice buffers [4] and thermal cycling [5]. Another integration scheme that has been used for GaAs on Si included a crystalline oxide buffer layer, viz. $SrTiO_3$ that was grown epitaxially on Si [6]. The $SrTiO_3$ lattice ($a_{STO} = 3.905$ Å) undergoes a 45° rotation to accommodate the high lattice mismatch with the underlying Si(0 0 1) ($a_{Si} = 5.431$ Å) leading to a strain of 1.7%. The GaAs lattice ($a_{GaAs} = 5.653$ Å) grown is now strained 2.3% with respect to the 45° rotated $SrTiO_3$ lattice, thereby enabling the reduction from the original 4% strain for the GaAs/Si system [7]. A two-step growth process utilizing a high temperature nucleation layer of GaAs, followed by a low-temperature GaAs layer at a higher growth rate was employed for this work. The surface termination conditions of the $SrTiO_3$ crystalline buffer layer have a strong effect on both the crystalline and surface quality of the final GaAs epitaxial growth. Prior work by Largeau et al. has shown the growth of GaAs islands on TiO_2 terminated $SrTiO_3$ films with the coexistence of wurtzite and cubic phases [8]. This study will investigate the effect of the $SrTiO_3$ surface terminations on the subsequent GaAs surface and epilayer quality. GaSb is another important III–V material with applications in thermo-photovoltaics [9], infrared detectors [10], and low-power high-frequency

* Corresponding author at: Materials Science, Engineering & Commercialization, Texas State University, San Marcos, TX 78666, United States. Tel.: +1 512 245 6165.
E-mail address: rdroopad@txstate.edu (R. Droopad).

electronics [11]. The growth of GaSb directly on Si is usually accomplished using an AlSb buffer layer [12]. For this work, the GaAs/STO/Si platform will be used as a virtual substrate for investigating the growth of GaSb layers on Si using the IMF-based growth on GaAs. The IMF array technique relieves the excess strain from the 8% lattice mismatch at the heterointerface, leading to the formation of highly crystalline GaSb under the optimized MBE growth conditions. The monolithic integration of GaSb on these Si-based virtual substrates will open up doors for high frequency, low-power tunnel-FETs and Esaki diodes [13]. In this paper we report on the effects of the oxide surface termination on the nucleation and subsequent growth of III–V semiconductors and the use of GaAs/STO/Si as virtual substrates for the growth of GaSb heterostructures.

2. Experimental procedure

The heterointegration approach was developed by growing GaAs films on Si wafers using a crystalline $SrTiO_3$ buffer layer resulting in templates of GaAs virtual substrates with a potential to grow complex III–V structures on a Si wafer. The concept of this integration was extended by growing GaSb epilayers onto these GaAs templates. Initially, 3" p-Si(0 0 1) wafers (on-axis and 4° miscut towards $\langle 1\,1\,0 \rangle$) were treated in a UV-ozone system to aid in the complete removal of carbon contaminants and then loaded into a load-lock section for an initial baking at 150 °C for 30 min. Then, the wafers were introduced into an oxide MBE chamber equipped with Sr and Ti effusion cells and a molecular oxygen source where 10 nm of $SrTiO_3$ (STO) with different surface terminations was grown on Si. Prior to the STO buffer layer growth, the Si wafers were cleaned using the de-oxidation procedure as developed by Wei et al. [14]. The entire growth process was monitored using in-situ reflection high electron energy diffraction (RHEED) to determine the growth mode and surface stoichiometry. STO growth was performed in two steps: first a nucleation layer of 2 unit cells was grown on the Si wafer at low temperature (300 °C) by co-depositing Sr and Ti under molecular O_2 environment at a partial pressure of 6×10^{-8} Torr followed by a high temperature (550 °C) anneal and subsequent growth of STO using an O_2 partial pressure of 10^{-7}–10^{-6} Torr. Typical growth rate used for the oxide film was 1 unit cell/min as determined by RHEED oscillations. Three different surface conditions of the STO film were chosen for this study: stoichiometric, Ti-terminated, and Sr-terminated. By default, the STO growth was performed under a stoichiometric regime (as evidence by a RHEED (1×1) reconstruction) that can be switched to either a Ti-rich or Sr-rich surface by closing the shutter for the respective metal cell and keeping the other one open until specific termination is achieved. The surface termination was monitored by RHEED as detailed in Ref. [6]. Following the growth of crystalline STO on Si, all the wafers were unloaded from the MBE cluster tool and stored under ambient conditions. Quarters of STO/Si wafers were then cut and loaded into a III–V MBE chamber for As-based semiconductor growths. Two sets of samples consisting of 0.5 μm and 1.5 μm GaAs were grown on the different STO/Si terminations to show the effect of the STO surface conditions on GaAs epilayer growth. The STO/Si samples were degassed at 580 °C for 15 min; then, a GaAs nucleation layer of 25 nm was grown at a temperature of 450 °C using an As_2/Ga ratio of 8 and a growth rate of 0.15 ML/s. Following this, the growth temperature was decreased to 380 °C and 475 nm or 1475 nm of GaAs layer was deposited at an As_2/Ga ratio of 15 and growth rate of 0.5 ML/s. Finally, a post-growth anneal was carried out at 580 °C for 15 min with the entire growth process being monitored using in-situ RHEED.

The $GaAs/SrTiO_3$/Si virtual substrates with the best crystalline quality and surface morphologies were then introduced in a different III–V MBE chamber with As and Sb valved crackers present.

Here an additional buffer layer of 0.5 μm GaAs was grown at 580 °C with a growth rate of 0.5 ML/s. Growth rate calibrations were performed previously on a GaAs substrate using RHEED intensity oscillations. Following this, a 0.5 μm layer of GaSb was grown on GaAs at 510 °C using the interfacial misfit (IMF) dislocation array technique as described by Huang et al. [15]. This technique involves the formation of 90° edge dislocations at the GaAs/GaSb interface, thereby relieving the inbuilt strain mostly at the interface in the form of a 2-D periodic array of misfit dislocations in the [1 1 0] and [$\bar{1}$ 1 0] direction. Heteroepitaxial GaSb films of extremely low dislocation density can be achieved using this technique. In this work, The GaSb surface quality was monitored as a function of the V-to-III flux ratios using the IMF array technique. The surface morphology of the grown samples was mapped using atomic force microscopy (AFM) in tapping mode with a Si probe tip and the structural properties of the films were analyzed ex-situ using a double crystal X-ray diffractometer.

3. Results and discussion

Although there is a large mismatch between the STO layer and the Si substrate ($\sim$28%), a 45° rotation of the STO lattice w.r.t. the Si lattice minimizes the mismatch ($\sim$1.7%) allowing for a high quality film with lower number of defect densities. Fig. 1 displays a typical 10 μm × 10 μm AFM image of a 10 nm STO layer grown on both nominal and vicinal 4° miscut Si(0 0 1) wafers. The surface morphology exhibits a very flat surface with a root mean square (RMS) roughness of around 1/2 a_{STO} for both the wafers. The surface quality is also corroborated in-situ by the streaky and sharp RHEED patterns displayed in the inset of Fig. 1(a) and (b). The different surface terminations of STO exhibit similar features in AFM micrographs and RHEED patterns. These results guarantee that the epitaxy of III–V films on STO/Si template is performed on extremely smooth surfaces.

III–V growth was started with a 25 nm of GaAs nucleation layer. Diffraction patterns at the end of the nucleation layer along [$\bar{1}$ 1 0] azimuth are shown for the Ti- and Sr-terminated STO films in Fig. 2. Both RHEED patterns are spotty indicating 3 dimensional growth of the nucleation layer with the formation of islands. The RHEED pattern of the GaAs nucleation layer grown on the Ti-terminated STO surface is spotty with ring-like features suggesting a polycrystalline nature of this layer, i.e. crystal grains with several orientations where, possibly, cubic and hexagonal phases could coexist (Fig. 2(a)). On the other hand, the nucleation on the Sr-terminated surface shows a well-ordered spotty RHEED pattern where the diffraction spots arrangement and interconnection is indicative of cubic monocrystalline faceted islands (Fig. 2(b)). Similar to this, the nucleation on stoichiometric STO exhibits the same behavior. From RHEED patterns, it is evident that the crystallographic relationship [1 1 0] GaAs‖[1 0 0] STO‖[1 1 0] Si exists confirming the 45° rotation of STO w.r.t to both the underlying Si and overlying GaAs epilayer.

GaAs films grown on STO show a strong dependency on the miscut of the Si substrate (on axis and offcut), the thickness of GaAs and the underlying termination of the STO as can be observed in AFM images of Fig. 3. In this figure, the topography of 1.5 μm thick GaAs film in a 10 μm x 10 μm AFM scan is shown as a function of these parameters. GaAs grown on on-axis STO/Si (0 0 1) presents a surface morphology consisting of clear antiphase domains that are isolated by well-defined boundaries (Fig. 3(a)) resulting, in general, from the heteroepitaxy of polar semiconductors grown on a nonpolar surfaces as in this case where the GaAs is grown on STO(0 0 1)/Si surface with no miscut on the starting Si substrate. Although the RMS roughness is high in this sample ($\sim$3.1 nm), the individual domains exhibit very flat surfaces as is

corroborated by the 4× streaky and slightly spotty RHEED pattern (inset of Fig. 3(a)). RHEED also confirms, in this sample, the 2-domain nature as seen in the AFM micrograph in which the 4-fold reconstruction from the (2×4) surface is present in the orthogonal [1 1 0] azimuths. The growth on miscut STO/Si templates promotes the growth of single domain GaAs as evidenced in AFM images (Fig. 3(c) and (d)), however, the growth is strongly dependent on the STO surface termination. GaAs grown on Ti-terminated STO surface depicts a grainy topography with a high RMS roughness of ~10 nm (Fig. 3(b)), this texture is in agreement with the spotty RHEED obtained at the end of the growth in inset of Fig. 3(b). On the other hand, GaAs layer grown on stoichiometric and Sr-terminated display flatter surfaces where antiphase domains are absent (Fig. 3(c) and (d)). Also, the RMS roughness has improved from 10 nm to as low as 2.7 nm and 0.8 nm for stoichiometric and Sr-rich surfaces, respectively. The stoichiometric termination shows a GaAs film mainly being flat but with small mound grains and holes that contributes to the roughness while GaAs on Sr-terminated STO surface is characterized by a very flat topography with just a few small holes and the lowest roughness a necessary requirement for device fabrication. The streaky RHEED patterns (insets Fig. 3(c) and (d)) are in correspondence with the observed surface features in both samples; (2×4) surface reconstruction is clearly seen at the growth temperature. In particular, the sample with the lowest roughness displays a RHEED pattern whose diffraction features are along a semicircle indicative of a very smooth surface. XRD analysis was

performed for the sample with the optimum surface quality according to AFM. Diffraction peaks are clearly observed from relaxed (2 0 0) STO planes and relaxed (2 0 0) and (4 0 0) GaAs lattice planes (Fig. 4). The wafer miscut inhibits the detection of the Si(4 0 0) planes since the Bragg condition is no longer satisfied in this orientation of the substrate.

We observe, that the best results for surface roughness (0.8 nm) are obtained for GaAs films grown on a Sr-terminated STO buffer layer for a 1.5 μm thick layer on Si(0 0 1) with a 4° miscut in the ⟨1 1 0⟩ direction (Fig. 5). As mentioned before, the crystalline quality and surface morphology of the GaAs epilayer depends strongly on the surface energy of the STO film which is governed by the surface termination. In order for GaAs to wet the STO surface properly leading eventually to a 2D growth mode, the surface energy of the STO surface should be greater than the sum of the GaAs surface energy and the interface energy [16]. The Sr-terminated STO provides enough energy to the surface to exceed this sum, leading to wetting of the GaAs layer and subsequent layer-by-layer growth responsible for high crystalline quality and optimum surface quality. As compared to the Ti-terminated STO, the surface energy is not enough to overcome this sum and leads to the formation of polycrystalline films which do not exhibit the 2D growth mode and are much rougher than the Sr-terminated case.

For the integration of GaSb onto silicon needed for the development of high mobility transistors in the next generation CMOS applications, the GaAs/STO/Si virtual substrate platform was used.
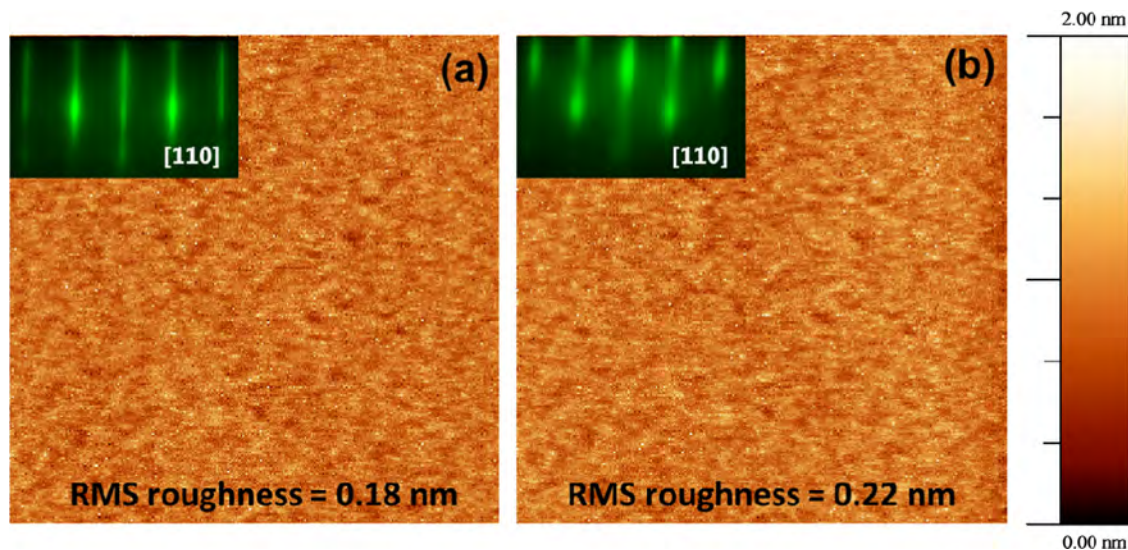
Fig. 1. AFM micrographs of 10 nm STO films grown on (a) nominal Si(0 0 1) substrate and (b) vicinal 4° miscut Si(0 0 1) towards ⟨1 1 0⟩ showing extremely low values of RMS roughness. Inset: RHEED patterns along the [1 1 0] direction for each case.
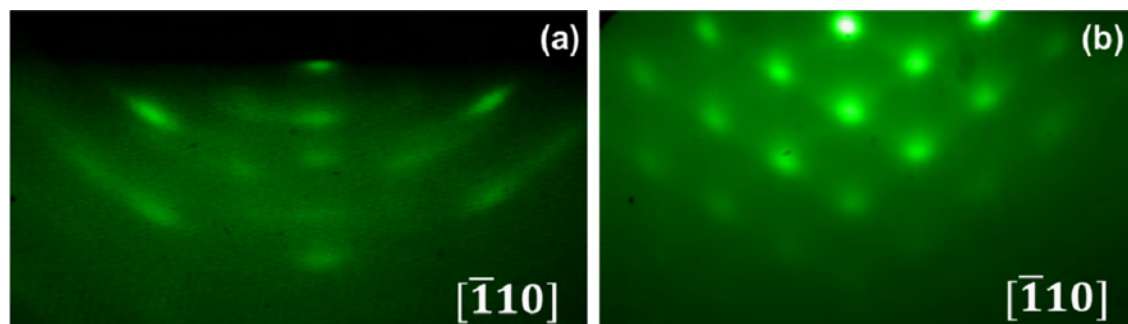
Fig. 2. RHEED patterns observed along the [$\bar{1}$ 1 0] direction during the GaAs nucleation layer growth on (a) Ti-terminated STO and (b) Sr-terminated STO.
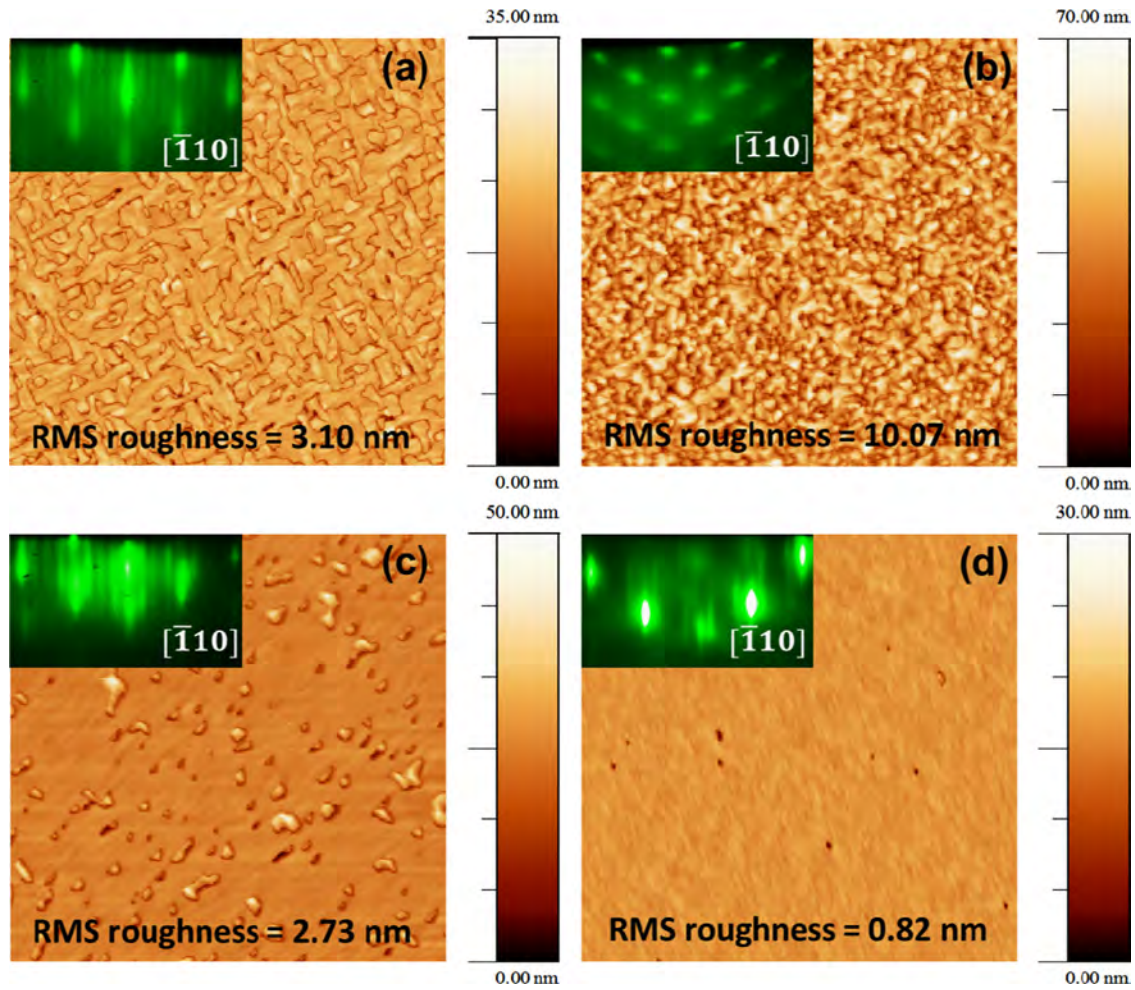
Fig. 3. AFM scans of 10 μm × 10 μm areas of the GaAs film surface on (a) nominal STO/Si(0 0 1) (b) Ti-terminated STO/miscut Si(0 0 1) (c) stoichiometric STO/miscut Si(0 0 1) (d) Sr-terminated STO/miscut Si(0 0 1). Inset: RHEED patterns along the [$\bar{1}$ 1 0] direction for each case.
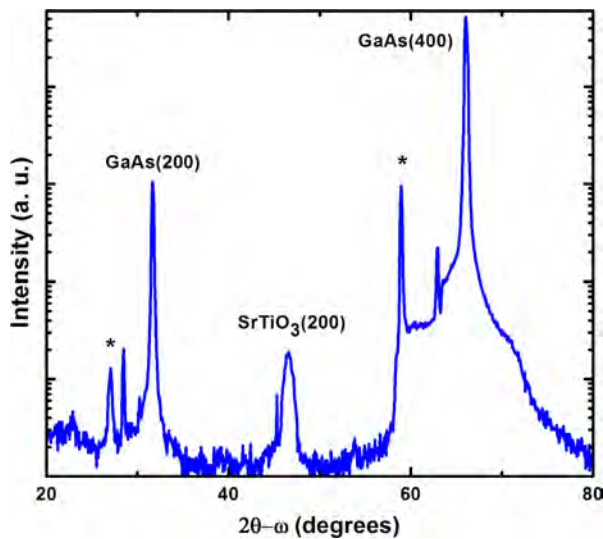
Fig. 4. Coupled 2Theta-omega XRD scan for GaAs grown on Sr-terminated STO/miscut Si(0 0 1) substrate. The symbol "*" represents the peaks arising from the Cu-k_β X-ray emission. The extra sharp peaks are related to instrument noise.

Fig. 5. The effect of STO surface termination and the thickness of the GaAs epilayer on the final surface quality of the GaAs in terms of RMS roughness using AFM.

Here a buffer layer of GaAs was first grown onto the GaAs/SrTiO₃/Si(0 0 1) virtual substrate with a 4° miscut in the ⟨1 1 0⟩ direction leading to a clear (2 × 4) reconstruction at a substrate temperature of 580 °C. The surface was then Ga-stabilized leading to a (4 × 2)

reconstruction by closing the As shutter. At this point, the introduction of Sb flux leads to a (2 × 8) reconstruction indicating atomic packing instead of tetragonal distortion, resulting in 90° pure edge dislocations for the formation of the IMF dislocation array. The substrate was then cooled down to 510 °C while
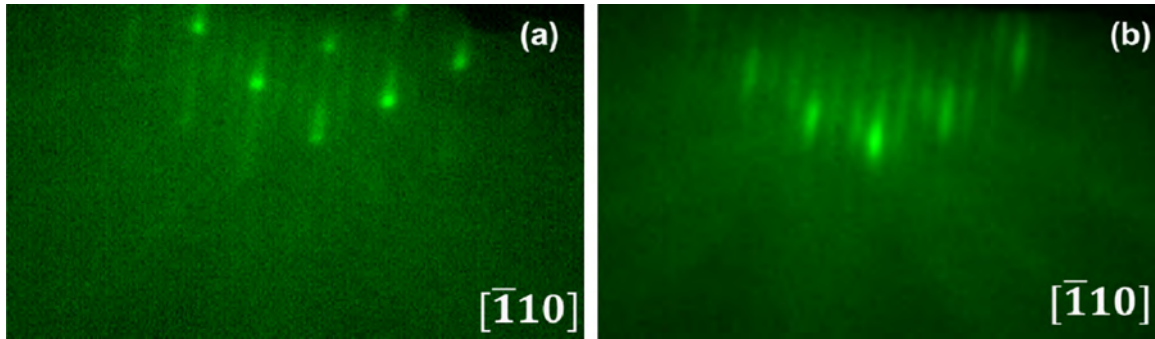
Fig. 6. RHEED patterns observed along the $[\bar{1}\,1\,0]$ direction during the GaSb growth on Ga-rich GaAs surface (a) initial stages showing GaSb islands and 2D growth and (b) (1×3) reconstruction after 50 nm GaSb showing two-dimensional growth.
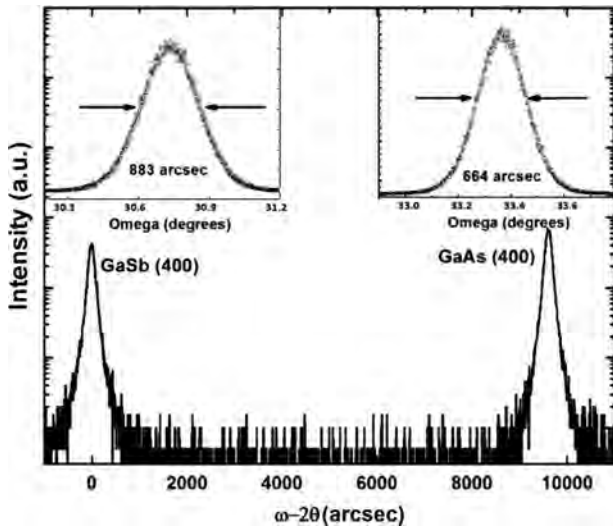
Fig. 7. Triple-axis omega-2theta scan for GaAs(4 0 0) and GaSb(4 0 0) showing complete relaxation of the GaSb epilayer and narrow FWHM for both peaks indicating high crystalline quality layers. Inset: Rocking curves for GaSb and GaAs (4 0 0) peaks.
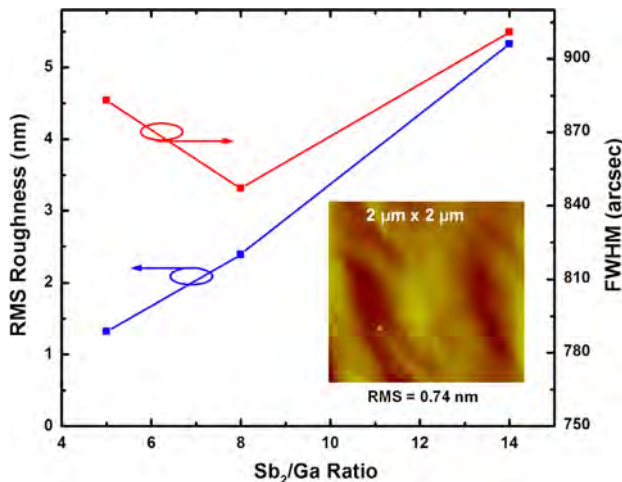
Fig. 8. RMS surface roughness and GaSb(4 0 0) rocking curve FWHM mapped as a function of Sb$_2$/Ga flux ratio. Inset: AFM micrograph of a 2 μm × 2 μm area showing extremely smooth surface quality for a flux ratio of 5.

maintaining the (2×8), and the GaSb deposition was then resumed with the growth showing Stranski–Krastanov (SK) mode as observed in the RHEED patterns for Fig. 6. Fig. 6(a) shows island growth after an initial thin layer of GaSb and as growth commences, the islands coalesce and the RHEED transforms into a

clear (1×3) surface reconstruction depicting layer by layer growth as in Fig. 6(b).

Fig. 7 shows the triple-axis omega-2theta scan for the GaAs (4 0 0) and GaSb(4 0 0) peaks which reveals a completely relaxed GaSb layer with respect to the underlying GaAs. The inset for this figure shows the respective omega rocking curves for GaSb and GaAs with FWHM values of 883 arcsecs and 664 arcsecs respectively indicating high crystalline quality with low density of dislocations in these films. To optimize the parameters for high quality growth of GaSb on the silicon-based virtual substrates, different V–III flux ratios were used; this was determined by measuring the beam equivalent pressures (BEP) using an ion gauge. Fig. 8 summarizes the rocking curve FWHM of the GaSb (4 0 0) peaks as a function of Sb/Ga flux ratio. AFM scans were also performed for all the samples to determine the growth parameters needed to produce the lowest RMS roughness, also shown in Fig. 8. The data shows that the minimum surface roughness was obtained for a V–III flux ratio of 5 and the optimum FWHM was obtained for a flux ratio 8 suggesting that a flux ratio window is available growth window exists for high surface and epilayer quality.

4. Conclusion

We have successfully demonstrated high quality growth of GaAs on SrTiO$_3$/Si substrates using solid-source MBE. The crystalline and surface quality of the GaAs films were monitored as a function of the surface termination of the STO layer. The Sr-terminated STO surface has sufficient surface energy to allow for wetting and 2D growth of the GaAs film and produces the best surface morphologies. Using the GaAs/STO/Si wafers as virtual substrates, GaSb films were grown on the Ga-rich GaAs surface via the IMF array technique. The growth of GaSb was optimized to achieve films with high crystalline quality and extremely low RMS surface roughness values using AFM. Successful monolithic integration of GaAs and GaSb on Si can lead to future III-V low cost CMOS devices as well as multifunctional devices on a single Si chip.

Acknowledgements

References

[1] Taur Yuan, D.A. Buchanan, Chen Wei, D.J. Frank, K.E. Ismail, Lo Shih-Hsien, G.A. Sai-Halasz, R.G. Viswanathan, H.J.C. Wann, S.J. Wind, Wong Hon-Sum, Proc. IEEE 85 (4) (1997) 486.

[2] Jesus A. del Alamo, Nature 479 (7373) (2011) 317.
[3] S.H. Huang, G. Balakrishnan, A. Khoshakhlagh, L.R. Dawson, D.L. Huffaker, Appl. Phys. Lett. 93 (7) (2008) 3.
[4] T. Soga, S. Hattori, S. Sakai, M. Takeyasu, M. Umeno, J. Appl. Phys. 57 (10) (1985) 4578.
[5] Y. Itoh, T. Nishioka, A. Yamamoto, M. Yamaguchi, Appl. Phys. Lett. 52 (19) (1988) 1617.
[6] R. Droopad, Z.Y. Yu, H. Li, Y. Liang, C. Overgaard, A. Demkov, X.D. Zhang, K. Moore, K. Eisenbeiser, M. Hu, J. Curless, J. Finder, J. Cryst. Growth 251 (1–4) (2003) 638.
[7] K. Eisenbeiser, R. Emrick, R. Droopad, Z. Yu, J. Finder, S. Rockwell, J. Holmes, C. Overgaard, W. Ooms, IEEE Electron Device Lett. 23 (6) (2002) 300.
[8] L. Largeau, J. Cheng, P. Regreny, G. Patriarche, A. Benamrouche, Y. Robach, M. Gendry, G. Hollinger, G. Saint-Girons, Appl. Phys. Lett. 95 (1) (2009) 011907.
[9] A.S. Licht, D.F. Demeo, J.B. Rodriguez, T.E. Vandervelde, in: A. Freundlich, J.F. Guillemoles (Eds.), Physics, Simulation, and Photonic Engineering of Photovoltaic Devices III, vol. 8981, Spie-Int Soc Optical Engineering, Bellingham, 2014.
[10] E.H. Aifer, E.M. Jackson, G. Boishin, L.J. Whitman, I. Vurgaftman, J.R. Meyer, J.C. Culbertson, B.R. Bennett, Appl. Phys. Lett. 82 (25) (2003) 4411.
[11] B.R. Bennett, R. Magno, J.B. Boos, W. Kruppa, M.G. Ancona, Solid-State Electron. 49 (12) (2005) 1875.
[12] G. Balakrishnan, S. Huang, L.R. Dawson, Y.C. Xin, P. Conlin, D.L. Huffaker, Appl. Phys. Lett. 86 (3) (2005) 3.
[13] D. Pawlik, B. Romanczyk, P. Thomas, S. Rommel, M. Edirisooriya, R. Contreras-Guerrero, R. Droopad, W.Y. Loh, M.H. Wong, K. Majumdar, W.E. Wang, P.D. Kirsch, R. Jammy, Int. Electron Devices Meet. (IEDM) (2012) 27.1.1.
[14] Wei Yi, Xiaoming Hu, Yong Liang, D.C. Jordan, Brad Craigo, Ravi Droopad, Z. Yu, Alex Demkov, John L. Edwards, William J. Ooms, J. Vac. Sci. Technol. B: Microelectron. Nanometer Struct. 20 (4) (2002) 1402.
[15] S.H. Huang, G. Balakrishnan, D.L. Huffaker, J. Nanosci. Nanotechnol. 11 (6) (2011) 5108.
[16] X. Zhang, A.A. Demkov, Hao Li, X. Hu, Yi Wei, J. Kulik, Phys. Rev. B 68 (12) (2003) 125323.
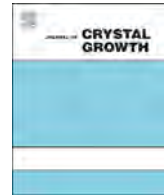
Theoretical and experimental study of highly textured GaAs on silicon using a graphene buffer layer

CrossMark

Yazeed Alaskar [a,b,1], Shamsul Arafin [a,1], Qiyin Lin [c], Darshana Wickramaratne [d], Jeff McKay [e], Andrew G. Norman [f], Zhi Zhang [g], Luchi Yao [h], Feng Ding [i], Jin Zou [g], Mark S. Goorsky [e], Roger K. Lake [d], Mark A. Zurbuchen [a], Kang L. Wang [a,*]

[a] Device Research Laboratory, Department of Electrical Engineering, University of California at Los Angeles, CA 90095, USA
[b] National Nanotechnology Research Center, King Abdulaziz City for Science and Technology, Riyadh 11442, Saudi Arabia
[c] Laboratory for Electron and X-ray Instrumentation, University of California at Irvine, CA 92697, USA
[d] Laboratory for Terahertz and Terascale Electronics, Department of Electrical and Computer Engineering University of California at Riverside, CA 92521, USA
[e] Department of Materials Science and Engineering, University of California at Los Angeles, CA 90095, USA
[f] National Renewable Energy Laboratory, Denver, CO 80401, USA
[g] Materials Engineering, The University of Queensland, St. Lucia, Qld 4072, Australia
[h] Shanghai Institute of Technical Physics, Chinese Academy of Science, Shanghai 200083, China
[i] Institute of Textiles and Clothing, Hong Kong Polytechnic University, Hong Kong, China

ARTICLE INFO

ABSTRACT

A novel heteroepitaxial growth technique, quasi-van der Waals epitaxy, promises the ability to deposit three-dimensional GaAs materials on silicon using two-dimensional graphene as a buffer layer by overcoming the lattice and thermal expansion mismatch. In this study, density functional theory (DFT) simulations were performed to understand the interactions at the GaAs/graphene hetero-interface as well as the growth orientations of GaAs on graphene. To develop a better understanding of the molecular beam epitaxy-grown GaAs films on graphene, samples were characterized by x-ray diffraction (θ–2θ scan, ω-scan, grazing incidence XRD and pole figure measurement) and transmission electron microscopy. The realizations of smooth GaAs films with a strong (111) oriented fiber-texture on graphene/silicon using this deposition technique are a milestone towards an eventual demonstration of the epitaxial growth of GaAs on silicon, which is necessary for integrated photonics application.

1. Introduction

Since the proposed concept and first experimental realization [1], van der Waals epitaxy (vdWE) has gained significant momentum within the research community. Recently, vdWE is viewed as a prospective alternative route of heteroepitaxy by which hetero-structures even with a lattice mismatch of as high as 40% can be grown with reasonably good crystal quality [2]. Although the original concept of vdWE was realized using two-dimensional (2D) layered semiconductors, such as $NbSe_2/MoS_2$; the growth of three-dimensional (3D) materials on top of a 2D surface is an extension of this growth idea [3]. This modification of vdWE is often referred to as quasivan der Waals epitaxy (QvdWE) or 3D–2D heteroepitaxy [4].

The epitaxial growth of optoelectronic materials, such as GaAs on silicon substrates, provides a unique opportunity to combine the advantages of superior optical properties with the capabilities of matured silicon technologies. Despite extensive efforts over the last 30 years, there has been little success in the growth of high-quality GaAs on Si. The main obstacles are lattice mismatch, polar-on-non-polar epitaxy, and thermal expansion mismatch between GaAs and Si [5,6]. Due to such intrinsic material-related problems, the grown GaAs thin films on Si are still far below the technologically acceptable limit, resulting poor performance in the devices made of such materials. In this regard, QvdWE could be considered as a method to overcome such problems. This technique employs layered two-dimensional materials as buffer layers which are self-passivated and inert, indicating a weak vdW interaction between the overlying–3D–semiconductor and the 2D-layer.

Among the large family of vdW materials, graphene, a single layer of sp^2-bonded carbon atoms, a thermally-stable material with high-decomposition temperature, could be an ideal choice as buffer layer material. Furthermore, due to its excellent optical

* Corresponding author.
  E-mail addresses: sarafin@ucla.edu (S. Arafin), wang@seas.ucla.edu (K.L. Wang).
[1] These authors contributed equally to this work.
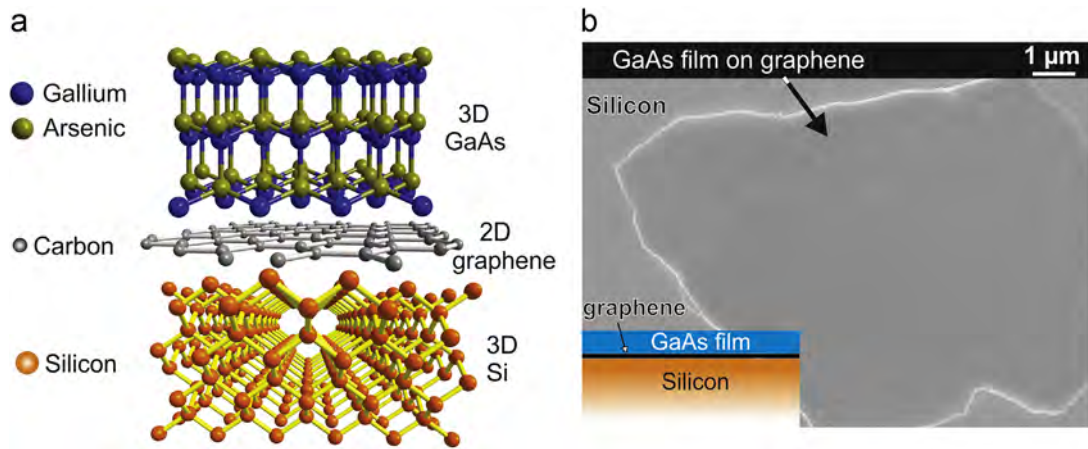
Fig. 1. (a) Atomic geometry of GaAs/graphene/Si, where GaAs and graphene are attached to each other by van der Waals interactions. (b) SEM plan-view image of the as-grown GaAs thin films on graphite flakes exfoliated atop Si (001) substrates, showing a smooth surface morphology.

transparency and electrical conductivity, graphene is a promising substrate for GaAs-based optoelectronic devices [7,8]. Hence, low-resistive, transparent and flexible ohmic contact could be formed on those devices.

A few experimental investigations [4,9,10] have already been reported on the growth of GaAs nanowires on Si using graphene. However, successful operation of nanowire-based devices is impeded by several intrinsic challenges which are primarily associated with the cylindrical geometry of NWs [11]. Thus far, nanowires still have not turned out to be the proper alternative of thin-film, when optical and electrical device characteristics are considered.

Using a 2D graphene buffer layer, the epitaxial growth mode of 3D GaAs materials on silicon substrate is shown schematically in Fig. 1(a) through a covalent bond diagram of the corresponding materials. GaAs which has a zinc-blende cubic crystal structure interacts with the underlying graphene layer with a honeycomb lattice structure via vdW forces. Fig. 1(b) shows an SEM image of molecular beam epitaxy (MBE) grown smooth GaAs films grown on gallium-terminated graphitic flakes lying on silicon substrate. Despite an ultrasmooth morphology of such GaAs films, the low adsorption and migration energies of gallium and arsenic atoms on graphene result in cluster-growth mode during crystallization of GaAs films at an elevated temperature. Details on the growth process and the associated physics can be found elsewhere [12].

2. Theoretical investigation

Density functional theory (DFT) calculations within the Perdew–Burke–Ernzerhof (PBE) type generalized gradient approximation (GGA) framework as implemented in the Vienna Abinitio Simulation Package (VASP) [13] were performed. Using a semi-empirical correction to the Kohn–Sham energies, vdW interactions were accounted for in all calculations [14]. A Monkhorst–Pack scheme was adopted to integrate over the Brillouin zone with a k-mesh $9 \times 9 \times 1$. A plane-wave basis kinetic energy cutoff of 400 eV was used. All structures are optimized until the largest force on the atoms is less than 0.01 eV/Å.

2.1. VdW hetero-interface study

The interface between zinc-blende (ZB) and wurtzite (WZ) GaAs on graphene is compared using ab-initio calculations. A $4 \times 4 \times 1$ graphene supercell is used with a $5 \times 5 \times 1$ GaAs supercell. The graphene/GaAs interfaces are Ga terminated. To saturate the dangling bonds pseudo-hydrogen atoms with fractional charge

Table 1
Binding energy values of zinc-blende and wurtzite GaAs surfaces on graphene.

	Binding energy/C atom (meV)	
	Zinc blende GaAs (111)	Wurtzite GaAs
Pristine	−43.21	−35.11
Ga-vacancy	−43.18	−33.98

of 0.75e were used. The binding energy $E_{binding}$ is calculated using the following expression:

$$E_{binding} = E_{graphene/GaAs} - E_{graphene} - E_{GaAs}$$

where $E_{graphene/GaAs}$ is the ground state energy of the graphene/GaAs heterostructure, $E_{graphene}$ is the ground state energy of the $4 \times 4 \times 1$ graphene supercell and E_{GaAs} is the ground state energy of the GaAs supercell.

To understand the nature of the heterointerface, the binding energy between graphene and the ZB and WZ GaAs surfaces is calculated. The binding energy describes the strength of the interactions at the epitaxial interface. Table 1 summarizes the binding energies between ZB GaAs (111) surface and WZ GaAs (0001) surface with graphene. The energies for a pristine interface and in the presence of a single point defect are compared. A point defect is introduced with the removal of a single Ga atom at the Ga-terminated graphene/GaAs interface.

Calculations of the binding energy indicate the ZB GaAs (111) phase is the preferred orientation on graphene; the ground state energy for this configuration is 8.1 meV/C-atom lower than the energy of WZ GaAs phase on graphene. With the presence of a single point-defect at the interface; the ZB GaAs phase remains the preferred orientation. Prior studies have demonstrated that the epitaxial relationship formed by GaAs and graphene can be affected by but is not limited to the orientation, strain, defect density at the interface [4]. Further calculations would elucidate which of these mechanisms governs the preferred GaAs phase when epitaxially grown atop graphene.

Interfaces dominated by vdW forces are known to lead to turbostratically misoriented interfaces. Hence, the effect of misorientation between the graphene–GaAs interface on the binding energy is also investigated. The binding energy is maximum for the misoriented structure and is minimum for the unrotated graphene/GaAs structure. The binding energies calculated as a function of rotation angle in Fig. 2 are the same order of magnitude as the binding energy of graphene on Cu (111) surfaces [15], where the interactions at this interface are also dominated by vdW forces. This
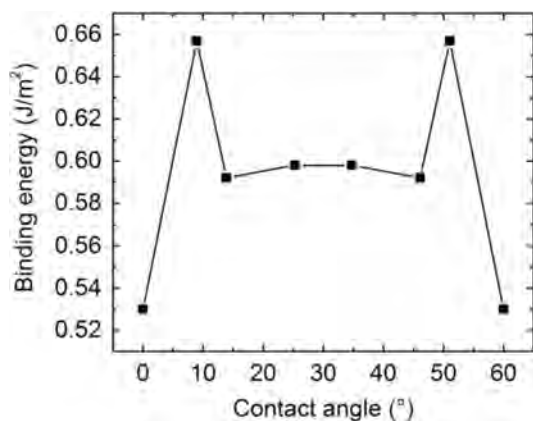
Fig. 2. Binding energy of the graphene/GaAs interface as a function of misorientation angle. The calculated binding energies are normalized with the planar area of the supercell used.

would also suggest that the graphene–GaAs interface is also governed by vdW interactions. The stronger binding energy in the misoriented structure suggests the strain in this structure is minimized. Furthermore, the higher binding energy would also suggest that the graphene–GaAs interface is likely to be misaligned when an epitaxial interface is formed, with an unrotated interface being the least preferred orientation configuration. The energy barrier to transition from a rotated interface to an unrotated interface in the graphene/GaAs structure can be as large as $0.13\ J/m^2$. For the supercells simulated, the total energy difference between the unrotated structure and the rotated structures is greater than the thermal energy k_BT at room temperature. This would suggest the interface between graphene and GaAs may remain misaligned at 300 K and higher growth temperatures as well.

2.2. Alternative QvdWE buffer layer materials

As wafer-scale growth of single monolayers of alternative vdW materials, such as h-BN and MoS_2 [16] approach the same quality as graphene, we consider the possibility of using these prototypical vdW materials as a buffer layer for our quasi-vdW epitaxy approach. Adsorption energy calculations were used to determine if monolayer and bilayer MoS_2 and h-BN would act as suitable buffer layers (in addition to graphene) to achieve QvdWE of GaAs. For calculations of the adsorption energy of Ga, Al, In and As on hBN and MoS_2, a $4 \times 4 \times 1$ supercell of monolayer (1L) MoS_2 and monolayer and bilayer (2L) hBN was used. For MoS_2, the 4p, 5s, 4d and 3s, 3p orbitals of Mo and S respectively are treated as valence in the PBE functional. For h-BN, the 2s, 2p orbitals of B and N are treated as valence. Calculation details for the adsorption energy and the Ga, Al, As and In pseudo-potentials used have been detailed in our previous study of adsorption energy of these elements on graphene [12]. Our prior studies of Al, Ga, As and In adsorption on graphene have shown that each element binds with approximately the same binding energy on to single layer and bilayer graphene; the favored binding site on the honeycomb lattice of graphene is unique to each element. Hence, the binding energy of the defect free GaAs surface is determined by the orientation of the Ga and As atoms above the honeycomb lattice. Table 2 summarizes the adsorption energy values for Al, Ga, As and In on h-BN and MoS_2.

The adsorption energy at each binding site for monolayer MoS_2 and monolayer and bilayer h-BN is approximately an order of magnitude lower than the adsorption energies calculated for Ga, Al, In and As on graphene. The strength of the adsorption energy can be characterized by the hybridization of the adsorbant elements on the vdW buffer layer material. Fig. 3 illustrates the projected

Table 2
Adsorption energy of Ga, Al, In and As on monolayer (1L) and bilayer (2L) h-BN and MoS_2. The favored adsorption site for each element and vdW material is listed in parentheses; for h-BN the favored site is when the adatom is on top of nitrogen (TN) or on top of the boron–nitrogen bond (B) and for MoS_2 the favored site is when the adatom is on top of the sulfur atom (T).

Adsorption energy			
	1L h-BN (meV/atom)	2L h-BN (meV/atom)	1L-MoS_2 (meV/atom)
Ga	131.6 (TN)	134.3 (TN)	234.6 (T)
Al	135.1 (TN)	101.1 (TN)	237.4 (T)
In	66.9 (B)	85.1 (TN)	573.1 (T)
As	296.9 (B)	341.5 (TN)	527.8 (T)
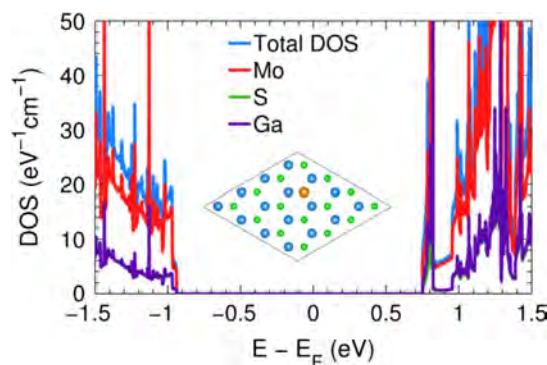
Fig. 3. Projected density of states for Ga adsorbed on the T-site of the MoS_2 supercell, total density of states (blue), Mo states (red), S states (green) and Ga states (magenta). Inset: Schematic of $4 \times 4 \times 1$ MoS_2 supercell with Ga adatom over S atom. (For interpretation of the references to color in this figure legend, the reader is referred to the web version of this article.)

density of states of a Ga atom adsorbed on the T-site of a monolayer MoS_2 supercell. The sp^2 orbitals of Ga are weakly hybridized with the 4d and 3p orbitals of Mo and S respectively. This is evidenced by the weak overlap of the Ga orbitals with the Mo and S orbitals of the valence band in MoS_2. In contrast, strong hybridization between the sp^2 orbitals of Ga with the sp^2 orbitals of carbon in graphene results in larger adsorption energies. The adsorption of Ga, Al, In and As atoms on 1L and 2L h-BN also results in weak hybridization with the sp^2 orbitals of boron and nitrogen which leads to lower adsorption energies when compared to graphene. The lower adsorption energies of Ga, Al, As and In atoms on the MoS_2 and h-BN surfaces would result in these adatoms being poorly anchored during the growth process, which in turn would lead to degradation in the morphology of the GaAs film. These initial calculations suggest that graphene remains an ideal candidate as a buffer material to enable vdW epitaxy when compared to h-BN and MoS_2.

3. Experimental procedure

X-ray diffraction experiments were performed at room temperature on a Rigaku SmartLab diffractometer equipped with a high accuracy/resolution four circle theta–theta goniometer, using a Cu Kα radiation and scintillation detector. The nearly parallel incident beam was collimated using a parabolic multilayer mirror. Sample was mounted horizontally on a motorized high precision Z-stage and Phi attachment. Full pole figure data was collected using an in-plane diffraction attachment with the axis β scanned from 0° to 360° at 50°/min speed at each α angle (step size 0.5° ranging from 0° to 90°). The incident slit (IS), length limit silts (H), and receiving slits (RS1/RS2) were 1 mm, 5 mm, 2 mm and 2 mm, respectively. For grazing
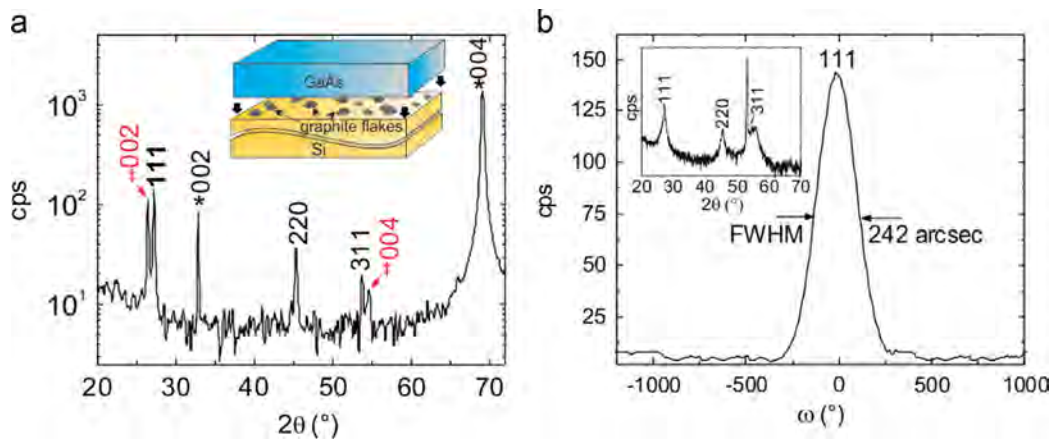
Fig. 4. XRD analyses of as-grown GaAs on exfoliated graphite flakes, (a) HRXRD θ–2θ scan, where multiple peaks correspond to zinc–blende (111), (220) and (311) GaAs, confirming polycrystallinity of the grown films. The (002) and (004) graphite peaks marked with doubledaggers (‡) indicate the multidomain graphite layers. The (002) and (004) peaks from Si (001) substrate are marked with asterisks (*). (b) The rocking curve of (111) GaAs peak, GIXRD 2θ scan profiles are shown in the inset. (For interpretation of the references to color in this figure, the reader is referred to the web version of this article.)
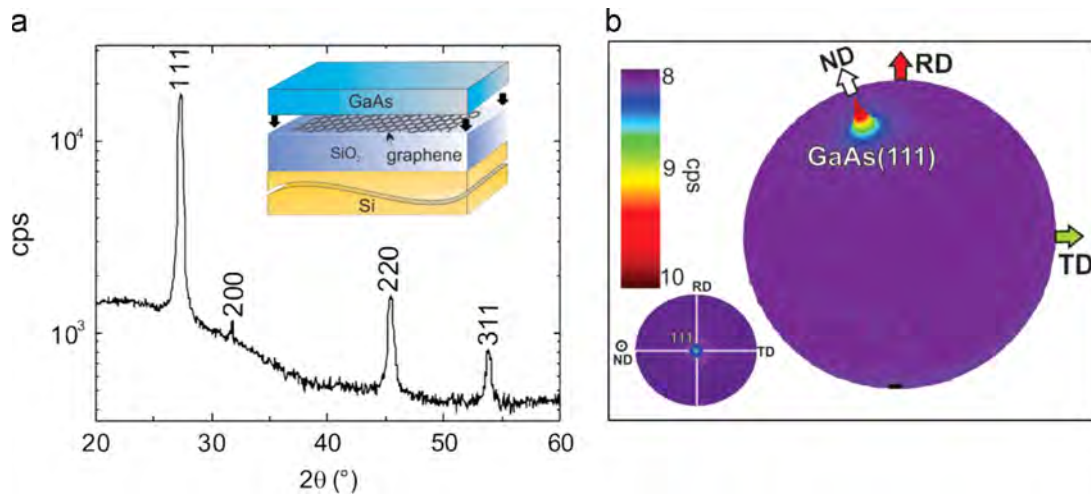
Fig. 5. XRD analysis and pole figure of as-grown GaAs on CVD graphene, (a) HRXRD θ–2θ scan, where multiple peaks correspond to zinc–blende (111), (200), (220) and (311) GaAs. (b) The 3D pole figure of (111) GaAs, showing a preferred orientation of the grown films. The stereographic projection of the (111) pole figure is shown as inset. (For interpretation of the references to color in this figure legend, the reader is referred to the web version of this article.)

incident x-ray diffraction (GIXRD), these slit conditions were used: IS=0.2 mm, H=5.0 mm, RS1=RS2=20.0 mm. The incident beam angle was fixed at 0.3°, while the 2θ arm was scanned from 20° to 60° at speed of 0.3°/min with its step size of 0.05°. As for radial $2\theta/\omega$-scan, the measurement conditions were IS=1.0 mm, H=5 mm, RS=20 mm, while scan speed was 0.5°/min with a step size=0.05°. For both GIXRD and $2\theta/\omega$ measurement, Soller slits were used to reduce the axial divergence of the incident and diffraction x-ray beam to 5°, and a 0.5° parallel slit analyzer (PSA) was used to improve 2θ angular resolution.

The cross-sectional specimen for transmission electron microscopy analysis was prepared by hand polishing using a tripod technique and final thinning using a Gatan precision ion polishing system (PIPS) (Gatan Model 691, operated at 4 keV). The structural characteristics of as-grown GaAs were then investigated using a Tecnai F20, operated at 200 keV.

4. Experimental results

Fig. 4(a) shows the out-of-plane XRD θ–2θ scan pattern for GaAs thin films grown on exfoliated graphite flakes over a 2θ range of 20–70°. The as–grown GaAs films exhibit polycrystalline nature, which

is confirmed by (111), (220) and (311) diffraction peaks. Apart from these three film-generating diffraction peaks, the (002) and (004) silicon substrate peaks are observed in the scan. The forbidden Si 002 peak at 2θ=32.9° is attributed to multiple diffractions (Umweganregung). Graphite (002) and (004) reflections are also found as labeled by the red-colored text in Fig. 4(a). The crystalline quality of the thin GaAs film on Ga-terminated graphene was characterized by XRD rocking-curve scans as shown in Fig. 4(b). The FWHM for the rocking curve of the GaAs (111) is 242 arcsec (0.067°), indicating good crystal quality for this orientation (and likely epitaxy). We note that the rocking curves of other surface-normal planes showed broad peaks which is reasonable since our vdW regions covered only a small percentage of an otherwise polycrystalline layer, yielding a strong background signal from the (majority) untemplated regions. The low-temperature grown GaAs on the flakes exhibits a strong (111) preferred-orientation texture. This is an essential step towards demonstration of epitaxy. If larger graphite flakes were used, a clear correlation between the graphene and the fiber texture could be confirmed by a featureless Φ-scan for an asymmetric peak, such as (115). As shown in the inset of Fig. 4(b), the GIXRD 2θ scan exhibits peaks at the expected locations for GaAs films, corresponding to the GaAs (111), (220), and (311), which indicates that the as-grown material is randomly oriented
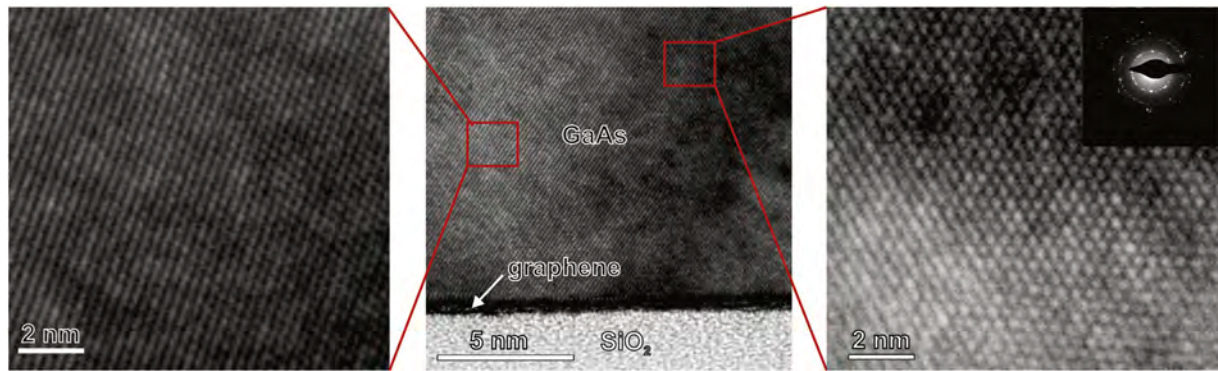
Fig. 6. Cross-sectional TEM image near the interface between GaAs film and CVDgraphene/SiO₂. Magnified TEM images of the solid red-square areas. To maximize ease of interpretation, the film growth direction is along the vertical direction of images. The corresponding SAED ring pattern is shown as inset.

polycrystalline. Note that there are two strong unlabeled peaks at $2\theta = 53°$ and $56.3°$ for these samples which could be due to graphitic regions.

To assess the quality of as-grown film and to benchmark our results, the full width at half-maximum (FWHM) of the XRD rocking curve could be compared with the prior reports of FWHM values obtained from GaAs on Si using conventional direct heteroepitaxy. By employing several direct growth approaches [17–20], micron thick buffer layer was deposited on silicon in order to obtain a FWHM value as low as 242 arcsec. However, the as-grown GaAs film via vdWE achieves the same FWHM with film thicknesses on the order of 25 nm. The two orders of magnitude improvement in the quality of our GaAs films can be attributed to the graphene buffer layer mitigating lattice and thermal mismatch between GaAs and the underlying substrate.

To verify crystalline quality of the material, the out-of-plane XRD θ–2θ scan pattern was performed for GaAs films grown on large-area CVD graphene over a 2θ range of 20–60°. As shown in Fig. 5(a), the θ–2θ scan is composed of ZB (111), (200), (220) and (311) GaAs peaks with unequal intensities. Therefore, the as-grown GaAs film on CVD graphene is confirmed to be polycrystalline.

The pole-figure has been proven to be one of the most powerful XRD techniques for studying texture in thin films. The strong (111) peak at the center of the pole figure as shown in 3D representation of Fig. 5(b) indicates that the as–grown films are preferably (111)-oriented along the surface normal. Also, the stereographic projection format of such pole figure is shown as an inset in Fig. 5(b). The FWHM of the surface normal peak and the degree of the preferred orientation are calculated to be 1.5° and 2.2%, suggesting strong fiber texture in the GaAs films. In a previous study, it was reported that (111) orientation is highly favored by the underlying graphene layer, exhibiting a triangular lattice symmetry. It should be noted that the XRD θ–2θ scan and pole figure data reported here were collected from the sample where the GaAs growth was performed on a blanket graphene layer sitting on SiO₂/(111)-oriented silicon substrates. This clearly suggests that the silicon substrate will have a negligible influence in defining the orientation of the grown layer.

Selected area electron diffraction (SAED) patterns obtained from the GaAs layer grown on CVD-graphene/SiO₂/Si contain a series of rings, which indicates the presence of a polycrystalline material. Using the diffraction pattern of the single crystal Si substrate as a reference, the lattice plane spacings of the diffraction pattern and the relative intensity of the diffraction rings suggest that a majority of GaAs is grown in the cubic ZB phase. Fig. 6 shows a high-resolution lattice image of an approximately 100 nm thick GaAs layer containing two grains in which a ⟨110⟩ direction is aligned close to parallel to the electron beam (see enlarged areas). The lattice fringe patterns observed are consistent with these grains being ZB in structure which is in good agreement with the theoretical findings. Defects such as microtwins and stacking faults were observed within some of the grains. The typical grain size observed in an approximately 100 nm think GaAs layer was between 20 and 60 nm.

5. Conclusion

In summary, we have reported the detailed theoretical and experimental characterization of MBE-grown GaAs thin films on graphene/silicon substrates using quasi-van der Waals epitaxy, which provides novel insights into the quality of grown material. From the theoretical study, we conclude that graphene as a buffer layer is more suitable than h-BN and MoS₂ in the case of the growth of 3D materials on 2D layered surfaces. By XRD measurements, it is verified that our as-grown GaAs films on graphene/silicon exhibit the polycrystalline nature with a strong [111]-oriented fiber texture. In the study of the GaAs/graphene hetero-interface, GaAs ZB crystal structure is experimentally found to be more stable than WZ GaAs, providing good agreement with the theoretical predictions. Since the CVDgrown graphene itself is polycrystalline, the as-grown materials on top of this 2D buffer layer cannot be single-crystalline. Therefore, future efforts will mainly focus on using single-domain graphene as a buffer layer, leading to single-crystalline GaAs which will serve as a potential and cost-effective route towards heteroepitaxial integration of GaAs on silicon in the developing field of silicon photonics.

References

[1] A. Koma, K. Sunouchi, T. Miyajima, Microelectron. Eng. 2 (1984) 129.
[2] T. Ueno, H. Yamamoto, K. Saiki, A. Koma, Appl. Surf. Sci. 113–114 (1997) 33.
[3] J. Kim, C. Bayram, H. Park, C.W. Cheng, C. Dimitrakopoulos, J.A. Ott, K.B. Reuter, S.W. Bedell, D.K. Sadana, Nat. Commun. 5 (2014) 4836.
[4] A.M. Munshi, D.L. Dheeraj, V.T. Fauske, D.C. Kim, A.T. van Helvoort, B. O. Fimland, H. Weman, Nano Lett. 12 (2012) 4570.

[5] C.-P. Chu, S. Arafin, T. Nie, K. Yao, X. Kou, L. He, C.-Y. Wang, S.-Y. Chen, L.-J. Chen, S.M. Qasim, M.S. BenSaleh, K.L. Wang, Cryst. Growth Des. 14 (2014) 593.

[6] C.-P. Chu, S. Arafin, G. Huang, T. Nie, K.L. Wang, Y. Wang, J. Zou, S.M. Qasim, M.S. BenSaleh, J. Vac. Sci. Technol. B 32 (2014) 02C111.

[7] K.S. Novoselov, Z. Jiang, Y. Zhang, S.V. Morozov, H.L. Stormer, U. Zeitler, J.C. Maan, G.S. Boebinger, P. Kim, A.K. Geim, Science 315 (2007) 1379.

[8] C.H. Lee, Y.J. Kim, Y.J. Hong, S.R. Jeon, S. Bae, B.H. Hong, G.C. Yi, Adv. Mater. 23 (2011) 4614.

[9] P.K. Mohseni, A. Behnam, J.D. Wood, C.D. English, J.W. Lyding, E. Pop, X. Li, Nano Lett. 13 (2013) 1153.

[10] A.M. Munshi, H. Weman, Phys. Status Solidi 7 (2013) 713.

[11] S. Arafin, X. Liu, Z. Mi, J. Nanophotonics 7 (2013) 074599.

[12] Y. Alaskar, S. Arafin, D. Wickramaratne, M.A. Zurbuchen, L. He, J. McKay, Q. Lin, M.S. Goorsky, R.K. Lake, K.L. Wang, Adv. Funct. Mater. 24 (2014) 6629.

[13] G. Kresse, J. Hafner, Phys. Rev. B 47 (1993) 558.

[14] S. Grimme, J. Comput. Chem. 27 (2006) 1787.

[15] X. Shi, Q. Yin, Y. Wei, Carbon 50 (2012) 3055.

[16] Y. Zhan, Z. Liu, S. Najmaei, P.M. Ajayan, J. Lou, Small 8 (2012) 966.

[17] M.E. Groenert, C.W. Leitz, A.J. Pitera, V. Yang, H. Lee, R.J. Ram, E.A. Fitzgerald, J. Appl. Phys. 93 (2003) 362.

[18] Y. Takano, M. Hisaka, N. Fujii, K. Suzuki, K. Kuwahara, S. Fuke, Appl. Phys. Lett. 73 (1998) 2917.

[19] K. Nozawa, Y. Horikoshi, Jpn. J. Appl. Phys. 30 (1991) 668.

[20] M. Tamura, T. Yodo, T. Saitoh, J. Palmer, J. Cryst. Growth 150 (1995) 654.
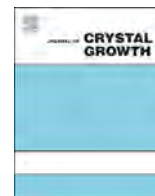
The impact of substrate selection for the controlled growth of graphene by molecular beam epitaxy

T. Schumann, J.M.J. Lopes *, J.M. Wofford, M.H. Oliveira Jr.[1], M. Dubslaff, M. Hanke, U. Jahn, L. Geelhaar, H. Riechert

Paul-Drude-Institut für Festkörperelektronik, Hausvogteiplatz 5–7, 10117 Berlin, Germany

ARTICLE INFO

ABSTRACT

We examine how substrate selection impacts the resulting film properties in graphene growth by molecular beam epitaxy (MBE). Graphene growth on metallic as well as dielectric templates was investigated. We find that MBE offers control over the number of atomic graphene layers regardless of the substrate used. High structural quality could be achieved for graphene prepared on Ni (111) films which were epitaxially grown on MgO (111). For growth either on Al_2O_3 (0001) or on $(6\sqrt{3} \times 6\sqrt{3})R30°$-reconstructed SiC (0001) surfaces, graphene with a higher density of defects is obtained. Interestingly, despite their defective nature, the layers possess a well defined epitaxial relation to the underlying substrate. These results demonstrate the feasibility of MBE as a technique for realizing the scalable synthesis of this two-dimensional crystal on a variety of substrates.

1. Introduction

Graphene, a single layer of carbon atoms arranged in a two-dimensional hexagonal lattice, is widely regarded as a revolutionary material, due primarily to its electronic properties [1–3]. The high charge carrier mobility and the ambipolar field effect measured in graphene are particularly appealing for electronic device applications [4]. Furthermore, it is known that ordered stacks of multiple graphene layers (e.g. bi- or trilayer graphene) also possess intriguing features, such as an electric field and stacking-order-dependent band structure [5–7]. These phenomena are not observed in monolayer graphene and open yet more exciting possibilities, such as the realization of devices with a gate-tunable band gap [7,8].

Hence, in terms of synthesis, a consensus has formed that the growth of high-quality, large-scale graphene films with precise control over the number of atomic layers is critical since it will enable applications where not only mono-, but also few-layer thick films will be required [9]. Although techniques such as SiC surface graphitization [10–12] and chemical vapor deposition (CVD) on Cu [13,14] have proved to be suitable for large-area synthesis, both have inherent drawbacks. The former method is restricted to a single substrate material (which happens currently to be costly). In addition, the controlled growth of a specific

number of graphene layers on SiC with complete thickness homogeneity remains challenging. CVD on Cu produces continuous graphene films which are exclusively one monolayer thick, since the precursor molecules are efficiently cracked only at the original, exposed metal surface. Similar to graphene growth on SiC, despite intensive ongoing research, the controlled formation of uniform few-layer graphene on Cu remains to be demonstrated. In this context, molecular beam epitaxy (MBE) appears to be a promising alternative. MBE is one of the most prominent techniques for the production of high-quality, single-crystal semiconductor films and multilayer heterostructures [15]. MBE typically does not involve catalytic surface processes, and thus holds promise for the growth of one to ∼few graphene layers on a wider variety of substrates, including insulators and semiconductors. Exact deposition rates and sub-monolayer thickness control are additional significant advantages offered by MBE which will be required to achieve well-controlled, layer-by-layer graphene growth.

Although it is a relatively new topic of study within the MBE community, there have been several attempts to prepare graphene by employing this method. Previously examined templates include Si [16,17], SiO_2 [18], SiC [19], Al_2O_3 [17,20–22], Ni [23,24], and mica [18,25]. The various substrates and growth conditions used during synthesis resulted in carbon materials with different structural quality and morphology, ranging from highly disordered sp^2-bonded carbon [16–18] or nanocrystalline (defective) graphene layers [17,20–22], to state-of-the-art quality graphene (either continuous layers [24] or isolated islands [25]). In spite of the apparent discrepancy between results, the collection of existing studies nevertheless already point to the fact that MBE is indeed a

---

* Corresponding author.
    E-mail address: lopes@pdi-berlin.de (J.M.J. Lopes).
[1] Permanent address: Departamento de Física, ICEx, Universidade Federal de Minas Gerais-UFMG, C.P. 702, 31270-901, Belo Horizonte, MG, Brazil.

promising technique for achieving the controlled growth of graphene over large areas. In addition, from a fundamental point of view, MBE is an ideal tool for generating a detailed understanding of nucleation and growth mechanisms due to its compatibility with in situ characterization. This is especially important as graphene growth has developed into a rich research field in its own right. It has already been shown to differ from conventional thin-film epitaxy in significant ways, following mechanisms such as van der Waals epitaxy and growth from below [18,21,24,25]. In this context, it is important to mention other studies regarding graphene growth in UHV (by both physical vapor deposition [PVD] and CVD) which have closely replicated MBE growth conditions. In particular, surface scientists have carefully examined graphene formation on metals such as Ru, Ir, Cu and Au, often using powerful in situ characterization techniques such as low-energy electron microscopy (LEEM). These studies have revealed a rich, complex array of growth phenomena [26–31]. This body of literature – of which the cited references are only a few examples – may not be MBE growth in the strictest terms, but does serve to illustrate the utility of a well-controlled, the UHV growth method in the study of graphene synthesis.

In this contribution we report research aimed at the controlled preparation of graphene layers by MBE. We focus specifically on how the choice of substrate impacts the properties of the resulting graphene film by comparing and contrasting results obtained for growth on three very different surfaces as illustrative examples: Ni (111) films which were epitaxially grown on MgO (111), Al_2O_3 (0001), and SiC (0001) (offering a $(6\sqrt{3} \times 6\sqrt{3})R30°$ C-rich surface reconstruction). These results demonstrate the potential of MBE for the realization of the controlled epitaxial growth of graphene films (mono- to few-layer thick) with substrate flexibility.

2. Experimental

Graphene growth was performed in a dedicated MBE system with a base pressure of 1×10^{-10} mbar. The system is equipped with a solid carbon source composed of a resistively heated highly oriented pyrolytic graphite (HOPG) filament that operates nominally
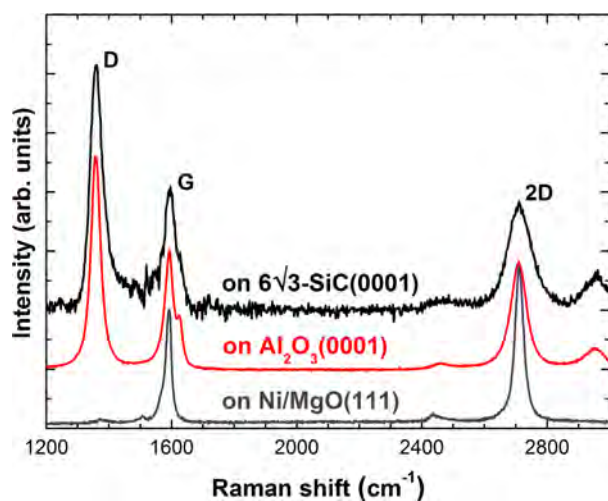
Fig. 1. Raman spectra of MBE grown graphene films on Ni/MgO (111) (gray), Al_2O_3 (0001) (red), and reconstructed $6\sqrt{3}$-SiC (0001) substrates (black). The film grown on Ni/MgO (111) was deposited at a substrate temperature of 765 °C over 120 min (average thickness of 2 MLs) while those on Al_2O_3 and SiC were grown at 900 °C and deposition times of 240 min (average thickness of 1.5 MLs). The intensity is normalized with respect to the G peak, the spectra are offset for visibility, and the substrate related background signal is subtracted from the spectrum recorded on SiC. (For interpretation of the references to color in this figure legend, the reader is referred to the web version of this article.)

between 2200 and 2400 °C. In this temperature range the carbon flux is $\sim 6 \times 10^{12}$ atoms/cm^2 s. All substrates [the Ni/MgO (111) and SiC (0001) were sized 1 cm^2, and Al_2O_3 (0001) were full two-inch wafers] were degassed in a preparation chamber at 350 °C for 30 min before transfer to the growth chamber. Note that all substrates employed a 1 μm thick Ti film (deposited *ex situ* by RF-sputtering) on the backside to allow non-contact radiative heating. In the case of Ni/MgO (111), 150 nm thick epitaxial Ni (111) films were grown on MgO (111) in the same MBE cluster prior to carbon deposition. The 2.490 Å in-plane lattice parameter of the (111) Ni surface closely matches that of graphene. More details about the synthesis of the Ni (111) films can be found elsewhere [24]. For the SiC (0001) substrates, the surface preparation which allows for the creation of a $(6\sqrt{3} \times 6\sqrt{3})R30°$ reconstruction (referred to as $6\sqrt{3}$, for simplicity) is performed *ex situ* at high temperatures (~ 1450 °C) in a RF-furnace prior to introducing the sample to the MBE cluster. The thermal annealing procedures utilized for this can be found in Ref. [32]. The MBE growth of graphene was performed using different growth temperatures and times. The temperature chosen for graphene growth on Ni/MgO (111) was 765 °C, with deposition time ranging from 40 to 200 min. For Al_2O_3 (0001) and $6\sqrt{3}$-SiC (0001) growth temperatures ranging from 900 to 1000 °C were employed, with a growth time of 240 min. The structural properties of the grown films were investigated by Raman spectroscopy. The spectra shown in the next section, which were acquired with a spatial resolution of 1 μm and excitation wavelength of 482 nm, are representative of large-area growth by MBE. Analyses of different surface regions yielded similar results. In addition, scanning electron microscopy (SEM) and grazing-incidence X-ray diffraction (GID) were used to investigate the surface morphology and structure of the samples, respectively.

3. Results and discussions

Raman spectroscopy, which is a commonly accepted proxy for the crystalline quality of graphene [33,34], was used to examine the resulting films. Representative spectra are shown in Fig. 1 for graphene grown on each substrate examined here, with each displaying the characteristic peaks of sp^2-bonded carbon. The appearance of well-defined and intense G and 2D peaks is clear evidence for the formation of graphene. In the case of graphene grown on Ni/MgO (111) (gray spectrum), the negligible intensity of the D peak indicates that extremely few structural defects, such as point vacancies or rotational grain boundaries, are present in the film. This is corroborated by the narrow widths (full widths at half maxima–FWHM) of the G and 2D peaks, $w_G = 17$ cm^{-1} and $w_{2D} = 32$ cm^{-1}, which show the presence of a well-ordered crystal structure with a degree of perfection similar to that observed in exfoliated graphene flakes [33,34] and CVD-prepared layers [14]. The high crystalline quality of the graphene is consistent with its relatively low nucleation density on Ni/MgO (111) substrates (Fig. 4a), which is facilitated by significant carbon adatom diffusion on the metallic surface. This leads to a correspondingly low line-density of grain boundaries, regardless of the crystallographic orientation of the individual domains.

Raman spectra from graphene grown on Al_2O_3 (Fig. 1, red) and $6\sqrt{3}$-SiC (black) both reveal similar features. The intense defect-related D peaks but well-defined and symmetric G and 2D peaks in spectra from films grown on both dielectric substrates are characteristic of defective graphene [34,35]. The peak intensity ratios I_D/I_G are comparable for both samples (1.9 for Al_2O_3 and 2.1 for $6\sqrt{3}$-SiC). However, the FWHM of the peaks are considerably lower in case for growth on Al_2O_3 ($w_D = 34$ cm^{-1}, $w_G = 32$ cm^{-1}, and $w_{2D} = 56$ cm^{-1}) when compared with graphene synthesized on the $6\sqrt{3}$-SiC ($w_D = 43$ cm^{-1}, $w_G = 42$ cm^{-1}, and $w_{2D} = 75$ cm^{-1}). Empirical

estimates yield lateral domain sizes of few tens of nanometer in both cases [21,32].

This Raman analysis suggests that growth on Al_2O_3 (0001) yields graphene with a slightly higher structural quality than $6\sqrt{3}$-SiC (0001). These two substrates were chosen to investigate graphene growth directly on insulating surfaces because – in addition to the high growth temperatures their excellent thermal stability allows – their hexagonal surface symmetry may be conducive to graphene epitaxy. The $6\sqrt{3}$-SiC (0001) surface is a carbon rich reconstruction of the Si-face of hexagonal SiC. It is isomorphic to graphene, i.e. it possesses the same honeycomb carbon lattice structure and a similar lattice parameter as graphene [36,37] (note, however, it has about 30% of its atoms covalently bound to the SiC substrate [38]). Therefore, due to its similarities to graphene, such a surface can be employed as a template to investigate the quasi-homoepitaxial growth of graphene. Al_2O_3 (0001), on the other hand, has a hexagonal surface symmetry with a lattice parameter (4.750 Å) approximately twice that of graphene (2.461 Å) [39], making growth on this substrate heteroepitaxial. Thus, perhaps paradoxically, heteroepitaxy is more conducive to the formation of high-quality graphene (fewer defects/less disorder) in this instance than quasi-homoepitaxial growth. A possible explanation for the lower quality of graphene resulting from growth on $6\sqrt{3}$-SiC (0001) and Al_2O_3 (0001) (in comparison to films obtained on Ni/MgO (111) substrates) is an absence of epitaxial ordering with respect to the substrate. The formation of small, defective graphene crystals with random crystallographic orientations – which is usually not observed for graphene grown on metals [24,26,31] – would represent a fundamental obstacle to the growth of high-quality material on insulators. However, if the graphene nanocrystals are epitaxially aligned with the substrate they can coalesce into a single domain. Strict epitaxy may thus be a prerequisite for high-quality growth on dielectrics.

In order to investigate this aspect of graphene growth on these substrates we have conducted grazing incidence diffraction (GID) at beamline ID10 at the European Synchrotron Radiation Facility (ESRF) in Grenoble using an X-ray energy of 10 keV. This highly surface sensitive technique provides the possibility of not only measuring the lattice parameters of two-dimensional films with extraordinary precision, but also of gaining information about the in-plane relation of the films and their respective substrates. Fig. 2 presents line-scans over the graphene G (10–10) reflection in the radial direction (i.e. probing the distance of the lattice planes). For easier interpretation, the x-axis is scaled to represent the lattice parameter of graphene. The reflection obtained from graphene on
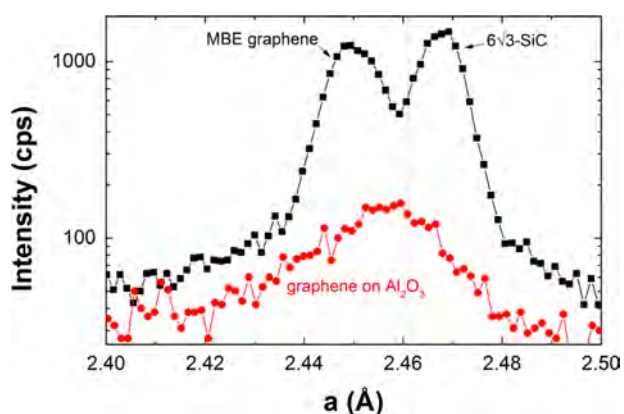
$6\sqrt{3}$-SiC (0001) shows a doublet structure with two peaks centered at 2.450 Å and 2.468 Å. The latter one can be assigned to the underlying C-rich reconstruction, as confirmed by reference measurements on a bare substrate. The peak at 2.450 Å therefore corresponds to the grown graphene, which means that the film possesses a lattice parameter ~0.45% smaller than that of relaxed graphite (2.461 Å) [39]. This shrinkage can be explained by the presence of point defects [32]. The scan recorded from the film on Al_2O_3 (0001) consists of a single peak, centered at 2.456 Å. The lattice contraction in comparison to graphite amounts only to ~0.20%, suggesting that the graphene lattice possesses fewer point defects in this case (in agreement with results obtained by Raman spectroscopy). On the other hand, the width of the peak is larger than for the growth on $6\sqrt{3}$-SiC (0001), which means that there is a broader variation in the graphene lattice parameter.

To investigate the in-plane orientation of the graphene films, line scans in the angular direction with an azimuthal range of 130° were performed, and are presented in Fig. 3(a). Only graphene peaks with a separation of 60° emerge, with an intensity that is two orders of magnitude higher than the background signal. Hence, the films possess a single crystallographic orientation with six-fold symmetry, as expected for graphene. Additional measurements (not shown here) reveal that the graphene films possess a single in-plane orientation with their respective substrates, and that this alignment is rotated by an angle of 30° [i.e. Al_2O_3/SiC (11–20) ∥ graphene (1–100)]. Remarkably, such an epitaxial alignment of the layers occurs even though previous results (obtained by X-ray photoelectron spectroscopy) revealed that they only weakly interact with the underlying substrate [21,32]. This indicates that van der Waals forces may play an important role in the process of epitaxial arrangement, although it is not yet possible to state that the whole process is purely based on this type of interaction, as it is expected for ideal van der Waals epitaxy [40]. Fig. 3(b) shows the in-plane alignment of the films with higher resolution. Even though the complete carbon lattice is aligned to the substrate, disorder and slight rotational misalignment between different domains is possible. The graphene grown on the $6\sqrt{3}$-SiC (0001) shows a narrow peak with a FWHM of 0.6°, indicating a strict epitaxial alignment to the substrate. In contrast, the width of the peak recorded from the film grown on Al_2O_3 (0001) amounts to 3.5°. Therefore, a larger degree of rotational disorder is present in the film and the epitaxial relation is less well defined when compared to growth on the quasi-homoepitaxial substrate. Note that the peak intensity for growth on Al_2O_3 is one order of magnitude lower compared with growth on $6\sqrt{3}$-SiC (0001). Nevertheless, since the peak's width in both radial and angular direction is larger, the integrated peak intensities are comparable for both samples, as expected given their similar thicknesses.

At first glance the Raman and GID analyses of graphene growth by MBE on these two substrates offer potentially contradictory results. As can be expected, growing on a (nearly) lattice matched substrate [$6\sqrt{3}$-SiC (0001)] leads to superior in-plane ordering in the graphene films when compared to growth on a heteroepitaxial substrate (Al_2O_3). However, these differences in epitaxial alignment seem not to be manifested in the structural quality, as determined by Raman spectroscopy, which revealed that the films on both substrates have similar characteristics, with even slightly narrower peaks widths obtained for the case of growth on Al_2O_3 (0001). This suggests that the final quality of graphene films is ultimately not limited by defects in grain boundary regions between graphene domains of different orientations, but rather by the presence of point defects. Or, alternatively, that coalescence between neighboring graphene domains does not take place without the incorporation of defects, regardless of the epitaxial relation between them.

Fig. 2. Radial line scans of the graphene (10–10) reflections (transformed to real space) recorded from graphene films grown on the $6\sqrt{3}$-SiC (0001) and on Al_2O_3 (0001). The x-axis is scaled to represent the lattice parameter of graphene, the dotted line marks the lattice parameter of relaxed graphite.

In addition to achieving epitaxial growth on different substrates, it is also desirable to exert control over the thickness of graphene films during synthesis. For the three substrates investigated here, the average thickness of the graphene film could easily be modulated with the growth time. This is an important benefit of solid-source MBE in comparison to CVD-based processes. Nevertheless, the existence of local thickness variations related to substrate features such as step edges cannot be excluded. This is particularly challenging during growth on Ni substrates.

We have employed SEM in conjunction with Raman spectroscopy to evaluate the thickness distribution within graphene films grown on Ni/MgO (111) (Fig. 4). We find that a complete mono-layer of graphene forms prior to any few-layer regions developing, which is consistent with monolayer graphene bound to the Ni surface being the energetically preferred state [41]. Upon completion of the first monolayer thicker regions of graphene begin to form, and rather than forming an additional continuous layer, they instead often form localized regions of thicker graphene. Despite the fact that the films offer thickness inhomogeneities, their average thickness scales well with deposition time, and indicate a growth rate of 1 monolayer of graphene each 60 min which enables precise, submonolayer thickness control. This growth rate indicates that $\sim 18\%$ of the carbon atoms impinging on the surface become incorporated into the graphene film, as compared to $\sim 7\%$
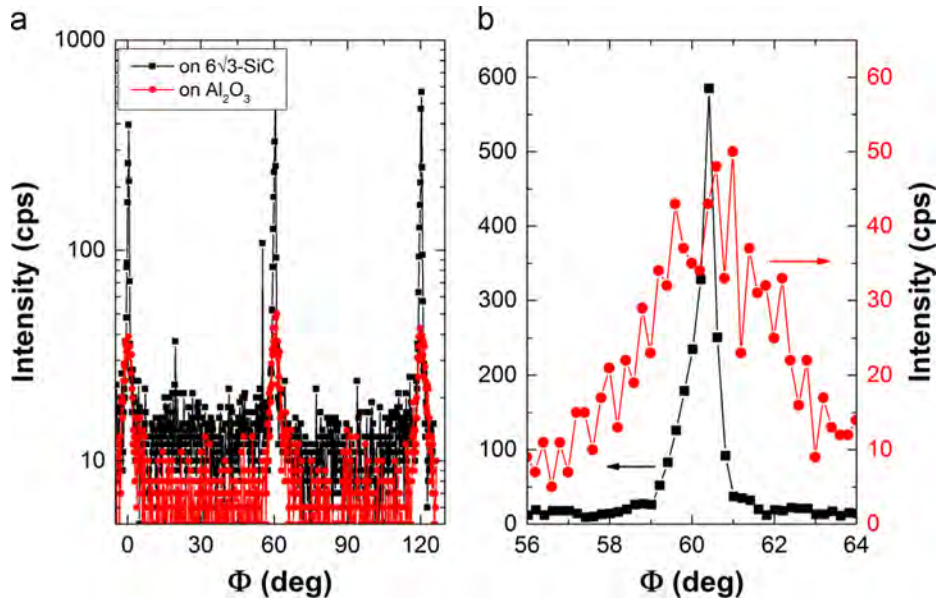
Fig. 3. Scans in the angular direction of the graphene (11–20) reflection [Al$_2$O$_3$ (3–300)/SiC(2–200) ∥ graphene (11–20)]. Note the different scales in (a) and (b).
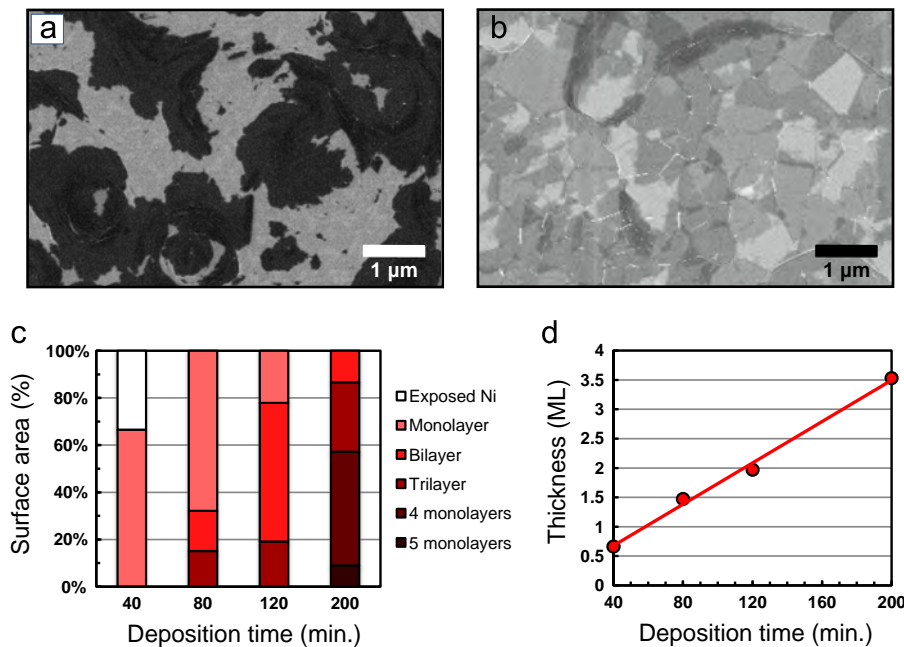
Fig. 4. SEM micrographs of graphene grown on Ni/MgO (111) for 40 min (a), and 200 min (b). The dark regions in (a) are graphene, while the lighter regions are exposed Ni, showing this film did not reach a full monolayer. The entire surface in (b) is covered in graphene, with the darker regions being thicker portions of the film. A complete monolayer of graphene forms prior to any multilayer formation (c), and the thickness disorder increases with deposition time. The average thickness of the graphene films scale well with deposition time (d).

for the dielectric substrates. The remaining carbon likely desorbs from the substrate surface prior to incorporation. In the case of the Ni/MgO (111) substrates, it may also dissolve into the metal. Because surface features have been shown to influence graphene growth, it is anticipated that further optimization of substrate surface will allow for increased thickness homogeneity [24,30,42].

4. Conclusions

The results presented here attest to the feasibility of employing MBE to controllably synthesize not only single-, but also few-layer thick graphene films on various templates. They also emphasize that more detailed investigations are still needed to completely elucidate the nucleation and growth mechanisms involved. It has been shown that state-of-the-art structural quality can be achieved for graphene grown on a metallic surface by MBE. For graphene layers prepared directly on insulators, a higher density of defects is verified. Nevertheless, the findings obtained for the latter case are particularly significant as they show that an epitaxial process takes place during MBE growth on these substrates [$6\sqrt{3}$-SiC (0001) and Al_2O_3 (0001)]. That strict epitaxy occurs on these substrates, which largely removes rotational disorder, means that the implementation of optimized synthesis conditions will enable the fabrication of large-area graphene films which possess a precise number of atomic layers, large domain sizes, and therefore offer excellent electronic properties.

Acknowledgments

References

[1] K.S. Novoselov, A.K. Geim, S.V. Morozov, D. Jiang, Y. Zhang, S.V. Dubonos I.V. Grigorieva, A.A. Firsov, Science 306 (2004) 666.
[2] C. Berger, Z. Song, T. Li, X. Li, A.Y. Ogbazghi, R. Feng, Z. Dai, A.N. Marchenkov E.H. Conrad, P.N. First, W.A. de Heer, J. Phys. Chem. B 108 (2004) 19912.
[3] Y. Zhang, Y.-W. Tan, H.L. Stormer, P. Kim, Nature 438 (2005) 201.
[4] M.S. Fuhrer, C.N. Lau, A.H. MacDonald, MRS Bull. 35 (2010) 289.
[5] J.B. Oostinga, H.B. Heersche, X. Liu, A.F. Morpurgo, L.M.K. Vandersypen, Nat. Mater. 7 (2008) 151.
[6] C.H. Lui, Z. Li, K.F. Mak, E. Cappelluti, T. Heinz, Nat. Phys. 7 (2011) 944.
[7] Y. Zhang, T.-T. Tang, C. Girit, Z. Hao, M.C. Martin, A. Zettl, M.F. Crommie Y.R. Shen, F. Wang, Nature 459 (2009) 820.
[8] B.N. Szafranek, D. Schall, M. Otto, D. Neumaier, H. Kurz, Nano Lett. 11 (2011) 2640.
[9] K.S. Novoselov, V.I. Falko, L. Colombo, P.R. Gellert, M.G. Schwab, K. Kim, Nature 490 (2012) 192.
[10] K.V. Emtsev, A. Bostwick, K. Horn, J. Jobst, G.L. Kellogg, L. Ley, J.L. McChesney, T. Ohta, S.A. Reshanov, J. Röhrl, E. Rotenberg, A.K. Schmid, D. Waldmann H.B. Weber, T. Seyller, Nat. Mater. 8 (2009) 203.
[11] W.A. de Heer, C. Berger, M. Ruan, M. Sprinkle, X. Li, Y. Hu, B. Zhang, J. Hankinson, E. Conrad, Proc. Natl. Acad. Sci. 108 (2011) 16900.
[12] M.H. Oliveira Jr., T. Schumann, M. Ramsteiner, J.M.J. Lopes, H. Riechert, Appl. Phys. Lett. 99 (2011) 111901.
[13] X. Li, W. Cai, J. An, S. Kim, J. Nah, D. Yang, R. Piner, A. Velamakanni, I. Jung, E. Tutuc, S.K. Banerjee, L. Colombo, R.S. Ruoff, Science 324 (2009) 1312.
[14] S. Bae, H. Kim, Y. Lee, X. Xu, J.-S. Park, Y. Zheng, J. Balakrishnan, T. Lei1 H.R. Kim, Y.I. Song, Y.-J. Kim, K.S. Kim, B Ozyilmaz, J.-H. Ahn, B.H. Hong, S. Iijima, Nat. Nanotech. 5 (2010) 574.
[15] W.P. McCray, Nat. Nanotech. 2 (2007) 259.
[16] J. Hackley, D. Ali, J. DiPasquale, J.D. Demaree, C.J.K. Richardson, Appl. Phys. Lett. 95 (2009) 133114.
[17] F. Maeda, H. Hibino, Jpn. J. Appl. Phys. 49 (2010) 04DH13.
[18] U. Wurstbauer, T. Schiros, C. Jaye, A.S. Plaut, R. He, A. Rigosi, C. Gutiérrez, D. Fischer, L.N. Pfeiffer, A.N. Pasupathy, A. Pinczuk, J.M. Garcia, Carbon 50 (2012) 4822.
[19] E. Moreau, S. Godey, F.J. Ferrer, D. Vignaud, X. Wallart, J. Avila, M.C. Asensio, F. Bournel, J.-J. Gallet, Appl. Phys. Lett. 97 (2010) 241907.
[20] S.K. Jerng, J.H. Lee, D.S. Yu, Y.S. Kim, J. Ryou, S. Hong, C. Kim, S. Yoon, S.H. Chun, J. Phys. Chem. C 116 (2012) 7380.
[21] M.H. Oliveira Jr, T. Schumann, R. Gargallo, F. Fromm, T. Seyller, M. Ramsteiner, A. Trampert, L. Geelhaar, J.M.J. Lopes, H. Riechert, Carbon 56 (2013) 339.
[22] S. Wang, L.F. dos Santos, U. Wurstbauer, L. Wang, L.N. Pfeiffer, J. Hone J.M. Garcia, A. Pinczuk, Solid State Commun. 189 (2014) 15.
[23] J.M. Garcia, R. He, M.P. Jiang, J. Yan, A. Pinczuk, Y.M. Zuev, K.S. Kim, P. Kim, K. Baldwin, K.W. West, L.N. Pfeiffer, Solid State Commun. 150 (2010) 809.
[24] J.M. Wofford, M.H. Oliveira Jr., T. Schumann, B. Jenichen, M. Ramsteiner, U. Jahn, S. Fölsch, J.M.J. Lopes, H. Riechert, New J. Phys. 16 (2014) 093055.
[25] G. Lippert, J. Dabrowski, Y. Yamamoto, F. Herziger, J. Maultzsch, M.C. Lemme, W. Mehr, G. Lupina, Carbon 52 (2013) 40.
[26] P.W. Sutter, J.-I Flege, E.A. Sutter, Nat. Mater. 7 (2008) 406.
[27] E. Loginova, N.C. Bartelt, P.J. Feibelman, K.F. McCarty, New J. Phys. 10 (2008) 93026.
[28] E. Loginova, N.C. Bartelt, P.J. Feibelman, K.F. McCarty, New J. Phys. 11 (2009) 063046.
[29] J.M. Wofford, S. Nie, K.F. McCarty, N.C. Bartelt, O.D. Dubon, Nano Lett. 10 (2010) 4890.
[30] S. Nie, J.M. Wofford, N.C. Bartelt, O.D. Dubon, K.F. McCarty, Phys. Rev. B 84 (2011) 155425.
[31] J.M. Wofford, E. Starodub, A.L. Walter, S. Nie, A. Bostwick, N.C. Bartelt, K. Thürmer, E. Rotenberg, K.F McCarty, O.D. Dubon, New J. Phys. 14 (2012) 053008.
[32] T. Schumann, M. Dubslaff, M.H. Oliveira Jr., M. Hanke, F. Fromm, T. Seyller, L. Nemec, V. Blum, M. Scheffler, J.M.J. Lopes, H. Riechert, New J. Phys. 15 (2013) 123034.
[33] A.C. Ferrari, J. Meyer, V. Scardaci, C. Casiraghi, M. Lazzeri, F. Mauri, S. Piscanec, D. Jiang, K.S. Novoselov, S. Roth, A.K. Geim, Phys. Rev. Lett. 97 (2006) 187401.
[34] A.C. Ferrari, D.M. Basko, Nat. Nanotechnol. 8 (2013) 235.
[35] L.G. Cançado, A. Jorio, E.H. Martins Ferreira, F. Stavale, C.A. Achete, R.B. Capaz, M.V.O. Moutinho, A. Lombardo, T.S. Kulmala, A.C. Ferrari, Nano Lett. 11 (2011) 3190.
[36] S. Goler, C. Coletti, V. Piazza, P. Pingue, F. Colangelo, V. Pellegrini, K.V. Emtsev, S. Forti, U. Starke, F. Beltram, S. Heun, Carbon 51 (2013) 249.
[37] T. Schumann, M. Dubslaff, M.H. Oliveira Jr., M. Hanke, J.M.J. Lopes, H. Riechert, Phys. Rev. B 90 (2014) 041403(R).
[38] K.V. Emtsev, F. Speck, T. Seyller, L. Ley, J. Riley, Phys. Rev. B 77 (2008) 155303.
[39] H. Hattab, A.T. N'Diaye, D. Wall, C. Klein, G. Jnawali, J. Coraux, C. Busse, R. van Gastel, B. Poelsema, T. Michely, F.-J. Meyer zu Heringdorf, M. Horn-von Hoegen, Nano Lett. 12 (2012) 678.
[40] A. Koma, Thin Solid Films 216 (1992) 72.
[41] R. Addou, A. Dahal, P. Sutter, M. Batzill, Appl. Phys. Lett. 100 (2012) 021601.
[42] J. Dabrowski, G. Lippert, T. Schroeder, G. Lupina, Appl. Phys. Lett. 105 (2014) 191610.

CrossMark
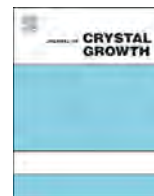
Quest for high-Curie temperature Mn$_x$Ge$_{1-x}$ diluted magnetic semiconductors for room-temperature spintronics applications

Tianxiao Nie *, Jianshi Tang, Kang L. Wang *

Device Research Laboratory, Department of Electrical Engineering, University of California, Los Angeles, CA 90095, USA

ABSTRACT

In this paper, we report the non-equilibrium growth of various Mn-doped Ge dilute magnetic semiconductor nanostructures using molecular-beam epitaxy, including quantum dots, nanodisks and nanowires. Their detailed structural and magnetic properties are characterized. By comparing the results with those in Mn$_x$Ge$_{1-x}$ thin films, it is affirmed that the use of nanostructures helps eliminate crystalline defects and meanwhile enhance the carrier-mediate ferromagnetism from substantial quantum confinements. Our systematic studies provide a promising platform to build nonvolatile spinFET and other novel spintronic devices based upon dilute magnetic semiconductor nanostructures.

© 2015 Elsevier B.V. All rights reserved.

1. Instruction

The International Technology Roadmap of Semiconductors (ITRS) has highlighted the demands of novel materials and devices to satisfy the challenges in the continuous scaling of CMOS with low power dissipation and low variability [1,2]. Spintronics, which utilizes the spin of electrons as another degree of freedom for information processing, offers a promising pathway to meet such challenges [2]. As a unique material system, diluted magnetic semiconductor (DMS), by introducing magnetic dopants into a semiconductor lattice, plays an irreplaceable role in developing peculiar spintronic devices due to the advantage of simultaneously utilizing the charge and spin of electrons for information processing [3,4]. Among various DMS materials, Mn-doped Ge DMS [5] has attracted tremendous attention due to its potentially high Curie temperature and high compatibility with the mature Si technology. Especially, the discovery of electric-field controlled ferromagnetism in Mn$_x$Ge$_{1-x}$ systems [5,6] opens up great possibilities to realize low-power spintronic devices with increased functionalities.

For room-temperature spintronics applications, single-crystalline Mn$_x$Ge$_{1-x}$ with high Curie temperature ($T_c > 300$ K) is highly desired. However, in practice it is very challenging. In the growth of Mn$_x$Ge$_{1-x}$ thin films, due to the extremely low Mn solubility in Ge, various intermetallic compounds (such as Mn$_5$Ge$_3$ and Mn$_{11}$Ge$_8$) are easily formed in a random and uncontrollable manner [7,8]. In fact, the acquisition of single-crystalline Mn$_x$Ge$_{1-x}$ DMS is in an extremely narrow growth window with poor reproducibility. In the pioneered

work, Park et al. [5] successfully obtained such genuine Mn$_x$Ge$_{1-x}$ thin film and demonstrated the hold-mediated ferromagnetism, which greatly stimulated the research in the Mn-doped Ge system. However, the achieved T_c was only 116 K, far away from most practical applications. Later research aimed to further increase the T_c and electric-field controllability at room temperature. However, extensive studies in Mn$_x$Ge$_{1-x}$ thin films have proved the origin of room-temperature ferromagnetism is likely attributed to the presence of metallic phase Mn$_5$Ge$_3$ ($T_c \sim 296$ K) [8–11], whose ferromagnetism cannot be controlled by external electric field. Recently, Jamet et al. [12] reported the formation of Mn$_x$Ge$_{1-x}$ thin film with T_c over 400 K, which was due to the coherent Mn$_x$Ge$_{1-x}$ nanocolumn with the new phase of MnGe$_2$. The narrow growth window and poor reproducibility made it difficult to produce high-quality Ge-based DMS for reliable spintronic devices [13]. To date, although great progress has been made in growing Mn$_x$Ge$_{1-x}$ DMS, the biggest challenge is still how to avoid the formation of intermetallic precipitates and secondary phases.

To circumvent this problem, the employment of nanostructures might open up a possibility to generate high-T_c DMS with no precipitates. Two distinctive advantages could be introduced by employing nanostructures. (1) When it comes to the one or zero dimensions, the cluster formation may be possibly limited because the strain induced by Mn substitute could be easily accommodated by the nano-architecture [14]. (2) When it comes to nanoscale structures, the quantum confinement effect emerges, which significantly enhances the exchange coupling between the confined holes and localized Mn [6,15]. In fact, previous report has demonstrated that a chemical vapor deposition (CVD)-grown Mn$_x$Ge$_{1-x}$ nanowires has a T_c over 300 K without any precipitation in the detection limitation of TEM [14]. Compared to the CVD method, the non-equilibrium technique of molecular beam epitaxy (MBE) [3] growth allows us to incorporate much higher Mn-doping concentration into

* Corresponding author.
    E-mail addresses: nietianxiao@gmail.com (T. Nie),
wang@seas.ucla.edu (K.L. Wang).

the Ge matrix beyond the solubility limit, which could facilitate to further increase the T_c.

In this work, we perform a systematic study on various MBE-grown Mn_xGe_{1-x} materials, and in particular, investigate the structural and magnetic properties of different nanostructures, including quantum dots, nanodisks and nanowires. By comparison with the Mn_xGe_{1-x} thin film, Mn_xGe_{1-x} nanostructures showed a much higher T_c over 400 K with minimized crystalline defects. Therefore, they provided a promising platform to build novel spintronic devices.

2. Mn_xGe_{1-x} thin film growth by MBE

As a control sample in our comparison study, Mn_xGe_{1-x} thin films were grown on Ge (111) substrate by a Perkin-Elmer solid source MBE with Ge and Mn Knudsen cells. Ge substrate was cleaned by immersing in acetone and isopropyl alcohol with ultrasonic agitation. After dipping in 1% diluted hydrofluoric acid (HF) solution, the substrate was directly transferred into the MBE chamber. The degassing was performed at 700 °C for 0.5 h. After that, a 45 nm-thick Mn_xGe_{1-x} was directly deposited onto the Ge substrate at 200 °C with a Ge growth rate 0.2 Å/s. The microstructure and composition of the samples were comprehensively characterized by transmission electron microscopy (TEM) equipped with energy-dispersive spectroscopy (EDS). The magnetic properties were measured by using a superconducting quantum interference device (SQUID).

Fig. 1(a) is a typical cross-sectional bright-field TEM image of the grown Mn_xGe_{1-x} film, in which some much dark regions are embedded in a relatively uniform contrast. It means other nanostructures were formed except for the relatively uniform doped MnGe as marked by red-dotted square. To understand the detailed structure, high-resolution TEM (HRTEM) was employed and typical [110] zone-axis TEM results are shown in Fig. 1(b)–(d). In Fig. 1(b), stacking faults (SFs) could be clearly observed in the Ge matrix, in which a triplet periodicity of (111) Ge lattice spacing in the SFs was explicitly featured [16]. The formation of SFs might come from the strain accumulation of Mn doping and lattice-mismatched precipitates. Fig. 1(c) was collected from the relatively uniform doped region and clearly displayed a very good crystallinity, exhibiting a DMS feature. We must mention that noticeable precipitates could be observed in our thin film sample, as shown in Fig. 1(d). It clearly shows another set of lattice structure different from the Ge matrix.

Using the lattice spacing of the Ge as the reference, we calculated the observed lattice spaces of the cluster, which matched with the (002) and (010) atomic planes of the hexagonal Mn_5Ge_3 phase [17,18]. Furthermore, it was confirmed that the Mn_5Ge_3 (002) plane was parallel to the Ge (111) plane. To determine the Mn doping concentration, EDS was carried out and the result showed the average Mn concentration was ~4%, as shown in Fig. 1(e).

The magnetic property of the grown Mn_xGe_{1-x} film was measured by SQUID, and the result is shown in Fig. 1(f). Clear magnetic hysteresis can be observed between 10 K and 250 K, and it disappeared around 300 K. To further determine the T_c and detect any magnetic precipitates, zero-field cooled (ZFC) and field cooled (FC) magnetization measurements were performed under a small magnetic field of 200 Oe. As shown in Fig. 1(g), the magnetization vanished near 300 K, indicating a T_c ~300 K, which further confirms the formation of Mn_5Ge_3 (T_c ~296 K) [12]. Two blocking temperatures coexisted in the ZFC curve, with the lower one at 20 K and the higher one at 200 K, which were attributed to Mn-rich coherent Mn_xGe_{1-x} nanostructures [13] and Mn_5Ge_3 precipitates [10], respectively. Both of them could be well resolved in the TEM characterization in Fig. 1(a), as indicated by white arrows and red-dotted squares.

Based upon the above TEM characterization and magnetic property measurement, Mn-rich Mn_xGe_{1-x} lattice-coherent phases and Mn_5Ge_3 clusters were hard to be eliminated in the thin film growth, which hampered the formation of single-crystalline Mn_xGe_{1-x} DMS with high T_c. Therefore, it is of great interest to further investigate the growth of Mn_xGe_{1-x} nanostructures.

3. Self-assembled Mn_xGe_{1-x} quantum dots by MBE

In our earlier work, we have successfully demonstrated the growth of Mn_xGe_{1-x} quantum dots (QDs) on p-type Si (100) substrate by MBE [6]. The growth of Mn_xGe_{1-x} QDs were carried out at 450 °C with Ge growth rate of 0.2 Å/s, abiding by the Stranski–Krastanow (SK) [19] growth mode. Cross-sectional TEM was employed to determine the structural characteristics of the grown Mn_xGe_{1-x} QDs, as shown in Fig. 2(a). It revealed a dome-shaped nanodot on top of the Si substrate with Mn diffusion underneath. Meanwhile, it shows a perfectly single crystallinity without any observable defects and precipitates in the QDs, implying a pure DMS system. The temperature-dependent hysteresis loops are shown in Fig. 2(b), in which the coercivity and saturated magnetic moment decreased with increasing temperature. However, even at 400 K, the
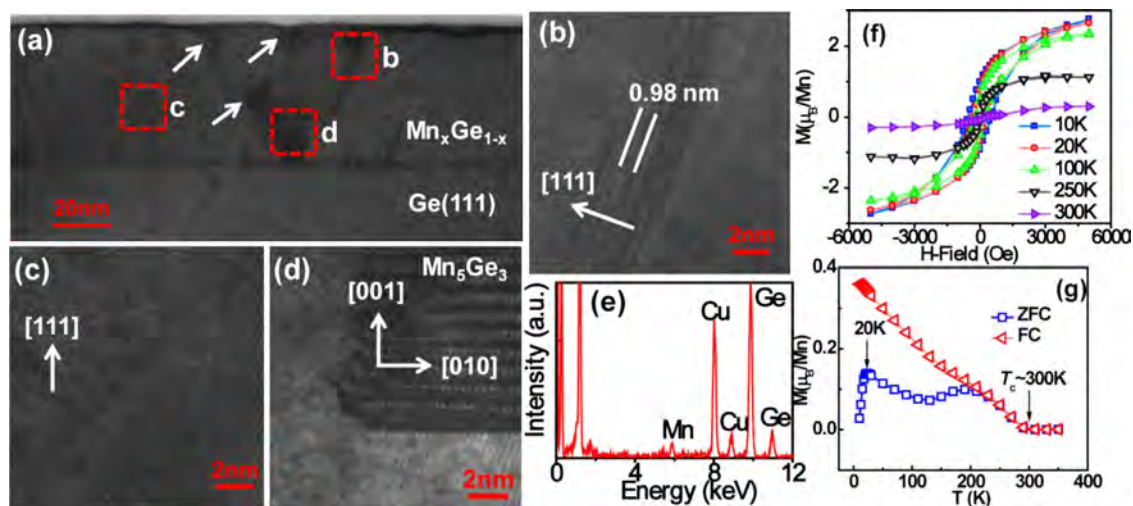
Fig. 1. (a) A typical cross-sectional TEM image of the Mn_xGe_{1-x} thin film. (b), (c) and (d) HRTEM images of stacking faults, Mn_xGe_{1-x} DMS region and Mn_5Ge_3 cluster in the film, respectively. (e) EDS spectrum confirming the ~4% Mn doping. (f) Temperature-dependent hysteresis loop of the Mn_xGe_{1-x} film. (g) ZFC and FC curves, showing a T_c ~300 K.

hysteresis loop still existed, indicating the T_c of Mn_xGe_{1-x} QDs was over 400 K. The fact of the high T_c in Mn_xGe_{1-x} QDs confirms that the use of nanostructures indeed helped enhance the T_c compared to thin films. Furthermore, using a metal-oxide-semiconductor (MOS) structure, the electric field control of ferromagnetism in the Mn_xGe_{1-x} QDs has been demonstrated, as shown in Fig. 2(c). The experimental data suggest the itinerant holes play an important role in mediating the ferromagnetism.

4. Nanolithography-patterned Mn_xGe_{1-x} nanodisks by MBE

In addition to the effort on the growth of Mn_xGe_{1-x} QDs, another type of nanostructures – Mn_xGe_{1-x} nanodisks were investigated by MBE growth on a SiO_2 patterned Si substrate. The SiO_2 pattern was fabricated on a Si substrate by nanolithography [20], which utilized the nanospheres to self-assembly form hexagonal close-packed pattern. By series of etching process, the hexagonal close-packed pattern could be inversely transferred to the SiO_2 mask. Fig. 3(a) is a typical AFM image of the SiO_2 mask, clearly showing a regular and repeatable nanohole pattern with a diameter of ∼100 nm. After cleaned by standard RCA process [21], the patterned substrate was transferred to the MBE chamber for Mn_xGe_{1-x} nanodisks growth. After removing the native oxide layer at 950 °C for 10 min, the substrate was cooled down to 250 °C for the Mn_xGe_{1-x} deposition with a Ge growth rate of ∼0.2 Å/s. Fig. 3(b) is a typical SEM image of the grown sample after removing the SiO_2 mask, which shows ordered Mn_xGe_{1-x} nanodisks with a diameter of 100 nm and uniform size distribution. The tilted

SEM view in Fig. 3(c) clearly demonstrates the ordered nanodisks are ∼20 nm high. To understand the detailed microstructure, cross-sectional HRTEM was employed and a typical image is shown in Fig. 3(d). A sharp interface between the Si substrate and the Mn_xGe_{1-x} nanodisks could be clearly observed with well-resolved lattice coherence. Careful examination could find there still exist some stacking faults in the Mn_xGe_{1-x} nanodisk, but without any noticeable precipitates, indicating a relatively good DSM system. Besides, EDS spectrum analysis in Fig. 3(e) shows a Mn doping concentration of ∼4%. Magnetic properties of the grown Mn_xGe_{1-x} nanodisks were further characterized in SQUID as well. Fig. 3(f) shows the temperature-dependent hysteresis loops with in-plane magnetic fields. The clear hysteresis loop at 300 K indicated that the T_c of the Mn_xGe_{1-x} nanodisks is above 300 K, affirming the enhancement of T_c in nanostructures. From the ZFC and FC curves as shown in Fig. 3(g), the non-zero magnetization at 400 K further indicates that the T_c is beyond 400 K. The separation of the ZFC and FC curves possibly arises from strain-induced anisotropy because of a large lattice mismatch between Si and Ge [6].

5. Pattern-assisted MBE growth of Mn_xGe_{1-x} nanowires

Besides to the above quasi-zero-dimensional QDs and nanodisks, one-dimensional Mn_xGe_{1-x} DMS nanowires were also grown by MBE on a Ge substrate with SiO_2 nanotrench patterns as the mask [22]. After removal of the native oxide by annealing at 600 °C for 30 min, the substrate was cooled down to 180 °C for the 60 nm-thick
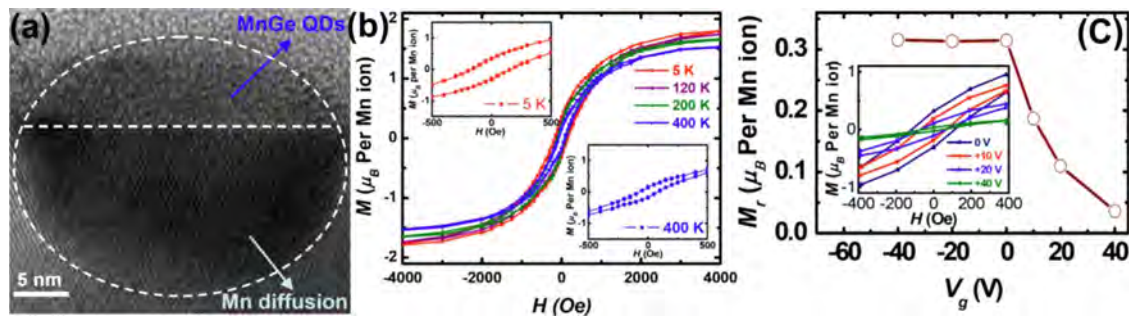
Fig. 2. (a) HRTEM image of a Mn_xGe_{1-x} QD. (b) Magnetic hysteresis loops from 5 K to 400 K. (c) Gate-dependent remnant moments and magnetic hysteresis loops (inset). Reproduced from Ref. [6].
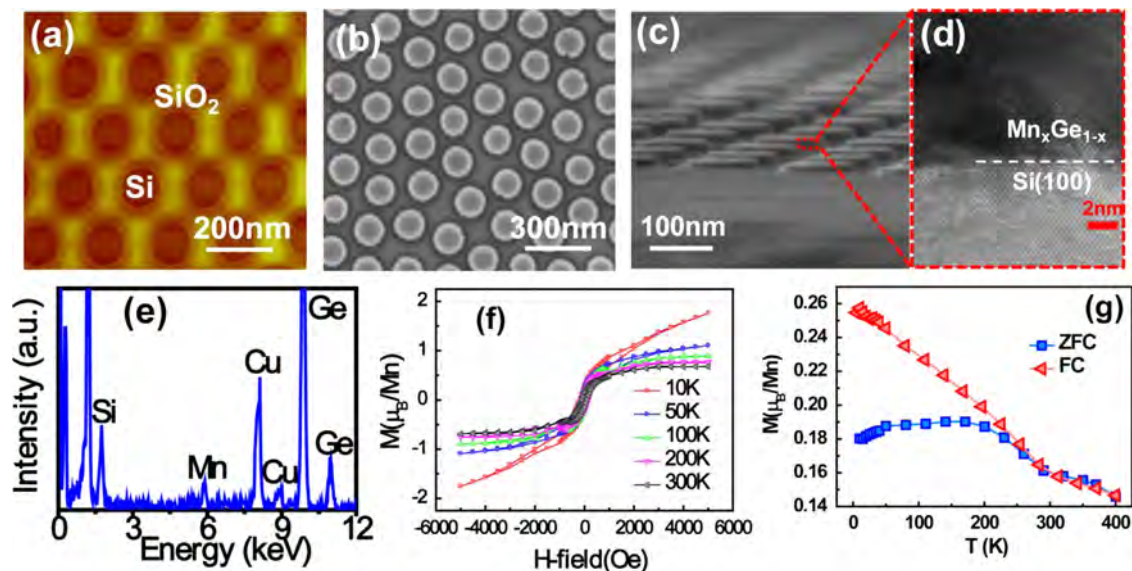
Fig. 3. (a) A typical AFM image of the ordered SiO_2 mask. (b) Top-view SEM image of the grown nanodisks with ∼100 nm diameter. (c) Cross-sectional SEM image, showing the height is ∼20 nm. (d) The corresponding HRTEM image, showing the coherent growth. (e) EDS spectrum showing a ∼4% Mn doping. (f) Temperature-dependent hysteresis loops. (g) ZFC and FC magnetization of the nanodisks with $H=100$ Oe.
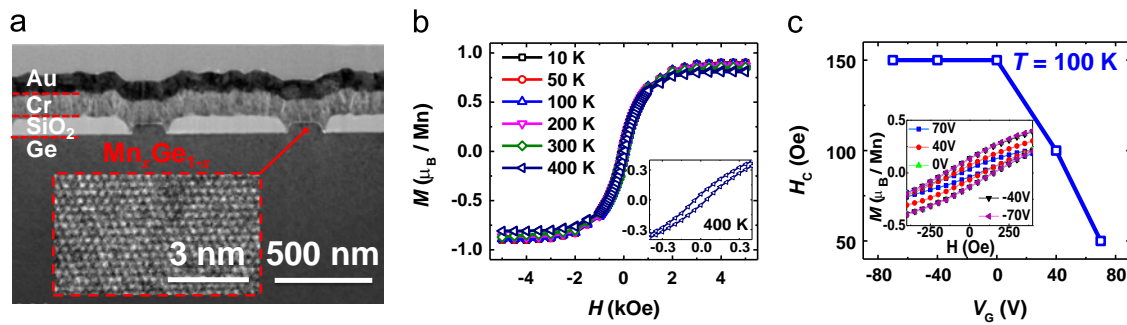
Fig. 4. (a) Cross-sectional and HRTEM images (inset) of the Mn_xGe_{1-x} nanowires. (b) Magnetic hysteresis loops from 10 K to 400 K. (c) Gate-dependent coercive fields and M–H loops (inset), indicating electric-field control of ferromagnetism in the Mn_xGe_{1-x} DMS nanowires.

Mn_xGe_{1-x} nanowire growth with a Ge growth rate of 0.2 Å/s. After the growth, cross-sectional TEM was used to investigate its structural characteristics, and a typical image is shown in Fig. 4(a). It shows that Mn_xGe_{1-x} nanowires are located on the Ge substrate and separated by the SiO_2 patterns. The inset HRTEM image clearly reveals a perfect crystallinity of the nanowire, in which no crystalline defects and MnGe precipitates were observed. Furthermore, magnetic properties of the grown Mn_xGe_{1-x} nanowires were measured by SQUID with in-plane magnetic fields. Fig. 4(b) shows the temperature-dependent magnetic hysteresis loops with temperature range from 10 K to 400 K. Clear hysteresis loop can still be observed even at 400 K, which provides a direct evidence of T_c beyond 400 K. To investigate the electric-field controlled ferromagnetism, a MOS structure similar to the one in Mn_xGe_{1-x} QDs was fabricated using the Mn_xGe_{1-x} nanowires as channel. By sweeping the gate voltage from positive to negative, the carrier density in the Mn_xGe_{1-x} DMS nanowires was modulated. Fig. 4(c) shows the gate-dependent coercivity, and the inset shows the magnified magnetic hysteresis loops recorded at various gate voltages. It is found that the coercivity decreased with increasing positive gate voltage, which depleted holes in the Mn_xGe_{1-x} nanowire. This result confirmed the ferromagnetism in the Mn_xGe_{1-x} nanowire was mediated by itinerant holes, similar to the scenario in the Mn_xGe_{1-x} QDs. Our results further confirmed that the use of DMS nanostructures could enhance the carrier-mediate ferromagnetism and meanwhile minimize crystal defects because of the quantum confinements.

6. Conclusion

In conclusion, we have demonstrated the MBE growth of various single-crystalline high-T_c Mn_xGe_{1-x} nanostructures, including QDs, nanodisks, and nanowires, in order to address the defects issue in the thin film growth. Detailed TEM structural analysis has excluded the presence of metallic precipitates or secondary phases in these nanostructures. Magnetic property characterizations show that the T_c is above 400 K. The enhancement in the carrier-mediated ferromagnetism and the single crystallinity is attributed to the substantial quantum confinement in nanostructures. Therefore, our findings provide great opportunities to build practical spintronic devices, such as DMS-based transpinor [22,23], using DMS nanostructures.

Acknowledgments

References

[1] K.L. Wang, F. Xiu, Quest of electric field controlled spintronics in MnGe, Thin Solid Films 518 (2010) S104–S112.
[2] K.L. Wang, Z. Zhao, A. Khitun, Spintronics for nanoelectronics and nanosystems, Thin Solid Films 517 (2008) 184–190.
[3] H. Ohno, Making nonmagnetic semiconductors ferromagnetic, Science 281 (1998) 951–956.
[4] H. Ohno, D. Chiba, F. Matsukura, T. Omiya, E. Abe, T. Dietl, Y. Ohno, K. Ohtani, Electric-field control of ferromagnetism, Nature 408 (2000) 944–946.
[5] Y.D. Park, A.T. Hanbicki, S.C. Erwin, C.S. Hellberg, J.M. Sullivan, J.E. Mattson, T.F. Ambrose, A. Wilson, G. Spanos, B.T. Jonker, A Group-IV, Ferromagnetic semiconductor: Mn_xGe_{1-x}, Science 295 (2002) 651–654.
[6] F. Xiu, Y. Wang, J. Kin, A. Hong, J. Tang, A.P. Jacob, J. Zou, K.L. Wang, Electric-field-controlled ferromagnetism in high-Curie-temperature $Mn_{0.05}Ge_{0.95}$ quantum dots, Nat. Mater. 9 (2010) 337–344.
[7] Y.D. Park, A. Wilson, A.T. Hanbicki, J.E. Mattson, T. Ambrose, G. Spanos, B.T. Jonker, Magnetoresistance of Mn:Ge ferromagnetic nanoclusters in a diluted magnetic semiconductor matrix, Appl. Phys. Lett. 78 (2001) 2739–2741.
[8] Y. Wang, J. Zou, Z. Zhao, X. Han, X. Zhou, K.L. Wang, Direct structural evidences of $Mn_{11}Ge_8$ and Mn_5Ge_2 clusters in $Ge_{0.96}Mn_{0.04}$ thin films, Appl. Phys. Lett. 92 (2008) 101913.
[9] R. Gunnella, L. Morresi, N. Pinto, R. Murri, L. Ottaviano, M. Passacantando, F. D'Orazio, F. Lucari, Magnetization of epitaxial MnGe alloys on Ge (111) substrates, Surf. Sci. 577 (2005) 22–30.
[10] F. Xiu, Y. Wang, K. Wang, Y. Zhou, X. Kou, J. Zou, K.L. Wang, MnGe magnetic nanocolumns and nanowells, Nanotechnology 21 (2010) 225602–225606.
[11] J. Chen, K.L. Wang, K. Galatsis, Electrical field control magnetic phase transition in nanostructured Mn_xGe_{1-x}, Appl. Phys. Lett. 90 (2007) 012501–012503.
[12] M. Jamet, A. Barski, T. Devillers, V. Poydenot, R. Dujardin, P. Bayle-Guillemaud, J. Rothman, E. Bellet-Amalric, A. Marty, J. Cibert, R. Mattana, S. Tatarenko, High-Curie-temperature ferromagnetism in self-organized $Ge_{1-x}Mn_x$ nanocolumns, Nat. Mater. 5 (2006) 653–659.
[13] T. Devillers, M. Jamet, A. Barski, V. Poydenot, P. Bayle-Guillemaud, E. Bellet-Amalric, S. Cherifi, J. Cibert, Structure and magnetism of self-organized GeMn nanocolumns on Ge(001), Phys. Rev. B 76 (2007) 205306–205317.
[14] M.I. van der Meulen, N. Petkov, M.A. Morris, O. Kazakova, X. Han, K.L. Wang, A.P. Jacob, J.D. Holmes, Single crystalline $Ge_{1-x}Mn_x$ nanowires as building blocks for nanoelectronics, Nano Lett. 9 (2008) 50–56.
[15] K.L. Wang, F. Xiu, Quest of electric field controlled spintronics in MnGe, Thin Solid Films 518 (2010) S104–S112.
[16] J.H. Lin, Y.Q. Wu, S. Tang, Y.L. Fan, X.J. Yang, Z.M. Jiang, J. Zou, Composition and strain measurements of Ge(Si)/Si(001) islands by HRTEM, J. Nanosci. Nanotechnol. 9 (2009) 2753–2757.
[17] Y.S. Dedkov, M. Holder, G. Mayer, M. Fonin, A.B. Preobrajenski, Spin-resolved photoemission of a ferromagnetic $Mn_5Ge_3(0001)$ epilayer on Ge(111), J. Appl. Phys. 105 (2009).
[18] T. Vinh Le, S. Aurélie, D. Minh-Tuan, F.O.-M. Sion, A.M. Lisa, P. Matthieu, Epitaxial growth and magnetic properties of Mn_5Ge_3/Ge and $Mn_5Ge_3C_x/Ge$ heterostructures for spintronic applications, Adv. Nat. Sci.: Nanosci. Nanotechnol. 4 (2013) 043002.
[19] T.-X. Nie, J.-H. Lin, Z.-G. Chen, Y.-M. Shao, Y.-Q. Wu, X.-J. Yang, Y.-L. Fan, Z.-M. Jiang, J. Zou, Thermally oxidized formation of new Ge dots over as-grown Ge dots in the Si capping layer, J. Appl. Phys. 110 (2011) 114304–114305.
[20] Y.W. Chen, B.Y. Pan, T.X. Nie, P.X. Chen, F. Lu, Z.M. Jiang, Z.Y. Zhong, Enhanced photoluminescence due to lateral ordering of GeSi quantum dots on patterned Si(001) substrates, Nanotechnology 21 (2010) 175701.
[21] C.-P. Chu, S. Arafin, T. Nie, K. Yao, X. Kou, L. He, C.-Y. Wang, S.-Y. Chen, L.-J. Chen, S.M. Qasim, M.S. BenSaleh, K.L. Wang, Nanoscale growth of GaAs on patterned Si (111) substrates by Molecular Beam Epitaxy, Cryst. Growth Des. 14 (2013) 593–598.
[22] J. Tang, T. Nie, K.L. Wang, Spin transport in Ge nanowires for diluted magnetic semiconductor-based nonvolatile transpinor, ECS Trans. 64 (2014) 613–623.
[23] J. Tang, C.-Y. Wang, L.-T. Chang, Y. Fan, T. Nie, M. Chan, W. Jiang, Y.-T. Chen, H.-J. Yang, H.-Y. Tuan, Electrical spin injection and detection in $Mn_5Ge_3/Ge/Mn_5Ge_3$ nanowire transistors, Nano Lett. 13 (2013) 4036–4043.
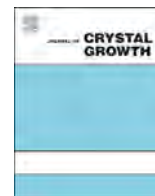
GaSb/GaAs quantum dots and rings grown under periodical growth mode by using molecular beam epitaxy

Hsuan-An Chen [a,b], Tung-Chuan Shih [c], Shiang-Feng Tang [d], Ping-Kuo Weng [d], Yau-Tang Gau [d], Shih-Yen Lin [a,b,c,*]

[a] Graduate Institute of Electronics Engineering, National Taiwan University, Taipei, Taiwan
[b] Research Center for Applied Sciences, Academia Sinica, Nankang, Taipei, Taiwan
[c] Department of Photonics, National Chiao-Tung University, Hsinchu, Taiwan
[d] National Chung-Shan Institute of Science & Technology, Taoyuan, Taiwan

ARTICLE INFO

ABSTRACT

GaSb/GaAs quantum dots (QDs) and quantum rings (QRs) are investigated. By using periodical growth interrupts, precise coverage control can be achieved for GaSb QD growth by using a single Ga source. With direct As irradiation to the substrate surface during the post soaking time, the soaking time can be effectively reduced while full ring morphologies and room-temperature QR luminescence can still be obtained by using this method.

1. Introduction

Compared with conventional type-I InAs quantum dots (QDs), GaSb/GaAs QDs and quantum rings (QRs) are of type-II band alignment and are believed to be promising candidates for memory device applications [1]. However, due to the difficult-to-control As/Sb interfaces, limited papers are published on theses nano-structures. In one previous publication, it has been demonstrated that with extend post-growth Sb soaking procedure, the dot morphology can be well maintained after GaAs capping layer growth [2]. The photo-luminescence (PL) intensities are also enhanced after the long post-growth soaking times. In this case, device applications such as room-temperature light-emitting devices and high-temperature operation quantum-dot infrared photodetectors are demonstrated by using this growth technique [3,4]. Lasing behavior of the type-II GaSb QDs in a microdisk cavity is also observed [5]. Compared with the simple extended post-growth Sb soaking time for GaAs QD growth, although the self-formed QRs after GaAs capping seems to be a promising approach for QR growth, there is no direct evidence that full ring morphology is obtained by using this approach [6]. Therefore, it has been proposed that by well controlling the Sb/background As flux ratios, either full- dot or ring morphologies can be obtained and observed before GaAs capping layer growth [7]. More significant PL intensities are also observed for QRs due to the more surrounding

electrons around the QRs and the less abrupt GaSb/GaAs interfaces. Compatible luminescence intensities with type-I InAs QDs and 1.3 μm luminescence are also observed for coupled- and InGaAs-capped QRs [8,9].

Although extended post-growth Sb soaking time does help in enhancing the luminescence intensities of GaSb QDs and QRs, the long growth interrupt may increase background impurity incorporation in the GaSb/GaAs interfaces. Due to the different growth rates of GaAs and GaSb, two Ga sources are usually required for the preparation of GaSb/GaAs nano-structures. Therefore, in this report, we have demonstrated that by using periodical growth interrupts, precise coverage control can be achieved for GaSb QD growth by using a single Ga source in reasonable time duration. With direct As irradiation to the substrate surface during the post Sb soaking procedure, the post-growth Sb soaking time can be effectively reduced while full ring

Table 1
The wafer structures of Samples A, B, C and D.

Sample	A	B	C	D
Post Soaking	60 s			
(Sb/As ratio)	No As	No As	0.25	0.05
GaSb QDs	3 ML GaSb			
Spacer layer	200 nm undoped GaAs			
Post soaking	60 s			
(Sb/As ratio)	No As	No As	0.25	0.05
GaSb QDs	3 ML GaSb			
Buffer layer	200 nm undoped GaAs			
350 mm SI GaAs Substrate				

* Correspondence to: 128 Sec. 2, Academia Rd., Nankang, Taipei, Taiwan 11529. Tel.: +886 2 27873187; fax: +886 2 27873122.
E-mail address: shihyen@gate.sinica.edu.tw (S.-Y. Lin).

morphologies and room-temperature QR luminescence can still be obtained via this method.

2. Experiment

All the samples discussed in this paper are grown on (100)-oriented semi-insulating GaAs substrates by using SVTA solid-source molecular beam epitaxy system (MBE). The wafer structures are shown in Table 1. The growth procedure is as following: (1) 200 nm undoped GaAs buffer layer growth, (2) 10 s. Sb pre-soaking procedure to form 1 mono-layer (ML) GaSb on GaAs surface, (3) periodical 2 MLs GaSb deposition for Samples B, C and D to form 3 MLs GaSb QDs, (4) 60 s. post-growth Sb soaking with controlled Sb/As flux ratios, (5) 200 nm undoped GaAs capping layer growth, (6) repeat steps (2)–(4) to form the uppermost GaSb layer for atomic-force
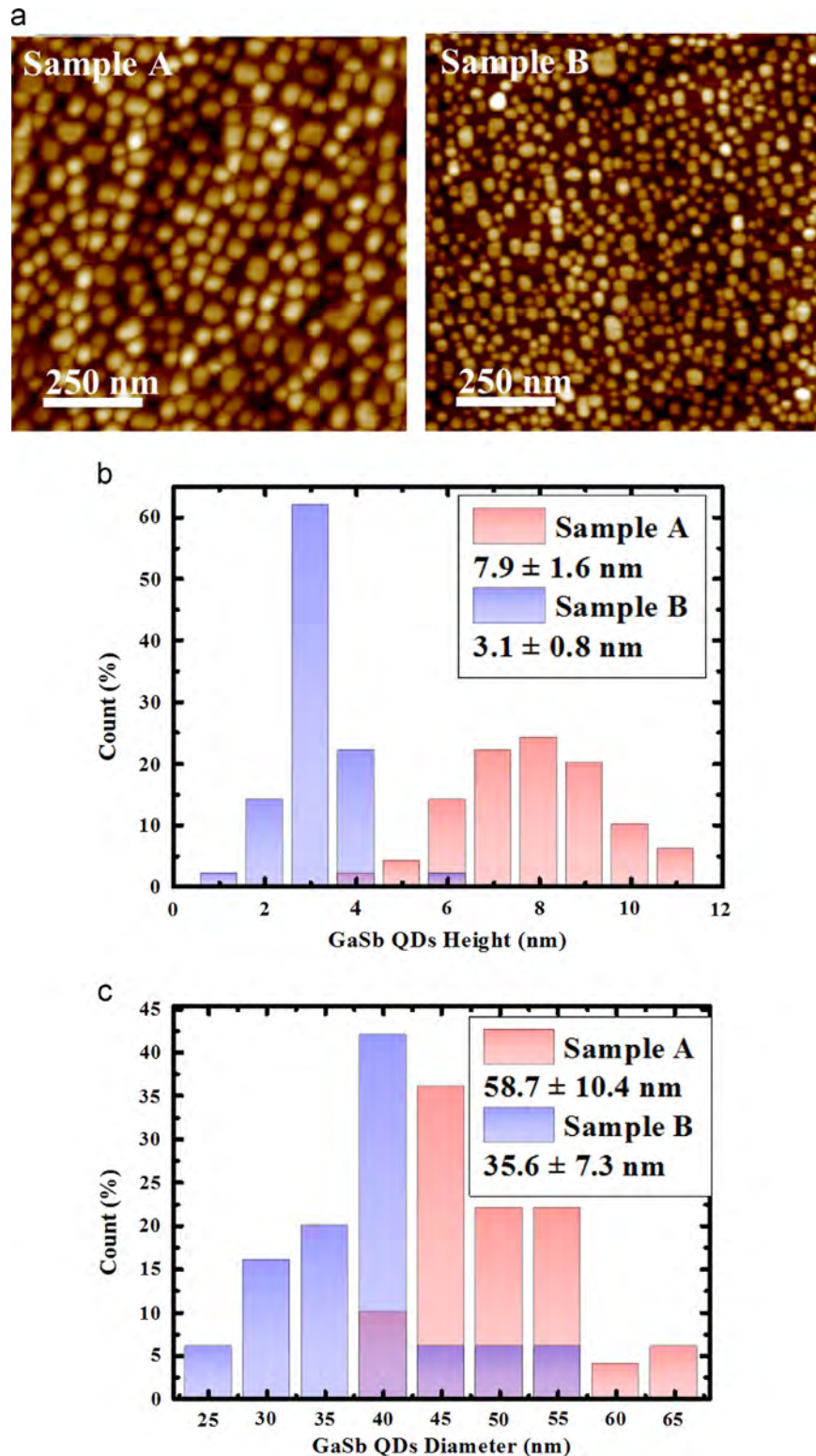
Fig. 1. (a) The 1×1 μm² AFM images of Samples A and B. (b) The dot diameter and (c) the dot height histograms of the two samples extracted from the AFM images.

microscopy (AFM) measurements. As$_4$ and Sb$_4$ are adopted for GaAs and GaSb material growth. The growth temperature for GaSb nanostructures is set at 470 °C with V/III ratio kept at 1. The growth rates of GaSb are determined by the thickness of 1.5 MLs GaSb divided by the appearance time of spotty reflection high-energy electron diffraction pattern (RHEED) [10]. For Sample A without growth interrupts, the growth time for 3 MLs GaSb deposition is 12 s. For sample B, C and D, six periods of 1 s. Ga shutter open and 4 s. interrupt are adopted by the periodical growth mode for 3 MLs GaSb deposition. The Sb shutter is kept open and the Ga source temperature and V/III ratios are the same for all the samples during GaSb growth. The shorter total Ga shutter open time for Samples B, C and D to achieve the same 3 MLs GaSb coverage suggests that higher GaSb growth rate is obtained by using periodical growth mode. The possible mechanism responsible for this phenomenon is the higher Ga sticking coefficient resulted from the effectively higher V/III ratios during GaSb growth for the three samples. The AFM measurements

are performed by using Veeco Innova SPM system. The PL measurements are performed by using the Jobin Yvon's NanoLog3 system coupled with a He–Ne laser as pumping source and a Janis cryostat to cool down the samples.

3. Result and discussion

The $1 \times 1\ \mu m^2$ AFM images of Samples A and B are shown in Fig. 1(a). As shown in the figure, slightly higher dot density $6.5 \times 10^{10}\ cm^{-2}$ is observed for Sample B than the value $4.1 \times 10^{10}\ cm^{-2}$ for Sample A. To investigate their diameter/height distributions, the dot diameter/height histograms of the two samples are shown in Fig. 1(b) and (c). The average dot diameters/heights of Samples A and B are 58.7/7.9 and 35.6/3.1 nm, respectively. As discussed in the experiment section, higher GaSb growth rate is obtained for Sample B with periodical growth mode due to the effectively higher V/III ratio. In this case, the less significant adatom migration of Sample B would result in higher dot density and smaller QDs in sizes [11]. Another phenomenon observed in the figure is the similar fluctuations ~20% in diameters and heights for the two samples. The results suggest that although Sample B is of longer adatom migration time (with additional 20 s. interrupt time), the possible dot uniformity improvement cancels out with its effectively higher GaSb growth rate such that similar size fluctuations are observed for the two samples.

It has been proposed elsewhere that full GaSb QD or QR morphologies can be obtained by well controlling the Sb/background As flux ratios during the post-growth Sb soaking procedure [7]. Although this method does provide a ready approach for full- dot or ring growth, it is difficult to verify actual Sb and As flux ratios reaching the substrate surfaces. Longer post Sb soaking time is also required by using this approach. Therefore, to achieve ring formation in a shorter post-growth Sb soaking time with controllable Sb and As flux ratios, Samples C and D with the same QD growth conditions as Sample B are prepared. During the shortened 60 s. post-growth Sb soaking time, the Sb/As ratios are kept at 0.25 and 0.05 with the As shutter open for Samples C and D, respectively. To investigate the growth evolution of GaSb QRs, the *in-situ* reflection high-energy electron diffraction (RHEED) patterns correspond to the growth procedure steps (2) to (4) are shown in Fig. 2(a), (b) and (c), respectively. Similar RHEED patterns evolution are observed for both Samples C and D. At step (2), the GaAs surface is soaked under Sb irradiation. In this case, the Sb atoms would exchange with As and take the As site. Then, a mono-layer of GaSb would be formed on the GaAs surface. The RHEED pattern would change from the GaAs 2×4 to GaSb 1×3 reconstruction
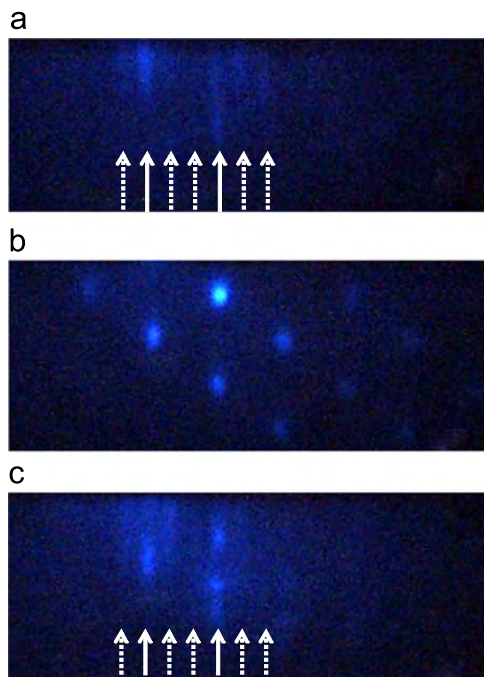
Fig. 2. The RHEED patterns correspond to different growth steps of (a) Sb presoaking procedure, (b) 3 ML GaSb QD formation and (c) post-growth Sb soaking procedure for GaSb QR growth. Similar RHEED patterns evolutions are observed for both Samples C and D. In (a) and (c), the solid arrow lines indicate the main lines while the dash arrow lines represent the 1/3 lines.
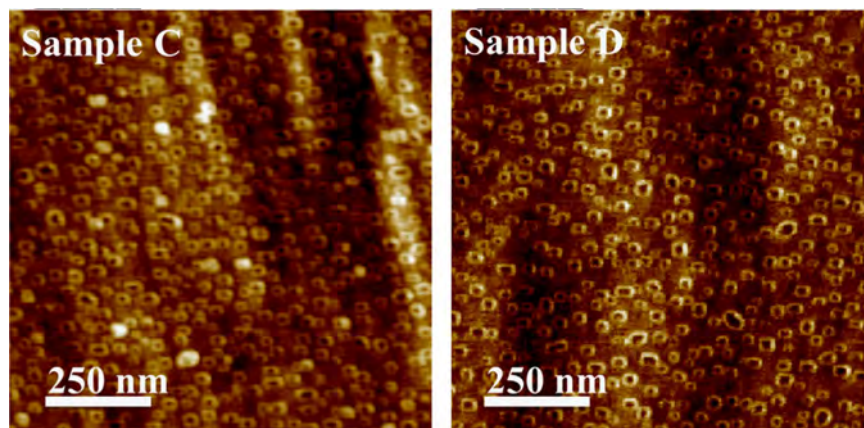
Fig. 3. The $1 \times 1\ \mu m^2$ AFM images of Samples C and D. The average heights 0.97 and 1.08 nm and the average diameters 44.586 nm and 42.742 nm are observed for the two samples, respectively.
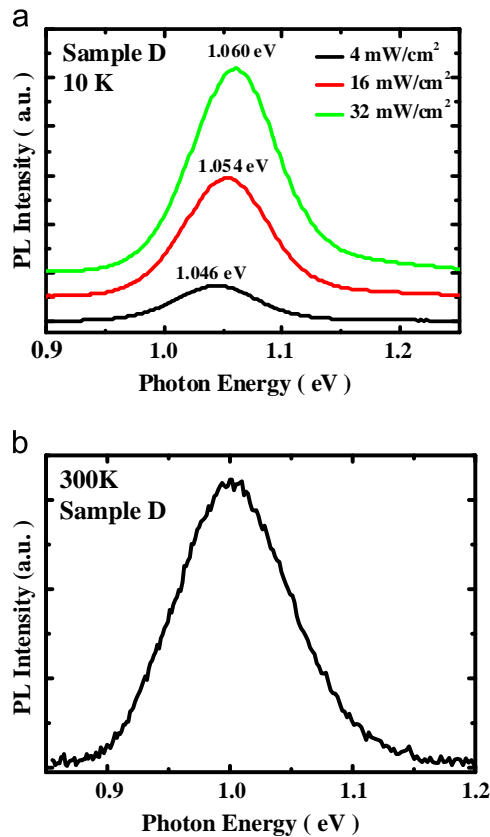
Fig. 4. (a) The 10 K power-dependent and (b) the room-temperature PL spectra of Sample D.

patterns as shown in Fig. 2(a). At step (3), periodical 2 ML GaSb is deposited on the pre-formed 1 ML GaSb layer such that in total 3 MLs of GaSb is grown on GaAs surface. Once the GaSb coverage reached the critical thickness 2.5 MLs including the pre-formed 1 ML GaSb, the 1×3 pattern would change into bright spotty RHEED pattern as shown in Fig. 2(b). At this stage, GaSb QDs are formed on the GaAs substrate. At the post-growth Sb soaking procedure step (3), with the direct As supply during this procedure, severe As-for-Sb exchange would take place. The bright spotty RHEED pattern would gradually change back to 1×3 pattern as shown in Fig. 2(c). After growth, the samples are moved out of the chamber for AFM measurements.

The $1 \times 1\ \mu m^2$ AFM images of Samples C and D are shown in Fig. 3. As shown in the figure, QD/QR mixture with total density of $4.1 \times 10^{10}\ cm^{-2}$ and full-ring morphologies with ring density $4.0 \times 10^{10}\ cm^{-2}$ and the average heights 0.97 and 1.08 nm are observed for Samples C and D, respectively. The much reduced ring heights ~ 1 nm of the two samples compared with the 3.1 nm dot height of Sample B would result in a near flat surface for RHEED observations. In this case, after the post-growth soaking Sb soaking procedure, although GaSb QRs are still on GaAs surfaces, the RHEED pattern shown in Fig. 2(c) would change back to 1×3 pattern. As shown in Fig. 3, with the lower As flux of Sample C, As-for-Sb exchange is not intense enough to convert all the dots to rings. The similar dot + ring and ring densities of the two samples with Sample A instead of Sample B suggest that smaller dots observed in Sample B may completely disappear during the intense As-for-Sb exchange process. In this case, reduced ring densities compared with Sample

B are observed for the two samples. The other supporting evidence comes from the similar ring outer diameters of Sample C and D with the dot diameter of Sample B.

One important characteristic for type-II hetero-structures is the PL peak blue shift with increasing pumping powers [3]. The 10 K PL spectra of Sample D under excitation power densities 4, 16 and 32 mW/cm^2 are shown in Fig. 4(a). The PL peak shift from 1.046 to 1.060 eV with increasing pumping power densities. The results suggest that the luminescence does come from the type-II GaSb/GaAs quantum rings. The major advantage of GaSb QDs and QRs prepared by using the extended post Sb soaking procedure is their superior optical characteristics and room-temperature luminescence [2]. The room-temperature PL spectrum of Sample D is shown in Fig. 4(b). The results suggests that by using periodical growth interrupts and direct As irradiations during the post-growth soaking procedure, high-quality GaSb QRs can also be obtained by using a single Ga source. Compared with the long 120 s. post Sb soaking time in previous publications [7], room-temperature luminescence can still be observed for the GaSb QRs prepared under reduced 60 s. post Sb soaking time with As atom directly irradiated on the substrates.

4. Conclusion

In conclusion, by using periodical growth interrupts, precise coverage control can be achieved for GaSb QD growth by using a single Ga source. With direct As irradiation to the substrate surface during the post Sb soaking procedure, the post-growth Sb soaking time can be reduced while full ring morphologies and room-temperature QR luminescence can still be observed by using this method. The periodical growth interrupts for GaSb QDs and direct As irradiation during the post Sb soaking procedure for GaSb QRs are proved to be a ready approach for the growth of GaSb nano-structures.

References

[1] A. Marent, M. Geller, A. Schliwa, D. Feise, K. Pötschke, D. Bimberg, N. Akçay, N. Öncan, Appl. Phys. Lett. 91 (2007) 242109.
[2] C.C. Tseng, S.C. Mai, W.H. Lin, S.Y. Wu, B.Y. Yu, S.H. Chen, S.Y. Lin, J.J. Shyue, M. C. Wu, IEEE J. Quantum Electron. 47 (2011) 335.
[3] S.Y. Lin, C.C. Tseng, W.H. Lin, S.C. Mai, S.Y. Wu, S.H. Chen, J.I. Chyi, Appl. Phys. Lett. 96 (2010) 123503.
[4] W.H. Lin, C.C. Tseng, K.P. Chao, S.C. Mai, S.Y. Kung, S.Y. Wu, S.Y. Lin, M.C. Wu, IEEE Photonics Technol. Lett. 23 (2011) 106.
[5] K.S. Hsu, T.T. Chiu, K.L. Wei-Hsun Lin, M.H. Chen, S.Y. Shih, Lin, Y.C. Chang, Appl. Phys. Lett. 98 (2011) 051105.
[6] M. Ahmad Kamarudin, M. Hayne, R.J. Young, Q.D. Zhuang, T. Ben, S.I. Molina, Phys. Rev. B 83 (2011) 115311.
[7] W.H. Lin, M.Y. Lin, S.Y. Wu, S.Y. Lin, IEEE Photonics Technol. Lett. 24 (2012) 1203.
[8] W.H. Lin, K.W. Wang, S.W. Chang, M.H. Shih, S.Y. Lin, Appl. Phys. Lett. 101 (2012) 031906.
[9] W.H. Lin, K.W. Wang, S.Y. Lin, M.C. Wu, IEEE Photonics Technol. Lett. 25 (2013) 97.
[10] K. Suzuki, R.A. Hogg, Y. Arakawa, J. Appl. Phys. 85 (1999) 8349.
[11] C.Y. Huang, M.C. Wu, J.J. Shen, S.Y. Lin, J. Appl. Phys. 103 (2008) 044301.
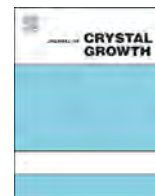
Fabrication of GaSb quantum rings on GaAs(0 0 1) by droplet epitaxy

CrossMark

Maetee Kunrugsa [a,*], Kar Hoo Patrick Tung [b], Aaron James Danner [b], Somsak Panyakeow [a], Somchai Ratanathammaphan [a]

[a] Semiconductor Device Research Laboratory (NANOTEC Center of Excellence), Department of Electrical Engineering, Chulalongkorn University, Bangkok 10330, Thailand
[b] Department of Electrical and Computer Engineering, National University of Singapore, Singapore 117576, Singapore

ABSTRACT

We report the achievement in the fabrication of self-assembled GaSb quantum rings (QRs) on GaAs (0 0 1) substrates by droplet epitaxy technique using molecular beam epitaxy. Surface morphology was characterized by atomic force microscopy. The QR formation can be described by the diffusion of Ga atoms out of an initial Ga droplet during crystallization with Sb flux. The understanding of the formation mechanism lights up the way to grow more complex GaSb nanostructures by droplet epitaxy. The optical properties of GaSb QRs in a GaAs matrix were investigated by photoluminescence (PL). Power- and temperature-dependent PL measurements were performed to study the carrier dynamics and to observe the characteristics of type-II band alignment.

© 2015 Elsevier B.V. All rights reserved.

1. Introduction

GaSb/GaAs quantum dots (QDs) are of interest owing to the staggered type-II band alignment where holes are strongly confined in the GaSb QDs, whereas electrons in a GaAs matrix form a shell around the QDs due to the Coulomb attraction. The spatial separation between electrons and holes makes the carrier lifetime become longer, which is promising for solar cells [1]. Moreover, the GaSb/GaAs QDs are plausible for the room-temperature charge storage devices as they possess the large hole confinement energy of 450 meV [2]. For the light-emitting applications, it seems that the GaSb/GaAs QDs are not suitable since the radiative recombination is less efficient in the type-II band alignment. Nevertheless, the photoluminescence (PL) and electroluminescence (EL) from the GaSb/GaAs QDs can be observed even at room temperature by performing the long Sb post-soaking [3]. The use of ring-shaped nanostructures or quantum rings (QRs) is another way to enhance the luminescence in the GaSb/GaAs system because there is more surface area for the recombination between the electrons in the GaAs matrix and the confined holes in the GaSb QRs [4]. A theoretical study also reveals that the GaSb/GaAs QRs are a good candidate for the observation of strong Aharonov–Bohm effect [5]. The GaSb QDs can be turned into the GaSb QRs by capping with a GaAs layer as a result of the As-for-Sb exchange reaction. Nonetheless, some QDs may still remain but in the smaller size,

affecting both the uniformity and the optical properties [6]. By the similar mechanism, the post-soaking with some Sb/As ratios on the GaSb QDs results in the formation of QRs [4]. Besides, the GaSb QRs can be formed by the molecular beam epitaxy (MBE) with an unusual growth procedure [7] or the metal–organic molecular beam epitaxy (MOMBE) with a partial-capping-and-regrowth technique [8]. These methods, however, require the special conditions and the complicated procedures. Therefore, we have demonstrated the utilization of droplet epitaxy, which is a simple method, in the fabrication of GaSb/GaAs QRs. The PL measurement was performed to study the optical properties of the QRs as well as the carrier dynamics.

2. Experimental procedure

GaSb QRs were grown on semi-insulating GaAs(0 0 1) substrates by droplet epitaxy technique using Riber Compact 21 solid-source MBE equipped with Sb valved-cracker cell. After the desorption of the native oxide at 580 °C under the As_4 flux of 8×10^{-6} Torr for 10 min, a 300-nm GaAs buffer layer was grown at 580 °C. Next, the substrate temperature (T_s) was reduced to 300 °C under the As_4 flux. When $T_s = 300$ °C, the As_4 flux was stopped supplying in order to eliminate the As atmosphere in the growth chamber. After that, it was needed to wait until the background pressure of the growth chamber was less than 5×10^{-9} Torr to prevent the initial reaction between Ga and As_4 during the Ga deposition. Then, the Ga amount of 3 monolayers (ML) (an equivalent amount of 3-ML GaAs grown under the As pressure)

* Corresponding author. Tel.: +668 5109 2131; fax: +662 251 8991.
E-mail address: k.maetee@gmail.com (M. Kunrugsa).

was deposited on the substrate surface at $T_s = 300\,°C$ with a deposition rate of 0.5 ML/s to form the liquid Ga droplets. Subsequently, T_s was decreased to $250\,°C$ and the Sb_4 flux of 5×10^{-7} Torr was irradiated to the substrate surface for 90 s to crystallize the Ga droplets into the GaSb nanocrystals. The formation of GaSb QRs after crystallization was indicated by the reflection high energy electron diffraction (RHEED) pattern featured by streaks and spots [9]. Finally, the sample was rapidly cooled down to room temperature. To confirm the existence of the Ga droplets after Ga deposition, another sample was provided by stopping the growth just after the Ga deposition at $T_s = 300\,°C$ without crystallization. Morphology of the Ga droplets and the GaSb QRs was investigated by atomic force microscopy (AFM) operated in dynamic mode.

For the PL study, the GaSb QRs were capped with a 150-nm GaAs layer. The details of the capping process have been reported

elsewhere [10]. A 514.5-nm Ar^+ laser having a spot size of ~0.3 mm was used as an excitation source. The PL spectra were detected by a cooled Ge detector. The power- and temperature-dependent PL measurements were also carried out.

3. Results and discussion

Fig. 1(a) shows an AFM image of Ga droplets having the density of $\sim1.8 \times 10^9$ cm^{-2}. A three-dimensional (3D) AFM image of a single Ga droplet and its cross-sectional profiles along [1 1 0] and [1 $\bar{1}$ 0] directions are depicted in Fig. 1(b). The average droplet size is 94 nm in diameter (*s*) and 10.6 nm in height (*t*). After the Ga droplets were exposed to the Sb_4 flux of 5×10^{-7} Torr for 90 s, the GaSb QRs were formed on the surface, as confirmed by the AFM image in Fig. 2(a) as well as the RHEED pattern consisting of
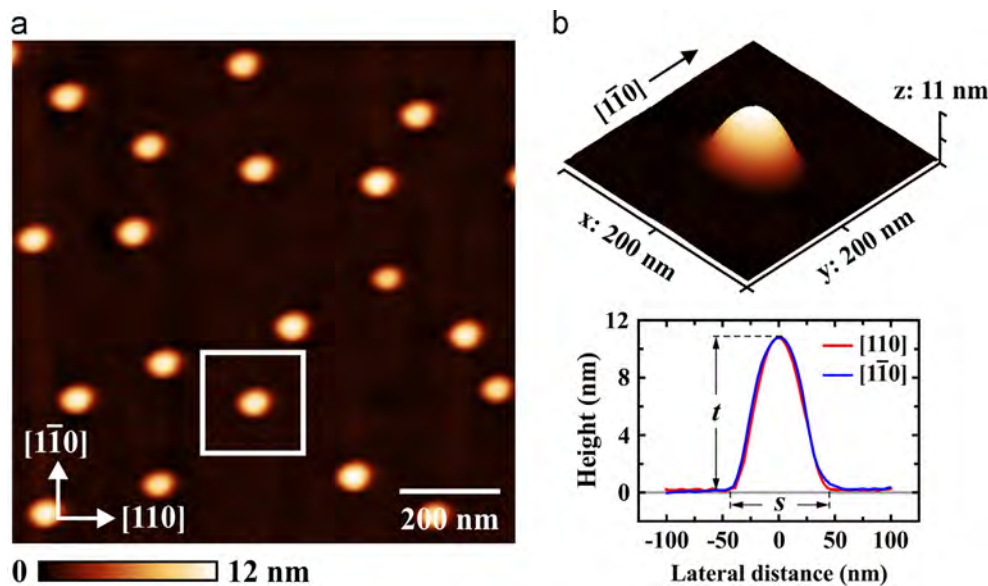
Fig. 1. (a) AFM image of Ga droplets. (b) Three-dimensional AFM image of a single Ga droplet (enclosed by a white square) with its cross-sectional profiles.
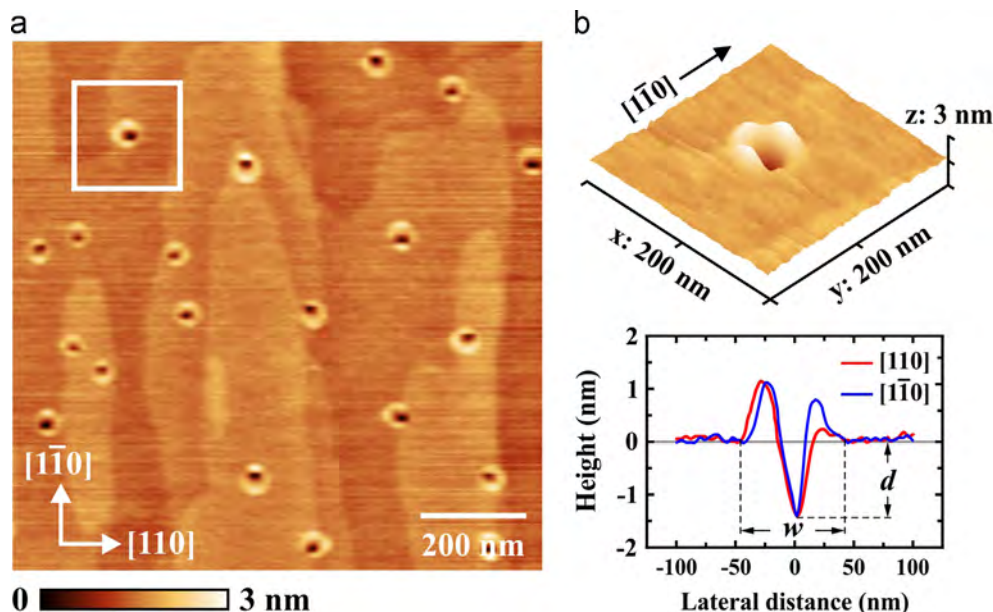
Fig. 2. (a) AFM image of GaSb QRs. (b) Three-dimensional AFM image of a single GaSb QR (enclosed by a white square) with its cross-sectional profiles.

streaks and spots. To make a closer look at the GaSb QR, the 3D AFM image of a single GaSb QR and its cross-sectional profiles are provided in Fig. 2(b). The average QR size is 96 nm in diameter (w) and 1.3 nm in depth (d). Compared with the droplet size, the larger average QR diameter indicates the outward diffusion of Ga atoms. Since the density of GaSb QRs is equivalent to the density of Ga droplets, it can be deduced that all Ga droplets were evolved into the GaSb QRs after crystallization with the Sb_4 flux.

The formation mechanism of the GaSb QR can be explained by the diffusion of Ga atoms from the initial Ga droplet. When Ga is deposited on the $c(4 \times 4)$ GaAs surface, the liquid Ga droplets are formed in consequence of Volmer-Weber-like growth mode. It results in a Ga-rich region at the interface between the Ga droplet and the GaAs surface. The GaAs surface underneath the droplet is thus dissolved into Ga and As atoms. Since the Sb_4 flux intensity used for the crystallization is not high, the periphery of Ga droplet would have more possibility to be crystallized into the GaSb nanocrystals. This is similar to the case of GaAs QRs grown by droplet epitaxy [11]. The growth of GaSb nanocrystals at the droplet periphery, therefore, has a higher rate than other parts and acts as the nucleation seed for the further GaSb growth. Because of the gradient of Ga atom concentration, Ga atoms from both the initial Ga droplet and the dissolved Ga atoms diffuse out of the droplet and react with the Sb_4 flux, giving rise to the lobe around the nanohole (see Fig. 2). The dissolved As atoms would be replaced by the Sb atoms due to the Sb-for-As exchange reaction [12]. Besides, the Sb-for-As exchange reaction turns the GaAs surface into the GaSb surface during crystallization. The shape of GaSb QRs is quite circular as a result of the isotropic diffusion of Ga atoms on the GaSb surface [13].

Fig. 3(a) shows the power-dependent PL measured at 7 K. The variation range of peak energy is around 1.103–1.122 eV for the GaSb QRs and 1.217–1.227 eV for the GaSb layer which is originated from the Sb-for-As exchange reaction during crystallization as above-mentioned. The excitation power (P) was varied from 5 to 150 mW. It is worth noting that the PL peak energies of GaSb QRs (E_{QR}) and GaSb layer (E_{layer}) shift to higher energies with increasing P (see Fig. 3(a)). This is a characteristic of the type-II band alignment [14]. The internal electric fields appeared at the GaSb/GaAs interfaces bend the conduction band into the triangular quantum wells (TQWs), giving rise to the quantized energy levels for electrons [15]. The increase of P enhances the accumulation of photogenerated carriers as well as the internal electric fields at the interfaces, resulting in the more bending conduction band and hence the raising up of electron quantization energy [15]. That is why E_{QR} and E_{layer} become blueshift when P increases. According to the TQW model, the electron quantization energy would increase proportionally with the third root of excitation power [15]. The plots of E_{QR} and E_{layer} as a function of the third root of excitation power ($P^{1/3}$) are shown in Fig. 3(b). The dependence of integrated PL intensities (IPLs) of GaSb QRs and GaSb layer on the excitation power is displayed in Fig. 3(c). As expected, E_{QR} increases linearly with $P^{1/3}$. Furthermore, the IPL of GaSb QRs is linearly dependent on P, implying that the carrier loss through the non-radiative recombination processes is negligible. It is noteworthy that E_{layer} becomes saturated when P exceeds 50 mW. This saturation behavior also appears in the IPL of GaSb layer. Such phenomena have been observed in the GaSb wetting layer (WL) in the growth of GaSb/GaAs QDs by a Stranski–Krastanov method and are attributed to the reduction of oscillator strength by screening within the 2D electron–hole plasma [16].

The temperature-dependent PL spectra taken by using $P = 100$ mW are displayed in Fig. 4(a). The PL spectra can be distinctly detected until 250 K. However, the observation of PL emissions at high temperatures reflects a good crystal quality. Fig. 4(b) shows the dependence of E_{QR} and E_{layer} on the temperature (T). Both E_{QR}
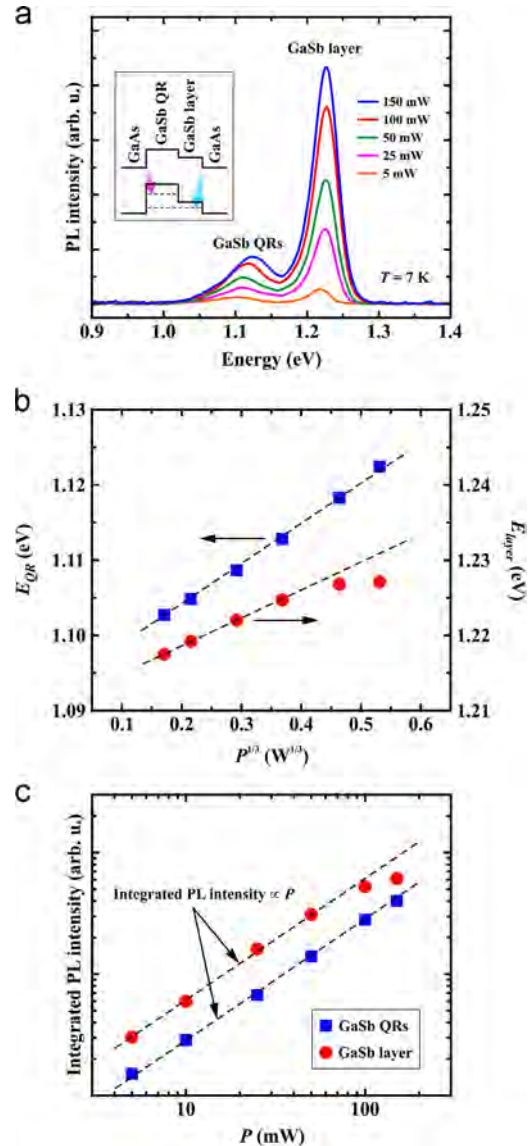
Fig. 3. (a) Power-dependent PL spectra at 7 K. The inset shows a schematic diagram of band alignment. (b) A plot of E_{QR} and E_{layer} as a function of the third root of excitation power. The dashed straight lines are guide for the eyes. (c) A log–log plot of integrated PL intensity as a function of the excitation power.

and E_{layer} exhibit the blueshift for the temperature range of 7–50 K and follow the band gap temperature dependence for high temperatures owing to the cumulative effects of the electron–phonon interaction and the thermal lattice expansion. The blueshift occurring at the low temperature range is another characteristic of the type-II band alignment and can be described by the more population of thermal-excited carriers, leading to the steeper TQW where the electron quantization energy is shifted up [15]. An Arrhenius plot of IPLs of GaSb QRs and GaSb layer is depicted in Fig. 4(c). The temperature dependence of IPL can be expressed by $I(T) = I_0/[1 + C\exp(-E_a/kT)]$ where I_0 is the IPL at 0 K, C is the constant, E_a is the activation energy, and k is the Boltzmann constant. The activation energy of ~ 160 meV is obtained for the GaSb QRs ($E_{a,QR}$) and ~ 215 meV for the GaSb layer ($E_{a,layer}$). $E_{a,layer}$ conforms to the calculated hole confinement energy for the GaSb WL (~ 207 meV) which is a similar structure to the GaSb layer [16], indicating that the PL quenching originates from the thermal escape of holes. From the carrier confinement point of view, the QRs confine the carriers in all three spatial directions like the QDs [17]. Thus, the GaSb QRs should have more activation energy than
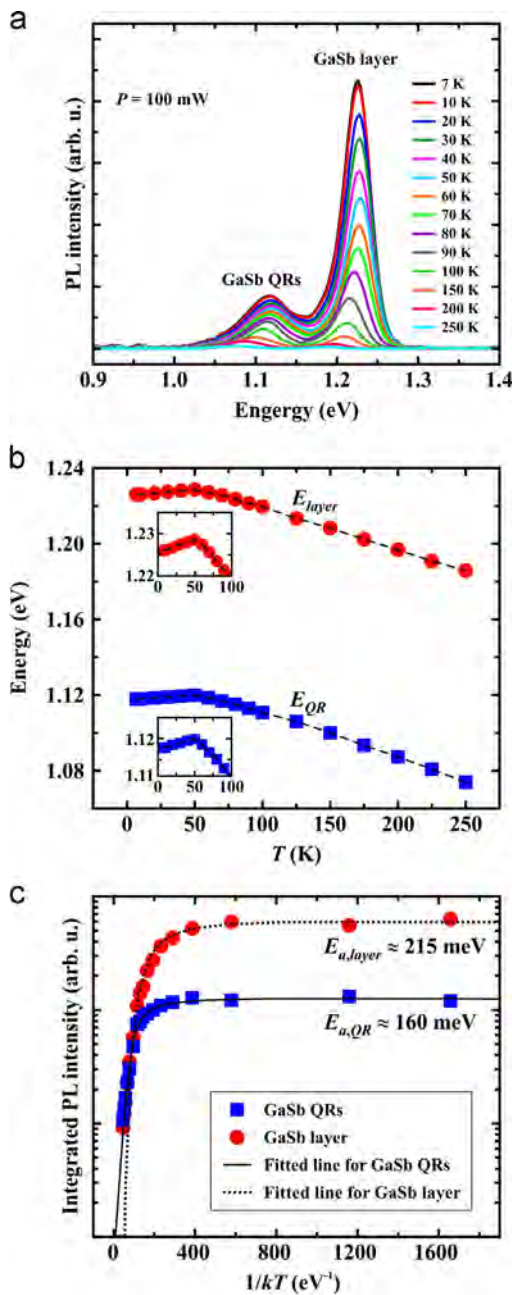
Fig. 4. (a) Temperature-dependent PL spectra obtained by using 100-mW excitation power. (b) A plot of E_{QR} and E_{layer} as a function of temperature. The dashed lines show the trends of variations. The insets are the magnified view in the temperature range of 0–100 K. (c) An Arrhenius plot of integrated PL intensity with the activation energy fit.

the GaSb layer. Nonetheless, we find that $E_{a,QR}$ is less than $E_{a,layer}$, implying that there should be a carrier transfer between the GaSb QRs and the GaSb layer. Fig. 4(c) reveals that the PL intensity of the GaSb layer decreases at the same time that the PL intensity of the GaSb QRs increases at $T = 175$ K ($1/kT \approx 66$ eV^{-1}), suggesting that the thermally escaped holes from the GaSb layer become captured into the GaSb QRs, and then contribute to the emission of the QRs.

That is why the PL intensity of the GaSb QRs drops slower than that of the GaSb layer.

4. Conclusion

We have successfully fabricated the self-assembled GaSb QRs on GaAs (0 0 1) substrates by droplet epitaxy technique. Each QR consists of the lobe around the nanohole as a result of the outward diffusion of Ga atoms from the initial droplet during crystallization with the Sb$_4$ flux. PL emission from the QRs, which can be observed at high temperatures, reveals the good crystal quality even the QRs were grown at the low temperature. The carrier dynamics and the signatures of type-II band alignment were investigated by the power- and temperature-dependent PL measurements.

References

[1] R.B. Laghumavarapu, A. Moscho, A. Khoshakhlagh, M. El-Emawy, L.F. Lester, D.L. Huffaker, Appl. Phys. Lett. 90 (2007) 173125.
[2] M. Geller, C. Kapteyn, L. Müller-Kirsch, R. Heitz, D. Bimberg, Appl. Phys. Lett. 82 (2003) 2706.
[3] S.-Y. Lin, C.-C. Tseng, W.-H. Lin, S.-C. Mai, S.-Y. Wu, S.-H. Chen, J.-I. Chyi, Appl. Phys. Lett. 96 (2010) 123503.
[4] W.-H. Lin, C.-C. Tseng, S.-Y. Wu, M.-H. Wu, S.-Y. Lin, M.-C. Wu, Phys. Status Solidi C 9 (2012) 314.
[5] M. Grochol, F. Grosse, R. Zimmermann, Phys. Rev. B 74 (2006) 115416.
[6] M.A. Kamarudin, M. Hayne1, Q.D. Zhuang, O. Kolosov, T. Nuytten, V.V. Moshchalkov, F. Dinelli, J. Phys. D: Appl. Phys. 43 (2010) 065402.
[7] S. Kobayashi, C. Jiang, T. Kawazu, H. Sakaki, Jpn. J. Appl. Phys. 43 (2004) L662.
[8] S. Odashima, S. Sakurai, M. Wada, I. Suemune, J. Cryst. Growth 323 (2011) 233.
[9] Á. Nemcsics, Ch. Heyn, A. Stemmann, A. Schramm, H. Welsch, W. Hansen, Mater. Sci. Eng. B 165 (2009) 118.
[10] M. Kunrugsa, S. Kiravittaya, S. Panyakeow, S. Ratanathammaphan, J. Cryst. Growth 402 (2014) 285.
[11] T. Mano, N. Koguchi, J. Cryst. Growth 278 (2005) 108.
[12] R. Timm, A. Lenz, H. Eisele, L. Ivanova, M. Dähne, G. Balakrishnan, D.L. Huffaker, I. Farrer, D.A. Ritchie, J. Vac. Sci. Technol. B 26 (2008) 1492.
[13] M. DeJarld, K. Reyes, P. Smereka, J.M. Millunchick, Appl. Phys. Lett. 102 (2013) 133107.
[14] F. Hatami, N.N. Ledentsov, M. Grundmann, J. Böhrer, F. Heinrichsdorff, M. Beer, D. Bimberg, S.S. Ruvimov, P. Werner, U. Gösele, J. Heydenreich, U. Richter, S.V. Ivanov, B.Ya. Meltser, P.S. Kop'ev, Zh.I. Alferov, Appl. Phys. Lett. 67 (1995) 656.
[15] N.N. Ledentsov, J. Böhrer, M. Beer, F. Heinrichsdorff, M. Grundmann, D. Bimberg, S.V. Ivanov, B.Ya. Meltser, S.V. Shaposhnikov, I.N. Yassievich, N.N. Faleev, P.S. Kop'ev, Zh.I. Alferov, Phys. Rev. B 52 (1995) 14058.
[16] D. Alonso-Álvarez, B. Alén, J.M. García, J.M. Ripalda, Appl. Phys. Lett. 91 (2007) 263103.
[17] R.J. Warburton, C. Schäflein, D. Haft, F. Bickel, A. Lorke, K. Karrai, J.M. García, W. Schoenfeld, P.M. Petroff, Nature 405 (2000) 926.
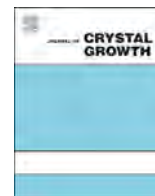
Molecular beam epitaxial growth of GaSb quantum dots on (0 0 1) GaAs substrate with InGaAs insertion layer

CrossMark

Kamonchanok Khoklang [a], Suwit Kiravittaya [b], Maetee Kunrugsa [a], Patchareewan Prongjit [a], Supachok Thainoi [a], Somchai Ratanathammaphan [a], Somsak Panyakeow [a,*]

[a] The Semiconductor Device Research Laboratory (SDRL), Department of Electrical Engineering, Faculty of Engineering, Chulalongkorn University, Bangkok 10330, Thailand
[b] Department of Electrical and Computer Engineering, Faculty of Engineering, Naresuan University, Phitsanulok 65000, Thailand

ARTICLE INFO

ABSTRACT

We report on the molecular beam epitaxial growth of self-assembled GaSb quantum dots (QDs) on (0 0 1) GaAs substrates with an insertion layer. The insertion layer, which is a 4-monolayers (MLs) $In_xGa_{1-x}As$ ($x=0.00$, 0.07, 0.15, 0.20 and 0.25), is grown prior to the QD growth. With this InGaAs insertion layer, the obtained QD density decreases substantially, while the QD height and diameter increase as compared with typical GaSb QDs grown on conventional (0 0 1) GaAs surface under the same growth condition. The GaSb QDs on GaAs have the dome shape with elliptical base and the elongation direction of the base is along the [1 1 0] direction. When the InGaAs insertion layer is introduced, the distinct elongation disappears and the QD sidewall shows facet-related surfaces with (0 0 1) plateau on top.

© 2015 Elsevier B.V. All rights reserved.

1. Introduction

For a few decades, semiconductor quantum dots (QDs) have gained considerable interests due to their promising properties for device applications. Many electronic and optoelectronic devices based on III–V QDs have been investigated [1–6]. They include lasers, light emitting diodes, photodetectors, photovoltaic cells and memories. Among these devices, self-assembled In(Ga)As/GaAs QD is a major dot system that has been investigated. However, GaSb/GaAs QDs, which have a type II band alignment, might be more suitable for some applications. For instance, GaSb/GaAs has been proposed to be used in charge-based memory device due to its large hole confinement [5]. Device performance will depend on the QD properties. It is therefore of interest to investigate structural properties of obtained QDs under various growth conditions in order to fine-tune them for any specific applications. In literature, different GaSb QD shapes have been reported [7,8]. For example, Jiang et al. [7] have shown that the elongation of GaSb QDs along the [1 1 0] direction can be controlled by changing the V/III ratio.

In this work, we report on the structural properties of free-standing self-assembled GaSb QDs when $In_xGa_{1-x}As$ insertion layers with $x=0.00$, 0.07, 0.15, 0.20 and 0.25 are introduced. All samples were grown by a molecular beam epitaxy (MBE) with an Sb valved-cracker cell and investigated by atomic force microscopy (AFM). The presence of indium in InGaAs insertion layer induces the substantial decrement of QD density, the enlargement of QD size (both height and diameter) and the transition from elongated QD shape to QD with facet-related sidewalls and (0 0 1) plateau on top.

2. Experiments

All samples were grown on semi-insulating (0 0 1) GaAs substrates in Riber Compact 21 solid-source MBE equipped with an Sb valved-cracker cell. After the deoxidation of surface oxide on GaAs substrate at 580 °C under As_4 atmosphere, GaAs buffer layer was grown at this temperature with the growth rate of 0.5 monolayer per second (ML/s). During the growth, reflection high-energy electron diffraction (RHEED) pattern was observed and well-prepared buffer layer ((0 0 1) GaAs surface) showed a clear (2×4) surface reconstruction. In order to grow the InGaAs insertion layer, the substrate temperature was ramped down to 500 °C. After the substrate temperature stabilized, 4-ML $In_xGa_{1-x}As$ was grown. This thickness is chosen so as to have a flat InGaAs surface without any surface relaxation [9]. When growing this layer, indium and gallium
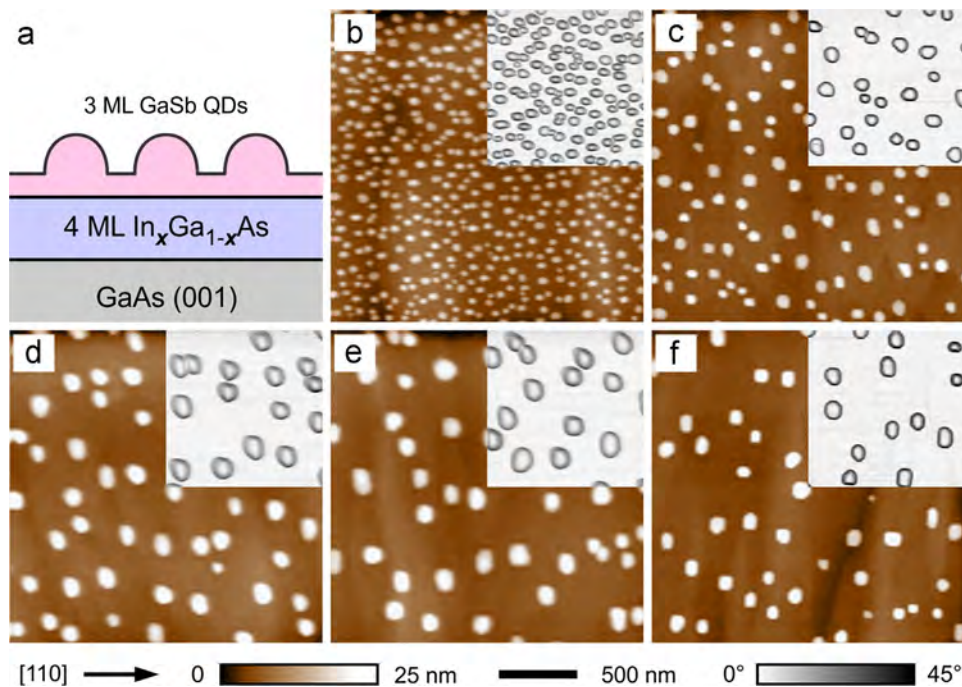
Fig. 1. (a) Schematic diagram of the investigated structure: GaSb QDs (3 ML) on top of 4-ML-thick $In_xGa_{1-x}As$ insertion layer. (b)–(e) 2×2 μm^2 AFM images of GaSb QDs on $In_xGa_{1-x}As$ with $x=0.00$, 0.07, 0.15, 0.20 and 0.25, respectively. Insets show a portion of the same AFM images with surface slope scale.

growth rates are changed in order to obtain the desired content of indium in InGaAs layer. For $x=0.07$, 0.15, 0.20, and 0.25, the indium rates are 0.025, 0.025, 0.025, and 0.033 ML/s and gallium rates are 0.33, 0.14, 0.10, and 0.10 ML/s, respectively. After the InGaAs insertion layer growth, the sample surface was soaked by Sb flux for 60 s. Self-assembled GaSb QDs are obtained by depositing 3-ML GaSb at the gallium growth rate of 0.1 ML/s. The V/III flux ratio (Sb/Ga) is kept constant at 4. After the growth, the sample was cooled down immediately. The surface morphology was characterized by an AFM (Seiko SPA-400) in dynamic force mode in air and the post-processing was done in MATLAB program.

3. Results and discussion

Fig. 1(a) shows a schematic diagram of investigated surface structure. Fig. 1(b)–(e) show 2×2 μm^2 AFM images of GaSb QDs on GaAs (Fig. 1(b)) and on $In_xGa_{1-x}As$ (Fig. 1(c)–(f)) surfaces. Insets of AFM images in Fig. 1(b)–(f) show a portion of the surface (obtained from the same AFM image) with surface slope scale [10]. Distinct surface morphology is observed when $In_xGa_{1-x}As$ layer is introduced, i.e., QD density substantially decreases and QD size increases. Gradual morphology changes are still observed when the indium content increases from $x=0.07$ (Fig. 1(c)) to 0.25 (Fig. 1(f)). This is due to the presence of different amount of indium in the InGaAs insertion layer.

Analysis of height and diameter distributions of GaSb QDs on different InGaAs insertion layers is displayed as histograms in Fig. 2. The data are obtained from the analysis of *individual QD* in each AFM image (shown in Fig. 1(b)–(e)). First, the QD base area is extracted from the largest closed-loop contour line of contour plots of the AFM data. The QD diameter is then calculated with a circular base approximation. The QD height is obtained from the difference between the height level of the largest closed-loop contour line and the maximum height data. Histograms of QD height and QD diameter are then fitted with Gaussian functions. Fitted center positions together with the fitted curves are shown in Fig. 2. From this figure, one can clearly see that both QD height and diameter increase when the InGaAs insertion layer is introduced. Abrupt change is observed when the indium content is changed from $x=0.0$ (no insertion layer) to $x=0.07$. By further increasing the indium content, the QD height and diameter increase except only at the indium content of $x=0.25$ where we observe the reduction of diameter. This non-monotonic diameter change might be due to the excessively high indium content on the surface. Indium adatoms might still present after 60-s Sb-soaking process because of their initially high content. Incorporating indium atoms into GaSb QDs induce high mismatch strain and enhance the growth of large aspect ratio QDs since the QD with a high ratio can relax more strain [11].

Fig. 2. Histograms of QD height and diameter distribution of GaSb QDs on $In_xGa_{1-x}As$ with $x=0.00$ (top), 0.07, 0.15, 0.20 and 0.25 (bottom). Solid lines are Gaussian function fits. Center position of the obtained Gaussian function fits are indicated in the figures.

Fig. 3 summarizes the structural variation of GaSb QDs on the $In_xGa_{1-x}As$ insertion layer as a function of indium content in the insertion layer. When the InGaAs insertion layer is introduced, the QD density reduces, whereas QD height and diameter increase, as depicted in Fig. 3(a)–(c). The initial GaSb QD density, which is about $120\ \mu m^{-2}$, decreases to less than $30\ \mu m^{-2}$, while the average QD height increases about 1.5 times (from 9.5 nm for $x=0.0$ to 14.5 nm for $x=0.07$) when the $In_{0.07}Ga_{0.93}As$ layer is inserted. These observations are attributed to the change of initial surface energy, interface energy as well as the strain energy of the QD system [11,12].
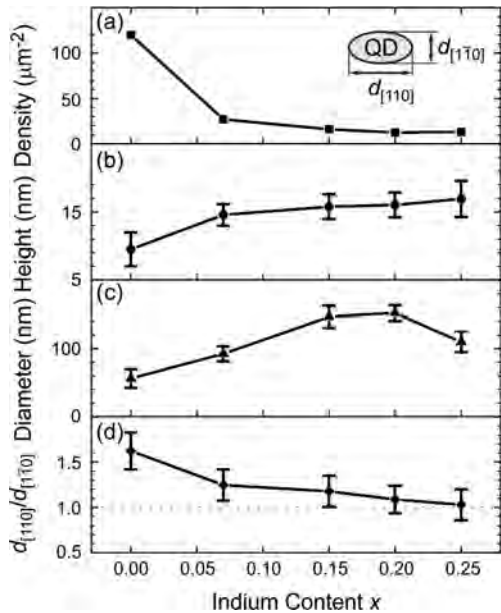
Fig. 3. Variations of (a) QD density, (b) average QD height, (c) average QD diameter and (d) degree of elongation (defined as $d_{[1\ 1\ 0]}/d_{[1\ \overline{1}\ 0]}$) as a function of indium content x in $In_xGa_{1-x}As$ insertion layer. Inset of (a) shows the definition of $d_{[1\ 1\ 0]}$ and $d_{[1\ \overline{1}\ 0]}$. The error bars in (b)–(d) are the standard deviation of the values.

To investigate the QD shape anisotropy, we define a degree of QD elongation as the ratio $d_{[1\ 1\ 0]}/d_{[1\ \overline{1}\ 0]}$, where $d_{[1\ 1\ 0]}$ and $d_{[1\ \overline{1}\ 0]}$ is the length of QD base along the [1 1 0] and [1 $\overline{1}$ 0] direction, respectively. Inset of Fig. 3(a) shows a schematic diagram of a QD with these lengths. Fig. 3(d) displays the degree of elongation as a function of indium content obtained from the AFM data. The elongation of GaSb QD shape gradually changes from a clear elongation along the [1 1 0] direction to almost isotropic (no elongation) QD shape. This change can relate to the distinct {1 1 n}-facet formation on QD surface when the InGaAs insertion layer is introduced and it will be explained below. It is noteworthy that this structural elongation influences the intrinsic properties of QDs such as their polarization dependency [7] and their transport properties [13].

For further quantifying the QD shape, a surface orientation mapping, which is so-called facet plot, is analyzed [10,14]. Fig. 4(a) shows the facet plot obtained from the QD surface of a GaSb QD without InGaAs insertion layer as compared that with $In_{0.07}Ga_{0.93}As$ insertion layer (Fig. 4(b)). From these plots (and also the insets of Fig. 1(b)–(f)), we can clearly see that the (0 0 1) surface as a plateau on top of each GaSb QD is present when InGaAs insertion layer is introduced. This plateau is also observed in other AFM images of GaSb QDs grown on InGaAs surface (not shown). Apart from this plateau, other facet surfaces, which are likely to orient along the {1 1 n} directions, are observed in the facet plot (see Fig. 4(b)). The facet-related surfaces are on the sidewall of the QDs. It is known from previous theoretical growth study that facet can form on the sidewall of QD due to its low surface energies [15]. This induces the so-called self-limiting growth, which stabilizes the QD size and shape. When indium content in the insertion layer increases, the sidewall facets tend to become steeper. However, due to the limited resolution of our AFM, we cannot fully identify the facet indices. Based on our investigation, we can draw simple illustrations for the shape of GaSb QD grown on GaAs and InGaAs surfaces as shown in Fig. 4(c) and (d), respectively. For GaSb QDs on GaAs, we obtain an elongated base QD with rather round shape, while the GaSb QDs on InGaAs show some facetted surfaces with the (0 0 1) plateau on top. Moreover, the height and diameter of GaSb QDs on InGaAs are larger than those on GaAs.
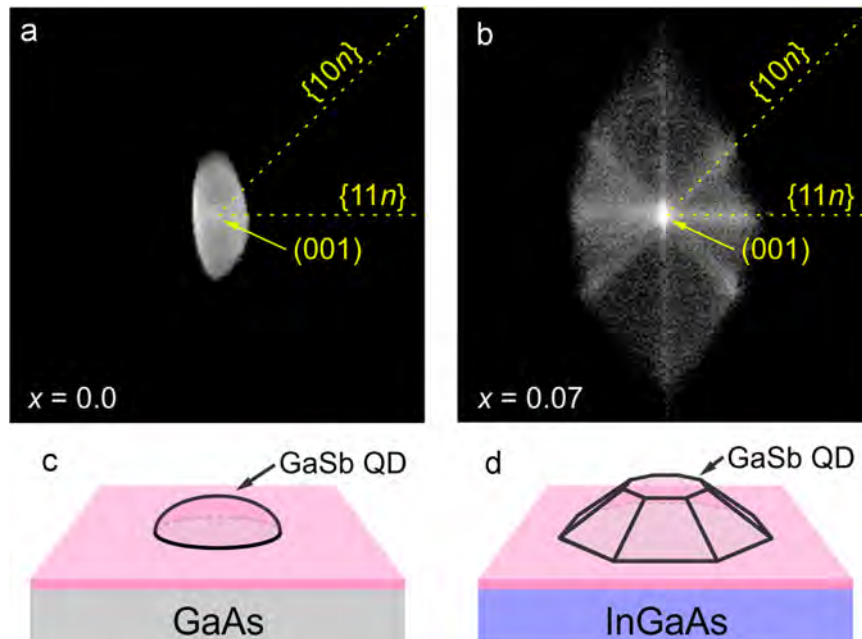
Fig. 4. Facet plots obtained from the QD surface of a GaSb QD (a) without and (b) with $In_{0.07}Ga_{0.93}As$ insertion layer. (c) and (d) are illustrations of GaSb QD on (0 0 1) GaAs surface and on (0 0 1) InGaAs surface. Relatively small QDs, which are elongated along the [1 1 0] direction, are observed for GaSb growth on GaAs, while large facet-related GaSb QDs are formed when InGaAs insertion layer is introduced before the QD growth.

4. Conclusions

We present an investigation of structural morphology of self-assembled GaSb QDs on (0 0 1) GaAs substrates. We have shown that when the InGaAs insertion layer is introduced, the obtained QD morphology considerably changes. The QD density decrement as well as QD size (height and diameter) enlargement are observed. Besides, the degree of QD elongation changes from a distinct elongation along the [1 1 0] direction to an isotropic shape when the indium content in InGaAs insertion layer increases. Finally, we have shown that the GaSb QDs on InGaAs have a clear (0 0 1) plateau on top and facet-related surfaces on the sidewalls.

References

[1] V.M. Ustinov, A.E. Zhukov, N.A. Maleev, A.R. Kovsh, S.S. Mikhrin, B.V. Volovik, Y.G. Musikhin, Y.M. Shernyakov, M.V. Maximov, A.F. Tsatsul'nikov, N.N. Ledentsov, Zh.I. Alferov, J.A. Lott, D. Bimberg, 1.3 μm InAs/GaAs quantum dot lasers and VCSELs grown by molecular beam epitaxy, J. Cryst. Growth 227-228 (2001) 1155–1161.
[2] J. Sabarinathan, P. Bhattacharya, P-C. Yu, S. Krishna, An electrically injected InAs/GaAs quantum-dot photonic crystal microcavity light-emitting diode, Appl. Phys. Lett. 81 (2002) 3876–3878.
[3] K. Hirakawa, S.-W. Lee, Ph. Lelong, S. Fujimoto, K. Hirotani, H. Sakaki, High-sensitivity modulation-doped quantum dot infrared photodetectors, Microelectron. Eng. 63 (2002) 185–192.
[4] K. Tanabe, D. Guimard, D. Bordel, Y. Arakawa, High-efficiency InAs/GaAs quantum dot solar cells by metalorganic chemical vapor deposition, Appl. Phys. Lett. 100 (2012) 193905.
[5] M. Hayne, R.J. Young, E.P. Smakman, T. Nowozin, P. Hoidgson, J.K. Garleff, P. Rambabu, P.M. Koenraad, A. Marent, L. Bonato, A. Schliwa, D. Bimberg, The structural, electronic and optical properties of GaSb/GaAs nanostructures for charge-based memory, J. Phys. D: Appl. Phys. 46 (2013) 264001.
[6] C.C. Tseng, W.-H. Lin, S.-Y. Wu, S.-H. Chen, S.-Y. Lin, The transition mechanisms of type-II GaSb/GaAs quantum-dot infrared light-emitting diodes, J. Cryst. Growth 323 (2011) 466–469.
[7] C. Jiang, T. Kawazu, S. Kobayashi, H. Sakaki, Molecular beam epitaxial of very large anisotropic GaSb/GaAs quantum dots, J. Cryst. Growth 301-302 (2007) 828–832.
[8] M. Kunrugsa, S. Kiravittaya, S. Sopitpan, S. Ratanathammaphan, S. Panyakeow, Molecular beam epitaxial growth of GaSb/GaAs quantum dots on Ge substrates, J. Cryst. Growth 401 (2014) 441–444.
[9] G.L. Price, Critical-thickness and growth-mode transitions in highly strained $In_xGa_{1-x}As$ films, Phys. Rev. Lett. 66 (1991) 469–472.
[10] S. Kiravittaya, A. Rastelli, O.G. Schmidt, Self-assembled InAs quantum dots on patterned GaAs(0 0 1) substrates: formation and shape evolution, Appl. Phys. Lett. 87 (2005) 243112.
[11] V.A. Shchukin, D. Bimberg, Spontaneous ordering of nanostructures on crystal surfaces, Rev. Mod. Phys. 71 (1999) 1125–1171.
[12] H. Eisele, M. Dähne, Critical thickness of the 2-dimensional to 3-dimensional transition in GaSb/GaAs(0 0 1) quantum dot growth, J. Cryst. Growth 338 (2012) 103–106.
[13] G. Li, C. Jiang, H. Sakaki, Anisotropic scattering of elongated GaSb/GaAs quantum dots embedded near two-dimensional electron gas, J. Nanosci. Nanotechnol. 11 (2010) 10792–10795.
[14] G. Costanini, A. Rastelli, C. Manzano, R. Songmuang, O.G. Schmidt, K. Kern, K. von Känel, Universal shapes of self-organized semiconductor quantum dots: striking similarities between InAs/GaAs(0 0 1) and Ge/Si(0 0 1), Appl. Phys. Lett. 85 (2004) 5673–5675.
[15] D.E. Jesson, G. Chen, K.M. Chen, S.J. Pennycook, Self-limiting growth of strained faceted islands, Phys. Rev. Lett. 80 (1998) 5156–5159.
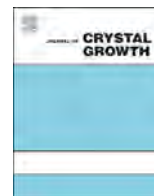
Electron g-factor and spin decoherence in GaAs quantum nanodisks fabricated by fully top-down lithography

Toru Tanaka [a], Takayuki Kiba [a,d], Akio Higo [b], Cedric Thomas [c,d], Yosuke Tamura [c], Seiji Samukawa [b,c,d], Akihiro Murayama [a,d,*]

[a] Graduate School of Information Science and Technology, Hokkaido University, Kita 14, Nishi 9, Kita-ku, Sapporo, Japan
[b] WPI-AIMR, Tohoku University, 2-1-1 Katahira, Aoba-ku, Sendai, Japan
[c] Institute of Fluid Science, Tohoku University, 2-1-1 Katahira, Aoba-ku, Sendai, Japan
[d] CREST Japan Science and Technology Agency, 5 Sanbancho, Chiyoda, Japan

ARTICLE INFO

ABSTRACT

GaAs nanodisks (NDs), with a thickness of 8 nm and a diameter of 15 nm, were directly fabricated from GaAs quantum wells (QW) by damage-free neutral-beam etching using bio-nanotemplates. We observed the electron g-factor and spin dephasing in NDs with different barrier heights in the lateral direction by means of time-resolved Kerr rotation. The magnitude of the g-factor depends on the degree of lateral confinement originating from enhanced penetration of the electron wavefunction from an ND into the surrounding AlGaAs barriers. The spin-dephasing time is also observed to be altered by ND formation.

1. Introduction

Carrier spin states, along with dynamics including precession of spin, in the quantum structures of III–V compound semiconductors have garnered considerable attention; since spin dynamics can be strongly affected by carrier momentum and scattering through spin–orbit interactions. Quantum nanodisks (NDs) of GaAs with desirable optical qualities have recently been grown from quantum wells (QWs) by fully top-down lithography, using damage-free neutral-beam etching aided by bio-engineering [1–4]. This fabrication method allows us to flexibly design the structural parameters of the NDs. Specifically, the thickness, diameter, and interval can be individually controlled by protein engineering [3,4]. This enables us to investigate effects of the lateral quantum confinement of carriers or excitons on spin dynamics. In fact, we have recently reported a significant suppression of exciton-spin relaxation in GaAs NDs by observing circularly polarized transient photoluminescence (PL) [5]. In this work, we expand on these methods to study transient optical Kerr effects under magnetic fields in GaAs NDs, which enables us to elucidate more detailed factors responsible for spin dynamics, such as the g-factor and relaxation of precession, i.e., spin dephasing.

2. Experiment

The GaAs NDs were prepared in a manner similar to that described in [3,4]. First, three layers of an 8-nm-thick GaAs/$Al_{0.15}Ga_{0.85}As$ QW were sandwiched by 100-nm-thick $Al_{0.15}Ga_{0.85}As$ barrier layers and a 1.4-μm-thick $Al_{0.30}Ga_{0.70}As$ bottom cladding layer was grown on a GaAs (100) substrate by metal–organic vapor phase epitaxy (MOVPE). The top part of each QW was capped with a 20-nm-thick GaAs layer. The sample was removed from the MOVPE environment and the surface was coated with ferritin supramolecules containing iron nanoparticles in their cavities. The average center-to-center distance of the dispersive ferritin molecules was 45 nm, which was set intentionally by attaching polyethylene–glycol polymer chains of a specific length to the exterior of the ferritin shell. The iron particles remaining after removal of the ferritin protein shells were then used as a mask for a subsequent etching. Neutral-beam etching allowed for the fabrication of nanoscale pillars containing a disk-shaped QW section, i.e., a GaAs ND, without optically inactive non-radiative centers. Finally, AlGaAs barriers and GaAs capping layers were re-grown by MOVPE. The barrier height in the lateral direction was varied solely by changing the Al composition of the re-grown AlGaAs barrier, e.g., $Al_{0.15}Ga_{0.85}As$ (GaAs ND1) and $Al_{0.30}Ga_{0.70}As$ (GaAs ND2). These samples permitted the investigation of quantum confinement effects on spin dynamics with lateral variation and constant vertical confinement. Such a systematic study of spin dynamics in quantum dots (QDs) with precisely controlled structural parameters has not yet been performed adequately using conventional QD systems prepared by the Stranski–Krastanov growth mode.

* Corresponding author at: Graduate School of Information Science and Technology, Hokkaido Univ., Kita 14, Nishi 9, Kita-ku, Sapporo, Japan.
  E-mail address: murayama@ist.hokudai.ac.jp (A. Murayama).
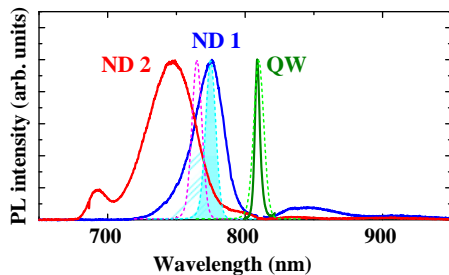
Fig. 1. PL spectra of GaAs QW (green), GaAs ND1 (blue) and GaAs ND2 (red) at 4 K. The laser spectra used for the time-resolved Kerr-rotation measurements are also shown as dashed lines with shaded area. (For interpretation of the references to color in this figure legend, the reader is referred to the web version of this article.)

Time-resolved Kerr effects were measured using a reflection-type pump–probe technique under magnetic fields of varied magnitude. Fundamental pulses of a mode-locked Ti: Sapphire laser with a pulse width of 160 fs and repetition rate of 80 MHz was used as a light source. Laser wavelengths were tuned in the resonant condition to the grand-state transition energy of each sample, which are shown in Fig. 1 together with the PL spectra. A balance photodiode, operated by a dual-chopped lock-in technique, was used for detecting the polarization change in the reflection probe light. The wavelengths of the pump/probe lights were tuned to the optical transition energies of the samples, which were determined by PL. Typical excitation-power values were 40 mW for the pump and 10 mW for the probe beams, respectively. The measurements were carried out in a magneto-optical cryostat equipped with a superconducting magnet. Temperature was fixed at 4 K and magnetic fields up to 6 T were applied with Voigt geometry.

3. Results and discussion

We observed two decaying components, with respective decay times of several picoseconds and several hundred picoseconds, of the Kerr signals in the Faraday geometry. These were used to quantify the longitudinal spin-relaxation dynamics. The slower decaying component can be observed above 100 K and is attributed to electron-spin relaxation because holes can thermally escape from the NDs at such high temperatures (owing to the relatively shallow potential confinement). Fig. 2 shows typical time-resolved Kerr rotation signals at 4 K in the Voigt geometry for the original GaAs QW and for the ND samples, where initial spin pumping was performed optically by circularly polarized pump pulses. The Kerr signal intensity is known to be proportional to the Kerr rotation angle (Θ_k); the electron-spin precession can be observed with a specific frequency determined by the g-factor, which is described by the following equation [6,7]:

$$\Theta_k = A \exp(-t/T_2) \cos(g\mu_B Bt/\hbar + \varphi), \tag{1}$$

where A is an initial amplitude proportional to the initial spin polarization generated along the optical axis, t is the time delay, T_2 is the spin dephasing time, g is the g-factor, μ_B is the Bohr magneton, and φ is a phase offset. We analyzed the transient Kerr signals by fitting with Eq. (1), and the absolute value of the electron g-factor ($g = |g|$) and spin dephasing time (T_2) were deduced. We excluded the initial amplitude change due to the effect of hole-spin from the analysis, which appeared in the initial time region (0–50 ps) [8–11] and decreased with increasing temperature (almost disappeared above 100 K). The solid lines in Fig. 1 denote these best-fit calculations. Magnitudes of the g-factor in the parent GaAs QW, GaAs ND1, and ND2 were found to be 0.16, 0.05, and 0.11, respectively. We also measured the magnetic-field
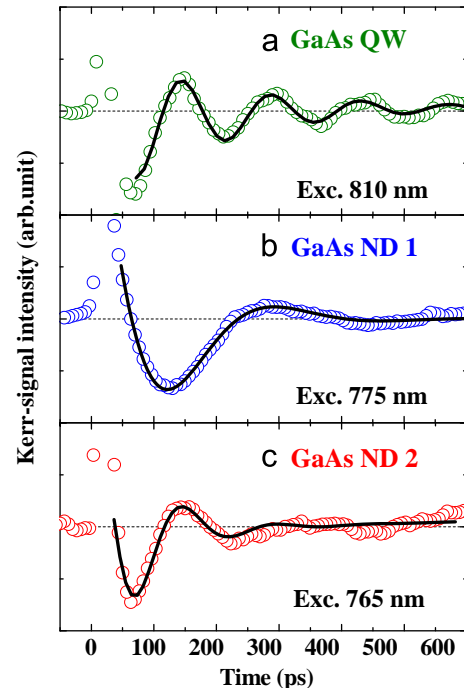
Fig. 2. Typical time-resolved Kerr-rotation signals (blue open circles) for (a) the original GaAs quantum well, (b) GaAs ND1 with $Al_{0.15}Ga_{0.85}As$ barriers, and (c) GaAs ND2 with $Al_{0.15}Ga_{0.85}As$ (vertical) and $Al_{0.30}Ga_{0.70}As$ (lateral) barriers at 4 K under a magnetic field of 4 T. Laser wavelengths used for the measurements are noted on the bottom-right corner of each plot. The solid lines denote best-fit calculations based on Eq. (1). (For interpretation of the references to color in this figure legend, the reader is referred to the web version of this article.)
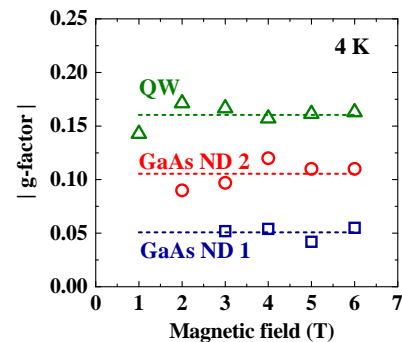
Fig. 3. Magnetic-field dependencies of the g-factor in the GaAs quantum well (green open triangles), GaAs ND1 (blue open squares), and ND2 (red open circles). Dotted lines are guides for the eyes. (For interpretation of the references to color in this figure legend, the reader is referred to the web version of this article.)

dependence and obtained magnitudes of the g-factor as a function of magnetic field, as plotted in Fig. 3. The magnitudes of the g-factor as a function of magnetic field are almost constant (within a ± 0.02 uncertainty for all samples).

First, we explain the g-factor of the parent GaAs QWs before etching. According to reference [10], the bandgap energy E_g and the electron g-factor of bulk $Al_xGa_{1-x}As$ can be theoretically estimated from the following equations:

$$E_g(x) = 1.549 + 1.04x + 0.47x^2 \text{[eV]}, \tag{2}$$

$$g_{bulk}(E_g) = -0.445 + 3.38(E_g - 1.519) - 2.21(E_g - 1.519)^2, \tag{3}$$

where x is the Al content. The g-factors are calculated to be $g_{bulk}(GaAs) = -0.44$, $g_{bulk}(Al_{0.15}Ga_{0.85}As) = +0.057$, and $g_{bulk}(Al_{0.3}Ga_{0.7}As) = +0.48$, according to Eqs. (2) and (3). The g-factor in a QW
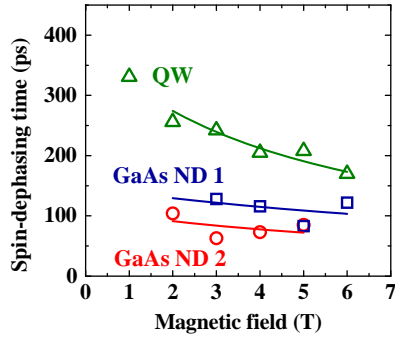
Fig. 4. Spin-dephasing time as a function of magnetic field in the GaAs quantum well (green open triangles), GaAs ND1 (blue open squares), and ND2 (red open circles). Solid lines are fits calculated by Eq. (4). (For interpretation of the references to color in this figure legend, the reader is referred to the web version of this article.)

can be additionally affected by the barrier material and well thickness, owing to the penetration of an electron wavefunction from the QW into the barrier. For example, the g-factor of an 8-nm-thick GaAs/Al$_{0.35}$Ga$_{0.65}$As QW was reported to be -0.1, which differs significantly from the above $g_{bulk}(GaAs) = -0.44$, and was shifted toward the value of $g_{bulk}(Al_{0.35}Ga_{0.65}As) = +0.58$ [12]. In our case, the g-factor obtained from the original QW is |0.16|. We calculate the three-dimensional electron wavefunction with the designed, and thus realistic, structural parameters, resulting in a penetrating wavefunction that cannot be ignored within the Al$_{0.15}$Ga$_{0.85}$As barrier. Therefore, we judge that the electron g-factor of the present GaAs QW is -0.16, which is similar to that obtained in [6] and the literature value in [13].

Next, we compare the g-factor of the GaAs ND1 with that of this parent QW. For ND1, the penetration depth of the electron wavefunction into the barrier is significantly larger than that of the parent QW (because of the additional lateral quantum confinement due to the ND's formation). It is worth noting that the additional lateral confinement by this Al$_{0.15}$Ga$_{0.85}$As barrier can significantly raise the potential of the electron ground state in the GaAs ND1, and thus the electron wavefunction can penetrate the barrier in the vertical direction in addition to the lateral direction. This situation leads to the conclusion that the g-factor of the ND1 is -0.05, where $+0.05$ for the ND1 is unlikely, considering that $g_{bulk}(Al_{0.15}Ga_{0.85}As) = +0.057$. We next consider the g-factor of the GaAs ND2, where only the lateral barrier height is higher than that of ND1. The electron wavefunction of ND2 penetrates the AlGaAs barrier more deeply because the higher Al content in the Al$_{0.3}$Ga$_{0.7}$As barrier can cause a marked increase in the ground-state potential for ND2. Therefore, the g-factor of ND2 can be estimated as $+0.11$, in a manner similar with the above discussion of ND1.

The spin-dephasing time T_2 is also deduced from the time-resolved Kerr-rotation signal using Eq. (1). T_2 for the QW, ND1, and ND2 are found to be 240, 130, and 70 ps, respectively, at 4 K and 4 T. The timescales of these T_2 values for the GaAs NDs are similar to those reported for a strain-induced GaAs QD with shallow potential confinements of carriers (91 ps) [7]. The magnetic-field dependencies of T_2 are shown in Fig. 4. For the QW, T_2 decreases as the magnetic field increases, whereas there is no clear trend for T_2 with the NDs. The magnetic-field dependence of this T_2 can be described by the following equation:

$$\frac{1}{T_2} = \frac{1}{T_2(B=0)} + \frac{\Delta g \mu_B B}{\sqrt{2}\hbar}, \tag{4}$$

where $T_2(B=0)$ is a spin-dephasing time without magnetic field and Δg is the inhomogeneous distribution of the g-factor [14]. $T_2(B=0)$ in the QW, ND1, and ND2 are 340, 140, and 90 ps, respectively. One possible reason for the shorter dephasing times

observed in the NDs is the broadened spectral width of our femtosecond laser used for pumping and probing. The observed Kerr oscillation can reflect an inhomogeneous distribution of g-factor if a number of NDs with slightly different sizes, and thus different bandgap energies, are excited by our laser. Integrating each oscillatory Kerr signal with slightly different g-values results in an oscillation signal with an averaged frequency (g-factor obtained by our measurements) and faster dumping than the essential oscillation in each ND. The difference in T_2 between ND1 (130 ps) and ND2 (70 ps) can be explained by this consideration, where the magnitude of the g-factor for ND2 ($+0.11$) is larger than that for ND1 (-0.05). If the inhomogeneous distribution width of the g-value is identical between these ND samples, the apparent (integrated) oscillatory Kerr signal with the larger average g-factor exhibits faster dumping because of the large amplitude fluctuation of each signal (compared to cases with smaller average g-factors). A study using spectrally limited measurements would be necessary to clarify this point.

4. Summary

We observe that the electron g-factor of GaAs NDs, which is responsible for precession of the spin, is significantly affected by the lateral quantum confinement artificially induced in planar QWs. This change in the g-factor can be attributed to enhanced penetration of the electron wavefunction from the NDs into the surrounding AlGaAs barriers, both in the vertical and lateral directions. The dephasing times for the electron-spin relaxation of these NDs are also modified from that of their parent QW sample.

References

[1] S. Samukawa, Ultimate top-down etching processes for future nanoscale devices: advanced neutral-beam etching, Jpn. J. Appl. Phys. 45 (2006) 2395.
[2] X.Y. Wang, C.H. Huang, R. Tsukamoto, P.A. Mortemousque, K.M. Itoh, Y. Ohno, S. Samukawa, Damage-free top-down processes for fabricating two-dimensional arrays of 7 nm GaAs nanodiscs using bio-templates and neutral beam etching, Nanotechnology 22 (2011) 365301.
[3] T. Kaizu, Y. Tamura, M. Igarashi, W. Hu, R. Tsukamoto, I. Yamashita, S. Samukawa, Y. Okada, Photoluminescence from GaAs nanodisks fabricated by using combination of neutral beam etching and atomic hydrogen-assisted molecular beam epitaxy regrowth, Appl. Phys. Lett. 101 (2012) 113108.
[4] Y. Tamura, T. Kaizu, T. Kiba, M. Igarashi, R. Tsukamoto, A. Higo, W. Hu, C. Thomas, M.E. Fauzi, T. Hoshii, I. Yamashita, Y. Okada, A. Murayama, S. Samukawa, Quantum size effects in GaAs nanodisks fabricated using a combination of the bio-template technique and neutral beam etching, Nanotechnology 24 (2013) 285301.
[5] T. Kiba, T. Tanaka, Y. Tamura, A. Higo, C. Thomas, S. Samukawa, A. Murayama, Impact of artificial lateral quantum confinement on spin relaxation in a two-dimensional GaAs electronic system, AIP Adv. 4 (2014) 107112.
[6] M. Poggio, G.M. Steeves, R.C. Myers, N.P. Stern, A.C. Gossard, D.D. Awschalom, Spin transfer and coherence in coupled quantum wells, Phys. Rev. B 70 (2004) 121305.
[7] A. Kanno, Y. Masumoto, Spin relaxation mechanism of strain-induced GaAs quantum dots studied by time-resolved Kerr rotation, Phys. Rev. B 73 (2006) 073309.
[8] T. Amand, X. Marie, P. Le Jeune, M. Brousseau, D. Robart, J. Barrau, R. Planel, Spin quantum beats of 2D excitons, Phys. Rev. Lett. 78 (1997) 1355–1358.
[9] T.A. Kennedy, A. Shabaev, M. Scheibner, A.L. Efros, A.S. Bracker, D. Gammon, Optical initialization and dynamics of spin in a remotely doped quantum well, Phys. Rev. B 73 (2006) 045307.
[10] I.A. Yugova, A. Greilich, D.R. Yakovlev, A.A. Kiselev, M. Bayer, V.V. Petrov, Y.K. Dolgikh, D. Reuter, A.D. Wieck, Universal behavior of the electron g factor in GaAs/Al$_x$Ga$_{1-x}$As quantum wells, Phys. Rev. B 75 (2007) 245302.

[11] F.G.G. Hernandez, G.M. Gusev, A.K. Bakarov, Tuning of the Landé g-factor in $Al_xGa_{1-x}As$/AlAs single and double quantum wells, J. Phys.: Conf. Ser. 456 (2013) 012015.

[12] A.A. Kiselev, E.L. Ivchenko, U. Rössler, Electron g factor in one- and zero-dimensional semiconductor nanostructures, Phys. Rev. B 58 (1998) 16353–16359.

[13] M.J. Snelling, E. Blackwood, C.J. McDonagh, R.T. Harley, C.T.B. Foxon, Exciton, heavy-hole, and electron g factors in type-I GaAs/$Al_xGa_{1-x}As$ quantum wells, Phys. Rev. B 45 (1992) 3922–3925.

[14] E.A. Zhukov, D.R. Yakovlev, M. Bayer, G. Karczewski, T. Wojtowicz, J. Kossut, Spin coherence of two-dimensional electron gas in CdTe/(Cd,Mg)Te quantum wells, Phys. Status Solidi (b) 243 (2006) 878–881.

CrossMark

High-density 1.54 µm InAs/InGaAlAs/InP(100) based quantum dots with reduced size inhomogeneity

Saddam Banyoudeh *, Johann Peter Reithmaier

Technische Physik, Institute of Nanostructure Technologies and Analytics (INA), CINSaT, University of Kassel, Heinrich-Plett-Str. 40, 34132 Kassel, Germany

ARTICLE INFO

ABSTRACT

Self-assembled InAs quantum dots (QDs) were grown by solid source molecular beam epitaxy. The impact of the growth parameters like the growth temperature of the InGaAlAs nucleation layer, V/III ratio and growth rate during growth of QD layers were carefully investigated by using atomic force microscopy and photoluminescence spectroscopy. The excellent size uniformity of InAs QDs grown on InP substrates are verified by narrow photoluminescence line widths of 17 meV for single QD layers and 26 meV for stacked QD layers, respectively. Both values measured at 10 K.

© 2015 Elsevier B.V. All rights reserved.

1. Introduction

In the last decade, the growth of self-assembled semiconductor quantum dot (QD) structures has attracted much interest from both fundamental physics and potential optoelectronic device applications operating at 1.55 µm and beyond, mainly driven by fiber-based applications, like classical optical communication [1] or quantum communication [2]. Mainly self-assembled semiconductor QDs formed via Stranski–Krastanov (SK) growth mode have supplied a potent active medium for optoelectronic devices such as laser diodes and light-emitting diodes [1,3–5]. For laser application, it is necessary to establish a high QD density with a homogenous size distribution and most likely round-shaped geometry for optimum 3D confinement. This results in device related performance properties like improved temperature stability, reduced threshold current and increased spectral and differential gain.

Several compounds as buffer layer and different growth parameters have been used to investigate the formation of InAs QDs based on InP substrate, such as strained InAs and $In_{0.32}Ga_{0.68}As$ layers or lattice matched InGaAsP and InAlAs as well as monolayer coverage dependence [6–8]. So far only a few studies regarding InAs QDs on lattice matched InGaAlAs as a buffer layer have been reported [9,10].

To increase the total QD density, stacked QD layers have been suggested [11]. Their photoluminescence (PL) spectrum showed an asymmetric shape and a broadened linewidth in comparison with the single layer QD sample [12]. In this work, the influence of V/III ratio, growth rate during QDs growth and growth temperature of the InGaAlAs nucleation layers on the formation of InAs QDs were carefully investigated by using photoluminescence (PL) measurements and atomic force microscopy (AFM).

2. Experimental details

All samples were grown on n-type InP(100) substrates by a modified Varian Gen-II solid source molecular beam epitaxy (SSMBE) system equipped with valved phosphorus and arsenic cracker sources. After thermal oxide desorption, the substrate was transferred to the growth chamber and set to 490 °C for 6 min under P_2 overpressure to remove the residual oxide. The structures consist of a 100 nm thick InP buffer layer and a nominally 6 monolayers (MLs) thick InAs layer, embedded in a 100 nm thick $In_{0.528}Ga_{0.234}Al_{0.238}As$ layer lattice matched to InP. The InAs QDs were grown in an As_2 mode. The structure is finalized with an uncapped nominally 6 MLs thick InAs QD layer on top for morphological characterization. The growth temperature of QDs was set to 490 °C. The InAs growth rate was 450 nm/h. The temperature was controlled by pyrometer. The beam equivalent pressure values are used to monitor the V/III ratio.

At the InGaAlAs/InP interface a growth interruption for 50 s was introduced to allow a well-defined exchange between the gases P_2 and As_2 without significant cross-contamination. In the case of stacked structures, similar growth conditions of the optimized parameters for single QD layers were applied, i.e., six periods of InAs QD layers separated by 20 nm thick InGaAlAs barrier layers were deposited.

3. Results and discussion

In Fig. 1, AFM images of an InAs QD layer with 6 MLs deposited on InGaAlAs are shown. The three samples were grown with

* Corresponding author.
E-mail address: s.banyoudeh@ina.uni-kassel.de (S. Banyoudeh).
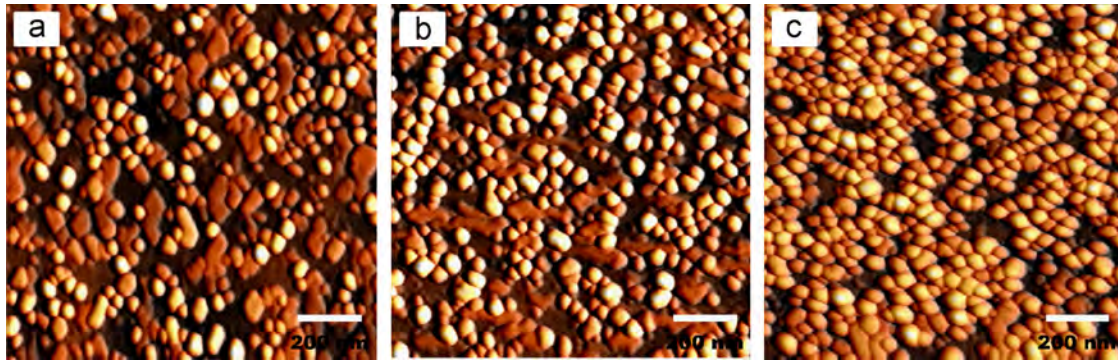
Fig. 1. AFM images (1×1) µm^2 of uncapped 6 MLs InAs QD layers grown on InGaAlAs. InAs QD layers were grown at 490 °C with a V/III ratio of 18, varying the growth temperature of the InGaAlAs nucleation layer from (a) 470 °C, (b) 485 °C to (c) 500 °C.

similar growth parameters, i.e., growth temperature of 490 °C, V/III ratio of 18 and InAs growth rate of 450 nm/h, but with different growth temperatures of the InGaAlAs nucleation layer ranging from 470 °C to 500 °C (from a to c, respectively). As can be seen, in addition to the formation of round-shaped InAs QDs, coalesced islands are observed. As the growth temperature of the InGaAlAs nucleation layer increases, the coalesced islands disappeared and the dot density significantly increased from 1.8×10^{10} cm^{-2} to 4.8×10^{10} cm^{-2}. This significant reduction of the degree of island coalescence with increasing growth temperature can be interpreted in terms of increasing the surface roughness of the nucleation layer, which causes a faster nucleation and therefore an enhanced suppression of adatom migration.

In Fig. 2, the corresponding PL measurements at low temperature show a shift to lower energies as the growth temperature of the InGaAlAs nucleation layer increases. The peaks centered at 0.84 eV, 0.83 eV and 0.80 eV, which are corresponding to the emission wavelengths of 1.47 µm, 1.49 µm and 1.54 µm, respectively. The full width at half-maximum (FWHM) strongly decreases from 30 meV to 22 meV as the growth temperature of the InGaAlAs nucleation layer increases, as shown in the inset of Fig. 2.

This significant change in the integral PL intensity, linewidth and dot density can be mainly attributed to the enhanced nucleation probability. The narrow PL line width of 21 meV reveals that highly uniform InAs QDs are formed on appropriately prepared InGaAlAs surfaces.

Further optimization of QD growth parameters is performed by small variations of the V/III ratio during the growth of the InAs QD layer while the InAs growth rate and temperature are maintained constant at 450 nm/h and 490 °C, respectively. Fig. 3 shows AFM images for four samples with a similar structure, including the reference sample (b). The V/III ratio decreased from 21 (a) to 18 (b), 15 (c) and finally to 12 (d). The corresponding surface dot densities are approximately 4.2×10^{10} cm^{-2}, 5.1×10^{10} cm^{-2} and 6.0×10^{10} cm^{-2} (from a to c, respectively). Besides increasing the QD density with increasing the V/III ratio, a shape transition from round-shaped QDs to QDashes at the lowest V/III ratio of 12 is observed. This transition can be attributed to an enhanced migration length of Indium adatoms, which is mostly favorable along [$\overline{0}$11] crystal direction [13].

Fig. 5 shows the PL spectra at 10 K for the four samples with different V/III ratios of 21, 18, 15 and 12 from right to left. The corresponding peaks are centered at around 0.79 eV, 0.80 eV, 0.81 eV and 0.84 meV. The difference in peak position can be mainly related to the QD size, in particular to the height. As seen from the height histograms in Fig. 4, the mean dot heights of QDs decrease with decreasing the V/III ratio in the samples a, c and d (in Fig. 3) from 21 to 12, respectively. In addition the height deviation decreases from
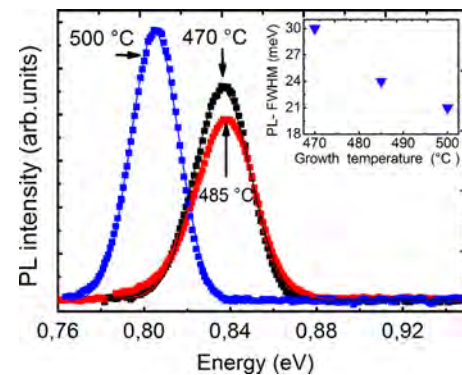
Fig. 2. PL spectra at 10 K of single InAs QD layers grown at 490 °C, on InGaAlAs grown at different temperature from 470 °C to 500 °C as labeled. Inset PL–FWHM values of the ensemble QD spectra as a function of InGaAlAs growth temperature measured at 10 K with a laser excitation power density of 10 W/cm^2, were extracted from the Gaussian fitting (solid curves).

2.24 nm to 1.97 nm (sample a and c in Fig. 3) as the V/III ratio decreases.

In the inset of Fig. 5, the dependence of the PL–FWHM on the V/III ratio is plotted. Starting from lower V/III ratios, the FWHM value can be reduced by decreasing the V/III ratio, mainly caused by the reduction of the migration length. Beyond a certain optimum condition (here about 18), the line width is increasing once again, presumably caused by excess As, which deteriorates the material and interface quality also known from quantum well growth. However, the doubling of the FWHM value at a V/III ratio of 12 is accompanied by a strong QD shape transition from circular-like QDs to QDash-like geometry, as seen in AFM images of Fig. 3(d), which enlarges the size variation effect. These results clearly show the high sensitivity of the optical as well as the morphological properties of InAs QDs on a moderate variation of the V/III ratio.

Another important growth parameter is the growth rate during deposition of the InAs QD layers. By growing the InAs QD layers at a higher growth rate of 570 nm/h and using a V/III ratio of 18, a very narrow PL–FWHM of 17 meV (Fig. 6) was achieved. These dots exhibit the narrowest linewidth for 1.55 µm emitting structure based on self-assembled QDs [9,14].

With similar growth conditions as used for optimized single QD layers, six periods of InAs QD layers were grown separated by 20 nm thick InGaAlAs barrier layers. Fig. 7 shows the PL measurements at 10 K for six stacked QD layers. The PL peak is centered at around 0.80 eV and the corresponding emission wavelength is around 1.54 µm with a PL–FWHM of 26 meV. In comparison to the reference single QD layer (Fig. 1c), The PL peak position is
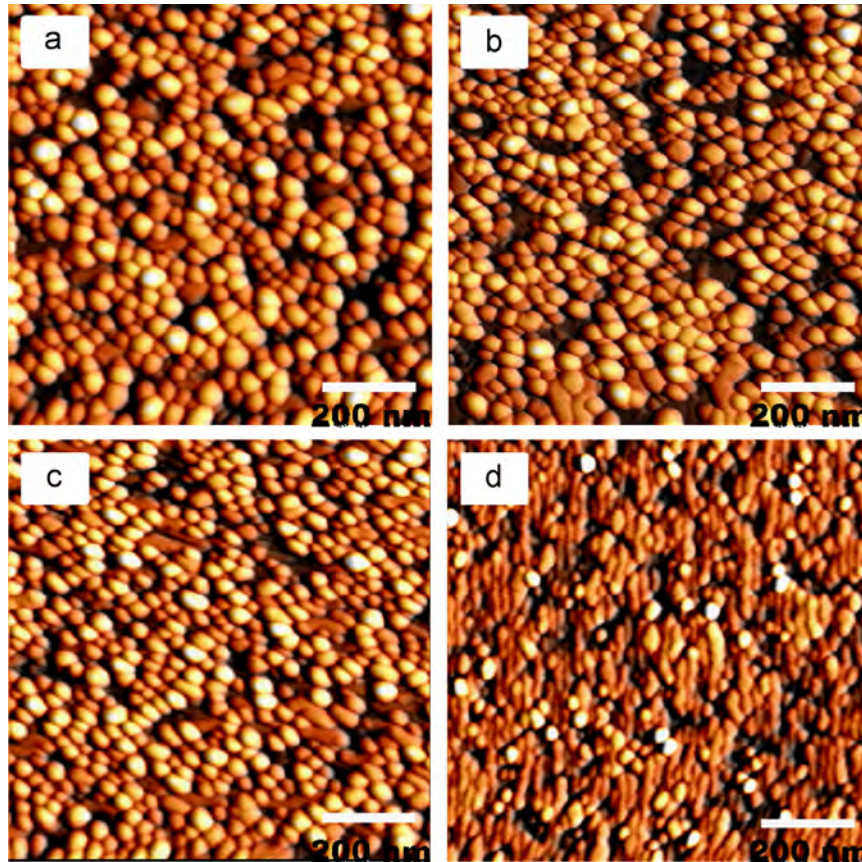
Fig. 3. AFM images of 1×1 μm^2 of InAs QDs grown on an InGaAlAs layer lattice matched to an InP(100) substrate after deposition of 6 MLs of InAs at 490 °C with different V/III ratios of (a) 21, (b) 18, (c) 15 and (d) 12, respectively.
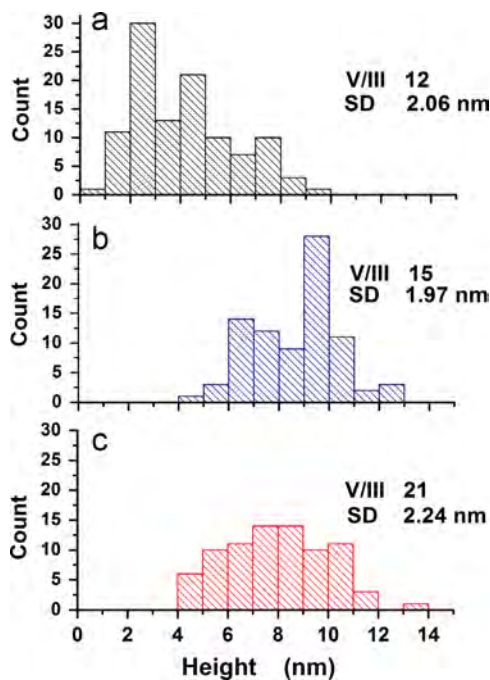
Fig. 4. The dot height histograms a, b and c, corresponding to the samples d, c and a in Fig. 3 after deposition of 6 MLs of InAs at 490 °C with different V/III ratios of 12, 15, and 21, respectively. The mean dot heights and the corresponding standard deviation (SD) in a, b and c are 4.02 nm, 8.02 nm, 8.92 nm and 2.07 nm, 1.97 nm, 2.24 nm, respectively.

Fig. 5. PL spectra at 10 K of 6 MLs InAs grown at 490 °C on InGaAlAs with different V/III ratio of 12, 15, 18 and 21 as labeled. The inset shows the PL–FWHM of a single InAs QD layer (6 MLs) grown at 490 °C on InGaAlAs grown at 500 °C as a function of V/III ratio. The solid curves show the Gaussian fitting, from which the data in the inset were extracted.

located at the same energy as for the reference sample with slightly broadened line width, which is caused by additional size fluctuation due to strain coupling.

4. Conclusions

In summary, the impact of the growth parameters on the dots formation, e.g., V/III ratio, growth temperature of InGaAlAs nucleation layer and growth rate of the QD layers was investigated. From AFM and PL results the nucleation of InAs QDs is obviously affected by the growth condition of the nucleation layer, i.e., the surface properties of the nucleation layer are very important for the QD formation process. By carefully optimizing the growth parameters a high dot density up to 6×10^{10} cm^{-2} and a very narrow line width of 17 meV were achieved. Under As$_2$ overpressure a shape
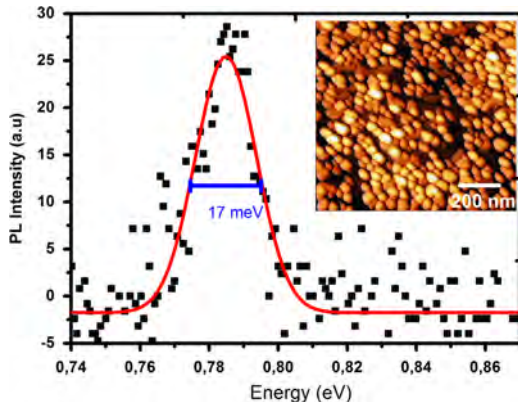
Fig. 6. PL spectrum of a single InAs QD layer (6 MLs) at 10 K and the corresponding Gaussian fit (red curve). Inset shows a $1 \times 1\ \mu m^2$ AFM scan of InAs QDs grown on top of the sample. The used growth rate and V/III ratio are 570 nm/h and 18, respectively. The used excitation power density is 0.2 W/cm^2. (For interpretation of the references to color in this figure legend, the reader is referred to the web version of this article.)
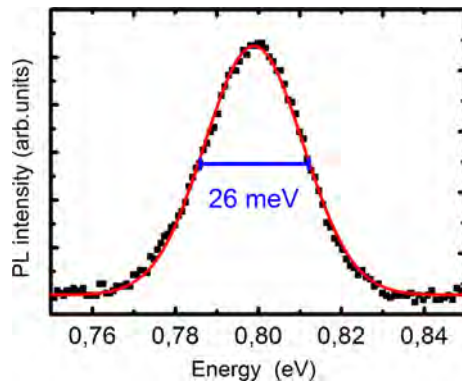
Fig. 7. PL spectra at 10 K for 6 stacked QD layers. The red curve is the Gaussian fit of the data points. (For interpretation of the references to color in this figure legend, the reader is referred to the web version of this article.)

transition from rounded QDs to QDashes at a relatively low V/III ratio of 12 was observed.

By stacking of QD layers additional broadening occurs due to strain coupling, which results in a linewidth of 26 meV for six layers. By compensating the strain coupling it should be possible to preserve the single QD layer quality also for lasers with multiple-QD layers. In comparison to previously realized QD lasers based on QD material with 31 meV line width and record-high modal gain [3] as well as large signal modulation characteristics [15] the new optimized growth conditions has the potential for nearly doubling the spectral gain, which will further enhance the modal and, respectively, the differential gain in high speed lasers.

Acknowledgments

References

[1] J.P. Reithmaier, A. Somers, S. Deubert, R. Schwertberger, W. Kaiser, A. Forchel, M. Calligaro, P. Resneau, O. Parillaud, S. Bansropun, M. Krakowski, R. Alizon, A. Hadass, H. Bilenca, V. Dery, G. Mikhelashvili, M. Eisenstein, I. Gioannini, T.W. Montrosset, M. Berg, J. van der Poel, B. Mørk, Tromborg, J. Phys. D 38 (2005) 2088.
[2] M. Benyoucef, M. Yacob, J.P. Reithmaier, J. Kettler, P. Michler, Appl. Phys. Lett. 103 (2013) 181120.
[3] D. Gready, G. Eisenstein, C. Gilfert, V. Ivanov, J.P. Reithmaier, IEEE Photonics Technol. Lett. 24 (2012) 809.
[4] C. Gilfert, V. Ivanov, N. Oehl, M. Yacob, J.P. Reithmaier, Appl. Phys. Lett. 98 (2011), pp. 201102-1-201102-3.
[5] R. Schwertberger, D. Gold, J.P. Reithmaier, A. Forchel, IEEE Photonics Technol. Lett. 14 (2002) 735.
[6] J.S. Kim, J.H. Lee, S.U. Hong, W.S. Han, H.S. Kwack, C.W. Lee, D.K. Oh, J. Cryst. Growth 259 (2003) 252.
[7] W.G. Jeong, P.D. Dapkus, U.H. Lee, J.S. Yim, D. Lee, B.T. Lee, Appl. Phys. Lett. 78 (2001) 1171.
[8] S.G. Li, Q. Gong, C.F. Cao, X.Z. Wang, L. Yue, Q.B. Liu, H.L. Wang, Y. Wang, Infrared Phys. Technol. 55 (2012) 205.
[9] C. Gilfert, E.-M. Pavelescu, J.P. Reithmaier, Appl. Phys. Lett. 96 (2010) 191903.
[10] X.Q. Huang, F.Q. Liu, X.L. Che, J.Q. Liu, W. Lei, Z.G. Wang, J. Cryst. Growth 270 (2004) 364.
[11] K. Akahane, N. Ohtani, Y. Okada, M. Kawabe, J. Cryst. Growth 245 (2002) 31.
[12] J.W. Oh, M.-Yi. Ryu, B. Jo, J.S. Kim, T.R. Harris, Y.K. Yeo, Thin Solid Film 541 (2013) 68.
[13] H. Dery, E. Benisty, A. Epstein, R. Alizon, V. Mikhelashvili, G. Eisenstein, R. Schwertberger, D. Gold, J.P. Reithmaier, A. Forchel, J. Appl. Phys. Lett. 95 (2004) 6103.
[14] Y. Yang, B. Jo, J. Kim, C.R. Lee, J.S. Kim, D.K. Oh, J.S. Kim, J.Y. Leem, J. Appl. Phys. Lett. 105 (2009) 053510.
[15] D. Gready, G. Eisenstein, V. Ivanov, C. Gilfert, F. Schnabel, A. Rippien, J.P. Reithmaier, IEEE Photonics Technol. Lett. 26 (2014) 11.
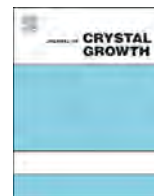
Terahertz emission from a coupled multilayer cavity with InAs quantum dots

Masanori Ogarane [a,*], Sho Katoh [a], Yoshinori Nakagawa [a,b], Ken Morita [c], Takahiro Kitada [a], Toshiro Isu [a]

[a] Center for Frontier Research of Engineering, Institute of Technology and Science, The University of Tokushima, 2-1, Minami-Josanjima-Cho, Tokushima 770-8506, Japan
[b] NICHIA Corporation, Anan, Tokushima 770-8601, Japan
[c] Graduate School of Engineering, Chiba University, Chiba 263-8522, Japan

ARTICLE INFO

ABSTRACT

InAs quantum dots (QDs) were introduced as efficient nonlinear materials into a GaAs/AlAs coupled multilayer cavity, which was recently demonstrated as a novel THz emission device based on difference-frequency generation (DFG) of the two cavity modes. The couple multilayer cavity containing QDs was grown by molecular beam epitaxy and the THz-DFG was measured using femtosecond laser pulses.

© 2015 Elsevier B.V. All rights reserved.

1. Introduction

Terahertz light sources based on semiconductor materials have been attracting considerable interest due to the wide range of possible application fields including wireless communication, spectroscopy, and transmission imaging. Several types of semiconductor devices, such as quantum cascade lasers (QCLs),[1–3] resonant tunneling diodes (RTDs), [4] and photo mixers,[5,6] have been studied and developed as cw terahertz light sources. There, however, still remain various problems in each type of device. For example, the emission power becomes insufficient for higher frequency operation of RTDs. Although remarkable progress has been made in the development of QCLs as compact light sources in recent years, near room temperature operation has not yet been demonstrated. Efficient wavelength conversion based on difference frequency generation (DFG) in III–V semiconductors is attractive for terahertz light sources operating at room temperature because of the large second-order nonlinearity and fundamental light emission by current injection. THz waves can be produced by DFG using a GaP crystal excited by two individual lasers [7–9].

Optical nonlinear phenomena in a semiconductor vertical microcavity are very interesting and useful to construct novel optical devices for dense parallel processing. A coupled cavity system has a unique feature of multiple cavity modes providing additional functionality. Recently, we have proposed a terahertz emission device with a coupled multilayer cavity structure utilizing DFG of the two cavity modes [10,11]. A GaAs/AlAs coupled multilayer cavity structure, which has two equivalent cavity layers coupled by an intermediate distributed Bragg reflector (DBR) multilayer, was fabricated on a (113)B GaAs substrate by

molecular beam epitaxy (MBE). Epitaxial growth on a non-(001) substrate is essential for terahertz DFG of the two cavity modes because the frequency mixing through the second-order nonlinear process is forbidden on a (001) substrate owing to crystal symmetry [12]. Strong sum-frequency generation (SFG) in the near-infrared region [13–15] and DFG in the terahertz region [16–18] were successfully demonstrated by simultaneous excitation of the two cavity modes in the coupled cavity structure using femtosecond laser pulse irradiation as the fundamental light sources. Since the strong internal light electric field due to the cavity effects, nonlinearity of the cavity layers is important to obtain strong non-linear optical response. Recently, we have demonstrated optical Kerr gate switches based on a GaAs/AlAs multilayer cavity structure with InAs quantum dots (QDs) embedded in strain-relaxed barriers [19–24]. We have observed 60 times enhancement of the optical Kerr signal from the cavity having InAs QDs compared with the cavity having no QDs [25]. The THz emission is expected to be also enhanced by introducing good nonlinear materials such as quantum dots (QDs) having resonance energy near the two mode frequencies.

In this paper, we grew the GaAs/AlAs coupled multilayer cavity structure having self-assembled InAs QDs by MBE. We observed monochromatic THz radiation due to the DFG of two cavity modes from a GaAs/AlAs coupled multilayer cavity having InAs QDs on a (113)B GaAs substrate using femtosecond laser pulses.

2. MBE growth of a coupled multilayer cavity with InAs quantum dots

The GaAs/AlAs coupled multilayer cavity structure with InAs quantum dots shown in Fig. 1 was grown on a 2-inch GaAs (113)B

* Corresponding author. Tel.: +81 88 656 7671; fax: +81 88 656 7674.
E-mail address: ogarane@frc.tokushima-u.ac.jp (M. Ogarane).
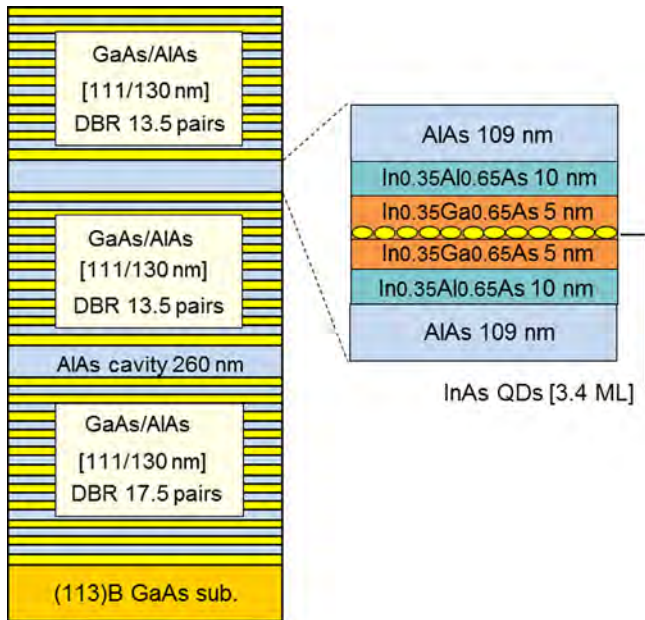
Fig. 1. Structure of the GaAs/AlAs coupled multilayer cavity with InAs quantum dots.
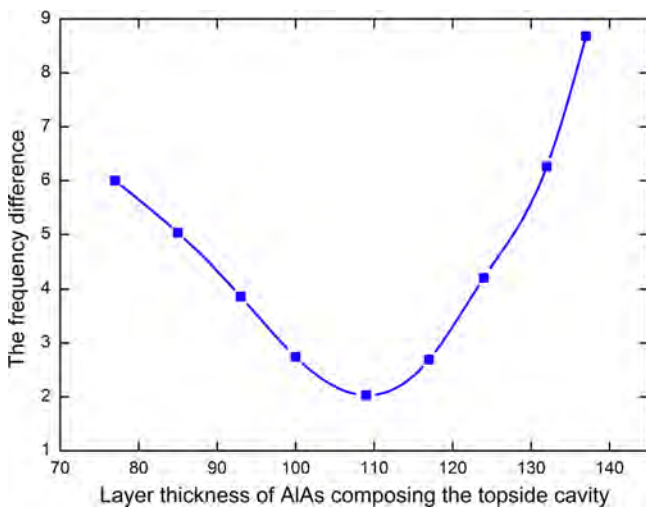
Fig. 2. The frequency difference of the two cavity modes for a coupled cavity where optical thickness of the top cavity is defferent from that of bottom cavity (260 nm).

Fig. 3. Reflection spectra measured at various positions of the epitaxial wafer.

substrate by solid-source MBE. Two half-wavelength ($\lambda/2$) cavities based on AlAs were coupled by a 13.5-period GaAs/AlAs distributed Bragg reflector (DBR) multilayer and 13.5- and 17.5-period DBRs were formed on both sides. The single self-assembled InAs QD layer (3.4 monolayer) was inserted only in the topside AlAs $\lambda/2$ cavity. The QDs were embedded in strain-relaxed $In_{0.35}Ga_{0.65}As$ layer (5 nm) to extend the resonance wavelength over 1.5 µm and they were sandwiched between two strain-relaxed $In_{0.35}Al_{0.65}As$ layers (10 nm) [25]. The average height and density of the QDs in each layer were estimated to be 6 nm and 6×10^{10} cm^{-2}, respectively. The top side cavity including QDs was grown at a substrate temperature (T_s) of 480 °C, while the bottom side cavity and DBR multilayers were grown at $T_s = 630$ °C under an As pressure of $\sim 1 \times 10^{-5}$ Torr. Growth rates of GaAs, AlAs, and InAs were 1.0, 1.0, and 0.35 µm/h, respectively. Since in this structure, materials of two cavity layers are different, it is difficult to grow the two cavity layers whose effective optical thicknesses were exactly the same as each other over the whole wafer. Therefore, two AlAs layers

(109 nm) composing the topside $\lambda/2$ cavity were grown without substrate rotation in order to make intentional thickness variation over the wafer.

3. Reflection spectra

Lateral thickness variation of the top cavity layer causes a slight variation of two cavity mode frequencies (ω_1, ω_2) in the 2-inch wafer. Fig. 2 shows calculated results of the frequency difference ($\omega_2 - \omega_1$) depending on the thickness of the AlAs layers in the top side cavity. When optical thicknesses of the two cavity layers were exactly the same as each other, frequency difference has minimum value. Fig. 3 shows optical reflection spectra measured at various wafer positions. Two reflection dips around 1.5 µm correspond to the cavity modes whose intensities depended on the measurement position. The frequency difference were changed at wafer positions and showed the minimum value at the position ($x = -5$ mm). Two reflection dips due to the cavity modes were observed at 1497 nm, 1513 nm. The frequency difference between two modes was 2.1 THz and the depths of the reflection dips were same values. These results corresponding to calculated results indicate that a coupled multilayer cavity structure with InAs QDs which has equivalent effective optical thicknesses of two cavity layers was successfully fabricated.

4. The time-domain THz measurements

Fig. 4 shows a schematic illustration of the THz time-domain measurement. Pump pulses of ~ 1.5 µm were produced by an optical parametric oscillator pumped by a Ti:sapphire laser, which has an output wavelength of ~ 0.81 µm and a repetition rate of 80 MHz. The pump pulses from the OPO typically have widths less than 150 fs. They were focused on the samples to a diameter of ~ 100 µm. The THz waveform emitted by the sample was detected using a dipole-type PC antenna with a gap of 6.0 µm, which was sensitive in the lower frequency range (< 3 THz) and was optically gated by a weak optical beam (10 mW) from the Ti:sapphire laser. The time delay between the optical pump pulse and the gated

probe pulse was controlled by a delay stage. A Ge filter was placed after the sample to prevent the strong pump pulse from irradiating the PC antenna. Both the sample and Photo-conductive (PC) antenna were in a N_2 atmosphere to prevent the THz radiation from absorption by water vapor.

Fig. 5 shows a time-domain THz waveform emitted from the coupled cavity with and without QDs. The excitation laser power was set to 160mW and the excitation wavelength was set to the central wavelength of the two cavity modes. The polarization of the excitation laser pulse was aligned in the [33−2] direction, and the detection polarization (which was parallel to the PC gap) was aligned in the same direction.[14,26] The relatively strong signal was observed around 0 ps in the THz waveform generated from both the coupled cavity with QDs and that without QDs. For the coupled cavity with QDs, we observed slowly decaying oscillations with a period of 0.48 ps after the initial monocycle signal. The oscillation period of 0.48 ps well agrees with the optical frequency difference between the two cavity modes (2.1 THz) shown in Fig. 3. On the other hand, such the oscillation was unclear for the coupled cavity without QDs because of poor nonlinearity of AlAs in the cavity layer. Fig. 6 shows the square Fourier Transform spectrum of Fig. 5. For the coupled cavity with QDs, the FT signal at 2.1 THz corresponds to the decaying oscillations with a period of 0.48 ps was clearly improved. These results indicate that the THz emission was successfully enhanced near the mode frequency difference of 2.1 THz when only a single QD layer was introduced in one of the AlAs cavity layers with poor nonlinearities.

Then, we noticed that the strong signal was observed around 0 ps in the THz waveform generated from both the coupled cavity with InAs QDs and that without QDs. We found that the THz waveform in the coupled cavity with QDs is different from the THz waveform observed so far.[16,17] Therefore, we compared THz waveform in the coupled cavity with QDs with simulated THz waveforms shown in Fig.7. The pump pulses are polarized in the [33−2] and [1−10] directions, while the polarization of THz-DFG was fixed in the [33−2] direction. In simulated waveform, when

the pump pulses are polarized in the [1−10] directions, the signal amplitude is smaller than that of the [33−2] direction. The sign of two waveforms are completely opposite each other. This is due to the anisotropy of the second nonlinear polarization of the Zinc Blend type structure but, the THz waveform in the coupled cavity with QDs is different from simulated waveform in initial rise. Moreover sign inversion was not observed when the pump pulse polarization was changed. THz waveforms in the coupled cavity with InAs QDs were not explained by the theoretical anisotropy of the second-order nonlinear polarization of the Zinc Blend type structure. In this paper, the QDs were embedded in strain-relaxed $In_{0.35}Ga_{0.65}As$ layer to extend the resonance wavelength over
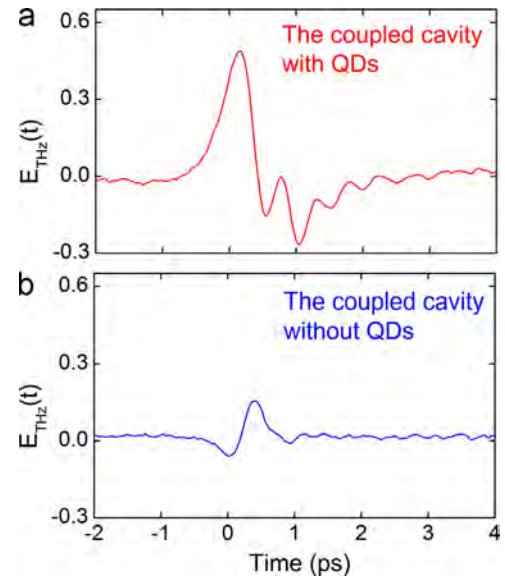
Fig. 5. Time-domain THz waveform from the coupled cavity samples with and without QDs.
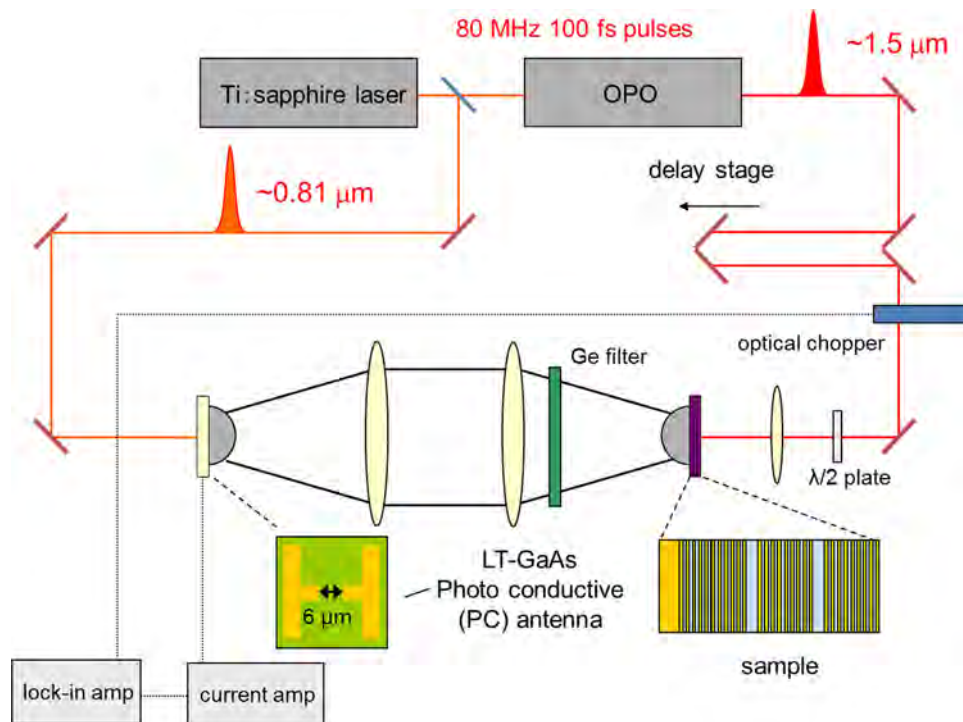
Fig. 4. Schematic illustration of experimental setup for the THz time-domain measurement.
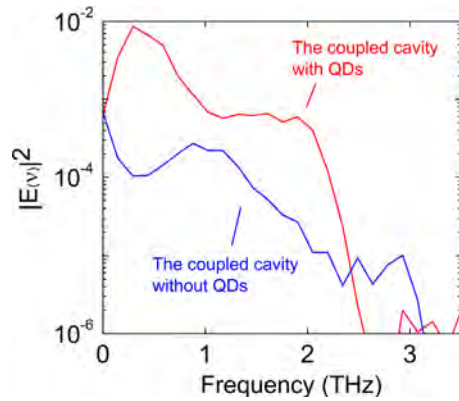
Fig. 6. The square FT spectrum of Fig. 5.
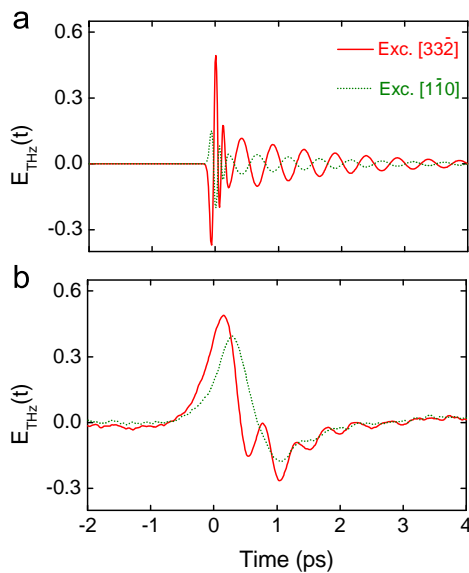
Fig. 7. (a) Simulated THz waveform and (b) measured THz waveform when the excitation laser pulses were polarized in the [33–2] (solid lines) and [1–10] (dotted lines).

1.5 μm. Therefore, real photo-excited carriers should be generated in the QDs by pump pulses of ∼1.5 μm. We think that photocurrents due to real photo-excited carriers in the QDs influence the THz waveform, but further investigation is necessary.

5. Conclusions

We grew the GaAs/AlAs coupled multilayer cavity with InAs quantum dots. We measured two cavity mode frequencies (ω_1, ω_2) over the 2-inch wafer whose cavity layer thickness has a slight lateral variation caused by the growth without the substrate rotation. The GaAs/AlAs coupled multilayer cavity with equivalent optical thickness of the two cavity layers was successfully fabricated by precise growth control and using the frequency difference changed at wafer positions. Time-domain THz waveform from the coupled cavity were measured using 100 fs laser pulses. The THz emission was successfully enhanced near the mode frequency difference of 2.1 THz, although only a single QD layer was introduced in one of the AlAs cavity layers. We found that THz waveforms in the coupled cavity having InAs QDs were not explained by the theoretical anisotropy of the second-order nonlinear polarization of the Zinc Blend type structure.

References

[1] R. Köhler, A. Tredicucci, F. Beltram, H.E. Beere, E.H. Linfield, A.G. Davies, D.A. Ritchie, R.C. Iotti, F. Rossi, Nature 417 (2002) 156.
[2] B.S. Williams, Nat. Photonics 1 (2007) 517.
[3] M.A. Belkin, J.A. Fan, S. Hormoz, F. Capasso, S.P. Khanna, M. Lachab, A.G. Davies, E.H. Linfield, Opt. Express 16 (2008) 3242.
[4] M. Asada, S. Suzuki, N. Kishimoto, Jpn. J. Appl. Phys. 47 (2008) 4375.
[5] S. Matsuura, M. Tani, K. Sakai, Appl. Phys. Lett. 70 (1997) 559.
[6] H. Ito, F. Nakajima, T. Furuta, K. Yoshino, T. Ishibashi, Electron. Lett. 39 (2003) 1828.
[7] T. Tanabe, K. Suto, J. Nishizawa, K. Saito, T. Kimura, Appl. Phys. Lett. 83 (2003) 237.
[8] T. Taniuchiand, H. Nakanishi, J. Appl. Phys. 95 (2004) 7588.
[9] I. Tomita, H. Suzuki, H. Ito, H. Takenouchi, K. Ajito, R. Rungsawang, Y. Ueno, Appl. Phys. Lett. 88 (2006) 071118.
[10] T. Kitada, F. Tanaka, T. Takahashi, K. Morita, T. Isu, Appl. Phys. Lett. 95 (2009) 111106.
[11] T. Kitada, F. Tanaka, T. Takahashi, K. Morita, T. Isu, Proc. SPIE 7937 (2011) 79371H.
[12] N. Yamada, Y. Ichimura, S. Nakagawa, Y. Kaneko, T. Takeuchi, N. Mikoshiba, Jpn. J. Appl. Phys. 35 (1996) 2659.
[13] F. Tanaka, T. Takahashi, K. Morita, T. Kitada, T. Isu, Jpn. J. Appl. Phys. 49 (2010) 04DG01.
[14] K. Morita, F. Tanaka, T. Takahashi, T. Kitada, T. Isu, Appl. Phys.Express 3 (2010) 072801.
[15] F. Tanaka, T. Takimoto, K. Morita, T. Kitada, T. Isu, Jpn. J. Appl. Phys. 50 (2011) 04DG03.
[16] K. Morita, S. Katoh, T. Takimoto, F. Tanaka, Y. Nakagawa, S. Saito, T. Kitada, T. Isu, Appl. Phys. Express 4 (2011) 102102.
[17] S. Katoh, T. Takimoto, Y. Nakagawa, K. Morita, T. Kitada, T. Isu, Jpn. J. Appl. Phys. 51 (2012) 04DG05.
[18] T. Kitada, S. Katoh, T. Takimoto, Y. Nakagawa, K. Morita, T. Isu, IEEE Photonics J. 5 (2013) 6500308.
[19] T. Kitada, T. Kanbara, K. Morita, T. Isu, Appl. Phys. Express 1 (2008) 092302.
[20] K. Morita, T. Takahashi, T. Kitada, T. Isu, Appl. Phys. Express 2 (2009) 082001.
[21] T. Takahashi, T. Mukai, K. Morita, T. Kitada, T. Isu, Jpn. J. Appl. Phys 49 (2010) 04DG02.
[22] K. Morita, T. Takahashi, T. Kanbara, S. Yano, T. Mukai, T. Kitada, T. Isu, Physica E 42 (2010) 2505.
[23] H. Ueyama, T. Takahashi, Y. Nakagawa, K. Morita, T. Kitada, T. Isu, Jpn. J. Appl. Phys. 51 (2012) 04DG06.
[24] K. Morita, H. Ueyama, Y. Yasunaga, Y. Nakagawa, T. Kitada, T. Isu, Jpn. J. Appl. Phys. 52 (2013) 04CG04.
[25] T. Kitada, T. Mukai, T. Takahashi, K. Morita, T. Isu, J. Cryst. Growth 311 (2009) 1807.
[26] T. Kitada, T. Kanbara, S. Yano, K. Morita, T. Isu, Jpn. J. Appl. Phys. 48 (2009) 080203.

CRYSTAL
GROWTH

CrossMark
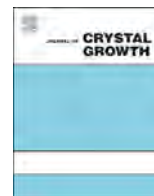
Molecular beam epitaxy grown indium self-assembled plasmonic nanostructures

Ricky Gibson [a,*], Michael Gehl [a], Jasmine Sears [a], Sander Zandbergen [a], Nima Nader [a,b,c], Patrick Keiffer [a], Joshua Hendrickson [b], Alexandre Arnoult [d], Galina Khitrova [a]

[a] College of Optical Sciences, University of Arizona, 1630 E University Blvd., Tucson, AZ 85721, USA
[b] Air Force Research Laboratory, Sensors Directorate, 2241 Avionics Circle, Wright-Patterson AFB, OH 45433, USA
[c] Solid State Scientific Corporation, 12 Simon St. Nashua, NH 03060, USA
[d] LAAS-CNRS, 7 Avenue du Colonel Roche, 31000, Toulouse, France

ARTICLE INFO

ABSTRACT

We describe molecular beam epitaxy (MBE) growth conditions for self-assembled indium nanostructures, or islands, which allow for the tuning of the density and size of the indium nanostructures. How the plasmonic resonance of indium nanostructures is affected by the island density, size, distribution in sizes, and indium purity of the nanostructures is explored. These self-assembled nanostructures provide a platform for integration of resonant and non-resonant plasmonic structures within a few nm of quantum wells (QWs) or quantum dots (QDs) in a single process. A $4\times$ increase in peak photoluminescence intensity is demonstrated for near-surface QDs resonantly coupled to indium nanostructures.

© 2015 Elsevier B.V. All rights reserved.

1. Introduction

The field of plasmonic nanostructures, where small volume structures can enhance electromagnetic fields that can be coupled to semiconductor quantum confined gain medium, is an expanding area of research. It has been shown that MBE grown silver films have improved optical constants, i.e. closer to intrinsic values, over e-beam or physical vapor deposited silver films [1]. This gives a possibility for improvements in the quality of plasmonic nanostructures or nano-antennas. It has also been shown that MBE can be used to grow site-controlled structures out of silver [2] and self-assembled structures with silver [3] and indium [4]. MBE growth allows for higher quality metallic nanostructures due to the improved optical constants and the self-assembly creates a clean interface between the metallic nanostructure and semiconductor underneath. In the self-assembled case there is also no need for fabrication or post-processing for optical experiments, eliminating possible sources of impurities and contamination. By tuning the sizes of these nanostructures the resonant wavelength can be tuned [5] to be in resonance with QWs [6,7] or QDs [8] just a few nanometers beneath the metallic structures. Growing these resonant indium islands in the same process as the semiconductor growth with MBE now opens up the possibility of encapsulating [9]

the islands with more semiconductor material, including gain material. This would allow for larger coupling effects and possibly compensating metamaterial losses.

Here we present MBE growth conditions for indium islands, which allow for the tuning of the density, to well below 1 μm^{-2}, and size, from $\sim$100 nm up to $\sim$1.5 μm, of the indium islands. The larger island diameters are a result of a slow indium growth in the 1 ML/hr range, allowing for migration of the indium atoms throughout the growth.

2. Materials and methods

All samples have been grown on (100) GaAs wafers. The indium island samples have been grown in two different machines. The first is a Riber 32P where the sources are mounted on the rear vertical wall of the MBE growth chamber and aimed at the substrate which is mounted 25° from vertical, and 13° away from the most uniform growth position. In this chamber we have utilized 500 μm thick, double-side polished, two inch wafers cleaved into quarters for sample growth. These quarter wafers are held in three inch molybdenum substrate mounts (molyblocks) for quarter wafers with two tabs along the perpendicular sides. The other chamber used is a Riber 412 where the sources are mounted on the bottom of the MBE growth chamber and aimed at the substrate which is mounted horizontally in a five inch platen and the substrate is centered in the platen. In this chamber the growth is done on

350 µm thick, single-side polished, full two inch wafers which are n-doped with silicon (10^{-18} cm^{-3}). This chamber was used for all samples discussed below that have been grown with doped semiconductor layers. Both chambers utilize effusion cells with 7 N (7N5) purity indium in the Riber 32P (Riber 412).

After de-oxidizing the substrate, >400 nm of GaAs is grown at a substrate temperature of ~580 °C. For samples grown with InGaAs QWs or InAs QDs the substrate temperature is dropped to ~485 °C for the growth of these structures. The QW or QDs are then capped with between 3 and 10 nm of GaAs grown at the same substrate temperature. For the indium island growth the substrate temperature is lowered by cutting off the current to the substrate heater. At a substrate temperature of ~300 °C the arsenic flux is cut off. Once the arsenic flux is off, the substrate heater is set at a constant current and the substrate is allowed to come to an equilibrium temperature, ~130 °C as measured with a type C thermocouple, while arsenic continues to be pumped out of the chamber. This time has been varied between 1 and 12 h. The indium island deposition then takes place with growth rates (beam equivalent pressure) between 0.27 ML/s (3.02×10^{-7} Torr) and 1 ML/hr or 0.00028 ML/s (3.97×10^{-10} Torr). In the latter case the indium cell temperature is only 60 °C above the standby temperature of the cell. The indium growth rate is given as the growth rate of InAs as calibrated from InAs QD growths.

Samples are characterized using atomic force microscopy (AFM), scanning electron microscopy (SEM), tunneling electron microscopy (TEM), energy dispersive x-ray spectroscopy (EDS), Fourier transform infrared (FTIR) transmission measurements, and photoluminescence (PL). By utilizing standard image processing techniques the sizes of the islands are extracted from AFM and SEM images.

3. Results

An interesting aspect of the indium island sample growths is the different distribution in island sizes achieved by the two different machines used. While there is expected to be small variations in substrate temperature and flux uniformity it is not expected that the indium islands grown in one chamber would have a Gaussian-like distribution in size while the other chamber would produce size distributions with a clear tail on the short side of the distribution. This is seen in Fig. 1(a) and (b) for the diameter
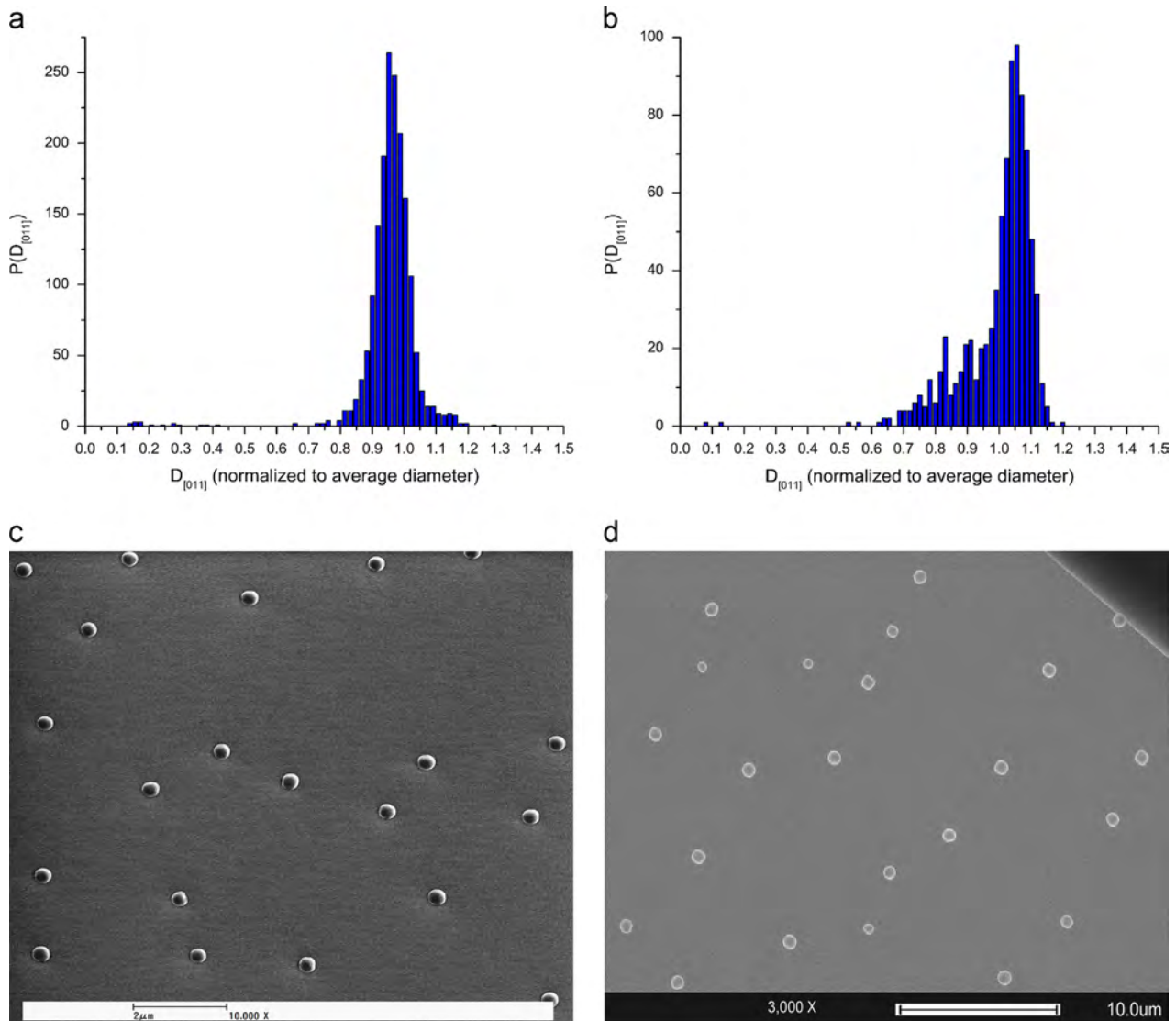
Fig. 1. Distribution of the diameter of the indium islands along the (011) crystal axis for a sample grown in the Riber 32 (a) and a sample grown in the Riber 412 (b). The distributions are scaled to their average diameter, which are 385 nm with a standard deviation of 34 nm and 834 nm with a standard deviation of 94 nm for samples shown in (a) and (b), respectively. (c) and (d) SEM images corresponding to the distributions in (a) and (b), respectively.

of the indium islands along the (011) crystal axis and can be seen along the (0–11) crystal axis as well as in the height of the indium islands, although this is not shown here. The indium island samples with the tail in the distribution are grown on silicon doped GaAs but this is not expected to affect the formation of the indium islands in such a manner. In either case the standard deviation of the distribution is ~10% of the average size for both samples. Both distributions in Fig. 1 are developed by analyzing the diameter of over 850 islands for each sample. The distribution with the tail looks similar to the asymptotic distribution of the Lifshitz–Slyozov $t^{1/3}$ growth law [10] which is familiar to the growth of II–VI QDs in a glass matrix [11]. The tailed distribution shown in Fig. 1(b) has a much narrower peak than the $t^{1/3}$ distribution but still suggests diffusion of the indium islands is taking place and the larger islands are growing at the expense of the smaller islands. From the corresponding SEM images in

Fig. 1(c) and (d) it can be seen that the indium islands tend to cluster for the Gaussian-like distribution of sizes and the samples showing the tail in the distribution seem to have some degree of order where they prefer to align together perpendicular to the (011) crystal axis (major flat) shown in upper right hand corner of Fig. 1(c). This direction is also parallel to the surface roughness of the sample seen on SEM images.

As discussed in the previous section, a wide range in growth rates or beam equivalent pressures are used, roughly a factor of 1000 between the highest and the lowest. By varying the growth rate and the amount of indium deposited the indium islands size can be varied between a diameter of 120 nm and a diameter of 1.5 μm, corresponding to heights of 50 nm and 445 nm. The densities achieved have been between 10 μm^{-2} and 0.007 μm^{-2}. Fig. 2 shows plasmonic resonances, measured using FTIR, of several indium island samples along with corresponding
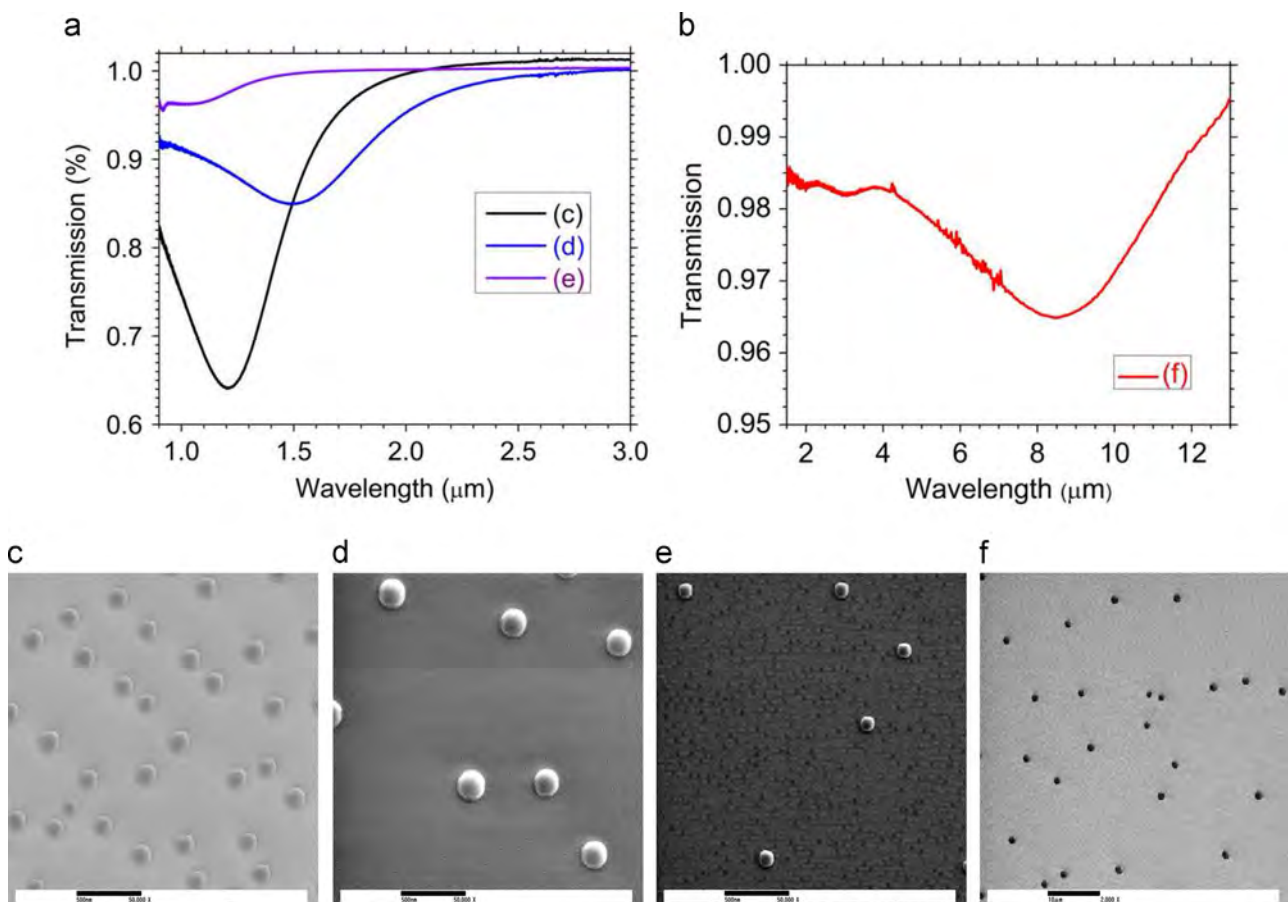
Fig. 2. (a) and (b) FTIR transmission measurements showing the plasmonic resonances of samples shown in the SEM images of (c), (d), (e), and (f). The scale bar in (c), (d), and (e) are 500 nm and in (f) is 10 μm.
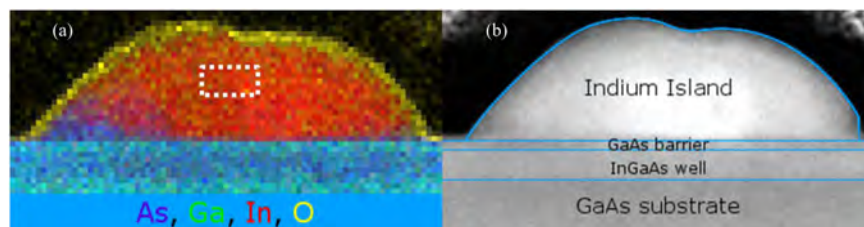
Fig. 3. (a) An EDS map of an island showing that it is predominantly indium (red) but also contains arsenic (violet), gallium (green), and oxygen (yellow). The white dashed box represents a 20 nm by 10 nm region where an indium concentration of 89.9% was measured. (b) A TEM image of the same island with the different regions of the structure outlined and labeled. (For interpretation of the references to color in this figure, the reader is referred to the web version of this article.)
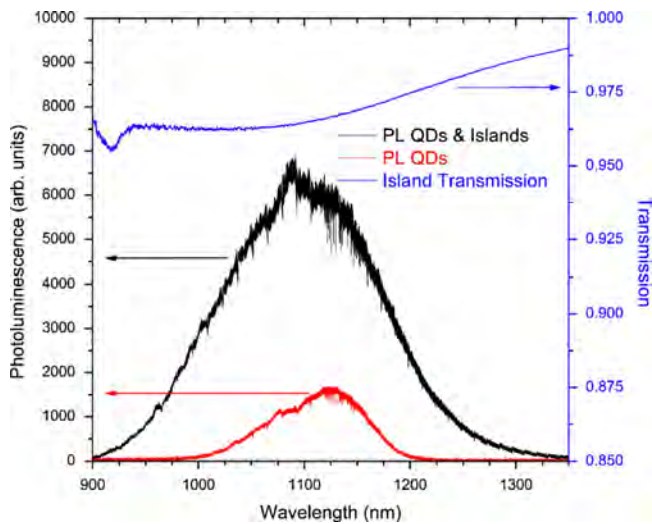
Fig. 4. PL of an indium island sample with 7 nm GaAs cap separating the InAs QDs and the indium islands (black), PL of just InAs QDs with a 7 nm GaAs cap (red), and the transmission spectra of the indium islands (blue). PL measured at 10.8 K and transmission measured at room temperature. (For interpretation of the references to color in this figure, the reader is referred to the web version of this article.)

SEM images for each sample. It is clear, that the larger islands have longer wavelength resonances and that a decrease in density of the indium islands decreases the collective transmission as measured by FTIR.

Using EDS measurements the chemical composition of several indium islands on a single sample have been determined. Before the sample is prepared for TEM and EDS measurements the sample is coated with carbon and platinum to protect the sample during processing of the TEM slice. As shown in Fig. 3(a), a color map showing the indium (red), gallium (green), arsenic (violet), and oxygen (yellow) mapping of a single island, the indium islands are predominantly indium. A TEM of the island with the sample structure outlined is shown in Fig. 3(b). In the dashed outline in the central area of the indium island in Fig. 3(a), representing a 20 nm by 10 nm section of the island, the indium concentration was measured to be 89.9% with only 5.6% gallium and 4.5% arsenic. Despite the presence of gallium and arsenic in the islands and an oxide layer covering the island the samples show a strong plasmonic resonance as shown in Fig. 2.

As described above, the indium islands can be grown in close proximity to InAs QDs where the separation between the indium islands and the QDs can be precisely controlled by the thickness of the GaAs capping layer. In Fig. 4 we show a $4\times$ increase in the peak intensity of the ensemble PL of InAs QDs when indium islands are present. The red data in Fig. 4 is from an InAs QD with a 7 nm GaAs cap but no indium islands. The black data is from a sample with similar InAs QDs and indium islands, at an island density of $\sim 1\ \mu m^{-2}$, with a 7 nm GaAs cap separating the InAs QDs from the indium islands. For both samples the density of the QDs is $\sim 80\ \mu m^{-2}$ and the QD size is ~ 25 nm in diameter and ~ 3.5 nm tall. The shift in the PL peak to a shorter wavelength enhanced QDs is from the indium island resonance being centered at a shorter wavelength and enhancing the shorter wavelength QDs more. The PL measurements are done at a temperature of 10.8 K with above band pumping from a 632.8 nm continuous wave HeNe laser. About 1.6 mW of pump power is focused to a $\sim 3\ \mu m$ diameter spot, using a high NA $100\times$ microscope objective. Also shown in Fig. 4 is the room temperature resonance of the indium islands, with dimension of 120 nm in diameter and 50 nm tall, as measured using an FTIR spectrometer. The resonance of the indium islands has been checked to not change between room temperature and 10 K but is not shown here.

4. Conclusion

Self-assembled plasmonic nanostructures that can be grown in the same process as III–V quantum emitters have been explored and a wide range in sizes and densities has been demonstrated. A $4\times$ increase in the peak PL of InAs QDs separated by 7 nm from the indium islands has been observed, demonstrating that the islands improve the luminescence of QDs and can in fact interact with them. This distance is less than the observed $1/e$ point, ~ 8 nm, of the coupling distance previously observed between a plasmonic structure and a QW [12] suggesting this is a useful platform to study coupling effects to III–V near-surface QDs. The increase in PL can be improved further by increasing the percentage of QD emission that is coupled to the plasmon mode [13] of on an indium island by controlling the position of the QDs relative to the plasmonic nanostructures or by using metals with lower losses as the plasmonic nanostructure [2]. An added interest of this platform is the ability to integrate superconducting structures, the indium islands, with III–V quantum emitters. The high indium concentration, up to $\sim 90\%$, will be beneficial for any superconducting experiments or applications.

References

[1] Y. Wu, C. Zhang, N.M. Estakhri, Y. Zhao, J. Kim, M. Zhang, X.-X. Liu, G.K. Pribil, A. Alù, C.-K. Shih, X. Li, Intrinsic optical properties and enhanced plasmonic response of epitaxial silver, Adv. Mater. 26 (35) (2014) 6106.
[2] A. Urbańczyk, R. Nötzel, Site-controlled Ag nanocrystals grown by molecular beam epitaxy—towards plasmonic integration technology, J. Appl. Phys. 112 (2012) 124302.
[3] Frank W.M. van Otten Adam Urbańczyk, Richard Nötzel, Self-aligned epitaxial metal-semiconductor hybrid nanostructures for plasmonics, Appl. Phys. Lett. 98 (24) (2011) 243110.
[4] A. Urbaczyk, G.J. Hamhuis, R. Nötzel, Coupling of single InGaAs quantum dots to the plasmon resonance of a metal nanocrystal, Appl. Phys. Lett. 97 (4) (2010) 043105.
[5] L. Novotny, Effective wavelength scaling for optical antennas, Phy. Rev. Lett. 98 (26) (2007) 266802.
[6] M. Gehl, S. Zandbergen, R. Gibson, M. Béchu, N. Nader, J. Hendrickson, J. Sears, P. Keiffer, M Wegener, G. Khitrova, Spectroscopic studies of resonant coupling of silver optical antenna arrays to a near-surface quantum well, J. Opt. 16 (11) (2014) 114016.
[7] N. Meinzer, M. Ruther, S. Linden, C.M. Soukoulis, G. Khitrova, J. Hendrickson, J.D. Olitzky, H.M. Gibbs, M. Wegener., Arrays of Ag split-ring resonators coupled to InGaAs single-quantum-well gain, Opt. Express 18 (23) (2010) 24140.

[8] A.G. Curto, T.H. Taminiau, G. Volpe, M.P. Kreuzer, R. Quidant, N.F. van Hulst., Multipolar radiation of quantum emitters with nanowire optical antennas, Nature Commun. 4 (2013) 1750.

[9] C.R. Haughn, E.H. Steenbergen, L.J. Bissell, E.Y. Chen, K.G. Eyink, J.M.O. Zide, M.F. Doty, Carrier transfer from InAs quantum dots to ErAs metal nanoparticles, Appl. Phys. Lett. 105 (10) (2014) 103108.

[10] I.M. Lifshitz, V.V. Slyozov, The kinetics of precipitation from supersaturated solid solutions, J. Phys. Chem. Solids 19 (1) (1961) 35.

[11] A.I. Ekimov, Optical properties of semiconductor quantum dots in glass matrix, Phys. Scr. 1991 (T39) (1991) 217.

[12] N. Meinzer, M. König, M. Ruther, S. Linden, G. Khitrova, H.M. Gibbs, K. Busch, M. Wegener, Distance-dependence of the coupling between split-ring resonators and single-quantum-well gain, Appl. Phys. Lett. 99 (11) (2011) 111104.

[13] A.V. Akimov, A. Mukherjee, C.L Yu, D.E. Chang, A.S. Zibrov, P.R. Hemmer, H. Park, M.D. Lukin, Generation of single optical plasmons in metallic nanowires coupled to quantum dots, Nature 450 (2007) 402.
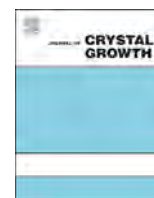
Photoluminescence study of the effect of strain compensation on InAs/AlAsSb quantum dots

Zhexin Zhao, Ramesh B. Laghumavarapu, Paul J. Simmonds, Haiming Ji, Baolai Liang *, Diana L. Huffaker

California NanoSystems Institute & Electrical Engineering Department, University of California—Los Angeles, Los Angeles, CA 90095, USA

ARTICLE INFO

ABSTRACT

We investigate stacked structures of InAs/AlAsSb/InP quantum dots using temperature- and power-dependent photoluminescence. The band gap of InAs/AlAsSb QDs is 0.73 eV at room temperature, which is close to the ideal case for intermediate band solar cells. As the number of quantum dot layers is increased, the photoluminescence undergoes a blue-shift due to the effects of accumulated compressive strain. This PL red shift can be counteracted using thin layers of AlAs to compensate the strain. We also derive thermal activation energies for this exotic quantum dot system.

© 2015 Elsevier B.V. All rights reserved.

1. Introduction

Intermediate band solar cells (IBSCs) are among the most promising candidates for next generation photovoltaics, offering high efficiency from a simple structure at low cost [1,2]. One possible method for creating the intermediate band is by inserting quantum dot (QD) layers into the active region of a solar cell [2–13]. The band alignments of current QD material systems, such as InAs/GaAs, InAs/GaAsN and GaSb/GaAs [3–5], are not optimal for implementing the theoretically predicted intermediate band for IBSCs. In comparison with InAs/GaAs and GaSb/GaAs, the InAs/AlAsSb QD system has band alignments that almost match the calculated ideal case [6]. Previous studies from our group show that this is a type-II QD system with strong electron confinement, that offers excellent optical characteristics for IBSCs [6]. We have successfully optimized both the MBE growth conditions to obtain high-quality stacked QD structures, and QD optical performance to create IBSC prototype devices [6,7].

So that QD IBSC devices can absorb solar energy more efficiently, it is important to obtain high QD density by stacking layers of dots. However, the compressive strain left over from the QD self-assembly process will also accumulate and cause defects in the stacked structure. It is therefore hard to achieve a large number of QD layers while maintaining high material quality. Strain compensation (SC) is a useful technique to deal with this problem [8–12]. We recently reported the use of thin tensile-strained AlAs layers to manage compressive strain in stacked layers of InAs/AlAsSb QDs [13]. The AlAs SC layers enable us to reduce residual strain in the QD stacks, so improving the overall optical quality and increasing carrier lifetime.

In this work we report the results of comprehensive photoluminescence (PL) spectroscopy measurements to fully understand the fundamental characteristics of strain-compensated InAs/AlAsSb QDs. With a view to implementing this exotic QD system in proof-of-principle IBSC devices, we are particularly interested to learn how the material properties change with increasing number of stacked QD layers, and what role the SC layers play.

2. Experiments

We studied four InAs/AlAsSb QD samples grown on InP(0 0 1) substrates by solid-source molecular beam epitaxy. Schematic diagrams of the sample structure are shown in Fig. 1 and the sample details are listed in Table 1. All samples have the following structure: a 500 nm AlAsSb buffer, a 5 monolayer (ML) GaAs cladding layer, 8 ML of InAs QDs, followed by a 5 ML GaAs$_{0.95}$Sb$_{0.05}$ capping layer [7], and then a 15 nm AlAsSb spacer. For sample B and sample C we repeated the whole QD section (including the GaAs cladding, the InAs QDs, the GaAsSb capping layer, and the AlAsSb spacer) 5 and 30 times, respectively. Sample D also has 30 QD layers, but with a 3 ML AlAs SC layer in the middle of each AlAsSb spacer. The 3 ML AlAs SC layer has been carefully designed to fully balance the strain in the stacked QD structure [13]. While the lattice constant of InAs is bigger than that of the InP substrate, the lattice constant of AlAs is smaller. The AlAs layers therefore introduce tensile strain that compensates the compressive strain caused by the InAs QDs in each period of the stack. We have previously reported the calculated band alignment for these strain compensated QD samples [13].

* Corresponding author.
  E-mail address: bliang@cnsi.ucla.edu (B. Liang).
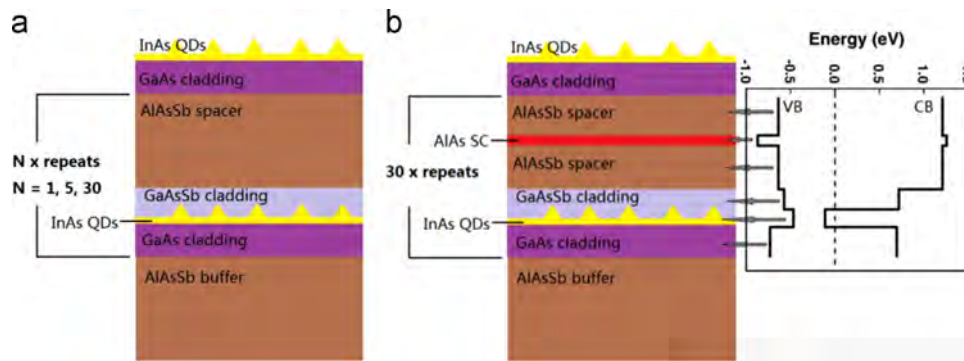
Fig. 1. Schematic diagram of InAs/AlAsSb QD samples (a) without, and (b) with an AlAs SC layer. The calculated band structure of the strain compensated sample is shown next to (b).

Table 1
Details of the four InAs/AlAsSb QD samples studied in this work.

Sample ID	A	B	C	D
No. of QD layers	1	5	30	30
Spacer thickness	–	15 nm	15 nm	15 nm
AlAs SC thickness	0 ML	0 ML	0 ML	3 ML

For PL measurements, the samples are placed in a cryostat (77–300 K). A 532 nm solid-state laser operated at 8 mW, 25 mW and 80 mW, is focused on the sample surface with a spot ∼125 μm in diameter. The PL signal is collected by a lens and then dispersed by a monochromator. A Hamamatsu Extended-InGaAs detector is used to measure the PL signal via standard lock-in technology. The PL spectra are fitted with Gaussian functions in order to derive the PL peak wavelength, FWHM and integrated PL intensity (IPL).

3. Experimental results and discussion

The PL spectra of the four samples are normalized to the maximum intensity of each spectrum in Fig. 2(a). The PL peak blue-shifts from 1587 nm to 1459 nm as the number of stacked QD layers increases from 1 to 30, while the 30-layer SC sample D emits at similar wavelength to the single QD layer sample A. The blue-shift from sample A to C may be attributed to the accumulated compressive strain, which tends to enlarge the band gap. However, with the introduction of the SC layers in sample D, the amount of strain in each period of the QD stack remains constant. So, even though sample D has 30 QD layers, the use of strain compensation means that it emits at almost the same wavelength as the single layer sample A. This trend holds throughout the temperature range from 77 K to room temperature (Fig. 2(b)).

Under the 8 mW excitation condition in Fig. 2(a), sample D has the strongest PL with peak intensity twice that of the other three samples. The integrated PL intensities (normalized to that of sample A) of samples A, B, C and D at 77 K (with a laser power of 8 mW) are found to be 1, 0.93, 1.43 and 3.48, respectively. Although increasing the number of layers of QDs may enhance light absorption, the simultaneous accumulation of strain also increases the occurrence of defects and deteriorates the optical quality. As a result, despite raising the number of stacked QD layers from 1 to 30 in samples A to C, the PL intensity remains essentially unchanged. However, in sample D the defects caused by excessive strain are reduced by the inclusion of the SC layers, and so the benefit of a large number of stacked QDs on the optical quality of the structure becomes apparent. We measure FWHM values of 82 nm, 103 nm, and 118 nm for samples A, B, and C, respectively. The broadening of the PL spectra with more QD layers may be due to the increasing inhomogeneity of QDs caused by stacking. It is also very interesting that the FWHM is 134 nm for sample D. Further

work will be needed to understand why the PL of sample D with SC layers is broader than that of sample C without SC layers.

The PL as a function of temperature from 77 to 300 K is shown in Fig. 3. In sample D, thermal quenching starts at a relatively low temperature, which is a characteristic of type-II QDs [14]. As the temperature increases, the PL peak energy shows a red shift for all samples due to the decrease of QD band gap predicted by the Varshni law [15],

$$E(T) = E(0) - \frac{\alpha T^2}{\beta + T} \qquad (1)$$

By fitting the temperature dependence of the peak PL energies using Eq. (1), we can obtain the Varshni parameters α, and β, while the transition energy at 0 K, $E(0)$, is offset in the four samples. Since in type-II QDs the PL peak energy is well known to depend on the excitation intensity [6,7,14], the fitting results also depend on the excitation intensity. Three different laser powers are thus used in the experiments to highlight this dependence and show the trend as excitation intensity approaches the solar power intensity (∼1 mW/mm²). The Varshni fitting for sample D is shown in Fig. 3(b) as an example and the corresponding values for all four samples are listed in Table 2. These Varshni fitting results are satisfactory when compared to the values for bulk InAs recommended by Vurgaftman et al.: $E(0)=0.417$ eV, $\alpha=0.276$ meV/K, and $\beta=93$ K [15]. In our QD system, the transition energy $E(0)$ is offset because of quantum confinement and the effect of strain on the band gap. Table 2 shows that increasing the number of QD layers raises $E(0)$, while in sample D, inserting SC layers reduces $E(0)$ to the value of the single QD layer sample A. Though α and β are a little different from the literature values above, they are within a tolerable range and reveal some interesting phenomenon. α and β change considerably from sample to sample, but the change is comparatively weak as a function of laser excitation power. Nevertheless, α for sample C is similar to that of sample D but differs significantly from samples A and B. We see the same trend for β. These results indicate that the number of stacked QD layers has stronger influence on α and β than the introduction of SC layers, or the pump laser power. An investigation of parameters α and β might therefore help reveal material properties that change as a result of stacking large numbers of QD layers.

It is worth noting from Fig. 3(b) that at a laser power of 8 mW the peak PL energy for sample D is 0.73 eV at 300 K. This value is very close to the optimal value (∼0.7 eV) for an IBSC [1]. IBSC theory predicts that only when the band alignment is close to the optimal case can the theoretical maximum power conversion efficiency be achieved. The careful design of the InAs/AlAsSb QD system for achieving highly efficient IBSCs is further confirmed by PL emission from the single QD layer sample A at 0.74 eV at 300 K. The peak PL energies for samples B and C are 0.78 eV, and 0.81 eV respectively at 300 K and the deviation from the optimal value
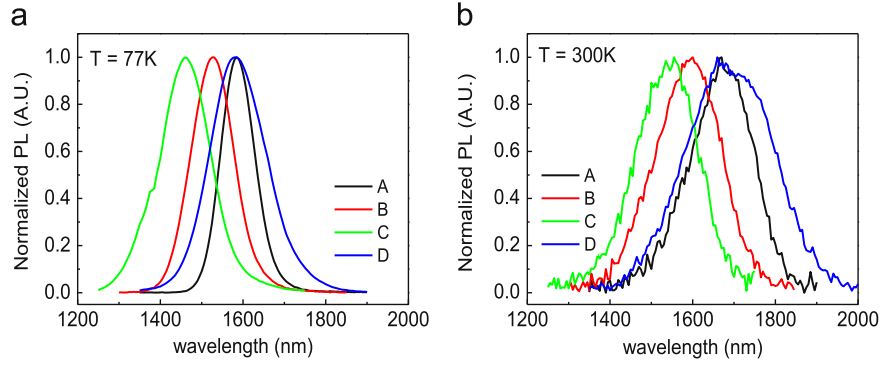
Fig. 2. (a) Normalized PL spectra measured with a laser power of 8 mW at 77 K. The PL intensities of samples B, C, and D are 0.74, 1.02 and 2.15 times the intensity of sample A, respectively. (b) Normalized PL spectra measured with a laser power of 25 mW at 300 K. The PL intensities of samples B, C, and D are 1.38, 0.95 and 1.82 times the intensity of sample A, respectively.
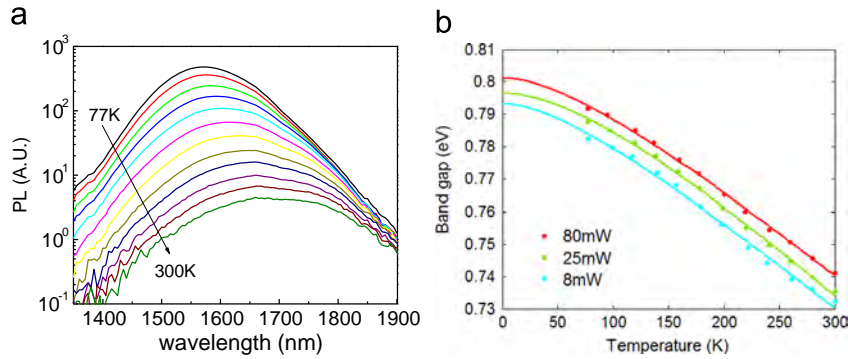
Fig. 3. (a) PL spectra of sample D measured at different temperatures from 77 K to 300 K using a laser power of 25 mW; (b) Varshni fitting of the peak PL energies from the spectra in Fig. 3(a) at three different laser excitation powers.

Table 2
Varshni equation fitting results for all four samples as a function of pump laser power.

Sample no.	A			B		
Laser power	8 mW	25 mW	80 mW	8 mW	25 mW	80 mW
$E(0)$ (eV)	0.790	0.796	0.805	0.822	0.828	0.835
α (meV/K)	0.220	0.223	0.212	0.204	0.199	0.191
β (K)	81	79	33	90	62	25
Sample no.	C			D		
Laser power	8 mW	25 mW	80 mW	8 mW	25 mW	80 mW
$E(0)$ (eV)	0.858	0.861	0.864	0.793	0.796	0.801
α (meV/K)	0.282	0.299	0.260	0.284	0.326	0.287
β (K)	158	185	129	106	170	125

Fig. 4. Linear fitting of ln(IPL) against 1000/T at high temperature for sample D. The slopes are annotated near the linear fitting.

grows larger with more QD layers. However, this deviation is eliminated when SC is applied to the QD system. The use of SC layers guarantees that the band alignment is still close to the optimal value, even when the number of QD layers is large, as it will need to be in a practical IBSC device.

Thermal activation energy, another critical parameter for carriers in a QD system, refers to the energy that the carriers need to escape from the QDs. The integrated PL intensity (IPL) is related to thermal activation energy (E_a) by [16],

$$IPL \propto \exp\frac{E_a}{kT} \tag{2}$$

We derive the thermal activation energy of the QDs from the thermal quenching processes close to room temperature. Fig. 4 shows the Arrhenius plot of IPL as a function of measurement temperature at three different pump powers—the example shown here is for sample D. The gradients of the linear fits at high temperature give the thermal activation energies and these are summarized for all four samples in Table 3. Thermal activation energy depends on the

excitation power density: higher excitation power leads to a lower measured activation energy. At the same power density, the thermal activation energy does not vary much between samples, except that sample C appears to be an outlier, showing higher thermal activation energies at all pump powers compared with the other three.

From the data in Table 3, we note that the activation energy of InAs/AlAsSb QDs decreases with increasing excitation laser power. Similar observations are reported by Le Ru et al. for the InAs/GaAs QD system [17]. If we can apply their model to the InAs/AlAsSb QD system, the average number of carriers captured in every QD may have an impact on the experimentally derived thermal activation energy. As the InAs/AlAsSb QD system has a type-II band alignment, after excitation, electrons will be confined in the QDs, with holes localized outside but close to the QDs. With stronger excitation laser power, on average every QD has more electrons in it and more holes near it. This leads to a distortion of the band structure, reducing the energy required by the carriers to escape the QDs.

Table 3
Thermal activation energies for the four samples at different excitation laser powers.

Activation energy (meV)	8 mW	25 mW	80 mW
Sample A	133	99	73
Sample B	130	102	74
Sample C	160	128	100
Sample D	126	101	79

To explain the inconsistency of sample C with the others in Table 3, we must consider that fact that it contains the highest number of stacked QD periods but no SC layers. As such, it is likely to have the highest defect density and hence a shorter carrier lifetime [13]. As a result, for a given pump laser power, each QD in sample C may, on average, have fewer carriers than the other three samples. The distortion of the band structure will therefore be less in sample C and so the measured activation energies are larger.

4. Conclusions

We have studied the photoluminescence response of InAs/AlAsSb QD structures. We see that stacking multiple layers of QDs leads to an accumulation of compressive strain, which increases the band gap and causes a blue-shift in the PL emission energy. Placing a carefully optimized tensile AlAs strain compensation layer in the AlAsSb spacer between each layer of QDs effectively balances the strain and improves the optical properties of the InAs dots. Through temperature and excitation power dependent PL measurements, we obtain Varshni parameters, as well as the thermal activation energies. We use these values to help us understand the carrier dynamics and the physical properties of these materials. The results presented here show that the strain compensated stacked InAs/AlAsSb QD system is a promising candidate with almost ideal band alignments for developing a high efficiency QD IBSC.

Acknowledgement

References

[1] A. Luque, A. Martí, Phys. Rev. Lett. 78 (1997) 5014.
[2] A. Luque, A. Martí, Adv. Mater. 22 (2010) 160.
[3] H. Jiang, J. Singh, Phys. Rev. B 56 (1997) 4696.
[4] F. Hatami, N.N. Ledentsov, M. Grundmann, J. Böhrer, F. Heinrichsdorff, M. Beer, D. Bimberg, S.S. Ruvimov, P. Werner, U. Gösele, J. Heydenreich, U. Richter, S.V. Ivanov, B.Y. Meltser, P.S. Kop'ev, Z.I. Alferov, Appl. Phys. Lett. 67 (1995) 656.
[5] F. Hatami, M. Grundmann, N.N. Ledentsov, F. Heinrichsdorff, R. Heitz, J. Böhrer, D. Bimberg, S.S. Ruvimov, P. Werner, V.M. Ustinov, P.S. Kop'ev, Z.I. Alferov, Phys. Rev. B 57 (1998) 4635.
[6] P.J. Simmonds, R.B. Laghumavarapu, M. Sun, A. Lin, C.J. Reyner, B. Liang, D.L. Huffaker, Appl. Phys. Lett. 100 (2012) 243108.
[7] M. Sun, P.J. Simmonds, R.B. Laghumavarapu, A. Lin, C.J. Reyner, H.-S. Duan, B. Liang, D.L. Huffaker, Appl. Phys. Lett. 102 (2013) 023107.
[8] P. Lever, H.H. Tan, C. Jagadish, J. Appl. Phys. 95 (2004).
[9] R.B. Laghumavarapu, M. El-Emawy, N. Nuntawong, A. Moscho, L.F. Lester, D.L. Huffaker, Appl. Phys. Lett. 91 (2007) 243115.
[10] Ryuji Oshima, Ayami Takata, Yoshitaka Okada, Appl. Phys. Lett. 93 (2008) 083111.
[11] Christopher G. Bailey, David V. Forbes, Ryne P. Raffaelle, Seth M. Hubbard, Appl. Phys. Lett. 98 (2011) 163105.
[12] C.G. Bailey, D.V. Forbes, S.J. Polly, Z.S. Bittner, Y. Dai, C. Mackos, R.P. Raffaelle, S.M. Hubbard, IEEE J. Photovoltaics 2 (2012) 269.
[13] P.J. Simmonds, M. Sun, R.B. Laghumavarapu, B. Liang, A.G. Norman, J.-W. Luo, D.L. Huffaker, Nanotechnology 25 (2014) 445402.
[14] K. Suzuki, R.A. Hogg, Y. Arakawa, J. Appl. Phys. 85 (1999) 8349.
[15] I. Vurgaftman, J.R. Meyer, L.R. Ram-Mohan, J. Appl. Phys. 89 (2001) 5815.
[16] Z. Xu, Z. Lu, X. Yang, Z. Yuan, B. Zheng, J. Xu, W. Ge, Y. Wang, J. Wang, L. Chang, Phys. Rev. B 54 (1996) 11528.
[17] E. Le Ru, J. Fack, R. Murray, Phys. Rev. B 67 (2003) 245318.
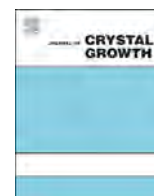
Novel selective area growth (SAG) method for regularly arranged AlGaN nanocolumns using nanotemplates

Koji Yamano [a], Katsumi Kishino [a,b,*], Hiroto Sekiguchi [c], Takao Oto [a], Akihiro Wakahara [c], Yoichi Kawakami [d]

[a] *Department of Engineering and Applied Sciences, Sophia University, 7-1 Kioi-cho, Chiyoda-ku, Tokyo 102-8554, Japan*
[b] *Sophia Nanotechnology Research Center, Sophia University, 7-1 Kioi-cho, Chiyoda-ku, Tokyo 102-8554, Japan*
[c] *Toyohashi University of Technology, 1-1 Hibarigaoka, Tempaku-cho, Toyohashi, Aichi 441-8580, Japan*
[d] *Kyoto University, Kyoto Univ. Katsura, Nishikyo-ku, Kyoto 615-8510, Japan*

ARTICLE INFO

ABSTRACT

We have demonstrated a novel selective area growth (SAG) method based on rf-plasma-assisted molecular beam epitaxy for AlGaN nanocolumns using nanotemplates. The nanotemplates, which were prepared on a metal-organic chemical vapor deposition-GaN template, consisted of a triangular lattice of nanopillars with a lattice constant from 200 to 400 nm. For nanopillars with a lattice constant of 400 nm, the gap width between adjacent pillars was varied from 30 to 130 nm. The well-controlled SAG of GaN nanocolumns was achieved on nanopillar arrays with gap widths of less than approximately 45 nm. The beam shadowing effect, which was induced in the high-density nanopillar arrays with small gaps, was a key mechanism in the SAG. This gap width condition for SAG was satisfied for lattice constants from 200 to 400 nm. Using the nanotemplate SAG technology, the SAG of AlGaN nanocolumn arrays was achieved for Al compositions of 0.13, 0.22, 0.43, and 1. Single-peak photoluminescence (PL) spectra of AlGaN were observed, whose wavelengths were close to the calculated bandgap wavelengths using the bandgaps of AlN (6.015 eV) and GaN (3.39 eV) and a bowing parameter of 0.98 eV.

1. Introduction

Nitride-semiconductor one-dimensional nanocrystals, which have various names such as nanocolumns, nanowires, nanorods, and nanopillars, have been extensively investigated in the last decade [1–5]. Freestanding vertical nanocolumns on substrates are attractive for applications to III–V nitride optoelectronic devices owing to their dislocation-free, efficient light extraction, and strain relaxation properties [3,6]. The periodic arrangement of GaN nanocolumns generates the photonic crystal effect in the nano-crystal system, which functions effectively to realize the radiation of a beam with high directionality from InGaN-based nanocolumn LEDs [7] and the surface-emitting lasing of InGaN nanocolumn arrays [8,9]. These phenomena have been actualized through precise control of the size and position of nanocolumns.

As a method of controlling the growth of nanocolumns, the selective area growth (SAG) of GaN nanocolumns has been developed on metal-organic chemical vapor deposition (MOCVD)-grown GaN template on sapphire substrates by MOCVD using a

SiN$_x$ mask [10] and by rf-plasma-assisted molecular beam epitaxy (rf-MBE) using a Ti mask [11,12]. Recently, the SAG of nanocolumns by rf-MBE on Si substrates has been reported using AlN buffer layers covered with patterned SiN$_x$ [13] and SiO$_2$ [14] masks and using thin GaN buffer layers with a Ti mask [15]. At the same time, the Ti-mask SAG technology on GaN/sapphire substrates has contributed to the realization of emission wavelength control via the nanocolumn diameter [16], the monolithic integration of nanocolumn LEDs with different emission colors [17], and green- and red-emitting nanocolumn LEDs [7,18].

However, the SAG of AlGaN using a Ti mask has not been achieved. This is because Al adatoms do not diffuse for a long distance on the surface of a Ti mask in the presence of nitrogen owing to the high bond energy between Al and N, which induces the spontaneous nucleation of AlGaN on the Ti mask, as shown in Fig. 1(a). Thus, it becomes difficult to perform the SAG of AlGaN at the mask openings with increasing Al composition.

In this study, we have demonstrated a novel method for the SAG of AlGaN nanocolumns based on rf-MBE using nanotemplates that consisted of top-down nanopillars. The nanopillars were prepared on a GaN template through electron beam lithography (EBL) and inductive coupling plasma (ICP) etching. The high-density nanopillar array with a high aspect ratio provides the beam shadowing effect, which enables AlGaN nanocolumns to be

* Corresponding author at: Department of Engineering and Applied Sciences, Sophia University, 7-1 Kioi-cho, Chiyoda-ku, Tokyo 102-8554, Japan.
 E-mail address: kishino@katsumi.ee.sophia.ac.jp (K. Kishino).

grown selectively on the tops of the underlying top-down nanopillars, as shown in Fig. 1(b). During the growth of AlGaN on the nanotemplate, Al and Ga beams are supplied to the concavo-convex surface of the nanopillar structure under the irradiation of atomic nitrogen. However, the sidewalls and gap regions of the structure are shadowed from the beam radiation by the neighboring nanopillars, suppressing the growth of AlGaN there and resulting in preferential growth on the tops of the nanostructures. As a result, the SAG of AlGaN is achieved (see Fig. 1(b)).

2. Growth of GaN on nanotemplates

Various GaN nanotemplates consisting of triangular-lattice nanopillar arrays with a lattice constant from 200 to 400 nm were

a
Ti-mask selective area growth

Nanoholes Ti mask

GaN template

Al   Ga

AlGaN

b
Nanotemplate selective area growth

Nanopillars

GaN template

Al   Ga

AlGaN
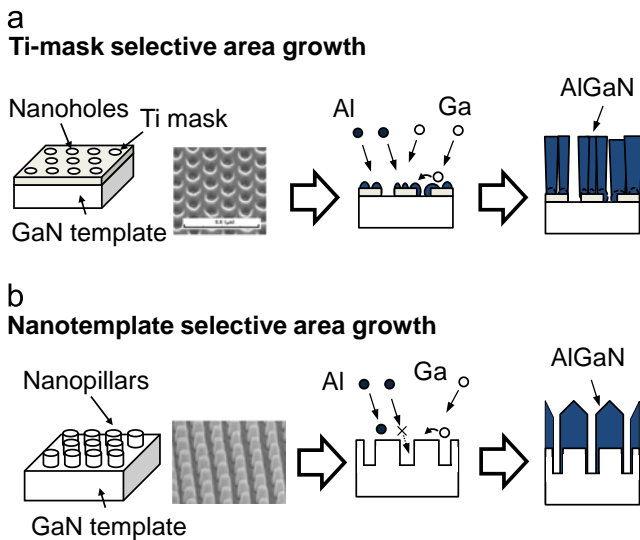
Fig. 1. Growth processes in selective area growth (SAG) methods; (a) Ti-mask SAG method and (b) nanotemplate SAG method proposed in this study. The bird's-eye-view SEM images in (a) and (b) are of the nanohole pattern and nanotemplate, respectively.

prepared on the same substrate. Owing to the etching property of ICP etching, the pillar height changed from 150 to 450 nm for a lattice constant of 400 nm when the gap width between adjacent pillars was increased from 30 to 130 nm. The pillar diameter changed from 160 nm (for a lattice constant of 200 nm) to 370 nm (for a lattice constant of 400 nm); thus, the aspect ratio of the nanopillars was 5–6. Using rf-MBE, Si-doped n-type GaN nanocolumns were grown on the GaN nanotemplates for 2 h at a substrate temperature T_{sub} of approximately 880 °C, which was measured using a pyrometer. The beam incident angle from the normal direction to the substrate surface was 40°, the beam equivalent pressure of Ga (P_{Ga}) was 3.0×10^{-4} Pa, and the flow rate of rf-plasma nitrogen was 0.7 sccm with a plasma input power of 450 W. The growth at a lower temperature enhanced the lateral growth, resulting in coalescence between neighboring nanocolumns. Here, to obtain a well-controlled SAG, we optimized the growth conditions and the growth window for SAG in terms of the growth temperature and nitrogen supply was similar to that for conventional Ti-mask SAG [12]. SAG on nanotemplates based on beam shadowing is suitable for the SAG of AlGaN as described later. The difference between the two types of SAG is that the enhanced nucleation at nanopillar tops in the initial growth stage promotes SAG in the former, while the suppressed nucleation on the Ti-mask promotes SAG in the latter Ti-mask SAG. However, in the latter, the sticking of AlN to the mask introduces a deficient SAG.

Fig. 2 shows top-view and bird's-eye-view scanning electron microscope (SEM) images of the underlying nanotemplates (before growth) and GaN nanocolumns grown on the nanotemplates (after growth) for patterns A, B and C, which consisted of nanopillars with small, large, and even larger gaps, respectively. Here, the lattice constant was 400 nm. For the samples in Fig. 2, the gap widths (W) in patterns A, B, and C were 45, 82, and 90–97 nm, respectively. Before the growth of GaN, the top surfaces of the nanopillars were flat, whereas the top shapes were different. The nanopillars were prepared by etching GaN through hexagonally shaped electron-beam resist masks, but in patterns B and C, large gaps were etched to form round nanopillars, as shown in Fig. 2, which was due to the isotropic nature of ICP etching. However, as a result of the growth of GaN nanocolumns on pattern B, the round
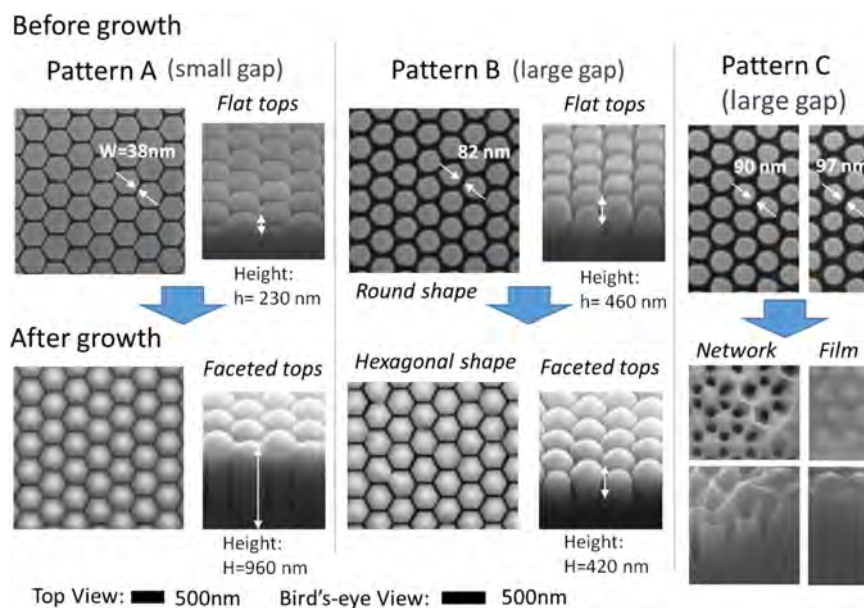
Fig. 2. SEM images of triangular-lattice nanotemplates (before growth) and nanocolumns (after growth) for different patterns of nanotemplates with a small gap width (pattern A), large gap width (pattern B), and even larger gap width (pattern C). The lattice constant was 400 nm for all patterns. The gap widths between adjacent nanopillars for patterns A, B, and C were 45, 82, and 90–97 nm, respectively, and the heights of the nanopillars and the grown nanocolumns for patterns A and B were 200 and 500 nm, and 950 and 420 nm, respectively. For pattern C, network or film of GaN was grown.
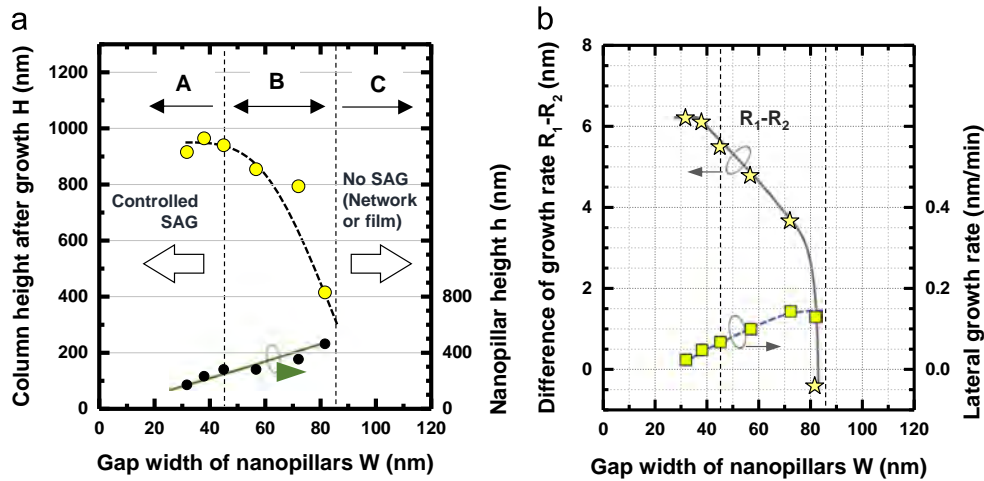
Fig. 3. (a) Nanocolumn height after the growth for 2 h and nanopillar height on nanotemplate before growth as a function of gap width of nanotemplate, and (b) difference between growth rates on nanopillar tops and in gap area (R_1–R_2), and lateral growth rate of nanocolumns as a function of gap width of nanotemplate.

shape of the pillars changed to a hexagonal shape, and the flat top surfaces changed to faceted pyramid surfaces. For pattern C with the largest gaps, the growth on the nanotemplate produced a network or film of GaN.

The beam shadowing effect changed with the gap width, resulting in a change in the nanocolumn height. For example, the nanocolumn height for pattern A was 960 nm and that for pattern B was 420 nm. Fig. 3(a) shows the nanocolumn height after growth (H) as a function of the gap width, where the initial nanopillar height before growth (h) is given at the bottom of the figure. For a gap width of less than 45 nm (pattern A in Fig. 2), taller GaN nanocolumns with a height from 900 to 1000 nm were obtained. When a gap width was larger than 45 nm (pattern B), the nanocolumn height decreased with increasing gap width, decreasing the beam shadowing effect, allowing more Ga atoms to reach the bottom of the gaps, and resulting in the growth of GaN, filling the gaps. When the gap width was very large (pattern C), the gaps were completely buried, resulting in a network or film of GaN on the entire area. To clarify the growth mechanism for a large gap, we evaluated the difference between the growth rates on the nanopillar tops (R_1) and in the gap area (R_2), using the formula $R_1 - R_2 = (H - h)/2$ for 2 h growth. The value of $R_1 - R_2$ decreased with increasing W and abruptly decreased when W approached ~80 nm, as shown in Fig. 3(b). $R_1 - R_2$ was slightly negative at $W = 82$ nm, probably due to error attributed to the measurement of H and h for different samples with the same pattern. The growth mechanism is as follows. With increasing gap width, the reduced shadowing effect of neighboring nanopillars increases the number of Ga atoms impinging on the nanopillar sidewalls, enhancing the diffusion of Ga to the bottom gap area; this results in the decreased value of $R_1 - R_2$. In the experiment, the increased imping-ing of Ga on the sidewalls enhanced the lateral growth of nanocol-umns with increasing W (see Fig. 3(b)).

The gap width of less than 45 nm required for SAG was satisfied for lattice constants from 200 to 400 nm; therefore the beam shadowing effect functioned effectively in promoting SAG under this condition. Fig. 4(a) shows the calculated incident atomic beam profile along the nanopillar axis of Ga impinging on the nanopillar sidewalls. We observed that the incident atomic flux dramatically decreases at the position $z = 200$ nm below the nanopillar top owing to beam shadowing by first- and second-neighbor nanopillars and no direct impingement of Ga on the gap bottom area occurs for gap widths calculated here. When the gap width is less than 40 nm, the incident atomic beam profile is well suppressed over a wide area on sidewalls. Thus, the diffusion of Ga to the bottom gap area does not occur, resulting in a controlled SAG. In fact, $R_1 - R_2$ did not change with the gap below a gap width of 40 nm. Note that the controlled SAG of GaN

nanocolumns occurred for a shallow concavo-convex surface of nanopillars with a height of ~200 nm, as shown in Fig. 3(b); then the calculation of Fig. 4(a) suggests that SAG of GaN nanocolumns occurs for nanopillars with a height less than 200 nm. The inset of Fig. 4(a) shows the incident atomic flux at $z = 50$ nm, which increases rapidly when the gap width is larger than 45 nm. The rapid increase in the incident atomic flux of Ga on the sidewalls enhances the diffusion of Ga to the bottom of the nanocolumns, decreasing the nanocolumn height and the difference in the growth rate between the nanopillar top and gap areas (see Fig. 3(a) and (b)). This growth behavior can be clearly observed in the cross-sectional SEM image of nanocolumns grown on nanopillar templates with the gap width tapered one-dimensionally from one end to the other shown in Fig. 4(b).

Transmission electron microscope (TEM) observation con-firmed that dislocation-free GaN nanocolumns were prepared by nanotemplate SAG in a similar way to Ti-mask SAG [12]; here the dislocations bent toward the sidewalls in the initial stage of growth and did not propagated to the upper region of the nanocolumns, as discussed below.

3. Dislocation filtering effect

We grew 40-pair Al$_{0.25}$Ga$_{0.75}$N (2 nm)/GaN (8 nm) superlattice (SL) template on GaN/sapphire by rf-MBE to prepare top-down AlGaN/GaN SL nanopillars, then GaN nanocolumns were grown on them, as shown in Fig. 5(a) and (b). This method is expected to enable us to integrate an AlGaN/GaN SL cladding region into nanocolumn emitters, such as nanocolumn lasers and/or LEDs. Fig. 5(c) shows a magnified cross-sectional TEM image of the AlGaN/GaN SL nanotemplate and the bottom region of the grown GaN nanocolumns. The horizontal lines indicate the stack of the short-period AlGaN/GaN superlattice. Note that the SL template included a large number of dislocations, which were generated at the boundary between the SL and the underlying GaN template and propagated through the SL region. However, when GaN nanocolumns were grown on the SL nanotemplate, the disloca-tions bent toward the sidewall and terminated in the bottom region of nanocolumns (i.e., at the initial stage of growth when the thickness was approximately 200 nm). The dislocation filtering effect [12] was also observed for the nanotemplate SAG.

4. SAG of AlGaN on nanotemplate

Four Si-doped AlGaN nanocolumns were grown for 30 min at a substrate temperature of approximately 900 °C by rf-MBE-based
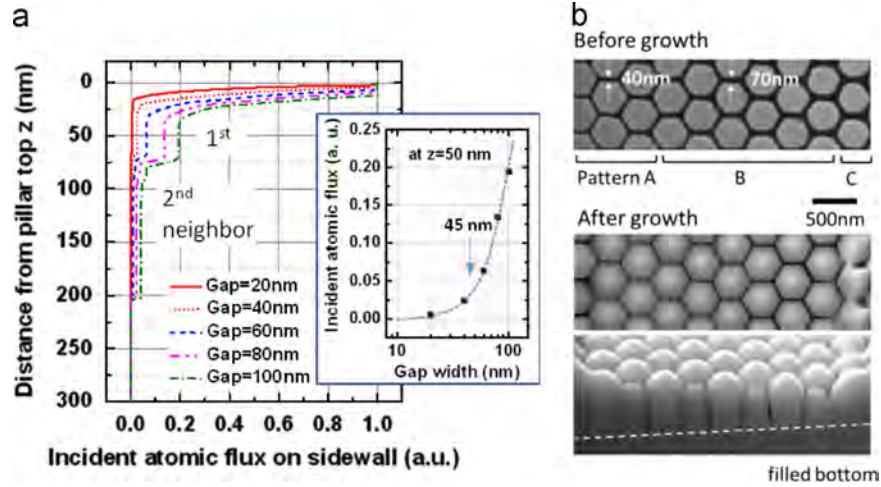
Fig. 4. (a) Calculated incident atomic beam profile along the nanopillar axis in the case of Ga impinging on the nanopillar sidewalls for gap widths from 20 to 100 nm. In the calculation, a triangular-lattice nanopillar array with a lattice constant of 400 nm is assumed. The inset shows the dependence of the incident atomic flux of Ga at the position 50 nm below the nanopillar top on the gap width. (b) Top-view and bird's-eye-view SEM images of GaN nanocolumns grown on a nanopillar template with the gap width tapered one-dimensionally from one end to the other.
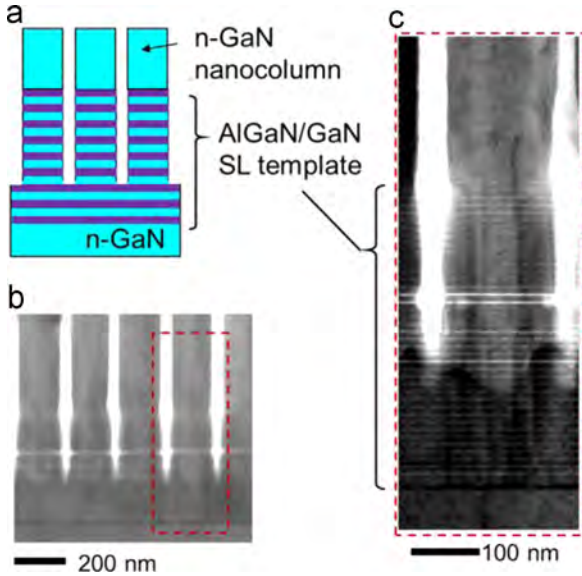
Fig. 5. n-Type GaN nanocolumns grown on AlGaN/GaN superlattice (SL) nanotemplate; (a) schematic diagram, (b) bright-field TEM image, and (c) magnified TEM image of rectangular region in (b) enclosed by dashed line.

nanotemplate SAG at $P_{Ga} = 3 \times 10^{-4}$ Pa, where the beam equivalent pressure of Al (P_{Al}) was controlled to 1×10^{-5}, 2.5×10^{-5}, 5×10^{-5}, and 1.5×10^{-4} Pa. The higher-temperature growth is expected to lead to AlGaN with higher crystal quality; in this study, AlGaN nanocolumns were grown at a temperature similar to that of GaN to control the Al composition of AlGaN by suppressing the excess evaporation of Ga induced at a higher temperature. But note that the growth temperature of AlGaN nanocolumns is higher than that of a standard film growth of AlGaN. Nitrogen was supplied through a nitrogen plasma cell with a flow rate of 1 sccm and a plasma input power of 450 W. Fig. 6 shows SEM and scanning ion microscope (SIM) images of the grown AlGaN nanocolumns. The lattice constant of the AlGaN nanocolumn array was 200 nm and that of the AlN nanocolumn array was 400 nm. The upper column shows SEM top-view images and the lower column shows bird's-eye-view SIM images. Nanocolumns were etched by FIB milling to reveal the vertical cross-sectional faces, whose SIM images were observed using the same FIB machine. The shapes of the nanocolumns were

observed to be hexagonal for all samples, and the boundaries between the AlGaN and the underlying GaN template were clearly distinguished in the SIM images, proving that the AlGaN nanocolumns were grown on the tops of the nanopillars.

The Al compositions (x_{Al}) of the grown AlGaN nanocolumns shown in Fig. 7 were evaluated by X-ray diffraction (XRD) measurement to be 0.13, 0.22, 0.43, and 1. x_{Al} increased linearly with increasing Al beam equivalent pressure ratio ($P_{Al}/(P_{Al}+P_{Ga})$) and reached unity at 0.333, as shown in Fig. 7, at which AlN nanocolumns with a periodic arrangement were grown (see the rightmost images in Fig. 6). The ratio between the fluxes of Al and Ga (J_{Al}/J_{Ga}) is calculated from P_{Al} and P_{Ga} as follows [19]:

$$\frac{J_{Al}}{J_{Ga}} = \frac{P_{Al}}{P_{Ga}} \times \frac{\eta_{Ga}}{\eta_{Al}} \left(\frac{T_{Al}M_{Ga}}{T_{Ga}M_{GAl}} \right)^{1/2} \tag{1}$$

where J_x is the flux of species x, η_x is its ionization efficiency, and T_x and M_x are the absolute temperature of the effusion cell and the molecular weight, respectively. Using Eq. (1) and the sticking coefficient of Ga (S_{Ga}) in the crystals, x_{Al} is expressed by

$$x_{Al} \sim \left[1 + S_{Ga} \cdot \frac{J_{Ga}}{J_{Al}} \right]^{-1} \tag{2}$$

where $S_{Al} \sim 1$ is assumed.

Fig. 8 shows the growth rate of AlGaN and the sticking coefficient of Ga calculated from Eq. (2) as a function of J_{Al}/J_{Ga}. The AlGaN nanocolumn arrays with a lattice constant of 400 nm were evaluated and the growth rate was found to increase monotonically with increasing Al flux. For a low J_{Al}/J_{Ga}, the sticking coefficient of Ga was nearly constant at $S_{Ga} \sim 0.6$. Owing to the smaller bonding energy between Ga and N, however, the sticking coefficient of Ga steadily decreased with increasing Al flux, as shown in Fig. 8. This phenomenon has also been reported for rf-MBE-grown AlGaN films [20], where the sticking coefficients of Al and Ga as a function of the arrival rate of group-III atoms were discussed for AlGaN films grown at 750 °C. Following the discussion in Ref. 20, under the nitrogen-rich growth conditions, all incident Al atoms were incorporated in the AlGaN film (i.e., $S_{Al} = 1$), while the sticking coefficient of Ga was constant ($S_{Ga} \sim 0.75$). However, under group-III-rich growth conditions, the Ga sticking coefficient deceased monotonically. The observed decrease in Ga sticking was explained as a result of the competition between Al and Ga to react
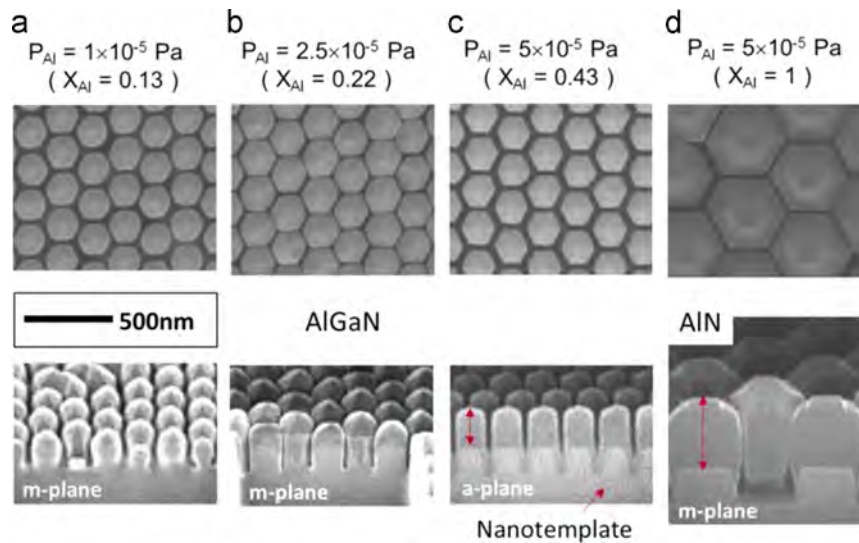
Fig. 6. SEM top-view (upper images) and SIM bird's-eye-view (lower images) images of the AlGaN nanocolumns with Al compositions from 0.13 to 1. The lattice constant of the AlGaN nanocolumns was 200 nm and that of the AlN nanocolumns was 400 nm. The cross-sectional SIM image for the $x_{Al} = 0.43$ sample shows the a-plane and the other images show the m-plane.
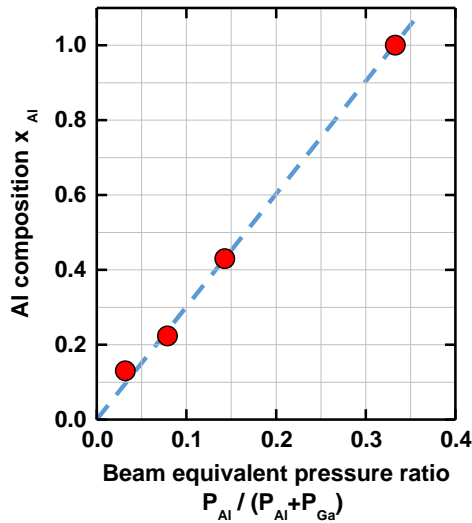
Fig. 7. Al composition (x_{Al}) of grown AlGaN as a function of the Al beam equivalent pressure ratio ($P_{Al}/(P_{Al} + P_{Ga})$).
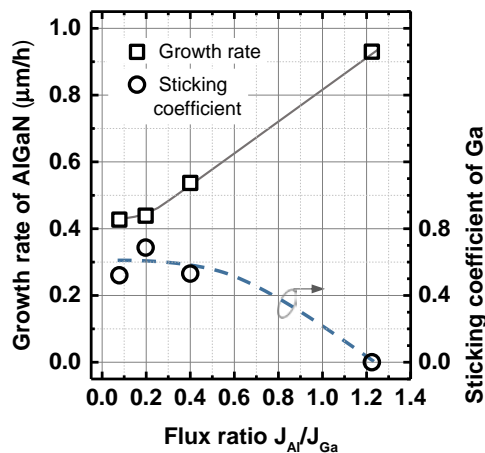
Fig. 8. Growth rate of AlGaN and sticking coefficient of Ga as functions of flux ratio J_{Al}/J_{Ga}. Squares and circles indicate the growth rate and sticking coefficient, respectively.

with the available active nitrogen. Thus, it is considered that a similar mechanism occurred in our experiment shown in Fig. 8.

5. Optical characteristics of AlGaN nanocolumns

Fig. 9(a) shows photoluminescence (PL) spectra of AlGaN nanocolumns measured at room temperature (RT) under excitation by an ArF excimer laser with a wavelength of 193 nm (pulse width: 4 ns and repetition rate: 25 Hz). Single-peak spectra of AlGaN were observed for all samples and the PL peak wavelength is plotted as a function of x_{Al} in Fig. 8(b). The solid line indicates the calculated bandgap wavelength using the bandgaps of AlN (6.015 eV) [21] and GaN (3.39 eV) [22] and a bowing parameter of 0.98 eV [23]; the experimental bandgaps were close to the calculated values. The PL peak wavelength of the AlN nanocolumns was 212 nm.

However, the excitation spot, whose size was approximately 100 μm, included an area outside the nanocolumns, and AlGaN with a slightly different Al composition was considered to be grown in the gap region. To evaluate the Al composition inside the nanocolumns, therefore, cathodoluminescence (CL) measurement was performed, where the center region of a nanocolumn was excited with an incident single spot electron beam whose diameter was less than ~100 nm. The single-point CL spectra of AlN and AlGaN ($x_{Al} = 0.43$) are shown in Fig. 10. The insets are monochromatic CL intensity mapping images of AlN and AlGaN evaluated at each emission peak wavelength, while scanning the electron beam over the whole area of the samples. As the excitation conditions, the acceleration voltage and emission current were 5 kV and 10 pA, respectively. In the images, hexagonally shaped nanocolumns appeared with homogeneous CL emission distributions inside the nanocolumn regions. Note that we did not observe specific dark regions in the crystals, which are usually produced by crystal dislocations. The single-peak CL emissions for AlN and AlGaN nanocolumns occurred at peak wavelengths of 209 and 290 nm, respectively. The CL peak wavelength of AlGaN with $x_{Al} = 0.43$ was identical to the calculated bandgap wavelength (see Fig. 8(b)). At the same time, the emission wavelengths of the freestanding bulk and homoepitaxial AlN crystals were 208 nm [21] and 207.8 nm [24], respectively, which are close to the CL peak wavelength of AlN nanocolumns.
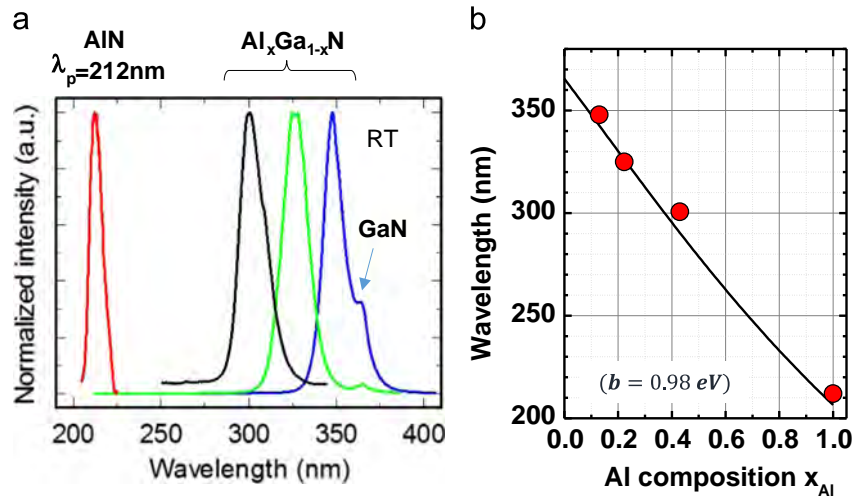
Fig. 9. (a) RT-PL spectra of AlGaN nanocolumns with x_{Al} of 0.13, 0.22, 0.43, and 1, and (b) peak wavelength of AlGaN as a function of Al composition. The solid line indicates the bandgap wavelength, calculated as $E_g = 6.015x + 0.339(1-x) - 0.98x(1-x)$.
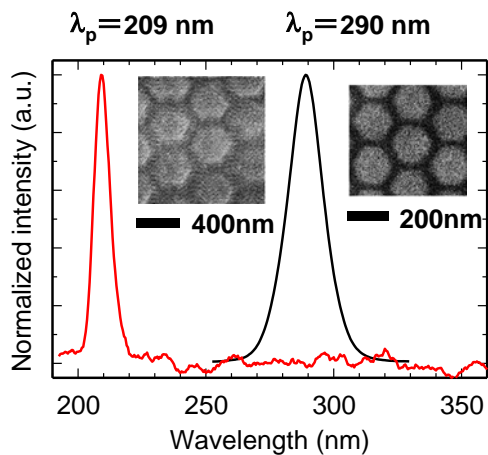
Fig. 10. Single-point CL spectra of $Al_{43}Ga_{57}N$, and AlN, when the center region of a nanocolumn was excited with an incident single spot electron beam. The inset images are the monolithic CL intensity mapping images taken at each CL peak wavelength while scanning the electron beam over the whole sample area.

6. Conclusion

The aim of this study was to develop an rf-MBE-based method for the SAG of AlGaN-based nanocolumns. We have demonstrated a novel SAG method based on nanotemplates consisting of a triangular lattice of nanopillars. Well-controlled SAG of GaN nanocolumns was obtained when the gap width between adjacent nanopillars was less than approximately 45 nm. Using this SAG technology, the successful SAG of AlGaN nanocolumn arrays was observed for Al compositions of 0.13, 0.22, 0.43, and 1. We observed single-peak photoluminescence (PL) spectra of AlGaN, the peak wavelengths of which were close to the calculated bandgap wavelengths using the bandgaps of AlN (6.015 eV) and GaN (3.39 eV) and a bowing parameter of 0.98 eV.

In this study, it was clarified that the beam shadowing effect, which was induced in the high-density nanopillar arrays with small gaps, had as a key role in accomplishing the SAG. During the growth of AlGaN on the nanotemplates, Al and Ga beams were supplied to the concavo-convex surfaces of the nanopillars.

However, the sidewalls and gap regions of the nanopillar structure were shielded from the beam by the neighboring nanopillars, resulting in preferential growth on the tops of the nanostructures.

References

[1] M. Yoshizawa, A. Kikuchi, M. Mori, N. Fujita, K. Kishino, Jpn. J. Appl. Phys. 36 (1997) L459.
[2] M. Yoshizawa, A. Kikuchi, N. Fujita, K. Kushi, H. Sasamoto, K. Kishino, J. Cryst. Growth 189/190 (1998) 138.
[3] S. Li, A. Waag, J. Appl. Phys. 111 (2012) 071101.
[4] W. Han, S. Fan, Q. Li, Y. Hu, Science 277 (1997) 1287.
[5] M.A. Sanchez-Garcia, E. Calleja, E. Monroy, F.J. Sanchez, F. Calle, E. Muñoz, R. Beresford, J. Cryst. Growth 183 (1998) 23.
[6] K. Kishino, A. Kikuchi, H. Sekiguchi, S. Ishizawa, Proc. SPIE 6473 (2007) 64730T.
[7] K. Kishino, K. Yamano, IEEE J. Quantum Electron. 50 (2014) 538.
[8] T. Kouno, K. Kishino, K. Yamano, A. Kikuchi, Opt. Express 17 (2009) 20440.
[9] S. Ishizawa, K. Kishino, R. Araki, A. Kikuchi, S. Sugimoto, Appl. Phys. Express 4 (2011) 055001.
[10] S.D. Hersee, X. Sun, X. Wang, Nano Lett. 6 (2006) 1808.
[11] H. Sekiguchi, K. Kishino, A. Kikuchi, Appl. Phys. Express 1 (2008) 124002.
[12] K. Kishino, H. Sekiguchi, A. Kikuchi, J. Cryst. Growth 311 (2009) 2063.
[13] K.A. Bertness, A.W. Sanders, D.M. Rourke, T.E. Harvey, A. Roshko, J.B. Schlager, N.A. Sanford, Adv. Funct. Mater. 20 (2010) 2911.
[14] T. Gotschke, T. Schumann, F. Limbach, T. Stoica, R. Calarco, Appl. Phys. Lett. 98 (2011) 103102.
[15] S. Albert, A. Bengoechea-Encabo, M.A. Sánchez-García, X. Kong, A. Trampert, E. Calleja, Nanotechnology 24 (2013) 175303.
[16] H. Sekiguchi, K. Kishino, A. Kikuchi, Appl. Phys. Lett. 96 (2010) 231104.
[17] K. Kishino, K. Nagashima, K. Yamano, Appl. Phys. Express 6 (2013) 012101.
[18] R. Vadivelu, Y. Igawa, K. Kishino, Jpn. J. Appl. Phys. 52 (2013) 08JE18.
[19] E.H.C. Parker, The Technology and Physics of Molecular Beam Epitaxy, Plenum Press, New York, ISBN 0-306-41860-6, 1985.
[20] E. Iliopoulos, T.D. Moustakas, Appl. Phys. Lett. 81 (2002) 295.
[21] M. Feneberg, R.A.R. Leute, B. Neuschl, K. Thonke, M. Bickermann, Phys. Rev. B 82 (2010) 075208.
[22] H.P. Maruska, J.J. Tietjen, Appl. Phys. Lett. 15 (1969) 327.
[23] M.R.H. Khan, Y. Koide, H. Itoh, N. Sawaki, I. Akasaki, Solid State Commun. 60 (1986) 509.
[24] M. Funato, K. Matsuda, R.B. Banal, R. Ishii, Y. Kawakami, Appl. Phys. Express 5 (2012) 082001.
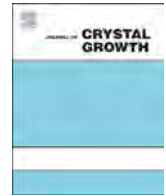
InGaP/GaAs/InGaAsP triple junction solar cells grown using solid-source molecular beam epitaxy

T. Sugaya [a,*], K. Makita [a], H. Mizuno [a], T. Mochizuki [b], R. Oshima [a], K. Matsubara [a], Y. Okano [b], S. Niki [a]

[a] National Institute of Advanced Industrial Science and Technology (AIST), Tsukuba, Ibaraki 305-8568, Japan
[b] Tokyo City University, Setagaya, Tokyo 158-8557, Japan

ARTICLE INFO

ABSTRACT

We report mechanically stacked InGaP (1.9 eV)/GaAs (1.42 eV)/InGaAsP (1.0 eV) triple junction solar cells fabricated with an advanced bonding technique using Pd nanoparticle arrays. High quality InGaP/GaAs tandem top and InGaAsP bottom cells are grown on GaAs and InP substrates, respectively using solid-source molecular beam epitaxy (MBE). The InGaAsP bottom cell has an open circuit voltage (V_{oc}) of 0.49 V, which indicates that high performance InGaAsP solar cells can be fabricated using solid-source MBE. A fabricated triple junction solar cell has a high efficiency of 25.6% with a high V_{oc} of 2.66 V.

© 2015 Elsevier B.V. All rights reserved.

1. Introduction

Multijunction solar cells have been studied to realize solar cells with ultra-high efficiency. InGaP/GaAs/Ge triple junction solar cells have been commercialized for space applications. There are two methods of fabricating multijunction solar cells. One is a monolithic epitaxial growth technique on GaAs or Ge substrates. InGaP/GaAs/InGaAs triple-junction solar cells grown monolithically on GaAs substrates have high efficiencies of 37.7% and 44.4% under AM1.5 and concentrator conditions, respectively [1]. This triple-junction solar cell utilizes metamorphic buffer growth, which is a very difficult technique that limits the choice of materials and cell combinations. Another method for fabricating multijunction solar cells is a semiconductor direct bonding technique applied to two different substrates [2–4]. 4- and 5-junction solar cells have been realized by using a technique for directly bonding GaAs and InP wafers, that makes it possible to connect GaAs-based 2- and 3-junction and InP-based 2-junction solar cells. 4- and 5-junction solar cells have the highest reported efficiencies of 44.7% and 38.8% under concentrator [5] and AM1.5 [6] conditions, respectively. The above multijunction structures are grown by metal organic chemical vapor deposition (MOCVD) because they require materials that include phosphorus such as InGaP and InGaAsP. Solid-source molecular beam epitaxy (MBE) has the potential to grow high quality phosphorus based materials, because it proceeds under ultra-high vacuum conditions

and uses ultra-high purity metal sources. These metal sources are far cheaper than the gas sources used in MOCVD. However, we require thick InGaP-based epitaxial layers for solar cell applications to obtain sufficient light absorption, and so we need a large-scale phosphorus source that is pyrophoric when venting or performing maintenance on an MBE chamber. Moreover, InGaAsP is very difficult to grow using solid-source MBE because we need precise control of the beam fluxes of two kinds of group-V atoms, for example As and P. Therefore, there have been a few reports on InGaP and InGaAsP solar cells and multijunction solar cells fabricated using solid-source MBE. Although InGaP/GaAs tandem solar cells have been fabricated using gas-source MBE, expensive gas sources are needed [7]. Recently, InGaP/GaAs/GaInNAsSb multijunction solar cells with a high efficiency of 44% and grown using MBE have been achieved under concentrator conditions [8]. However, the growth technique and procedure have not been described in detail.

In our earlier work, we reported a technique for growing InGaP material [9–12] and InGaP/GaAs tandem solar cells [13] using solid-source MBE. We have also proposed a new semiconductor bonding technology for mechanically stacked multi-junction solar cells by using conductive nanoparticle alignment [14]. This technique is very attractive for interconnecting different kinds of solar cells [15]. In this paper, we detail the optimal growth conditions for InGaAsP epitaxial films on (100) InP and describe the characteristics of InGaAsP solar cells fabricated using solid-source MBE. Moreover, we report mechanically stacked InGaP (1.90 eV) /GaAs (1.42 eV) /InGaAsP (1.0 eV) triple junction solar cells. GaAs-based InGaP/GaAs top and InP-based InGaAsP bottom cells grown by solid-source MBE are mechanically stacked for the first time.

---

* Corresponding author. Tel.: +81 29 861 5466; fax: +81 29 861 5615.
E-mail address: t.sugaya@aist.go.jp (T. Sugaya).

2. Experiments

We grew $In_{0.775}Ga_{0.225}As_{0.489}P_{0.511}$ layers with an energy gap of 1.0 eV on InP (100) substrates at growth rates of 1.0 μm/h. A 400 nm InP buffer layer was grown at 450 °C prior to the $In_{0.775}Ga_{0.225}As_{0.489}P_{0.511}$ layer growth. The growth temperature of the $In_{0.775}Ga_{0.225}As_{0.489}P_{0.511}$ layer was varied from 380 to 420 °C. The In and Ga fluxes were constant at 1.0×10^{-6} and 1.7×10^{-7} Torr, respectively. The As_2 and P_2 fluxes were generated by using arsenic and phosphorus valved cracker cells, respectively. We used red phosphorus and arsenic ingots as solid sources. The P_4 molecules were cracked into P_2 at 825 °C, and the As_4 molecules were cracked into As_2 at 950 °C. The As_2 pressures were varied from 0.9×10^{-6} to 1.2×10^{-6} Torr under a constant P_2/As_2 flux ratio, during the InGaAsP growth. The As_2 and P_2 beam intensities were controlled by the aperture size of the valved cracker outlet. Photoluminescence (PL) measurement was performed to study the optical properties of the InGaAsP films.

For solar cell applications, InGaAsP p–n junctions were grown on a p^+-InP (100) substrate. The sample structures are shown in detail in Fig. 1. The growth temperature and the growth rate were 400 °C and 1 μm/h, respectively. The p-InGaAsP layer thickness was 2 μm and an n^+-InP window layer was grown. The n^+-InGaAs was grown on the InP window as an electrode contact layer. After the growth, the front electrode was formed using photolithography and a lift-off technique. AuGe/Ni/Au and Ti/Au were used for the front and back electrodes, respectively. The n^+-InGaAs contact layer was removed by chemical etching using the front electrode as an etching mask. Anti-reflection coating (ARC) was not employed.

Triple junction solar cells were fabricated using an advanced bonding technique [14]. InGaP/GaAs tandem top cells were grown [13] and separated from the GaAs substrates by using a selective etching method called the epitaxial lift-off technique. The InGaP/GaAs top cells were connected to the InGaAsP bottom cells on the InP substrates through Pd nanoparticle arrays as shown in Fig. 2. We employed a moth-eye-type low-reflection film as an ARC for a triple junction solar cell. A conductive Pd nanoparticle alignment was formed on the InGaAsP bottom cell by using a self-assembled block copolymer (polystyrene-block-poly-2-vinylpyridine). The optical absorption loss at the interface was very small because of the extremely small nanoparticle thickness (~ 10 nm) and low surface coverage ($< 12\%$). Therefore, both a low bonding resistance ($< 1 \ \Omega \ cm^2$) and a low interfacial optical loss ($< 2\%$) were possible.

The performances of the InGaAsP and the triple junction solar cells were measured under standard conditions of AM1.5 G,
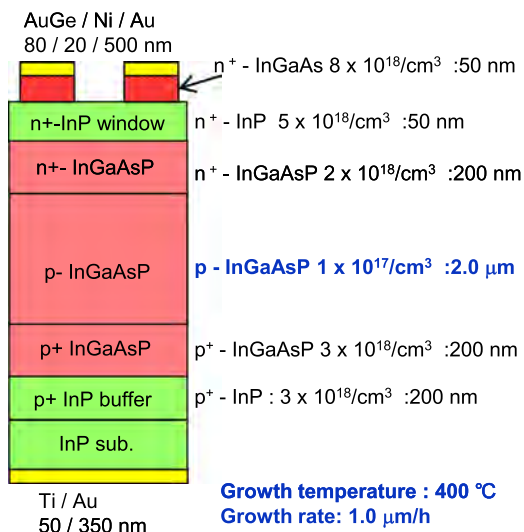
Fig. 1. Schematic layer structure of an InGaAsP solar cell grown on an p^+-InP (001) substrate.
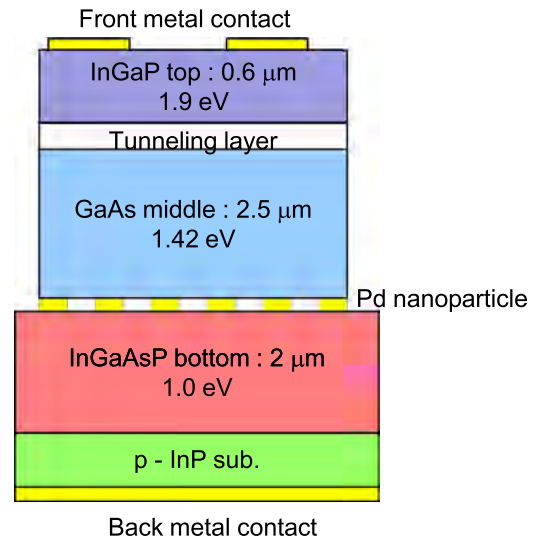
Fig. 2. Schematic layer structure of an InGaP/GaAs/InGaAsP triple junction solar cell fabricated using Pd nanoparticle arrays.
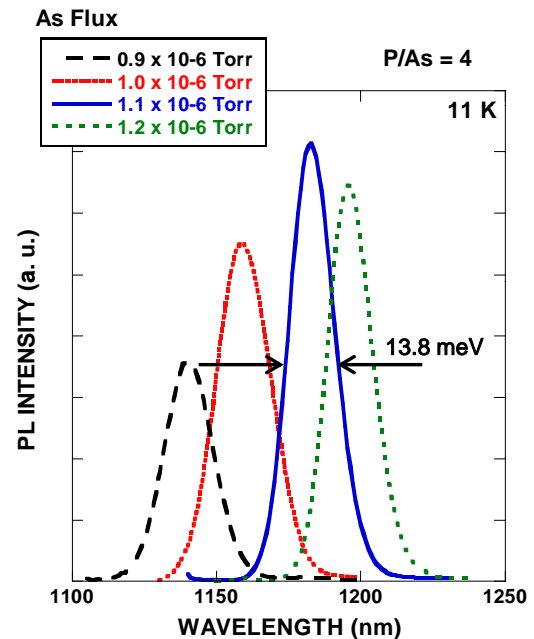
Fig. 3. PL spectra of 500 nm-thick InGaAsP epitaxial films measured at 11 K. The As_2 pressures were varied from 0.9×10^{-6} to 1.2×10^{-6} Torr under a constant P/As_2 flux ratio of 4.

100 mW/cm², and 25 °C. The external quantum efficiency (EQE) of the solar cells was measured directly under a constant photon irradiation of $10^{14}/cm^2$.

3. Results and discussion

Fig. 3 shows the PL spectra of 500 nm-thick InGaAsP epitaxial films measured at 11 K. The growth temperature and growth rate of the InGaAsP layers were 400 °C and 1.0 μm/h, respectively. The As_2 pressures were varied from 0.9×10^{-6} to 1.2×10^{-6} Torr under a constant P_2/As_2 flux ratio of 4. Each InGaAsP peak has a narrow PL peak with a full-width at half-maximum of ~ 14 meV, which indicates the growth of high quality InGaAsP films. However, the PL peak wavelengths are very sensitive to changes in the As_2 pressure and we need precise control of the group-V fluxes to obtain high quality InGaAsP films using solid-source MBE. The PL wavelength of
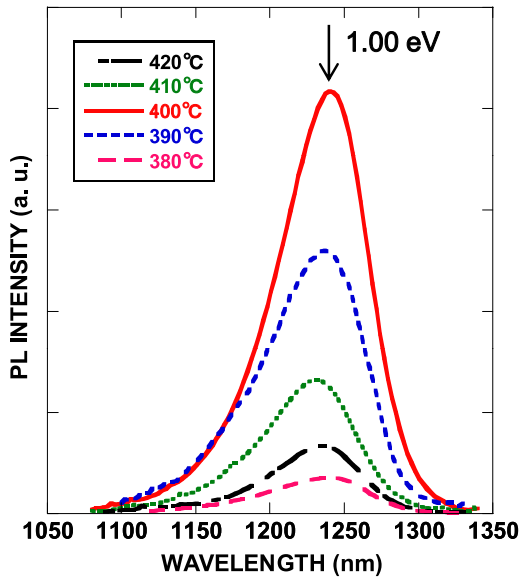
Fig. 4. PL spectra of InGaAsP epitaxial layers with a growth thickness of 500 nm measured at room temperature. The growth temperature was varied from 380 to 420 °C.
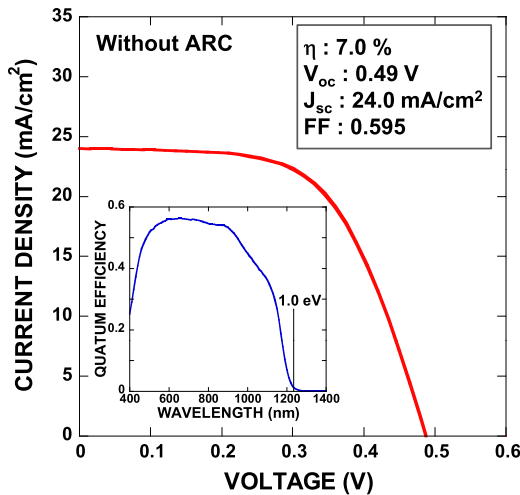
Fig. 5. *I–V* curve of an InGaAsP solar cell grown at 400 °C with the inset showing its EQE spectrum.

InGaAsP films at room temperature corresponded to 1.03, 1.01, 0.99 and 0.98 eV for As$_2$ fluxes of 0.9×10^{-6}, 1.0×10^{-6}, 1.1×10^{-6} and 1.2×10^{-6} Torr, respectively, during growth. To grow InGaAsP films with a 1.0 eV emission at room temperature, we employed P$_2$ and As fluxes of 3.7×10^{-6} and 1.0×10^{-6} Torr, respectively.

Fig. 4 shows the PL spectra of 500 nm-thick InGaAsP epitaxial films measured at room temperature. The growth temperature of the InGaAsP layers was varied from 380 to 420 °C. The P and As fluxes were 3.7×10^{-6} and 1.0×10^{-6} Torr, respectively. The InGaAsP layer grown at 400 °C had a stronger and narrower PL peak. The PL peak energy was 1.00 eV, which corresponds to the In$_{0.775}$Ga$_{0.225}$As$_{0.489}$P$_{0.511}$ bulk transition lattice-matched to the InP substrates. The slight deviation of PL peak of the InGaAsP layer was due to fluctuations in the P and As fluxes. High quality InGaAsP films lattice-matched to InP can be grown by precisely controlling the group-V fluxes using solid-source MBE.

Fig. 5 shows the *I–V* curves of an InGaAsP solar cell grown at 400 °C with the inset indicating its EQE spectrum. The EQE spectrum reveals the fabrication of an InGaAsP solar cell with an energy gap of 1.0 eV. The InGaAsP solar cell has a high open circuit
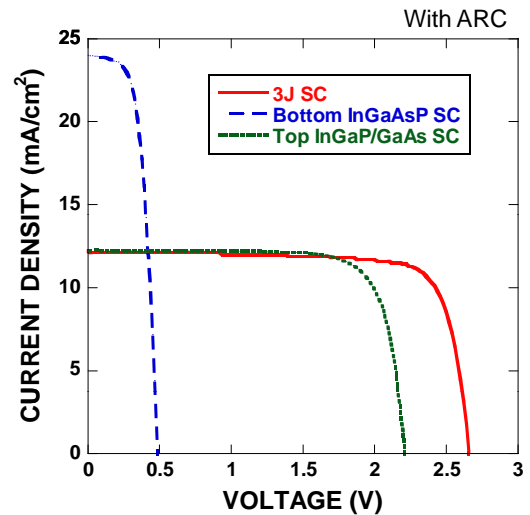
Fig. 6. *I–V* characteristics of a triple junction solar cell with its top tandem and bottom cells.

Table 1
The device parameters of a triple junction solar cell with its bottom and top cells.

	I_{sc} (mA/cm^2)	V_{oc} (V)	F.F.	η (%)
3J SC	12.1	**2.66**	0.791	**25.6**
Bottom	24.0	0.49	0.595	7.0
Top cell	12.1	2.20	0.794	21.1

voltage of 0.49 V with a conversion efficiency of 7.0% without ARC, which indicates that high quality InGaAsP solar cells can be fabricated by using solid-source MBE.

An InGaP/GaAs tandem top cell is connected to the above-mentioned InGaAsP bottom cell by using an advanced bonding technique with Pd nanoparticle arrays. Fig. 6 shows the *I–V* characteristics of the fabricated triple junction solar cell with the top tandem and bottom cells, recorded under AM1.5 solar spectrum illumination. The device parameters of each cell are also summarized in Table 1. The excellent V_{oc} of 2.66 V is nearly equal of the sum of those of the top and bottom cells. A high conversion efficiency of 25.6% and a high fill factor of 0.791 are observed with the triple junction cell. These results indicate the possibility of achieving high-efficiency multijunction solar cells grown by solid-source MBE. Moreover, these results suggest that our bonding method is highly useful for heterogeneous cell combinations of multijunction solar cells.

4. Conclusion

In conclusion, we have detailed the solid-source MBE growth conditions for realizing high quality InGaAsP epitaxial films. The photoluminescence measurements indicate that the InGaAsP composition is very sensitive to changes in the As$_2$ pressure. We need precise control of the group-V fluxes to obtain high quality InGaAsP films. A growth temperature of 400 °C is suitable for high quality InGaAsP epitaxial growth. The InGaAsP bottom cell has an efficiency of 7.0% with a high V_{oc} of 0.49 V. The InGaAsP solar cell is used as the bottom cell of InGaP/GaAs/InGaAsP triple junction solar cells fabricated using Pd nanoparticle arrays. A fabricated triple junction solar cell has a high efficiency of 25.6% with a high V_{oc} of 2.66 V, which indicates that solid-source MBE offers the possibility of

growing high quality multijunction solar cells that include phosphorus based materials such as InGaP and InGaAsP.

Acknowledgment

References

[1] T. Takamoto, H. Washino, H. Juso, Proceedings of the 40th IEEE Photovoltaic Specialists Conference, 2014, pp. 1.
[2] J.M. Zahler, K. Tanabe, C. Ladous, T. Pinnington, F.D. Newman, H.A. Atwater, Appl. Phys. Lett. 91 (2007) 012108.
[3] M.J. Archer, D.C. Law, S. Mesropian, M. Haddad, C.M. Fetzer, A.C. Ackerman, C. Ladous, R.R. King, H.A. Atwater, Appl. Phys. Lett. 92 (2008) 103503.
[4] J. Boisvert, D. Law, R. King, D. Bhusari, X. Liu, A. Zakaria, W. Hong, S. Mesropian, D. Larrabee, R. Woo, A. Boca, K. Edmondson, D. Krut, D. Peterson, K. Rouhani, B. Benedikt, and N.H. Karam, Proceedings of the 35th IEEE Photovoltaic Specialists Conference, 2010, pp. 123.
[5] F. Dimroth, M. Grave, P. Beutel, U. Fiedeler, C. Karcher, T.N.D. Tibbits, E. Oliva, G. Siefer, M. Schachtner, A. Wekkeli, A.W. Bett, R. Krause, M. Piccin, N. Blanc, C. Drazek, E. Guiot, B. Ghyselen, T. Salvetat, A. Tauzin, T. Signamarcheix, A. Dobrich, T. Hannappel, K. Schwarzburg, Prog. Photovolt. 22 (2014) 277.
[6] P. Chiu, D. Law, R. Woo, S.B. Singer, D. Bhusari, W. Hong, A. Zakaria, J.C. Boisvert, S. Mesropian, R.R. King, and N.H. Karam, Proceedings of the 40th IEEE Photovoltaic Specialists Conference, 2014, pp. 11.
[7] J. Haapamaa, M. Pessa, G. La Roche, Sol. Energy Mater. Sol. Cells 66 (2001) 573.
[8] H. Yuen, V. Sabnis, and M. Wiemer, Proceedings of the 40th International Symposium on Compound Semiconductors, 2013, TuA2-1.
[9] T. Sugaya, A. Takeda, R. Oshima, K. Matsubara, S. Niki, Y. Okano, J. Cryst. Growth 378 (2013) 576.
[10] T. Sugaya, R. Oshima, K. Matsubara, S. Niki, J. Cryst. Growth 378 (2013) 430.
[11] T. Sugaya, R. Oshima, K. Matsubara, S. Niki, J. Appl. Phys. 114 (2013) 014303.
[12] T. Sugaya, A. Takeda, R. Oshima, K. Matsubara, S. Niki, Y. Okano, Appl. Phys. Lett. 101 (2012) 133110.
[13] T. Sugaya, K. Makita, A. Takeda, R. Oshima, K. Matsubara, Y. Okano, S. Niki, Jpn. J. Appl. Phys. 53 (2014) 05FV06.
[14] H. Mizuno, K. Makita, K. Matsubara, Appl. Phys. Lett. 101 (2012) 191111.
[15] K. Makita, H. Komaki, H. Mizuno, H. Sai, T. Sugaya, R. Oshima, H. Shibata, K. Matsubara, and S. Niki, Proceedings of the 28th European Photovoltaic Solar Energy Conferenceand Exhibition, 2013, pp. 2279.
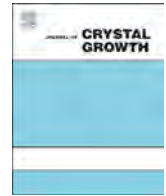
Recombination current in AlGaAs/GaAs superlattice solar-cells grown by molecular beam epitaxy

CrossMark

A. Kawaharazuka [a,b,c,*], J. Nishinaga [a,b,c], Y. Horikoshi [a,b,c]

[a] Kagami Memorial Laboratory for Materials Science and Technology, Waseda University, 2-8-26 Nishi-Waseda, Shinjuku, Tokyo 169-0051, Japan
[b] Faculty of Science and Engineering, Waseda University, 3-4-1 Okubo, Shinjuku, Tokyo 169-8555, Japan
[c] CREST, Japan Science and Technology Agency, Kawaguchi Center Building, 4-1-8 Honcho, Kawaguchi, Saitama 332-0012, Japan

ARTICLE INFO

ABSTRACT

We investigate the effect of the recombination current of p–i–n junction solar-cells. We develop a simple evaluation method of the recombination and diffusion current component of the solar-cells based on the measured three characteristic values: short circuit current, open circuit voltage, and fill factor without the knowledge in the details of the device structure. The advantage of the developed technique is its simplicity and wide applicability to various p–i–n junction solar-cells. We apply the method to GaAs bulk and AlGaAs/GaAs superlattice solar-cells. Obtained parameters well reproduce the whole current-voltage characteristics. The diode current is almost dominated by the recombination current at the maximum-output voltage for both GaAs bulk and superlattice cells. The higher contribution of the recombination current in the superlattice solar-cell is due to the quality of the AlGaAs barriers and the AlGaAs/GaAs interfaces. This result indicates that the good crystalline quality is important to enhance the efficiency of the solar-cells.

© 2015 Elsevier B.V. All rights reserved.

1. Introduction

Recently, needs for solar-cells are more and more increasing [1–3]. High absorbance is one of the key issues to enhance the efficiency especially for thin film sorlar-cells [4]. Superlattices (SLs) are attractive materials for the active layer of such thin film solar-cells because of their higher photo-absorbance due to the quantum confinement and excitonic enhancement effect [5–8]. In addition to the good optical properties, transport characteristics are also important for the high device performance. The recombination current due to deep trapping centers [9,10] is one of the critical factors, which degrade the efficiency [11], since p–i–n junction solar-cells have wide depletion layer and are operated at low injection condition as diodes. It is less significant for light emitting devices such as light emitting diodes and laser diodes because these devices are usually operated at high injection conditions. The diffusion current overcomes the recombination current and becomes dominant component at higher bias voltages. Compared with the ideal case, in which the current is determined by diffusion process, the recombination component decreases the fill factor due to the slow increase with the bias. Its mid-gap nature prevents the photon recycling process. Furthermore, temperature stability is lower because of the $2kT$ factor. The origin of the recombination centers is defects formed during the crystal growth

and device processing. It directly reflects the crystalline quality and interface imperfection. The effect is more important for SL solar-cells, which contain AlGaAs alloy and AlGaAs/GaAs hetero-interfaces in the active layer. Therefore, an evaluation method of the recombination current applicable to the actual solar-cells are desirable for possible feed-back to the fabrication processes.

In this paper, we discuss the recombination current of the p–i–n junction solar-cells. We have developed a simple method to obtain the recombination component of the fabricated devices based on the measured current-voltage (I–V) characteristic of the solar-cells. Our approach is to separate the diffusion and the recombination current components from measured solar-cell characteristic values: short circuit current density J_{sc}, open circuit voltage V_{oc}, and fill factor FF. These three values are the most important properties directly extracted from the I–V measurement. Since these values are reported in the literatures together with the efficiency [12], our method is widely applicable to various solar-cells without knowing the precise device structure. After the theoretical formulation in Section 2 and experimental procedure in Section 3, we discuss the analyses on the p–i–n junction solar-cells consisting of GaAs bulk and AlGaAs/GaAs SL active layers grown by molecular beam epitaxy (MBE) in Section 4.

2. Theoretical

The equivalent circuit [13] of the solar-cell taking the diffusion ($n=1$) and recombination ($n=2$) current into account is depicted in Fig. 1(a). Diffusion (D_1) and recombination (D_2) current components

a

b
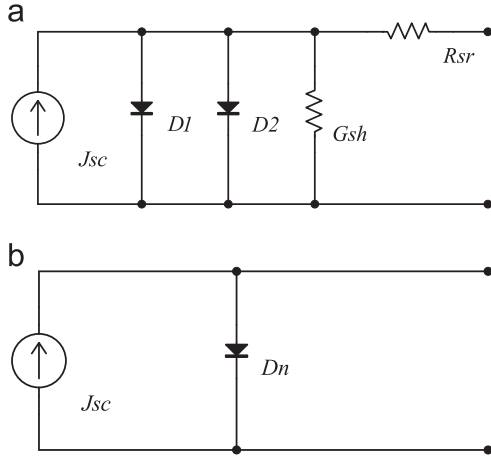
Fig. 1. Equivalent circuit of the p–i–n junction solar-cell in (a) diffusion-recombination model and (b) ideality factor model.

are separately described as diodes connected parallel to the current source, which represents the photo-generated current under illumination. Shunt conductance and series resistance are expressed by G_{sh} and R_{sr}, respectively. To simplify the model and reducing the parameters, we assume that the shunt conductance and series resistance are negligibly small. The assumption is reasonable since the shunt current is much lower than the photo-generated current and the voltage drop due to the series resistance becomes prominent in much higher injection conditions. In this case, the solar-cell current density is expressed as

$$J(V) = t_s J_{Sun}(E > E_g) - J_1(e^{qV/kT} - 1) - J_2(e^{qV/2kT} - 1), \qquad (1)$$

where t_s is the absorbance of the illumination light (here including the reflection loss). J_{Sun} is the integrated incident photon flux above the bandgap converted to current density by multiplying by elementary charge. J_1 and J_2 are the reverse saturation current density of the diffusion and recombination component, respectively. Other symbols have their usual meanings. The bandgap E_g of the active layer is required to define J_{Sun}. Since the bandgap depends on the material and the structure as well in superlattices, direct measurement or numerical estimation is necessary. However, J_{Sun} is used only to find t_s from J_{sc} according to the relation

$$J_{sc} = J(0) = t_s J_{Sun}(E > E_g). \qquad (2)$$

When t_s is out of interest and J_{sc} is left as a resulting parameter, preliminary device informations are not required. The parameters J_1 and J_2 can be solely determined by characteristic values obtained from the I–V measurement. The advantage of our method is its simplicity that enables the wide range of application. Simulations often require the precise parameters, which specify the physical properties of the materials and device structures. Some of them are very difficult to estimate directly from the measurement on the actual solar-cell devices although they strongly depend on the crystal growth and device processing. On the other hand, three parameters, t_s, J_1, and J_2 are solely determined from measured J_{sc}, V_{oc}, and FF, in our approach.

Another model with ideality factor n is often used for evaluating the cell performance. From the point of view of the circuit, this is equivalent to replace four components D_1, D_2, G_{sh}, and R_{sr} with one ideal diode D_n parameterized by J_n and n, as shown in Fig. 1(b). The current density is expressed as

$$J(V) = t_s J_{Sun}(E > E_g) - J_n(e^{qV/nkT} - 1). \qquad (3)$$

This simplification is useful because the diode operation is described with single exponential term. Accordingly, the efficiency and the other characteristic values can be analytically obtained in

closed form by using Lambert W function. However, it should be noted that the parameters J_n and n are phenomenological and have no physical interpretation. There are no simple relations between parameters used in two models.

We employ a fitting technique to determine the parameters of both models from the measured characteristics values. Actually, this is equivalent to parameter transformation by numerically solving the non-linear simultaneous equations because the number of both input and output parameters are the same. We use the standard solar spectral irradiance (air mass 1.5 global tilt) based on the observation [14].

3. Experimental

The solar-cell structures are grown by MBE. They are based on the AlGaAs/GaAs p–i–n diode with a SL or GaAs bulk active layer. On the n-type GaAs(001) substrate, 1 µm of Si-doped n-type GaAs layer, 2-µm-thick undoped SL or GaAs active layer followed by 10-nm-thick Be doped p-type $Al_{0.5}Ga_{0.5}As$ window, and 5-nm-thick p-type GaAs cap are sequentially grown to fabricate p–i–n diode structure. The unit structure of the SL is 2-nm-thick $Al_{0.5}Ga_{0.5}As$ barrier and 5-nm-thick GaAs well. The doping concentration of Si is 1×10^{18} cm^{-3} and the concentration of Be is 1×10^{18} cm^{-3} for $Al_{0.5}Ga_{0.5}As$ and 2×10^{18} cm^{-3} for GaAs. We employ 10-nm-thick window to avoid the possible absorption loss. Au–Ge–Ni and Au–Zn are evaporated on back- and top-side of the sample respectively and annealed to form ohmic electrodes for electric measurements. For the details of the growth and device structures, refer to Ref. [8]. We measure I–V characteristics at room temperature under Air-Mass 1.5, 100 mW/cm^2 (one-sun) illumination.

4. Results and discussion

We evaluate the device with the GaAs bulk active layer. The measured J–V characteristic is shown in Fig. 2. Experimentally obtained characteristic values are $J_{sc} = 26.81$ mA/cm^{-2}, $V_{oc} = 0.993$ V and FF=83.12%. The resulting efficiency is 22.13%. We assume the bandgap of GaAs at room temperature as 1.423 eV [15]. First we analyze the cell properties by using the diffusion-recombination model. Obtained parameters of $t_s = 84\%$, $J_1 = 2.1 \times 10^{-16}$ mA/cm^2 and $J_2 = 5.6 \times 10^{-8}$ mA/cm^2 well reproduce the whole J–V curve, without taking G_{sh} and R_{sr} into account, as shown in Fig. 2(a). The saturation current density of the diffusion component J_1 is within reasonable range expected from the device structure. Therefore, we consider the recombination component J_2 is reliable. We separately plot the diffusion and recombination components by using the obtained parameters. It is clearly seen that the current is dominated by the recombination component especially in the low bias region, where the reverse injection current of the diode is much lower than the short circuit current, as shown in Fig. 3. The ratio of the recombination component is as high as 92% at the bias for maximum output power ($V_{max} = 0.870$ V). Contribution from the diffusion component increases with increasing the bias voltage due to the steeper exponential characteristic. Even at the open circuit voltage, however, the diffusion current is only 48%. Around the favorable operating points, the recombination current determines the solar-cell performance. This result clearly reveals that the reduction of the recombination process in the active layer is important for high efficiency. Since the thickness of the active layer is mainly determined by the optical characteristics to fully absorb the incident light, it is necessary to reduce the recombination rate by reducing the defect density. High crystalline quality based on the growth is essential for the higher solar-cell performance. Next, we apply the ideality factor model to the same experimental data. The whole curve is well

Fig. 2. Mesured (open circle) *J–V* characteristic of the GaAs bulk solar-cell is plotted with fitted curve (solid line) obtained by (a) diffusion-recombination and (b) ideality factor models.
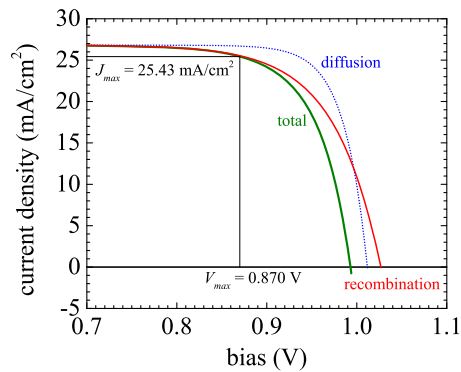
Fig. 3. Recombination (thin solid line) and diffusion (thin dotted line) components of the current of the GaAs bulk solar-cell are plotted with total (thick solid line) current.

Fig. 4. Measured (open circle) *J–V* characteristic of the AlGaAs/GaAs SL solar-cell is plotted with fitted curve (solid line) obtained by (a) diffusion-recombination and (b) ideality factor models.
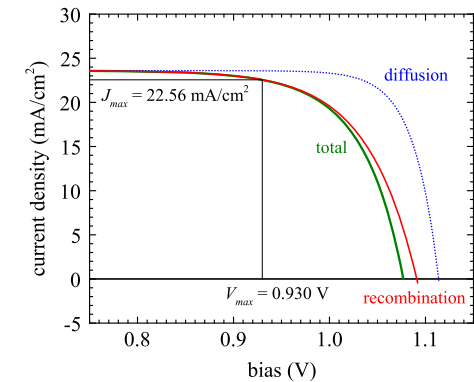
Fig. 5. Recombination (thin solid line) and diffusion (thin dotted line) components of the current of the AlGaAs/GaAs SL solar-cell are plotted with total (thick solid line) current.

reproduced by J_n of 1.1×10^{-9} mA/cm^2 and n of 1.6. The result is shown in Fig. 2(b). There is no significant difference between two theoretical curves. However, physical interpretation of obtained parameters are unknown and no simple relations can be found between J_1, J_2 and J_n, n. Quantitative evaluation of the recombination current is not possible.

We perform the same analyses on the SL solar-cell. Measured characteristic values are $J_{sc} = 23.60$ mA/cm^2, $V_{oc} = 1.077$ V and $FF = 82.57\%$. The efficiency is 20.98%, which is slightly lower than that of the GaAs cell. We assume the bandgap of 1.519 eV, which is numerically calculated from the SL structure. Because the bandgap is wider than that of GaAs, lower J_{sc} and higher V_{oc} are reasonable. Fitted parameters of $t_s = 83\%$, $J_1 = 3.5 \times 10^{-18}$ mA/cm^2, and $J_2 = 1.4 \times 10^{-8}$ mA/cm^2 well reproduce the whole *J–V* curves, as shown in Fig. 4(a). Obtained J_1 roughly agree with the estimation

from the device design. Each component calculated from the obtained parameters is plotted in Fig. 5. In nearly whole region, the current is determined by the recombination process. At the voltage for the maximum output ($V_{max} = 0.930$ V), 98% of the current is contribution from the recombination. It is still 76% at the open circuit voltage. The higher contribution of the recombination current in the SL cell may be attributed to the incorporation of Al and the hetero-interface in the active region since the physical origin of the recombination current is the deep defect centers. These results clearly indicate that it is essential to grow SL active layers with high purity and interface perfection. High crystalline quality is necessary as well as optimized photo-absorption for further enhancement of

the efficiency of the solar-cells based on the AlGaAs/GaAs hetero-structure p–i–n junctions.

The saturation current density of the recombination [13,9] is expressed as

$$J_2 = \frac{qW_D}{\tau_r}n_i = \frac{qW_D}{\tau_r}\sqrt{N_cN_v}e^{-E_g/2kT}, \qquad (4)$$

where W_D is the depletion width (active layer thickness), τ_r is the lifetime of the recombination. N_c and N_v are effective density of states in conduction and valence band, respectively. We roughly estimate the lifetime assuming the same effective density of states of GaAs in both bulk and SL cells. The assumption is reasonable because the SL used in the experiment forms the mini-band and the density of states may be close to the three dimensional one. The estimated lifetime is 1.2 µs for the GaAs and 0.76 µs for the SL. The recombination in the AlGaAs/GaAs superlattice is about 1.5 times faster than that in the GaAs bulk. The slight increase in the recombination rate may affect the current component through the exponential term. Therefore, high crystalline quality is indeed important for the solar-cell performance.

We note here that the performance of solar-cells should be characterized by physical parameters. The recombination current is directly related to the crystalline quality and gives the useful information for the growth and device processing. When employing the numerical fitting, both diffusion-recombination and ideality factor modes are very simple to treat. There is no advantage to use phenomenological parametrization using n value. The fill factor and open circuit voltage are the complicated functions of t_s, J_1 and J_2. Discussing the cell performance based only on V_{oc} or FF may lead to the misunderstanding of the physical background of the characteristics. The diffusion-recombination model discussed above is still applicable to devices with finite shunt conductance and/or series resistance by including these values to the current model as fitting parameters. In this case, we need to perform the fitting to the whole measured J–V curve because the three input characteristic values are not sufficient to determine all parameters. Practically, the analysis is not complicated when the measured J–V data are available.

5. Conclusion

We have developed the simple evaluation method of the recombination current in solar-cells. The three characteristic values, short circuit current, open circuit voltage, and fill factor determine the diffusion and recombination current components. Our approach is very simple and thus widely applicable to various p–i–n junction solar-cells because the precise information about the device structure and consisting materials are not necessary. We apply the method to GaAs bulk and AlGaAs/GaAs SL solar-cells. Obtained parameters well reproduce the whole J–V characteristics in both cases. It is revealed that the diode current are almost dominated by the recombination process at the maximum-output voltage. The higher contribution of the recombination current in the SL solar-cell is due to the quality of the AlGaAs barriers and the AlGaAs/GaAs interfaces. The good crystalline quality is indeed important for high efficiency solar-cells. Phenomenological ideality factor model also well reproduces the measured data. However, physical interpretation is impossible and the relations between the J_n, n and J_1, J_2 are not obvious.

References

[1] V. Avrutin, N. Izyumskaya, H. Morkoç, Semiconductor solar cells: recent progress in terrestrial applications, Superlattices Microstruct. 49 (4) (2011) 337–364.
[2] H. Cotal, C. Fetzer, J. Boisvert, G. Kinsey, R. King, P. Hebert, H. Yoon, N. Karam, III–V multijunction solar cells for concentrating photovoltaics, Energy Environ. Sci. 2 (2) (2009) 174–192.
[3] A. Goetzberger, C. Hebling, H.W. Schock, Photovoltaic materials, history, status and outlook, Mater. Sci. Eng. R 40 (1) (2003) 1–46.
[4] M.A. Green, Thin-film solar cells: review of materials, technologies and commercial status, J. Mater. Sci.—Mater. Electron. 18 (S1) (2007) 15–19.
[5] A. Kawaharazuka, K. Onomitsu, J. Nishinaga, Y. Horikoshi, Effect of excitons on the absorption in the solar-cell with AlGaAs/GaAs superlattice grown by molecular beam epitaxy, J. Cryst. Growth 323 (1) (2011) 504–507.
[6] J. Nishinaga, A. Kawaharazuka, K. Onomitsu, K.H. Ploog, Y. Horikoshi, Effect of excitons in AlGaAs/GaAs superlattice solar cells, Jpn. J. Appl. Phys. 50 (5) (2011) 052302–052305.
[7] J. Nishinaga, A. Kawaharazuka, K. Onomitsu, K.H. Ploog, Y. Horikoshi, Excitonic absorption on AlGaAs/GaAs superlattice solar cells, Phys. Status Solidi C 9 (2) (2012) 330–333.
[8] J. Nishinaga, A. Kawaharazuka, K. Onomitsu, Y. Horikoshi, High-absorption-efficiency superlattice solar cells by excitons, Jpn. J. Appl. Phys. 52 (11) (2013) 112302–112304.
[9] W. Shockley, W.T. Read, Statistics of the recombinations of holes and electrons, Phys. Rev. 87 (5) (1952) 835–842.
[10] R.N. Hall, Electron–hole recombination in germanium, Phys. Rev. 87 (2) (1952) 387.
[11] W. Shockley, H.J. Queisser, Detailed balance limit of efficiency of p–n junction solar cells, J. Appl. Phys. 32 (3) (1961) 510–519.
[12] M.A. Green, K. Emery, Y. Hishikawa, W. Warta, E.D. Dunlop, Solar cell efficiency tables (version 44), Prog. Photovolt.: Res. Appl. 22 (7) (2014) 701–710.
[13] S.M. Sze, K.K. Ng, Physics of Semiconductor Devices, 3rd edition, Wiley-Interscience, New Jersey, 2006.
[14] International Standard, IEC 609043, Photovoltaic Devices. Part 3. Measurement Principles for Terrestrial Photovoltaic (PV) Solar Devices with Reference Spectral Irradiance Data, 2nd edition, International Electrotechnical Commission, April 2008.
[15] I. Vurgaftman, J.R. Meyer, L.R. Ram-Mohan, Band parameters for III–V compound semiconductors and their alloys, J. Appl. Phys. 89 (11) (2001) 5815–5875.
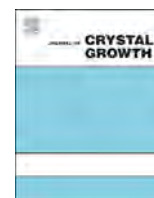
Effects of surface barrier layer in AlGaAs/GaAs solar cells

Hiroyuki Urabe [a,b,*], Makoto Kuramoto [a,b], Tomohiro Nakano [a,b], Atsushi Kawaharazuka [b],
Toshiki Makimoto [a,b], Yoshiji Horikoshi [a,b]

[a] *School of Science and Engineering, WASEDA University, 3-4-1, Okubo, Shinjuku, Tokyo 169-8555, Japan*
[b] *JST–CREST, 4-1-8, Honcho, Kawaguchi, Saitama 332-0012, Japan*

ARTICLE INFO

ABSTRACT

In this paper, we report the effects of surface barrier layers on the characteristics of AlGaAs/GaAs solar cells. The external quantum efficiency (EQE) spectra for AlGaAs barrier samples with different barrier layer AlAs fractions and thickness of the surface barrier layer were measured to increase the solar cell efficiency. The results show that the surface barrier layer is effective to block diffusing photoexcited electrons to the surface while the thicker barrier layer absorbs higher energy photons to generate carriers which recombine at the surface. The optimal surface barrier structure is a 50 nm thick $Al_{0.7}Ga_{0.3}As$.

© 2015 Elsevier B.V. All rights reserved.

1. Introduction

Solar cells have attracted attention as renewable energy for these days [1–3]. Among these solar cells, thin-film solar cells are required for cost reduction. The thin active layers, however, have low light absorption, so high absorption coefficient is essential to spread thin-film solar cells. Si has an indirect transition type energy band structure, while GaAs has a direct transition type energy band structure. GaAs absorption coefficient steeply goes up from absorption edge and reaches to ten to the fifth power, so the GaAs system is suitable for the thin-film solar cells. Moreover, the GaAs has an optimum band-gap energy of around 1.4 eV which gives the maximum efficiency of single junction solar cells which is called the Shockley–Queisser limit [4]. In order to exceed the limit, various ideas are produced such as intermediate band structures [5,6] and multi p–n junction systems [7,8]. Compound semiconductor solar cells suffer from considerable surface recombination. Recently it has been shown that a barrier layer in the surface region is effective to block diffusing electrons toward the surface region and thus improve the solar cell efficiency [9]. In this paper, we report the effects of surface barrier layers on the characteristics of AlGaAs/GaAs solar cells.

There are two major recombination processes. One is a recombination in the absorption layer. The other is surface recombination. These should be reduced because these are taken as loss of photoexcited carriers. In order to reduce them, it is necessary to grow high quality layers and give careful attention to aluminum purifying and growth rate. It is desirable that the aluminum cell is

baked for an hour before every growth and that the growth rate is lower than 1.5 ML/s. It is also necessary to insert potential barriers in order to reduce the diffusion to the surface. Fig. 1 shows a schematic band structure of the AlGaAs/GaAs p–i–n diode solar cell made in this study. The large arrows show carrier flows which are attributed to drift currents due to the internal electric field. Photocurrent extracted from solar cells mainly consists of these drift currents. The small arrows show carrier flows which are attributed to diffusion currents. They flow in the reverse direction to the drift currents. Therefore, the diffusion currents become loss for solar cells, so they should be reduced in order to realize high efficiency solar cells. In this structure, the diffusion currents are blocked by these barriers to reduce surface recombination.

In this study, we investigate the effects of surface barrier layer in AlGaAs/GaAs p–i–n diode solar cells using the EQE spectra and solar cell characteristics. The results obtained in this study demonstrate the importance of surface barrier conditions to improve solar cell efficiency.

2. Experimental procedure

AlGaAs/GaAs solar cell structures with different AlAs fractions (x) are grown at 630 °C by MBE. First, a 2 μm thick n-type GaAs layer, a 100 nm thick n-type AlGaAs barrier layer, a 2.2 μm thick p–i–n GaAs layer followed by a p-type AlGaAs barrier layer and a 5 nm thick p-type GaAs cap were sequentially grown on an n-type GaAs(001) substrate. Fig. 2 shows a schematic device structure of the AlGaAs/GaAs solar cell. Since photoabsorption strongly depends on surface layers, a backside barrier thickness was fixed

* Corresponding author.
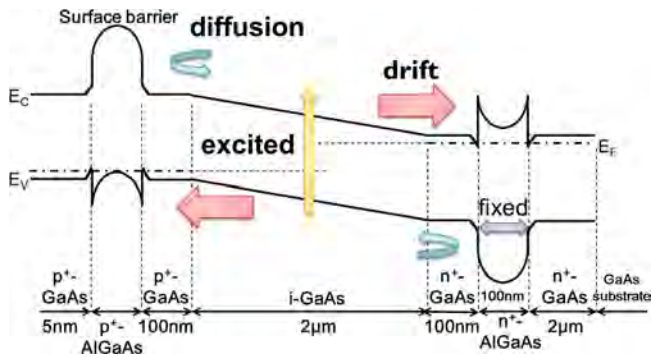
Fig. 1. Schematic band structure of the AlGaAs/GaAs, p–i–n diode solar cell.

Fig. 3. EQE spectra for the 10 nm barrier samples, with different AlAs fractions.

Table 1
Solar cell characteristics for the 10 nm barrier samples, with different AlAs fractions.

x	0	0.3	0.5	0.7
Solar cell efficiency [%]	11.1	14.6	14.9	14.9
Fill factor [%]	81.7	74.9	75.5	73.9
J_{sc} [mA/cm^2]	15.1	22.7	22.1	22.6
V_{oc} [V]	0.901	0.858	0.897	0.894
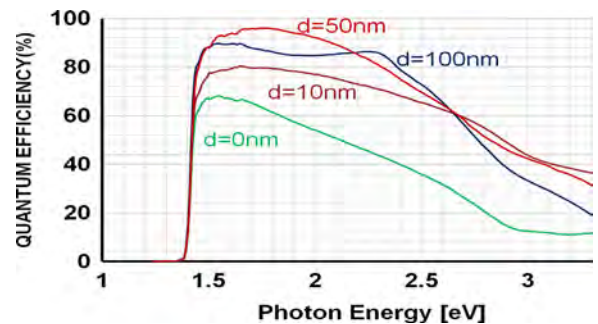
Fig. 4. EQE spectra for Al$_{0.7}$Ga$_{0.3}$As barrier samples, with different surface barrier layer thicknesses.

at 25 °C with solar radiation of an air-mass1.5 spectrum at 100 mW/cm^2.

3. Results and discussion

Fig. 3 compares the EQE spectra for the 10 nm surface barrier samples with different AlAs fractions; $x=0$, 0.3, 0.5, 0.7. Without surface barrier layer, the EQE value drops steeply at higher photon energies. This is caused by intense electrons diffusion to the surface. So the surface barrier layer effectively increases the EQE value especially at higher photon energies. The three arrows in Fig. 3 indicate the band gap energies of the surface barrier layer. This result indicates that the EQE value starts to decrease beyond the band gap of the surface barrier layer. For $x=0.7$, the EQE value starts to decrease beyond the indirect band gap of the surface barrier layer (around 2.0 eV) and decreases more steeply beyond the direct band gap. Table 1 shows solar cell characteristics for the 10 nm barrier samples with different AlAs fractions. It shows that the solar cell characteristics are improved as the barrier layer AlAs fraction increases. The barrier layer AlAs fraction increase causes high J_{sc} and V_{oc} although no systematic change is observed in the FF values. The highest solar cell efficiency is obtained for the samples with $x > 0.5$.

Fig. 2. Schematic layer structure of the AlGaAs/GaAs solar cell.

and surface barrier thickness and AlAs fraction were changed in this study. The AlAs fraction with surface and backside barrier layer was changed from 0 to 0.7. The doping concentration of Si is 10^{18} cm^{-3} and that of Be is 10^{19} cm^{-3}.

Next, the x value is fixed at 0.7 and surface barrier layer thickness was changed from 0 to 100 nm. EQE values were measured using photocurrents and current–voltage characteristics

Table 2
Solar cell characteristics for $Al_{0.7}Ga_{0.3}As$ barrier samples, with different surface barrier layer thicknesses.

d [nm]	0	10	50	100
Solar cell efficiency [%]	11.1	15.0	18.3	17.7
Fill factor [%]	81.7	88.6	80.8	81.2
J_{sc} [mA/cm^2]	15.1	20.8	23.7	23.2
V_{oc} [V]	0.901	0.913	0.954	0.939
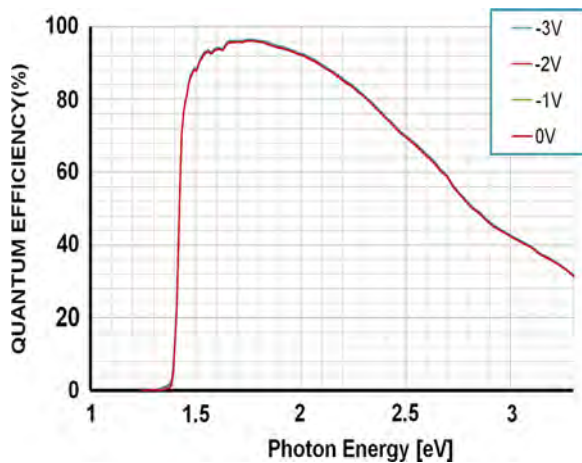
Fig. 5. EQE spectra for 50 nm thick $Al_{0.7}Ga_{0.3}As$ barrier samples, with different reverse bias voltages.

Fig. 4 compares the EQE spectra for $Al_{0.7}Ga_{0.3}As$ barrier samples with different surface barrier layer thicknesses. The EQE value is enhanced at lower photon energies for the samples with a surface barrier layer. This result shows that the barrier layer effectively blocks the diffusion of photoexcited electrons to the surface. However, the EQE drops gradually at higher photon energies. This implies that the barrier layer absorbs higher energy photons to generate carriers which recombine at the surface. Table 2 shows solar cell characteristics for $Al_{0.7}Ga_{0.3}As$ barrier samples with different barrier layer thicknesses. Among the present experiments, the highest J_{sc} and V_{oc} are obtained at the barrier layer thickness of 50 nm. When the thickness is further increased to 100 nm, J_{sc} and V_{oc} decrease. These results show that the optimized barrier layer thickness is 50 nm.

In the experiment so far, we focused the effects of the surface barrier on the diffusion current. Finally, we investigate the carrier trapping effect at the interface between GaAs and the barrier layer. Fig. 5 compares the EQE spectra for 50 nm thick $Al_{0.7}Ga_{0.3}As$ barrier samples with different reverse bias voltages. If the carrier trapping centers exist at the interface, the EQE value with the reverse bias voltage would be enhanced. However, the EQE spectra are independent of the reverse bias voltage as shown in Fig. 5, so no carriers are trapped at the interface between GaAs and the barrier layer.

4. Conclusions

In conclusion, the effects of surface barrier layer in AlGaAs/GaAs solar cells have been investigated by changing the AlAs fraction and the surface barrier layer thickness. The EQE spectra and solar cell characteristics for the samples with a surface barrier and no surface barrier reveal that the surface barrier is effective to block the diffusion of photoexcited electrons to the surface. As a result, the solar cell efficiency was improved from 11.1% to 18.3%. However, a thicker surface barrier layer causes absorption of higher energy photons. In this study, these results indicate that the optimized barrier is a 50 nm thick $Al_{0.7}Ga_{0.3}As$.

Acknowledgments

References

[1] A. Goetzberger, C. Hebling, H.-W. Schock, Mater. Sci. Eng. R 40 (2003) 1–46.
[2] M. Bosi, C. Pelosi, Prog. Photovolt. Res. Appl. 15 (2007) 51–68.
[3] H. Cotal, C. Fetzer, J. Boisvert, G. Kinsey, R. King, P. Hebert, H. Yoon, N. Karam, Energy Environ. Sci. 2 (2009) 174–192.
[4] W. Shockley, H.J. Queisser, J. Appl. Phys. 32 (1961) 510–519.
[5] A. Luque, A. Marti, A.J. Nozik, MRS Bull. 32 (2007) 236–241.
[6] A. Luque, A. Marti, Adv. Mater. 22 (2010) 160–174.
[7] A. Yakimov, S.R. Forrest, Appl. Phys. Lett. 80 (2002) 1667–1669.
[8] J. Gilot, M.M. Wienk, R.A.J. Janssen, Appl. Phys. Lett. (143512), 90(2007) 1-3.
[9] A. Kawaharazuka, K. Onomitsu, J. Nishinaga, Y. Horikoshi, J. Cryst. Growth 323 (2011) 504–507.
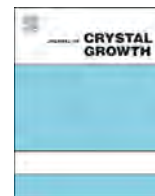
Optical properties of Al$_x$Ga$_{1-x}$As/GaAs superlattice solar cells

Makoto Kuramoto [a,b,*], Hiroyuki Urabe [a,b], Tomohiro Nakano [a,b], Atsushi Kawaharazuka [a,b], Jiro Nishinaga [a,b], Toshiki Makimoto [a], Yoshiji Horikoshi [a,b]

[a] Faculty of Science and Engineering, Waseda University, 3-4-1, Okubo, Shinjuku, Tokyo 169-8555, Japan
[b] JST-CREST, 4-1-8, Honcho Kawaguchi, Saitama 332-0012, Japan

ARTICLE INFO

ABSTRACT

The effect of excitons in Al$_x$Ga$_{1-x}$As/GaAs superlattice solar cells has been investigated. We have shown that the superlattice active layers are effective to improve the solar cell performances because of the exciton enhanced photo-absorption. External quantum efficiency spectra show sharp and intense increase at the absorption edge due to excitonic absorption. This result indicates that excitonic photo-absorption can be stabilized at room temperature by using a superlattice structure. Optical properties of superlattice solar cells depend on the superlattice parameters because they determine the excitonic confinement effect, the tunneling effect and the sub-band structure. In this study, we compare external quantum efficiency for solar cells with different superlattice parameters to optimize the structure. The optimal barrier layer thickness is determined to be 1 nm for the Al$_{0.5}$Ga$_{0.5}$As/GaAs superlattice solar cell with 2-μm-thick active layer.

1. Introduction

In recent years, demands for solar cells have considerably increased as a renewable energy source. However, further improvement in efficiency, fabrication cost and lifetime are inevitable to make them a practical power source [1,2,3]. While thinning the solar cells is advantageous for cost reduction, the photo-absorption efficiency drops at the same time, resulting in a decrease in solar cell efficiency. Thus, highly absorptive thin absorption layers are needed for thin film solar cells to keep the original efficiency. As one of the methods to enhance the absorption of thin films, we focus on the effect of excitons in solar cells.

In order to enhance the photo-absorption by excitonic transition at room temperature, materials with high exciton binding energy are desirable. However, semiconductor materials with high excitonic binding energy are generally wide-bandgap semiconductors, like GaN and ZnO, whose excitonic binding energies are as high as of 30 meV and 60 meV. Therefore, their bandgap energies do not match well with the solar power spectrum. Even in the semiconductor materials with low excitonic binding energies, the excitonic absorption can be enhanced considerably by constructing superlattices (SLs) [4,5]. The Al$_x$Ga$_{1-x}$As/GaAs system is one of the candidates, since it has direct bandgap around 1.4 eV, which is optimized bandgap predicted by Schockley–Queisser approach [6]. The layer structure of solar cells with this system can also be precisely controlled by moleculer beam epitaxy (MBE). Although

the excitonic binding energies of approximately 4–8 meV in GaAs are much smaller than the thermal energy at room temperature [7], efficient photo-absorption by excitonic transition can be obtained even at room temperature in solar cells by the confinement structure of SL [8–10]. We have found that the characteristics of SL solar cells strongly depend on the design of the consisting SL layers, so it is necessary to optimize the SL parameters for solar cells.

In this paper, we discuss the optical properties of solar cells with different Al$_x$Ga$_{1-x}$As/GaAs SL parameters. The overall efficiency and external quantum efficiency (EQE) spectra are found to be less sensitive to the Al content x and well width of SL. So the value x of Al$_x$Ga$_{1-x}$As barrier is fixed at 0.5, while the thickness of GaAs well is kept constant at 5 nm for all the experiment. On the other hand, optical properties strongly depend on barrier thickness, since the Al$_{0.5}$Ga$_{0.5}$As barrier thickness mainly determines excitonic confinement effect, tunneling effect and the sub-band structure. The EQE is also found to be sensitive to the total thickness of SL. From these facts, Al$_{0.5}$Ga$_{0.5}$As barrier layer thickness and total SL layer thickness are varied in the SL solar cells in this experiment. The EQE spectra thus obtained are compared to optimize the SL parameters.

2. Experimental procedure

We grew p–i–n junction solar cells with Al$_{0.5}$Ga$_{0.5}$As/GaAs SL active layer by MBE on n-type (001) GaAs substrates at 600 °C. These solar cells consist of a 1-μm-thick Si-doped n-type GaAs buffer layer,

* Corresponding author: Tel.: +81 3 5286 3429.
  E-mail address: kura-anfield@ruri.waseda.jp (M. Kuramoto).

a 100-nm-thick Si-doped n-type $Al_{0.5}Ga_{0.5}As$ layer, a 1- or 2 μm-thick $Al_{0.5}Ga_{0.5}As$/GaAs SL absorption layer, a 10-nm-thick Be-doped p-type $Al_{0.5}Ga_{0.5}As$ surface barrier layer and a 5-nm-thick Be-doped p-type GaAs cap layer successively grown on n-type (001) GaAs substrates. The thickness of GaAs well in the SL active layer is fixed at 5 nm, while the thickness of $Al_{0.5}Ga_{0.5}As$ barrier is varied between 0.5 nm and 3 nm. The Si and Be doping concentrations are 8×10^{18} cm^{-3} and 2×10^{19} cm^{-3}, respectively. Au–Ge–Ni and Au–Zn electrodes were evaporated on back and surface sides, respectively. The samples were annealed at 350 °C for 1 min to form ohmic contacts. Fig. 1 shows a schematic layer structure of the SL solar cell. We measured EQE at room temperature in short circuit conditions to evaluate the solar cell performance.

3. Results and discussion

Fig. 2(a) and (b) shows the EQE spectra of the solar cell with the 1-μm-thick active layer measured at room temperature. The steep rise at the absorption edge around 1.5 eV clearly indicates the beginning of excitonic absorption. The decrease of EQE in the higher energy region is probably caused by the surface reflection. A distinct dip appears around 1.7 eV in the spectrum of the solar cell with 2-nm-thick barrier as shown in Fig. 2(a).

To investigate the origin of this dip, we performed theoretical calculation on the active layer thickness dependence of the absorption rate. Fig. 3(a) and (b) shows absorption rates as function of photon energy (horizontal axis) and SL active layer thickness (vertical axis). Equi-absorption rate lines are indicated in the figure by 5% step. In these calculations, the absorption by excitonic transition is also taken into account. In Fig. 3(a) distinct low absorption region appears around 1.7 eV, which has been attributed to the energy gap between the first and the second sub-band transition. According to the calculated results for 1-μm-thick SL layer, the absorption rate around 1.7 eV is less than 75% when the barrier layer thickness is 2 nm, while for the 1 nm barrier layer cell it is more than 80%. This slight difference in the absorption rate may cause the experimental results shown in Fig. 2 where more distinct dip in EQE is observed for the SL solar cell with 2-nm-thick barrier layer, than that with 1-nm-thick barrier layer. Thus, the dip in EQE shown in Fig. 2 is caused by the energy gap between the first and the second sub-band transition. This difference in the gap is observed more clearly in the 2-μm-thick SL active layer solar cells. That is, the low absorbance region around 1.7 eV disappears completely for the 2-μm-thick SL active layer with the barrier layer thickness of 1 nm. Therefore, the 2-μm-thick SL active layer with 1-nm-thick barrier is more preferable for high efficiency solar cells.

The calculated results in Fig. 3 predict that the low absorption region around 1.7 eV disappears when the SL absorption layer thickness exceeds approximately 2.4 μm for the 2-nm-thick barrier solar cell. They also suggest that, for the 2-μm-thick SL layer cell, the low absorption rate region near 1.7 eV completely disappears for the 1-nm-thick barrier solar cell. Since the low absorption region near 1.7 eV still remains for 2-nm-thick barrier layer cell, there could be a large difference in EQE spectra between 1- and 2-nm-thick barrier solar cells with a 2-μm-thick SL absorption layer.
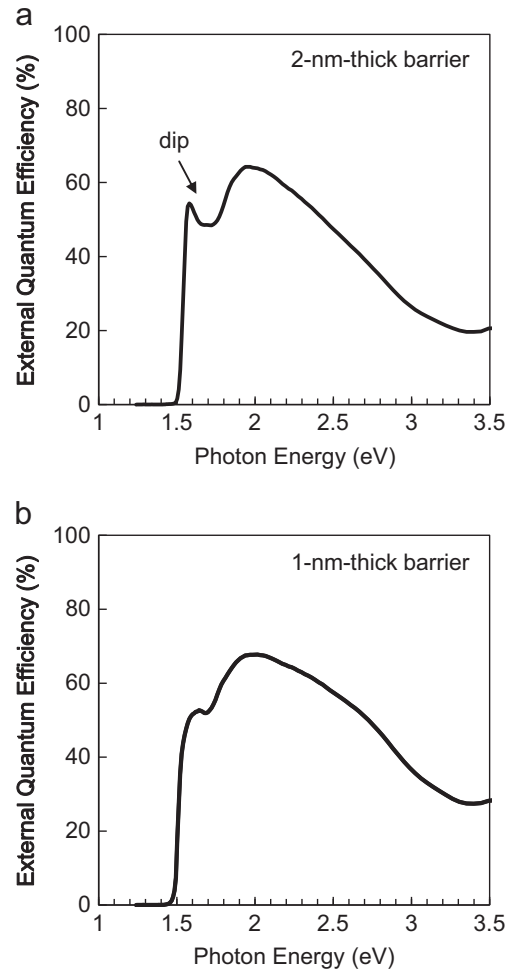
Fig. 2. The EQE spectra measured at room temperature of the solar cells for 1-μm-thick active layer with (a) 2-nm-thick and (b) 1-nm-thick barrier layers.
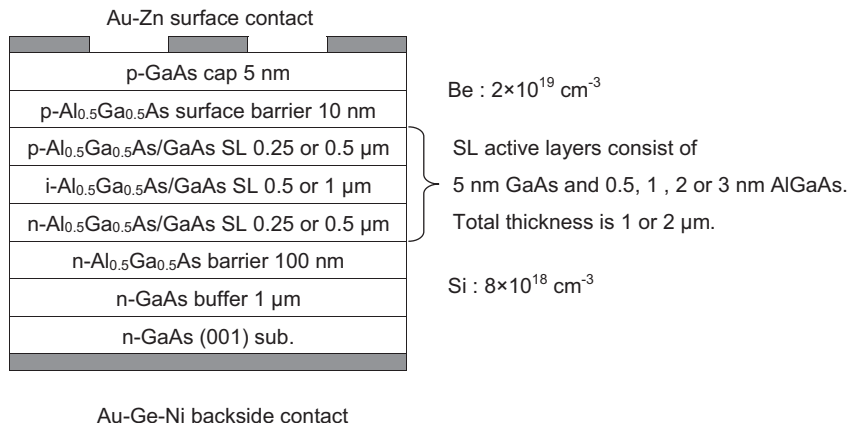
Fig. 1. Schematic layer structure of the SL solar cell grown on an n-type (001) GaAs substrate by MBE.
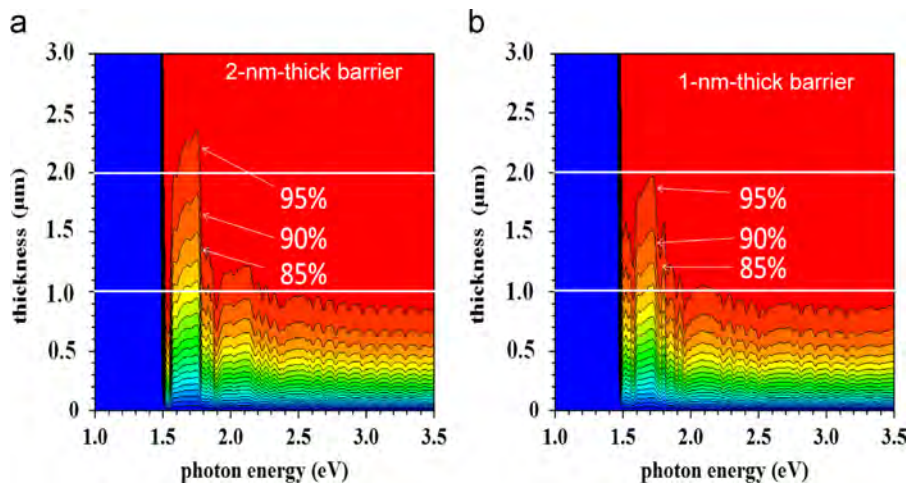
Fig. 3. Simulated absorption rate of the SLs with (a) 2-nm-thick and (b) 1-nm-thick barrier layers. The absorption rate is shown in 5% step.
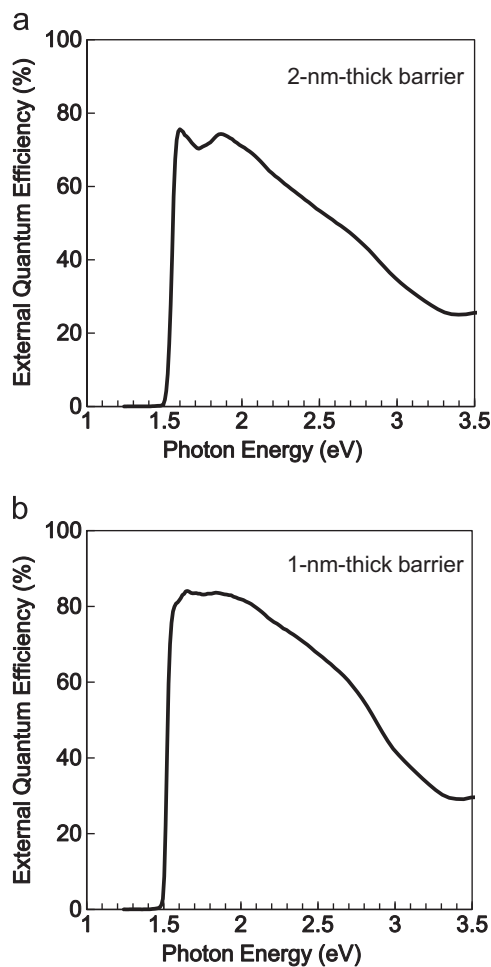
Fig. 4. The measured EQE spectra of the solar cells for 2-μm-thick active layer with (a) 2-nm-thick and (b) 1-nm-thick barrier layers.

To verify theoretical predictions, SL solar cells with a 2-μm-thick active layer were grown. Fig. 4(a) and (b) shows EQE spectra of the solar cells with the 2-μm-thick active layer. As expected, a dip around 1.7 eV is also observed in the measured spectrum for the 2-nm-thick barrier as shown in Fig. 4(a). This dip indicates insufficient absorption even for the 2-μm-thick absorption layer when the barrier layer thickness is 2 nm. The spectrum of 1-nm-thick barrier solar cell shows no clear dip as shown in Fig. 4(b).
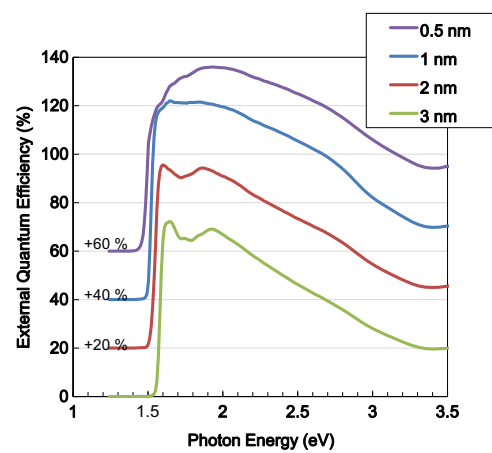
Fig. 5. The measured EQE spectra for the 2-μm-thick active layer with 0.5-, 1-, 2- and 3-nm-thick barrier layers.

To investigate the barrier thickness influence on the EQE in detail, SL solar cells with various Al0.5Ga0.5As barrier thicknesses are also grown. The SL active layer thickness is fixed at 2 μm, while the barrier layer thicknesses are varied between 0.5 nm and 3 nm. Fig. 5 compares the measured EQE spectra of different barrier thickness cells. The gradual shifts of absorption edge are observed because the effective bandgap depends on the $Al_{0.5}Ga_{0.5}As$ barrier thickness. The spectrum of 3-nm-thick barrier solar cell also shows a clear dip around 1.7 eV. On the other hand, the steep absorption edge disappears in the thinnest 0.5-nm-thick barrier solar cell, which is often observed in a bulk material. From these results in Fig. 5, the optimal SL barrier thickness is 1 nm.

4. Conclusion

We have investigated the effect of excitons in $Al_{0.5}Ga_{0.5}As$/GaAs SL solar cells to increase the photo-absorption. The optical characteristics of the SL strongly depend on the design of the SL structure, so the SL structure for solar cells has been optimized. In this paper, we have changed $Al_{0.5}Ga_{0.5}As$ barrier thickness in the SL and total thickness of the active layer, while the GaAs well width is fixed at 5 nm. A dip around 1.7 eV is observed in the EQE spectra for the SL solar cells with 2- and 3-nm-thick barrier layers. The origin of this dip is related to the energy gap between the first and the second sub-band transition. The measured EQE spectra of the thinner barrier solar cells show no clear dip as expected from

the theoretical calculation. A high intensity uniform spectrum without the dip is preferable for a high absorption rate, that is, high solar cell efficiency. However, the steep absorption edge disappears in the thinnest 0.5-nm-thick barrier solar cell. Considering these results, the optimal structure is the solar cell with the 2-μm-thick SL active layer consisting of 1-nm-thick barrier.

Acknowledgment

References

[1] A. Goetzberger, C. Hebling, H.-W. Schock, Mater. Sci. Eng. R40 (2003) 1–46.
[2] M. Bosi, C. Pelosi, Prog. Photovolt.: Res. Appl. 15 (2007) 51–68.
[3] H. Cotal, C. Fetzer, J. Boisvert, G. Kinsey, R. King, P. Hebert, H. Yoon, N. Karam, Energy Environ. Sci. 2 (2009) 174–192.
[4] H Iwamura, H. Kobayashi, H. Okamoto, Jpn. J. Appl. Phys. 23 (1984) L795.
[5] P.M. Young, H. Ehrenreich, P.M. Hui, N.F. Johnson, J. Appl. Phys. 74 (1993) 7369.
[6] W. Shockley, H.J. Queisser, J. Appl. Phys. 32 (1961) 510–519.
[7] M.D. Sturge, Phys. Rev. 127 (1962) 768.
[8] A Kawaharazuka, K. Onomitsu, J. Nishinaga, Y. Horikoshi, J. Cryst. Growth 323 (2011) 504–507.
[9] J. Nishinaga, A. Kawaharazuka, K. Onomitsu, K.H. Ploog, Y. Horikoshi, Jpn. J. Appl. Phys. 50 (2011) 052302.
[10] J. Nishinaga, A. Kawaharazuka, K. Onomitsu, Y. Horikoshi, Jpn. J. Appl. Phys. 52 (2013) 112302.
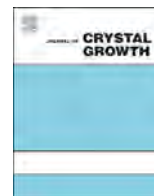
Effects of continuously graded or step-graded In$_x$Al$_{1-x}$As buffer on the performance of InP-based In$_{0.83}$Ga$_{0.17}$As photodetectors

CrossMark

S.P. Xi, Y. Gu, Y.G. Zhang *, X.Y. Chen, L. Zhou, A.Z. Li, Hsby. Li

State Key Laboratory of Functional Materials for Informatics, Shanghai Institute of Microsystem and Information Technology, Chinese Academy of Sciences, Shanghai 200050, China

A B S T R A C T

InP-based high indium content In$_{0.83}$Ga$_{0.17}$As photodetector structures with lattice mismatch up to 2.1% have been grown by gas source molecular beam epitaxy system. The photodetectors using continuously graded and step-graded In$_x$Al$_{1-x}$As buffer structures were grown and demonstrated. The effects of the buffer scheme were investigated by the measurements of atomic force microscopy, high-resolution X-ray diffraction, photoluminescence and device performance. Results show that the full relaxation of the photodetector structure has been achieved by using continuously graded InAlAs buffer. Superior optical properties and lower dark currents can be reached for the photodetector structure with continuously graded buffer layer.

© 2015 Elsevier B.V. All rights reserved.

1. Introduction

There are great needs for the infrared photodetectors (PDs) covering 1–3 μm short wave infrared range, due to their very important applications in spatial remote sensing, earth observation, night vision, etc [1–3]. Among varieties of PDs in this band, InGaAs detectors are widely used. The In$_{0.53}$Ga$_{0.47}$As PDs lattice matched to InP substrate with cut-off wavelength of about 1.7 μm have been well investigated mainly for the fiber communication applications. To extend the cut-off wavelength of the InGaAs PDs from 1.7 μm to 2.6 μm, the indium fraction of InGaAs should be increased from 0.53 to 0.83, which introduces a quite large lattice mismatch of about +2.1% between the InGaAs absorption layer and the InP substrate. Once the highly lattice mismatched InGaAs layers are directly grown on InP substrates, poor material with high threading dislocation density will be induced. Therefore a suitable buffer layer between the In$_{0.83}$Ga$_{0.17}$As absorption layer and InP substrate is needed to prevent the propagation of threading dislocations and improve the material quality. So far many material systems have been demonstrated for the buffer layers of high indium InGaAs materials, such as InGaAs [4–6], AlGaInAs [7], InAlAs [8,9] and InAsP [10–12]. Among them, InAlAs buffers own the wider bandgap than InGaAs in the case of the same indium composition, thus are suitable for the back illumination PD structure. Besides, the composition control of group III elements is very convenient by molecular beam epitaxy. On the other hand,

several kinds of buffer schemes have been used to improve the quality of metamorphic materials, such as step-graded [8,12,13], superlattice [14] and continuously graded buffers [4,15,16]. Comparing with the superlattice, continuously graded and step-graded buffers are more convenient from the view point of growth technology. However, the investigation of the different behaviors of continuously graded and step-graded buffers is still insufficient. In this work, In$_{0.83}$Ga$_{0.17}$As PDs with cut-off wavelength of 2.6 μm were grown on InP substrate by gas source molecular beam epitaxy (GSMBE). Through a comprehensive comparison, the effects of continuously graded and step-graded InAlAs buffers on both the material and device properties of the PDs were investigated.

2. Experimental details

The samples were grown on (001)-oriented InP epi-ready substrates by using a VG Semicon V80H GSMBE system. The elements indium, gallium and aluminum were used as group III sources, and their fluxes were temperature controlled. Arsine and phosphine high-pressure cracking cells were used as group V sources. Their fluxes were controlled by adjusting the pressure. The cracking temperature was around 1000 °C, measured by thermocouple. Standard beryllium and silicon effusion cells were used as p-type and n-type doping sources, and the doping levels were also controlled by changing the temperatures. The lowest background pressure of this GSMBE system is less than 10^{-10} Torr, while the pressure during growth is typically in the 10^{-5} Torr range. The surface oxide

desorption of the InP substrate was carried out under P_2 flux at substrate temperature around 530 °C [17,18].

Two PD structures with indium content of about 0.83 in the InGaAs absorption layer were grown for the cut-off wavelength around 2.6 μm. In the growth, a 0.2 μm N^+ doped InP buffer layer was initially deposited to generate a smooth surface. After that, a 0.1 μm N^+ doped $In_{0.52}Al_{0.48}As$ (lattice matched to InP) buffer layer was grown for both samples. Then a 1.9 μm N^+ continuously graded and step-graded $In_xAl_{1-x}As$ buffer layer was grown for samples A and B, respectively. The indium composition was continuously graded from 0.52 to 0.83 in the InAlAs buffer of sample A. In sample B, four 0.475 μm InAlAs layers with step-graded indium compositions of 0.60, 0.68, 0.76 and 0.83 were grown. The thickness of the whole buffer layers is 1.9 μm, which is the same as that of sample A. After the growth of InAlAs buffer layers, a 1.5 μm N^- $In_{0.83}Ga_{0.17}As$ absorption layer and a 0.6 μm P^+ $In_{0.83}Al_{0.17}As$ cap layer were grown for both samples A and B. The growth rates of all the layers were around 1 μmh^{-1}.

After growth, the morphologies of the grown samples were observed using an atomic force microscope (AFM). The X-ray diffraction scan curves and reciprocal space mapping (RSM) were measured using a Philips X'pert MRD high resolution X-ray diffractometer (HRXRD) equipped with a four-crystal Ge (220) monochromator. The photoluminescence (PL) spectra were measured using a Nicolet Megna 860 Fourier transform infrared (FTIR) spectrometer, in which a liquid-nitrogen cooled InSb detector and CaF_2 beam splitter were used. A diode-pumped solid-state (DPSS) laser with the wavelength of 532 nm was used as the excitation source. The wafers were also processed into mesa-type PDs. The mesas were defined by using photolithography, and then passivated by Si_3N_4 using plasma enhanced chemical vapor deposition (PECVD). After sputtering the contact metals and an alloy step, the wafers were diced into chips. A HP4156A semiconductor analyzer was used to perform the dark current measurements.

3. Results and discussions

Fig. 1 shows the AFM images with 20×20 μm^2 scan area measured in a contact mode. Both of the samples exhibit a cross-hatching pattern surface, which is associated with the two types of misfit dislocations oriented along the [110] and [110] directions, corresponding to the group V and III atom-based cores, respectively [19]. The AFM measurements reveal that the root-

mean-square (RMS) roughness for sample B is 7.3 nm, lower than that of 10.3 nm for sample A. Nevertheless, the differences of morphologies for these samples are unobvious and thus inadequate to judge the quality of the samples and further evaluations are needed.

To determine the structural properties of the grown wafers, X-ray diffraction measurements were implemented. Fig. 2 shows the typical HRXRD ω–2θ scan curves in the (004) direction and Table 1 lists the extracted results. Two main peaks can be observed in each scan curve, where the relatively narrower peak corresponds to the InP substrate and the broader peak corresponds to the $In_{0.83}Ga_{0.17}As$ absorption and $In_{0.83}Al_{0.17}As$ cap layers. The signals from these two layers with almost the same indium content are merged together. The full width at half maximum (FWHM) of the scan curves for samples A and B is 869 s and 902 s, respectively. It suggests the slightly degraded crystalline quality of the step-graded buffer, which is consistent with the results of for InGaAs graded buffers [20]. From the estimation of full relaxation, the indium content of the epitaxy layers is around 0.80 and 0.82 for samples A and B, respectively. To further understand the strain relaxation mechanism, it is necessary to perform RSM measurements

The relaxation states and residual strains of the samples were investigated by the RSM measurements with both symmetric (004) and asymmetric (224) reflections as shown in Fig. 3, where the intensities are in the logarithmic scale. The vertical and horizontal axes represent the reciprocal lattice in the [001] (q_y) and [110] (q_x) directions. In all of the mapping figures, the
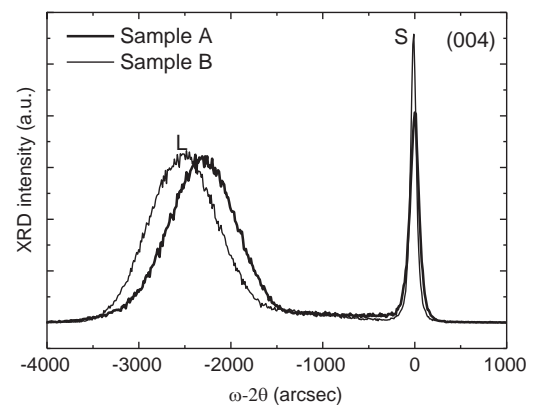
Fig. 2. (004) ω–2θ scan curves of sample A and B.
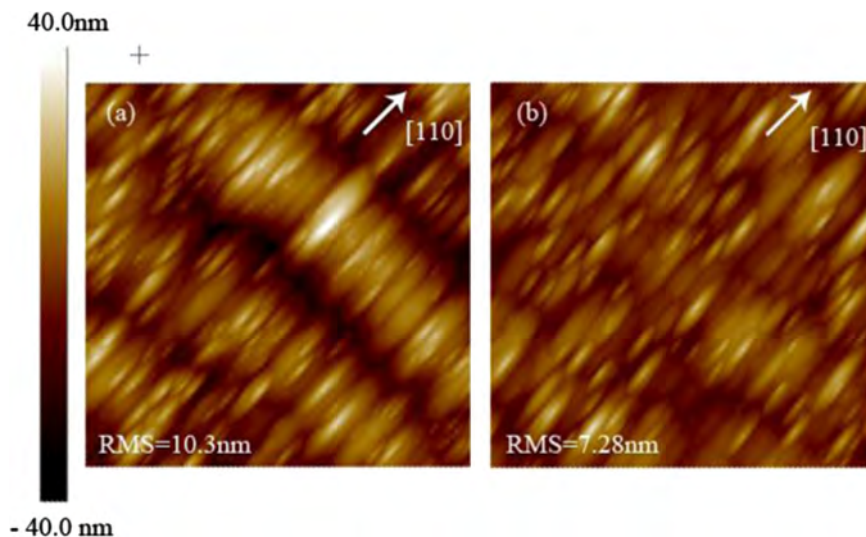
Fig. 1. Contact mode AFM images of (a) sample A and (b) sample B with 20×20 μm^2 scan area.

relatively narrow and circular peaks correspond to InP substrate (denoted as S). The diffraction features from individual epitaxy layers are distinguished in the RSMs. For the epitaxy layer signals, the graded buffer layers can be observed in the q_y direction for both of the samples. The two epitaxy layer peaks with relatively strong intensities correspond to the $In_{0.83}Ga_{0.17}As$ absorption layer (denoted as L1) and $In_{0.83}Al_{0.17}As$ cap layer (denoted as L2), respectively. They are elliptical with a larger diffused scattering perpendicular to the normal line due to the existence of dislocations. L1 and L2 were assigned by measuring the HRXRD curves in the same directions before and after the etching of the $In_{0.83}Al_{0.17}As$ cap layer. The layer peak was shifted towards the substrate side after the etching. In the (004) RSMs of the samples, the position of maximum diffraction intensity for each epitaxial layer is almost centered along the vertical line drawn through the substrate's reciprocal lattice point (RLP), indicating a small lattice

Table 1
Results from XRD measurements of (004) ω–2θ scan curves.

Sample	L-intensity (a.u.)	L-FWHM (arcsec)	Relaxed indium content	Relaxed mismatch (%)
A	5341	869	0.80	1.83
B	5424	902	0.82	1.97

tilt with respect to the substrate. For the asymmetric (224) reflections, the full relaxation and full pseudomorphic lines with respect to the substrate were drawn for reference. The glancing incidence was used, and the intensities of substrate peaks are weaker than those of layer peaks due to the thick epilayers. For sample A, the center of the layer contours indicate that the material is almost fully relaxed, on the other side, the center of layer contours is below the full relaxation line, which suggests that the epitaxy layers are not relaxed sufficiently. The indium content in the InGaAs absorption layers of sample A and B are 0.806 and 0.805, respectively, as listed in Table 2. The residual strain is 1.07×10^{-3} for sample A and -0.55×10^{-3} for sample B, corresponding to the relaxation degrees of 105.4% and 96.8%. The epitaxy layer of sample A with continuously graded buffer is fully relaxed regardless of the experimental error.

The optical quality of the epilayers, which is correlated with the performance of the optoelectronic device in a more straightforward way, is evaluated using PL measurements, and the results are shown in Fig. 4, noticing that the water absorption bands have affected the PL signals in the wavelength range of 2.5–2.8 μm at 300 K. Two PL peaks can be observed for each sample. The stronger one with the longer wavelength at around 2.53 μm corresponds to the InGaAs absorption layer, and the weaker one centering at 1.7 μm corresponds to the InAlAs cap layer. The wavelength of sample B is slightly shorter than that of sample A

Fig. 3. Symmetric (004) and asymmetric (224) reciprocal space maps of (a) sample A and (b) sample B.

Table 2
Results from symmetric (004) and asymmetric (224) RSMs.

Sample	Parallel mismatch (%)	Perpendicular mismatch (%)	Cubic mismatch (10^{-2})	Indium content	Relaxation degree (%)	Tilting angle (deg)	Residual strain (10^{-3})
A	2.01	1.79	1.90	0.806	105.4	0.06	1.07
B	1.83	1.96	1.89	0.805	96.8	−0.03	−0.55
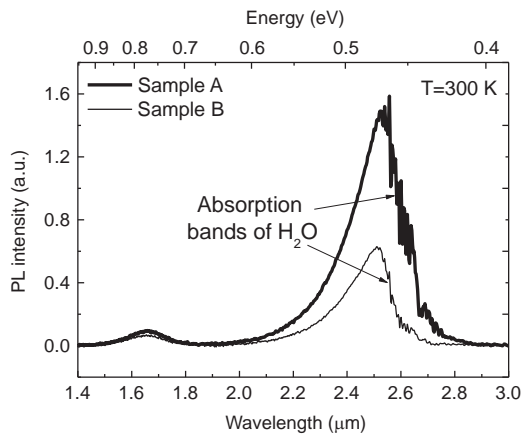
Fig. 4. PL spectra at 300 K of sample A and B.
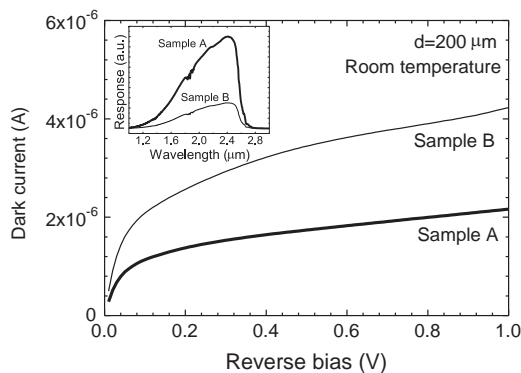
Fig. 5. Dark current versus the reverse bias voltage of sample A and B at room temperature. The inset shows the response spectra at room temperature and zero bias.

due to the relatively larger residual strain of sample B. It can be seen that by using continuously graded InAlAs buffer layer, the PL intensity of sample A is about doubled comparing to that of sample B. It suggests the larger number of non-radiative recombination centers in the InGaAs absorption layer of sample B.

To confirm the quality of the wafers, the response spectra and dark currents of the PDs were measured for the mesa-type devices with 200 μm diameter. The inset of Fig. 5 shows the response spectra of the PDs at room temperature and zero bias, where the water vapor absorption bands around 1.9 μm and 1.4 μm could be clearly seen. The 50% cut-off wavelengths of these two samples are almost the same at about 2.57 μm. In the measured spectra, sample A shows a much larger response than that of sample B. Fig. 5 shows the dark current versus the reverse bias voltage at room temperature for the two samples. At a reverse bias of $V_R = 10$ mV, the dark currents are 259 nA (8.25×10^{-4} A/cm²) and 473 nA (1.51×10^{-3} A/cm²) for samples A and B, respectively. The larger response and lower dark current of sample A is consistent with its superior structural and PL properties.

Comparing to sample B, sample A with continuously graded InAlAs buffer layer shows improved device performance.

4. Conclusion

In$_{0.83}$Ga$_{0.17}$As PD structures with continuously graded and step-graded InAlAs buffer layers have been grown on InP substrates by GSMBE. X-ray diffraction measurements show that the continuously graded InAlAs buffer is effective to lead to the full relaxation of epitaxy layers. Superior optical properties are revealed by the PL measurements. For the PDs with 200 μm mesa diameter, the dark currents at reverse bias of 10 mV are 259 nA (8.25×10^{-4} A/cm²) and 473 nA (1.51×10^{-3} A/cm²) at room temperature for samples A and B, respectively. The optical response is increased for the PD with continuously graded buffer and the cut-off wavelengths of the two devices are both around 2.57 μm. It can be concluded that the PD applying continuously graded InAlAs buffer shows superior performances than that using step-graded InAlAs buffer.

References

[1] R.W.M. Hoogeveen, R.J. vander A, A.P.H. Goede, Infrared Phys. Technol. 42 (2001) 1.
[2] M.A. Forte-Possion, C. Brylinski, J. Di Persio, X. Hugon, B. Vilotitch, C. Le Nobel, J. Cryst. Growth 124 (1992) 782.
[3] Q.L. Kleipool, R.T. Jongma, A.M.S. Gloudemans, et al., Infrared Phys. Technol. 50 (2007) 30.
[4] T.M. Zhang, G.Q. Miao, Y.X. Jin, H. Jiang, Z.M. Li, H. Song, J. Alloy. Compd. 458 (2008) 363.
[5] B. Lee, J.H. Beak, J.H. Lee, S.W. Choi, S.D. Jung, W.S. Han, E.H. Lee, Appl. Phys. Lett. 68 (1996) 2973.
[6] M.T. Bulsara, C. Leitz, E.A. Fitzgerald, Appl. Phys. Lett. 72 (1998) 1608.
[7] M. Haupt, K. Kohler, P. Ganser, S. Emminger, S. Muller, W. Rothemund, Appl. Phys. Lett. 69 (1996) 412.
[8] D. Lee, M.S. Park, Z. Tang, H. Luo, R. Beresford, C.R. Wie, J. Appl. Phys. 1 (2007) 101.
[9] Y.G. Zhang, Y. Gu, Z.B. Tian, K. Wang, A.Z. Li, X.R. Zhu, Y.L. Zheng, J. Cryst. Growth 311 (2009) 1881.
[10] J.A. Czaban, D.A. Thompson, B.J. Robinson, Semicond. Sci. Technol. 22 (2007) 408.
[11] L. Ji, S.L. Lu, Y.M. Zhao, et al., J. Cryst. Growth 363 (2013) 44.
[12] M.K. Hudait, Y. Lin, P.M. Sinha, J.R. Lindemuth, S.A. Ringel, J. Appl. Phys. 100 (2006) 1.
[13] P. Kidd, D.J. Dunstan, H.G. Colson, et al., J. Cryst. Growth 169 (1996) 649.
[14] M. Wada, H. Hosomatsu, Appl. Phys. Lett. 64 (1994) 1265.
[15] J. Tersoff, Appl. Phys. Lett. 62 (1993) 693.
[16] H. Choi, Y. Jeong, J. Cho, et al., J. Cryst. Growth 311 (2009) 1091.
[17] Y. Gu, C. Li, K. Wang, Hsby Li, Y.Y. Li, Y.G. Zhang, J. Infrared Millim. Waves 29 (2010) 81.
[18] Y. Gu, Y.G. Zhang, K. Wang, X. Fang, C. Li, L. Zhou, A.Z. Li, Hsby Li, J. Cryst. Growth 378 (2013) 65.
[19] M.K. Hudait, Y. Lin, D.M. Wilt, et al., Appl. Phys. Lett. 82 (2003) 3212.
[20] M. D'Hondt, I. Moerman, P. Demeester, Electron. Lett. 34 (1998) 910.

CrossMark
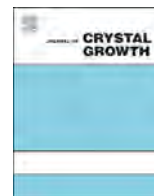
Position-sensitive multi-wavelength photon detectors based on epitaxial InGaAs/InAlAs quantum wells

T. Ganbold [a,b], M. Antonelli [c], G. Cautero [c], R.H. Menk [c], R. Cucini [c], G. Biasiol [a,*]

[a] IOM CNR, Laboratorio TASC, Area Science Park Basovizza, 34149 Trieste, Italy
[b] Graduate School of Nanotechnology, University of Trieste, 34128 Trieste, Italy
[c] Elettra – Sincrotrone Trieste S.C.p.A., Area Science Park Basovizza, 34149 Trieste, Italy

ARTICLE INFO

ABSTRACT

Beam monitoring in synchrotron radiation or free electron laser facilities is extremely important for calibration and diagnostic issues. Here we propose an *in-situ* detector showing fast response and homogeneity for both diagnostics and calibration purposes. The devices are based on $In_{0.75}Ga_{0.25}As/In_{0.75}Al_{0.25}As$ QWs, which offer several advantages due to their direct, low-energy band gap and high electron mobility at room temperature. A pixelation structure with 4 quadrants was developed on the back surface of the device, in order to fit commercially available readout chips.

The QW devices have been tested with collimated monochromatic X-ray beams from synchrotron radiation. A rise in the current noise with positive bias was observed, which could be due to deep traps for hole carriers. Therefore, an optimized negative bias was chosen to minimize dark currents and noise. A decrease in charge collection efficiency was experienced as the beam penetrates into deeper layers, where a dislocation network is present. The prototype samples showed that individual currents obtained from each quadrant allow the position of the beam to be monitored for all the utilized energies. These detectors have a potential to estimate the position of the beam with a precision of about 10 μm.

© 2015 Elsevier B.V. All rights reserved.

1. Introduction

In modern synchrotron radiation (SR) and free electron lasers (FEL), developed as light sources for scientific and technological applications, simultaneous monitoring of the position and the intensity of the photon beam is becoming of increasing importance due to the unavoidable instabilities of the delivered light beams. Several solid-state, on-axis photon beam position monitoring (pBPM) detectors have been reported in the literature [1–3]. Recently, we have proposed the use of epitaxially grown quantum well (QW) devices for photon beam detection [4–6]. Such structures allow reducing the direct semiconductor band gap down to 0.6 eV in the well layer, and thus have the ability to detect photons over a broad energy range, spanning from visible to X-rays. Furthermore, the high density and mobility of carriers in the 2D Electron Gas (2DEG) forming inside the QW allow the development of fast and efficient photon detectors with sub-nanosecond response times. In older experiments, QWs were segmented into four quadrants, allowing to monitor the position of a photon beam with a precision down to 800 nm [7].

However, in order to fit commercial readout chips, the readout electrodes cannot lie on the side hit by the photon beam. Therefore, in this work we have developed pixelated structures on the back surface of the QW by metal deposition and optical lithography techniques, while leaving the QW unsegmented. In order to provide uniform readout electrodes, the four quadrants were covered by Au/Ge/Ni metallic layers. Photo-generated carriers can be collected at the readout electrodes under a bias, while the beam is hitting the device from the QW side. The device was mounted on a carrier board placed on an XY movable stage, which is in turn driven by stepper motors inside a UHV-compatible chamber.

The QW detectors were tested in a conventional X-ray tube in order to compare the position sensitivity with respect to detectors fabricated on bulk GaAs. Then, results for three experiments performed with QW detectors at the X-Ray Fluorescence (XRF) beamline, Elettra, Italy, are reported in this paper. The precision of the beam-position estimation was evaluated at three different photon energies. Additionally, charge collection efficiency (CCE) for photo-generated carriers is reported and discussed.

2. Growth and fabrication

The epitaxial structure of all devices was grown on a 500-μm-thick, semi-insulating GaAs substrate (Fig. 1). After a 200 nm GaAs

* Corresponding author. Tel.: +39 040 3756439; fax: +39 040 226767.
E-mail address: biasiol@iom.cnr.it (G. Biasiol).
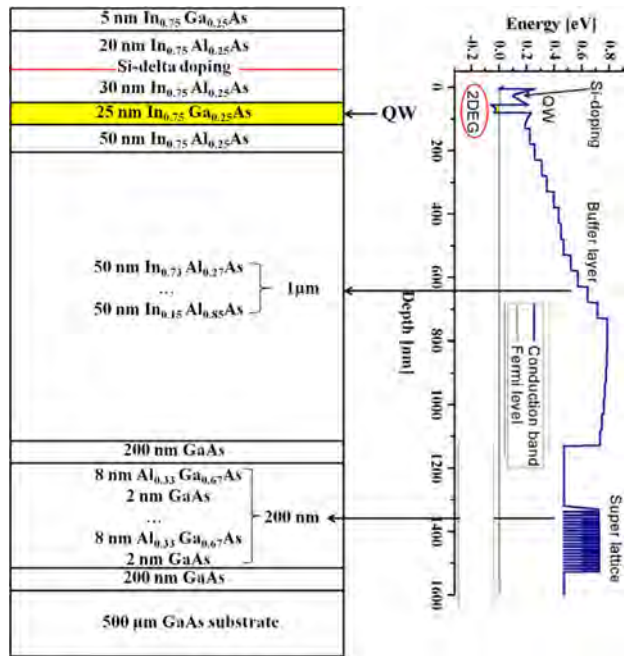
Fig. 1. Layout of the device structure with the simulated profile of the conduction band.

Fig. 2. (a) Photolithographic development on the samples; (b) schematic view of the fabricated devices and of the experimental setup.

Table 1
Parameters and results for the three photon beams used. The different columns show photon energies, spot sizes, photon fluxes, precisions of position estimation and charge collection efficiencies.

E_{ph} (keV)	Spot size (μm^2)	Flux (ph/s)	Position estimation precision (μm)	CCE (%)
2.14	500 × 500	3.0×10^8	10	27
5.0	200 × 200	1.0×10^8	12	20
10.0	200 × 200	1.0×10^8	19	10

layer for surface smoothing, a GaAs/AlGaAs (2 nm/8 nm) super-lattice (SL) was introduced to block impurities from the substrate. Another 200 nm GaAs was inserted before starting an $In_xAl_{1-x}As$ step-graded buffer layer (BL) with an In concentration x increasing from 0.15 to 0.75. The BL consists of a series of 50 nm steps, grown by keeping the Al flux constant and ramping the In cell tempera-ture at each step, without growth interruptions. This BL was used to grow metamorphic 2DEG structures on GaAs substrates in almost unstrained $In_xGa_{1-x}As$ layers with $x \geq 0.7$ [8–11] as a way to block the dislocation network, generated at the hetero-interface between mismatched layers, below the QW region. Growth details can be found in Refs. [10,11].

The active region of the sample consists, from the top of the BL to the free surface, of a 50 nm $In_{0.75}Al_{0.25}As$ lower barrier, a 25 nm $In_{0.75}Ga_{0.25}As$ QW where the 2DEG forms, a 50 nm $In_{0.75}Al_{0.25}As$ upper barrier doped by Si delta 30 nm apart from the QW and a 5 nm $In_{0.75}Ga_{0.25}As$ cap. The band structure was simulated by using a 1D Poisson–Schrodinger solver package [12]. As the chemical composition of the BL changes, a "staircase" band structure is shown by the simulation, followed by the QW region (Fig. 1).

Pixelated structures were fabricated on the back surface of a 5×5-mm^2 dice cut from the grown wafers. 4 readout quadrants made of Au/Ge/Ni (130 nm/60 nm/30 nm) pads with a 100 μm wide clearance were deposited by means of metal evaporation on the back side of the dice, while the QW was left unsegmented (Fig. 2a). A single 400 nm Al electrode was deposited on the QW side of the die for biasing (Fig. 2b). A device with the same structure was fabricated on a 350 μm-thick bare GaAs wafer with no epitaxial layers in order to compare it with the QW devices in terms of position sensitivity and photo-current values.

Hall measurements at room temperature were performed to characterize the charge density n and the carrier mobility μ in the QW, resulting in 7.7×10^{11} cm^{-2} and $\mu = 1.1 \times 10^4$ cm^2 V^{-1} s^{-1}, respectively. Top-to-bottom resistance was found to be of the order of 100 MΩ, mostly determined by the substrate resistivity. The speed of the proposed QW devices was tested in response to ultra-short laser pulses. The acquired signals showed sub-ns response, with 100 ps rise/fall times, i.e., a factor of 6 faster than state-of-the-art commercial diamond detectors [13].

3. Experiment

Position sensitivities of QW and bulk GaAs devices were compared on a conventional crystallographic X-ray tube with a silver target. Such a source provides a white beam with photon energies ranging from 6 keV to 50 keV with an intensity peak at 22 keV. The spot size has been reduced by a pinhole and a double-slit collimator to 500 μm (FWHM) at the interaction point.

Full characterization of the QW devices was performed at the XRF beamline at Elettra – Sincrotrone Trieste S.C.p.A. The beamline is optically designed to present the beam parameters needed for high-level measurements in spectroscopy as well as in microscopy. In particular, experimental chambers can be placed temporarily at the beamline to make use of its monochromatic beam. Three experiments were performed with monochromatic beams at photon energies of 2.14 keV, 5 keV and 10 keV (Table 1). A photon flux of 10^8 ph/s was roughly estimated by an ion chamber for the two higher energies with a spot size of 200 μm. Since photon absorption of air increases below 4 keV, the spot size of the beam at 2.14 keV was set to 500 μm, in order to reach a comparable value of the impinging flux (3×10^8 ph/s).

The samples were placed and wire-bonded onto printed-circuit boards, provided with bias and signal connectors, which are fed into the readout electronics (AH501 picoammeter). This board was mounted onto an XY movable stage driven by stepper motors, which is hosted in a compact chamber and allows fine mesh scans of the photon beam to be carried out during the measurements.

4. Results and discussion

The dark current summing from the 4 quadrants was measured under a bias voltage from -30 V to 30 V range in 5 V intervals at

room temperature (see Fig. 3, dots). A smaller dark current was recorded for negative biases, with respect to positive ones, saturating from about −15 V. Additionally, an increase of the current noise was observed with positive bias, which could be due to deep traps for hole carriers, as shown in Fig. 3, squares. The maximum and minimum values of RMS noise were recorded as 2.7 nA and 0.02 nA at 30 V and −30 V bias voltages, respectively. Therefore, a bias voltage of −15 V was chosen for the measurements as the optimal bias in terms of dark currents and noise. This can be an advantage of these devices with respect to other solid-state position-sensitive detectors which require higher voltages [2].

To assess the role of the QW in the position monitoring capabilities of our devices we have compared the performance of detectors fabricated on QW epitaxial samples and on bulk GaAs. From a mesh scan of both the QW and GaAs devices with a 500 μm X-ray beam, the QW detector shows enhanced photon beam position sensitivity with respect to bulk GaAs (Fig. 4). Responses of the all channels are more uniform and the difference between the photocurrent and the dark current of the QW is higher than the bulk GaAs. The 4 pixels on the surface can be more clearly distinguished due to the much smaller cross talk between the pixels in the QW detector (Fig. 4a). Thus, segmentation of the QW allows us to electrically isolate the pixels much better than the bulk GaAs despite the geometrical configurations of these detectors being the same. Moreover, the total photocurrent was higher in the QW detector then in GaAs, even for lower electric fields (1.13 nA at a field of −0.03 V/μm, with respect to 1.06 nA at −0.04 V/μm). The higher photocurrent in the QW detector could be due to the fact that photo-generated electrons drifting through the sample give their kinetic energy to the carriers in the 2DEG forming inside the QW and allow them to escape from the potential well, and thus to give an additional contribution to the total photocurrent. This mechanism could be considered as a charge amplification effect due to the high charge density in the 2DEG [14].

In order to determine the response of all channels as the X-ray beam moves across the device, scans of photocurrent acquired along a square-shaped path (shown in the inset of Fig. 5c) were recorded. As shown in Fig. 5, all channels were homogeneously responding to the beam exposure during the scan, at all utilized energies.

While the beam is shifting from one quadrant to the next one, a sharp switch in currents between two neighbor quadrants is shown in the reported results. The individual currents obtained from each readout electrode prove that our prototype detector allows to effectively monitor the beam position. The beam position was estimated by using the *difference-over-sum* technique [15] for all energies and then plotted in terms of the real position, as determined by the XY stepper (Fig. 6). The estimate is represented in Fig. 6b by the dots, relative to each of the scan lines. The deviation of this curve from the fitting sigmoidal function (continuous line) suggests a precision of 10 μm for the position monitoring of a 500-μm-wide monochromatic beam at 2.14 keV. The precisions of the position estimation degraded to12 μm at 5 keV and 19 μm at 10 keV (see Table 1). The much poorer spatial resolution with respect to devices fabricated on the same semiconductor heterostructures but with the segmentation applied to the QW [7] could be ascribed to two separate effects. First, a cross talk between the pixels is likely to take place if the QW is not segmented as carriers in the 2DEG, which contribute to the photocurrent, is free to move around the whole device area and is not confined in a single pixel. Furthermore, we observe a loss of resolution as the photon energy increases. Since the penetration depth increases with the photon energy, with the beam eventually reaching the deeper layers of the BL where dislocations are present, we infer that such dislocations play the role of traps for the photo-generated carriers, which reduce the signal level and thus the resolution.

Finally, the charge collection efficiency (CCE) for photo-generated carriers was evaluated by comparing the acquired photocurrents with the ones expected from the incident photon flux (considering a pair-generation energy of 4.2 eV for GaAs [16]). The CCE was 27% at 2.14 keV, 20% at 5 keV, and dropped to only 10% at 10 keV (see Table 1). This could be due to the closeness of the highest excitation energy to the Ga K absorption edge (around 10.3 keV [17]), causing a decrease of the number of photo-generated carriers.

5. Conclusions

We have developed a position sensitive photon detector based on epitaxial InGaAs/InAlAs QWs. The QW photon detector response to a 500 μm X-ray beam shows a better spatial resolution with respect to a device fabricated on bulk GaAs. Photo-currents with low noise were recorded for low negative bias voltages, with
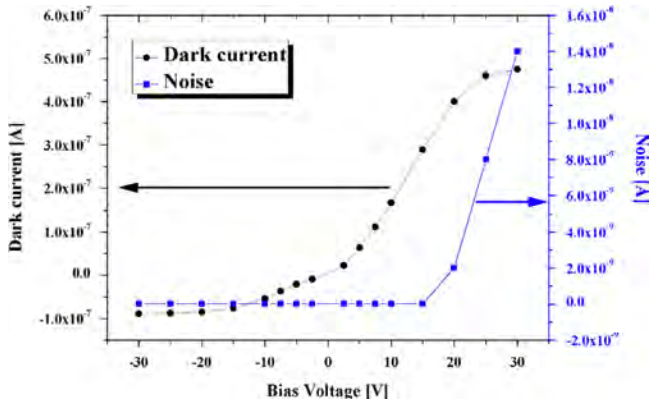
Fig. 3. Dark current (dots) and current noise (squares) of the QW device in terms of bias voltage.
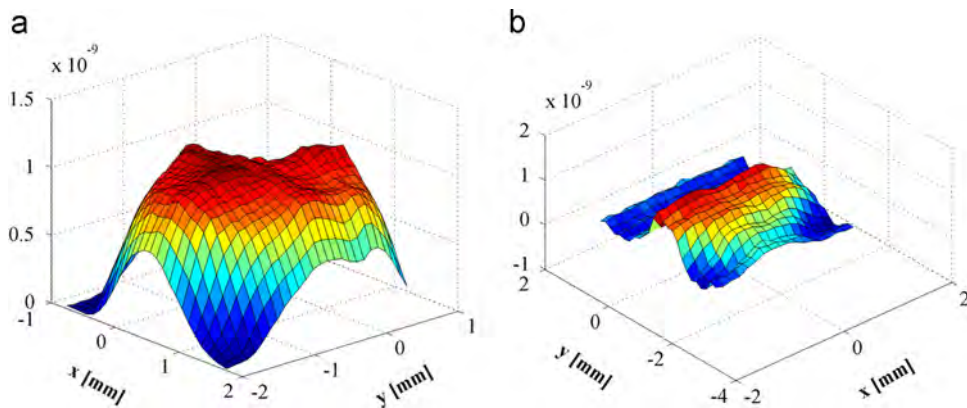
Fig. 4. Mesh scan with a conventional X-ray tube performed on: (a) the QW detector and (b) the GaAs detector.
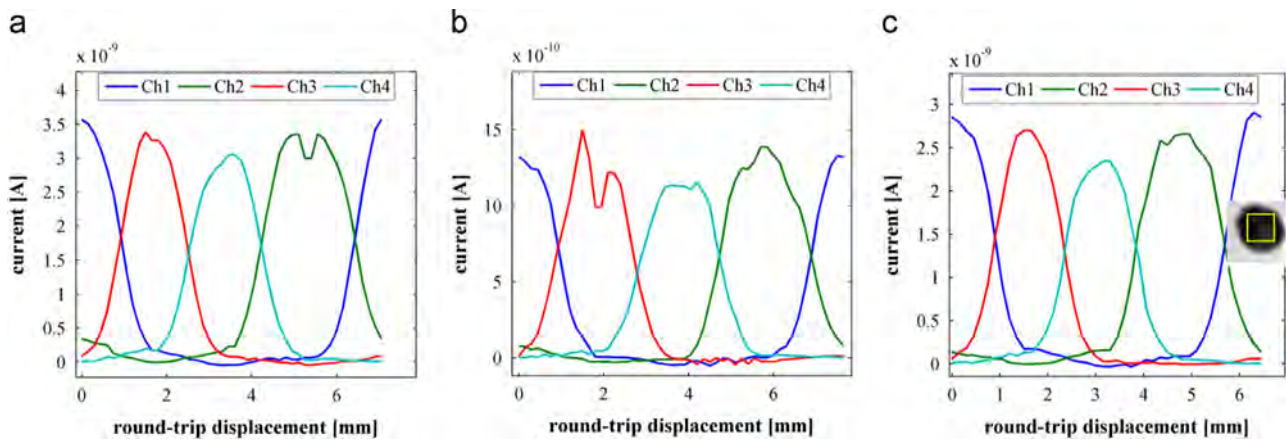
Fig. 5. Current line scans along a square-shaped path around the surface of the QW device, as sketched in the inset of panel (c); (a) at 2.14 keV, (b) at 5 keV and (c) at 10 keV.
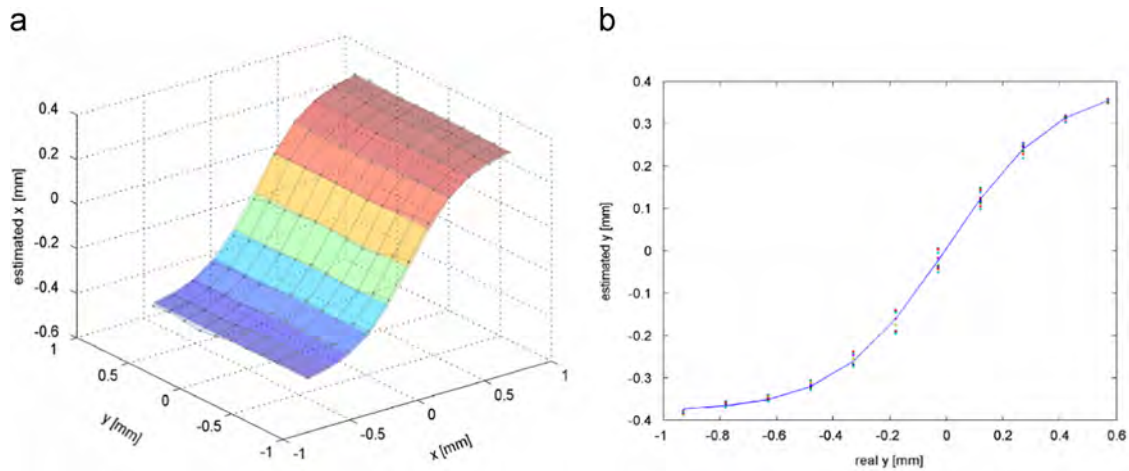
Fig. 6. Estimated position from the total currents from Fig. 5 in terms of real beam position at energy of 2.14 keV: (a) 2D horizontal position estimation and (b) 1D vertical position estimation.

respect to other beam monitoring photon detectors such as diamond-based pBPMs, which work at higher bias. The beam positions were estimated with SR light at energies of 2.14 keV, 5 keV and 10 keV. The finest estimation precision recorded was 10 μm for a spot size of 500 μm with 2.14 keV photon energy. The position of the 10 keV beam with 200 μm spot size was estimated with a much lower precision of 19 μm, as the incident photon penetrates deeper into the dislocated InAlAs buffer layer. Furthermore, the low CCE recorded at 10 keV could be caused by the fact that the excitation energy was close to the Ga K absorption edge. The much lower spatial resolution with respect to front-segmented QW detectors [7] is imputable to the higher cross talk between the quadrants caused by the lack of QW segmentation. In order to improve the resolution and at the same time allow the insertion into commercial readout chips, we are currently developing a device where both sides are pixelated, with the readout electrodes deposited on the back side, and the QW segmented with the same structure and subsequently covered by a single bias electrode.

References

[1] R.G. VanSilfhout, S. Manolopoulos, N.R. Kyele, K. Decanniere, Sens. Actuators A 133 (2007) 82.
[2] M. Di Fraia, M. Antonelli, A. Tallaire, J. Achard, S. Carrato, R.H. Menk, G. Cautero, D. Giuressi, W.H. Jark, F. D'Acapito, A. De Sio, E. Pace, J. Phys. Conf. Ser. 425 (2013) 212001.
[3] J. Smedley, A. Héroux, J. W. Keister, M. Gaowei, E. Muller, J. Bohon, K. Attenkofer, and J. Distel, in: Proceedings of the Particle Accelerator Conference, New York, NY, USA, MOP207, 483, 2011.
[4] M. Antonelli, M. Di Fraia, A. Tallaire, J. Achard, S. Carrato, R.H. Menk, G. Cautero, D. Giuressi, W.H. Jark, G. Biasiol, T. Ganbold, K. Oliver, C. Callegari, M. Coreno, A. De Sio, E. Pace, Proc. SPIE (2012) 85040D.
[5] M. Antonelli, M. Di Fraia, S. Carrato, G. Cautero, R.H. Menk, W.H. Jark, T. Ganbold, G. Biasiol, C. Callegari, M. Coreno, A. De Sio, E. Pace, Nucl. Instrum. Methods A 730 (2013) 164.
[6] M. Antonelli, T. Ganbold, R.H. Menk, G. Cautero, W.H. Jark, D.M. Eichert, G. Biasiol, J. Instrum. 9 (2014) C05034.
[7] T. Ganbold, M. Antonelli, G. Biasiol, G. Cautero, H. Jark, D.M. Eichert, R. Cucini, R.H. Menk, J. Instrum. 9 (2014) C12043.
[8] S. Gozu, T. Kita, Y. Sato, S. Yamada, M. Tomizawa, J. Cryst. Growth 227–228 (2001) 155.
[9] S. Löhr, S. Mendach, T. Vonau, C. Heyn, W. Hansen, Phys. Rev. B 67 (2003) 1.
[10] F. Capotondi, G. Biasiol, D. Ercolani, V. Grillo, E. Carlino, F. Romanato, L. Sorba, Thin Solid Films 484 (2005) 400.
[11] F. Capotondi, G. Biasiol, I. Vobornik, L. Sorba, F. Giazotto, A. Cavallini, B. Fraboni, J. Vac. Sci. Technol. B 22 (2004) 702.

[12] Snider. G., ⟨http://www3.nd.edu/~gsnider/⟩ (n.d.).
[13] T. Ganbold, M. Antonelli, G. Biasiol, G. Cautero, R..Cucini, D.M. Eichert, W.H. Jark, and R.H. Menk, in: Proceedings of FEL, Basel, Switz., 2014.
[14] T. Ganbold, M. Antonelli, G. Biasiol, R. Cucini, G. Cautero, R.H. Menk, J. Instrum. 10 (2015) C03009.

[15] R.H. Menk, D. Giuressi, F. Arfelli, L. Rigon, AIP Conf. Proc. 879 (2007) 1109.
[16] G. Bertuccio, D. Maiocchi, J. Appl. Phys. 92 (2002) 1248.
[17] J.A. Bearden, F. Burr, Rev. Mod. Phys. 39 (1967) 125.
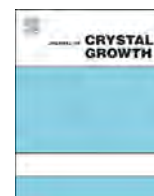
Optimization of InAlAs buffers for growth of GaAs-based high indium content InGaAs photodetectors

CrossMark

X.Y. Chen [a], Y. Gu [a], Y.G. Zhang [a,*], S.P. Xi [a], Z.X. Guo [b], L. Zhou [a], A.Z. Li [a], Hsby. Li [a]

[a] State Key Laboratory of Functional Materials for Informatics, Shanghai Institute of Microsystem and Information Technology, Chinese Academy of Sciences, Shanghai 200050, China
[b] Key Laboratory of Automobile Materials, Ministry of Education, College of Materials Science and Engineering, Jilin University, Nanling Campus, Changchun 130025, China

ABSTRACT

The impact of buffer schemes on the strain relaxation and structural characteristics of $In_{0.83}Ga_{0.17}As$ photodetector structures with relatively high lattice mismatch (5.9%) grown on GaAs substrate by gas source molecular beam epitaxy has been investigated. Reduction of surface roughness, full widths at half maximum of X-ray diffraction signals and threading dislocations, as well as an enhancement of photoluminescence intensity were observed for the $In_{0.83}Ga_{0.17}As$ photodetector structure with fixed-composition $In_{0.83}Al_{0.17}As$ buffer compared to those with continuously graded $In_xAl_{1-x}As$ buffer. The role of fixed-composition $In_{0.83}Al_{0.17}As$ buffer layer is investigated, and it is believed that a couple monolayers of $In_{0.83}Al_{0.17}As$ at the initial growth stage can provide high density of nucleation site by the formation of quantum dots at the interface and thus to reduce the strain energy caused by the large lattice mismatch between $In_{0.83}Al_{0.17}As$ and GaAs.

© 2015 Elsevier B.V. All rights reserved.

1. Introduction

The ternary III–V compound semiconductor, $In_xGa_{1-x}As$ ($0 < x < 1$), with features such as relatively high carrier mobility, wide direct band gap ranging from 0.35 to 1.42 eV, high reliability and radiation resistance, has wide application in short-wave infrared (SWIR) region. Especially, the demands for the so-called extended wavelength $In_xGa_{1-x}As$ ($x > 0.53$) PDs and arrays are increasing dramatically due to their important applications including earth observation, spatial remote sensing, and night vision, etc. [1,2]. So far, $In_xGa_{1-x}As$ ($x > 0.53$) PDs are often fabricated on InP substrates, and the cutoff wavelength has been extended up to 2.9 μm by using gas source molecular beam epitaxy (GSMBE) [3]. When $In_xGa_{1-x}As$ PDs were transferred to GaAs substrates, the major difficulty would be that the nearly 4% increased lattice mismatch for the same indium content x [4,5]. However, GaAs substrates hold the advantages of higher robustness, lower cost and larger size as compared to InP substrates. Moreover, integration of GaAs-based devices enjoys merits of presently highly developed GaAs integrated circuits. The key point would be the reduction of

threading dislocations in InGaAs due to the relatively high lattice mismatch with respect to GaAs. So far, although numerous researches have been carried out to investigate the dislocation behaviors of misfit dislocations in the lattice mismatched systems, few of them focused on the material of $In_xGa_{1-x}As/GaAs$ ($0.53 < x < 1$). Therefore, the nucleation mechanism at the interface between $In_xGa_{1-x}As$ ($0.53 < x < 1$) and GaAs is still relatively vague. To release the strain, continuously graded metamorphic InAlAs layers are commonly employed as buffers for InP-based InGaAs PDs in our previous experiments. For the case of GaAs-based InGaAs PD structure with a higher lattice mismatch, the performance of InGaAs PD would be influenced by the grading slope, buffer thickness and relaxation degree of the continuously graded buffers. In this experiment, a fixed-composition InAlAs layer, which takes forms of a uniform composition and an abrupt growth on GaAs, has been adopted as a buffer regime to accommodate and release the strain, as expected that the threading dislocation density would be reduced for further epilayer growth. Through a comprehensive comparison, the effects of InAlAs buffer strategies on the material quality and defect behaviors of GaAs-based $In_{0.83}Ga_{0.17}As$ PD structures with the continuously graded and fixed-composition InAlAs buffers were investigated. Based on XTEM images of the two typical PD structures, the misfit dislocation formation mechanism was also investigated in the fixed

* Corresponding author. Tel.: +86 21 62511070; fax: +86 21 52419931.
E-mail address: ygzhang@mail.sim.ac.cn (Y.G. Zhang).

compositional $In_{0.83}Al_{0.17}As$ buffer with respect to the continuously graded $In_xAl_{1-x}As$ buffer. It was found that the differences between the two buffer regimes not only exist in the magnitude order of dislocation density, but also in the location they originate and the way they distribute. The results will be very helpful for understanding of dislocation behaviors in growth of metamorphic materials with relatively high lattice mismatch, and further designing appropriate buffer layers for fabrication of high indium content InGaAs photodetectors with low dark current density.

2. Experiments

$In_{0.83}Ga_{0.17}As/In_{0.83}Al_{0.17}As$ p-i-n heterojunction structures with different buffer schemes were grown by GSMBE on semi-insulated (100) GaAs epi-ready substrates (Table 1). Growth condition was exactly the same as our previous study [5]. Each wafer consisted of a 2.5-μm-thick N^+ InAlAs buffer layer and a 1.5-μm-thick n^- $In_{0.83}Ga_{0.17}As$ absorption layer followed by a 530-nm-thick P^+ InAlAs cap. For the deposition of structure with continuously graded InAlAs buffer, GaAs growth was followed by a 0.1-μm-thick highly Si-doped N^+ $In_{0.1}Al_{0.9}As$ layer grown at 530 °C, then the 2.5-μm-thick highly Si-doped N^+ $In_xAl_{1-x}As$ buffer layer with In composition x graded from 0.1 to 0.86 and substrate temperature graded from 530 to 460 °C was grown. There is a compositional overshoot in the end of the $In_xAl_{1-x}As$ buffer layer with respect to the following epilayers [6]. For the structure with fixed-composition $In_{0.83}Al_{0.17}As$ buffer, the $In_{0.83}Al_{0.17}As$ layer grown on GaAs at a constant substrate temperature of 490 °C was also 2.5 μm thick. The doping level in each layer of both structures was kept uniform. To investigate the effect of interfacial layer on the behavior of threading dislocations in epilayers, PD structures with InAs wetting layer inserted between the fixed-composition $In_{0.83}Al_{0.17}As$ layer and the GaAs substrate were also grown for comparison. These samples were defined as samples A, B, C and D hereafter respectively, as listed in Table 1. The $In_{0.83}Ga_{0.17}As$ absorption layer and $In_{0.83}Al_{0.17}As$ cap were grown at 490 °C and a constant group III growth rate of 1 μm/h was used for the epilayer growth.

The strain relaxation and defect properties of the PD structures were characterized using triple axis X-ray diffraction (XRD), atomic force microscopy (AFM), photoluminescence (PL), and cross-sectional transmission electron microscopy (XTEM). Triple axis XRD measurements were carried out with a Philips X'pert MRD high resolution X-ray diffractometer (HRXRD) equipped with a four-crystal Ge (220) monochromator. AFM measurements were carried out with a Bruker Dimension-Icon Atomic Force Microscope System. The microstructure of the interface of InAlAs/GaAs heterostructure and the epilayer was detected by transmission electron microscopy (TEM, JEM-2100F, JEOL) operating at 200 kV.

3. Results and discussions

AFM scan over 20×20 μm^2 were performed to investigate the surface morphology for samples A and B. Slightly rumpled cross-hatch patterns of the two PD structures were observed, as shown in Fig. 1(a) and (b). The cross-hatch pattern is associated with the strain fields of misfit dislocations aligned with the [110] and [1−10]

directions [7], which should be related to the different growth rates around the dislocations. Compared to sample A, the cross-hatch patterns of sample B is less pronounced. Meanwhile, to distinguish the surface features, 3D AFM images of the two typical samples are shown in Fig. 1(c) and (d). Different shapes and diameters of 3D mounds align along the [110] direction on the surface of the two samples. These 3D mounds results from the asymmetric diffusion of group III atoms on the sample surface due to the non-uniform strains [8]. They undulate and overlap more significantly for sample A with a width of about 1 μm, and a length of 4–5 μm which are larger than those of sample B. Root-mean-square (RMS) roughnesses of all the samples are summarized in Table 1. It can clearly be seen that the RMS values are both very high. For the PD structure with continuously graded InAlAs buffer, the RMS roughness is a little higher than that with fixed-composition $In_{0.83}Al_{0.17}As$ buffer. These surface features should be associated with the different alloy grading profile in the buffer layers underneath, i.e., different mechanisms of strain relaxation. When the thickness of the epilayer is beyond the critical value, the misfit strain would relax by introducing misfit dislocations. While a large misfit strain could not release enough by dislocation arrays. Other strain relaxation mechanism such as surface undulation would become predominant, which relaxes part of the strain but increases the surface roughness [9,10]. The larger RMS value and larger size of 3D mounds on the structural surface of sample A reflect that the strain-reliving surface roughening is more serious in the structure with continuously graded InAlAs buffer than other samples with fixed-composition $In_{0.83}Al_{0.17}As$ buffer.

Lattice relaxation degree and alloy composition can be determined by HRXRD using two symmetrical (004) rocking curves recorded 180° apart in Phi and two asymmetrical (224) rocking curves recorded at the same Phi value with a low angle of incidence. It was observed that samples with fixed-composition $In_{0.83}Al_{0.17}As$ buffer exhibited a little larger degree of relaxation than sample A with continuously graded $In_xAl_{1-x}As$ buffer, as shown in Table 1. The lattice relaxation has been proved to be associated with the misfit dislocation formation at the film/substrate interface [11]. Moreover, the full width at half maximum (FWHM) in XRD spectrum is related to the threading dislocation density and other crystal imperfections [12]. Fig. 2 shows the normalized HRXRD rocking curves for (004) reflections of all samples. The lattice misfit between the layers of $In_{0.83}Ga_{0.17}As$ or $In_{0.83}Al_{0.17}As$ and the GaAs substrate is both about 5.9%. Therefore the relatively broader peaks appearing at about 31° include the $In_{0.83}Al_{0.17}As$ cap layer peak and $In_{0.83}Ga_{0.17}As$ absorption layer peak. The broad peak of sample A reflects the continuously grading profile of $In_xAl_{1-x}As$ ($x=0.1\rightarrow0.86$) buffer which ultimately combined with the $In_{0.83}Ga_{0.17}As$ peak. While samples B–D with fixed compositional $In_{0.83}Al_{0.17}As$ buffers showed much lower FWHM value of $In_{0.83}Ga_{0.17}As$ layers probably mainly due to the thicker fixed-composition $In_{0.83}Al_{0.17}As$ layer in the buffer. Furthermore, the FWHM was ameliorated by inserting 5 MLs InAs quantum dots (QDs) at the $In_{0.83}Al_{0.17}As$/GaAs interface for sample C with a narrowest value of 410 s, but degraded to 511 s by increasing the thickness of InAs layer to 50 nm for sample D, as illustrated in Fig. 2. This indicates that the intermediate layer at the interface between $In_{0.83}Al_{0.17}As$ and GaAs plays an important

Table 1
Buffer schemes and measured results for four samples.

Sample	Buffer scheme	XRD FWHM (arc sec)	Relaxation degree (%)	In composition	AFM RMS (nm)
A	2.5 μm $In_xAl_{1-x}As$ buffer, x grades from 0.1 to 0.86	1782	94.8	0.84	11.6
B	2.5 μm $In_{0.83}Al_{0.17}As$	544	97.5	0.82	8.1
C	5 MLs InAs QDs+2.5 μm $In_{0.83}Al_{0.17}As$	410	98.3	0.83	8.8
D	50 nm InAs+2.5 μm $In_{0.83}Al_{0.17}As$	511	98.8	0.82	8.6
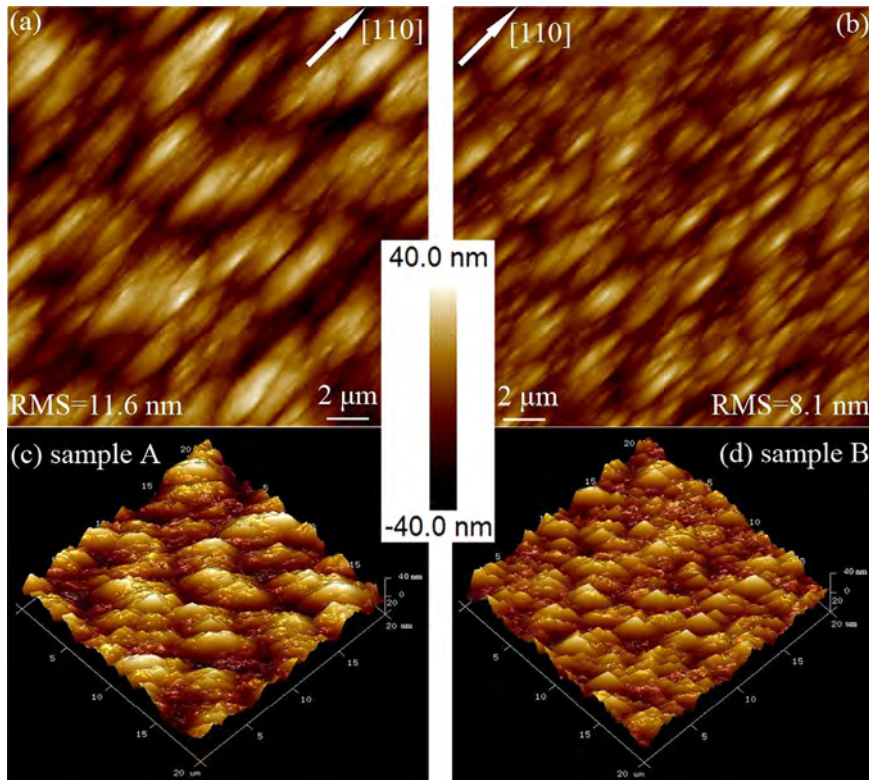
Fig. 1. AFM images of samples A and B. The scan area is $20 \times 20\ \mu m^2$.
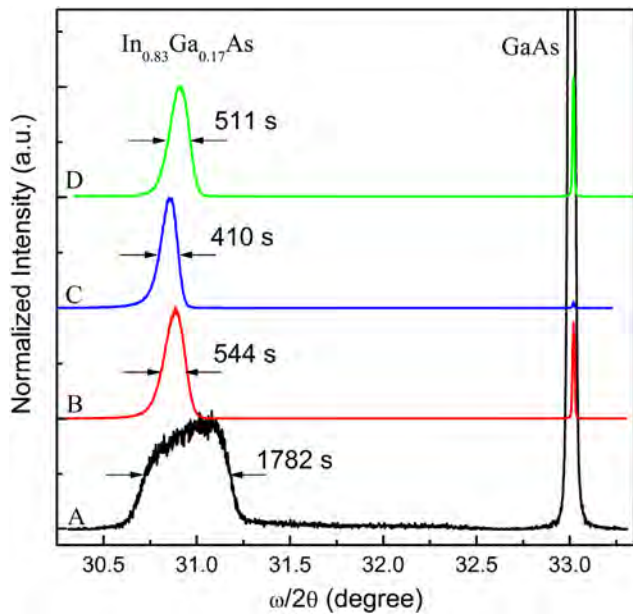
Fig. 2. (004) ω-2θ high resolution XRD patterns.

role in the blocking of threading dislocations. The 5 MLs InAs QDs may be beneficial to the confinement of misfit dislocations in the inactive region, while the confinement effect is weakened when the thickness of InAs was increased.

To compare the crystal quality, PL measurements were performed by using a Nicolet Megna 860 Fourier transform infrared (FTIR) spectrometer, using the 532 nm line of diode-pumped solid-state (DPSS) laser as excitation source with the excitation power of 500 mw, and the PL spectrum was detected by InSb detector through a GaF_2 beam splitter. Fig. 3 shows the PL spectra measured at 300 K
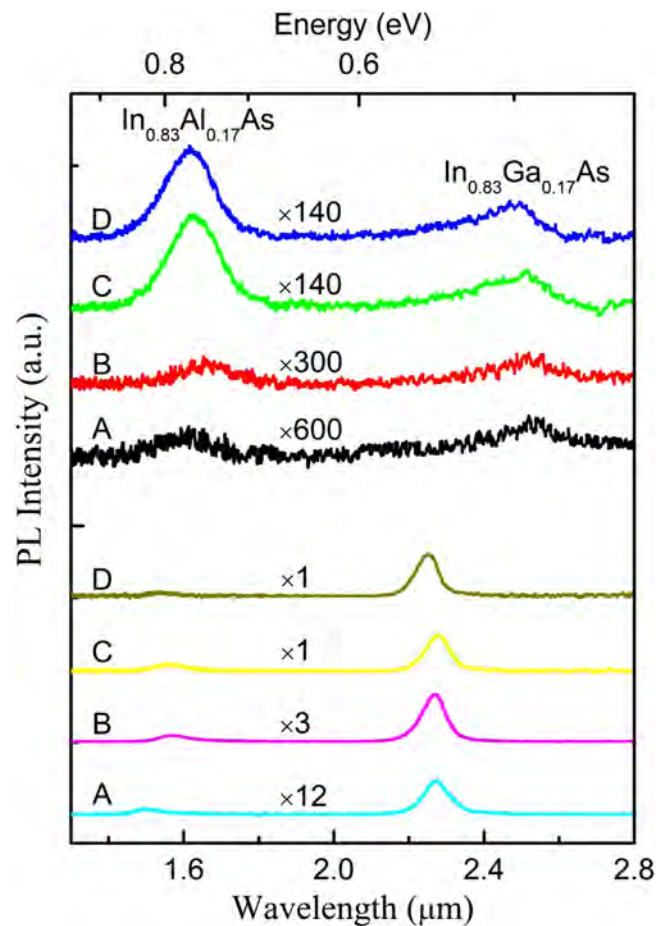
Fig. 3. PL spectra at 300 K and 10 K of samples A–D.

and 10 K. Two PL envelopes can be observed for each sample. The PL envelopes with the centers located at around 1.62 µm at 300 K correspond to the $In_{0.83}Al_{0.17}As$ cap layer, which blue-shift to about 1.53 µm at 10 K. The other PL envelopes with the centers blue-shifting from 2.54 µm at 300 K to about 2.27 µm at 10 K correspond to the $In_{0.83}Ga_{0.17}As$ absorption layers for all samples. The PL intensity of the $In_{0.83}Ga_{0.17}As$ absorption layers for samples A–C increased in sequence at both 300 K and 10 K, indicating that the numbers of non-radiative recombination centers decreased when the buffer scheme was changed from continuously graded $In_xAl_{1-x}As$ layer to fixed-composition $In_{0.83}Al_{0.17}As$ layer. This is in good agreement with the AFM and XRD results, and the dislocation blocking mechanism should be analyzed.

Fig. 4 shows the XTEM images of the two typical PD structures. For each sample, XTEM images were taken from three different areas. These images reveal the structure and distribution of dislocations in both the two types of InAlAs buffers. For sample A, the epitaxy of the InAlAs buffer was started with a 0.1-µm-thick $In_{0.1}Al_{0.9}As$ layer, then the continuously graded $In_xAl_{1-x}As$ layer was grown with In composition x graded from 0.1 to 0.86. Therefore, it can be seen that the misfit dislocation networks was separated by some distance from the interface between $In_{0.1}Al_{0.9}As$ and GaAs. They were distributed almost throughout the growth of the $In_xAl_{1-x}As$ (0.1 < x < 0.86) layer. As we discussed above, strain in this structure released dominantly by surface roughening, which deteriorates the surface morphology of the PD structure and leads to a large RMS roughness. And researchers have also demonstrated that stain-relieving defects originated from surface ripple troughs [13]. By this means, the misfit dislocations would be generated by gliding of dislocation half loops from the surface through the epilayer. Fig. 4(a) shows that high dense dislocation arrays accumulated in the lower area of the $In_xAl_{1-x}As$ layer. Many vertical dislocations with long dislocation length, thread from the tangling area through the epilayer along the [100] direction and propagate to the top active region of the PD structure.

Instead, when using the fixed-composition $In_{0.83}Al_{0.17}As$ layer as buffer, the dislocations are short and most of them are not perpendicular to the sample surface, as shown in Fig. 4(b). It has been proven that the dislocation generation mechanism in the hetero-epitaxy of $In_xGa_{1-x}As$ (0 < x < 1) on GaAs could be also affected by the initial growth mechanism except for the lattice mismatch [14]. The relaxation process in sample C may start with a layer-to-island transition (Stranski–Kranstanov growth mode) after the deposition of a couple MLs of $In_{0.83}Al_{0.17}As$ on GaAs with the lattice mismatch of 5.9%. Above the critical thickness, the accumulated strain in the two dimensional [2D] $In_{0.83}Al_{0.17}As$ buffer layer will release by the formation of three-dimensional [3D] structures [15,16]. Thus the $In_{0.83}Al_{0.17}As$ QDs will form at the beginning of growth of the fixed-composition $In_{0.83}Al_{0.17}As$ layer. Then large numbers of misfit dislocations would generate, react and form misfit dislocations networks to release the large compressive strain. In this way, the formation of $In_{0.83}Al_{0.17}As$ QDs at the initial stage of the buffer layer may provide high density of nucleation sites [8] and act as core of misfit dislocations. This brings large degree of relaxation and only small residue strain remaining in the following epilayers, as shown in Table 1. The relaxation process is promptly due to the substantial lattice mismatch and the core locates close to the $In_{0.83}Al_{0.17}As$/GaAs interface. This is in accord with the small critical thickness value of $In_{0.83}Al_{0.17}As$ due to the relatively large lattice mismatch with GaAs. Therefore, most of the misfit dislocations are inhibited to propagate a long distance by the island growth at the interface in sample B. Moreover, many point defects would exist in the high In content $In_{0.83}Al_{0.17}As$ layer, which may also interact with misfit dislocations and block their movements. This also enhances the possibility of threading dislocation annihilation. Therefore, sample B with fixed-composition $In_{0.83}Al_{0.17}As$ buffer shows a relatively low threading dislocation density, even though the multiplication of dislocations happened with increasing the thickness of $In_{0.83}Al_{0.17}As$. Therefore, introducing QDs to the interface between the $In_{0.83}Al_{0.17}As$ buffer and the GaAs substrate will be beneficial to reducing threading dislocation density in the $In_{0.83}Ga_{0.17}As$ absorption layer. It is expected that the action of QDs will be enhanced by inserting a thin InAs wetting layer at the $In_{0.83}Al_{0.17}As$/GaAs interface because of a higher lattice mismatch. However, a larger thickness of the InAs wetting layer may bring about undesired effects such as degraded interfacial quality of the relaxed InAs layer. This explains the variation trends of FWHM values of XRD for samples C and D.

As a result, the $In_{0.83}Al_{0.17}As$ layer grown atop on the 5 MLs InAs QD/fixed-composition $In_{0.83}Al_{0.17}As$ buffer would be acted as a final virtual substrate, which may favor the growth of the $In_{0.83}Ga_{0.17}As$ PD structure because they match well with each other. Further mesa
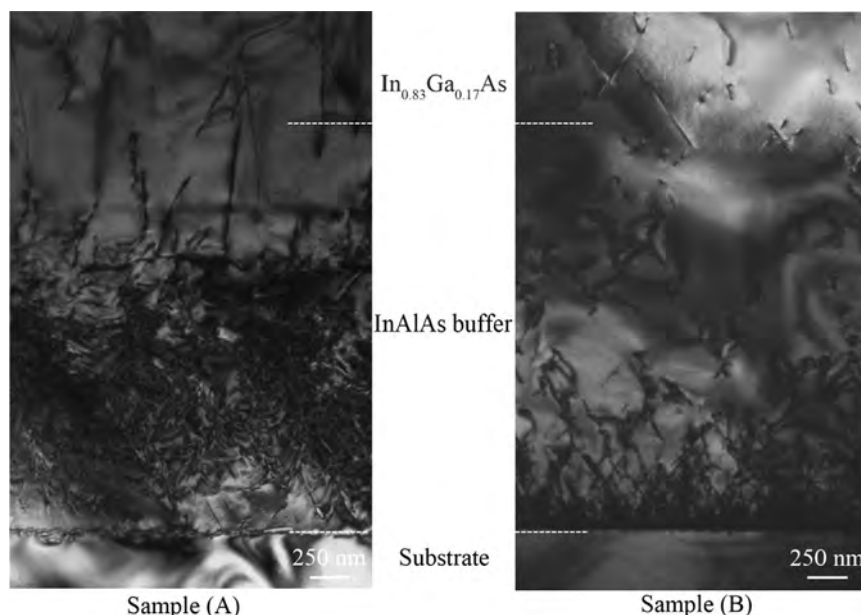
Fig. 4. XTEM images of (a) sample A and (b) sample B.

device studies will check the material qualities and the thickness and the growth temperature of the $In_{0.83}Al_{0.17}As$ buffer layer should be optimized in the next step.

4. Conclusion

In conclusion, characteristics of GaAs-based $In_{0.83}Ga_{0.17}As$ PD structures were compared by utilizing different InAlAs buffer strategies. The normal scans of a 4-circle X-ray diffraction indicated that a higher strain relaxation degree of PD structures with fixed-composition $In_{0.83}Al_{0.17}As$ buffer than that with continuously graded InAlAs buffer. The RMS roughness, structural and optical properties of $In_{0.83}Ga_{0.17}As$ PD structures can be improved by using fixed-composition $In_{0.83}Al_{0.17}As$ buffer as well. It is also essential to reduce the strain energy caused by the relatively high lattice mismatch by designing interfacial intermediate layer. This would help confine the threading dislocation in the inactive region by introduction of interfacial dislocations. The use of fixed-composition $In_{0.83}Al_{0.17}As$ buffer may be beneficial in the metamorphic device design because of faster lattice relaxation process and better structural characteristics.

Acknowledgments

References

[1] R.W.M. Hoogeveen, A.R.J. van der, A.P.H. Goede, Infrared Phys. Technol. 42 (1) (2001) 1–16.
[2] P. Merken, L. Zimmermann, J. John, G. Borghs, C.V. Hoof, S. Nemeth, Electron. Lett. 38 (2002) 588–590.
[3] Y.G. Zhang, Y. Gu, Gas source MBE Grown Wavelength Extending InGaAs Photodetectors, Chapter 17, InTech, 2011, ISBN: 978-953-307-163-3.
[4] L. Zhou, Y.G. Zhang, X.Y. Chen, Y. Gu, Hsby. Li, Y.Y. Cao, S.P. Xi, J. Phys. D Appl. Phys. 47 (2014) 085107.
[5] X.Y. Chen, Y.G. Zhang, Y. Gu, L. Zhou, Y.Y. Cao, X. Fang, Hsby. Li, J. Cryst. Growth 39 (2014) 75–80.
[6] X. Fang, Y. Gu, Y.G. Zhang, L. Zhou, K. Wang, Hsby. Li, K.H. Liu, Y.Y. Cao, J. Infrared Millim. Waves 32 (2013) 481–490.
[7] S.B. Samavedan, E.A. Fitzgerald, J. Appl. Phys. 81 (1997) 3108.
[8] Y.X. Song, S.M. Wang, I. Tangring, Z.H. Lai, M. Sadeghi, J. Appl. Phys. 106 (2009) 123531.
[9] J. Tersoff, Appl. Surf. Sci. 102 (1996) 1–2.
[10] R.M. France, J.F. Geisz, M.A. Steiner, B. To, M.J. Romero, W.J. Olavarria, R.R. King, J. Appl. Phys. 111 (2012) 103528.
[11] A.M. Andrews, J.S. Speck, A.E. Romanov, M. Bobeth, W. Pompe, J. Appl. Phys. 91 (2002) 1933.
[12] J.E. Ayers, J. Cryst. Growth 135 (1994) 71.
[13] A.G. Cullis, A.J. Pidduck, M.T. Emeny, Phys. Rev. Lett. 75 (12) (1995) 2368.
[14] S.Z. Chang, T.C. Chang, S.C. Lee, J. Appl. Phys. 73 (1993) 4916.
[15] G.Y. Zhou, Y.H. Chen, C.G. Tang, L.Y. Liang, P. Jin, Z.G. Wang, J. Appl. Phys. 108 (2010) 083513.
[16] F. Patella, F. Arciprete, M. Fanfoni, A. Balzarotti, Appl. Phys. Lett. 88 (2006) 161903.

CRYSTAL
GROWTH

ELSEVIER
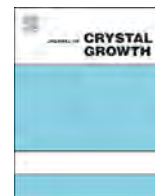
XBₙn and XBₚp infrared detectors

P.C. Klipstein *

SemiConductor Devices, P.O. Box 2250, Haifa 31021, Israel

ARTICLE INFO

ABSTRACT

XBₙn and XBₚp barrier detectors grown from III–V materials on GaSb substrates have recently been shown to exhibit a low diffusion limited dark current and a high quantum efficiency. Two important examples are InAsSb/AlSbAs based XBₙn devices with a cut-off wavelength of $\lambda_C \sim 4.1$ μm, and InAs/GaSb Type II superlattice (T2SL) based XBₚp devices, with $\lambda_C \sim 9.5$ μm. The former exhibit background limited performance (BLIP) at F/3 up to ~ 175 K, which is a much higher temperature than observed in standard generation-recombination limited devices, such as InSb photodiodes operating in the same Mid Wave IR atmospheric window. The Long Wave IR (LWIR) T2SL XBₚp device has a BLIP temperature of ~ 100 K at F/2. Using the $\mathbf{k} \cdot \mathbf{p}$ and optical transfer matrix methods, full spectral response curves of both detectors can be predicted from a basic knowledge of the layer thicknesses and doping. The spectral response curves of LWIR gallium free InAs/InAs$_{1-x}$Sb$_x$ barrier devices have also been simulated. These devices appear to have a lower quantum efficiency than the equivalent InAs/GaSb XBₚp devices.

© 2015 Elsevier B.V. All rights reserved.

1. Introduction

High performance photodiode Focal Plane Array (FPA) detectors that operate in the Mid or Long Wave Infra-Red (MWIR or LWIR) "windows" of the atmosphere are often made from Mercury Cadmium Telluride (MCT), because of the potential tunability of the band gap and the low "diffusion" limited dark current [1]. However, the need for high quality Cadmium Zinc Telluride substrates makes them expensive and difficult to scale to large areas. For this reason InSb FPAs are often preferred in the MWIR, even though they must operate at a few tens of degrees colder, in order to suppress the generation-recombination (G-R) current created in the photodiode depletion region [2]. Recently, InAs/GaSb Type II superlattices (T2SLs) have emerged as another competitor to MCT because, like MCT, they also offer tunability over the full MWIR and LWIR ranges. Although they are also G-R limited, the G-R problem has recently been overcome using a patented XBₙn/XBₚp technology [3,4] which can be implemented in the MWIR or LWIR in III–V devices grown on commercial GaSb substrates. It provides a low diffusion limited dark current as in MCT, but with many of the advantages of III–V materials, including the potential for scalability to large areas at affordable cost. In this work barrier devices grown lattice matched to GaSb are discussed based on a bulk InAsSb/AlSbAs XBₙn architecture for the MWIR and an InAs/GaSb T2SL XBₚp architecture suitable for both the

MWIR and LWIR. The T2SL results are compared with those of an alternative T2SL design, based on InAs/InAs$_{1-x}$Sb$_x$.

2. XBₙn devices

Schematic band diagrams for an InAsSb XBₙn detector at operating bias [5] are shown in Fig. 1. The detector has a cut-off wavelength close to 4.1 μm and is based on a heterostructure design that can be grown with high quality on GaSb or even GaAs [6] substrates, using Molecular Beam Epitaxy (MBE). The device contains an n- or p-type contact layer made from InAs$_{1-x}$Sb$_x$ or GaSb (X), a barrier layer made from n-type AlSb$_{1-y}$As$_y$ (Bₙ), and an active layer made from n-type InAs$_{1-x}$Sb$_x$ (n). By excluding the depletion region from the photon absorbing layer the G-R current is strongly suppressed. Exclusion is achieved by ensuring that the barrier and photon absorbing layers are both doped n-type. It also creates the interesting situation of a completely unipolar nBₙn device which behaves in many ways like a photovoltaic detector with a gain of one, even though it contains no p–n junction [4].

When the G-R current is suppressed, the result is a large increase in operating temperature for a detector with a given dark current, as depicted by the red arrow in Fig. 2. As shown in the Figure, the G-R current has a lower slope than the diffusion current, because it is activated with approximately half the energy. The two contributions are equal at the crossover temperature T_0, which increases with the active layer (AL) band gap energy [5]. The effect of changing the barrier layer (BL) polarity is shown in Fig. 3. If the barrier has the opposite doping polarity to the

* Fax: +972 4 990 2686.
E-mail address: philip_k@scd.co.il
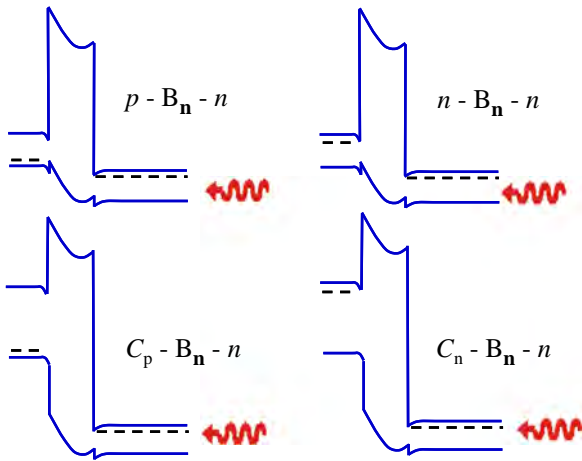
Fig. 1. The four contact configurations of an XB_nn device (shown at operating bias).
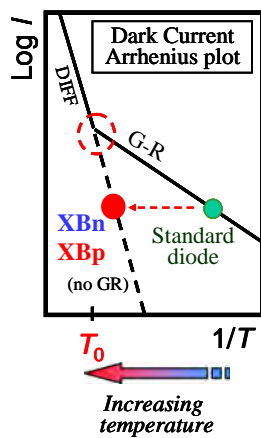
Fig. 2. Schematic T-dependence of I_{dark} in a p–n diode (green dot) and a XB_nn or XB_pp barrier detector (red dot) with the same active layer material. (For interpretation of the references to colour in this figure legend, the reader is referred to the web version of this article.)
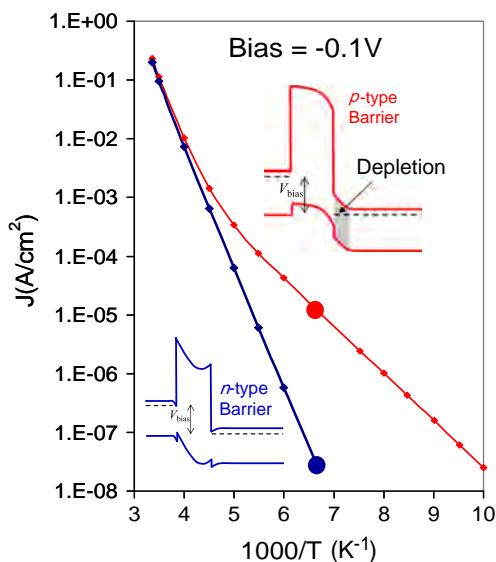
Fig. 3. Log J_{dark} vs $1000/T$ for two identical InAsSb/AlSbAs nBn devices with opposite barrier doping polarities (red $= p$, blue $= n$). Active layer band gap wavelength, $\lambda_G = 4.1\ \mu m$ at 150 K (Insets: band profiles at operating bias). (For interpretation of the references to colour in this figure legend, the reader is referred to the web version of this article.)

photon absorbing layer, then a depletion region develops in the photon absorbing layer and a large G-R current ensues. Fig. 3 shows two nominally identical devices with opposite barrier polarities, each operating at a bias of -0.1 V. The nB_nn device exhibits a single straight line, characteristic of diffusion limited behaviour, while the nB_pn device exhibits two slope behaviour, characteristic of a crossover from diffusion limited behaviour at high temperatures to G-R limited behaviour at low temperatures. The dark current at 150 K (enlarged points in Fig. 3) is $100\times$ greater for the detector with the p-type barrier because it is already G-R limited. For a typical quantum efficiency of 70% at F/3, this results in a lower background limited performance (BLIP) temperature of ~ 140 K, compared with ~ 175 K for the detector with the n-type barrier. The BLIP temperature is defined as the temperature at which the dark current equals the photocurrent.

Fig. 4 shows a series of images registered at F/3.2 and different operating temperatures up to 225 K for a 15 μm pitch FPA detector flip-chip bonded to SCD's Pelican-D 640 $\times$ 512 digital silicon read-out integrated circuit (ROIC). The FPA has a quantum efficiency (QE) of ~ 80%. There is no discernable degradation in image quality until ~ 193 K, as expected for a BLIP temperature of ~ 175 K. Such high imaging temperatures, up to nearly 200 K, allow considerable reductions in size, weight and power of the complete integrated XB_nn detector/cooler assembly. Further details of the radiometric performance of these XB_nn detectors may be found in Refs. [7,8].

3. XB_pp devices

In this section two types of barrier device will be discussed, where the active layer is based on a InAs/GaSb T2SL or a gallium free InAs/InAs$_{1-x}$Sb$_x$ T2SL, in all cases lattice matched to a GaSb substrate. The latter have attracted attention recently due to their longer minority carrier lifetime in low doped material [9,10]. Since the T2SL valence mini-band is generally very narrow and small hole mobilities have been reported in several cases [11,12], the present analysis is based on a pB_pp architecture, where the minority carriers in the AL are electrons.

3.1. InAs/GaSb

Fig. 5(a) shows a schematic band structure for an XB_pp device based on an InAs/GaSb T2SL AL and a InAs/AlSb T2SL BL. The individual InAs layers are terminated with indium and the AlSb or GaSb layers are terminated with antimony, in order to create "InSb" like interfaces with the correct amount of strain for lattice matching between the T2SL and the GaSb substrate [13]. In (b) the edges of the mini-bands shown in (a) are sketched for a unipolar pB_pp device at operating bias, where all T2SL regions are doped p-type [4]. The advantage of the barrier device is demonstrated in Fig. 6, which compares the dark current in a standard LWIR n-on-p diode based solely on InAs/GaSb, with that for a LWIR pB_pp device based on the design in Fig. 5. Both devices have a p-type AL with a band gap wavelength close to 10 μm. The barrier device (blue) is diffusion limited down to 77 K, while the diode (red) is G-R limited at this temperature, with a dark current over $20\times$ larger (solid points). The dark current in our pB_pp devices is within one order of magnitude of MCT Rule-07 [14], which is the performance standard for state of the art MCT photo-diodes [1].

In order to predict the detector photo-response, it is first necessary to calculate the T2SL absorption spectrum. Fig. 7 shows measured (grey) and simulated (black) absorption spectra at 77 K for two InAs/GaSb T2SL structures with cut-off wavelengths in the MWIR and LWIR respectively. The widths of the individual InAs and GaSb layers in a single period were determined with a typical accuracy of 0.2 monolayers (MLs), by finding a single pair of rate
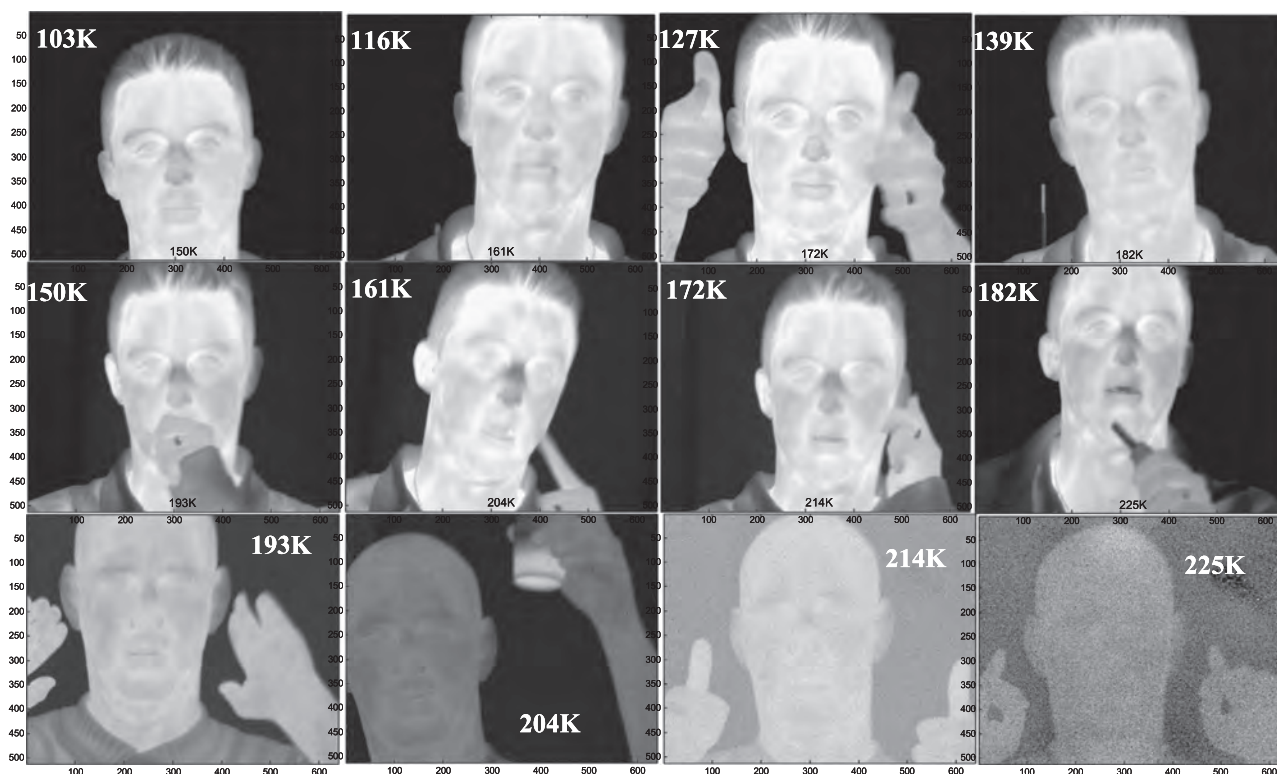
Fig. 4. Images at FPA temperatures between 103 and 225 K for a 15 μm pitch 640 × 512 XB$_n$n FPA at F/3.2.
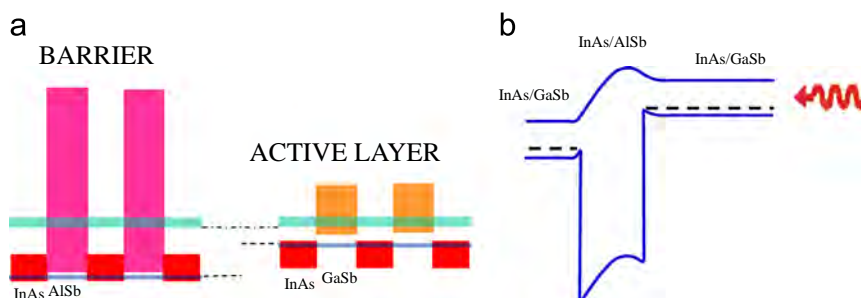
Fig. 5. (a) Alignment between mini-bands in the active and barrier layers of a T2SL XB$_p$p device, super-imposed on the band gaps of InAs, GaSb and AlSb. (b) Schematic profile of band edges in an operating pB$_p$p device, based on the mini-bands shown in (a).

constants that when multiplied by the measured group III beam fluxes and shutter timings of the MBE reactor gave the best fit to the precisely measured periods of over 30 different T2SLs [13]. The layer widths of the MWIR and LWIR InAs/GaSb T2SLs in Fig. 7 were 8.4/13.7 ML and 14.4/7.2, respectively. The absorption spectra for these layer widths were calculated using the $\mathbf{k} \cdot \mathbf{p}$ treatment described in Ref. [13]. This treatment has only seven fitting parameters which are two independent Luttinger parameters (γ_1 and γ_2 for InAs, from which the non-independent parameters, γ_3 of InAs and γ_1, γ_2 and γ_3 of GaSb are calculated), three interface parameters, the valence band offset, and an optical matrix element scaling parameter. It can be seen that the simulated spectra reproduce the measured spectra quite well, including a large peak at 2–3 μm due to a very high joint density of states (JDOS) for $HH_2 \rightarrow E_1$ transitions which are allowed at the zone boundary.

Using the simulated absorption spectra it is possible to calculate the full spectral response of an FPA detector with a InAs/GaSb AL, based on an optical transfer matrix technique [15]. In the present case it is assumed that the detector is ideal with no losses of photo-carriers due to recombination in the bulk or at the surface [16]. Fig. 8 compares the simulated and measured QE values at 77 K (weighted by the 300 K black body radiation

spectrum and averaged over a spectral window of 7.6–9.5 μm) for a series of LWIR pB$_p$p test devices with AL thickness values from 1.5–6.0 μm and a cut-off wavelength of ∼9.5 μm. Details of the method of measurement are given in Ref. [17]. Although the InAs/AlSb BL makes no contribution to the response, the $\mathbf{k} \cdot \mathbf{p}$ treatment described above is also used to design the correct layer widths in the BL of the grown devices [16]. The solid line in Fig. 8 is for the simulation when no anti-reflection coating (ARC) is used and the dashed line is when an ARC is used. The detector structures include a mirror on the contact layer (CL) to reflect 80% of the light back for a second pass. Measured QE values are shown as points and they all appear quite close to the respective simulated curves. Fig. 8 shows that it is possible to achieve QE values above 60% for an AL thickness of 4.5 μm.

The inset in Fig. 8 shows the typical bias dependence of the QE at 77 K for a 100 × 100 μm^2 test device. The signal does not reach its full value until a positive applied bias of ∼0.6 V, because this bias is needed to overcome the electrostatic barrier to minority carriers caused by the negative space charge in the depleted p-type BL (see Fig. 5(b)). This behaviour is typical of XB$_n$n and XB$_p$p barrier devices and highlights the dependence of the operating bias (V_{OP}) on barrier doping (N_A) and width (W). Both

of these parameters increase the height of the electrostatic barrier and thus increase the operating bias. The operating bias varies approximately as $V_{OP}=V_0+aN_AW^2$, where V_0 is a small constant and a is also a constant.

3.2. InAs/InAsSb

The measured and simulated absorption spectra for a 12.8/12.8 InAs/InAs$_{0.815}$Sb$_{0.185}$ T2SL at 77 K are shown as solid lines in Fig. 9(a). Parameter values used in the fit are given in Ref. [16]. Unlike for the case of no common atom superlattices such as InAs/GaSb where the interface parameters make a large first order contribution and thus play a critical role, in common atom superlattices such as InAs/InAs$_{1-x}$Sb$_x$ the interface contribution is due to a much weaker second order interaction and it has been assumed that for these superlattices it can safely be neglected [16,18]. Fig. 9 shows that this assumption is justified because there is good agreement between measurement and simulation, with the main features in the measured spectrum also appearing in the calculation. The period of the simulated T2SL is very close to that

measured by high resolution X-ray diffraction and the composition of the layers is close to that deduced from the calibration of the MBE growth. It should be noted that in this T2SL the ternary material exhibits very strong bowing of its bandgaps and Luttinger parameters. Since experimental measurements of the former are well documented in the literature [19], while the latter are calculated from values already determined above for γ_1 and γ_2 in InAs, our $\mathbf{k} \cdot \mathbf{p}$ treatment is able to handle the bowing effects quite efficiently [16]. Also shown in Fig. 9(a) as a dashed line is the measured absorption spectrum of a 8.5/10.8 InAs/GaSb T2SL with the same cut-off wavelength as the gallium free T2SL (a $\mathbf{k} \cdot \mathbf{p}$ treatment of this T2SL may be seen in Ref. [13]). The InAs/GaSb T2SL has a larger and more abrupt absorption edge than the InAs/InAs$_{0.815}$Sb$_{0.185}$ T2SL, although at shorter wavelengths the spectra effectively merge. The more abrupt absorption edge for InAs/GaSb T2SLs is probably attributable to a more step-like two-dimensional JDOS, where both electrons and holes have large band offsets. In

Fig. 6. Log J_{dark} vs. 1000/T in pB_pp barrier device (bias=0.6V) and n–p diode (bias=0.1V), each with a p-type InAs/GaSb active layer with a bandgap wavelength of $\lambda_G \sim 10\,\mu m$ (mesa area=100×100 μm^2). Solid points are for 77 K. (For interpretation of the references to colour in this figure, the reader is referred to the web version of this article.)
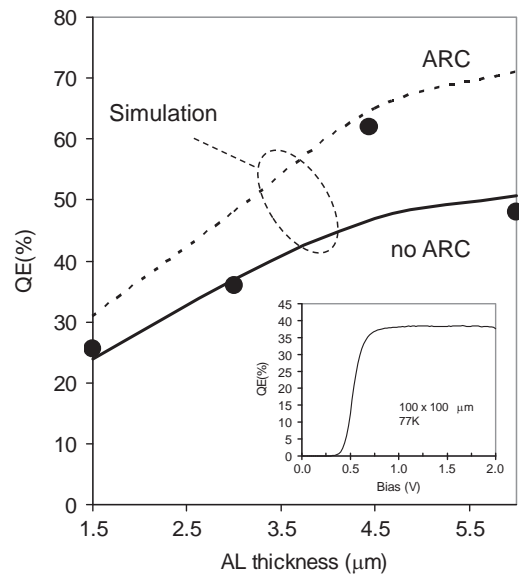
Fig. 8. Simulated (lines) and measured (dots) QE values at 77 K averaged over the 300 K black body spectrum from 7.6 μm to the cut-off wavelength of $\sim 9.5\,\mu m$, for pB_pp test devices with AL thicknesses from 1.5–6.0 μm. The simulation assumes there are no losses of photo-generated carriers. An anti-reflection coating (ARC) is included for the dashed line. A mirror on the contact layer reflects 80% of the light back for a second pass through the AL. Inset: example of QE vs. bias for a 100 × 100 μm^2 test device.

Fig. 7. Measured (solid grey) and simulated (solid black) absorption spectra at 77 K for (a) 8.4/13.7 MWIR and (b) 14.4/7.2 LWIR InAs/GaSb T2SLs (dimensions in ML). The large peaks at short wavelengths are from zone boundary $HH_2 \rightarrow E_1$ transitions. The dip at ~4.2 μm in the measured spectra is an artifact due to strong atmospheric absorption and can be ignored.
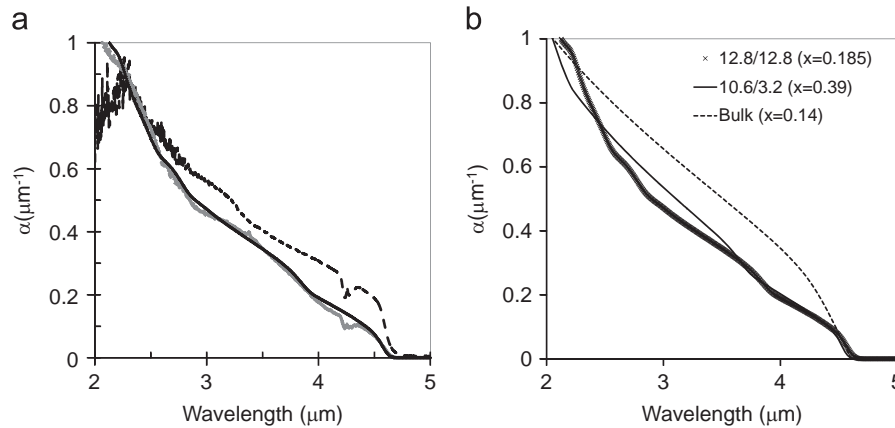
Fig. 9. Comparison of absorption spectra at 77 K showing (a) measured (solid grey) and simulated (solid black) spectra for a 12.8/12.8 InAs/InAs$_{0.815}$Sb$_{0.185}$ T2SL (dashed line is a comparison with the measured spectrum of a 8.5/10.8 InAs/GaSb T2SL) and (b) simulated spectra for a 12.8/12.8 InAs/InAs$_{0.815}$Sb$_{0.185}$ T2SL (points), a 10.6/3.2 InAs/InAs$_{0.61}$Sb$_{0.39}$ T2SL (solid line) and bulk InAs$_{0.86}$Sb$_{0.14}$ (dashed line).

the gallium free case, the conduction band offset is quite small giving a more three-dimensional electron dispersion, and hence a less abrupt JDOS.

Fig. 9(b) shows that increasing the antimony content of the InAs$_{1-x}$Sb$_x$ T2SL layer from $x=0.185$ (crosses) to $x=0.39$ (solid line) has almost no effect on the absorption coefficient in the 3–5 μm wavelength range. The layer thicknesses are changed from 12.8/12.8 to 10.6/3.2 in order to maintain the same cut-off wavelength. For comparison, a bulk layer with $x=0.14$ is also shown. The bulk absorption coefficient is calculated using the phenomenological formula derived in Ref. [15]. It is significantly larger than for the T2SLs, but the bulk material is no longer lattice matched to a GaSb substrate. For lattice matched InAs/InAs$_{1-x}$Sb$_x$ T2SLs, it seems that the region of greatest practical interest near the absorption edge has relatively little sensitivity to antimony content, provided the T2SL period is small enough for there to be significant confinement of both electrons and holes.

Finally the spectral response at 77 K has been calculated for two LWIR pB$_p$$p$ detectors, in which the AL is either a 13.8/7 InAs/GaSb T2SL or a 31.5/9.5 InAs/InAs$_{0.61}$Sb$_{0.39}$ T2SL. In each case the cut-off wavelength is 9.9 μm, chosen because it is well matched to the LWIR atmospheric transmission window. Both detectors reflect 80% of the light back for a second pass through the AL which has a thickness of 5 μm, and it is assumed, as above, that there are no losses of photo-carriers at the surface or in the bulk. The back-side of the detector has an anti-reflecting coating, and the response spectrum was averaged over several different thicknesses of a transparent thin GaSb substrate in order to suppress Fabry–Perot oscillations. When averaged over the 300 K black body radiation spectrum in the LWIR atmospheric window (from 7.6 to 9.8 μm), the average QE is $<\text{QE}>=44\%$ for the InAs/InAs$_{0.61}$Sb$_{0.39}$ T2SL and $<\text{QE}>=67\%$ for the InAs/GaSb T2SL. For this AL thickness, the gallium free T2SL is thus expected to exhibit about 2/3 of the QE of the InAs/GaSb T2SL. In fact, the present model can be used to show that the absorption coefficient increases slightly at higher antimony content and the average QE can thus be increased to 49% for the same cut-off wavelength in a 20.5/3.7 gallium free T2SL with $x=0.6$. However, the cut-off wavelength then becomes very sensitive to small variations in the thickness of the ternary layer, and there may also be issues of Sb segregation at such high antimony concentrations [20].

It should be mentioned that although the InAs/AlSb BL has a valence band offset (VBO) with respect to the LWIR InAs/GaSb AL of more than twice the AL band gap, the VBO in the case of the InAs/InAs$_{0.61}$Sb$_{0.39}$ AL is predicted to be slightly less than the AL bandgap. This VBO is less than the minimum value required for a diffusion limited dark current, which in general should be greater than the AL bandgap [3,4,5]. Although the result of the model is somewhat sensitive to the values of the interface parameters deduced for the InAs/AlSb T2SL in Ref. [16], it highlights the fact that the band edges in InAs/InAs$_{1-x}$Sb$_x$ T2SLs are lower in energy than those in InAs/GaSb T2SLs. The use of gallium free T2SLs in diffusion limited pB$_p$$p$ detectors with an InAs/AlSb BL is therefore limited to cut-off wavelengths longer than some minimum value, which is in the region of 10 μm. In order to make a gallium free diffusion limited device with a shorter cut-off wavelength, one possibility is to use an nB$_n$$n$ structure, for example with an AlGaSbAs alloy BL which has a very large conduction band offset. However, such a detector may suffer from a low minority carrier mobility due to the very narrow T2SL valence band dispersion. This case has been discussed in detail in Ref. [16], where the hole diffusion length was estimated to be ~1 μm by scaling results reported for an InAs/GaSb T2SL with a similar valence band structure. If the hole diffusion length falls below the AL thickness, the QE is reduced significantly from that shown in Fig. 10, due to poor carrier collection. However, in the light of recent measurements by Haddadi et al. [21], the hole diffusion length in the InAs/InAs$_{1-x}$Sb$_x$ T2SL may in fact be significantly larger (≥ 6 μm). Its effect on the QE will then be much less than previously suggested.

4. Summary

MWIR XB$_n$$n$ and LWIR XB$_p$$p$ barrier devices have been fabricated from InAsSb/AlSbAs and InAs/GaSb T2SL heterostructures, respectively. In each case it has been possible to achieve a high QE and a diffusion limited dark current close to the MCT Rule-07 value. This has led to a high BLIP temperature of ~175 K at F/3 for the MWIR device, and ~100 K at F/2 for the LWIR device. The measured QE of T2SL detectors with AL thicknesses between 1.5 and 6 μm agrees quite well with that predicted from a model based on $\mathbf{k} \cdot \mathbf{p}$ theory and an optical transfer matrix calculation, assuming no losses of photo-generated carriers (internal QE of 100%). The same model has also been used to simulate the absorption coefficient of InAs/InAs$_{1-x}$Sb$_x$ T2SLs, and to compare the spectral response curves of pB$_p$$p$ devices based on T2SLs of both types. For short period gallium free structures, the absorption spectrum appears to exhibit little dependence on antimony concentration over a useful range of wavelengths near the absorption edge, especially for MWIR T2SLs, and shows good agreement with experiment for the case of a 12.8/12.8 InAs/InAs$_{0.815}$Sb$_{0.185}$ T2SL with a cut-off wavelength of ~4.6 μm. For an optimised LWIR
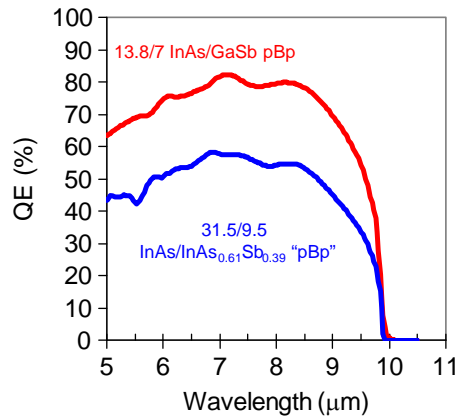
Fig. 10. Simulated spectral response for pB_pp detectors with antireflection coatings and no losses of photo-generated carriers, based on a 13.8/7 InAs/GaSb T2SL (red) and a 31.5/9.5 InAs/InAs$_{0.61}$Sb$_{0.39}$ T2SL (blue). 80% of the light is reflected back for a second pass and AL thickness is 5 μm. (For interpretation of the references to colour in this figure legend, the reader is referred to the web version of this article.)

pB_pp detector made from a 5 μm thick InAs/GaSb T2SL AL with a cut-off wavelength of 9.9 μm (and an InAs/AlSb T2SL BL), a model of the spectral response predicts a QE of ~67% when averaged over the 300 K black body radiation spectrum in a transmission window from 7.6 to 9.8 μm. For the equivalent detector based on an InAs/InAs$_{0.61}$Sb$_{0.39}$ T2SL, however, the predicted average QE is only about 2/3 of the InAs/GaSb value. This difference can be attributed to the smaller absorption coefficient of the InAs/InAs$_{1-x}$Sb$_x$ T2SL near the cut-off wavelength. Since the bands of the gallium free T2SL are lower than those for an InAs/GaSb T2SL, it was also noted that an InAs/AlSb T2SL BL appears to be too low for diffusion limited behaviour in a gallium free pB_pp device when the AL cut-off wavelength is shorter than about 10 μm. For this wavelength range an nB_nn architecture can be used with a tall AlGaSbAs alloy BL. However, device performance may be affected by the narrow T2SL valence mini-band and hence a short hole diffusion length.

Acknowledgements

References

[1] W.E. Tennant, in: Proceeding of the U.S. Workshop on the Physics & Chemistry of II–VI Materials, Chicago, 2009.
[2] A. Glozman, E. Harush, E. Jacobsohn, O. Klin, P.C. Klipstein, T. Markovitz, V. Nahum, E. Saguy, J. Oiknine-Schlesinger, I. Shtrichman, M. Yassen, B. Yofis, E. Weiss, Proc. SPIE 6206 (2006) 62060M.
[3] P.C. Klipstein, Depletionless photodiode with suppressed dark current…, US Patent 7,795,640, 2 July 2003.
[4] P.C. Klipstein, Unipolar semiconductor photodetector with suppressed dark current…, US Patent 8,004,012, 6 April 2006.
[5] P.C. Klipstein, XB*n* barrier photodetectors for high sensitivity and high operating temperature infrared sensors, Proc. SPIE 6940 (2008) 6940-2U.
[6] E. Weiss, O. Klin, S. Grossmann, N. Snapi, I. Lukomsky, D. Aronov, M. Yassen, E. Berkowicz, A. Glozman, P.C. Klipstein, A. Fraenkel, I. Shtrichman, J. Cryst. Growth 339 (2012) 31.
[7] P.C. Klipstein, Y. Gross, D. Aronov, M. ben Ezra, E. Berkowicz, Y. Cohen, R. Fraenkel, A. Glozman, S. Grossman, O. Klin, I. Lukomsky, T. Markowitz, L. Shkedy, I. Strichman, N. Snapi, A. Tuito, M. Yassen, E. Weiss, Proc. SPIE 8704 (2013) 87041S.
[8] Y. Karni, E. Avnon, M. ben Ezra, E. Berkowicz, O. Cohen, Y. Cohen, R. Dobromislin, I. Hirsh, O. Klin, P.C. Klipstein, I. Lukomsky, M. Nitzani, I. Pivnik, O. Rozenberg, I. Shtrichman, M. Singer, S. Sulimani, A. Tuito, E. Weiss, Proc. SPIE 9070 (2014) 90701F.
[9] E.H. Steenbergen, B.C. Connelly, G.D. Metcalfe, H. Shen, M. Wraback, D. Lubyshev, Y. Qiu, J.M. Fastenau, A.W.K. Liu, S. Elhamri, O.O. Cellek, Y.-H. Zhang., Appl. Phys. Lett. 99 (2011) 251110.
[10] B.V. Olson, E.A. Shaner, J.K. Kim, J.F. Klem, S.D. Hawkins, L.M. Murray, J.P. Prineas, M.E. Flatté, T.F. Boggess, Appl. Phys. Lett. 101 (2012) 092109.
[11] R. Rehm, M. Walther, J. Schmitz, F. Rutz, A. Wörl, R. Scheibner, J. Ziegler, Proc. SPIE 7660 (2010) 76601G.
[12] B.V. Olson, (Ph. D. thesis), University of Iowa, ⟨http://ir.uiowa.edu/etd/2596⟩, 2013.
[13] Y. Livneh, P.C. Klipstein, O. Klin, N. Snapi, S. Grossman, A. Glozman, E. Weiss, Phys. Rev. B 86 (2012) 235311;
Y. Livneh, P.C. Klipstein, O. Klin, N. Snapi, S. Grossman, A. Glozman, E. Weiss Erratum, Phys. Rev. B 90 (2014) 039903.
[14] P.C. Klipstein, E. Avnon, Y. Benny, R. Fraenkel, A. Glozman, S. Grossman, O. Klin, L. Langoff, Y. Livneh, I. Lukomsky, M. Nitzani, L. Shkedy, I. Shtrichman, N. Snapi, A. Tuito, E. Weiss, Proc. SPIE 9070 (2014) 90700U.
[15] P.C. Klipstein, O. Klin, S. Grossman, N. Snapi, B. Yaakobovitz, M. Brumer, I. Lukomsky, D. Aronov, M. Yassen, B. Yofis, A. Glozman, T. Fishman, E. Berkowicz, O. Magen, I. Strichman, E. Weiss, Proc. SPIE 7608 (2010) 76081V.
[16] P.C. Klipstein, Y. Livneh, A. Glozman, S. Grossman, O. Klin, N. Snapi, E. Weiss J. Electron. Mater. 43 (2014) 2984.
[17] P.C. Klipstein, O. Klin, S. Grossman, N. Snapi, I. Lukomsky, D. Aronov, M. Yassen, A. Glozman, T. Fishman, E. Berkowicz, O. Magen, I. Strichman, E. Weiss, Opt. Eng. 50 (2011) 061002.
[18] P.C. Klipstein, Y. Livneh, O. Klin, S. Grossman, N. Snapi, A. Glozman, E. Weiss, Infrared Phys. Technol. 59 (2013) 53.
[19] K.H. Hellwege , O. Madelung (Eds.), Physics of Group IV Elements and III–V Compounds, Landolt-Börnstein New Series, Group III, Vol. 17a, Springer, Berlin, 1982, pp. 634–635.
[20] R.A. Stradling, in: Proceedings of the XXVI International School of Semiconducting Compounds, Jaszowiec, 1997.;
R.A. Stradling, Acta Physica Polonica A92 (1997) 851.
[21] A. Haddadi, G. Chen, R. Chevallier, A.M. Hoang, M. Razeghi, Appl. Phys. Lett. 105 (2014) 121104.

CRYSTAL
GROWTH
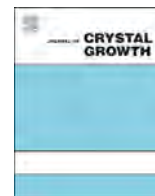
AlInAsSb for M-LWIR detectors

CrossMark

W.L. Sarney [a,*], S.P. Svensson [a], D. Wang [b], D. Donetsky [b], G. Kipshidze [b], L. Shterengas [b],
Y. Lin [b], G. Belenky [b]

[a] U.S. Army Research Laboratory, 2800 Powder Mill Rd, Adelphi, MD 20783, United States
[b] Dept. of Electrical and Computer Engineering, Stony Brook University, Stony Brook, NY 11794, United States

A R T I C L E   I N F O

A B S T R A C T

Growth of unrelaxed and unstrained $Al_zIn_{1-z}As_ySb_{1-y}$ with a lattice constant=6.23 Å was demonstrated. $InAs_{1-x}Sb_x$ with this lattice constant produces a bandgap corresponding to absorption in the long-wavelength infrared range. The structures were grown on GaSb substrates, using a lattice constant shifting buffer layer. Good photoluminescence intensity was shown, ranging from 2.0 to 4.5 μm, demonstrating the potential for development of multi-color infrared detectors that can cover both the mid- and long-wavelength infrared bands.

Published by Elsevier B.V.

1. Introduction

It has long been recognized that $InAs_{1-x}Sb_x$ has the smallest bandgap among the III–V compound semiconductors [1]. The bandgap is considerably smaller than that of either end-point binary due to a large bowing parameter, C. Until recently it was assumed that the value of C was 0.67 eV [2], which precluded $InAs_{1-x}Sb_x$ from reaching the long-wavelength infrared (LWIR) band. However, by using appropriately designed lattice constant shifting buffer layers, we have demonstrated that it is possible to produce unstrained and unrelaxed $InAs_{1-x}Sb_x$, which allows the true intrinsic properties of the alloy to be measured [3–7]. The bowing parameter is in fact 0.87 eV, which allows bandgaps corresponding to wavelengths over the entire 8–12 μm band [6].

$InAs_{1-x}Sb_x$ exhibits surface electron accumulation, similar to InAs [7]. This means that it is not possible to produce a p-n-diode in mesa configuration without employing an effective surface insulation process. This has not been accomplished for InAs and certainly not for long wavelength infrared (LWIR) $InAs_{1-x}Sb_x$. Detector devices can still be made using various barrier designs. [8–12]. In these types of structures a large bandgap layer is used, and surface leakage is blocked; either due to its inherent absence of surface electron accumulation and/or oxidation due to the high Al-content typically used in such designs.

It is also of interest to consider multi-color nBn detector structures using bulk $InAs_{1-x}Sb_x$ for the LWIR band. By combining it with χInAsSb with the same lattice constant, where χ could be Ga or Al, we could reach, for example, the mid-wave IR (MWIR)

range. Of the two choices we would be reluctant to employ Ga due to its general detrimental effect on minority carrier lifetimes [13] and the fact that it would require more Ga than Al to achieve the same increase of the χInAsSb bandgap. Here we will present the first study of the design and growth of $Al_zIn_{1-z}As_ySb_{1-y}$ layers with lattice constants corresponding to LWIR $InAs_{1-x}Sb_x$.

2. Experimental

The material studied here was grown in a Gen II Veeco solid-source molecular beam epitaxy (MBE) system equipped with As and Sb valved cracker sources. Epi-ready, exact-oriented (001) GaSb substrates from WaferTech LLC were used. The $Al_zIn_{1-z}As_ySb_{1-y}$ layers were grown at 415 °C at a growth rate of 1 μm/hr.

In order to estimate the required amount of Al needed to accomplish a desired increase in the InAsSb bandgap, we used the quaternary interpolation scheme proposed by Glisson et al.[14]. We used the binary bandgaps and ternary bowing parameters from reference [15], except for $InAs_{1-x}Sb_x$ where we used C=0.87 eV.

In Fig. 1 we show the predicted energy positions of the Γ, X and L valleys as a function of the Sb composition, x, in $InAs_{1-x}Sb_x$. For each x, the $InAs_{1-x}Sb_x$ lattice constant was first calculated and the mole fractions z and y of $Al_zIn_{1-z}As_ySb_{1-y}$ that lattice match to it were determined. We see that a very large range of bandgaps are achievable.

We chose a lattice constant, a=6.23 Å for this series. An AlGaInSb grade from a=6.0959 Å was used like in Refs. [3–7]. When adding Al to InAsSb the Sb/As composition needs to be appropriately adjusted. Our strategy was thus to first determine the flux ratios that produce the higher Sb/As mole fractions in InAsSb, then to use that information to achieve the a=6.23 Å lattice constant for each added amount
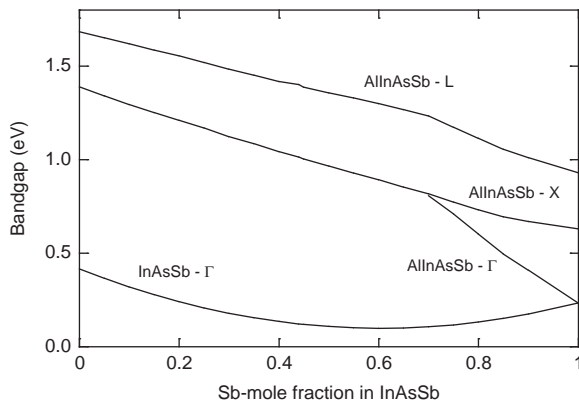
Fig. 1. The bandgaps of InAsSb and lattice matching AlInAsSb as a function of Sb-composition in InAsSb.
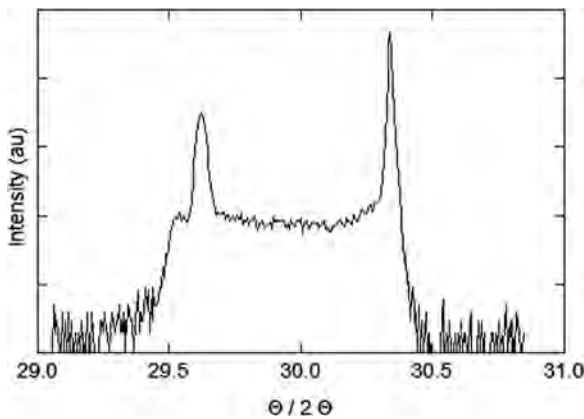
Fig. 2. Representative triple axis XRD with the Al containing peak on the left and the GaSb substrate on the right.
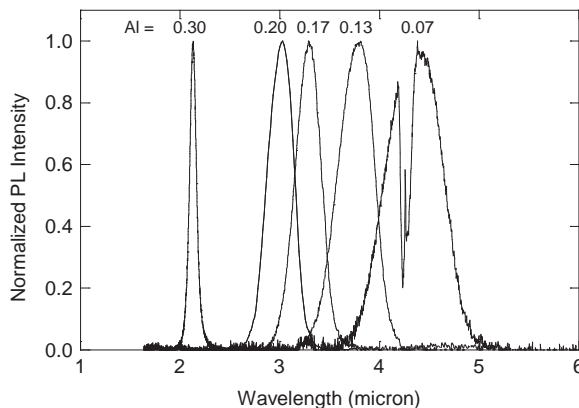
Fig. 3. Normalized photoluminescence peaks for AlInAsSb samples with a lattice constant of 6.23 Å. The range of Al-mole fractions are as noted.

of Al. The compositions and strain state were verified with symmetric (004) and asymmetric (115) triple axis x-ray diffraction (XRD) with a $180°$ rotation in phi. Fig. 2 shows a representative (004) XRD result, this particular sample had a $Al_{0.07}InAsSb_{0.47}$ (left side XRD peak) grown onto a graded structure on the GaSb substrate (right side XRD peak). The bandgaps of all films where measured at 77 K with photoluminescence (PL).

3. Results

The PL data is shown in Fig. 3. We observe strong signals for the entire sample set and we can easily cover the entire 3–5 μm, MWIR
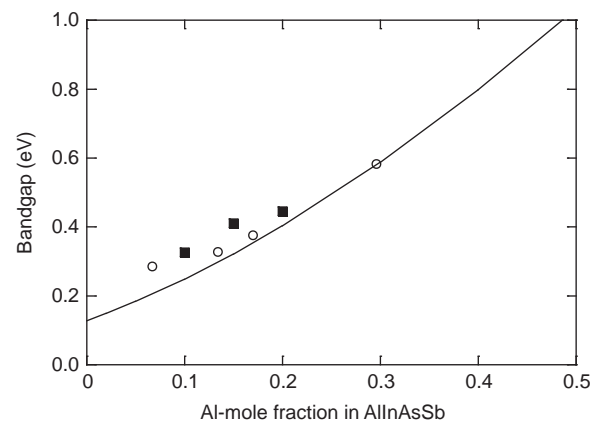
Fig. 4. $Al_zIn_{1-z}As_ySb_{1-y}$ bandgaps as a function of Al-mole fraction in AlInAsSb with a lattice constant of of 6.23 Å. The line represents the predictions using the interpolation scheme described in the text.

range. Comparing the bandgaps with the interpolation prediction in Fig. 4, we observe overall good agreement, with a few data points showing larger than expected bandgaps. The origin of this deviation is not known at present. It could possibly be due to compensating errors in the x and y compositions since the XRD shows that the $Al_zIn_{1-z}As_ySb_{1-y}$ film is very well lattice matched both in and out of plane to the underlying virtual substrate.

4. Conclusions

We have demonstrated that by using a lattice constant shifting buffer technology, the lattice constant itself can be a design parameter. We chose a lattice constant suitable for using our predetermined relationship between the Sb/As flux and the resulting group V mole fraction, to design a set of $Al_zIn_{1-z}As_ySb_{1-y}$ layers with increasing Al-content, while keeping the lattice constant the same. The structures exhibited strong PL signals corresponding to the predicted bandgaps and covered the entire MWIR band. This demonstrates the feasibility of development of multi-color monolithic, bulk III–V IR detector materials.

Acknowledgments

References

[1] A.G. Thompson, J.C. Woolley, Energy-gap variation in mixed III–V alloys, Can. J. Phys. 45 (1967) 255.
[2] Z.M. Fang, K.Y. Ma, D.H. Jaw, R.M. Cohen, G.B. Stringfellow, Photoluminescence of InSb, InAs, and InAsSb grown by organometallic vapor phase epitaxy, J. Appl. Phys. 67 (1990) 7034.
[3] G. Kipshidze, T. Hosoda, W.L. Sarney, L. Shterengas, G. Belenky, High-power 2.2-um diode lasers with metamorphic arsenic-free heterostructures, IEEE Photonics Technol. Lett. 23 (2011) 317.
[4] D. Wang, Y. Lin, D. Donetsky, L. Shterengas, G. Kipshidze, G. Belenky W.L. Sarney, H. Hier, S.P. Svensson, Unrelaxed bulk InAsSb with novel absorption, carrier transport and recombination properties for MWIR and LWIR photodetectors, Proc. SPIE 8353 (2012) 835312-1–835312-11.
[5] G. Belenky, D. Donetsky, G. Kipshidze, D. Wang, L. Shterengas, W.L. Sarney, S. P. Svensson, Appl. Phys. Lett. 99 (2011) 141116.
[6] S.P. Svensson, W.L. Sarney, H. Hier, Y. Lin, D. Wang, D. Donetsky, L. Shterengas, G. Kipshidze, G. Belenky, Band gap of InAs1 − xSbx with native lattice constant, Phys. Rev. B 86 (2012) 245205.

[7] W.L. Sarney, S.P. Svensson, H. Hier, G. Kipshidze, D. Donetsky, D. Wang, L. Shterengas, G. Belenky, Structural and luminescent properties of bulk InAsSb, J. Vac. Sci. Technol. B. 30 (2012) 02B105.

[8] S.P. Svensson, F.J. Crowne, H.S. Hier, W.L. Sarney, W.A. Beck, Y. Lin, D. Donetsky, S. Suchalkin, G. Belenky, Background and Interface Electron Populations in InAs0.58Sb0.42, Semiconductor Science & Technology 30 (2015) 035018.

[9] A.M. White, Infrared Detectors, U.S. Patent 4679063, (Filed 1983, awarded; 1987).

[10] P. Klipstein, Depletion-less photodiode with suppressed dark current and method for producing the same, US Patent 7795640, (Filed 2004, awarded; 2010).

[11] S. Maimon, G.W. Wicks, Nbn detector, an infrared detector with reduced dark current and higher operating temperature, Appl. Phys. Lett. 89 (2006) 151109.

[12] D. Wang, D. Donetsky, G. Kipshidze, Y. Lin, L. Shterengas, G. Belenky, W. L. Sarney, S.P. Svensson, Metamorphic InAsSb based barrier photodetectors for the long wavelength infrared region, Appl. Phys. Lett. 103 (2013) 051120.

[13] S.P. Svensson, D. Donetsky, D. Wang, H.S. Hier, F.J. Crowne, G. Belenky, Growth of type II strained layer superlattice, bulk InAs and GaSb materials for minority lifetime characterization, J. Cryst. Growth 334 (2011) 103.

[14] T.H. Glisson, J.R. Hauser, M.A. Littlejohn, C.K. Williams, Energy bandgap and lattice constant contours of III–V quaternary alloys, J. Electron. Mater. 7 (1978) 1.

[15] I. Vurgaftman, J.R. Meyer, L.R. Ram-Mohan, Band parameters for III–V compounds semiconductors and their alloys, J. Appl. Phys. 89 (2001) 5815.

CrossMark
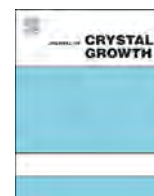
Comparison of semi-insulating InAlAs and InP:Fe for InP-based buried-heterostructure QCLs

Y.V. Flores [a,*], A. Aleksandrova [a], M. Elagin [a], J. Kischkat [a], S.S. Kurlov [a], G. Monastyrskyi [a], J. Hellemann [a], S.L. Golovynskyi [b], O.I. Dacenko [c], S.V. Kondratenko [c], G.G. Tarasov [b], M.P. Semtsiv [a], W.T. Masselink [a]

[a] Department of Physics, Humboldt University Berlin, Newtonstrasse 15, D-12489 Berlin, Germany
[b] Institute of Semiconductor Physics, National Academy of Sciences, pr. Nauki 45, 03028 Kyiv, Ukraine
[c] Taras Shevchenko National University of Kyiv, 64 Volodymyrs'ka St., 01601 Kyiv, Ukraine

ARTICLE INFO

ABSTRACT

In a previous work [Flores et al., J. Cryst. Growth 398 (2014) 40] [3] we demonstrated the advantages of using a thin InAlAs spacer layer in the fabrication of buried-heterostructure quantum-cascade lasers (QCLs), as it improves the morphology of the interface between the laser core and the InP:Fe lateral cladding. In this paper we investigate aspects of InAlAs, which are relevant for its role as insulating lateral cladding of the laser sidewalls: carrier traps, electrical resistivity, and functionality as a sole lateral cladding. We find that a thin InAlAs spacer layer not only improves the regrowth interface morphology, but also eliminates interface-related shallow electronic states, thus improving the electrical resistivity of the interface. We further find that bulk InAlAs grown by gas-source molecular-beam epitaxy as well as InP:Fe are semi-insulating at room temperature, with specific resistivities of $3 \times 10^7\ \Omega\,cm$ and $2 \times 10^8\ \Omega\,cm$, respectively. Both materials have also a high thermal activation energy for electrical conductivity (0.79 eV and 0.68 eV, respectively). In order to compare the performance of InP:Fe and InAlAs as a lateral cladding, lasers were fabricated from the same QCL wafer with differing stripe insulation materials. The resulting lasers differ mainly by the lateral insulation material: SiO_2, InP:Fe (with InAlAs spacer), and pure InAlAs. All devices show a similar performance and similar temperature dependence, indicating insulating properties of InAlAs adequate for application in lateral regrowth of buried-heterostructure QCLs.

© 2015 Elsevier B.V. All rights reserved.

1. Introduction

The quantum-cascade laser (QCL) is a unipolar laser in which the laser transition is between conduction subbands. QCL structures are made using molecular-beam epitaxy (MBE), metal-organic vapor-phase epitaxy (MOVPE), and gas-source MBE (GSMBE). The GSMBE technique offers the following advantages for the growth of QCL structures: (i) easy handling of phosphides and arsenides in a single chamber within the same growth run, (ii) ability to grow strain-compensated heterostructures with very high internal strain for short-wavelength intersubband transitions and for maximized gain, and (iii) the ability to fabricate buried-heterostructure lasers through overgrowth of stripes in the same chamber and at very similar process temperatures as the primary wafer growth.

GSMBE allows furthermore the growth of strain-compensated heterostructures containing a higher degree of strain than is possible with vapor phase epitaxy, including up to 2-nm thick AlAs barriers on InP [1–3]. High AlAs barriers also allow the design of QCL active regions with low thermal escape charge carriers into the quasi-continuum and a sufficiently deep relaxation region. New insights into the physics of carriers scattering in QCLs suggest new structures to avoid carrier leakage and non-radiative scattering due to interface roughness and phonons [4–7]. These new designs allow for high characteristic temperatures T_0 and T_1, and low threshold current densities at room temperature and above.

Buried heterostructure (BH)-QCLs using insulating material that is epitaxially overgrown over the etched laser stripes provide the best heat extraction from the active region. Insulating iron-doped indium-phosphide (InP:Fe) can be overgrown with a high interface quality by GSMBE at approximately the same growth temperatures as the primary wafer growth, thus avoiding thermal relaxation of the highly strained AlAs barriers [1–3].

* Corresponding author. Tel.: +49 30 20937645.
E-mail address: floresyu@physik.hu-berlin.de (Y.V. Flores).

Continuous-wave (cw) operation, which is an essential performance aspect for the broadening of QCL applications, was demonstrated up to a temperature of 210 K with thin epi-down-mounted narrow (7 µm-wide) QCL stripes using InP:Fe as lateral cladding [3].

In the previous studies we improved heat extraction capabilities of InP:Fe-covered BH-QCLs using a thin (20 nm) InAlAs spacer layer between the laser ridge sidewalls and the InP:Fe insulating layers. This led furthermore to a clear improvement of the crystal quality of the interface, which is otherwise populated by void-like defects playing against an efficient heat extraction out of the laser core [3].

In this paper we reinforce our argumentation of using a thin InAlAs spacer layer for the fabrication of highly thermally conductive BH-QCLs. In particular, we present thermally stimulated current (TSC) measurements suggesting that InAlAs plays a crucial role in the suppression of surface states between the InP:Fe layer and the InP substrate. We demonstrate that InAlAs layers guarantee high electrical insulation through room-temperature resistivity values up to $3 \times 10^7 \, \Omega$ cm. This high resistivity translates into leakage currents through the InAlAs layers in QCLs of only several milliamperes, an insignificant current compared to laser drive currents of several amperes.

2. Electrical properties of thin InAlAs and InP:Fe layers

2.1. Thermal stimulated current measurement

The thermally-stimulated current (TSC) measurement is a well-suited technique to investigate the formation of trap levels induced by the epitaxial growth of InP:Fe and, generally, for the investigation of deep levels in both crystalline and amorphous semiconductors [8]. In contrast to other techniques as, for example, deep-level transient spectroscopy (DLTS), this technique allows the investigation of deep traps in highly resistive structures with in-plane charge carrier transfer.

The TSC measurements were temperature-driven and measured after the excitation of the samples with near-infrared (1.3 eV photon energy) light for 1 min and subsequent delay time of 20 s. The power density of the excitation signal was 300 µW/cm² and the heating rate was about 10 K/min. We used furthermore a current amplifier and standard direct current detection equipment. In dots were used to contact the top surface of the upper layer (inset in Fig. 1).

Fig. 1 shows the measured TSC current as a function of temperature for a 2 µm-thick highly doped InP:Fe layer grown over a semi-insulating InP:Fe substrate (dark gray line). We observe three TSC peaks at 85.8, 121, and 232 K. Using the empirical relation, $E_a \approx 23 k_B T$
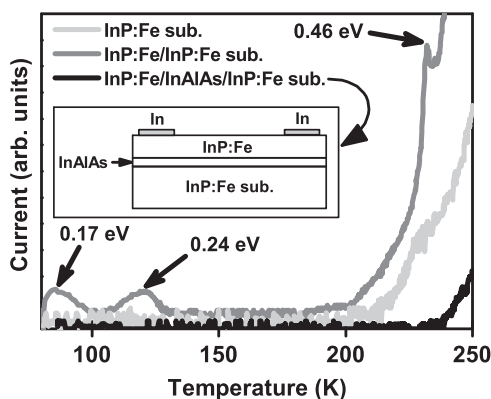
[9], this leads to activation energies of, respectively, E_a=0.17, 0.24, and 0.46 eV below the conduction band E_c. The deepest level observed with activation energy 0.46 eV below E_c corresponds to the major electron trap that was observed at undoped and doped InP [10,11].

Furthermore, other trap levels such as 0.24 eV and 0.32 eV associated with P-vacancies, or, 0.52 eV, associated with native point defects, can evolve under different grow stages [11]. The second TSC peak can be attributed to the well known electron trap associated with P-vacancies with an activation energy of 0.24 eV. The peaks from Fe levels (0.68 eV, Fig. 3) cannot be observed because the Fe acceptor is a also a recombination center [12]. No TSC current is observed after light excitation of the pure 350 µm-thick semi-insulating InP:Fe substrate (light gray line in Fig. 1).

In a previous study we reported the improved crystal quality and the heat extraction capabilities of BH-QCLs using InP:Fe lateral cladding. This improvement was achieved placing a thin (20 nm) $In_{0.52}Al_{0.48}As$ spacer layer between the laser ridge sidewalls and the InP:Fe insulating layers [3]. As we show next, such a spacer layer has also interesting consequences for our MBE-grown InP:Fe/InP:Fe (substrate) system.

The black line of Fig. 1 represents the measured TSC current for the same material system as in the dark gray line, yet with a 0.18 µM-thick $In_{0.52}Al_{0.48}As$ spacer layer grown in between. The spacer layer is Be-doped with a doping concentration of $4 \times 10^{17} \, cm^{-3}$ in order to compensate the background n-doping. No TSC peaks are observed. The MBE growth of InAlAs in AsH_3 atmosphere seems to have the interesting faculty to suppress shallow trap states, which are, as the evidence suggests, mostly located at the surface between the InP:Fe layer and the semi-insulating substrate.

2.2. Activation energy and specific resistivity

With the goal of integrate InAlAs and InP:Fe layers in the fabrication of QCLs we investigate their electrical transport characteristics.

The room-temperature resistivity is determined from current–voltage measurements. Fig. 2 shows the current density as a function of applied electric field for a 4 µm InAlAs film grown over a highly conductive InP:S substrate. Here, again, the InAlAs layer was doped with Be-atoms acting as shallow acceptors in order to compensate the background n-doping. The Be doping concentration was $4 \times 10^{17} \, cm^{-3}$. For measurements, we evaporated and annealed ohmic Au:Cr contacts to the both the top surface of the InAlAs and to the substrate (inset in Fig. 2).

A room-temperature resistivity $3 \times 10^7 \, \Omega$ cm is measured from the linear region up to a 20 kV/cm electric field. This value is approximately one order of magnitude lower than the measured

Fig. 1. Direct current measured after the excitation of the samples with near-infrared light as a function temperature. Arrows indicate the estimated activation energies, corresponding to peak TSC values at 85.8, 121, and 232 K. The heating rate was about 10 K/min. The inset is a schematic representation of a sample's geometry used for measurement.
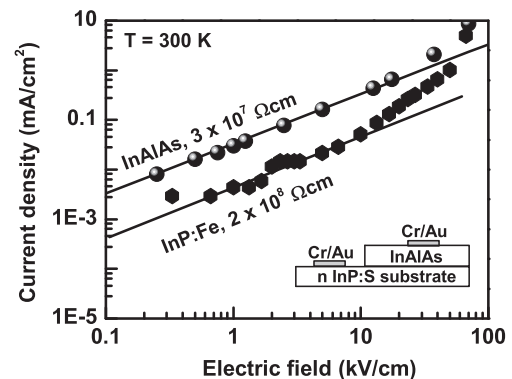
Fig. 2. Measured current density as a function of electric field for a 4 µm InAlAs (dots) and a 3 µm InP:Fe film at room temperature. Solid lines show best fits to the data, resulting in the indicated resistivities. The inset is a schematic representation of the sample's geometry used for measurements.

room-temperature resistivity of a 3 µM InP:Fe film, which achieves values up to 2×10^8 Ω cm (Fig. 2, solid hexagons). The measured value of 3×10^7 Ω cm is, however, still a good result: leakage currents through InAlAs layers in QCLs with such high resistivity would lie in the milliamperes order of magnitude, an insignificant current compared to laser drive currents of several amperes.

Finally, we measure the resistivity as a function of temperature of thin InAlAs and InP:Fe layers. Results are summarized in Fig. 3. For InAlAs, the measured resistivity values range between 2.4 and 0.3×10^5 Ω cm for the temperature range 390–440 K. These values are by a factor 2–3 smaller than the measured values for the semi-insulating InP:Fe layer. Using an exponential fit we obtain a thermal activation energy for InAlAs of about 0.79 eV below the conduction band. We attribute this value to a deep trap level induced by the Al atoms. The measured activation energy for the InP:Fe layer, 0.68 eV, corresponds to the activation energy for the deep Fe-acceptor [12,2].

3. Implications for laser performance

We investigate the application of InAlAs and InP:Fe as cladding layers in BH-QCLs. For our study we choose a mid-infrared QCL design emitting at the central wavelength of 5.7 µm. The active region design is based on the strain-compensated InGaAs/InAlAs heterosystem and includes highly strained AlAs extraction barriers [13–17,6]. The high conduction band discontinuity achieved by the AlAs barriers reduces carriers leakage and contributes to a high temperature performance of the lasers. The layer thicknesses in nm are *3.8*/1.7/*2.0*/2.5/[0.5]/2.5/*2.0*/2.3/[0.5]/*2.3*/**1.0**/1.7/[0.5]/1.7/**1.0**/1.6/[0.5]/1.6/**1.0**/<u>1.5</u>/[0.5]/1.5/**1.0**/<u>1.3</u>/[0.5]/1.3/*2.8*/<u>1.2</u>/[0.5]/1.2/[0.5]/<u>3.4</u>/<u>0.8</u>/[0.5]/0.8. AlAs layers are in bold, $In_{0.53}Ga_{0.47}As$ layers are in roman, $In_{0.52}Al_{0.48}As$ layers are in italics, and InAs layers are in square brackets. Underlined layers are doped to 5×10^{17} cm^{-3}.

The QCL structure containing 40 active periods was grown on a low-doped ($n = 2 \times 10^{17}$ cm^{-3}) InP:S substrate, which serves as the lower cladding layer. The epitaxial growth was carried out, as all samples presented in this work, in a Riber Compact 21T GSMBE system, which uses solid sources for the group-III elements, while As and P are supplied by pre-cracked arsine (AH_3) and phosphine (PH_3). The epitaxy sequence consists of 100 nm InP:Si ($n = 1 \times 10^{17}$ cm^{-3}), 250 nm of lattice matched InGaAs:Si spacer ($n = 7 \times 10^{16}$ cm^{-3}), the 2.2 µm-thick active region (40 cascades), 250 nm of lattice matched InGaAs:Si spacer ($n = 7 \times 10^{16}$ cm^{-3}), 3 µm ($n = 1 \times 10^{17}$ cm^{-3}) InP:Si, and 1 µm ($n = 3 \times 10^{18}$ cm^{-3}) InP:Si top cladding.
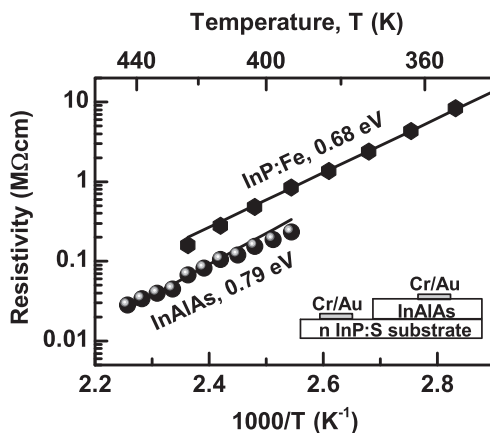
Fig. 3. Measured resistivity as a function of reciprocal temperature for a 4 µm InAlAs (dots) and a 5 µm InP:Fe film. Solid lines represent best fits to the data, resulting in the indicated activation energies. The inset is a schematic representation of the sample's geometry used for measurements.

After the primary growth of the laser structure, the wafer was cleaved and the quarter wafers were processed into laser ridges. The processing steps included conventional photo-lithography techniques, wet chemical etching, and lift-off [18,3]. The processing of each quarter wafer differs in the resulting laser shape, width, and in the used material for lateral cladding:

- Quarter wafer A was processed into laser ridges of width $w = 25$ µm using a 30 µm wide SiO_2 dielectric etch-mask oriented along the (1$\bar{1}$0) crystallographic direction. Stripes were etched in a HBr : HCl : H_2O_2 : H_2O (10:5:1:50) solution. Electrical insulation and lateral optical confinement of the laser mode were achieved by reactive magnetron sputtering deposition of approximately 500 nm SiO_2 described elsewhere [18].
- Quarter wafer B was processed into 10.5 µm-width stripes oriented perpendicular to the (1$\bar{1}$0) crystallographic direction using a 10 µm wide SiO_2 dielectric etch-mask. The stripes with etched with the same solution as in quarter wafer A, rinsed with deionized water and dried with nitrogen. Because of the crystallographic orientation the etched stripes the sidewalls are tilted by 45° with respect to the direction of growth. The sample was loaded into the MBE for regrowth of InAlAs of 2.7 µm-thick. No InP:Fe overgrowth followed. After the regrowth the etch-mask was removed in buffered HF and so the access to the top laser contact was achieved.
- Quarter wafer C and D were processed into narrow laser ridges of 9.3 µm and 14.4 µm width, respectively, using the method described in Ref. [3]. After etching the laser stripe along the (1$\bar{1}$0) crystallographic direction as in the case of sample A, the sample was loaded into the MBE loadlock for regrowth. The wafer was heated in an AsH_3 flux and the regrowth started with the 20-nm InAlAs spacer layer. Immediately after, the gas flux was switched to PH_3 and the overgrowth continued with InP:Fe (2.5 µm-thick) [3]. It is important to note that both the primary growth of the laser structure and the secondary growth (InAlAs and InP:Fe) were carried out in the same GSMBE system.

Top metallization was done in all samples by thermal evaporation of Cr/Au. After processing, laser bars of different length were cleaved and soldered epi-up into Cu heat sinks. Laser facets were left uncoated. The devices were mounted in a nitrogen-low cryostat for temperature-dependent measurements and the laser heat sink temperature was registered using a Pt100 thermocouple. Key characteristics of laser bars fabricated from samples A, B, C, and D are summarized in Table 1.

Fig. 4 shows the measured threshold current density J_{th} as a function of temperature for 4 mm-long stripes of samples A, B, C, and D. The lasers were operated in pulsed mode with 100 ns current pulses and a repetition frequency of 10 kHz (0.1%d.c). Higher threshold current densities are measured for narrower stripes (samples B, C, and D) as for the wide stripes (sample A). This trend has been observed before and is related to the poorer optical confinement capabilities of the laser mode in narrower stripes (see for example Ref. [3]). As a matter of fact, following 1/L-measurements, a lower modal gain coefficient (laser gain pro injected current density) g_c is measured for sample C (8.0 cm/kA at 300 K) as for sample A (11.5 cm/kA at 300 K). And an even smaller modal gain coefficient is measured for sample B (2.35 cm/kA at 300 K). We attribute the small g_c for sample B to the poor optical confinement of the laser mode. However, it is not clear why sample B should have such a bad optical confinement, especially if we consider the fact that the refractive index of the InAlAs burying layer should be more or less similar than InP (samples C and D).

The measured threshold current densities at room temperature for samples A, B, C, and D, are, respectively, 1.76, 10.15, 3.12, and 2.25 kA/cm² ($L = 4$ mm). We observe a reduction of J_{th} by ~30% in

Table 1

Summarized characteristics of $L = 4$ mm-long laser bars fabricated from quarter wafers A, B, C, and D. w represents the laser stripe width, J_{th} is the threshold current density, g_c is the modal gain coefficient, and T_0 is the threshold current characteristic temperature. J_{th} and g_c are measured for a heat sink temperature of 300 K. T_0 is measured within the temperature range $100 - 300$ K.

Sample	Lateral cladding	w (μm)	J_{th} (kA/cm^2)	g_c (cm/kA)	T_0 (K)
A	[500 nm] SiO$_2$	25	1.76	11.5	150
B	[2.7 μm] InAlAs	10.5	10.15	2.35	151
C	[20 nm] InAlAs/[2.5 μm] InP:Fe	9.3	3.12	8.0	150
D	[20 nm] InAlAs/[2.5 μm] InP:Fe	14.4	2.25	11.0	151
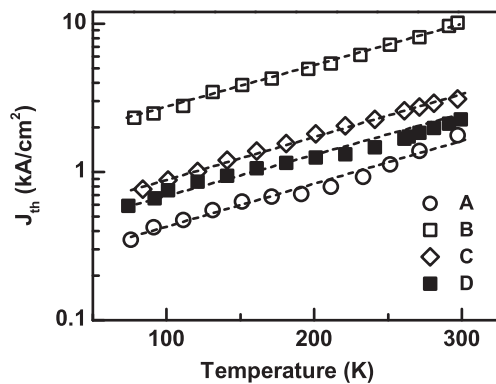
Fig. 4. Measured threshold current density as a function of temperature for QCL stripes of 4 mm length. All devices were fabricated from the same wafer and operated in pulsed mode with 100 ns current pulses and a repetition frequency of 10 kHz. Dashed lines represent exponential fits to the data, resulting in nearly the same threshold current characteristic temperatures $T_0 \approx 150$ K for all samples. Further characteristics are specified in Table 1.
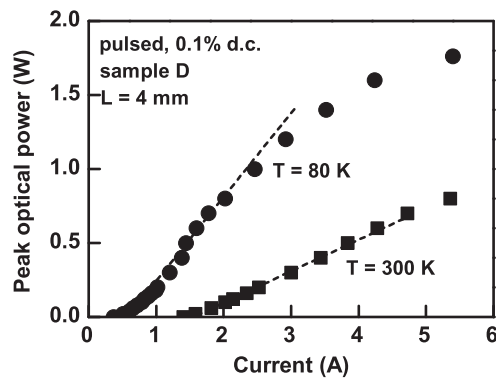
Fig. 5. Measured peak optical power as a function of injection current for a 14.4 μm-wide stripe BH-QCL using InAlAs/InP:Fe lateral cladding. The dashed lines represent linear fits to the data resulting in differential slope efficiencies of 0.7 W/A at 80 K and 0.22 at 300 K.

sample D with respect to sample C. We attribute this fact to the better optical confinement capabilities of the wider stripe D. The threshold voltage is nearly the same for all samples $U_{th} \approx 17$ V.

The waveguide loss α_w, estimated from 1/L-measurements, is in all samples nearly the same ($\alpha_w \approx 18$ cm^{-1} at 300 K). This is expected because the waveguide loss is mainly determined by the free carrier absorption in the active region and the highly doped vertical cladding layers, which is in all samples the same. Furthermore, as suggested by the same threshold current characteristic temperature $T_0 \approx 150$ K

measured for all samples (Table 1), no temperature-driven leakage current paths are activated by the presence of the InAlAs layer.

Fig. 5 shows the measured peak optical power as a function of injection current for sample D at two different heat sink temperatures. We measure differential slope efficiencies as high as 0.7 W/A at 80 K and 0.22 at 300 K, which corresponds to a quantum efficiency per cascade of 8% and 2.5%, respectively.

4. Conclusions

Thin InAlAs layers not only improve the morphology of the interface between the laser core and the InP:Fe layers in BH-QCLs, improving heat extraction out of the laser core and allowing cw operation [3], but also offers excellent electrical insulation due to room-temperature resistivities up to 3×10^7 Ω cm. We observe furthermore the suppression of shallow trap levels in InP:Fe when growing an InAlAs spacer between highly doped InP:Fe and a semi-insulating InP:Fe substrate. Fabrication of a BH-QCL using InP:Fe lateral cladding with an InAlAs spacer led to a room-temperature threshold current density in pulsed operation mode of 2.25 kA/cm^2 for a 4 mm $\times$ 14.4 μm laser stripe with emission wavelength of 5.7 μm.

Acknowledgements

References

[1] M. Chashnikova, G. Monastyrskyi, A. Aleksandrova, M. Klinikmüller, M.P. Semtsiv, W.T. Masselink, Appl. Phys. Lett. 100 (2012) 213504.
[2] M.P. Semtsiv, A. Aleksandrova, M. Elagin, G. Monastyrskyi, J.-F. Kischkat, Y.V. Flores, W.T. Masselink, J. Cryst. Growth 378 (2013) 125.
[3] Y.V. Flores, M. Elagin, S.S. Kurlov, A. Aleksandrova, G. Monastyrskyi, J. Kischkat, M.P. Semtsiv, W.T. Masselink, J. Cryst. Growth 398 (2014) 40.
[4] J.B. Khurgin, Y. Dikmelik, P.Q. Liu, A.J. Hoffman, M.D. Escarra, K.J. Franz, C.F. Gmachl, Appl. Phys. Lett. 94 (2009) 091101.
[5] Y.T. Chiu, Y. Dikmelik, P.Q. Liu, N.L. Aung, J.B. Khurgin, C.F. Gmachl, Appl. Phys. Lett. 101 (2012) 171117.
[6] D. Botez, J. Shin, J. Kirch, C. Chang, L. Mawst, T. Earles, IEEE J. Sel.Top. Quantum Electron. 19 (4) (2013) 1200312, and references therein.
[7] Y.V. Flores, S.S. Kurlov, M. Elagin, M.P. Semtsiv, W.T. Masselink, Appl. Phys. Lett. 103 (2013) 161102.
[8] D.S. Misra, A. Kumar, S.C. Agarwal, Phys. Rev. B 31 (1985) 1047.
[9] A.G. Milnes, Deep Impurities in Semiconductors, Wiley, New York, 1973.
[10] A.A. Iliadis, W. Lee, O.A. Aina, IEEE Electron Device Lett. 10 (1989) 370.
[11] H. Asahi, Y. Kawamura, M. Ikeda, H. Okamoto, J. Appl. Phys. 52 (1981) 2852.
[12] A. Dadgar, R. Engelhardt, M. Kuttler, D. Bimberg, Phys. Rev. B 56 (1997) 10241.
[13] Q.K. Yang, C. Mann, F. Fuchs, R. Kiefer, K. Köhler, N. Rollbühler, H. Schneider, J. Wagner, Appl. Phys. Lett. 80 (2002) 2048.
[14] J.C. Shin, M. D'Souza, Z. Liu, J. Kirch, L.J. Mawst, D. Botez, I. Vurgaftman, J.R. Meyer, Appl. Phys. Lett. 94 (2009) 201103.
[15] D. Botez, S. Kumar, J.C. Shin, L.J. Mawst, I. Vurgaftman, J.R. Meyer, Appl. Phys. Lett. 97 (2010) 071101.
[16] Y. Bai, N. Bandyopadhyay, S. Tao, E. Selcuk, S. Slivken, M. Razeghi, Appl. Phys. Lett. 97 (2010) 251104.
[17] M.P. Semtsiv, Y. Flores, M. Chashnikova, G. Monastyrskyi, W.T. Masselink, Appl. Phys. Lett. 100 (2012) 163502.
[18] M.P. Semtsiv, M. Ziegler, S. Dressler, W.T. Masselink, N. Georgiev, T. Dekorsy, M. Helm, Appl. Phys. Lett. 85 (2004) 1478.
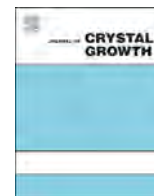
Molecular beam epitaxy growth of antimony-based mid-infrared interband cascade photodetectors

Zhao-Bing Tian [a,*], Ted Schuler-Sandy [a], Sanjay Krishna [a], Dinghao Tang [b], David J. Smith [b]

[a] Center for High Tech Materials, University of New Mexico, Albuquerque, NM 87106, USA
[b] Department of Physics, Arizona State University, Tempe, AZ 85287, USA

ABSTRACT

The molecular beam epitaxial growth and optimization of antimony-based interband cascade photodetectors, on both GaSb and GaAs substrates, are presented. Material characterization techniques, including X-ray diffraction, atomic force microscopy, and cross-sectional transmission electron microscopy, are used to evaluate the epitaxial material quality. This work has led to the demonstration of mid-infrared photodetectors operational up to a record-high 450 K, and a dark current density as low as 1.10×10^{-7} A/cm^2 at 150 K. The results also suggest that further improved material quality and device performance can be expected via optimization of growth parameters.

© 2015 Elsevier B.V. All rights reserved.

1. Introduction

The InAs/GaSb type-II strained layer superlattice (T2-SL) is widely regarded as a viable alternative to the dominant HgCdTe technology for infrared (IR) detection [1]. Over the past decade, significant progress in both scientific and technological aspects has been made [2]. Despite the relatively short carrier lifetime in InAs/GaSb T2-SLs, researchers managed to take advantage of the great versatility in energy band alignment. The detector performances are steadily approaching the well-investigated HgCdTe and InSb technologies [1,2]. Driven by the increasing demand to shrink the size, weight, and power consumption (SWaP) of IR imaging systems, the development of high operating temperature (HOT) IR detectors and imagers is of great interest. The key issue/challenge for the InAs/GaSb T2-SL HOT applications is the relatively short carrier lifetime, which results in pronounced generation-recombination noise and inferior photo-carrier collection at HOTs, therefore degrading the attainable detector performances. One possible way to promote the photo-carrier extraction in InAs/GaSb T2-SL photodetectors at HOTs is to use a multijunction/stage design with multiple thin absorbers, such as Interband Cascade (IC) detectors [3–7]. The multi-stage design could also be beneficial for detector noise suppression, by means of incorporating unipolar barriers and designing devices to operate under/near zero-bias conditions [5–7].

This paper describes the development of HOT InAs/GaSb T2-SL photodetectors. By adopting the so-called IC structure [4–9], high

performance mid-IR detectors operational well above room temperatures are realized. By uniquely combining several different carrier transport mechanisms, many distinctive and highly desirable features are obtained in IC photodetectors [4–7]. The devices consist of multiple stages that are electrically connected in series. In each stage, there are three different regions: an electron barrier (eB), an InAs/GaSb T2-SL absorber, and an electron relaxation (eR) region.

The basic operation principle of IC detectors is shown in Fig. 1: the incoming photons are absorbed in the moderately thin InAs/GaSb T2-SL region, creating photo-excited electrons. Due to the existence of unipolar barriers to the left of the absorber, photo-generated electrons can only travel towards the right. The electrons will then travel through the eR region via ultra-fast longitudinal optical-phonon assistance inter-subband relaxation, and subsequently tunnel into the valence band of the next stage. By implementing this ultra-fast electron transport channel into the device, a large lifetime contrast (between carrier recombination and transport) is created in the IC detectors, despite the short carrier lifetime in InAs/GaSb T2-SLs. Combined with the implementation of unipolar barriers and its zero-bias operation capabilities, IC detectors are capable of very high temperature operation [6,7].

In order to facilitate such a relatively complicated device concept, a quantum-engineered AlSb/InAs/GaSb-based layered structure is adopted. As shown in Fig. 1, an IC photodetector consists of several alternating chirped superlattice or coupled quantum wells (QWs) regions, whose constituent materials and layer thicknesses vary. The eB region is made of GaSb/AlSb multiple QWs, the absorber consists of InAs/GaSb superlattices, and the eR region is made of a series of InAs/AlSb coupled QWs. The optimum growth conditions for these constituent materials, for example the growth temperature for InAs/InSb and AlSb, are quite different. More

---
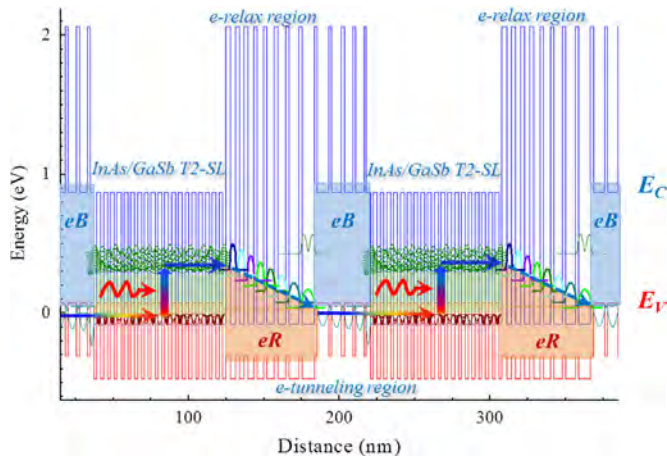
Fig. 1. Band structure diagram in (two-stage) interband cascade photodetectors. Incoming photons are absorbed in the InAs/GaSb T2-SL absorbers, generating electron–hole pairs. Electrons diffuse into the electron relaxation region, and then effectively transport into the valence band of the next stage, through fast LO phonon-assisted inter-subband relaxation and interband tunneling.

importantly, as the operation of IC detectors depends entirely on the proper energy band alignment, enabled by the quantum-confinement effect in the QW structures, these layer thicknesses are critical and therefore need to be precisely controlled. This is particularly true for mid-IR IC devices, where thinner QW layers are used and the band alignment is more sensitive to layer thickness variations. In addition, the strain in each stage and in individual regions has to be balanced in order to ensure better crystal quality. Therefore, the growth of such a complicated IC detector structure is very challenging, particularly for epitaxial systems without redundant sources. This paper elaborates the epitaxial growth and optimization of mid-IR IC photodetectors.

2. Experimental procedure

The materials are grown with a Veeco Gen-10 molecular beam epitaxy (MBE) system, which is equipped with group-III SUMO cells and group-V valved crackers. For the group-III SUMO cells, the tip filament for Gallium and Indium cells are kept at higher temperatures (100–120 °C higher than the base temperatures) to reduce the spitting/oval defects, and a cold-lipped Aluminum SUMO cell is used to avoid source material creeping. For the group-V As and Sb crackers, the cracking zone temperatures are set to 900 °C (a mixture of dimers and monomers). The growth rates of the group-III sources are determined by multiple-point Reflection High-Energy Electron Diffraction (RHEED) oscillations, and are routinely verified by monitoring the beam equivalent pressure (BEP) of each source, as well as from constituent layer thicknesses in superlattice calibration samples. The optimum growth temperatures, growth rates and V/III ratios are determined by the optical (maximum photoluminescence PL intensity) and crystal qualities (as determined from the surface morphology and X-ray diffractions) through a series of superlattice calibration samples prior to the growth of device wafers.

The typical MBE growth sequence for IC detectors grown on (001) GaSb substrates is as follows: the substrate is transferred into the growth chamber for oxide desorption, performed under excess Sb flux at 540–550 °C, as determined by an InGaAs pyrometer. Complete oxide desorption from the GaSb substrate is ensured by a streaky 1×3 RHEED reconstruction pattern. The substrate is then cooled down to ~ 500 °C for a 200–400 nm p-GaSb buffer layer growth, to obtain a smooth surface. The GaSb buffer layer, which is doped to 5×10^{18} cm^{-3} with Beryllium, also serves as the bottom contact. The 5-stage IC structure is subsequently grown, with the overall strain

balanced in each individual region. In this work, strain balancing is achieved by two approaches – proper device structure design and carefully tuned growth sequence and parameters. The growth is then finalized by a thin (10–15 nm) n-InAs top contact layer doped with Tellurium. For the cascade stage growth, the substrate temperature is set at 400–420 °C. During the growth of InAs/GaSb T2-SL absorber region, the growth rate of InAs is 0.9 Å/sec, with an As/In ratio of ~ 3, and the GaSb growth rate is 0.9 Å/sec, with a Sb/Ga ratio of 4.5. InSb-like interfacial layers are used in the InAs/GaSb T2-SL absorber regions for better crystal and optical quality [10]. Because of the existence of residual As flux during the GaSb layer growth and the higher sticking coefficient of As over Sb, about 9% Arsenic was found to be incorporated into the GaSb thin layers. In fact, As incorporation is found in all Sb-containing layers, which will require further attention in fine tuning the device design and strain balancing.

There has also been considerable interest in the development of high performance IR photodetectors on GaAs substrates, to further reduce cost and enable large-format focal plane arrays (FPAs). The major challenge here is to properly accommodate the 7.8% lattice mismatch between GaAs and GaSb, which could produce excessive amount of threading dislocations, resulting in severely degraded crystal quality and carrier lifetime. Nonetheless, due to the uniquely high lifetime contrast in IC detectors, one would expect IC detectors to be less susceptible to the inferior material quality. In this study, for IC detectors grown on (001) GaAs substrates, an interfacial misfit array (IMF) method [11] is adapted. After the oxide desorption on GaAs substrate, a 300-nm GaAs layer is first deposited to obtain a smooth surface, and then the sample is exposed to excess Sb overpressure while the substrate temperature is brought down to ~ 500 °C. An 800-nm p-GaSb buffer layer (which also serves as the bottom contact) is then grown. The 5-stage mid-IR IC device structure is grown subsequently, with identical growth parameters.

After growth, the crystal quality and surface morphology of the epitaxial structures are characterized by X-ray diffraction (XRD), atomic force microscopy (AFM), and cross-sectional transmission electron microscopy (TEM). The samples are then processed into single-pixel devices, to further characterize electrical and optical performances of the detector. One sample grown on GaSb substrate is processed into a 320×256 FPA, and IR images acquired by the mid-IR IC FPA are demonstrated.

3. Results and discussion

The sample surface morphology and crystal quality are evaluated by optical and electron microscopy, AFM, XRD, and room temperature photoluminescence (PL). The XRD rocking curves are recorded in the vicinity of the symmetrical (004) GaSb diffraction spot. The representative XRD pattern of an IC detector sample is shown in Fig. 2, and the inset is an enlarged view of the rocking curve close to the substrate peak. Sharp satellite peaks up to 8th order are observed, indicating high structural quality of the samples. The InAs/GaSb T2-SL absorber overall shows good material quality, as indicated by the strong room temperature PL (not included here) and the sharp satellite peaks in XRD rocking curves (the FWHM of the satellite peaks is around 26 arcseconds, as measured from InAs/GaSb T2-SL calibration samples). The overall strain in the epitaxial structure is within 50 arcseconds for the 5-stage IC detector samples. The extracted period of the cascade stage is around 220 nm, which is in good agreement with the device design (about 0.4% thicker than the design).

The wafers are then processed into single-pixel photodetectors for device performance evaluation. These mid-IR IC detectors are operational up to 450 K under zero-bias, as shown in Fig. 3a. To the best of our knowledge, this is the highest operation temperature reported for IR photodetectors [7,9]. The promising optical performance of IC detectors is attributed to the high lifetime contrast and efficient
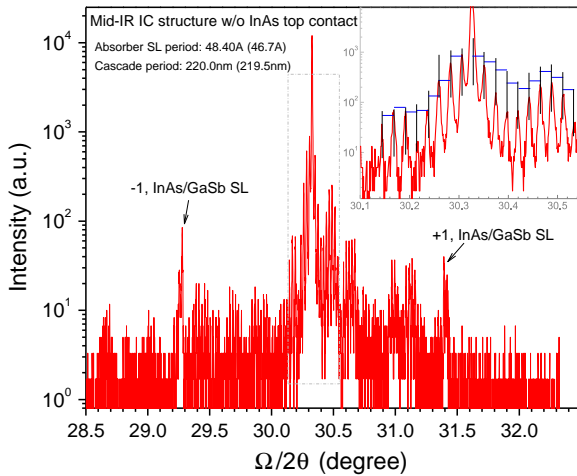
Fig. 2. XRD pattern of 5-stage antimony-based mid-IR IC detector grown on GaSb substrate. The inset shows satellite peaks that arise from periodicity between cascaded stages.

Fig. 3. (a) Zero-bias response spectra of 5-stage mid-IR interband cascade photo-detector at several operating temperatures. The atmospheric CO_2 absorption at 4.2 μm and water absorption lines around 2.7 μm are clearly seen. (b)Thermal image acquired by the 320×256 IC FPA operating at 80 K.

photo-carrier extraction. The IC device also shows very low dark current over the whole temperature range [6,9]. The dark current density is as low as 1.10×10^{-7} A/cm^2 at 150 K, which is better than that estimated from HgCdTe *Rule07* [6,12]. Because of the optimized MBE growth and improved device design, the 5-stage mid-IR IC detector has obtained a Johnson-limited D^* of 1.81×10^{11} and 1.59×10^9 cm Hz$^{1/2}$/W at 150 K and room temperature, respectively. The sample is further processed into the first IC focal plane array (FPA), and is hybridized with a standard commercial read-out circuit (Indigo ISC9705) [7]. The pixel size for the 320×256 IC FPA is 24×24 μm^2, with a filling-factor of 72%. Even with the 0.7-μm total absorber (corresponds to an external quantum efficiency of 3.1% for our 5-stage design) and non-optimal fabrication, the mid-IR IC FPA is operational above 180 K, with a noise equivalent temperature difference (NEDT) of 28 mK at 120 K [7]. Fig. 3b is a thermal image acquired with the IC FPA operated at 80 K. The blood vein is clearly visible, indicating very good temporal and spatial resolution for the IC IR images.

Despite the excellent performance of the IC detectors, the AFM topography results suggest that the MBE growth of these mid-IR IC detector wafers can be further improved. The surface morphology shows slightly rough surfaces. The typical RMS roughness obtained from the 5×5 μm^2 AFM scans is around 3.5 Å. In order to gain some further insights into the material growth, one mid-IR IC detector sample is examined by cross-sectional TEM. As shown in Fig. 4a, the layer structures in each region of the IC detector are well defined and clearly visible, and no structural defects are observed across large lateral distances. Nonetheless, some interfacial roughness is observed in the AlSb/InAs eR regions. The roughness could be either introduced from the non-optimum MBE growth condition or due to the oxidization of thin AlSb layers.

To further investigate the observed excess roughness in AlSb/InAs eR region, a set of AlSb/InAs superlattice samples are then grown and characterized in detail. Our result indicates that greatly improved crystal quality and smoother surfaces can be obtained by increasing the growth temperature to 415–470 °C during the AlSb/InAs region growth [13]. Since the optimal MBE growth temperature for InAs/GaSb T2-SL is around 400–420 °C, a lower substrate temperature is desirable for IC detector growth. Fig. 5 shows the XRD rocking curves and AFM surface topography as obtained from AlSb/InAs superlattice calibration samples grown at different substrate temperatures. Sample A grown at 415 °C clearly shows sharper satellite peaks, and the surface is much smoother than sample B grown at 400 °C. The RMS roughness of the InAs/AlSb
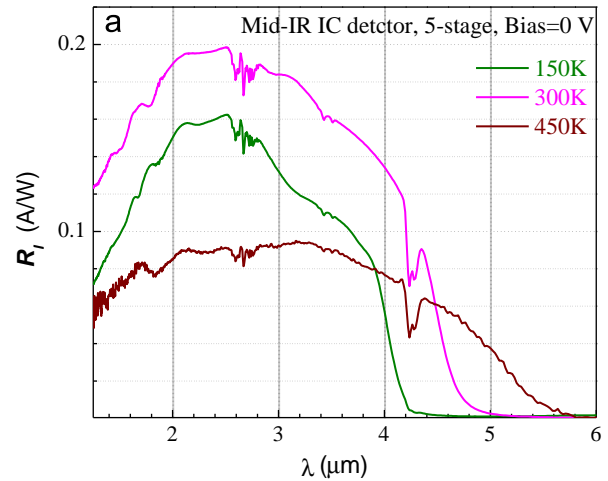
superlattice has improved from 3.5 nm to 0.6 nm by fine tuning the MBE growth temperature. The recently fabricated single-pixel IC device, which implemented with the InAs/AlSb eR growth optimization, has shown improved dark current performance. Detailed investigation is underway and will be reported elsewhere.

To enable low-cost and large-format IR FPA technology, our effort has also extended to the development of IC detectors on GaAs substrates. By using an interfacial misfit array between GaAs and GaSb layers, the 7.78% lattice mismatch is accommodated by the formation of periodic 2D 90° misfit dislocations along the interface [10]. With the IMF technology, the XRD FWHM peak of the 0.5-μm-thick GaSb buffer layer grown on GaAs substrate is around 290 arc-seconds. The relatively broad FWHM of the GaSb layer is attributed to the small residual strain (less than 2%) in the epitaxial layer [14]. As expected, the IC structure grown on GaAs has a much rougher surface, as shown by the AFM scan in the inset of Fig. 6, with RMS roughness of 1.95 nm over the 5×5 μm^2 area. The surface morphology is very similar to the typical fluctuation reported for IMF method in the literature [15]. Fig. 6 shows the XRD rocking curves for IC detectors grown on GaAs and GaSb substrates.

Despite the non-optimal growth of the mid-IR IC detector on a GaAs substrate, the single-pixel devices are operational well above room temperature. The dark current density is as low as 12.4 μA/cm^2 at 200 K, which is only two times higher than that of an IC detector grown on GaSb. The Johnson-limited D^* is 1.44×10^9 cm Hz$^{1/2}$/W at 300 K, which shows significant improvement (about 2.5 times
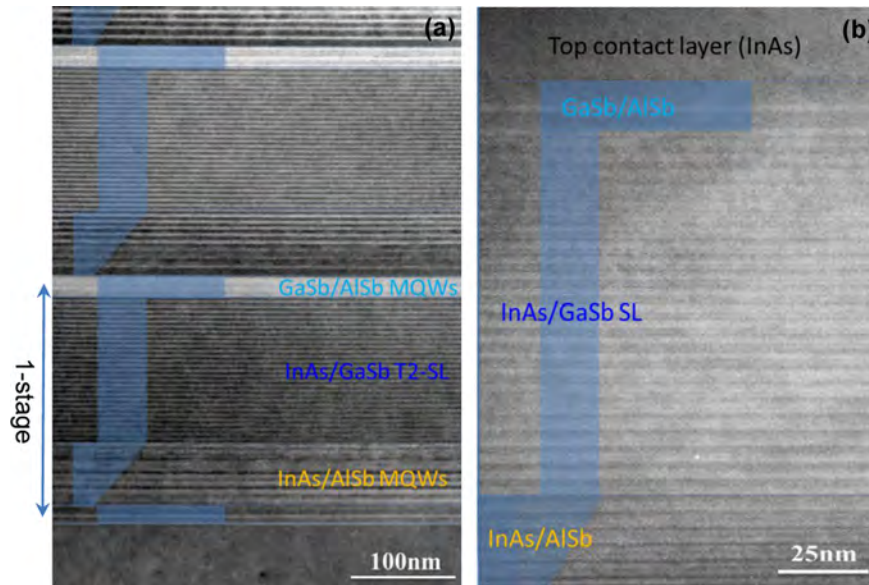
Fig. 4. Cross-sectional TEM images acquired from a 5-stage mid-IR interband cascade photodetector structure. (a) Two stages immediately above the substrate; and (b) one cascade stage close to the top InAs contact layer.
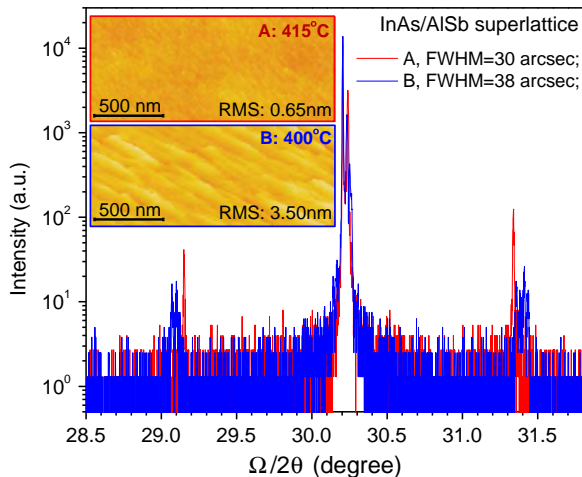
Fig. 5. XRD rocking curves of AlSb/InAs superlattices grown at different temperatures on GaSb substrates: sample A is grown at 415 °C, and sample B is grown at 400 °C. The insets are the surface morphology of AFM scans from the two samples.

Fig. 6. XRD pattern of a 5-stage antimony-based mid-IR IC detector grown on GaAs substrate, along with a reference XRD rocking curve obtained from an IC detector sample grown on GaSb substrate. The inset is AFM topography of IC detector sample grown on GaAs.

higher) over the best previously reported result [16]. It is expected that, by optimizing the buffer layer technology to accommodate the residual strain (for example, by using a thicker GaSb buffer layer grown at lower temperature), the material quality can be further improved, and better device performance would be achieved.

lattice mismatch, the device shows comparable performance to IC devices grown on GaSb substrates. Further improvements in material quality are expected by refining the growth parameters, and better device performance should also be achieved.

4. Summary

In summary, MBE growth optimization of quantum-engineered mid-IR interband cascade photodetectors is presented. With its complex structure and a wide range of MBE growth parameters, we have first focused on obtaining better optical and crystal quality. This allows the demonstration of mid-IR IC detectors operational well above room temperature. The dark current is as low as at 1.10×10^{-7} A/cm^2 and Johnson-limited D^* at 1.81×10^{11} cm Hz$^{1/2}$/W at 150 K. In addition, the development of mid-IR IC detectors on a GaAs substrate is also reported. By using the interfacial misfit array method and 0.8-μm-thick GaSb buffer layer to accommodate the 7.8%

John M. Cowley Center for High Resolution Electron Microscopy at Arizona State University.

References

[1] A. Rogalski, Recent progress in infrared detector technologies, Infrared Phys. Technol. 54 (2011) 136.

[2] L. Zheng, M. Tidrow, S. Bandara, L. Aitcheson, T. Shih, Update on III-V antimonide-based superlattice FPA development and material characterization, Proc. SPIE 8012 (2011) 80120S.

[3] J. Piotrowski, P. Brzozowski, K. Jozwikowski, Stacked multi-junction photodetectors for long-wavelength radiation, J. Electron. Mater. 32 (2003) 672.

[4] R.Q. Yang, Z. Tian, Z. Cai, J.F. Klem, M.B. Johnson, H.C. Liu, Interband cascade infrared photodetectors with superlattice absorbers, J. Appl. Phys. 107 (2010) 054514.

[5] Z. Tian, R.T. Hinkey, R.Q. Yang, Y. Qiu, D. Lubyshev, J.M. Fastenau, Amy W.K. Liu, M.B. Johnson, Type-II InAs/GaSb superlattice midwave infrared photodetectors based on interband cascade structures for high temperature operations, J. Appl. Phys. 111 (2012) 024510.

[6] Z.B. Tian, T. Schuler-Sandy, S. Krishna, Electron barrier study of mid-wave infrared interband cascade photodetectors, Appl. Phys. Lett. 103 (2013) 083501.

[7] Z.B. Tian, S.E. Godoy, H.S. Kim, T. Schuler-Sandy, J.A. Montoya, S. Krishna, High operating temperature interband cascade focal plane arrays, Appl. Phys. Lett. 105 (2014) 051109.

[8] R.Q. Yang, Z. Tian, J.F. Klem, T.D. Mishima, M.B. Santos, M.B. Johnson, Interband cascade photovoltaic devices, Appl. Phys. Lett. 96 (2010) 063504.

[9] Z.B. Tian, S.E. Godoy, T. Schuler-Sandy, H.S. Kim, J.A. Montoya, S. Krishna, Mid-wave infrared interband cascade photodetectors and focal plane arrays, Proc. SPIE 9070 (2014) 90701K.

[10] J.R. Waterman, B.V. Shanabrook, R.J. Wagner, M.J. Yang, J.L. Davis, J.P. Omaggio, The effect of interface bond type on the structural and optical properties of GaSb/InAs superlattices, Semicond. Sci. Technol. 8 (1993) S106.

[11] S.H. Huang, G. Balakrishnan, A. Khoshakhlagh, A. Jallipalli, L.R. Dawson, D.L. Huffaker, Strain relief by periodic misfit arrays for low defect density GaSb on GaAs, Appl. Phys. Lett. 88 (2006) 131911.

[12] W.E. Tennant, Rule 07 revisited: still a good heuristic predictor of p/n HgCdTe photodiode performance? J. Electron. Mater. 39 (2010) 1030.

[13] D. Xu, A.P. Litvinchuk, X. Wang, A. Delaney, H. Le, S.S. Pei, Structure stability of short-period InAs/AlSb superlattices, J. Cryst. Growth 251 (2003) 547.

[14] A. Jallipalli, G. Balakrishnan, S.H. Huang, T.J. Rotter, K. Nunna, B.L. Liang, L.R. Dawson, D.L. Huffaker, Structural analysis of highly relaxed GaSb grown on GaAs substrates with periodic interfacial array of 90° misfit dislocations, Nanoscale Res. Lett. 4 (2009) 1458.

[15] W. Zhou, X. Li, S. Xia, J. Yang, W. Tang, K.M. Lau, High hole mobility of GaSb relaxed epilayer grown on GaAs substrate by MOCVD through interfacial misfit dislocations array, J. Mater. Sci. Technol. 28 (2012) 132.

[16] B.M. Nguyen, D. Hoffman, E.K. Huang, S. Bogdanov, P.Y. Delaunay, M. Razeghi, M.Z. Tidrow, Demonstration of midinfrared type-II InAs/GaSb superlattice photodiodes grown on GaAs substrate, Appl. Phys. Lett. 94 (2009) 223506.

Journal of Crystal Growth
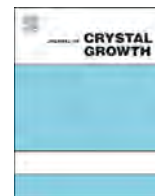
MBE-grown long-wavelength interband cascade lasers on InAs substrates

Lu Li [a,*], Hao Ye [a], Yuchao Jiang [a], Rui Q. Yang [a,*], Joel C. Keay [b], Tetsuya D. Mishima [b], Michael B. Santos [b], Matthew B. Johnson [b]

[a] School of Electrical and Computer Engineering, University of Oklahoma, Norman, OK 73019, USA
[b] Homer L. Dodge Department of Physics and Astronomy, University of Oklahoma, Norman, OK 73019, USA

ARTICLE INFO

ABSTRACT

An interband cascade (IC) laser structure with an emission wavelength designed to be near 11 μm was grown by molecular beam epitaxy on an InAs substrate. Defects and surface smoothness, as well as the overall crystalline quality, were characterized by optical microscopy, atomic force microscopy and X-ray diffraction. The maximum operating temperatures of a broad-area IC laser device in CW and pulsed modes were 97 K and 130 K, respectively, at an emission wavelength of 11 μm, which is the longest wavelength among interband lasers based on III–V semiconductor materials. The pulsed threshold current density at 80 K was measured to be 72 A/cm^2. The performance of this IC laser device may be limited by intersubband absorption loss in the active region and an unidentified carrier leakage channel.

Published by Elsevier B.V.

1. Introduction

With increasing emission wavelength, conventional interband lasers suffer from the limitation of the bandgaps of available semiconductor alloys, the difficulty of material growth, and the increase in free-carrier absorption loss and Auger recombination. IV–VI semiconductor lasers that can operate at low temperatures in the long-wavelength infrared region [1], have a relatively high threshold current and low output power, partly because IV–VI growth and device processing are still immature compared to those for the III–V material systems. Interband cascade (IC) lasers [2] that contain type-II quantum-well (QW) active regions, as a counterpart to the well-known intersubband quantum cascade (QC) lasers [3], have the same advantages of a cascade configuration and the ability to tailor their wavelength without being directly limited by the bandgaps of the constituent materials. Furthermore, the power consumption of IC lasers can be much lower than that of QC lasers, which will benefit some applications especially where energy cost is a concern.

IC lasers made of InAs/GaSb/AlSb materials on GaSb substrates have demonstrated superior performance in the wavelength range from 3 to 6 μm [4]. However, extending to longer wavelengths is difficult because the cladding regions, which consist of hundreds of InAs/AlSb superlattice (SL) layers, have to be significantly thickened to accommodate the longer optical wave decay length. These thick SL layers increase the complexity of the molecular beam epitaxy (MBE) growth, as well as the thermal resistance of the device due to the much lower thermal conductivity of SL layers compared to bulk binary materials. For longer wavelengths, IC lasers with InAs plasmon cladding layers grown on InAs substrates would have significant benefits because of the lower refractive index and the higher thermal conductivity of the InAs plasmon cladding layers. These benefits have been demonstrated with room temperature operation beyond 6 μm [5], as well as lasing up to 10.4 μm [6]. In this paper, we report the MBE growth of an InAs-based IC laser structure with an emission wavelength at 11 μm, the longest lasing wavelength achieved for III–V interband semiconductor lasers. The maximum operating temperatures reached for a broad-area device were 97 and 130 K in CW and pulsed mode, respectively.

2. Epitaxial growth and material characterizations

The IC laser structure was grown on an epi-ready S-doped ($n \sim 2.5 \times 10^{18}$ cm^{-3}) InAs substrate using an Intevac GEN II MBE system equipped with a valved As cracker and an unvalved Sb cracker. The growth temperature was monitored by an IRCON Modline 3 infrared pyrometer, which was calibrated using the GaSb surface reconstruction transition from (1×3) to (2×5) [7]. The growth rates for group III sources (In, Ga and Al) were calibrated by intensity oscillations of the reflection high-energy

* Corresponding author. Tel.: +1-405-431-0092.
E-mail addresses: lilu@ou.edu (L. Li), rui.q.yang@ou.edu (R.Q. Yang).

electron diffraction (RHEED) patterns prior to the growth of the IC laser structure. Moderate growth rates were adopted to grow Ga- and Al-containing alloys, compared to a low growth rate (0.22 ML/s) for InAs, which was found to be optimum in our previous growths of laser structures [8]. The cracker zones for both As and Sb were kept at 900 °C to provide stable beams mostly composed of As_2 and Sb_2, respectively. While the flux ratios of Sb_2/Ga and Sb_2/Al were both maintained around 3, the As_2/In flux ratio was kept near 8 to achieve a slight As_2 overpressure as determined by the observation of an As-rich (2×4) surface under RHEED observation. During growth, the As-valve position was kept constant and only the shutter was used to control the As flux for the different layers. The whole structure was grown at 400 °C as a compromise between the optimal growth windows for the thick InAs layers and the ultra-thin InAs/AlSb/Ga(In)Sb layers in the cascade regions.

After the oxide desorption process described in Ref. [8] was completed, the growth was initiated with a 2.3 μm highly n-doped (Si, $\sim 7 \times 10^{18}$ cm^{-3}) InAs layer as a bottom plasmon waveguide cladding layer. Then a (~ 1.9 μm) unintentionally doped InAs separate confinement layer (SCL) was grown, followed by the 20 cascade stages (46.2 nm per stage) for achieving an optical gain that is sufficient to overcome the likely increased optical loss expected for the longer wavelength range. Next, a top (~ 2.5 μm) unintentionally doped InAs SCL was grown and the growth ended with 35 nm of highly n-doped (Si, $\sim 7 \times 10^{18}$ cm^{-3}) InAs as the top contact layer. Each cascade stage was composed of an n-type electron injector made of InAs/AlSb multiple QWs, an active region (InAs/Ga$_{0.65}$In$_{0.35}$Sb/InAs, 38/28/33.5 Å, similar to "W"-shape QWs [9]) and a hole injector (GaSb/AlSb QWs). Because InAs has the smallest lattice constant among all the alloys in the IC laser structure, strain balance for the whole structure to the InAs substrate was achieved by using AlAs interfaces in the electron/hole injection regions. Otherwise, there was no intentional shutter sequence at the interfaces between the ultra-thin alloy layers. Some of the InAs QWs in the electron injector were heavily n-doped to $\sim 2.3 \times 10^{18}$ cm^{-3} to rebalance the hole concentration [10]. The entire growth time exceeded 30 h as the total thickness was close to 8 μm.

After growth, the wafer was first assessed by differential interference contrast (DIC) microscopy for surface defects and texture. The surface defect density ranged from 7×10^3 to 2×10^4 cm^{-2} over the wafer. This density is comparable to the average etch pit density (EPD) of $\sim 1.5 \times 10^4$ cm^{-2} for the InAs substrate, as specified by the substrate supplier. Despite the long growth time for this thick structure, there was no appreciable increase in the defect density. Besides the limited defect density, the surface looks flat and featureless. The surface smoothness was quantified using an Asylum MFP-3D-BIO atomic force microscope (AFM). The AFM image (Fig. 1) shows uniform steps with atomic step edges, as expected from the InAs substrate miscut of $\sim 0.35°$ from (100) toward (111)A. On the 2 μm × 2 μm scan area the root-mean-square (RMS) roughness is only 0.1 nm.

The crystalline quality of the IC laser structure was characterized using a Philips MRD X-ray diffraction (XRD) system. Fig. 2 (top) shows experimental data from an XRD omega/2θ scan around the InAs (004) reflection for the IC laser structure. Numerous sharp and narrow satellite peaks over $\pm 3°$ around the InAs substrate peak were observed (> 30 orders at each side of the substrate peak with FWHM less than 30''), indicating that the structure has an excellent crystalline quality. A simulated XRD curve (Fig. 2, bottom) based on the designed IC laser structure was calculated using a commercial XRD simulator (X'pert Epitaxy). The average thickness per stage in the cascade region of the IC laser structure (47.5 nm as derived from the spacing of the satellite peaks) is only 3% more than design value. The experimental and simulated curves are nearly identical to each
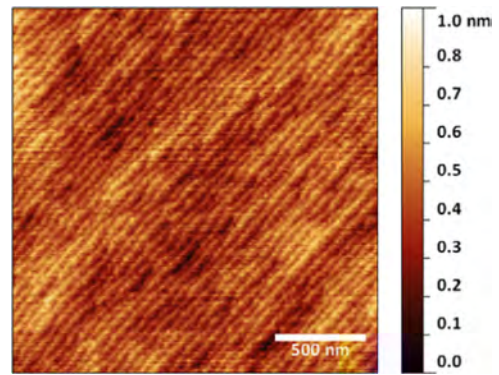
Fig. 1. A 2 μm X 2 μm atomic force microscope image of the IC laser structure's surface.
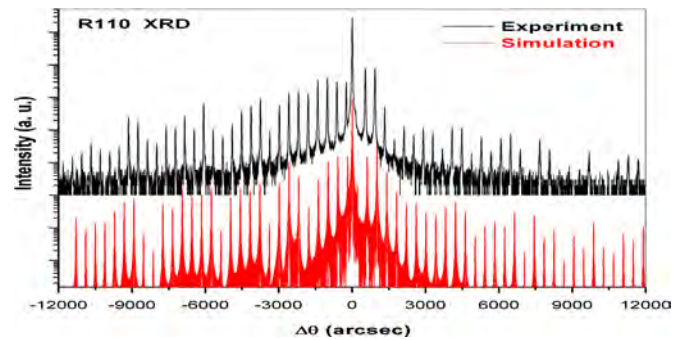
Fig. 2. (Top) Experimental XRD curve from an omega/2θ scan around the InAs (004) reflection for the IC laser structure. (Bottom) Corresponding simulated XRD curve calculated for the designed structure.

other, demonstrating that the MBE growth was well controlled over the long growth time.

3. Device results and discussion

In order to reduce the influences of device processing and quickly evaluate the device performance, broad-area IC lasers were fabricated. The 150-μm-wide mesas were defined using UV contact lithography and wet-chemical etching. The etching proceeded to the bottom SCL to prevent lateral current spreading. A 220-nm-thick, 90-μm-wide SiO$_2$ insulating layer was deposited and lithographically defined (through lift-off) on the center of the mesa stripe, followed by the deposition and lithographic defining (through lift off) of a 30/300-nm-thick and 100-μm-wide Ti/Au layer that contacted the top InAs layer for current injection. After thinning the wafer down to ~ 150 μm, the processing was finished by Ti/Au metallization on the substrate side of the wafer. All the depositions were done using magnetron sputtering. A schematic of the processed broad-area device is shown in Fig. 3. The SiO$_2$ insulating layer combined with the top metal layer, constitute the dielectric-metal hybrid top cladding layers used to confine optical wave [11]. Our waveguide simulation suggests that the confinement factor and free-carrier absorption loss in this 20-stage laser (without accounting for possible absorption loss due to intersubband transitions in the active region) are very similar to the previous 15-stage 9.1 μm IC lasers reported in Ref. [6].

The fabricated broad-area laser wafer was cleaved into bars with a cavity length ranging from 1 to 2 mm, which were mounted epi-side up on a copper heat sink with indium solder and then wire bonded. The emission spectra were acquired by a Nicolet Fourier transform infrared (FTIR) spectrometer equipped with a liquid nitrogen cooled mercury cadmium telluride (MCT) detector. In CW
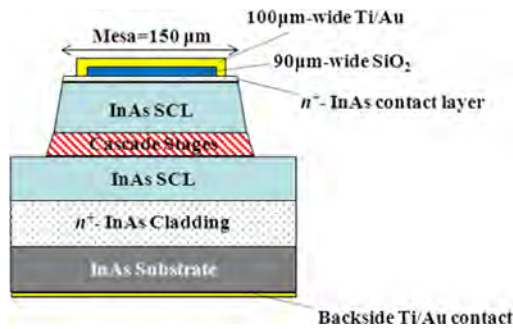
Fig. 3. Schematic of the processed broad-area IC laser.
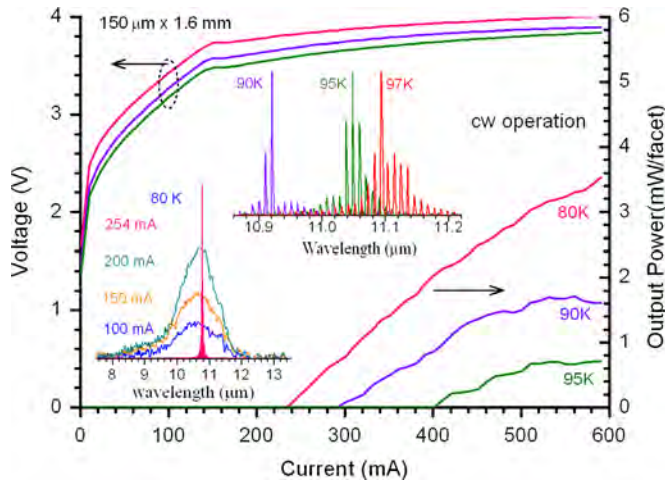
Fig. 4. Current–voltage–light characteristics for a 150-μm-wide device in cw operation. The insets show the cw lasing spectra at heat-sink temperatures of 80–97 K, and emission spectra at 80 K with several injection currents before threshold.

Fig. 5. Light–current curves for the broad-area IC laser in pulsed mode at temperatures of 80 K to 130 K. The arrows point to threshold currents where spectra were taken. The inset shows the pulsed spectra at several temperatures.

mode, a 1.6-mm-long device lased near 10.8 μm at 80 K, and was operated at up to 97 K with an emission wavelength at 11.1 μm, as shown in the inset to Fig. 4. The threshold current density at 80 K in CW mode was 95 A/cm^2, much higher than the $\sim$10 A/cm^2 for IC lasers near $\sim$9 μm operated under the same conditions [6]. The threshold voltage was 3.9 V at 80 K, corresponding to a voltage efficiency of 61% that is lower than a typical value (e.g. 90%) for InAs-based IC lasers.

Additionally, current–voltage characteristics exhibited some abnormal behavior—i.e., the slope that corresponds to the differential resistance had an abrupt drop well before the current reached the threshold, as shown in Fig. 4. Emission spectra were taken at several injection current levels around that point ($\sim$150 mA) at 80 K to examine whether the device had lased or not. As shown in the inset to Fig. 4, electroluminescence peaks at currents below the threshold ($\sim$230 mA) were broad ($>$120 nm) in contrast to the narrow lasing spectrum. This confirmed that the device did not lase before the current reached 230 mA. Other IC lasers from the same wafer also exhibited an abrupt drop in differential resistance at various current densities before threshold. The devices, which had this pre-threshold drop in the differential resistance at smaller currents, had higher threshold currents, suggesting a correlation with defect related leakage and material non-uniformity. The abrupt drop in differential resistance might be caused by the activation of a carrier leakage channel, which increases the threshold current density and reduces the output power. The device at 80 K had an output power of $\sim$3.6 mW/facet at 600 mA (Fig. 4), which is much lower than our previous 9 μm IC lasers [6].

Nevertheless, the threshold input power density (370 W/cm^2 in CW mode at 80 K) was much lower than that of QC lasers at similar wavelengths [12,13]. The threshold current density and voltage of QC lasers are typically around several hundreds of A/cm^2 and 10 V, respectively. In pulsed mode (1 μs at 5 kHz), our device lased at temperatures up to 130 K near 11.2 μm (inset to Fig. 5), the longest wavelength achieved among III–V interband lasers. The light intensity did not increase rapidly immediately after reaching the threshold and the slope was initially small at the threshold as shown by the light–current (L–I) characteristics in Fig. 5. Hence, it was difficult to accurately determine the threshold current by L–I curves. The threshold current was then obtained from the lasing spectra by varying current. At 80 K, the threshold current density was 72 A/cm^2, which was about 24% lower than that in cw mode, suggesting substantial heating for broad-area lasers in cw operation even at 80 K.

The 11 μm IC lasers did not perform as well as our previous 9 μm IC lasers in terms of threshold current densities and output powers. The threshold current density can be expressed as $J_{th} = q(N_{tr} + \frac{\alpha_i + \alpha_m}{a\Gamma})/\tau$, where N_{tr} is the transparency carrier density, τ is the carrier lifetime, Γ is the optical confinement factor, $a = dg/dN$ is the differential material gain, α_m is the mirror loss, and α_i is the internal loss which includes the waveguide loss (mainly free carrier absorption loss) and the absorption loss in the active region due possibly to intersubband transitions. The transparency carrier density depends on the band structure (see [14,15]) and is nearly insensitive to the lasing wavelength in type-II QWs at low temperatures (e.g. 80 K), based on observed threshold current densities for type-II IC lasers over a wide spectral range. The typical transparency current density is small at low temperatures (e.g. 1–3 A/cm^2 at 80 K). Hence, at 80 K, there is a negligible difference between N_{tr} for the 11 μm and 9 μm IC lasers, as their active regions are very similar. For the same reason and because the differential material gain, dg/dN, is proportional to the wavefunction overlap in the active region, the difference in dg/dN between the 11 μm and 9 μm IC lasers would not be larger than 10%. Considering the similar confinement factor and comparable mirror losses (because both their facets were uncoated), the much higher threshold current density in this 11 μm IC laser might be caused only by a significantly reduced lifetime, τ, and increased internal loss, a_i. The reduced carrier lifetime could be related to more defects and an increased Auger recombination. However, a large increase in Auger recombination at 80 K is unlikely because

the lasing wavelength was increased only from 9.1 to 10.8 μm, unless the threshold carrier concentration was greatly increased.

If the carrier leakage channel was not activated, an increase in threshold carrier concentration could only be caused by a considerable increase of internal optical loss based on the above discussion, which is consistent with the significant reduction of attainable output power. This is because the increased Auger recombination alone would not necessarily lower the output power, while the internal optical loss would do so. Hence, the lower performance of these long wavelength IC lasers could be primarily attributed to the combination of a possibly activated leakage channel and a large increase of internal optical loss beyond the common free-carrier absorption (the free-carrier absorption loss is similar to what was calculated in our 9 μm IC lasers). Although the cause of a high internal absorption loss is not clear at this stage, intersubband absorption loss in the active region is a possibility. Intersubband absorption loss occurs in QW structures [14], but in principle can be eliminated or alleviated by removing resonant intersubband transitions through quantum engineering. To fully understand and address this issue, further investigations are needed.

4. Conclusions

We have investigated the MBE growth of IC laser structures on InAs substrates, and demonstrated the longest lasing wavelength ever achieved by interband lasers based on III–V materials. Optical microscopy, AFM and XRD measurements showed that the material quality of the IC laser structure was quite good in terms of surface defects, smoothness and crystalline quality. A 150-μm × 1.6-mm IC laser operated at 11 μm at temperatures up to 97 K in CW mode and 130 K in pulsed mode. The threshold current density was noticeably higher and the output power lower than for our shorter wavelength IC lasers. This reduced performance was mainly attributed to a possible activated leakage channel and a significantly increased internal optical loss, not to the Auger recombination expected for increasing wavelength. At this stage, we do not fully understand why the threshold current density of this long wavelength IC laser was so much higher ($>7\times$) with only a modest increase in lasing wavelength compared to our 9 μm IC lasers. Further investigations are required to achieving better understanding and improved device performance.

References

[1] E. Kapon, Semiconductor Lasers II: Materials and structures, Optics and Photonics, Academic Press, United States of America, 1998.
[2] R.Q. Yang, Superlattices Microstruct. 17 (1995) 77–83.
[3] J. Faist, F. Capasso, D.L. Sivco, C. Sirtori, A.L. Hutchinson, A.Y. Cho, Science 264 (1994) 553–556.
[4] I. Vurgaftman, W.W. Bewley, C.L. Canedy, C.S. Kim, M. Kim, C.D. Merritt, J. Abell, J.R. Meyer, IEEE J. Sel. Top. Quant. Electron. 19 (2013) 1200210.
[5] M. Dallner, S. Höfling, M. Kamp, Electron. Lett. 49 (2013) 286–287.
[6] Z. Tian, L. Li, H. Ye, R.Q. Yang, T.D. Mishima, M.B. Santos, M.B. Johnson, Electron. Lett. 48 (2012) 113–114.
[7] A.S. Bracker, M.J. Yang, B.R. Bennett, J.C. Culbertson, W.J. Moore, J. Cryst. Growth 220 (2000) 384–392.
[8] H. Ye, L. Li, R.T. Hinkey, R.Q. Yang, T.D. Mishima, J.C. Keay, M.B. Santos M.B. Johnson, J. Vac. Sci. Technol. B 31 (2013) 03C135.
[9] J.R. Meyer, C.A. Hoffman, F.J. Bartoli, L.R. Ram-Mohan, Appl. Phys. Lett. 67 (1995) 757–759.
[10] I. Vurgaftman, W.W. Bewley, C.L. Canedy, C.S. Kim, M. Kim, C.D. Merritt, J. Abell, J.R. Lindle, J.R. Meyer, Nat. Commun. 2 (2011) 585.
[11] Z. Tian, Y. Jiang, L. Li, R.T. Hinkey, Z. Yin, R.Q. Yang, T.D. Mishima, M.B. Santos, M.B. Johnson, IEEE J. Quant. Electron. 48 (2012) 915.
[12] A. Tahraoui, A. Matlis, S. Slivken, J. Diaz, M. Razeghi, Appl. Phys. Lett. 78 (2001) 416–418.
[13] S. Slivken, Y. Bai, B. Gokden, S.R. Darvish, M. Razeghi, Proc. SPIE 7608 (2010) 76080B.
[14] Y.-M. Mu, R.Q. Yang, J. Appl. Phys. 84 (1998) 5357–5359.
[15] R.Q. Yang, Y.-M. Mu, SPIE 3628 (1999) 104–112.
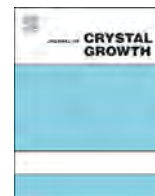
Wavelength tuning of InAs quantum dot laser by micromirror device

CrossMark

J.Y. Yan [a], Q. Gong [a,*], C.Z. Kang [a], H.X. Xu [a], C.F. Cao [a], Y.Y. Li [a], S.M. Wang [a,1], H.L. Wang [b]

[a] State Key Laboratory of Functional Materials for Informatics, Shanghai Institute of Microsystem and Information Technology, Chinese Academy of Sciences, 865 Changning Road, Shanghai 200050, People's Republic of China
[b] Department of Physics, Qufu Normal University, Qufu 273165, People's Republic of China

ARTICLE INFO

ABSTRACT

We report on the InAs quantum dot (QD) external cavity laser (ECL) using a digital mirror device (DMD) as the key component for wavelength tuning. The InAs QD laser diode was grown by gas source molecular-beam epitaxy, which had a broad gain profile. Single mode operation was achieved with the side mode suppression ratio of 21 dB when the optical feedback was provided by a mirror pattern consisting of 9 micromirrors. Moreover, two-color lasing was demonstrated with two laser lines having frequency difference in the THz range. The incorporation of DMD in the ECL enables great flexibility and many unique features, such as high tuning speed independent of the tuning step, two-color or multi-color lasing, and adjustable intensity for individual laser lines.

© 2015 Elsevier B.V. All rights reserved.

1. Introduction

A unique feature of quantum dot (QD) lasers is that their gain profile is much broader than the conventional quantum well (QW) lasers, which is extremely desirable for realizing broadband tunable external cavity lasers (ECLs) [1,2]. In classical ECL configurations, i.e., Littman and Littrow, the function of wavelength tuning is achieved by mechanically rotating the grating or the cavity mirror. Thus, a broad wavelength tuning range needs significant rotation movement of the grating or mirror, which may drastically degrade the reliability and reproducibility of the whole system. Recently, a concept of Fourier transform ECL (FTECL) was developed by Breede et al. [3,4] to tune QW lasers for the purposes of fast tuning and multiple-color lasing. In this paper, we propose that the FTECL concept can be utilized to perfectly solve the problem mentioned above by using a digital micromirror device (DMD) to choose the optical feedback for the QD laser. Each micromirror can be electronically turned on or off in order to adjust the optical feedback. In this way, the movement of mirror/grating in the Littman/Littrow configuration can be completely replaced by control of the micromirrors at desired locations, resulting in good reliability and reproducibility of the broadband tunable QD ECL.

Regarding the laser diode for tunable laser, broad gain profile is one of the very desirable properties. Growth of self-assembled QDs in Stranski–Krastanov (SK) mode has been demonstrated as a very

efficient way to obtain high density of zero-dimensional nanostructures [5]. In addition, these densely packed QDs have very good optical properties and can be used as active material for high performance QD lasers [6–9]. Due to the basic nature of the SK growth mode, the QD assembly always has relative broad size distribution, leading to a gain profile much wider than that of QWs. This feature is very useful for broadly tunable lasers. Previously, we studied external cavity tunable InAs/GaAs and InAs/InP [2] QD lasers with broad tunable range in Littrow configuration. In this work, we modified the setup by using a DMD to generate optical feedback, which brings unique features and flexibility to the ECL system.

2. Experimental setup

The QD lasers were grown on n-type GaAs (100) substrates by gas source molecular-beam epitaxy (GSMBE). In the GSMBE system, pure metal gallium, indium, and aluminum are used to provide III element flux, while AH_3 gas is introduced into a high temperature injector and thermally decomposed there at 1000 °C. After oxide desorption, a 500 nm-thick Si-doped GaAs buffer layer was grown, followed by a 1500 nm-thick Si-doped $Al_{0.3}Ga_{0.7}As$ layer for the optical confinement. The active region consisted of five-stacked InAs QD layers embedded in a 160 nm-thick $Al_{0.15}Ga_{0.85}As$ layer. GaAs spacers (40-nm-thick) were inserted into the adjacent QD layers. Finally, the structure was finished by growing 1500 nm-thick Be-doped $Al_{0.3}Ga_{0.7}As$ cladding layer and 200 nm-thick Be-doped GaAs contact layer. Each QD layer was formed by deposition of nominally 2.2 monolayers (MLs) InAs with growth rate of 0.12 ML/s.

The background pressure in the growth chamber was 1.5×10^{-5} Torr during growth. Ridge waveguide laser diodes were fabricated with strip width of 6 μm. Both facets of the laser diode were left as-cleaved without coating. The LD chips were soldered on copper heat sinks by thin indium films.

The QD laser diode was mounted in a FTECL setup illustrated in Fig. 1. Firstly, the laser beam was collimated by a lens, and then diffracted by a grating. A second lens was used to focus the diffracted light, resulting in a series of focused light spots, where the DMD was placed. Note that the beam only contains light of Fabry–Perot mode existing in the internal cavity of laser diode. Therefore on the focal plane of the second lens there are a series of laser spots corresponding to diffracted beams with discrete wavelengths. The beam size for a single mode is estimated as about 20 μm. The DMD was controlled to reflect the light either back to the laser diode or just to the free space. In the former case an external cavity is formed between the laser facet and the DMD, leading to optical feedback to the laser diode, i.e., reduction of mirror loss of the whole system.

The DMD consists of an array of micromirrors with dimensions of 13.68×13.68 μm². Each micromirror can be electronically controlled to rotate $\pm 12°$, corresponding to an "on" and "off" state. The micromirrors with "on" state will generate optical feedback to the laser diode, while that with "off" state will not. Therefore, we can choose the mirror patterns corresponding to one or more focused laser spots on the focal plane to reflect the laser beam back and generate optical feedback to the QD laser diode.

3. Results and discussions

3.1. Tuning by a column of micromirrors

The wavelength tuning of the system was tested by using a single column of micromirrors for feedback. As shown in Fig. 2, single mode lasing at different wavelengths was observed by
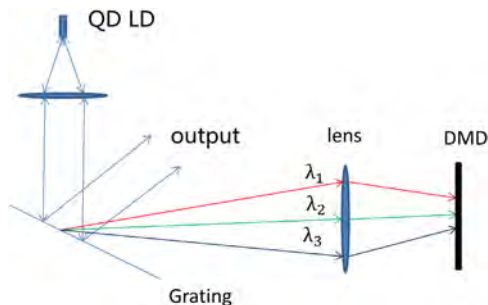
Fig. 1. Schematic illustration of the FTECL setup with a InAs QD laser, a grating, two lenses, and a DMD.
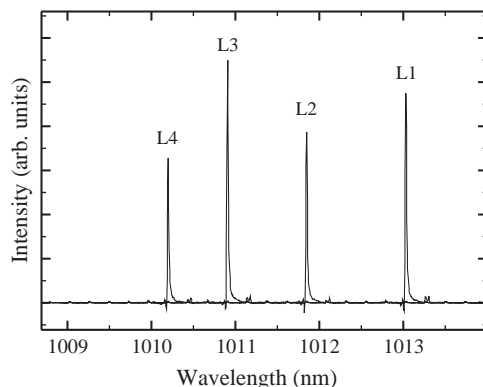
Fig. 2. Lasing spectra of the InAs QD ECL with optical feedback provided by activating single column of micromirrors with different column numbers.

activating different columns of micromirrors. For example, single mode lasing at 1013.1 nm was realized by activating the single column of micromirrors with column number of L1. On the other hand, lasing occurred at 1010.2 nm when the active column was at number L4. Note that the tuning speed of the system was mainly limited by the operation speed of DMD, e.g., in the kHz range. It is worthy to note that such a high tuning speed is independent of the wavelength tuning gap, because just one command is needed to change the mirror pattern whatever the pattern is. So this system has an advantage over the conventional Littrow or Littman configuration, where large tuning gap usually needs more time to gain enough rotation angle of the grating or mirror.

3.2. Optimization of the mirror pattern

In order to obtain the optical feedback as large as possible, we optimized the reflecting mirror pattern. A pattern consisted of 9 micromirrors was found to fit the focused laser spot very well, resulting in high quality lasing spectrum in single mode, as shown in Fig. 3. The side mode suppression ratio was measured as 21 dB, when the feedback was provided by the optimized pattern shown in the inset of Fig. 3. Adding more active mirrors to the optimized mirror pattern did not improve the laser performance, indicating that the focused laser spot was completely covered by the mirror pattern and maximum optical feedback was achieved. The output power was measured as a few mW, depending on the injection current.

3.3. Two-color lasing

Single mode operation was obtained by activating one mirror pattern as mentioned above. If more mirror patterns were added, more laser lines would appear, given that each mirror pattern covers the corresponding focused laser spot in space. For example, two-color lasing was obtained by just activating two mirror patterns, as shown in Fig. 4. The separated mirror patterns are shown in the inset, while the distance between two patterns determines the wavelength difference between the two lasing lines. The diffraction capability of grating and the focal length of the lens together define the dependence of the wavelength difference on the distance between the active patterns. It is worth noting that the wavelength difference of the two-color lasing shown Fig. 4 is 3.56 nm, i.e., 1.04 THz difference in frequency. Therefore, this system is able to generate two laser lines with frequency difference in the THz range, which might be used in THz generation by the technique of frequency mixing. Moreover, by activating proper mirror patterns, multiple lasing lines with desirable wavelengths can be obtained.
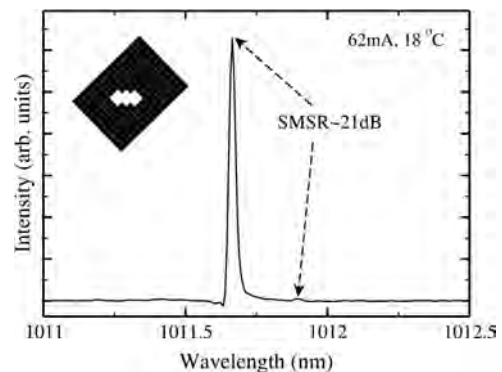
Fig. 3. Lasing spectrum of the InAs QD ECL with the optical feedback provided by the optimized mirror pattern consisting of 9 micromirrors, which are shown in the inset.
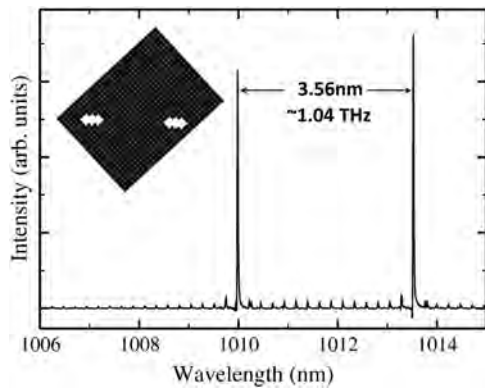
Fig. 4. Lasing spectrum of the QD ECL when there were two active mirror patterns. The spectrum consisted of two lasing lines with a wavelength difference determined by the distance between the mirror patterns.
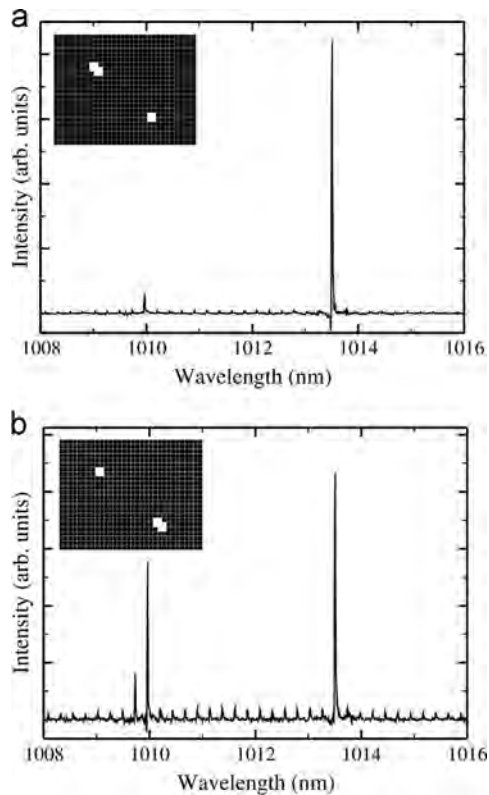
Fig. 5. (a) Lasing spectrum of the InAs QD ECL working in two-color mode, where one laser line was much stronger than the other. (b) Lasing spectrum after modifying the active mirror patterns. The insets show the active mirror patterns corresponding to the spectra.

3.4. Intensity adjustment of the laser lines

In the case of two-color lasing discussed above, the relative intensities of the two laser lines are mainly determined by the optical gain and loss, which vary as a function of the wavelength. Therefore, the intensity of the individual lasing line should be very sensitive to the optical feedback provided by the active mirror pattern. In other words, the active mirror pattern reduces the mirror loss of the external cavity, thus, enhances the optical feedback. The concept

was proved by the results shown in Fig. 5. We started with a two-color lasing case, where one laser line had much higher intensity than the other, as shown in Fig. 5(a). Then the active mirror patterns were changed by increasing the optical feedback for the low intensity laser line, and, decreasing the optical feedback for the high intensity laser line, as shown in the insets. Indeed, the relative intensities of the two laser lines became more close, as shown in Fig. 5(b). The original low intensity laser line was enhanced in intensity, while the high intensity one was suppressed. Therefore, fine regulation of the strength of optical feedback is very effective to adjust the intensity of an individual laser line. This method might be very important to balance the intensity of two or even more lasing lines when the system is working in multi-color mode.

4. Conclusion

We have investigated the InAs QD ECL using a DMD as the key component for wavelength tuning. The system has fast tuning speed, and, in particular, the tuning speed is intrinsically independent of the wavelength tuning gap. High quality of single mode spectrum was achieved by using the optimized mirror pattern consisting of 9 micromirrors. Moreover, it is quite convenient to realize two-color or multi-color operation by just activating two or more mirror patterns. The wavelength difference between the laser lines can be adjusted by the distance between the mirror patterns. Two laser lines with frequency difference in the THz range were demonstrated. In addition, the intensities of the laser lines can be adjusted by fine regulation of the mirror patterns when the system is working in the multi-color mode. We have shown that this system has much more flexibility than the conventional Littrow and Littman configurations.

References

[1] P.M. Varangis, H. Li, G.T. Liu, T.C. Newell, A. Stintz, B. Fuchs, K.J. Malloy, L. F. Lester, Low-threshold quantum dot lasers with 201 nm tuning range, Electron. Lett. 36 (18) (2000) 1544–1545.
[2] P. Chen, Q. Gong, C.F. Cao, S.G. Li, Y. Wang, Q.B. Liu, L. Yue, Y.G. Zhang, S.L. Feng, C.H. Ma, H.L. Wang, High performance external cavity InAs/InP quantum dot lasers, Appl. Phys. Lett. 98 (12) (2011) 121102.
[3] M. Breede, S. Hoffmann, J. Zimmermann, J. Struckmeier, M. Hofmann, T. Kleine-Ostmann, P. Knobloch, M. Koch, J.P. Meyn, M. Matus, S.W. Koch, J.V. Moloney, Fourier-transform external cavity lasers, Opt. Commun. 207 (2002) 261–271.
[4] M. Breede, C. Kasseck, C. Brenner, N.C. Gerhardt, M. Hofmann, R. Höfling, Micromirror device controlled tunable diode laser, Opt. Lett. 43 (8) (2007) 456–457.
[5] D. Leonard, M. Krishnamurthy, C.M. Reaves, S.P. Denbaars, P.M. Petroff, Direct formation of quantum-sized dots from uniform coherent islands of InGaAs on GaAs surfaces, Appl. Phys. Lett. 63 (23) (1993) 3203–3205.
[6] D.L. Huffaker, G. Park, Z. Zou, O.B. Shchekin, D.G. Deppe, 1.3 μm room-temperature GaAs-based quantum-dot laser, Appl. Phys. Lett. 73 (18) (1998) 2564–2566.
[7] M. Grundmann, The present status of quantum dot lasers, Physica E 5 (2000) 167–184.
[8] Z. Mi, P. Bhattacharya, S. Fathpour, High-speed 1.3 μm tunnel injection quantum-dot lasers, Appl. Phys. Lett. 86 (15) (2005) 153109.
[9] C.S. Lee, W. Guo, D. Basu, P. Bhattacharya, High performance tunnel injection quantum dot comb laser, Appl. Phys. Lett. 96 (10) (2010) 101107.
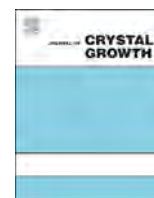
Effects of well widths and well numbers on InP-based triangular quantum well lasers beyond 2.4 μm

Y. Gu, Y.G. Zhang *, X.Y. Chen, Y.Y. Cao, L. Zhou, S.P. Xi, A.Z. Li, Hsby. Li

State Key Laboratory of Functional Materials for Informatics, Shanghai Institute of Microsystem and Information Technology, Chinese Academy of Sciences, Shanghai 200050, China

ABSTRACT

The effects of well widths and well numbers of InGaAs triangular quantum well lasers in 2.30–2.44 μm range using antimony-free material system on InP substrates are investigated. The triangular quantum well was equivalently formed by using gas source molecular beam epitaxy grown InAs/In$_{0.53}$Ga$_{0.47}$As digital alloy and the pseudomorphic growth was confirmed by the X-ray diffraction measurements. Lasing at 2.30 μm above 330 K under continuous wave operation has been achieved for the laser with four 13 nm quantum wells. By increasing the well width to 19 nm, the continuous wave wavelength has been extended to 2.44 μm at 290 K, whereas the epitaxial quality and laser performances are deteriorated. For those lasers with well width up to 19 nm, the moderate reduction of the quantum well numbers can restrict the strain accumulation and improve the laser performances. Continuous wave lasing at 2.38 μm above 300 K has been achieved.

© 2015 Elsevier B.V. All rights reserved.

1. Introduction

Semiconductor laser diodes emitting in 2–2.5 μm wavelength range are very attractive for free space communications and light detection and ranging (LIDAR) due to the low absorption by atmospheric water molecules in this range [1]. Such devices are also of great interests in atmospheric pollution monitoring and medical diagnostics by tunable diode laser absorption spectroscopy (TDLAS) gas sensing [2]. Furthermore, it is also desired for the characterization and evaluation of photodetectors and focal plane arrays operating in this wavelength range, because wavelength match is very important to determine their actual features [3]. Compressively strained type-I InGaAs quantum well (QW) lasers on InP substrate offer an attractive alternative to traditional GaSb-based structures for semiconductor lasers in this wavelength range. The emission wavelength can be tailored by the indium composition and well width of InGaAs QWs, and the main obstacle is how to control the significant strain and keep good structural quality in the QWs when increasing the indium contents [4,5]. To improve the material quality, several methods have been applied, such as growing the QWs at a relatively low temperature [6], applying a relatively high growth rate [7], and using surfactant [8]. By using 5 nm thick pure InAs in the QWs, lasers extended to 2.33 μm have been demonstrated under continuous wave (CW)

operation at room temperature (RT) [9,10]. On the other hand, the use of triangular QW instead of rectangular one can increase the lasing wavelength while keeping the same strain extent [11,12]. The triangular QW can be grown by digital alloy technology, which is very effective to restrain the formation of three dimensional growth in the strained QW thus improve the laser performances [13,14]. By this approach, the InAs/InGaAs triangular QW lasers on InP substrate with wavelength up to 2.4 μm have been reported recently [15]. To control the strain in the QW, the QW structures, especially the well widths and numbers, play a very crucial role. In this work, InAs/InGaAs triangular QW lasers with different well widths and well numbers were demonstrated and investigated in detail. The well widths were changed to tailor the wavelength, and the well numbers were adjusted to optimize the laser performances.

2. Experiments

The epitaxial laser wafers were all grown on *n*-type (001)-oriented InP epi-ready substrates in a VG Semicon V80H gas source molecular beam epitaxy (GSMBE) system. The elemental indium, gallium and aluminum were used as group III sources, while As$_2$ and P$_2$ cracked from Arsine and phosphine were used as group V sources. The InP substrates were at first heated to about 500 °C measured by thermocouple under P$_2$ flux to carry out the surface oxide desorption and then reduced to 440 °C for growth.

* Corresponding author. Tel.: +86 21 62511070; fax: +86 21 52419931.
 E-mail address: ygzhang@mail.sim.ac.cn (Y.G. Zhang).

a

p-InGaAs contact, 300 nm	
p-InP cladding, 1700 nm	
uid-InGaAsP waveguide, 120 nm	
uid-triangular QWs	
uid-InGaAsP waveguide, 120 nm	
n-InP buffer, 1000 nm	
n-InP substrate	

b
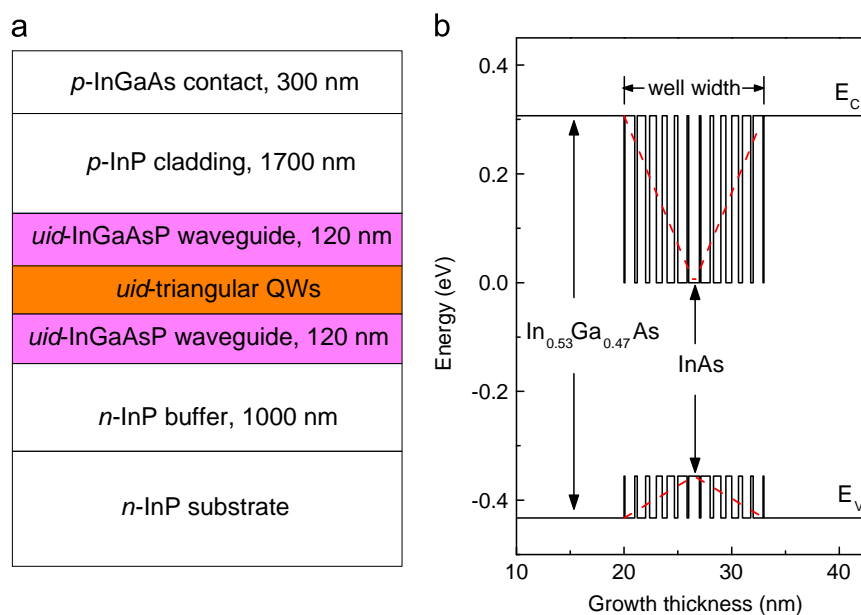
Fig. 1. (a) Schematic structure of the grown triangular QW laser samples. (b) Schematic diagram of the appeared (solid line) and effective (dotted line) band energy of the digital alloy for one QW.

Table 1
The well widths and numbers of samples 1–3.

Sample no.	Well width (nm)	Well number
1	13	4
2	19	4
3	19	2

As shown in Fig. 1(a), the growth started from a 1000-nm silicon doped *n*-type InP buffer, followed by a 120-nm unintentionally doped (*uid*) lattice-matched InGaAsP ($E_g = 1.1$ eV) waveguide layer which was grown at 460 °C. The substrate temperature was then decreased to 420 °C to grow the *uid* active triangular QWs. In the QW regions, the indium composition was approximately increased from 0.53 to 1 and then decreased to 0.53, which was approximated by using InAs/In$_{0.53}$Ga$_{0.47}$As digital alloy technology. Fig. 1 (b) shows the appeared and effective band energy of one QW. The designed period thickness of the digital alloy including one InAs layer and one In$_{0.53}$Ga$_{0.47}$As layer was 1 nm. The thicknesses of the InAs layer (d_1) and In$_{0.53}$Ga$_{0.47}$As layer ($1-d_1$) are obtained from $d_1 + 0.53 \times (1-d_1) = \alpha$, where α is the expected average indium composition in each short period. These layers are very thin, and the thinnest layer is even thinner than one monolayer, therefore these thin layers are supposed to intermix during the growth. When growing the QW structures, only the Ga shutter was opening and closing, without any growth interruption. The growth rates of InAs and InGaAs were 0.152 and 0.287 nm/s, respectively. Three samples with different well widths and well numbers were grown and the parameters were listed in Table 1. In$_{0.53}$Ga$_{0.47}$As layers were grown as barriers and the barrier thickness were 20 nm except for the first and last barrier layers, which were thickened to 100 nm to enhance the confinement. Therefore, the active QW layers were grown keeping the indium and gallium fluxes unchanged. Afterwards, a 120-nm *uid* InGaAsP upper waveguide, a 1700-nm beryllium doped *p*-type InP upper cladding layer and a 300-nm *p*-type In$_{0.53}$Ga$_{0.47}$As contact layer were grown at 440 °C. The substrate was undergoing rotation during the growth to get uniform thickness.

After growth, the structural properties of the wafers were characterized by X-ray diffraction (XRD) scanning curves using a Philips X'pert MRD high resolution X-ray diffractometer equipped with a four-crystal Ge (220) monochromator. Then, the ridge waveguide lasers with strip width of 6 μm were fabricated by using standard lithography and wet chemical etching. 300-nm Si$_3$N$_4$ layers were deposited by plasma enhanced chemical vapor deposition for isolation, and 4-μm-wide windows were opened on the top of the ridges. Sputtered Ti/Pt/Au and evaporated Ge/Au/Ni/ Au were formed as top *p*-type and bottom *n*-type contacts, respectively. After an alloyed step, the wafers were diced into bars of 800 μm leaving as-cleaved laser facets, mounted on copper heat sinks, wire bonded and installed into an Oxford Optistat DN-V variable temperature liquid nitrogen cryostat. The lasers were CW driven by a Keithley 2420 source meter, and the spectral characteristics were characterized by a Nicolet 860 Fourier transform infrared spectrometer using a liquid-nitrogen cooled InSb detector and a CaF$_2$ beam splitter. For the *I–P* measurements, a Coherent EMP1000 power meter was used.

3. Results and discussions

The XRD (004) $\omega/2\theta$ scanning curves of the grown laser wafers with various well widths and numbers in the active QW region are shown in Fig. 2, the strongest peak corresponds to InP and the envelope signals in the left side correspond to the active QWs. The XRD curves at different positions on the wafer are nearly the same indicating the pretty good uniformity of the QWs. Distinct satellite peaks are observed in sample 1. For sample 2 where the QW number is still four but the well width increases to 19 nm, the satellite peaks in the measured XRD curve become dimer, indicating the deteriorated QW quality with the rough heterostructure interfaces due to the accumulated strain. For sample 3, the satellite peaks become much more distinct for the QW number of two and keeping the well width of 19 nm, suggesting that the material quality of 19 nm QWs is improved by decreasing the QW number from four to two. In Fig. 2, the simulated curves from lattice dynamics for samples 1–3 are also shown. The simulated curves were all achieved by the simulation from the exact structure as designed. The good agreements of the diffraction peaks between the measured and simulated curves confirm the pseudomorphic
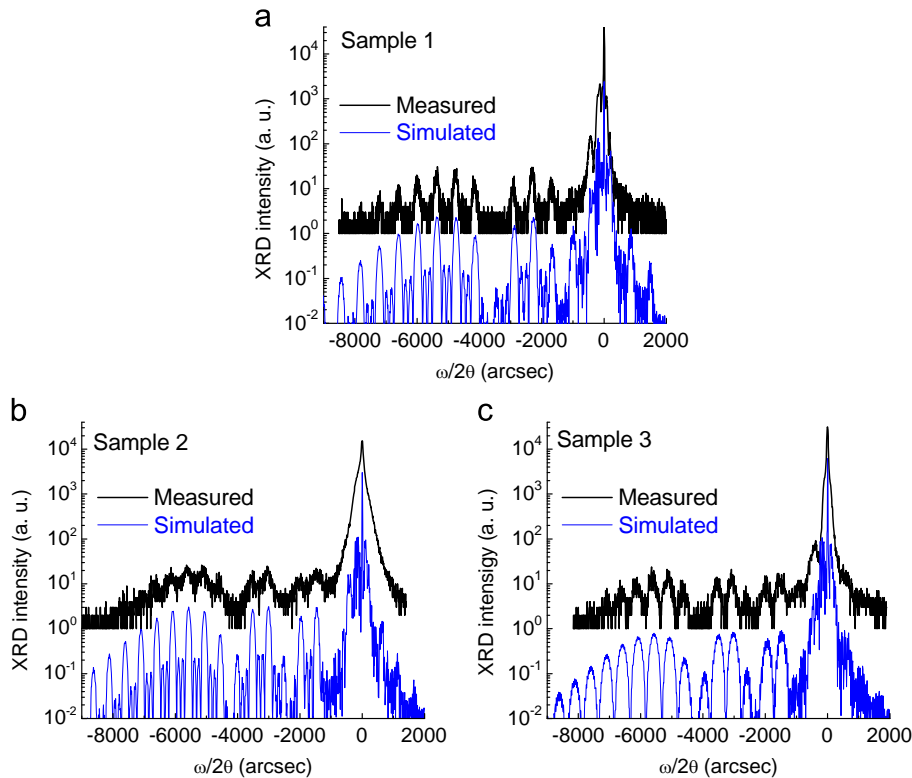
Fig. 2. Measured (upper curve) and simulated (bottom curve) XRD (004) $\omega/2\theta$ scan curves of the triangular QW laser samples 1–3.

growth of all samples. For these whole laser structures, the PL signals from QWs cannot be observed as about 2 μm thick top layers were grown on the QWs. In the PL measurements of QW test samples with different well widths, the PL intensity was observed a bit decreased as the increased QW width [16,17].

As shown in Fig. 3 the temperature dependent CW lasing wavelengths of the lasers have shown various performances, and the typical lasing spectra of samples 1–3 are shown in Fig. 4. The lasing wavelength is 2.30 μm at 300 K for sample 1 with four 13 nm QWs, and redshifts to 2.44 μm at 290 K as the well width increases to 19 nm for sample 2. However, the maximum lasing temperature is decreased from 330 K for sample 1 to 290 K for sample 2 due to the deteriorated material quality. For the 19 nm QW lasers, as the well number decreases from four to two, the maximum lasing temperature is increased to beyond 300 K and the lasing wavelength is around 2.38 μm at 300 K for sample 3. From linear fitting, the temperature dependent wavelength shift values are 1.00 nm/K, 1.41 nm/K and 1.01 nm/K for samples 1, 2 and 3, respectively. It is noted that the lasing wavelengths of sample 2 are longer than those of sample 3 at all temperatures. It is probably because that the QW wave functions are partly coupled as the carrier confinement is relatively weak in this triangular QW structure due to the inclined energy band.

Fig. 5 shows the light output characteristics of the three triangular QW lasers under CW operation. The output power is about 34 mW/facet at 350 mA injection current at 200 K and 15 mW/facet at 300 K for sample 1 with 13 nm QWs. The threshold current is about 17 mA at 200 K and increases to 58 mA at 300 K. As the well width increases to 19 nm while keeping four QWs in the active region (sample 2), the power at 200 K is decreased to only 11 mW/facet at 350 mA injection current. The threshold current of sample 2 is significantly increased to 72 mA and 260 mA at 200 K and 290 K, respectively. As the QW number of 19 nm QW laser decreases from four to two, the output power is increased to 16 mW/facet at 350 mA injection current at 200 K
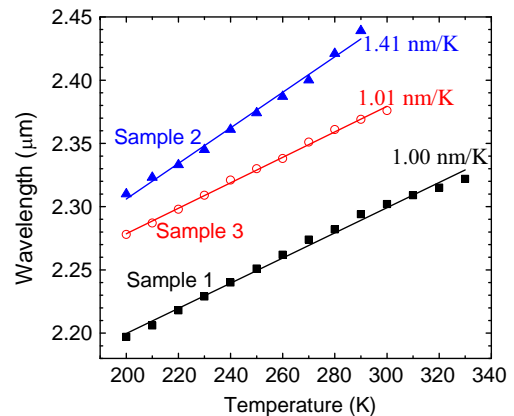
Fig. 3. Temperature dependence of the CW lasing wavelengths for the triangular QW laser samples 1–3. The temperature dependent wavelength shift values for the three samples are all indicated.

although there are less QWs in the active region. The maximum output power at 300 K is 1.8 mW/facet. The threshold current of sample 3 is reduced to about 10 mA at 200 K and 96 mA at 300 K. The improved output characteristics are mainly due to the better material quality.

The laser threshold current densities at various temperatures and derived characteristic temperatures for the three samples are shown in Fig. 6. For sample 1 with the 13 nm QWs, the threshold current density is about 1.2 kA/cm^2 at 300 K (300 A/cm^2 per QW). Two different slopes of the threshold current density exist in different temperature ranges. The characteristic temperature T_0 is derived to be about 75 K in the temperature range of 200–290 K, and decreases to 36 K in the temperature range of 290–330 K. For sample 2 with the increased well width of 19 nm, the threshold current density is significantly increased. The characteristic temperature T_0 is about 81 K and 48 K in the temperature ranges of 200–260 K and 260–
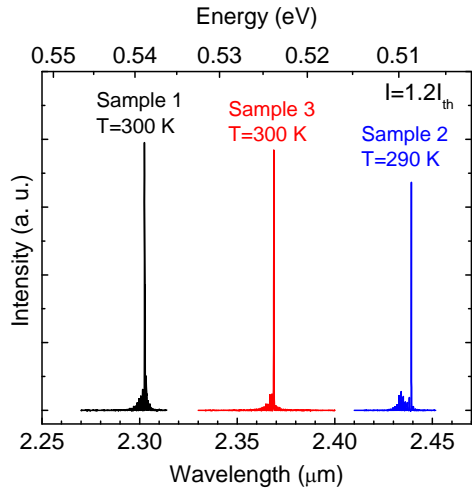
Fig. 4. CW lasing spectra of the triangular QW laser sample 1 at 300 K, sample 2 at 290 K and sample 3 at 300 K injected by 1.2 times of the threshold current.

Fig. 6. Temperature dependence of threshold current densities and characteristic temperatures (T_0) of samples 1–3. Two different T_0 values are derived in different temperature ranges for each sample.

sample 1 probably due to the less QWs of sample 3, however the threshold current density of sample 3 increases much more quickly as the temperature increases, reaching 2.0 kA/cm^2 at 300 K. The characteristic temperature T_0 of sample 3 is 50 K and 22 K for 200–280 K and 280–300 K temperature ranges, smaller than those of samples 1 and 2, which is probably because of the reduced gain as the decreased QW number. For this kind of highly strained triangular QW laser, a tradeoff should be considered between the strain control and sufficient gain. For the structure with thinner QWs, more QW number can be applied to achieve higher output power. In our experience, the performances of the 4 QWs laser structures do not degrade a lot when the well width enlarged from 10 nm to 16 nm [14,15]. As a rough estimation, 4 QWs could be around the maximum QW number for the 16 nm QW laser structure, but more QW number could be applied for thinner QWs whereas less QW number for wider QWs.

Fig. 5. Output powers at various temperatures and voltages at 300 K as a function of injected currents of samples 1–3.

290 K respectively, both close to those of sample 1. Comparing to those of sample 2, the threshold current density of sample 3 is significantly reduced as the well number decreases from four to two. At 200 K the threshold current density of sample 3 is even smaller than that of

4. Conclusion

In conclusion, InP-based InGaAs triangular QW lasers with different well widths and numbers have been grown by GSMBE. The triangular QW was equivalently formed by using InAs/In$_{0.53}$Ga$_{0.47}$As digital alloy with carefully adjusted growth thickness of each layer. X-ray diffraction measurements have confirmed the pseudomorphic growth. For the laser with four 13 nm QWs, CW lasing at 2.30 μm above 330 K has been achieved. By increasing the QW width to 19 nm, the CW lasing wavelength is extended to 2.44 μm at 290 K although the material qualities and laser performances are deteriorated. For the 19 nm triangular QW lasers, the reduction of the QW number from four to two can improve the laser performances and CW lasing at 2.38 μm above 300 K has been achieved.

References

[1] A. Bauer, K. Rößner, T. Lehnhardt, M. Kamp, S. Höfling, L. Worschech, A. Forchel, Semicond. Sci. Technol. 26 (2011) 014032.
[2] W. Lei, C. Jagadish, J. Appl. Phys. 104 (2008) 091101.

[3] Y. Gu, Y.G. Zhang, K. Wang, X. Fang, C. Li, L. Zhou, A.Z. Li, Hsby. Li, J. Cryst. Growth 378 (2013) 65.
[4] S. Forouhar, A. Ksebdzov, A. Larsson, H. Temkin, Electron. Lett. 28 (1992) 1431.
[5] J.S. Wang, H.H. Lin, L.W. Sung, IEEE J. Quantum Electron. 34 (1998) 1959.
[6] S. Jourba, M. Gendry, P. Regreny, G. Hollinger, J. Cryst. Growth 201/202 (1999) 1101.
[7] S. Kim, J. Kirch, L. Mawst, J. Cryst. Growth 312 (2010) 1388.
[8] T. Sato, M. Mitsuhara, T. Watanabe, Y. Kondo, Appl. Phys. Lett. 87 (2005) 211903.
[9] T. Sato, M. Mitsuhara, Y. Kondo, Electron. Lett. 43 (2007) 1143.
[10] T. Sato, M. Mitsuhara, N. Nunoya, T. Fujisawa, K. Kasaya, F. Kano, Y. Kondo, IEEE Photonics Technol. Lett. 20 (2008) 1045.
[11] G. Boehm, M. Grau, O. Dier, K. Windhorn, E. Roenneberg, J. Rosskopf, R. Shau, R. Meyer, M. Ortsiefer, M.-C. Amann, J. Cryst. Growth 301–302 (2007) 941.
[12] Y. Gu, Y.G. Zhang, S. Liu, Chin. Phys. Lett. 24 (2007) 3237.
[13] S. Jourba, M. Gendry, O. Marty, M. Pitaval, G. Hollinger, Appl. Phys. Lett. 75 (1999) 220.
[14] Y.Y. Cao, Y.G. Zhang, Y. Gu, X.Y. Chen, L. Zhou, Hsby. Li, IEEE Photonics Technol. Lett. 26 (2014) 571.
[15] Y. Gu, Y.G. Zhang, Y.Y. Cao, L. Zhou, X.Y. Chen, Hsby Li, S.P. Xi, Appl. Phys. Express 7 (2014) 032701.
[16] Y. Gu, Y.G. Zhang, K. Wang, A.Z. Li, Y.Y. Li, J. Cryst. Growth 311 (2009) 1935.
[17] Y.Y. Cao, Y. Gu, Y.G. Zhang, Y.Y. Li, X. Fang, A.Z. Li, L. Zhou, Hsby. Li, J. Infrared Millim. Waves 33 (2014) 213.

CrossMark
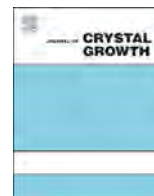
Specific detection of mercury(II) irons using AlGaAs/InGaAs high electron mobility transistors

Chengyan Wang, Yang Zhang*, Min Guan*, Lijie Cui, Kai Ding, Bintian Zhang, Zhang Lin, Feng Huang, Yiping Zeng

The Key Laboratory of Semiconductor Materials Science, Institute of Semiconductors, Chinese Academy of Sciences, Beijing 100083, China

ABSTRACT

As one of the most environmentally important cations, mercury(II) iron has the biological toxicity which impacts wild life ecology and human health heavily. A Hg^{2+} biosensor based on AlGaAs/InGaAs high electron mobility transistors with high sensitivity and short response time is demonstrated experimentally. To achieve highly specific detection of Hg^{2+}, an one-end thiol-modified ssDNA with lots of T thymine is immobilized to the Au-coated gate area of the high electron mobility transistors by a covalent modification method. The introduction of Hg^{2+} to the gate of the high electron mobility transistors affects surface charges, which leads to a change in the concentration of the two-dimensional electron gas in the AlGaAs/InGaAs high electron mobility transistors. Thus, the saturation current curves can be shifted with the modification of the gate areas and varied concentrations of Hg^{2+}. Under the bias of 100 mV, a detection limit for the Hg^{2+} as low as 10 nM is achieved. Successful detection with minute quantity of the sample indicates that the sensor has great potential in practical screening for a wide population. In addition, the dimension of the active area of the sensor is $20 \times 50~\mu m^2$ and that of the entire sensor chip is $1 \times 2~mm^2$, which make the Hg^{2+} biosensor portable.

© 2015 Elsevier B.V. All rights reserved.

1. Introduction

As one of the most environmentally important cations, mercury(II) irons (Hg^{2+}) has the biological toxicity which impacts wild life ecology and human health heavily [1–4]. Hg^{2+} can be enriched through food chain, enter the human body, and cannot be biodegradable. Methyl-mercury can cause irreversible damage on human brain tissue (cerebral cortex, cerebellum), leading to minamata disease, which cannot be cured [5]. Therefore, a portable sensor which can detect Hg^{2+} sensitively is desirable.

Recently, biosensors based on high electron mobility transistors (HEMTs) have been demonstrated for the detection of a variety of chemical and biological substances [6–13]. The two dimensional electron gas (2DEG) of GaN HEMTs is produced by piezoelectric polarization and spontaneous polarization at the interface between AlGaN layer and GaN layer. Because of its sensitivity of the change of the charge on the gate surface, AlGaN/GaN HEMTs have been studied for application of detecting DNA [6], Hg^{2+} [10], glucose [12] and so on. In addition to piezoelectric polarization and spontaneous polarization, the 2DEG in AlGaAs/InGaAs HEMTs is mainly provided by

δ-doping Si layer. AlGaAs/InGaAs HEMTs, along with higher mobility, lower operating voltage and mature production process, also exhibit their advantages in biosensors [14]. The selective detection of Hg^{2+} in aqueous solution by using the coordinate interaction between Hg^{2+} and bis-thymine has been approved. The thymine-rich olignonucleotide probe can capture free Hg^{2+}, forming T-Hg-T [15–18]. In this letter, we functionalized the Au-coated gate area with ssDNA to detect Hg^{2+} in solution. We demonstrated that AlGaAs/InGaAs HEMTs could be used to detect Hg^{2+}, and the limit of the detection was as low as 10 nM.

2. Experiments and measurements

2.1. Fabrication of HEMT devices

In this letter, the AlGaAs/InGaAs HEMT structures for biosensors were grown by Veeco GENII solid source molecular beam epitaxy (MBE) system on (1 0 0) semi-insulating GaAs substrates [19–21]. The samples for devices fabrication have an undoped 300 nm thick GaAs buffer layer, a 15 nm thick $In_{0.2}Ga_{0.8}As$ channel layer, a 4 nm thick $Al_{0.3}Ga_{0.7}As$ spacer layer, a Si δ-doping layer, a 25 nm thick $Al_{0.3}Ga_{0.7}As$ barrier layer, and a 30 nm thick GaAs cap layer which is heavily doped with Si of $3 \times 10^{18}~cm^{-3}$. Fig. 1 shows

* Corresponding authors. Tel.: +86 1082304101.
E-mail addresses: zhang_yang@semi.ac.cn (Y. Zhang),
guanmin@semi.ac.cn (M. Guan).
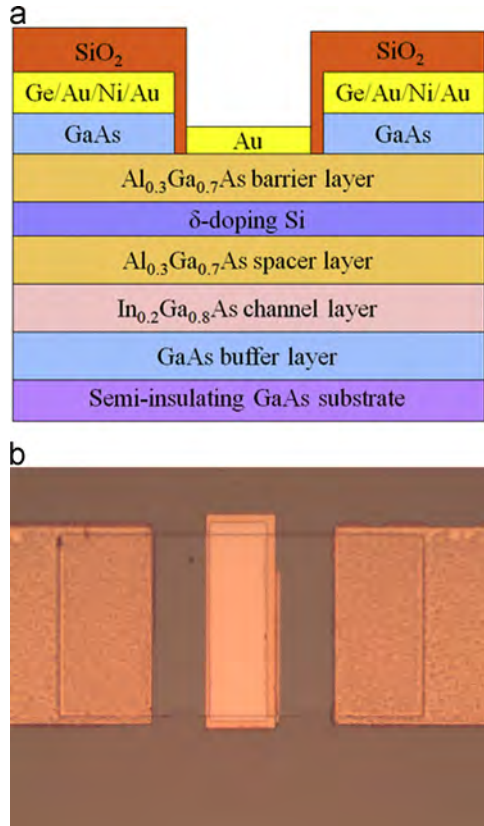
Fig. 1. (a) Cross-sectional schematic drawing of the AlGaAs/InGaAs HEMT. (b) Top view photomicrograph of the HEMT with a 40 nm Au film covering the gate region.

Fig. 2. Wet etching of GaAs along with different lattice planes: (a) $(0 -1 1)$ lattice plane, (b) $(0 1 1)$ lattice plane.

Fig. 3. (a) Drain–source currents of the AlGaAs/InGaAs HEMT: V_g varies from -100 mV to 400 mV; (b) I_d–V_g curve of the AlGaAs/InGaAs HEMT.

the cross-sectional schematic drawing of the AlGaAs/InGaAs HEMT and the top view photomicrograph of the HEMT with a 40 nm Au film covering the gate region. The 2DEG density and electron mobility were obtained by the Hall measurement respectively at 77 K ($n_s = 2.2 \times 10^{12}$ cm^{-2}, $\mu = 2.2 \times 10^4$ cm^2 V^{-1} s^{-1}) and 300 K ($n_s = 2.3 \times 10^{12}$ cm^{-2}, $\mu = 5025$ cm^2 V^{-1} s^{-1}). Sequentially, the epitaxial wafer proposed above was processed into HEMT devices. Mesa isolation was performed by wet chemical etching using H$_3$PO$_4$/H$_2$O$_2$ solution. The Ge/Au/Ni/Au ohmic contact metal was evaporated on the source and drain with a gap of 100 μm, followed by annealing at 420 °C for 20 s under flowing N$_2$, and the resistivity about $10^{-6}\Omega$ cm^2 was gotten. A 40 nm Au film was deposited at the 20×50 μm^2 gate area by electron beam evaporator. A 200 nm SiO$_2$ passivation layer was deposited immediately, and then SiO$_2$ on top of the gate area was removed for liquid solution and pads of the electrodes for measurements. The area of the sensors chip fabricated was only 1×2 mm^2, which makes the Hg^{2+} biosensor portable.

During the process of the HEMT device fabrication, removing the heavily doped GaAs cap layer over Al$_{0.3}$Ga$_{0.7}$As selectively was a very important step. A citric acid/H$_2$O$_2$ solution was prepared with optimized proportion, and the etching selectivity of GaAs over Al$_{0.3}$Ga$_{0.7}$As could reach up to 112. Fig. 2 shows that the solution etched GaAs epitaxial layer anisotropically. When the gate is parallel with $(0 -1 1)$ lattice plane, GaAs epitaxial layer will get a sidewall of the shape in Fig. 2(a), and the sidewall of the shape in Fig. 2(b) will be obtained when the gate is parallel with $(0 1 1)$ lattice plane. Therefore, the gate was chosen to be parallel with the main orientation of edges of the semi-insulating GaAs substrate in order to receive the gate recess in Fig. 2(b).

The current–voltage characteristics of the AlGaAs/InGaAs HEMT test pattern were given in Fig. 3. Fig. 3(a) shows the drain–source current at bias voltage from 0 V to 3 V measured at different V_g
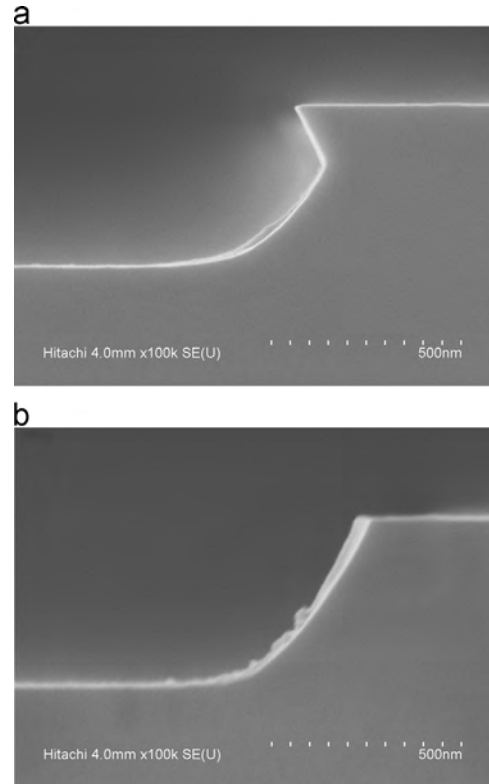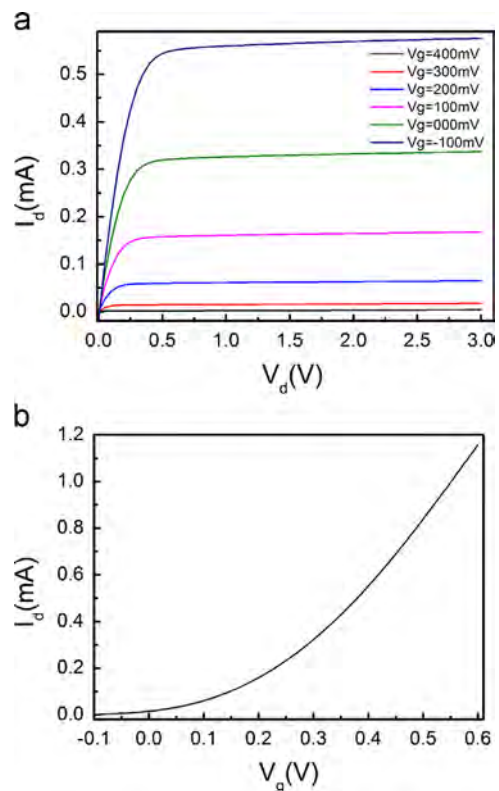
(V_g changes from -100 mV to 400 mV). The device had typical current saturation curve of HEMTs at the bias voltage from 0 V to 3 V, and the drain–source current increased when the gate voltage

Fig. 4. Schematic illustration of the selective detection of Hg^{2+}. The Au-coated gate area is functionalized with ssDNA, which can selectively react with Hg^{2+}, forming T-Hg-T.
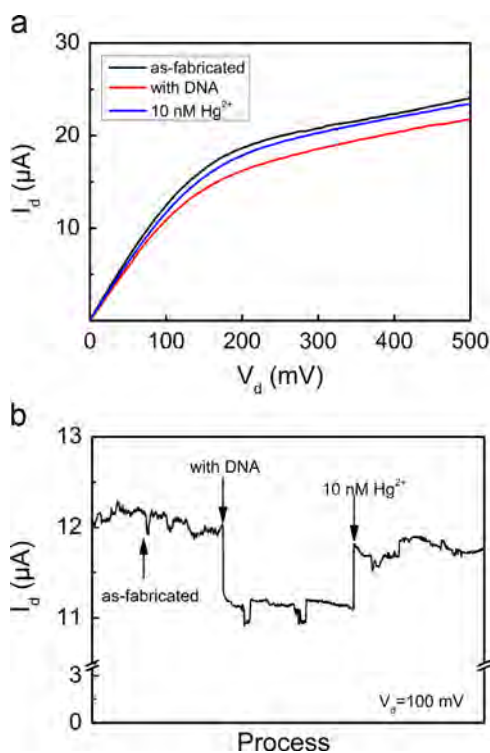
Fig. 5. (a) Drain−source currents of the AlGaAs/InGaAs HEMT sensor: before gate functionalization (as-fabricated HEMT, top line), after functionalized with ssDNA (bottom line), and after exposed to 10 nM $HgCl_2$ (middle line). (b) Changes of drain−source current at a constant bias voltage of 100 mV.

changed from −100 mV to 400 mV. The I_d–V_g curve at 100 mV bias voltage was shown in Fig. 3(b). It is clear that the drain–source current is sensitive to the gate voltage, meaning the device can be used to detect Hg^{2+} if we can immobilize Hg^{2+} on the surface of the gate area. The test pattern has $50 \times 50\ \mu m^2$ ohmic contacts of source and drain with a gap of 20 μm, and a 40 nm Au-coated gate area of $10 \times 50\ \mu m^2$.

2.2. Specific detection of mercury(II) irons

Fig. 4 represents mechanism of the Hg^{2+} detection process. Before the detection of Hg^{2+}, the sensing surface was functionalized with 5′thiol-modified oligonucleotide probe (5′-(SH)ATTCTTTCTT CCCCCCGGTTGTTTGTTT-3′, ssDNA). In our work, the Au-coated gate area of the HEMT fabricated above was immersed in 10 μM ssDNA twelve hours at room temperature. After the formation of Au–S bonding through the strong interaction between gold and the thiol-group of the ssDNA, the device was washed with water to remove unreacted ssDNA, and then dried with a nitrogen stream. When the sensor was exposed to 10 nM Hg^{2+} in aqueous solution, the

thiolated ssDNA probe immobilized on the Au-coated gate area would selectively capture free Hg^{2+}, forming a stable hairpin structure (T-Hg^{2+}-T). The distribution of the charges on the gate surface is varied, leading to a change in the concentration of the two-dimensional electron gas in the AlGaAs/InGaAs HEMTs. Thus, the drain–source current can be shifted. A CHI 660D electrochemical workstation was used to measure the drain–source current characteristics of the HEMT sensor at room temperature.

3. Results and discussions

Fig. 5 shows the drain–source current of the sensors as a function of the bias voltage from 0 V to 500 V measured before gate fuctionalization (as-fabricated HEMT), after functionalized with ssDNA, and after exposed to 10 nM Hg^{2+} solution. The drain–source current decreased after functionalized with ssDNA, and it was increased when exposed in Hg^{2+} solution. Under 100 mV bias voltage, the drain–source current changed from 11.97 μA to 11.13 μA when the gate of HEMT device was functionalized with ssDNA, and it increased to 11.74 μA immediately when the sensor was exposed to 10 nM Hg^{2+} solution. The response time is less than 10 s. It means that the sensor can be used to detect Hg^{2+}, and the limit can be down to 10 nM at least.

The mechanism of the sensor can be explained as follow. At the interface of AlGaAs/InGaAs heterojunction, a triangle potential well forms at the side of InGaAs channel layer, and electrons will be accumulated and trapped in the well. The depth and width of the well can be modulated by the gate potential, which has an impact on the 2DEG concentration, then affects the drain–source current. Due to the high mobility of the AlGaAs/InGaAs HEMT, the sensor is very sensitive to the potential changes at the gate. When the ssDNA was immobilized on the gate area, a negative potential was introduced to the gate, resulting the decrease in the 2DEG concentration and the drain–source current. Similarly, because of the positive potential provided by Hg^{2+}, the drain–source current increased apparently (6.61 μA) when the ssDNA immobilized on the gate captured Hg^{2+}.

4. Conclusion

In summary, we have shown that Hg^{2+} can be detected by using AlGaAs/InGaAs HEMTs. Based on the functionalization of the gate by ssDNA, we can detect Hg^{2+} sensitively and rapidly. The detection limit for the Hg^{2+} of as low as 10 nM is achieved under the bias of 100 mV. Successful detection with minute quantity of the sample indicates that the sensor has great potential in practical screening for a wide population.

References

[1] A. Wolkin, D. Hunt, C. Martin, K.L. Caldwell, M.A. McGeehin, Blood mercury levels among fish consumers residing in areas with high environmental burden, Chemosphere 86 (2012) 967–971.
[2] Olaf Malm, Gold mining as a source of mercury exposure in the Brazilian Amazon, Environ. Res. 77.2 (1998) 73–78.
[3] A. Renzoni, F. Zino, E. Franchi, Mercury levels along the food chain and risk for exposed populations, Environ. Res. 77.2 (1998) 68–72.

[4] Dean W. Boening, Ecological effects, transport, and fate of mercury: a general review, Chemosphere 40.12 (2000) 1335–1351.

[5] Masazumi Harada, Minamata disease: methylmercury poisoning in Japan caused by environmental pollution, CRC Crit. Rev. Toxicol. 25.1 (1995) 1–24.

[6] ByoungSam Kang, et al., Electrical detection of deoxyribonucleic acid hybridization with AlGaN/GaN high electron mobility transistors, in: MRS Proceedings. Vol. 955. Cambridge University Press, 2006.

[7] B.S. Kang, et al., Prostate specific antigen detection using AlGaN/GaN high electron mobility transistors, Appl. Phys. Lett. 91.11 (2007) (112106–112106).

[8] K.H. Chen, et al., c-erbB-2 sensing using AlGaN/GaN high electron mobility transistors for breast cancer detection, Appl. Phys. Lett. 92.19 (2008) (192103–192103).

[9] Yu-Lin Wang, et al., Fast detection of a protozoan pathogen, Perkinsus marinus, using AlGaN/GaN high electron mobility transistors, Appl. Phys. Lett. 94.24 (2009) 243901.

[10] Hung-Ta Wang, et al., Fast electrical detection of Hg(II) ions with AlGaN/GaN high electron mobility transistors, Appl. Phys. Lett. 91.4 (2007) (042114–042114).

[11] H.T. Wang, et al., Electrical detection of kidney injury molecule-1 with AlGaN/GaN high electron mobility transistors, Appl. Phys. Lett. 91.22 (2007) (222101–222101).

[12] B.S. Kang, et al., Enzymatic glucose detection using ZnO nanorods on the gate region of AlGaN/GaN high electron mobility transistors, Appl. Phys. Lett. 91.25 (2007) (252103–252103).

[13] S.C. Hung, et al., Detection of chloride ions using an integrated Ag/AgCl electrode with AlGaN/GaN high electron mobility transistors, Appl. Phys. Lett. 92.19 (2008) 193903.

[14] Kai Ding, et al., Specific detection of alpha-fetoprotein using AlGaAs/GaAs high electron mobility transistors, Electron Device Lett. 35 (3) (2014) 333–335.

[15] Yoshiyuki Tanaka, et al., 15N–15NJ-coupling across HgII: direct observation of HgII-mediated TT base pairs in a DNA duplex, J. Am. Chem. Soc. 129.2 (2007) 244–245.

[16] Guido H. Clever, Corinna Kaul, Thomas Carell, DNA—metal base pairs, Angew. Chem. Int. Ed. 46.33 (2007) 6226–6236.

[17] Zhiqiang Zhu, et al., Highly sensitive electrochemical sensor for mercury(II) ions by using a mercury-specific oligonucleotide probe and gold nanoparticle-based amplification, Anal. Chem. 81.18 (2009) 7660–7666.

[18] Yoko Miyake, et al., MercuryII-mediated formation of thymine-HgII-thymine base pairs in DNA duplexes, J. Am. Chem. Soc. 128.7 (2006) 2172–2173.

[19] Xin Cao, et al., Using photoluminescence as optimization criterion to achieve high-quality InGaAs/AlGaAs pHEMT structure, J. Cryst. Growth 227 (2001) 127–131.

[20] Xin Cao, et al., Photoluminescence of AlGaAs/InGaAs/GaAs pseudomorphic HEMTs with different thickness of spacer layer, J. Cryst. Growth 231.4 (2001) 520–524.

[21] Xin Cao, et al., The keys to get high transconductance of AlGaAs/InGaAs/GaAs pseudomorphic HEMTs devices, Solid-State Electron. 45.5 (2001) 751–754.

CRExssMark
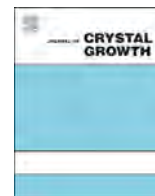
High hole mobility InGaSb/AlSb QW field effect transistors grown on Si by molecular beam epitaxy

Pei-Chin Chiu [a], Hsuan-Wei Huang [a], Wei-Jen Hsueh [a], Yu-Ming Hsin [a], Cheng-Yu Chen [a], Jen-Inn Chyi [a,b,*]

[a] Department of Electrical Engineering, National Central University, Jhongli 32001, Taiwan, ROC
[b] Optical Sciences Center, National Central University, Jhongli 32001, Taiwan, ROC

ARTICLE INFO

ABSTRACT

Growth of InGaSb/AlSb high hole mobility quantum well field effect transistors (QW FETs) on Si substrates with a step-graded GaAsSb metamorphic buffer layer by molecular beam epitaxy is explored. With an optimized growth temperature for the InGaSb/AlSb QW, hole mobility of 770 cm^2/V s and 3060 cm^2/V s have been achieved at room temperature and 77 K, respectively. It is also found that the twins in the samples do not cause significant anisotropic behavior of the InGaSb QW FETs in term of gate direction.

1. Introduction

III–V field effect transistors (FETs) have great potential for high performance low power consumption logic circuits on Si substrates due to their high mobility and low bandgap characteristics [1–3]. While the developments on the n-channel devices for complementary circuits have been successful in the last few years, the progress on p-channel devices is rather limited. Antimonide-based heterostructure is one of the promising candidates for p-channel devices since exciting results, hole mobility of 1500 cm^2/V s with sheet concentration of 7×10^{11} cm^{-2}, have been demonstrated on InGaSb/Al(Ga)Sb QW structures [4]. The antimonide heterostructure is also favored because the lattice constant of the stained InGaSb layer is close to that of InAs. This makes the integration with InAs n-channel FETs for complementary circuits much easier since they can share the same buffer layer on Si. Up to date, high hole mobility InGaSb/Al(Ga)Sb p-channel devices have been demonstrated on GaAs substrates, but the reports of III–V p-channel devices on Si substrates remain few [5–7]. In 2012, Takei et al. demonstrated the integration of InGaSb/AlSb p-channel FETs on Si substrates using epitaxial layer transfer technology [8]. An InAs/InGaSb/InAs structure was grown on a GaSb substrate by molecular beam epitaxy (MBE), and then transferred onto a Si substrate by polydimethylsiloxane. A maximum effective hole mobility of ~820 cm^2/V s at room temperature was achieved. The placement issue of this approach has to be overcome before

it can be utilized for mass production. In 2014, Madisetti et al. reported their studies on the metal-oxide-semiconductor (MOS) capacitors of InGaSb-QW structure, which was directly grown on a Si-on-insulator substrate with a metamorphic buffer layer by MBE. Although a lot of defects including twins were observed in the buffer layer, the InGaSb/AlSb QWs exhibited a maximum hole mobility of 632 cm^2/V s with a sheet hole density of 7.6×10^{11} cm^{-2}, and sheet resistance over 12,000 Ω/sq [9]. In this work, InGaSb p-channel QW FETs were grown on Si by MBE and characterized. Hole mobility as high as 770 cm^2/V s with sheet resistance of 8100 Ω/sq at room temperature was obtained by modifying the growth temperature of QW. The effects of twins on the transport properties were also investigated.

2. Experiments

Fig. 1 shows the layer structure of the samples studied in this work. These samples were prepared by solid source MBE. The group V materials, Sb and As were supplied by two valved crackers, respectively. Vicinal (100) Si p-type substrates with 6 degrees tilted toward the [1–10] direction were used to reduce the formation of anti-phase domain [10]. Before the commencement of epitaxial growth, the substrate was heated at 720 °C for 1 h to remove the hydrogen atoms and residual contaminants on the surface. The growth was started with a 3 nm-thick GaAs nucleation layer using migration-enhanced epitaxy, then a multi-step graded GaAsSb layer was grown at 500 °C. The Sb conetent in each step layer was approximately 5%, 10% and 23% as verified by X-ray diffraction reciprocal space maps of the (004) and (115)

reflections. Afterwards, a 1500 nm-thick AlSb and a 300 nm-thick AlGaSb buffer layers were grown at 540 °C and 500 °C, respectively. To increase hole mobility, a lattice mismatch of approximately 2.0% was intentionally introduced to the $In_{0.4}Ga_{0.6}Sb$ channel layer so as to induce a compressive strain in the channel layer. The growth temperature for the active region, including InGaSb channel and AlSb barrier, was 380 °C, 360 °C and 340 °C for each sample. Because the growth temperature was outside the temperature range (400–1000 °C) of the pyrometer used in the work, the growth temperature of InGaSb/AlSb QW was estimated by linear interpolation from the curve of growth temperature versus power consumption of the substrate heater. The properties of these samples were assessed by temperature-dependent Van der Pauw Hall measurements, atomic force microscopy (AFM), and transmission electron microscopy (TEM). The buffer resistance

exceeded 1 M Ω/sq and allowed the assessment of real transport properties of the QW channel. The ohmic contacts for Hall measurements were formed by alloying indium balls at 200 °C for only 10 s to avoid excessive indium diffusion to the Si substrate that causes parallel conduction.

3. Results and discussion

Table 1 summarizes the carrier transport properties of the InGaSb/AlSb QW structures determined by Hall effect measurements at room temperature and 77 K. As the growth temperature is reduced from 380 °C to 360 °C, the hole mobility at room temperature increases from 630 cm²/V s to 770 cm²/V s. The higher hole mobility at 77 K of the InGaSb/AlSb QW grown at 360 °C against 380 °C, i.e. 3060 cm²/V s versus 2490 cm²/V s, implies that it contains less defects, probably because of the reduced lattice relaxation and defects generation with decrease of the growth temperature [6,11]. Notably, a repeated experiment on the growth of 360 °C gives hole mobility of 838 cm²/V s with a sheet carrier concentration of 9.5×10^{11} cm^{-2} at room temperature. Further reducing the growth temperature to 340 °C reduces the hole mobility at room temperature and 77 K to 312 cm²/V s and 964 cm²/V s, respectively. Fig. 2 reveals the reflection high energy electron diffraction (RHEED) patterns during the growth of the upper AlSb barrier at 360 °C and 340 °C in the [1–10] direction. Reducing the growth temperature of QW to 340 °C results in a rough upper AlSb barrier surface as evidenced by the spotty RHEED pattern in Fig. 2(b). Fig. 3 displays the AFM images of these samples. The root mean square roughness increases from 2.5–2.7 nm for the QW grown at 380 °C and 360 °C to 3.4 nm for that grown at 340 °C. Therefore, the reduction of hole mobility of the QW grown at 340 °C could be attributed to the degradation of the upper AlSb barrier grown at low temperature.

TEM images on the mutually perpendicular ($1\bar{1}0$) and (110) planes of the InGaSb/AlSb QW FET grown at 360 °C are presented in Fig. 4. Figs. 4(a) and (b) reveal that, although some threading dislocations and planar defects are generated at the GaAs and Si interface and blocked at the GaAsSb/AlSb interface, there are twins penetrating the QW channel layer. The effects of twins on the growth of InGaSb/AlSb QW are investigated by high resolution cross-sectional TEM as displayed in Fig. 4(c). The growth fronts of the AlSb buffer and subsequent InGaSb layer are altered by the penetrating twins. The presence of planar defects is also confirmed by Fig. 4(d), which shows many short stripes in the AlSb buffer layer and is attributable to the overlap of micro-twins or probably

Fig. 1. Layer structure of the InGaSb QW FETs grown on Si substrate.

| InAs 2 nm |
| $In_{0.5}Al_{0.5}As$ 5 nm |
| GaSb 0.6 nm |
| AlSb 11 nm |
| InGaSb QW 7.5 nm |
| AlSb 10 nm |
| $Al_{0.7}Ga_{0.3}Sb$ 300 nm |
| AlSb 1550 nm |
| $GaAs_{0.77}Sb_{0.23}$ 50 nm |
| $GaAs_{0.90}Sb_{0.10}$ 50 nm |
| $GaAs_{0.95}Sb_{0.05}$ 50 nm |
| GaAs 3 nm |
| Si substrate p-type |

Table 1
Summary of Hall effect measurements on InGaSb QW FETs grown at three different temperatures.

Growth temperature (°C)	380 (Sample A)	360 (Sample B)	340 (Sample C)
Hall mobility (cm²/V s) (300 K)	630	770	312
Sheet concentration (cm^{-2}) (300 K)	1.29×10^{12}	1.04×10^{12}	1.90×10^{12}
Hall mobility (cm²/V s) (77 K)	2490	3060	964
Sheet concentration (cm^{-2}) (77 K)	1.15×10^{12}	1.14×10^{12}	1.35×10^{12}

Fig. 2. RHEED patterns along the [1–10] direction during the growth of the upper AlSb barrier for the samples grown at (a) 360 °C and (b) 340 °C.

stacking faults. The micrographs indicate that the observed micro-twins prefer to lie on the (111) and ($\overline{1}\,\overline{1}$1) planes.

It has been reported that twins play an important role in the transport properties of InAs and InSb n-channel QWHFETs [12–14]. Twins are scattering centers, which degrade carrier transport property, especially when the transport direction is perpendicular to the twin-induced line features observed on the surface. They cause strong anisotropic I–V characteristics in n-channel InAs QW FETs [14]. It is desirable to know whether the twins cause anisotropic characteristics of p-channel InGaSb QW FETs. An

optical lithographic process is used to fabricate 2 µm gate-length devices on the sample grown at 360 °C. The distance between source and drain is 12 µm. Pd/Ti/Pt/Au (20/40/40/50 nm) metal stack deposited by e-beam evaporator is used for the ohmic contact pads and Ti/Pt/Au (20/40/300 nm) metal stack is the Schottky gate metal. Mesa isolation is defined by dry etching in an inductively coupled plasma etcher using $BCl_3/Cl_2/Ar$. Two types of devices are fabricated on the wafer. One type of the devices have their drain current flowing along the [1–10] direction, while that of the other type is along the [110] direction. Shown in Fig. 5
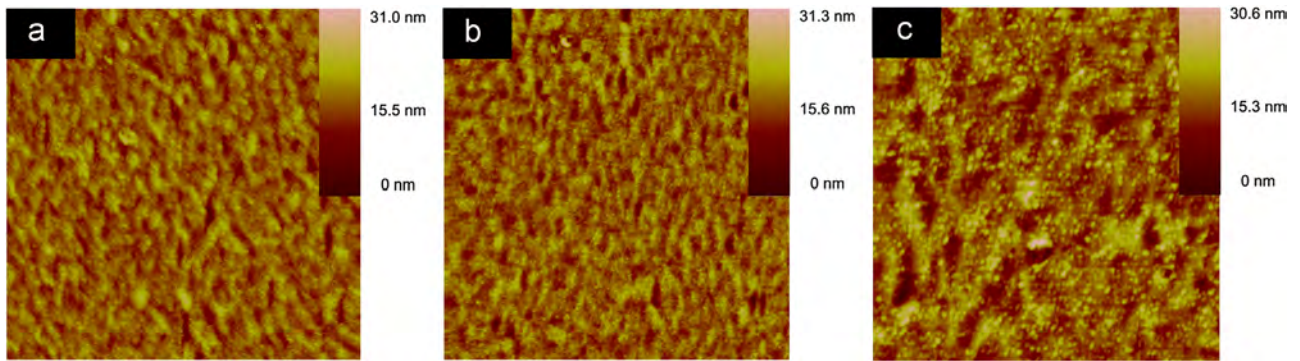
Fig. 3. AFM images (10 µm × 10 µm) of the InGaSb QWs grown at (a) 380 °C, (b) 360 °C, and (c) 340 °C.
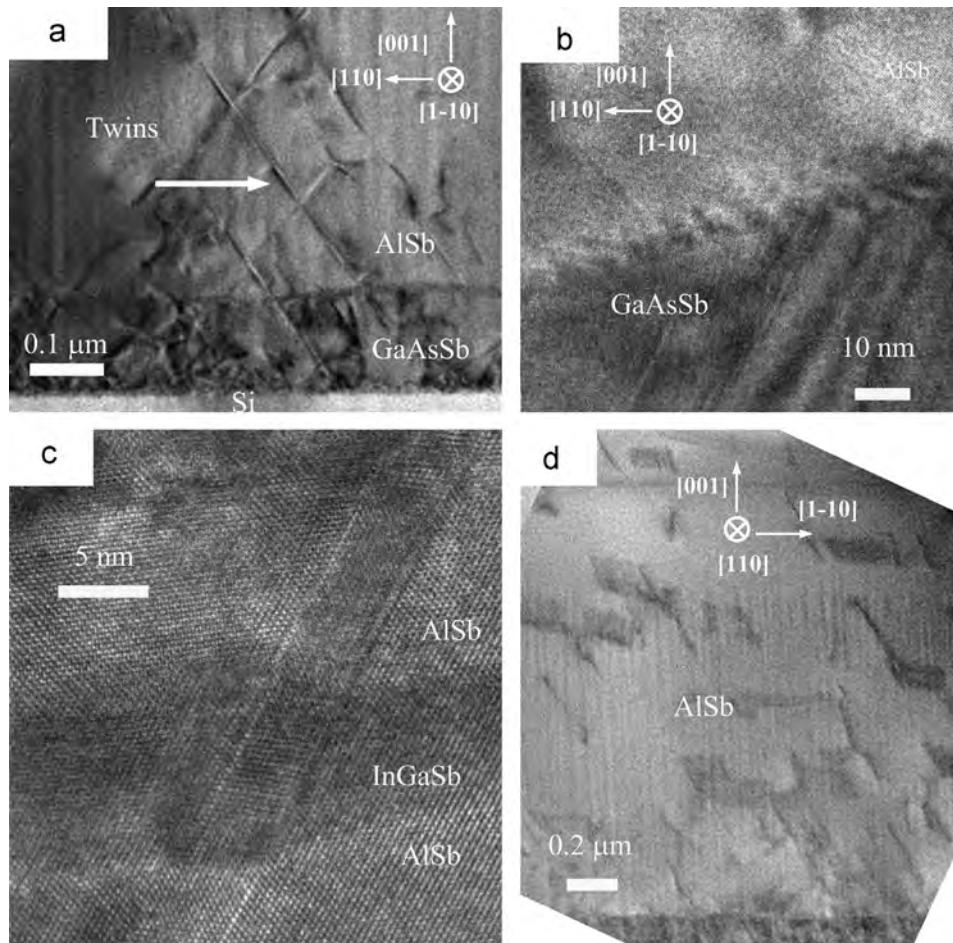
Fig. 4. (a) [1–10] cross-sectional TEM micrograph of the sample grown at 360 °C, (b) the image near the GaAsSb/AlSb interface, (c) high resolution image near the QW, and (d) [110] cross-sectional TEM image of the same sample.
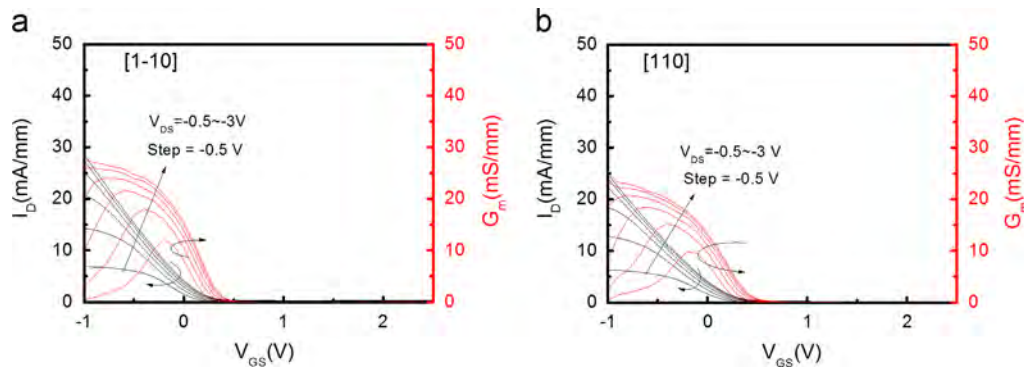
Fig. 5. (a) Transfer characteristics of InGaSb QW FETs with drain current flowing along the (a) [1–10] and (b) [110] directions.

are the transfer characteristics of these devices. The threshold voltage of both types of devices is 0.5 V. The devices with drain current along the [1–10] direction have a maximum drain current density of 28.5 mA/mm and a peak transconductance (Gm_{peak}) of 28 mS/mm at $V_{GS} = -1$ V and $V_{DS} = -3$ V. The devices with drain current along the [110] direction have a maximum drain current density of 25 mA/mm and a Gm_{peak} of 25 mS/mm at $V_{GS} = -1$ V and $V_{DS} = -3$ V. The differences in these electrical properties between the two types of devices are less 15%, unlike the case of InAs QW n-channel FETs. This implies that InGaSb QW FETs are less susceptible to twins [14]. It is postulated what may have been responsible for this is the short mean-free-path of holes in the InGaSb QW. The mean-free-path of a hole in InGaSb QW, which has a hole mobility of 770 cm^2/V s with a sheet concentration of 1×10^{12} cm^{-2}, is estimated to be about 13 nm. This value is far shorter than the average distance between the twins (~ 0.12 μm) estimated from the TEM image. A shorter mean-free-path corresponds to a lower likelihood for the holes to meet the twins. Hence, the transport of holes is less sensitive to the scattering resulting from the twins than that of electrons in the channel.

4. Conclusions

In conclusion, InGaSb/AlSb QW FETs have been grown on Si substrates with a step- graded GaAsSb metamorphic buffer layer by MBE. Using a growth temperature of 360 °C for InGaSb/AlSb QW, hole mobility of 770 cm^2/V s and 3060 cm^2/V s has been achieved at room temperature and 77 K, respectively. Further reduction in growth temperature increases surface roughness and lower mobility. It is also found that although the growth fronts of AlSb and InGaSb are affected by the penetrating twins, the impact of twins to the isotropic behavior of p-channel InGaSb QW FETs is insignificant. This could be attributed to the short means-free-path of holes in the InGaSb QW.

Acknowledgments

References

[1] G. Dewey, M.K. Hudait, K. Lee, R. Pillarisetty, W. Rachmady, M. Radosavljevic, T. Rakshit, R. Chau, Carrier Transport in high-mobility III–V quantum-well transistors and performance impact for high-speed low-power logic applications, IEEE Electron. Device Lett. 29 (2008) 1094–1097.

[2] S. Oktyabrsky, P. Ye (Eds.), Fundamentals of Compound Semiconductor MOSFETs, Springer, New York, 2010.

[3] J.A. del Alamo, Nanometre-scale electronics with III–V compound semiconductors, Nature 479 (2011) 317–323.

[4] B.R. Bennett, M.G. Ancona, J.B. Boos, B.V. Shanabrook, Mobility enhancement in strained p-InGaSb quantum wells, Appl. Phys. Lett. 91 (2007) 042104.

[5] J.B. Boos, B.R. Bennett, N.A. Papanicolaou, M.G. Ancona, J.G. Champlain, R. Bass, B.V. Shanabrook, High mobility p-channel HFETs using strained Sb-based materials, Electron. Lett. 43 (2007) 834–835.

[6] H.-C. Ho, Z.-Y. Gao, H.-K. Lin, P.-C. Chiu, Y.-M. Hsin, J.-I. Chyi, Device characteristics of InGaSb/AlSb high-hole-mobility FETs, IEEE Electron. Device Lett. 33 (2012) 964–966.

[7] A. Nainani, Z. Yuan, T. Krishnamohan, B.R. Bennett, J.B. Boos, M. Reason, M.G. Ancona, Y. Nishi, K.C. Saraswat, In$_x$Ga$_{1-x}$Sb channel p-metal-oxide-semiconductor field effect transistors: effect of strain and heterostructure design, J. Appl. Phys. 110 (2011) 014503.

[8] K. Takei, M. Madsen, H. Fang, R. Kapadia, S. Chuang, H.S. Kim, C.H. Liu, E. Plis, J. Nah, S. Krishna, Y.L. Chueh, J. Guo, A. Javey, Nanoscale InGaSb heterostructure membranes on Si substrates for high hole mobility transistors, Nano Lett. 12 (2012) 2060–2066.

[9] S.K. Madisetti, V. Tokranov, A. Greene, S. Novak, M. Yakimov, S. Oktyabrsky, S. Bentley, A.P. Jacob, GaSb on Si: structural defects and their effect on surface morphology and electrical properties, Mater. Res. Soc. Symp. Proc. 1635 (2014) 115–120.

[10] M. Grundmann, A. Krost, D. Bimberg, Low-temperature metalorganic chemical vapor deposition of InP on Si(001), Appl. Phys. Lett. 58 (1991) 284–286.

[11] P.R. Berger, K. Chang, P. Bhattacharya, J. Singh, K.K. Bajaj, Role of strain and growth conditions on the growth front profile of In$_x$Ga$_{1-x}$As on GaAs during the pseudomorphic growth regime, Appl. Phys. Lett. 53 (1988) 684–686.

[12] T.D. Mishima, J.C. Keay, N. Goel, M.A. Ball, S.J. Chung, M.B. Johnson, M.B. Santos, Anisotropic structural and electronic properties of InSb/Al$_x$In$_{1-x}$Sb quantum wells grown on GaAs (001) substrates, J. Cryst. Growth 251 (2003) 551–555.

[13] L. Desplanque, S. El Kazzi, J.L. Codron, Y. Wang, P. Ruterana, G. Moschetti, J. Grahn, X. Wallart, AlSb nucleation induced anisotropic electron mobility in AlSb/InAs heterostructures on GaAs, Appl. Phys. Lett. 100 (2012) 262103.

[14] G. Moschetti, H. Zhao, P.-Å. Nilsson, S. Wang, A. Kalabukhov, G. Dambrine, S. Bollaert, L. Desplanque, X. Wallart, J. Grahn, Anisotropic transport properties in InAs/AlSb heterostructures, Appl. Phys. Lett. 97 (2010) 243510.

CrossMark
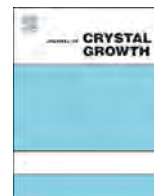
Ultraviolet light emitting diodes by ammonia molecular beam epitaxy on metamorphic (20$\bar{2}$1) AlGaN/GaN buffer layers

Erin C. Young *, Benjamin P. Yonkee, Feng Wu, Burhan K. Saifaddin, Daniel A. Cohen, Steve P. DenBaars, Shuji Nakamura, James S. Speck

Materials Department, University of California, Santa Barbara, CA 93106, United States

ARTICLE INFO

ABSTRACT

In this paper we demonstrate ultraviolet (UV) light emitting diodes (LEDs) grown on metamorphic AlGaN buffers on freestanding GaN (20$\bar{2}$1) substrates by ammonia assisted molecular beam epitaxy (MBE). Misfit and related threading dislocations were confined to the stress relaxed, compositionally graded buffer layers, and single quantum well devices emitting at 355, 310 and 274 nm were grown on top of the graded buffers. The devices showed excellent structural and electrical (I–V) characteristics.

Published by Elsevier B.V.

1. Introduction

Efficient UV light sources with sub-300 nm emission wavelengths are of interest for many applications, including both detection and decontamination of chemicals and biological agents such as viruses and bacteria. While the wurtzite GaN–AlN ternary materials system has suitable band gap (3.4–6.0 eV) for emission over the entire UV spectral range, and progress is being made in reported efficiencies of LEDs at shorter wavelengths [1], by visible LED standards external quantum efficiencies remain relatively low (< 10%). Major challenges associated with UV light emitters are efficient p-type doping with Mg in the wide band gap $Al_xGa_{1-x}N$ semiconductor, as well as the lack of commercially available AlN substrates. As a result the majority of UV device development has been carried out on non-native substrates, leading to high extended defect densities in device heterostructures [1]. While freestanding GaN substrates have become available in recent years, growth of high Al content, deep UV quantum well (QW) devices are not possible on *c*-plane GaN due to tensile coherency stresses that result in fracture of the heteroepitaxial films [2]. Alternatively, the primary relaxation mechanism of AlGaN grown on semipolar orientations of GaN is not cracking, but misfit dislocation (MD) array formation via low energy slip on the basal c-plane [3]. Recent work has shown that growth of stress relaxed buffers on semipolar orientations of GaN is viable for extending the range of wavelengths possible for laser diodes on GaN substrates for both visible [4] and near UV emission [5], and that

graded, relaxed $Al_xGa_{1-x}N$ buffers with *x* up to 0.6 can be generated for device growth with low ($\sim 10^6/cm^2$) threading dislocation density (TDD) by MBE [6]. While relatively unexplored as a growth technique for UV devices, MBE has recently been shown to be viable for growth of near UV semipolar GaN based lasers [7], as well as nanostructured UV devices [8–10] and high internal quantum efficiency (IQE) active regions [11]. In this work, we demonstrate planar, metamorphic UV LEDs on relaxed AlGaN buffers on (20$\bar{2}$1) GaN substrates with by ammonia-assisted MBE with emission wavelengths from 355 nm down to 274 nm with excellent I–V characteristics. While the band gap of GaN is absorbing for photons with wavelengths in the UV spectrum, resulting in significant absorption losses in a fully processed device, we propose that the substrate can be easily removed via growth of sacrificial InGaN quantum wells and a photoelectrochemical etch process which has been successfully developed and applied for GaN based lasers [12]. Future UV devices on GaN substrates could subsequently be processed in a flip-chip geometry.

In this study, LED structures were grown with emission wavelengths of 355 nm, 310 nm, and 274 nm to investigate the impact of increasing $Al_xGa_{1-x}N$ alloy content *x* on the device properties and performance. All samples were grown by NH_3-assisted MBE in a Veeco Gen 930 equipped with solid source effusion cells for group III elements Al and Ga, and p- and n- type dopant elements Mg and Si respectively. The devices were grown on freestanding (20$\bar{2}$1) GaN substrates from Mitsubishi Chemical Corporation at temperatures between 850–900 °C. Growth conditions were N-rich with NH_3 fluxes on the order of 10^{-4} Torr and metal fluxes on the order of 10^{-7} Torr. Graded buffers were grown as described in [6]. p-AlGaN and GaN layers were grown at 750 °C,

as the lower temperature was found to maximize acceptor concentrations in ammonia MBE grown p-GaN [13]. Mg concentrations were in the 10^{19}/cm³ range and Si concentrations were in the 10^{18}/cm³ range as determined by secondary ion mass spectroscopy of calibration samples. Compositions and strain state of the films were determined using high resolution X-ray diffraction (XRD) and structurally characterized with cathodoluminescence (CL) and high resolution scanning transmission electron microscopy (STEM/TEM). Optical and electrical properties were studied via room temperature (RT) photoluminescence (PL) and electroluminescence (EL) measurements. The 355 nm LED was processed for EL quick test with Ti/Au n-contacts, Pd/Au p-type contacts, and a thin Pd/Au current spreading layer, while the I–V characteristics of the 310 and 274 nm LEDs were measured with indium contacts.

Before LED heterostructures were grown, continuously graded $Al_xGa_{1-x}N$ buffer layers were developed and characterized. A symmetric, on-axis (2 0 1) XRD reciprocal space map for a 500 nm thick graded buffer with 500 nm of $Al_{0.52}Ga_{0.48}N$ is shown in Fig. 1(a), indicating the change in lattice parameter and strain state of the film with increasing Al content. The offset in Q_x between the GaN substrate and $Al_{0.52}Ga_{0.48}N$ layer is due to tilt introduced by the edge component of MDs associated with stress relaxation of the lattice mismatch between the GaN and $Al_xGa_{1-x}N$ buffer [3], and the buffer was determined to be 90% relaxed in the in-plane projected-c direction. Threading dislocations from the substrates (typical TDD $\sim 5 \times 10^6$/cm²) were assumed to be the source for the MDs [4]. For the same sample, Fig. 1(b) shows two CL images taken at excitation voltages of 5 kV and 15 kV, corresponding to electron penetration depths in $Al_{0.52}Ga_{0.48}N$ of approximately 150 nm and 1000 nm respectively. Cracking was not observed in the graded buffer layer films developed in this study. While dark lines associated with non-radiative

recombination regions around MDs are observed for the 15 kV image, no dark lines associated with MDs or dark spots associated with threading dislocations are observed for the 5 kV images, indicating a high structural quality, low defect density template for subsequent quantum well device growth. This has been confirmed via high resolution TEM data, shown in Fig. 1(c) for a typical LED structure grown on a relaxed buffer, in this case the 310 nm LED heterostructure. The cross sectional image was taken looking down the projected c-axis of the $(20\overline{2}1)$ crystal, and shows the $Al_xGa_{1-x}N$ buffer continuously graded in x from GaN to the desired buffer layer composition, in this case x=0.36. The strain contrast visible in the 500 nm thick buffer region of the TEM image is associated with MDs lying along the a-axis throughout the thickness of the graded region, with $b=(1/3)\langle 11\overline{2}0\rangle$ type burgers vectors [3,6]. While some threading dislocations are generated in the graded region, they do not propagate vertically through subsequent epitaxial layers. XRD reciprocal space maps for each LED (not shown) provided further confirmation that the active regions of the LED devices were coherent (metamorphic) to the relaxed, graded buffer layers.

EL and I–V data for the 355 nm LED are shown in Fig. 2(a) and (b) respectively. The LED heterostructure consisted of an n-type buffer graded from GaN to $Al_{0.20}Ga_{0.80}N$ followed by 500 nm of n-$Al_{0.20}Ga_{0.80}N$ and an active region of a single 10 nm GaN quantum well with a 250 nm p– $Al_{0.20}Ga_{0.80}N$ cap, and 10 nm p+ GaN contact layer. The device showed strong EL emission at 355 nm and excellent turn-on voltage of 3.6 V at 20 mA. Light output power of the device is shown in Fig. 2(b) and was measured with a UV calibrated Newport photodetector under CW conditions. The processed device had thick Au metal pads for current probing and a thin metal layer (2/3 nm of Pd/Au) for current spreading through which the light was measured. The total area of the metal contacts
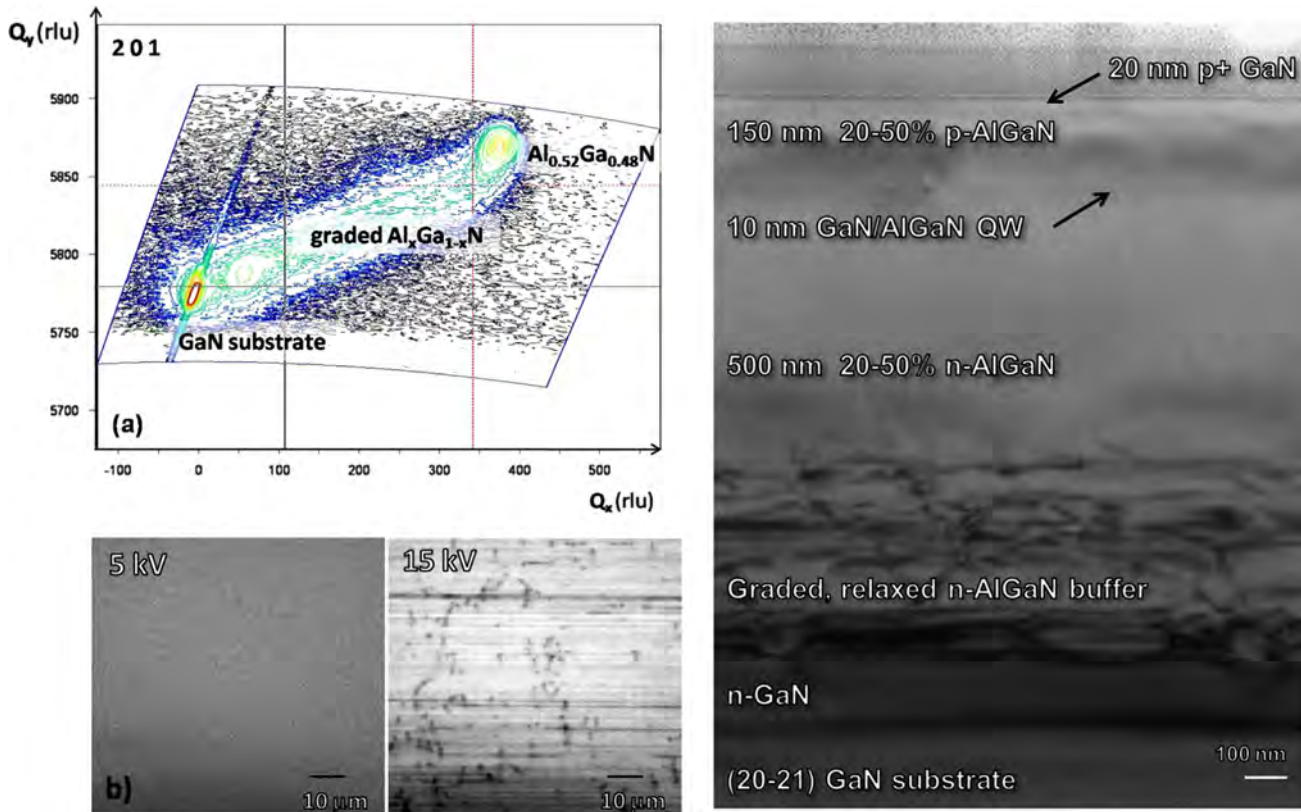
Fig. 1. (a) Symmetric 2 0 1 reciprocal space map taken with X-rays incident along the projected c-direction, showing relaxation of buffer layer graded from GaN to $Al_{0.52}Ga_{0.48}N$. (b) Panchromatic CL images of graded buffer taken at 5 kV and 15 kV corresponding respectively to 150 nm and 1000 nm electron penetration depths. (c) High resolution cross sectional TEM image down the projected c-axis for a typical $Al_xGa_{1-x}N$ UV LED heterostructure, coherent to relaxed buffer.
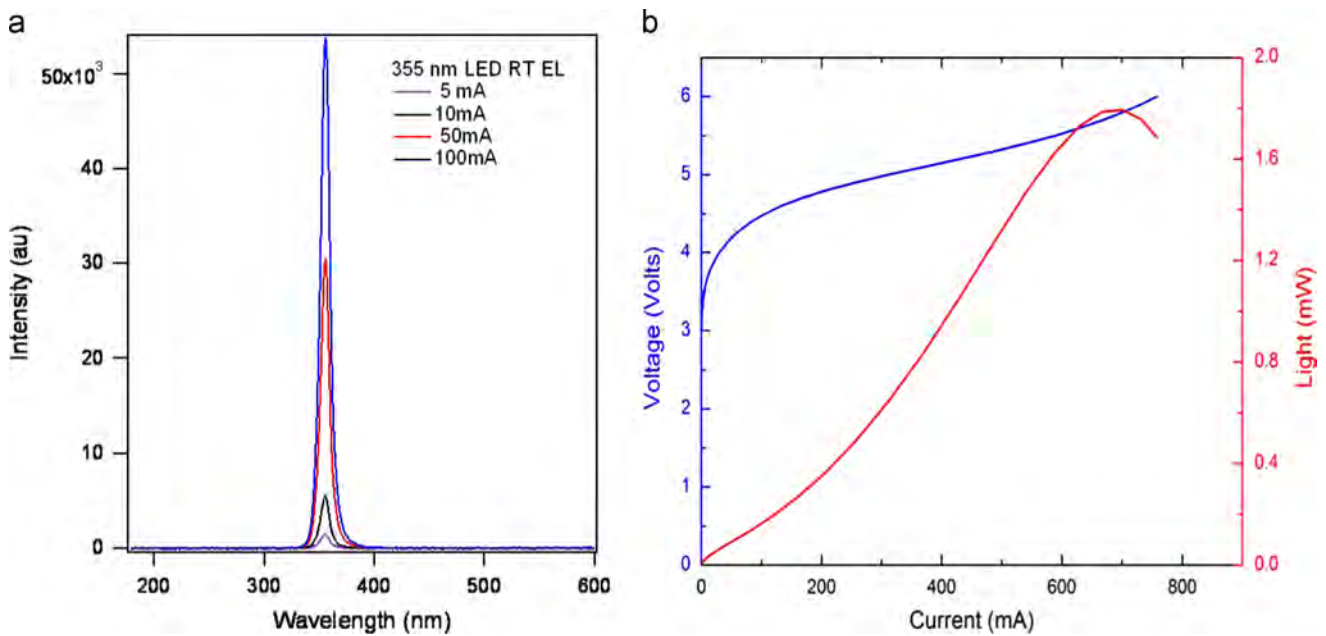
Fig. 2. (a) 355 nm LED room temperature electroluminescence spectra with increasing current and (b) *I–V* characteristics and light output power. Voltage is 3.6 V at 20 mA and max power is 1.8 mW. Extraction efficiency for this structure is estimated at ~1%.
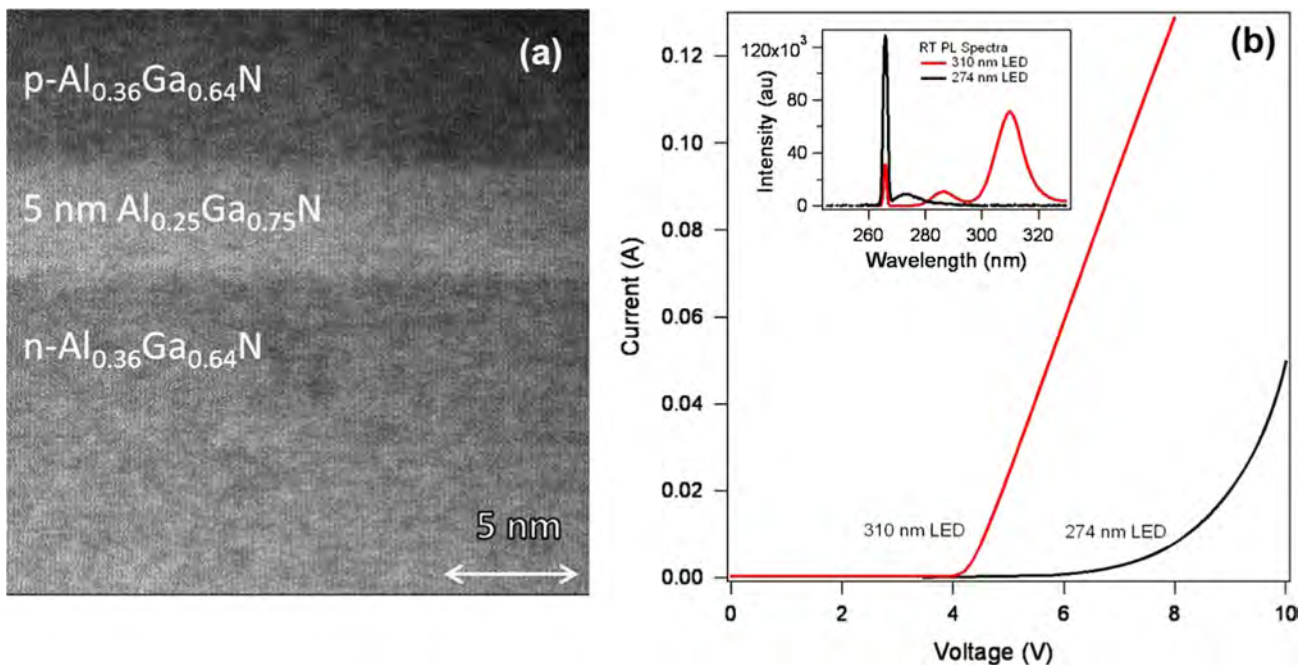
Fig. 3. (a) High resolution *z*-contrast STEM image of the active region of a 310 nm LED heterostructure and (b) *I–V* curves and room temperature photoluminescence spectra (inset) for 310 nm and 274 nm LED heterostructures with indium contacts. At 20 mA, voltage is 4.8 V for the 310 nm LED and 8.9 V for the 274 nm LED. PL peak at 285 nm for the 310 nm LED is attributed to luminescence from the buffer layer. Peak at 266 nm is due to the PL excitation laser.

and current spreading layer was designed so that 1 mA corresponded to 1 A/cm^2. This device showed promising peak output power of 1.8 mW and no efficiency droop up to 500 A/cm^2. Assuming a single extraction cone upwards and taking into account absorption in the p-GaN contact, surface reflection, and transmission through the metal current spreading layer extraction efficiency is only estimated to be about 1% for this test structure. The same epitaxial structure could be expected to exhibit much higher output power in a flip chip geometry with substrate removal. In addition, the epitaxial growth conditions and device structure are relatively unoptimized. From the quick test

measurement, internal quantum efficiency for the active region was estimated to be about 20%, which also agrees well with IQE estimates of the material from low temperature PL measurements. Further optimization of epitaxy and device structure, for example inclusion of an electron blocking layer (EBL), could also be expected to yield efficiency improvements.

Results for two LED heterostructures with 310 nm and 274 nm emission are shown in Fig. 3. The 310 nm device had a graded buffer with final composition Al$_{0.36}$Ga$_{0.64}$N, and an Al$_{0.25}$Ga$_{0.75}$N QW, while the 274 nm device was graded to Al$_{0.50}$Ga$_{0.50}$N and had an Al$_{0.40}$Ga$_{0.40}$N QW. Both structures had 150 nm of p− AlGaN and

a 10 nm p+ GaN contact layer above the QW. *Z-* contrast STEM (Fig. 3a) indicates that the active region of the 310 nm device had planar interfaces, and no cracking was observed in this hetero-structure with TEM or CL. Optical microscopy did indicate the presence of some cracks in the 274 nm LED sample, with spacing on the order of hundreds of microns. Photoluminescence spectra, as well as *I–V* curves for these two device heterostructures with indium n- and p-contacts are shown in Fig. 3(b). *I–V* for the 310 nm LED is linear with a sharp turn-on voltage of 4.8 V, just above the band gap of the quantum well material, at 20 mA. Turn on voltage is higher, 8.9 V at 20 mA, and *I–V* is less linear for the 274 nm LED. In addition, the PL intensity for the 274 nm LED is an order of magnitude lower than the peak PL intensity for the 310 nm LED. The PL peak at 285 nm in the spectrum for the 310 nm LED is attributed to luminescence from the $Al_{0.36}Ga_{0.64}N$ buffer layer. No buffer emission was observed for the 274 nm LED as it is likely lower or at the same wavelength as the 266 nm PL excitation laser. The drop in PL intensity with shorter wavelength is not unexpected as this follows the trend seen by many research groups as compiled by Kneissel et al [14]. However, since we know that the extended defect density for these devices was compara-tively low ($\sim 10^6/cm^2$), more work is required to elucidate the cause of the efficiency drop, which may be related to oxygen incorporation or the presence of other point defects generated at the relatively low MBE growth temperatures. The highest effi-ciency deep UV LEDs reported to date were grown by metal organic chemical vapor deposition at temperatures exceeding 1300 °C [15].

In summary, preliminary UV LEDs on commercially available $(20\bar{2}1)$ GaN substrates have been demonstrated by ammonia MBE. The LEDs with emission wavelengths longer than 300 nm showed excellent electrical characteristics, low extended defect densities and promising optical emission for relatively unoptimized growth conditions and device structures. In particu-lar, improvements to internal and external quantum efficiency could be realized by a number of modifications to device design including introduction of EBLs and use of multiple QW active regions as well as optimization of growth conditions for p-AlGaN and p-GaN contact layers. Substrate removal and a flip chip device process are under development to assess the material quality of ammonia-MBE AlGaN with improved extraction efficiency.

References

[1] M. Shatalov, et al., Semicond. Sci. Technol. 29 (2014) 084007.
[2] S.J. Hearne, et al., Appl. Phys. Lett. 76 (2000) 1534.
[3] E.C. Young, et al., Appl. Phys. Express 3 (2010) 111002.
[4] P.S. Hsu, et al., Appl. Phys. Lett. 103 (2013) 161117.
[5] D.A. Haeger, et al., Appl. Phys. Lett. 100 (2012) 161107.
[6] E.C. Young, et al., Appl. Phys. Lett. 101 (2012) 142109.
[7] M. Sawicka, et al., Appl. Phys. Lett. 102 (2013) 251101.
[8] J. Verma, et al., Appl. Phys. Lett. 104 (2014) p021105.
[9] S. Carnevale, et al., Nano Lett. 12 (2) (2012) 915–920.
[10] K.H. Li et al. International workshop on nitride semiconductors, Wroclaw, Poland, August, 2014.
[11] A. Bhattacharyya, et al., Appl. Phys. Lett. 94 (2009) 181907.
[12] C.O. Holder, et al., Appl. Phys. Express 5 (2012) 092104.
[13] C.A. Hurni, et al., Appl. Phys. Lett. 101 (2012) 102106.
[14] M. Kneissel, et al., Semicond. Sci. Technol. 26 (2011) 014036.
[15] M. Ippommatsu, et al. Development of AlGaN DUV-LED 10th Conference on Lasers and Electro-Optics Pacific Rim (CLEO-PR) Kyoto, Japan, July 2013.

CRYSTAL GROWTH
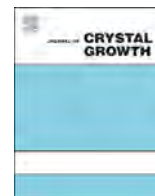
InGaN pn-junctions grown by PA-MBE: Material characterization and fabrication of nanocolumn electroluminescent devices

CrossMark

I. Gherasoiu [a,*], K.M. Yu [b,c], L. Reichertz [b], W. Walukiewicz [b]

[a] State University of New York Polytechnic Institute, Utica, NY, United States
[b] Material Sciences Division, Lawrence Berkeley National Laboratory, Berkeley, CA, United States
[c] Department of Physics and Materials Science, City University of Hong Kong, Kowloon, Hong Kong

ARTICLE INFO

ABSTRACT

PN junctions are basic building blocks of many electronic devices and their performance depends on the structural properties of the component layers and on the type and the amount of the doping impurities incorporated.

Magnesium is the common p-type dopant for nitride semiconductors while silicon and more recently germanium are the n-dopants of choice.

In this paper, therefore we analyze the quantitative limits for Mg and Ge incorporation on GaN and InGaN with high In content. We also discuss the challenges posed by the growth and characterization of InGaN pn-junctions and we discuss the properties of large area, long wavelength nanocolumn LEDs grown on silicon (1 1 1) by PA-MBE.

© 2015 Elsevier B.V. All rights reserved.

1. Introduction

Nitride semiconductors containing indium have a direct band gap spanning from 0.65 eV (InN) to 3.4 eV (GaN) [1]. This large range in the band gap of InGaN alloys could allow the fabrication of full-spectrum solar cells as well as long wavelength LEDs.

For device applications, controllable doping of InGaN is essential and requires the reduction of electron background due to native and/or crystalline defects, especially in alloys with high indium content. For this reason, the InGaN alloys have been subject of sustained work targeting the synthesis of layers with high crystalline quality and high indium fraction (> 30%) [2,3].

Even when high quality GaN substrates are available their usefulness for the growth of thick or high indium fraction ($x > 30$%) $In_xGa_{1−x}N$ layers is limited by the formation of misfit dislocations at the InGaN/GaN interface.

As a result, the operation of the nitride devices is typically hampered by the presence of threading dislocations originating at these interfaces. One approach suggested for the mitigation of the dislocation effects and for the control of the indium segregation in InGaN alloys is the growth of nano-structured devices [4–6].

In this work we report a detailed study on Mg and Ge doping of InGaN and describe the fabrication of large area green and yellow InGaN nanocolumn LEDs on Si (1 1 1) substrates. Finally we

discuss the mechanism responsible for the reduction of the electroluminescence intensity of these nanocolumn devices.

2. Materials and methods

The films were grown using 2 in. insulating GaN-on-sapphire templates and the growth of GaN and InGaN films was initiated by depositing 200 nm of nominally un-doped GaN, using a production-style plasma-assisted molecular beam epitaxy system (PA-MBE). The samples of GaN doped with magnesium were grown at 605° C. All InGaN films were grown at a substrate temperature of 545° C, except where indicate differently, using the same indium flux and have a thickness of 300 nm. Mg cell temperature was increased such that the equivalent beam pressure (BEP) at the sample surface ranged from $\sim 1 \times 10^{-9}$ Torr to 1.6×10^{-7} Torr. The light emitting diode structures have been grown on 4 in. p-type silicon (1 1 1) wafers. The typical structure is Si(1 1 1)/AlN/n-GaN/n-InGaN/p-InGaN/p-GaN and the estimated thickness of the Ga containing layers (n-GaN/NC-InGaN/p-GaN) is 300 nm/850 nm–1000 nm/160 nm. During the growth of the nanocolumns In and Ga fluxes were set for BEP 3×10^{-7} Torr, and 4×10^{-8} Torr respectively while the Nitrogen plasma had a total flow of 18 sccm with an approximate BEP of 1.4×10^{-4} Torr. The growth temperature for these samples, at the substrate surface, was between 515°C and 525°C.

The composition and the thickness of the films were evaluated by Rutherford backscattering spectrometry (RBS) and secondary ion mass spectrometry (SIMS), while crystallinity of the film was

* Corresponding author.
E-mail address: gherasi@sunyit.edu (I. Gherasoiu).

evaluated using the ion channeling. Electrical properties of the films were determined using Hall effect and electrochemical capacitance voltage (ECV) measurements . Finally, optical emission from photoluminescence (PL) and the electroluminescence (EL) were measured using an OceanOptics spectrometer.

3. Results and discussion

The properties of Mg doped GaN and InGaN films with indium fraction up to 40% have been investigated. Normalized ion channeling yield, χ has been used as a measure of the crystalline quality. The effect of magnesium incorporation on the structural quality of GaN films is presented in Fig. 1. The decrease of the channeling yield at surface, in comparison with the channeling yield at 500 nm, suggests the improvement of crystal structure with the progression of growth. The comparison also indicates that the differences in doping behavior that are seen in the mid region (p&n) of the graph in Fig. 1 are not caused by crystal defects whether buried or at surface.

Fig. 1 suggests that the crystalline perfection of the Mg doped GaN degrades as the Mg concentration in the film increases. Drastic degradation of the film crystallinity occurs at Mg concentrations of ~ 6–$7 \times 10^{20}/\text{cm}^3$. The plot also indicates that, for the experimental conditions described, hole conduction can be achieved and maintained up to a magnesium concentration of $\sim 2 \times 10^{20}/\text{cm}^3$. This is in agreement with our previous report [7] that the p-type conduction domain is followed by a sudden transition to n-type conduction ensued around a Mg concentration of $7 \times 10^{20}/\text{cm}^3$. The inclusion of new SIMS measurements in this data set suggests that between $2 \times 10^{20}/\text{cm}^3$ and ~ 6–$7 \times 10^{20}/\text{cm}^3$ the material conductivity, as measured by Hall method, can be dominated by either electrons or holes as can be seen in Fig. 1.

The crystlline quality of the n-type samples in this region, as suggested by the normalized ion channeling, appears to be similar to p-type samples that have incorporated less Mg and therefore does not seem to be the cause of the electron conduction. The evolution of GaN crystallinity for one of these samples is presented in Fig. 2.

At the interface with the insulating template, the film exhibits increased lattice disorder that is reflected in the relative larger ion channeling yield. As the growth advances the channeling yield decreases in a linear fashion and the trend does not change with the arrival of Mg at the growth surface. The mobility associated with hole carriers has been found to be correlated with the Mg
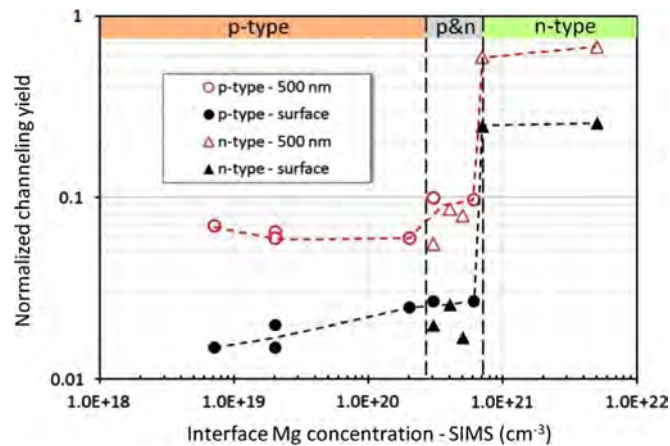
Fig. 2. Evolution of the GaN crystalline quality as expressed by the ion channeling yield during the film growth and magnesium doping. Mg concen-tration has been determined by SIMS.
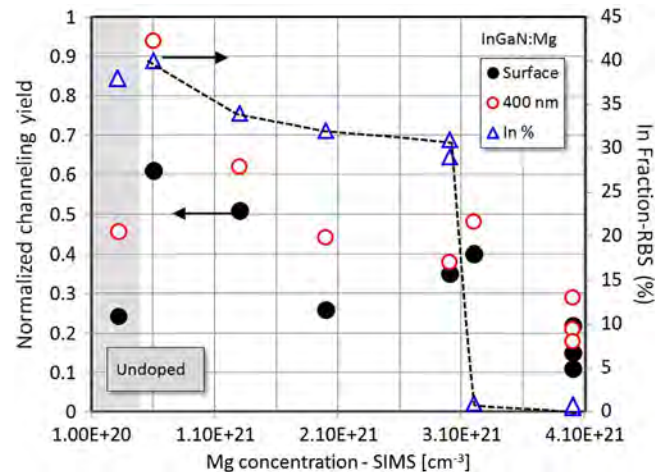
Fig. 3. Effect of magnesium incorporation on the $In_xGa_{1-x}N$ indium fraction and crystalline quality, as reflected by the ion channeling yield.

concentration. The hole mobility can be modeled, with a good correlation coefficient ($R^2 = 0.885$), by a power law of the impurity density with a negative scaling coefficient ($\alpha = -5.1$). The correlation between the hole mobility and the Mg concentration is an indication of the origin of the p-type conduction with Mg ionization. The measurements show that high hole mobility (10–12 $\text{cm}^2/\text{V s}$) is associated with the lower Mg concentration ($2 \times 10^{19}/\text{cm}^3$) while the hole mobility decreases ($\sim 2 \text{ cm}^2/\text{V s}$) with the increase of the magnesium concentration.

For the n-type samples, the electron mobility does not correlate well with the increase of the Mg concentration suggesting that extended defects originating in the Mg doping process rather than point defects are responsible for the generation of the conduction electrons. The large density of Mg in this growth regime could hamper the nitrogen incorporation leading to the formation of nitrogen vacancies (V_N) and the formation of Mg_{Ga}–V_N complexes [8,9]. The electron mobilities are in the range from 50 $\text{cm}^2/\text{V s}$ ($5 \times 10^{18}/\text{cm}^3$-Hall density) to 152 $\text{cm}^2/\text{V s}$ ($1 \times 10^{18}/\text{cm}^3$-Hall density) for Mg concentrations larger than $3 \times 10^{20}/\text{cm}^3$. InGaN films with indium fractions up to 40% as estimated by RBS have been grown and doped with Mg and Ge. Channeling yield has been used to evaluate the crystalline

Fig. 1. Effect of magnesium incorporation in GaN as expressed by the ion channeling yield. Mg concentration has been determined by SIMS. Low values of the channeling yield are associated whit a low density of structural defects while higher scattering rates result due lattice imperfections.

quality of the films, with and without Mg doping. The evolution of the yield with the increase of the Mg concentration is presented in Fig. 3.

The incorporation of indium determines the degradation of the InGaN film crystalline quality when compared with GaN, the ion channeling yield being about one order of magnitude larger in the case of InGaN films, whether measured at surface (0.2–0.26) or 400 nm below (0.37–0.46). The channeling yield therefore cannot be used to accurately represent the effect of Mg incorporation. In this case the magnesium incorporation limit has been determined based on the competition between In and Mg for the group III lattice site. This substitution is characterized by a threshold with respect to indium incorporation, as can be seen in Fig. 3.

The determination of the electrical characteristics of the InGaN films doped with Mg is challenging for a couple of reasons. On one hand, Mg-doped layers are typically grown on top of thin un-doped InGaN films that exhibit native n-type conductivity. The relatively large defect density of the InGaN films with high indium fraction (> 20%) ensures that the metal contacts used for the fabrication of the Hall samples have a high likelihood to contact both layers, p-type and n-type. This results in Hall measurements where the mobility and carrier concentration reflect predominantly the n-type layer, since the contacts with this material are usually ohmic.

On the other hand, for InGaN films with indium fraction larger than 35% the Fermi level becomes pinned above the conduction band edge and as a result electrons accumulate at the surface. The conductivity measurement of such films will reflect mostly the surface electron accumulation, obscuring to a large extent the properties of the carriers in the bulk.

Germanium has been used as n-type dopant for both GaN and InGaN layers. For these layers, we have determined the electron concentration and mobility using Hall measurements. For both GaN and InGaN we have found electrons concentrations in the range from 1×10^{18}/cm^3 to 7×10^{20}/cm^3. At low electron

concentration the mobility in the films reaches the maximum while with increasing carrier concentration, associated with increased Ge incorporation, the electron mobility saturates and converges for both films to values around 40 cm^2/V-s.

The goal of analyzing the doping characteristics of the GaN and InGaN layers was to allow the growth of p–n junction devices with optimized properties. The presence of dislocations leads to a decrease of the device performance, as represented by the external quantum efficiency (EQE). Another factor contributing to the low operation efficiency of the nitride devices is the charge polarization that leads to the quantum confined Stark effect (QCSE).

A possible solution attempting to overcome these detrimental properties concerns the growth of nanocolumn based devices. The nanocolumns growth can eliminate or reduce the density of misfit dislocations [4], and suppress the effect of the polarization field if the p-n junctions are fabricated along the radial direction that coincides with the direction of non-polar III-nitride planes.

In this context, the catalyst-free growth appears as an attractive alternative that allows the growth of high crystalline quality nitrides with no need for substrate patterning. In Fig. 4, the schematic of the structures grown is presented. The goal of the growth was three fold: (1) to nucleate and grow InGaN nanocolumns, (2) to form pn-junctions in InGaN by doping the upper side of the columns with Mg, and (3) to grow a continuous p-type GaN cap layer that could isolate the junction region from the device surface. The accurate evolution stage of the nanostructures cannot be evaluated in-situ. Therefore, to reach the goals of InGaN nanocolumn growth and of a continuous p-GaN cap-layer, a series of samples have been grown under identical growth conditions. For these samples the growth was stopped at essential stages, as indicated by RHEED and schematically represented in Fig. 4, to study the surface morphology. The surface of the samples has been imaged by SEM and the pictures obtained for each of these 3 stages are presented in Fig. 5.

Fabrication of nanocolumns using a catalyst-free approach resulted in an average surface density, regardless of the cross-sectional size column density of $\sim$23 μm^{-2} and the nanocolumns occupy approximately 76% of the growth plane surface. The estimated diameters of the nanocolumns range from $\sim$100 nm up to $\sim$300 nm. The majority (64%) of them have cross-sections that can be approximated by circles with diameters between 150 nm and 200 nm and if the diameters up to 300 nm are included the proportion of nanocolumns in this range reaches 90%.

The predominance of the diameters between 150 nm and 200 nm suggests that the lateral growth is limited and most of the material is deposited along the c-axis of the nanocolumn which is expected for the nitrogen-rich PA-MBE growth. This observation is in agreement with the model proposed by Foxon et al. [10]. For the case of our structures another mechanism is obvious. As the diameter of the nanocolumns increases, the space available between the columns decreases to the point where the arrival of the precursors is impeded by a shadowing effect.
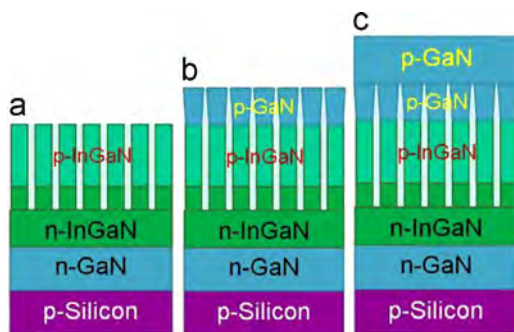
Fig. 4. Schematic of the main growth steps of the nanocolumn LED. (a) Nucleation and development of the InGaN nanocolumns, (b) start of the nanocolumn coalescence, (c) fully coalesced GaN:Mg cap layer.
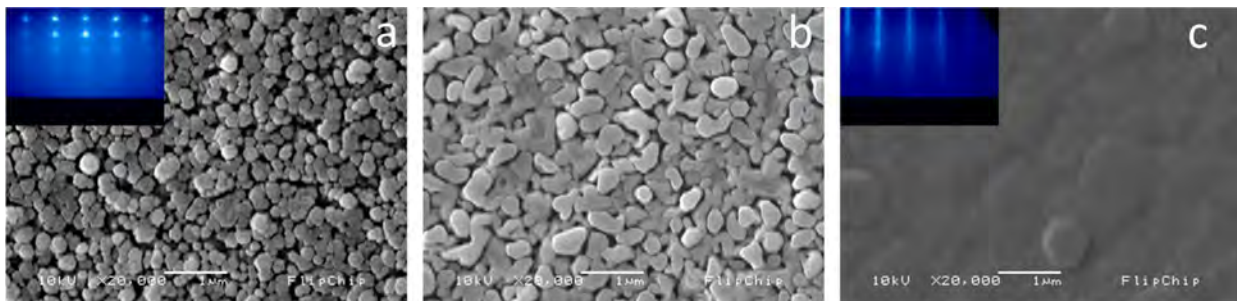
Fig. 5. In$_x$Ga$_{1-x}$N nanocolumn: scanning electron microscope (SEM) top view of the nanocolumns during the growth of the device. (a) InGaN:Mg nanocoulumns, (b) start of the GaN:Mg nanocolumn coalescence, (c) fully coalesced GaN:Mg cap layer.
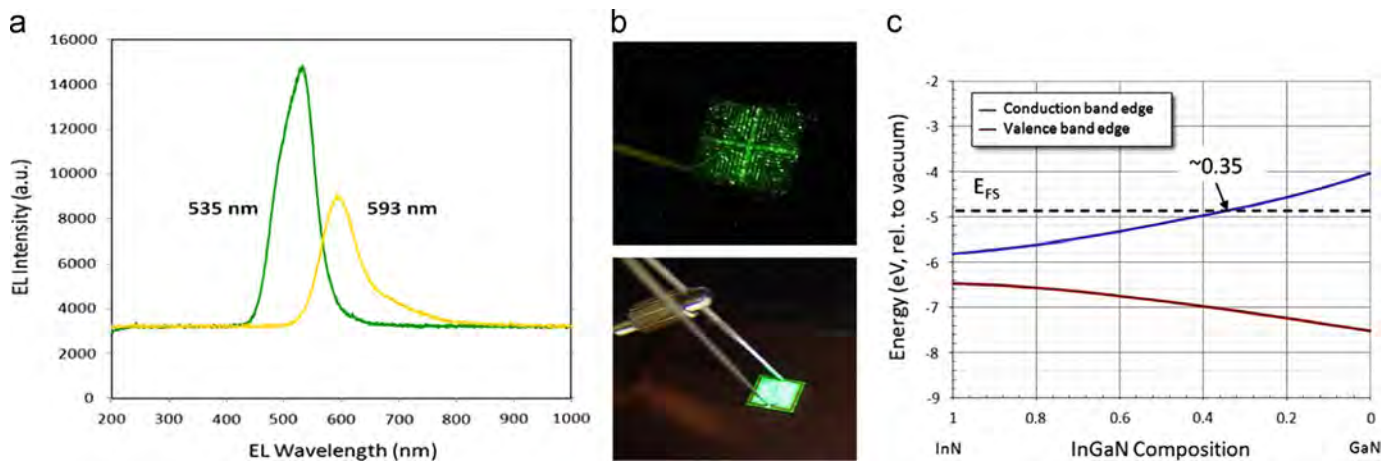
Fig. 6. In$_x$Ga$_{1-x}$N nanocolumn LEDs: (a) electroluminescence at room temperature, (b) low current and high current optical view of a 5 × 5 mm LED, (c) energy with respect to vacuum of the conduction and valence band edges, as a function of In$_x$Ga$_{1-x}$N composition.

Two different samples have been used to measure the electroluminescence. The EL intensity for the two structures is presented in Fig. 6(a). In Fig. 6(b) the emission of large area (5 × 5) mm, green LED is presented at low and high current. At low current the columnar emitters are visible (top).

Although the current injection characteristics were the same for the two structures, it is noticeable that the intensity of the yellow LED is reduced by almost 40% when compared to the intensity of the green LED. The decrease of the emission intensity has been known to occur in correlation with the increase of the indium fraction in the quantum wells of the GaN/InGaN LEDs [11].

While most of the work has been focused toward the mitigation of the carrier separation in the quantum wells (QCSE), the reduction of the polarization through the use of non-polar substrates has not provided the desired advance. More recently, the use of strain compensation techniques have allowed the achievement of larger than 1 W light power output [12]. However, the external quantum efficiency for these structures has remained below 3% demonstrating the conversion process inefficiency.

It has been demonstrated that the density of the threading dislocations is a factor in the degradation of the light emission efficiency in GaN [13]. The resilience of the III-nitrides to the presence of dislocations with densities in the range from 10^8 cm^{-2} to 10^{10} cm^{-2} is due in large part to the potential barriers separating the surface of these dislocations from the bulk of the semiconductor volume, either n-doped or p-doped. Excited carriers can overcome the barriers ($E_e = 0.55$ eV, $E_h = 0.9$ eV) under light excitation and this behavior has been manifested and studied as photoconductivity. The presence of external bias and injection charges at the surface of the dislocations can also alter the band bending and the width of the barrier. However, the strongest effect on the barrier height is associated with the increase of indium fraction in InGaN, as can be seen from Fig. 6(c). In n-type GaN the conduction band edge is pinned above the Fermi stabilization level (E_{FS}) and a thin region at the surface is depleted from electrons [14]. The increase of the indium fraction reduces gradually the barrier height such as at ~35% indium fraction the relative energy of the conduction band coincides with the Fermi stabilization level and the flat band condition is reached. For InGaN with indium fractions larger than 35% the conduction band edge is pinned below the Fermi level (E_{FS}), allowing electrons to accumulate at the material surface. We speculate that this gradual reduction of the potential barrier at the InGaN surface is responsible for the increase of the leakage currents in InGaN p–n junctions and is the mechanism that governs the gradual reduction in the external quantum efficiency of the light emitting diodes (LEDs) with the increase of the indium fraction in the active region. This phenomenon is also known as the "Green Gap". The emission wavelength corresponding to 35% indium fraction is ~583 nm, located in the yellow band of the visible spectrum.

4. Concluding remarks

The quantitative limits of Mg and Ge doping of GaN and InGaN have been explored and the effect of impurity incorporation has been evaluated with respect to the impact on material crystalline quality, carrier mobility and carrier density. For the case of InGaN, the competition between In and Mg determines the upper limit for p-type doping. We have found that for Mg fluxes larger than 1×10^{-7} Torr (BEP) corresponding to Mg volume density of more than 3×10^{21} cm^{-3} indium incorporation has been largely prevented.

InGaN nanocolumn p–n junctions were grown on silicon (1 1 1) using a buffer layer of n-AlN/n-GaN and p-GaN as cap layer. The p–n junction were located in the InGaN column volume. The coalescence of the p-GaN layer has been successfully employed for the separation of the metal deposition from the p–n junction region. The electroluminescence of these structures has been measured with wavelengths of 535 nm (green) and 593 nm (yellow). The intensity of the yellow LED has shown a decrease of almost 40% when compared with that of the green LED.

We propose that the EQE decrease associated with the increase of the In fraction in the active region of LEDs, known as the "Green Gap", is determined by the decrease of the energy barrier separating the surface of threading dislocations from the volume of the semiconductor structure. Our assertion is based on indirect evidence obtained performing photovoltaic experiments and on the calculated position of the band gap edges with respect to Fermi stabilization energy.

References

[1] J. Wu, W. Walukiewicz, K.M. Yu, W. Shan, J.W. Ager III, E.E. Haller, H. Lu, W. J. Schaff, W.K. Metzger, S. Kurtz, J. Appl. Phys. 94 (2003) 6477.
[2] I. Gherasoiu, L.A. Reichertz, K.M. Yu, J.W. Ager III, V.M. Kao, W. Walukiewicz, Phys. Status Solidi C 8 (7–8) (2011) 2466–2468.
[3] I. Gherasoiu, K.M. Yu, L.A. Reichertz, V.M. Kao, M. Hawkridge, J.W. Ager III, W. Walukiewicz, Phys. Status Solidi B 247 (7) (2010) 1747–1749.
[4] S. Li, A. Waag, J. Appl. Phys. 111 (2012) 071101.
[5] L.-Y. Chen, Y.-Y. Huang, C.-S. Chang, J.J. Huang, in: Proceedings of the CS MANTECH Conference, Portland, Oregon, USA, May 17th-20th, 2010.
[6] A. Kikuchi, M. Tada, K. Miwa, K. Kishino, in: Proceedings of SPIE, Vol. 6129, 2006, 612905.
[7] I. Gherasoiu, K.M. Yu, L.A. Reichertz, W. Walukiewicz, Phys. Status Solidi C 11 (3–4) (2014) 381–384.
[8] M.A. Reshchikov, D.O. Demchenko, J.D. McNamara, S. Fernandez-Garrido, R. Calarco, Phys. Rev. B 90 (2014) 035207.
[9] M.A. Reshchikova, H. Morkoç, J. Appl. Phys. 97 (2005) 061301.
[10] C.T. Foxon, S.V. Novikov, J.L. Hall, R.P. Campion, D. Cherns, I. Griffiths, S. Khongphetsak, J. Cryst. Growth 311 (2009) 3423.
[11] C. Wetzel, M. Zhu, Y. Li, W. Hou, L. Zhao, W. Zhao, S. You, C. Stark, Y. Xia, M. DiBiccari, T. Detchprohm, in: Proceedings of the SPIE 7422, Ninth International Conference on Solid State Lighting, August 18, 2009. http://dx.doi.org/10.1117/12.829513, 742204.
[12] Shinji Saito, Rei Hashimoto, Jongil Hwang, Shinya Nunoue, Applied Physics Express 6 (11) (2013) 111004.
[13] Sergey Yu. Karpov, Yuri N. Makarov, Appl. Phys. Lett. 81 (23) (2002) 4721–4723.
[14] S.X. Li, K.M. Yu, J. Wu, R.E. Jones, W. Walukiewicz, J.W. Ager III, W. Shan, E. E. Haller, Hai Lu, William J. Schaff, Phys. Rev. B 71 (R) (2005) 161201.

CrossMark
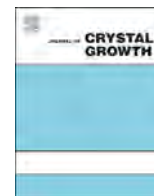
High power nitride laser diodes grown by plasma assisted molecular beam epitaxy

G. Muziol [a,*], M. Siekacz [a,b], H. Turski [a], P. Wolny [a], S. Grzanka [a,b], E. Grzanka [a,b],
A. Feduniewicz-Żmuda [a], J. Borysiuk [c,d], K. Sobczak [c], J. Domagała [c],
A. Nowakowska-Siwińska [b], I. Makarowa [b], P. Perlin [a,b], C. Skierbiszewski [a,b]

[a] Institute of High Pressure Physics, Sokolowska 29/37, 01-142 Warsaw, Poland
[b] TopGaN Ltd, ul Sokołowska 29/37, 01-142 Warsaw, Poland
[c] Institute of Physics, Polish Academy of Sciences, Al. Lotników 32/46, 02-668 Warsaw, Poland
[d] Faculty of Physics, University of Warsaw, Pasteura 5, 02-093 Warsaw, Poland

ARTICLE INFO

ABSTRACT

The influence of waveguide design on performance of nitride based laser diodes (LDs) grown by plasma assisted molecular beam epitaxy is studied. A large improvement in threshold current density and slope efficiency of LDs is observed when an InGaN interlayer with 8% In content is introduced between multi-quantum-well region and electron blocking layer. This dependence is attributed to reduction of internal losses due to lower optical mode overlap with highly absorptive Mg-doped layers. This led to demonstration of blue LD operating at $\lambda = 450$ nm with high optical power of 500 mW per facet.

© 2015 Elsevier B.V. All rights reserved.

1. Introduction

In the past two decades nitride optoelectronic devices had been developed to commercial standards and became widely available. The epitaxial structures of all of the commercial light emitting diodes and laser diodes (LDs) are grown by Metal Organic Vapor Phase Epitaxy (MOVPE) [1]. However, the recent progress in understanding the new growth mechanism for nitrides in Plasma Assisted Molecular Beam Epitaxy (PAMBE) [2–4] together with a remarkable control of growth parameters has renewed interest in MBE technology as a possible alternative in some applications [5]. The main difference in growth of III–N compounds between PAMBE and MOVPE is the growth temperature which in case of PAMBE is 200–300 °C lower than in MOVPE.

Optimization process of epitaxial design of LD requires comprehension of factors such as strain distribution, voltage drop, carrier injection, optical confinement and optical losses just to name a few. In this paper we will focus on optical losses generated by epitaxial layers. In the past decade many researchers focused on this problem and found Mg-doped layers to be responsible for generation of the optical losses [6]. As a solution to this problem it had been proposed by Uchida et. al [7] to insert an undoped AlGaN interlayer between multi-quantum-well (MQW) region and Mg-doped layers to reduce

the optical mode overlap with highly absorptive layers and thus reduce the internal losses.

Low temperature PAMBE proved to be technology of choice for growth of high quality InGaN layers. Application of InGaN layers as waveguides in LDs opens up new design possibilities for more efficient LDs [8].

In this paper we investigate properties of LDs with InGaN waveguide grown by PAMBE. We focus on the influence of $In_{0.08}Ga_{0.92}N$ interlayer between MQW region and electron blocking layer (EBL) on threshold current density and slope efficiency of blue ($\lambda = 450$ nm) LDs.

2. Experimental

The growth of LD structures presented in this work was performed in a customized VG V90 MBE reactor equipped with two Veeco RF plasma sources, operating at 240–450 W power for 0.8–2 sccm of N_2 flow. All of the LDs were grown on bulk Ammono–GaN substrates with threading dislocation density (TDD) in the order of 10^4 cm^{-2}, grown by an ammono-thermal method [9]. The epi-ready substrates were prepared by mechanical polishing and mechano-chemical polishing. The crystals had miscut 0.5 degree towards [1–100] direction. The growth of GaN and AlGaN cladding layers were performed at 720 °C under gallium-rich, while InGaN layers were grown at 650 °C under indium-rich conditions. Growth of AlGaN in EBL was performed at 650 °C with indium as a surfactant.
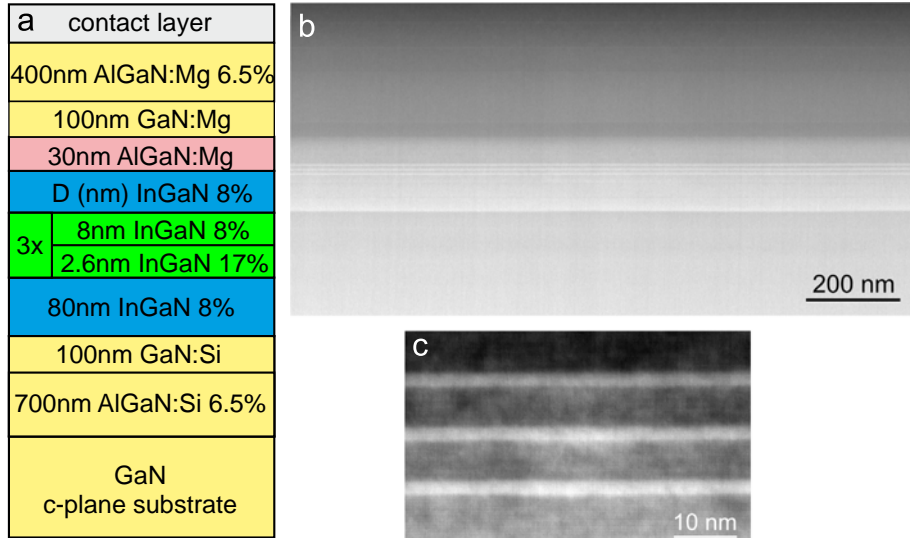
Fig. 1. (a) Schematics of LD structure (b) large area HAADF–STEM cross-section image showing no extended defects (c) HAADF–STEM image of MQW region.
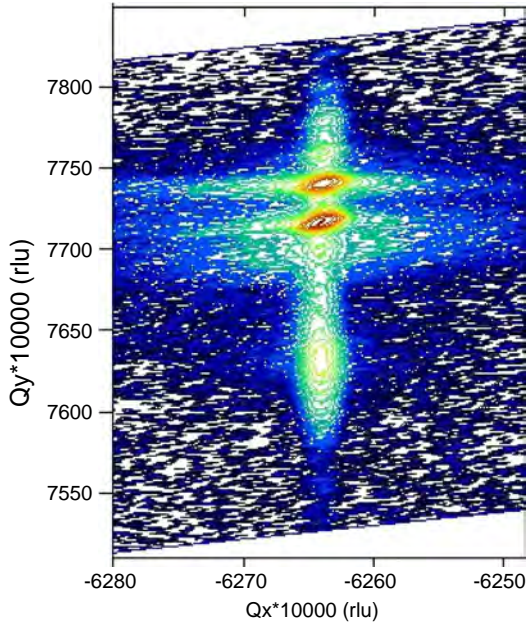
Fig. 2. Reciprocal space map of asymmetric ($\overline{1}1\overline{1}4$) reflection of full LD structure with thick InGaN waveguides showing no relaxation.

Growth rate for all layers apart from MQW was equal to supplied nitrogen flux of 0.35 μm/h. The MQWs were grown using 1 μm/h of N flux. The nitrogen flux was calibrated during GaN growth under Ga rich conditions. Details of the InGaN growth mechanism in PAMBE can be found in Ref. [4,10].

3. Laser diode structure

Fig. 1(a) presents schematics of the LD design. The laser structures consist of a 700 nm $Al_{0.065}Ga_{0.935}N$:Si cladding layer, a 100 nm GaN: Si, a 80 nm undoped $In_{0.08}Ga_{0.92}N$ waveguide, an active region composed of three 2.6 nm $In_{0.17}Ga_{0.83}N$ QWs separated by 8 nm $In_{0.08}Ga_{0.92}N$ quantum barriers. Then the $In_{0.08}Ga_{0.92}N$ interlayer is grown with thickness changed from 5 to 60 nm. The EBL is composed of AlGaN with a Mg doping level of 3×10^{19} cm^{-3}. This is followed by

a 500 nm GaN:Mg cladding layer or 100 nm GaN:Mg and 400 nm $Al_{0.065}Ga_{0.935}N$:Mg to further enhance optical confinement. The LD structure is capped with 60 nm $In_{0.01}Ga_{0.99}N$:Mg acting as a contact layer.

Fig. 1(b) shows a large area high-angle annular dark field scanning transmission electron microscopy (HAADF–STEM) image of LD with the thickest InGaN interlayer $D = 60$ nm taken in a TITAN CUBED 80–300 system operating at 300 kV equipped with Cs-corrector. Cross-sectional STEM specimens were prepared by a standard method, based on mechanically prethinning of the samples followed by an Ar ion milling procedure. In this LD the total thickness of $In_{0.08}Ga_{0.92}N$ was 160 nm and we did not observe creation of any extended defects after growth of such thick InGaN layers. Fig. 1(c) shows magnification of the MQW region. Furthermore, we investigated the whole LD structure using X-ray reciprocal space mapping. We used an Philips X'Pert MRD X-ray diffractometer equipped with a fourfold Ge (220) monochromator, a threefold Ge (220) analyzer, and an X-ray mirror. Fig. 2 presents the reciprocal space map of asymmetric ($\overline{1}1\overline{1}4$) reflection of LD with the thickest $In_{0.08}Ga_{0.92}N$ interlayer $D = 60$ nm. As can be seen from Fig. 2 the there is no relaxation and the InGaN waveguide is fully strained to GaN substrate.

The LDs are processed as ridge waveguide lasers with mesa etched to a depth of 470 nm. Mirrors of the resonator were cleaved and facets were left uncoated.

4. Influence of waveguide design on lasing threshold

Fig. 3(a) presents threshold current density of LDs as a function of $In_{0.08}Ga_{0.92}N$ interlayer thickness D. We observed a dramatic reduction of threshold current density which we attribute to a decrease of internal optical losses due to a smaller optical mode overlap with Mg-doped layers. This is also confirmed by slope efficiency measurement. The slope efficiency is related to internal losses through the following equation [11]:

$$\frac{dP}{dI} = \eta_i \left(\frac{\alpha_m}{\alpha_m + \alpha_{int}} \right) \frac{h\nu}{q} \tag{1}$$

where η_i is the injection efficiency, α_{int} are internal losses, $\alpha_m = (1/2L)\ln(R_1 R_2)$ are mirror losses, where L is the resonator length and R_1 and R_2 are reflectivities of front and rear mirrors. Fig. 3(b) shows a significant increase of slope efficiency with the thickness of the InGaN interlayer. According to Eq. (1) this may be
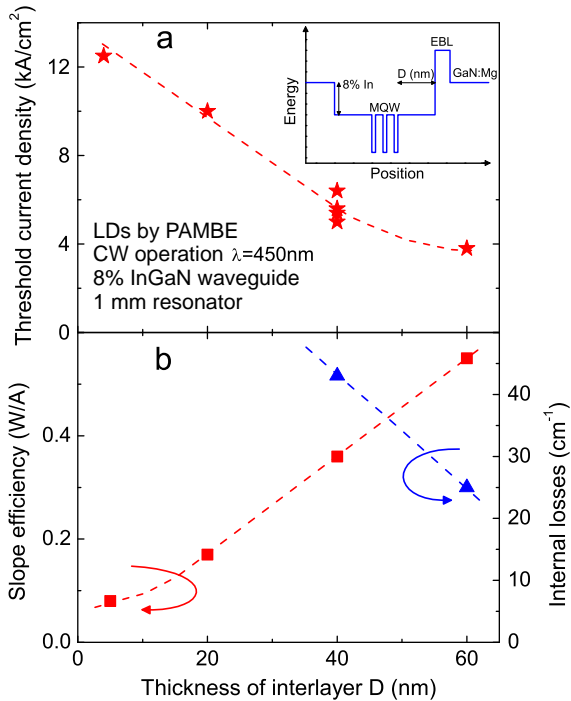
Fig. 3. (a) Threshold current density of LDs as a function of InGaN interlayer thickness between MQW and Mg-doped region. Inset shows a simplified conduction band profile with placement of the interlayer marked as D. (b) Dependance of slope efficiency and internal losses on thickness of InGaN interlayer.
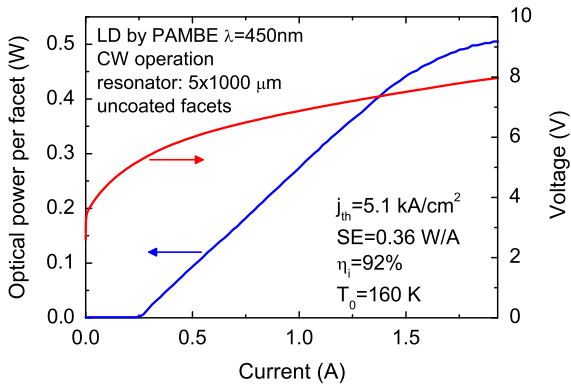
Fig. 4. Light-current–voltage characteristics of high power LD grown by PAMBE.

due to a change in η_i or α_{int} since all of the LDs had the same $\alpha_m = 17$ cm^{-1}. It is highly unlikely that injection efficiency increases for LDs with larger distance between MQW and EBL but to validate that the change in slope efficiency is caused solely by α_{int} we have measured internal losses of these devices using the Hakki-Paoli technique [12]. Fig. 3(b) presents the α_{int} data which confirms the decrease of optical losses for LDs with increased thickness of InGaN interlayer.

5. High power LD by PAMBE

The decrease of internal losses has led to a significant improvement in parameters of LDs grown by PAMBE. Fig. 4 shows light-current–voltage characteristics of a high power LD with In$_{0.08}$Ga$_{0.92}$N waveguide. The thickness of interlayer between MQW and EBL in this LD is 40 nm. It is important to stress that the facets of this LD are without coating so the optical power is emitted equivalently in both directions. The maximum observed optical power was 500 mW per facet.

6. Summary

In this work we investigated the influence of waveguide design on performance of blue LDs grown by PAMBE. In particular we showed that inserting an InGaN interlayer between MQW region and EBL with high In content of 8% significantly reduces the threshold current density and increases slope efficiency. Interlayer with thickness up to 60 nm had been successfully grown and showed no relaxation of laser structure. This had led to demonstration of high power blue LDs with 500 mW of optical power per facet.

References

[1] S. Nakamura, et al., The Blue Laser Diode: The Complete Story, 2nd ed., Springer, New York, 2000.
[2] J. Neugebauer, T.K. Zywietz, M. Scheffler, J.E. Northrup, H. Chen, R.M. Feenstra, Phys. Rev. Lett. 90 (2003) 056101.
[3] C. Skierbiszewski, M. Siekacz, H. Turski, G. Muziol, M. Sawicka, P. Wolny, G. Cywiński, L. Marona, P. Perlin, P. Wiśniewski, M. Albrecht, Z.R. Wasilewski, S. Porowski, Appl. Phys. Express 5 (2012) 112103.
[4] C. Skierbiszewski, H. Turski, G. Muziol, M. Siekacz, M. Sawicka, G. Cywiński, Z.R. Wasilewski, S. Porowski, J. Phys. D: Appl. Phys. 47 (2014) 073001.
[5] C. Skierbiszewski, M. Siekacz, H. Turski, G. Muziol, M. Sawicka, A. Feduniewicz-Żmuda, G. Cywiński, C. Cheze, S. Grzanka, P. Perlin, P. Wiśniewski, Z.R. Wasilewski, S. Porowski, Appl. Phys. Express 5 (2012) 022104.
[6] M. Kuramoto, C. Sasaoka, N. Futagawa, M. Nido, A.A. Yamaguchi, Phys. Status Solidi A 192 (2) (2002) 329–334.
[7] S. Uchida, M. Takeya, S. Ikeda, T. Mizuno, T. Fujimoto, O. Matsumoto, T. Tojyo, M. Ikeda, J. IEEE Sel. Top. Quantum Electron. 9 (5) (2003) 1252–1259.
[8] C. Skierbiszewski, M. Siekacz, H. Turski, G. Muziol, M. Sawicka, A. Feduniewicz-Zmuda, J. Smalc-Koziorowska, P. Perlin, S. Grzanka, Z.R. Wasilewski, R. Kucharski, S. Porowski, J. Vac. Sci. Technol. B 30 (2012) 02B102.
[9] R. Dwiliński, R. Doradziński, J. Garczyński, L. Sierzputowski, A. Puchalski, Y. Kanbara, K. Yagi, H. Minakuchi, H. Hayashi, J. Cryst. Growth 310 (2008) 3911–3916.
[10] H. Turski, M. Siekacz, Z.R. Wasilewski, M. Sawicka, S. Porowski, C. Skierbiszewski, J. Cryst. Growth 367 (2013) 115.
[11] L.A. Coldren, S.W. Corzine, Diode Lasers and Photonic Integrated Circuits, 1st ed., Wiley, New York, 1995.
[12] B.W. Hakki, T.L. Paoli, J. Appl. Phys. 44 (1973) 4113.